NOTE TO USERS

This reproduction is the best copy available.

UMI®

Université d'Ottawa • University of Ottawa

PERMISSION DE REPRODUIRE ET DE DISTRIBUER LA THÈSE

PERMISSION TO REPRODUCE AND DISTRIBUTE THE THESIS

NOM DE L'AUTEUR / NAME OF AUTHOR:	Patrick Mercier
ADRESSE POSTALE / MAILING ADDRESS:	A-6 de la Cime Gatineau, Quebec J8Z 3N8
GRADE / DEGREE:	**ANNÉE D'OBTENTION / YEAR GRANTED**
Ph.D - Physics	2003
TITRE DE LA THÈSE / TITLE OF THESIS:	
Crystal Chemistry of Natural and Synthetic Trioctahedral Micas: Exploring the Limits of Geometric Crystal Chemical Models	

L'auteur permet, par la présente, la consultation et le prêt de cette thèse en conformité avec les règlements établis par le bibliothécaire en chef de l'Université d'Ottawa. L'auteur autorise aussi l'Université d'Ottawa, ses successeurs et cessionnaires, à reproduire cet exemplaire par photograhie ou photocopie pour fins de prêt ou de vente au prix coûtant aux bibliothèques ou aux chercheurs qui en feront la demande.

Les droits de publication par tout autre moyen et pour vente au public demeureront la propriété de l'auteur de la thèse sous réserve des règlements de l'Université d'Ottawa en matière de publication de thèses.

The author hereby permits the consultation and the lending of this thesis pursuant to the regulations established by the Chief Librarian of the University of Ottawa. The author also authorizes the University of Ottawa, its successors and assignees, to make reproductions of this copy by photographic means or by photocopying and to lend or sell such reproductions at cost to libraries and to scholars requesting them.

The right to publish the thesis by other means and to sell it to the public is reserved to the author, subject to the regulations of the University of Ottawa governing the publication of theses.

N.B. LE MASCULIN COMPREND ÉGALEMENT LE FÉMININ

22-SEP-2003

DATE

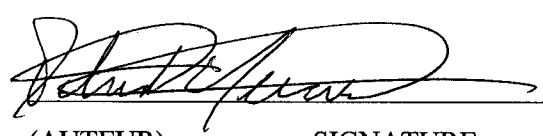

(AUTEUR) SIGNATURE (AUTHOR)

Université d'Ottawa · University of Ottawa

Université d'Ottawa · University of Ottawa

FACULTÉ DES ÉTUDES SUPÉRIEURES ET POSTDOCTORALES

FACULTY OF GRADUATE AND POSTDOCTORAL STUDIES

MERCIER, Patrick

AUTEUR DE LA THÈSE - AUTHOR OF THESIS

Ph. D. (Physics)

GRADE - DEGREE

Department of Physics

FACULTÉ, ÉCOLE, DÉPARTEMENT - FACULTY, SCHOOL, DEPARTMENT

TITRE DE LA THÈSE - TITLE OF THE THESIS

Crystal Chemistry of Natural and Synthetic Trioctahedral Micas: Exploring the limits of Geometric Chemical Models

D. Rancourt

DIRECTEUR DE LA THÈSE - THESIS SUPERVISOR

EXAMINATEURS DE LA THÈSE - THESIS EXAMINERS

J. Armitage

S. Desgreniers

A. Lalonde

M. Nespolo

J.-M. De Koninck, Ph.D.

LE DOYEN DE LA FACULTÉ DES ÉTUDES SUPÉRIEURES ET POSTDOCTORALES

SIGNATURE

DEAN OF THE FACULTY OF GRADUATE AND POSTDOCTORAL STUDIE

CRYSTAL CHEMISTRY OF NATURAL AND SYNTHETIC TRIOCTAHEDRAL MICAS: EXPLORING THE LIMITS OF GEOMETRIC CRYSTAL CHEMICAL MODELS

By

Patrick H.J. Mercier

A thesis submitted to the
Faculty of Graduate and Postdoctoral Studies
in partial fulfilment of the requirements
for the degree of Doctor of Philosophy

Department of Physics

University of Ottawa
Ottawa, Ontario
22 September 2003

© Patrick H.J. Mercier, Ottawa, Canada, 2003

National Library of Canada
Acquisitions and Bibliographic Services
395 Wellington Street
Ottawa ON K1A 0N4
Canada

Bibliothèque nationale du Canada
Acquisitions et services bibliographiques
395, rue Wellington
Ottawa ON K1A 0N4
Canada

Your file Votre référence

Our file Notre référence

The author has granted a non-exclusive licence allowing the National Library of Canada to reproduce, loan, distribute or sell copies of this thesis in microform, paper or electronic formats.

L'auteur a accordé une licence non exclusive permettant à la Bibliothèque nationale du Canada de reproduire, prêter, distribuer ou vendre des copies de cette thèse sous la forme de microfiche/film, de reproduction sur papier ou sur format électronique.

The author retains ownership of the copyright in this thesis. Neither the thesis nor substantial extracts from it may be printed or otherwise reproduced without the author's permission.

L'auteur conserve la propriété du droit d'auteur qui protège cette thèse. Ni la thèse ni des extraits substantiels de celle-ci ne doivent être imprimés ou autrement reproduits sans son autorisation.

0-612-85378-0

Canada

Abstract

Seventy-five synthetic powder trioctahedral mica samples (between Mg, Co, Ni, and Fe end members, with different degrees of oxidation, vacancy and Al/Si contents, and including an OH/F substitution series) were studied by room-temperature powder X-ray diffraction. The iron-bearing samples were studied by ^{57}Fe Mössbauer spectroscopy. Subsets of the samples were also characterized by scanning electron microscopy combined with energy dispersive spectroscopy, optical microscopy, X-ray fluorescence spectroscopy, and gas chromatography. Lattice parameters (refined under the 1*M* stacking polytype, space group *C*2/*m*) were determined for all powder samples and iron site populations ($^{[4]}Fe^{3+}$, $^{[6]}Fe^{3+}$, and $^{[6]}Fe^{2+}$) were obtained from Mössbauer spectroscopy.

The geometry of coordination polyhedrons from 170 published single crystal structure refinements of trioctahedral-1*M* mica structures (128 natural, 42 synthetic, space group *C*2/*m*) was analysed in detail. Sixty-five published structural refinements corresponding to other stacking polytypes and space groups ($2M_1$, *C*2/*c* = 46; $2M_2$, *C*2/*c* = 4; 2*O* : *Pnmn* = 2, *Ccmm* = 1; 3*T*, $P3_112$ = 12) were used together with the 170 trioctahedral-1*M* single-crystal refinements and the 75 synthetic powder results to establish the validity of the $b = \sqrt{3}a$ relationship. The latter relation is not imposed by any space-group symmetry, except for stacking polytype 3*T*, and it would follow from octahedral cations that are arranged in an ideal hexagonal pattern.

Fractional atomic coordinates were derived in terms of the atomic positions in a 1*M* unit cell of C2/*m* space-group type for each known homogenous mica polytype. These coordinates ensure that all TOT layers in each stacking polytype structure are the same 1*M*-type TOT layer, and were used via simulated powder diffraction intensities to determine polytypic contents in our synthetic powder samples.

A hierarchical sequence of geometrical models was developed, starting from the usual distortions (octahedral flattening and counter-rotation, tetrahedral rotation) towards additional features as they are shown to be required (geometric meso-octahedral sheet, tetrahedral elongation via apical bond adjustment, tetrahedral basal flattening). A complete geometric crystal chemical model for the unit cell of a geometric homo-octahedral 1*M* structure was developed in terms of a minimal number of empirical parameters (octahedral, tetrahedral, and interlayer bond lengths, flattening angles of octahedral and tetrahedral sheets, and tetrahedral rotation angle).

We examined the extent to which the lattice parameter variations of synthetic powder samples with known chemical compositions, oxidation states, and site populations can be

understood in terms of our geometric crystal chemical models, in comparison with the 128 natural and 42 synthetic 1*M* single-crystals. A key difficulty in testing the models on synthetic powders was to establish appropriate characteristic cation-specific bond lengths, which are shown to vary systematically from bond distances obtained using Shannon's radii.

The relation $(c/a)\cos\beta^* = 1/3$ was found to hold exactly (within experimental error) for all synthetic powders whereas it does not hold in general for synthetic and natural 1*M* single-crystals. The above relation is predicted to hold for geometric homo-octahedral sheets (having equal *M*1 and *M*2 site bond lengths) and not to hold for geometric meso-octahedral sheets (having unequal *M*1 and *M*2 site bond lengths). The counter-rotation of the *M*2 site of 1*M* single-crystals exactly (within experimental error) follows the geometric meso-octahedral sheet model, which, assuming a uniform octahedral sheet height and site-specific *M*1 and *M*2 bond lengths, predicts site-specific flattening angles and a counter-rotation angle for the *M*2 site which is uniquely determined by the bond length difference between the *M*1 and *M*2 sites. A geometric meso-octahedral 2:1 layer silicate was shown to require corrugated tetrahedral sheets composed of bond-distorted tetrahedra. Key geometric meso-octahedral distortions in 1*M* single-crystals were identified and elucidated: i) intra-layer top-bottom displacements within a TOT layer; and ii) a tetrahedral bending angle between the apical bond and the pyramidal base formed by the three basal bonds. Plots of lattice parameter *b* versus average-octahedral-bond-length allowed the following distinction to be made: Unoxidized divalent synthetic solid solution series tend to evolve along constant flattening-angle lines whereas trivalent octahedral cation and vacancy bearing natural single-crystals and synthetic powders follow trends with varying flattening angles. We found that the bond length of a given interlayer cationic species monotonously increases as the tetrahedral rotation angle α decreases in trioctahedral-1*M* single-crystals. An upper limit of tetrahedral rotation of $\alpha = 9.5^\circ$ was demonstrated to occur in trioctahedral-1*M* K-rich micas having an $<AlSi_3>$ sheet, for both synthetic powders and natural single-crystals.

Other attempts at applying geometric crystal chemical models and at identifying structuro-chemical relationships from structural refinement data will benefit from the perspective of our more complete and systematic approach based on pursuing simple geometrical models using 'regular' coordination polyhedrons and characteristic cation-specific bond lengths up to the limit beyond which such models are shown to necessarily breakdown because of unavoidable 'non-regular' polyhedral distortions.

Statement of Originality

This thesis was done under the supervision of Dr. Denis G. Rancourt from the Department of Physics of the University of Ottawa, and further advice was provided by Dr. André E. Lalonde from the Department of Earth Sciences. The following describes the extent of my personal involvement in the various parts of the thesis.

Experimental methods and sample characterization (Chapters 2 and 3)

Samples were synthesized by: Dr. Jean-Louis Robert at the CNRS-Orléans, France; Dr. Rob G. Berman at the Geological Survey of Canada, Ottawa, Canada; and Dr. Guenther Redhammer at the University of Salzburg, Austria. Acquisition of samples was made by my supervisor. Corresponding details of sample synthesis and pre-measurement heat treatment are given in Section 3.2.

I performed all the tasks associated to the detailed powder X-ray diffraction analysis of seventy-five (75) synthetic powder trioctahedral mica samples reported in this thesis: sample preparation and data analysis (Section 2.1), collection of diffractograms for each sample (Appendix A), identification of impurity peaks in the diffractograms (summary in Section 3.3; details in Appendices F to N), determination of stacking polytype contents (Chapter 4 and Section 5.2), and lattice parameter refinements (including error analysis; Section 5.1) .

Accurate ferric and ferrous iron site populations (within ~0.2 % of total Fe) of the fifty-three (53) iron-bearing samples were determined from Mössbauer spectroscopy (Section 2.2) using recent data treatment and spectral analysis methods and software developed in Dr. D.G. Rancourt's laboratory, that includes (Section 2.2): i) analytic methods for removing the spectral distortions associated to the effects of absorber thickness; and ii) a powerful Voigt-based fitting method that allows arbitrary-shape quadrupole splitting distributions for each site.

The room-temperature Mössbauer spectra of the 15 samples shown in Appendix B were collected by my supervisor. In the context of this thesis, I have determined the iron site populations for 13 out of the 15 samples shown in Appendix B (two samples were ignored due to significant magnetite impurity peaks seen in the Mössbauer spectra). The populations of the remaining samples were retrieved from my M.Sc. thesis and elsewhere in the literature (see Section 3.5). Fitting parameters for the thirteen (13) thin-limit spectra (generated using the above mentioned methodology; see Section 2.2) are tabulated in Appendix O.

The impurity contents of selected samples (Section 3.3) was also ascertained by scanning

electron microscopy (SEM) combined with energy-dispersive spectroscopy (EDS) (Section 2.3), and by optical microscopy (Section 2.4). I assisted two persons for these measurements: Mrs. Pam Hunt at the Geological Survey of Canada for taking the SEM micrographs and EDS X-ray microanalysis spectra that are shown in Appendix C; and Dr. A.E. Lalonde for collecting the photomicrographs that are displayed in Appendix D.

Because of limited sample amounts, only one sample was examined by X-ray fluorescence spectroscopy (Section 2.5) and gas chromatography (Section 2.6). Elemental analyses provided by these two methods are summarized in Section 3.4.

With the assistance of Mr. Ron Hartree at the University of Ottawa, I have developed a calibration requiring only 250 mg of samples for major-element analysis using a wavelength-dispersive X-ray fluorescence spectrometer. I have also determined the precision and accuracy of the calibration for relevant major elements.

Gas chromatography was performed at the G.G. Hatch Isotope Laboratories of the University of Ottawa with the help of Mrs. Wendi Abdi and Mr. Gilles St-Jean. I have developed a procedure to establish the hydrogen contents of small amounts (1-100 mg) of powder (crystallite size = 0.1-20 μm) samples of layer silicate by gas chromatography. Chromatograms taken in the run corresponding to the one sample studied are given in Appendix E.

Main results (Chapters 4 and 5)

Stacking polytype contents. An area of concern is the complexities introduced by the possible presence of a mixture of stacking polytypes in the samples studied. To deal with this problem, I have derived fractional atomic coordinates for each observed homogenous mica polytype ($2M_1$ and $2M_2$, s.g. *C*2/*c*; 2*O*, s.g. *Ccmm*; and 3*T*, s.g. $P3_112$) in terms of the atomic positions in a standard 1*M* mica layer (these calculations are explained in Chapter 4 and given in Appendix U). By treating the various polytypes as different crystalline phases built of the same 1*M* unit in the simulation of a polytypic mixture, one then establishes clear criteria for identification based on the presence or absence of a Bragg peak at a 2θ position corresponding to a given stacking polytype. The polytypic contents of thirty-six (36) powder samples of four different solid solution series, determined as explained above, are presented in Section 5.2. Several workers have established criteria for the identification of mica polytypes by powder X-ray diffraction, but it is here attempted for the first time via a set of fractional atomic coordinates which ensures that the TOT layers of each stacking polytype are the same 1*M*-type TOT layer.

Lattice parameters. I investigated all factors determining the precision and accuracy of lattice parameters (Section 5.1, Appendices V and X): choice of method for evaluation of peak positions, observational and systematic errors on line positions, effect of indexing scheme on refinement results, etc. Lattice parameters refined for the 75 samples are given in Appendix W.

Models, data analysis, data representations, and interpretations (Chapter 6)

Many synthetic mica solid solution series were studied, between Mg, Co, Ni, and Fe end members, with different degrees of oxidation (induced by hydrothermal synthesis conditions or by heat-treatment), vacancy and Al/Si contents, and including an OH/F substitution series. I have examined the extent to which their lattice parameter variations with known chemical compositions, oxidation states, and site populations can be understood in terms of simple geometric crystal chemical models, in comparison with published crystal structure refinements of 170 single-crystal 1*M* samples (128 natural, 42 synthetic). This is the largest suite of synthetic trioctahedral mica samples ever studied in this way.

Relation to M.Sc. thesis. My M.Sc. thesis focussed on the experimental determination of the iron site populations of the nine (9) annite (Fe end-member) samples considered in this thesis, which were synthesized by Drs. R.G. Berman and J.-L. Robert using the C-CH_4 and Ni-NiO buffers at various equilibration temperatures. A structural model for the lateral misfit of tetrahedral and octahedral sheets of 'real' annite was proposed, that gives definite predictions on the ferric and ferrous iron site populations and includes a cation size dependent octahedral flattening, tetrahedral rotation, and the effect of octahedral/tetrahedral sheet differential thermal expansion. The latter model was based on cationic and anionic radii and has been redefined in terms of bond lengths during my Ph.D.

Geometric crystal chemical models. A hierarchical sequence of progressively more realistic geometrical models for octahedrons and tetrahedrons in layer silicates is developed. The geometrical models for geometric homo-, meso-, and hetero-octahedral sheets of layer silicates were derived by Mr. James R. Evans (University of Ottawa); I adapted his results to the geometry of a conventional 1*M* layer. I have generalized the currently available tetrahedral sheet models to allow tetrahedral elongation (or compression) via apical bond adjustment and/or tetrahedral basal flattening. A complete geometric crystal chemical model for the unit-cell of a geometric homo-octahedral 1*M* structure is worked out in terms of a minimal number of empirical parameters

(octahedral, tetrahedral, and interlayer bond lengths, flattening angles of octahedral and tetrahedral sheets, and tetrahedral rotation angle). I have used such simple geometrical models as a guide in the interpretation of the structural properties of the 170 single-crystal 1*M* samples considered (published refinements) and the 75 synthetic powder samples. A key difficulty in testing the predictions of the models on synthetic powder samples was to establish characteristic cation-specific bond lengths appropriate for these structures. The cation-specific bond lengths which were derived are shown to vary systematically from bond distances calculated using Shannon's radii for network silicates and oxides. Bond lengths specific to layer silicates have also been proposed by [Weiss *et al.* 1985, 1992], but I have argued that these are incorrect.

Distortions of real layer silicates. I have shown that the relation $(c/a)\cos\beta^* = 1/3$ holds exactly (within experimental error) for all synthetic powder samples whereas it does not hold in general for synthetic and natural 1*M* single-crystals of *C*2/*m* symmetry. From the models of [Donnay *et al.* 1964a] and [Evans 2001], the above relation is predicted to hold for geometric homo-octahedral sheets (having equal *M*1 and *M*2 site bond lengths) and not to hold for geometric meso-octahedral sheets (having unequal *M*1 and *M*2 site bond lengths), respectively. I have shown that the counter-rotation of the *M*2 sites of 1*M* samples exactly (within experimental error) follows the geometric meso-octahedral sheet model of [Evans 2001], that assumes only octahedral flattening, uniform thickness, and site-specific *M*1 and *M*2 bond lengths. Limits to simple geometrical models are demonstrated by showing that a geometric meso-octahedral 2:1 layer silicate requires corrugated tetrahedral sheets composed of bond-distorted tetrahedra. The following geometric meso-octahedral distortions were noted in 1*M* structures: i) intra-layer top-bottom displacements within a TOT layer; and ii) a tetrahedral bending of the apical bond with respect to the pyramidal base formed by the three basal bonds. I have shown that plots of lattice parameter *b* versus the average octahedral cation-oxygen bond length are particularly instructive and allow the following distinction to be made: unoxidized synthetic solid series tend to evolve along constant flattening angle lines whereas trivalent octahedral cation and vacancy bearing natural single-crystal and synthetic powder samples follow trends with varying flattening angles. I have found that the bond length of a given interlayer cationic species monotonously varies as a function of the tetrahedral rotation angle α. An upper limit of $\alpha = 9.5°$ is demonstrated to occur for K-rich micas having an $<AlSi_3>$ sheet, for both synthetic powders and natural single-crystals.

Original contributions. The following manuscripts, largely based on the results of Chapter 6, are currently planned or in preparation:

P.H.J. Mercier, R.J. Evans, D.G. Rancourt, *et al. Consequences and rare exceptions of in-plane pseudo-hexagonal symmetry in micas.*

P.H.J. Mercier, D.G. Rancourt, *et al. Fundamental difference between synthetic and natural trioctahedral micas: Homo-octahedral versus meso-octahedral sheets.*

P.H.J. Mercier, D.G. Rancourt, *et al. Upper limit of the tetrahedral rotation angle and factors affecting the octahedral flattening angle in synthetic and natural trioctahedral micas.*

P.H.J. Mercier, D.G. Rancourt, *et al. Real layer silicates must have corrugated tetrahedral sheets composed of bond distorted tetrahedra.*

Publications and presentations at conferences

Some of the results of this work (and my M.Sc.thesis, when indicated) have been reported in articles and presentations at various conferences:

D.G. Rancourt, **P.H.J. Mercier**, D.J. Cherniak, S. Desgreniers, H. Kodama, J.-L. Robert, and E. Murad. (2001) *Mechanisms and crystal chemistry of oxidation in annite: Resolving the hydrogen-loss and vacancy reactions* Clays and Clay Minerals 49: 455-491

P.H.J. Mercier, D.G. Rancourt, and R.G. Berman. (1999) *Control of site populations, at synthesis, by inter-sheet differential thermal expansion in a 2:1 layer silicate.* H. Kodama, A.R. Mermut, and J.K. Torrance (eds.), Clays for our future - Proceedings of the 11th International Clay Conference, Ottawa, Canada, 1997.

P.H.J. Mercier, D.G. Rancourt, and R.G. Berman. (1996) *Aspects of the Crystal Chemistry of Annite Mica.* Conference Proceedings, Volume 50, International Conference on the Applications of the Mössbauer Effect, ICAME-1995. I. Ortalli (Ed.), Italian Physical Society, p.789-792 [M.Sc.]

D.G. Rancourt, **P.H.J. Mercier**, E.J. Evans, M. Grodzicki, A.A.T. Shabani, and A.E. Lalonde. *Resolving the hydrogen-loss and vacancy reactions in the oxidation of Fe-bearing layer silicates.* Eighth Latin American Conference on the Applications of the Mössbauer Effect, Panama City, Panama. 22-27 September 2002 (*poster*)

D.G. Rancourt, **P.H.J. Mercier**, D.J. Cherniak, and S. Desgreniers. *Development of a single-mineral multi-variable geosensor based on the crystal chemistry of biotite.* 41st meeting of the United Kingdom Mössbauer Discussion Group, hosted by the Royal Society of Chemistry, University of Greenwich, London, 4-5 September 2000. (*keynote talk given by my supervisor*)

P.H.J. Mercier, A.A.T. Shabani, D.G.Rancourt, A.E. Lalonde, R.G. Berman, and J.-L. Robert. *Quadrupole splitting distributions of biotite.* International Conference on the Applications of the Mössbauer Effect, Garmish-Partenkirchen, Germany, Aug 28 - Sep 3, 1999 (*selected oral contribution).*

P.H.J. Mercier, D.G. Rancourt, and J.-L. Robert. *Étude expérimentale de la solution solide annite-sydérophyllite: impact de la teneur an aluminium sur la cristallochimie des micas.* 67e Congrès de l'Acfas, Ottawa, Ontario, 10-14 May 1999 (*oral presentation*).

P.H.J. Mercier, D.G. Rancourt, and R.G. Berman. *Control of site populations, at synthesis, by inter-sheet differential thermal expansion in a T-O-T layer silicate.* 11th International Clay Conference, Ottawa, Canada, June 15-21, 1997 (*oral presentation*).

P.H.J. Mercier, D.G. Rancourt, R.G. Berman, and J.-L. Robert. *Quadrupole splitting distributions of layer silicates from Mösbauer spectroscopy.* 11th International Clay Conference, Ottawa, Canada, 15-21 juin 1997 (*poster*).

P.H.J. Mercier, D.G. Rancourt, and R.G. Berman. *An ^{57}Fe Mössbauer spectroscopy study of synthetic layer silicates of the phlogopite-annite series having various Al-contents.* Congrès annuel de l'Association canadienne des physiciens, Ottawa, Canada, 16-19 juin 1996 (*oral presentation*).

P.H.J. Mercier, D.G Rancourt, and R.G. Berman. *Lower bound on Fe^{3+}/Fe_{tot} in synthetic annite mica.* International Conference on the Applications of the Mössbauer Effect. Rimini, Italy, September 10-16, 1995 (*poster*) [M.Sc.]

Acknowledgements

First and foremost, I thank my supervisor, Dr. Denis G. Rancourt, for his trust and financial support, for collecting the Mössbauer spectra, and for his guidance and encouragements. Dr. Rancourt is rigorous in his thinking; he expects nothing less from his students; that is what makes him so hard, so good. Thank you, Denis, for teaching me how to do science.

I thank Dr. André E. Lalonde for the optical microscopy measurements and his advice provided on numerous occasions.

I thank Drs. J.-L. Robert, R.G. Berman, and G. Redhammer for the syntheses of the samples.

I thank Dr. G. Redhammer for sharing results of structural refinements of synthetic single-crystal samples prior to their publication.

I thank the following technicians for their help: Mr. Ron Hartree (X-ray fluorescence spectroscopy), Mrs. Pam Hunt (scanning electron microscopy combined with energy-dispersive spectroscopy), and Mrs. Wendi Abdi and Mr. Gilles St-Jean (gas chromatography).

I thank fellow graduate student Jim Evans for fully working out the geometrical models of an octahedral sheet, as well as for the numerous enlightening discussions.

I thank all my colleagues and friends who helped me at various at various stages during my Ph.D. studies and in the production of the thesis: Drs. Meizhen Dang, Ken Lagarec, and Amir A.T. Shabani; Pierre-Jean Thibeault, Jean-François Meunier; Serge Lafontaine, Francis Leblanc, Marc Ducharme, Éric Thériault; Micheline Cormier-Guay, Emmanuelle Guay.

Financial support from Ontario Graduate Scholarships in Science and Technology in association with Golder Associates (1999-2000) and Noranda (2000-2001) is gratefully acknowledged.

I will now move to thank the people who contributed to this project in a more personal way. For that part, I will switch to my mother tongue ...

Je remercie ma conjointe, Emmanuelle Guay, pour m'avoir supporté et soutenu au cours des trois dernières années, même à travers mes périodes tourmentées. Ma Belle Emmanuelle, maintenant que tout est fini, je ne peux vraiment pas voir comment j'aurais pu y arriver sans avoir connu la fraîcheur que tu apportes à ma vie. Tu es ma plus précieuse découverte.

Je remercie les parents d'Emmanuelle, André et Micheline, pour leur générosité et leur hospitalité.

Je remercie Annie Thériault et toute sa famille.

Je remercie mes amis, *Les Boys* , pour leur support moral — et financier lors de nos mémorables fins de semaine.

Je remercie ma famille au grand complet, *des deux côtés*.

Je remercie mes parents, Jean-Paul et Pauline, ainsi que mon frère, Bruno, qui sont toujours là pour m'aider et me supporter du mieux qu'ils le peuvent.

Enfin, je dédie cette thèse à la mémoire de mon autre frère, Régis, qui demeurera toujours ma source d'inspiration la plus profonde.

Table of Contents

List of Tables

List of Figures

List of Appendices

Chapter 1. Introduction

In this chapter, we first give a preliminary background on layer silicates and the crystal chemistry of mica minerals. We then briefly explain the basic crystal chemical notions used in the understanding of the structures of minerals and inorganic solids. The motivation, perspective, and approach entailed in the long term project pursued in our group are next described along with the scope of the thesis. Finally, a section clarifies the nomenclature of a few important terms used throughout the thesis. An overview of the thesis organization is presented at the end of this introductory chapter.

1.1 Background on layer silicates and the crystal chemistry of the micas

Layer silicates — also called sheet silicates or phyllosilicates — are both common rock forming minerals and important clay minerals. All layer silicates can be conceived as constructed from two types of structural units: sheets of corner-linked tetrahedra and sheets of edge-linked octahedrons. Various cations are found within both the tetrahedral and octahedral sites. The tetrahedrons are usually occupied by Si^{4+}, Al^{3+}, and Fe^{3+}, whereas cations which are usually found in the octahedrons include Fe^{2+}, Fe^{3+}, Al^{3+}, Mg^{2+}, and others.

Depending on the arrangement of the tetrahedral and octahedral sheets, phyllosilicates are described according to their layer type and water content (hydrous *vs.* anhydrous). The assemblage formed by linking one tetrahedral sheet and one octahedral sheet is known as a 1:1 [or T:O] layer. A 2:1 [or T:O:T or TOT] layer links two tetrahedral sheets on either sides of an octahedral sheet. According to Chapter 1 of [Bailey 1988a]: "Hydrous phyllosilicate minerals can be classified conveniently on the basis of layer type (1:1, 2:1, or modulated), layer charge (x) per formula unit, and type of interlayer into several major groups. Further subdivision into subgroups is made on the basis of the octahedral sheet type (dioctahedral [if two-thirds of the octahedral sites are occupied by a cation] or trioctahedral [if all octahedral sites are occupied]) and into species by chemical composition or, occasionally, by the geometry of superposition of individual layers and interlayers. Such a classification scheme for non-modulated hydrous phyllosilicates is given in Table 1 [of the quoted reference]. The structures of the major groups of non-modulated hydrous phyllosilicates are shown diagrammatically in Figure 2 [of the quoted reference]." For further details concerning the classification, nomenclature, and structure of hydrous phyllosilicates other than micas, consult [Bailey 1988a].

Mica minerals belong to the 2:1 sheet silicates. Classification of the mica species is done on the basis of ideal end-member compositions such as those listed in Table 1.1. Structural information on mica and other layer silicates at a more technical level can be found in [Brindley & Brown 1984; Bailey 1984, 1988a; Mottana *et al.* 2002]. An up to date account of the nomenclature and stoichiometry of mica species is given in [Rieder *et al.* 1998]. Figure 1.1 shows the basic features of the mica structure.

Micas are divided into three families according to the symmetry of occupancy of the octahedral sheets in the TOT layers [Ďurovič 1994; Nespolo & Ďurovič 2002; Ferraris & Vivaldi 2002]: i) *homo-octahedral* micas have an octahedral sheet of symmetry $H(\overline{3})1m$, where all three octahedral sites *M*1, *M*2, and *M*3 (see Figure 6.1 of Section 6.1 below) are occupied by the same kind of crystallochemical entity (i.e., by the same the kind of ion or by the same statistical average of different kinds of ions including vacancies); ii) *meso-octahedral* micas have an octahedral sheet of symmetry $P(\overline{3})1m$, where two of the octahedral sites are occupied by the same kind of crystallochemical entity and the third by a different one; and iii) *hetero-octahedral* micas have an octahedral sheet of symmetry $P(3)12$, where each of the three octahedral sites is occupied by a different crystallochemical entity. Two types of TOT layers can also be distinguished in micas: 'M1 layers' have the origin of the octahedral sheet in the *M*1 site, whereas 'M2 layers' have the origin of the octahedral sheet in either the *M*2 or the *M*3 site [Nespolo 2001; Nespolo & Ďurovič 2002; Ferraris & Vivaldi 2002].

As stated in Chapter 1 of [Bailey 1984]: "In its simplest terms the crystal structure of a mica consists of negatively charged 2:1 layers that are compensated and bonded by large, positively charged, interlayer cations. [...] Each tetrahedral sheet is of composition T_2O_5 (T = tetrahedral cation), and within each sheet individual tetrahedra are linked with neighbouring tetrahedra by sharing three corners each (the basal oxygens) to form an hexagonal mesh pattern of the sort illustrated in Figure 1a [of the quoted reference]. The fourth tetrahedral corner (the apical oxygen) points in a direction normal to the sheet and at the same time forms part of an immediately adjacent octahedral sheet in which individual octahedra are linked laterally by sharing octahedral edges (Fig. 1b [of the quoted reference]). In a 2:1 layer the upper and lower planes of anions that comprise an octahedral sheet are also the common planes of junction with two oppositely directed tetrahedral sheets, as in Figure 1c [of the quoted reference]. These planes of junction consist of the shared apical oxygens plus unshared OH groups [or F or Cl anions] that lie at the center of each tetrahedral six-fold ring at [approximately] the same *z*-level as the apical oxygens."

In the octahedral sheet, as explained above, each octahedron shares four corners with the

tetrahedral sheet, leaving two corners occupied by OH groups. If the OH groups are on the same edge of an octahedron, the octahedron is said to be a *cis* site (the *cis* sites correspond to the *M*2 and *M*3 sites; see Figure 6.1 of Section 6.1 below). If the OH groups are opposite to one another on the diagonal of an octahedron, the octahedron is said to be a *trans* site (the *trans* sites correspond to the *M*1 sites; see Figure 6.1 of Section 6.1 below).

Because the apical oxygens of the tetrahedral sheets are shared with the octahedral sheets, the size matching of the two sheets is of critical importance in the formation of a stable mica structure. In annite, for example, the ideal end-member stoichiometry (Table 1.1) is never attained due to sheet structural mismatch constraints between the larger $[Fe^{2+}{}_3]$ octahedral and the smaller $<Al^{3+}Si^{4+}{}_3>$ tetrahedral sheet, which require some Fe^{3+} to be present even under highly reducing conditions [Hazen & Wones 1972, 1978; Mercier 1996; Mercier *et al.* 1996, 1999; Redhammer *et al.* 1993]. On the other end, it is a well known fact that in phlogopite (Table 1.1) the $<Al^{3+}Si^{4+}{}_3>$ tetrahedral sheet is larger than the $[Mg^{2+}{}_3]$ octahedral sheet [Radoslovich & Norrish 1962; Wones 1963a; Redhammer *et al.* 1995].

Inter-sheet lateral commensurateness and bond matching are ensured via several structural mechanisms (e.g, bond length altering, octahedral sheet flattening, tetrahedral rotation, tetrahedral sheet corrugation, etc.; see Chapter 6), as well as various oxidation and chemical substitution reactions, including: the oxybiotite or oxyannite reaction, involving loss of structural H

(1.1) $$Fe^{2+} + (OH)^{-} \rightleftarrows Fe^{3+} + O^{2-} + H\uparrow,$$

an Fe vacancy substitution, involving loss of structural Fe

(1.2) $$3\,Fe^{2+} \rightleftarrows 2\,Fe^{3+} + {}^{[6]}\square + Fe\uparrow$$ (where $\square$ indicates a vacancy),

a change in Al/Si ratio, involving an Al/Si substitution

(1.3) $$Fe^{2+} + Si^{4+} + Al\uparrow \rightleftarrows Fe^{3+} + Al^{3+} + Si\uparrow,$$

an Fe^{3+}/Al^{3+} exchange between the octahedral and tetrahedral sheets

(1.4) $$^{[4]}Al^{3+} + {}^{[6]}Fe^{3+} \rightleftarrows {}^{[6]}Al^{3+} + {}^{[4]}Fe^{3+}$$

and Tschermak's substitution

(1.5) $$^{[6]}(Fe^{2+}, Mg^{2+}) + {}^{[4]}Si^{4+} \rightleftharpoons {}^{[6]}Al^{3+} + {}^{[4]}Fe^{3+} \quad .$$

In the above equations and in general, the prefixes $^{[4]}$ and $^{[6]}$ designate tetrahedral and octahedral coordination, respectively.

1.2 Preliminary crystal chemical notions

The basic ideas used in the understanding of the structures of minerals and inorganic solids are that atoms have a specific size and that crystals can be considered as polymerizations of coordination polyhedra. For a recent review of the state-of-the-art of the field dealing with the fundamental crystal chemistry aspects of minerals, consult [Merlino 1997]. The latter reference also includes a separate chapter on the crystallography of mica polytypes [Nespolo *et al.* 1997a].

Currently, there exist two readily available ways for predicting the bond length of a given cation in a specific coordination: tables of ionic radii [Shannon & Prewitt 1969, 1970; Shannon 1976], and an empirical method that calculates bond lengths by means of a few bond-valence parameters [Brown & Altermatt 1975; Brown 1977, 1987]. Both of these methods are based on systematic, statistical analyses of crystal structure data obtained from inorganic solids. More recently, [Weiss *et al.* 1985; 1992] carried out a statistical evaluation of crystal-structure data for several (~100) phyllosilicates, where multiple regressions were used to obtain bond lengths and ionic radii specific to layer silicates. Numerous statistical studies have also been performed in order to establish relationships between lattice parameters and chemical compositions of micas (e.g., see [Bailey 1984; Smoliar-Zviagina 1993; Guidotti *et al.* 1989, 1993; Radoslovich 1962]).

As will be explained in the next section, the main emphasis of this work is to compare predictions made using simple geometrical models to measured crystal chemical properties of micas. In the vast literature published on the crystal chemistry of micas, there are relatively few papers dealing specifically with such an approach (for examples, see [Pauling 1930, 1960; Franzini & Schiaffino 1963; Donnay *et al.* 1964; Drits 1969; Tepikin *et al.* 1969; McCauley & Newnham 1971; Hazen & Wones 1972; Takeda & Morosin 1975; Appelo 1978; Toraya 1981]). Consult Volumes 13 [Bailey 1984] and 46 [Mottana *et al.* 2002] of the Reviews in Mineralogy and Geochemistry published by the Mineralogical Society of America for a series of papers addressing various aspects of mica crystal chemistry (in particular, see: [Brigatti & Guggenheim 2002; Ferraris & Vivaldi 2002; Nespolo & Durovic 2002]).

1.3 Motivation, perspective, approach, and scope

The ultimate goal of the long term project (not achieved in this thesis) pursued in our group is to develop a fundamental crystal chemical understanding of the links between the equilibration conditions (total pressure, temperature, prevailing gas fugacities, ambient chemical potentials, etc.), the crystallographic structures, and the chemical compositions of a broad array of 2:1 layer silicates.

One motivation of this long term project is to develop a single-mineral multi-variable geosensor based on the crystal chemistry of biotite, which is already the basis of a widely used oxygen fugacity gauge in petrology [Eugster & Wones 1965; Speers 1984]. As biotites are very common constituents of igneous and metamorphic rocks, a knowledge of the intricacies explaining their crystal chemistry immediately leads to their use in evaluating rock genesis or re-equilibration conditions. Most of the currently available geothermometers and geobarometers are based on thermodynamic compositional equilibrium between various minerals that coexist in rocks and are not single-mineral sensors.

Of the many ways one can begin to solve such a vast research problem, a straightforward initial step was adopted: to test the limits of a hierarchy of progressively more realistic simple geometrical models in explaining the crystal chemical properties of trioctahedral micas. It is hoped that the resulting crystal chemical understanding will help in uncovering and correctly describing key links between observed mineral properties and synthesis or equilibration conditions.

The thesis itself consists of a detailed study of the structural properties of 75 synthetic trioctahedral mica samples of different chemical compositions (trioctahedral 2:1 solid solution series having divalent and trivalent cationic, vacancy, and anionic substitutions in the octahedral sheets) which were investigated mainly by powder X-ray diffraction and characterized by several complementary methods. A large number of published crystal structure refinements (235 samples) are also considered. The geometry of the coordination polyhedrons of 170 trioctahedral-1*M* mica structures of *C*2/*m* symmetry is analysed in great detail (128 natural, 42 synthetic). Sixty-five (65) structural refinements corresponding to other stacking polytypes and space groups ($2M_1$, *C*2/*c* = 46; $2M_2$, *C*2/*c* = 4; $2O$: *Pnmn* = 2 , *Ccmm* = 1; $3T$, $P3_112$ = 12) are also used in a more limited way (to ascertain the validity of the studied $b = \sqrt{3}a$ relationship). No structural refinements of subgroup symmetries were considered. All this has lead to uncovering and/or establishing certain crystal chemical relationships that will undoubtedly be useful in the long term objectives mentioned above.

1.4 Nomenclature clarification

The official classification of micas into the homo-octahedral, meso-octahedral, or hetero-octahedral family is based on refinements of site-specific octahedral occupancies (mean electron counts), which correspond to differences in scattering powers of the cations populating each of the three octahedral sites (*M*1, *M*2 , and *M*3). On the other hand, [Weiss *et al.* 1992] identified eight possible configurations of the octahedral sheet based on differences between the average cation-anion bond lengths <M1-O>, <M2-O>, and <M3-O> refined in each of the three octahedral sites. According to their categorisation, three types of octahedral sheets are possible [Weiss *et al.* 1992]:

I. <M1-O> = <M2-O> = <M3-O>

II. (a) <M1-O> > <M2-O> = <M3-O>

(b) <M1-O> = <M3-O> > <M2-O> or <M1-O> = <M2-O> > <M3-O>

(c) <M1-O> < <M2-O> = <M3-O>

(d) <M1-O> = <M2-O> < <M3-O> or <M1-O> = <M3-O> < <M2-O>

III. (a) <M1-O> > <M3-O> > <M2-O> or <M1-O> > <M2-O> > <M3-O>

(b) <M3-O> > <M3-O> > <M2-O> or <M2-O> > <M1-O> > <M3-O>

(c) <M3-O> > <M2-O> > <M1-O> or <M2-O> > <M3-O> > <M1-O> .

As noted by [Weiss *et al.* 1992], the above situation is complicated because sometimes, in a given refinement, the average electron densities of two distinct octahedral sites are different but there is no significant difference between the average bond lengths of these two sites, or vice versa (e.g., see also [Brigatti & Guggenheim 2002]).

In this thesis, we use the terms *geometric homo-octahedral*, *geometric meso-octahedral*, and *geometric hetero-octahedral* to refer to each of three octahedral sheet types I , II, and III described by [Weiss *et al.* 1992], respectively. Note that the latter classification is based on the average bond lengths refined in the three distinct octahedral sites, not on the refinements of site-specific octahedral occupancies. When used without the qualifying adjective *geometric*, the terms *homo-octahedral*, *meso-octahedral*, and *hetero-octahedral* strictly refer to the official classification based on the symmetry of occupancy of the octahedral sheets as judged by the refinements of site-specific mean electron counts [Nespolo & Ďurovič 2002].

1.5 Organization of the thesis

After this introduction, we present the experimental methods and data treatment that were used in this thesis (Chapter 2). The next chapter deals with the synthesis, treatment, and characterization of the 75 synthetic powder samples that were studied (Chapter 3). Chapter 4 proposes a method to resolve the different stacking polytypes that may be present in a given mica sample. Chapter 5 first investigates all factors determining the precision and accuracy of lattice parameters obtained via powder X-ray diffraction, and then applies the method explained in Chapter 4 to determine stacking polytype contents in our synthetic powder samples. The core of the thesis is in Chapter 6, where a hierarchical sequence of geometrical models is presented and then tested against measured structural properties of natural and synthetic trioctahedral micas. Chapter 7 presents a discussion of the main findings made in our detailed analysis of trioctahedral mica structures performed using geometric crystal chemical models. Chapter 8 summarizes the main results and conclusions of this thesis.

Species	Composition
annite	$\{K\}[Fe_3^{2+}]\langle AlSi_3\rangle O_{10}(OH)_2$
phlogopite	$\{K\}[Mg_3]\langle AlSi_3\rangle O_{10}(OH)_2$
siderophyllite	$\{K\}[Fe_2^{2+}Al]\langle Al_2Si_2\rangle O_{10}(OH)_2$
eastonite	$\{K\}[Mg_2Al]\langle Al_2Si_2\rangle O_{10}(OH)_2$
tetra-ferri-annite	$\{K\}[Fe_3^{2+}]\langle Fe^{3+}Si_3\rangle O_{10}(OH)_2$
tetra-ferriphlogopite	$\{K\}[Mg_3]\langle Fe^{3+}Si_3\rangle O_{10}(OH)_2$
tainiolite	$\{K\}[Mg_2Li]\langle Si_4\rangle O_{10}F_2$
polythionite	$\{K\}[Li_2Al]\langle Si_4\rangle O_{10}F_2$
trilithionite	$\{K\}[Li_{1.5}Al_{1.5}]\langle AlSi_3\rangle O_{10}F_2$
norrishite	$\{K\}[LiMn_2^{3+}]\langle Si_4\rangle O_{10}F_2$
preiswerkite	$\{Na\}[Mg_2Al]\langle Al_2Si_2\rangle O_{10}(OH)_2$
clintonite	$\{Ca\}[Mg_2Al]\langle Al_3Si\rangle O_{10}(OH)_2$
kinoshitalite	$\{Ba\}[Mg_3]\langle Al_2Si_2\rangle O_{10}(OH)_2$
paragonite	$\{Na\}[Al_2\square]\langle AlSi_3\rangle O_{10}(OH)_2$

Series	Composition
biotite	Trioctahedral micas between, or close to, the annite-phlopite and syderophyllite-eatonite joins; dark micas without Li.
lepidolite	Trioctahedral micas on, or close to, the trilithionite-polythionite join; light micas with substantial Li.

Table 1.1. Classification of some ideal end-member compositions of the micas following [Rieder *et al.* 1998].

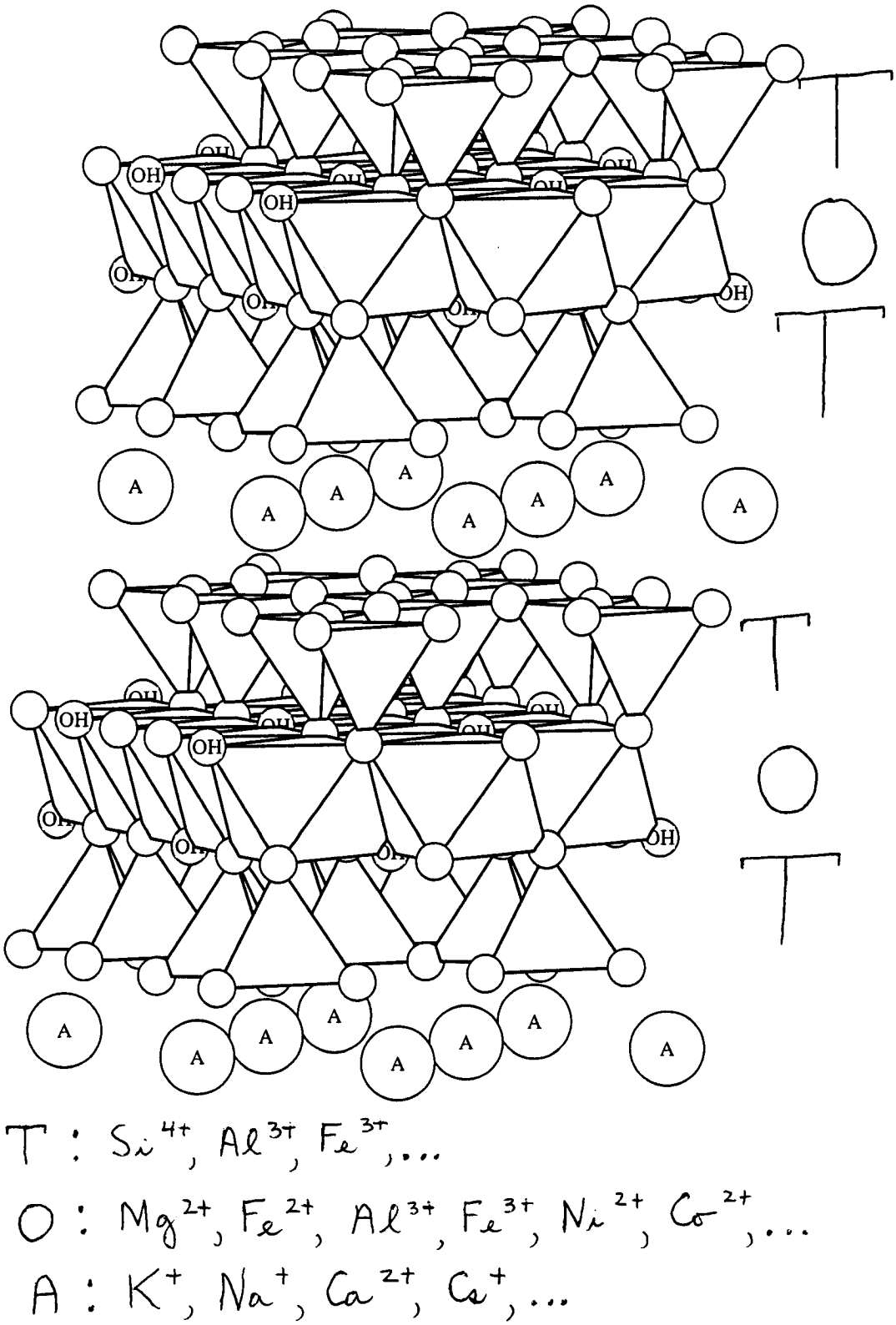

Figure 1.1. Mica structure.

Chapter 2. Experimental Methods and Data Treatment

In this chapter, I describe the experimental methods used in this work. For each method, I give an explanation of: the physical basis of the analytical signal that is measured, the apparatus, the data acquisition, the data treatment, the analytical procedures, and the physical properties that are extracted from the measurements.

2.1 Powder X-ray diffraction

Powder X-ray diffraction (pXRD) is the primary experimental method used in this study. An excellent review of the powder diffraction method is made in [Langford & Louër 1996]. For a complete and up to date reference describing diffraction theory and practice, consult the International Tables for Crystallography [Wilson 1992]. There also exist several monographs devoted to various aspects of X-ray diffraction (XRD): basic theory and experimental methods [James 1948, 1962; Wilson 1949, 1970; Warren 1969], powder diffractometry [Jenkins & Snyder 1996; Klug & Alexander 1974; Wilson 1963; Bish & Post 1989], quantitative X-ray diffractometry [Zevin & Kimmel 1995], Rietveld analysis [Young 1995], and diffraction physics [Cowley 1995; Guinier 1963]. Fundamentals of crystallography can be found in a number of texts, e.g. [Burns & Glazer 1990; Giacovazzo 1992]. For an introduction to solid state physics, I refer the reader to [Kittel 1986; Ashcroft & Mermin 1976].

2.1.1 Apparatus

The pXRD patterns were collected with a Philips X'Pert PW3710 twin-goniometer automated powder diffractometer using Cu-K_α radiation emitted from a 12 mm long line focus sealed X-ray tube. This system employs the Bragg-Brentano parafocusing geometry. A two-dimensional view

of the Bragg-Brentano geometric arrangement is shown in Figure 2.1. A divergent beam of radiation coming from the line of focus (F) of the X-ray tube passes first through a divergent slit (DS) , then through a first set of Soller slits (SS1), through a beam mask (BM), before striking the specimen (S) at an angle θ with respect to the sample plane. The diffracted X-rays leave the specimen at an angle 2θ with respect to the incident beam (and θ with respect to the sample plane), pass through a second set of Soller slits (SS2), through the receiving slit (RS), through the scatter slit (ScS), to the detector. In order to establish the parafocusing condition, the axes of the line of focus of the X-ray tube and of the receiving slit are at an equal distance r_f from the axis of the goniometer.

The receiving slit assembly is coupled to the goniometer and moves around a goniometer circle of radius R, centred about the axis of the goniometer, in order to scan a range of 2θ angles. The source-to-specimen and the specimen-to-receiving-slit distances are both equal to R. For θ-2θ scans, the goniometer rotates the specimen about the same axis as that of the detector, but at half the rotational speed. The surface of the specimen thus remains tangential to the focussing circle r_f .

The system is equipped with two goniometers arranged in a vertical θ-2θ configuration. The goniometers have Soller slits placed in both the primary (incident) and secondary (diffracted) paths of the X-rays. The aperture angle of the Soller slits Δ is equal to 2.3 degrees. Soller slits are made of parallel thin metal foils (at right angle with respect to the direction of the axis of the goniometer) whose spacing and length determine Δ (Δ is equal, in radians, to the spacing of the foils divided by the length of the foils) [Wilson 1963].

The left goniometer has a radius R of 230 mm. It is equipped with a graphite crystal secondary beam monochromator with gas-filled proportional detector, and a non-rotating sample holder. Both the divergent and the receiving slits are adjustable via independently computer-controlled stepper motors.

The right goniometer has a radius R of 173 mm. This side is fitted with a Kevex solid-state detector having sufficient energy resolution to select only the Cu-K_α radiation, and a sample holder that can spin the specimen around an axis perpendicular to the surface of the sample. The divergent slit is an original variable divergent slit system (i.e., mechanically belt-

driven by the θ-axis of the goniometer) that gives a constant specimen irradiation length of 12 mm. The receiving slits are interchangeable and of fixed size.

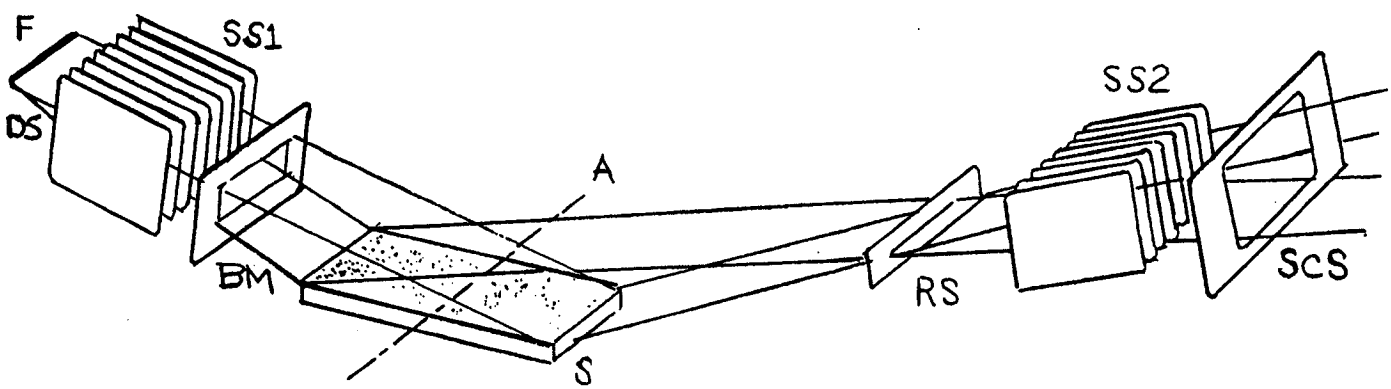

Figure 2.1. The Bragg-Brentano geometric arrangement (detector not shown). Symbols are described in the text.

Inserted in the path of the X-rays between the divergence slit and the specimen, the beam mask determines the axial length of the sample that is illuminated. While smaller beam mask sizes give rise to narrower and better resolved diffraction line profiles, there is a corresponding loss in the intensity diffracted since less sample gets irradiated.

The height of the scatter slit fixes the vertical length of the sample (i.e., the length of the sample perpendicular to the direction of the axis of the goniometer) that is seen by the detector. A scatter slit reduces the background intensity and ensures that the radiation going to the detector is restricted to the X-rays diffracted by the sample.

The function of the divergent slit is to limit the vertical divergence of the X-ray beam. The illuminated length L of the sample is given by [Jenkins & Snyder 1996]:

$$L = \frac{2R\sin\theta\tan(\delta/2)}{(\sin\theta)^2 - (\cos\theta)^2 \cdot (\tan[\theta(\delta/2)])^2} \tag{2.1}$$

where δ is the divergence angle resulting from the aperture of the divergent slit, and R is the goniometer radius. When δ is small ($< 4°$), the second term in the denominator becomes insignificant with respect to the first, and Equation (2.1) reduces to

$$L = \frac{2R\tan(\delta/2)}{\sin\theta} \tag{2.2}$$

The difference between a variable divergence slit and a fixed divergence slit is that the latter produces a fixed divergence angle while the former gives a fixed sample illumination length.

2.1.2 Data collection

Given the small amounts of material available (10-100 mg), samples were mounted as acetone smears on a single-crystal silicon wafer low-background holder. This method of sample

preparation minimizes the specimen-transparency error, provided that the smears are thin enough. A thick smear produces diffraction lines that are shifted towards higher diffractometer angle.

Most diffractograms were collected on the left goniometer in a step-scanning mode from 5 to 80 °2θ, with a step of 0.01 °2θ, and a counting time per step ranging from 3 to 5 seconds. Appendix A presents all the diffractograms collected in this work. Diffractograms are usually referred to as MER*XXX*, where *XXX* is the label number of a given diffractogram.

I also investigated the effects associated to the sizes of the receiving slit, the beam mask, the scatter slit, and the divergent slit. Changing the size of the receiving slit affects both the width and intensity of a given line. In general, as the intensity increases, the resolution of the line decreases, and vice versa. When the beam size is close to the size of the receiving slit, optimum intensity and resolution are obtained. I took a series of measurements on a disk made with a powder of Si crystallites mixed with a resin. In doing so, I established the optimal experimental configuration to consist of a receiving slit height of 0.1 mm and a beam mask width of 10 mm.

The majority of the diffractograms were measured using a variable divergence slit having a 12 mm specimen irradiation length in combination with a 1° scatter slit. Under these conditions, the size of the divergent slit is larger than that of the scatter slit above a certain 2θ angle. Following Equation 2.2, the angle δ subtended by a variable divergent slit is

$$\delta = 2 \cdot \arctan\left(\frac{l \cdot \sin\theta}{2R}\right) \quad , \tag{2.3}$$

where l is the fixed sample illumination length imposed by the variable divergent slit, θ is the Bragg angle (half of the diffraction angle), and R is the radius of the goniometer. Therefore, when the diffraction angle is greater than the value

$$2\theta_o = 2 \cdot \arcsin\left(\frac{2R \tan(\delta_{SeS}/2)}{l}\right), \tag{2.4}$$

where δ_{ScS} is the actual size of the scatter slit in angular units, the diffracted beam is partly blocked by the scatter slit. As a result the length of the sample seen by the detector is no longer constant above $2\theta_o$, but varies as

$$l_{2\theta>2\theta_o} = \frac{2R \cdot \tan[\delta_{ScS}/2]}{\sin\theta}, \tag{2.5}$$

following Eq. 2.4.

With a thin smear and a 1° scatter slit, this implies a constant *effective diffracting volume* up to $2\theta_o = 29.15°$ on the right goniometer ($R = 173$ mm) and up to $2\theta_o = 39.09°$ on the left goniometer ($R = 230$ mm).

2.1.3 Lattice parameter refinement

CELREF is a personal computer (PC) version – initiated on PC by P.C. Burns – of the unit-cell parameters refinement program developed by D.E. Appleman and H.T. Evans for the U.S. Geological Survey [Appleman & Evans 1973]. The reader is referred to the latter publication for a detailed description of the program. The program accepts as input any combination of indexed and unindexed powder diffraction data, along with crystal system, extinction criteria, and approximate lattice parameters. Even though the program is old, it can still run as a DOS-driven application on Windows 95/98/NT systems.

Calculated and observed peak positions are matched according to the following acceptance criterion when the observations are indexed

$$\left|\sqrt{w_i}\left(\theta_i - \text{ARCSIN}\left(0.5 \cdot \lambda \cdot \sqrt{Q_{hkl}}\right)\right)\right| \leq \text{TOL}\ , \tag{2.6}$$

where: θ_i is the observed Bragg angle, w_i is a user-defined weight assigned to the observation, λ

is the X-ray wavelength of the radiation being used, and TOL is the specified tolerance (which can be fixed by the user or determined according to predefined criteria by the program). The value of Q_{hkl} corresponds to the (hkl) indices assigned to the reflection as

$$Q_{hkl} = h^2a^{*2} + k^2b^{*2} + l^2c^{*2} + 2kl\,b^*c^*\cos\alpha^* + 2hl\,a^*c^*\cos\beta^* + 2hk\,a^*b^*\cos\gamma^* \quad , \tag{2.7}$$

where a^*, b^*, c^*, α^*, β^*,and γ^* are the reciprocal cell parameters.

A match is accepted if and only if the difference between the observed and calculated Bragg angle, $\Delta\theta$, is less than the specified tolerance. The program then uses the $\Delta\theta$ values to obtain corrections (shifts) to the reciprocal cell parameters by least-squares analysis. Refinement ends when the reciprocal cell parameter shifts are sufficiently small.

At this point, estimated standard deviations (ESDs) of both the reciprocal and direct cell parameters are computed using the covariance matrix of the least-squares algorithm (for an introduction to the principles of least-squares analysis, consult [Press *et al.* 1996]). All least-squares and error calculations are based on the $\Delta\theta$ values; i.e. the program assumes that the observational error occurs in the determination of θ. In Subsection 5.1.4, I will compare ESDs output by the CELREF program to errors calculated using other methods.

2.1.4 Line-profile refinement and structure factor calculation

XFIT is an interactive and graphical X-ray line profile fitting software program that works under the MS Windows operating system (95/98 and some NT versions), written in the C^{++} programming language. It integrates the familiar pseudo-Voigt and split-Pearson functions, together with a fundamental parameter convolution approach [Cheary & Coelho 1992,1998a, 1998b] to generating line profiles. In the present work, I used the fundamental parameter (FP) approach implemented in XFIT to perform line-profile refinement.

XFIT also incorporates a program, Koalariet, which runs through XFIT using an input

file that consists of readable key words. Koalariet offers the possibility to define parameters, and subsequently refine these parameters in the context of a Rietveld refinement. Koalariet can also execute conventional Rietveld analysis and perform structure factor calculation.

In the FP approach, the line shape (diffraction-line-intensity-profile) is synthesized from the Cu K_α emission profile, the physical variables of the diffractometer, and some specimen-dependent parameters. In addition to the integrated intensities and 2θ positions of the line profiles, both diffractometer- and specimen-dependent parameters may be refined, and constitute the convolution parameters that are used to generate the aberration profiles.

The Cu Kα emission spectrum consists of two major components, $K\alpha_1$ and $K\alpha_2$, which makeup ~99 % of the intensity, and the Kα satellite group of lines in the high-energy tail (lower λ values, i.e. lower-angle side of a diffraction line) which makes up the rest. As explained in [Cheary & Coelho 1992], the Cu spectrum displays a different level of asymmetry in the $K\alpha_1$ and $K\alpha_2$ components; both of these lines are actually two-line structures arising from the fine structure of the $K\alpha_1$ and $K\alpha_2$ transitions. Although in theory each of these lines is also asymmetric, it has been shown that a Lorentzian shape is quite adequate for describing each of these four lines.

In the FP approach, the Cu Kα spectrum emission profile can be represented by a sum of up to five Lorentzian lines, the four Kα lines and the satellite group, and each one of these is expressed as a unit area Lorentzian. Parameters defining the emission profile are stored in a specific file (LAM file) that is used by the program to generate the peaks.

Table 2.1 lists the data contained in the LAM file that I have used to generate the emission profile lines of a peak for line-profile refinements. $E_{o,k}$, $E_{h,k}$, and $E_{A,k}$ are parameter names used to identify the wavelength λ, the full width at half maximum Γ (which is proportional to the lifetime of the excited state giving rise to the emission line), and the relative intensity of the k-th emission line, respectively. The relative areas of the emission lines under a peak are determined by the $E_{A,k}$ values.

The position of a particular k-th emission line of a given peak i, $2\theta_{i,k}$, is determined from the following equations:

$$
\begin{aligned}
2d_{hkl} &= E_{o,r}/\sin\theta_i \\
E_{o,k} &= 2d_{hkl}\sin\theta_k = \left(E_{o,r}/\sin\theta_i\right)\cdot\sin\left(\theta_i + \Delta\theta_{i,k}\right) \\
\Delta 2\theta_{i,k} &= \left(\frac{E_{o,i}}{E_{o,r}} - 1\right)\cdot\left(\frac{360\tan\theta_i}{\pi}\right) \\
2\theta_{i,k} &= 2\theta_r + \Delta 2\theta_{i,k}
\end{aligned}
\qquad (2.9)
$$

where the subscript r refers to the line having the highest $E_{A,k}$ value. The full width parameter at half maximum of an emission line, $H_{i,k}$ (in °2θ), is determined by the relation

$$
H_{i,k} = \left(\lambda_{h,k}/\lambda_{o,r}\right)\cdot\frac{180\tan\theta}{\pi} \qquad . \qquad (2.10)
$$

Emission line	$E_{o,k}$ λ (Å)	$E_{h,k}$ Γ (Å ×10^{-3})	$E_{A,k}$ relative intensity (dimensionless)
satellites	1.534753	3.6854	0.0159
$K\alpha_{1a}$	1.540596	0.437	0.5691
$K\alpha_{1b}$	1.541058	0.6	0.0762
$K\alpha_{2a}$	1.54441	0.52	0.2517
$K\alpha_{2b}$	1.544721	0.62	0.0871

Table 2.1 Relative intensities, wavelengths, and lifetime widths of the emission lines used in line-profile fitting to generate the Cu Kα emission profile. Symbols are described in the text.

The peak (reflection) dependent parameters are its integrated intensity, A_i, and the position, $2\theta_i$, of the emission line having the highest $E_{A,k}$ value. The peak parameter A_i determines the total area under all of the emission lines of a peak. Before scaling by the A_i parameter, the area under all of the emission lines is scaled to unity.

The emission profile, $L(x)$ (where x is the observed angle on the diffractometer) is convoluted with the diffractometer aberration functions, $D_i(2\phi)$, and the total instrumental profile of a peak, $g(x)$, is a convolution of these functions and the emission profile,

$$g(x) = \mathbf{L}*\mathbf{D}_1*\mathbf{D}_2*\mathbf{D}_3*\cdots*\mathbf{D}_n \tag{2.11}$$

where n is the number of instrumental terms included in the convolution. I refer the reader to the original publications [Cheary & Coelho 1992,1998a, 1998b], as well as the documents that come with the program for a full description of the methods and the details concerning the generation of the aberration profiles.

The diffractometer-dependent parameters include: the flat-surface fixed divergence angle (FSFA) in degrees, the flat-surface fixed sample illumination length (FSFL) in mm, the target (source) size (TA) in mm, the specimen tilt (ST) in mm, and the receiving slit width (SW) in mm. The axial divergence aberration function parameters are: the receiving slit length (SL) in mm, the sample length (SAML) in mm, the source length (SOUL) in mm, the primary Soller slit aperture angle (PS) in degrees, and the secondary Soller slit aperture angle (SS) in degrees.

Specimen-dependent factors may also be taken into account through the following aberration parameters: the linear absorption coefficient of the specimen (AB) in cm^{-1}, a Gaussian shape strain (STR) expressed as a percentage, and a Lorentzian shape crystallite size (CS) in Å. The STR parameter is related to the Gaussian full width at half maximum ($FWHM_G$) by

$$\mathrm{FWHM_G} = \frac{4\sqrt{2\ln 2}\cdot\tan\theta\cdot\mathrm{STR}}{100} \quad (\text{in } ^\circ 2\theta), \tag{2.12}$$

whereas the CS parameter is defined in terms of the Lorentzian FWHM ($FWHM_L$) as

$$\text{FWHM}_L = \frac{180}{\pi} \cdot \frac{E_{o,r}}{\text{CS} \cdot \cos\theta} \quad \text{(in °2θ)}, \tag{2.13}$$

where $E_{o,r}$ has been defined above.

The quality of the fit of a given pXRD pattern is judged according to the following profile agreement indicators (used mainly to follow the progress of a given refinement):

$$R_{wp} = \sqrt{\frac{\sum \frac{(Y_{obs} - Y_{cal})^2}{Y_{obs}}}{\sum Y_{obs}}}, \tag{2.14}$$

$$R_{wp}' = \frac{\sum |Y_{obs} - Y_{cal}|}{\sum |Y_{obs} - Bkg|}, \tag{2.15}$$

$$R_{exp} = \sqrt{\frac{N - P}{\sum Y_{obs}}}, \tag{2.16}$$

$$GOF = \frac{R_{wp}}{R_{exp}} = \sqrt{\frac{\sum \frac{(Y_{obs} - Y_{cal})^2}{Y_{obs}}}{N - P}}, \tag{2.17}$$

where: R_{wp} is the R-weighted pattern factor, R_{wp}' is the R-weighted pattern prime factor, R_{exp} is the expected factor, *GOF* is the goodness-of-fit factor, Y_{obs} is the observed intensity at a particular diffractometer angle, Y_{cal} is the calculated intensity at a particular diffractometer angle, N is the total number of observations that make up the pXRD pattern, and P is the number of parameters being fitted in the refinement.

2.2 Mössbauer spectroscopy

Mössbauer spectroscopy is a nuclear spectroscopy that relies on recoilless emission (i.e., without loss of energy due to recoil of the nucleus and without thermal broadening) and subsequent absorption of a γ-ray photon by a nucleus of the sample. [Rancourt 1998] gives an overview of the Mössbauer spectroscopy method. In that article, the author "start[s] from the basics and describe[s] all the physical and chemical concepts that are required to perform correct spectral analysis and interpretation in order to give a complete and up to date treatment so that one may appreciate and use published Mössbauer results. A complete bibliography, including electronic sources [and a number of textbooks and monographs on Mössbauer spectroscopy], is also given" [Rancourt 1998].

Powder absorbers were prepared as described elsewhere [Mercier 1996; Rancourt *et al.* 1994a]. Uniform absorbers are required for thickness-effect corrections, so the following procedure was used. Approximately 20 mg of samples (Table 2.2) was spread evenly and sandwiched between two waxed paper sheets held with clear tape in aluminum holders with 5/16 or 1/2 inch diameter windows. Because of the small particle size of our synthetic samples (see SEM micrographs in Appendix C and [Mercier 1996]), such a procedure ensures that no texture is present in the absorbers [Rancourt *et al.* 1994b].

Transmission ^{57}Fe Mössbauer spectra were collected using a <30 mCi ^{57}Co rhodium matrix single-line thin source with a constant-acceleration drive on a velocity range of ±4 mm/s. This range gives an optimal resolution for the biotite pattern. The same experimental set-up as that described in [Mercier 1996] was used to collect the spectra. Data was acquired on 1024 channels and folded to give a flat background and a zero-velocity position corresponding to the centre shift of metallic α-Fe at RT. The folded raw spectra that I have analysed in this project are presented in Appendix B.

All RT spectra were corrected for thickness effects as described elsewhere [Rancourt 1994; Rancourt *et al.* 1994a, 1994b; Rancourt 1989]. In order to treat thickness effects properly, each spectrum is first fitted with an arbitrary number of Voigt lines to obtain a statistically ideal fit. Intrinsic absorber cross sections (CRS) are then extracted from the Voigt fits and used to

generate thin-limit spectra (TLS). The TLS are fitted using a Voigt-based quadrupole splitting distribution (QSD) method [Rancourt & Ping 1991].

The Rancourt and Ping methodology used here is described in detail elsewhere [Rancourt & Ping 1991; Rancourt *et al.* 1994a, 1994b]. Consult [Rancourt & Ping 1991] for all Mössbauer parameter definitions and a detailed description of the relevant notation. All steps of the analysis procedure were carried out using the Recoil software developed in Dr. D.G. Rancourt's laboratory by Dr. K. Lagarec and now commercialized by ISA Inc. (http//:pages.infinit.net/klagarec/recoil/).

Sample	Weigth (±0.1 mg)	Area (cm^2)
$Fe_{1.2}Mg_{1.8}$JLR	30.0	0.495
$Fe_{1.8}Mg_{1.2}$JLR	25.6	0.495
$Fe_{2.4}Mg_{0.6}$JLR	21.0	0.495
$Fe_{0.75}Mg_{2.25}$RGB	22.2	0.495
$Fe_{1.5}Mg_{1.5}$RGB	22.3	0.495
$Fe_{2.25}Mg_{0.75}$RGB	22.3	0.495
$Fe_{3.0}Mg_{0.0}$RGB	18.7	0.495
$Fe_{25}Mg_{75}$Bi33rRGB	25.7	0.495
$Fe_{50}Mg_{50}$Bi38rRGB	20.8	0.495
$Fe_{75}Mg_{25}$Bi32rRGB	20.8	0.495
Fe_{100}Bi35rRGB	19.9	1.267
$Fe_{25}Mg_{75}$Bi31rRGB	49.0	1.267
$Fe_{75}Mg_{25}$Bi30rRGB	59.4	1.267

Table 2.2. Mössbauer absorber characteristics.

2.3 Scanning electron microscopy combined with energy dispersive spectroscopy

Scanning electron microscopy (SEM) combined with energy dispersive spectroscopy (EDS) permits the observation and characterization of the physical nature and chemical composition of the surfaces of solids on a micrometer or submicrometer scale. The monograph by [Goldstein *et al.* 1992] provides an excellent overview of the SEM and EDS X-ray microanalysis techniques. In their introductory chapter, [Goldstein *et al.* 1992] summarize the basic capabilities of each method as follows: "[In SEM], the signals of greatest interest are the secondary and backscattered electrons, since these vary according to the differences in surface tomography as the electron beam sweeps across the specimen. The secondary-electron emission is confined to a volume near the beam's impact area, permitting images to be obtained at relatively high resolution. [... In EDS X-ray microanalysis], the primary radiation of interest is the characteristic X rays emitted as a result of electron bombardment. The analysis of characteristic X-rays can yield both qualitative identification and quantitative compositional information of a specimen".

In this work, SEM of selected samples prepared as carbon-coated loose powder mounts was performed with a JEOL JSM 6400 system at the Geological Survey of Canada, Ottawa. The EDS X-ray microanalysis was used to look for and identify impurity phases. All SEM micrographs and all EDS X-ray microanalysis spectra are presented in Appendix C.

2.4 Optical microscopy

Optical microscopy is by far the most utilized characterization method in the geosciences for the examination of minerals and rocks. An introductory understanding of the technique is given by R. Telle and G. Petzow in Chapter 5 of [Lifshin 1992]. Optical properties of the micas under the polarizing microscope are summarized by R.E. Wilcox in Chapter 6 of [Bailey 1984], where it is assumed that the reader is acquainted with the theory of optical crystallography which can be found elsewhere [Bloss 1961].

In this thesis, I report on transmission optical microscopy investigations of selected samples (see Chapter 3 and Appendix D) conducted with Dr. André E. Lalonde at the University of Ottawa using either a Meiji ML9400 or a Nikon ECLIPSE E600 POL polarizing microscope. The Nikon microscope was equipped with a digital photo camera, that allowed photomicrographs to be taken. Samples were mounted between two glass plates by immersion in a liquid of known refractive index.

2.5 X-ray fluorescence spectroscopy

X-ray fluorescence (XRF) spectroscopy provides the means for identification and quantification of the chemical composition of a sample by measuring the characteristic X-ray line intensity corresponding to a given chemical element and then relating this intensity to elemental concentration. An introduction to the principles and practice of XRF elemental analysis is given by R. Jenkins in Chapter 9 of [Lifshin 1992] (and references therein). Consult [Ahmedali 1989] for a recent overview of advances in methodology of XRF analysis in the geological sciences.

The XRF experimental method and data treatment that I have carried out in this project are described in [Rancourt *et al.* 2001]: "The XRF elemental analyses were obtained using a Philips PW2400/00 sequential [angle-dispersive] X-ray spectrometer. Because of limited sample amounts, an XRF analysis was performed only for sample [IKO-Ann (see Chapter 3)]. For this purpose, a new calibration was developed that used only 250 mg of sample in preparing fused disks with 4.0750 g of flux material (3.2000 g $Li_2B_4O_7$; 0.8750 g $LiBO_2$). The new calibration was based on a complete suite of international standards. Precision was evaluated by performing several analyses on the same fused disk and was found to be 0.01 wt.% or better (error in the mean) for the relevant major oxides (Fe_2O_3, SiO_2, Al_2O_3, and K_2O). Accuracy was evaluated by measuring five relevant standards, that had not been used in establishing the calibration, and was estimated (average absolute deviations) to be 0.2, 0.3, 0.1, and 0.01 wt.% for Fe_2O_3, SiO_2, Al_2O_3, and K_2O, respectively."

2.6 Gas chromatography

Gas chromatography (GC) of light elements (C, H, N, S) was performed with the CE Instruments model EA-1110 elemental analyser located in the Department of Earth Sciences at the University of Ottawa. With this instrument, the sample is vaporized by combustion and injected into the head of a chromatographic column. Elution is brought about by the flow of an inert gaseous mobile phase and the analyte (sample) signal is measured using thermal conductivity (thermistor) detection. For an introduction to the principles of chromatography, consult [Skoog & Leary 1992].

Quantification was achieved by using time-integrated thermistor signals and run-specific calibrations for C, H, N, and S. In any given run, several standards (typically 10-20) are measured (before, between, and after analyte measurements) and used to construct a calibration line for each element. The names and chemical compositions of the standards that were employed are as follows: BBOT, $C_{0.7253}H_{0.0609}N_{0.0651}S_{0.0744}$; SUL, $C_{0.4184}H_{0.0468}N_{0.1627}S_{0.1862}$; and LCYS, $C_{0.2999}H_{0.0503}N_{0.1166}S_{0.2669}$. These same standard materials are used several times with different sample weights in a given run. Chromatograms collected and analysed in this project are presented in Appendix E, along with the details of the run.

"The calibration curves were found to be linear, within a precision of 0.01 wt.% or better, and were constrained to intersect with the origin in order to avoid systematic errors at the smallest measured values. Detection limit and accuracy were evaluated from the distributions of repeated values for standards and were found to be 0.01 wt.% or better for all elements, including H. All relevant factors that can affect the integrated signals were evaluated, including: sorbed water on the Sn combustion capsule; sorbed water on the sample itself; sorbed water on V_2O_5 combustion agent when used; and the errors in evaluating the integrated signals" [Rancourt *et al.* 2001].

Chapter 3. Sample Synthesis, Treatment, and Characterization

3.1 Hydrothermal synthesis and thermodynamic stability fields

As stated in [Chou & Cygan 1990]: "The pioneering work of [Eugster 1957] on the solid oxygen buffer technique provides a convenient way to control redox states in hydrothermal experiments. Information on the technique's basic theory, the experimental setups as well as its variations, and its applications are contained in papers by [Huebner 1971] and [Chou 1987a]. The basic experimental assembly consists of two nested capsules (Figure 1 [of their paper]) and has often been referred to as the double-capsule technique. The mineral assemblage under study and water are sealed in the inner capsule, constructed of either Pt or one of the Ag-Pd alloys, which are highly permeable to hydrogen. This charge system, together with an oxygen buffer assemblage and water, is in turn sealed in a larger outer capsule, made of either Au or Ag, which are relatively impermeable to hydrogen."

The buffer is usually composed of a metal with its most reduced oxide (e.g., Ni-NiO) or of two oxides with different cation oxidation states (e.g., magnetite, Fe_3O_4, and wüstite, $Fe_{1-x}O$). A buffer mixture resists changes in oxygen fugacity, f_{O_2} (or hydrogen fugacity, f_{H_2}), at constant total pressure, P, and temperature, T. At a fixed P-T condition, therefore, the fugacities of the gas species are fixed by equilibration of the fluid with the solid phases of the buffer, assuming that equilibrium redox states of the buffer system is achieved and maintained during the hydrothermal experiment.

However, the above assumption is not necessarily valid mainly due to the slow kinetics of the buffer reaction and/or the high rate of hydrogen leakage through the buffer container, as indicated by redox measurements of buffer systems made using the hydrogen sensor techniques [Chou & Cygan 1990; Chou & Eugster 1976; Chou 1978, 1987a, 1987b]. Therefore, some of the published data on mineral stability relations in $P-T-f_{O_2}$ or $P-T-f_{H_2}$ space may not be reliable.

Experimental phase relations of the micas are reviewed by D.A. Hewitt and D.R. Wones in Chapter 7 of [Bailey 1984]. Measured thermodynamic stability fields of trioctahedral micas relevant here are those of annite [Chou 1997; Dachs & Benisek 1997; Cygan *et al.* 1996; Dachs 1994; Eugster & Wones 1962], ferriannite [Wones 1963b], phlogopite-biotite solid solution [Wones & Eugster 1965], and Tschermak's substituted biotite [Benisek *et al.* 1996].

3.2 Sample synthesis and treatment

Nominal compositions and synthesis or treatment conditions of samples studied are listed in Table 3.1. In total, nine different sample series having the following structural formulas were investigated:

(3.1) $$\{K^{1+}\}[Co^{2+}_{3-w}\,Mg^{2+}_{w}]<Al^{3+}\,Si^{4+}_{3}>O^{2-}_{10}(OH)^{1-}_{2}$$

(Co-Mg JLR),

(3.2) $$\{K^{1+}\}[Mg^{2+}_{3-w}\,Ni^{2+}_{w}]<Al^{3+}\,Si^{4+}_{3}>O^{2-}_{10}(OH)^{1-}_{2}$$

(Mg-Ni JLR),

(3.3) $$\{K^{1+}\}[Fe^{2+}_{3-x-y-w}\,Mg^{2+}_{w}\,Fe^{3+}_{x}\,Al^{3+}_{y}]<Al^{3+}_{1-y}\,Si^{4+}_{3}\,Fe^{3+}_{y}>O^{2-}_{10+x+y}(OH)^{1-}_{2-x-y}$$

(Fe-Mg JLR),

(3.4) $$\{K^{1+}\}[Fe^{2+}_{3-x-y-w}\,Mg^{2+}_{w}\,Fe^{3+}_{x}\,Al^{3+}_{y}]<Al^{3+}_{1-y}\,Si^{4+}_{3}\,Fe^{3+}_{y}>O^{2-}_{10+x+y}(OH)^{1-}_{2-x-y}$$

(Fe-Mg RGB Al-normal),

(3.5) $$\{K^{1+}\}[Fe^{2+}_{3-x-y-w}\,Mg^{2+}_{w}\,Fe^{3+}_{x}\,Al^{3+}_{y}]<Al^{3+}_{1-y-v}Si^{4+}_{3}Fe^{3+}_{y+v}>O^{2-}_{10+x+y}(OH)^{1-}_{2-x-y}$$

(Fe-Mg RGB Al-poor),

(3.6) $\{K^{1+}\}[Fe^{2+}_{3-w-x}\ Mg^{2+}_{w}\ Fe^{3+}_{x}\ Al^{3+}_{v}]<Al^{3+}_{1+v}Si^{4+}_{3+v}>O^{2-}_{10+x}(OH)^{1-}_{2-x}$

(Fe-Mg RGB Al-rich),

(3.7) $\{K^{1+}\}[Fe^{2+}_{3-x-y-w}\ Ni^{2+}_{w}\ Fe^{3+}_{x}\ Al^{3+}_{y}]<Al^{3+}_{1-y}Si^{4+}_{3}Fe^{3+}_{y}>O^{2-}_{10+x+y}(OH)^{1-}_{2-x-y}$

(Fe-Ni GR),

(3.8) $\{K^{1+}\}[Fe^{2+}_{3-x-y}\ Fe^{3+}_{x}\ Al^{3+}_{y}]<Al^{3+}_{1-y}Si^{4+}_{3}Fe^{3+}_{y}>O^{2-}_{10+x+y}(OH)^{1-}_{2-z-x-y}F_{z}$

(annite-fluoroannite),

(3.9) $\{K^{1+}\}[Fe^{2+}_{3-x-y-3t}\ Fe^{3+}_{x+y+2t}\ \square_{t}]<Al^{3+}_{1-y}Si^{4+}_{3}Fe^{3+}_{y}>O^{2-}_{10+x+y}\ (OH)^{1-}_{2-x-y}$

(annite-oxyannite-ferrioxyannite),

where { }, [ ], and < > represent the interlayer, octahedral, and tetrahedral sites, respectively, and the symbol □ designates an octahedral vacancy.

The determination of the actual values of *w*, *x*, *y*, *u*, *v*, and *t* occurring in the mica phase of each sample, which are induced via various reactions (e.g., structural H loss via the oxybiotite reaction, Al/Fe exchange, Tschermak's substitution, etc.), will be discussed later.

In all syntheses that are studied in this work, no attempt was made to ascertain the attained fugacity values by the hydrogen sensor technique [Chou & Cygan 1990].

Details of the synthesis of the Co-Mg, Mg-Ni, and Fe-Mg JLR series can be found in [Diaz 1999]. These syntheses were performed by Dr. Jean-Louis Robert (JLR) at the CRSCM-CNRS Orléans, France. The starting materials were mechanical mixtures of gels prepared according to the method of [Hamilton & Henderson 1968]. Hydrogen fugacity was buffered by the nickel-nickel oxide (Ni-NiO) assemblage [Eugster & Wones 1962; Huebner & Sato 1970; Chou 1987a] using a variation of the double-capsule method devised by [Eugster 1957]. This variation of the Eugster's method, which was developed at the CRSCM-CNRS Orléans, permits the production of several hundreds of mg of sample during a single hydrothermal experiment.

Syntheses of the Fe-Mg RGB Al-normal, Al-poor, and Al-rich series were performed by Dr. Rob G. Berman (RGB) at the Geological Survey of Canada, Ottawa. Hydrothermal

experiments were conducted in cold-seal hydrothermal apparatus, with pressure vessels made from Haynes Alloy #25 (stellite) and CH_4 or H_2O as the pressure medium. Each pressure vessel was monitored by a 60,000 psi digital strain sensor (within 0.2 % linearity), calibrated to a Heise-Bourdon tube gauge certified by the manufacturer as accurate to within 0.1 % of full scale (0-50,000 psi). Temperatures were controlled and continually monitored by a digital data acquisition and control system made by Sciemetric Inc., Ottawa, Ontario, Canada. Between 100 to 150 mg of each starting stoichiometric mix was sealed in 4 mm O.D. - 3.8 mm I.D. Au capsules with pure H_2O or approximately 10 mg of $KHCO_3$ solution, prepared by adding 10 wt.% $KHCO_3$ to distilled water. The $KHCO_3$ solution was used instead of pure water to enhance reaction rates. All RGB syntheses were equilibrated with the graphite-methane (C-CH_4) buffer [Eugster & Skippen 1967; Chou 1987b].

Samples $Fe_{3.0}Mg_{0.0}$RGB and Fe_{100}RGB-Bi35 were synthesized from stoichiometric mixtures of $KSi_3O_{6.5}$ glass, prepared by the method of [Schairer & Bowen 1955], iron oxalate (FeC_2O_4•2H2O), and γ-Al_2O_3. The remaining samples of the Fe-Mg RGB Al-normal and Al-rich series were synthesized from iron oxalate, MgO, γ-Al_2O_3, K_2CO_3, and cristobalite (SiO_2), mixed to give nominal compositions listed in Table 3.1. MgO, γ-Al_2O_3, and cristobalite were prepared by firing MgO, $Al(OH)_3$, and silicic acid, respectively, at 1000 °C for 20 hours. As for the Fe-Mg RGB Al-poor sample series, they "were synthesized from stoichiometric mixes of $KSi_3O_{6.5}$ glass, prepared by the method of [Schairer & Bowen 1955], iron oxalate (FeC_2O_4•2H_2O), Al_2O_3 glass, and MgO. The latter two oxides were fired at 1000 °C for 20 hours prior to weighing" [Rancourt *et al.* 1994b].

The synthesis of the Fe-Ni GR sample series was done by Dr. Guenther Redhammer (GR) and is desribed in [Redhammer 1998]. These samples were synthesized by standard hydrothermal techniques ("Tuttle-type cold-seal autoclaves, horizontal furnaces, temperature control and regulation by use of Ni/NiCr thermocouples and electronic regulators, online control by a computer" [Redhammer 1998]) from oxide mixtures at redox conditions defined by the Ni-NiO buffer.

The synthesis of annite-fluoroannite sample series is detailed in [Rancourt *et al.* 1996]: "The starting products were mixtures of gels, prepared according to the gelling method of

[Hamilton & Henderson 1968], and dried solid fluorides, mechanically added to the gels in order realize the desired bulk stoichiometries [Table 3.1, present work]. Several fluorides were tested (FeF_2, AlF_3, and KF): all gave reproducible micas and phase assemblages. All experiments were performed in Tuttle-type externally heated pressure vessels at 720 °C, 1 kbar P_{H_2O}, with run durations of one week. The oxygen fugacity was controlled by the double capsule method of [Eugster 1957] using the magnetite-wüstite (MW) assemblage as a solid buffer."

Samples of the annite-oxyannite -ferrioxyannite are described in [Rancourt *et al.* 2001]: "The starting sample was the same synthetic annite sample [labelled as sample IKO-Ann in the present work] that has been characterized in detail by cryogenic and ambient temperature ^{57}Fe Mössbauer spectroscopy, high-field and low-field magnetometry, pXRD, SEM and IR [Rancourt *et al.* 1994a, 1994b]. The original synthesis yielded a large amount of product (10 g) and was not synthesized as previously incorrectly stated in [Rancourt *et al.* 1994a; Mercier 1996] but rather as follows. A hot-seal type autoclave having an internal volume 44 cm^3 was used in which ~10 g of stoichiometric starting gel was sealed in a silver tube and the correct amount of water was added to produce a synthesis pressure of 1 kbar at the synthesis temperature [T_{SYN}] of 600 °C. The relatively large amount of water (~14 cm^3) can take up a considerable amount of dissolved K. In order to ensure K stoichiometry of the annite product, therefore, the water was actually replaced by a 2 M solution of K, as KCl. This gave rise to a certain amount (~10 wt.%) of KCl impurity phase in the dry product that is described below and that does not otherwise affect the synthesis since Cl is not easily incorporated into mica structures [Volfinger *et al.* 1985]. [...]

The oxidized samples were prepared by heating small amounts (typically 20-100 mg) of [sample IKO-Ann] in air at different set temperatures for 5 h [...]. The quench was accomplished by simply pulling the sample and its open-ended quartz tube out of the furnace. The resulting quench rate is not expected to affect the results significantly, given what is known about the kinetics of the relevant reactions."

Sample Name	Nominal Composition	*P* (kbar)	Pressure Medium	T_{SYN} , T_{TR} (°C)	Buffer	Run Duration
Co-Mg JLR series						
$Co_{0.3}Mg_{2.7}$JLR	$\{K\}[Co_{0.3}Mg_{2.7}]<AlSi_3>O_{10}(OH)_2$	1	H_2O	600	Ni-NiO	2 weeks
$Co_{0.6}Mg_{2.4}$JLR	$\{K\}[Co_{0.6}Mg_{2.4}]<AlSi_3>O_{10}(OH)_2$	"	"	"	"	"
$Co_{0.9}Mg_{2.1}$JLR	$\{K\}[Co_{0.9}Mg_{2.1}]<AlSi_3>O_{10}(OH)_2$	"	"	"	"	"
$Co_{1.2}Mg_{1.8}$JLR	$\{K\}[Co_{1.2}Mg_{1.8}]<AlSi_3>O_{10}(OH)_2$	"	"	"	"	"
$Co_{1.5}Mg_{1.5}$JLR	$\{K\}[Co_{1.5}Mg_{1.5}]<AlSi_3>O_{10}(OH)_2$	"	"	"	"	"
$Co_{1.8}Mg_{1.2}$JLR	$\{K\}[Co_{1.8}Mg_{1.2}]<AlSi_3>O_{10}(OH)_2$	"	"	"	"	"
$Co_{2.1}Mg_{0.9}$JLR	$\{K\}[Co_{2.1}Mg_{0.9}]<AlSi_3>O_{10}(OH)_2$	"	"	"	"	"
$Co_{2.4}Mg_{0.6}$JLR	$\{K\}[Co_{2.4}Mg_{0.6}]<AlSi_3>O_{10}(OH)_2$	"	"	"	"	"
$Co_{2.7}Mg_{0.3}$JLR	$\{K\}[Co_{2.7}Mg_{0.3}]<AlSi_3>O_{10}(OH)_2$	"	"	"	"	"
$Co_{3.0}Mg_{0.0}$JLR	$\{K\}[Co_{3.0}Mg_{0.0}]<AlSi_3>O_{10}(OH)_2$	"	"	"	"	"
Mg-Ni JLR series[1]						
$Mg_{0.0}Ni_{3.0}$JLR-OH	$\{K\}[Mg_{0.0}Ni_{3.0}]<AlSi_3>O_{10}(OH)_2$	1	H_2O	600	Ni-NiO	2 weeks
$Mg_{0.0}Ni_{3.0}$JLR-OD	$\{K\}[Mg_{0.0}Ni_{3.0}]<AlSi_3>O_{10}(OD)_2$	"	"	"	"	"
$Mg_{0.3}Ni_{2.7}$JLR	$\{K\}[Mg_{0.3}Ni_{2.7}]<AlSi_3>O_{10}(OD)_2$	"	"	"	"	"
$Mg_{0.6}Ni_{2.4}$JLR	$\{K\}[Mg_{0.6}Ni_{2.4}]<AlSi_3>O_{10}(OD)_2$	"	"	"	"	"
$Mg_{0.9}Ni_{2.1}$JLR	$\{K\}[Mg_{0.9}Ni_{2.1}]<AlSi_3>O_{10}(OD)_2$	"	"	"	"	"
$Mg_{1.2}Ni_{1.8}$JLR	$\{K\}[Mg_{1.2}Ni_{1.8}]<AlSi_3>O_{10}(OD)_2$	"	"	"	"	"
$Mg_{1.5}Ni_{1.5}$JLR	$\{K\}[Mg_{1.5}Ni_{1.5}]<AlSi_3>O_{10}(OD)_2$	"	"	"	"	"
$Mg_{1.8}Ni_{1.2}$JLR	$\{K\}[Mg_{1.8}Ni_{1.2}]<AlSi_3>O_{10}(OD)_2$	"	"	"	"	"
$Mg_{2.1}Ni_{0.9}$JLR	$\{K\}[Mg_{2.1}Ni_{0.9}]<AlSi_3>O_{10}(OD)_2$	"	"	"	"	"
$Mg_{2.4}Ni_{0.6}$JLR	$\{K\}[Mg_{2.4}Ni_{0.6}]<AlSi_3>O_{10}(OD)_2$	"	"	"	"	"
$Mg_{2.7}Ni_{0.3}$JLR	$\{K\}[Mg_{2.7}Ni_{0.3}]<AlSi_3>O_{10}(OD)_2$	"	"	"	"	"
$Mg_{3.0}Ni_{0.0}$JLR	$\{K\}[Mg_{3.0}Ni_{0.0}]<AlSi_3>O_{10}(OD)_2$	"	"	"	"	"
Fe-Mg JLR series						
$Fe_{0.0}Mg_{3.0}$JLR	$\{K\}[Fe_{0.0}Mg_{3.0}]<AlSi_3>O_{10}(OH)_2$	1	H_2O	600	Ni-NiO	2 weeks
$Fe_{0.6}Mg_{2.4}$JLR	$\{K\}[Fe_{0.6}Mg_{2.4}]<AlSi_3>O_{10}(OH)_2$	"	"	"	"	"
$Fe_{1.2}Mg_{1.8}$JLR	$\{K\}[Fe_{1.2}Mg_{1.8}]<AlSi_3>O_{10}(OH)_2$	"	"	"	"	"
$Fe_{1.8}Mg_{1.2}$JLR	$\{K\}[Fe_{1.8}Mg_{1.2}]<AlSi_3>O_{10}(OH)_2$	"	"	"	"	"
$Fe_{2.4}Mg_{0.6}$JLR	$\{K\}[Fe_{2.4}Mg_{0.6}]<AlSi_3>O_{10}(OH)_2$	"	"	"	"	"
$Fe_{3.0}Mg_{0.0}$JLR	$\{K\}[Fe_{3.0}Mg_{0.0}]<AlSi_3>O_{10}(OH)_2$	"	"	"	"	"
Fe-Mg RGB Al-normal series						
$Fe_{0.75}Mg_{2.25}$RGB	$\{K\}[Fe_{0.75}Mg_{2.25}]<AlSi_3>O_{10}(OH)_2$	2	CH_4 or H_2O	700	C-CH_4	7-13 d
$Fe_{1.5}Mg_{1.5}$RGB	$\{K\}[Fe_{1.5}Mg_{1.5}]<AlSi_3>O_{10}(OH)_2$	2	"	700	C-CH_4	"
$Fe_{2.25}Mg_{0.75}$RGB	$\{K\}[Fe_{2.25}Mg_{0.75}]<AlSi_3>O_{10}(OH)_2$	2	"	700	C-CH_4	"
$Fe_{3.0}Mg_{0.0}$RGB	$\{K\}[Fe_{3.0}Mg_{0.0}]<AlSi_3>O_{10}(OH)_2$	2	"	700	C-CH_4	"

[1] Used deuterenated water (D_2O) instead of distilled water in all but one synthesis of this series.

Table 3.1. Nominal compositions and synthesis or treatment conditions of samples studied.

Sample Name	Nominal Composition	P (kbar)	Pressure Medium	T_{SYN}, T_{TR} (°C)	Buffer	Run Duration
Fe-Mg RGB Al-poor series						
$Fe_{25}Mg_{75}$RGBp	$\{K\}[Fe_{0.75}Mg_{2.25}]<AlSi_3>O_{10}(OH)_2$	2	CH_4 or H_2O	675	C-CH_4[1]	7-13 d
$Fe_{50}Mg_{50}$RGBp	$\{K\}[Fe_{1.5}Mg_{1.5}]<AlSi_3>O_{10}(OH)_2$	2	"	650	C-CH_4[1]	"
$Fe_{75}Mg_{25}$RGBp	$\{K\}[Fe_{2.25}Mg_{0.75}]<AlSi_3>O_{10}(OH)_2$	2	"	700	C-CH_4[1]	"
Fe_{100}RGBp	$\{K\}[Fe_3]<AlSi_3>O_{10}(OH)_2$	2	"	715	C-CH_4[1]	"
Fe-Mg RGB Al-rich series						
$Fe_{25}Mg_{75}$Bi33r	$\{K\}[Fe_{0.575}Mg_{1.725}Al_{0.7}]<Al_{1.7}Si_{2.3}>O_{10}(OH)_2$	2	CH_4 or H_2O	650	C-CH_4	7-13 d
$Fe_{50}Mg_{50}$Bi38r	$\{K\}[Fe_{1.1}Mg_{1.1}Al_{0.8}]<Al_{1.8}Si_{2.2}>O_{10}(OH)_2$	2	"	650	C-CH_4	"
$Fe_{75}Mg_{25}$Bi32r	$\{K\}[Fe_{1.725}Mg_{0.575}Al_{0.7}]<Al_{1.7}Si_{2.3}>O_{10}(OH)_2$	2	"	650	C-CH_4	"
Fe_{100}Bi35r	$\{K\}[Fe_{2.45}Al_{0.55}]<Al_{1.55}Si_{2.45}>O_{10}(OH)_2$	2	"	700	C-CH_4	"
$Fe_{25}Mg_{75}$Bi31r	$\{K\}[Fe_{0.575}Mg_{1.725}Al_{0.7}]<Al_{1.7}Si_{2.3}>O_{10}(OH)_2$	2	"	650	C-CH_4[1]	"
$Fe_{75}Mg_{25}$Bi30r	$\{K\}[Fe_{1.725}Mg_{0.575}Al_{0.7}]<Al_{1.7}Si_{2.3}>O_{10}(OH)_2$	2	"	650	C-CH_4[1]	"
Fe-Ni GR series						
$Fe_{0.0}Ni_{3.0}$GR	$\{K\}[Fe_{0.0}Ni_{3.0}]<AlSi_3>O_{10}(OH)_2$	4	H_2O:oil[2]	700	Ni-NiO	7-13 d
$Fe_{0.2}Ni_{2.8}$GR	$\{K\}[Fe_{0.2}Ni_{2.8}]<AlSi_3>O_{10}(OH)_2$	"	"	"	"	"
$Fe_{0.6}Ni_{2.4}$GR	$\{K\}[Fe_{0.6}Ni_{2.4}]<AlSi_3>O_{10}(OH)_2$	"	"	"	"	"
$Fe_{1.0}Ni_{2.0}$GR	$\{K\}[Fe_{1.0}Ni_{2.0}]<AlSi_3>O_{10}(OH)_2$	"	"	"	"	"
$Fe_{1.4}Ni_{1.6}$GR	$\{K\}[Fe_{1.4}Ni_{1.6}]<AlSi_3>O_{10}(OH)_2$	"	"	"	"	"
$Fe_{1.8}Ni_{1.2}$GR	$\{K\}[Fe_{1.8}Ni_{1.2}]<AlSi_3>O_{10}(OH)_2$	"	"	"	"	"
$Fe_{2.2}Ni_{0.8}$GR	$\{K\}[Fe_{2.2}Ni_{0.8}]<AlSi_3>O_{10}(OH)_2$	"	"	"	"	"
$Fe_{2.6}Ni_{0.4}$GR	$\{K\}[Fe_{2.6}Ni_{0.4}]<AlSi_3>O_{10}(OH)_2$	"	"	"	"	"
annite-fluoroannite series						
Ann-$F_{0.0}(OH)_{2.0}$	$\{K\}[Fe_3]<AlSi_3>O_{10}F_{0.0}(OH)_{2.0}$	1	H_2O	720	MW	1 w
Ann-$F_{0.4}(OH)_{1.6}$	$\{K\}[Fe_3]<AlSi_3>O_{10}F_{0.4}(OH)_{1.6}$	1	"	"	"	"
Ann-$F_{0.8}(OH)_{1.2}$	$\{K\}[Fe_3]<AlSi_3>O_{10}F_{0.8}(OH)_{1.2}$	1	"	"	"	"
Ann-$F_{1.0}(OH)_{1.0}$	$\{K\}[Fe_3]<AlSi_3>O_{10}F_{1.0}(OH)_{1.0}$	1	"	"	"	"
Ann-$F_{1.1}(OH)_{0.9}$	$\{K\}[Fe_3]<AlSi_3>O_{10}F_{1.1}(OH)_{0.9}$	1	"	"	"	"
Ann-$F_{1.2}(OH)_{0.8}$	$\{K\}[Fe_3]<AlSi_3>O_{10}F_{1.2}(OH)_{0.8}$	1	"	"	"	"
Ann-$F_{1.6}(OH)_{0.4}$	$\{K\}[Fe_3]<AlSi_3>O_{10}F_{1.6}(OH)_{0.4}$	1	"	"	"	"
annite-oxyannite-ferrioxyannite series						
IKO-Ann	$\{K\}[Fe_3]<AlSi_3>O_{10}(OH)_2$	1	H_2O	600	n/a	3 w
EM250	*Sample IKO-Ann annealed	n/a	n/a	250*	n/a	n/a
EM300	in air at these temperatures	"	"	300*	"	"
EM350	for 5 hours.	"	"	350*	"	"
EK350		"	"	350*	"	"
EK370		"	"	370*	"	"
EM400		"	"	400*	"	"
EM450		"	"	450*	"	"
EM500		"	"	500*	"	"
EM550		"	"	550*	"	"
EM600		"	"	600*	"	"

[1] Using 10 wt.% $KHCO_3$ solution instead of distilled water in the inner capsule.

[2] 20:1 ratio [Redhammer *et al*. 1993].

Table 3.1. Continued.

3.3 Sample characterization and impurity content

In this thesis, samples were characterized primarily by pXRD (powder X-ray diffraction) and Mössbauer spectroscopy. In addition, selected samples were also characterized by optical microscopy and SEM/EDS. In the production of synthetic mica samples, it is important to ascertain whether the run product is a single phase. All diffractograms were searched for the presence of peaks belonging to phases other than mica that are known to occur or that can occur from the bulk starting stoichiometries (Table 3.2).

Preliminary optical examination (i.e., right after synthesis) of the run products of all syntheses by Drs. J.-L. Robert, R.G. Berman, and G. Redhammer indicated almost complete reaction of all starting materials, and that mica was the main phase of all samples. This is confirmed by the characterization of the impurity content of the samples that was performed in this work, which is summarized in Table 3.3.

Samples of the Fe-Mg RGB Al-poor, annite-fluoroannite, and annite-oxyannite-ferrioxyannite series have already been characterized in [Rancourt *et al.* 1994b], [Rancourt *et al.* 1996], and [Rancourt *et al.* 2001], respectively. Slightly different conclusions than those given in the first two papers cited above were reached regarding the impurities that can be detected by pXRD, presumably because those studies used diffractograms of lesser quality.

All reflections that are observed in any given diffractogram of a particular sample can be indexed to belong either to an known impurity phase or to one of the various mica stacking polytypes, except for a few cases noted in Table 3.3. The identification of the impurity reflections detected in the diffractograms was done on the basis of pXRD patterns calculated using published crystal structure refinements retrieved from the crystal structure database that is available interactively on the web site of the Mineralogical Society of America (www.minsocam.org). I used the software programs XFIT (described in Chapter 2) or POWDER CELL Version 2.3 [Krauss & Nolze 1996] to simulate the impurity patterns. In the case of the presence of a mixture of mica stacking polytypes, I have determined the reflections belonging to each stacking polytype using the stacking polytype crystal structure models that are presented in Chapter 4. The stacking polytype content of the samples is discussed in Section 5.3. Results of

the identification of reflections observed for each sample series studied are presented in Appendix F to N, inclusively.

Impurity phase	Composition
kalsilite	KAlSiO4
sanidine	$KAlSi_3O_8$
olivine	$(Fe,Mg,Ni,Co)_2SiO_4$
almandine garnet	$Fe_3Al_2Si_3O_{12}$
hematite	Fe_2O_3
corrundum	Al_2O_3
leucite	$KAlSi_2O_6$
topaz	$Al_2(F,OH)_2[SiO_4]$
ilmenite	$MgSiO_3$
quartz	SiO_2
α-cristobalite	SiO2
brucite-type	$(Mg,Co,\ldots)(OH)_2$
cordierite	$(Mg,Fe,\ldots)_2Al_4Si_5O_{18}$
sillimanite	Al_2SiO_5
magnetite-type	$(Fe,Co,\ldots)_3O_4$
oxide	FeO, MgO, CoO
potassium oxide	KO_2, K_2O
hollandite	$KAlSi_3O_8$

Table 3.2. Impurity phases that were searched for in the diffractograms.

Sample	Impurities[1] detected by pXRD[2]	Impurities[1] detected by other methods[3,4]
Co-Mg JLR[5]	below detection limit	not measured
$Co_{0.3}Mg_{2.7}$JLR	below detection limit	not measured
$Co_{0.6}Mg_{2.4}$JLR	below detection limit	not measured
$Co_{0.9}Mg_{2.1}$JLR	below detection limit	not measured
$Co_{1.2}Mg_{1.8}$JLR	Sa	not measured
$Co_{1.5}Mg_{1.5}$JLR	Sa	not measured
$Co_{1.8}Mg_{1.2}$JLR	Sa	not measured
$Co_{2.1}Mg_{0.9}$JLR	Sa	not measured
$Co_{2.4}Mg_{0.6}$JLR	Sa	Sa, ~5% (SEM/EDS)
$Co_{2.7}Mg_{0.3}$JLR	Sa	not measured
$Co_{3.0}Mg_{0.0}$JLR	Sa	not measured
Mg-Ni JLR[5]		
$Mg_{0.0}Ni_{3.0}$JLR-OH	below detection limit	Sa, ~5% (OM)
$Mg_{0.0}Ni_{3.0}$JLR-OD	below detection limit	not measured
$Mg_{0.3}Ni_{2.7}$JLR	below detection limit	Sa, ~5% (OM)
$Mg_{0.6}Ni_{2.4}$JLR	below detection limit	not measured
$Mg_{0.9}Ni_{2.1}$JLR	below detection limit	not measured
$Mg_{1.2}Ni_{1.8}$JLR	below detection limit	not measured
$Mg_{1.5}Ni_{1.5}$JLR	below detection limit	Sa, ~5% (OM)
$Mg_{1.8}Ni_{1.2}$JLR	below detection limit	not measured
$Mg_{2.1}Ni_{0.9}$JLR	below detection limit	not measured
$Mg_{2.4}Ni_{0.6}$JLR	below detection limit	Sa, ~5% (OM)
$Mg_{2.7}Ni_{0.3}$JLR	below detection limit	not measured
$Mg_{3.0}Ni_{0.0}$JLR	Fo, Sa	not measured
Fe-Mg JLR[5]		
$Fe_{0.0}Mg_{3.0}$JLR	below detection limit	not measured
$Fe_{0.6}Mg_{2.4}$JLR	below detection limit	Mag (MBS)
$Fe_{1.2}Mg_{1.8}$JLR	below detection limit	not measured
$Fe_{1.8}Mg_{1.2}$JLR	Unknown[6], ?%	not measured
$Fe_{2.4}Mg_{0.6}$JLR	below detection limit	not measured
$Fe_{3.0}Mg_{0.0}$JLR	Sa	Sa, ~5% (OM); Mag (MBS)
Fe-Mg RGB Al-normal		
$Fe_{0.75}Mg_{2.25}$RGB	below detection limit	not measured
$Fe_{1.5}Mg_{1.5}$RGB	below detection limit	not measured
$Fe_{0.75}Mg_{2.25}$RGB	Sa	not measured
$Fe_{3.0}Mg_{0.0}$RGB	Fa, Sa	Fa, ~5%; Sa, ~5% (SEM/EDS both[7])

[1] Sa = sanidine ($KAlSi_3O_8$); Mag = magnetite (Fe_3O_4); Fa = fayalite (Fe_2SiO_4); Fo = forsterite (Mg_2SiO_4)

[2] No quantification was attempted by pXRD.

[3] MBS = Mossbauer spectroscopy; OM = optical microscopy.

[4] Expressed as Vol.% visually estimated, except for MBS where no quantification was attempted.

[5] See also [Diaz 1999].

[6] A peak from an unkown phase is detected at *d*-spacing 3.218 Angstroms (27.70 °2θ) in this sample.

[7] See [Mercier 1996]. In that reference, this sample is denoted as RB-25.

Table 3.3. Impurity phase content of the samples (continued on next page).

Sample	Impurities[1] detected by pXRD[2]	Impurities[1] detected by other methods[3,4]
Fe-Mg RGB Al-poor[5]		
$Fe_{25}Mg_{75}$RGBp	Lct	not measured
$Fe_{50}Mg_{50}$RGBp	Lct , Kls	Lct, ~5% (OM)
$Fe_{75}Mg_{25}$RGBp	Lct , Kls	not measured
Fe_{100}RGBp	Lct, Sa	not measured
Fe-Mg RGB Al-rich		
$Fe_{25}Mg_{75}$Bi33r	?Cor	Cor (SEM/EDS, [Berman, pers.comm.])
$Fe_{25}Mg_{75}$Bi38r	?Cor , ?Alm	Cor (SEM/EDS, [Berman, pers.comm.])
$Fe_{75}Mg_{25}$Bi32r	below detection limit	Cor (SEM/EDS, [Berman, pers.comm.])
Fe_{100}Bi35r	Fa , Alm	Cor (SEM/EDS, [Berman *et al*. 1995])
$Fe_{25}Mg_{75}$Bi31r	below detection limit	Cor (SEM/EDS, [Berman, pers.comm.])
$Fe_{75}Mg_{25}$Bi30r	below detection limit	Cor (SEM/EDS, [Berman, pers.comm.])
Fe-Ni GR		not measured
$Fe_{0.0}Ni_{3.0}$GR	?Sa	Sa, ~5% (OM)
$Fe_{0.2}Ni_{2.8}$GR	below detection limit	not measured
$Fe_{0.6}Ni_{2.4}$GR	below detection limit	not measured
$Fe_{1.0}Ni_{2.0}$GR	below detection limit	not measured
$Fe_{1.4}Ni_{1.6}$GR	below detection limit	not measured
$Fe_{1.8}Ni_{1.2}$GR	below detection limit	not measured
$Fe_{2.2}Ni_{0.8}$GR	below detection limit	not measured
$Fe_{2.6}Ni_{0.4}$GR	below detection limit	not measured
Ann-fluoroAnn[6]		not measured
Ann-$F_{0.0}(OH)_{2.0}$	Fa , Sa	Mag (SQUID)
Ann-$F_{0.4}(OH)_{1.6}$	Fa , Sa	not measured
Ann-$F_{0.8}(OH)_{1.2}$	Sa	not measured
Ann-$F_{1.0}(OH)_{1.0}$	Fa , Sa	not measured
Ann-$F_{1.1}(OH)_{0.9}$	Fa , Sa	not measured
Ann-$F_{1.2}(OH)_{0.8}$	below detection limit	not measured
Ann-$F_{1.6}(OH)_{0.4}$	Tpz , ?Fa , ?Sa	not measured
Ann-oxy-ferrioxy[7]		
IKO-Ann	KCl, x%	KCl (SEM/EDS[8])
EM250	KCl, x%	not measured
EM300	KCl, x%	α-Fe_2O_3, a-Fe oxide (Raman, MBS)[10]
EM350[9]	?KO_2, %	α-Fe_2O_3, a-Fe oxide (Raman, MBS)[10]
EK350	KCl, x%; Unknown[11]	α-Fe_2O_3, a-Fe oxide (Raman, MBS)[10]
EK370	KCl, x%	α-Fe_2O_3, a-Fe oxide (Raman, MBS)[10]
EM400	KCl, x%; Hem, x%	α-Fe_2O_3, a-Fe oxide (Raman, MBS)[10]
EM450	KCl, x%; ?KO_2, x%; Hem, x%	α-Fe_2O_3, a-Fe oxide (Raman, MBS)[10]
EM500	KCl, x%; ?KO_2, x%; Hem, x%	α-Fe_2O_3, a-Fe oxide (Raman, MBS)[10]
EM550	KCl, x%; ?KO_2, x%; Hem, x%	α-Fe_2O_3, a-Fe oxide (Raman, MBS)[10]
EM600	KCl, x%; ?KO_2, x%; Hem, x%	α-Fe_2O_3, a-Fe oxide (Raman, MBS)[10]

[1] Sa = sanidine ($KAlSi_3O_8$); Mag = magnetite (Fe_3O_4); Fa = fayalite (Fe_2SiO_4); Cor = corundum (Al_2O_3)
Hem = hematite (Fe_2O_3); Lct = leucite ($KAlSi_2O_6$); Kls = kalsilite ($KAlSiO_4$); Alm = almandine ($Fe_3Al_2Si_3O_{12}$);
Top = topaz ($Al_2[F,OH]_2SiO_4$). A ? sign indicates that only one or two peaks could unambiguously be attributed to this phase.

[2] No quantification was attempted by pXRD.

[3] MBS = Mossbauer spectroscopy; OM = optical microscopy, Raman = Raman spectroscopy; SQUID = SQUID magnetometry.

[4] Expressed as Vol.% visually estimated, except for MBS and SQUID where no quantification was attempted.

[5] See also [Rancourt *et al*. 1994b].

[6] See also [Rancourt *et al*. 1996].

[7] See also [Rancourt *et al*. 2001].

[8] See [Mercier 1996]. In that reference, this sample is denoted as HK-NNO.

[9] This sample was treated with chloroform to remove MBS absorber grease, which apparently removed KCl and produced KO_2.

[10] See [Rancourt *et al*. 2001] for a quantification of the relative amounts of the α-Fe_2O_3 and a-Fe oxide phases w.r.t. the mica phase.

[11] Two small unidentified peaks are seen at 3.52 and 3.50 Angstoms (25.28 and 25.43 $^o2\theta$, respectively) in this sample.

Table 3.3. Continued.

3.4 Elemental analyses of sample IKO-Ann

Results of the elemental analyses of sample IKO-Ann performed in this thesis are reported in [Rancourt *et al.* 2001]: "The XRF results, with accuracies calculated as explained [... in Section 2.5], can be stated as follows, with elemental amounts expressed as weight percentages of assumed oxides: 41.3(2)% Fe_2O_3, 30.2(3)% SiO_2, 8.6(1)% Al_2O_3, 14.55(1)% K_2O, and -2(%) LOI (i.e. gain). The total is consistent with the known KCl impurity and the fact that Cl was not analysed and the known ferric/ferrous ratio of the sample. Of all usual elements, the only significant impurity was one of 1860(80) ppm of Co (0.2% Co), probably arising from an impurity in the starting materials. We expect Co to behave as Fe^{2+} in the annite structure. If we ignore the Co, the relevant elemental ratios and their accuracies can be expressed as: Al/Si = 0.337(5), Fe/Si = 1.03(1), and K/Si = 0.615(6), compared to the ideal values of [...] $\frac{1}{3}$, 1 and $\frac{1}{3}$, respectively. The Al:Si:Fe ratio, therefore, is ideal within experimental error. At worst, there is a small excess of Fe (or Fe + Co), and no evidence for octahedral vacancies. The excess K is understood in terms of the synthesis method, as described [... in Section 3.2], and the excess (calculated as a weight ratio, KCl/annite = 12.3 %) is in quantitative agreement with the amounts of KCl estimated by pXRD, that fall in the range KCl/annite = 6-19 % (Table 2 [of the quoted reference]). These amounts of KCl are also consistent with the large crystal (~10 μm) crystals of KCl that are seen in SEM micrographs that have compositions confirmed by EDS [Mercier 1996].

The GC [gas chromatography] gives an independent evaluation of the total in [... sample IKO-Ann]. The result based on 10 different analyses is 0.33(1) wt.% H (one standard deviation error), in excellent agreement with the NRA result [nuclear reaction analysis result reported in the quoted reference]. [...] No S was detected. A small N signal is near the detection limit. There is also 0.122(1) wt.% C probably substituting for Si in the annite structure."

3.5 Iron site populations from room-temperature Mössbauer spectroscopy

As explained in [Rancourt *et al.* 2001]: "Since accurate Fe-site populations were required in this application [...], it was necessary to perform full absorber thickness corrections. [... I] used the procedure of [Rancourt 1989, 1996] that is implemented in Recoil [to accomplish this task]. This involves generating a synthetic thin-limit spectrum using the raw folded data, that is completely corrected for absorber thickness effects, both spectral shape and relative and absolute intensities. Such corrected spectra are then analysed in the same way as the raw folded spectra, using QSDs and HFDs. The only required user-supplied parameter for this exact correction is the average recoil-less fraction of the absorber material [Rancourt *et al.* 1993]. This recoil-less fraction has been measured to be $f_a = 0.5$ for synthetic annite [Royer 1991; Rancourt *et al.* 1994a], which is the value [... I] have used. It is important to note that the precise value of f_a, where, for example, $f_a = 0.7$ gives the same results within experimental error. [... It] is found that thickness effects cause systematic errors of several percent or more in site populations".

In obtaining site populations from Mössbauer spectroscopy, there is always the possibility that the site-specific or cation-species-specific recoil-less fractions may not be equal in a given sample [Rancourt 1989]. In the present work, equal recoil-less fractions were assumed for all Fe-sites in a given sample. For a complete explanation of the reasons validating that assumption, see [Rancourt *et al.* 2001].

The thin limit (or thickness corrected) spectra of the JLR and RGB samples were fitted with a 1-1-3 model: one tetrahedral Fe^{3+} site having one Gaussian component in its QSD, an octahedral Fe^{3+} site also having one Gaussian component, and an octahedral Fe^{2+} site with three Gaussian components in its QSD. All spectra were thickness corrected such that to each raw spectrum there corresponds a simulated thin-limit spectrum. The fitting parameters of the room-temperature thin-limit spectra of the JLR and RGB samples are given in Appendix O.

Table 3.4 gives the $<Fe^{3+}>$, $[Fe^{3+}]$, and $[Fe^{2+}]$ site populations of all iron-bearing samples. Site populations of Fe-Ni GR, annite-fluoroannite, and annite-oxyannite-ferrioxyannite samples were taken from [Redhammer pers.comm.], [Rancourt *et al.* 1996], and [Rancourt *et al.* 2001], respectively. All these studies employ the same methodology that is used here.

Sample	$<Fe^{3+}>/Fe_{tot}$ (%)	$[Fe^{3+}]/Fe_{tot}$ (%)	$[Fe^{2+}]/Fe_{tot}$ (%)	Fe_{oxide}/Fe_{tot} (%)
Fe-Mg JLR				
$Fe_{0.6}Mg_{2.4}$JLR	not used, Mag	not used, Mag	not used, Mag	not used, Mag
$Fe_{1.2}Mg_{1.8}$JLR	3.69(40)	11.38(46)	84.9(56)	b.d.l.[2]
$Fe_{1.8}Mg_{1.2}$JLR	2.52(32)	14.21(37)	83.26(44)	b.d.l.
$Fe_{2.4}Mg_{0.6}$JLR	4.40(29)	13.11(32)	82.49(39)	b.d.l.
$Fe_{3.0}Mg_{0.0}$JLR	not used, Mag	not used, Mag	not used, Mag	not used, Mag
Fe-Mg RGB Al-normal				
$Fe_{0.75}Mg_{2.25}$RGB	3.2(9)	3.5(9)	93.3(12)	b.d.l.
$Fe_{1.5}Mg_{1.5}$RGB	5.08(41)	2.23(49)	92.7(6)	b.d.l.
$Fe_{2.25}Mg_{0.75}$RGB	7.82(17)	2.47(23)	89.71(27)	b.d.l.
$Fe_{3.0}Mg_{0.0}$RGB	6.57(17)	3.08(20)	90.35(26)	b.d.l.
Fe-Mg RGB Al-poor				
$Fe_{25}Mg_{75}$RGBp	8.35	4.55	87.10	b.d.l.
$Fe_{50}Mg_{50}$RGBp	12.37	5.02	82.61	b.d.l.
$Fe_{75}Mg_{25}$RGBp	16.01	5.75	78.24	b.d.l.
Fe_{100}RGBp	16.09	6.37	77.54	b.d.l.
Fe-Mg RGB Al-rich				
$Fe_{25}Mg_{75}$Bi33r	b.d.l.	2.42(22)	97.58(22)	b.d.l.
$Fe_{50}Mg_{50}$Bi38r	b.d.l.	4.85(24)	95.15(24)	b.d.l.
$Fe_{75}Mg_{25}$Bi32r	b.d.l.	1.86(16)	98.14(16)	b.d.l.
Fe_{100}Bi35r	b.d.l.	5.26(35)	94.74(35)	b.d.l.
$Fe_{25}Mg_{75}$Bi31r	b.d.l.	10.88(23)	89.12(23)	b.d.l.
$Fe_{75}Mg_{25}$Bi30r	b.d.l.	3.51(11)	96.49(11)	b.d.l.
Fe-Ni GR				
$Fe_{0.2}Ni_{2.8}$GR	23.1	4.1	72.8	--
$Fe_{0.6}Ni_{2.4}$GR	11.0	7.6	81.4	--
$Fe_{1.0}Ni_{2.0}$GR	8.8	9.3	81.9	--
$Fe_{1.4}Ni_{1.6}$GR	8.6	10.0	81.4	--
$Fe_{1.8}Ni_{1.2}$GR	8.1	12.1	79.8	--
$Fe_{2.2}Ni_{0.8}$GR	8.9	10.6	80.5	--
$Fe_{2.6}Ni_{0.4}$GR	7.2	12.1	80.7	--
Ann-fluoroAnn				
Ann-$F_{0.0}(OH)_{2.0}$	4.46	2.99	92.55	b.d.l.
Ann-$F_{0.4}(OH)_{1.6}$	b.d.l.	3.56	96.44	b.d.l.
Ann-$F_{0.8}(OH)_{1.2}$	b.d.l.	4.16	95.84	b.d.l.
Ann-$F_{1.0}(OH)_{1.0}$	b.d.l.	2.24	97.76	b.d.l.
Ann-$F_{1.1}(OH)_{0.9}$	b.d.l.	2.64	97.36	b.d.l.
Ann-$F_{1.2}(OH)_{0.8}$	b.d.l.	3.00	97.00	b.d.l.
Ann-$F_{1.6}(OH)_{0.4}$	b.d.l.	8.28	91.72	b.d.l.
Ann-oxy-ferrioxy				
IKO-Ann	4.0(2)	7.0(2)	89.0(2)	b.d.l.
EM250	4.22(56)	9.28(63)	86.50(78)	b.d.l.
EM300	5.15(44)	20.78(44)	74.07(53)	b.d.l.
EM350	4.85(50)	47.35(45)	47.80(45)	b.d.l.
EK350	4.14(44)	52.08(38)	43.78(34)	b.d.l.
EK370	not modelled	66.80(15)	30.18(11)	3.02(16)
EM400	not modelled	79.80(31)	13.03(20)	7.17(29)
EM450	not modelled	88.86(38)	b.d.l.	11.14(38)
EM500	not modelled	89.40(32)	b.d.l.	10.60(32)
EM550	not modelled	88.35(35)	b.d.l.	11.65(35)
EM600	not modelled	88.09(34)	b.d.l.	11.91(34)

[1] Number in parentheses are one-sigma uncertainties estimated with the bootstrap method (see [Press *et al*. 1992] and references therein) implemented in Recoil.

[2] b.d.l.: Below detection limit (~0.1-2 %) for the Mössbauer spectrum collected on that sample.

Table 3.4. Iron site populations from Mössbauer spectroscopy for all Fe-bearing samples.

Chapter 4. Resolving the Different Stacking Polytypes

The identification and quantification of the individual crystalline phases in a mixture consisting of either various layer silicates or different stacking polytypes of a given mineral is a difficult problem that has been the subject of extensive work (e.g., see [Bailey 1984, 1988b; Reynolds 1985; Plançon 1981; Drits & Tchoubar 1990; Takeda & Ross 1995; Nespolo *et al.* 1997b, 2000; Ďurovič *et al.* 1984; Weiss & Wiewiora 1986]).

In this thesis, the problem of resolving the different mica stacking polytypes was handled in the following manner. Given the current knowledge regarding the occurrences of the various mica polytypes (see Sections 4.1 and 4.2), a set of fractional atomic coordinates was worked out for each common polytype by applying the proper generating (stacking) operations to a conventional 1*M* mica unit cell of space-group type *C*2/*m*. The coordinates that were derived ensure that all TOT layers in each stacking polytype structure are the same 1*M*-type TOT layer. It was then possible to calculate structure factors, simulate pXRD patterns, and establish clear criteria for the proper identification and quantification of the different stacking polytypes.

4.1 Introduction to mica polytypism

A concise introductory description of mica polytypism and its different stacking polytypes is given in [Nespolo 2001]:

> "Polytypism arises from the stacking of the M [TOT] layer along the *c* axis: the geometrical operation relating pairs of layers is a two-fold axis in the interlayer, and adjacent layers result rotated by $n \times 60^{\circ}$ ($0 \le n \le 5$) about c^*. Polytypes in which the position of any layer relative to the others and the transition from it to adjacent ones are the same or equivalent for all layers are termed *homogeneous* [Zvyagin 1988]. Homogeneous polytypes have successive M [TOT] layers rotated always by the same angle, apart from the sign, and correspond to the so-called "simple polymorphs" in [Smith & Yoder 1956]. By using [Ramsdell 1947] notation, homogeneous polytypes are identified as 1*M*, $2M_1$, 3*T*, $2M_2$, 2*O*, and 6*H* [...]. The remaining polytypes are termed *inhomogeneous* and correspond to the "complex polymorphs" in [Smith & Yoder 1956].

Mica polytypes are then suitably classified into three kinds, depending on the geometrical equivalence of layer pairs [Ďurovič *et al.* 1984; Nespolo 1999]: 1) *subfamily-A polytypes:* successive layers are rotated by $2n \times 60°$ only [1*M*, $2M_1$, and 3*T*]; 2) *subfamily-B polytypes:* successive layers are rotated by $(2n+1) \times 60°$ only [$2M_2$, 2*O*, and 6*H*]; 3) *mixed-rotation polytypes:* successive layers are rotated by both $2n \times 60°$ and $(2n+1) \times 60°$ (in all cases $0 \leq n \leq 5$) [...]."

The ideal space-group types of the six homogeneous polytypes are: *C*2/*m* (1*M*), *C*2/*c* ($2M_1$ and $2M_2$), $P3_{1,2}12$ (3*T*), *Ccmm* (2*O*), and $P6_{1,5}22$ (6*H*) [Zvyagin 1962].

4.2 Stacking polytype repartition

As summarized by [Ferraris *et al.* 2001]:

"Subfamily A polytypes are by far more common and among them 1*M* and $2M_1$ are the most abundant in trioctahedral and dioctahedral micas, respectively [Bailey 1984; Abbot &Burnham 1988]. The 3*T* polytype occurs particularly for phengitic compositions, ideally $KAl_{1.5}(Mg,Fe)_{0.5}[Si_{3.5}Al_{0.5}O_{10}](OH)_2$ (see [Ivaldi *et al.* 2001]); its occurrence in trioctahedral micas is also known (e.g. [Ross *et al.* 1966]), but the small number of structural reports might be due to difficulty of distinguishing it from a three-individual twin of 1*M* [... or to ambiguity in indexing the 3*T* polytype (Nespolo & Kogure 1998)]. Subfamily B polytypes are rarer and 6*H* is so far unknown; $2M_2$ occurs mainly in lepidolites (e.g. see [Guggenheim 1981]). A 'non-orthodox' 2*O* polytype has been reported in anandite, $BaFe^{2+}{}_3(Mg,Fe)_{0.5}[Si_3Fe^{3+}O_{10}]OHS$, from Sri Lanka and structurally refined [Giuseppetti & Tadini 1972; Filut *et al.* 1985] in the space-group type *Pnmn*. Because of ordering between S and OH, neither the structure nor its building layers can be described on the basis of *C*-centred cell common to all mica polytypes: this anandite does not represent a true mica polytype. The presence of S seems essential to stabilise the structure, which shows coordination 13 for Ba in the interlayer (12 O plus S). A 2*O* polytype has been reported in a synthetic fluor-phlogopite [Sunagawa *et al.* 1968], on the basis of surface observation only (the space-group type was not investigated), and a short 2*O* sequence has been observed by High Resolution Transmission Electron Microscopy (HRTEM) in a matrix of a [Ti-containing] magnesian annite [Kogure & Nespolo 1999].

[Lazarenko *et al.* 1978] observed by electron diffraction associated $2O$ and $1M$ polytypes of lepidolite, $(K_{1.03}Na_{0.01}Rb_{0.02}Ca_{0.02})$ $(Li_{1.49}Al_{0.89}Fe^{3+}_{0.05}Fe^{2+}_{0.39}Mg_{0.03}Ti_{0.02})$ $(Si_{3.58}Al_{0.42}O_{10})F_{1.59}(OH)_{0.41}$, within fine-lamellar aggregates; no crystal data were reported".

In the above quoted reference [Ferraris *et al.* 2001], the first structure determination of a $2O$ polytype in space-group type *Ccmm* is reported to occur in association with a $1M$ polytype.

Figure 4.1 shows a histogram representing the repartition of the different stacking polytypes amongst the selection of published crystal structures considered in this thesis. In total, two hundred thirty-five (235) mica structures were retrieved from the literature; these are compiled in separate databases for each of the $1M$, $2M_1$, $2M_2$, $2O$ and $3T$ polytypes in Appendices P to T, respectively.

In the case of the $1M$ database, a complete set of crystal structure data (including octahedral, tetrahedral, and interlayer bond lengths and angles, etc.) was extracted from each crystal structure refinement for the purpose of comparisons with simple geometrical models (see Chapter 6).

All crystal structures belonging to the $1M$, $2M_1$, $2M_2$, and $2O$ stacking polytypes are built from the M1 layer type, whereas the $3T$ polytype comprises structures that are built from M1 or M2 layer types (recalling Section 1.1, an M1 layer has the origin of the octahedral sheet in the $M1$site whereas an M2 layer has the origin of the octahedral sheet in either the $M2$ or the $M3$ site). It is important to point out that the selection of structural refinements considered in this thesis amounts to approximately 90 % of all published crystal structure refinements of micas. The remaining 10 % of structural refinements which were not included correspond to homogeneous stacking polytypes refined in subgroup symmetries: $1M$ polytype, space group $C2$ (which comprises structures built by M1 or M2 layer type), $2M_1$ polytype, space groups Cc and $C1$; and $3T$ polytype, space group $C12(1)$ (which also comprises structures built by M1 or M2 layer type) (for examples, see [Brigatti & Guggenheim 2002; Nespolo & Ďurovič 2002]).

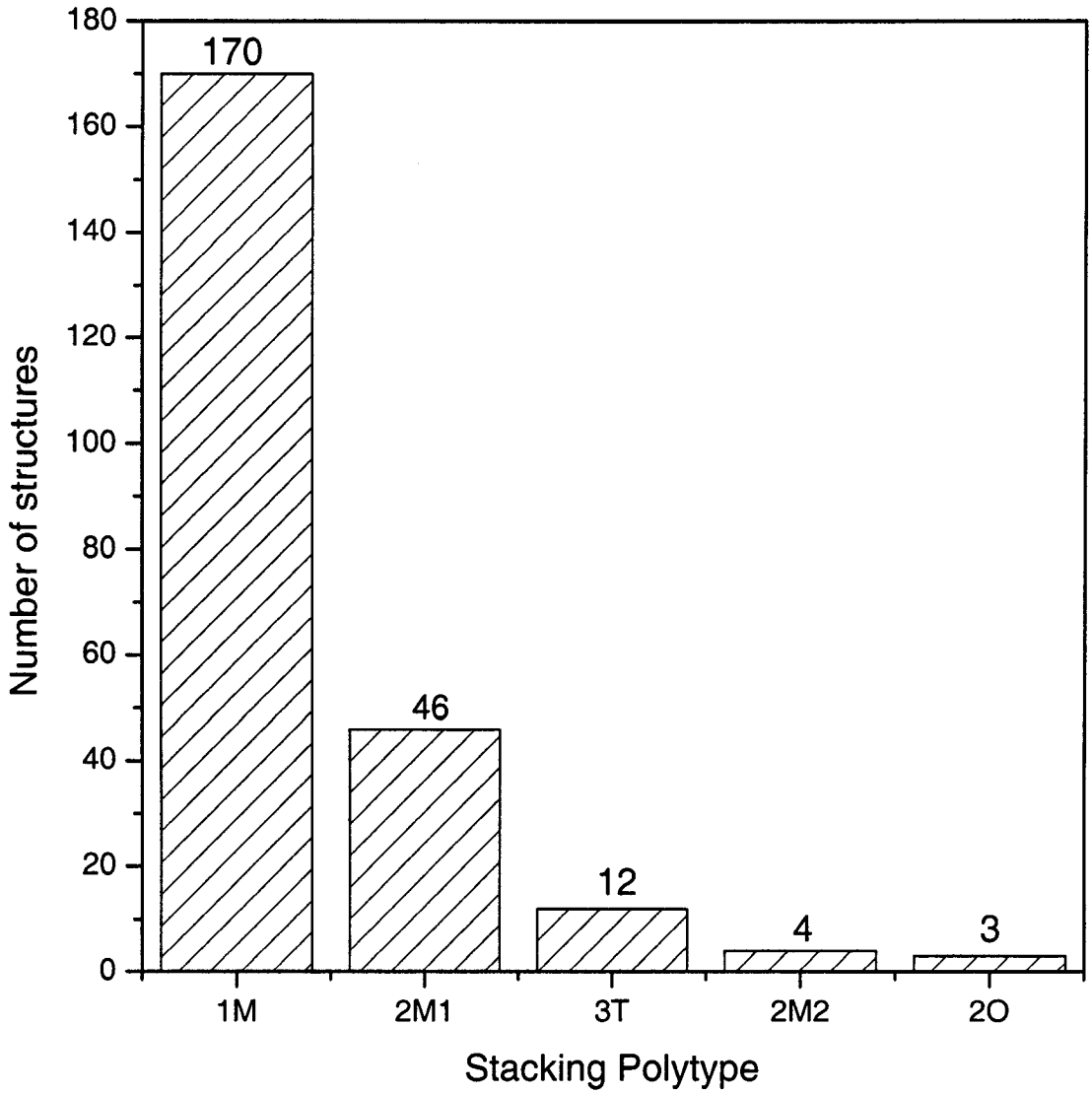

Figure 4.1. Histogram showing the repartition of mica polytypes amongst the selection of published crystal structure refinements (235 samples) considered in this thesis.

4.3 Crystal-structure models for selected stacking polytypes

For each selected stacking polytype (Table 4.1), fractional atomic coordinates were derived in terms of atomic positions in the unit cell of a conventional M layer (standard 1*M* layer). Tables 4.2 to 4.5 give fractional atomic coordinates for the $2M_1$, $2M_2$, $2O$, and $3T$ polytypes, respectively. Since the $6H$ polytype has never been observed in nature and that there exist only one crystal structure refinement of questionable quality for an inhomogeneous mica polytype [Rule *et al.* 1987], fractional atomic coordinates were not worked out for those polytypes.

Following the treatment of [Zvyagin 1962], one can show (see Maple worksheets contained in Appendix U) that these sets of fractional atomic coordinates (Tables 4.2 to 4.5) are exact and self-consistent provided that a few assumptions are made and a few appropriate steps are taken, which can be outlined as follows:

1. Transform fractional atomic coordinates from those of the 1*M* structure to orthogonal trimetric atomic coordinates $x'/a, y/b, z'/c'$, which, according to [Donnay *et al.* 1964]: "can be calculated in a rectangular system of axes Ox, Oy, Oz', in which Ox and Oy are the usual monoclinic axes], Oz' is normal to the cleavage plane (001), and $c' = c \sin\beta^*$ [$= c^*$; $\beta^* = 180° - \beta_{1M}$] is the interplanar distance d(001) [$= d_{001}$]. As consequences we have:

$$z/c = z'/c' ,$$

$$x = x' + z' \cot\beta^* = x' + z \cos\beta^* ,$$

$$x/a = x'/a + (z/c)(c/a)\cos\beta^* \quad " .$$

This coordinate transformation can be done using the transformation matrix 1*M*_to_*abc** listed in Table 4.1. The rectangular system of axes Ox, Oy, Oz' is hereafter referred to as *abc**, whereas the systems of axes of the different stacking polytypes are referred to as abc_{2M_1}, etc.

2. Apply an origin displacement that brings an *M*1 cation at $(0,0,0)_{abc^*}$ by adding translation vector $[1/2 \cdot c_{1M}/a_{1M} \cdot \cos\beta^* , 0 , -1/2]$ to atomic positions obtained from Step 1 above.

3. Build atomic coordinates of each individual n-th layer of the N-layer polytype ($N = 2$ for $2M_1$, $2O$, and $2M_2$; $N = 3$ for $3T$) by carrying out the following procedure:

   i) rotate all atoms of a standard cell about an axis parallel to c^* which goes through $M1$ located at $(0,0,0)_{abc^*}$, so that the orientation of the n-th layer (see Figure 1 of [Zvyagin 1962]) corresponds to its symbol and its respective position in the stacking sequence (Table 4.1) — for example, with polytype $2M_1$, the stacking sequence is $\overline{BA}$, hence $\overline{B}$ and $\overline{A}$ coincide with the first ($n = 1$) and second ($n = 2$) layer, respectively;

   ii) adjust z/c coordinates for all atoms of each n-th layer;

   iii) add an appropriate stacking vector to the rotated atomic coordinates of individual layers having $n \geq 2$;

   iv) add a centring vector that takes $M1$ cations of each n-th layer to their proper symmetry positions with respect to the centre of symmetry of the relevant space group specific for the given polytype — in the case of polytype $3T$, steps iii) and iv) were combined into individual vectors to be added to each n-th layer; and

   v) transform atomic coordinates expressed in the abc^* system to fractional atomic coordinates specific to each stacking polytype — this was accomplished using the appropriate coordinate transformation matrices given in Table 4.1 (see also Appendix U).

In the case of the 3T polytype, once the above procedure was applied, another centring vector needed to be added in order to obtain a set of fractional atomic coordinates consistent with that of [Guven & Burnham 1967 (M1 layer type); Brown 1978 (M2 layer type)].

Rotation matrices given in Table 4.1 are exact if $b_{1M} = \sqrt{3} \cdot a_{1M}$ (or $b = \sqrt{3} \cdot a$; if there are no subscripts in the label of the lattice parameters, this refers to a standard $1M$ cell). This assumption follows from the in-plane pseudo-hexagonal symmetry of mica layers (Section 6.1).

In the treatment presented above and in Table 4.1 below, please note that the Zvyagin's stacking symbols used here [Zvyagin 1962] are the oldest and have since been abandoned by the

author [Zvyagin *et al.* 1979; Zvyagin 1985]. The modern symbols are numerical, the correspondences being 3 – 2 – 1 – 6 – 5 – 4 for $C - \overline{A} - B - \overline{C} - A - \overline{B}$, respectively. Notice also that the complete stacking symbol of a given polytype actually includes three symbols for each TOT layer used in building the stacking sequence: two for each half-layer, one for the interlayer region (which is always 0 in the case of micas). Shortened symbols giving only one digit for each TOT layer within the stacking sequence of a given polytype are also used, but only in cases of polytypes entirely built by M1 layers. For a review of the state-of-the-art in the field of mica polytypes, see [Nespolo & Ďurovič 2002].

Rotation angle about an axis parallel to c^* through M1	Layer type [Zvyagin 1962]	Rotation matrices (if $b = 3^{1/2} \cdot a$) [Takeda 1966]	Coordinate transformation matrices
0°	C	$\begin{bmatrix} 1 & 0 & 0 \\ 0 & 1 & 0 \\ 0 & 0 & 1 \end{bmatrix}$	$abc_{1M}\text{TO}abc^* = \begin{bmatrix} 1 & 0 & -c_{1M}/a_{1M}\cos\beta^*_{1M} \\ 0 & 1 & 0 \\ 0 & 0 & 1 \end{bmatrix}$
60°	$\overline{A}$	$\begin{bmatrix} ½ & -½ & 0 \\ ½ & ½ & 0 \\ 0 & 0 & 1 \end{bmatrix}$	$abc^*\text{TO}abc_{2M_1} = \begin{bmatrix} 1 & 0 & c_{1M}/a_{1M}\cos\beta^*_{1M} \\ 0 & 1 & 0 \\ 0 & 0 & 1 \end{bmatrix}$
120°	B	$\begin{bmatrix} -½ & -½ & 0 \\ ½ & -½ & 0 \\ 0 & 0 & 1 \end{bmatrix}$	$abc^*\text{TO}abc_{3T} = \begin{bmatrix} 0 & 2 & 0 \\ -1 & 1 & 0 \\ 0 & 0 & 1 \end{bmatrix}$
180°	$\overline{C}$	$\begin{bmatrix} -1 & 0 & 0 \\ 0 & -1 & 0 \\ 0 & 0 & 1 \end{bmatrix}$	$abc^*\text{TO}abc_{2M_2}(a\text{ - unique}) = \begin{bmatrix} 1 & 0 & c_{1M}/a_{1M}\cos\beta^*_{1M} \\ 0 & 1 & 0 \\ 0 & 0 & 1 \end{bmatrix}$
-120°	A	$\begin{bmatrix} -½ & ½ & 0 \\ -½ & -½ & 0 \\ 0 & 0 & 1 \end{bmatrix}$	$abc_{2M_2}(a-\text{unique})TOabc_{2M_2}(b-\text{unique}) = \begin{bmatrix} 0 & 1 & 0 \\ -1 & 0 & 0 \\ 0 & 0 & 1 \end{bmatrix}$
-60°	$\overline{B}$	$\begin{bmatrix} ½ & ½ & 0 \\ -½ & ½ & 0 \\ 0 & 0 & 1 \end{bmatrix}$	

Selected stacking polytype	Stacking sequence [Zvyagin 1962]	Space group type	Space group No.	Lattice parameter relationships	Translation operations required (*SV* : stacking vector; *CV* : centring vector)
$2M_1$	$\overline{BA}$	$C2/c$	15	$a_{2M_1} = a_{1M}$; $b_{2M_1} = b_{1M}$ $c_{2M_1} = 2 \cdot c_{1M} \cdot \sin\beta_{1M}/\sin\beta_{2M_1}$ $\sin\beta_{2M_1} = \sqrt{1/\left(1+\left[1/\left(4\tan^2\beta^*_{1M}\right)\right]\right)}$	$SV_{n=2} = [1/2 - 1/2 c_{1M}/a_{1M}\cos\beta^*_{1M}, 0, 1/2]_{abc^*}$ $CV = [3/4, 1/4, 0]_{abc^*}$
$3T$	CBA	$P3_112$	151	$a_{3T} = a_{1M}$ $c_{3T} = 3 \cdot c_{1M}\sin\beta_{1M}$	$SV_{n=1} = [0, -1/3 \cdot (1/2 - 1/2 c_{1M}/a_{1M}\cos\beta^*_{1M}), 0]_{abc^*}$ $SV_{n=2} = [(1/2 - 1/2 c_{1M}/a_{1M}\cos\beta^*_{1M}), 1/6 \cdot (1/2 - 1/2 c_{1M}/a_{1M}\cos\beta^*_{1M}), 1/3]_{abc^*}$ $SV_{n=3} = [-(1/2 - 1/2 c_{1M}/a_{1M}\cos\beta^*_{1M}), 1/6 \cdot (1/2 - 1/2 c_{1M}/a_{1M}\cos\beta^*_{1M}), 2/3]_{abc^*}$
$2O$	$\overline{C}C$	$Ccmm$	63	$a_{2O} = a_{1M}$; $b_{2O} = b_{1M}$ $c_{2O} = 2 \cdot c_{1M}\sin\beta_{1M}$	None required
$2M_2$	$A\overline{B}$	$C2/c$	15	$a_{2M_2} = b_{1M}$; $b_{2M_2} = a_{1M}$ $c_{2M_1} = 2 \cdot c_{1M} \cdot \sin\beta_{1M}/\sin\beta_{2M_2}$ $\sin\beta_{2M_2} = \sqrt{1/\left(1+\left[3/\left(4\tan^2\beta^*_{1M}\right)\right]\right)}$	$SV_{n=2} = [0, 1/2 - 1/2 c_{1M}/a_{1M}\cos\beta^*_{1M}, 1/2]_{abc^*}$ $CV = [1/4, -1/4, 0]_{abc^*}$

Table 4.1. Selected stacking polytypes. The information listed here was used to derive fractional atomic coordinates for each polytype.

Atom	Multiplicity	Wyckoff letter	Site symmetry	x/a	y/b	z/c
I (interlayer)	4	e	2	0	$1/4(c_{1M}/a_{1M})\cos(180-\beta_{1M})$	1/4
M1 (*trans*)	4	d	-1	3/4	1/4	0
M2 (*cis*)	8	f	1	3/4 - 3/2*M2y	1/4 - 1/2*M2y	0.0
O4 (OH/F site)	8	f	1	1 - 1/2*O4x	1/2*O4x + (1/4-1/2*O4z)$(c_{1M}/a_{1M})\cos(180-\beta_{1M})$	1/4-1/2*O4z
O31 (apical)	8	f	1	3/4 - 1/2*O3x - 3/2*O3y	1/4 + 1/2*O3x - 1/2*O3y + (1/4-1/2*O3z)$(c_{1M}/a_{1M})\cos(180-\beta_{1M})$	1/4-1/2*O3z
O32 (apical)	8	f	1	1/4 - 1/2*O3x + 3/2*O3y	3/4 + 1/2*O3x + 1/2*O3y + (1/4-1/2*O3z)$(c_{1M}/a_{1M})\cos(180-\beta_{1M})$	1/4-1/2*O3z
T1 (T-cation)	8	f	1	3/4 - 1/2*Tx + 3/2*Ty	1/4 + 1/2*Tx + 1/2*Ty + (1/4-1/2*Tz)$(c_{1M}/a_{1M})\cos(180-\beta_{1M})$	1/4 - 1/2*Tz
T2 (T-cation)	8	f	1	3/4 - 1/2*Tx - 3/2*Ty	1/4 + 1/2*Tx - 1/2*Ty + (1/4-1/2*Tz)$(c_{1M}/a_{1M})\cos(180-\beta_{1M})$	1/4 - 1/2*Tz
O11 (basal)	8	f	1	1/4 - 1/2*O1x	3/4 + 1/2*O1x + (1/4-1/2*O1z)$(c_{1M}/a_{1M})\cos(180-\beta_{1M})$	1/4-1/2*O1z
O21 (basal)	8	f	1	3/4 - 1/2*O2x + 3/2*O2y	1/4 + 1/2*O2x + 1/2*O2y + (1/4-1/2*O2z)$(c_{1M}/a_{1M})\cos(180-\beta_{1M})$	1/4-1/2*O2z
O22 (basal)	8	f	1	3/4 - 1/2*O2x - 3/2*O2y	1/4 + 1/2*O2x - 1/2*O2y + (1/4-1/2*O2z)$(c_{1M}/a_{1M})\cos(180-\beta_{1M})$	1/4-1/2*O2z

Table 4.2. Fractional atomic coordinates used for crystal-structure model of stacking polytype $2M_1$.

Atom	Multiplicity	Wyckoff letter	Site symmetry	x/a	y/b	z/c
I (interlayer)	4	e	2	0	$1/2 - 1/4(c_{1M}/a_{1M})\cos(180-\beta_{1M})$	1/4
M1 (*trans*)	4	c	-1	1/4	1/4	0
M2 (*cis*)	8	f	1	3/4 - 1/2*M2y	3/2*M2y - 1/4	0.0
O4 (OH/F site)	8	f	1	1 - 1/2*O4x	$1 - 1/2*O4x + (-1/4+1/2*O4z)(c_{1M}/a_{1M})\cos(180-\beta_{1M})$	1/4-1/2*O4z
O31 (apical)	8	f	1	1/4 - 1/2*O3x - 1/2*O3y	$1/4 - 1/2*O3x + 3/2*O3y + (-1/4+1/2*O3z)(c_{1M}/a_{1M})\cos(180-\beta_{1M})$	1/4-1/2*O3z
O32 (apical)	8	f	1	3/4 - 1/2*O3x + 1/2*O3y	$3/4 - 1/2*O3x - 3/2*O3y + (-1/4+1/2*O3z)(c_{1M}/a_{1M})\cos(180-\beta_{1M})$	1/4-1/2*O3z
T1 (*T*-cation)	8	f	1	1/4 - 1/2*Tx - 1/2*Ty	$1/4 - 1/2*Tx + 3/2*Ty + (-1/4+1/2*Tz)(c_{1M}/a_{1M})\cos(180-\beta_{1M})$	1/4 - 1/2*Tz
T2 (*T*-cation)	8	f	1	3/4 - 1/2*Tx + 1/2*Ty	$3/4 - 1/2*Tx - 3/2*Ty + (-1/4+1/2*Tz)(c_{1M}/a_{1M})\cos(180-\beta_{1M})$	1/4 - 1/2*Tz
O11 (basal)	8	f	1	1/4 - 1/2*O1x	$1/4 - 1/2*O1x + (-1/4+1/2*O1z)(c_{1M}/a_{1M})\cos(180-\beta_{1M})$	1/4-1/2*O1z
O21 (basal)	8	f	1	1/4 - 1/2*O2x - 1/2*O2y	$1/4 - 1/2*O2x - 3/2*O2y + (-1/4+1/2*O2z)(c_{1M}/a_{1M})\cos(180-\beta_{1M})$	1/4-1/2*O2z
O22 (basal)	8	f	1	3/4 - 1/2*O2x + 1/2*O2y	$3/4 - 1/2*O2x + 1/2*O2y + (-1/4+1/2*O2z)(c_{1M}/a_{1M})\cos(180-\beta_{1M})$	1/4-1/2*O2z

Table 4.3. Fractional atomic coordinates used for crystal-structure model of stacking polytype $2M_2$.

Atom	Multiplicity	Wyckoff letter	Site symmetry	x/a	y/b	z/c
I (interlayer)	4	c	2mm	$1/2 + 1/2(c_{1M}/a_{1M})\cos(180-\beta_{1M})$	0	1/4
M1 (*trans*)	4	a	2/m..	0	0	0
M2 (*cis*)	8	e	2..	0	M2y	0
O4 (OH/F site)	8	f	m..	$1/2 + O4x + (1/2-O4z)(c_{1M}/a_{1M})\cos(180-\beta_{1M})$	0	1/4-1/2*O4z
O3 (apical)	16	h	1	$O3x + (1/2-O3z)(c_{1M}/a_{1M})\cos(180-\beta_{1M})$	O3y	1/4-1/2*O3z
T (*T*-cation)	16	h	1	$Tx + (1/2-Tz)(c_{1M}/a_{1M})\cos(180-\beta_{1M})$	Ty	1/4 - 1/2*Tz
O1 (basal)	8	f	m..	$O1x + (1/2-O1z)(c_{1M}/a_{1M})\cos(180-\beta_{1M})$	0	1/4-1/2*O1z
O2 (basal)	16	h	1	$O2x + (1/2-O2z)(c_{1M}/a_{1M})\cos(180-\beta_{1M})$	O2y	1/4-1/2*O2z

Table 4.4. Fractional atomic coordinates used for crystal-structure model of stacking polytype 2*O*.

Atom	Multiplicity	Wyckoff letter	Site symmetry	x/a	y/b	z/c
I (interlayer)	3	b	..2	$1/3(c_{1M}/a_{1M})\cos(180-\beta_{1M})$	$-1/3(c_{1M}/a_{1M})\cos(180-\beta_{1M})$	5/6
*M*1 (*trans*)	3	a	..2	$1/3 + 1/6 - 1/6(c_{1M}/a_{1M})\cos(180-\beta_{1M})$	$-\{ 1/3 + 1/6 - 1/6(c_{1M}/a_{1M})\cos(180-\beta_{1M}) \}$	1/3
*M*2 (*cis*)	3	a	..2	$1/3 + 1/6 - M2y - 1/6(c_{1M}/a_{1M})\cos(180-\beta_{1M})$	$-\{ 1/3 + 1/6 - M2y - 1/6(c_{1M}/a_{1M})\cos(180-\beta_{1M}) \}$	1/3
*M*3 (*cis*)	3	a	..2	$1/3 + 1/6 + M2y - 1/6(c_{1M}/a_{1M})\cos(180-\beta_{1M})$	$-\{ 1/3 + 1/6 + M2y - 1/6(c_{1M}/a_{1M})\cos(180-\beta_{1M}) \}$	1/3
O4 (OH/F site)	6	c	1	$1/3(c_{1M}/a_{1M})\cos(180-\beta_{1M})$	$1 - O4x + (O4z-1/3)(c_{1M}/a_{1M})\cos(180-\beta_{1M})$	1/3*O4z -1/6
O31 (apical)	6	c	1	$2*O3y + 1/3(c_{1M}/a_{1M})\cos(180-\beta_{1M})$	$1/2 - O3x + O3y + (O3z-1/3)(c_{1M}/a_{1M})\cos(180-\beta_{1M})$	1/3*O3z -1/6
O32 (apical)	6	c	1	$1 - 2*O3y + 1/3(c_{1M}/a_{1M})\cos(180-\beta_{1M})$	$1/2 - O3x - O3y + (O3z-1/3)(c_{1M}/a_{1M})\cos(180-\beta_{1M})$	1/3*O3z -1/6
T1 (T-cation)	6	c	1	$1 - 2*Ty + 1/3(c_{1M}/a_{1M})\cos(180-\beta_{1M})$	$1/2 - Tx - Ty + (Tz-1/3)(c_{1M}/a_{1M})\cos(180-\beta_{1M})$	1/3*Tz -1/6
T2 (T-cation)	6	c	1	$2*Ty + 1/3(c_{1M}/a_{1M})\cos(180-\beta_{1M})$	$1/2 - Tx + Ty + (Tz-1/3)(c_{1M}/a_{1M})\cos(180-\beta_{1M})$	1/3*Tz -1/6
O11 (basal)	6	c	1	$1/3(c_{1M}/a_{1M})\cos(180-\beta_{1M})$	$1/2 - O1x + (O1z-1/3)(c_{1M}/a_{1M})\cos(180-\beta_{1M})$	1/3*O1z -1/6
O21 (basal)	6	c	1	$1 - 2*O2y + 1/3(c_{1M}/a_{1M})\cos(180-\beta_{1M})$	$1/2 - O2x - O2y + (O2z-1/3)(c_{1M}/a_{1M})\cos(180-\beta_{1M})$	1/3*O2z -1/6
O22 (basal)	6	c	1	$2*O2y + 1/3(c_{1M}/a_{1M})\cos(180-\beta_{1M})$	$1/2 - O2x + O2y + (O2z-1/3)(c_{1M}/a_{1M})\cos(180-\beta_{1M})$	1/3*O2z -1/6

Table 4.5. Fractional atomic coordinates for stacking polytype 3*T*.

Chapter 5. Lattice Parameters and Stacking Polytype Contents

5.1 Lattice parameters: reproducibility, precision, and accuracy

The precision and accuracy of the lattice parameters ultimately depend on the degree of precision and accuracy of the line positions. In this section, I answer the following questions: What method should we use to evaluate the peak positions? What is the error associated to the reproducibility of the position of the diffraction lines? What is the magnitude of the observational error on the line positions in a given diffractogram? To what degree are the line positions accurate? Do we need to correct the line positions for any systematic errors? What is the precision on each of the refined lattice parameters? What is the accuracy on each of the refined lattice parameters?

Throughout this section, the following terms have the following meanings:

i) *reproducibility* refers to a set of diffractograms of a *given smear* collected under an identical experimental configuration, one after the other, and without removing the sample from the holder and replacing it on the diffractometer;

ii) *precision* refers to diffractograms of a *given sample* collected using different smears or different experimental conditions (e.g., different sizes of scatter slit, etc.); and

iii) *accuracy* refers to the uncertainty of a line position or of a lattice parameter when compared to a *certified* value.

5.1.1 Evaluation of the peak positions

In this subsection, I compare the results of two methods that were considered for the evaluation of the Cu $K\alpha_1$ peak positions: i) visual estimation, and ii) line-profile fitting of the diffraction lines using the FP approach implemented in XFIT (Subsection 2.1.4).

With the first method, I carefully examine each diffraction line of a pXRD pattern on an expanded angular scale and visually estimate the angle where the intensity profile of a given diffraction line has a maximum. The software program CELREF Beta Version by Laugier (www.inpg.fr/LMPG/) provides a user-friendly interface to perform this task. This method is simple and is equivalent to other common methods that rely on peak-finding routines based on second-derivative algorithms.

The separation of the $K\alpha_1$ and $K\alpha_2$ line, $\Delta\theta_{\alpha_1-\alpha_2}$, increases with the diffraction angle as

$$\Delta\theta_{\alpha_1-\alpha_2} = 2\left(\frac{\Delta\lambda}{\lambda}\right)\tan\theta \quad \text{(in radians)}, \tag{5. 1}$$

where $\Delta\lambda = \lambda_{\alpha_2} - \lambda_{\alpha_1}$ and $\lambda = \left(\lambda_{\alpha_2} + \lambda_{\alpha_1}\right)/2$. The $K\alpha$ doublet thus contributes a certain amount of broadening to a diffraction line. However, the intensity of the $K\alpha_1$ line is approximately twice as that of the $K\alpha_2$ line. So the broadening induced is asymmetric in nature. In the cases where the $K\alpha$ doublet is well resolved, we unambiguously assign $K\alpha_1$ line positions to the peaks with the lower 2θ values. In other cases where the $K\alpha$ doublet is not resolved, the $K\alpha_2$ contribution always appears as a shoulder on the high-angle side of the diffraction line and is progressively less apparent as 2θ decreases. In light of the above considerations, it is therefore correct (as a first-approximation) to attribute the Cu $K\alpha_1$ position to the angle corresponding to the maximum intensity of a diffraction line.

With the second method, I carry out a line-profile fitting for each diffraction line observed in a diffractogram using the FP approach implemented in XFIT (Subsection 2.1.4). I utilized a LAM file containing the data of Table 2.1 to generate the emission profile of a peak. The background was modelled as up to a 9th order orthonormalized Chebyshev polynomial. For each peak, a unique CS parameter was found sufficient to adequately model each line-profile, so that no other specimen-dependent parameters were adjusted. All diffractometer-dependent parameters were fixed at the actual values of the experimental configuration; namely, TA = 0.04 mm, ST = 0 mm, SW = 0.1 mm, SL = 18 mm, SAML = 10 mm (the size of the beam mask used),

SOUL = 12 mm, PS = 2.3°, and SS = 2.3°. In addition, I imposed a FSFL = 12 mm or a FSFA = 1° or 2°, which ever was appropriate, in order to properly account for the combination of divergent and scatter slits used in recording the diffractograms (as explained in Chapter 2, see explanations leading to Eqns. 2.1 to 2.4).

I have determined the $K\alpha_1$ line positions by these two methods for several diffractograms from samples IKO-Ann and $Ni_{3.0}$JLR, and from various standard reference materials (SRMs): SRM640b, silicon powder [Raspberry, 1987]; SRM640c, silicon powder [Freiman & Trahey 2000a]; and SRM660a, lanthanum hexaboride powder [Freiman & Trahey 2000b] (see Appendix V for details).

Table V.1 (Appendix V) compares the results yielded by each method. The $K\alpha_1$ line positions determined by the visual estimation method, $2\theta_{vis}$, the $K\alpha_1$ line positions obtained by the FP line-profile fitting method, $2\theta_{prf}$, and the differences between $K\alpha_1$ line positions extracted by each method, $\text{Diff.} = 2\theta_{vis} - 2\theta_{prf}$, are tabulated in separate columns. The average value of the differences $2\theta_{vis} - 2\theta_{prf}$ corresponding to a single diffractogram, <Diff.>, and the standard deviation of these differences, $\sigma_{Diff.}$, excluding outliers, are indicated at the bottom of the column corresponding to each diffractogram. Outliers always coincide with diffraction lines having weak intensities.

Additionally, Figures 5.1 and 5.2 illustrate the results of Table V.1 for various diffractograms measured on the left and right goniometers, respectively. On both Figures 5.1 and 5.2, each graph shows the differences, $\text{Diff.} = 2\theta_{vis} - 2\theta_{prf}$, for the various peaks observed in a single diffractogram. For each diffractogram, the values of <Diff.> and $\sigma_{Diff.}$ are also indicated.

For the diffractograms collected from acetone smears of sample IKO-Ann on either the left or right goniometer, the behaviours of the differences displayed are the same for all diffractograms. The values of <Diff.> and $\sigma_{Diff.}$ range from -0.0012 to 0.0213 °2θ and from 0.0140 to 0.0277 °2θ, respectively (Table V.1, Appendix V). The values of <Diff.> are mostly positive, indicating that the visual estimation method usually gives 2θ values that are slightly greater than the FP line-profile fitting method. However, the <Diff.> values are of the same order or less than the $\sigma_{Diff.}$ values, thereby revealing that these systematic differences are relatively

small compared to the width of the distribution of the differences $\text{Diff.} = 2\theta_{vis} - 2\theta_{prf}$ for a given diffractogram.

In the case of diffractograms measured on the left goniometer from SRMs, the values of Av. Diff. and $\sigma_{Diff.}$ range from -0.0054 to 0.0014 °2θ and from 0.0009 to 0.0068 °2θ, respectively; on the right goniometer, Av. Diff. and $\sigma_{Diff.}$ take on values of 0.0043 and 0.0088 °2θ and of 0.0064 and 0.0092 °2θ, respectively.

On the left goniometer, differences demonstrated by SRMs have <Diff.> and $\sigma_{Diff.}$ values which are approximately one order of magnitude smaller. It can also be noted that four <Diff.> values are positive and two others are negative. The reflections of the SRMs are much thinner than diffraction lines observed from acetone smears of sample IKO-Ann, because SRMs introduce a minimal amount of sample-induced line broadening. As a result, the peak positions are much more constrained and the resolution of the diffraction lines is better.

The distinctions between differences in line positions from acetone smears of sample IKO-Ann and those of SRMs are clearly exhibited in Figures 5.1 and 5.2. We can observe that the scatter is much larger for the IKO-Ann graphs than in the graphs corresponding to mixtures of SRMs. Further, the scatter of IKO-Ann graph does not seem to vary with the evolution of the 2θ angle for both goniometers (Figures 5.1 and 5.2).

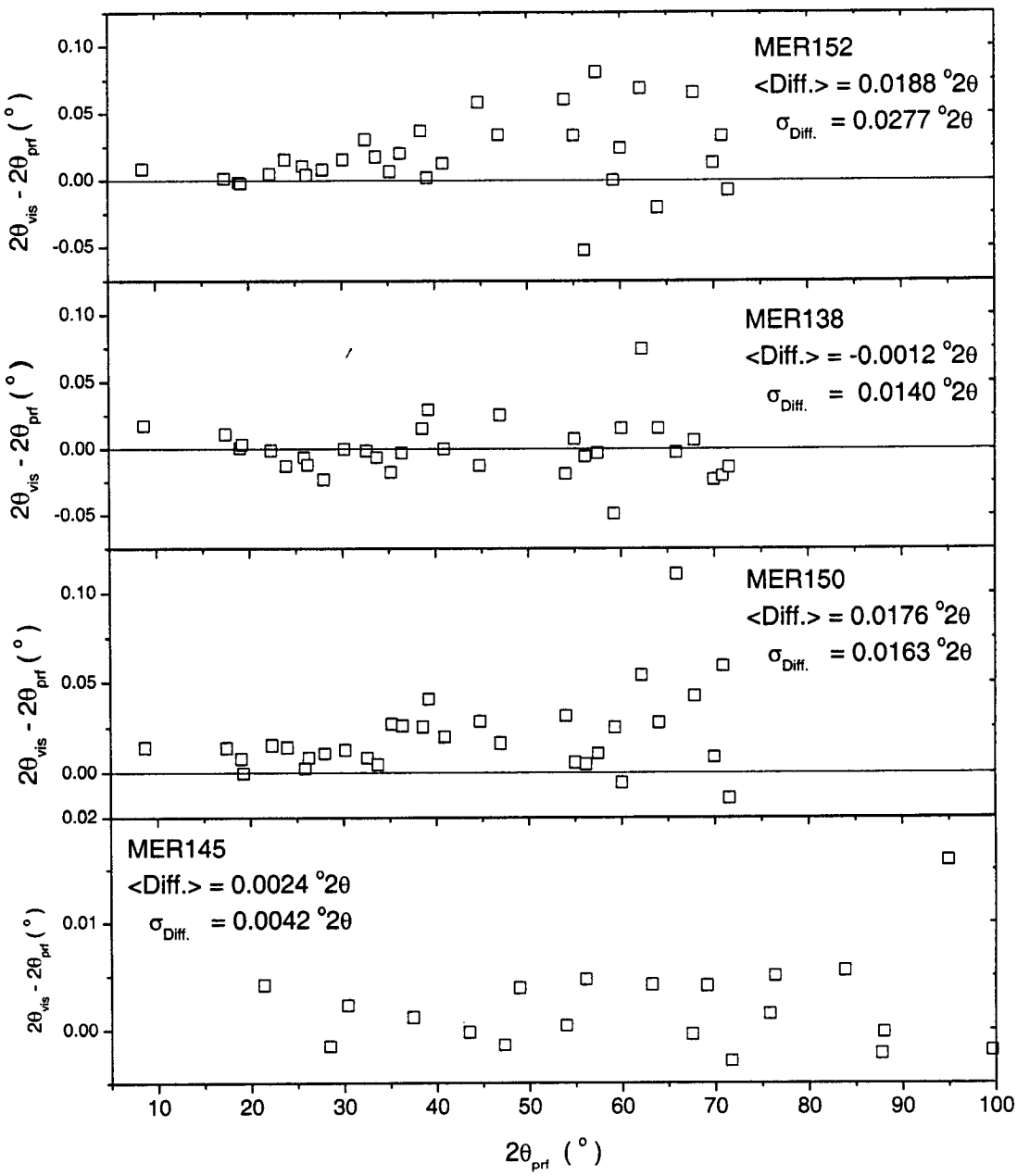

Figure 5.1. Comparison of $K\alpha_1$ line positions obtained by the visual estimation and FP line-profile fitting methods for selected diffractograms measured on the left goniometer (see text for a description of the content of the figure).

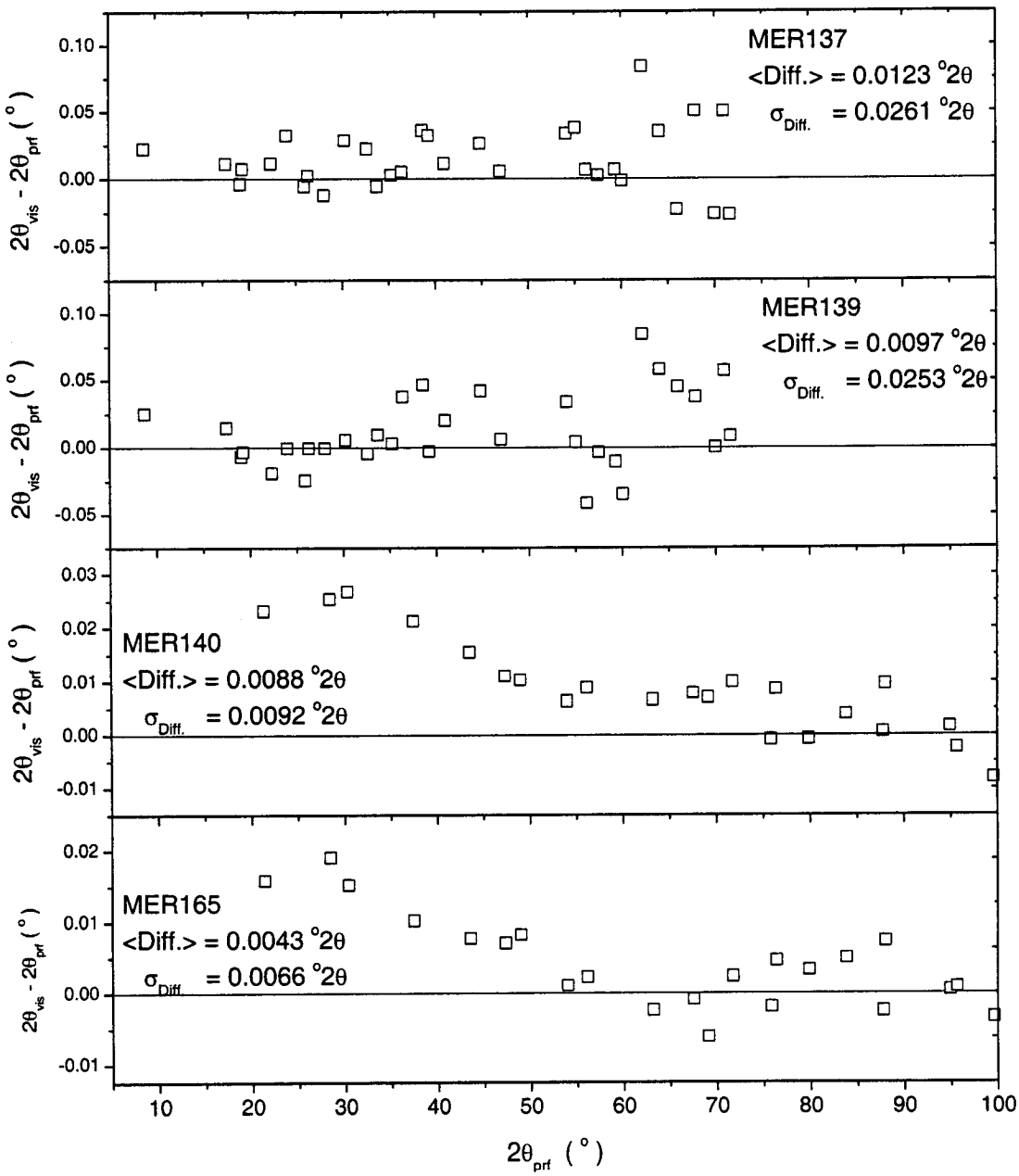

Figure 5.2. Comparison of $K\alpha_1$ line positions obtained by the visual estimation and FP line-profile fitting methods for selected diffractograms measured on the right goniometer (see text for a description of the content of the figure).

Assuming that the measurement errors of line positions in a given diffractogram can be determined for each method, and since $\sigma_{Diff.}$ is proportional to $\sqrt{\sigma_{vis}^2 + \sigma_{prf}^2}$ (assuming uncorrelated errors into error propagation), where σ_{vis} and σ_{prf} are the measurement errors of line positions in a given diffractogram evaluated by visual estimation and FP fitting, respectively, then the fact that $\sigma_{Diff.}$ values are approximately one order of magnitude larger for IKO-Ann than for SRMs means that line positions are established more precisely in the case of SRMs. I will estimate the measurement errors of each method in the next two subsections.

In the case of the right goniometer, Figure 5.2 also shows that the scatter in the IKO-Ann graphs is much larger than in those of SRMs. On the other hand, we notice a systematic increase in the differences below $2\theta \approx 50^0$ as the diffractometer angle decreases in the case of SRMs (Figure 5.2).

I impute this artifact to the following factors: i) the Kevex detector of the right goniometer yields more counts for the same sample than the gas-filled proportional counter of the left goniometer, thereby causing the resolution of the reflections and the signal-to-noise to be augmented on the right goniometer; ii) the asymmetry of the peak is larger on the right than on the left goniometer because axial divergence is enhanced due to the smaller radius of the right goniometer; iii) as a result of i) and ii), the peaks on the right goniometer can be observed with high enough resolution and asymmetry to give rise to the systematics described above.

In summary, I conclude that: i) for diffractograms measured on the left goniometer from both IKO-Ann and SRMs, as well as for diffractograms recorded on the right goniometer from IKO-Ann, the visual estimation method gives $K\alpha_1$ line positions that are slightly greater than those obtained by the FP line-profile fitting method; and ii) in the case of diffractograms from SRMs recorded on the right goniometer, the differences between the $K\alpha_1$ line positions obtained by the two methods significantly augment as 2θ decreases when the diffractometer angle is below $2\theta \approx 50^0$. In the next three subsections, I will determine the precision and accuracy associated to each method and establish the extent to which these relatively small peak position differences play an important role.

5.1.2 Reproducibility of the peak positions

In order to find out the reproducibility of the peak positions, three diffractograms (MER151, MER152, and MER153) of a single smear of sample IKO-Ann were collected on the left goniometer under an identical experimental configuration, one after the other, and without removing the silicon wafer from the sample holder and putting it back in between each measurement. This sequence of measurements allows one to single out the following factors of the many sources of error: i) peculiarities of the diffraction patterns of the samples (i.e., degree of overlap of reflections, line broadening due to microstructural properties, etc.); ii) the quality of the experimental data (i.e., signal-to-noise, degree of resolution of the reflections, etc.); and iii) instrumental contributions related to the control of the goniometer's 2θ positions, the variable divergence slit, and the receiving slit.

Having evaluated the $K\alpha_1$ line positions of each peak j observed in the diffraction pattern of sample IKO-Ann for each of the diffractograms MER151-152-153 separately (Table V.1), by both the visual estimation and the FP line-profile methods, I have computed the average position of each reflection j as:

$$2\theta_j^{mean} = \frac{1}{K}\sum_{k=1}^{K} 2\theta_{j,k} \quad , \tag{5.2}$$

where k designates a particular diffractogram in the set of K diffractograms. Then, the standard deviation of the position of the j-th reflection is given by:

$$\sigma_j = \sqrt{\frac{1}{K-1}\sum_{k=1}^{K}\left(2\theta_{j,k} - 2\theta_j^{mean}\right)^2} \quad . \tag{5.3}$$

With $K = 3$, however, it must be realized that the σ_j values overestimate the measurement error of the position of a given reflection in most cases.

I have also computed the average value, $\left(\sigma_j\right)_{av}$, and standard deviation, $\left(\sigma_j\right)_{sd}$, of the σ_j values. If we assume that the σ_j values are independent measurements of the error in the peak position at various 2θ angles across a diffractogram, and that the nature of the errors is the same for all peaks at all 2θ, then: i) $\left(\sigma_j\right)_{av}$ represents an estimation of the overall magnitude of the observational error on the line positions in a given diffractogram; and ii) $\left(\sigma_j\right)_{sd}$ gives a measure of the uncertainty of $\left(\sigma_j\right)_{av}$.

Figure 5.3 shows the standard deviations, σ_j, versus mean position, $2\theta_j^{mean}$, of each diffraction peak j computed from the measured $K\alpha_1$ line positions on diffractograms MER151-152-153 (Table V.1). The average value, $\left(\sigma_j\right)_{av}$, and standard deviation, $\left(\sigma_j\right)_{sd}$, of the σ_j values, obtained using relations similar to those of Eqns. 5.2 and 5.3 (excluding the outliers that are circled on each graph), are indicated on the graph corresponding to each method. Since diffractograms MER151-152-153 correspond to repeated measurements under an identical experimental configuration, the $\left(\sigma_j\right)_{av}$ and $\left(\sigma_j\right)_{sd}$ values reported in Figure 5.3 provide an estimate of the reproducibility error on the peak positions from our samples for each method.

The visual estimation method gives $\left(\sigma_j\right)_{av}$ and $\left(\sigma_j\right)_{sd}$ values of 0.016 and 0.013 °2θ, respectively, whereas those obtained by FP line-profile fitting are approximately three times smaller, yielding $\left(\sigma_j\right)_{av}$ and $\left(\sigma_j\right)_{sd}$ values equal to 0.0054 and 0.0042 °2θ, respectively. Thus, the FP line-profile fitting method is more precise than that of visual estimation in terms of determining the peak positions for our samples.

In conclusion, because of the reproducibility error, the ultimate precision of the $K\alpha_1$ line positions which can be achieved is of 0.005 to 0.01 °2θ with the FP line-profile fitting method and of 0.01 to 0.02 °2θ with the visual estimation method.

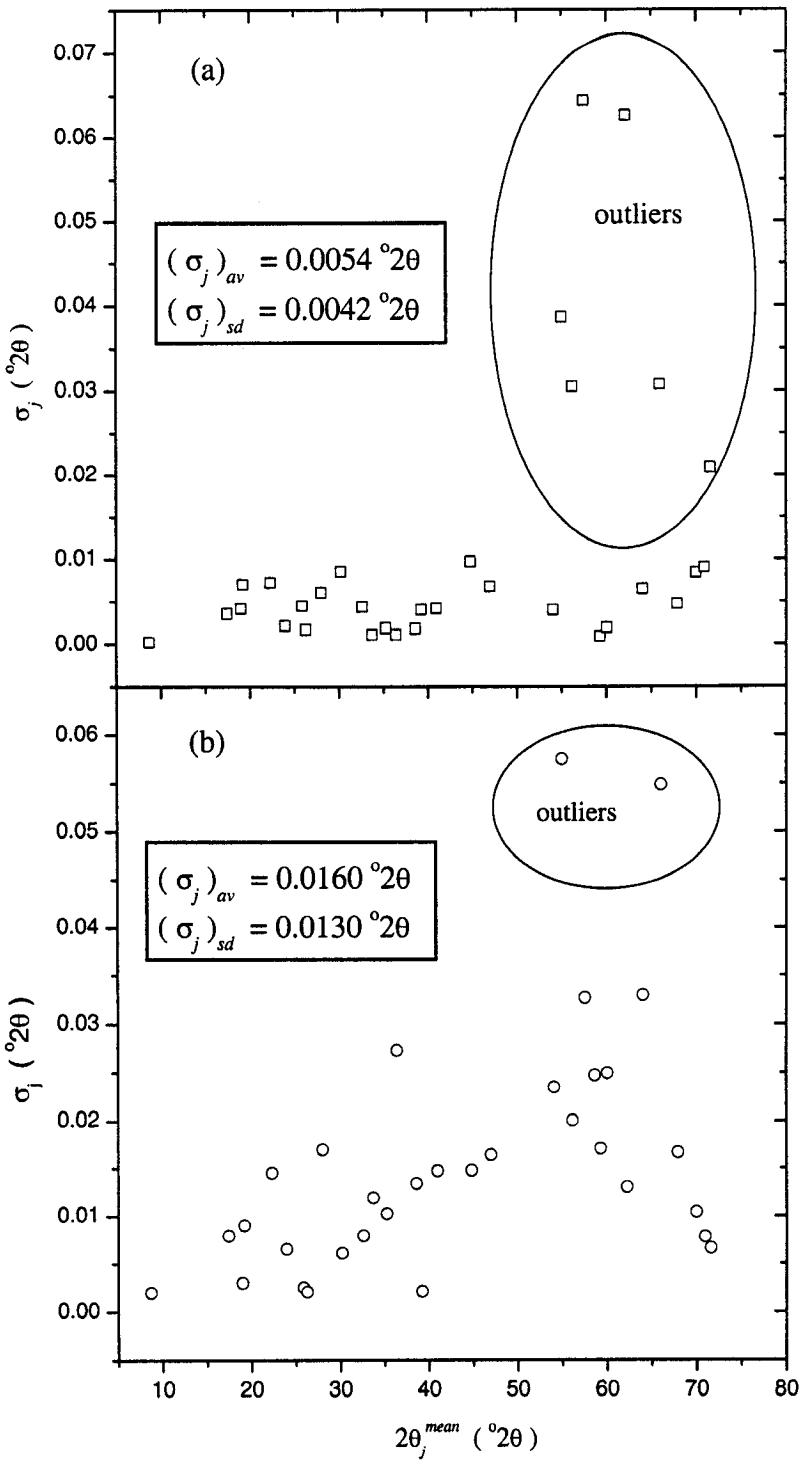

Figure 5.3. Reproducibility error evaluated by: (a) the FP line-profile fitting method, and (b) the visual estimation method. Symbols are explained in the text, along with a description of the content of the figure.

5.1.3 Precision and accuracy of the peak positions

Besides the random reproducibility error, that is mainly determined by the noise level in the data, systematic and non-statistical random errors are attributable to a combination of the following factors: uniformness of smears (thickness, distribution of material over the diffracting sample area, etc.), exact position of goniometer's reference surface from one measurement to another (i.e., the effect of putting the sample in and out), amount of noise present (tolerated) in the data, differences in experimental configurations (e.g., different sizes of scatter slit, etc.), and sample-dependent properties (e.g., degree of overlap between reflections, particle-size broadening, etc.).

Table V.2 (Appendix V) compares values of $\left(\sigma_j\right)_{av}$ and $\left(\sigma_j\right)_{sd}$ computed from $K\alpha_1$ line positions reported in Table V.1 for various sets of diffractograms. For sets of diffractograms from IKO-Ann and for both the visual estimation and the FP line-profile fitting methods, one sees that $\left(\sigma_j\right)_{av}$ and $\left(\sigma_j\right)_{sd}$ values are of the same order as those established in the preceding subsection for the reproducibility error. Thus, it seems that factors external to those associated to the reproducibility error do not significantly augment the magnitude of the observational error on the peak positions for diffractograms from sample IKO-Ann. Since the diffractograms of all the samples are similar to those of IKO-Ann, I therefore conclude that the peak positions in a given diffractogram can be measured within a precision of ~0.0075 °2θ with FP line-profile fitting and of ~0.015 °2θ with visual estimation.

Note also that $\left(\sigma_j\right)_{av}$ and $\left(\sigma_j\right)_{sd}$ values obtained from considering diffractograms of SRMs are approximately the same for both the visual estimation and the FP line-profile fitting methods, ranging from 0.0010 to 0.0050 °2θ for both $\left(\sigma_j\right)_{av}$ and $\left(\sigma_j\right)_{sd}$. As explained earlier, because SRMs introduce a minimal amount of sample-induced line broadening, the resolution of the diffraction lines is better and the peak positions are more constrained. So in the case of SRMs, the peak positions can be measured with a precision error smaller than 0.005 °2θ with either visual estimation or FP line-profile fitting.

Let us turn to the accuracy of the line positions. Figures 5.4 (left goniometer) and 5.5 (right goniometer) compare 2θ values determined from certified SRMs's lattice parameters [Freiman & Trahey 2000a, 2000b; Raspberry 1987], $2\theta_{cert.}$, to $K\alpha_1$ line positions evaluated by

visual estimation and FP fitting, assuming $\lambda_{\alpha_1} = 1.5406$ Å.

The diffractograms referred to in Figures 5.4 and 5.5 were ran at various points in time. For the sets of measurements ran in November 2001 (MER140-145-148 and SRM640c_6NOV2001) and March 2002 (MER154-165), on both the left and right goniometers, one sees that the scatter on the y-axis of all graphs of Figures 5.4 and 5.5 is of the order of the precision error on line positions from SRMs established earlier in the current subsection, such that all points, within an uncertainty of ±0.005 °2θ, usually follow monotonic decreasing trends in going from low to high angles.

On the left goniometer, for measurements ran in November 2001 and March 2002, the points scatter around values of $\left(2\theta_{vis} - 2\theta_{cert.}\right)$ and $\left(2\theta_{prf} - 2\theta_{cert.}\right)$ nearly equal to zero for all $2\theta_{cert.}$ values, except for a slight interval towards lower $2\theta_{cert.}$ values where small positive values of $\left(2\theta_{vis} - 2\theta_{cert.}\right)$ and $\left(2\theta_{prf} - 2\theta_{cert.}\right)$ are observed as the general trend. The latter feature is more pronounced with the visual estimation method. On the other end, MER064 (November 1998) and s002_hkl (March 1999) display net differences $\left(2\theta_{vis} - 2\theta_{cert.}\right)$ and $\left(2\theta_{prf} - 2\theta_{cert.}\right)$ ranging from 0.030 and 0.025 °2θ with visual estimation and FP fitting, respectively, at low $2\theta_{cert.}$ values, down to approximately zero as $2\theta_{cert.}$ increases. The decrease is more regular with FP fitting.

On the right goniometer, values of differences $\left(2\theta_{vis} - 2\theta_{cert.}\right)$ diminish monotonically from 0.010 °2θ at 20° to -0.025 °2θ at 100°. As for the differences $\left(2\theta_{prf} - 2\theta_{cert.}\right)$, they first evolve on a plateau at -0.015 °2θ up to $2\theta \approx 50^0$, and then decrease progressively to -0.025 °2θ at 100°. This difference in behaviour of line positions from visual estimation and FP fitting on the right goniometer has already been explained in the context of Figure 5.2.

In summary, Figures 5.4 and 5.5 provide the state of the goniometers's alignment at the times specified above. Corrections to line positions for any systematic errors would have to come, at least partially, from considerations related to these two figures. However, as will be demonstrated in the next subsection, given the precision error on the refined lattice parameters, no such corrections are necessary.

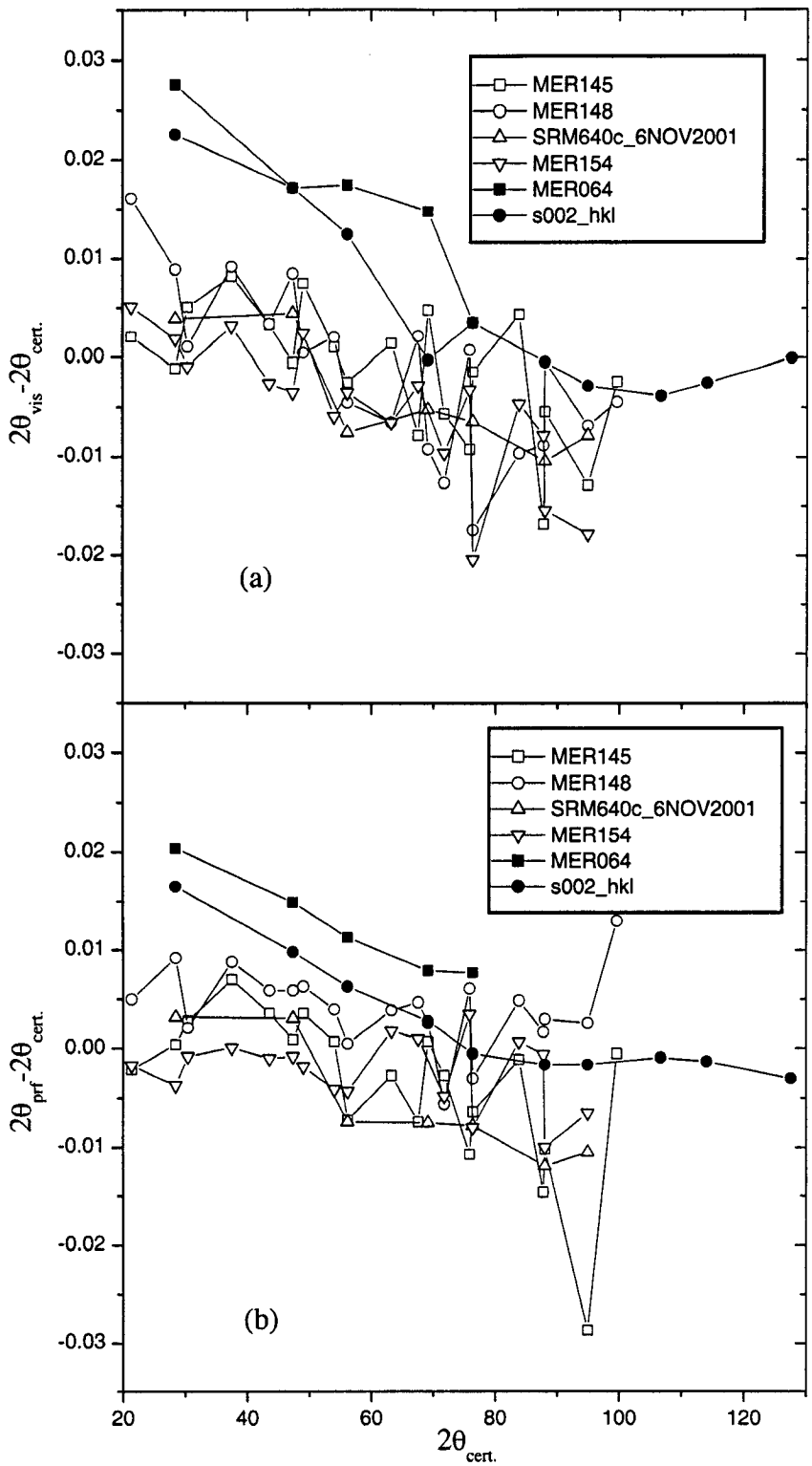

Figure 5.4. Comparison of certified 2θ values of SRMs to $K\alpha_1$ line positions determined on the left goniometer by : (a) visual estimation, and (b) FP line-profile fitting (see text for a description of the content of the figure).

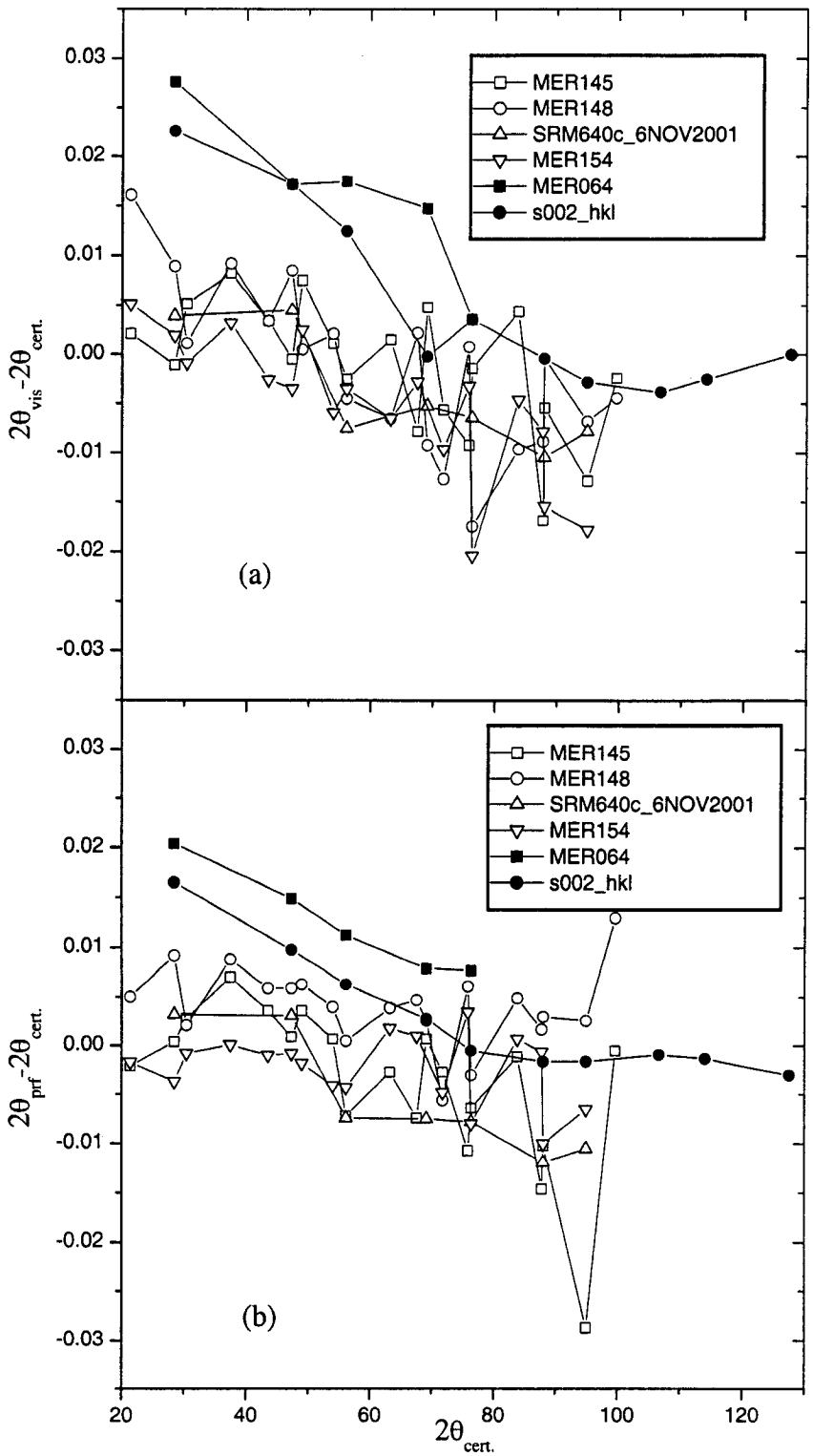

Figure 5.5. Comparison of certified 2θ values of SRMs to $K\alpha_1$ line positions determined on the right goniometer by : (a) visual estimation, and (b) FP line-profile fitting (see text for a description of the content of the figure).

5.1.4 Precision and accuracy of the lattice parameters

Lattice parameters were refined using 23 to 35 reflections for each sample. Indexing was done assuming the 1*M* stacking polytype following Table 5.1, so that 40 to 55 *hkl* values were assigned successfully in each of the diffractograms. Results of all lattice parameter refinements performed for each of the samples (which are obtained from CELREF output files) are tabulated in Appendix W.

Table 5.1 also gives the results of a structure factor calculation performed with the Koalariet program (Section 2.1.4) using the fractional coordinates of [Donnay *et al.*1964] with: a = 5.3948 Å, b = 9.3440 Å, c = 10.3557 Å, $\beta = 100°$, d_o = 2.090 Å, and d_i = 1.680 Å. On the basis of that calculation, all reflections were given equal weight in a given refinement.

Figures 5.6, 5.7, 5.8, and 5.9 compare values of lattice parameters a, b, c, and β, respectively, determined from various diffractograms of samples IKO-Ann and $Ni_{3.0}$JLR with $K\alpha_1$ line positions evaluated by visual estimation and FP fitting. The line positions were not corrected for any systematic errors. The letters A, B, and C refer to groups of diffractograms ran on a given diffractometer at different points in time.

In Figures 5.6-5.10, the solid lines that are shown through the lattice parameters obtained from IKO-Ann diffractograms MER149-153 correspond to a different indexing scheme, where only one *hkl* value was assigned per 2θ reflection. One immediately notes that the scatters of the lattice parameters gets larger as a result of such a procedure. Given what is known about the structure of these materials (Table 5.1), therefore, the latter indexing scheme is wrong, whereas the one of Table 5.1 is more appropriate.

For sample IKO-Ann, values of a (Figure 5.6) cluster around three different values depending on the diffractograms considered: ~5.393 Å for MER135, MER137, and MER139; ~5.394 Å for MER136 and MER138 (left goniometer, Fall 1999; see Table V.2); and ~5.397 Å for MER149 to MER153 (left goniometer, Fall 2000). As for sample $Ni_{3.0}$JLR, values of a determined from line positions evaluated by FP fitting are systematically higher than those refined using line positions visually estimated. Values of a can again be divided into three separate groups for sample $Ni_{3.0}$JLR: ~5.300 Å for MER143; ~5.297 Å for MER131; and ~5.299

Å for MER146 and MER147.

Lattice parameter *b* values (Figure 5.7) closely mirror the behaviours displayed by *a*. Values of *b* for the first, second, and third group of sample IKO-Ann diffractograms are of ~9.342, ~9.343, and ~9.345 Å, respectively. As for sample $Ni_{3.0}$JLR, values of *b* refined are of ~9.180, ~9.175, and ~9.178 Å, for the first, second, and third groups, respectively. More importantly, for almost each case where the value of *b* established by FP fitting is smaller than the one determined from visual estimation, the opposite trend is observed for *a*, and vice-versa. The latter behaviour is true for all $Ni_{3.0}$JLR diffractograms considered and for most of IKO-Ann diffractograms as well.

Lattice parameter *c* values (Figure 5.8) clearly divide themselves into separate groups according to the method that was used to determine the line positions, so that values of *c* obtained from visual estimation are systematically lower than those from FP fitting. With IKO-Ann, FP fitting values level at ~10.324, ~10.328, and ~10.332 Å, for the first, second, and third group, respectively, while those from visual estimation range from ~10.316 to ~10.328 Å and do not clearly distribute themselves into specific groups. In the case of sample $Ni_{3.0}$JLR, values of *c* from visual estimation fall between ~10.276 to ~10.284 Å, whereas those from FP fitting are of ~10.288, ~10.282, and ~10.286 Å for the first, second, and third group, respectively.

Lattice parameter β values (Figure 5.9) show a systematics inverse to that of *c*: in most cases, values of β from visual estimation are higher than those from FP fitting. For sample IKO-Ann, β values from visual estimation range from ~100.04° to ~100.06°, and those from FP fitting are of ~100.04° for the first group, and of ~100.035° for the second and third group. As for sample $Ni_{3.0}$JLR, values of *b* cover an interval between ~99.88° to ~99.90° with both visual estimation and FP fitting.

Let us now establish the precision of the refined lattice parameters. Figure 5.10 compares: i) standard deviations of lattice parameter values evaluated from diffractograms MER149 to MER153 by visual estimation and FP fitting; ii) standard deviations errors calculated by a synthetic method that uses a predefined Gaussian error width to generate 100 different line position data sets for each lattice parameter refinement (the code of the program used for that purpose is given in Appendix X); and iii) estimated standard deviations (ESDs) output by the

CELREF program (which is based on a linear least-squares refinement).

Although the measurement errors of line positions are more precise by FP fitting than by visual estimation (Subsection 5.1.3), it does not seem that the precision of the refined lattice parameters is influenced by the method used to measure the line positions. Indeed, the standard deviations of lattice parameters determined from diffractograms MER149 to MER153 are of the same order of magnitude for both the visual estimation and FP fitting methods. Likewise, the standard deviations calculated by the synthetic method evolve in the same manner for both methods as the assumed Gaussian error width is increased. In the case of ESDs, most of them are slightly larger with visual estimation, but remain of the same order of magnitude as those from FP fitting.

However, lattice parameters extracted from visual estimation and FP fitting differ systematically. The differences exhibited by the refined values of a, b, c, and β for each method are mainly due to the fact the visual estimation method generally gives higher 2θ positions than the FP fitting method (Subsection 5.1.1). Consequently, this causes lattice parameter tradeoffs to occur to accommodate for that effect. Besides that, diffractograms were measured under various state of goniometer's alignment on either side.

In view of all of the above considerations, I conclude that: i) the precision of the lattice parameter measurements is the same with either visual estimation or FP fitting; ii) the one standard deviation (1σ) *precision* errors of lattice parameters are 0.001 Å in a and in b, 0.003 Å in c, and 0.01° in β ; and iii) the 1σ accuracy of the lattice parameters are 0.005 Å for a and b, 0.01 Å for c, and 0.02° for β.

hkl	m_{hkl}	2θ	$\|F_{hkl}\|^2$
001	2	8.66	34168
002	2	17.38	5937
020	2	18.97	2675
110	4	19.19	3579
111	4	22.27	7788
11-2	4	23.94	19229
022	4	25.84	29471
003	2	26.19	61054
112	4	27.92	32883
11-3	4	30.17	27829
023	4	32.54	17556
-201	2	33.30	516
130	4	33.30	1027
200	2	33.70	67941
13-1	4	33.70	135708
004	2	35.17	31085
20-2	2	35.24	887
131	4	35.24	1775
201	2	36.35	42037
13-2	4	36.36	84013
22-1	4	38.60	10347
132	4	39.20	32208
20-3	2	39.20	16078
041	4	39.53	9718
13-3	4	40.89	122646
202	2	40.89	61333
005	2	44.38	9966
133	4	44.74	87760
20-4	2	44.74	43870
13-4	4	46.87	41642
203	2	46.87	20824
204	2	53.94	65949
13-5	4	53.95	131926
311	4	54.96	8955
31-3	4	54.96	24579

hkl	m_{hkl}	2θ	$\|F_{hkl}\|^2$
152	4	56.10	22608
24-3	4	56.11	12085
242	4	57.41	15341
15-3	4	57.41	12002
060	2	59.26	101970
33-1	4	59.26	203940
135	4	59.17	89711
20-6	2	59.17	44793
061	4	60.02	39214
330	4	60.01	39150
33-2	4	60.02	39278
13-6	4	61.92	45069
205	2	61.92	22499
062	4	62.25	14809
331	4	62.25	14790
007	2	63.84	22016
063	4	65.89	20468
332	4	65.89	20466
33-4	4	65.89	20470
136	4	67.70	142360
20-7	2	67.71	71181
40-1	2	69.70	3764
26-1	4	69.70	7487
40-2	2	69.93	47489
260	4	69.93	95207
064	4	70.81	60626
333	4	70.81	60585
33-5	4	70.82	60667
261	4	71.55	68887
40-3	2	71.55	34444
26-3	4	73.38	45930
401	2	73.37	22989
008	2	74.35	22419

Table 5.1. Indexing scheme followed for the determination of lattice parameters using the CELREF program (Subsection 2.1.3). Also shown are structure factor F^2_{hkl} values that are explained in text. The framed *hkl* values were assigned together to a given 2θ position.

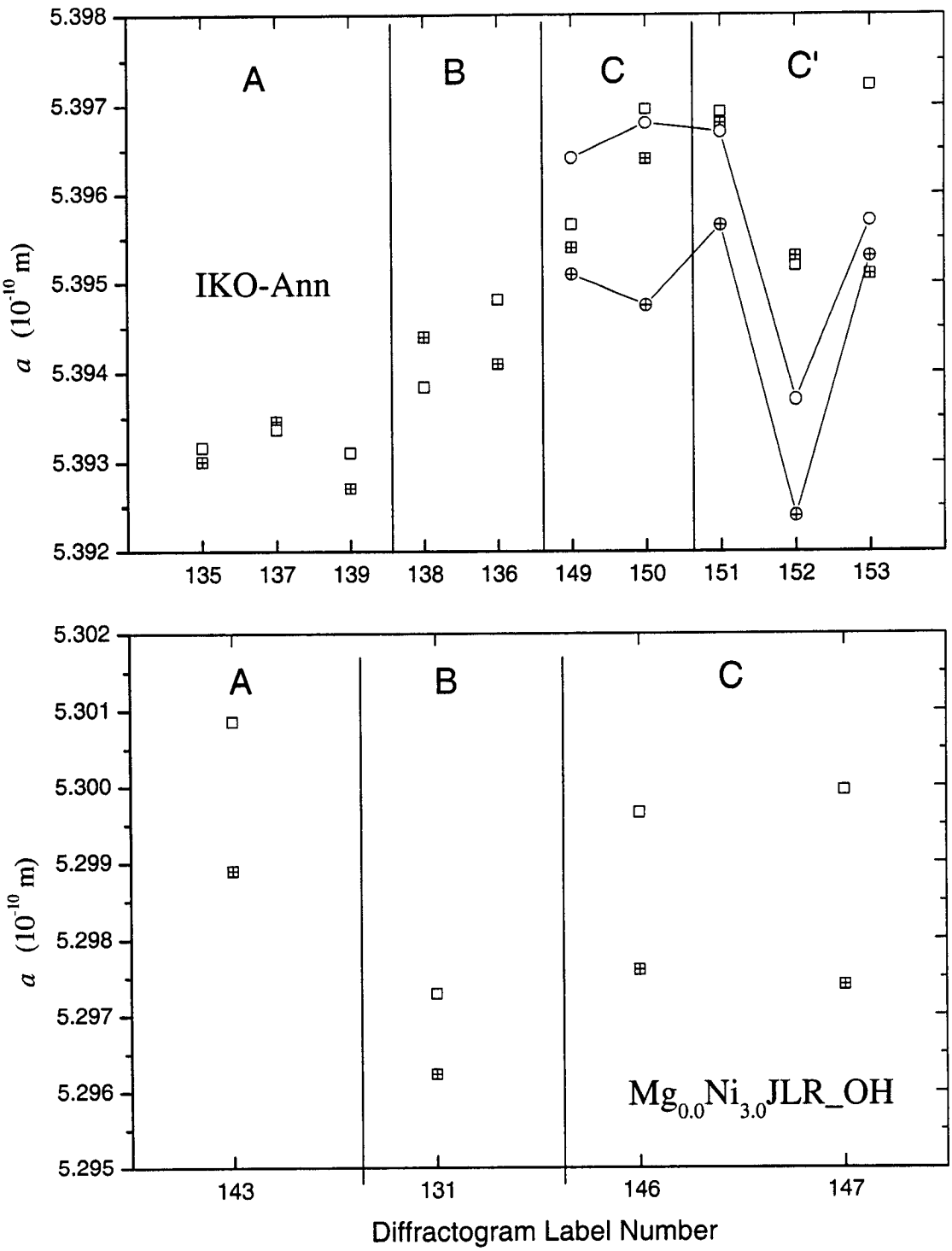

Figure 5.6. Values of lattice parameter a determined from various diffractograms of samples IKO-Ann (top) and $Ni_{3.0}$JLR (bottom) with $K\alpha_1$ positions evaluated by visual estimation (plus-squares) and FP fitting (open-squares).

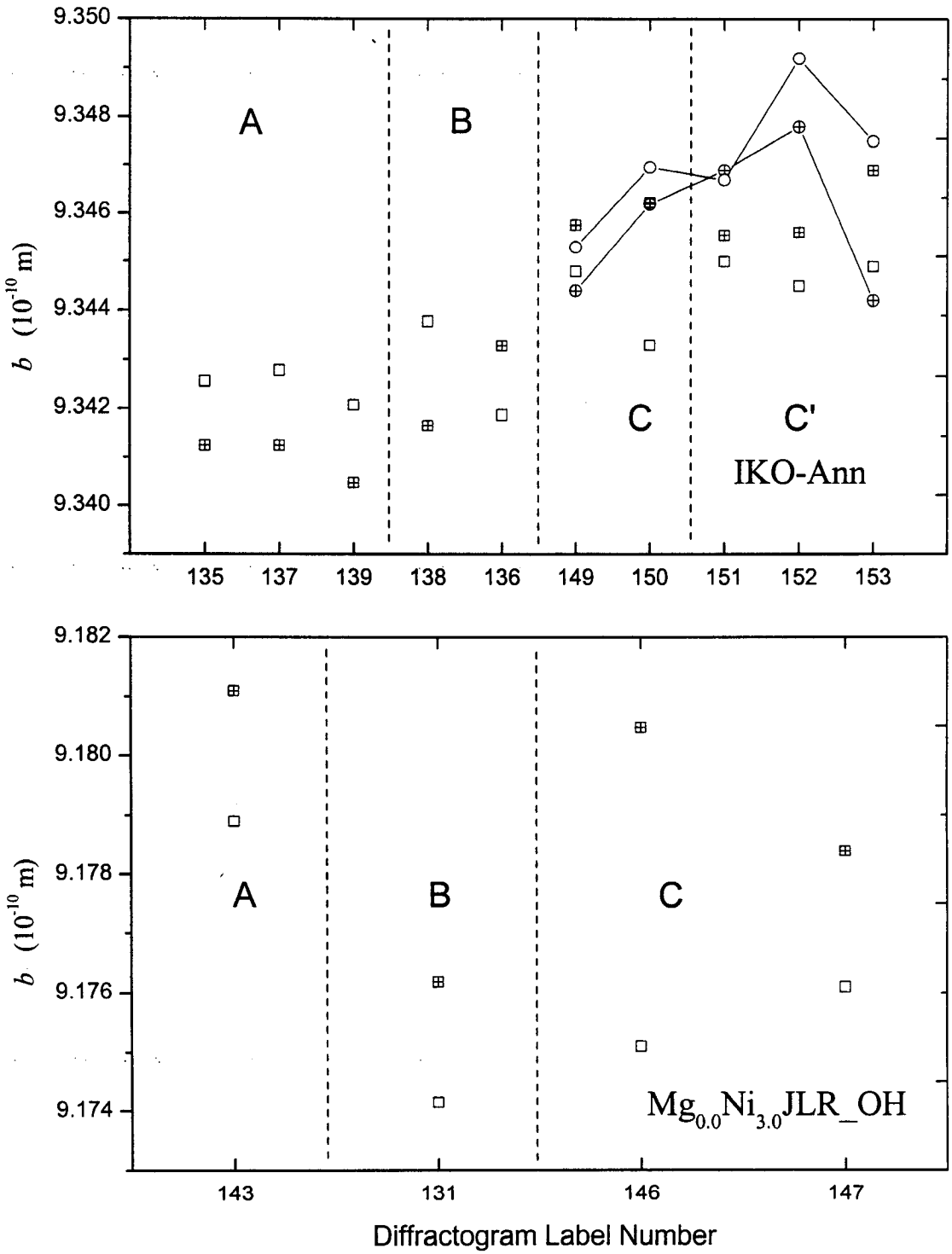

Figure 5.7. Values of lattice parameter b determined from various diffractograms of samples IKO-Ann (top) and $Ni_{3.0}$JLR (bottom) with $K\alpha_1$ positions evaluated by visual estimation (plus-squares) and FP fitting (open-squares).

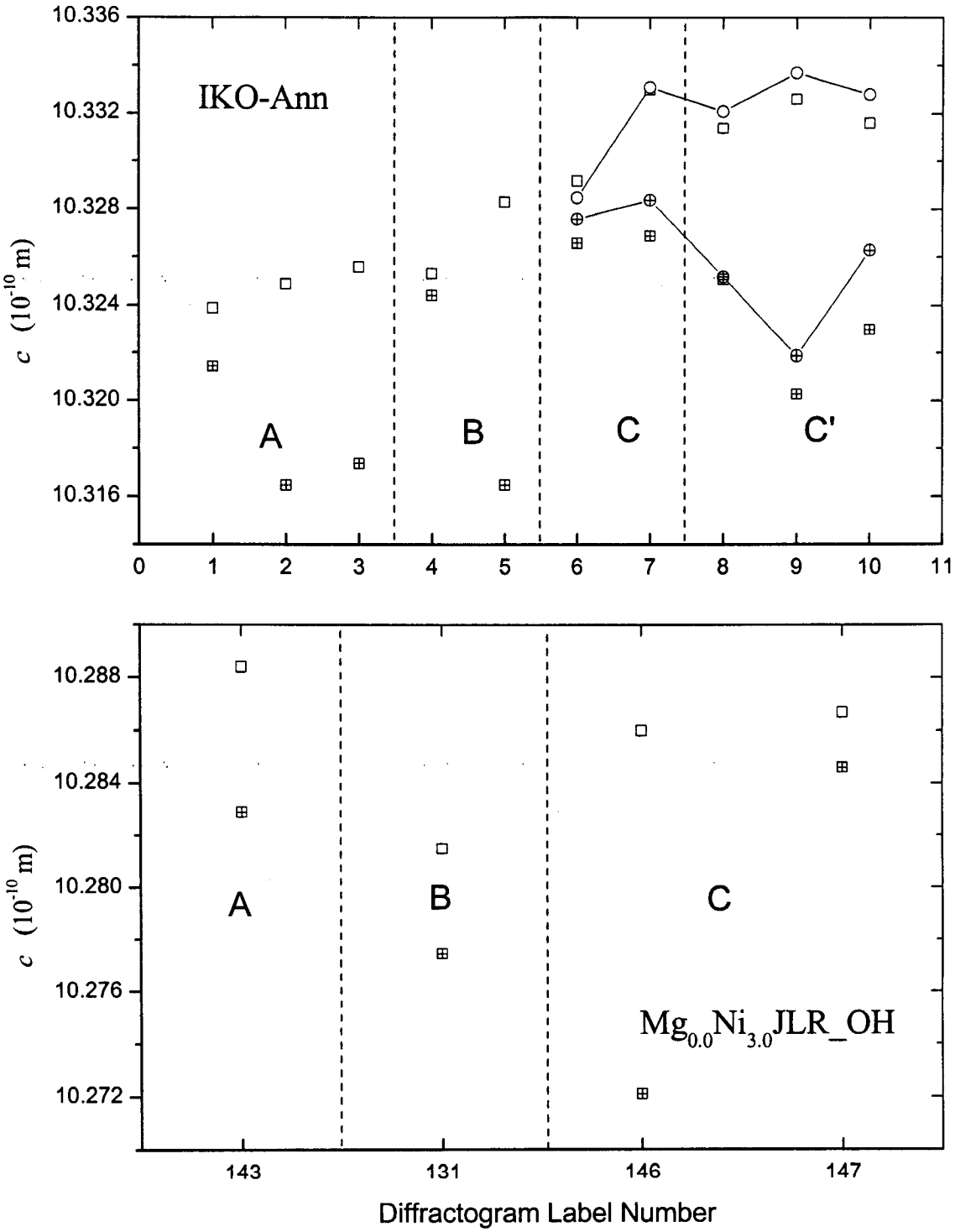

Figure 5.8. Values of lattice parameter c determined from various diffractograms of samples IKO-Ann (top) and $Ni_{3.0}$JLR (bottom) with $K\alpha_1$ positions evaluated by visual estimation (plus-squares) and FP fitting (open-squares).

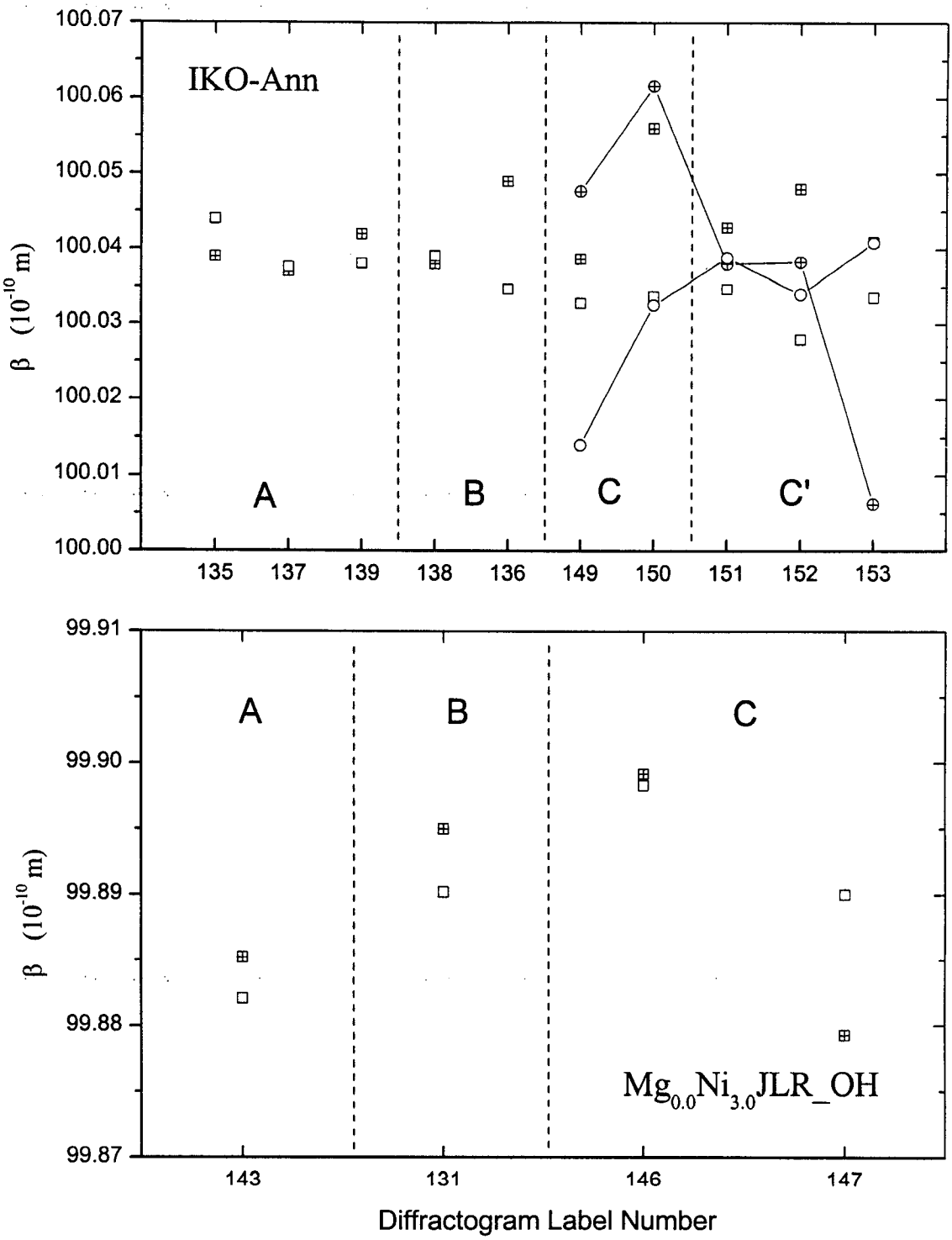

Figure 5.9. Values of lattice parameter β determined from various diffractograms of samples IKO-Ann (top) and $Ni_{3.0}$JLR (bottom) with $K\alpha_1$ positions evaluated by visual estimation (plus-squares) and FP fitting (open-squares).

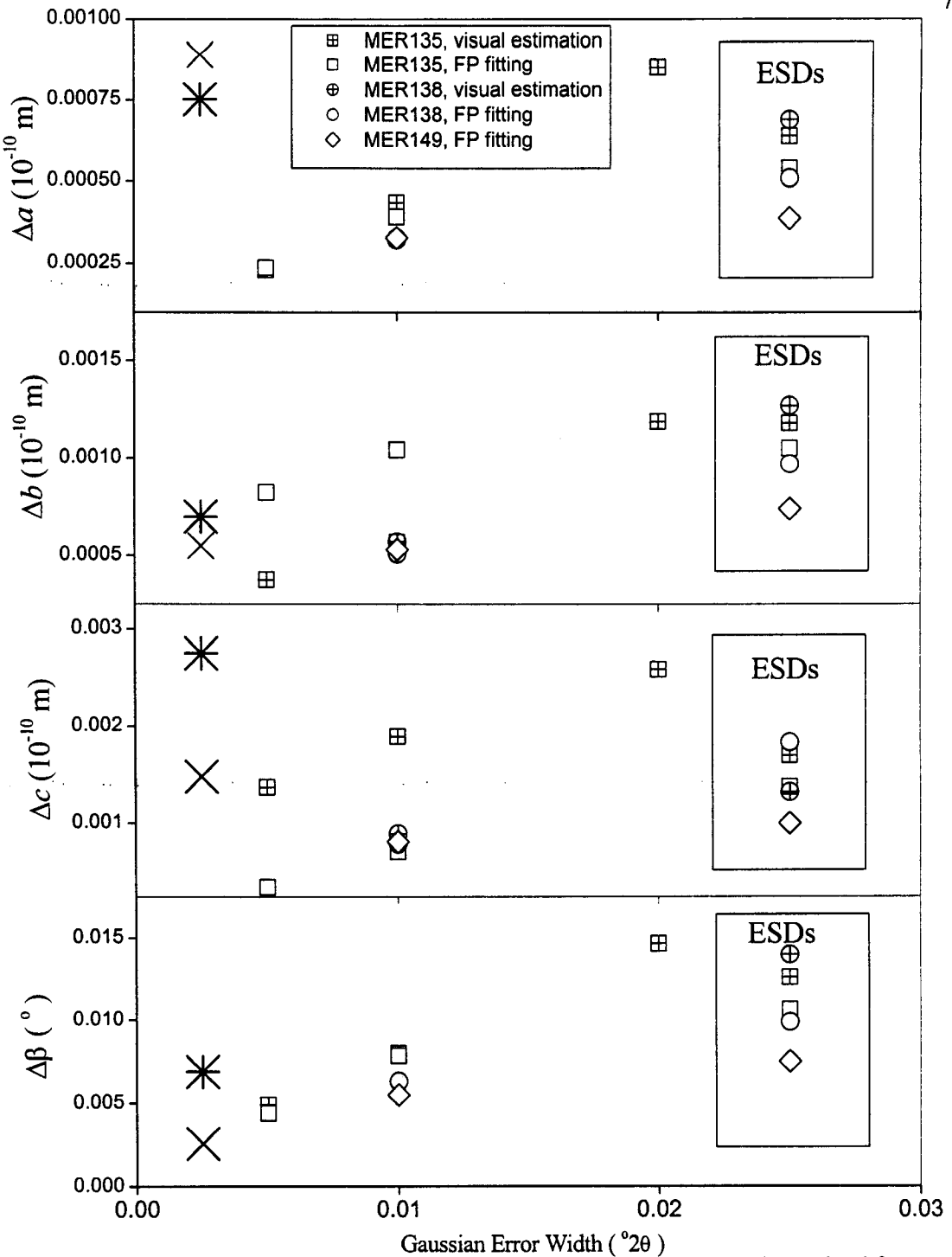

Figure 5.10. Comparison of : i) standard deviations of lattice parameters determined from diffractograms MER149 to MER153 by visual estimation (large stars) and FP fitting (large crosses), left; ii) standard deviations obtained by the synthetic method as a function of the assumed Gaussian error width, middle; and iii) ESDs output by CELREF, right.

5.2 Stacking polytype contents

Table 5.2 gives the results of structure factor calculations obtained for the $2M_1$, $2M_2$, $2O$, and $3T$ stacking polytypes using the fractional coordinates of Tables 4.2, 4.3, 4.4, and 4.5, respectively (see also Table 4.1). In these calculations, the same starting $1M$ unit cell as that of Table 5.1 was used — that is, the fractional coordinates of [Donnay *et al.*1964] with:
a = 5.3948 Å, b = 9.3440 Å, c = 10.3557 Å, β = 100°, d_o = 2.090 Å, and d_t = 1.680 Å.

In Table 5.2, the structure factor F^2_{hkl} values were divided by the squared volume of a given unit cell volume, V_c^2, as well as multiplied by the multiplicity of the reflection, m_{hkl}, to allow comparison between the different stacking polytypes. One notes that based on the presence or absence of a Bragg peak at a 2θ position corresponding to a given stacking polytype, one then has a clear set of criteria for the identification (and quantification, using our models) of mixtures of homogeneous stacking polytypes by powder X-ray diffraction. The criteria are in agreement with the accepted view that stacking polytype $3T$ cannot be distinguished from $1M$, whereas $2O$ is clearly recognizable if present in relatively large amounts.

Table 5.3 compiles the reflections of given sample observed at 2θ positions corresponding to other stacking polytypes than $1M$ (via the equations enumerated in Table 4.1) for various synthetic solid solution series. From these results, one concludes that the samples in Mg-Ni JLR and Co-Mg JLR series contain a mixture of stacking polytypes ($1M$, $2M_1$, and $2M_2$), whereas the other solid solution series appear to be nearly pure $1M$ stacking polytype samples.

a	5.3948				5.3948				9.3440			
b	9.3440				9.3440				5.3948			
c	10.3557		$1M$		20.4759		$2M_1$		20.6333		$2M_2$	
b	100				95.04				98.68			
Vc	514.1				1028.2				1028.2			

2θ	*hkl*	m_{hkl}	F^2_{hkl}	I_{hkl}^*	*hkl*	m_{hkl}	F^2_{hkl}	I_{hkl}	*hkl*	m_{hkl}	F^2_{hkl}	I_{hkl}
8.66	001	2	34168	**0.259**	002	2	136671	**0.259**	00-2	2	136671	**0.259**
17.38	002	2	5937	**0.045**	004	2	23747	**0.045**	004	2	23747	**0.045**
18.97	020	2	2675	0.020	020	2	2680	0.005				
18.97												
19.03									110	4	14609	0.055
19.19	110	4	3579	0.054	11-1	4	23081	0.087	11-1	4	3574	0.014
19.84												
20.89												
22.27	111	4	7788	0.118	11-3	4	46587	0.176	11-3	4	7788	0.029
23.07					02-3	4	147092	0.557				
23.94	11-2	4	19229	0.291	113	4	42628	0.161	20-4	2	38458	0.073
23.94									113	4	19203	0.073
24.86					11-4	4	74750	0.283	11-4	4	74750	0.283
25.84	022	4	29471	0.446	02-4	4	29524	0.112				
25.84												
26.19	003	2	61054	**0.462**	00-6	2	244217	**0.462**	00-6	2	244217	**0.462**
26.86					114	4	96795	0.366	114	4	96795	0.366
27.92	112	4	32883	0.498	11-5	4	6085	0.023	204	2	65766	0.124
27.92									11-5	4	32852	0.124
29.03					02-5	4	11922	0.045				
30.17	11-3	4	27829	0.421	115	4	3811	0.014	115	4	27810	0.105
30.17									20-6	2	55659	0.105
31.34					11-6	4	69052	0.261	11-6	4	69052	0.261
32.54	023	4	17556	0.266	02-6	4	17588	0.067				
32.54												
33.17									020	2	39755	0.075
33.17									31-1	4	79772	0.302
33.30	-201	2	516	0.004	200	2	2055	0.004				
33.30	130	4	1027	0.016	130	4	0.231	0.000				
33.50									312	4	127682	0.483
33.50									02-1	4	127797	0.484
33.50									310	4	127996	0.484
33.70	200	2	67941	0.514	20-2	2	271416	0.513				
33.70	13-1	4	135708	2.054	131	4	569662	2.155				
33.77									116	4	36564	0.138
34.34									311	4	121737	0.461
34.34									02-2	4	121639	0.460
34.34									31-3	4	121640	0.460
35.02												
35.17	004	2	31085	**0.235**	00-8	2	124341	**0.235**	008	2	124341	**0.235**
35.24	20-2	2	887	0.007	202	2	3550	0.007				
35.24	131	4	1775	0.027	13-3	4	57844	0.219				
35.77									312	4	69303	0.262
35.77									31-4	4	69278	0.262
35.77									02-3	4	69233	0.262
36.30												
36.35	201	2	42037	0.318	20-4	2	168027	0.318				
36.35	13-2	4	84013	1.272	133	4	225018	0.851				
37.60												
37.68									313	4	170727	0.646
37.68									02-4	4	170684	0.646
37.68									31-5	4	170548	0.645
38.50												
38.60	22-1	4	10347	0.157	200	4	10366	0.039	22-1	4	30990	0.117
38.95												
39.20	132	4	32208	0.487	13-5	4	271437	1.027	221	4	30207	0.114
39.20	20-3	2	16078	0.122	204	2	64417	0.122				
39.53	041	4	9718	0.147	22-3	4	9683	0.037				
39.53												
42.74									315	4	391461	1.481
42.74									02-6	4	391519	1.481
42.74									31-7	4	391352	1.481

$$^{*}I_{hkl} = m_{hkl} \times F^2_{hkl} / Vc^2$$

Table 5.2. Structure factor calculations obtained for the $2M_1$, $2M_2$, $2O$, and $3T$ stacking polytypes. See text for explanations. Continued on next page.

	1M				2O				3T			
a	5.3948				5.3948				5.3948			
b	9.3440				9.3440							
c	10.3557				20.3968				30.5952			
b	100				90				120			
Vc	514.1				1028.2				771.1			
2θ	***hkl***	m_{hkl}	F^2_{hkl}	I_{hkl}*	**hkl**	m_{hkl}	F^2_{hkl}	I_{hkl}	***hkl***	m_{hkl}	F^2_{hkl}	I_{hkl}
8.66	001	2	34168	**0.259**	002	2	136671	**0.259**	003	2	76878	**0.259**
17.38	002	2	5937	**0.045**	004	2	23747	**0.045**	006	2	13358	**0.045**
18.97	020	2	2675	0.020	020	2	10702	0.020	010	6	6027	0.061
18.97					110	4	5361	0.020				
19.03												
19.19	110	4	3579	0.054					011	12	8045	0.162
19.84									012	12	1168	0.024
20.89									013	12	2120	0.043
22.27	111	4	7788	0.118					014	12	17523	0.354
23.07					113	8	79405	0.601				
23.94	11-2	4	19229	0.291					015	12	43226	0.872
23.94												
24.86												
25.84	022	4	29471	0.446	024	4	117883	0.446	016	12	66390	1.340
25.84					114	8	59049	0.447				
26.19	003	2	61054	**0.462**	006	2	244217	**0.462**	009	2	137372	**0.462**
26.86												
27.92	112	4	32883	0.498					017	12	73940	1.492
27.92												
29.03					115	8	187745	1.421				
30.17	11-3	4	27829	0.421					018	12	62588	1.263
30.17												
31.34												
32.54	023	4	17556	0.266	026	4	70223	0.266	019	12	39548	0.798
32.54					116	8	35175	0.266				
33.17					200	2	40017	0.076	110	6	0.05	
33.17					130	4	79510	0.301				
33.30	-201	2	516	0.004					111	6	0.18	
33.30	130	4	1027	0.016								
33.50					131	8	255595	1.934				
33.50					201	4	127881	0.484				
33.50												
33.70	200	2	67941	0.514					112	6	458210	4.623
33.70	13-1	4	135708	2.054								
33.77												
34.34					202	4	121738	0.461				
34.34					132	8	243277	1.841				
34.34												
35.02									01.10	12	16858	0.340
35.17	004	2	31085	**0.235**	008	2	124341	**0.235**	00.12	2	69942	**0.235**
35.24	20-2	2	887	0.007					114	6	0.05	
35.24	131	4	1775	0.027								
35.77					203	4	69348	0.262				
35.77					133	8	138466	1.048				
35.77												
36.30					117	8	23389	0.177				
36.35	201	2	42037	0.318					115	6	283614	2.862
36.35	13-2	4	84013	1.272								
37.60									01.11	12	3467	0.070
37.68					134	8	341368	2.583	116	6	0.009	
37.68					204	4	170591	0.645				
37.68												
38.50									020	6	11592	0.117
38.60	22-1	4	10347	0.157					021	12	23310	0.470
38.95									022	12	23119	0.467
39.20	132	4	32208	0.487					117	6	0.06	
39.20	20-3	2	16078	0.122								
39.53	041	4	9718	0.147	222	8	19366	0.147	023	12	21813	0.440
39.53					042	4	38873	0.147				
42.74					136	8	783039	5.926				
42.74					206	4	391294	1.481				
42.74												

$$^{*}I_{hkl} = m_{hkl} \times F^2_{hkl} / Vc^2$$

Table 5.2. Continued.

Sample	$2M_1$	$2M_1$	$2M_1$	$2M_1$	$2M_1$					
	02-3	11-4	114	02-5	11-6					
		$2M_2$	$2M_2$		$2M_2$	$2M_2$	$2M_2$	$2M_2$	$2M_2$	$2M_2$
		11-4	114		11-6	311...	312...	313...	315...	317...
Co-Mg JLR										
$Co_{0.3}Mg_{2.7}$JLR	X	X	X	X			X		X	
$Co_{0.6}Mg_{2.4}$JLR	X	X	X	X	X		X	X	X	X
$Co_{0.9}Mg_{2.1}$JLR	X	X	X	X	X		X	X	X	X
$Co_{1.2}Mg_{1.8}$JLR	X	X	X	X	X	X	X	X	X	X
$Co_{1.5}Mg_{1.5}$JLR	X	X	X	X	X	X	X	X	X	X
$Co_{1.8}Mg_{1.2}$JLR	X	X	X	X	X	X	X	X	X	X
$Co_{2.1}Mg_{0.9}$JLR	X	X	X	X	X	X	X	X	X	X
$Co_{2.4}Mg_{0.6}$JLR	X	X	X	X	X	X	X	X	X	X
$Co_{2.7}Mg_{0.3}$JLR	X	X	X	X	X	X	X	X	X	X
$Co_{3.0}Mg_{0.0}$JLR	X	X	X	X	X	X	X	X	X	X
Mg-Ni JLR										
$Mg_{0.0}Ni_{3.0}$JLR-OH	X	X	X	X	X	X	X	X	X	X
$Mg_{0.0}Ni_{3.0}$JLR-OD	X	X	X	X	X	X	X	X	X	X
$Mg_{0.3}Ni_{2.7}$JLR	X	X	X	X	X	X	X	X	X	X
$Mg_{0.6}Ni_{2.4}$JLR	X	X	X	X	X	X	X	X	X	X
$Mg_{0.9}Ni_{2.1}$JLR	X	X	X	X	X	X	X	X	X	X
$Mg_{1.2}Ni_{1.8}$JLR	X	X	X	X	X	X	X	X	X	
$Mg_{1.5}Ni_{1.5}$JLR		X	X	X	X		X		X	
$Mg_{1.8}Ni_{1.2}$JLR				X	X		X		X	
$Mg_{2.1}Ni_{0.9}$JLR										
$Mg_{2.4}Ni_{0.6}$JLR									X	
$Mg_{2.7}Ni_{0.3}$JLR									X	
$Mg_{3.0}Ni_{0.0}$JLR	X	X	X	X					X	
Fe-Mg JLR										
$Fe_{0.0}Mg_{3.0}$JLR									X	
$Fe_{0.6}Mg_{2.4}$JLR									X	
$Fe_{1.2}Mg_{1.8}$JLR									X	
$Fe_{1.8}Mg_{1.2}$JLR									X	
$Fe_{2.4}Mg_{0.6}$JLR										
$Fe_{3.0}Mg_{0.0}$JLR										
Fe-Ni GR										
$Fe_{0.0}Ni_{3.0}$GR									X	
$Fe_{0.2}Ni_{2.8}$GR										
$Fe_{0.6}Ni_{2.4}$GR		X	X	X	X	X	X	X	X	X
$Fe_{1.0}Ni_{2.0}$GR		X	X	X	X	X	X	X	X	X
$Fe_{1.4}Ni_{1.6}$GR								X	X	
$Fe_{1.8}Ni_{1.2}$GR								X	X	
$Fe_{2.2}Ni_{0.8}$GR								X	X	
$Fe_{2.6}Ni_{0.4}$GR								X		

Table 5.3. Stacking polytype contents of synthetic samples belonging to various solid series of this thesis. See text for explanations.

Chapter 6. Testing of Geometrical Models

Simple geometrical models for the mica structure have been presented by [Pauling 1930], [Radoslovich 1961], [Donnay *et al.* 1964a], and [Takeda & Morosin 1975]. In the chronological order that they appeared, these are in fact a hierarchical sequence of modifications of one another; they are often referred to and used for various purposes (e.g., see [Hazen & Wones 1972; Takeda 1967; Takeda & Ross 1995; Nespolo *et al.* 1999; Mercier *et al.* 1996,1999; Rancourt *et al.* 2001]), as well as severely criticized [Weiss *et al.* 1985; Lin & Guggenheim 1983]. In this chapter we shall explore the limits of applicability of simple geometrical models, including those cited above and more sophisticated ones, in the prediction and interpretation of the crystal chemical properties of micas.

6.1 In-plane pseudo-hexagonal symmetry of mica layers

In layer silicates, the axes *a* and *b* are chosen to lie in a plane parallel to the layers, so that the *c* axis is the direction along which the layers stack one over another. The shortest distance connecting two *trans*-coordinated octahedral cations (*M1* sites) defines the *a* axis (Figure 6.1), whereas the *b* axis lies perpendicular to *a*. If the octahedral cations are arranged in a perfectly hexagonal pattern, then it can be shown that $b = \sqrt{3} \cdot a$.

Figures 6.2 and 6.3 show measured lattice parameters *b* as a function of *a* for synthetic samples reported in Section 5.2 and for single-crystal refinements of mica structures belonging to various stacking polytypes tabulated in Appendices P to T, inclusively. Both Figures 6.2 and 6.3 demonstrate that the straight line relationship $b = \sqrt{3} \cdot a$ is closely obeyed, except for a few structures of single-crystals that are discussed below. Such a relationship is not imposed by any of the known mica space groups corresponding to the different stacking polytypes, except for polytype $3T$ where it arises from the space group symmetry (trigonal). Note also that with stacking polytype $2M_2$, *a* and *b* are interchanged.

In the case of synthetic samples, it was found that the few exceptions where this relationship did not appear to hold could always be traced to an error in indexing one or more of the reflections or to an error in tabulating one or more of the peak positions. In practice, therefore, when dealing with synthetic *2:1* layer silicates, agreement with this relationship is valid evidence that a lattice parameter refinement has been done correctly.

Exceptions noted in Figure 6.3 can be explained as follows. Structure 1*M* No. 80 is the only known occurrence of norrishite, ideally $\{K^{1+}\}[Li^{1+}Mn^{3+}{}_2]\langle Si_4\rangle O_{12}$ [Tyrna & Guggenheim 1991]. The geometry of the *2:1* layer observed in this mineral is complicated due to three separate effects [Brigatti & Guggenheim 2002]: i) large displacement of octahedral *M2* cation, ii) elongation of octahedrons owing to Jahn-Teller effects, and iii) chemical ordering of Li^{1+} and Mn^{3+} on the *M1* and *M2* sites, respectively. Structure 2*O* No. 2 is an anandite specimen, ideally $\{Ba^{2+}\}[Fe^{2+}{}_3]\langle Si^{4+}{}_3Fe^{3+}\rangle O_{10}(OH)S$, which was refined in a symmetry reduced from *Ccmm* to *Pnmn* as a result of ordering of tetrahedral Fe^{3+} and Si, octahedral Fe and some Mg that is present, and the anions OH and S [Filut *et al.* 1985]. The remaining two anomalies are $2M_1$ structures. No. 26 is a crystal recovered by cooling after the dehydroxylation of a paragonite (ideally $\{Na^{1+}\}[Al^{3+}{}_2\square]\langle Si^{4+}{}_3Al^{3+}\rangle O_{10}(OH)_2$) specimen at 700 °C according to the reaction $2\ OH^- \rightarrow O^{2-} + H_2O\uparrow$ [Comodi & Zanazzi 2000]; after heat treatment, the composition is nominally $\{Na^{1+}\}[Al^{3+}{}_2\square]\langle Si^{4+}{}_3Al^{3+}\rangle O_{11}$ and an *M2* site with a near five-fold coordination is hence formed. Lastly, No. 33 is the structure of a lepidolite (Table 1.1) for which the refinement in *C2/c* symmetry indicated no tetrahedral ordering but ordering of octahedral cations so that *M1* = $Li_{0.93}[Mg,Mn,Fe]^{2+}{}_{0.06}Fe^{3+}{}_{0.01}$ and *M2* = $Al_{0.58}Li_{0.35}\square_{0.07}$; several tests were also performed which established that the true symmetry most likely is $C\bar{1}$ [Swan & Bailey 1981].

The $b = \sqrt{3} \cdot a$ relationship is a direct consequence of the hexagonal in-plane pseudo-symmetry of the mica layers, especially of the octahedral sheets. To the extent that this pseudo-symmetry is not broken by some features such as chemical order or peculiar site distortions, which were present for all exceptions pointed above, this relationship is expected to hold exactly.

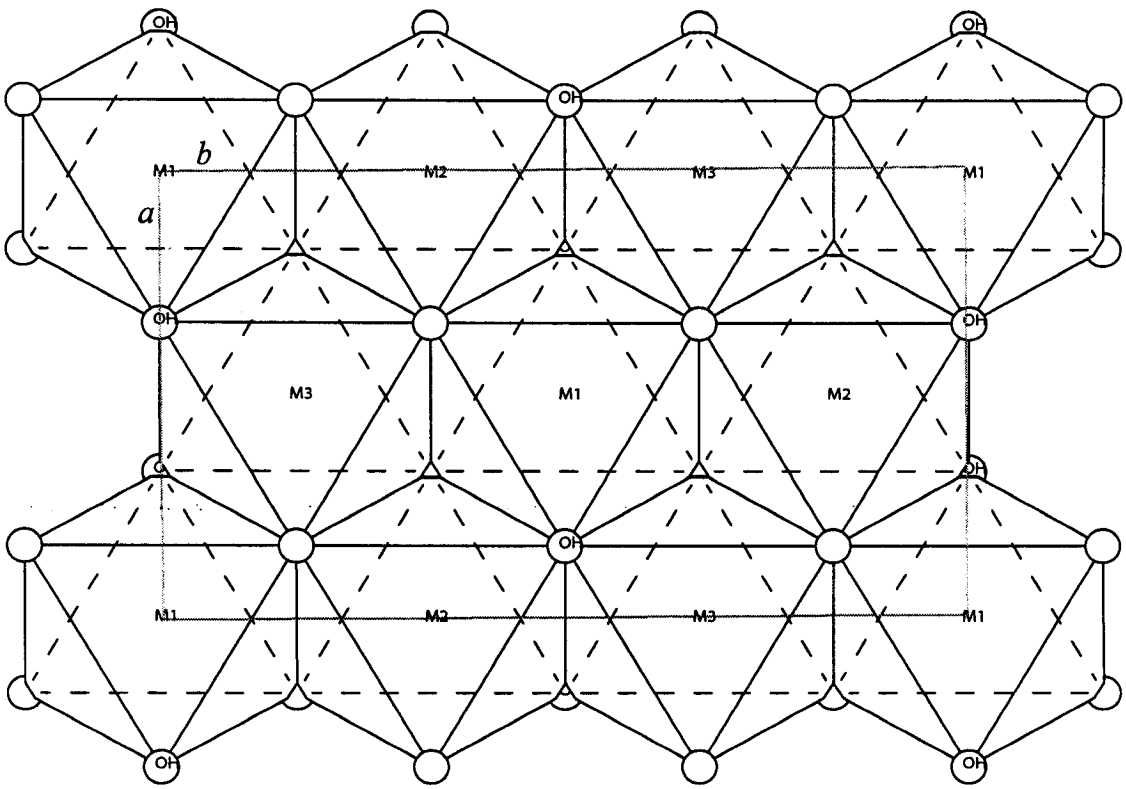

Figure 6.1. Diagram illustrating the *a* and *b* axes. *M*1 and *M*2/*M*3 symbols refer to octahedral cations that are *trans*- and *cis*- coordinated, respectively.

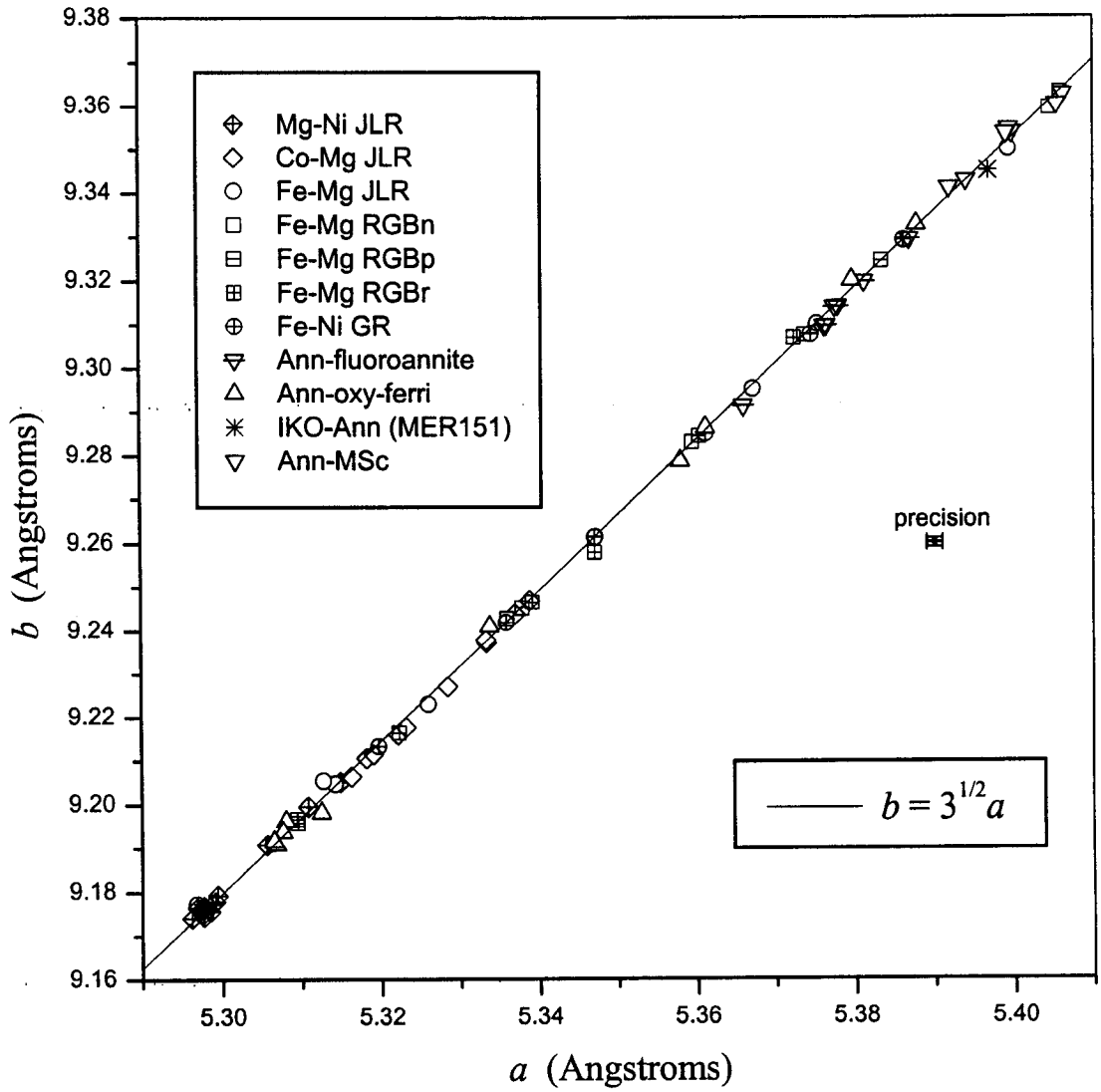

Figure 6.2. *b vs. a* for synthetic samples studied in this thesis. The labelled symbols indicated in the legend refer to the various sample solid solution series described in Table 3.1. The Ann-MSc symbol refers to the synthetic annite samples studied in [Mercier 1996].

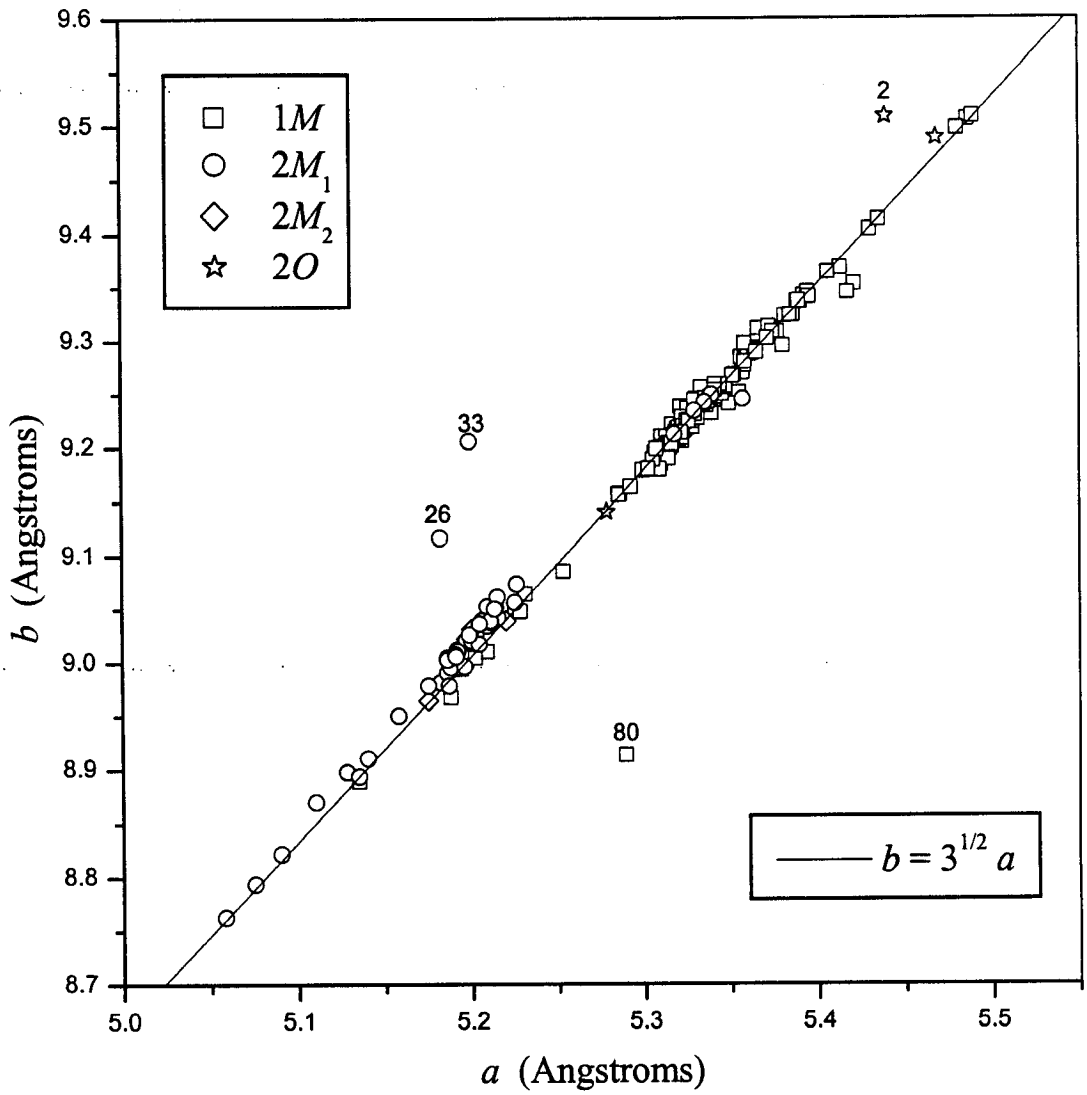

Figure 6.3. *b vs. a* for single-crystal structure refinements tabulated in Appendices P to T, inclusively. Notable exceptions are numbered with the corresponding structure No. given in the appropriate appendix. See text for a discussion of these anomalies.

6.2 Geometrical models

In Chapter 4, fractional atomic coordinates for each common stacking polytype were obtained by applying proper generating operations to a conventional 1*M* mica unit cell of space-group type *C*2/*m*. We will now present a hierarchy of progressively more realistic simple geometrical models of octahedrons and tetrahedrons, that will then be used to develop a crystal structure models for the 1*M* mica structure using idealized polyhedral networks.

6.2.1 An octahedron in an octahedral sheet

There are two distortions that preserve the bond length of an octahedron of a given height (Figure 6.4): i) iso-bond flattening, and ii) counter-rotation.

Iso-bond flattening is measured by the angle ψ between a line given by the direction of an octahedral bond length (*M-O*) and a line normal to the upper and lower triangular faces running through the central (octahedral) cation, *M*. If the height of an octahedron is decreased as a result of flattening alone (Figure 6.4b), then the upper and lower triangular faces are expanded (or vice-versa), maintaining their equilateral shape.

In an ideal octahedron (Figure 6.4a), the flattening angle is given by

(6.1) $$\psi_{ideal} = \arctan\left(\sqrt{2}\right) \cong 54.74^{\circ}.$$

As pointed out in [Donnay *et al.* 1964a], ψ_{ideal} is the cube-octahedron angle that can be read directly as the angle between the diagonal of a cube and the side edge contributing to the cosine of the angle. The following relationships also hold:

(6.2) $$\sin\psi_{ideal} = \sqrt{2/3} \quad ; \quad \cos\psi_{ideal} = \sqrt{1/3}\ .$$

The height of an octahedron, h_o, with bond length d_i and flattening ψ_i is given by:

(6.3) $$h_o = 2d_i \cos\psi_i .$$

As a consequence of flattening, the edges of an octahedron are no longer equal. The six unshared

edges that make up the upper and lower triangular faces are of length

(6.4) $$e_u^i = \sqrt{3} \cdot d_i \cdot \sin\psi_i$$

and the remaining six shared edges (i.e., shared with other octahedrons in the sheet) are of length

(6.5) $$e_s^i = d_i \sqrt{3 \cdot \cos^2\psi_i + 1} \quad .$$

It then follows that

(6.6) $$\left(\frac{e_s}{e_u}\right)_i = \sqrt{\frac{4}{\sin^2\psi_i} - 3} \qquad \text{or} \qquad \sin^2\psi_i = \frac{4}{3 \cdot \left[1 + \left(e_s/e_u\right)_i^2\right]} \quad ,$$

from which it can be obtained using Eqs. 6.1 to 6.6 that for an ideal octahedron:

(6.7) $$e_s^i = e_u^i = \sqrt{2} \cdot d_i \, .$$

Counter-rotation arises from rotating an octahedron's upper and lower triangular faces in opposite directions (Figure 6.4c). The counter-rotation angle, δ_i , is measured by the angle through which each triangular face is rotated. We will assume that if the rotation angle is positive, then the upper triangular face is rotated clockwise and the lower triangular face is rotated anti-clockwise.

As can be seen in Figure 6.4c, counter-rotation can be combined with iso-bond flattening. In this case the unshared edge lengths remain of the length given by Eq. 6.4, whereas the shared edges split into two groups of three, where the edge lengths of the two groups are:

(6.8a) $$e^{i}_{s+} = \sqrt{\left[2d_i \sin\psi_i \cos\left(60^o + \delta_i\right)\right] + h_o^2}$$ and

(6.8a) $$e^{i}_{s-} = \sqrt{\left[2d_i \sin\psi_i \cos\left(60^o - \delta_i\right)\right] + h_o^2}$$.

A demonstration that iso-bond flattening and counter-rotation together are enough to fit octahedrons of different sizes in a plane is made in [Evans 2001], where it is shown that one needs three different sized octahedral sites, each with a bond length d_i, a flattening ψ_i, and a counter-rotation δ_i, to make an octahedral sheet of uniform height h_o.

The flattening angles ψ_i of the three sites are determined from the three bond lengths d_i and the height of the octahedral sheet h_o as

(6.9) $$\frac{h_o}{2} = d_{M1}\cos\psi_{M1} = d_{M2}\cos\psi_{M2} = d_{M3}\cos\psi_{M3},$$

where $M1$, $M2$, and $M3$ designate each individual octahedral site.

Further, [Evans 2001] demonstrates that the following relations stem from fitting three different sized octahedrons of uniform height in a plane:

(6.10a)
$$\begin{aligned} d_{M1}\cos\left(60^\circ - \delta_{M1}\right)\sin\psi_{M1} &= d_{M2}\cos\left(60^\circ + \delta_{M2}\right)\sin\psi_{M2} \\ d_{M2}\cos\left(60^\circ - \delta_{M2}\right)\sin\psi_{M2} &= d_{M3}\cos\left(60^\circ + \delta_{M3}\right)\sin\psi_{M3} \\ d_{M3}\cos\left(60^\circ - \delta_{M3}\right)\sin\psi_{M3} &= d_{M1}\cos\left(60^\circ + \delta_{M1}\right)\sin\psi_{M1} \end{aligned}$$

and

(6.10b)
$$\begin{aligned} e_u^{M1}\cos\left(60^\circ - \delta_{M1}\right) &= e_u^{M2}\cos\left(60^\circ + \delta_{M2}\right) \\ e_u^{M2}\cos\left(60^\circ - \delta_{M2}\right) &= e_u^{M3}\cos\left(60^\circ + \delta_{M3}\right) \\ e_u^{M3}\cos\left(60^\circ - \delta_{M3}\right) &= e_u^{M1}\cos\left(60^\circ + \delta_{M1}\right) \end{aligned}$$

Despite the different sizes and shapes of the octahedrons in such a *geometric hetero-octahedral* sheet (following the nomenclature defined in Section 1.4), the cations are positioned in an ideal simple hexagonal lattice (this is also proven by [Evans 2001]).

Before we end this section, let us recall a few important points. Iso-bond flattening and counter-rotation do not alter the bond length of a given octahedron. This means that with only those two distortions acting, the *M-O* distance is equal to the *M-OH* distance in a given octahedron. The latter point is a rather important approximation, that will be discussed in Section 6.3 in the context of an overview of observed polyhedral distortions in 1*M* mica structures refined in space-group type *C*2/*m*.

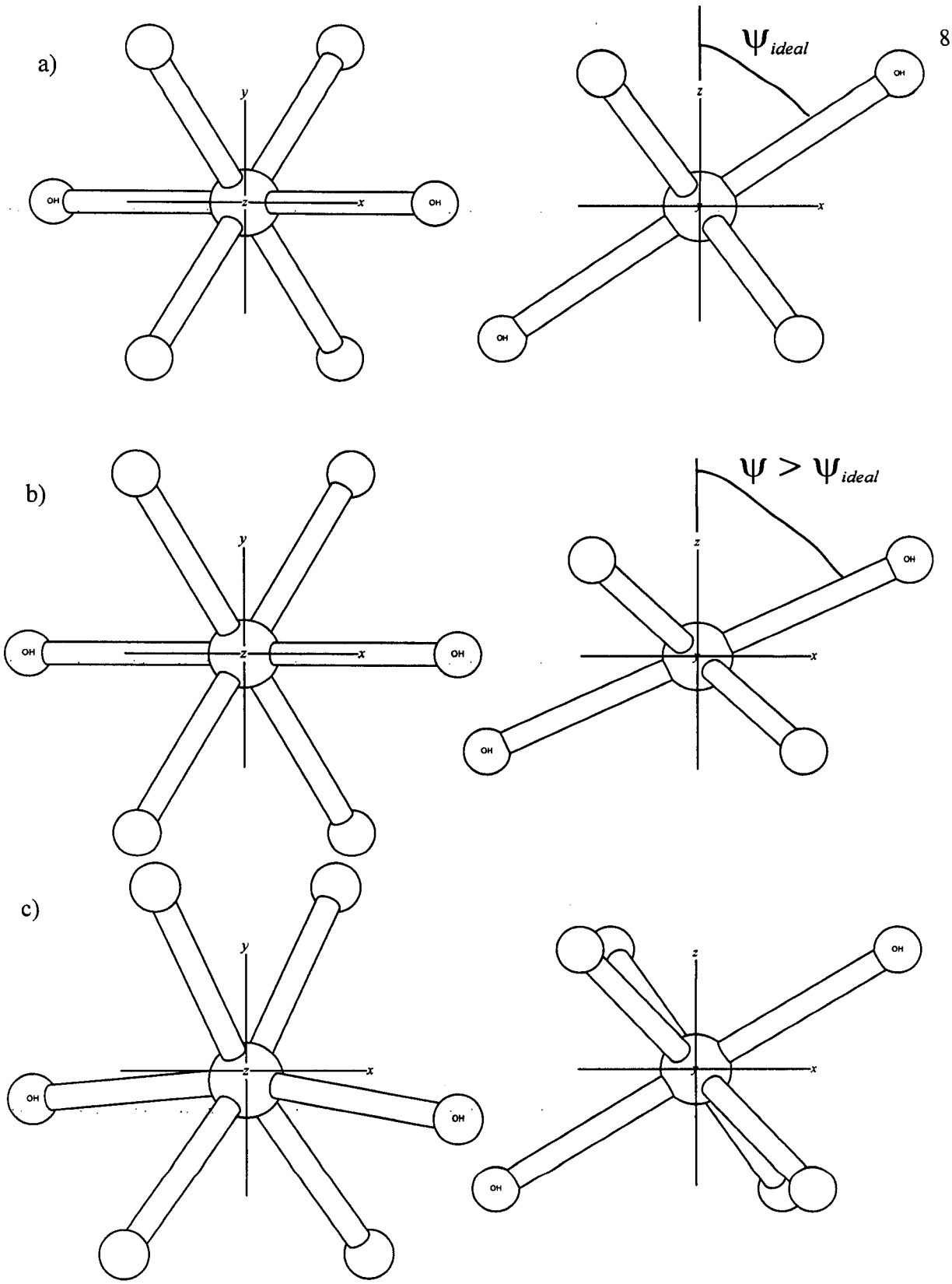

Figure 6.4. Geometrical models for an octahedron: a) ideal octahedron; b) iso-bond flattened octahedron; and c) iso-bond flattened and counter-rotated octahedron.

6.2.2 Geometric homo-octahedral sheet

From Eqns. 6.4, 6.9 and 6.10 it can be seen that if $d_{M1} = d_{M2} = d_{M3} = d_o$, then

$$\begin{aligned} \psi_{M1} = \psi_{M2} = \psi_{M3} = \psi \\ e_u^{M1} = e_u^{M2} = e_u^{M3} = e_u = \sqrt{3} \cdot d_o \cdot \sin\psi \\ \delta_{M1} = \delta_{M2} = \delta_{M3} = 0 \end{aligned} \tag{6.11}$$

Hence, when all bond lengths are equal, there is no counter-rotation, and iso-bond flattening is the only distortion that is applied uniformly to all octahedral sites. This type of octahedral sheet, which was first introduced by [Donnay *et al.* 1964a], is referred to as a *geometric homo-octahedral* sheet (following the nomenclature defined in Section 1.4).

In a geometric homo-octahedral sheet, the in-plane a and b lattice parameters can be expressed as (Figure 6.5):

$$\begin{aligned} a = 3 \cdot d_o \cdot \sin\psi = \sqrt{3} \cdot e_u \\ b = 3 \cdot \sqrt{3} \cdot d_o \cdot \sin\psi = 3 \cdot e_u \end{aligned} \tag{6.12}$$

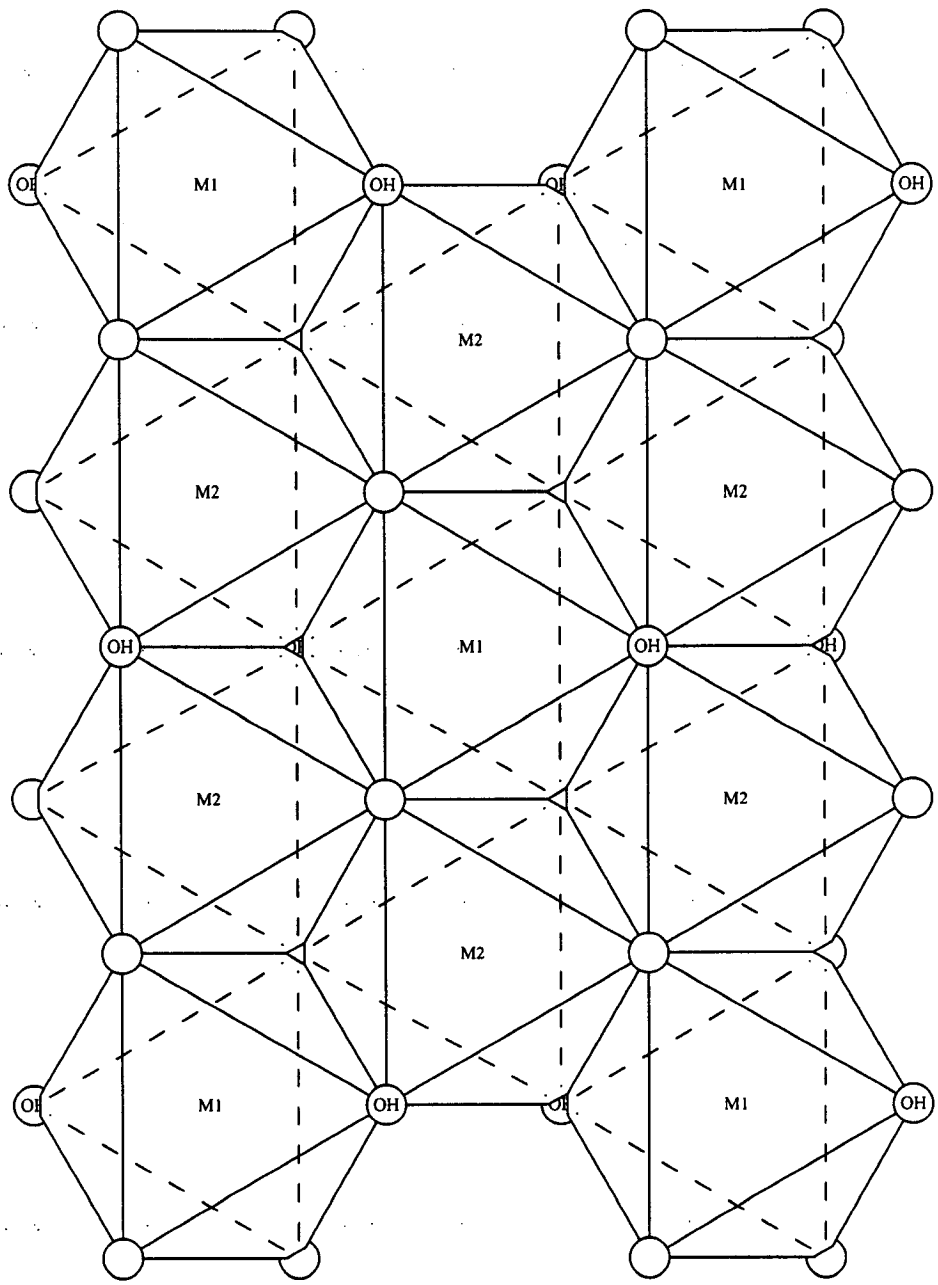

Figure 6.5. Geometrical model for a geometric homo-octahedral sheet.

6.2.3 Geometric meso-octahedral sheet

When only two bond lengths are equal, e.g. $d_{M1} \neq d_{M2} = d_{M3}$, then one finds (using Eqns. 6.4, 6.9, and 6.10):

$$\psi_{M1} \neq \psi_{M2} = \psi_{M3}$$
$$\delta_{M1} = 0 \quad , \quad \delta_{M2} = -\delta_{M3} \tag{6.13}$$

The two octahedrons with equal bond lengths and flattening angles have equal and opposite counter-rotation angles, whereas the distinct octahedral site has zero counter-rotation. This type of octahedral network is referred to as a *geometric meso-octahedral* sheet (Figure 6.6) following the nomenclature defined in Section 1.4.

From the results of [Evans 2001], it can be shown that:

$$a = 2 \cdot d_{M1} \sin\psi_{M1} + 2 \cdot d_{M2} \sin\psi_{M2} \sin\left(30° - \delta\right) = \frac{2}{\sqrt{3}}\left[e_u^{M1} + e_u^{M2} \sin\left(30° - \delta\right)\right]$$
$$b = \sqrt{3} \cdot d_{M1} \sin\psi_{M1} + 2 \cdot \sqrt{3} \cdot d_{M2} \sin\psi_{M2} \cos\delta = e_u^{M1} + 2 \cdot e_u^{M2} \cos\delta \tag{6.14}$$

In the latter equation, the notation was simplified in accordance with Eq. 6.12. If $\delta > 0$, then $d_{M1} > d_{M2}$; and vice-versa.

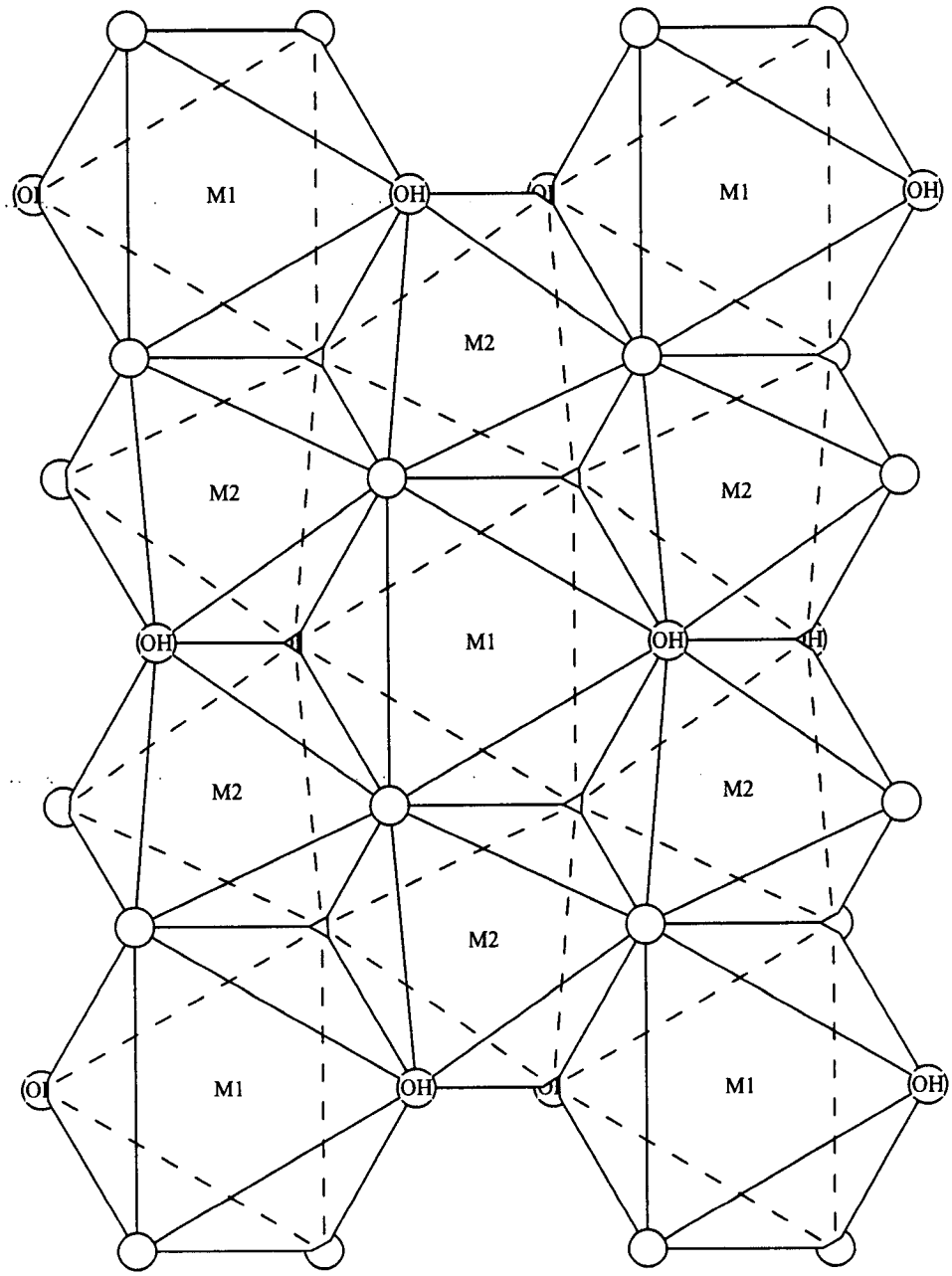

Figure 6.6. Geometrical model for a geometric meso-octahedral sheet.

6.2.4 A single tetrahedron

Consider the triangular pyramid displayed in Figure 6.7, which has the tetrahedral cation T as its summit and one basal oxygen atom, O_{bas}, for each corner of its base. If the O_{bas} atoms form an equilateral triangle of edge length e_t^{bas}, and T lies on a perpendicular through the centre of mass of the equilateral basal triangle, then the following relationships can be obtained from such a construction:

$$
\begin{aligned}
e_t^{bas} &= 2 \cdot d_t^{bas} \cdot \sin\left(\tau_{bas}/2\right) \\
h_t^{bas} &= d_t^{bas} \sqrt{1 - \frac{4}{3} \cdot \sin^2\left(\tau_{bas}/2\right)} \\
\varepsilon_{bas} &= \arccos\left[\frac{2}{\sqrt{3}} \sin\left(\tau_{bas}/2\right)\right]
\end{aligned}
\qquad (6.15)
$$

In the above expressions, the symbols have the following meanings: h_t^{bas} is the height of the pyramid; d_t^{bas} is the T-O_{bas} bond length; ε_{bas} is the angle that makes a T-O_{bas} bond with respect to the basal-oxygen plane; and τ_{bas} is the value of the three O_{bas}-T-O_{bas} angles.

One can construct various shapes of tetrahedrons using the above described pyramid as a building block. This approach is consistent with the shapes of actual tetrahedra in layer silicates, as will be shown below. If the apical oxygen atom O_{api} is placed on the same perpendicular through the basal equilateral triangle as T, then the following three types of tetrahedrons and their associated modes of distortion can be considered: i) the ideal tetrahedron (Figure 6.8); ii) iso-bond-basal-flattened tetrahedrons (Figure 6.9); and iii) aniso-bond tetrahedrons (Figure 6.10).

In an ideal tetrahedron (Figure 6.8) with tetrahedral bond length d_t and tetrahedral edge length e_t, one has

$$
\begin{aligned}
d_t &= d_t^{api} = d_t^{bas} \\
e_t &= e_t^{bas} = e_t^{api} = 2 \cdot \sqrt{2/3} \cdot d_t \\
\tau_{bas} &= \tau_{api} = \tau_{ideal} = 2 \cdot \psi_{ideal} \cong 109.47^\circ \\
\varepsilon_{bas} &= 2 \cdot \psi_{ideal} - 90^\circ \\
h_t &= h_t^{bas} + d_t = 4/3 \cdot d_t
\end{aligned}
\qquad (6.16)
$$

where: d_t^{api} is the length of the T-O_{api} bond; e_t^{api} is the length of the three O_{api}-O_{bas} lateral edges; τ_{api} is value of the three O_{api}-T-O_{bas} angles; ψ_{ideal} is the cube-octahedron angle described by Eqns. 6.1 and 6.2; and h_t is the height of the tetrahedron. There are no distortion in an ideal tetrahedron: all T-O bonds have the same length and all O-T-O angles are the same.

In iso-bond-basal-flattened tetrahedrons (Figure 6.9) all T-O bond lengths are equal but the τ_{bas} angle is allowed to vary — hence the 'iso-bond-basal-flattened' label ('iso-bond' for short). The relationships characterizing an iso-bond tetrahedron can be written as

$$\begin{aligned} d_t &= d_t^{bas} = d_t^{api} \\ h_t &= d_t + h_t^{bas} \\ e_t^{api} &= \sqrt{h_t^2 + 1/3 \cdot \left(e_t^{bas}\right)^2} \\ \tau_{api} &= 90^\circ + \varepsilon_{bas} \end{aligned} \quad , \tag{6.17}$$

where h_t^{bas}, e_t^{bas}, and ε_{bas} are given by Eq. 6.15. Hence, it can be seen that an iso-bond tetrahedron is fully defined by specifying its bond length d_t and one other parameter. An iso-bond tetrahedron has two 'degrees of freedom'. This geometrical model of a tetrahedron was first presented by [Takeda & Morosin 1975].

In the case of an aniso-bond tetrahedron (Figure 6.10), the T-O_{api} bond length is not equal to the T-O_{bas} bond length — hence the 'aniso-bond' label. The relationships describing an aniso-bond tetrahedron can then be expressed as

$$\begin{aligned} d_t^{bas} &\neq d_t^{api} \\ h_t &= d_t^{api} + h_t^{bas} \\ e_t^{api} &= \sqrt{h_t^2 + 1/3 \cdot \left(e_t^{bas}\right)^2} \\ \tau_{api} &= 90^\circ + \varepsilon_{bas} \end{aligned} \quad , \tag{6.18}$$

where h_t^{bas}, e_t^{bas}, and ε_{bas} are also given by Eq. 6.15. An aniso-bond tetrahedron described Eq. 6.18 has three degrees of freedom: d_t^{bas} and d_t^{api}, and one other parameter. We are the first to consider aniso-bond tetrahedra in simple geometrical models of layer silicates.

6.2.5 Tetrahedral sheet

In layer silicates, tetrahedrons are linked together by sharing basal oxygen atoms as shown in Figure 6.11. If the following assumptions are made:

i) the basal oxygen atoms in each tetrahedral sheet are coplanar and their plane orientation in (001);
ii) the basal faces of tetrahedrons are equilateral triangles articulated at their vertices (Figure 6.11); and
iii) the orthohexagonal relationship $b = \sqrt{3} \cdot a$ is rigorously obeyed;

then [Donnay *et al.* 1964b] have shown that by rotating each tetrahedron by an angle α about an axis perpendicular to the (001) plane, the lateral size of the tetrahedral sheet is reduced.

In terms of the tetrahedral rotation angle α and the basal edge length e_t^{bas} of the equilateral faces, it follows that the in-plane *a* and *b* lattice parameters are given by

$$a = 2 \cdot e_t^{bas} \cdot \cos \alpha$$
$$b = 2 \cdot \sqrt{3} \cdot e_t^{bas} \cdot \cos \alpha \qquad (6.19)$$

Tetrahedral sheet models having ideal tetrahedra with $\alpha = 0°$ and $\alpha \neq 0°$ are referred to as the *Pauling model* and the *Trigonal model*, respectively (e.g., [Nespolo 1999; Ferraris & Vivaldi 2002]).

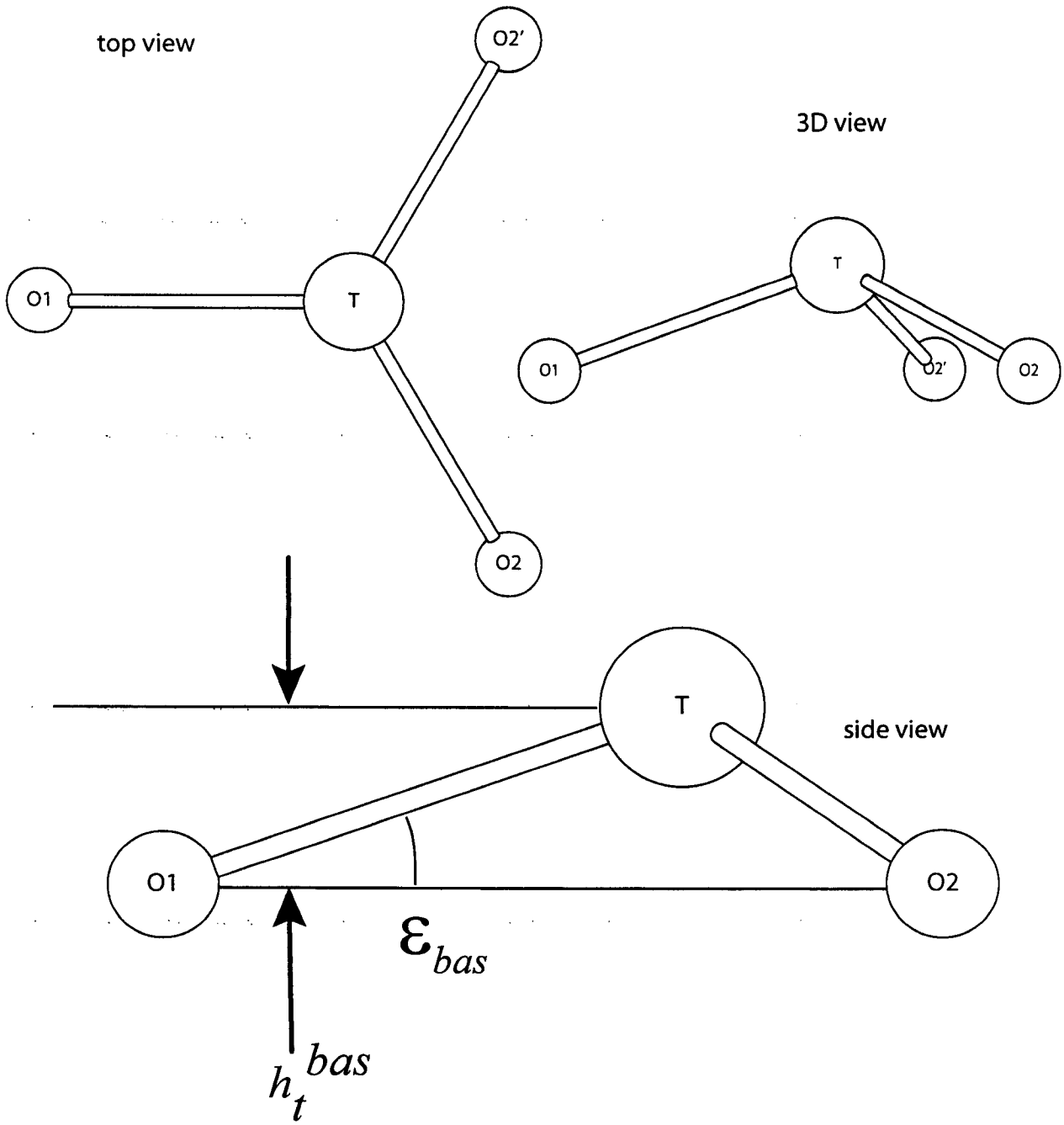

Figure 6.7. Pyramid formed by the tetrahedral cation *T* and the three basal oxygen atoms (denoted O1, O2, and O2'). The various symbols that are shown are explained in the text.

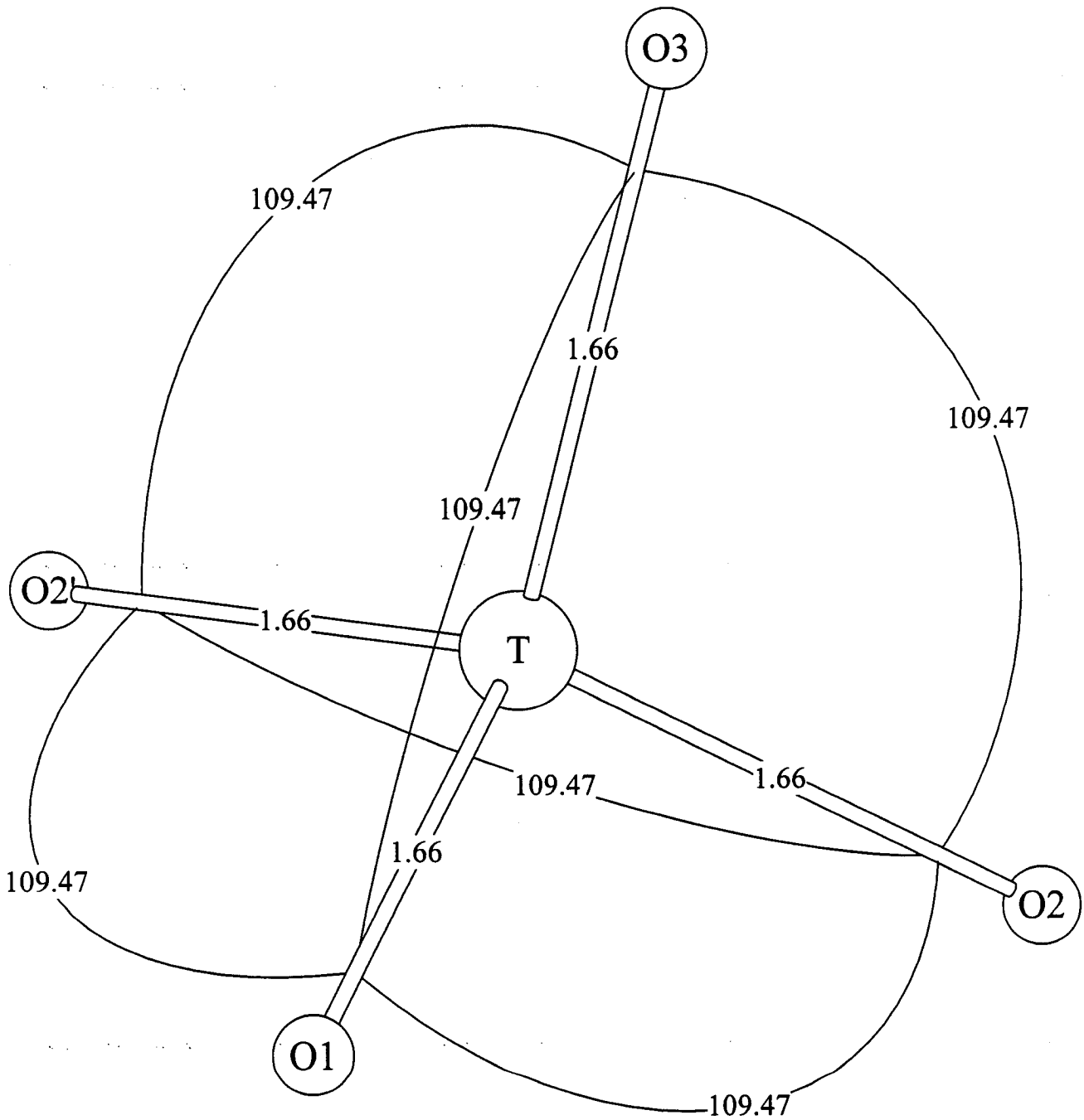

Figure 6.8. An ideal tetrahedron. The tetrahedral cation *T* is equidistant from the three basal oxygen atoms (denoted O1, O2, and O2') and the apical oxygen atom (O3), and all O-T-O angles have the same value (~109.47°).

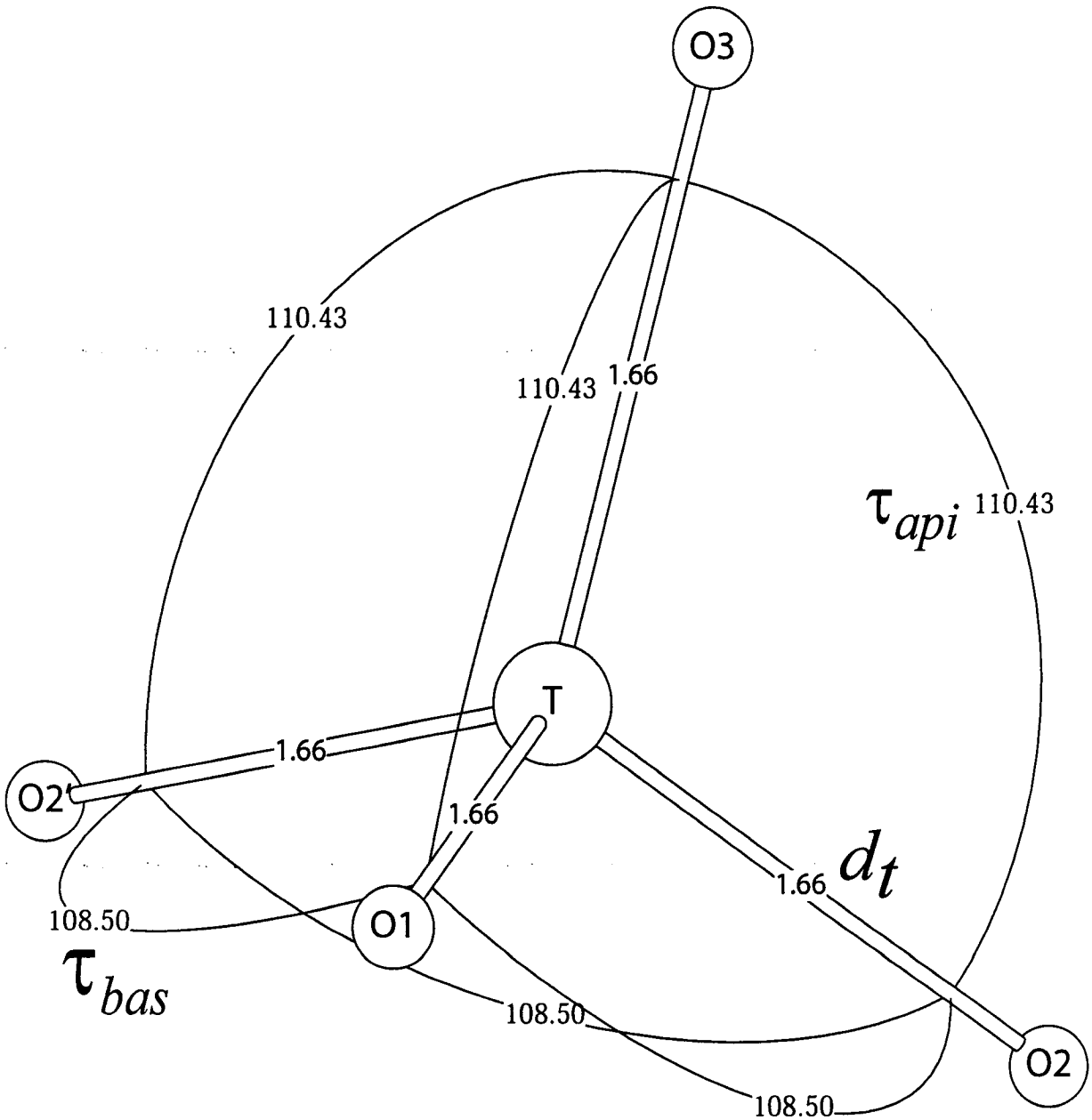

Figure 6.9. An iso-bond-basal-flattened tetrahedron (iso-bond tetrahedron for short). The tetrahedral cation *T* is equidistant from the three basal oxygen atoms (denoted O1, O2, and O2') and the apical oxygen atom (O3), but the value of the three O_{bas}-*T*-O_{bas} angles is allowed to vary.

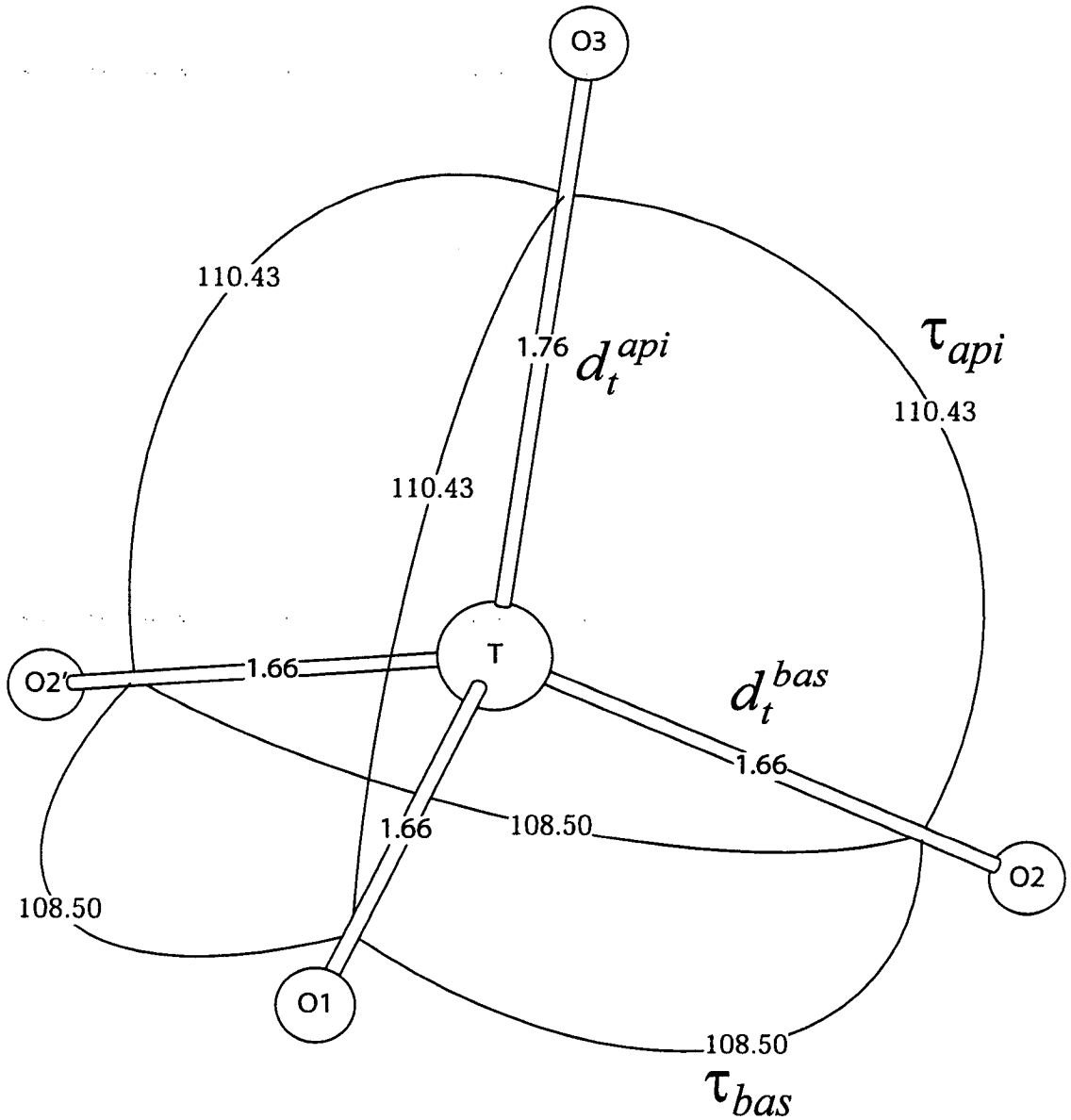

Figure 6.10. An aniso-bond tetrahedron. The distance between tetrahedral cation *T* and the one of the three basal oxygen atoms (denoted O1, O2, and O2') is different from the distance between *T* and the the apical oxygen atom (O3), and the value of the three O_{bas}-*T*-O_{bas} angles is allowed to vary.

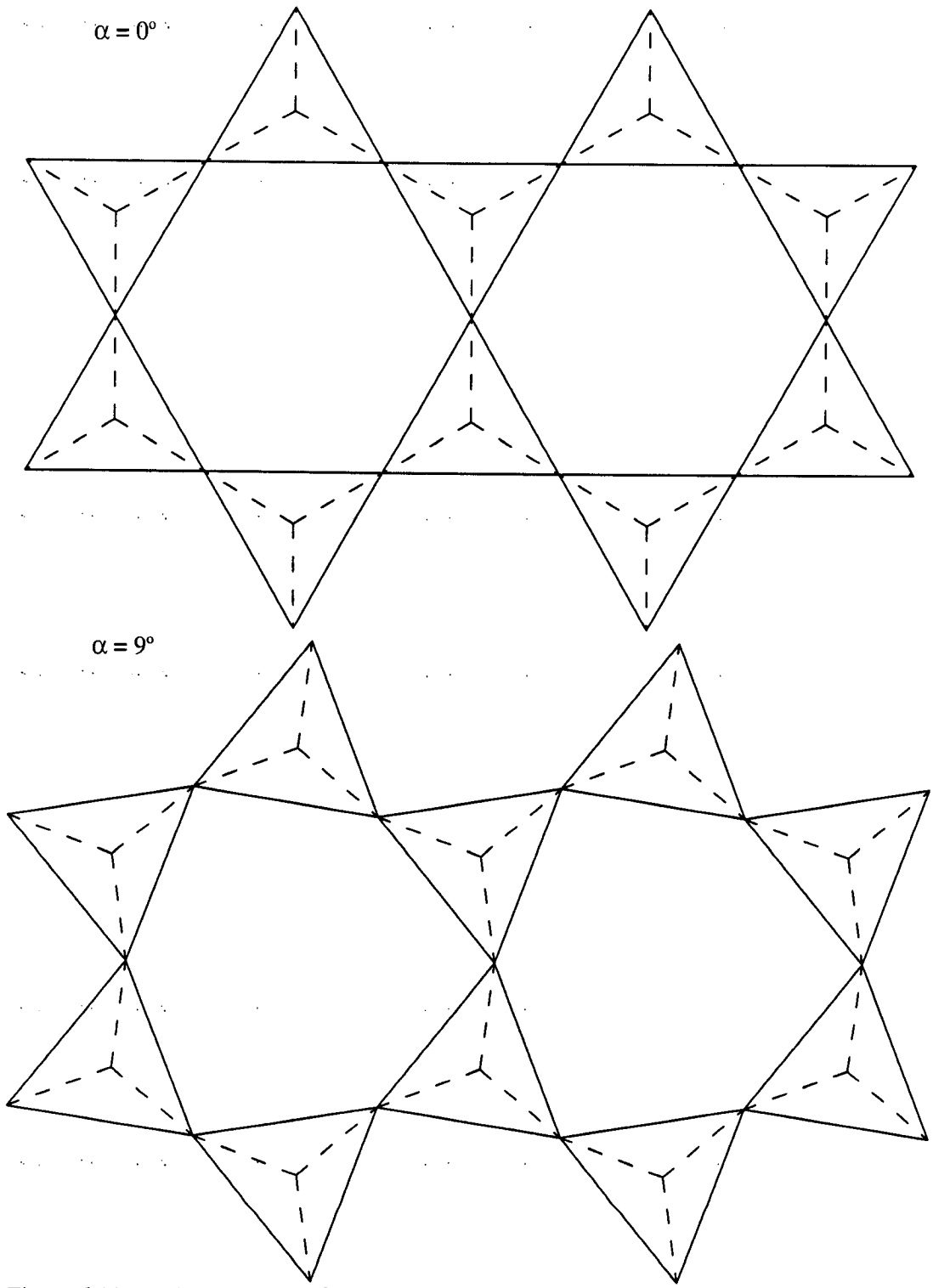

Figure 6.11. Arrangement of tetrahedrons in a tetrahedral sheet. The various symbols that are shown are explained in the text.

6.2.6 Crystal structure model for a 1*M* mica unit layer

It is now possible to construct a complete crystal structure model using idealized polyhedral networks. Consider a geometric homo-octahedral sheet to which is attached two tetrahedral sheets via the apical oxygen atoms, one above and another below, that are comprised of tetrahedrons that have their equilateral triangular basal faces lying in two single planes whose orientation is parallel to the plane of octahedral cations (Figure 6.12).

Suppose the interlayer cations lie directly above and below the OH/F groups on perpendiculars through to the *a*-*b* plane, which also go through the geometric centres of the hexagons formed by: i) the lower and upper tetrahedral apical oxygen atoms; ii) the lower and upper tetrahedral cations; and iii) the lower and upper tetrahedral basal oxygen atoms. Then, in the case of such an idealized homo-octahedral network, it can be seen (Figure 6.12) that the projections in the *a*-*b* plane of the sides of the hexagons formed by the apical oxygen atoms and tetrahedral cations are superimposed one over another, and their length is equal to *b*/3. The basal edge length of the equilateral triangular faces is related to the *a* and *b* lattice parameters via Eq. 6.19.

One now needs to define the *c* and β lattice parameters (Figure 6.13). The *c*-axis has a length equal to the norm of the shortest vector linking an interlayer cation lying below the octahedral and lower tetrahedral sheets on one end, to another interlayer cation located above the octahedral and upper tetrahedral sheets on the other end. For the conventional 1*M* mica unit layer, the origin of the unit cell is chosen so that the interlayer and *trans*-octahedral cations occupy special symmetry positions 2*b* and 2*c* of space-group type *C*2/*m* (space-group type No. 12; first setting), respectively [Pabst 1955; Donnay *et al.* 1964a, 1964b].

In the case on an idealized geometric homo-octahedral network as described above, it can be demonstrated that the projection of the *c*-axis on the *a*-*b* plane is

$$c \cdot \cos\beta^* = \frac{a}{3}, \tag{6.20}$$

where $\beta^* = \left(180^\circ - \beta\right)$. The vector that consists of this projection is illustrated on Figures 6.12 and 6.13, and is referred to as the interlayer stacking vector. The in-plane axes corresponding to the conventional 1*M* unit layer, a_{1M} and b_{1M}, are also indicated.

One can easily notice on Figure 6.13 that the interlayer spacing, d_{int}, is related to *c* by

$$c^2 = \frac{a^2}{9} + \left[d_{int} + h_o + 2 \cdot h_t\right]^2 \quad , \tag{6.21}$$

where h_o and h_t are the heights octahedral and tetrahedral sheets, respectively.

Let us now focus on the geometry of the interlayer site (Figure 6.14). As a result of tetrahedral rotation, one observes that the basal oxygen atoms form 'inner' and 'outer' octahedrons around each interlayer cation *A*. In terms of the basal edge length e_t^{bas} and the tetrahedral rotation angle α, the inner and outer bond lengths of the interlayer site can be written as [Takeda & Morosin 1975]:

$$\left(A-O\right)_{in}{}^2 = \nu^2 + \left\{e_t^{bas} - e_t^{bas}\left[\frac{\sqrt{3}}{3}\sin\alpha + \left(1-\cos\alpha\right)\right]\right\}^2$$

$$\left(A-O\right)_{out}{}^2 = \nu^2 + \left\{e_t^{bas} + e_t^{bas}\left[\frac{\sqrt{3}}{3}\sin\alpha - \left(1-\cos\alpha\right)\right]\right\}^2 \tag{6.22}$$

where

$$\nu = 1/2 \cdot \left[c \cdot \sin\beta - h_o - 2 \cdot h_t\right] \quad . \tag{6.23}$$

The subscripts 'in' and 'out' denote the inner and outer octahedrons, respectively.

Noting that the inner and outer interlayer octahedrons hence built are flattened but not counter-rotated, one can then define flattening angles for each of these octahedrons, which are referred to as ϕ_{in} and ϕ_{out}. The inner and outer interlayer octahedrons have a height equal to the interlayer spacing d_{int}; the orientations of their lower and upper triangular faces are opposite from one to another. The relationships giving ϕ_{in} and ϕ_{out} are simply

$$\cos\phi_{in} = \frac{d_{int}/2}{\left(A-O\right)_{in}}$$

$$\cos\phi_{out} = \frac{d_{int}/2}{\left(A-O\right)_{out}} \quad , \tag{6.24}$$

where $\left(A-O\right)_{in}$ and $\left(A-O\right)_{out}$ are given by Eq. 6.21.

The interlayer spacing d_{int} can be expressed as a function of the lattice parameter a, the tetrahedral rotation α, and the inner interlayer $(A-O)_{in}$ as (following [Franzini & Schiaffino 1963]):

(6.25a) $$d_{int} = \sqrt{4\cdot(A-O)_{in}{}^2 - a^2\left[1-\frac{\sqrt{3}}{3}\cdot\tan\alpha\right]^2}$$

(6.25b) $$d_{\text{int}} = \sqrt{4\cdot(A-O)_{in}{}^2 - 4\left(e_t^{bas}\right)^2\left[\cos\alpha - \frac{1}{\sqrt{3}}\sin\alpha\right]^2}$$.

We now have a complete set of equations that can be used to specify the coordinates of all atoms in a 1*M* mica unit layer comprised of a geometric homo-octahedral sheet, that depend on the particular shapes assumed for the tetrahedrons. Table 6.1 summarizes the characteristics of the different models presented in this section.

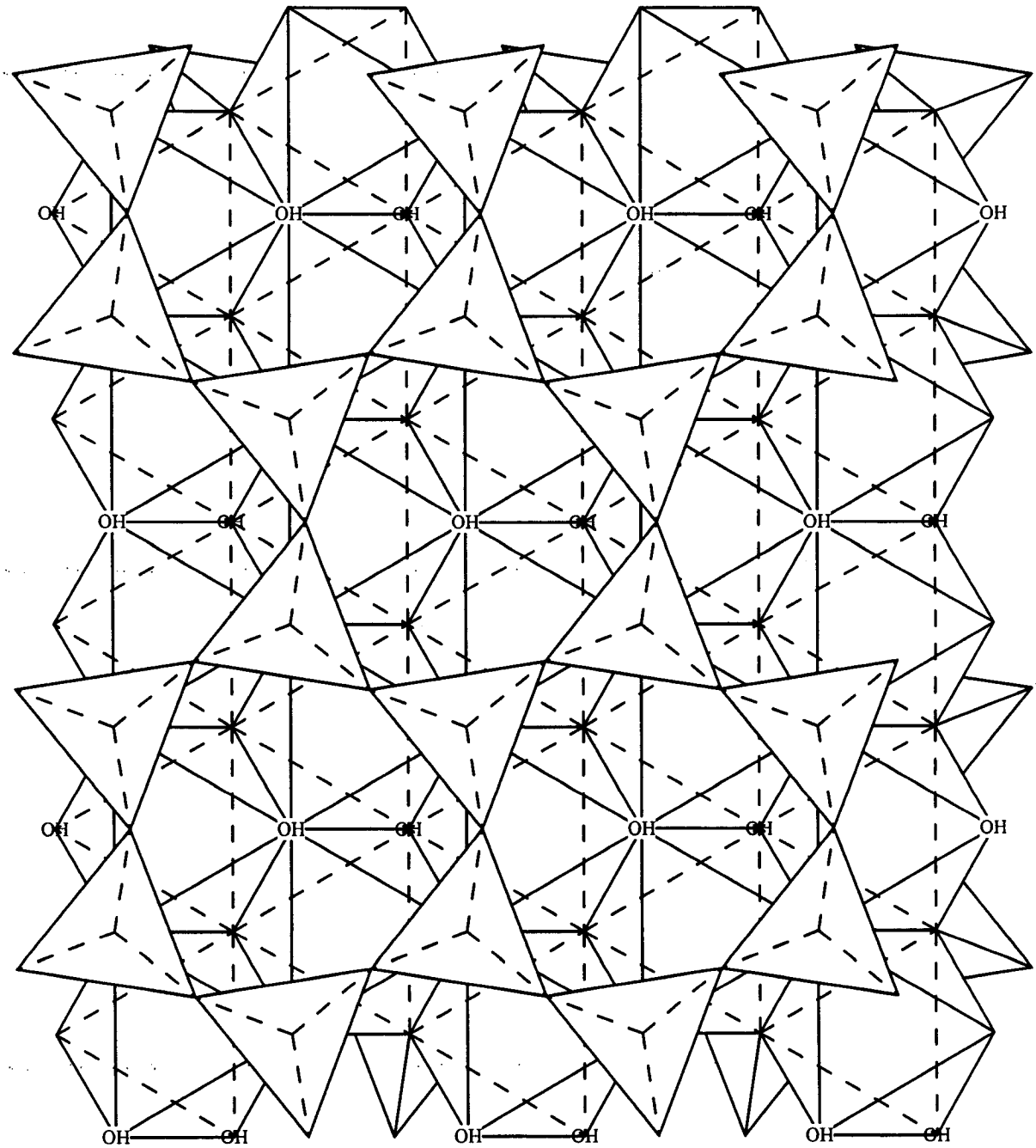

Figure 6.12. Crystal structure model for a geometric homo-octahedral sheet to which is attached two tetrahedral sheets via the apical oxygen atoms. The interlayer cations are placed directly above the OH/F groups on a perpendicular to the *a-b* plane.

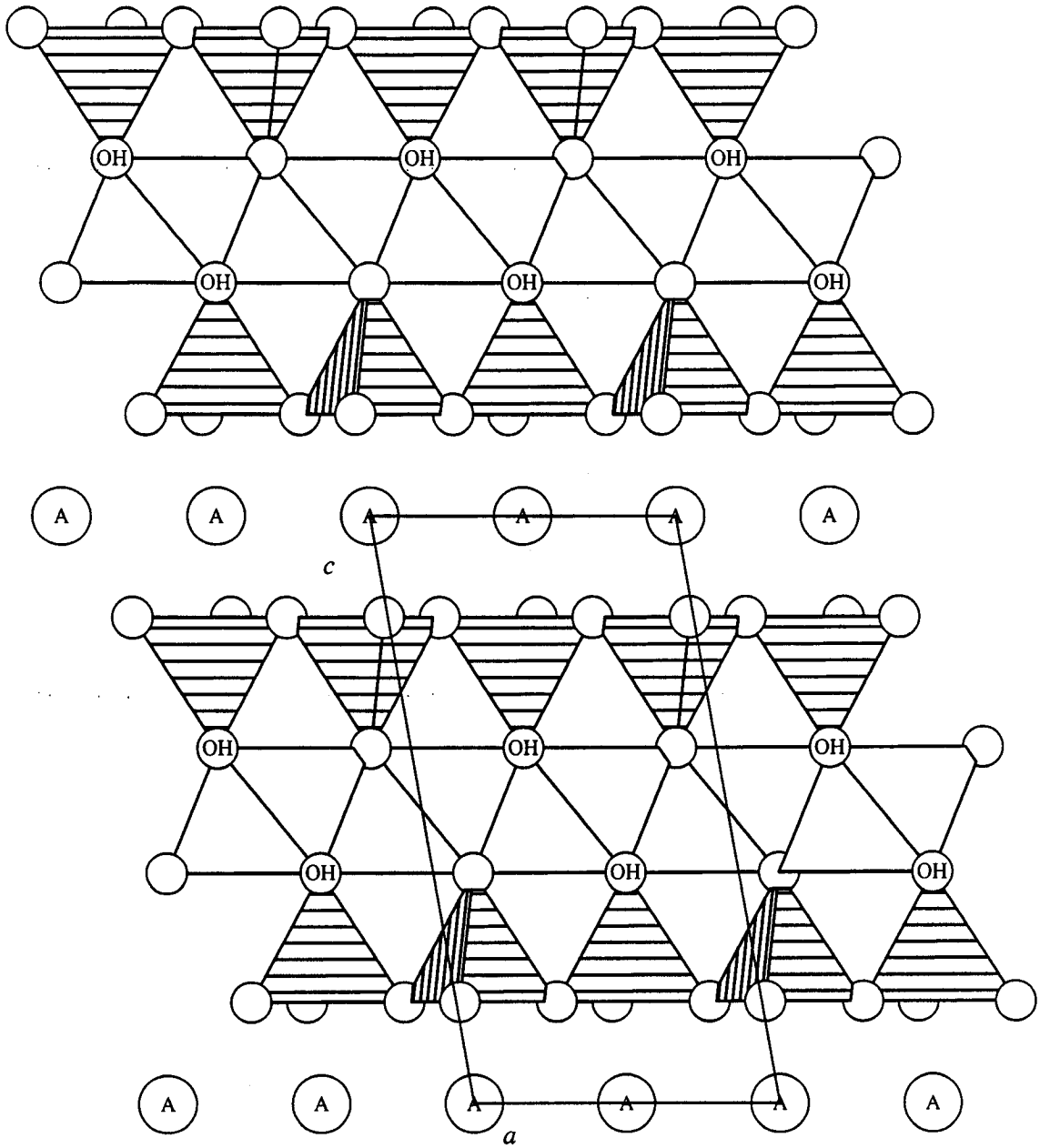

Figure 6.13. (0-10) projection showing the position of the *a* and *c* axes for the conventional 1*M* mica unit layer.

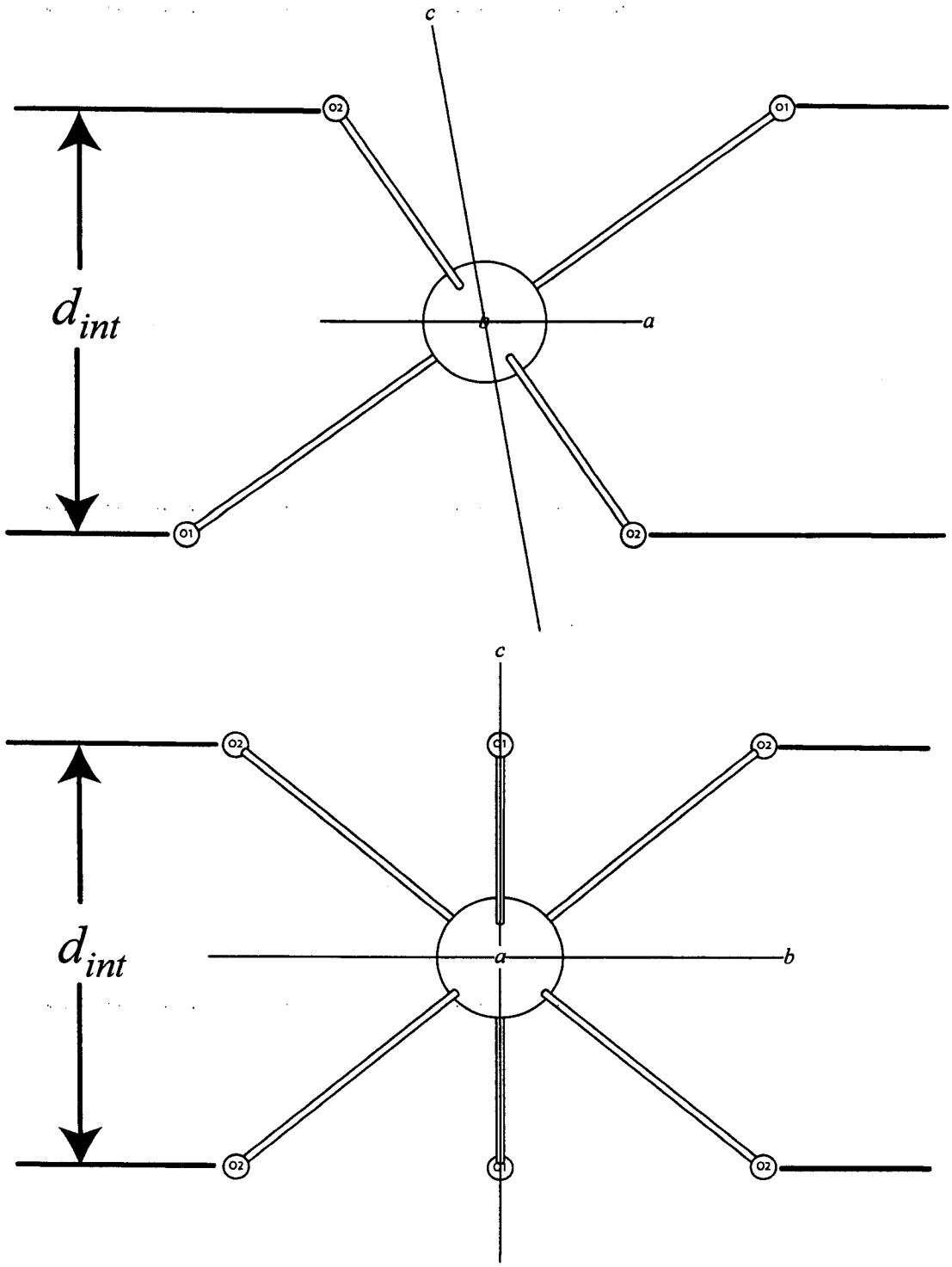

Figure 6.14. Geometry of the inner octahedron located in the interlayer site. See text for an explanation of the various symbols that are shown.

Model Type	Specified Parameters	Parameters that follow
geometric homo-octahedral sheet attached to tetrahedral sheets composed of:	d_o, h_o	a, b, ψ
i) ideal tetrahedrons	d_t, α	a,b,h_t
ii) iso-bond tetrahedrons	d_t, τ_{bas}	h^t_{bas} ,a,b,h_t
iii) aniso-bond tetrahedrons	d_t^{bas}, τ_{bas}	h^t_{bas} ,a,b, τ_{api}
	d_t^{api}	h_t
interlayer site	$(A\text{-}O)_{in}$	d_{int} , c , β
geometric meso-octahedral sheet	h_o, δ_{M2}, d_{M1} (or d_{M2})	d_{M2} (or d_{M1}), ψ_{M1}, ψ_{M2}, a, b
A tetrahedral sheet composed of ideal, iso-bond, or aniso-bond tetrahedrons cannot fit on top of a geometric meso-octahedral sheet (see Subsection 6.3.3 below)		
geometric hetero-octahedral sheet: not considered in this thesis		

Table 6.1. Summary of the different geometrical models presented in Section 6.2.

6.3 Comparison of geometrical models with single-crystal 1*M* structures

The vast majority of 1*M* mica structures have been refined in the space-group type *C*2/*m* (see [Brigatti & Guggenheim 2002]). Excluding hydrogen atoms, this symmetry provides eight independent crystallographic sites (Table 6.2): one interlayer cation site, *A*; two octahedral cation sites, *M*1 and *M*2; one tetrahedral site cation site, *T*; two basal oxygen anion sites, *O*1 and *O*2; one apical oxygen anion site, *O*3; and one OH/F anion site, *O*4. We have compiled 170 crystal structure refinements of 1*M* structures, tabulated in Appendix P, for the purpose of comparisons with our geometrical models that are reported in this thesis.

Table 6.3 lists the crystallographically independent cation-anion bond lengths, anion-anion distances (edge lengths), and selected bond angles for the octahedral, tetrahedral, and interlayer sites, along with their multiplicities. The quantities specified in Table 6.3 were calculated for all 1*M* structures tabulated in Appendix P and are compiled therein.

Atom	Multiplicity	Wyckoff	Site Symmetry
A	2	b	2/*m*
M1	2	c	2/*m*
M2	4	h	2
T	8	j	1
O1	4	i	m
O2	8	j	1
O3	8	j	1
O4	4	i	*m*

Table 6.2. Independent crystallographic sites for the conventional 1*M* mica unit layer, space-group type *C*2/*m*.

	Octahedral sheet		
	Bond Lengths	Unshared Edges	Shared Edges
	(M1-O3) x 4	(O3-O3) x 2	(O3-O3) x 2
	(M1-O4) x 2	(O3-O4) x 4	(O3-O4) x 4
	(M2-O3) x 2	(O3-O3') x 2	(O3-O3) x 1
	(M2-O3') x 2	(O3-O4) x 2	(O3-O4) x 2
	(M2-O4) x 2	(O3'-O4) x 2	(O3-O3) x 2
			(O4-O4) x 1
	Tetrahedral sheet		
	Bond Lengths	Edges	Angles
Basal	(T-O1)	(O1-O2) x 1	τ (O1-T-O2)
	(T-O2)	(O1-O2') x 1	τ (O1-T-O2')
	(T-O3)	(O2-O2') x 1	τ (O2'-T-O2)
Apical	(T-O3)	(O3-O1) x 1	τ (O1-T-O3)
		(O3-O2) x 1	τ (O2-T-O3)
		(O3-O2') x 1	τ (O2'-T-O3)
	Interlayer Bond lengths		
		$(A\text{-}O1)_{in}$ x 2	
		$(A\text{-}O2)_{in}$ x 4	

Table 6.3. Crystallographically independent cation-anion bond lengths, anion-anion distances (edge lengths), and selected bond angles for the octahedral, tetrahedral, and interlayer sites, along with their multiplicities.

6.3.1 Distortions of octahedrons

Figures 6.15 and 6.16 show the variations of individual cation-anion distances as a function of average octahedral bond lengths for the *M*1 and *M*2 sites, respectively, for a suite of crystal structure refinements of 1*M* structures tabulated in Appendix P .

In the *M*1 octahedrons, (M1-O3) and (M1-O4) distances increase linearly with the average <M1-O> at slightly different rates. In contrast with [Toraya 1981], who concluded an almost constant difference of 0.05 Å between (M1-O3) and (M1-O4), it is observed that the differences between these two distances increase as <M1-O> decreases. Note that the study of [Toraya 1981] was based on a survey including only fifteen (15) 1*M* mica structures, whereas Figure 6.15 includes 170 structures.

In the case of *M*2 octahedrons (Figure 6.16), the systematics displayed by the variations of the (M2-O3), (M2-O3'), and (M2-O4) distances with the average <M2-O> are somewhat poorer. In general (M2-O3) and (M2-O3') are larger than (M2-O4) for a given structure, except for Rietveld-refined synthetic annite-syderophyllite structures which display the opposite behaviour — i.e., (M2-O4) > (M2-O3), (M2-O3') (see Figure 6.16, bottom). The three M2-O distances increase more or less linearly with <M2-O> at approximately the same rate, except for a few samples that are numbered individually on a separate blow-up (Figure 6.16, bottom).

Extrema and notable exceptions in Figures 6.15 and 6.16 are (see Table 1.1 for nomenclature): lepidolite, Nos. 28, 65, 144; paragonite, No. 147; clintonite, Nos. 46-48, 68, 129-134; preiswerkite, Nos. 51-52; norrishite, No. 80; synthetic tetra-Ge-phlogopite, Nos. 71, 79; synthetic Cs-tetra-ferri-annite, Nos. 44-45; a Mn-rich biotite sample, No. 32; an annite sample, No. 165; oxybiotite, Nos. 27, 53; a synthetic Mn-F-Mg-mica sample, No. 74; a hydrogenated-biotite sample, No. 67; Rietveld-refined synthetic annite-syderophyllite samples, Nos. 55-62; and some biotite specimens, Nos. 1, 96, 100-102 ($[Ti]_{apfu} \approx 0.6$), 114-115 & 118 ($[Ti]_{apfu} \approx 0.4$, Ba-rich), 145, 150.

The observation that M-O4 distances are smaller than M-O3 distances for the *M*1 and *M*2 sites can be (partially) understood in terms of an electrostatic repulsion between the interlayer cations and the OH-group protons. The interlayer cations exert electrostatic forces on the protons that cause a displacement (depression) of the OH groups towards the plane of octahedral cations, that is also most likely accompanied with a certain bending of the O-H dipole direction. The overall effect is that the apical oxygen atoms located in the *O*3 site are *not* coplanar with the OH-groups of the *O*4 site, i.e. $O3_z \neq O4_z$.

Such effects (unequal M-O bond lengths and non-co-planar O3 and O4 atoms) were not

taken into account in the geometrical models presented in Section 6.2 and shall now be addressed. Consider the distorted *M*1 and *M*2 octahedrons that are shown in Figure 6.17. If the depression of the O4 sites occurs on axes perpendicular to the plane of octahedral cations, then, in terms of the (M1-O3) bond length and the observed depression $(O4z - O3z)\cdot c\cdot \sin\beta$, one can predict the (M1-O4) bond length to be given by:

$$(M1-O4) = \sqrt{\begin{array}{l}(M1-O3)^2 \sin^2\psi_{M1-O3} + \\ \left[(M1-O3)\cos\psi_{M1-O3} - (O4z-O3z)c\sin\beta\right]^2\end{array}} \tag{6.26}$$

where ψ_{M1-O3} represents the flattening angle of the individual (M1-O3) bond length with respect to the *c**-direction. Using the *O*3 positions reported in Appendix P, ψ_{M1-O3} can be written as

$$\psi_{M1-O3} = \arccos\left[\frac{(\tfrac{1}{2} - O3z)c\sin\beta}{(\mathrm{M1-O3})}\right] \tag{6.27}$$

Similarly, one can also predict the (M2-O4) bond lengths. In this case, since the (M2-O3) and (M2-O3') distances are not necessarily equal, three separate predictions can be obtained:

$$(M2-O4) = \sqrt{\begin{array}{l}(M2-O3)^2 \sin^2\psi_{M2-O3} + \\ \left[(M2-O3)\cos\psi_{M2-O3} - (O4z-O3z)c\sin\beta\right]^2\end{array}}$$

$$(M2-O4) = \sqrt{\begin{array}{l}(M2-O3')^2 \sin^2\psi_{M2-O3'} + \\ \left[(M2-O3')\cos\psi_{M2-O3'} - (O4z-O3z)c\sin\beta\right]^2\end{array}}$$

$$(M2-O4) = \sqrt{\begin{array}{l}\left[\frac{(M2-O3)+(M2-O3')}{2}\right]^2 \sin^2\psi_{M2-O3} + \\ \left[\left(\frac{(M2-O3)+(M2-O3')}{2}\right)\cos\left(\frac{\psi_{M2-O3}+\psi_{M2-O3'}}{2}\right) - (O4z-O3z)c\sin\beta\right]^2\end{array}} \tag{6.28}$$

where

$$\Psi_{M2\text{-}O3} = \arccos\left[\frac{(\tfrac{1}{2} - O3z)c\,\sin\beta}{(\mathrm{M2 - O3})}\right]$$

(6.28)

$$\Psi_{M2\text{-}O3'} = \arccos\left[\frac{(\tfrac{1}{2} - O3z)c\,\sin\beta}{(\mathrm{M2 - O3'})}\right]$$

Figure 6.18 compares observed (M1-O4) and (M2-O4) bond lengths to predictions made using Eqs. 6.25 and 6.27. Extrema and notable exceptions in Figure 6.18 are the same as those discerned for Figures 6.15 and 6.16, with the addition of two structures: biotite, No. 143 ($[Ti]_{apfu} \approx 0.3$); and ferrokinoshitalite, No. 81.

The degree to which the data points coincide with each of the 1:1 correspondence lines indicates how adequate our O4-site depression model of Figure 6.17 is insofar as predicting individual octahedral bond lengths on a given crystallographic *M*-site. The agreement of the model with the data is within ~0.02 Å and ~0.04 Å for the *M*1 and *M*2 sites, respectively, excluding the above mentioned exceptions.

Cases severely incongruent with the *O*4-site depression model for either the *M*1 or *M*2 sites are: norrishite, No. 80; and biotite, No. 145. There is nothing special with the latter biotite specimen except for a relatively high agreement factor *R* of 13.5 % , whereas norrishite was already pointed out in Figure 6.3 as a exception to the hexagonal pseudo-symmetry demonstrated by the $b = \sqrt{3} \cdot a$ relationship (Section 6.1). In addition, Rietveld-refined synthetic annite-syderophyllite structures Nos. 55-62 are systematically shifted from the 1:1 correspondance lines.

It is interesting to notice that clintonite (Nos. 46-48, 68, 129-134), preiswerkite (Nos. 51-52), lepidolite (Nos. 28, 65, 144), and paragonite (No. 147) structures agree with the model in the case of *M*1 sites except for Nos. 68 and 147, but not for *M*2 sites where it is seen (Figure 6.18) that predicted values are smaller than observed (M2-O4) bond lengths in all cases — the ideal octahedral sheet content of each species is $[Mg_2Al]$ for clintonite and preiswerkite, $[Li_{2\text{-}1.5}Al_{1\text{-}1.5}]$ for lepidolite, and $[Li_2\square]$ for paragonite.

On the other hand, there are structures — namely, oxybiotite, Nos. 27, 53; a tetra-Ge-mica, No. 71; a hydrogenated-biotite, No. 67; biotite, Nos. 96, 100-102, 114-115 & 118, 143, 145, 150 — that display an opposite behaviour: predicted values are higher than observed (M2-O4) bond lengths, whereas (M1-O4) predicted and observed distances show a fair agreement. In general, these structures also stand out on Figure 6.16 (bottom).

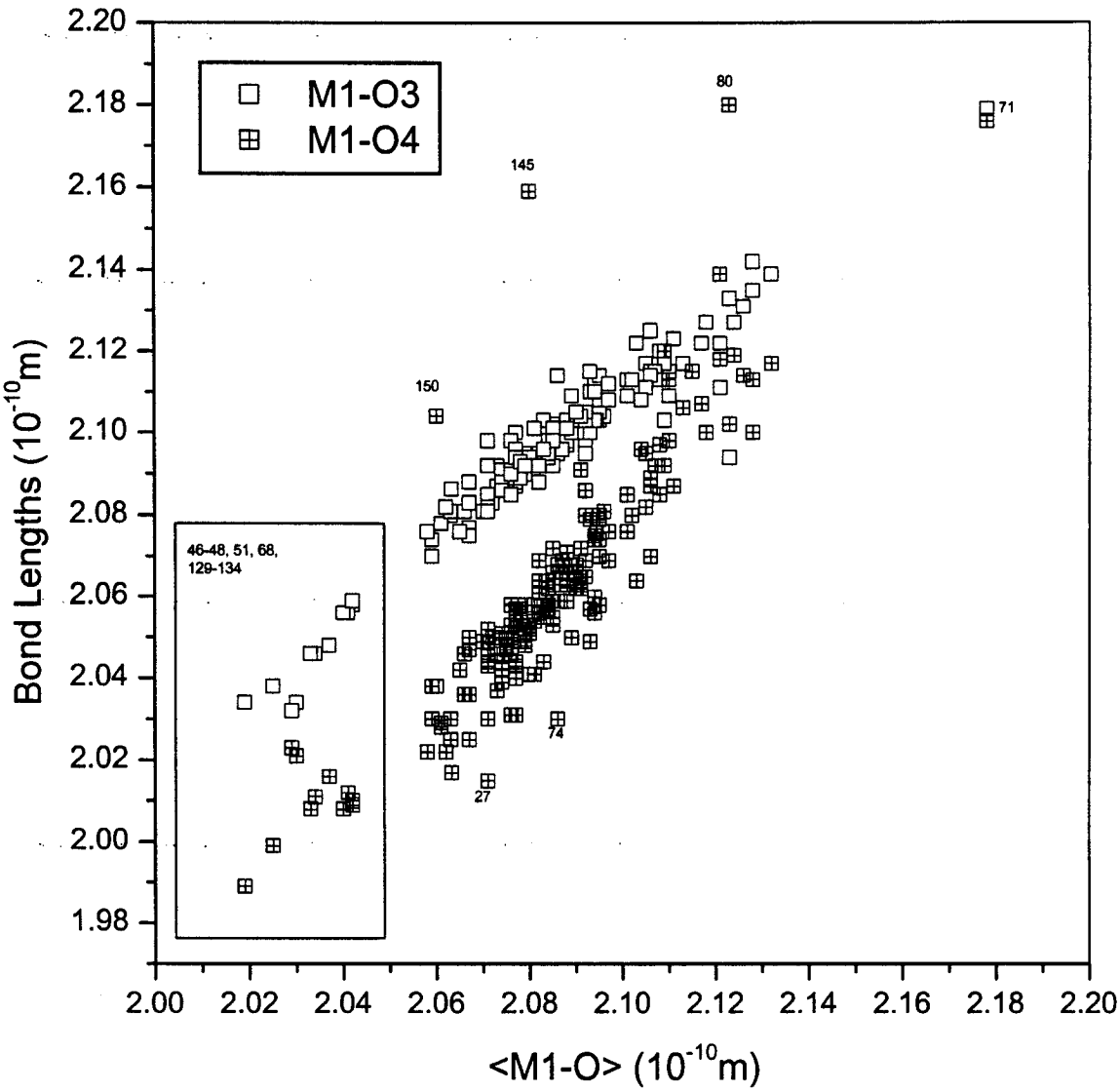

Figure 6.15. Variations of individual bond lengths for the *M*1 sites. Samples labelled with their corresponding structure Nos. (Appendix P) are discussed in the text.

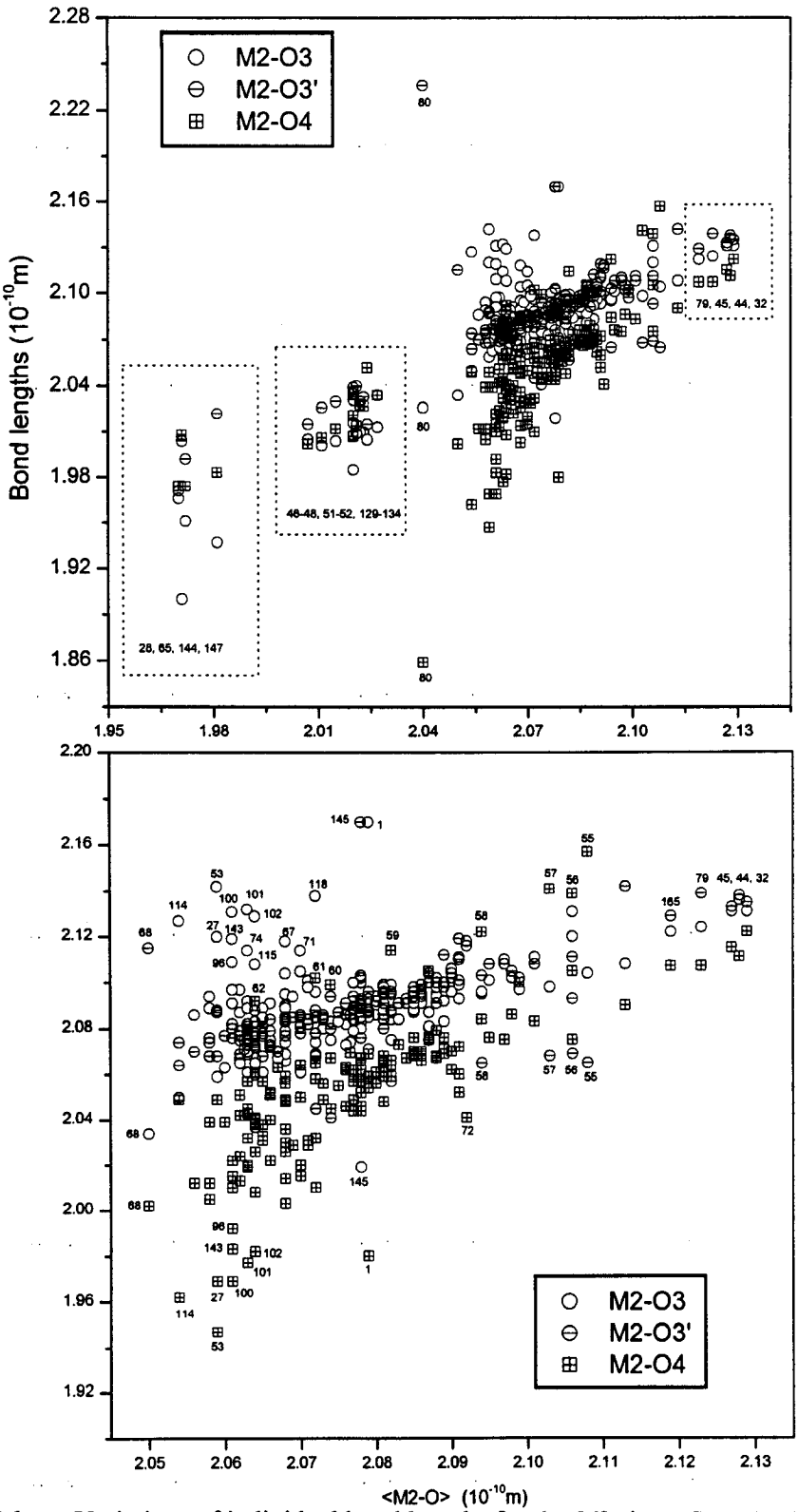

Figure 6.16. Variations of individual bond lengths for the *M*2 sites. Samples labelled with their corresponding structure Nos. (Appendix P) are discussed in the text.

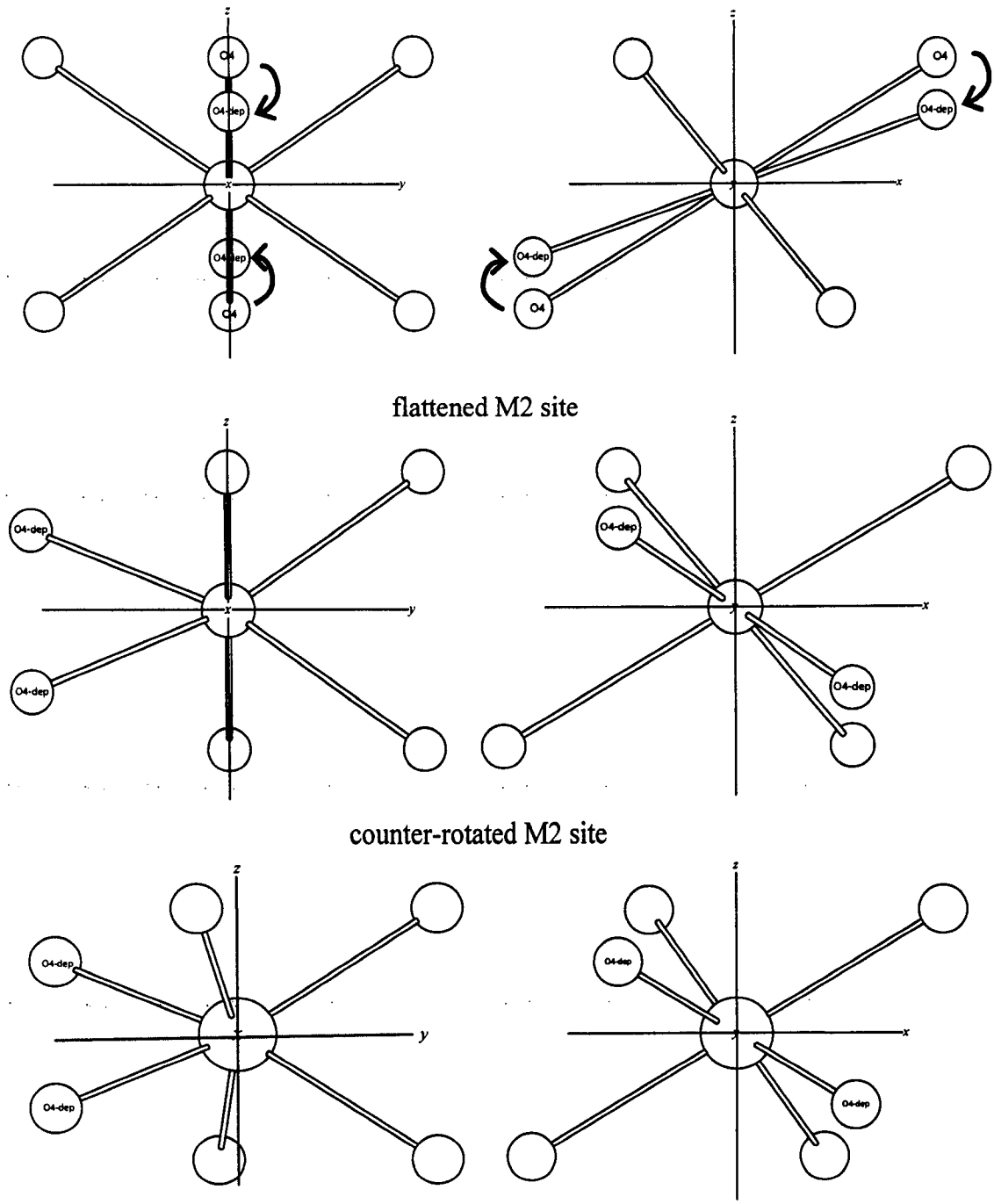

Figure 6.17. Geometrical model for the depression of the *O*4 site. See text for an explanation of the model.

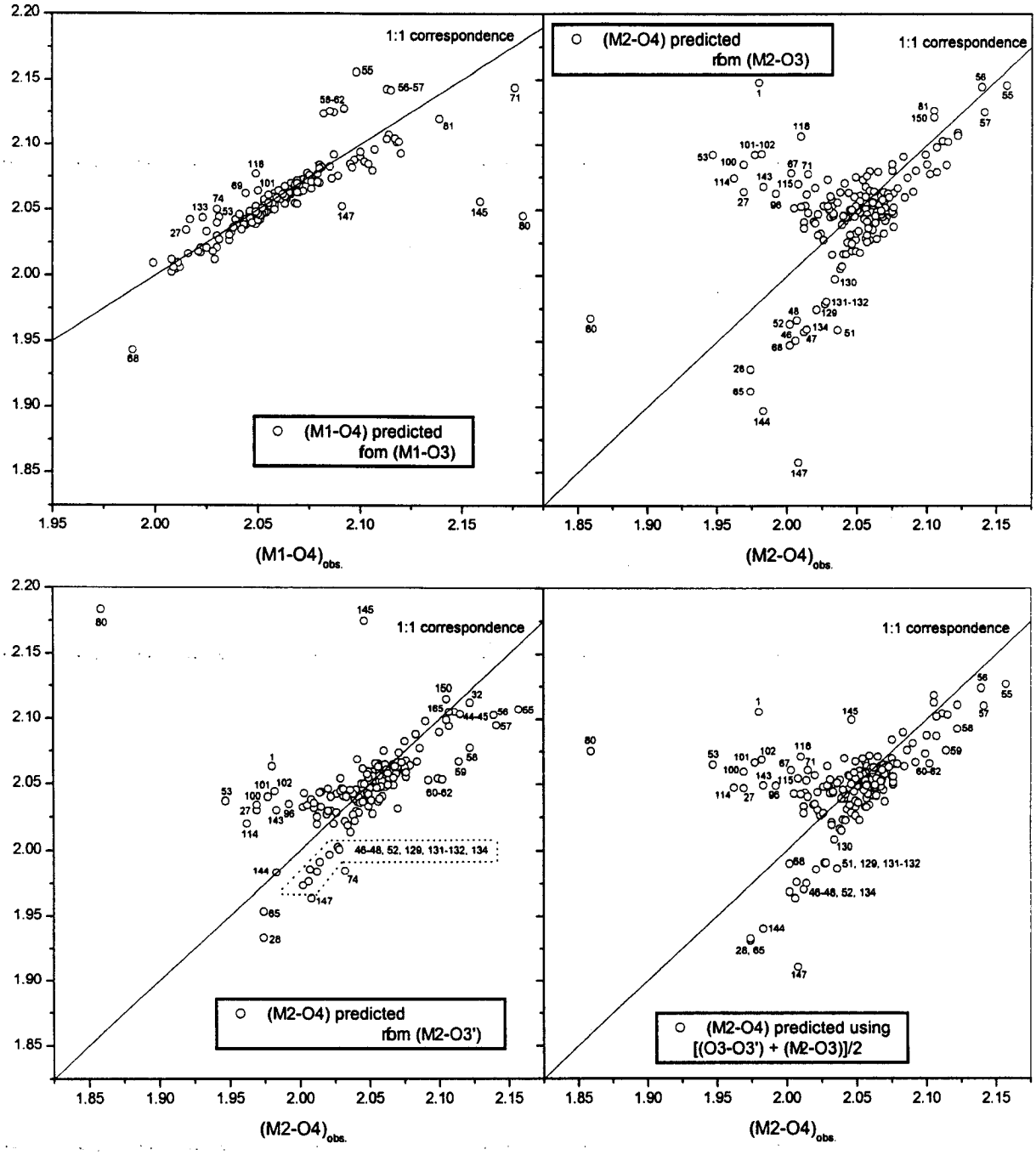

Figure 6.18. Comparison of observed (M1-O4) and (M2-O4) bond lengths with predictions made using the *O*4-depression model presented in Figure 6.17.

Let us now examine the systematics displayed by the octahedral edges. Figures 6.19 and 6.20-6.21 show the variations of individual *shared edge* lengths with their average values $\langle e_s \rangle$ in *M*1 and *M*2 octahedrons, respectively. The solid lines drawn in these figures indicate a 1:1 correspondence between the *x* and *y* axes. Notable exceptions are the same as those pointed out for Figures 6.15, 6.16, and 6.18.

In *M*1 octahedrons (Figure 6.19), (O3-O3) and (O3-O4) increase approximately linearly along the 1:1 correspondence lines, showing more scatter for the (O3-O3) edges. In accordance with our *O*4-site depression model (Figure 6.17), (O3-O3) edge lengths are usually larger than those of (O3-O4). In *M*2 octahedrons (Figure 6.20 and 6.21), the lengths of the shared edges are generally in the order (O3-O3) > (O3-O4) > (O4-O4), and are hence also in agreement with our *O*4 depression model.

Among the four individual shared edge lengths of *M*2 octahedrons (Figure 6.21), two of them refer to edges shared between *M*1 and *M*2 octahedrons, $(O3\text{-}O3)^{M1\text{-}M2}$ and $(O3\text{-}O4)^{M1\text{-}M2}$, and the remaining two correspond to edges shared between two *M*2 octahedrons, $(O3\text{-}O3)^{M2\text{-}M2}$ and $(O4\text{-}O4)^{M2\text{-}M2}$. As previously explained in Subsection 6.2.1, the shared edge lengths also depend on the angle of counter-rotation of a given octahedron.

Counter-rotation angles of *M*2 octahedrons, δ_{M2}, were calculated in a manner similar to [Weiss *et al.* 1985] (i.e. $\delta_{M2} = \delta_{Weiss}/2$, see Figure 6.27 below) and are tabulated in Appendix P. In *M*1octahedrons, when obtained as in [Weiss *et al.* 1985], counter-rotation angles are zero by symmetry.

The relationships between shared edge lengths and counter-rotation angles are illustrated Figure 6.22, where differences $[(O3\text{-}O3)^{M1\text{-}M2} - (O3\text{-}O3)^{M2\text{-}M2}]$ and $[(O3\text{-}O4)^{M1\text{-}M2} - (O4\text{-}O4)^{M2\text{-}M2}]$ are plotted as a function of δ_{M2}. In an ideally flattened and counter-rotated octahedron, as mentioned in Subsection 6.2.1, $O3z = O4z$ and the six shared edges of a given octahedron fall into two groups of three, where the edge lengths for each group are given by Eq. 6.8. In 1*M* structures, however, $O3z \neq O4z$ and one additional degree of freedom is hence possible.

Nevertheless, as emphasized by the short-dash lines drawn on Figure 6.22 as guides to the eye, the plotted differences evolve linearly with δ_{M2}, the scatter being much narrower in cases involving *O*3 atoms only. This means that shared edge lengths depend first on the degree of counter-rotation, and then on the amount of depression of the *O*4 site.

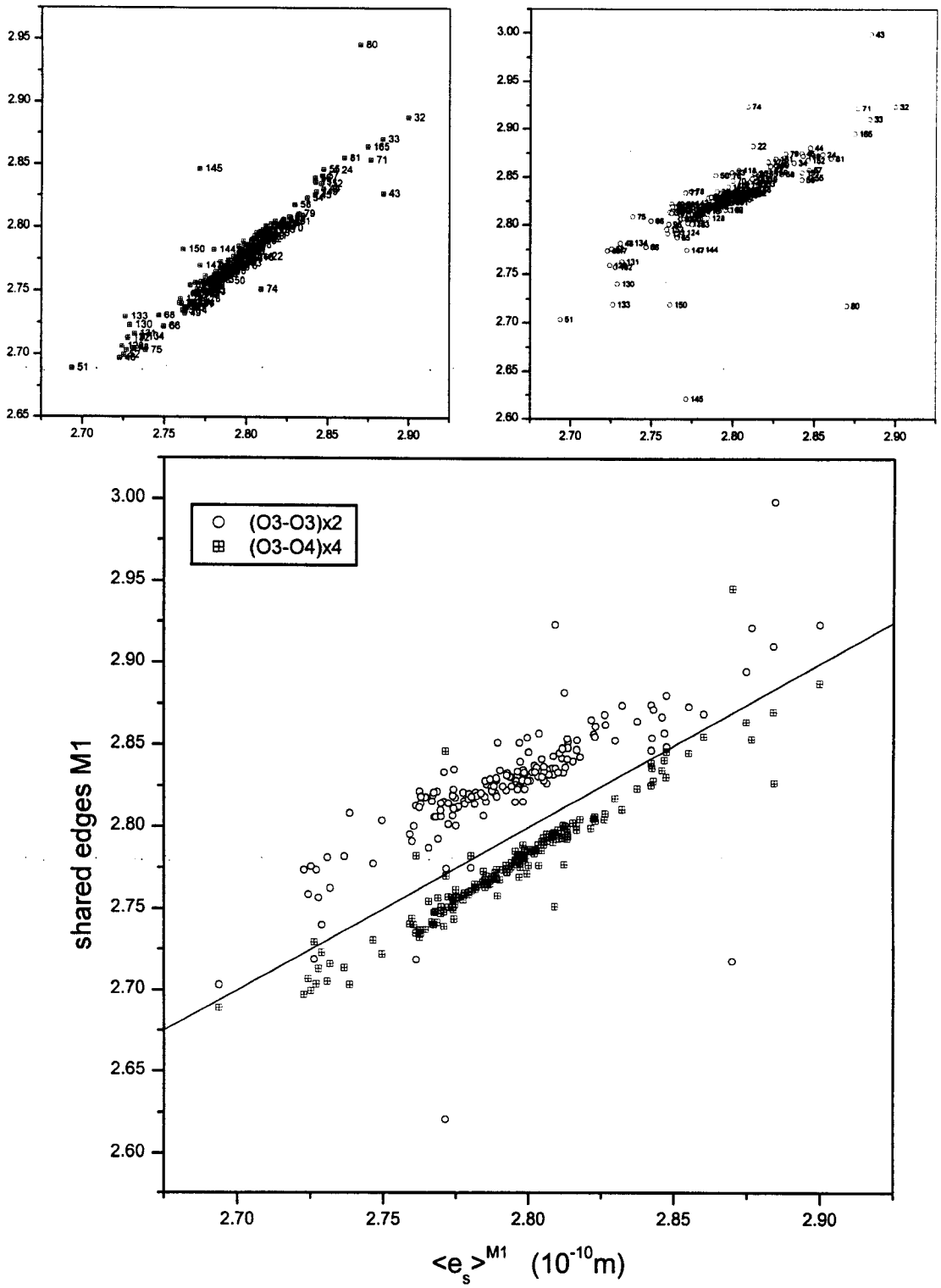

Figure 6.19. Variations of individual shared edges with their averages values for the *M*1 octahedrons. The solid line is a 1:1 correspondence between *x* and *y* axes.

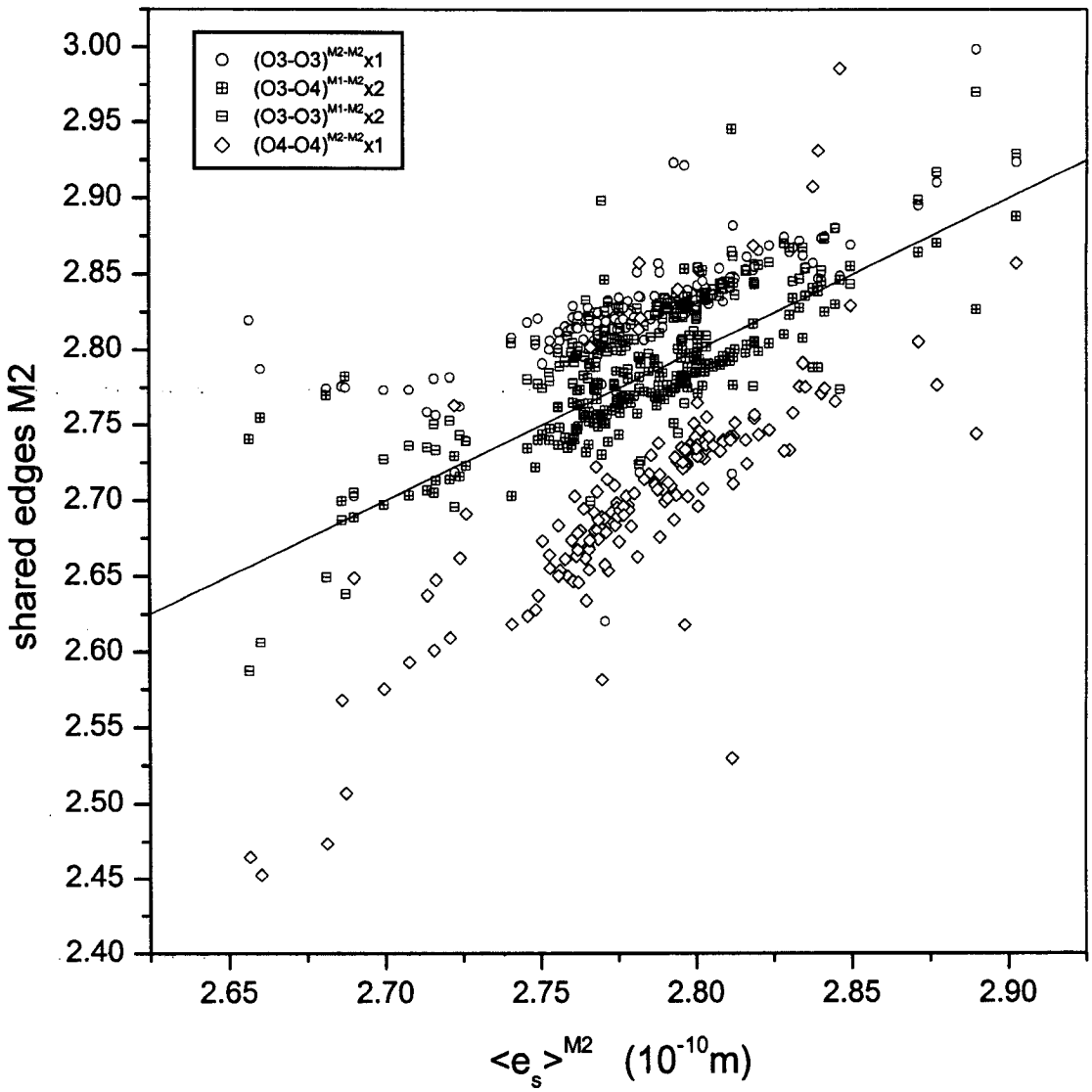

Figure 6.20. Variations of individual shared edges with their average values for the *M*2 octahedrons. The solid line is a 1:1 correspondence between *x* and *y* axes.

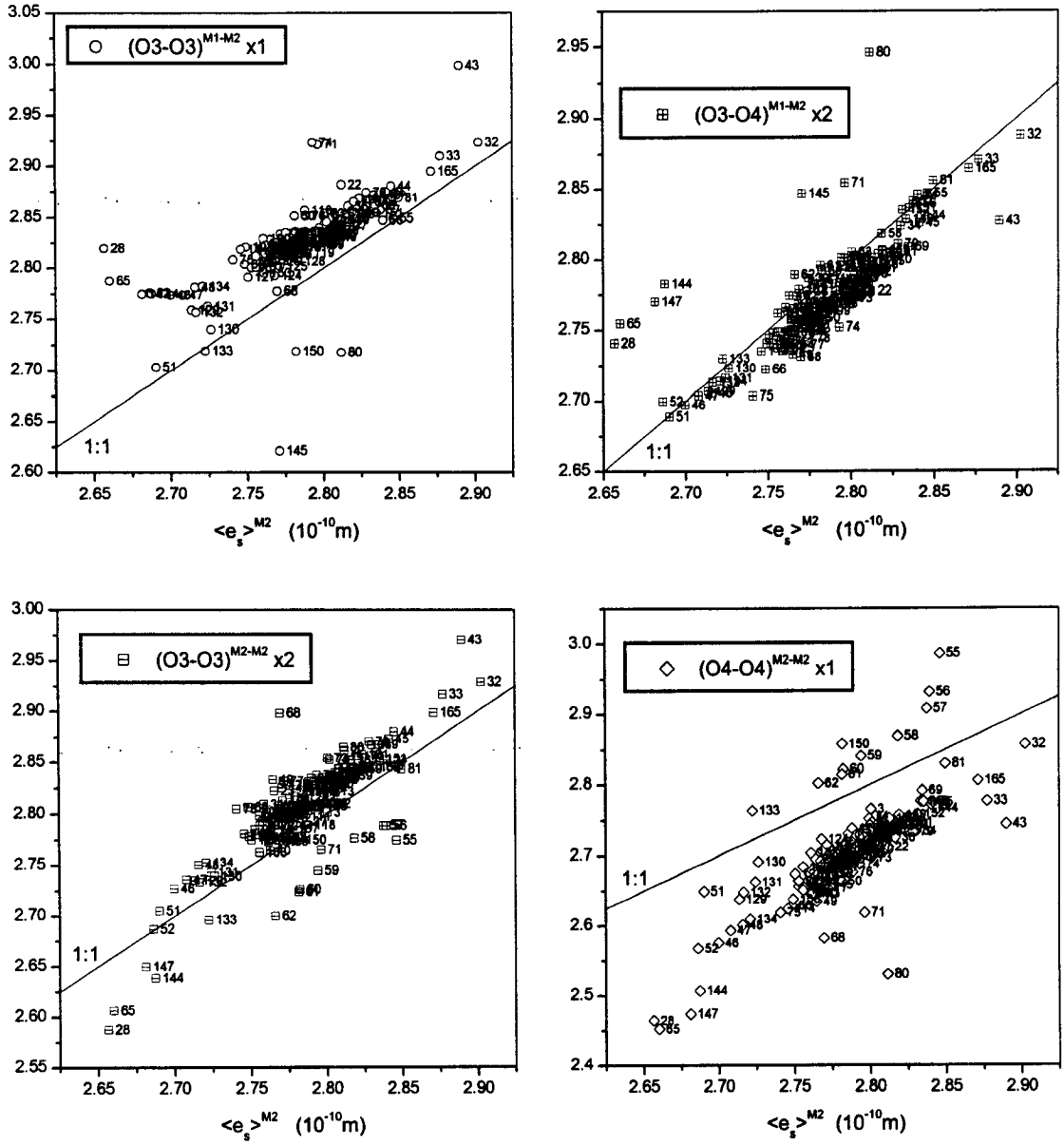

Figure 6.21. Identification of data points plotted in Figure 6.20. The solid lines are 1:1 correspondence between *x* and *y* axes.

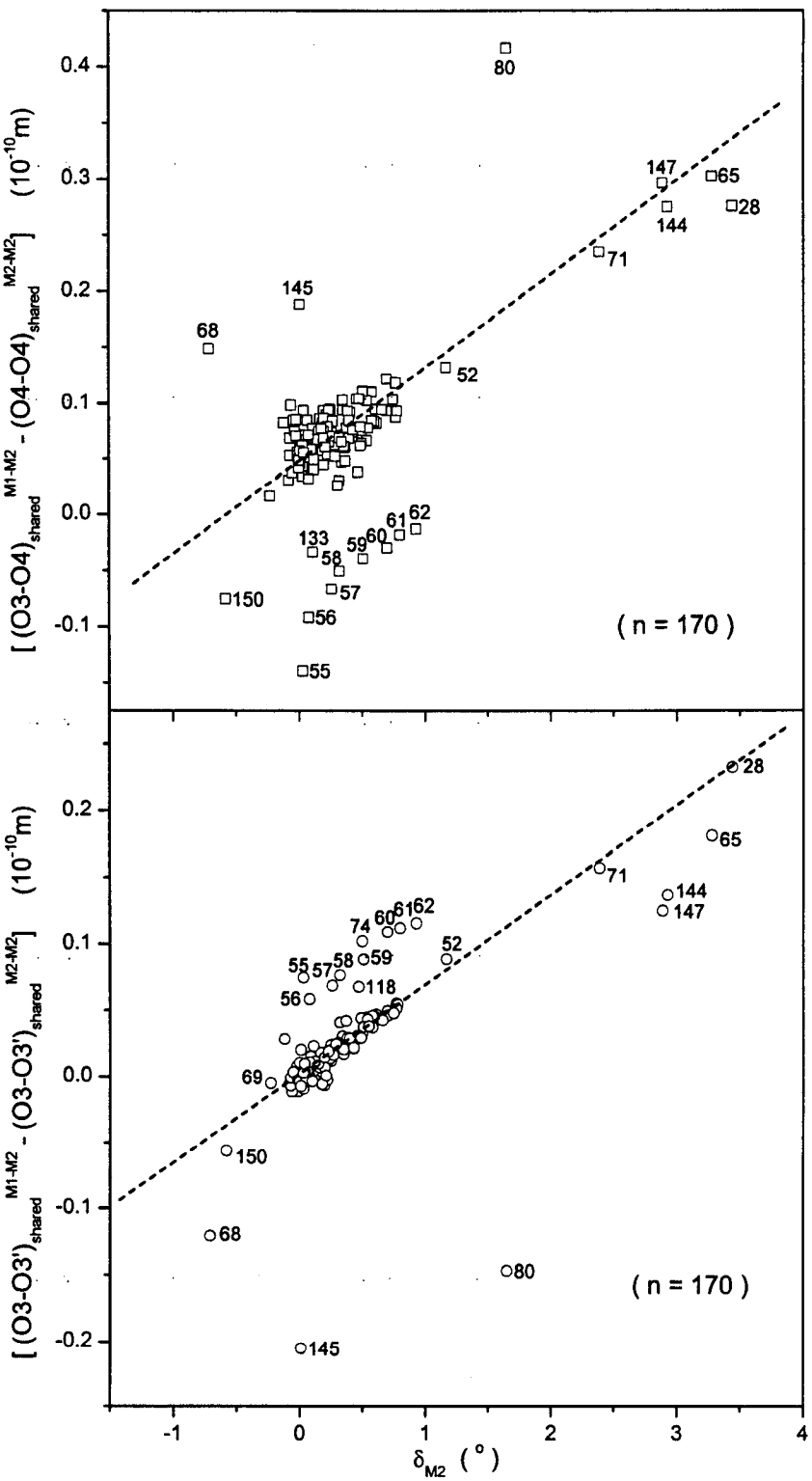

Figure 6.22. Shared edge length differences in *M*2 octahedrons as a function of counter-rotation angles δ_{M2}. The dashed lines are guides to the eye.

Figures 6.23 and 6.24-6.25 present the variations of individual *unshared edge* lengths with their average values $<e_u>$ in *M*1 and *M*2 octahedrons, respectively. Given the space-group symmetry positions occupied by the *M*1, *O*3, and *O*4 atoms, it follows that in *M*1 octahedrons top and bottom triangular faces formed by unshared edges are at least isosceles, with an *M*1 cation lying at the centre of mass of each *M*1 octahedron. When (O3-O4) and (O3-O3) distances are equal, the triangular faces are equilateral; Figure 6.23 gives the extent to which this is the case.

On the other hand, from space-group symmetry positions, an *M*2 cation is not necessarily at the centre of mass of an *M*2 octahedron, while top and bottom triangular faces formed by the unshared edges are in principle scalene. However, Figure 6.24 (bottom) demonstrates that *M*2 triangular faces are actually at least isosceles, (O3'-O4) being essentially always equal to (O3-O3'). The only exception to this observation is the norrishite structure, No. 80.

The ratio between the two uneven side lengths of an isosceles triangle can be taken as a measure of its 'degree of isosceles-ness'. In Figure 6.26, ratios (O3-O4)/(O3-O3') for *M*1octahedrons are plotted as a function of ratios {[(O3-O3')+(O3'-O4)]/2}/(O3-O4)} for *M*2 octahedrons. Given that the data points approximately follow the 1:1 correspondence line between the *x* and *y* axes, one concludes that the degree of isosceles-ness of *M*1 and *M*2 octahedrons are related one to another.

The latter observation can be linked to the in-plane distortion angle ε_{M1}, which is defined as the angle between the direction of the *a* axis and the projection of an (M1-O3) bond length on the *a-b* plane (see Figure 6.27). For an ideal or flattened octahedron located at the *M*1 site, $\varepsilon_{M1} = 60^{\circ}$; this condition applies for geometric homo-octahedral and geometric meso-octahedral sheets (Figures 6.5 and 6.6, respectively), but it is not imposed by the space-group symmetry of the *O*3 site in a 1*M* structure. Values of ε_{M1} were calculated for *M*1 octahedrons and are tabulated in Appendix P.

Figure 6.28 shows ratios (O3-O4)/(O3-O3') and {[(O3-O3')+(O3'-O4)]/2]}/(O3-O4) for *M*1and *M*2 octahedrons, respectively, as a function of ε_{M1}. Besides the usual exceptions noted so far, one can observe linear correlations between unshared edge length ratios and ε_{M1} for both *M*1 and *M*2 octahedrons, which are brought into relief by the short-dash lines drawn as guides to the eye. Therefore, the degree of isosceles-ness of top and bottom unshared triangular faces of *M*1 and *M*2 octahedrons is caused by the in-plane distortion angle ε_{M1} of the *M*1 site.

Even though unshared edge lengths are not affected by counter-rotation in an ideally flattened and counter-rotated octahedron (see Subsection 6.2.1), one could nonetheless expect a relation to hold between ε_{M1} and δ_{M2} since the isosceles-ness of *M*1 and *M*2 unshared faces are linked together through ε_{M1}. However, as shown in Figure 6.29, where values of ε_{M1} are

plotted as a function of δ_{M2}, there is no correlation between these two parameters.

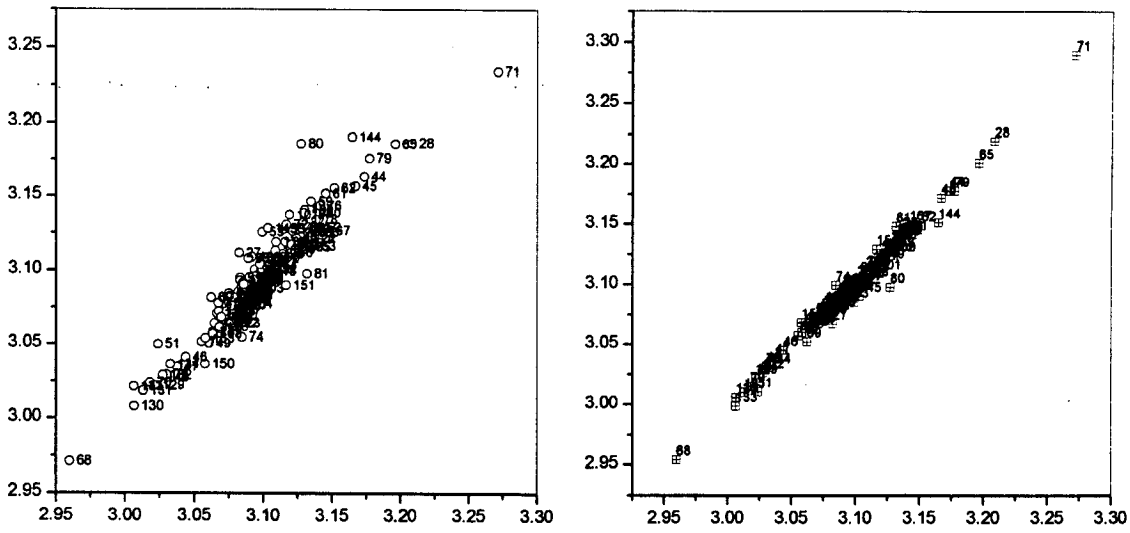

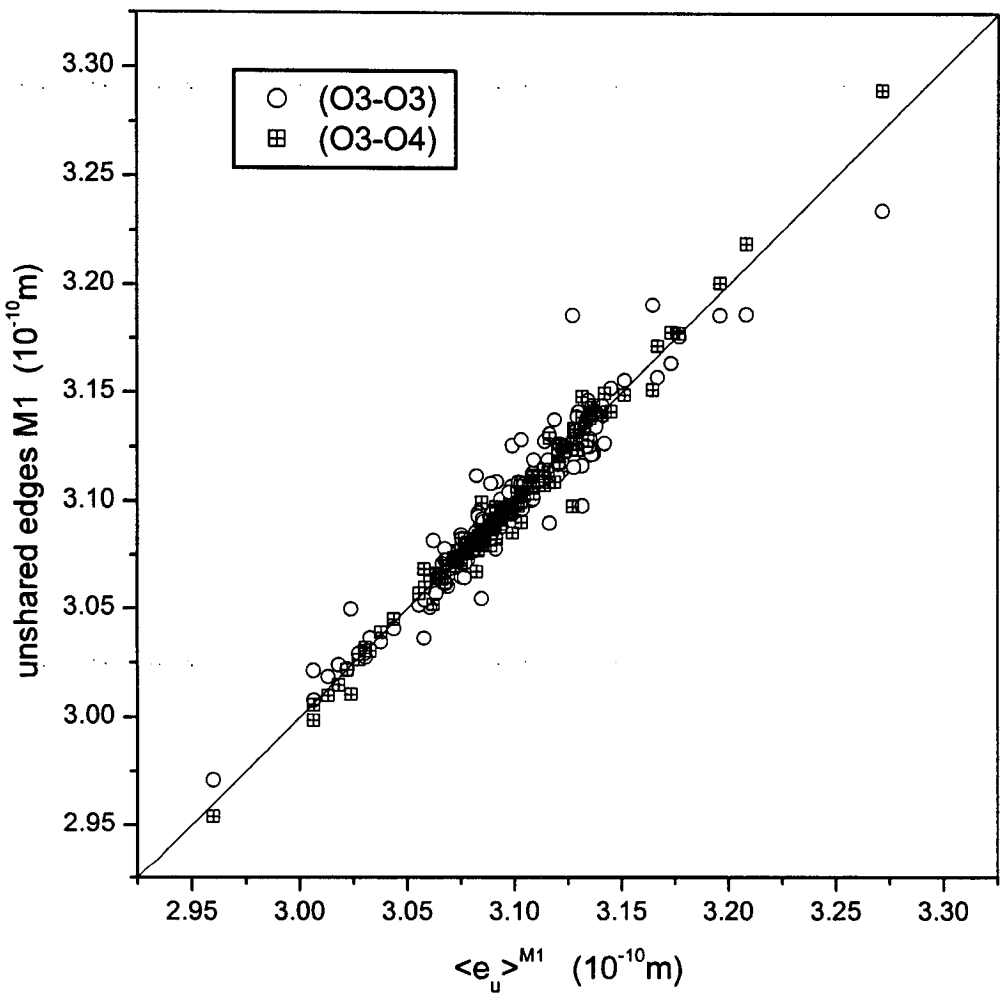

Figure 6.23. Variations of individual unshared edges with their average values for the *M*1 octahedrons. The solid line is a 1:1 correspondence between the *x* and *y* axes.

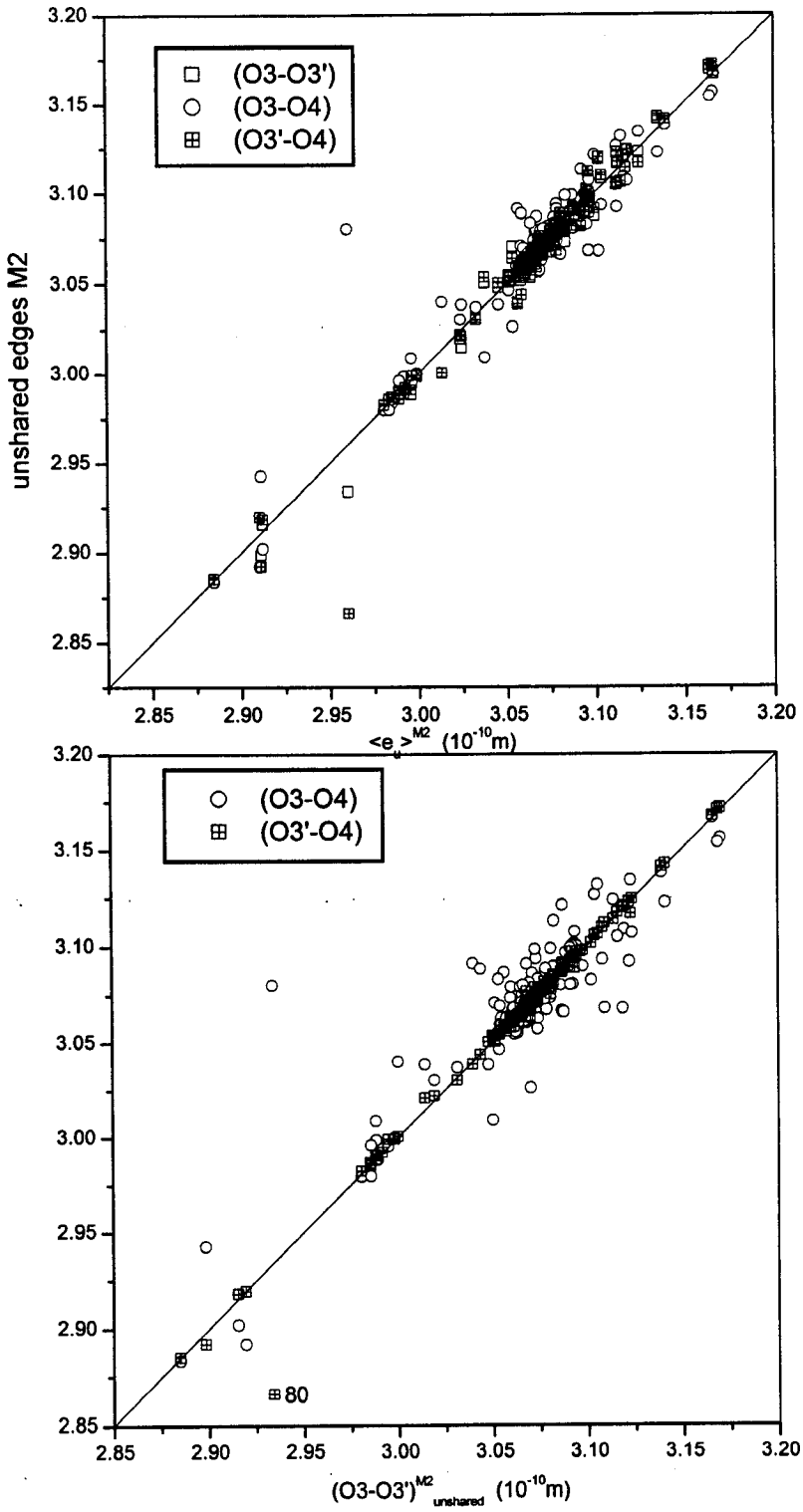

Figure 6.24. Variations of individual unshared edges with their average values for the *M*2 octahedrons. The solid line are 1:1 correspondence between the *x* and *y* axes.

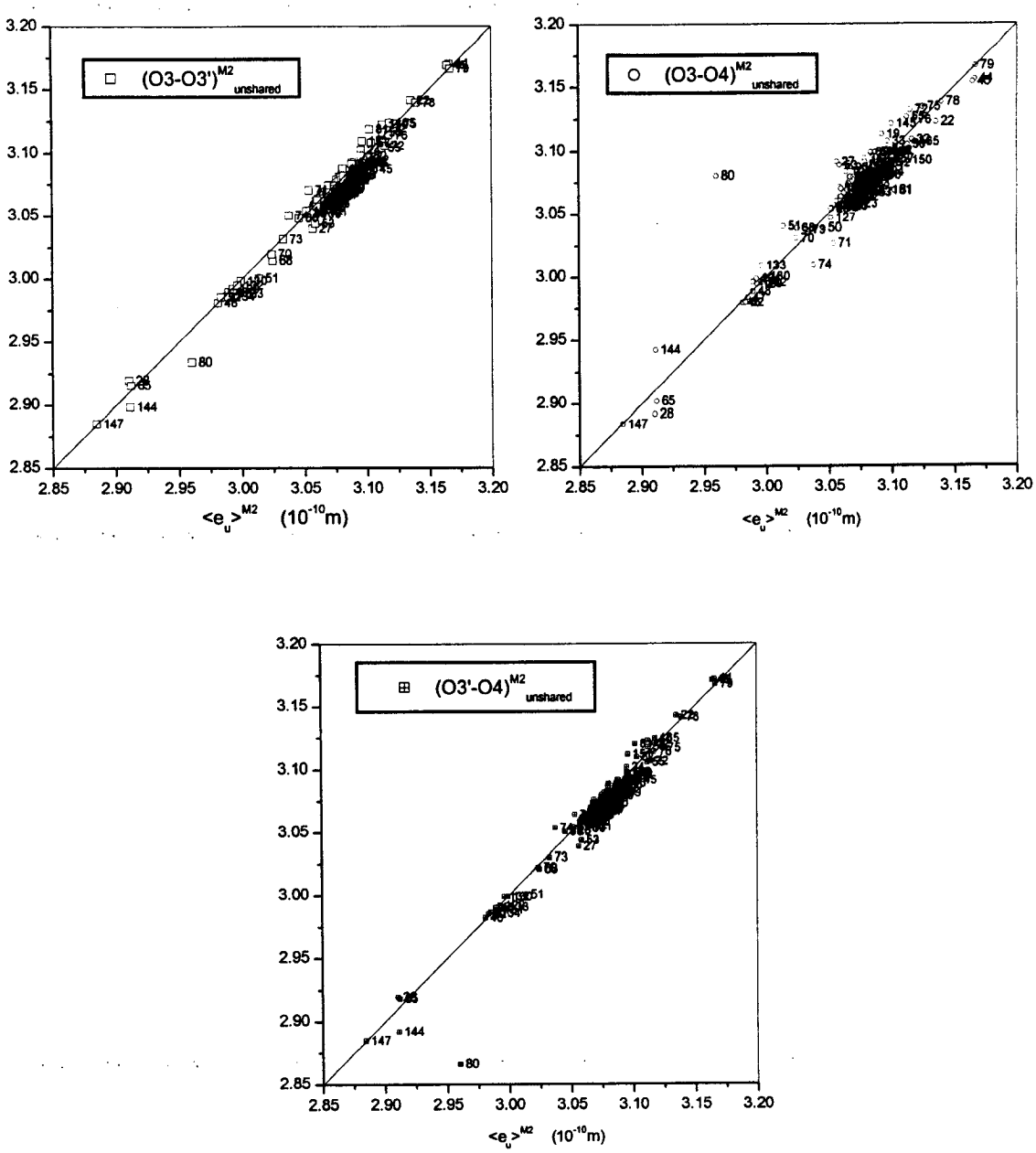

Figure 6.25. Identification of data points plotted in Figure 6.24. The solid line are 1:1 correspondence between the *x* and *y* axes.

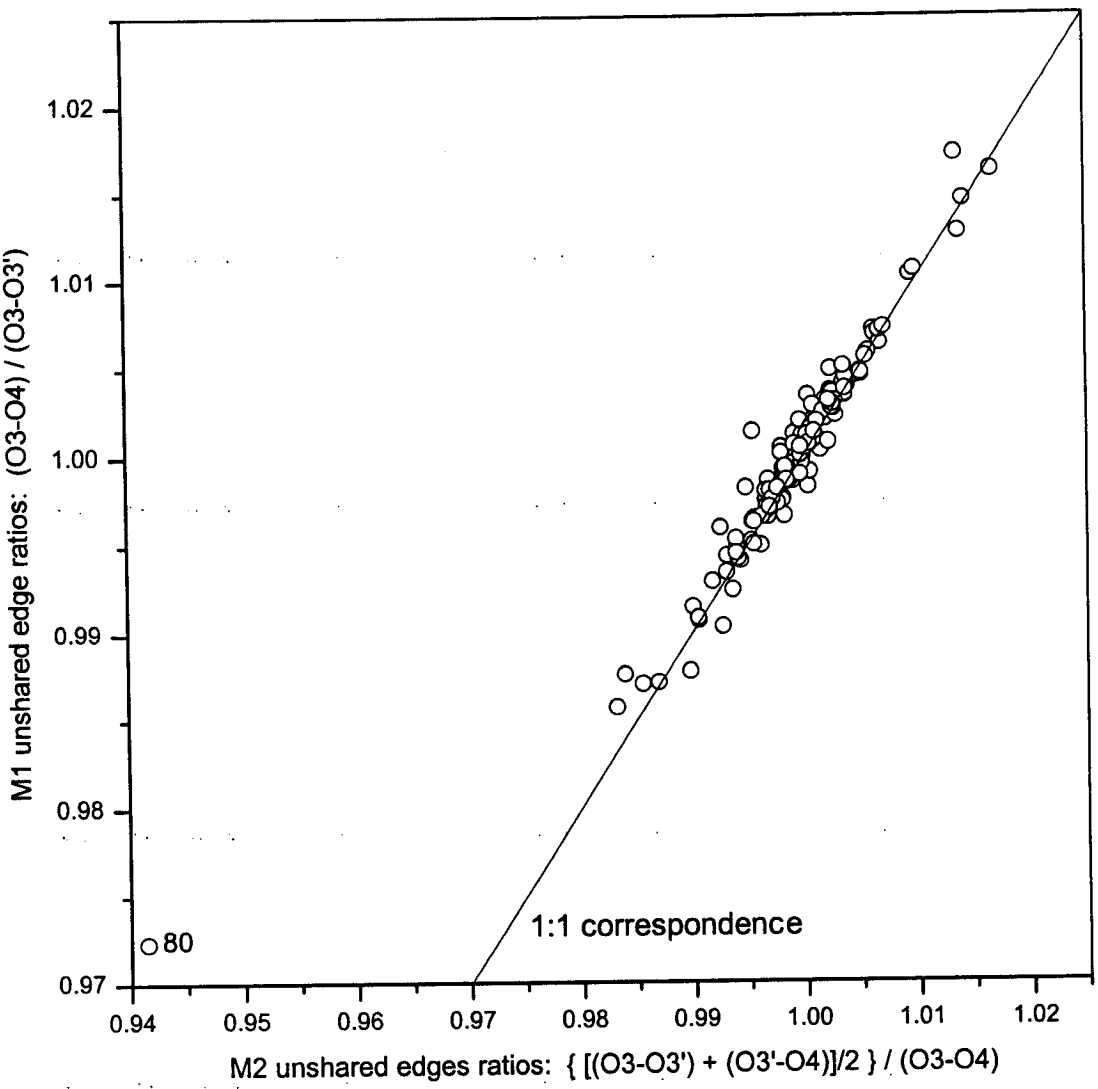

Figure 6.26. Unshared edge length ratios of *M*1 *vs*. *M*2 sites. The solid line is a 1:1 correspondence between the *x* and *y* axes.

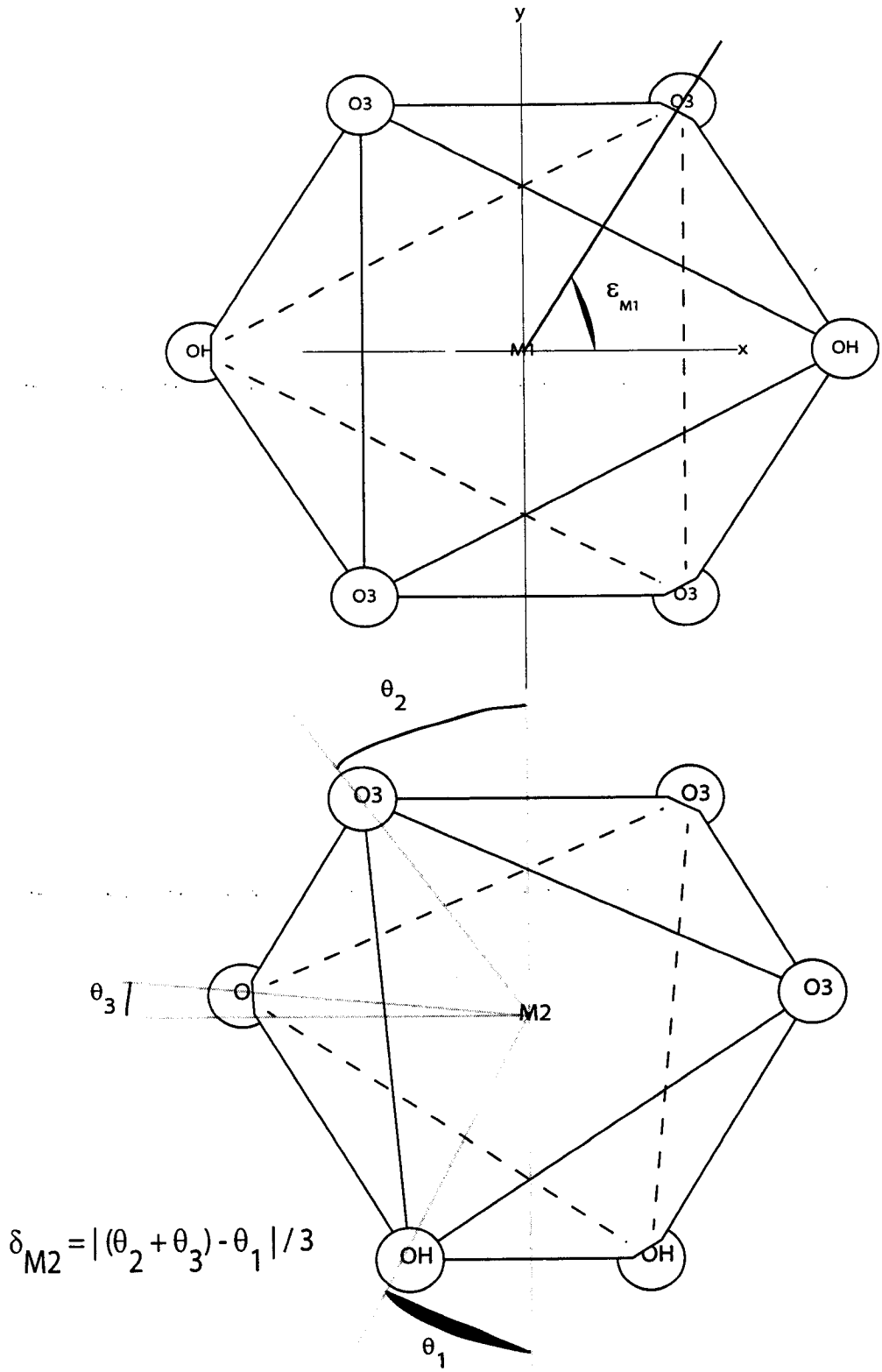

Figure 6.27. Calculation of in-plane distortion angle ε_{M1} (top) and counter-rotation angle δ_{M2} (bottom).

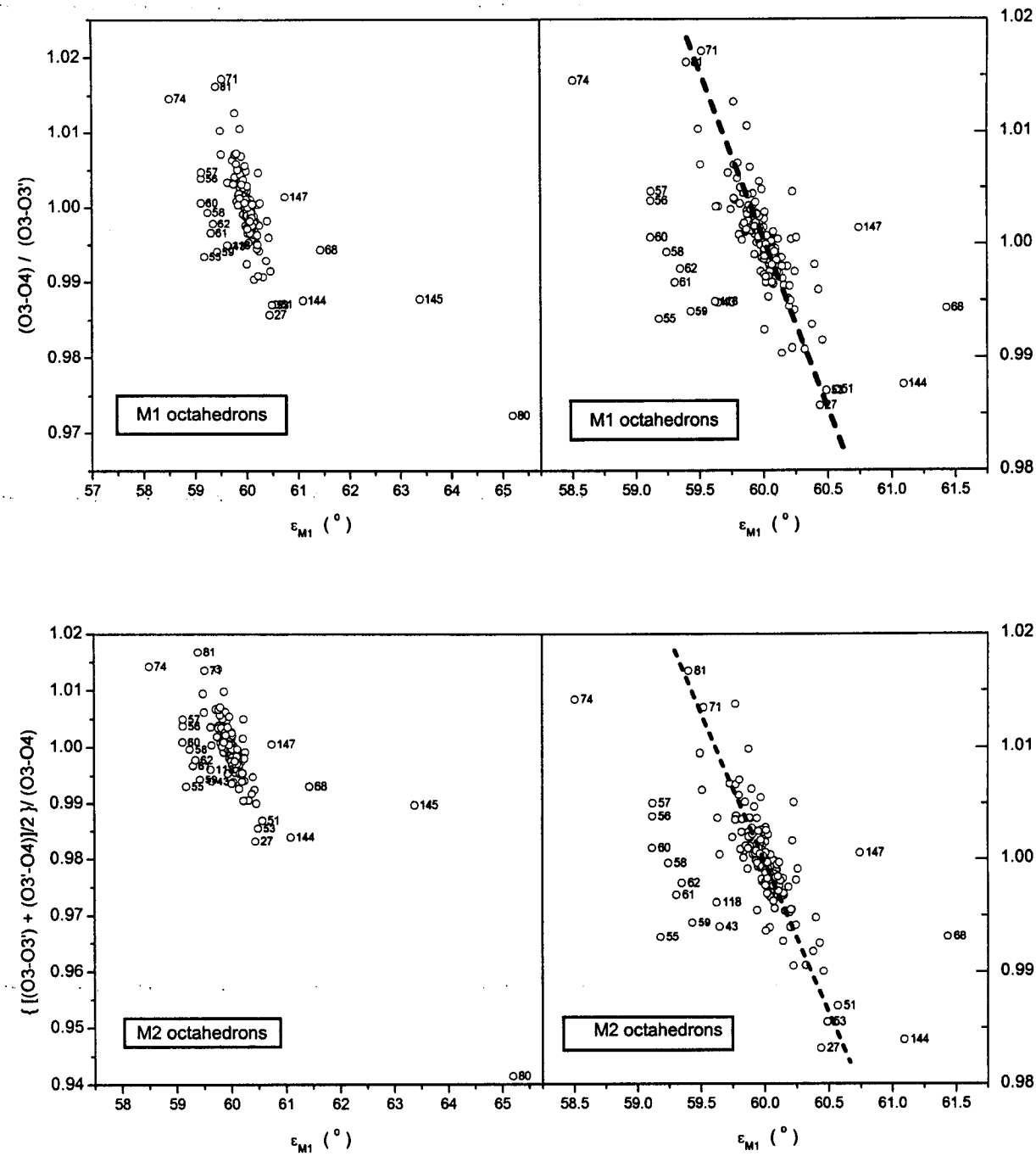

Figure 6.28. Unshared edge length ratios for $M1$ and $M2$ octahedrons as a function of in-plane distortion angle ε_{M1}. Short-dash lines are guides to the eye.

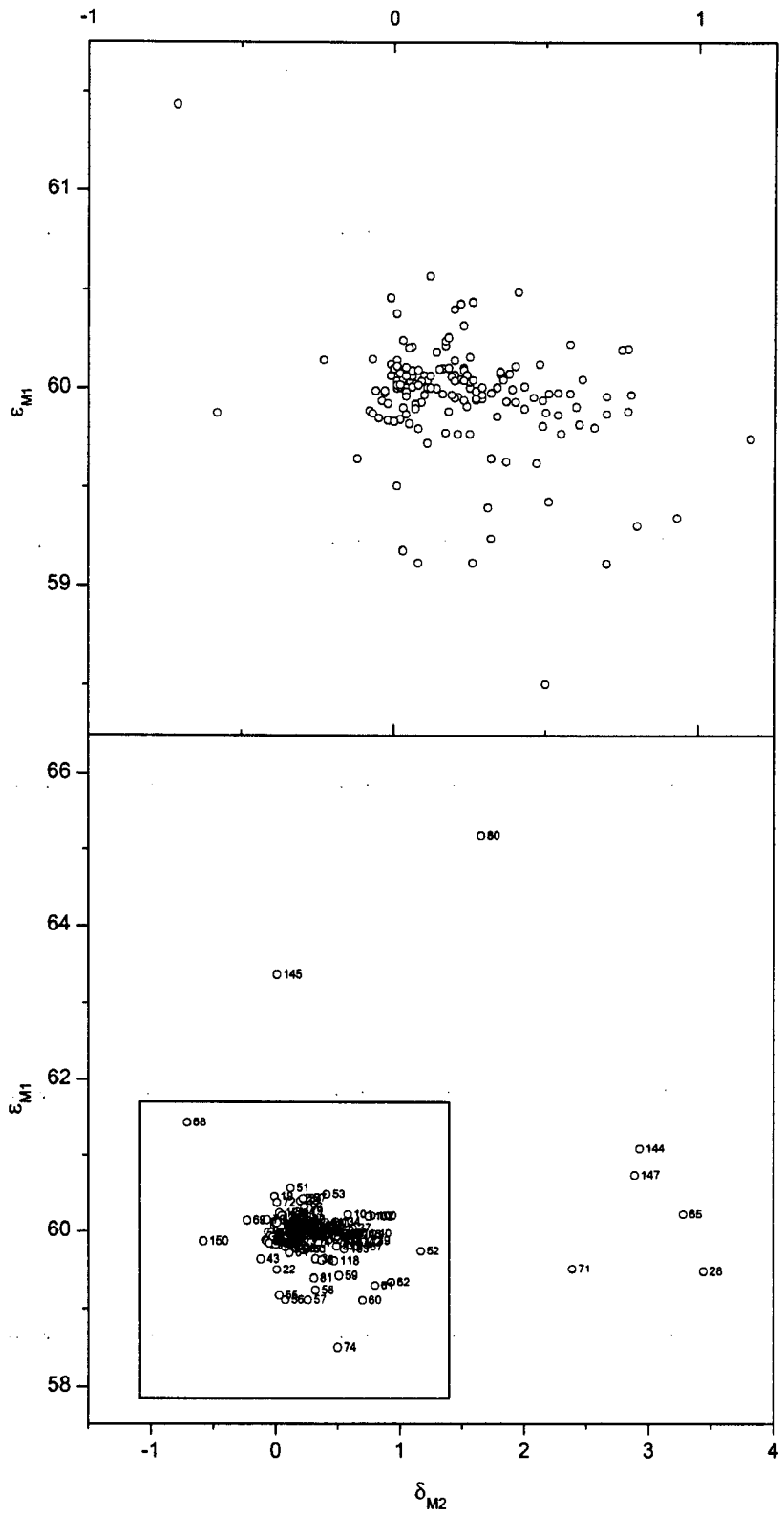

Figure 6.29. In-plane distortion angle ε_{M1} as a function of counter-rotation angle δ_{M2}. The top graph is a blow-up of the insert delimited by solid lines in the bottom graph.

6.3.2 Octahedral sheet distortions

In the preceding subsection, individual bond lengths and edge lengths of *M*1 and *M*2 sites were investigated thoroughly. In the present subsection, we now turn to octahedral sheet distortions.

Figures 6.30 and 6.31 compare lattice parameter predictions made for *a* and *b*, respectively, that were achieved using either: i) a geometric homo-octahedral sheet model via Eq. 6.12 (Figure 6.5) , or ii) a geometric meso-octahedral sheet model via Eq. 6.14 (Figure 6.6).

In the case of geometric homo-octahedral predictions, the average octahedral sheet bond length, <M-O>, and flattening angle, <ψ>, are given by:

(6.30) $$\langle M\text{-}O\rangle = (\langle M1\text{-}O\rangle + 2 \cdot \langle M2\text{-}O\rangle) /3$$

(6.31) $$\langle \psi \rangle = (\psi_{M1} + 2 \cdot \psi_{M2}) /3$$

where ψ_{M1} and ψ_{M2} are obtained from the average octahedral sheet height h_o,

(6.32) $$h_o = 2 \cdot c \cdot \sin\beta \left(\frac{1}{2} - \frac{O4z + 2 \cdot O3z}{3} \right),$$

and the average bond lengths of each of the *M*1 and *M*2 sites, <M1-O> or <M2-O>, as

(6.33) $$\psi_{M1} = \arccos\left[\frac{h_o}{2 \cdot \langle M1 - O \rangle} \right]$$
$$\psi_{M2} = \arccos\left[\frac{h_o}{2 \cdot \langle M2 - O \rangle} \right] .$$

Values of <M-O>, <ψ>, <M1-O>, <M2-O>, h_o, ψ_{M1} and ψ_{M2} are compiled in Appendix P. For geometric meso-octahedral predictions, values of counter-rotation angle δ_{M2} calculated as in Figure 6.27 (and referred to in Subsection 6.3.1) are used.

As can be ascertained from the narrow scatter of data points along the 1:1 correspondence lines drawn on each graph displayed in Figures 6.30 and 6.31, geometric homo-octahedral and geometric meso-octahedral predictions (*y*-axis) give equally good agreements with the observed *a* and *b* lattice parameters (labelled as a_{obs} and b_{obs} in Figures 6.30 and 6.31) to within ~0.005 Å.

Equivalent expressions involving unshared edges of top and bottom triangular faces of *M*1 and *M*2 octahedrons, that are also obtained using Eqs. 6.12 and 6.14, give similar agreements (not shown).

Norrishite structure No. 80 constitutes the only outlier discernable in Figures 6.30 and 6.31. It is interesting to note that predicted values of *b* are larger for this sample than observed values, whereas the opposite takes place for *a*. Indeed, this is due to a break of the $b = \sqrt{3}a$ relationship in this sample (Subsection 6.1).

Therefore, to the extent that peculiar site distortions such as those acting in norrishite are absent (which are presumably due to Jahn-teller effects, see [Tyrna & Guggenheim 1991] and [Brigatti & Guggenheim 2002]), in-plane *a* and *b* lattice parameters are adequately predicted using simple geometrical models involving a geometric homo-octahedral sheet or a geometric meso-octahedral sheet, regardless of the individual bond lengths and edge lengths actually occurring on the *M*1 and *M*2 sites.

Consider now the geometry of a geometric meso-octahedral sheet more closely as in Figure 6.61 (Subsection 6.2.3). As previously mentioned, the projection of the *O*3 atom on the *a*-*b* plane must lie on a line making a 60° angle with the direction of the *a* axis. Clearly then, the situation when $\delta_{M2} = 0$ corresponds to a geometric homo-octahedral sheet.

The sides of the triangle delimited by the projections of the *M*1, *M*2, and *O*3 atoms on the *a*-*b* plane are of lengths: $d_{M1}\sin\psi_{M1}$ for M1-$O3_{xy}$, $d_{M2}\sin\psi_{M2}$ for M1-$O3_{xy}$, and $a/\sqrt{3}$ for *M*1-*M*2. Hereafter, the subscript 'xy' is used to designate a projection on the *a*-*b* plane. Using a few trigonometric identities and a sine law applied specifically to this triangle, one can show that the following relation holds

$$\frac{a/\sqrt{3}}{\sin(120^\circ - \delta_{M2})} = \frac{d_{M1}\sin\psi_{M1}}{\sin 30^\circ} = \frac{d_{M2}\sin\psi_{M2}}{\sin(30 + \delta_{M2})}, \tag{6.34}$$

from which it can be derived that:

$$\frac{d_{M1}\sin\psi_{M1} - d_{M2}\sin\psi_{M2}}{a} = \frac{1}{\sqrt{3}}\left[\frac{\sin(30^\circ + \delta_{M2}) - \sin 30^\circ}{\sin(120^\circ - \delta_{M2})}\right]. \tag{6.35}$$

Equation 6.35 will serve as a basis to explore in-plane intra-layer displacements in Subsection 6.3.5 below.

Next, isolating $d_{M1}\sin\psi_{M1}$ and $d_{M2}\sin\psi_{M2}$ separately in terms of a and δ_{M2} in Eq. 6.35, combined with Eq. 6.9 using Pythagoras' theorem, the following relations arise:

$$d_{M1}{}^2 = \frac{h_o{}^2}{4} + \left(\frac{a}{\sqrt{3}} \cdot \frac{\sin\left[30^\circ + \delta_{M2}\right]}{\sin\left[120^\circ - \delta_{M2}\right]} \right)^2 \tag{6.36a}$$

$$d_{M2}{}^2 = \frac{h_o{}^2}{4} + \left(\frac{a}{\sqrt{3}} \cdot \frac{\sin 30^\circ}{\sin\left[120^\circ - \delta_{M2}\right]} \right)^2 . \tag{6.36b}$$

By subtracting Eq. 6.36b from Eq. 6.36a and factoring out a, one then finds the dimensionless relationship:

$$\frac{d_{M1}{}^2 - d_{M2}{}^2}{a^2} = \frac{1}{3} \frac{\sin^2\left[30^\circ + \delta_{M2}\right] - \sin^2 30^\circ}{\sin^2\left[120^\circ - \delta_{M2}\right]} . \tag{6.37}$$

Eq. 6.37 brings about an interesting geometrical property of an ideal geometric meso-octahedral sheet: The size difference of $M1$ and $M2$ octahedrons is uniquely determined by the degree of counter-rotation of the $M2$ octahedron. The latter relation has not previously been given.

Figure 6.32 shows the normalized size difference $[\langle M1\text{-}O\rangle^2 - \langle M2\text{-}O\rangle^2]/a^2$ plotted as function of counter-rotation angle δ_{M2} expressed in radians. The solid line drawn in this graph represents a first-order Taylor expansion of the right-hand side of Eq. 6.37 around $\delta_{M2} = 0$, which yields

$$\left[d_{M1}{}^2 - d_{M2}{}^2 \right] / a^2 = 2/9 \cdot \sqrt{3} \cdot \delta_{M2} + \ \ldots Order\left(\delta_{M2}{}^2 \right) . \tag{6.38}$$

The agreement of data points in Figure 6.32 with Eq. 6.38 is remarkable around $\delta_{M2} \approx 0$ and gets worst as δ_{M2} increases, as expected with a Taylor expansion. Norrishite structure No. 80 is again the only exception, but it agrees proportionally better with the predictions than in the case of a and b (Figures 6.30 and 6.31).

Therefore, in accordance with a geometric meso-octahedral sheet model, the normalized size difference $[\langle M1\text{-}O\rangle^2 - \langle M2\text{-}O\rangle^2]/a^2$ observed in $1M$ mica structures solely depends on the counter-rotation angle δ_{M2}, despite local distortions actually occurring on $M1$ and $M2$ sites.

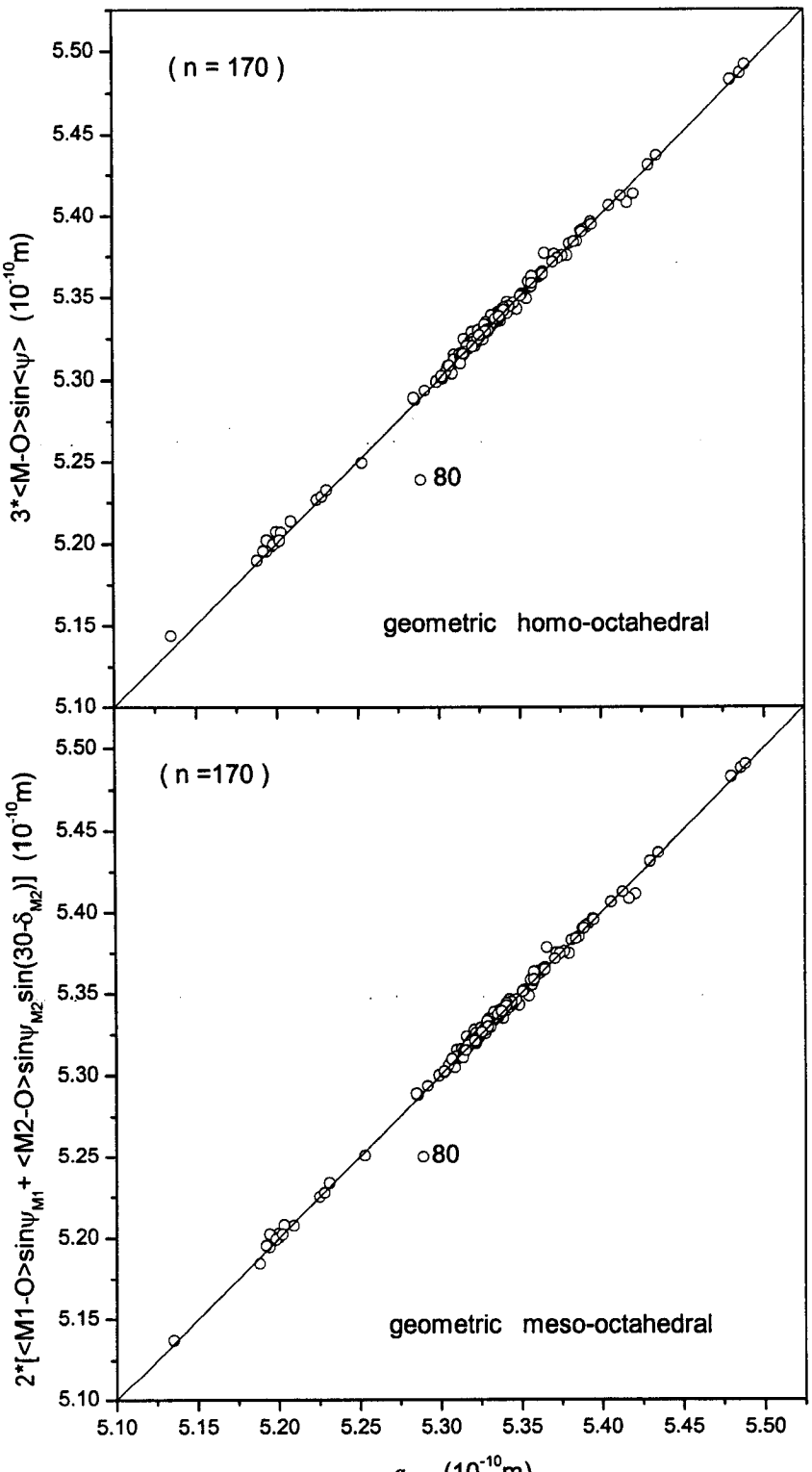

Figure 6.30. Comparison of observed a values (x-axis) to predictions made using a geometric homo-octahedral (top) and a geometric meso-octahedral (bottom) sheet model via Eqs. 6.12 and 6.14, respectively.

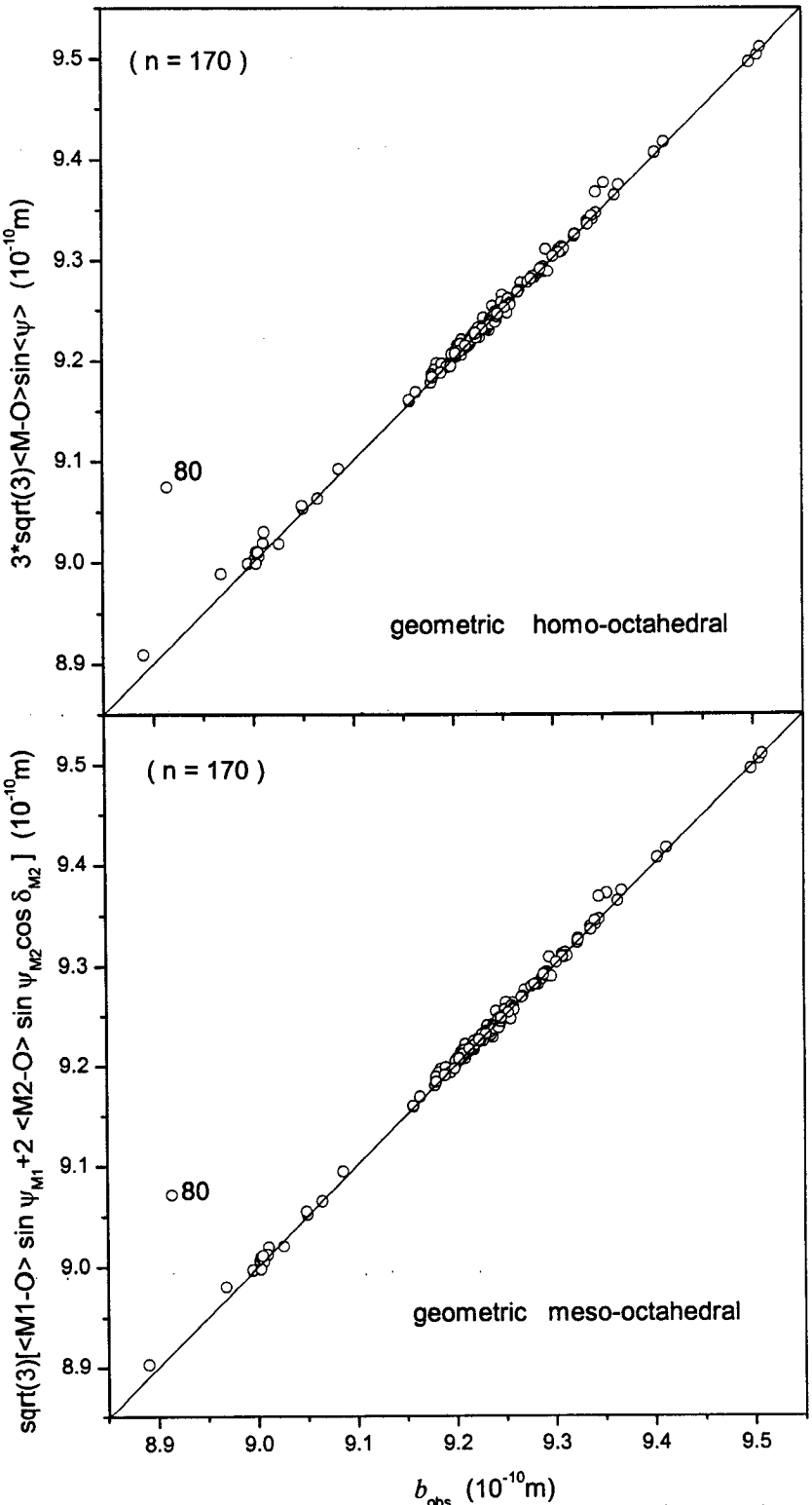

Figure 6.31. Comparison of observed b values (x-axis) to predictions made using a geometric homo-octahedral (top) and a geometric meso-octahedral (bottom) sheet model via Eqs. 6.12 and 6.14, respectively.

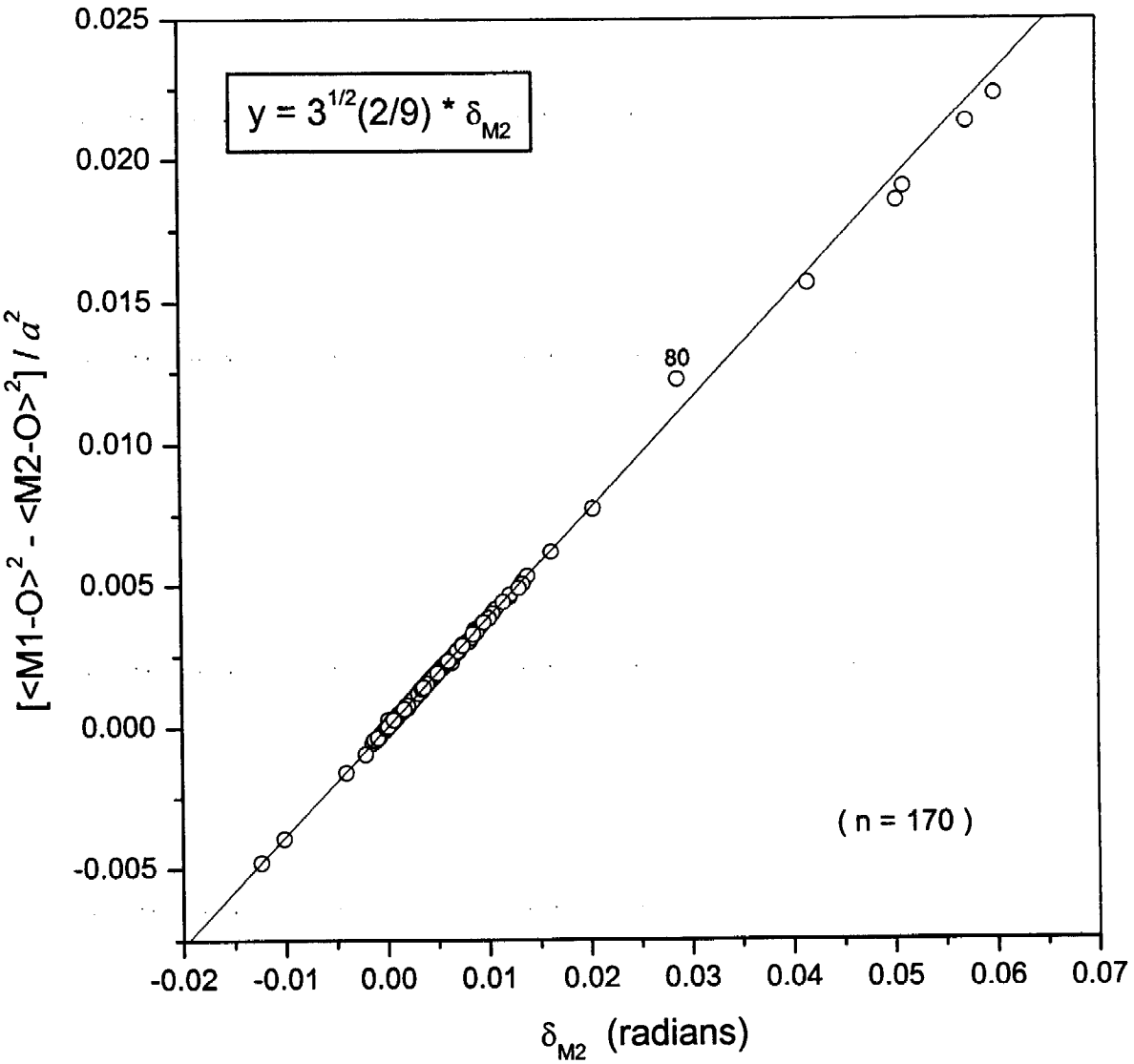

Figure 6.32. Normalized squared octahedral size difference $[\langle M1\text{-}O\rangle^2 - \langle M2\text{-}O\rangle^2]/a^2$ plotted as function of counter-rotation angle δ_{M2} expressed in radians.

6.3.3 Distortions of tetrahedrons and tetrahedral sheets

Figures 6.33, 6.34, and 6.35 show individual distances as functions of average lengths for the following quantities, respectively (see Table 6.3 for symbols and nomenclature): i) (T-O1), (T-O2), (T-O2'), and (T-O3) distances *vs.* the average basal tetrahedral bond length $\langle T\text{-}O\rangle_{bas}$; ii) basal edge lengths (O1-O2), (O1-O2'), and (O2-O2') *vs.* the average length $\langle O\text{-}O\rangle_{bas}$; and iii) apical edge lengths (O3-O1), (O3-O2), and (O3-O2') *vs.* the average length $\langle O\text{-}O\rangle_{api}$.

As is well known (see [Brigatti & Guggenheim 2002]for a recent review), Figures 6.34, 6.35, and 6.36 show that bond and edge lengths fall into separate groups that depend on the chemical composition of the tetrahedral sheets: $\langle Al_{\sim 1}Si_{\sim 3}\rangle$ (not labelled, except if falling outside the main trend); $\langle Al_{\sim 3}Si_{\sim 1}\rangle$, Nos. 46-48, 68, 129-134; $\langle Al_{\sim 2}Si_{\sim 2}\rangle$, Nos. 51-52; $\langle Al_{\sim 1\text{-}2}Si_{\sim 2\text{-}1}\rangle$, Nos. 55-62, 163; $\langle Al_{\sim 1}Ge_{\sim 3}\rangle$, Nos. 75, 78-79; $\langle Ge_{\sim 4}\rangle$, Nos. 71, 72-76; and $\langle Si_{\sim 4}\rangle$, Nos. 28, 65, 69-70, 73-74, 77, 80, 144 (see details in Appendix P).

Histograms displaying the distributions of basal and apical edge lengths, O_{bas}-T-O_{bas} and O_{bas}-T-O_{api} angles, and individual T-O bond lengths are presented in Figures 6.36, 6.37, and 6.38, respectively. For edge lengths and O-T-O angles, all three different values of a given type are included in a single distribution for each type. The main peaks appearing on all of these distributions correspond to the $\langle Al_{\sim 1}Si_{\sim 3}\rangle$ samples.

Clearly, apical edge (Figure 6.36) and O_{bas}-T-O_{api} (Figure 6.37) distributions are centred around larger values than basal edge and O_{bas}-T-O_{bas} ones. In fact, for 144 out of the 170 samples studied (≈85 %), all three values of apical edge lengths or O_{bas}-T-O_{api} angles in a given sample are larger than any of their basal counterparts. The few exceptions to this observation come from the following samples: a tetra-ferri-annite sample, No. 22; clintonite samples, Nos. 46-48, 68, 129-134; Rietveld-refined synthetic annite-syderophyllite samples, Nos. 55-62; the sample having the largest Ti-content in the tetrahedral sheet, No. 69 ($\langle Si^{4+}_{3.63}\ Al^{3+}_{0.02}\ Fe^{3+}_{0.035}Ti^{4+}_{0.305}\rangle$); a paragonite sample, No. 147; and two biotite samples, Nos. 19,145.

When apical edge lengths are larger than basal edge ones, it can be unambiguously concluded that the shapes of tetrahedrons are elongated with respect to an ideal tetrahedron (or compressed along the direction perpendicular to the elongation). However, one cannot ascribe that the elongation is caused by the larger size of the O_{bas}-T-O_{api} angles with respect to the O_{bas}-T-O_{bas} angles, because the elongation (or compression) also depends on bond lengths.

In examining the histograms showing the distributions of individual tetrahedral bond lengths (Figure 6.38), one sees that the apical (T-O3) bond length distribution is fairly similar to the three basal bond length distributions — namely (T-O1), (T-O2), and (T-O2'). The largest

difference is that $<Al_{-3}Si_{-1}>$, $<Al_{-1}Ge_{-3}>$, and $<Ge_{-4}>$ samples are more distinctively resolved on basal bond length distributions than on the apical one. Nonetheless, values of mean (<x>) and standard deviation (SD) of the sample population corresponding to each distribution of bond length are equal within error (Table 6.4). On the basis of the distributions of individual bond lengths and *O-T-O* angles, therefore, one might tentatively ascribe the elongation of tetrahedrons established above to be caused by an enlargement apical *O-T-O* angles at equal *T-O* bond lengths. However, as will be shown below, this is not usually the case.

Table 6.4 give values of mean (<x>) and standard deviation (SD) for each of the individual *T-O* distributions, as well as for various distributions that are discussed below.

Individual T-O bond lengths		
x	<x> (10^{-10} m)	SD (10^{-10} m)
(T-O1)	1.668(2)*	0.026(1)
(T-O2)	1.666(2)	0.028(1)
(T-O2')	1.668(2)	0.027(1)
(T-O3)	1.667(2)	0.029(2)
Sample-specific distortion parameters		
x	<x> (%)	SD (%)
100 [(T-O1)-$<T\text{-}O>_{bas}$] / $<T\text{-}O>_{bas}$	0.03(2)	0.23(1)
100 [(T-O2)-$<T\text{-}O>_{bas}$] / $<T\text{-}O>_{bas}$	-0.07(3)	0.38(2)
100 [(T-O2')-$<T\text{-}O>_{bas}$] / $<T\text{-}O>_{bas}$	0.04(3)	0.36(2)
100 [(T-O3)-$<T\text{-}O>_{bas}$] / $<T\text{-}O>_{bas}$	0.0(1)	1.28(7)
100 [(O1-O2)-$<O\text{-}O>_{bas}$] / $<O\text{-}O>_{bas}$	-0.07(4)	0.49
100 [(O1-O2')-$<O\text{-}O>_{bas}$] / $<O\text{-}O>_{bas}$	0.04(3)	0.43
100 [(O2-O2')-$<O\text{-}O>_{bas}$] / $<O\text{-}O>_{bas}$	0.03(1)	0.14
100 [(O3-O1)-$<O\text{-}O>_{api}$] / $<O\text{-}O>_{api}$	0.11(3)	0.38
100 [(O3-O2)-$<O\text{-}O>_{api}$] / $<O\text{-}O>_{api}$	-0.10(3)	0.44
100 [(O3-O2')-$<O\text{-}O>_{api}$] / $<O\text{-}O>_{api}$	-0.01(2)	0.31
100 [$\tau_{O1\text{-}T\text{-}O2}$ - $<\tau>_{bas}$] / $<\tau>_{bas}$	-0.05(4)	0.55
100 [$\tau_{O1\text{-}T\text{-}O2'}$ - $<\tau>_{bas}$] / $<\tau>_{bas}$	0.01(4)	0.48
100 [$\tau_{O2\text{-}T\text{-}O2'}$ - $<\tau>_{bas}$] / $<\tau>_{bas}$	0.04(2)	0.21
100 [$\tau_{O3\text{-}T\text{-}O1}$ - $<\tau>_{api}$] / $<\tau>_{api}$	0.14(3)	0.43
100 [$\tau_{O3\text{-}T\text{-}O2}$ - $<\tau>_{api}$] / $<\tau>_{api}$	-0.10(4)	0.47
100 [$\tau_{O3\text{-}T\text{-}O2'}$ - $<\tau>_{api}$] / $<\tau>_{api}$	-0.04(3)	0.36

* Numbers in parentheses are one standard deviation errors and refer to the last digit.

Table 6.4. Values of mean, <x>, and standard deviation, SD, of various distributions discussed in the text.

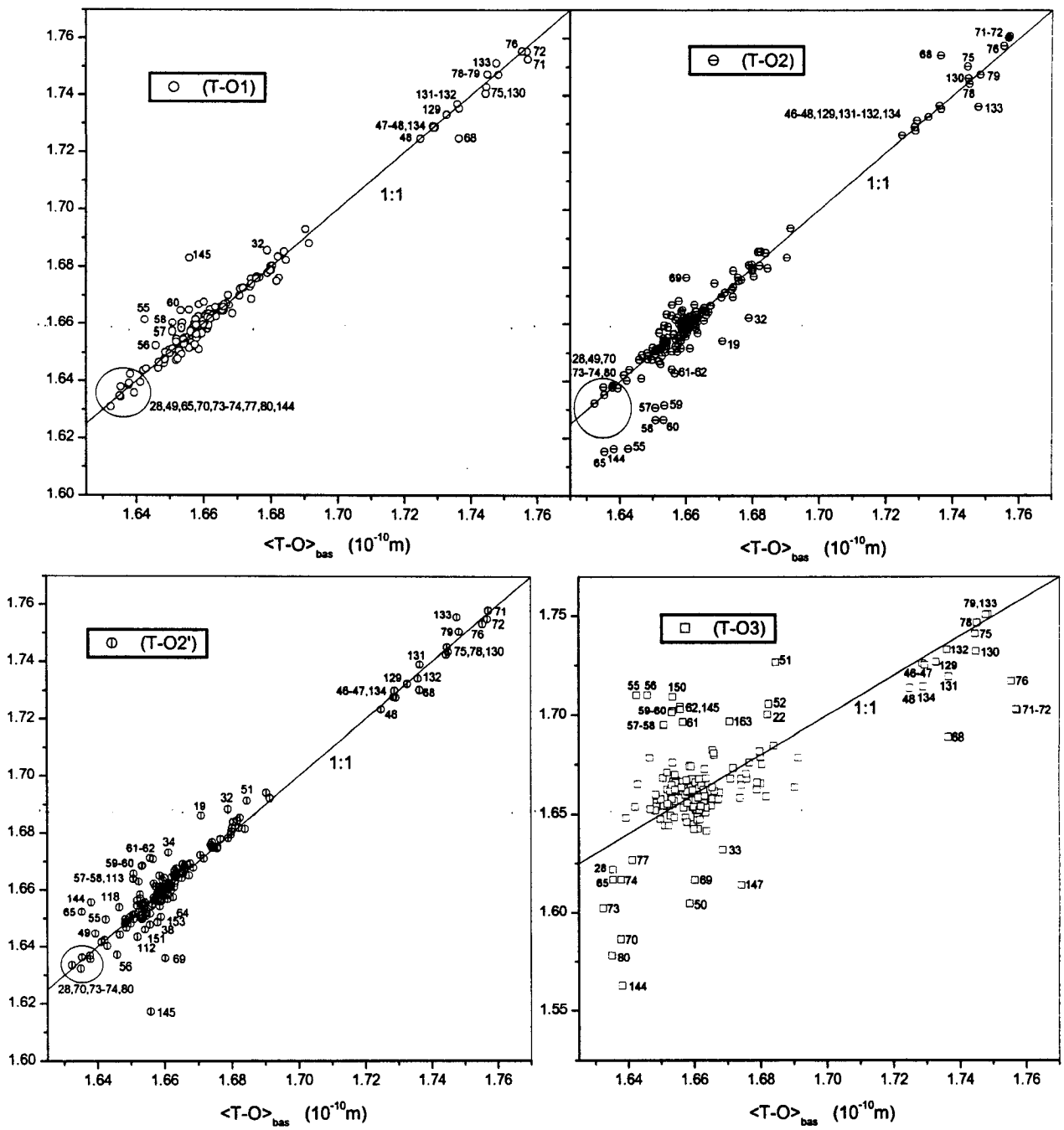

Figure 6.33. Evolution of individual *T-O* distances as a function of the average basal tetrahedral bond lengths, $\langle T\text{-}O\rangle_{bas}$ (= 1/3[(T-O1) + (T-O2) + (T-O2')]).

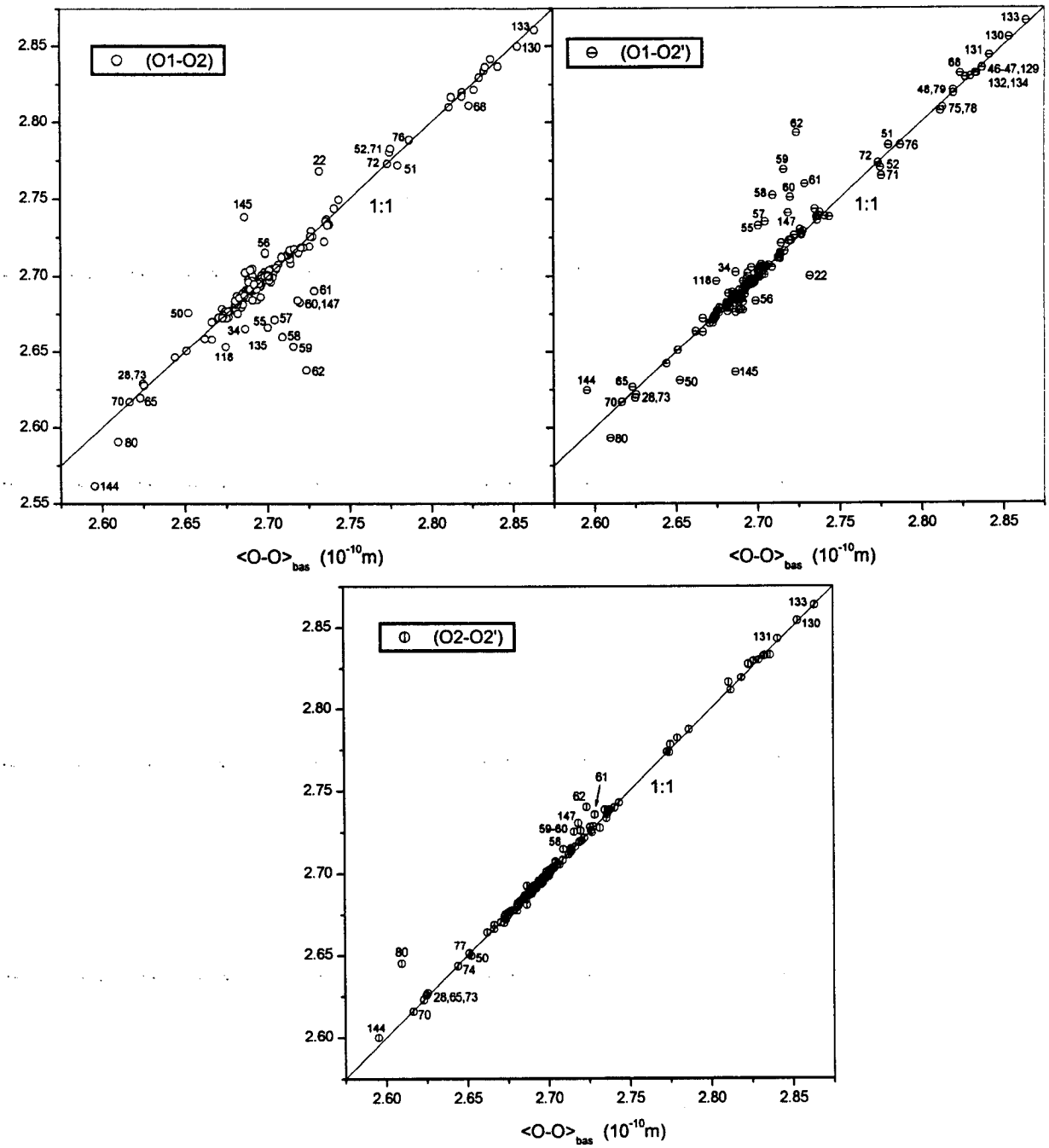

Figure 6.34. Evolution of basal edge lengths (O1-O2), (O1-O2'), and (O2-O2') as a function of their average lengths $\langle O\text{-}O \rangle_{bas}$.

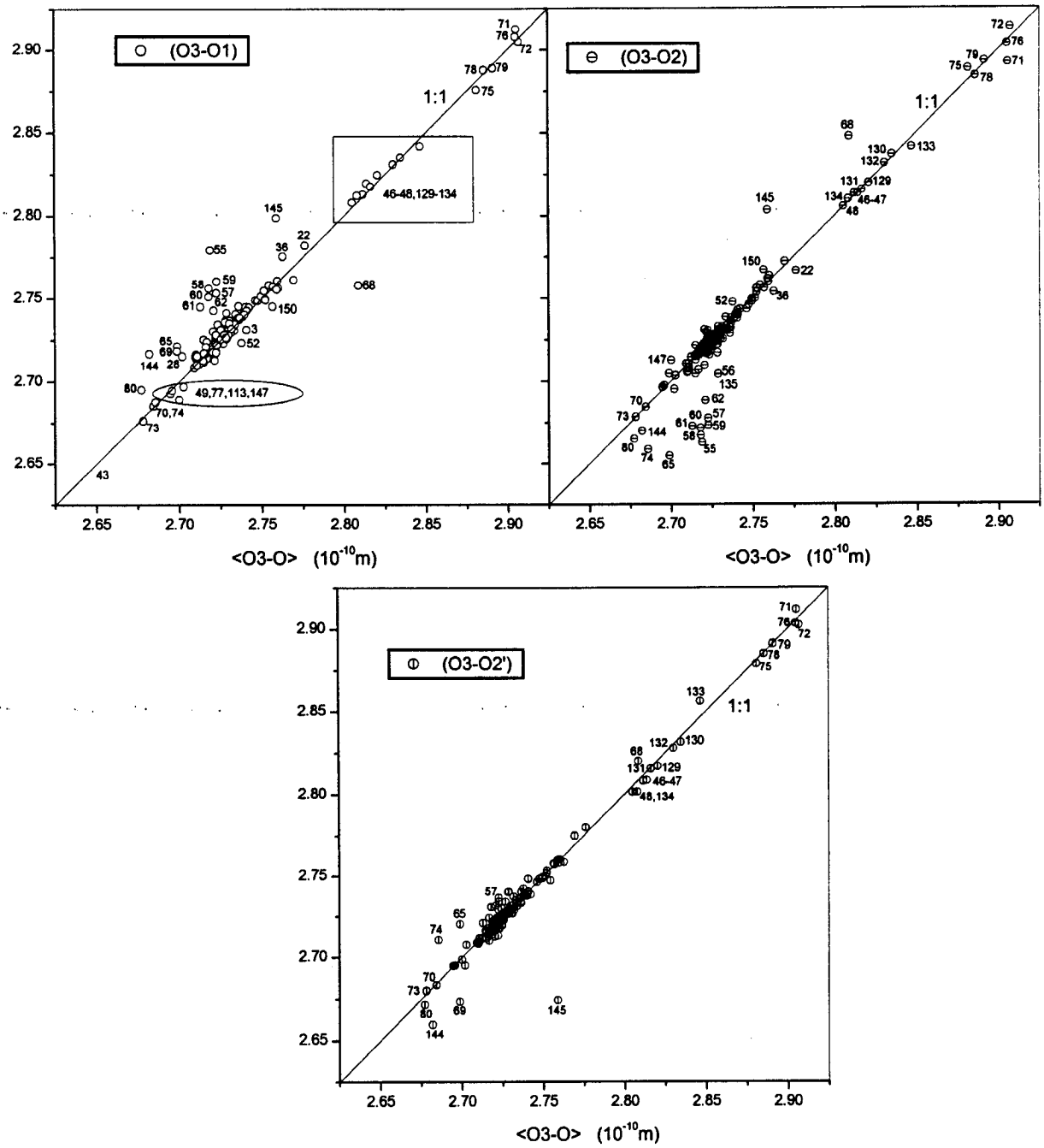

Figure 6.35. Evolution of apical (or lateral) edge lengths (O3-O1), (O3-O2), and (O3-O2') as a function of their average lengths $\langle O\text{-}O\rangle_{api}$.

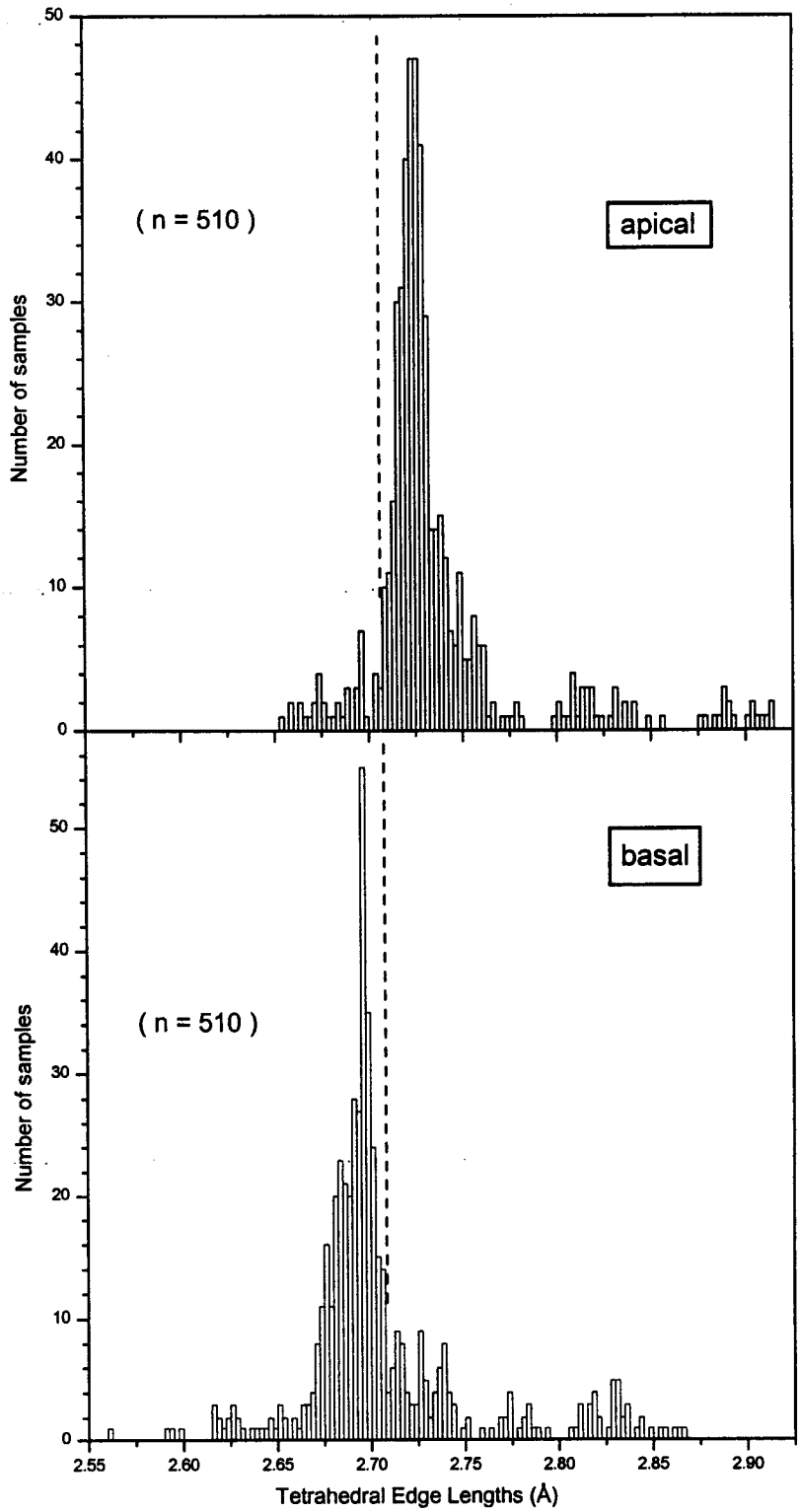

Figure 6.36. Histogram showing the distributions of apical and basal tetrahedral edge lengths. All three different edge length values of a given type are included in a single distribution.

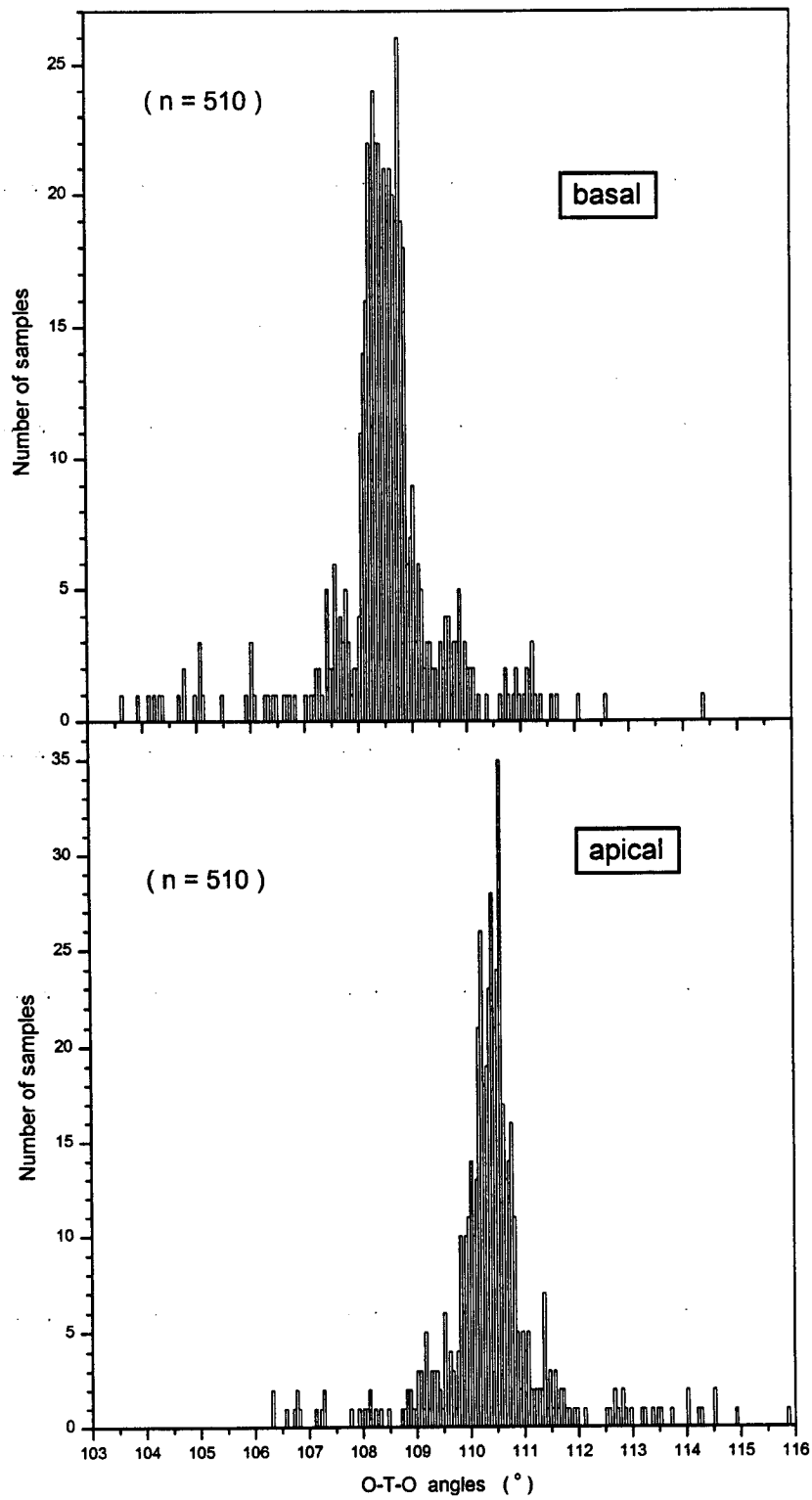

Figure 6.37. Histogram showing the distributions O_{bas}-T-O_{bas} (basal) and O_{bas}-T-O_{api} (apical) angles. All three different *O-T-O* angle values of a given type are included in a single distribution.

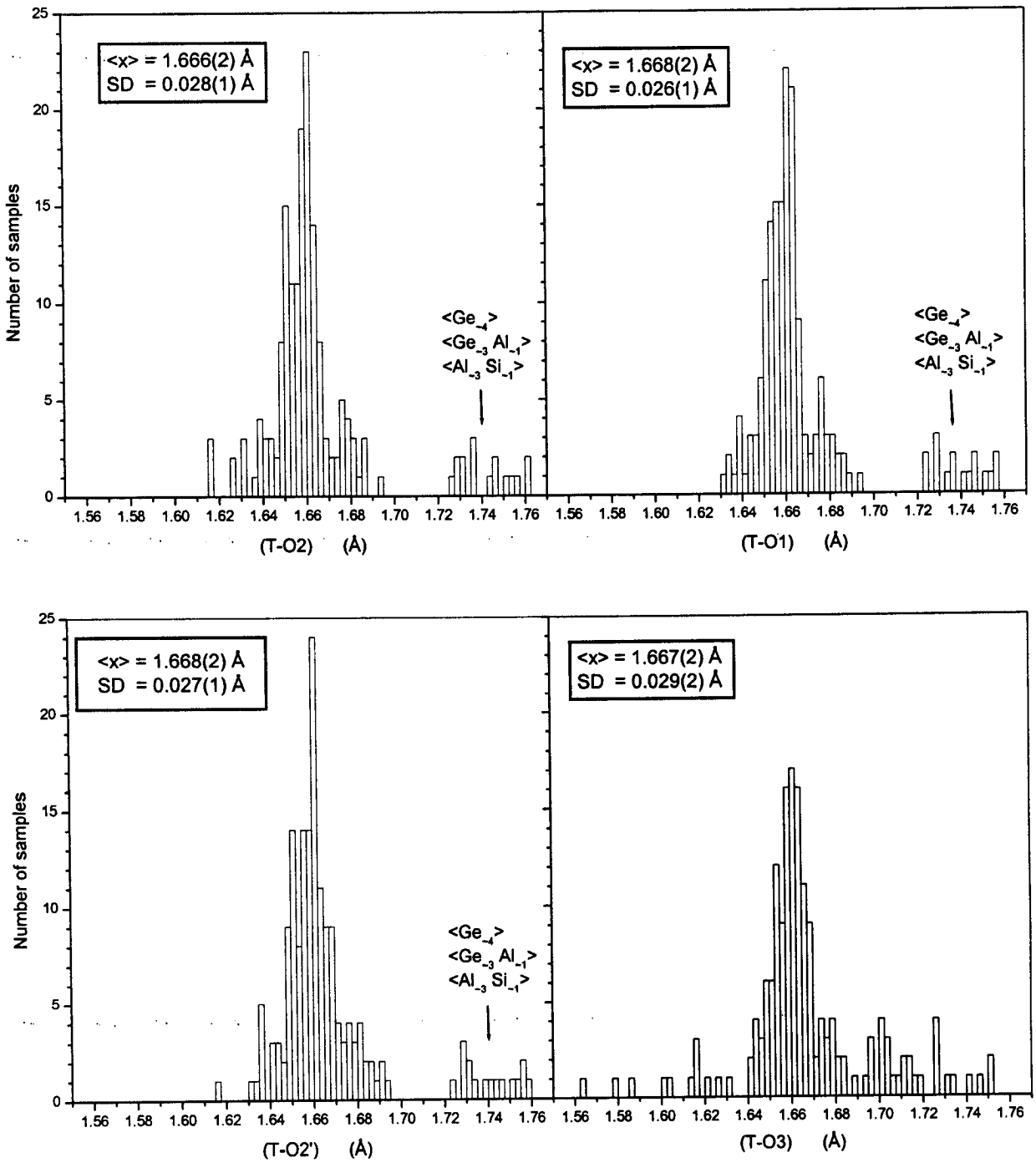

Figure 6.38. Histograms showing the distributions of individual *T-O* bond lengths.

In order to obtain structural information about tetrahedral distortions, distributions of the following sample-specific dimensionless individual bond length, edge length, and angle distortion parameters were investigated:

$$BLD_i = (100\ \%)\ [\ (T\text{-}O)_i - \langle T\text{-}O\rangle_{bas}\ ]\ /\ \langle T\text{-}O\rangle_{bas} \quad (6.39a)$$

$$ELD^{bas}{}_i = (100\ \%)\ [\ (O\text{-}O)_i - \langle O\text{-}O\rangle_{bas}\ ]\ /\ \langle O\text{-}O\rangle_{bas} \quad (6.39b)$$

$$ELD^{api}{}_i = (100\ \%)\ [\ (O\text{-}O)_i - \langle O\text{-}O\rangle_{api}\ ]\ /\ \langle O\text{-}O\rangle_{api} \quad (6.39c)$$

$$AD^{bas}{}_i = (100\ \%)\ [\ \tau_i - \langle\tau\rangle_{bas}\ ]\ /\ \langle\tau\rangle_{bas} \quad (6.39d)$$

$$AD^{api}{}_i = (100\ \%)\ [\ \tau_i - \langle\tau\rangle_{api}\ ]\ /\ \langle\tau\rangle_{api} \quad (6.39e)$$

In the above equations, the symbols have the following meanings: i) *i* refers to an individual bond length $(T\text{-}O)_i$, edge length $(O\text{-}O)_i$, or *O-T-O* angle τ_i; ii) τ is the symbol used herein below to designate an *O-T-O* angle; iii) $\langle\tau\rangle_{bas}$ is the average of the three O_{bas}-*T*-O_{bas} angles in a given tetrahedron of a given structure refinement of a given sample; iv) $\langle\tau\rangle_{api}$ is the average of the three O_{api}-*T*-O_{bas} angles in a given tetrahedron of a given structure refinement of a given sample; v) $\langle T\text{-}O\rangle_{bas}$ = [(T-O1)+(T-O2)+(T-O2')]/3 ; $\langle O\text{-}O\rangle_{bas}$ = [(O1-O2)+(O1-O2)+(O2-O2')]/3; and $\langle O\text{-}O\rangle_{api}$ = [(O3-O1)+(O3-O2)+(O3-O2')]/3. For Eq. 6.39b, only individual basal edge lengths were considered; and similarly so for Eqs. 6.39c-6.39e. Values of mean (<x>) and standard deviation (SD) for the distributions of parameters calculated from Eqs. 6.39 are compiled in Table 6.4.

In examining the BLD_i distributions (Eq. 6.39a) shown in Figure 6.39, the most striking feature is that the apical $BLD_{T\text{-}O3}$ distribution is unequivocally larger than any of the three basal BLD_i distributions. According to <x> and SD values (Table 6.4), all BLD_i distributions are centred around zero and the $BLD_{T\text{-}O3}$ distribution is approximately three to five times wider than the basal BLD_i distributions. Contrary to individual *T-O* bond length distributions (Figure 6.38), which suggested equal *T-O* bond lengths, Figure 6.39 clearly establishes that the apical (T-O3) bond length can differ significantly from the basal *T-O* bond lengths, in a given structure of a given sample. The $BLD_{T\text{-}O3}$ parameter is a direct measure of the extent to which this is the situation, provided that the basal *T-O* bond lengths are sufficiently close amongst each other.

Excluding a few outliers, the central peaks of the three basal BLD_i distributions are well constrained around zero (Figure 6.39). In fact, as indicated by values of <x> and SD given in Table 6.4, distributions of $ELD^{bas}{}_i$, $ELD^{api}{}_i$, $AD^{bas}{}_i$, and $AD^{api}{}_i$ parameters all behave similarly or have even smaller widths (not shown; except for $ELD^{bas}{}_i$, see Figure 6.46 below). To the extent that the population of 170 samples considered here is representative of the ensemble of possible

individual tetrahedral distortions occurring in 1*M* mica structures (and possibly layer silicates in general), this means that average tetrahedral distortion parameters $\langle T\text{-}O\rangle_{bas}$, $\langle O\text{-}O\rangle_{bas}$, $\langle O\text{-}O\rangle_{api}$, $\langle\tau\rangle_{bas}$, and $\langle\tau\rangle_{api}$ are valid indicators of tetrahedron shapes, with fractional sample specific deviations of at most ~0.1-0.5 % , except (T-O3) with 1.3 % (Table 6.4)

In order to illustrate the point made above, Figure 6.40 compares simple geometrical model predictions made from Eqs. 6.15-6.18 (Section 6.2.4) to average tetrahedral distortion parameters actually observed in the structures. The predictions are shown as solid lines, whereas data points come from values of $\langle T\text{-}O\rangle_{bas}$, $\langle\tau\rangle_{bas}$, $\langle\tau\rangle_{api}$, and h_t^{bas} tabulated in Appendix P. The parameter h_t^{bas} is the *euclidian* distance between the tetrahedral cation and the plane formed by the three basal oxygen atoms in a given tetrahedron, whose values were determined using analytic geometry formulae. Given the remarkable agreement of experimental data with predictions, it is concluded that simple geometrical models of ideal, iso-bond-basal-flattened, or aniso-bond tetrahedrons — which are all constructed using a rigid base formed by three basal *T-O* bonds having an equal length (see Section 6.2.4) — are valid representations of actual tetrahedrons found in trioctahedral-1*M* micas.

It is interesting to point out the evolution of sample compositions along the solid-line predictions shown in Figure 6.40. The combined charge per formula unit of interlayer and tetrahedral cations progressively increases from ~15+ to ~17+ as one goes from compressed — $\tau_{bas} > \tau_{ideal}$ ($\tau_{ideal} \approx 109.47°$) — to elongated — $\tau_{bas} < \tau_{ideal}$ — tetrahedrons. This is attributed to size of the cations that occupy both the tetrahedral and interlayer cations.

In contrast with the above noted distinct evolution of tetrahedron's shapes with compositions, a surprising feature is that the tetrahedron's height h_t[1] and the apical bond length (T-O3) do not evolve in the same manner as a function of $\langle\tau\rangle_{bas}$ (Figure 6.41). Excluding $\langle Ge_{-4}\rangle$ and $\langle Ge_{-3}Al_{-1}\rangle$ samples, (T-O3) increases somewhat regularly with $\langle\tau\rangle_{bas}$, extending over a range of ~12.0 % around its mean ($\langle T\text{-}O3\rangle$ = 1.667(2) Å; see Table 6.4), whereas h_t does not apparently vary in a manner that is related to $\langle\tau\rangle_{bas}$, remaining ~4.5 % around its mean ($\langle h_t\rangle$ = 2.247(3) Å; see Figure 6.41). This situation is paradoxical: the apical bond length increases as tetrahedrons are compressed (i.e. as $\langle\tau\rangle_{bas}$ increases), whereas the height of the tetrahedrons stays approximately the same whether the tetrahedrons are elongated or compressed. This strange behaviour will be rationalized below.

In addition to a tetrahedral flattening via τ angles (i.e. elongation or compression) and to

---

[1] Values of h_t reported in Appendix P were determined using analytic geometry formulae; in a given tetrahedron, h_t is the distance between the apical O3 oxygen atom and the plane formed by the three basal oxygen atoms.

a frequent difference in length between apical and basal bonds, there are two additional tetrahedral distortions that occur.

One of these distortions is pointed out here for the first time. It consists of a bending that makes the apical (T-O3) bond with respect to the pyramidal base formed by the three basal *T-O* bonds. In a given tetrahedron, this distortion is conveniently measured by the angle η between a line given by the direction of the (T-O3) bond and a line running from tetrahedral cation *T* to the geometric centre of the triangle formed by the three basal edges (Figure 6.42a). In an ideal, iso-bond-basal-flattened or aniso-bond tetrahedron, $\eta = 180^{\circ}$.

The other distortion is referred to as tetrahedral corrugation [Brigatti & Guggenheim 2002]. This distortion manifests itself as an out-of-plane twisting of the basal *O*2 oxygen atoms located in the [110] tetrahedral chains (Figure 6.42b), determining a departure from coplanarity of the basal triangle formed by the three basal edges. Basal-oxygen plane corrugation is determined by the parameter Δz :

$$\Delta z = \left(O1z - O2z\right) \cdot c \sin\beta \quad . \tag{6.40}$$

Figure 6.42 presents the distributions of Δz and $\left(180^{\circ} - \eta\right)$ found in 1*M* structures, along with an illustration of the degree of correlation between these two parameters (Table 6.5). A positive value of η was given if $O1z > O2z$, and vice versa for negative η values. Although the correlation is affected by the presence of a few outliers, a definite trend can be discerned. There now remains to establish the nature of the link between two distortions.

[Lee & Guggenheim 1981] demonstrated that the corrugation of the basal oxygen atom plane Δz is related to differences in distance between apical oxygen atoms linked to octahedrons of different size. In a recent study covering more than 200 mica structures (146 trioctahedral and 55 dioctahedral), [Brigatti & Guggenheim 2002] have also confirmed that there exits such a relationship by plotting Δz as a function of the maximum difference in octahedral bond length between the two octahedral sites having the largest and smallest average bond lengths in a given structure, i.e. $[\langle M\text{-}O\rangle_{max} - \langle M\text{-}O\rangle_{min}]$. In light of results presented in Section 6.3.2, Figure 6.44 displays Δz as a function of the normalized squared size difference $[\langle M1\text{-}O\rangle^2 - \langle M2\text{-}O\rangle^2]/a^2$ (see Eq. 6.37); similar correlations are found if the difference $[\langle M1\text{-}O\rangle - \langle M2\text{-}O\rangle]$ is considered instead (Table 6.5). Given the similar results that the above independent investigations have yielded, therefore, it appears evident that octahedral size differences play an important role in tetrahedral corrugation.

It shall now be demonstrated that the origin of tetrahedral plane corrugation can be

understood in terms of geometrical considerations associated to the matching of a tetrahedral sheet to a geometric meso-octahedral sheet and that this explains the correlation illustrated in Figure 6.44.

Consider the two in-plane (001) projections shown in Figure 6.45, which both display a tetrahedral sheet fitting on top of a geometric meso-octahedral sheet. Certain elements are common to both top and bottom diagrams: i) the basal edges of the tetrahedrons (solid lines) are drawn as coplanar triangular basal faces rotated by a specified α, which are attached to a geometric homo-octahedral sheet having certain lateral *a* and *b* dimensions (with $b = \sqrt{3} \cdot a$, following Section 6.1) ii) the apical O3 oxygen atoms (filled circles) are placed at positions corresponding to a geometric meso-octahedral sheet having $d_{M1} > d_{M2}$ and the same *a* and *b* as the overlying tetrahedral sheet; and iii) the thicker solid lines designate the basal edges (O2-O2') that lie along the *a*-axis direction.

Focus first on the top diagram (Figure 6.45). In this case, the apical edges of the tetrahedrons (dashed lines) are shown as if they belonged to ideal, iso-bond or aniso-bond tetrahedrons, that fit on top a geometric homo-octahedral sheet. In such a situation, one sees that when the three basal edges of a given tetrahedron are coplanar, then, in any given tetrahedron, there is a lateral shift $\vec{\Delta}$ between the position of the geometric centre of the basal triangular face — which is also the position of the apical oxygen atom in a homo-octahedral sheet — and the position of the apical oxygen atom belonging to the meso-octahedral sheet. of the bottom diagram.

Consider now the bottom diagram (Figure 6.45), where the $\vec{\Delta}$ vectors are indicated by a tiny arrow sign on each tetrahedron. In this case, each apical edge links one of the three basal oxygen atoms to an apical O3 atom belonging to the geometric meso-octahedral sheet. If the basal edges are coplanar, then one can clearly see that the three apical edges must have different lengths. In a tetrahedron of such shape, moreover, if a cation *T* is placed at a point equidistant from its four coordinating oxygen atoms (or at any points where the three basal *T-O* bond lengths are equal), then one must have that $\eta \neq 180^{\circ}$ (Figure 6.42a). From the developments made in this paragraph, one concludes that unless tetrahedrons were severely distorted beyond what is observed, a tetrahedral sheet comprised of coplanar basal equilateral triangular faces cannot fit on top of a geometric meso-octahedral sheet.

In examining Figure 6.45 more closely, one can appreciate that a straightforward means to regularize the tetrahedrons' shapes is to incline the basal faces in directions given by the $\vec{\Delta}$ vectors. Without changing the *a* and *b* dimensions, an effective way to accomplish this task is through an adjustment of the *z*-coordinates of the O1 atoms, keeping the O2 atoms fixed, which

immediately leads to tetrahedral corrugation, and to unequal basal edge lengths. If the O1 atoms are also allowed to move laterally in a direction parallel to *a* (i.e. along the [110] direction), then both apical and basal edges can more closely equalize their lengths amongst each other, with the end result that the shape of each tetrahedron is more regular and that a more typical tetrahedral bonding symmetry is recovered for each cation *T*.

The logical reasoning undergone in the above treatment sheds light on a few issues pertaining to the crystal chemistry of 2:1 layer silicates. First, a tetrahedral sheet composed of tetrahedrons having a simple geometrical shape (be it ideal, iso-bond, or aniso-bond) cannot be arranged to match a geometric meso-octahedral sheet. This, therefore, is a fundamental limit of simple geometrical models. That is, the usual (stretched, expanded, flattened, counter-rotated, rotated) regular coordination polyhedra (octahedrons and tetrahedrons) cannot be assembled such that the tetrahedral and octahedral sheets match in a geometric meso-octahedral 2:1 layer silicate (i.e., one with <M1-O> ≠ <M2-O>).

Another finding is that tetrahedral corrugation is particularly favourable. From a network point of view, corrugation is economical: it does not change the lateral *a* and *b* dimensions, it does not alter the connectivity of the bonds, and it only requires a unidimensional displacement of one single atomic site in the crystal structure. Corrugation can therefore be viewed as the favoured non-planar cooperative response of the tetrahedral sheet to the presence of a meso-octahedral sheet, which arises under the driving influence of strong *T-O* bonds wanting to stabilize at similar lengths in a regular tetrahedral bonding symmetry.

In comparing the SD values obtained for distributions of sample-specific distortion parameters compiled in Table 6.4, one notes an increasing trend that will now be explained. Most notably, (O2-O2') basal edges give the thinnest of not only all ELD^{bas}_{i} distributions (Figure 6.46), but also all other sample-specific distortion parameters considered. Then come the SD values of the distributions of $BLD_{T\text{-}O1}$ and $AD^{bas}_{O2\text{-}T\text{-}O2'}$ parameters, which are followed by the other two basal BLD_{i} distributions, essentially reflecting the fact that basal *T-O* bonds always equilibrate at similar lengths. The rest of the SD values obtained for distributions of ELD^{api}_{i}, the other two AD^{bas}_{i}, and AD^{api}_{i} parameters are all equal or larger than those previously mentioned, in accordance with the idea that individual bond length, edge length, and angle distortions taking place within a single tetrahedron are consequences of the tetrahedrons being corrugated as a result of the presence of geometric meso-octahedral sheets.

The significantly larger distribution of the $BLD_{T\text{-}O3}$ parameter can be understood as follows. Each O3 atom is constrained by bonding to three octahedral cations (in the trioctahedral case) that are usually not the same whereas the tetrahedral basal oxygen atoms have no such

strong covalent bonding constraints. This may explain why the $BLD_{T\text{-}O3}$ parameter is not correlated with any other distortion parameters such as $[\langle M1\text{-}O\rangle^2-\langle M2\text{-}O\rangle^2]/a^2$, $(180^\circ-\eta)$, Δz, or α (see Table 6.5).

Finally, Figure 6.47 demonstrates that the lateral extension of the tetrahedral sheets of trioctahedral-1*M* micas can always be accounted for in terms of simple geometrical models via Eq. 6.19 (Subsection 6.2.5). In the above results, it was shown that the average basal edge length $\langle O\text{-}O\rangle_{bas}$ is virtually always equal to the length of the basal (O2-O2') edges located along the [110] tetrahedral chains (Figure 6.46). The case of the only exception, norrishite sample No. 80, is due to a break of the $b = \sqrt{3}a$ pseudo-hexagonal symmetry (see Section 6.1).

In a given 1*M* structure, Figure 6.48 shows that the tetrahedral rotation can be evaluated using two different methods: i) by the average tetrahedral rotation angle α,

$$\alpha = \sum_{i=1}^{6} \alpha_i \quad , \tag{6.41}$$

where $\alpha_i = |120\text{-}\phi_i|$ and where ϕ_i is one of the six different angles between basal edges of neighbouring tetrahedrons articulated in the tetrahedral rings of a 1*M* structure; or ii) by the angle $\alpha_{(O2\text{-}O2')\text{-}[110]}$ that makes the basal (O2-O2') edges with respect to the *a*-axis direction,

$$\alpha_{(O2\text{-}O2')\text{-}[110]} = \arctan\left[\sqrt{3}(1-4\cdot O2y)\right]. \tag{6.42}$$

Figure 6.48 illustrates the extent to which the above point is valid; the only exceptions are Rietveld-refined synthetic samples (Nos. 55-62) and samples for which the R-values are relatively high.

In conclusion, whereas simple geometrical models cannot provide the exact positions of each atom within a given tetrahedron due to the presence of meso-octahedral sheets in *2:1* layer silicates, the lateral extension of the tetrahedral sheets can be accurately predicted from simple geometric considerations despite local distortions actually occurring in individual tetrahedrons.

	$[\langle M1\text{-}O\rangle^2-\langle M2\text{-}O\rangle^2]/a^2$	Δz	$(180^\circ-\eta)$	$BLD_{T\text{-}O3}$	α
$[\langle M1\text{-}O\rangle^2-\langle M2\text{-}O\rangle^2]/a^2$	-	0.556	0.692	-0.186	-0.003
Δz		-	0.803	-0.466	0.229
$(180^\circ-\eta)$			-	-0.441	0.126
$BLD_{T\text{-}O3}$				-	0.181
α					-

Table 6.5. Correlation coefficients between various tetrahedral distortion parameters.

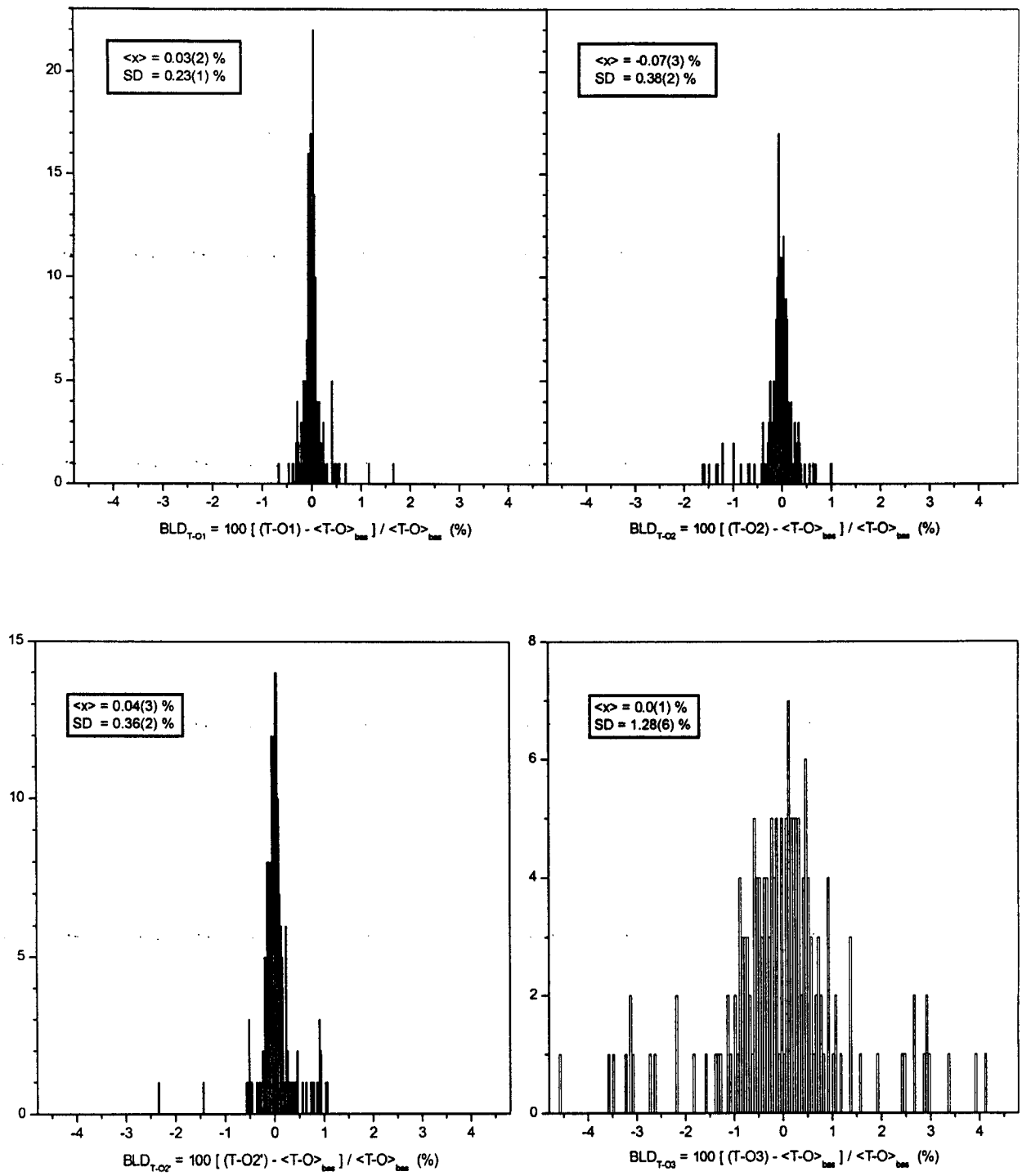

Figure 6.39. Histograms showing the distributions of BLD_i parameters (Eq. 6.39a).

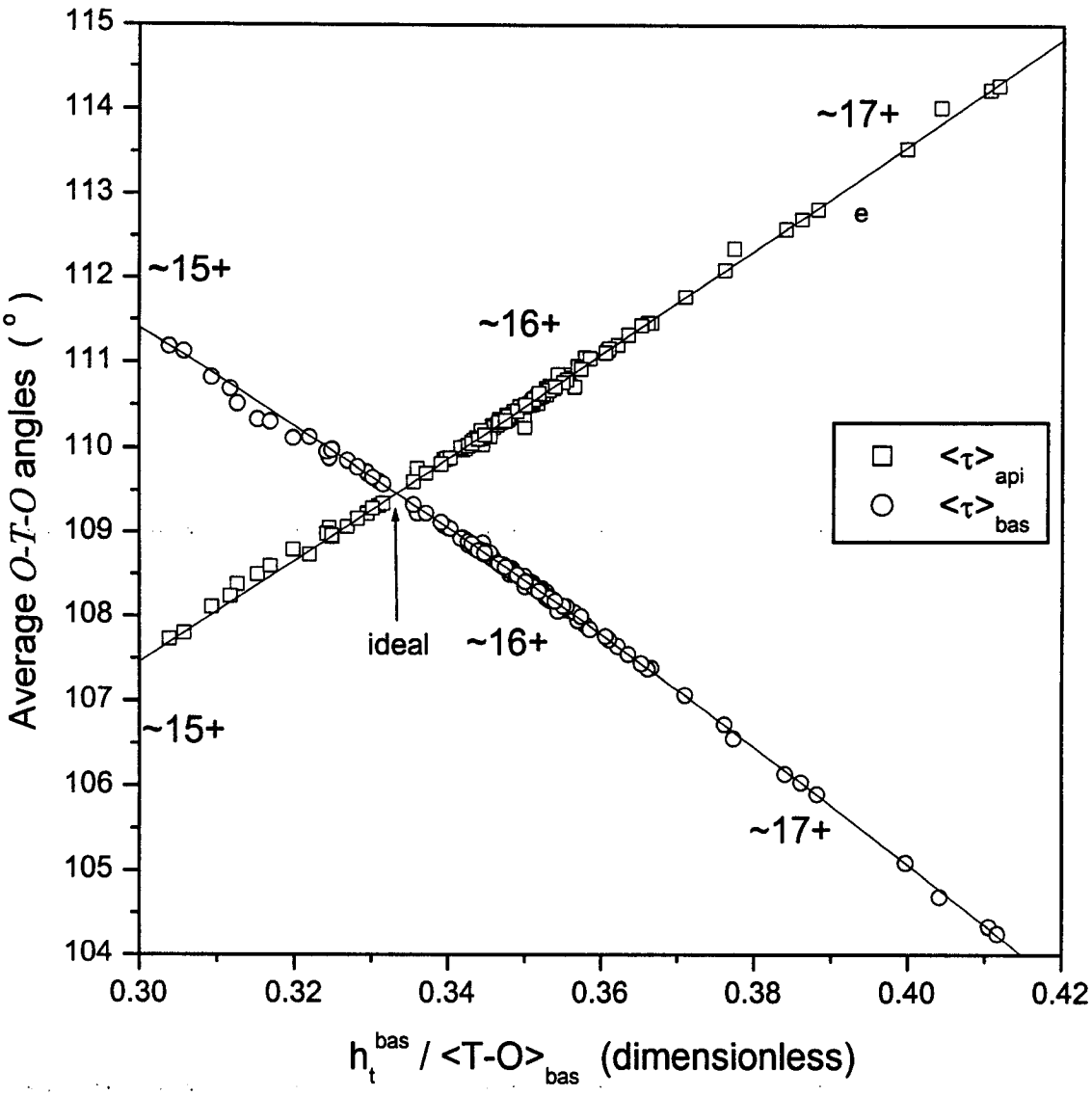

Figure 6.40. Comparison of simple geometrical model predictions (solid lines) to average tetrahedral distortion parameters actually observed in the structures. See text for a detailed description of the figure.

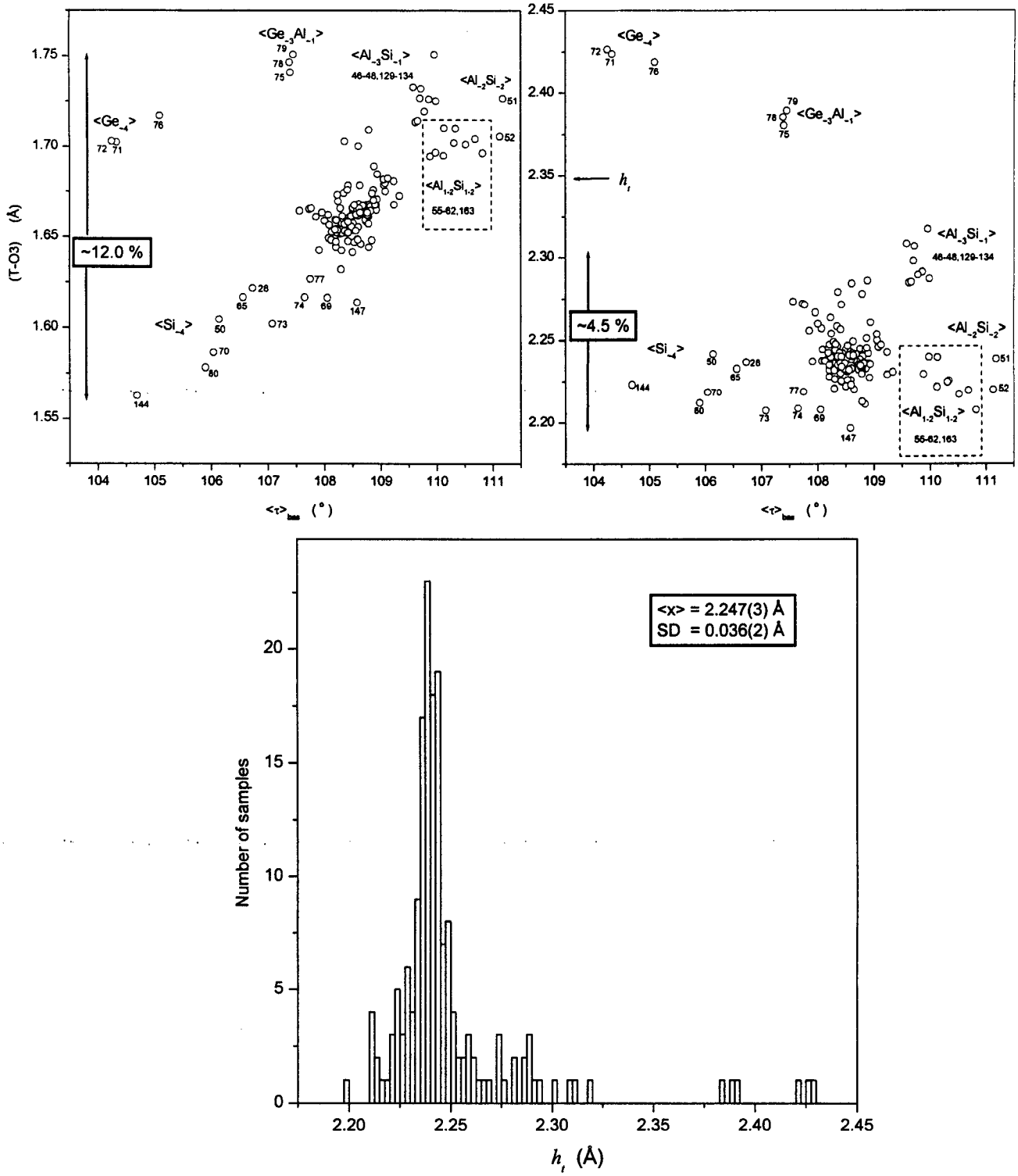

Figure 6.41. Evolution of tetrahedron's height h_t and apical bond length (T-O3) as a function of the average basal flattening angle $\langle\tau\rangle_{bas}$. An histogram showing the distribution of h_t values is also presented.

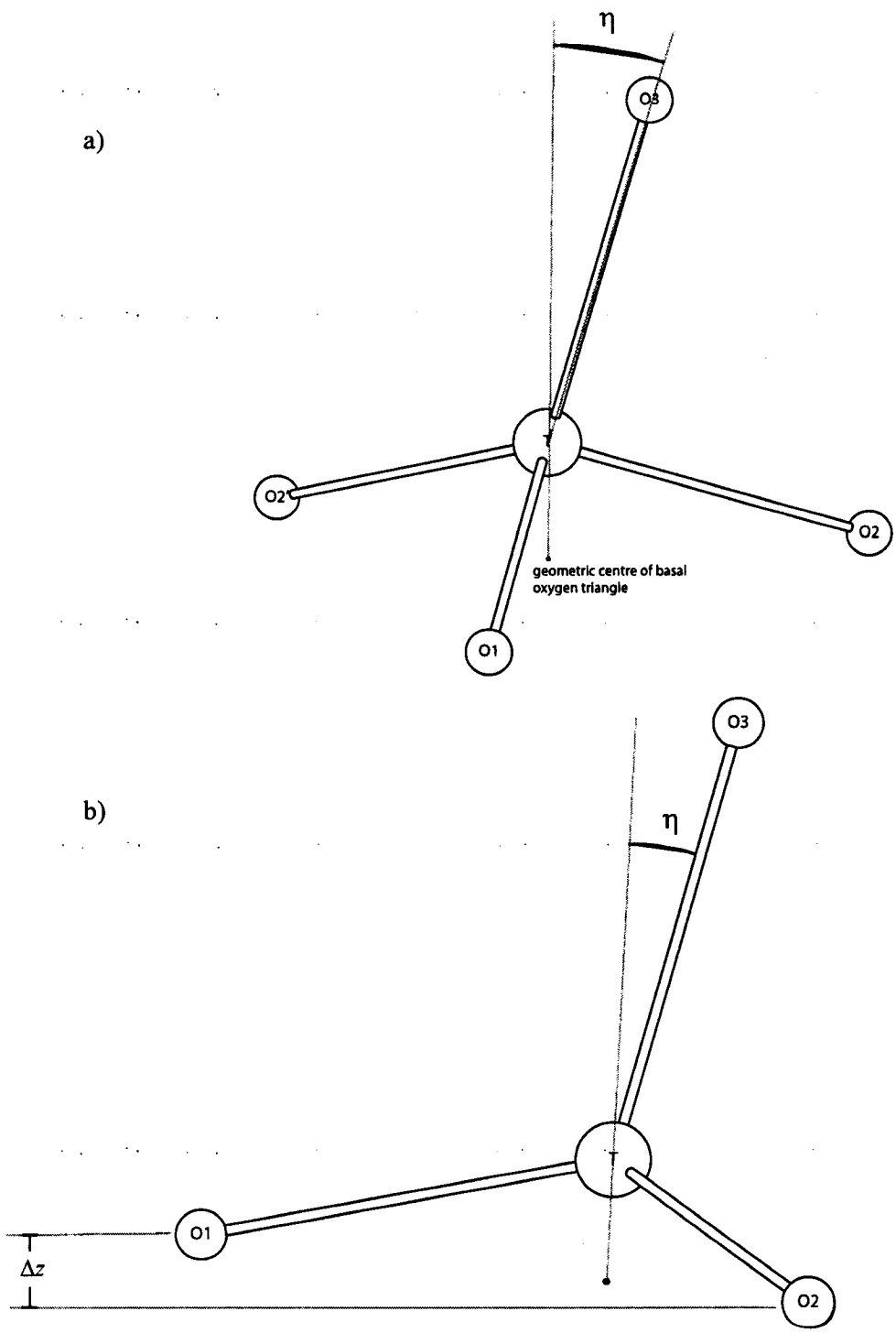

Figure 6.42. Diagrams depicting two tetrahedral distortions: a) bending of the apical (T-O3) bond with respect to the pyramidal base formed by the three basal bonds; and b) tetrahedral corrugation. See text for a description of the various symbols.

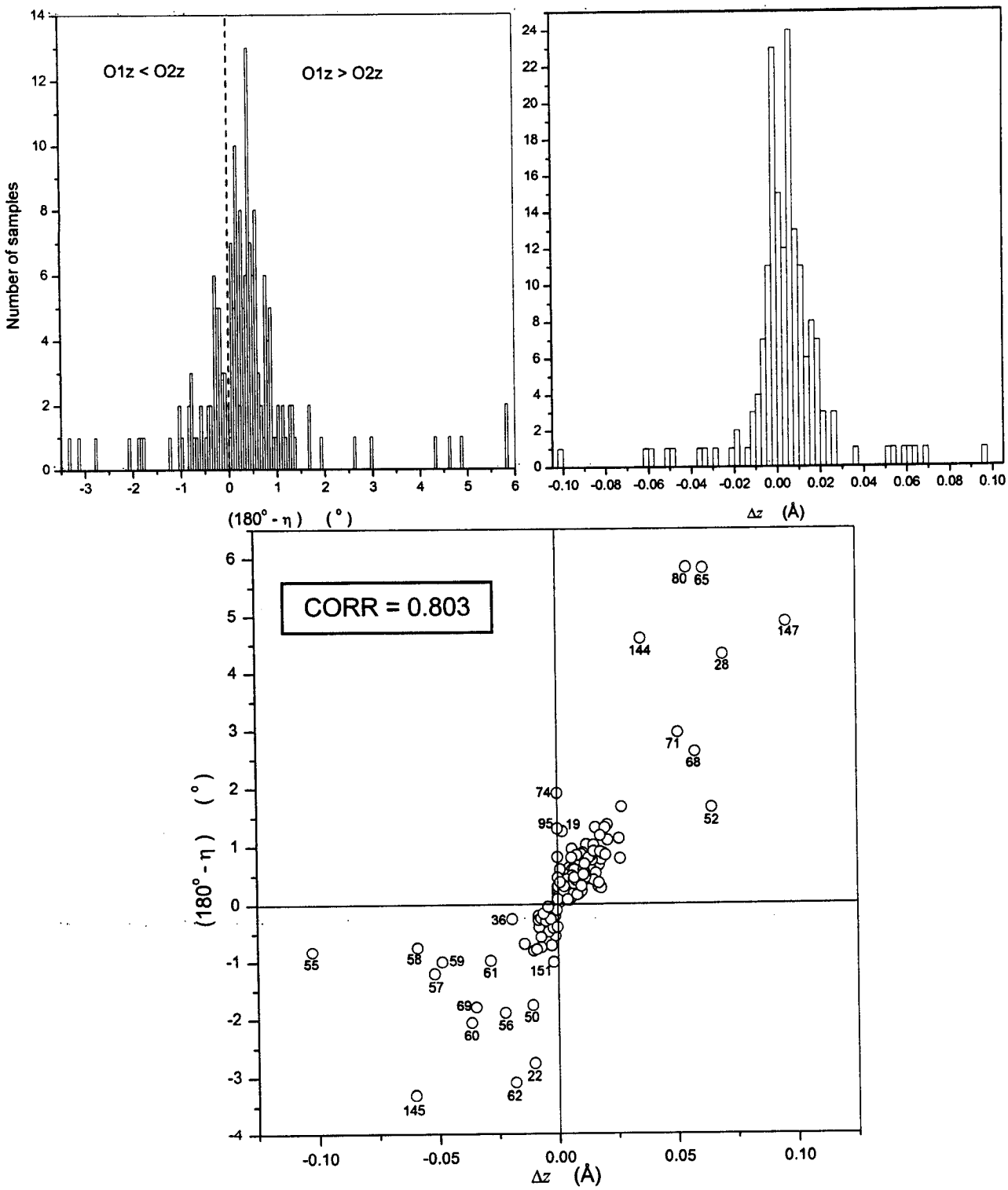

Figure 6.43. Histograms showing the distributions of Δz and $(180°-\eta)$ values, along with an illustration of the degree of correlation between Δz and $(180°-\eta)$. The value of the correlation coefficient (CORR) is also indicated.

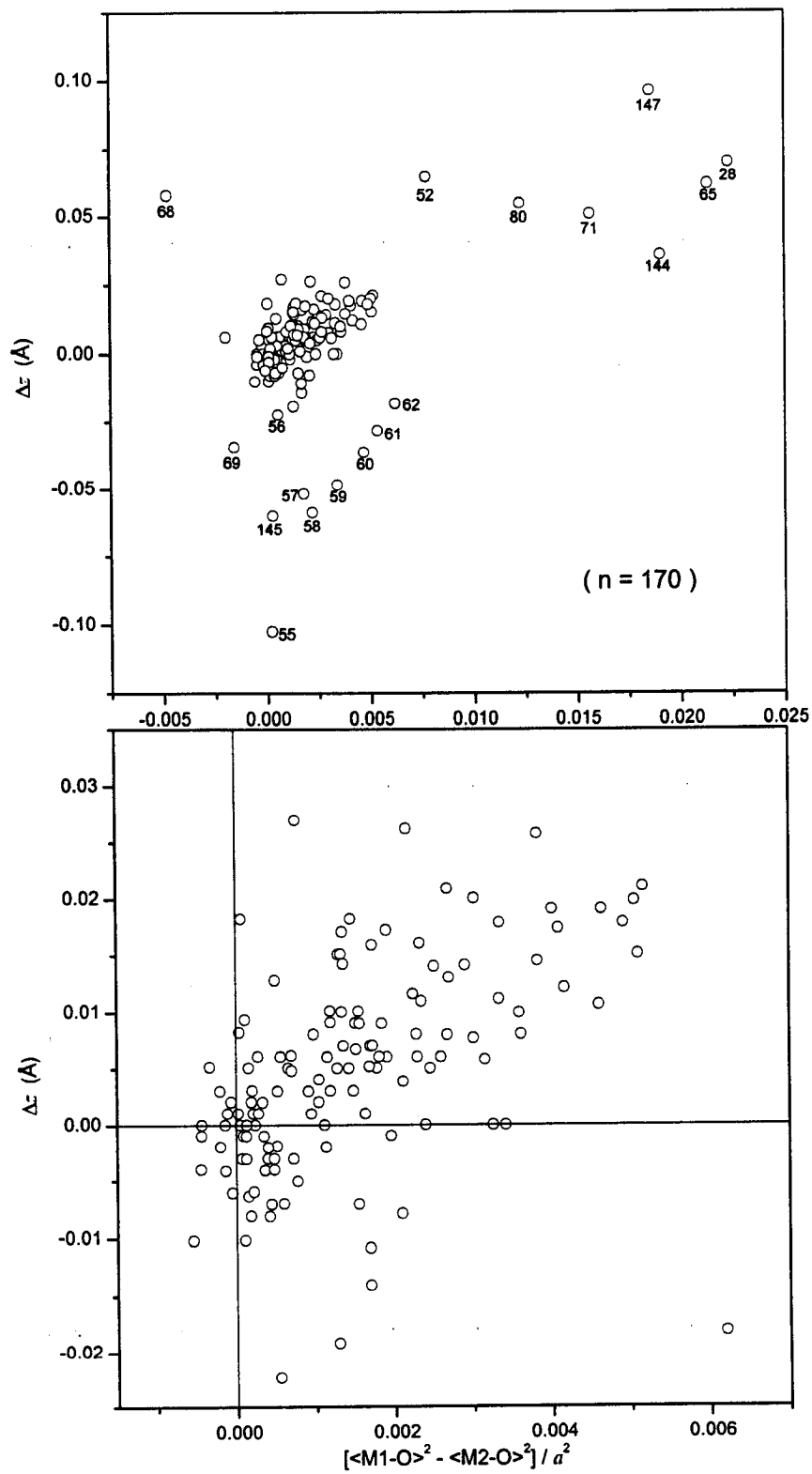

Figure 6.44. Basal oxygen plane corrugation Δz *vs.* dimensionless squared octahedral size difference $[<M1\text{-}O>^2-<M2\text{-}O>^2]/a^2$.

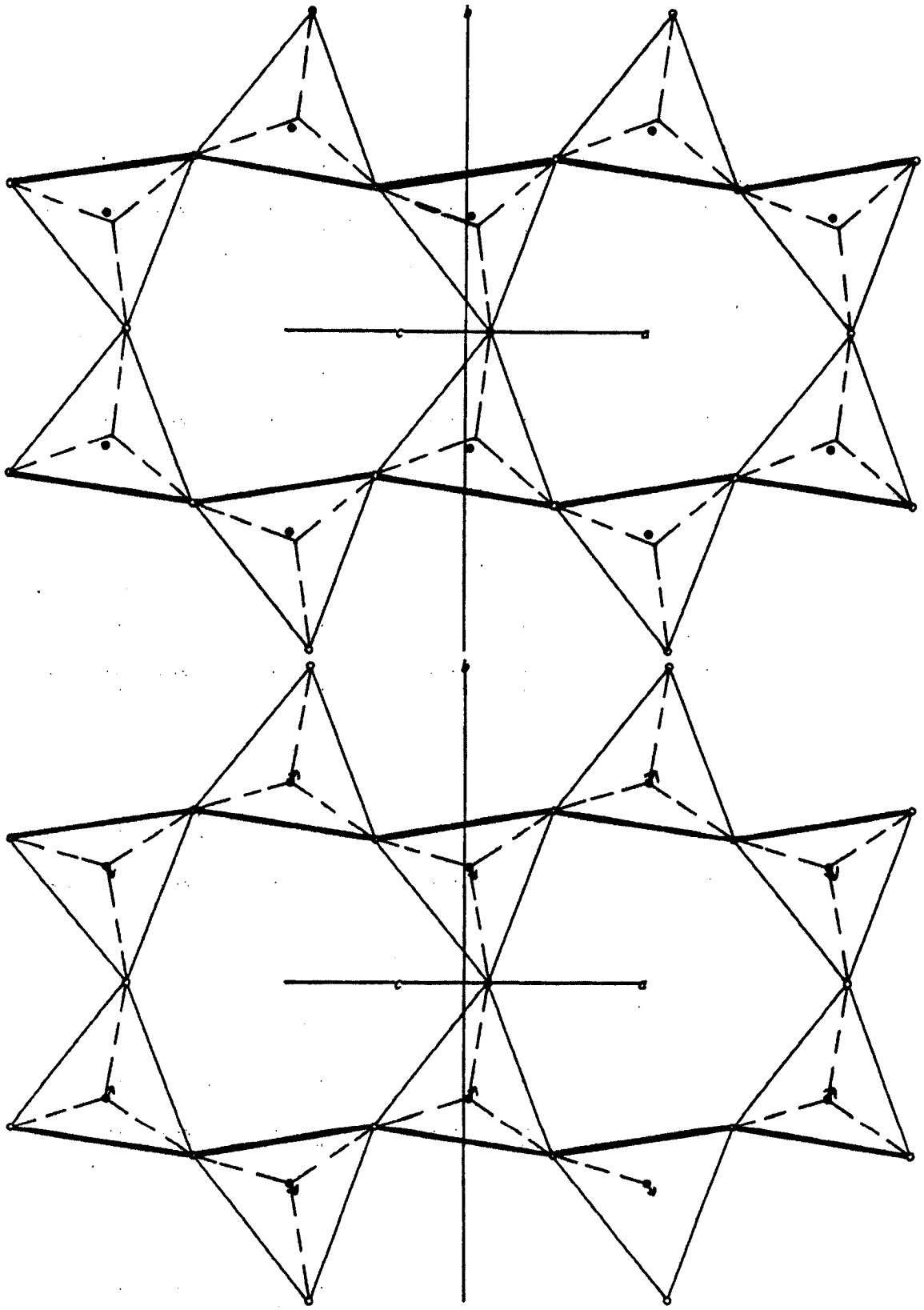

Figure 6.45: In-plane (001) projections of a tetrahedral sheet fitting on top of a geometric meso-octahedral sheet. See text for a detailed description of the figure.

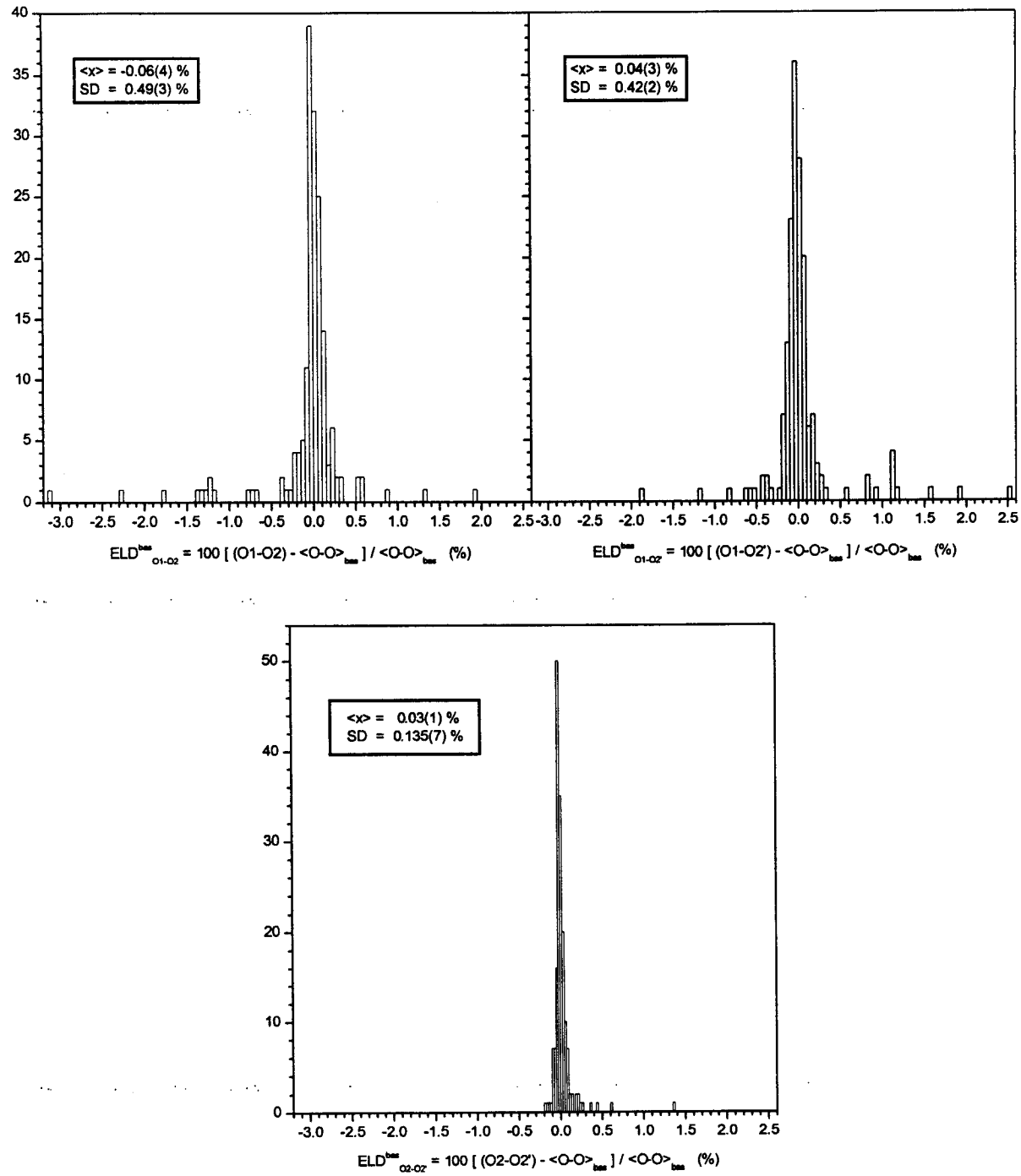

Figure 6.46. Histograms showing the distributions of ELD^{bas}_i parameters (Eq. 6.39b).

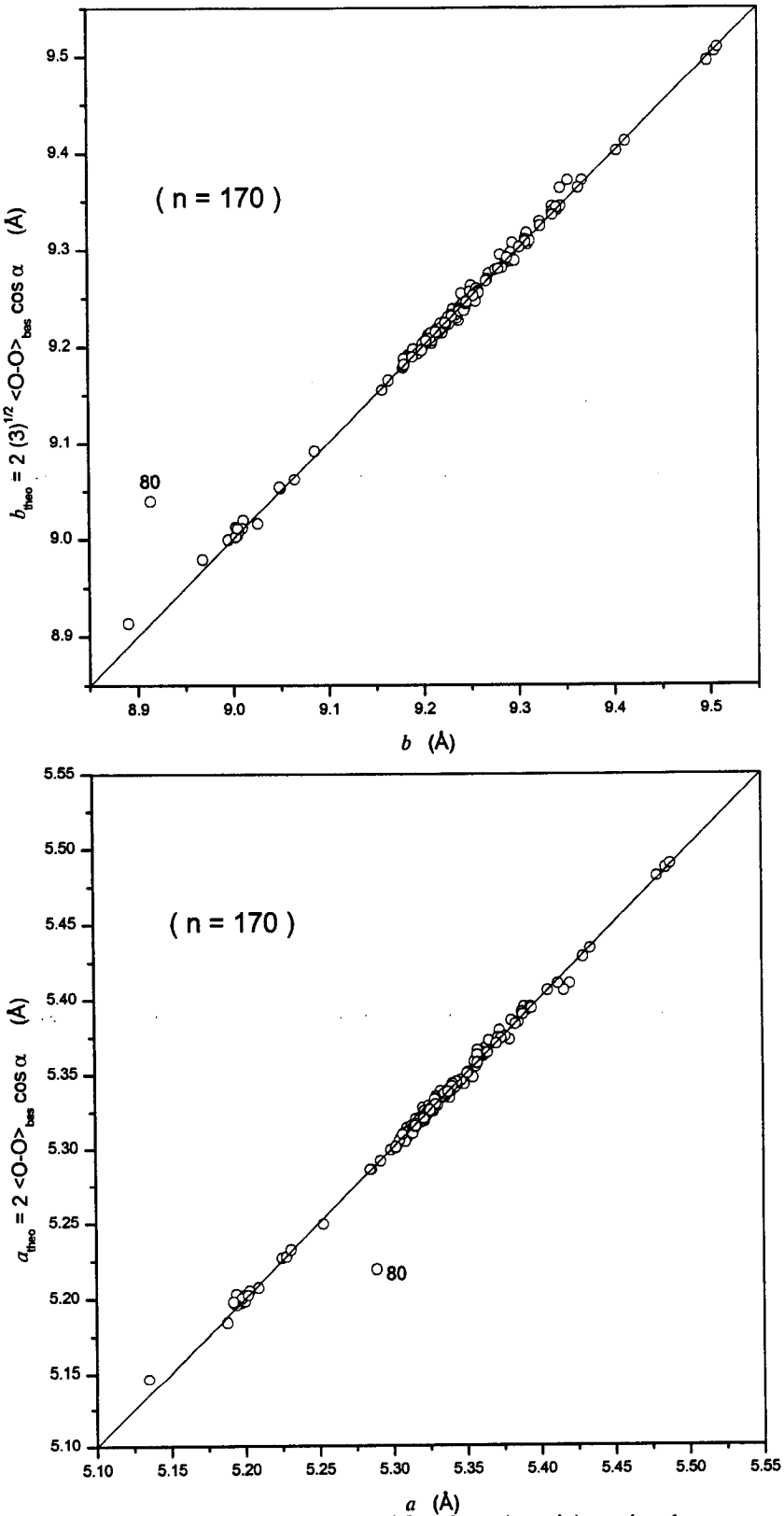

Figure 6.47. Comparison of observed a and b values (x-axis) to simple geometrical model predictions made using Eq. 6.19 (Subsection 6.2.5).

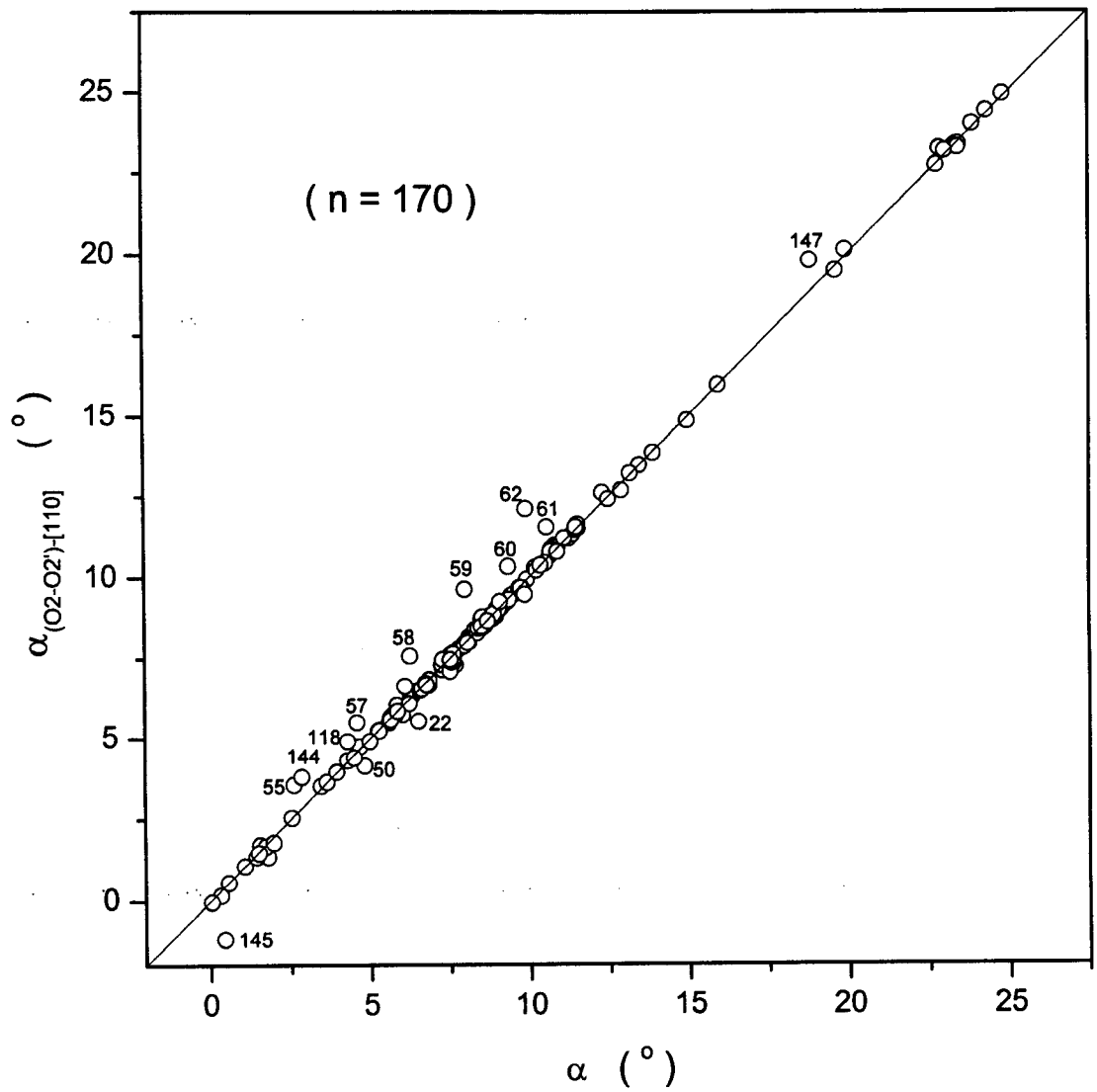

Figure 6.48. Comparison of the average tetrahedral rotation angle α (Eq. 6.41) to the angle $\alpha_{(O2\text{-}O2')\text{-}[110]}$ that makes the basal (O2-O2') edges with respect to the *a*-axis direction (Eq. 6.42).

6.3.4 Interlayer site distortions

Figures 6.49, 6.50, and 6.51 show individual distances as functions of average lengths for the following quantities, respectively (see Table 6.3 for symbols and nomenclature): i) individual inner interlayer site bond lengths $(A\text{-}O1)_{in}$ and $(A\text{-}O2)_{in}$ as functions of the average inner interlayer site bond length $\langle A\text{-}O\rangle_{in}$ (= 1/6·[2·(A-O1) + 4·(A-O2)]); ii) individual basal inner interlayer edge lengths $(O1\text{-}O2)^{bas}_{in}$ and $(O2\text{-}O2)^{bas}_{in}$ as functions of the average basal inner interlayer edge length $\langle(O\text{-}O)^{bas}\rangle_{in}$ (=1/6·[4·$(O1\text{-}O2)^{bas}_{in}$ + 2·$(O2\text{-}O2)^{bas}_{in}$]); and iii) individual lateral inner interlayer edge lengths $(O1\text{-}O2)^{lat}_{in}$ and $(O2\text{-}O2)^{lat}_{in}$ as a function of the average lateral inner interlayer edge length $\langle(O\text{-}O)^{lat}\rangle_{in}$ (=1/6·[4·$(O1\text{-}O2)^{lat}_{in}$ + 2·$(O2\text{-}O2)^{lat}_{in}$]). In addition, Figures 6.49-6.51 present histograms displaying the distributions of normalized size differences (100%)[$(A\text{-}O1)_{in}$ - $(A\text{-}O2)_{in}$]/$\langle A\text{-}O\rangle_{in}$, (100%)[$(O1\text{-}O2)^{bas}_{i}$ - $(O2\text{-}O2)^{bas}_{in}$]/$\langle(O\text{-}O)^{bas}\rangle_{in}$, and (100%)[$(O1\text{-}O2)^{lat}_{in}$ - $(O2\text{-}O2)^{lat}_{in}$]/$\langle(O\text{-}O)^{lat}\rangle_{in}$, respectively.

Histograms displaying the distributions of *A-O* bond lengths and interlayer distances d_{int} are presented in Figure 6.52, whereas the distributions of basal and lateral inner interlayer edge lengths are given in Figure 6.53. For bond and edge lengths, the two different values of a given type (basal or lateral) are included in a single distribution for each type. The main peaks appearing on all of these distributions correspond to the $\{K^{1+}\}$ samples.

The interlayer distance d_{int} is the thickness of the interlayer region calculated from the z coordinates of basal oxygen atoms (compiled in Appendix P) as:

$$d_{int} = 2 \cdot c \sin\beta \cdot \left(1/3 \cdot \left[O1z + 2 \cdot O2z\right]\right) . \tag{6.43}$$

Values of d_{int} and all quantities plotted in Figures 6.49-6.53 are tabulated in Appendix P.

As is well known (e.g., see [Brigatti & Guggenheim 2002]), Figures 6.49-6.53 demonstrate that inner interlayer site bond lengths, basal and lateral edge lengths, and interlayer distances fall into separate groups that depend on the chemical composition of the interlayer sites: $\{K^{1+}_{-1}\}$, $\{Na^{1+}_{-1}\}$, $\{Ca^{2+}_{-1}\}$, and $\{Cs^{1+}_{-1}\}$.

In examining the distributions of normalized size differences (100%)[$(A\text{-}O1)_{in}$ - ($A\text{-}O2)_{in}$]/$\langle A\text{-}O\rangle_{in}$, (100%)[$(O1\text{-}O2)^{bas}_{in}$ - $(O2\text{-}O2)^{bas}_{in}$]/$\langle(O\text{-}O)^{bas}\rangle_{in}$, and (100%)[$(O1\text{-}O2)^{lat}_{in}$ - ($O2\text{-}O2)^{lat}_{in}$]/$\langle(O\text{-}O)^{lat}\rangle_{in}$ shown in Figures 6.49-6.51, one notes that excluding a few outliers, all distributions are well constrained around zero, with fractional sample-specific deviations of at most only ~0.5-0.7 % for each distribution. This means that the shapes of inner interlayer site octahedrons can be adequately given from the average geometric parameters $\langle A\text{-}O\rangle_{in}$,

$<(O\text{-}O)^{bas}>_{in}$, and $<(O\text{-}O)^{lat}>_{in}$.

Another important distortion parameter is the inner interlayer octahedron flattening angle ϕ_{in} , that can be obtained from either: i) the average inner interlayer site bond length $<A\text{-}O>_{in}$ and the interlayer distance d_{int} via Eq. 6.24 (Subsection 6.2.6),

$$\phi_{in} = \arccos\left[\frac{d_{int}/2}{<A-O>_{in}}\right] \quad ; \tag{6.44}$$

or ii) the average basal $<(O\text{-}O)^{bas}>_{in}$ and lateral $<(O\text{-}O)^{lat}>_{in}$ inner interlayer edge lengths via Eq. 6.6 (Subsection 6.2.1),

$$\phi_{in} = \arcsin\sqrt{\frac{4}{3\left(1+\left[\frac{<(O-O)^{lat}>_{in}}{<(O-O)^{bas}>_{in}}\right]^2\right)}} \quad . \tag{6.45}$$

In the $1M$ structural refinements that were investigated, values of ϕ_{in} obtained from Eqs. 6.44 and 6.45 are equal to each other to within $\pm 0.02°$; both of these ϕ_{in} values are compiled in Appendix P.

Let us now look into the matching of interlayer site octahedrons to tetrahedral sheets. Figure 6.54 compares observed interlayer distances d_{int} to predictions made from Eq. 6.25 (Subsection 6.2.6) using the values compiled in Appendix P for the lattice parameter a , the average inner interlayer bond length $<A\text{-}O>_{in}$,the average basal tetrahedral edge length $<O\text{-}O>_{bas}$, and the average tetrahedral rotation angle α (as defined in Eq. 6.41, Subsection 6.3.3). The solid lines that are drawn in Figure 6.55 correspond to a 1:1 correspondence between the x and y axes of each graph. Given the remarkable agreement between theoretical and observed values of d_{int} , therefore, Figure 6.54 clearly demonstrates that when all relevant crystal chemical parameters are properly taken into account via Eq. 6.25, simple geometrical models of tetrahedrons and inner interlayer octahedrons are sufficient to explain the matching of tetrahedral sheets to interlayer octahedrons. The case of the only notable exception, norrishite sample No. 80, is due to a break of the $b = \sqrt{3}a$ relationship (see Section 6.1).

The fact that all relevant crystal chemical parameters are necessary is emphasized in Figure 6.55, where the evolutions of the interlayer distance d_{int} and the inner interlayer octahedron flattening angle ϕ_{in} are plotted as functions of the average tetrahedral rotation angle α . The lines (solid, dashed, or dotted) that are shown in Figure 6.55 correspond to predictions made on the

basis of Eq. 6.25b (Subsection 6.2.6), which specifies that the position of a given line depends on the particular values of inner interlayer octahedron bond length, $(A\text{-}O)_{in}$, and tetrahedral basal edge length, e_t^{bas}, that are assumed. All together, Figure 6.55 allows one to visualize that at a fixed $(A\text{-}O)_{in}$ interlayer bond length, when the basal tetrahedral triangular faces rotate by α due to an increase of the basal edge length e_t^{bas}, then the interlayer distance d_{int} increases via the flattening angle ϕ_{in} of the inner interlayer octahedron. That is, as the tetrahedral rings close up, the interlayer cations move away from the tetrahedral sheets.

In Figure 6.55, we now focus on the $\{K^{1+}\}$ samples. If the basal tetrahedral edge length e_t^{bas} is constrained to a range of values between 2.67 and 2.72 Å — that is consistent with the variation of basal edge length values observed for these samples (see samples labelled as $<Al_{\sim 1}Si_{\sim 3}>$ in Figure 6.36, Subsection 6.3.3) — then in order to cover the full range of observed values for d_{int} or ϕ_{in}, one needs to vary $(A\text{-}O)_{in}$ from 3.05 to 2.90 Å. From a crystal chemistry perspective, one expects a cation in octahedral coordination to have a specific bond length, especially within a given type of network. In the present case, however, the extent of the inner interlayer octahedral bond length variation for K^{1+} is estimated at ~5.0 % (=100[3.05 - 2.90]/2.975) for the $<Al_{\sim 1}Si_{\sim 3}>\{K_{\sim 1}\}$ samples. By contrast, the basal edge length variation is of only ~1.8 % (=100[2.72 - 2.67]/2.695) for the same group of samples, despite the effect that sample-to-sample differences in Al:Si ratios within this group exert on tetrahedral sheets' dimensions.

In view of the above considerations, the immediate question to ask is: What could be the origin of such a large bond length variation for the K^{1+} cation in trioctahedral micas ? Useful insights into this situation is offered by considering the interatomic distance (A-O4) between the interlayer *A* cation and the O4-site anion. The O4 anion is the OH/F/Cl anion of the octahedral sheet, that is directly above and below the interlayer cation.

Figure 6.56 displays the average inner interlayer bond length $<A\text{-}O>_{in}$, the interlayer distance d_{int}, and the lattice parameter *c* as functions of the (A-O4) distance. The dashed lines drawn in Figure 6.56 are linear regressions through the data. Different clusters of samples can be identified depending on the chemical composition of the interlayer sites, except for Rietveld-refined (Nos. 55-62) and Ge-containing (Nos. 71-72, 75-76, 78-79) samples which stand out separately. As indicated by the R-values of the fits, positive correlations with (A-O4) can be discerned for both *c* and d_{int}, while in the case of $<A\text{-}O>_{in}$, there might be a slight negative correlation. If the large variation of bond lengths for the K^{1+} cations were due to interactions between interlayer *A* cations and O4-site anions, then it is reasonable to believe that signs of this would be reflected in a behaviour dependent on the (A-O4) distance. This is precisely the case

here: irrespective of the exact nature of the interaction between the interlayer *A* cations and the O4 site anions, Figure 6.56 gives reasonable evidence that the (A-O4) distance is a key factor determining the length of the *c*-axis and the interlayer distance d_{int} , for a given identity of interlayer *A* cation.

Although half of d_{int} contributes to the (A-O4) distance along *c** (i.e., these two parameters are geometrically related one to another), the physical mechanisms contributing to each of these interatomic distances are quite distinct: the interlayer distance d_{int} follows from the bonding of the interlayer cations with the basal oxygen atoms that are part of the tetrahedral sheets (Figures 6.54 and 6.55), whereas the (A-O4) distance is a consequence of both interactions between the interlayer *A* cation and the O4 anion and the geometry of the T-O-T network. In any case, the (A-O4) distance is a convenient crystal chemical parameter to consider.

That being said, if the length of the *c*-axis predominantly depends on the character of the *A*-O4 interaction and on the type of interlayer cation, then it should not be much affected by the cationic species contained in the tetrahedral and octahedral sheets. Indeed, this is shown in Figure 6.57, where the *c* lattice parameter is plotted as a function of the interlayer distance d_{int}, as well as a function of the overall *T-O-T thickness*[1] , the latter quantity being a measure of the intralayer distance along *c** between the average positions of two basal-oxygen planes that comprise the octahedral sheet and the two tetrahedral sheets (values of *T-O-T thickness* are compiled in Appendix P). Whereas a clear relationship (R = 0.882) is exhibited between *c* and d_{int}, one can see that no net relation (R = 0.299) exists between the *c*-axis length and the *T-O-T thickness*. Given that *c* and d_{int} are also related to the (A-O4) distance (Figure 6.56), therefore, in the ensemble of trioctahedral-1*M* mica samples considered here, it clearly appears that the interaction between the interlayer *A* cation and the O4-site anion effectively controls the *c*-axis length, rather than being determined by the cationic species contained in the octahedral and tetrahedral sheets, for a given interlayer cation species.

There now remains to establish the nature of the physical mechanisms responsible for the behaviours observed in Figures 6.56 and 6.57, that should also explain the large bond length variation noted in Figure 6.55 for the K^{1+} cation in trioctahedral micas. Fortunately, as was reported in [Rancourt *et al.* 2001], enlightening leads into this situation are given by the lattice parameters of synthetic samples studied in this thesis.

In Figure 6.58, *c* is plotted *versus a* for all synthetic samples (refer to Table 3.1 for

---

[1]The *T-O-T thickness* was determined from the z coordinates of basal oxygen atoms and is equal to:

$$c \sin\beta \, [1 - 2/3 \cdot (O1z + 2 \cdot O2z)] .$$

nomenclature of the various solution series; consult Section 5.2 or Appendix W for values of the lattice parameters); for the sake of comparison, values of *c versus a* for single-crystal structure refinements are shown in Figure 6.59. In synthetic samples, for a given tetrahedral-site composition, one can see that although *a* varies as expected with the average octahedral radius (as does *b*, by virtue of the $b = \sqrt{3} \cdot a$ relationship explained in Section 6.1), *c* is relatively constant within a given solid solution for all series that have near-saturation amounts of structural OH groups. Figure 6.58, therefore, gives strong evidence that the above interpretation of Figures 6.56 and 6.57, in terms of a *c*-axis length being controlled by the nature of the *A*-O4 interaction rather than by the cationic species contained in the *2:1* layers, is correct. In addition, Figure 6.58 convincingly demonstrates that the presence of structural OH *versus* F in the O4-site is a crucial factor determining *c*.

Figure 6.60 separately shows the evolutions of the *c* lattice parameters for the annite-fluoroannite (Ann-FAnn) and the annite-oxyannite-ferrioxyannite (oxidized) series (Table 3.1) as functions of the nominal F content [X_F] and the heat-treatment temperature T_{TR}, respectively (consult Section 3.2 for details of the sample synthesis and heat-treatment conditions). Although the overall differences in the magnitude of *c* are similar in both series (~0.20 Å for oxidized; ~0.21 Å for Ann-FAnn), the most striking feature is the discontinuity in *c* that takes place in the oxidized samples between treatment temperatures T_{TR} = 350 and 370°C.

As explained in [Rancourt *et al.* 2001], the abrupt change in behaviour seen in the oxidized samples is interpreted as a *pillaring collapse* transition that occurs near the point where the OH concentration becomes zero as oxidation proceeds. Moreover, the gradual pre-transition decrease in *c* can be tentatively attributed to progressive OH-dipole bending away from the *c* axis, as more and more of the electrostatic interlayer compressional force is countered by fewer and fewer OH groups (whose protons oppose the K^{1+} interlayer cations). Such bending is consistent with the fact that, as the Fe^{3+}/Fe^{2+} ratio (Table 3.3) increases with the samples being oxidized more and more, a larger and larger fraction of the remaining OH groups see $^{[6]}Fe^{2+}$-$^{[6]}Fe^{2+}$-$^{[6]}Fe^{3+}$ or $^{[6]}Fe^{2+}$-$^{[6]}Fe^{3+}$-$^{[6]}Fe^{3+}$ nearest-neighbour configurations, rather than the dominant $^{[6]}Fe^{2+}$-$^{[6]}Fe^{2+}$-$^{[6]}Fe^{2+}$ configuration of the unoxidized starting IKO-Ann sample [Gilkes *et al.* 1972a, 1972b].

Before we end this subsection, it is important to state that tetrahedral corrugation does not affect any of the conclusions reached above regarding the inner interlayer *A* octahedron. This can be easily visualized by drawing the actual distortions that occur in the interlayer as a result of tetrahedral corrugation (not shown).

In conclusion, the results presented in this subsection can be summarized as follows: i) the interlayer site distortions can be adequately modelled using an iso-bond flattened octahedron;

ii) the matching of interlayer octahedrons to tetrahedral sheets is fully understood in terms of simple geometrical models via Eq. 6.25 (Subsection 6.2.4); iii) a large bond length variation is observed for K^{1+} in trioctahedral-1*M* micas; iv) the *c*-axis length is controlled by the nature of O4-site anion and its interaction with the interlayer *A* cation; and v) the large bond length variation for K^{1+} can be understood as arising from *A*-O4 interactions, which depend on the degree of OH-dipole bending away from the *c* axis introduced by M^{3+} to M^{2+} cationic substitutions in the octahedral sheets and on the degree of OH/F and OH/Cl substitutions.

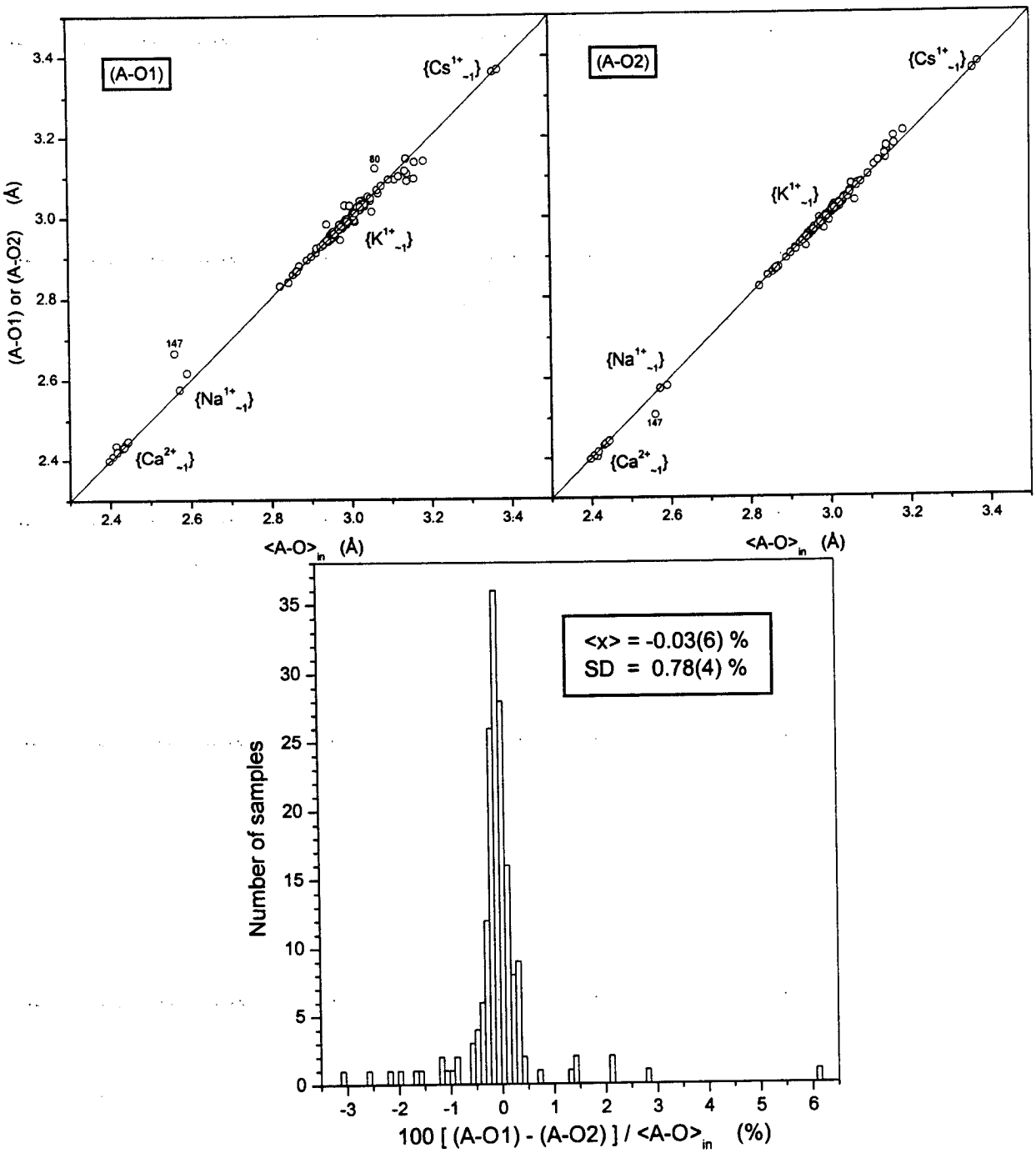

Figure 6.49. Evolution of individual inner *A-O* distances $(A\text{-}O1)_{in}$ and $(A\text{-}O2)_{in}$ as a function of the average inner interlayer site bond length $\langle A\text{-}O\rangle_{in}$ (=1/6·[2·(A-O1)+4·(A-O2)]). The solid lines that are shown represent a 1:1 correspondence between the *x* and *y* axes. A histogram displaying the distribution of the normalized size difference between the two inner *A-O* distances, (100 %) $[(A\text{-}O1)_{in} - (A\text{-}O2)_{in}] / \langle A\text{-}O\rangle_{in}$, is also shown.

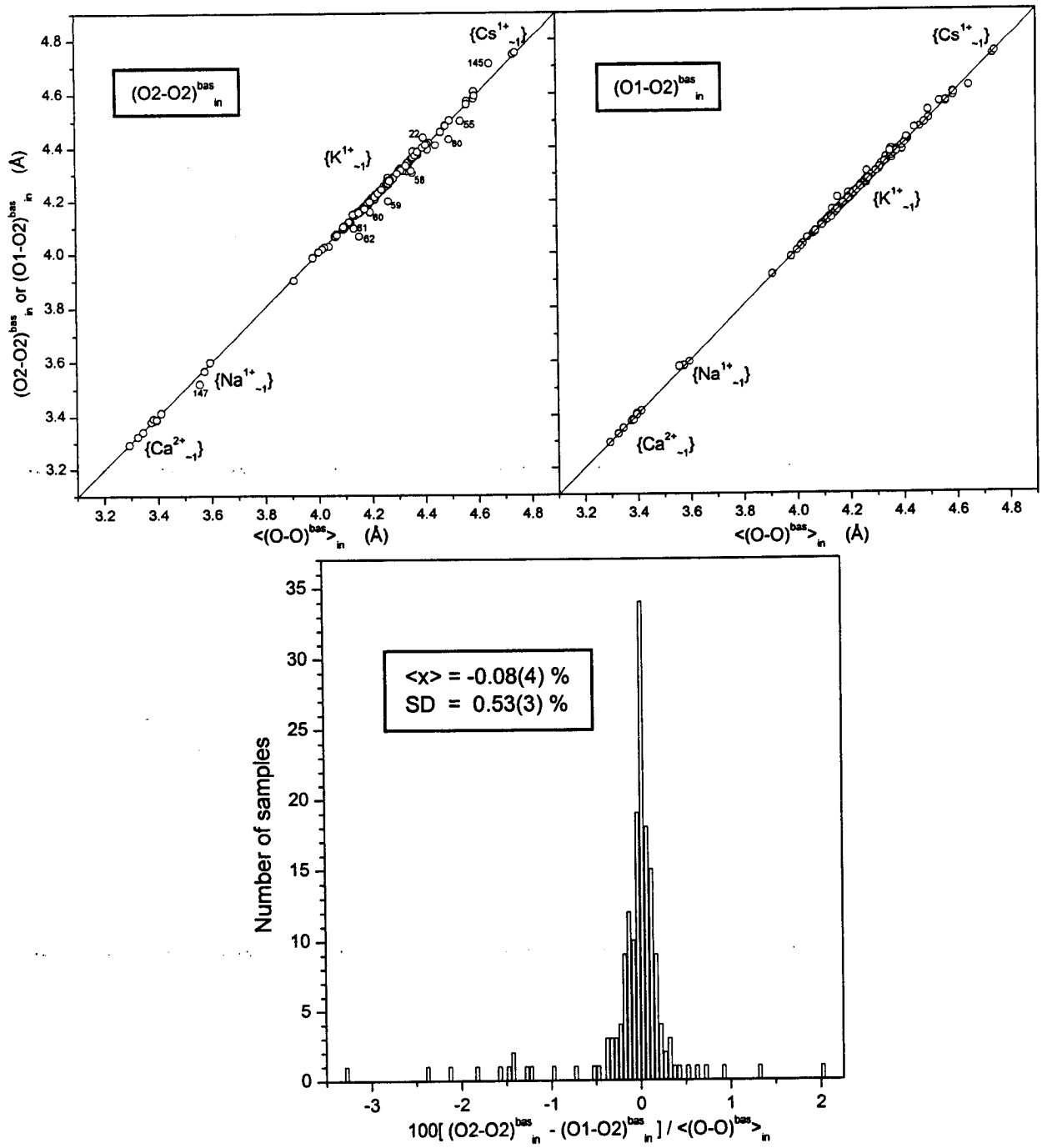

Figure 6.50. Evolution of basal inner interlayer edge lengths $(O1\text{-}O2)^{bas}_{in}$ and $(O2\text{-}O2)^{bas}_{in}$ as a function of the average basal inner interlayer edge length $\langle(O\text{-}O)^{bas}\rangle_{in}$ $(=1/6\cdot[4\cdot(O1\text{-}O2)^{bas}_{in} + 2\cdot(O2\text{-}O2)^{bas}_{in}])$. The solid lines that are shown represent a 1:1 correspondence between the *x* and *y* axes. An histogram displaying the distribution of the normalized size difference between the two inner basal distances, (100 %) $[(O1\text{-}O2)^{bas}_{in} - (O2\text{-}O2)^{bas}_{in}] / \langle(O\text{-}O)^{bas}\rangle_{in}$, is also shown.

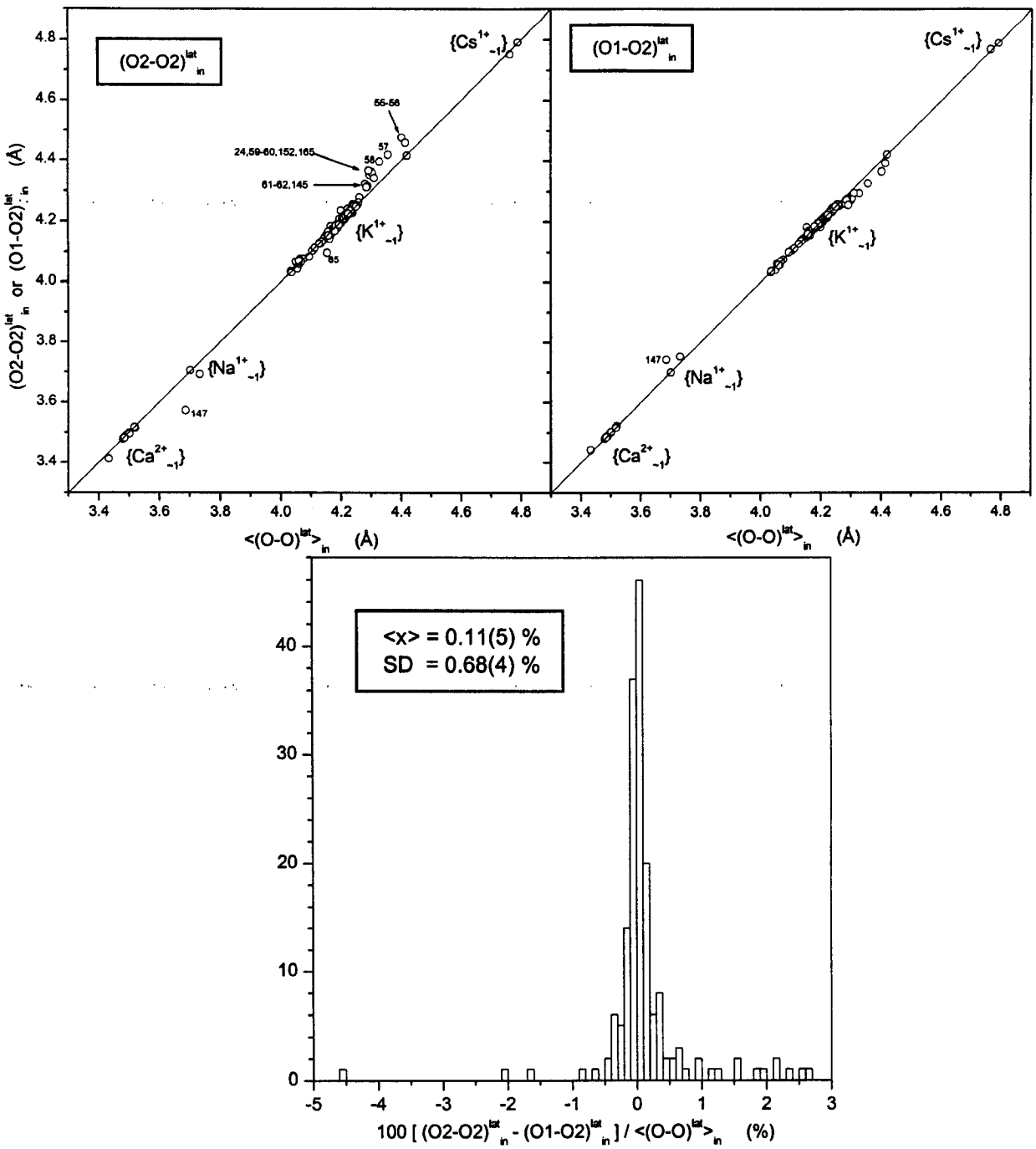

Figure 6.51. Evolution of lateral inner interlayer edge lengths $(O1\text{-}O2)^{lat}_{in}$ and $(O2\text{-}O2)^{lat}_{in}$ as a function of the average lateral inner interlayer edge length $\langle(O\text{-}O)^{lat}\rangle_{in}$ $(=1/6\cdot[4\cdot(O1\text{-}O2)^{lat}_{in} + 2\cdot(O2\text{-}O2)^{lat}_{in}])$. The solid lines that are shown represent a 1:1 correspondence between the *x* and *y* axes. A histogram displaying the distribution of the normalized size difference between the two inner basal distances, (100 %) $[(O1\text{-}O2)^{lat}_{in} - (O2\text{-}O2)^{lat}_{in}] / \langle(O\text{-}O)^{lat}\rangle_{in}$, is also shown.

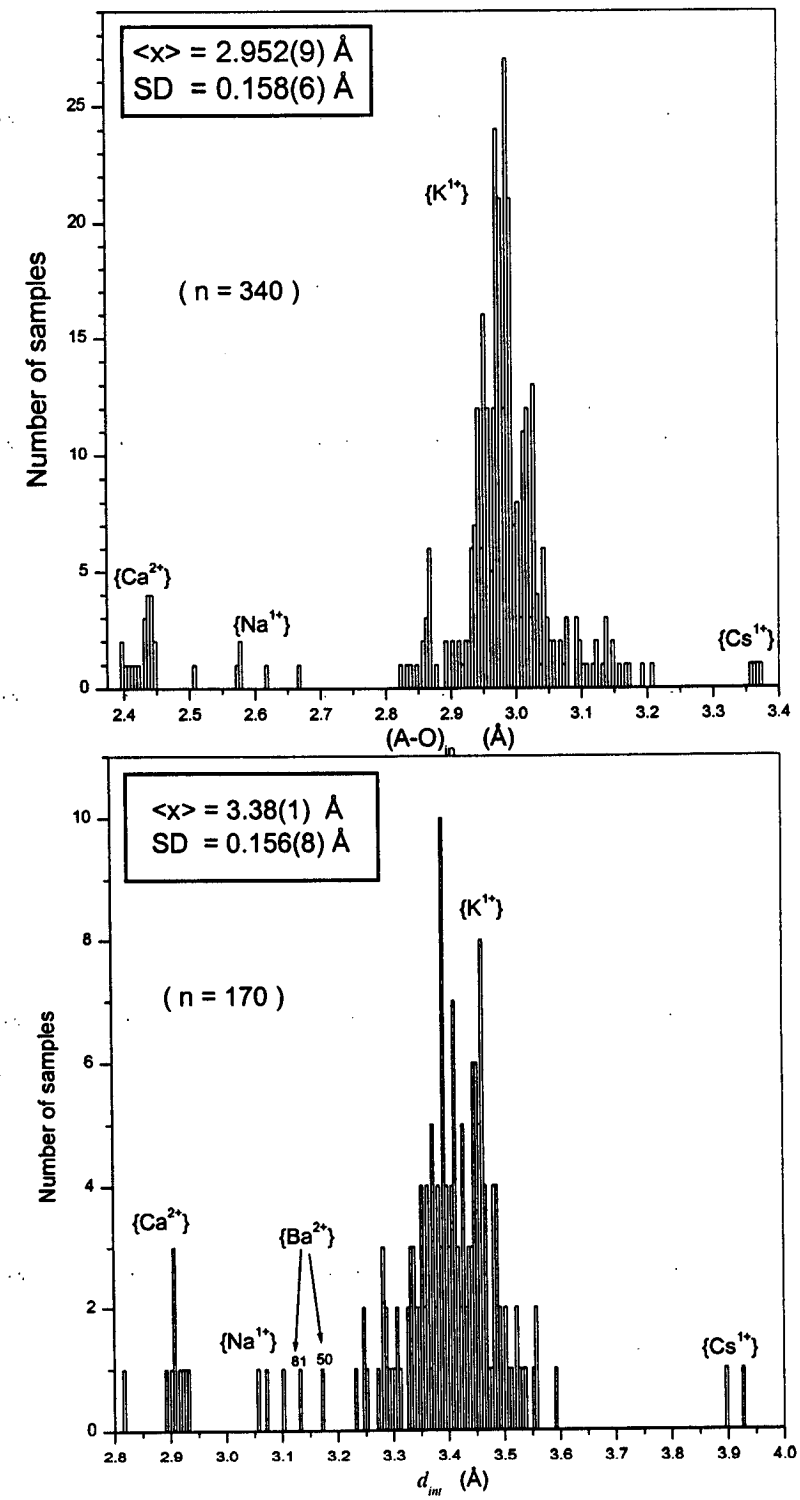

Figure 6.52. Histograms showing the distributions of inner *A-O* bond lengths (top) and interlayer distances d_{int} (bottom) observed in 1*M* structures. The two different inner interlayer bond lengths $(A\text{-}O1)_{in}$ and $(A\text{-}O2)_{in}$ are included in a single distribution.

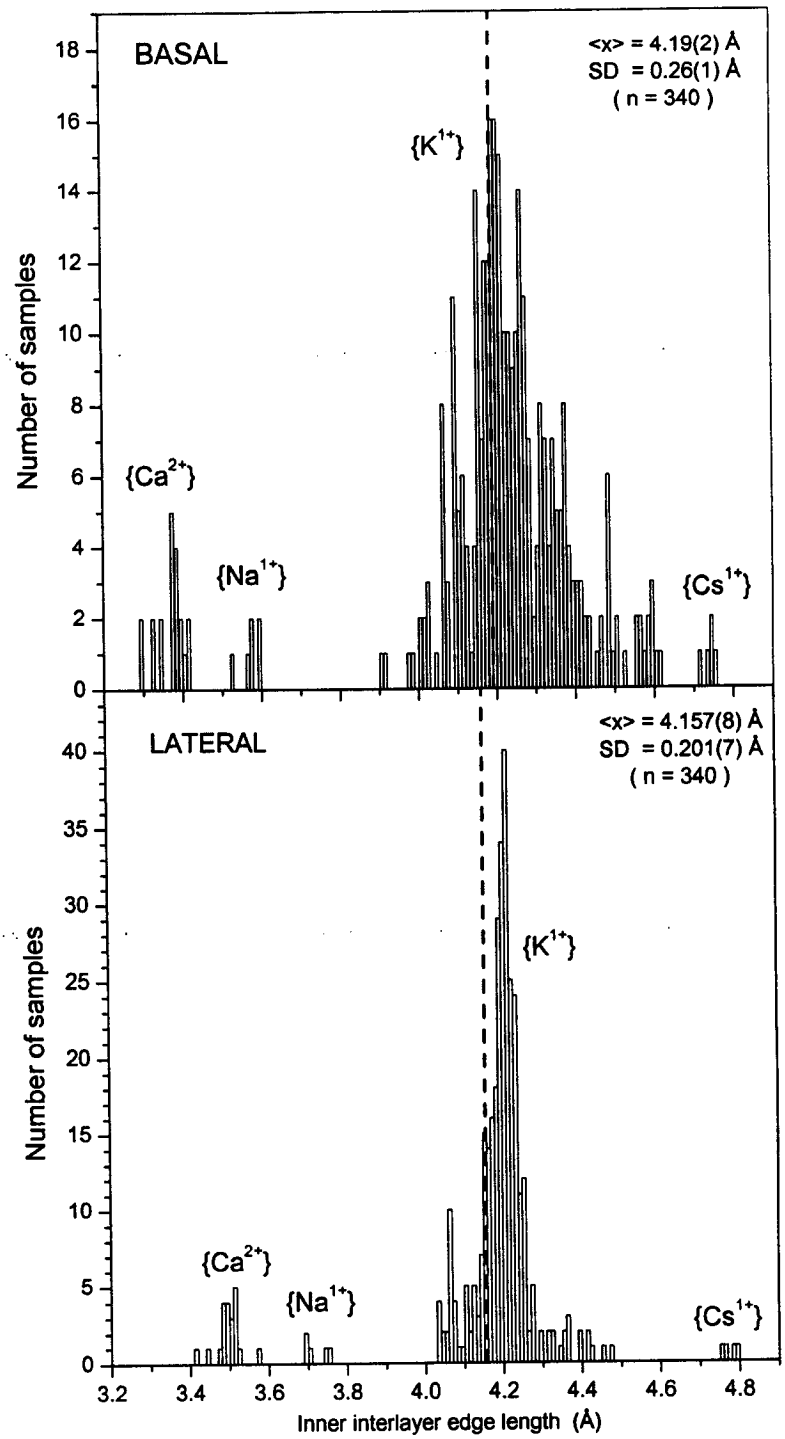

Figure 6.53. Histograms showing the distributions of basal (top) and lateral (bottom) inner interlayer edge lengths observed in 1*M* structures. The two different edge length values of a given type are included in a single distribution for each type. The dashed-lines indicate the average edge length values <x> of each distribution.

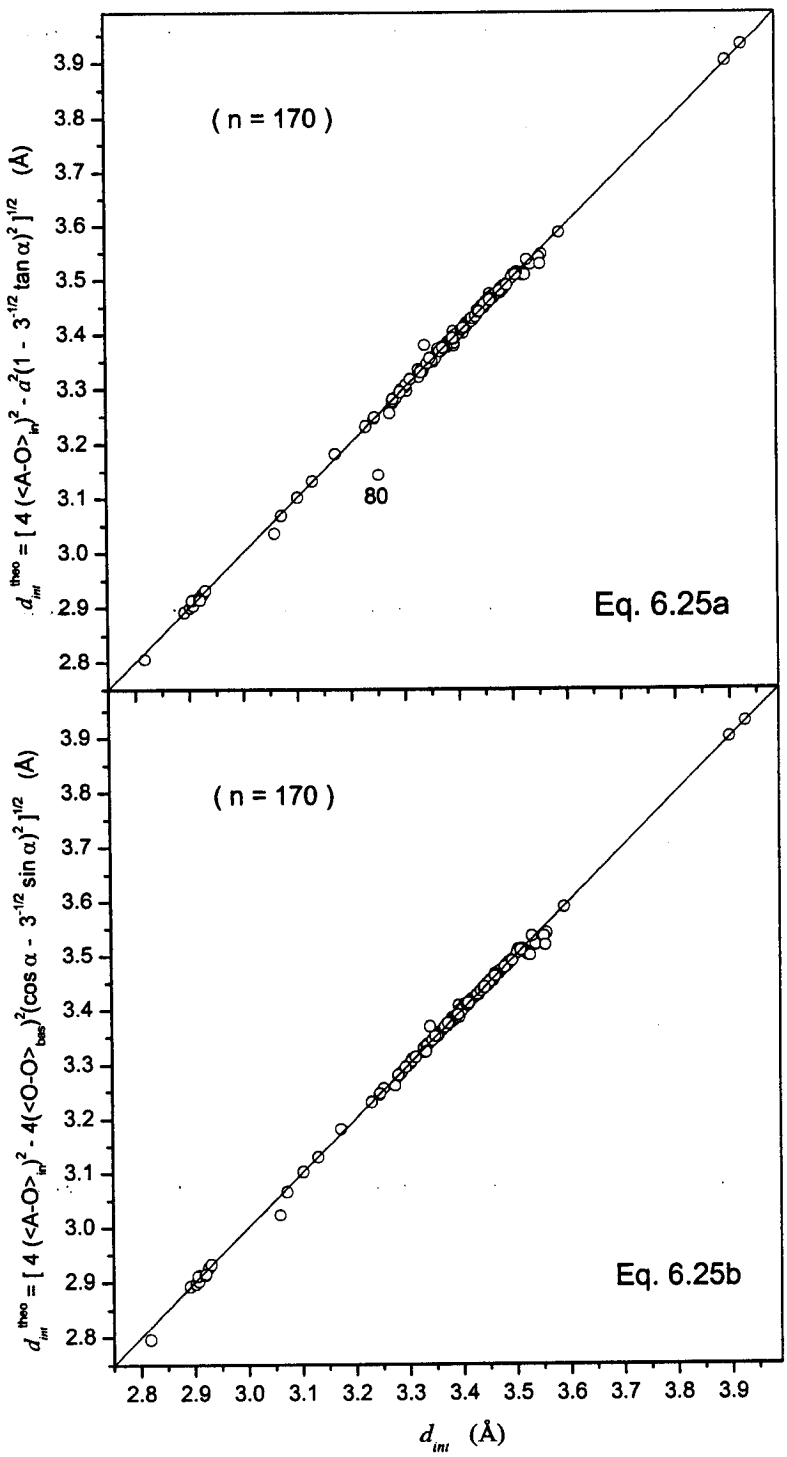

Figure 6.54. Comparison of observed interlayer distances d_{int} (x-axis) to simple geometrical predictions made from Eq. 6.25 (Subsection 6.2.6). The solid lines indicate a 1:1 correspondence between the x and y axes. See text for a detailed description of the figure.

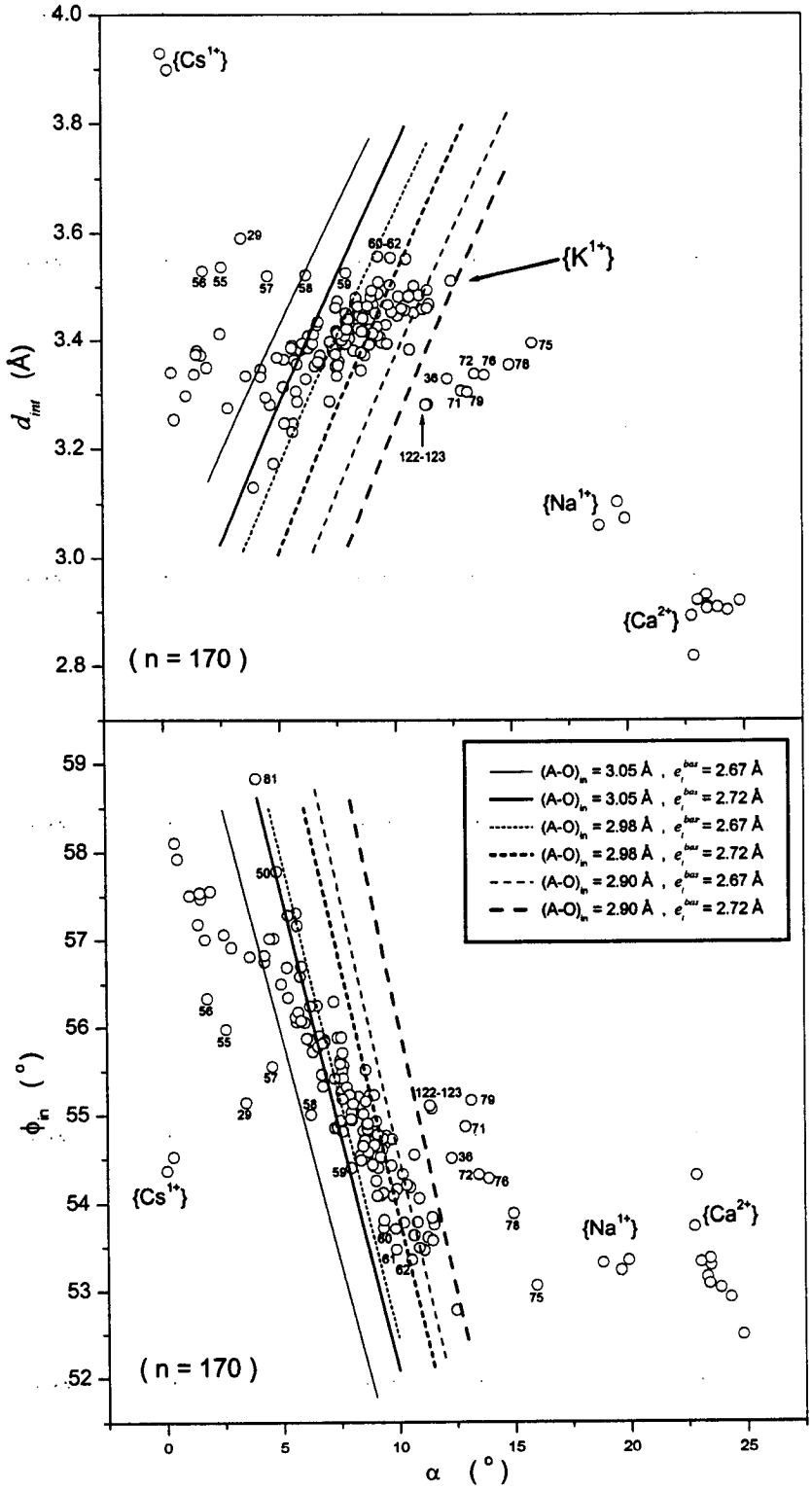

Figure 6.55. Plots of interlayer distance d_{int} and average inner interlayer octahedron flattening angle ϕ_{in} as functions of the average tetrahedral rotation angle α. The various lines (solid, dashed, or dotted) give predictions made from Eq. 6.25b. See text for a detailed description of the figure.

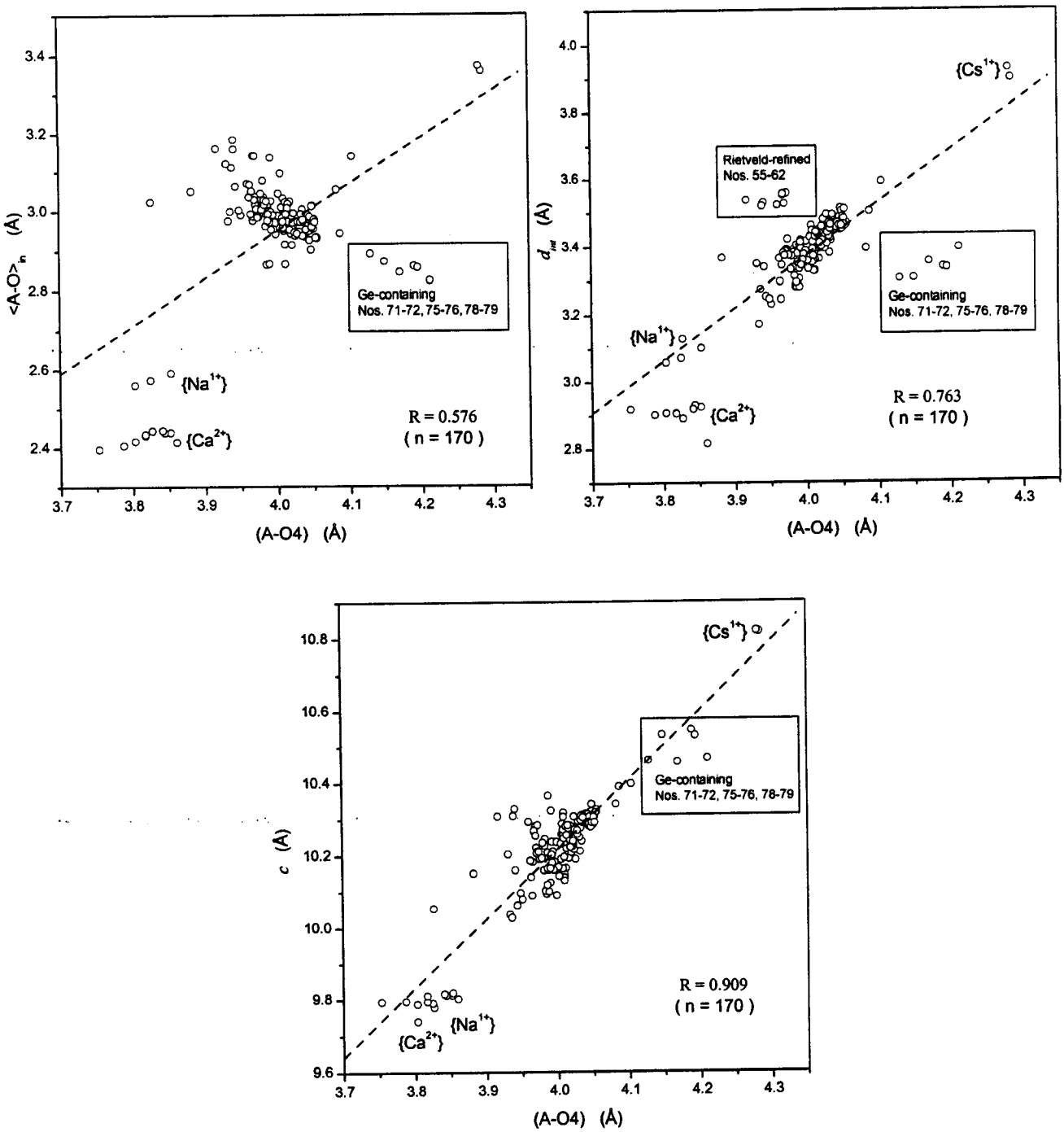

Figure 6.56. Plots of average inner interlayer bond length $\langle A\text{-}O\rangle_{in}$, interlayer distance d_{int}, and lattice parameter c as functions of the (A-O4) distance. The dashed lines that are shown are best straight-line fits through the data. See text for a detailed description of the figure.

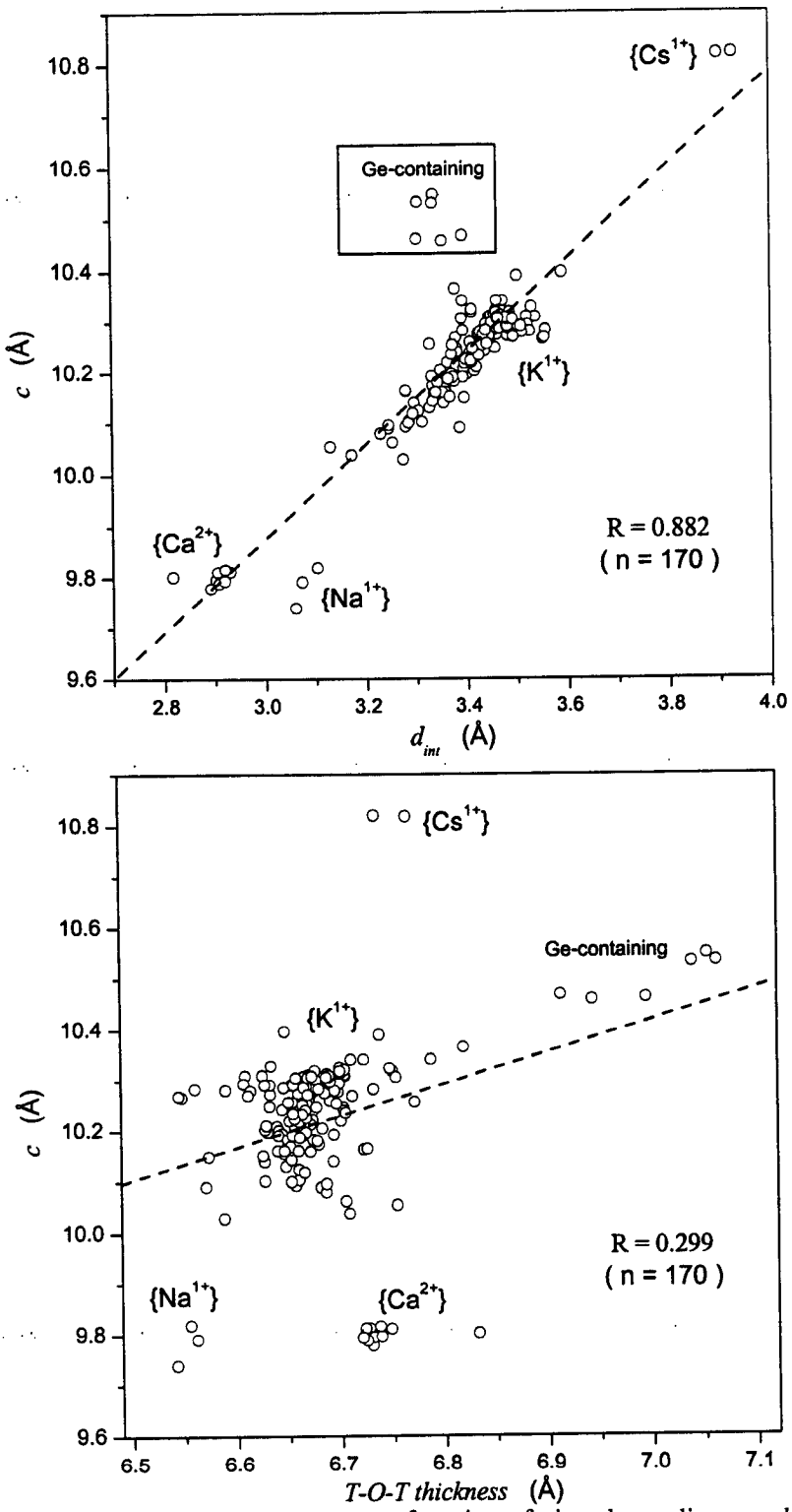

Figure 6.57. Plots of lattice parameter c as a function of: interlayer distance d_{int} (top) ; and overall *T-O-T thickness* (bottom). The dashed lines that are shown are best straight-line fits through the data. See text for a detailed description of the figure.

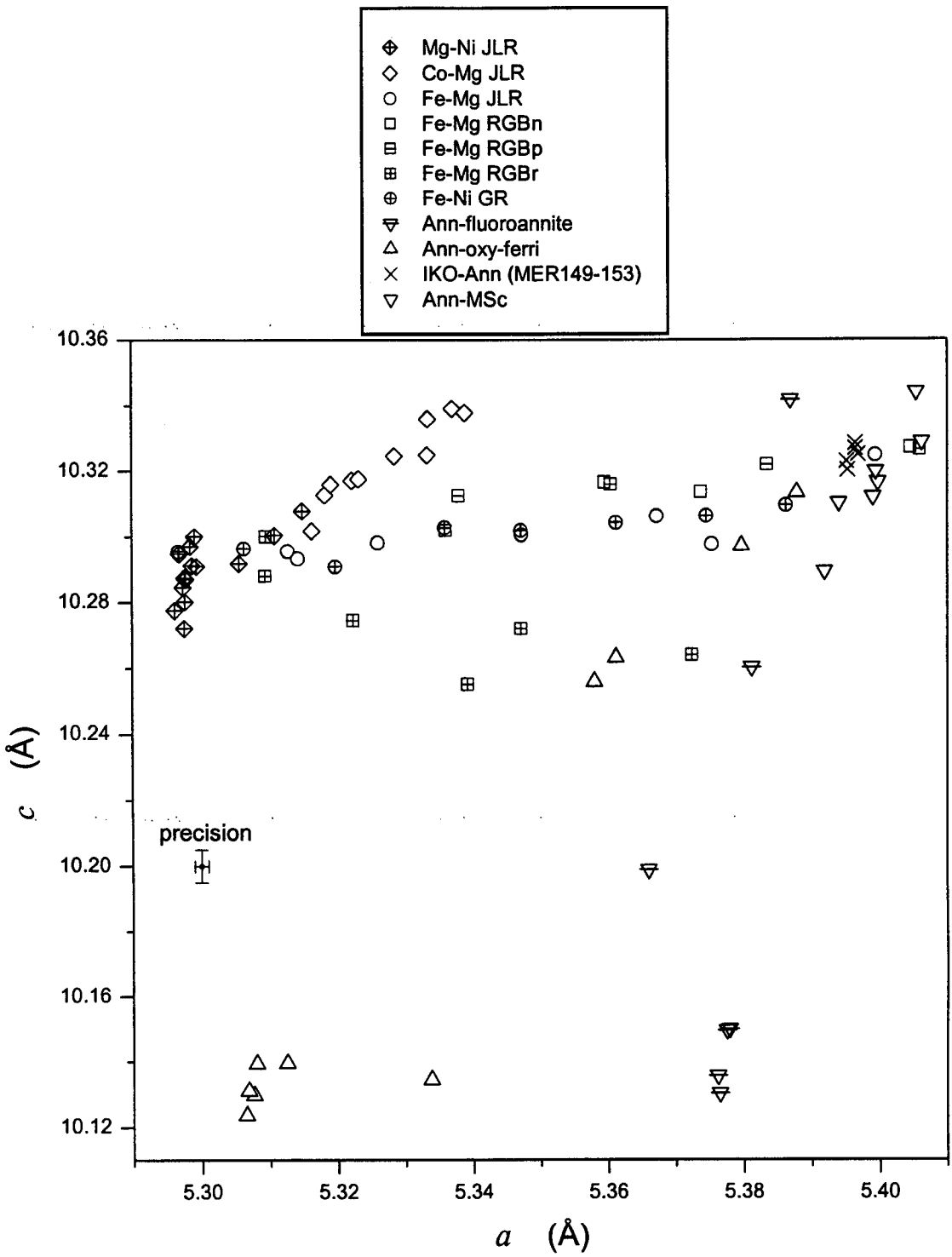

Figure 6.58. *c vs. a* for synthetic samples studied in this thesis. The labelled symbols indicated in the legend refer to the sample solid solutions series described in Table 3.1. The Ann-MSc refers to the synthetic annite samples studied in [Mercier 1996].

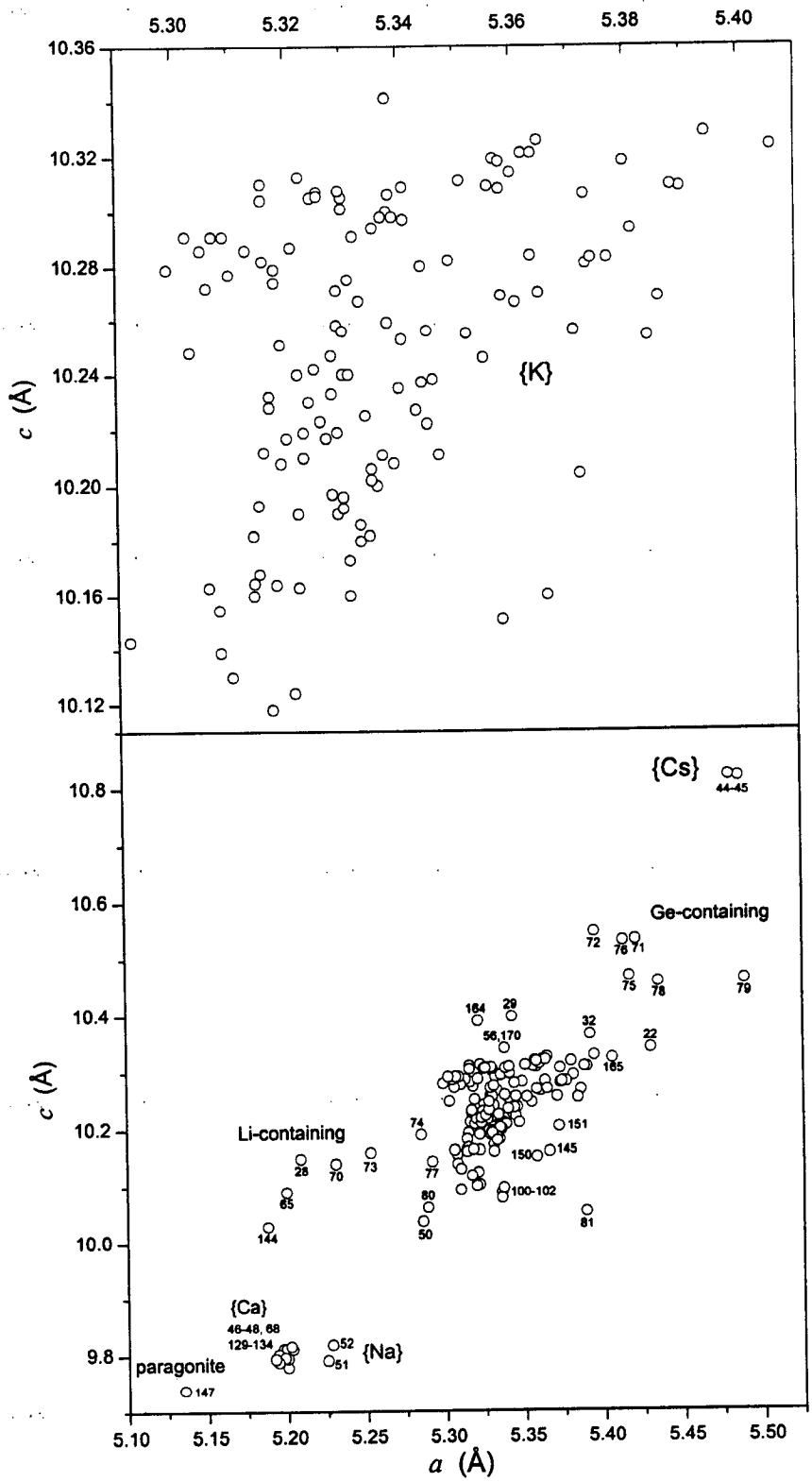

Figure 6.59. *c vs. a* for single-crystal structure refinements of 1*M* structures tabulated in Appendix P. The top graph is a blow-up of a region having the same scale as the plot of *c vs. a* for synthetic samples shown in the previous page.

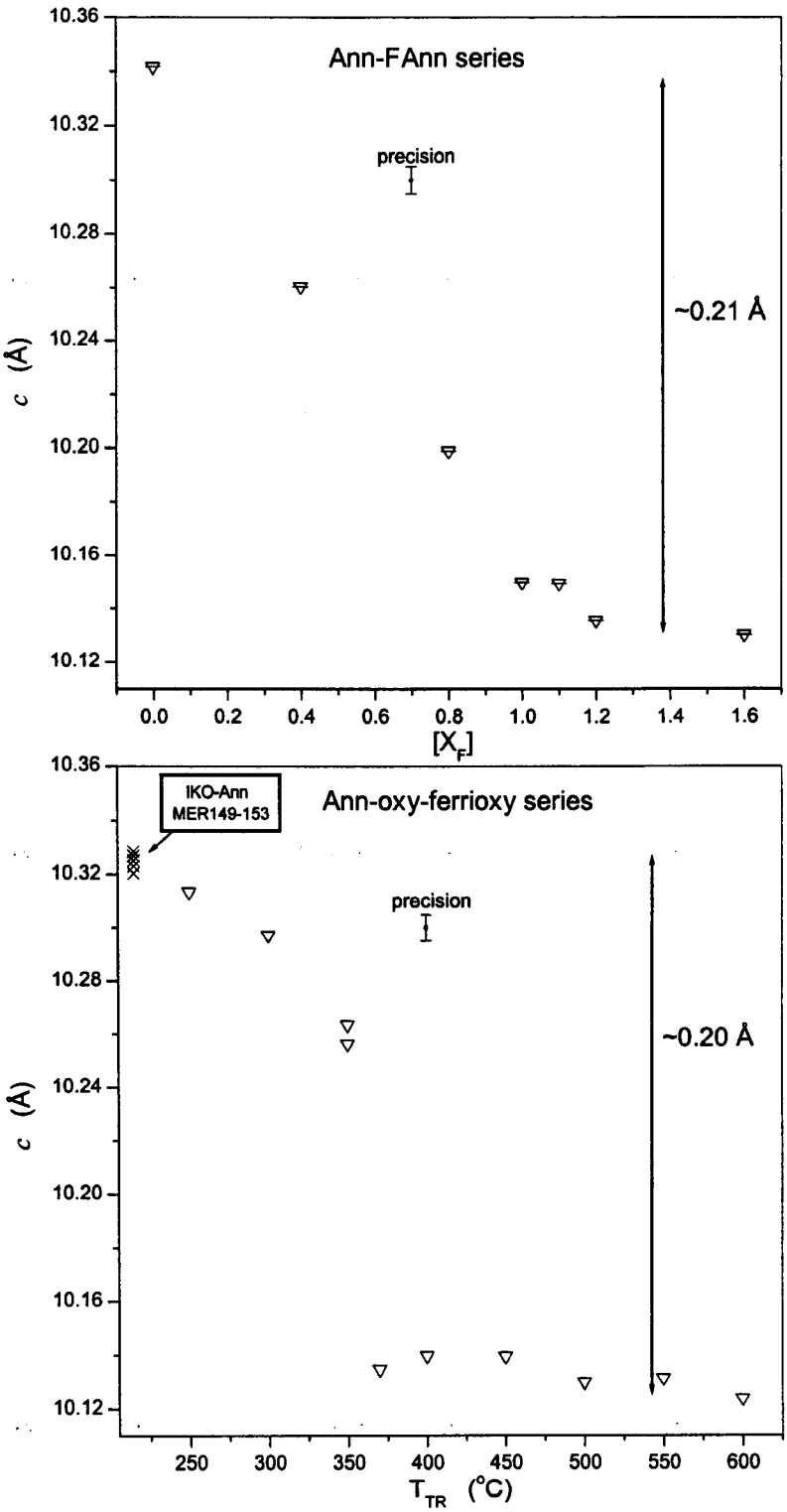

Figure 6.60. Evolutions of *c* for the annite-fluoroannite (top) and the annite-oxyannite-ferrioxyannite (bottom) series as functions of the nominal F content [X_F] and the heat-treatment temperature T_{TR}, respectively. Consult Section 3.2 for details of sample synthesis and heat-treatment conditions (Table 3.1).

6.3.5 Geometric meso-octahedral nature of in-plane intra-layer displacements

In Subsection 6.3.2, it was shown that the normalized squared octahedral size difference $[\langle M1\text{-}O\rangle^2 - \langle M2\text{-}O\rangle^2]/a^2$ observed in 1*M* structures is a single variable function of the counter-rotation angle of the *M*2 octahedron (Figure 6.32), in accordance with a geometric meso-octahedral sheet model (Subsection 6.2.3). In this subsection, it shall now be established that the in-plane intra-layer displacements between atoms of a given type located above and below the octahedral-cation plane are related to the geometric meso-octahedral character of the octahedral sheets.

Consider the in-plane projection of a geometric meso-octahedral sheet pictured in Figure 6.61, which displays the lateral shift vectors $\vec{\Delta}$ occurring between the positions that *O*3 and *O*4 atoms take when $d_{M1} > d_{M2}$ and the positions that these atoms would adopt in a geometric homo-octahedral sheet having the same *a* and *b* lattice parameters. As a result of the lateral shifts introduced by the $\vec{\Delta}$ vectors, the projections in the *a*-*b* plane of the O3 and O4 atoms lying above and below the octahedral-cation plane are no longer superimposed one over the other, as in a geometric homo-octahedral sheet.

Let us now determine the magnitude of the lateral shift vectors $\vec{\Delta}$. Using a sine law, one can show that the small shaded triangle illustrated in Figure 6.61 gives rise to the following relation:

$$\frac{\left\|\vec{\Delta}\right\|}{\sin \delta_{M2}} = \frac{d_{M2} \sin \psi_{M2}}{\sin 60^\circ} \quad . \tag{6.46}$$

In the above expression, the symbols have the following meanings: i) $\left\|\vec{\Delta}\right\|$ is the norm of a single $\vec{\Delta}$ vector; ii) δ_{M2} is the counter-rotation angle of an *M*2 octahedron; iii) d_{M2} is the *M*-*O* bond length of an *M*2 octahedron; and iv) ψ_{M2} is the flattening angle of an *M*2 octahedron.

In a manner similar as above, another relationship involving $\left\|\vec{\Delta}\right\|$, δ_{M2}, d_{M2}, and ψ_{M2} can be obtained from the sides of the triangle delimited by thick solid lines drawn in Figure 6.61:

$$\frac{a/3 + \left\|\vec{\Delta}\right\|}{\sin\left(30^\circ + \delta_{M2}\right)} = \frac{d_{M2} \sin \psi_{M2}}{\sin 30^\circ} \quad . \tag{6.47}$$

This triangle (i.e., the one delimited by thick solid lines) was also considered in the derivations of Eqs. 6.34 and 6.35 (Subsection 6.3.2).

Next, by equating Eqs. 6.46 and 6.47, one obtains an expression for the magnitude of the lateral shift vectors $\vec{\Delta}$ in terms of the lattice parameter a and the counter-rotation angle δ_{M2}:

$$\frac{\|\vec{\Delta}\|}{a} = \frac{1}{3}\left[\frac{\sin\delta_{M2}}{\sqrt{3}\sin\left(30^\circ+\delta_{M2}\right)-\sin\delta_{M2}}\right] . \tag{6.48}$$

Recalling Eq. 6.35, one has

$$\frac{d_{M1}\sin\psi_{M1}-d_{M2}\sin\psi_{M2}}{a} = \frac{1}{\sqrt{3}}\left[\frac{\sin\left(30^\circ+\delta_{M2}\right)-\sin 30^\circ}{\sin\left(120^\circ+\delta_{M2}\right)}\right] . \tag{6.35}$$

We hence have a set of parametric equations that depend on the counter-rotation angle δ_{M2}. As a function of δ_{M2}, Eq. 6.48 provides a means to obtain theoretical values of in-plane intra-layer displacements between atoms of a given type located above and below the octahedral-cation plane, whereas Eq. 6.35 gives the in-plane size difference of $M1$ and $M2$ octahedrons.

In order to test the above ideas, however, one must first define appropriate in-plane intra-layer displacements for each atom-type of the 1M structure. This was accomplished by taking in-plane distances along a[1] between the projections of various geometric entities on the a axis: i) the distance ID_{xy}^{O3} between the (001) projections of the geometric centres of upper and lower hexagons formed by O3 atoms (Figure 6.61); ii) the distance ID_{xy}^{O4} between the (001) projections of an upper and a lower O4 atoms (Figure 6.61); iii) the distance ID_{xy}^{T} between the (001) projections of the geometric centres of upper and lower hexagons formed by T atoms (Figure 6.62a); iv) the distance $ID_{xy}^{O1\text{-}O2}$ between the (001) projections of the geometric centres of an upper and a lower hexagons formed by basal O1 and O2 oxygen atoms (Figure 6.62b); and v) the distance ID_{xy}^{A} between the projections of two interlayer A cations, one located above the octahedral-cation plane and the other below (Figure 6.62c).

In terms of the fractional coordinates and lattice parameters tabulated for 1M structures in

[1]In the 1M structure, in-plane intra-layer stagger between atoms of a given type located above and below the octahedral-cation plane only occur along the a-axis direction.

Appendix P, one can show that the in-plane intra-layer displacements ID_{xy}^{O3}, ID_{xy}^{O4}, ID_{xy}^{T}, $ID_{xy}^{O1\text{-}O2}$, and ID_{xy}^{A} specified above (Figures 6.61 and 6.62) can be expressed as follows:

(6.49a) $$ID_{xy}^{O3}/a = 2\left[O3x - O3z\,(c/a)\cos\beta^*\right]$$

(6.49b) $$ID_{xy}^{O4}/a = 2\left[O4x + (1/2 - O4z)(c/a)\cos\beta^*\right]$$

(6.49c) $$ID_{xy}^{T}/a = 2\left[Tx - Tz(c/a)\cos\beta^*\right]$$

(6.49d) $$ID_{xy}^{O1\text{-}O2}/a = 1/6\left[2 - 4\cdot O1x - 8\cdot O2x + 2(c/a)\cos\beta^*(2\cdot O1z + 4\cdot O2z - 3)\right]$$

(6.49e) $$ID_{xy}^{A}/a = (c/a)\cos\beta^*$$

The values given by Eqs. 6.49a-6.49e are referred to as 'normalized' in-plane intra-layer displacements.

Figures 6.63-6.67 show the evolutions of normalized in-plane intra-layer displacements ID_{xy}^{O3}/a, ID_{xy}^{O4}/a, ID_{xy}^{T}/a, $ID_{xy}^{O1\text{-}O2}/a$, and ID_{xy}^{A}/a as functions of the in-plane normalized octahedral size difference $[\langle M1\text{-}O\rangle \sin\psi_{M1} - \langle M2\text{-}O\rangle \sin\psi_{M2}]/a$, respectively. These figures allow direct comparisons with the predictions made from Eqs. 6.35 and 6.48.

The solid-line predictions that are shown in Figures 6.63-6.67 stem from the following considerations. In a geometric meso-octahedral sheet, it can be seen in Figure 6.61 that when $d_{M1} > d_{M2}$, then $ID_{xy}^{O3} > a/3$ and $ID_{xy}^{O4} < a/3$; or vice-versa when $d_{M1} < d_{M2}$. By comparison, $ID_{xy}^{O3} = ID_{xy}^{O4} = a/3$ in a geometric homo-octahedral sheet. Given that tetrahedral *T* cations, basal O1 and O2 oxygen atoms, and interlayer *A* cations are all linked to apical O3 oxygen atoms via the tetrahedral sheets in a TOT network, therefore, it is expected that in-plane intra-layer displacements involving *T*, O1, O2, and *A* atoms will behave similarly as those of O3 atoms.

Indeed, this is shown in Figures 6.63-6.67. Except for the few usual outliers, one observes that the data points display a fair agreement with the solid-line predictions made on the basis of Eqs. 6.35 and 6.48, especially for O3 and O4 atoms. This, therefore, represents strong evidence that in-plane intra-layer displacements between atoms of a given type located above and below the octahedral-cation plane are predominantly a direct consequence of the geometric meso-octahedral character of the octahedral sheets.

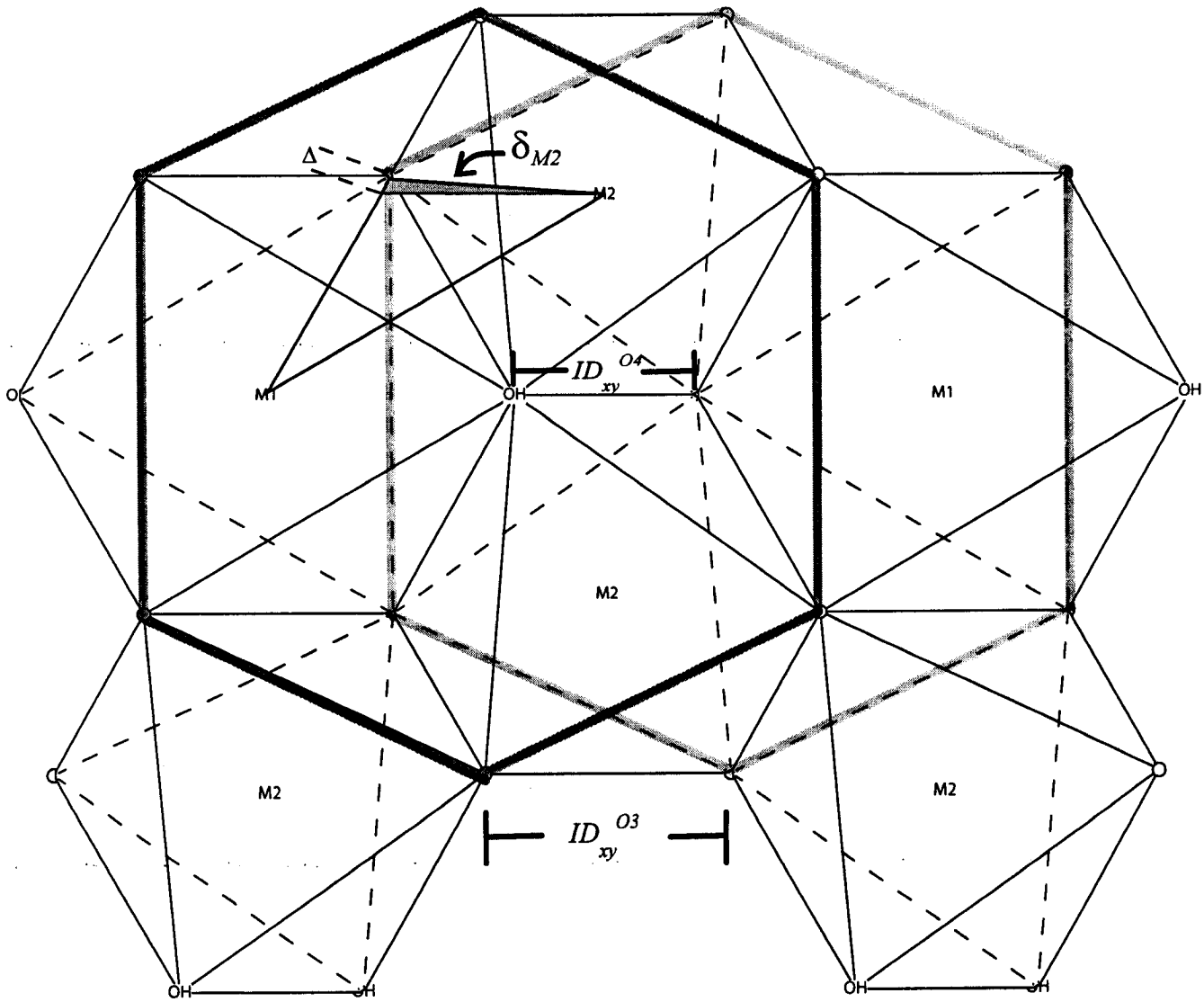

Figure 6.61. Illustration of a geometric meso-octahedral sheet showing the lateral shift vectors $\vec{\Delta}$ that occur when $d_{M1} > d_{M2}$. The in-plane intra-layer displacements ID_{xy}^{O3} and ID_{xy}^{O4} are also shown. See text for a detailed explanation of the use of the two triangles that are drawn.

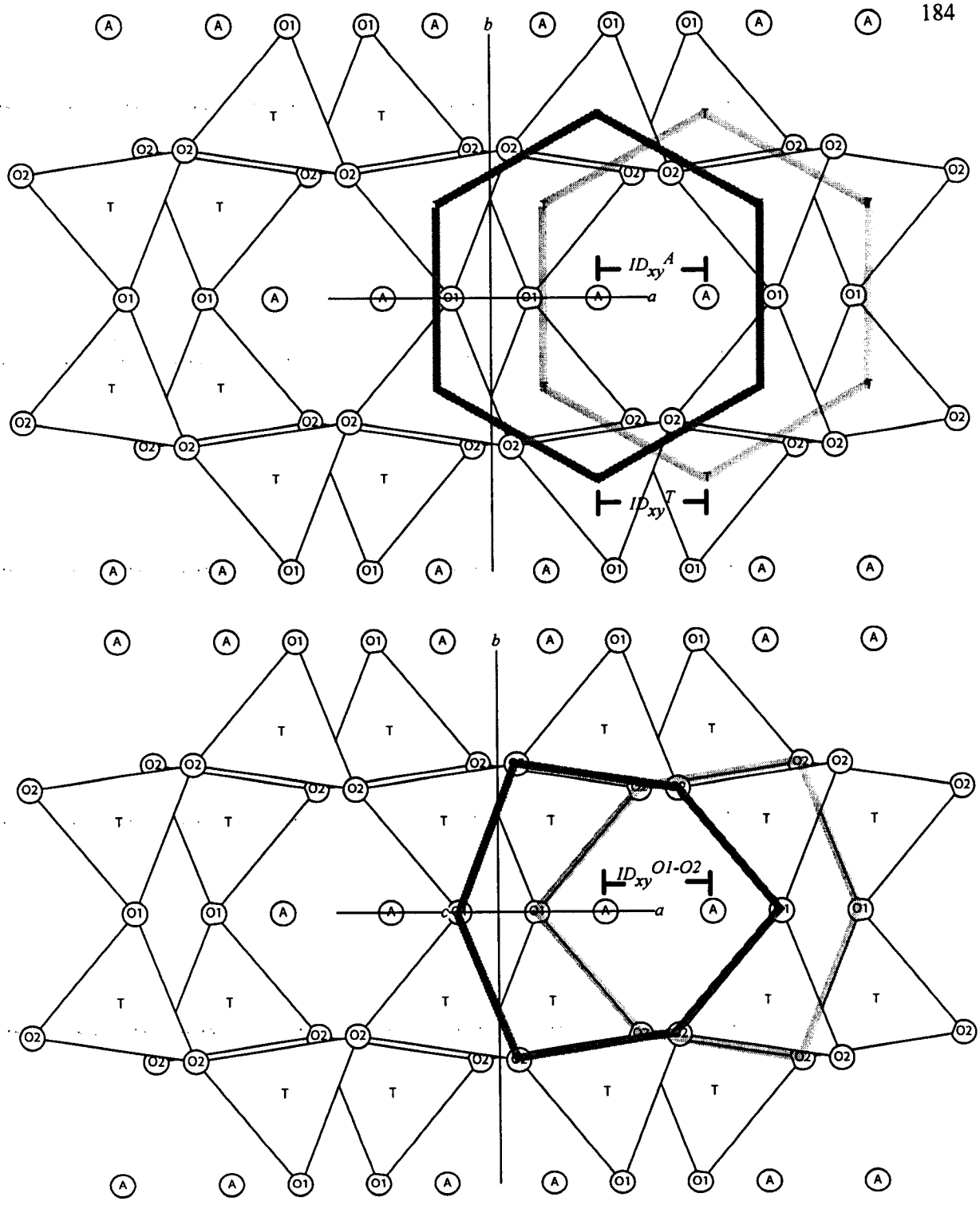

Figure 6.62. Diagrams illustrating in-plane intra-layer displacements that were considered: ID_{xy}^{T}, $ID_{xy}^{O1\text{-}O2}$, and ID_{xy}^{A}.

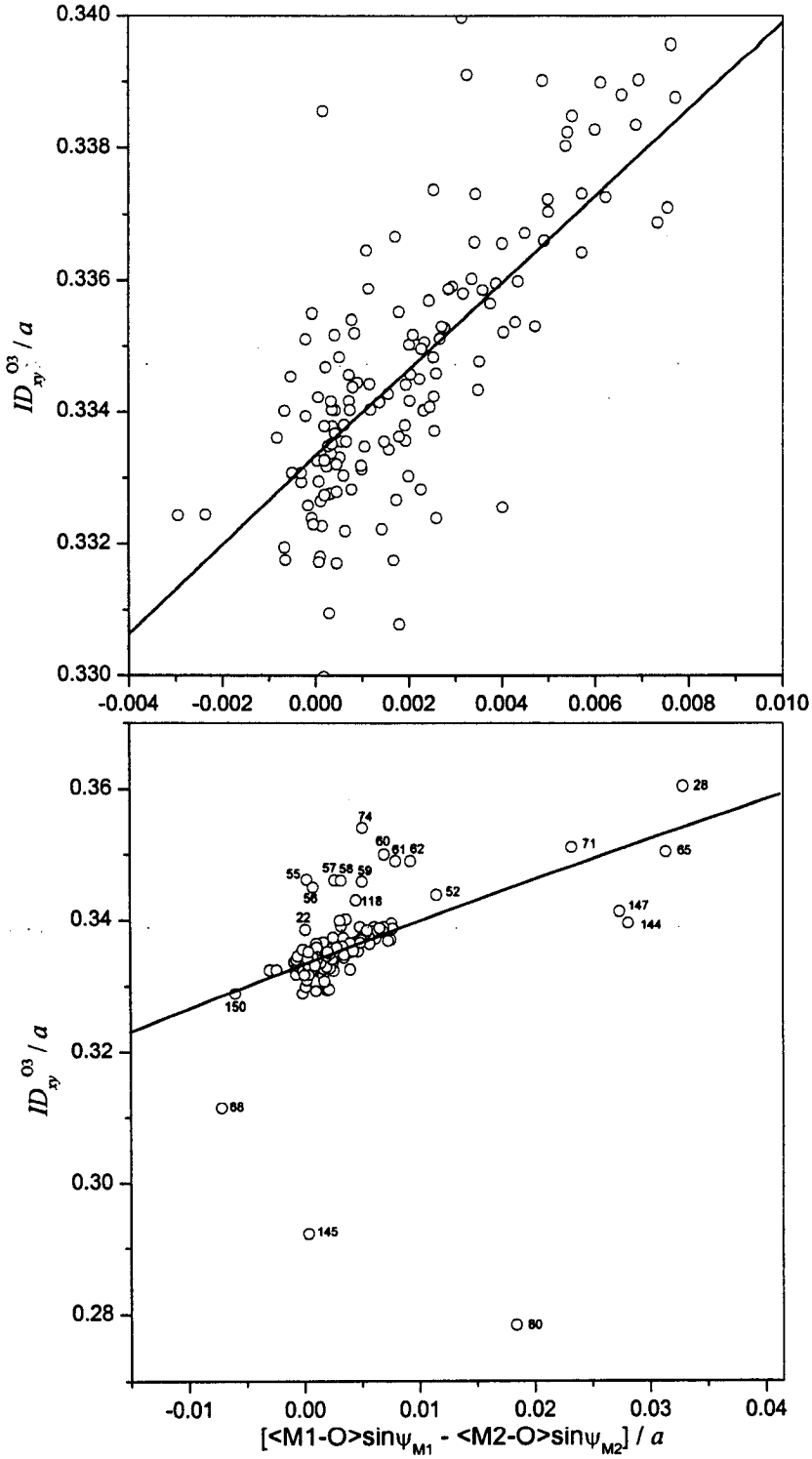

Figure 6.63. Evolution of normalized in-plane intra-layer displacement ID_{xy}^{O3} / a as a function of the normalized size difference $[<M1\text{-}O>\sin\psi_{M1} - <M2\text{-}O>\sin\psi_{M2}]/a$. The solid lines that are shown correspond to predictions made on the basis of Eqs. 6.35 and 6.48.

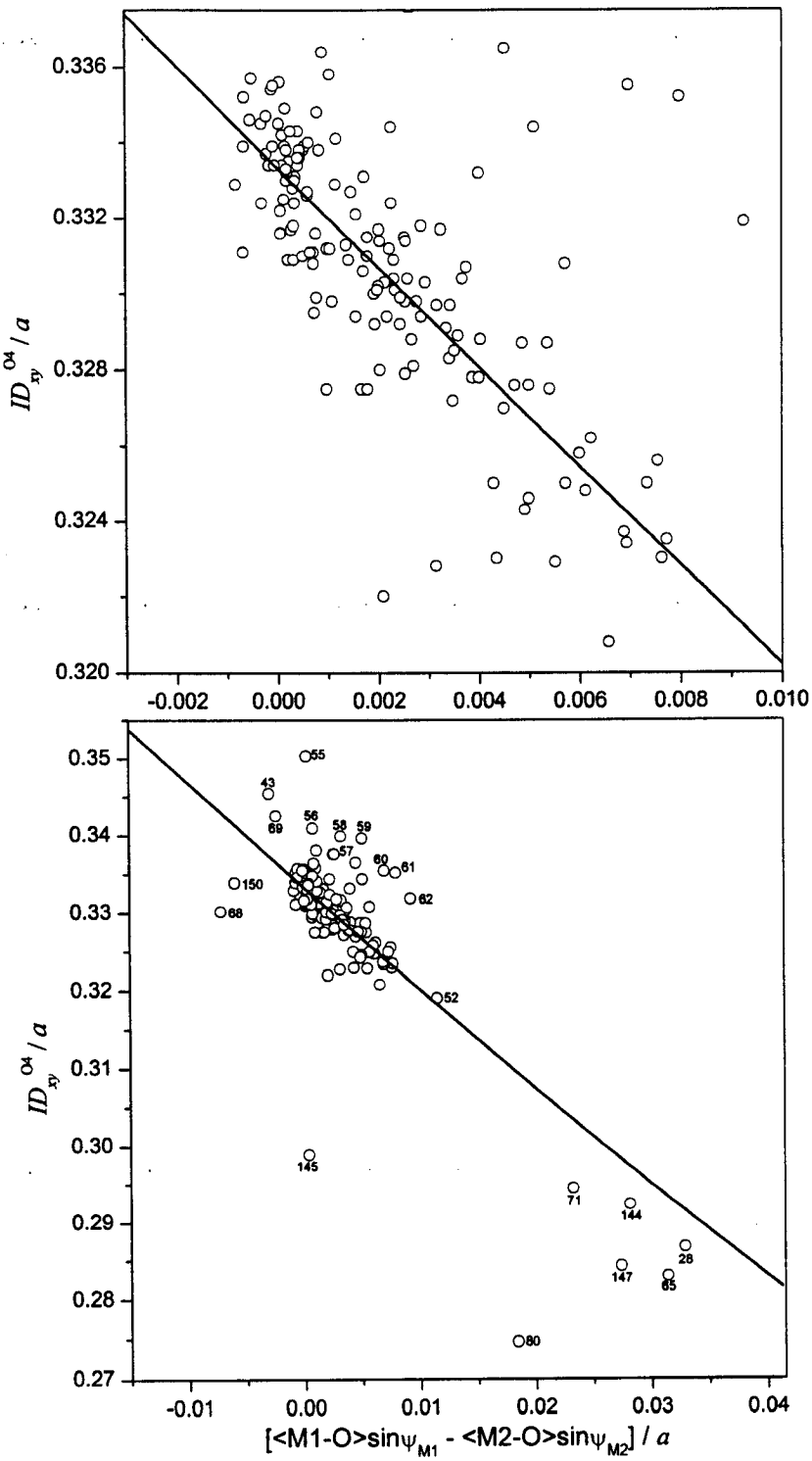

Figure 6.64. Evolution of normalized in-plane intra-layer displacement ID_{xy}^{O4} / a as a function of the normalized size difference [<M1-O>sinψ$_{M1}$ - <M2-O>sinψ$_{M2}$]/a . The solid lines that are shown correspond to predictions made on the basis of Eqs. 6.35 and 6.48.

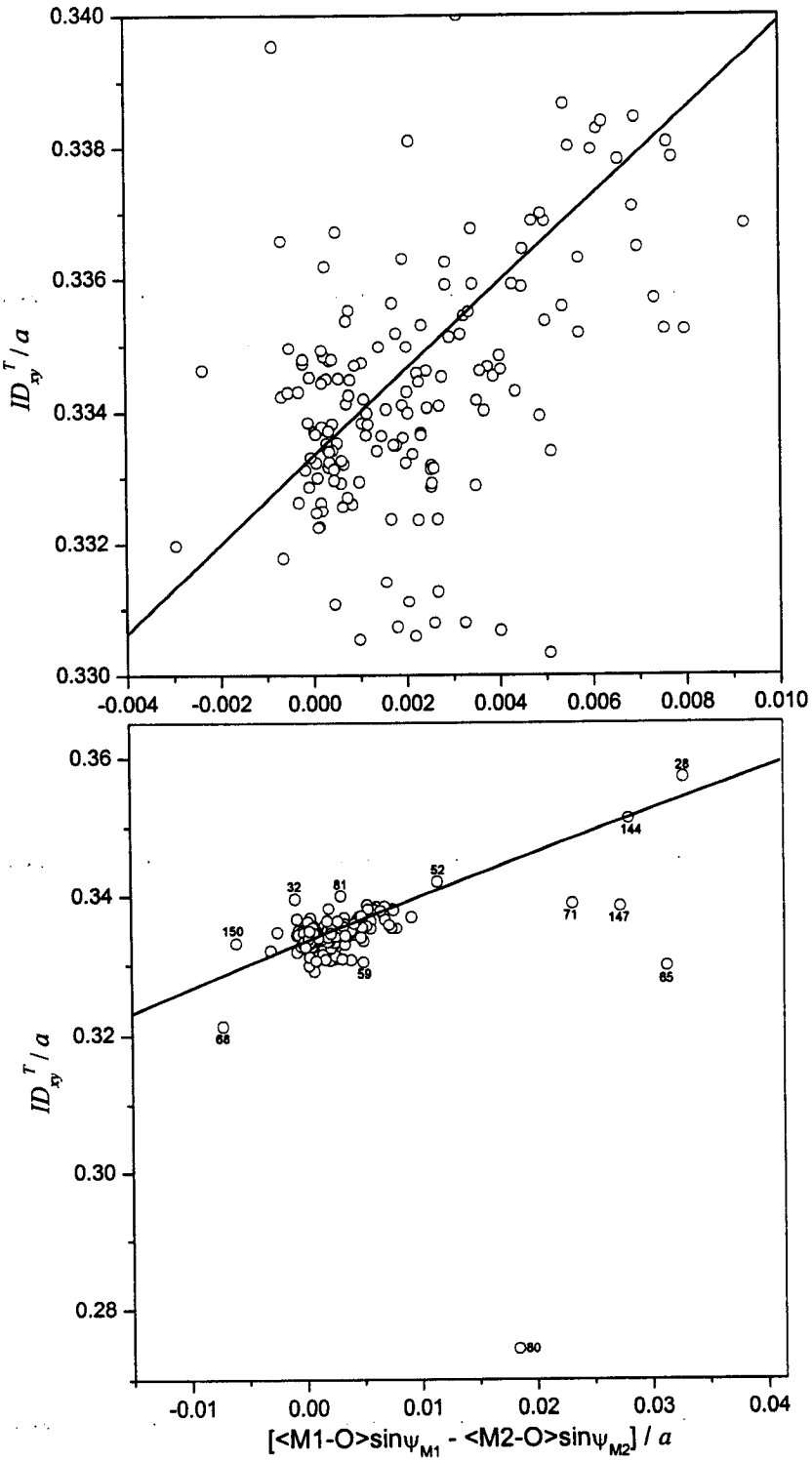

Figure 6.65. Evolution of normalized in-plane intra-layer displacement ID_{xy}^{T} / a as a function of the normalized size difference $[\langle M1\text{-}O\rangle \sin\psi_{M1} - \langle M2\text{-}O\rangle \sin\psi_{M2}]/a$. The solid lines that are shown correspond to predictions made on the basis of Eqs. 6.35 and 6.48.

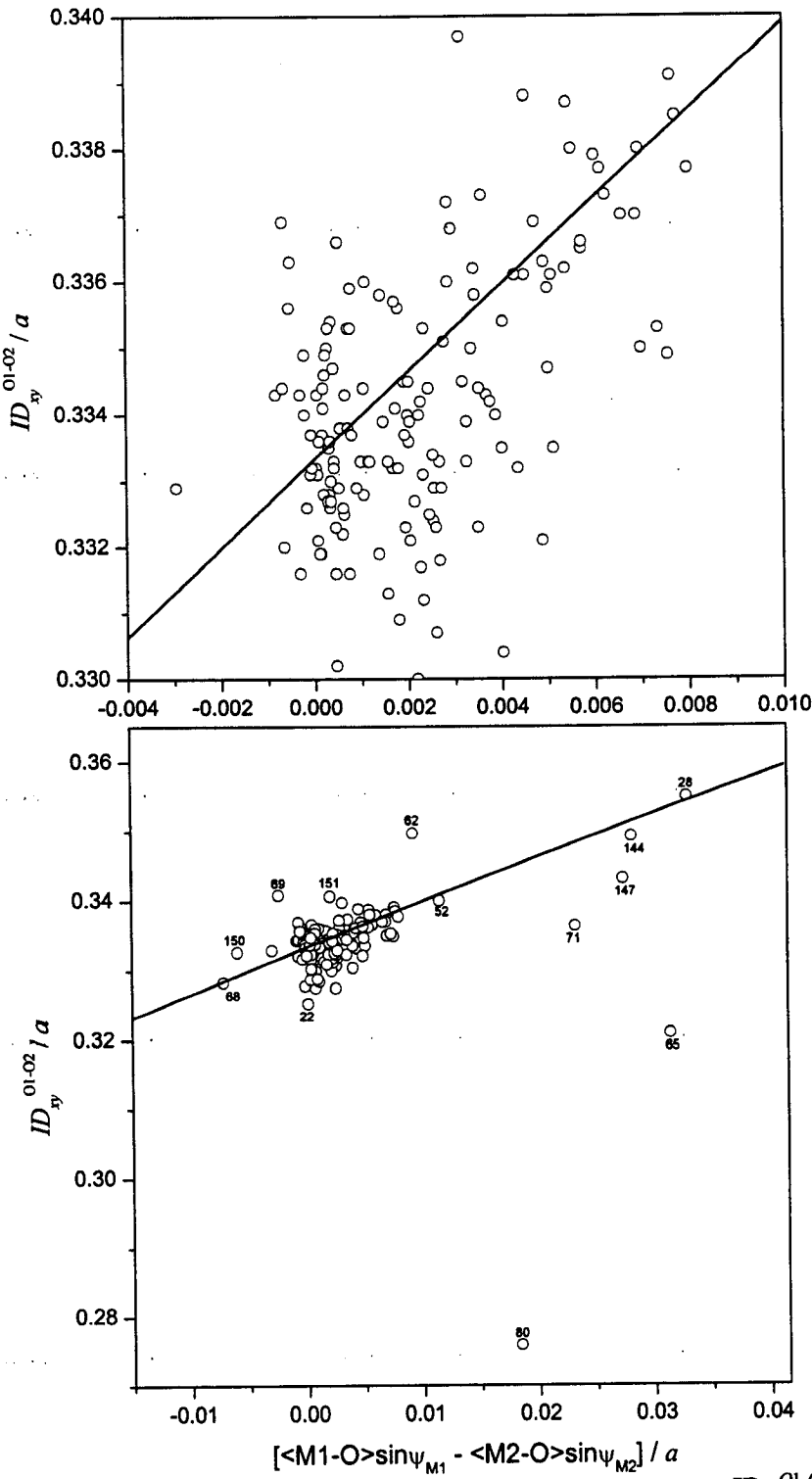

Figure 6.66. Evolution of normalized in-plane intra-layer displacement $ID_{xy}^{O1\text{-}O2} / a$ as a function of the normalized size difference $[<M1\text{-}O>\sin\psi_{M1} - <M2\text{-}O>\sin\psi_{M2}]/a$. The solid lines that are shown correspond to predictions made on the basis of Eqs. 6.35 and 6.48.

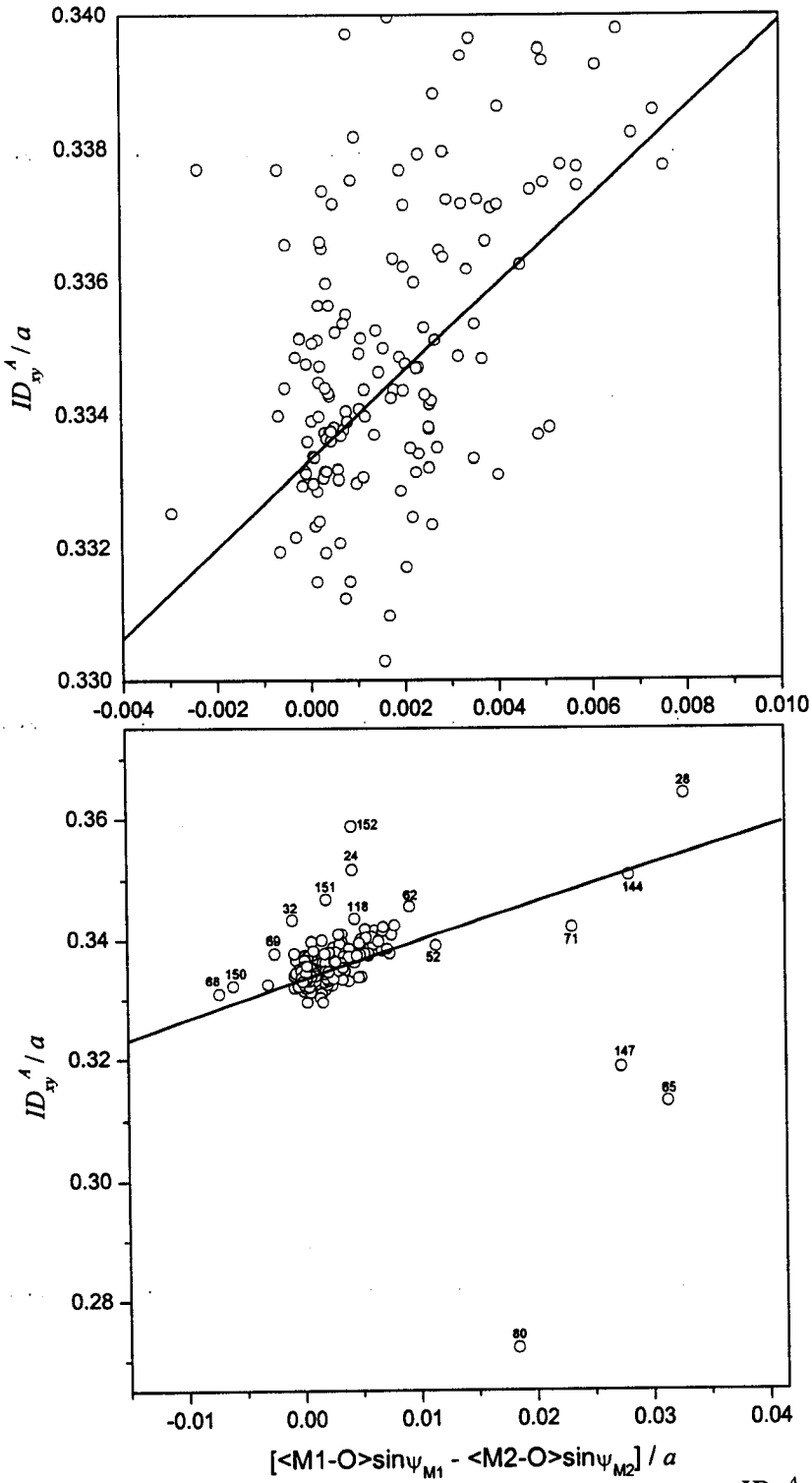

Figure 6.67. Evolution of normalized in-plane intra-layer displacement ID_{xy}^{A} / a as a function of the normalized size difference $[<M1\text{-}O>\sin\psi_{M1} - <M2\text{-}O>\sin\psi_{M2}]/a$. The solid lines that are shown correspond to predictions made on the basis of Eqs. 6.35 and 6.48.

6.3.6 Fundamental difference between synthetic and natural samples

The normalized intra-layer displacement $(c/a)\cos\beta^*$ (where $\beta^* = 180° - \beta$) is referred to as the 'intralayer shift' or 'intralayer stagger' [Brigatti & Guggenheim 2002; Ferraris & Vivaldi 2002]. In a geometric homo-octahedral 2:1 layer silicate, one has $(c/a)\cos\beta^* = 1/3$ (Subsection 6.2.6).

Figure 6.69 displays the distribution of $(c/a)\cos\beta^*$ for the 170 single-crystal structure refinements of 1*M* samples compiled in Appendix P. Clearly, one observes that the distribution is asymmetric and not centred on the dashed line drawn at $(c/a)\cos\beta^* = 1/3$. In light of the previous subsection, therefore, this is attributed to the presence of geometric meso-octahedral sheets in these samples.

It is important to verify the extent to which synthetic and natural samples differ. Figure 6.70 compares the distributions of $(c/a)\cos\beta^*$ for: i) the 128 single-crystal structure refinements of natural 1*M* samples; ii) the 42 single-crystal structure refinements of synthetic 1*M* samples; iii) the 170 single-crystal structure of 1*M* samples, natural and synthetic, on an expanded scale relative to Figure 6.69; and iv) the 75 synthetic samples investigated by powder X-ray diffraction in this thesis. As indicated by the standard deviation (SD) values of the distributions, the synthetic single-crystal distribution is approximately twice thinner than the natural single-crystal one, whereas the distribution of $(c/a)\cos\beta^*$ for the synthetic powder samples of this thesis is one order of magnitude thinner than the two single-crystal distributions.

An alternate way to visualize the above situation is via the plots of $c\cdot\cos\beta^*$ *versus* a presented in Figures 6.71 and 6.72. The solid lines that are shown in each graph of these figures correspond to $(c/a)\cos\beta^* = 1/3$, whereas the error bars reported for the synthetic samples of this thesis incorporate the precision errors of each lattice parameter using the common error propagation method (assuming uncorrelated errors). While in the case of single-crystal structure refinements no clear trend is noticeable, one finds that, within error, the synthetic samples of this thesis agree with the $(c/a)\cos\beta^* = 1/3$ relationship which is predicted for a geometric homo-octahedral 2:1 layer silicate.

From this subsection, therefore, the following conclusions are made: i) strong evidence for a fundamental difference between synthetic and natural samples is found, presumably due to some degree of chemical ordering that is present in natural samples (which causes a geometrical meso-octahedral structure to occur) and not in synthetic ones; and ii) a crystal structure model based on a geometric homo-octahedral network is valid for the synthetic powder samples of this thesis.

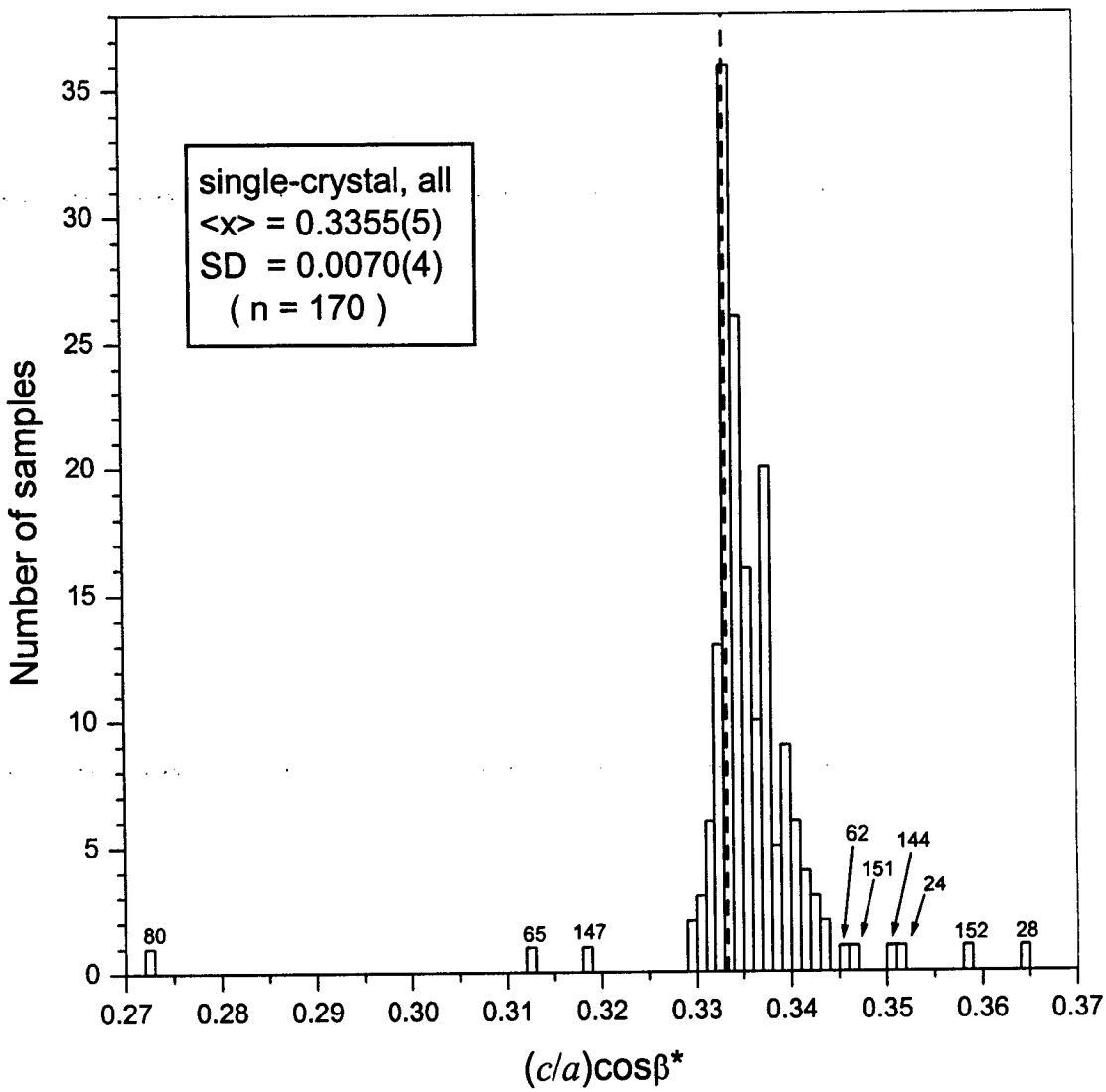

Figure 6.69. Histogram showing the distribution of $(c/a)\cos\beta^*$ for the 170 single-crystal structure refinements of 1*M* samples compiled in Appendix P. The dashed line that is shown corresponds to $(c/a)\cos\beta^* = 1/3$.

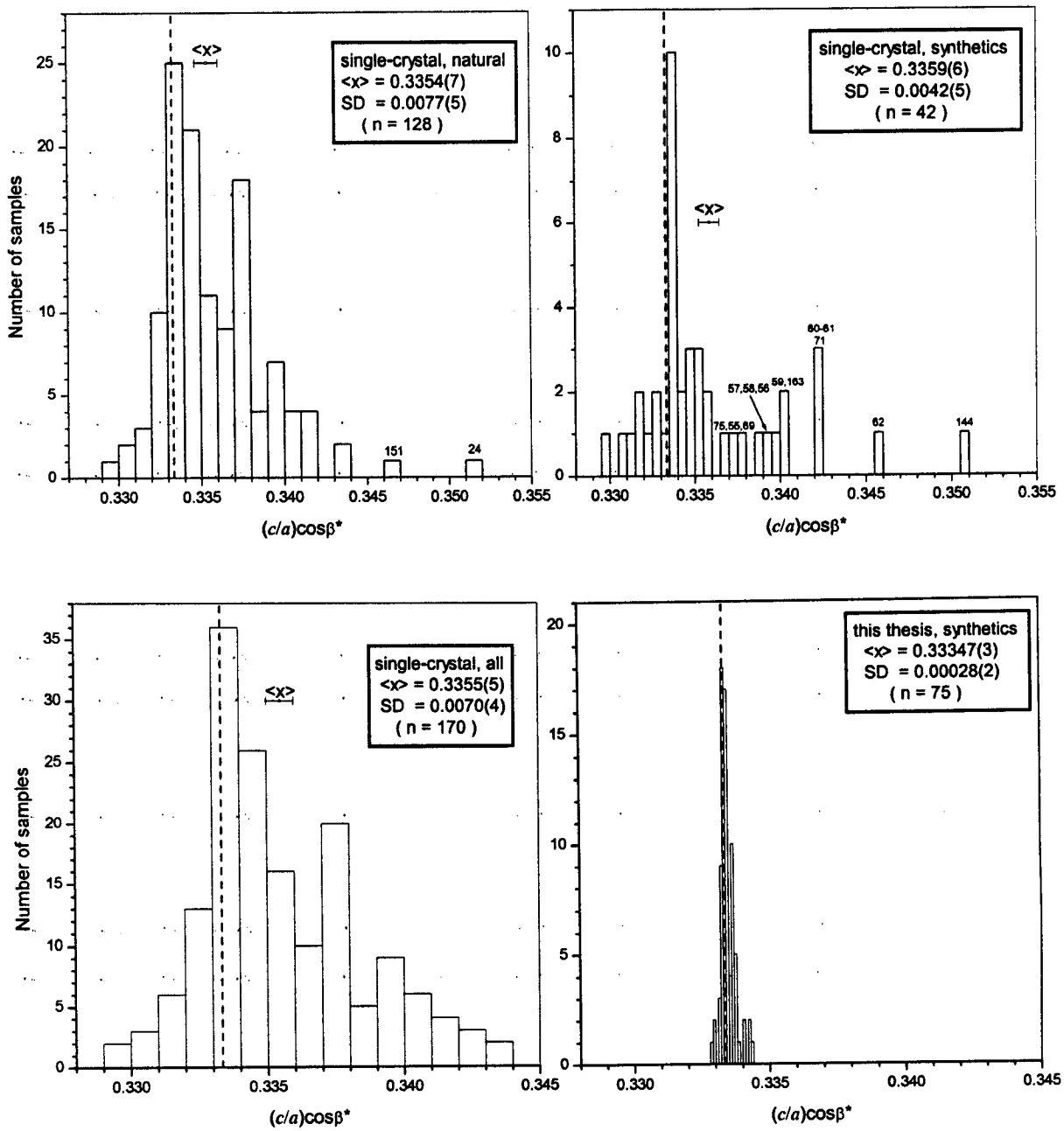

Figure 6.70. Comparison of the distributions of $(c/a)\cos\beta^*$ for: (a) the 128 single-crystal structure refinements of natural 1*M* samples; (b) the 42 single-crystal structure refinements of synthetic 1*M* samples; (c) the 170 single-crystal structures of 1*M* samples, natural and synthetic, on an expanded scale; and (d) the 75 synthetic samples investigated by powder X-ray diffraction in this thesis. The vertical dashed lines correspond to $(c/a)\cos\beta^* = 1/3$.

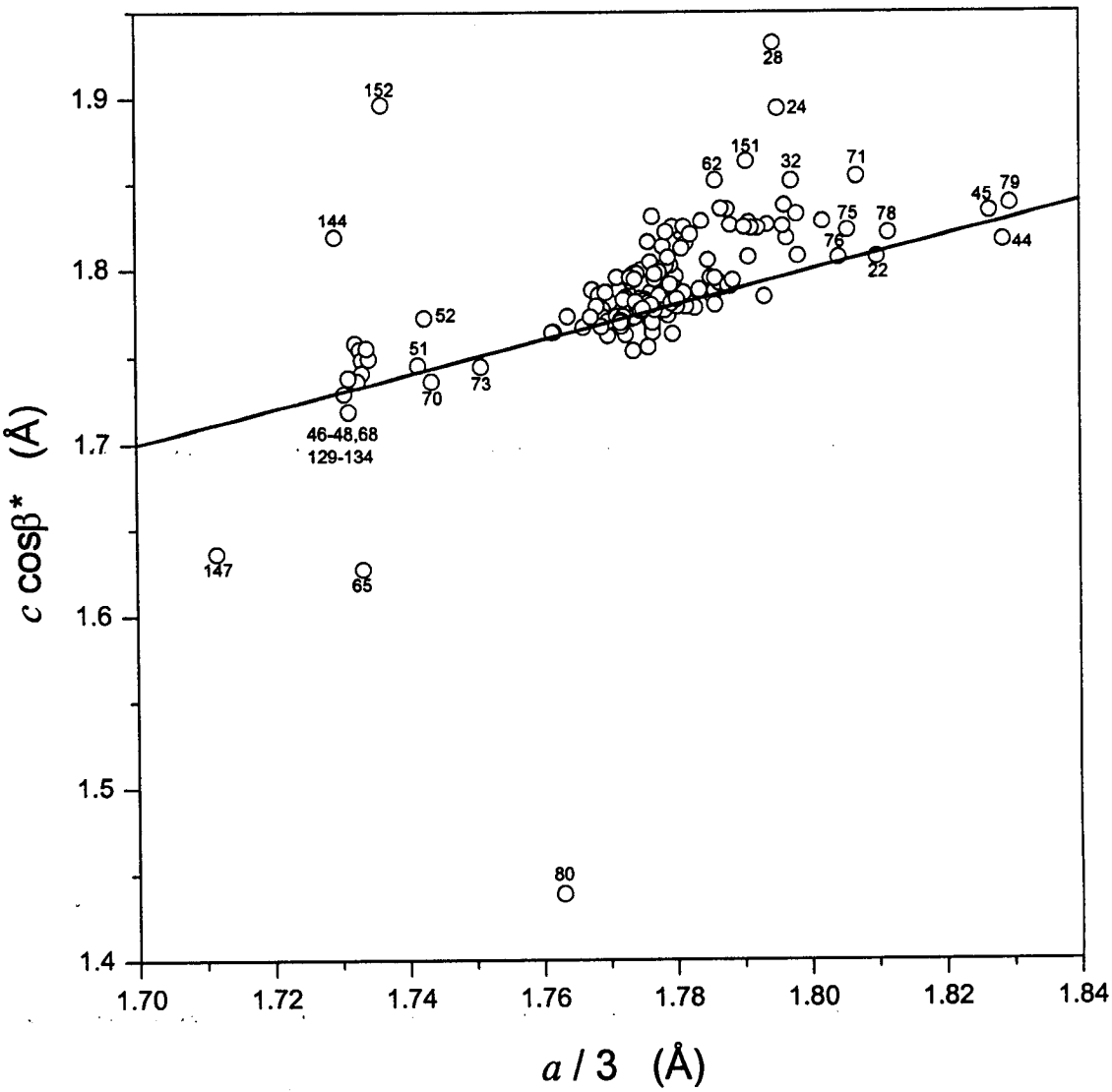

Figure 6.71. Evolution of $c\cos\beta^*$ *versus* a for the 170 single-crystal structure refinements of 1*M* samples compiled in Appendix P. The solid straight line corresponds to $(c/a)\cos\beta^* = 1/3$.

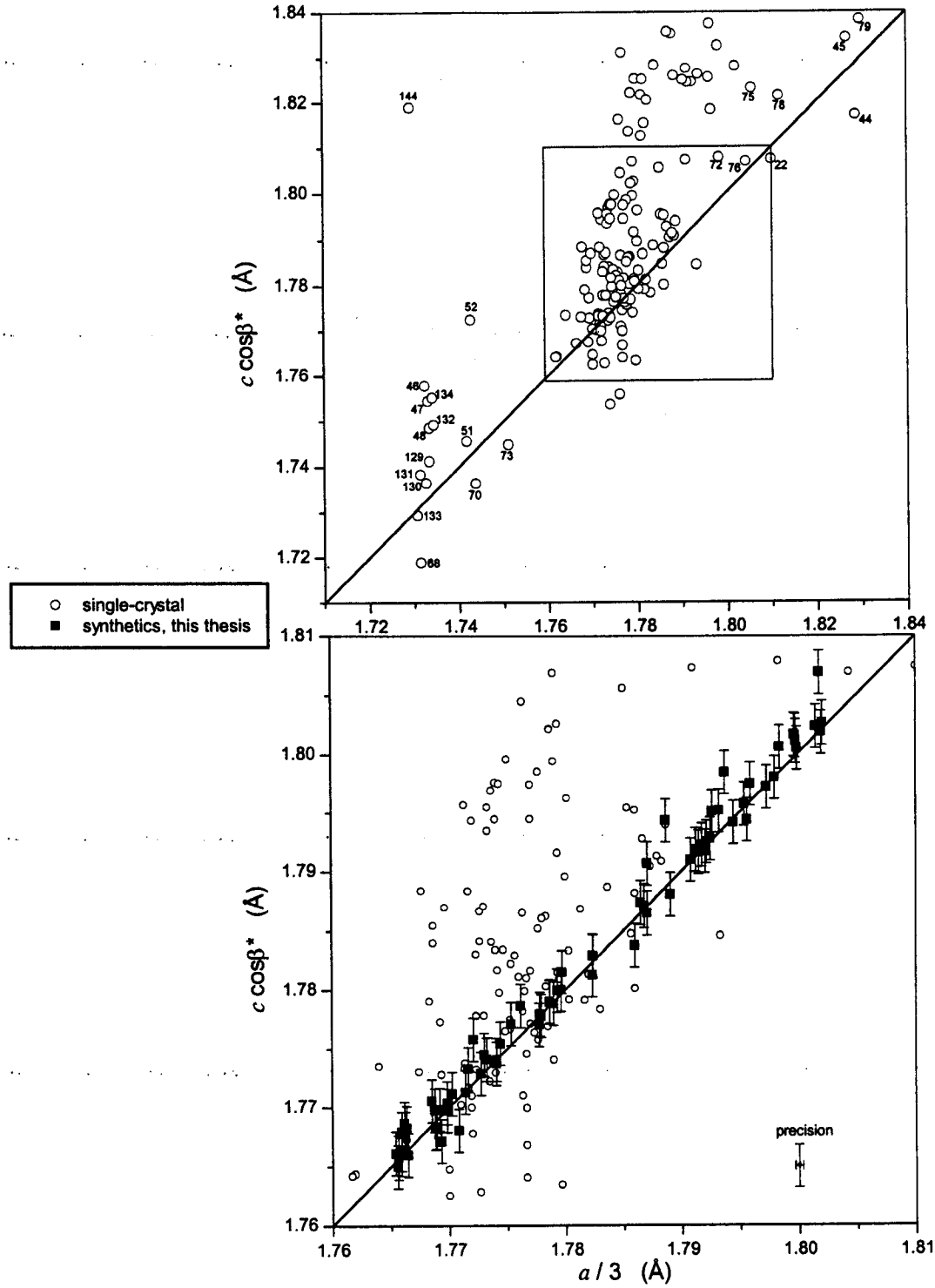

Figure 6.72. Comparisons of the evolutions of $c\cos\beta^*$ *versus* a for: i) the 170 single-crystal structure refinements of 1*M* samples (open circles), on two different expanded scales (top and bottom); and ii) the 75 synthetic samples investigated by powder X-ray diffraction in this thesis (filled squares with error bars). The solid lines correspond to $(c/a)\cos\beta^* = 1/3$.

6.4 Comparative analysis of single-crystal and synthetic powder samples

In this section, crystal chemical quantities calculated from the lattice parameters of synthetic powder samples (reported in Section 5.2) are compared to measured properties in single-crystal 1*M* structures. In accordance with the findings of the previous section, all calculations are based on a geometric homo-octahedral crystal structure model having no tetrahedral corrugation.

For the purpose of comparisons, single-crystal 1*M* samples were categorized into groups (see Appendix P) depending on the chemical compositions of the samples. There are four groups of single-crystal samples with compositions similar to our powder samples: i) sixty-seven biotite samples close to the annite-phlogopite join with $Al_{apfu} \leq 1.3$[1], labelled as '[Ann-Phl]'; ii) thirty-nine biotite samples more towards the eastonite-syderophyllite join with $Al_{apfu} > 1.3$, labelled as 'aluminous-[Ann-Phl]'; iii) twelve tetra-ferri biotite samples with $\langle Fe^{3+} \rangle_{apfu} > 0.4$), labelled as 'tetra-ferri-[Ann-Phl]'; and iv) two oxy-biotite samples (Nos. 27 and 53), labelled as 'oxy-Bt'.

6.4.1 Cation-specific bond lengths

The cation-specific octahedral and tetrahedral bond lengths used in this work to extract structural information from lattice parameters are given in Table 6.6. The procedure employed to establish these bond lengths is explained in this subsection, whereas the case of interlayer-site bond lengths is addressed in Subsections 6.4.4.

Figure 6.73 compares the values of average octahedral sheet bond length <M-O> (defined in Eq. 6.30) observed for the 170 single-crystal refinements of 1*M* structures (tabulated in Appendix P) to the following quantities: i) values of the mean octahedral bond length $\langle d_o \rangle^{Shannon}$ calculated using a set of bond lengths obtained from the tables of ionic radii given in [Shannon 1976] (Table 6.6); and ii) values of the mean octahedral bond length $\langle d_o \rangle^{Weiss}$ calculated using the cation-specific bond distances of [Weiss *et al.* 1992] averaged for *cis* and *trans* occupancies (Table 6.6).

Values of $\langle d_o \rangle^{Shannon}$ and $\langle d_o \rangle^{Weiss}$ were obtained from the chemical compositions (tabulated in Appendix P) reported for each sample as follows:

$$\langle d_o \rangle^{\text{Shannon or Weiss}} = \sum_i d_i(M) \cdot x_i \quad . \tag{6.50}$$

---

[1] X_{apfu} = number of atoms X per formula unit.

In the above equation, the symbols have the following meanings: i) the subscript '*i*' denotes a particular cation; ii) $d_i(M)$ refers to a cation-specific octahedral bond length; and iii) x_i represents the atomic fraction of cation *i* contained in the octahedral sites of a given sample. In the calculation of $<d_o>^{Shannon}$, the vacancy bond length value of Weiss was taken. Similarly, for $<d_o>^{Weiss}$, the $d_i(M)$ values of Shannon were used if there were no bond length provided by [Weiss *et al.* 1992] for given cations.

Values of $d_i(M)$ for Weiss and Shannon bond lengths are given in Table 6.6. For the sake of comparison, cation-specific *M-O* distances computed by the bond-valence parameters of [Brown & Altermatt 1985] are also presented in Table 6.6. Note that Shannon and Brown cation-specific bond lengths are equal to within 0.001 – 0.012 Å. In Figure 6.73, the data points display a poor agreement with the 1:1 correspondence solid lines that are shown. A similar poor agreement is observed if Brown's cation-specific $d_i(M)$ bond lengths are considered instead (not shown).

Figure 6.74 compares the evolutions of the average octahedral bond length <M-O> as a function of $<d_o>^{Shannon}$ for single-crystal structure refinements of: i) twenty-seven well characterized olivine samples with variable chemical compositions in the octahedral sites, $(Ni,Mg,Co,Fe)_2SiO_4$ [Myake *et al.* 1987; Böstrom 1987; Lager & Meagher 1978; Morimoto *et al.* 1974; Birle *et al.* 1968; Smyth 1975; Smyth & Hazen 1973; Rajamani *et al.* 1975; Hazen 1976, 1977; Nord *et al.* 1982]; and ii) six end-member trioctahedral mica samples having substitutions in the octahedral sheets, $\{K\}[Ni,Mg,Co]_3<AlSi_3>O_{10}(OH)_2$ [Redhammer & Roth 2002; Redhammer pers. comm.]. Single-crystal refinements of 1*M* structures belonging to the [Ann-Phl], aluminous-[Ann-Phl], tetra-ferri-[Ann-Phl], and oxy-Bt groups are also shown.

In examining Figure 6.74, one observes that olivine and [Ni, Mg, Co]-end-member mica samples fall on two distinct lines whose slopes differ from that of the 1:1 correspondence solid lines that are shown. In contrast, no clean trend can be discerned for the 1*M* structures, other than the fact that Shannon cation-specific bond lengths definitively over evaluate the mean octahedral bond length in the region between Mg^{2+} and Fe^{2+}, and vice-versa for many samples with an <M-O> size smaller than Mg^{2+}. Given that <M-O> values of well-characterized olivine and end-member mica samples vary linearly — as expected over a small range of average bond lengths — with the $<d_o>^{Shannon}$ values, the scatter observed for the 1*M* structures is attributed to uncertainties in the chemical compositions of these samples.

The dashed lines drawn in Figure 6.74 correspond to a linear regression through the six [Ni, Mg, Co]-end-member trioctahedral mica samples (samples not shown), that were used to establish the cation-specific octahedral $d_i(M)$ values for Ni^{2+}, Mg^{2+}, and Co^{2+} specified in Table

6.6. The errors of these cation-specific bond lengths were obtained from the linear regression analysis results using standard error calculation procedures.

In the case of Fe^{2+}, Fe^{3+}, and Al^{3+} cations, the adopted cation-specific bond lengths are the mid-points between the values predicted by Shannon bond lengths (solid lines) and the ones yielded by the linear regression described above (dashed lines). The individual errors on these cation-specific bond lengths are estimated by taking half of the difference between two corresponding values for a given cation. The corresponding values are given in Table 6.6.

Let us now turn to tetrahedral bond lengths. Figure 6.75 presents the average basal tetrahedral bond length $\langle T\text{-}O\rangle_{bas}$ as a function of the reported Si_{apfu} (where X_{apfu} = number of atoms X per formula unit), along with the distribution of Si_{apfu} values for the 170 single-crystal samples. In examining this figure, the first observation is that only 10 % of the structures (17 out 170) have a near-ideal annite-phlogopite Si_{apfu} value of ~3. Moreover, there appears to be no simple relationship between $\langle T\text{-}O\rangle_{bas}$ and $[Si]_{apfu}$, presumably due to the fact that the tetrahedral sheets contain not only Si^{4+}, but also other cations such as Al^{3+}, Fe^{3+}, and Ti^{4+}, in different amounts.

Given the above situation, cation-specific basal tetrahedral bond lengths were determined as follows. In Figure 6.75, the black squares represent the $T\text{-}O_{bas}$ distances that were assumed for $\langle Al_{1.1}Si_{2.9}\rangle$, $\langle FeSi_3\rangle$, and $\langle Al_{2.8}Si_{1.2}\rangle$ tetrahedral sheets (Table 6.6). The $T\text{-}O_{bas}$ and Si_{apfu} values adopted for $\langle Al_{1.1}Si_{2.9}\rangle$ and $\langle FeSi_3\rangle$ correspond to, respectively: i) the average $T\text{-}O_{bas}$ value of the [Ni, Mg, Co]-end-member mica samples referred to above [Redhammer & Roth 2002; Redhammer pers. comm.]; and ii) the $\langle T\text{-}O\rangle_{bas}$ value of the synthetic tetra-ferri-annite sample of [Donnay *et al.* 1964a]. In the case of $\langle Al_{2.8}Si_{1.2}\rangle$, the adopted $T\text{-}O_{bas}$ distance corresponds the average $\langle T\text{-}O\rangle_{bas}$ and Si_{apfu} values that one obtains from this cluster of samples.

Values of cation-specific basal tetrahedral bond length $d_t^{bas}(T)$ were then derived by solving the set of three linear equations given by combining the assumed $T\text{-}O_{bas}$ distances and chemical compositions for $\langle Al_{1.1}Si_{2.9}\rangle$, $\langle FeSi_3\rangle$, and $\langle Al_{2.8}Si_{1.2}\rangle$ tetrahedral sheets. The values of $d_t^{bas}(T)$ hence acquired for Si^{4+}, Al^{3+}, and Fe^{3+} are compiled in Table 6.6; in Figure 6.75, the open square represents the value of $d_t^{bas}(T)$ thus predicted for Si^{4+}. For the sake of comparison, an appropriate set of bond lengths computed from the tables of ionic radii of [Shannon 1976] is also presented in Table 6.6. No error evaluation was attempted for the cation-specific tetrahedral bond lengths, but bond lengths consistent with Shannon values were also tested.

cation-specific octahedral bond lengths (Å) $d_t(M)$				
M cation	Weiss	Brown	Shannon	This work
Ni^{2+}	-	2.060	2.057	2.0617(25)
Mg^{2+}	2.083	2.099	2.087	2.0759(22)
Co^{2+}	-	2.098	2.112	2.0876(25)
Fe^{2+}	2.110	2.140	2.147	2.126(11)
Fe^{3+}	2.053	2.015	2.012	2.0263(71)
Al^{3+}	1.919	1.907	1.902	1.945(22)
Ti^{4+}	2.073	1.965	1.972	-
Li^{1+}	2.107	2.129	2.127	-
Cr^{3+}	2.040	1.980	1.982	-
Mn^{3+}	-	2.016	2.012	-
Mn^{2+}	2.140	2.196	2.197	-
Vacancy	2.210	-	-	2.210

cation-specific basal tetrahedral bond lengths (Å)				
T-sheet	This work d_t^{bas} or $T\text{-}O_{bas}$	*T* cation	Shannon $([4]T\text{-}[3]O) - ([4]T\text{-}[4]O)$	This work $d_t^{bas}(T)$
$\langle Al_{1.1}Si_{2.9}\rangle$	1.659	Si^{4+}	1.62 - 1.64	1.610
$\langle FeSi_3\rangle$	1.682	Al^{3+}	1.75 - 1.77	1.788
$\langle Al_{2.8}Si_{1.2}\rangle$	1.735	Fe^{3+}	1.85 - 1.87	1.898

Table 6.6. Cation-specific octahedral and basal tetrahedral bond lengths used in this work to extract structural information from lattice parameters. See text for detailed explanations of the other values compiled in this table.

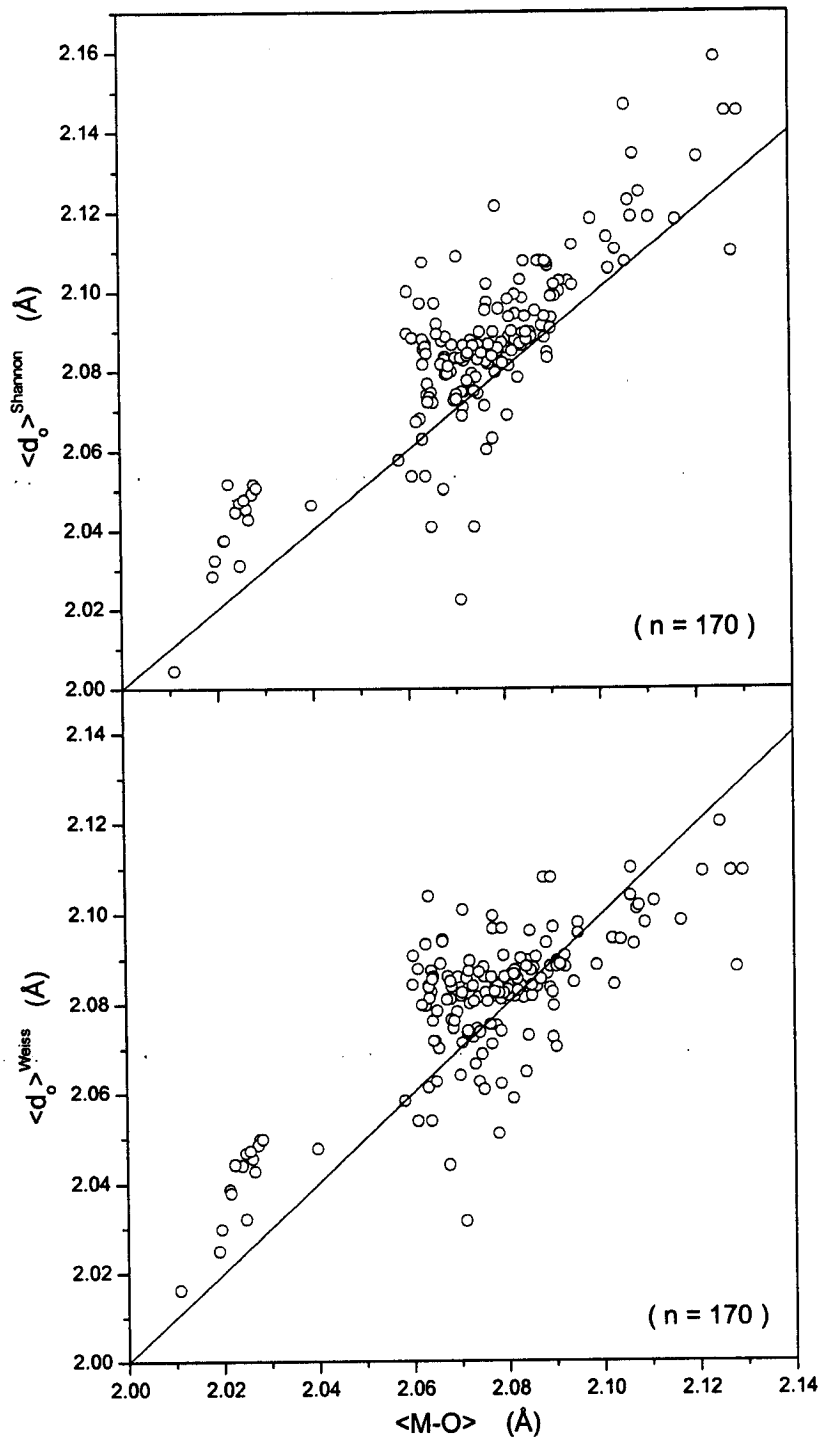

Figure 6.73. Comparison of the values of average octahedral bond length <M-O> (defined in Eq. 6.30) observed for the 170 single-crystal refinements of 1*M* structures to values of mean octahedral bond lengths $\langle d_o \rangle^{Shannon}$ (top) and $\langle d_o \rangle^{Weiss}$ (bottom) calculated from Eq. 6.50.

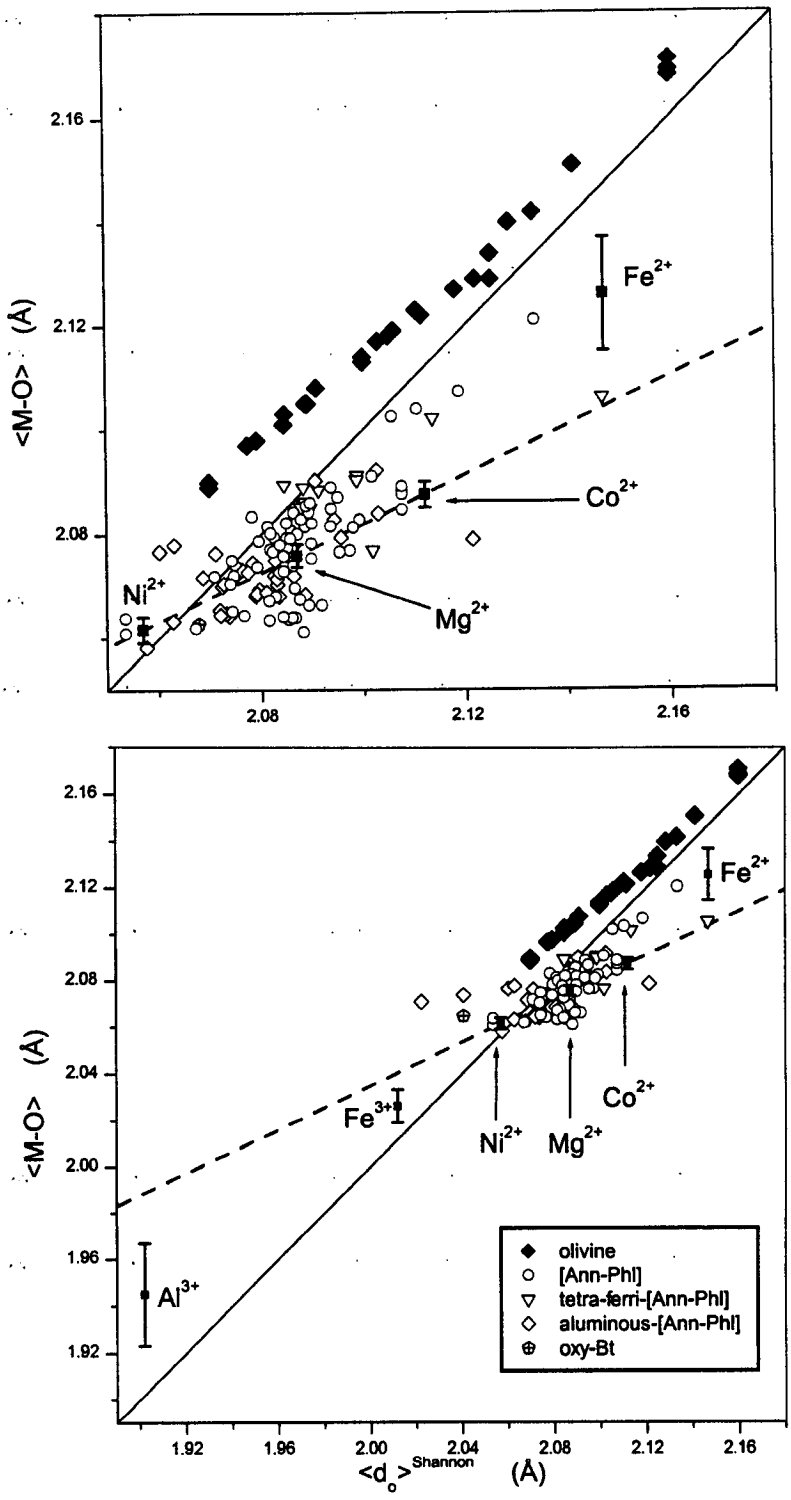

Figure 6.74. Evolution of <M-O> as a function of $<d_o>^{Shannon}$ for single-crystal structure refinements of selected samples. See text for detailed explanations of the content of this figure.

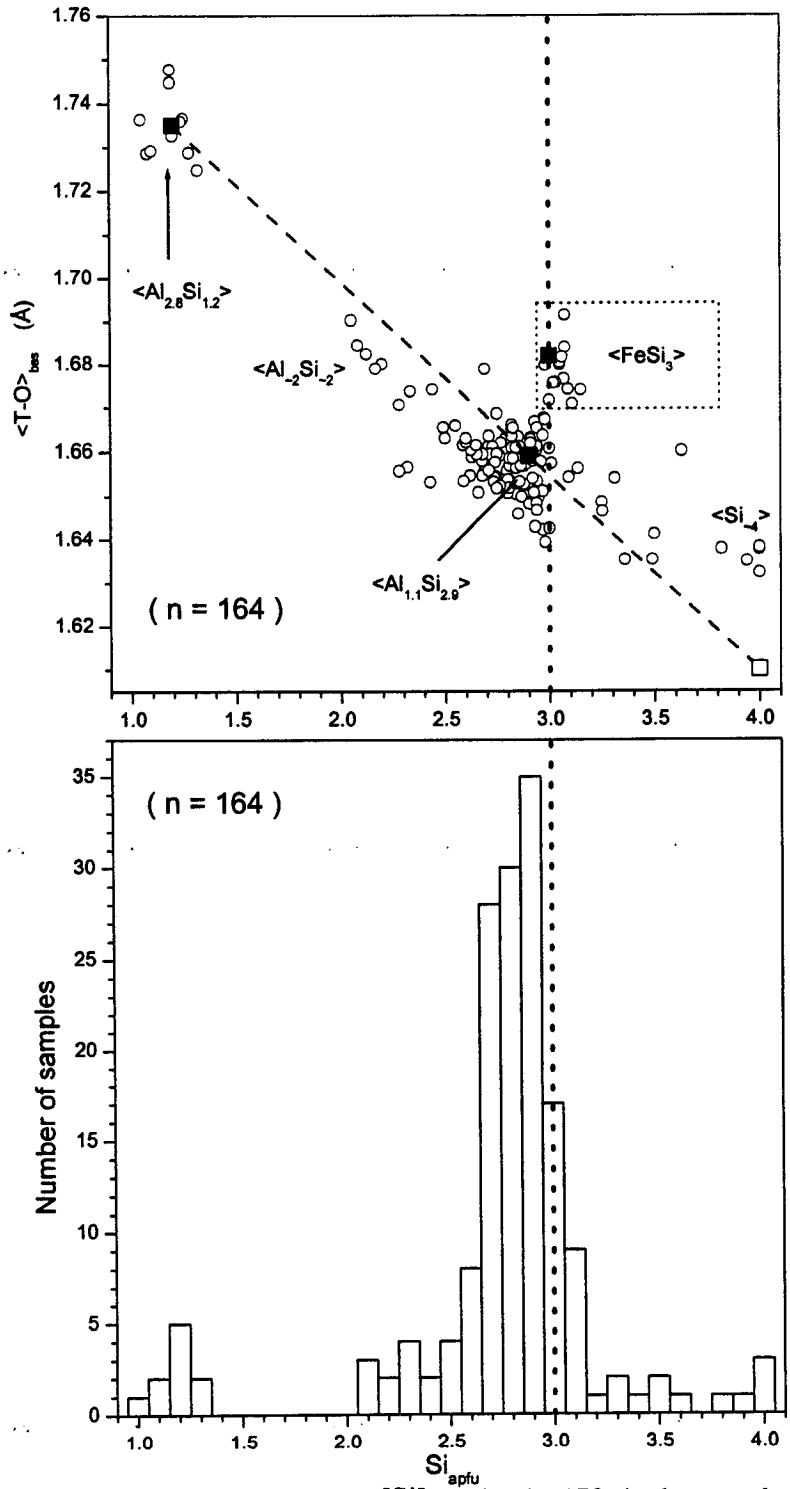

Figure 6.75. Evolution of $\langle T\text{-}O\rangle_{bas}$ *versus* $[Si]_{apfu}$ for the 170 single-crystal structure refinements of 1*M* samples compiled in Appendix P, along with the distribution of $[Si]_{apfu}$ values. The vertical dotted lines correspond to $[Si]_{apfu} = 3$. See text for a detailed explanation of the content of this figure.

6.4.2 *b* as a function of the mean octahedral bond length

Figures 6.76 and 6.77 show *b versus* the mean octahedral bond length, [D], calculated for various solid solution series studied in this thesis, whereas Figures 6.78 and 6.79 display *b* as a function of the average octahedral sheet bond length <M-O> for the various groups of single-crystal 1*M* samples. Some octahedral flattening $\psi = constant$ (dotted lines) and octahedral sheet height $h_o = constant$ (dashed lines) predictions made via Eq. 6.12 (Subsection 6.2.2) — that are valid for both *geometric homo-octahedral* and *geometric meso-octahedral* ideal octahedral sheet models — are shown as reference in these figures.

For a given sample, [D] is calculated as in Eq. 6.50 using the cation-specific octahedral bond lengths of Table 6.6, the nominal composition of the sample (Eqs. 3.1-3.4, 3.6, and 3.9; Table 3.1), and the measured ferric and ferrous iron site populations obtained from Mössbauer spectroscopy (Table 3.3, Section 3.5), assuming that any amounts of tetrahedral ferric iron <Fe^{3+}> occurs through Al/Fe exchange between octahedral and tetrahedral sheets (i.e., via Eq. 1.4). In the case of the annite-oxyannite-ferrioxyannite series, following [Rancourt *et al.* 2001], annite-oxyannite ($Fe^{2+} + OH^- \rightleftharpoons Fe^{3+} + O^{2-} + H\uparrow$; Eq. 1.1) and oxyannite-ferrioxyannite ($3\ Fe^{2+} \rightleftharpoons 2\ Fe^{3+} + {}^{[6]}\square + Fe\uparrow$; Eq. 1.2) stoichiometries were assumed at $T_{TR} \leq 350$ °C and $T_{TR} \geq 370$ °C, respectively.

As illustrated in Figure 6.77, the differences in crystal chemical behaviours seen in Figure 6.76 between the "divalent" (Co-Mg JLR, Mg-Ni JLR, Fe-MgJLR, Fe-Mg RGBn, and Fe-Ni GR) and "trivalent" (Ann-oxy-ferrioxy and Fe-Mg RGBr) solid solution series do not depend on the particular values of cation-specific octahedral bond lengths that are assumed. The error bars displayed along the *x*-axis of Figure 6.77 represent the maximum variations in [D] values obtained for each sample using the individual errors of the cation-specific $d_i(M)$ values given in Table 6.6.

Moreover, as explained in [Rancourt *et al.* 2001], the break observed in the behaviour of the Ann-oxy-ferrioxy series between $T_{TR} = 350$ and 370 °C occurs irrespective of any particular stoichiometries assumed for these samples. That is, any combination of the oxybiotite reaction ($Fe^{2+} + OH^- \rightleftharpoons Fe^{3+} + O^{2-} + H\uparrow$; Eq. 1.1) and the Fe vacancy substitution ($3\ Fe^{2+} \rightleftharpoons 2\ Fe^{3+} + {}^{[6]}\square + Fe\uparrow$; Eq. 1.2) gives a discontinuity such as the one shown in Figures 6.76 and 6.77.

One notes that the positions of the solid-solution lines of the divalent series move progressively from $\psi = 58.5°$ to higher $\psi = constant$ angle predictions as the Fe^{3+}/Fe^{2+} ratio of the given series increases (see Table 3.3, Section 3.5). This is clearly shown in Figure 6.80, where calculated flattening angle $\psi_{calculated}$ values (via Eq. 6.12, Subsection 6.2.2) are plotted as a

function of [D] .

By contrast, Figures 6.81 and 6.82 show that in 1*M* single-crystal samples, the average flattening angle <ψ> always decreases with increasing average octahedral bond length <M-O>, within a given solid solution series or a particular group of samples. For samples with chemical compositions similar to our synthetic powder samples, the range of <ψ> values observed is closely delimited by the values of $\psi_{calculated}$ that were obtained for the Ni-Mg JLR, Co-Mg JLR, and Ann-oxy-ferrioxy solid solution series (Figure 6.81).

In examining Figure 6.81 attentively, one notes a higher degree of correlation between <ψ> and <M-O> for [Ann-Phl] samples, as compared to other pertinent groups of single-crystal samples. Similarly, Figures 6.83 and 6.84 show that the individual octahedral-site flattening angles ψ_{M1} and ψ_{M2} also increase with decreasing <M1-O> and <M2-O> distances. However, one observes that the correlation is higher for *M*2 than for *M*1 sites. [Redhammer & Roth 2002] and [Brigatti et al. 1991] have also made similar observations.

The above trends, in terms of an increasing flattening as the bond length decreases, do not appear to be present in our synthetic divalent solid solution series on the basis of the bond lengths that were considered (Table 6.6). This is puzzling and could indicate an important difference between natural single-crystal and synthetic powder samples. Note however that the *b* *vs.* [D] (Figure 6.76) behaviour of the synthetic Al-rich Fe-Mg RGBr series has a slope similar to the one observe in the plot of *b vs.* <M-O> (Figure 6.78) for natural [Ann-Phl] single-crystal samples.

As revealed in Figures 6.83 and 6.84, the effect that high-charge cations (such as Al^{3+}, Fe^{3+}, and Ti^{4+}) may induce in the octahedral sheets of micas seems to play an important role. This has been the subject of many studies, where the authors have mainly attempted to establish links between various measured structural parameters and the chemical compositions of the samples (e.g., see [Alietti *et al.* 1995, 1997; Brigatti & Guggenheim 2002; Brigatti & Poppi 1993; Brigatti *et al.* 1991, 1996a, 1996b, 1998, 2000a, 2000b, 2001; Cruciani & Zanazzi 1994; Redhammer *et al.* 2000; Redhammer & Roth 2002]).

More work is required to fully understand the results presented in this subsection. Finally, as will be discussed below, the plateau in *b* values observed for the Mg-Ni JLR series Figures 6.76-6.78) is attributed to a maximum limit of the tetrahedral rotation angle for trioctahedral K-rich micas having an $<Al_1Si_3>$ tetrahedral sheet.

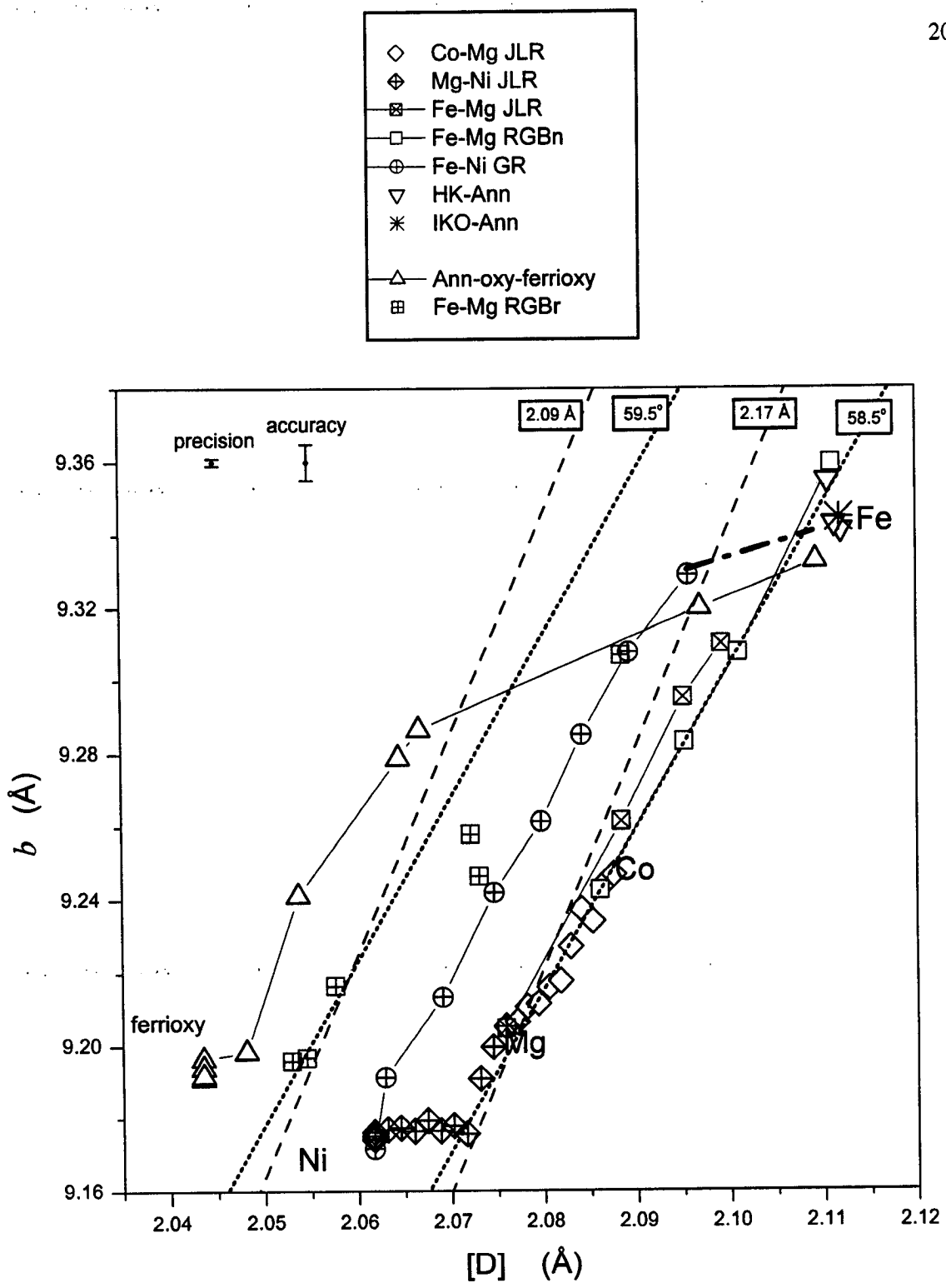

Figure 6.76. Lattice parameter *b* as a function of the mean octahedral bond length [D] calculated for various solid solution series studied of this thesis. The precision and accuracy of *b* are also indicated.

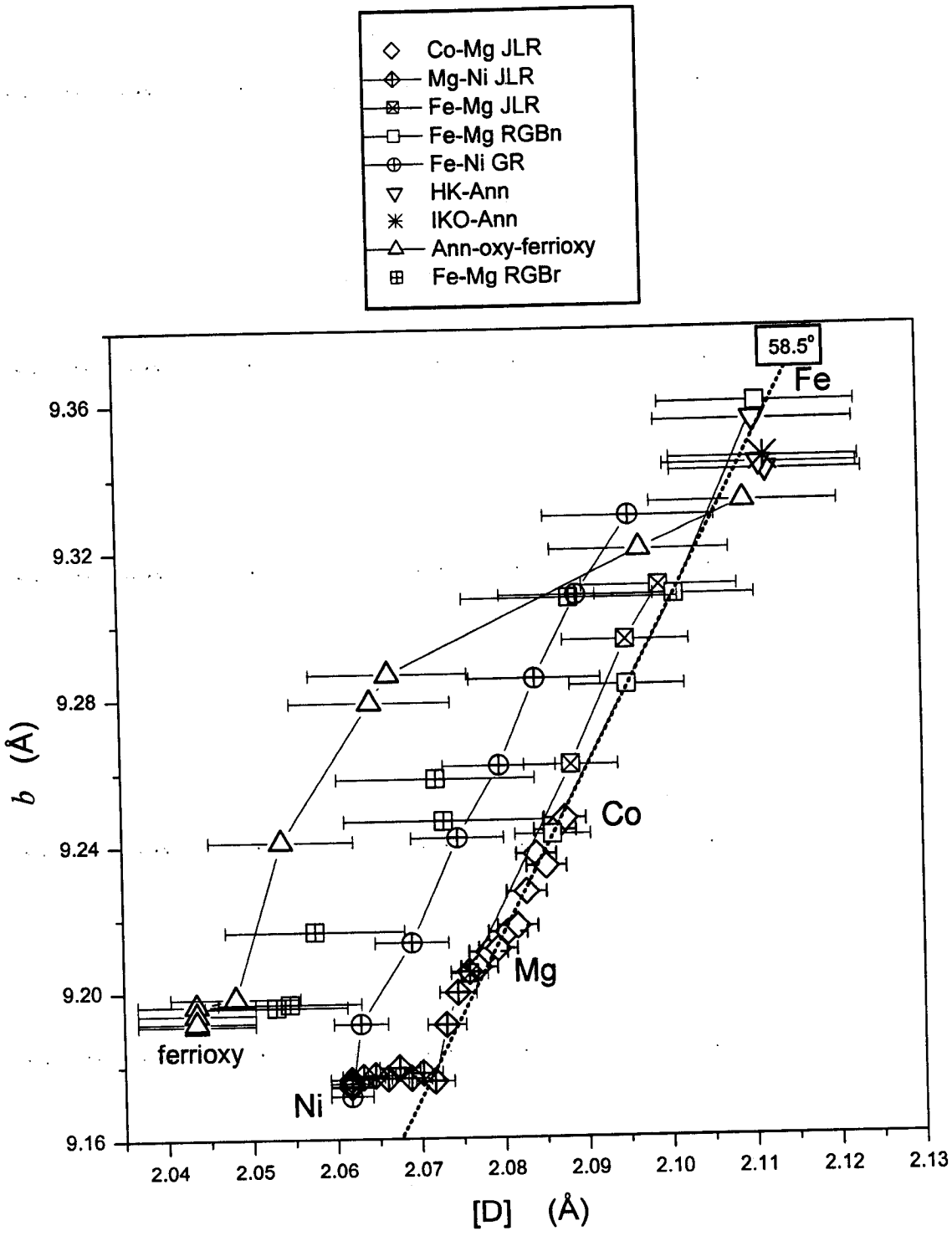

Figure 6.77. Plot of *b versus* [D] showing the maximum variations of [D] values, displayed *x*-axis error bars, that were obtained using the individual errors of the cation-specific $d_i(M)$ values stipulated in Table 6.6.

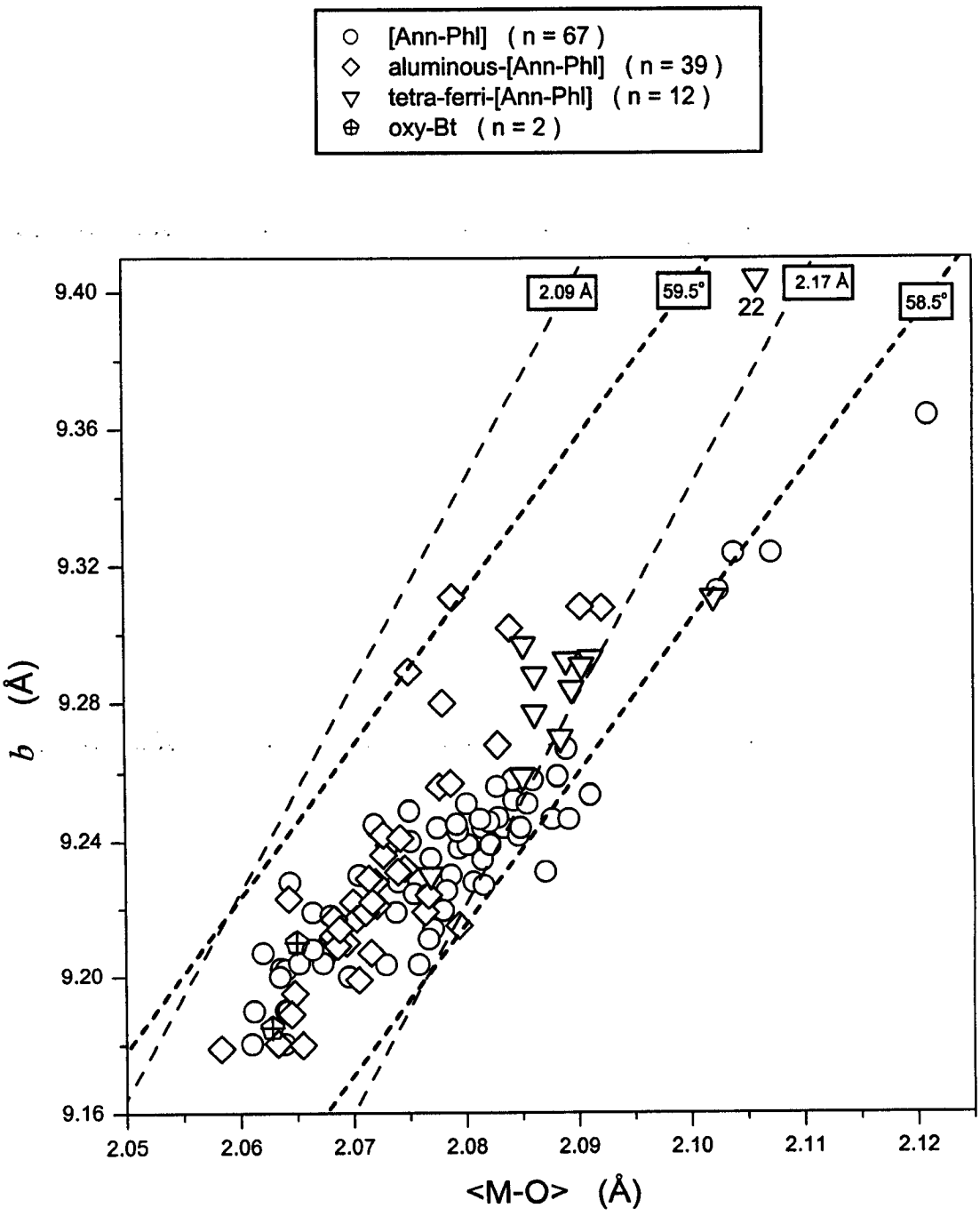

Figure 6.78. *b* as a function of the average octahedral sheet bond length <M-O> for groups of single-crystal 1*M* samples having chemical compositions similar to our synthetic samples.

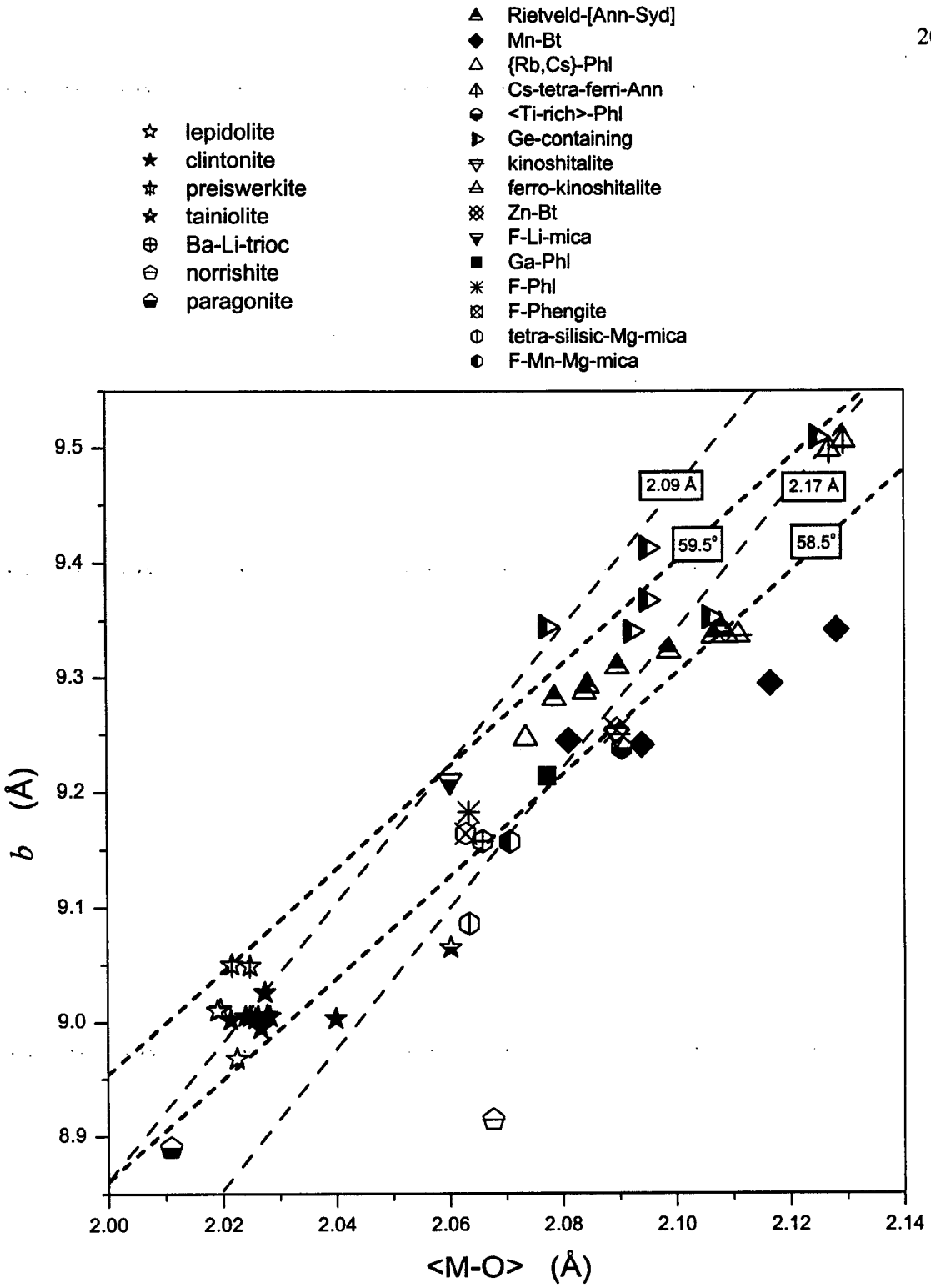

Figure 6.79. *b versus* <M-O> for other groups of single-crystal 1*M* samples. Consult Appendix P for the nomenclature of the various groups.

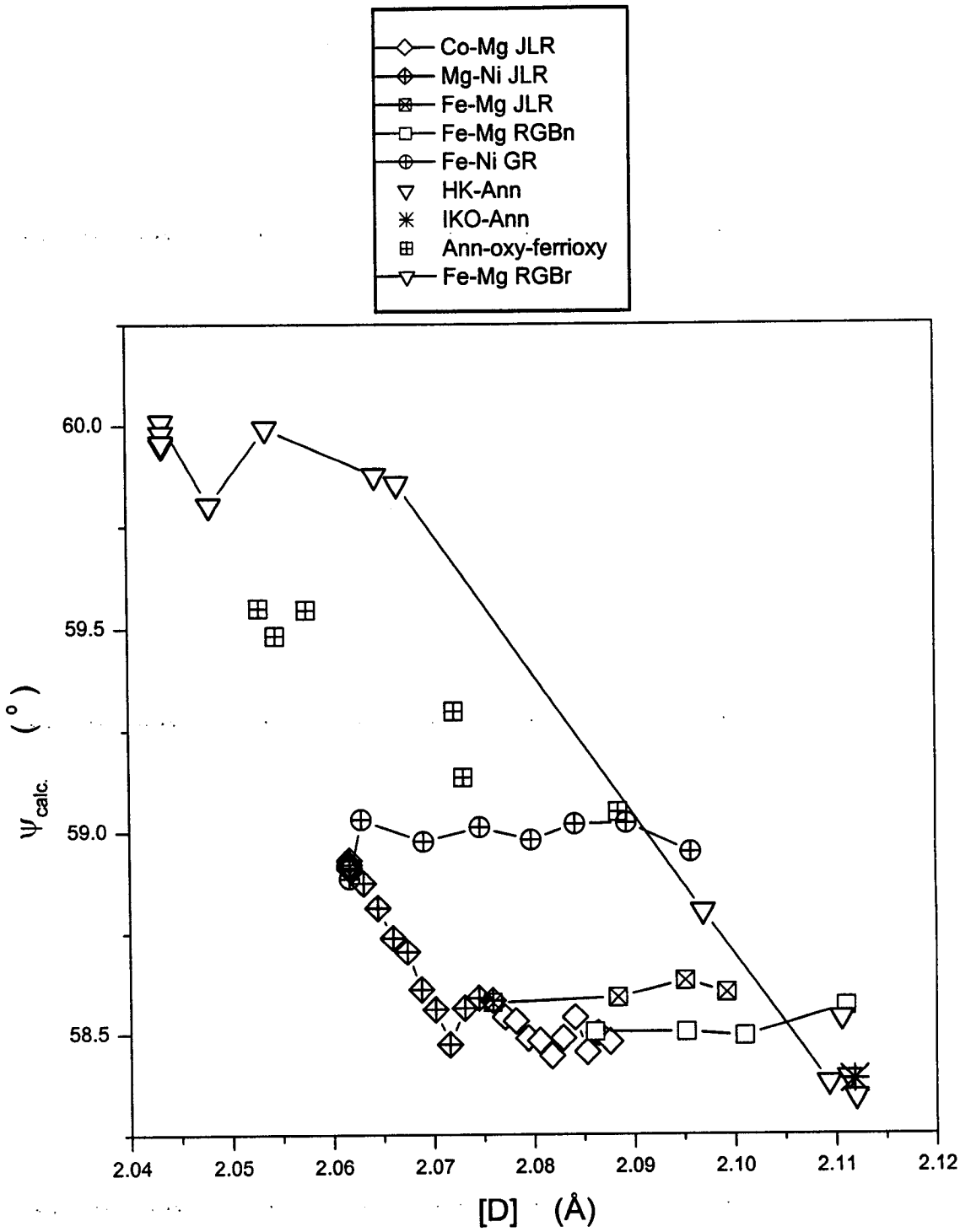

Figure 6.80. Flattening angle $\psi_{calculated}$ as a function of the mean octahedral bond length [D].

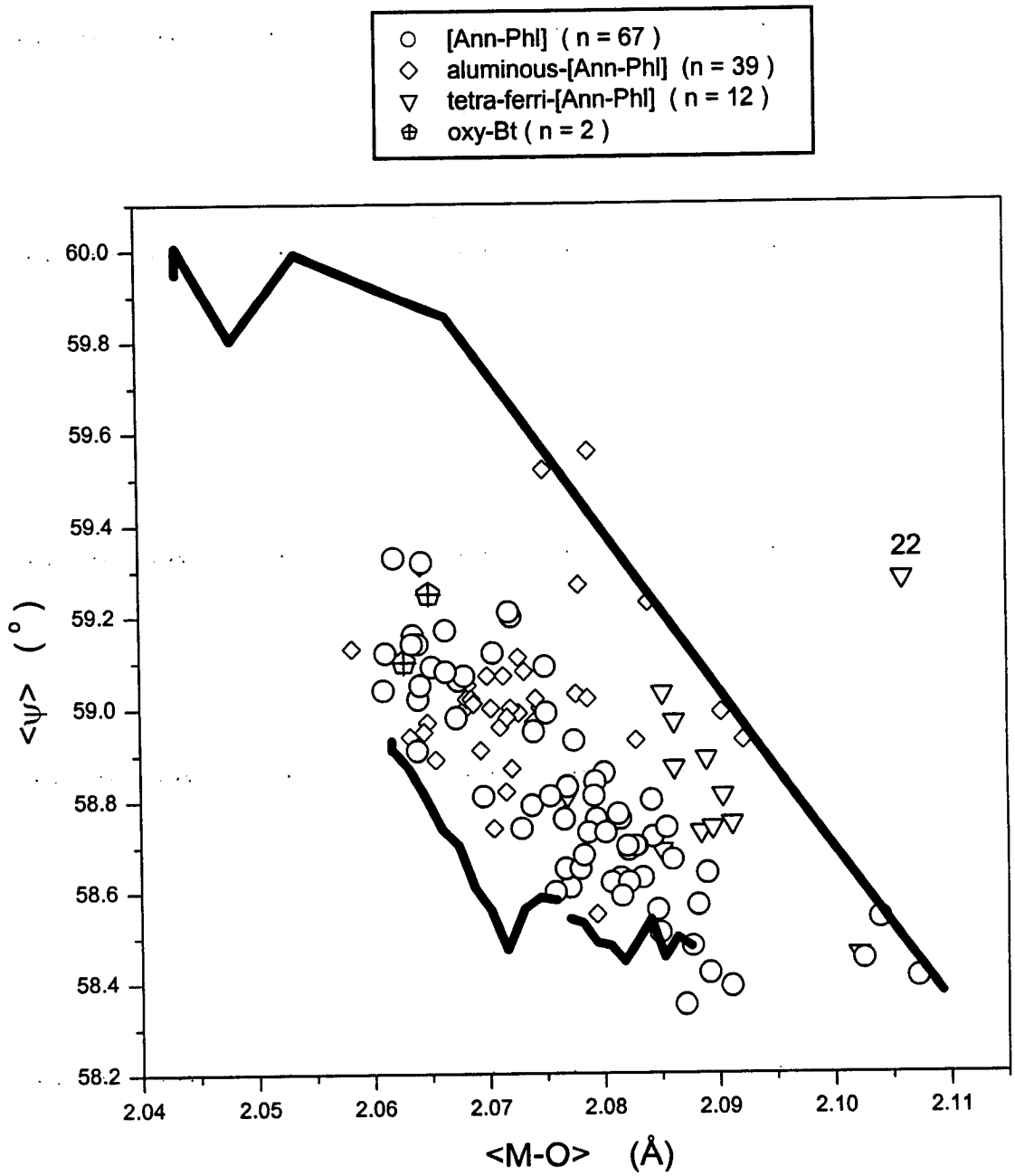

Figure 6.81. Flattening angle <ψ> as a function of average octahedral bond length <M-O> for pertinent single-crystal samples. The thick dark lines correspond to $\psi_{calculated}$ and [D] values of the Mg-Ni JLR, Co-Mg JLR, and Ann-oxy-ferrioxy series.

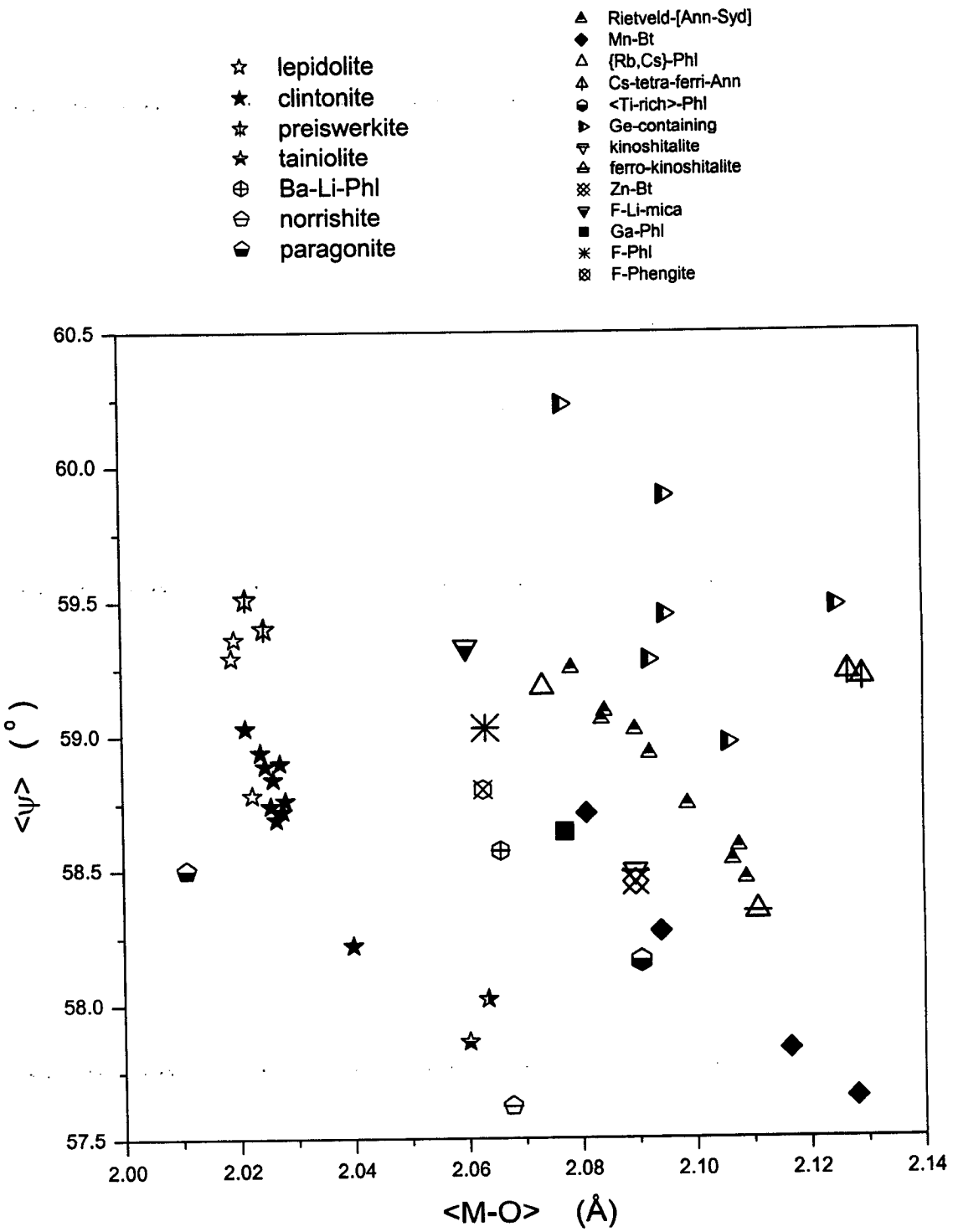

Figure 6.82. Flattening angle <ψ> as a function of average octahedral bond length <M-O> for other groups of single-crystal samples. Consult Appendix P for the nomenclature of the various groups.

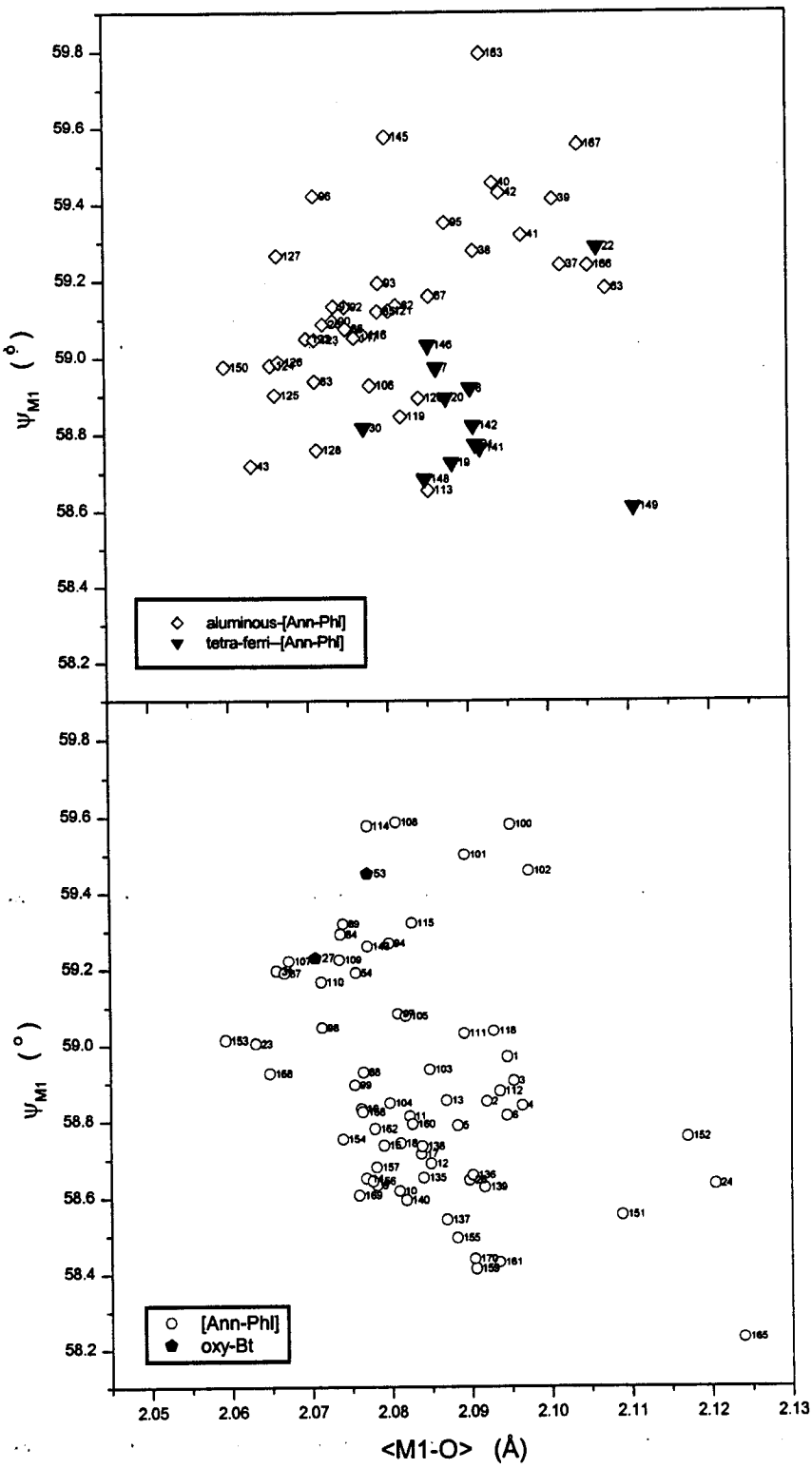

Figure 6.83. Flattening angle ψ_{M1} of the *M*1 site as a function of mean <M1-O> distance for pertinent groups of single-crystal samples.

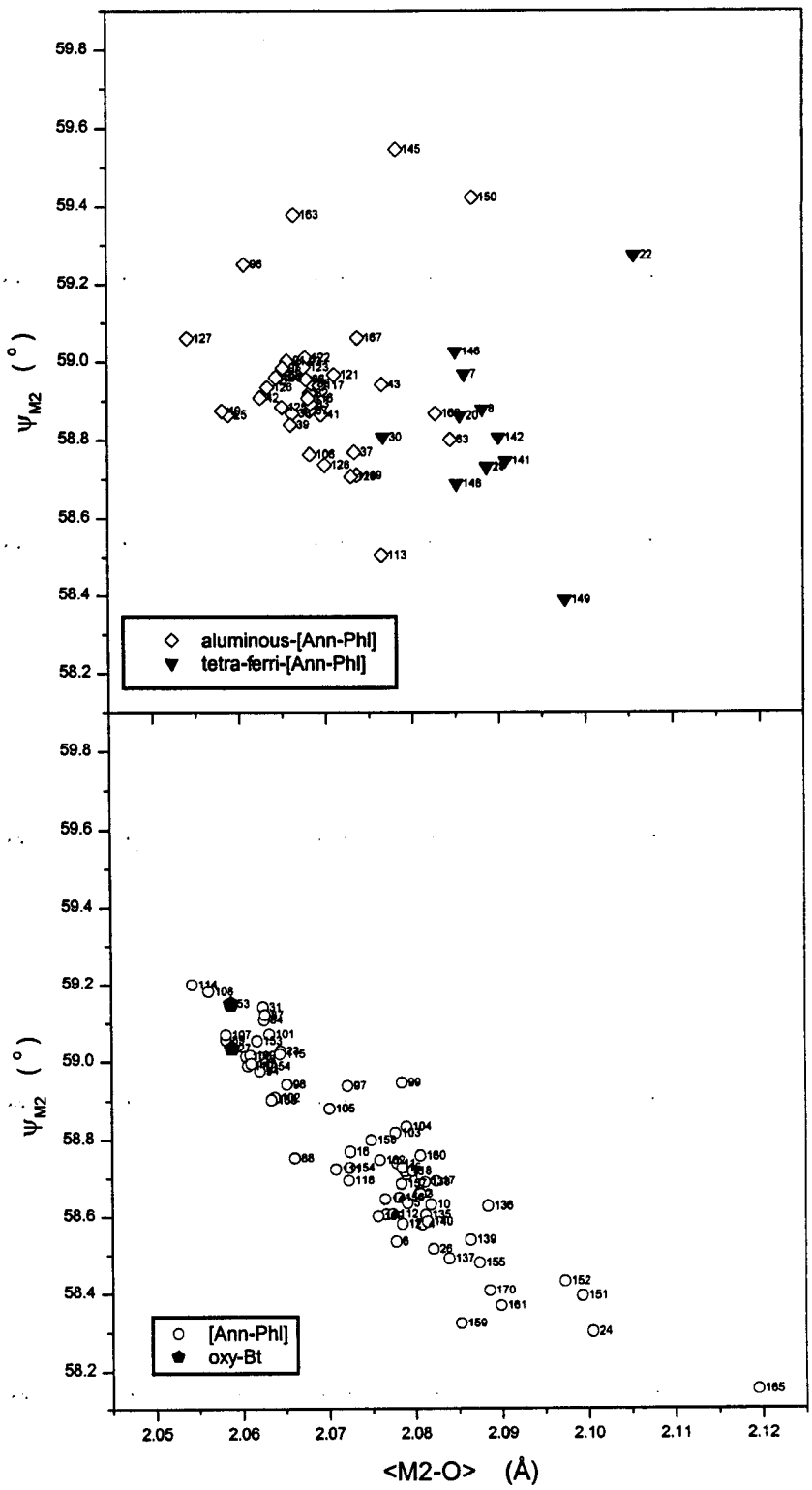

Figure 6.84. Flattening angle ψ_{M2} of the *M*2 site as a function of mean <M2-O> distance for pertinent groups of single-crystal samples.

6.4.3 Tetrahedral rotation limits

Figure 6.85 displays the average basal edge length $\langle O\text{-}O\rangle_{bas}$ as a function of the average basal tetrahedral bond length $\langle T\text{-}O\rangle_{bas}$ for the 170 single-crystal samples. The lines (solid, dashed, and dotted) that are shown in this graph correspond to tetrahedral flattening O_{bas}-T-O_{bas} angle $\tau_{bas} = constant$ predictions made via Eq. 6.15 (Subsection 6.2.4). One observes that the $\{K\}\langle Al_{\sim 1}Si_{\sim 3}\rangle$ samples closely follow the $\tau_{bas} = 108.5°$ solid-line prediction, whereas other groups of samples having different tetrahedral sheet contents cluster at other particular positions.

Figure 6.86 shows the tetrahedral rotation angle, $\alpha_{calculated}$, as a function of the octahedral-to-tetrahedral cation-oxygen bond length ratio, $[D]/\langle T\rangle_{bas}$, for various solid solution series of synthetic powder samples studied in this thesis. $\langle T\rangle_{bas}$ is the mean basal tetrahedral bond length calculated in the same manner as for [D] via Eq. 6.50 (see Subsection 6.2.4). For a given sample, $\alpha_{calculated}$ is obtained from the (measured) b and (calculated) $\langle T\rangle_{bas}$ values via substitution of Eq. 6.15 into 6.19, assuming that $\tau_{bas} = 108.5°$ (Figure 6.85).

The various predictions that are displayed as thin solid lines in Figure 6.86 are obtained by equating Eqs. 6.12 and 6.15 (Subsection 6.2.4) at a given octahedral flattening angle ψ with $\tau_{bas} = 108.5°$ (Figure 6.85). As illustrated by the positions of the small arrows that are drawn, the point of initiation of the lower limit on α moves progressively from lower to higher $[D]/\langle T\rangle_{bas}$ ratio, which depends on both octahedral ψ and tetrahedral τ_{bas} flattening angles that are assumed in the calculations.

The lower limit on α corresponds to the point where the tetrahedral sheets cannot laterally fit on top of the octahedral sheets. On the basis of the structural parameters that were taken to occur for octahedrons and tetrahedrons in the above described calculations, one sees that all the Fe-end-member synthetic samples fall in a regime where octahedral and tetrahedral sheets cannot be matched, as predicted by [Hazen & Wones 1972, 1978].

In Figure 6.86, a higher limit on α seen for the Mg-Ni JLR series occurs irrespective of any set of cation-specific basal tetrahedral bond lengths taken between Shannon values (Table 6.6) and the ones determined in this thesis (Table 6.6, Figure 6.85, Subsection 6.2.1). The only difference is that one obtains different *plateau* values for α. Here, with the structural parameters that are assumed, one calculates a higher limit on $\alpha \cong 9.5°$.

Figures 6.87 and 6.88 show the average tetrahedral rotation α as a function of the ratio $\langle M\text{-}O\rangle/\langle T\text{-}O\rangle_{bas}$ for the single-crystal samples on an overall and expanded scale, respectively. The dashed-dotted horizontal lines displayed in these figures are drawn at the same α positions as those illustrated in Figure 6.86. Note also that Figure 6.88 has the same scale as Figure 6.86.

In examining Figure 6.88, one sees that the density of the data points is higher near the dashed-dotted line positioned at $\alpha = 9.5°$. [Redhammer & Roth 2002] have made similar observations by plotting the average tetrahedral rotation angle α as a function of the mean octahedral cation radii, calculated using the tables of [Shannon 1976], for a subset of single-crystal 1*M* samples considered in this thesis.

Figures 6.89 presents the distribution of α for all single-crystal 1*M* structures. One observes the distribution to be clearly asymmetric. All samples outside the main trend displayed by the biotite samples belong to groups that have significantly different tetrahedral-sheet contents, except for paragonite which is a dioctahedral mica.

Figures 6.90 shows the the distributions of α for the [Ann-Phl], aluminous-[Ann-Phl], and tetra-ferri-[Ann-Phl] groups separately. Overall, Figure 6.90 demonstrates strong evidence that, indeed, a higher limit appears to be present at $\alpha \cong 9.5°$ for the [Ann-Phl] samples. Morever, as discussed by [Hazen & Wones 1978], Figure 6.90 presents strong evidence for the proposed higher limit on α to be tetrahedral composition dependent

Whereas the lower limit on α is understood as arising from a lateral misfit between octahedral and tetrahedral sheets, the higher limit on α cannot be attributed to a structural mechanisms based on the geometrical models that were tested. Therefore, the higher α-limit is tentatively attributed to some combination of intra-tetrahedral-sheet inter-cation repulsion and local bonding constraints on tetrahedrons.

From the results of this subsection, one concludes that: i) an O_{bas}-T-O_{bas} angle of 108.5° is favoured for an $<Al_1Si_3>$ tetrahedral sheet; and ii) strong evidence supports that the break in b seen in the Mg-Ni JLR series is due to a higher limit of tetrahedral rotation for an $<Al_1Si_3>$ sheet of ~9.5° .

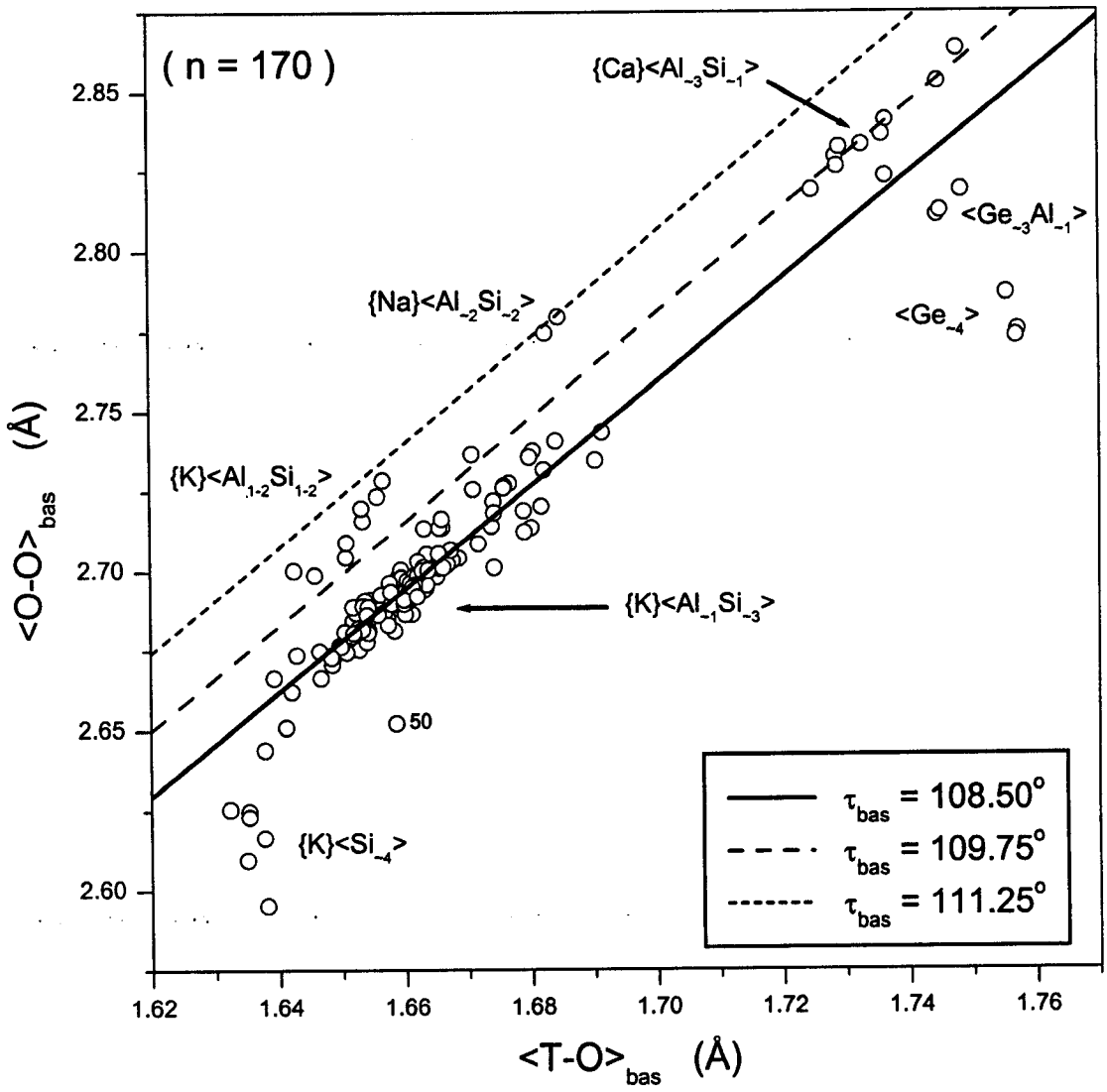

Figure 6.85. Average basal edge length $\langle O\text{-}O\rangle_{bas}$ as a function of the average basal tetrahedral bond length $\langle T\text{-}O\rangle_{bas}$ for the 170 single-crystal samples. The various lines correspond to predictions that are explained in the text.

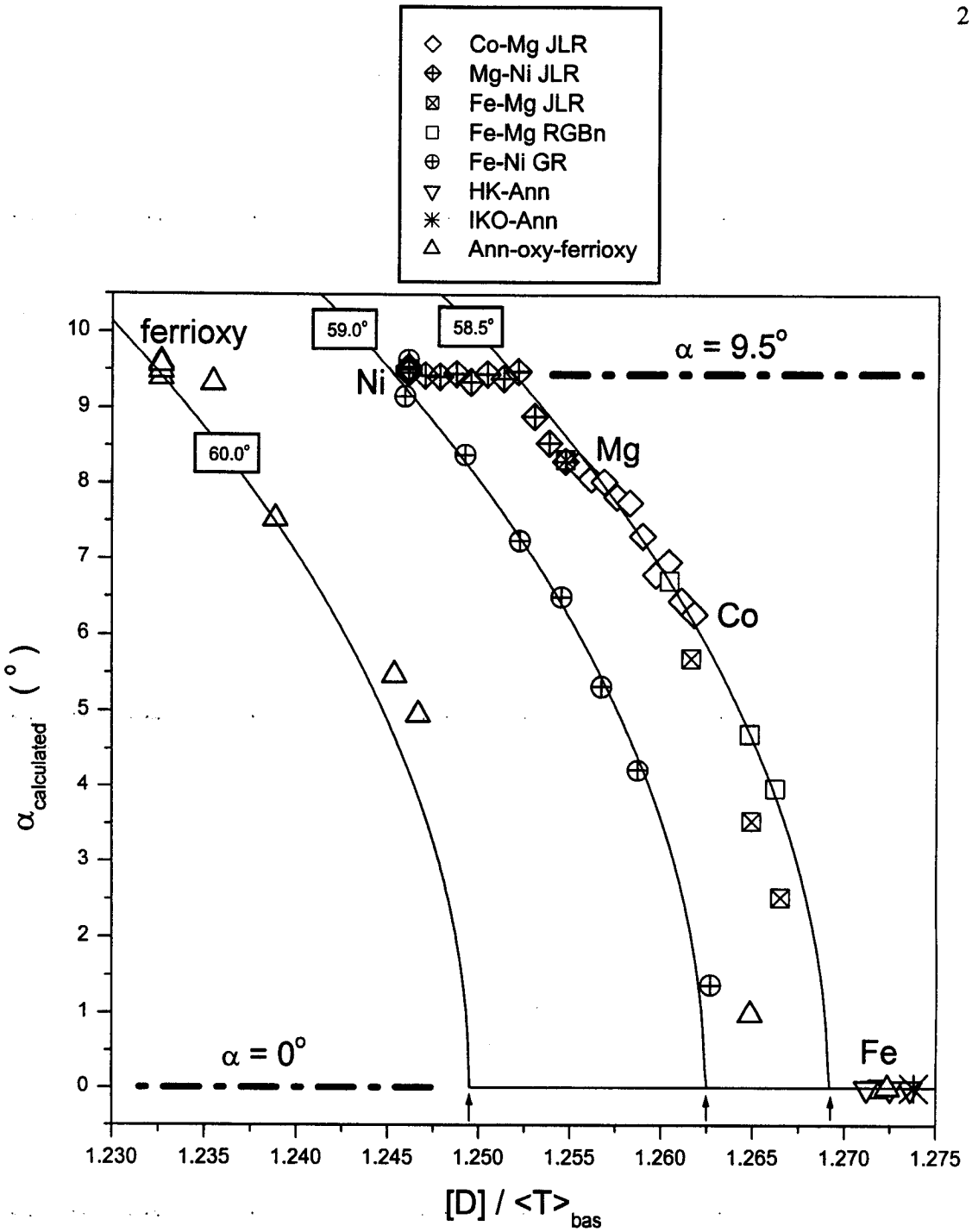

Figure 6.86. Tetrahedral rotation angle $\alpha_{calculated}$ as a function of the octahedral-to-tetrahedral cation-oxygen ratio [D]/<T>$_{bas}$ calculated for various solid solution series of synthetic powder samples studied in this thesis.

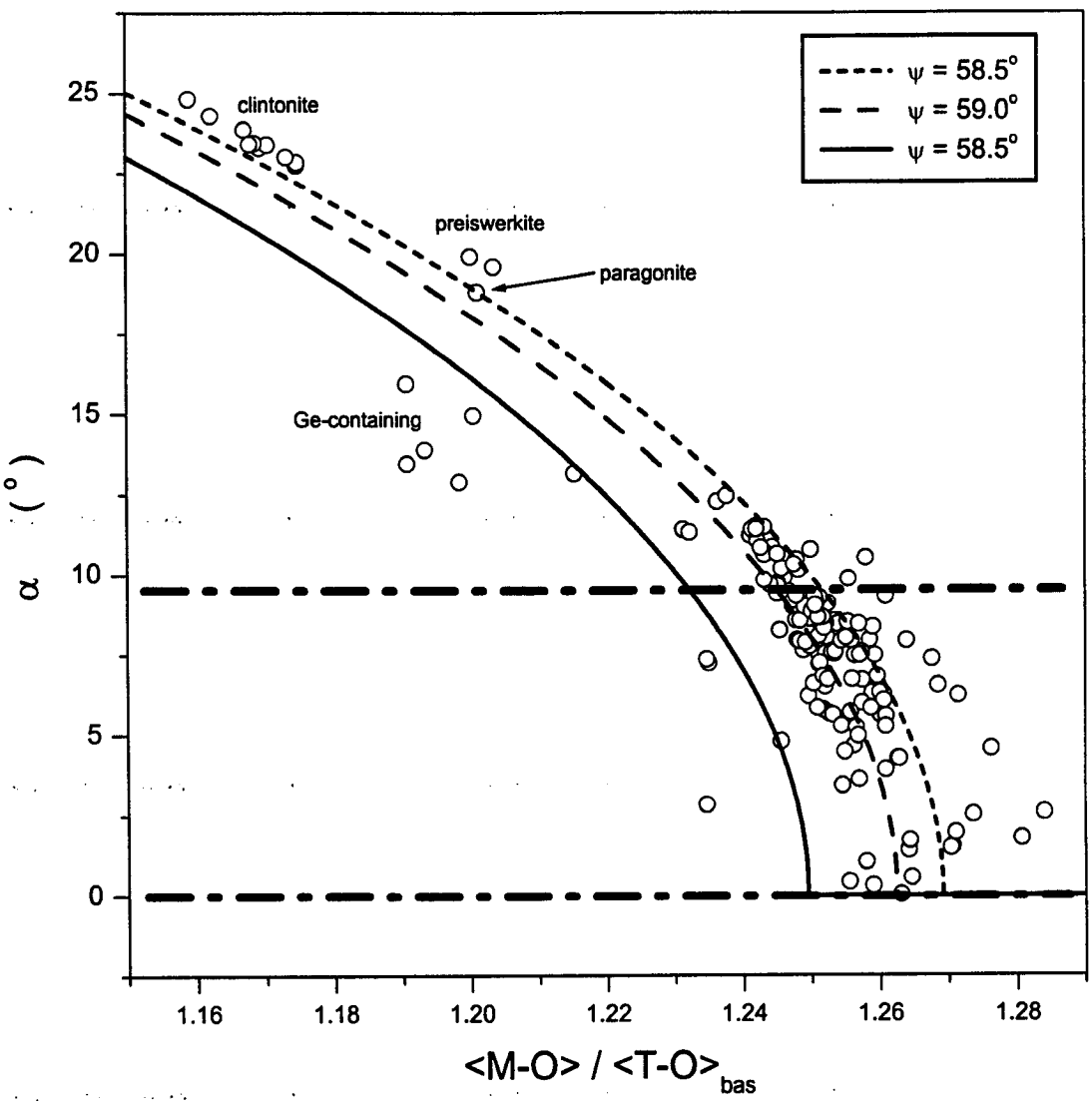

Figure 6.87. Average tetrahedral rotation α as a function of the ratio $\langle M\text{-}O\rangle/\langle T\text{-}O\rangle_{bas}$ observed for the 170 single-crystal samples.

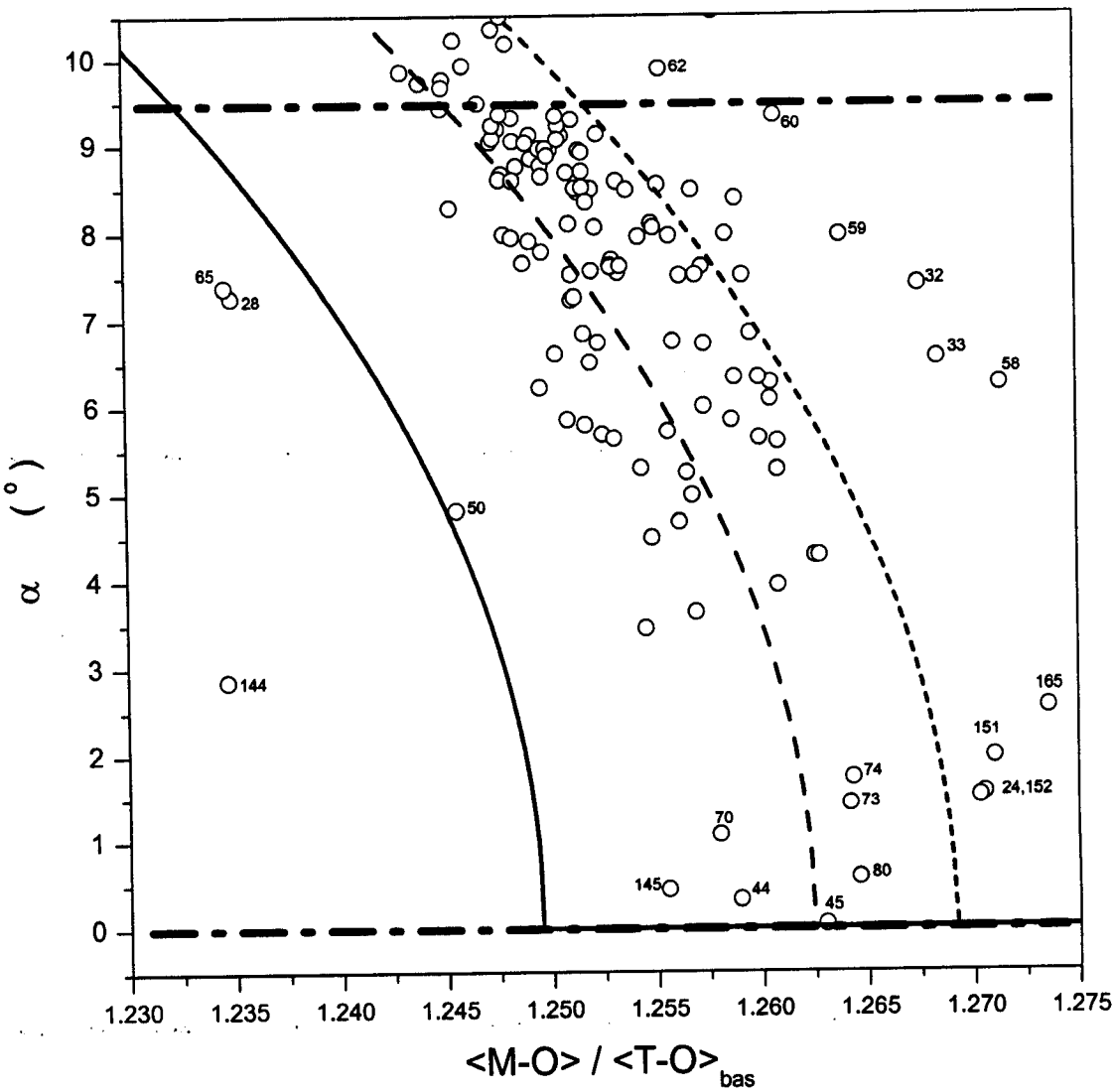

Figure 6.88. Plot of α *versus* <M-O>/<T-O>$_{bas}$ for the single-crystal samples, displayed on the same scale as in Figure 6.86.

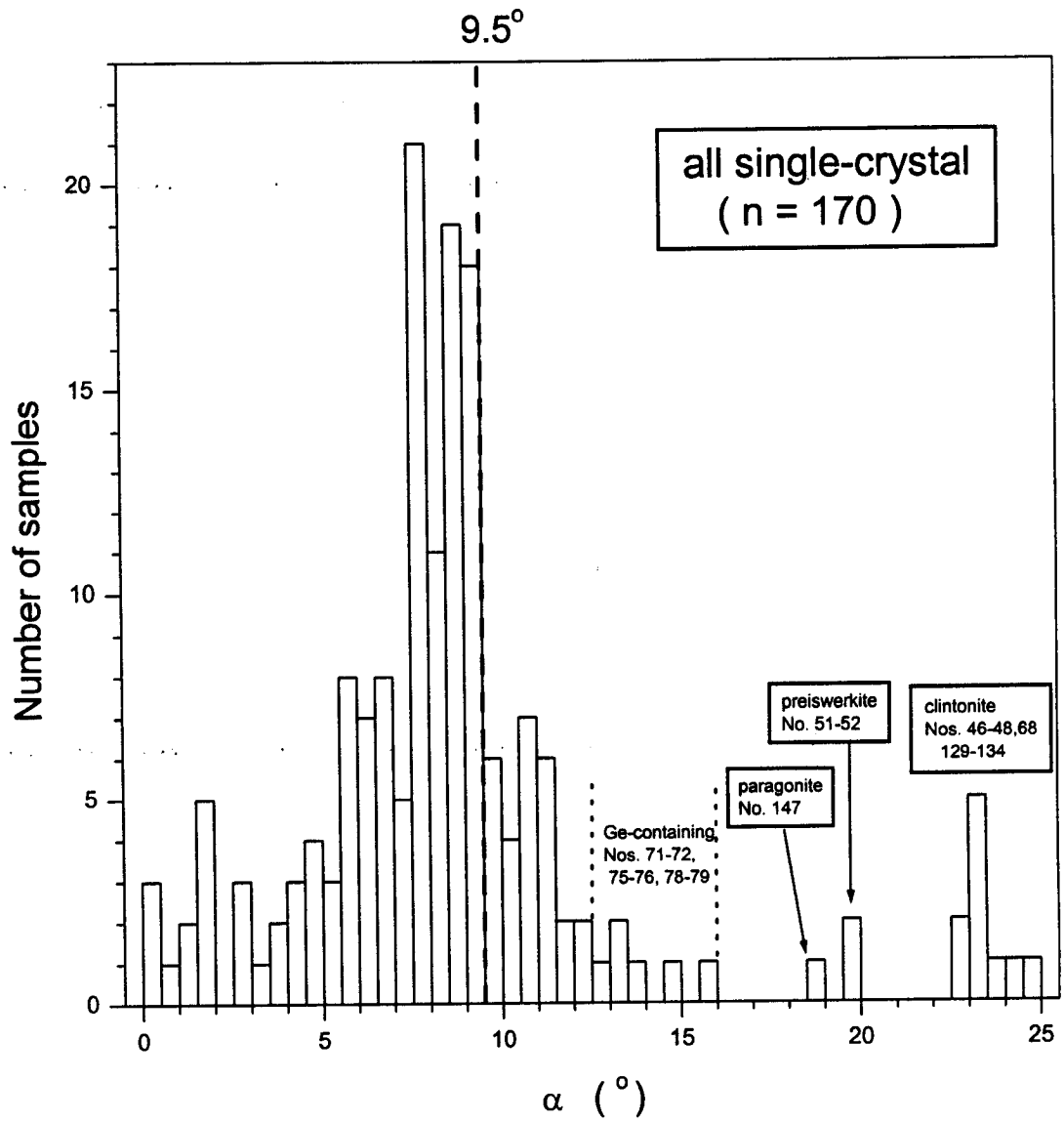

Figure 6.89. Distribution of the average tetrahedral rotation α for the 170 single-crystal samples.

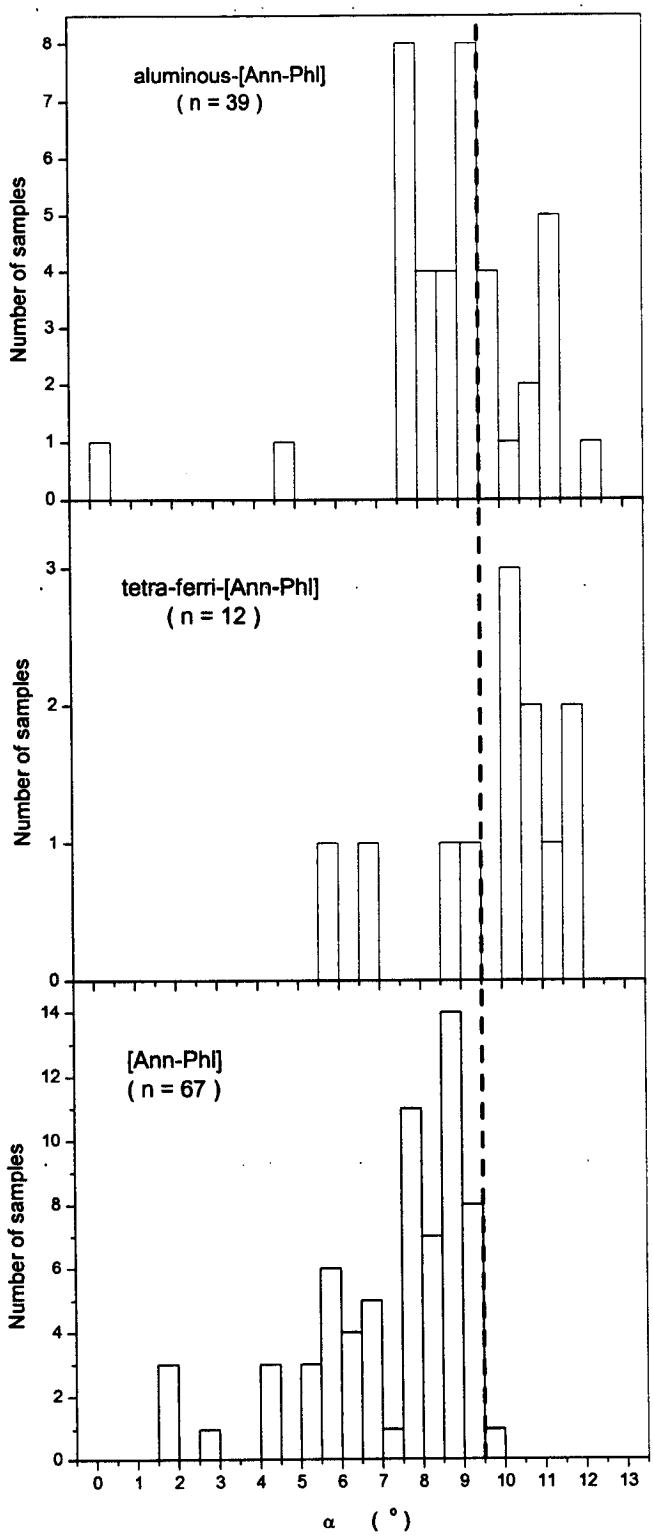

Figure 6.90. Distributions of α for the [Ann-Phl], aluminous-[Ann-Phl], and tetra-ferri-[Ann-Phl] groups of single-crystal samples.

6.4.4 Interlayer bond lengths and interlayer spacings

From an appropriate combination of equations described in Section 6.2:

i) Eqs. 6.3 and 6.12 for octahedral sheets;
ii) Eq. 6.16 (ideal tetrahedron) or Eq. 6.17 (iso-bond-basal-flattened tetrahedron) or Eq. 6.18 (aniso-bond tetrahedron), and Eq. 6.19 for tetrahedral sheets;
iii) Eq. 6.25 for interlayer spacing d_{int}; and
iv) Eq. 6.21 for lattice parameter c;

one can adjust the inner interlayer bond length to the measured c for a given synthetic sample.

In the results that are presented in this subsection, only iso-bond-basal-flattened tetrahedrons were considered in testing.

Figure 6.91 shows the adjusted inner interlayer bond length, $(A\text{-}O)_{in}^{adjusted}$, as a function of the lattice parameter a, for various solid solution series of synthetic powder samples. On the same graph, Figure 6.91 also displays the average inner interlayer bond length, $\langle A\text{-}O\rangle_{in}$, as a function of a for pertinent groups of single-crystal samples. For the Al-rich Fe-Mg RGBr series, Figure 6.91 presents results obtained by assuming two different values of the O_{bas}-T-O_{bas} angle (τ_{bas} = 108.5° and 109.5°), whereas τ_{bas} =108.5° for other solid solution series. In these figures, one notes a complicated behaviour that is hard to understand.

A similar complicated behaviour is observed in Figure 6.92, where calculated interlayer spacing $d_{int}^{calculated}$ and interlayer spacing d_{int} are plotted as function of a, for synthetic powder and pertinent single-crystal samples, respectively.

On the other hand, Figure 6.93 and 6.94 show a linear correlation between: i) the average inner interlayer bond length $\langle A\text{-}O\rangle_{in}$ as function of the average tetrahedral rotation, α, observed for the 170 single-crystal biotite-1M samples (Figure 6.93); and ii) the adjusted inner interlayer bond length, $(A\text{-}O)_{in}^{adjusted}$, as a function of the calculated tetrahedral rotation angle, $\alpha_{calculated}$, for various solid solution series of synthetic powder samples (Figure 6.94).

From this subsection, therefore, one concludes that for a given interlayer cation species, the inner interlayer bond length monotonously increases as the tetrahedral rotation angle α decreases.

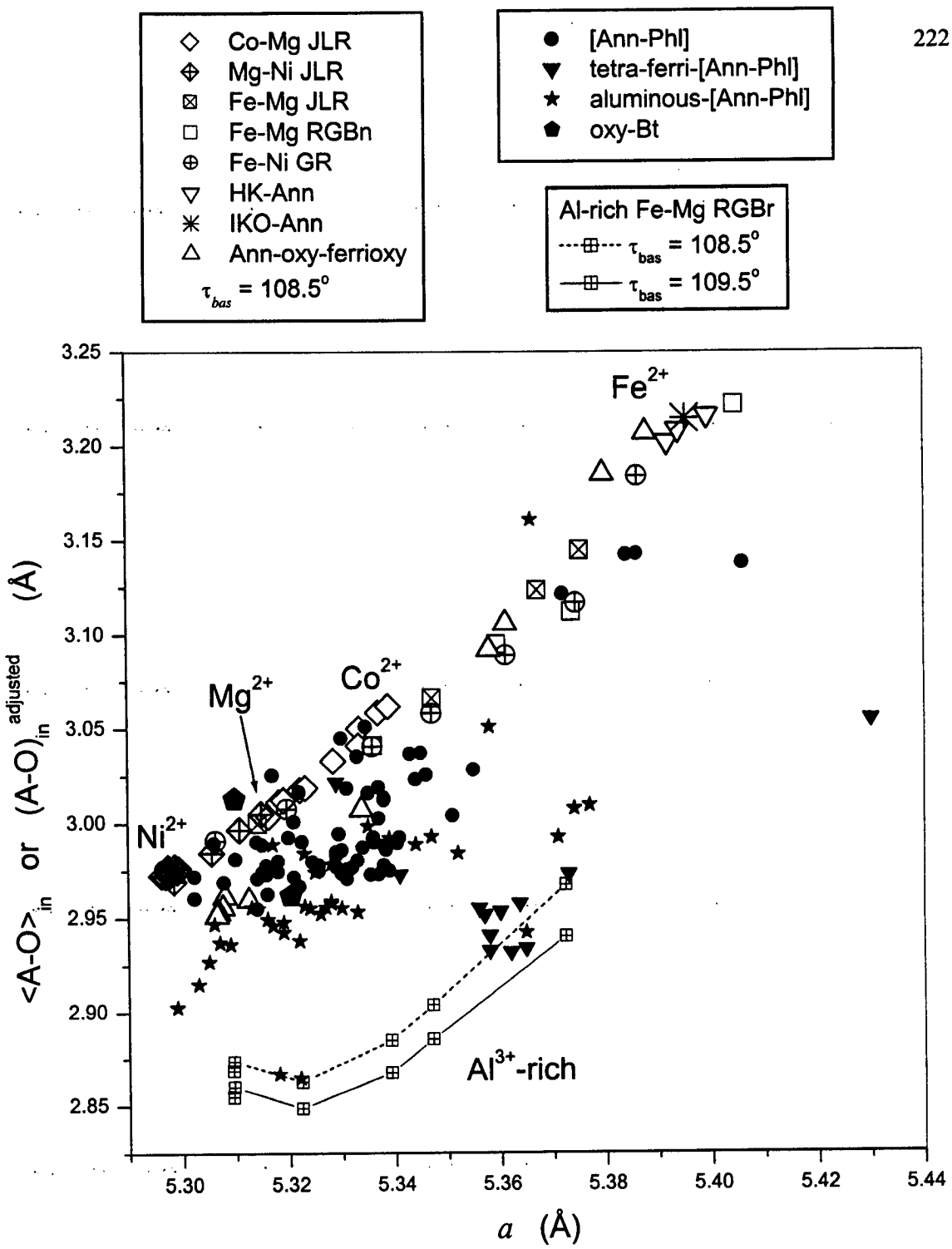

Figure 6.91. Adjusted inner interlayer bond length, $(A\text{-}O)_{in}^{adjusted}$, as a function of the lattice parameter a, for various solid solution series of synthetic powder samples. Also shown is the average inner interlayer bond length, $\langle A\text{-}O\rangle_{in}$, as a function of a for pertinent groups of single-crystal samples.

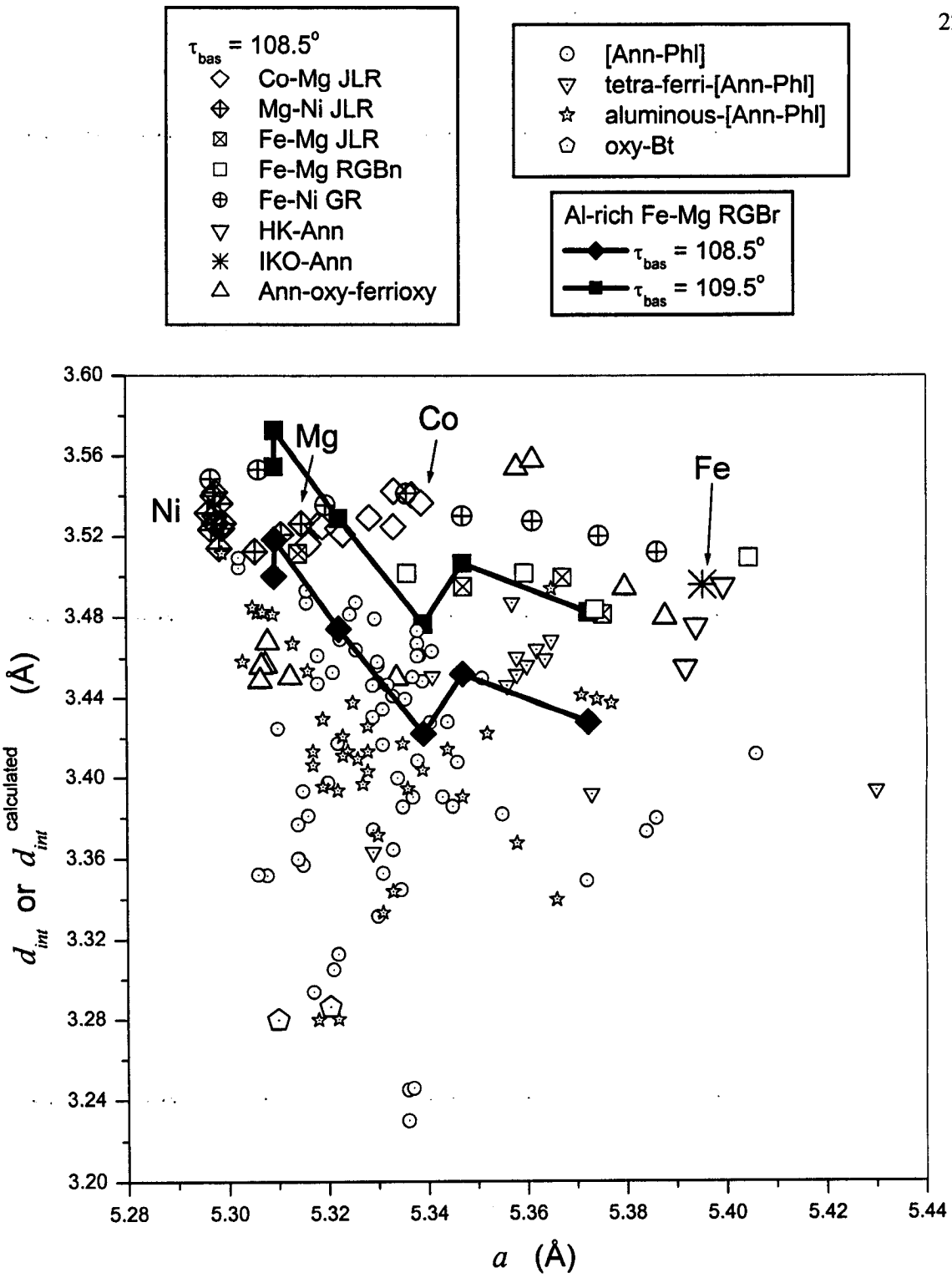

Figure 6.92. Calculated interlayer spacing, $d_{int}^{\text{calculated}}$, and interlayer spacing, d_{int}, as functions of a, for synthetic powder and single-crystal samples, respectively.

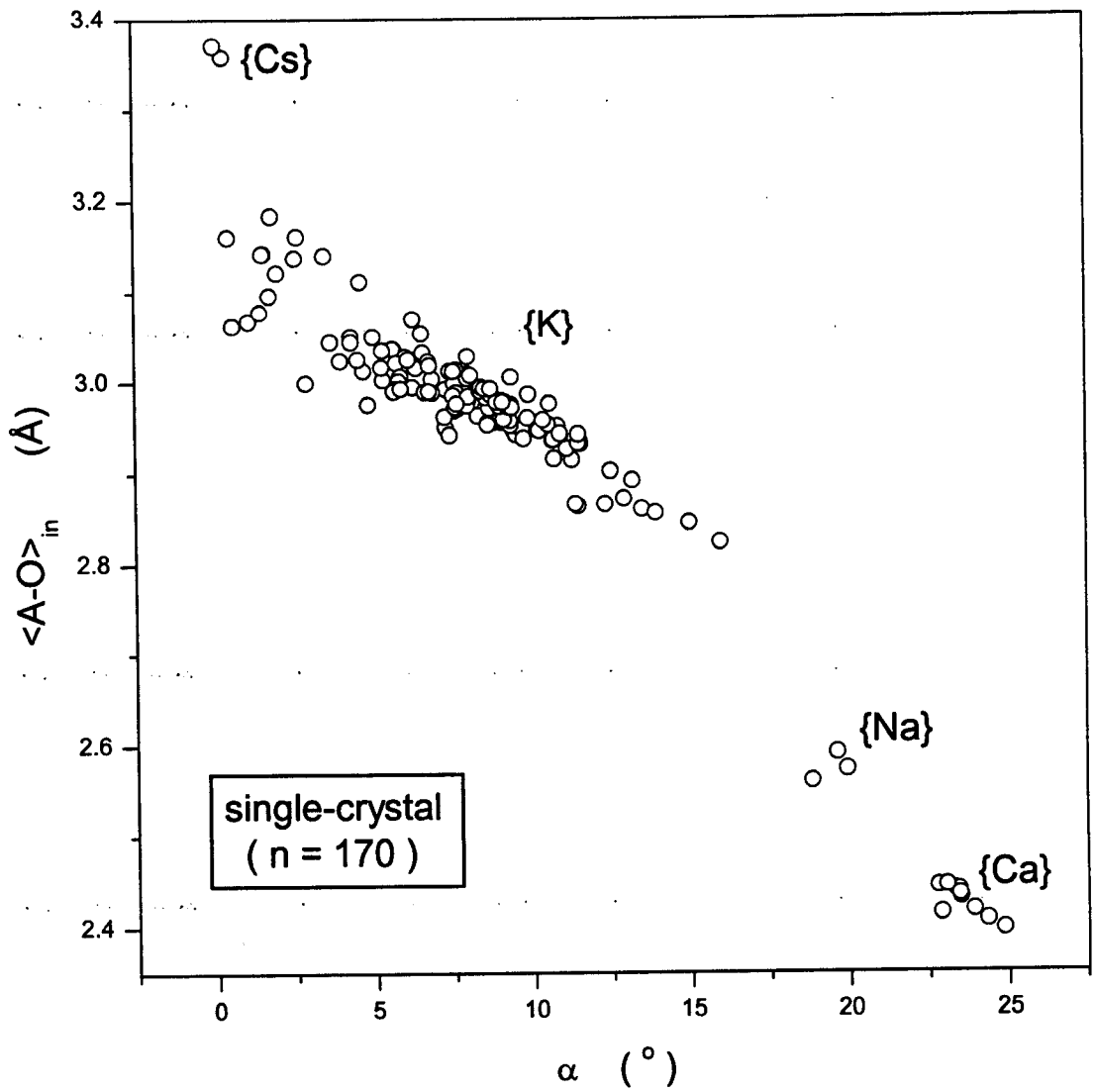

Figure 6.93. Average inner interlayer bond length $\langle A\text{-}O\rangle_{in}$ as function of the average tetrahedral rotation, α, observed for the 170 single-crystal 1*M* samples.

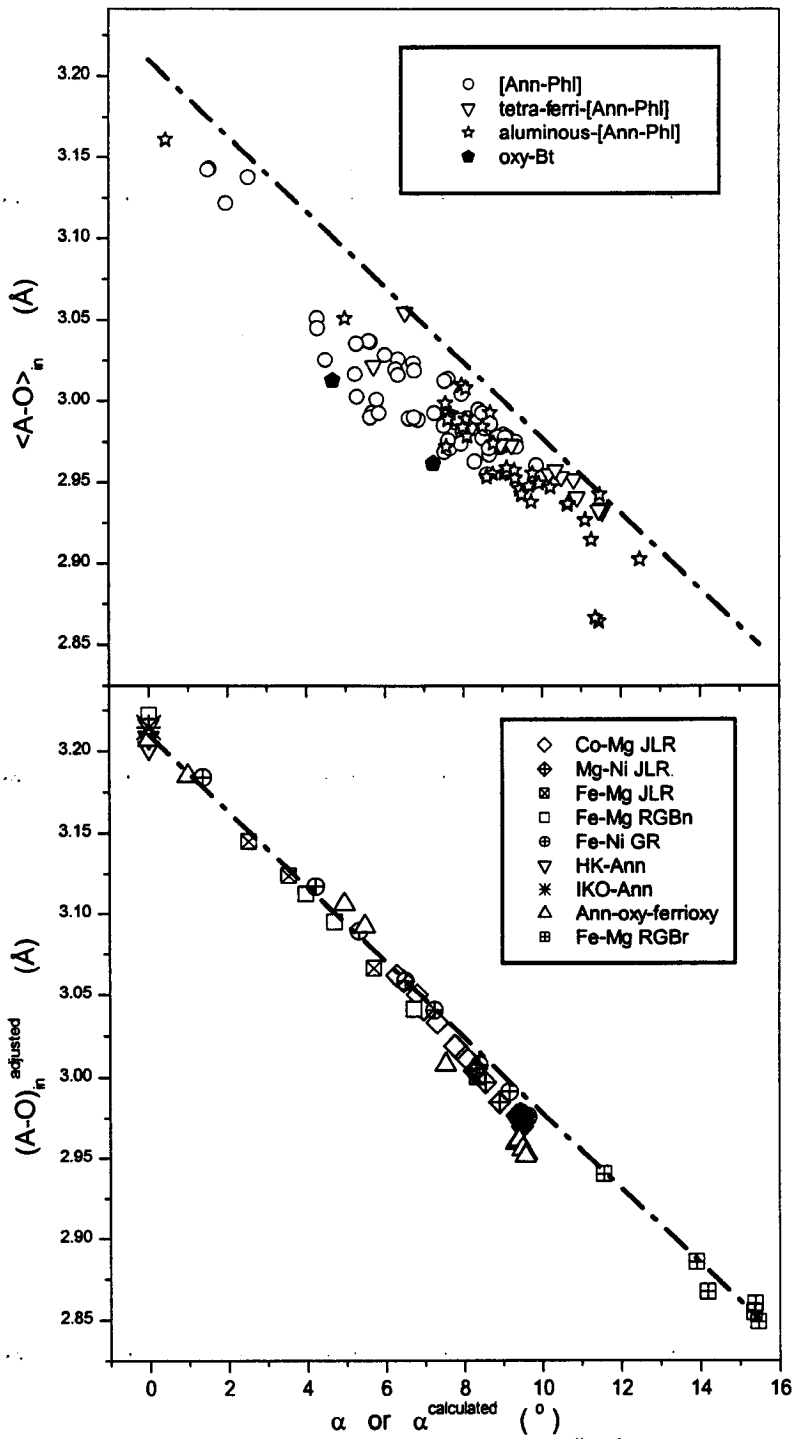

Figure 6.94. Adjusted inner interlayer bond length, $(A\text{-}O)_{in}^{adjusted}$, as a function of the calculated tetrahedral rotation angle, $\alpha_{calculated}$, for various solid solution series of synthetic powder samples. Also shown are inner interlayer bond length, $\langle A\text{-}O\rangle_{in}$, as function of the average tetrahedral rotation, α, for the [Ann-Phl], aluminous-[Ann-Phl], and tetra-ferri-[Ann-Phl] groups of single-crystal samples.

Chapter 7. Discussion

7.1 Rationale of the crystal chemical approach

The ultimate crystal chemical model would predict exactly the atomic coordinates of all atoms in the average unit cell, given the stoichiometry and degree and type of any chemical order. In trioctahedral micas, the large chemical variability of the octahedral, tetrahedral, and interlayer sites complicates the modelling of the crystal structure, as does the inherent misfit between the constituent octahedral and tetrahedral sheets. Moreover, the different crystallographically distinct cationic sites may be occupied by different ion populations either in an ordered or a disordered way, Al^{3+} and Fe^{3+} (and Ti^{4+} ?) may populate both octahedral and tetrahedral sites, and Fe and Mn may be present in different oxidation states (Fe^{2+} and Fe^{3+}; Mn^{2+} and Mn^{3+}). To account for all this complexity, an approach based on a simple conceptual framework is therefore highly desirable.

Following the main premiss of crystal chemistry, we assume that the average cation-anion bond length of a given crystallographically distinct cationic site in the average unit cell is a precise measure of the average chemical composition of that site and its coordinating anions. In contrast, chemical data obtained by electron microprobe analysis (and other analytic methods) are often incorrect because oxidation states, water (hydrogen), and light elements (such as Li) are not directly measured. Nonetheless, all subtleties pertaining to the average cationic contents, the geometries, and the dimensions of the different coordinating polyhedrons in the average unit cell of a given crystallographic structure are reflected in the measured diffraction intensities analysed in a structural refinement.

Consequently, we have adopted an approach where cation-specific bond lengths are used to predict the average bond sizes of the different cationic sites in octahedral and tetrahedral sheets (Subsection 6.4.1), while in the case of interlayer sites, we admit and show that the bond length of a given interlayer cationic species monotonously varies with the tetrahedral rotation angle (see Subsection 6.4.4, as well as Section 7.5 below). In this way, the average bond length of a given cationic site stems directly from its average chemical (cationic) composition.

In the various crystallographic structures of micas, the polyhedrons hosting the cations actually differentiate their bond lengths and angles in different ways depending on the space-group type and the polytype. These adjustments are understood to arise from, at least in part,

internal strains, connected with the presence of chemical composition differences from one unit cell to another in the crystal and to the structural misfit between tetrahedral and octahedral sheets, that depend on temperature and pressure [Ferraris & Vivaldi 2002; Bailey 1984a; Zanazzi & Pavase 2002].

For the above reasons, it is a well known fact that geometric crystal chemical models based on site-specific (uniform) cation-anion bond lengths only approximately give the atomic positions obtained in actual crystal structure refinements of micas. However, the extent to which such models are valid had never been determined or exploited to the extent presented here.

In the remaining of this chapter, we now discuss the main findings that were made following our approach founded on geometric crystal chemical models.

7.2 Fundamental difference between natural and synthetic trioctahedral-1*M* micas: geometric meso-octahedral versus geometric homo-octahedral sheets.

Based on the powder X-ray diffraction measurements of many solid solution series of synthetic powder samples (between Mg, Ni, Co, and Fe end members, with different degrees of oxidation, vacancy, and Al/Si contents, and including an OH/F substitution series; 75 samples indexed as 1*M* polytype, space-group type *C*2/*m*) and on the published crystal structures of 170 trioctahedral-1*M* micas (refined in space-group type *C*2/*m*) comprising both (42) synthetic and (128) natural single-crystal samples, we have shown that the relation

$$(c/a)\cos\beta^* = 1/3$$

holds exactly (within experimental error) for all synthetic powder samples (Figure 6.72, Subsection 6.3.6) whereas it does not hold in general for the natural or synthetic single-crystal samples (Figures 6.69-6.71, Subsection 6.3.6). This relation is not imposed by the *C*2/*m* space-group symmetry.

The $(c/a)\cos\beta^* = 1/3$ relation holds in the crystal structure model proposed by Donnay *et al.* [Donnay *et al.* 1964a] for a 1*M* unit cell of *C*2/*m* space-group symmetry (Eq. 6.20, Subsection 6.2.6), that assumes a geometric homo-octahedral sheet of uniform height in which the bond lengths (and flattening angles) of all octahedral sites are *equal* (Subsection 6.2.2). On the other hand, as explained in Subsection 6.3.5, the $(c/a)\cos\beta^* = 1/3$ relation is not expected to

hold in general when the bond lengths of the *M*1 and *M*2 sites are *unequal* in a 1*M* structure of *C*2/*m* symmetry; the same conclusion was also reached by [Bailey 1984a] following a reasoning similar to ours. We have derived and rigorously validated the latter conclusion by considering the geometric meso-octahedral sheet model of [Evans 2001] (Subsection 6.2.3), which, assuming only a uniform octahedral sheet height, predicts site-specific bond lengths and flattening angles for the *M*1 and *M*2 sites, and a counter-rotation angle for the *M*2 site, δ_{M2}, that is uniquely determined by the bond length difference between the *M*1 and *M*2 sites.

In our analysis, the geometric meso-octahedral character of the 170 trioctahedral-1*M* single-crystals is also corroborated by several parameters of the structure refinements:

1) The normalized squared octahedral size difference $[\langle M1\text{-}O\rangle^2 - \langle M2\text{-}O\rangle^2]/a^2$ variation with the counter-rotation angle δ_{M2} (Figure 6.32, Subsection 6.3.2) exactly (within experimental error) follows our geometric meso-octahedral sheet predictions (Eqs. 6.37 and 6.38, Subsection 6.3.2), for 169 out of 170 trioctahedral-1*M* single-crystals. The only exception corresponds to a norrishite sample that breaks the $b = \sqrt{3} \cdot a$ relationship (Figure 6.3, Subsection 6.1).

2) The normalized in-plane intra-layer displacements between atoms located above and below the octahedral-cation plane (Eqs. 6.49a-6.49e; Figures 6.61 and 6.62) evolve in fair agreement with geometric meso-octahedral predictions (Eqs. 6.35 and 6.48) as a function of the normalized in-plane size difference $[\langle M1\text{-}O\rangle \sin\psi_{M1} - \langle M2\text{-}O\rangle \sin\psi_{M2}]/a$ (Figures 6.63-6.67, Subsection 6.3.5).

We conclude that our synthetic powder samples (usually having particle diameters in the range 0.01-10 μm) are geometric homo-octahedral whereas single-crystals (typical size of 0.05×0.05×0.01 mm or larger) are geometric meso-octahedral. The synthetic powders appear not to have had the time to equilibrate into a minimal free energy state, possibly because average diffusion hoping times occurring in those syntheses (compared to synthesis times) are larger than under synthesis conditions that lead to single-crystals (e.g., fluxing agents used in single-crystal syntheses, geological conditions and large petrogenesis equilibration times of natural samples), whereas all the single-crystal samples have to some extent exploited the free energy advantage of sorting smaller and larger cations into distinct crystallographic sites in a (geometric) meso-octahedral sheet structure. These results suggest further experimental work in which the conditions for and kinetics of meso-octahedral chemical ordering could be studied.

7.3 Factors affecting octahedral sheets in trioctahedral-1*M* micas

Many authors have studied the geometry of cationic sites in the octahedral sheets of trioctahedral-1*M* micas (e.g., [Bailey 1984a; Toraya 1981; Lin & Guggenheim 1983; Weiss *et al.* 1985, 1992; Alietti *et al.* 1995, 1997; Brigatti & Davoli 1990; Brigatti & Poppi 1993; Brigatti *et al.* 1991, 1996b, 2000a, 2000b, 2001; Cruciani & Zanazzi 1994; Brigatti & Guggenheim 2002; Redhammer & Roth 2002]), but so far only a few researchers have emphasized the utility of geometrical models in assessing both the octahedral topology (i.e., the octahedral dimensions and the octahedral distortions) and the complex crystal chemistry of these minerals (e.g., [Hazen & Wones 1972; Hazen & Burnham 1973; Hazen & Finger 1982]).

The exact agreement (within experimental error) of the geometric meso-octahedral sheet model with observations in trioctahedral-1*M* micas of *C*2/*m* symmetry (Eqs. 6.37-6.38; Figure 6.32) permits the identification of two rigorous parameters to quantify or predict the effects of different octahedral cation ordering patterns in these structures: i) the normalized squared octahedral size difference, $[\langle M1\text{-}O\rangle^2 - \langle M2\text{-}O\rangle^2]/a^2$, and ii) the counter-rotation angle of the *M*2 site, δ_{M2} .

The latter two parameters, uniquely related via Eq. 6.37, are dimensionless quantities free from peculiarities due to chemical substitutions. Noting that the flattening angles of *M*1 and *M*2 sites are given by Eq. 6.9, one then has that the flattening angle difference $[\psi_{M1} - \psi_{M2}]$ is also uniquely determined by one of the above parameters.

Several authors have noted correlations between differences of structural parameters characterizing the *M*1 and *M*2 sites in trioctahedral-1*M* micas of *C*2/*m* symmetry [Brigatti & Davoli 1990; Brigatti *et al.* 1991; Redhammer & Roth 2002; Lin & Guggenheim 1983; Alietti *et al.* 1997], but none of them have stressed that such relationships can be explained by geometrical models that admit site-specific uniform bond lengths for *M*1 and *M*2 sites in an octahedral sheet of uniform height. We have demonstrated this for the first time.

Weiss *et al.* [Weiss *et al.* 1985, 1992] have noticed high correlations by plotting absolute differences of ψ angles in a sheet — that is $|\psi_{M1} - \psi_{M2}|$, $|\psi_{M2} - \psi_{M3}|$, and $|\psi_{M3} - \psi_{M1}|$ — against corresponding differences of counter-rotation δ angles. They have also recognized that these correlations were the consequence of the octahedral sheet's uniform thickness but they have only derived linear regression equations that predict ψ and δ angles separately for each site, as functions of the mean bond lengths of the individual octahedral sites. Such an approach cannot possibly predict atomic coordinates correctly, because it does not properly take into account the constraints imposed by the uniform height of the octahedral sheet.

Using the geometric meso-octahedral and geometric hetero-octahedral sheet models of [Evans 2001], we suggest that rigorous geometrical relationships, similar to Eq. 6.37, could also be established for meso-octahedral and hetero-octahedral (dioctahedral or trioctahedral) mica structures of other space-group types and polytypes. The main advantage of the geometrical models of [Evans 2001] is that they directly (and correctly) predict the atomic coordinates in an octahedral sheet of uniform height as a function of site-specific uniform bond lengths, allowing rigorous parameters to be defined to follow octahedral chemical ordering.

The vast majority of the trioctahedral-1*M* micas considered (151 out of 170 samples) have <M1-O> > <M2-O> and $\psi_{M1} > \psi_{M2}$. This has been described as the normal ordering pattern [Toraya 1981; Bailey 1984a; Guggenheim 1984] in which enlargement of *M*1 with respect to *M*2 is believed to be caused by partitioning of high-charge, smaller cations into *M*2, while low-charge, larger cations and vacancies tend to occupy *M*1. This mode of ordering is in agreement with the propositions of [Hazen & Wones 1972], who suggested that octahedral flattening is primarily a function of the mean cation radius [R] inside an octahedron (where [R] is obtained using the cation-specific radii of [Shannon & Prewitt 1969, 1970; Shannon 1976]).

On the other hand, [Lin & Guggenheim 1983] argued that the flattening of each octahedral cationic site in an octahedral sheet is mainly dependent on the field strengths of the neighbouring sites, where the field strength of an individual site is equal to its valence divided by its mean cation radius. Alternatively, [Weiss *et al.* 1985] asserted that the flattening ψ and counter-rotation δ angles of any particular octahedron in a sheet are due to the interaction in the whole sheet rather than in the octahedron alone.

Our results give a different perspective to the above debate regarding the nature of octahedral flattening (cation-specific versus whole-sheet control?). We have shown that plots of lattice parameter *b* versus the average octahedral sheet bond length are particularly instructive and allow the following distinction to be made. Unoxidized synthetic divalent solid solution series (between Mg^{2+}, Ni^{2+}, Co^{2+}, and Fe^{2+}) tend to evolve along constant flattening angle lines as the mean octahedral bond length increases (Figure 6.76, Subsection 6.4.2), whereas trivalent octahedral cation (Fe^{3+} and Al^{3+}) and vacancy bearing synthetic solid solution series (Figure 6.76, Subsection 6.4.2) and natural biotite-1*M* single-crystals (Figure 6.78, Subsection 6.4.2) follow trends with decreasing flattening angles as the average bond length of the sheet increases (see also Figures 6.80-6.81, Subsection 6.4.2).

Given that the geometric homo-octahedral and geometric meso-octahedral sheet models both predict the same constant flattening-angle lines on a graph of *b versus* average-octahedral-bond-length and that both these models accurately predict *b* (Figures 6.30-6.31, Subsection

6.3.2), this means that the scatter in the plot of *b vs.* <M-O> for the biotite-1*M* single-crystals displayed in Figure 6.78 (Subsection 6.4.2) cannot be attributed to octahedral cation ordering, and hence must to a large extent be due to variations in the cationic compositions of the octahedral sheets, that cause different average octahedral flattening angles to occur.

The *b* versus mean-octahedral-bond-length behaviours of synthetic powder samples are consistent with the fact that natural Fe-rich micas tend to have greater octahedral Al^{3+} concentrations as compared to natural phlogopite crystals (e.g., see [Foster 1960; Redhammer & Roth 2002]). Substitution of Al^{3+} for divalent cations in the octahedral sheets of trioctahedral micas accompanies a corresponding substitution of Al^{3+} for Si^{4+} in the tetrahedral sheets. Thus excess Al^{3+} in the annite-phlogopite series has the dual effect of increasing the average bond size of the tetrahedral sheet, while decreasing the average octahedral bond length. Therefore, the octahedral sheets of trioctahedral-1*M* micas are also influenced by the octahedral-to-tetrahedral sheet mismatch, especially in the proximity of a tetrahedral rotation limit. This is discussed further in Section 7.5 below. In this way, a plot of *b versus* average-octahedral-bond-length is a particularly instructive data representation in assessing the average octahedral flattening that results from complex crystal chemical substitutions.

We conclude that the average octahedral flattening of trioctahedral-1*M* micas of *C*2/*m* symmetry is determined by both the octahedral cationic composition and the tetrahedral-to-octahedral sheet mismatch, whereas the individual flattening angles of *M*1 and *M*2 sites depend solely on the degree of octahedral *M*1/*M*2 chemical ordering which occurs. Our crystal chemical analysis is important because it provides rigorous analysis tools (*b vs.* <M-O> graph, $[\langle M1\text{-}O\rangle^2 - \langle M2\text{-}O\rangle^2]/a^2$, δ_{M2}) to accurately follow key crystal chemical parameters (average octahedral flattening, 'geometric' octahedral ordering) that may affect the stability relationships of these micas. For example, the degree of octahedral ordering is an important factor contributing to the overall energy and the stability of a mica structure; this may have important consequences in the formulation of mica-based (single-mineral or multi-mineral) geothermometers and geobarometers [Cruciani & Zanazzi 1994].

7.4 Geometric meso-octahedral 2:1 layer silicates must have corrugated tetrahedral sheets composed of bond-distorted tetrahedrons

In its simplest form, the architecture of the TOT layers in micas and other 2:1 layer silicates is consistent with flat tetrahedral sheets lying on either sides of a flat octahedral sheet. This

assumption is made in most crystal chemical models of layer silicates by providing tetrahedral-to-octahedral sheet matching via tetrahedral rotation, that does not involve out of plane tetrahedral tilting in order to match a given octahedral sheet having some mean octahedral bond length and flattening angle.

Using tetrahedral sheet models involving coplanar basal equilateral faces rotated by a specified tetrahedral rotation angle α (Eqs. 6.15-6.19; Figures 6.8-6.11, Subsections 6.2.4 and 6.2.5) together with the geometric homo- and meso-octahedral sheet models of [Evans 2001] (Subsections 6.2.2 and 6.2.3), we have rigorously demonstrated that flat tetrahedral sheets having tetrahedral apical bonds perpendicular to the *ab*-plane are only possible in 2:1 layer silicates having a geometric homo-octahedral sheet (see explanations related to Figure 6.45, Subsection 6.3.3). This means that via unavoidable structural constraints, *a tetrahedral sheet comprised of coplanar equilateral triangular basal faces cannot be arranged to match a geometric meso-octahedral sheet.*

For a 1*M* structure of *C*2/*m* symmetry, we have shown that a straightforward means to accommodate a geometric meso-octahedral sheet is to have lowered (*M*1 > *M*2) or raised (*M*1 < *M*2) O1 atoms relative to (O2-O2') basal edges (Subsection 6.3.3). [Lee & Guggenheim 1981] and [Appelo 1978] have also recognized that basal-oxygen plane corrugation is an effective way to provide linkage between octahedral and tetrahedral sheets in the presence of differently sized octahedral sites, but they have not demonstrated that such corrugation *must* occur when there is *M*1/*M*2 chemical ordering.

Basal-oxygen plane corrugation (Δz) is small but significant in trioctahedral-1*M* micas of *C*2/*m* symmetry (Figure 6.29, Subsection 6.3.1; Figure 6.32, Subsection 6.3.2), whereas it is much larger in dioctahedral-2M_1 micas having space-group type *C*2/*c*, where usually the *M*1 site is vacant while Al^{3+} occupies the *M*2 site (e.g., see [Bailey 1984; Brigatti & Guggenheim 2002]). A good correlation is observed between Δz and the size difference of *M*1 and *M*2 sites (e.g., plot of $[\langle M1\text{-}O\rangle^2 - \langle M2\text{-}O\rangle^2]/a^2$ *vs.* Δz , Figure 6.44, Subsection 6.3.3; see also [Brigatti & Guggenheim 2002]).

In addition, we have established that basal tetrahedral corrugation cannot simply be accomplished by cooperative tilting of tetrahedrons having a simple geometrical shape, as the tetrahedrons themselves *must* be distorted in the process such as to have isosceles or scalene triangular basal-oxygen faces (Figure 6.45, Subsection 6.3.3), which means that the tetrahedrons require unequal basal bond lengths arising from unavoidable structural constraints. Several tetrahedral distortion parameters of the 170 single-crystal 1*M* refinements also support these findings: i) the progressive widths of the distributions of sample-specific tetrahedral distortion

parameters that characterize the degree to which individual bond lengths, edge lengths, and bond angles differ within a given tetrahedron (Eqs. 6.39-6.39e, Table 6.4, Figures 6.39 and 6.46, Subsection 6.3.3); and ii) the strong correlation between Δz and the tetrahedral bending angle η between the apical bond and the pyramidal base formed by the three basal bonds (Figures 6.42 and 6.43, Subsection 6.3.3).

We conclude that geometric meso-octahedral 2:1 layer silicates must have corrugated tetrahedral sheets composed of bond-distorted tetrahedrons, as we expect similar arguments as those explained above to hold for all types of 2:1 layer silicates where geometric meso-octahedral sheets occur. Since tetrahedral corrugation develops in direct response to the degree to which the size of $M1 \neq M2$ and is well represented as such in the average unit cell, tetrahedral distortions due to corrugation are to be distinguished from local distortions due to local chemical variations caused by Al/Si disorder.

It has been proposed [Appelo 1978, 1979; Abbott & Burnham 1988] that basal-oxygen plane corrugation Δz may control the relative stability of $1M$ and $2M_1$ mica polytypes, the latter becoming energetically favoured when Δz increases. One also expects that the relative stability of mica polytypes is affected by Δz on geometric grounds by considering the interlayer cation configurations which result from Δz in the different homogeneous mica polytypes [Ferraris & Vivaldi 2002; Guven 1971; Takéuchi 1965]. Our results imply that the free energy advantage of sorting smaller and larger cations into differently sized $M1$ and $M2$ sites in a geometric meso-octahedral arrangement must be at least partly compromised by an energy increase associated with bond-distorted tetrahedrons. This could also be an important factor in determining the relative stability of $1M$ and $2M_1$ structures, the two most common mica polytypes.

7.5 Upper limit of tetrahedral rotation in trioctahedral-1*M* K-rich micas

Recently, [Redhammer & Roth 2002] have pointed out that a tetrahedral rotation of about 9.5° seems to be an upper limit for K-rich micas having an $<AlSi_3>$ tetrahedral-sheet composition. An upper limit of the tetrahedral rotation angle α had been proposed by [Hewitt & Wones 1975], who suggested that the size of the interlayer cation may control the maximum amount of tetrahedral rotation that can occur in a stable mica. The latter authors also suggested that the upper limit on α was the reason why Al-substitutions in synthetic biotite solid solutions cease at a tetrahedral composition of $<Al_{1.75}Si_{2.25}>$ and an octahedral composition of $[(Fe,Mg)_{2.25}Al_{0.75}]$ (which is approximately the compositions targeted in the Fe-Mg RGB Al-rich solid solution

series, see Table 3.1).

The crux of the argument of [Hewitt & Wones 1975] was based on calculated α-rotation angles and interlayer K-O bond lengths obtained using the nomogram of [Donnay *et al.* 1964] (their Figure 4), who assumed ideal tetrahedrons (and lattice parameter $\beta = 100°$) in their calculations. The α-rotation and K-O bond lengths that [Hewitt & Wones 1975] hence obtained for their most aluminous synthetic biotites ranged from 12° and 2.89 Å in their Mg-free samples to 14° and 2.77 Å in their Fe-free samples. Given that the accepted range of bond lengths for potassium in 6- to 12-fold coordination indicate that K-O bond lengths nearby the lower limit of 2.76 Å (6-fold) would be relatively unstable [Shannon & Prewitt, 1969, 1970; Shannon 1976], this then led these authors to propose that the interlayer site controls the maximum value of α and thus the maximum amount of Al-substitution, because Al-substitution in trioctahedral biotite enlarges the misfit between the octahedral and tetrahedral sheets and thereby increases the amount of necessary tetrahedral rotation α. However, tetrahedrons of actual biotite are not ideal and this strongly affects calculated α-rotation and interlayer bond lengths (e.g., [Takeda & Morosin 1975]).

The *O-T-O* angles of actual tetrahedrons are affected by both tetrahedral and interlayer contents [Takéuchi 1975; Brigatti & Guggenheim 2002] (see also Figure 6.40, Subsection 6.3.3). In trioctahedral true K-rich micas, the average basal O_{bas}-T-O_{bas} angle $\langle\tau\rangle_{bas}$ decreases as Si^{4+} increases relative to Al^{3+} in the tetrahedral sheet. We have illustrated this effect by plotting the average basal edge length $\langle O\text{-}O\rangle_{bas}$ as a function the average basal bond length $\langle T\text{-}O\rangle_{bas}$ actually refined for the 170 trioctahedral-1*M* mica structures (Figure 6.85, Subsection 6.4.3), in comparison with simple geometrical model $\tau_{bas} = constant$ prediction lines (Eqs. 6.15, Subsection 6.2.4). This convenient data representation allows us to conclude that: i) specific O_{bas}-T-O_{bas} angles are preferred for a given tetrahedral composition in trioctahedral-1*M* true micas (as well as O_{api}-T-O_{bas} angles, via Eq. 6.15; see Figure 6.40, Subsection 6.2.4); and ii) an O_{bas}-T-O_{bas} angle of 108.5° is favoured for K-rich micas having an $\langle AlSi_3\rangle$ tetrahedral sheet.

The inner (i.e., shortest first nearest neighbour) interlayer site bond length of a given cationic species monotonously decreases as the tetrahedral rotation α increases (Figures 6.93-6.94, Subsection 6.4.4), as would be expected since the interlayer-cation coordination progressively goes from 12-fold (α=0°) to 6-fold (α=30°) as a function of α [Weiss *et al.* 1992]. The range of average inner interlayer site bond lengths actually observed in natural biotite-1*M* single-crystals goes from 2.85 to 3.15 Å (Figures 6.91 and 6.94, Subsection 6.4.4), whereas the accepted bond lengths for potassium between 6- and 12-fold coordination range from 2.76 to 3.16 Å [Shannon 1976].

Contrary to [Hewitt & Wones 1975], we find that the smaller K-O bonds do not appear to be constrained by the monotonous interlayer site bond length reduction with increasing tetrahedral rotation. The range of K-O bond lengths that we have obtained from the measured *c* lattice parameters of our synthetic powder samples is also consistent with these findings (Figures 6.91 and 6.94, Subsection 6.4.4). The large K-O bond lengths (~3.22 Å) of our synthetic annite (Fe end-member) samples are not unreasonable considering that natural Fe^{2+}-rich micas usually have a significant content of octahedral Al^{3+} [Foster 1960; Redhammer & Roth 2002], which increases α and thus reduces the K-O bonds. Our synthetic annite samples are actually the most Fe^{2+}-rich, $AlSi_3$ micas one can produce [Redhammer *et al.* 1993; Mercier *et al.* 1996, 1999].

To analyse the structural misfit between octahedral and tetrahedral sheets, we have plotted the evolution of the tetrahedral rotation angle α as a function of the ratio of (mean-octahedral-bond-length)/(mean-basal-tetrahedral-bond-length) for both our synthetic powders and the 170 trioctahedral-1*M* single-crystals (Figures 6.86-6.88, Subsection 6.4.3). From this data representation, in comparison with octahedral and tetrahedral constant-flattening-angle prediction lines (explained in Subsection 6.4.4), we have demonstrated that the plateau of *b* lattice parameters measured in the Mg-Ni JLR solid solutions series actually corresponds to an upper limit of tetrahedral rotation angle at $\alpha \cong 9.5°$.

By chemical substitution of a smaller Ni^{2+} for a larger Mg^{2+} in the octahedral sheets at a constant $<AlSi_3>$ tetrahedral composition, one expects the dimensional tetrahedral-to-octahedral sheet misfit to progressively grow so that α becomes larger as the average octahedral bond size is reduced. Given that the behaviour in *b* is real, therefore, this constitutes the first direct experimental evidence of the existence a lower limit of lateral extension concurrent with an upper limit of α-rotation at a given tetrahedral composition.

The distributions of α for the groups of biotite-1*M* single-crystals having different tetrahedral compositions also support the above findings (Figure 6.90, Subsection 6.4.3): i) an upper limit of $\alpha \cong 9.5°$ occurs in trioctahedral-1*M* K-rich samples having an $<AlSi_3>$ tetrahedral sheet; and ii) the upper limit of α-rotation appears to be tetrahedral composition dependent.

We conclude that the tetrahedral-sheet composition is the main controlling factor for both the *O-T-O* angles and the upper limit of tetrahedral rotation α in trioctahedral-1*M* true micas, whereas the monotonous variation of the inner interlayer site bond length of a given cationic species with α does not appear to be a limiting factor in K-rich micas. In trioctahedral-1*M* K-rich micas having an$<AlSi_3>$ tetrahedral sheet, an O_{bas}-*T*-O_{bas} angle of 108.5° is favoured and an upper limit of tetrahedral rotation of $\alpha \cong 9.5°$ is present in both synthetic powder and natural single-

crystal samples. The presence of well defined limiting upper values of α-rotation as a function of tetrahedral compositions at room temperature may explain the Al-substitution limits in synthetic biotite solid solutions.

Chapter 8. Conclusions

The main conclusions and results of this work are as follows.

- Fractional atomic coordinates were derived in terms of the atomic positions in a 1*M* unit cell of space-group type *C*2/*m* for each known homogeneous mica polytype of ideal space-group type ($2M_1$ and $2M_2$, s.g. *C*2/*c*; 2*O*, s.g. *Ccmm* ; 3*T*, s.g. $P3_112$) (Chapter 4). The coordinates ensure that all TOT layers in each stacking polytype structure are the same 1*M*-type TOT layer, and were used to determine stacking polytype contents in our synthetic powder samples (Subsection 5.2).

- The relationship

$$b = \sqrt{3}a$$

that would rigorously follow from hexagonal symmetry of an octahedral sheet is found to hold within experimental error for all synthetic powder samples studied and for the great majority (231 of 235) of natural and synthetic single-crystal samples (having various degrees of geometric meso-octahedral and geometric homo-octahedral character) and including all stacking polytypes (Figures 6.2 and 6.3, Section 6.1).

- The four noted exceptions to the observed $b = \sqrt{3}a$ rule

  Norrishite sample 1*M* No. 80
  Anandite sample 2*O* No. 2
  Dehydroxylated paragonite sample $2M_1$ No. 26
  Lepidolite sample $2M_1$ No. 33

presumably correspond to deviations from in-plane pseudo-hexagonal symmetry induced for example by chemical order (Section 6.1).

- The relation

$$(c/a)\cos\beta^* = 1/3$$

is found to hold exactly (within experimental error) for all (75) synthetic powder samples (indexed assuming 1*M* stacking polytype, space-group type C2/m) whereas it does not hold in general for the (128) natural and (42) synthetic single-crystal trioctahedral-1*M* mica structural refinements of *C*2/*m* symmetry (Figures 6.69-6.72, Subsection 6.3.6). The latter relation is predicted to hold for geometric homo-octahedral sheets (having equal *M*1 and *M*2 site bond lengths; Subsection 6.2.2) and not to hold for geometric meso-octahedral sheets (having unequal *M*1 and *M*2 site bond lengths; Subsection 6.2.3) (Figure 6.61-6.62, Subsection 6.3.5; Section 7.2).

- Certain in-plane intra-layer displacements within a TOT layer between atoms located above and below the octahedral-cation plane are predominantly a direct consequence of the geometric meso-octahedral character of the octahedral sheets in trioctahedral-1*M* single-crystals (Figures 6.63-6.67, Subsection 6.3.5; Section 7.2).

- All trioctahedral-1*M* mica structural refinements that follow the $b = \sqrt{3}a$ rule have octahedral counter-rotation angles δ_{M2} that exactly (within experimental error) follow the geometric meso-octahedral sheet model, which, assuming only a uniform octahedral thickness and site-specific *M*1 and *M*2 bond lengths, predicts site-specific flattening angles and a counter-rotation angle for the *M*2 site, δ_{M2}, that is uniquely determined by the bond length difference between the *M*1 and *M*2 sites (Subsection 6.2.3; Eqs. 6.37-6.38, Figure 6.32, Subsection 6.3.2; Section 7.3).

- The exact agreement (within experimental error) of the geometric meso-octahedral sheet model with observations in trioctahedral-1*M* micas of *C*2/*m* symmetry (Eqs. 6.37, Figure 6.32, Subsection 6.3.2) permits the identification of two key parameters to quantify or predict the effects of different octahedral *M*1/*M*2 chemical (cationic) ordering patterns in these structures (Section 7.3): i) the normalized squared octahedral size difference, $[\langle M1\text{-}O\rangle^2 - \langle M2\text{-}O\rangle^2]/a^2$, and ii) the counter-rotation angle of the M2 site, δ_{M2}.

- Plots of lattice parameter *b* as a function the mean octahedral cation-anion bond length are particularly instructive and allow the following distinction to be made. Unoxidized synthetic divalent solid solution series (between Mg^{2+}, Ni^{2+}, Co^{2+}, and Fe^{2+}) tend to evolve along constant flattening angle lines as the mean octahedral bond length increases, whereas trivalent octahedral cation (Fe^{3+} and Al^{3+}) and vacancy bearing synthetic solid solution series and natural biotite-1*M* single-crystals follow trends with decreasing flattening angles as the average bond length of the octahedral sheet increases (Figure 6.76-6.78, Subsection 6.4.2; Section 7.3).

- The average octahedral flattening angle of trioctahedral-1*M* micas of *C*2/*m* symmetry is determined by both the octahedral cationic composition and the tetrahedral-to-octahedral sheet mismatch, whereas differences in flattening angles of *M*1 and *M*2 sites depend on the degrees of octahedral *M*1/*M*2 chemical ordering which occur (Section 7.3).

- Flat tetrahedral sheets having tetrahedral apical bonds perpendicular to the *ab*-plane are only possible in 2:1 layer silicates having geometric homo-octahedral sheets. Because of unavoidable structural constraints, a tetrahedral sheet comprised of coplanar equilateral triangular basal faces cannot be arranged to match a geometric meso-octahedral sheet. For a 1*M* structure of *C*2/*m* symmetry, a straightforward means to accommodate a geometric meso-octahedral sheet is to have basal-oxygen plane corrugation. (Figure 6.45, Subsection 6.3.3; Section 7.4)

- The predicted tetrahedral sheet corrugation is seen to be in direct response to the difference in *M*1 and *M*2 bond lengths (Figure 6.44, Subsection 6.3.3) and corresponds to lowering (*M*1 > *M*2) or raising (*M*1 < *M*2) of O1 atoms relative to (O2-O2') basal edges (Figure 6.45, Subsection 6.3.3; Section 7.4).

- Tetrahedral corrugation cannot simply be accomplished by cooperative tilting of tetrahedrons having a 'regular' geometrical shape, as the tetrahedrons themselves *must* be distorted in the process such as to have isosceles or scalene basal-oxygen triangular faces and unequal basal bond lengths arising from unavoidable structural constraints (Figure 6.45, Subsection 6.3.3; Section 7.4).

- The inner (i.e., shortest first near neighbour) interlayer site bond length of a given interlayer cation species monotonously increases as the tetrahedral rotation angle α decreases in trioctahedral-1*M* micas, for both synthetic powders and natural single-crystals (Figures 6.93 and 6.94, Subsection 6.4.4; Section 7.5).

- Specific *O-T-O* angles are preferred for a given tetrahedral sheet composition in trioctahedral-1*M* true micas (Figure 6.40, Subsection 6.3.3; Figure 6.85, Subsection 6.4.3; Section 7.5). For K-rich micas having an $<AlSi_3>$ tetrahedral composition, an O_{bas}-T-O_{bas} angle of 108.5° is favoured and an upper limit of tetrahedral rotation of $\alpha \approx 9.5°$ is present, for both synthetic powders and natural single-crystal samples (Subsection 6.4.3; Section 7.5).

- Other attempts at applying geometric crystal chemical models and at identifying structuro-chemical relationships from structural refinement data will benefit from the perspective of our more complete and systematic approach based on pursuing simple geometrical models using 'regular' coordination polyhedrons and characteristic cation-specific bond lengths up to the limit beyond which such models are shown to necessarily breakdown because of unavoidable 'non-regular' polyhedral distortions.

References

Abbott RN, Burnham CW (1988) Polytypism in micas: A polyhedral approach to energy calculations. American Mineralogist 73:105-118

Ahmedali ST (1989) X-ray fluorescence analysis in the geological sciences : advances in methodology. Short course 7:297 pp.

Alietti E, Brigatti MF, Poppi L (1995) The crystal structure and chemistry of high-aluminum phlogopite. Mineralogical Magazine 59:149-157

Alietti E, Brigatti MF, Poppi L (1997) Clintonite-1*M*: Crystal chemistry and its relationships to closely associated Al-rich phlogopite. American Mineralogist 82:936-945

Amisano-Canesi A, Chiari G, Ferraris G, Ivaldi G, Soboleva SV (1994) Muscovite- and phengite-3*T*: crystal structure and conditions of formation. European Journal of Mineralogy 6:489-496

Appelo CAJ (1978) Layer deformation and crystal energy of micas and related minerals. I. Structural models for 1M and $2M_1$ polytypes. American Mineralogist 63:782-792

Appelo CAJ (1979) Layer deformation and crystal energy of micas and related minerals. II. Deformation of the coordination units. American Mineralogist 63:782-792

Appleman DE, Evan HT (1973) Indexing and least-squares refinements of powder diffraction data. US Geol Surv Comput Contrib 20

Ashcroft NW, Mermin ND (1976) Solid State Physics. 826 pp.

Backhaus KO (1983) Structure refinement of a 1M-lepidolite. Crystal research and technology 18:1253-1260

Bailey S (1984) Micas. Reviews in mineralogy 13: 584 pp.

Bailey S (1984a) Crystal chemistry of the true micas. Reviews in mineralogy 13:13-60

Bailey S (1988a) Hydrous phyllosilicates (exclusive of micas). Reviews in mineralogy 19: 725 pp.

Bailey S (1988b) X-ray diffraction identification of the polytypes of mica, serpentine, and chlorite. Clays and Clay Minerals 36:193-213

Benisek A, Dachs E, Redhammer G, Tippelt G, Amthauer G (1996) Activity-composition relationship in Tschermak's substituted Fe biotites at 700°C, 2 kbar. Contribution to Mineralogy and Petrology 125:85-99

Berman RG, Aranovich YA, Rancourt DG (1995) Phase equilibrium constraints on the stability of biotite. Part 2: Fe-Al biotite in the system K_2O-FeO-Al_2O_3-SiO_2-H_2O. Current Research 1995-E; Geological Survey of Canada, 263-270.

Bigi S, Brigatti MF (1994) Crystal chemistry and microstructures of plutonic biotite. American Mineralogist 79:63-72

Birle JD, Tettenhorst R. (1968) Refined muscovite structure. Mineralogical Magazine 36:883-886

Bloss (1961) An introduction to the method of optical crystallography. Saunders College Publishing 294 pp.

Bohlen SR, Peacor DR, Essene EJ (1980) Crystal chemistry of a metamorphic biotite and its significance in water barometry. American Mineralogist 65:55-62

Brigatti MF, Guggenheim S (2002) Mica Crystal Chemistry and the Influence of Pressure, Temperature, and Solid Solution on Atomistic Models. Reviews in mineralogy and geochemistry 46:1-97

Brigatti MF, Davoli P (1990) Crystal-structure refinements of 1M plutonic biotites. American Mineralogist 75:305-313

Brigatti MF, Frigieri P, Ghezzo C, Poppi L (2000a) Crystal chemistry of Al-rich biotites coexisting with muscovites in peraluminous granites. American Mineralogist 85:436-448

Brigatti MF, Lugli C, Poppi L, Foord EE, Kile DE (2000b) Crystal chemistry variations in Li- and Fe-rich micas from Pikes Peak batholith (central Colorado). American Mineralogist 85:1275-1286

Brigatti MF, Frigieri P, Poppi L (1998) Crystal chemistry of Mg-, Fe-bearing muscovites-2M1. American Mineralogist 83:775-785

Brigatti MF, Galli E, Poppi L (1991) Effect of Ti substitution in biotite-1*M* crystal chemistry. American Mineralogist 76:1174-1183

Brigatti MF, Luca M, Poppi L, Vaccaro C (2001a) Crystal chemistry of trioctahedral micas-1*M* from the alto paranaiba igneous province, southeastern Brasil. Canadian Mineralogist 39:1333-1345

Brigatti MF *et al.* (2001b) Chromium-containing muscovite: crystal chemistry and XANES spectroscopy. European Journal of Mineralogy 13:377-389

Brigatti MF, Lugli C, Poppi L, Elburg Marlina (1998) Crystal chemistry of biotites from mafic enclaves in the Warburton granodiorite, Lachlan Fold Belt (Australia. European Journal of Mineralogy 10:855-864

Brigatti MF, Medici L, Poppi L (1996a) Refinement of the structure of natural ferriphlogopite. Clays and Clay Minerals 44:540-545

Brigatti MF, Medici L, Saccana E, Vaccaro C (1996b) Crystal chemistry and petrological significance of Fe3+-rich phlogopites from the Tapira Carbonatite Complex (Brazil). American Mineralogist 81:913-927 Notes: reviewer's comments of Rancourt and Lalonde also in File, separate.

Brindley GW, Brown G (1984) Crystal Structures of Clay Minerals. Mineralogical Society 495 pp.

Brown BE (1978) The crystal structure of a 3*T* lepidolite. American Mineralogist 63:332-336

Brown I (1977) Predicting Bond Lengths in Inorganic Crystals. Acta Crystallographica B33:1305-1310

Brown I (1987) Recent Developments in the Bond Valence Model of Inorganic Bonding. Phys Chem Minerals 15:30-34

Brown I, Altermatt D (1985) Bond-Valence Parameters Obtained from a Systematic Analysis of the Inorganic Crystal Structure Database. Acta Crystallographica B41:244-247

Burnham CW, Radoslovich EW Refinement of the crystal structures of coexisting muscovite and paragonite. Notes: Thirtennth National Conference on Clays and Clay Minerals.

Burns G, Glazier AM (1990) Space Groups for Solid State Scientists .343 pp.

Catti M, Ferraris G, Hull S, Pavese A (1994) Powder neutron diffraction study of 2*M*1 muscovite at room pressure and at 2 GPa. European Journal of Mineralogy 6:171-178

Catti M, Ferraris G, Ivaldi G (1989) Thermal strain analysis in the crystal structure of muscovite at 700 C. European Journal of Mineralogy 1:625-632

Cheary RW, Coelho AA (1998a) Axial divergence in a conventional X-ray powder diffractometer. I. theoretical foundations. J. Appl. Cryst. 31:851-861

Cheary RW, Coelho AA (1998b) Axial divergence in a conventional X-ray powder diffractometer. II. Realization and evaluation in a fundamental-parameter profile fitting procedure. J. Appl. Cryst. 31:862-868

Cheary RW, Coelho AA (1992) A fundamental parameters approach to X-ray line-profile fitting. J. Appl. Cryst. 25:109-121

Chou I (1987b) Calibration of the graphite-methane buffer using the f_{H2} sensors at 2-kbar pressure. American Mineralogist 72:76-81

Chou I (1987a) Oxygen Buffer and Hydrogen Sensor Techniques at Elevated Pressures and Temperatures. Hydrothermal Experimental Techniques 61-99

Chou I-M (1997) The use and misuse of the of the fH2 sensors: a discussion of the paper by Dachs (1994). Contribution to Mineralogy and Petrology 128:302-305

Chou I-M, Cygan GL (1990) Auantative redox control and measurements in hydrothermal experiments. Fluid-mineral interactions: a tribute to H.P. Eugster, J.Spencer and I.-M. Chou (ed.) The Geochemical Society, Special Publication no.23-15

Comodi P, Zanazzi PF (2000) Structural thermal behavior of paragonite and its dehydroxylate: a high-temperature single-crystal study. Phys Chem Minerals 27:377-385

Comodi P, Zanazzi PF, Weiss Z, Rieder M, Drabek M (1999) "Cs-tetra-ferri-annite:" High-pressure and high temperature behavior of a potential nuclear waste disposal phase. American Mineralogist 84:325-332

Cowley JM (1995) Diffraction Physics.431 pp.

Cruciani G, Zanazzi PF (1994) Cation partitioning and substitution mechanisms in 1M phlogopite: A crystal chemical study. American Mineralogist 79:289-301

Cygan GL, Chou IM, Sherman DM (1996) Reinvestigation of the annite = sanidine + magnetite + H2 reaction using the f_{H2}-sensor technique. American Mineralogist 81:475-484

Dachs (1994) Annite stability revised. 1. Hydrogen-sensor data for the reaction, annite = sanidine + magnetite +H2O. Contribution to Mineralogy and Petrology 117:229-240

Dachs E, Benisek A (1997) Annite stability revised: hydrogen-sensor data for the reaction annite = sanidine + magnetite + H2: additional results and reply to Chou. Contribution to Mineralogy and Petrology306-311

Diaz PM (1999) Étude des interactions cations compensateurs / feuillets dans les argiles : contribution a la connaissance des mécanismes de rétention sélective.135 pp.

Donnay G, Donnay J, Takeda H (1964a) Trioctahedral One-Layer Micas. II. Prediction of the Structure from Composition and Cell Dimensions. Acta Crystallographica 17:1374-1381

Donnay G, Morimoto N, Takeda H, Donnay JDH (1964b) Trioctahedral one-layer micas. I. Crystal structure of a synthetic iron mica. Acta Crystallographica 17:1369-1373

Drits V (1969) Some general remarks on the structure of trioctahedral micas. Proc 4th International Clay Conference, Tokyo51-59

Drits VA, Tcoubar C (1990) X-Ray Diffraction by Disordered Lamellar Structures. Springer-Verlag371

Durovic S, Weiss Z, Backhaus K-O (1984) Polytypism of micas. II. Classification and abundance of MDO polytypes. Clays and Clay Minerals 32:464-474

Eugster H (1957) Heterogenous reactions involving oxydation and reduction at high pressures and temperatures. Journal of Chemical Physics 26:1760-1761

Eugster H, Skippen GB (1967) Igneous and metamorphic reactions involving gas equilibria. Researches in Geochemistry, P.H. Abelson (ed.). John Wiley and Sons377-396

Eugster H, Wones D (1965) Stability of biotite: Experiment, theory and application. Physics and Chemistry of Minerals 50:1228-1272

Eugster H, Wones D (1962) Stability Relations of the Ferruginous Biotite, Annite. Journal of Petrology 3:82-125

Evans RJ (2001) The Electric Field Gradient of Octahedral Fe^{2+} in Layer Silicates. M.Sc. Thesis. University of Ottawa, Canada 210 pp.

Ferraris G, Gula A, Ivaldi G, Nespolo M, Sokolova E, Uvarova Y, Khomyakov AP (2001) First structure determination of an MDO-2*O* mica polytype associated with a 1*M* polytype. European Journal of Mineralogy 13:1013-1023

Ferraris G, Ivaldi G (2002) Structural Features of Micas. Reviews in mineralogy and geochemistry 46:117-153

Filut MA, Rule AC, Bailey SW (1985) Crystal structure refinement of anandite-2*O*r, a barium- and sulfur-bearing trioctahedral mica. American Mineralogist 70:1298-1308

Foster (1960) Interpretations of the composition of Trioctahedral micas. U.S. Geol. Surv. Prof. Pap. 354B:11-46

Franzini M, Schiaffino L (1963) On the crystal structure of bioties. Zeischrift für Kristallographie Bd.119:297-309

Franzini M (1969) The A and B Mica Layers of the Crystal Structure of Sheet Silicates. Contribution to Mineralogy and Petrology 21:203-224

Freiman SW, Trahey NM (2000a) Standard Reference Material 640c.

Freiman SW, trahey NM (2000b) Standard Reference Material Certificate 660a.

Giacovazzo C (1992) Fundamentals of Crystallography. International Union of Crystallography; Oxford University Press 654 pp.

Gilkes R, Young R, Quirk J (1972) The oxidation of octahedral iron in biotite. Clays Clay Minerals 20:303-315

Giuseppetti G, Tadini C (1972) The crystal structure of 2 *O* brittle mica: anandite. Tschermaks Min. Petr. Mitt. 18:169-184

Goldstein *et al.* (1992) Scanning Electron Microscopy and X-Ray Microanalysis. Plenum Press 820 pp.

Guggenheim S (1981) Cation ordering in lepidolite. American Mineralogist 66:1221-1232

Guggenheim S (1984) The Brittle Micas. Reviews in Mineralogy 13: 61-104

Guggenheim S, Bailey SW (1975) Refinement of the Margarite Structure in Subgroup Symmetry. American Mineralogist 60:1023-1029

Guggenheim S, Bailey SW (1977) The refinement of zinnwaldite-1M in subgroup symmetry. American Mineralogist 62:1158-1167

Guggenheim S, Chang Y-H, van Groos AFF (1987) Muscovite dehydroxylation: High-temperature studies. American Mineralogist 72:537-550

Guggenheim S, Frimmel HE (1999) Ferrokinoshitalite, a new species of brittle mica from the broken hill mine, South Africa: structural and mineralogical characterization. Canadian Mineralogist 37:1445-1452

Guidotti C, Cheney J, Conatore P (1975) Interrelationship between Mg/Fe Ratio and Octahedral Al Content in Biotite. American Mineralogist 60:849-853

Guidotti C, Mazzoli C, Sassi F, Blencoe J (1992) Compositional controls on the cell dimensions of 2M1 muscovite and paragonite. European Journal of Mineralogy 4:283-297

Guidotti C, Sassi F, Blencoe J (1989) Compositional controls on the a and b cell dimensions of 2M1 muscovite. European Journal of Mineralogy 1:71-84

Guinier A (1963) X-Ray Diffraction, In Crystals, Imperfect Crystals, and Amorphous Bodies .378 pp.

Guven N (1971) The crystal structures of $2M_1$ phengite and $2M_1$ muscovite. Zeitschrift fur Kristallographie 134:198-212

Guven N, Burnham CW (1967) The crystal structure of 3*T* muscovite. Zeitschrift fur Kristallographie 125:163-183

Hamilton DL, Henderson CMB (1968) The preparation of silicate compositions by gelling method. Mineralogical Magazine 36:832-838

Hawthorne FC, Teertstra DK, Cerny P (1999) Crystal-structure refinement of a rubidian cesian phlogopite. American Mineralogist 84:778-781

Hazen RM, Wones DR (1978) Predicted and observed compositional limits of trioctahedral micas. American Mineralogist 63:885-892

Hazen RM, Wones DR (1972) The effect of cation substitutions on the physical properties of trioctahedral micas. American Mineralogist 57:103-129

Hazen RM, Burnham CW (1973) The Crystal Structures of One-Layer Phlogopite and Annite. American Mineralogist 58:889-900

Hazen RM, Finger LW, Velde D (1981) Crystal structure of a silica- and alkali-rich trioctahedral mica. American Mineralogist 66:586-591

Hewitt DA, Wones DR (1975) Physical Properties of Some Synthetic Fe-Mg-Al Trioctahedral Biotites . American Mineralogist 60:854-862

Huebner JS (1971) Buffering Techniques for Hydrostatic Systems at Elevated Pressures. Research Techniques for High Pressure and High Temperature123-177

Huebner JS, Sato M (1970) The oxygen fugacity-temperature relationships of manganese oxyde and nickel-nickel oxyde buffers. American Mineralogist 55:377-396

Ivaldi G, Ferraris G, Curetti N, Compagnoni R (2001) Coexisting 3*T* and 2 *M*1 polytypes of phengite from Cima Pal (Val Savenca, western Alps): Chemical and polytypic zoning and structural characterisation. European Journal of Mineralogy 13:1025-1034

James RW (1948) The optical principles of the diffraction of X-Rays. The Crystalline State II:622 pp.

Jenkins R, Snyder RL (1996) Introduction to X-Ray Powder Diffractometry.403 pp.

Joswig W (1972) Neutronenbeugungsmessungen an einem 1M-Phlogopit. N. Jb. Mineral. Mh.1-11

Kato T, Miura Y, Yoshii M, Maeda K (1979) The crystal structures of 1M-kinoshitalite, a new barium brittle mica and 1M-manganese trioctahedral micas. Mineralogical Journal 9:392-408

Kittel C (1986) Intorduction to Solid State Physics. Wiley, New York

Klug HP, Alexander LE (1974) X-Ray Diffraction Procedures, For Polycrystalline and Amorphous Materials.966 pp.

Knurr RA, Bailey SW (1986) Refinement of Mn-substituted muscovite and phlogopite. Clays and Clay Minerals 34:7-16

Kogure T, Banfield F (2000) New insights into the mechanism for chloritization of biotite using polytype analysis. American Mineralogist 85:1202-1208

Kogure T, Nespolo M (1999) First occurence of a stacking sequence including (+/- 60o, 180o) rotations in Mg-rich annite. Clays and Clay Minerals 47:784-792

Kraus W, Nolze G (1996) Powder cell - a program for the representation and manipulation of crystal structures and calculation of the resulting X-ray powder patterns. J. Appl. Cryst. 29:301-303

Lalonde A, Rancourt D, Chao G (1996) Fe-bearing trioctahedral micas from Mont Saint-Hilaire, Québec, Canada. Mineralogical Magazine 60:447-460

Langford JI, Louër D (1996) Powder Diffraction. Prog. Phys. 59:131-234

Lee HL, Guggenheim S (1981) Single crystal refinement of pyrophyllite-1*Tc*. American Mineralogist 66:350-357

Lifshin E (1992) Characterization of materials.

Lin C-Y, Bailey SW (1984) The crystal structure of paragonite-2M1. American Mineralogist 69:122-127

Lin J-C, Guggenheim S (1983) The crystal structure of Li,Be-rich brittle mica : a dioctahedral-trioctahedral intermediate. American Mineralogist 68:130-142

Lister JS, Bailey SW (1967) Chlorite polytypism: IV. Regulaer two-layer structures. American Mineralogist 52:1614-1631

MacKinney JA, Mora CI, Bailey SW (1988) Structure and crystal chemistry of clintonite. American Mineralogist 73:365-375

McCauley J, Newnham R (1971) Origin and prediction of ditriogonal distortions in micas. American Mineralogist 56:1626-1638

McCauley JW, Newnham RE (1973) Structure refinement of a barium mica. Zeitschrift fur Kristallographie 137:360-367

McCauley JW, Newnham RE, Gibbs GV (1973) Crystal structure analysis of synthetic fluorophlogopite. American Mineralogist 58:249-254

Mercier PHJ (1996) An 57-Fe Mössbauer spectroscopy study of the effects of different equilibration temperatures and oxygen fugacity buffers on the Fe^{2+} and Fe^{3+} site populations in synthetic annite mica. M.Sc. Thesis 141pp.

Mercier PHJ, Rancourt DG, Berman RG, Robert J-L (1999) Control of site population, at synthesis, by inter-sheet thermal expansion in a 2:1 layer silicate. In: Clays for our future. Proceedings of the 11th International Clay Conference p. 221-227

Mercier PHJ, Rancourt DG, Berman RG (1996) Aspects of the crystal chemistry of annite mica. Conference Proceedings, Volume 50, International Conference on the Application of the Mössnauer Effect, ICAME-1995. I. Ortalli (Ed.), Italian Physical Society, p. 789-792

Merlino S (1997) Modular Aspects of Minerals. European Mineralogical Union Notes in Mineralogy 1: 448 pp.

Mizota T, Kato T, Harada K (1986) The crystal structure of masutomilite, Mn analogue of zinnwaldite. Mineralogical Journal 13:13-21

Mottana A, Sassi FP, Thompson JB, Guggenheim S (2002) Micas: Crystal Chemistry and Metamorphic Petrology. Reviews in mineralogy and geochemistry 46: 499 pp.

Nespolo M (1999) Analysis of family reflections of OD mica polytypes, and its application to twin identification. Mineralogical Journal 21:53-85

Nespolo M (2001) Perturbative theory of mica polytypism. Role of the M2 layer in the formation of inhomogeneous polytypes. Clays and Clay Minerals 49:1-23

Nespolo M, Durovic S (2002) Crystallographic Basis of Polytypism and Twinning in Micas. Reviews in Mineralogy and Geochemistry 46:155-279

Nespolo M, Ferraris G, Takeda H (2000) Identification of two allotwins of mica polytypes in reciprocal space through the minimal rhombus unit. Acta Crystallographica B56:639-647

Nespolo M, Kogure T (1998) On the indexing of 3T mica polytype. Z.Kristallogr. 213:

Nespolo M, Takeda H, Ferraris G (1997a) Crystallography of mica polytypes. EMU Notes in Mineralogy 1: 81-118

Nespolo M, Takeda H, Ferraris G, Kogure T (1997b) Composite twins of 1M mica: derivation and identification. Mineralogical Journal 19:173-186

Novak M *et al.* (1999) Boron-bearing 2*M*1 polylithionite and 2*M*1+1*M* boromuscovite from an elbaite pegmatite at Recice, western Moravia, Czech Republic. European Journal of Mineralogy 11:669-678

Oberti R, Ungaretti L, Tlili A, Smith DC, Robert J-L (1993) The crystal structure of preiswerkite. American Mineralogist 78:1290-1298

Ohta T, Takeda H, Takeuchi Y (1982) Mica polytypism: similarities in the crystal structures of coexisting 1M and 2M1 oxybiotite. American Mineralogist 67:298-310

Pabst A (1955) Redescription of the single layer structure of the micas. American Mineralogist 40:967-975

Pauling L (1960) The nature of the chemical bond and the structure of molecules and crystals: An introduction to modern structural chemistry.505-563

Pauling L (1930) The structure of the micas and related minerals. Proceedings of the National Academy of Sciences 16:123-129

Pavese A, Ferraris G, Pischedda V, Ibberson R (1999) Tetrahedral order in phengite 2*M*1 upon heating, from powder neutron diffraction, and thermodynamic consequences. European Journal of Mineralogy 11:309-320

Pavese A, Ferraris G, Prencipe M, Ibberson R (1997) Cation site ordering in phengite 3*T* from the Dora-Maira massif (western Alps): a variable-temperature neutron powder diffraction study. European Journal of Mineralogy 9:1183-1190

Pavlishin VI, Semenova TF, Rozhdestvenskaya IV (1981) Protolithionite-3*T*: the structure, typomorphism and practical importance. Mineral. Zhurnal 3:47-60

Plançon A (1981) Diffraction by Layer Structures Containing Different Kinds of Layers and Stacking Faults. J. Appl. Cryst. 14:300-304

Press WH, Flannery BP, Teukolsky SA, Vetterling WT (1986) Numerical Recipes. Cambridge University Press

Radoslovich (1961) Surface symmetry and cell dimensions of layer-lattice silicates. Nature 191:67-68

Radoslovich E (1963) The cell dimensions and symmetry of layer-lattice silicates IV: interatomic forces. American Mineralogist 48:76-98

Radoslovich E (1962) The cell dimensions and symmetry of layer-lattice silicates, regression relations. American Mineralogist 48:617-635

Radoslovich E, Norrish K (1962) The cell dimensions and symmetry of layer-lattice silicates, some structural considerations. American Mineralogist 47:599-616

Radoslovich EW (1960) The structure of muscovite, KAl2(Si3Al)O10(OH)2. Acta Crystallographica 13:919-932

Ramsdell LS (1947) Studies on silicon carbide. American Mineralogist 32:64-82

Rancourt DG (1989) Accurate site populations from Mössbauer spectroscopy. Nuclear Instruments and Methods in Physics Research B44:199-210

Rancourt DG (1996) Analytic methods for Mössbauer spectral analysis and complex materials. Mössbauer Spectroscopy Applied to Magnetism and Materials Science105-124

Rancourt DG (1998) Mössbauer spectroscopy in clay science. Hyperfine Interactions 114:3-38

Rancourt DG (1994b) Mössbauer Spectroscopy of Minerals. III. Octahedral-site Fe^{2+} Quadrupole Splitting Distributions in the Phlogopite-Annite Series. Physics and Chemistry of Minerals 21:258-267

Rancourt DG *et al.* (1994a) Determination of accurate $^{[4]}Fe^{3+}$, $^{[6]}Fe^{3+}$, and $^{[6]}Fe^{2+}$ site populations in synthetic annite by Mössbauer spectroscopy. American Mineralogist 79:51-62

Rancourt DG, Mercier PHJ, Cherniah DJ, Desgreniers S, Hodama H, Robert J-L, Murad E (2001) Mechanisms and crystal chemistry of oxydation in annite: resolving the hydrogen-loss and vacancy reactions. Clays and Clay Minerals 49:455-491

Rancourt DG, Ping JY (1991) Voigt-based methods for arbitrary-shape static hyperfine parameter distributions in Mössbauer spectroscopy. Nuclear Instruments and Methods in Physics Research 8:85-87

Rancourt DG, Ping JY, Boukili B, Robert JL (1996) Octahedral-site Fe^{2+} quadrupole splitting distributions from Mössbauer spectroscopy along the (OH, F)-annite series. Physics and Chemistry of Minerals 23:63-71

Rancourt DG, Tume P, Lalonde A (1993) Kinetics of the $(Fe^{2+}+OH^{-})_{mica}$ –> $(Fe^{3+}+O^{2-})_{mica}+H$ Oxidation Reaction in Bulk single-Crystal Biotite studied by Mössbauer Spectroscopy. Phys Chem Minerals 20:276-284

Rasberry SD (1987) Standard Reference Material Certificate 640b.

Rayner JH (1974) The crystal structure of phlogopite by neutron diffraction. Mineralogical Magazine 39:850-856

Redhammer G (1998) Characterization of synthetic trioctahedral micas by Mössbauer spectroscopy, special issure of Hyperfine Interaction entitled Mössbauer Spectroscopy in Clay Science, edited by D.G. Rancourt.

Redhammer G, Beran E, Dachs E, Amthauer G (1993) A Mössbauer and X-ray diffraction study of annites synthesized at different oxygen fugacities and crystal chemical implications. Phys Chem Minerals 20:382-394

Redhammer G, Roth G (2002) Single-crystal structure refinements and crystals chemistry of synthetic trioctahedral micas $KM_3(Al^{3+}, Si^{4+})_4O_{10}(OH)_2$, where $M=Ni^{2+}$, Mg^{2+}, Co^{2+},Fe^{2+}, or Al^{3+}. American Mineralogist 87:1464-1476

Redhammer GJ, Beran A, Schneider J, Amthauer G, Lottermoser W (2000) Spectroscopic and structural properties of synthetic micas on the annite-syderophyllite binary: synthesis, crystal structure refinements, Mossbauer, and infrared spectroscopy. American Mineralogist 85:449-465

Reynolds RC (1985) NEWMOD, a Computer Program for the Calculation of Basal X-Ray Diffraction Intensities of Mixed-Layered Clays.

Richardson SM, Richardson Jr. JW (1982) Crystal structure of a pink muscovite from Archer's Post, Kenya: implications for reverse pleochroism in dioctahedral micas. American Mineralogist 67:69-75

Rieder M *et al.* (1998) Nomenclature of the micas. Clays and Clay Minerals 46:586-595

Robert J-L, Gaspérin M (1985) Crystal Structure Refinement of Hendricksite, a Zn- and Mn-rich Trioctahedral Potassium Mica: a Contribution to the Crystal Chemeistry of Zinc-Bearing Minerals. Tschermaks Min. Petr. Mitt. 34:1-14

Robert J-L, Volfinger M, Barrandon J-N, Basutçu M (1983) Lithium in the interlayer space of synthetic trioctahedral micas. Chemical Geology 40:337-351

Ross M, Takeda H, Wones D (1966) Mica polytypes: Systematic description and identification. Science 151:191-193

Royer M (1991) Site-specific 57-Fe Mössbauer recoiless fractions in true tri-octahedral micas. M.Sc. Thesis. University of Ottawa, Canada

Rule AC, Bailey SW, Livi KJT, Veblen DR (1987) Complex stacking sequences in a lepidolite from Tordal, Norway. American Mineralogist 72:1163-1169

Rule AC, Bailey SW (1985) Refinement of the crystal structure of phengite-2M1. Clays and Clay Minerals 33:403-409

Russell R, Guggenheim S (1999) Crystal structures of near-end-member phlogopite at high temperatures and heat-treated Fe-rich phlogopite: The influence of the O,OH,F site. Canadian Mineralogist 37:711-720

Sartori F (1976) The crystal structure of a 1M lepidolite. Tschermaks Min. Petr. Mitt. 23:65-75

Sartori F (1977) The crystal structure of a 2M1 lepidolite. Tschermaks Min. Petr. Mitt. 24:23-37

Sartori F, Franzini M, Merlino S (1973) Crystal structure of a 2M2 lepidolite. Acta Crystallographica 29:573

Schairer JF, Bowen NL (1955) The system K_2 0-Al_2O_3-SiO_2. American Journal of Science 253:681-746

Semenova TF, Rozhdestvenskaya IV, Frank-Kamenetskii VA (1977) Refinement of the crystal structure of tetraferriphlogopite. Kristallografiya 22:1196-1201

Semenova TF, Rozhdestvenskaya IV, Frank-Kamenetskii VA, Pavlishin VI (1983) Crystal structure of tetraferriphlogopite and tetraferribiotite. Mineral. Zhurnal 5:41-49

Shannon R.D. (1976) Revised effective ionic radii and systematic studies of interatomic distances in halides and chalcogenides. Acta Crystallographica A32:751

Shannon R.D., Prewitt CT (1969) Effective ionic radii in oxides and fluorides. Acta Crystallographica B25:925

Shannon R.D., Prewitt CT (1970) Revised values of effective ionic radii. Acta Crystallographica B26:1046

Sidorenko DV, Zvyagin BB, Soboleva SV (1977) The crystal structure of 3*T* paragonite. Kristallografiya 22:976-981

Sidorenko DV, Zvyagin BB, Soboleva SV (1977) Refinement of the crystal structure of 2*M*, paragonite by the method of high-voltage electron diffraction. Kristallografiya 22:971-974

Skoog DA, Leary JJ (1992) Principles of instrumental analysis.700 pp.

Smith JV, Yoder HS (1956) Experimental and theoretical studies of the mica polymorphs. Mineral. Mag. 31:209-235

Smith JV, Yoder HS (1956) Experimental and theoretical studies of the mica polymorphs. Mineralogical Magazine 31:209-235

Smoliar-Zviagina BB (1993) Relationships between structural parameters and chemical composition of micas. Clay Minerals 28:603-624

Smyth JR *et al.* (2000) Crystal structures and compressibilities of synthetic 2*M*1 and 3*T* phengite micas. European Journal of Mineralogy 12:955-963

Soboleva SV, Sidorenko DV, Zvyagin BB (1977) The crystal structure of paragonite 1M. Kristallografiya 22:510-514

Speer JA (1984) Micas in igneous rocks. Reviews in Mineralogy 13:299-356

Sunagawa I, Endo Y, Daimon N, Tate I (1968) Nucleation, growth and polytypism of pluor-phlogopite from the vapour phase. Journal of crystal growth 3,4:751

Swanson TH, Bailey SW (1981) Redetermination of the lepidolite-2M1 structure. Clays Clay Minerals 29:81-90

Takeda H (1967) Determination of the Layer Stacking Sequence of a New Complex Mica Polytype: A 4-layer Lithium Fluorophlogopite. Acta Crystallographica 22:845-853

Takeda H, Morosin B (1975) Comparison of Observed and Predicted Structural Parameters of Mica at High Temperature. Acta Crystallographica B31:2444-2452

Takeda H, Burnham CW (1969) Fluor-polylithionite: a lithium mica with nearly hexagonal (Si2O5)2- ring. Mineralogical Journal 6:102-109

Takeda H, Donnay JDH (1966) Trioctahedral one-layer micas. III. Crystal structures of a synthetic lithium fluormica. Acta Crystallographica 20:638-646

Takeda H, Haga N, Sadanaga R (1971) Structural investigation of polymorphic transition between 2M2-, 1M- lepidolite and 2M1 muscovite. Mineralogical Journal 6:203-215

Takeda H, Ross M (1975) Mica polytypism: Dissimilarities in the crystal structures of coexisting 1M and 2M1 biotite. American Mineralogist 60:1030-1040

Takeda H, Ross M (1995) Mica polytypism: Identification and origin. American Mineralogist 80:715-724

Takéuchi Y (1965) Structures of brittle micas. Clays and Clay Minerals 13:1-25

Takéuchi Y (1975) Structures of brittle micas. The distortion of Si(Al) tetrahedra in sheet silicates. Contribution Caly Mineralogy. T. Sudo Volume, K Henmi (Ed.) p. 1-6

Tateyama H, Shimoda S, Sudo T (1974) The crystal structure of synthetic MgIV mica. Zeitschrift fur Kristallographie 139:196-206

Tepikin EV, Drits VA, Alexandrova VA (1969) Crystal structure of iron biotite and construction of structural models for trioctahedral micas. Proc 4th International Clay Conference, Tokyo43-49

Toraya H (1981) Distortions of octahedra and octahedral sheets in 1*M* micas and the relation to their stability. Zeitschrift fur Kristallographie 157:173-190

Toraya H, Iwai S, Marumo F, Dalmon M, Kondo R (1976) The crystal structure of tetrasilisic potassium fluor mica, KMg2.5Si4O10F2. Zeitschrift fur Kristallographie 146:42-52

Toraya H, Iwai S, Marumo F, Hirao M (1978) The crystal structure of a germanate mica, KMg3Ge3AlO10F2. Mineralogical Journal 9:221-230

Toraya H, Iwai S, Marumo F, Hirao M (1977) The crystal structure of taeniolite, KLiMg2Si4O10(OH)2. Zeitschrift fur Kristallographie 146:73-83

Toraya H, Iwai S, Marumo F, Hirao M (1978) The crystal structures of germanate micas, KMg2.5Ge4O10F2 and KLiMg2Ge4O10F2. Zeitschrift fur Kristallographie 148:65-81

Toraya H, Iwai S, Marumo F, Nishikawa T, Hirao M (1978) The crystal structure of synthetic mica, KMg2.75Si3.5Al0.5O10F2. Mineralogical Journal 9:210-220

Toraya H, Marumo F (1983) The crystal structure of a germanate mica KMg[2.5+x]Ge[4-2x]Al[2x]O10F2 (x~0.14) and distortion of (Ge, Al)O4 tetrahedra. Mineralogical Journal 11:222-231

Toraya H, Marumo F (1981) Structure variation with octahedral cation substitution in the system of germanate micas, KMg[3-x]Mn[x]Ge3AlO10F2. Mineralogical Journal 10:396-407

Toraya H, Marumo F, Hirao M (1983) Synthesis and the crystal structure of a manganoan fluoromica, K(Mg2.44Mn.24)(Si3.82Mn.18)O10F2. Mineralogical Journal 11:240-247

Tyrna PL, Guggenheim S (1991) The crystal structure of norrishite, $KLiMn_2^{3+}Si_4O_{12}$: An oxygen-rich mica. American Mineralogist 76:266-271

Veitch LG, Radoslovich EW (1963) The cell dimensions and symmetry of layer-lattice silicates. III. Octahedral ordering. American Mineralogist 48:62-75

Warren BE (1969) X-Ray Diffraction.381 pp.

Weiss Z (1986) Polytypism of Micas. III. X-ray diffraction identication. Clays and Clay Minerals 34:53-68

Weiss Z, Rieder M, Chmielova M (1992) Deformation of coordination polyhedra and their sheets in phyllosilicates. European Journal of Mineralogy 4:665-682

Weiss Z, Rieder M, Chmielova M, Krajicek J (1985) Geometry of the octahedral coordination in micas: a review of refined structures. American Mineralogist 70:747-757

Weiss Z, Rieder M, Smrcok L, Petricek V, Bailey SW (1993) Refinement of the crystal structures of two "protolithionites". European Journal of Mineralogy 5:493-502

Weiss Z, Wiewóra (1986) Polytypism of micas. III. X-ray diffraction identification. Clays and Clay Minerals 34:53-58

Wilson A (1963) Mathematical Theory of X-Ray Powder Diffractometry.128 pp.

Wilson AJC (1970) Elements of X-Ray Crystallography. 256 pp.

Wilson AJC (1992) International Tables for Crystallography. Mathematical, Physical and Chemical Tables C:V-XXIX

Wilson AJC (1949) X-Ray Optics, The Diffraction of X-Rays by Finite and Imperfect Crystals.127 pp.

Wones D, Eugster H (1965) Stability of Biotite: Experiment, Theory, and Application. American Mineralogist 50:1228-1273

Wones DR (1963) Phase equilibria of "ferriannite", KFe3+2Fe+3Si3O10(OH)2. American Journal of Science 261:581-595

Zanazzi PF, Pavase A (2002) Behavior of Micas at High Pressure and High Temperature. Reviews in mineralogy and geochemistry 46:99-116

Zevin L, Kimmel G. (1995) Quantitative X-ray diffractometry .372 pp.

Zheng H, Bailey SW (1989) Structures of intergrown triclinic and monoclinic IIb chlorites from Kenya. Clays and Clay Minerals 37:308-316

Zhoukhlistov AP, Zvyagin BB, Soboleva SV, Fedetov AF (1973) The crystal structure of the dioctahedral mica 2M2 determined by high voltage electron diffraction. Clays and Clay Minerals 21:465-470

Zvyagin BB (1988) Polytypism in crystal structures. Comput. Math. App. 16:569-581

Zvyagin BB (1962) A theory of polymorphism of micas. Soviet Physics-Crystallography 6:571-580

Zvyagin BB (1985) Polytypism in contemporary crystallography. Soviet Physics Crystallography 32:394-399

Zvyagin BB *et al.* (1979) High voltage electron diffraction in the study of layered minerals. Moscow: Nauks Press, 223 pp. (In Russian)

Appendix A. Diffractograms collected

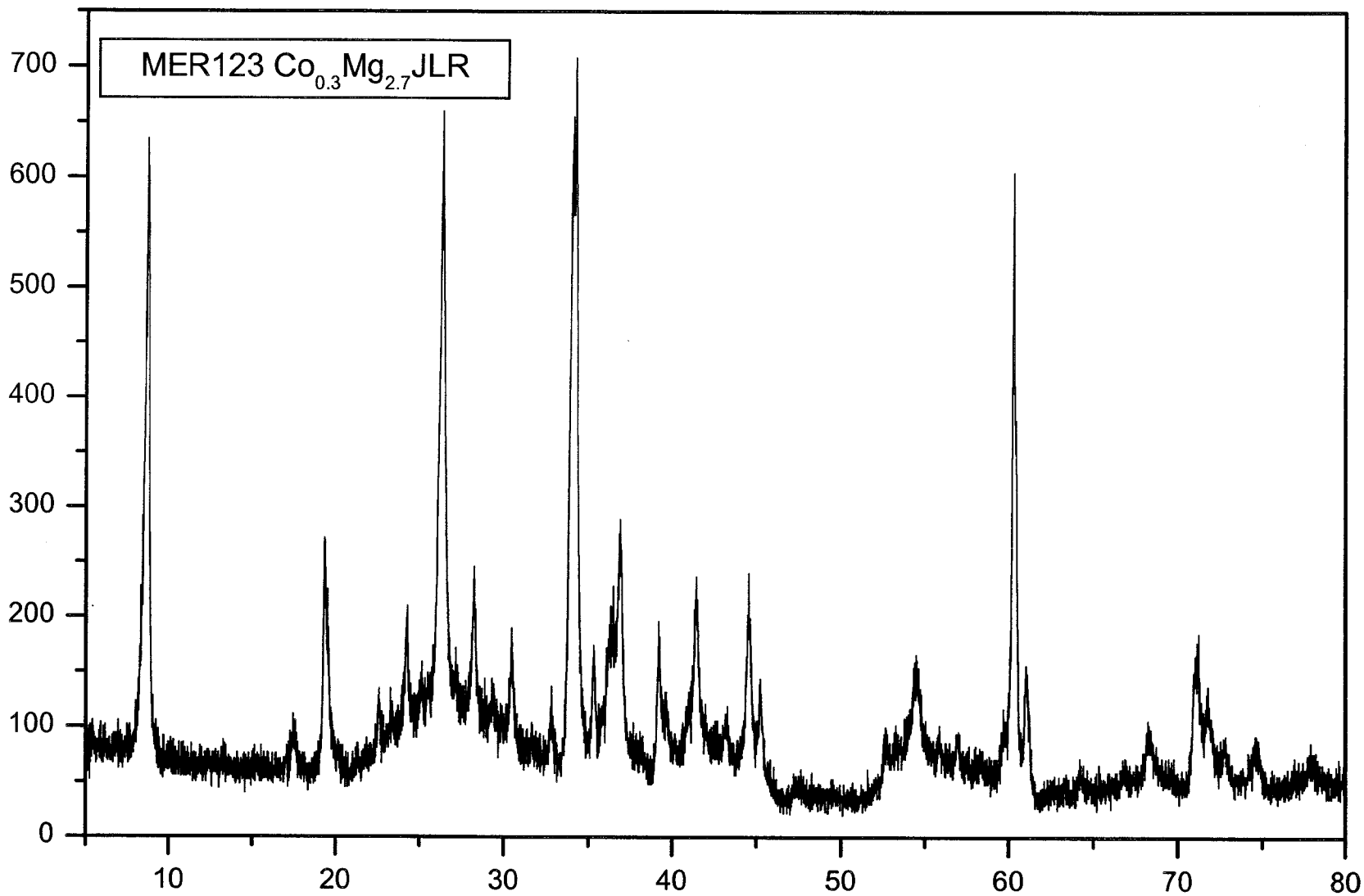
MER123 $Co_{0.3}Mg_{2.7}JLR$
700
600
500
400
300
200
100
0
10
20
30
40
50
60
70
80

AI

A2

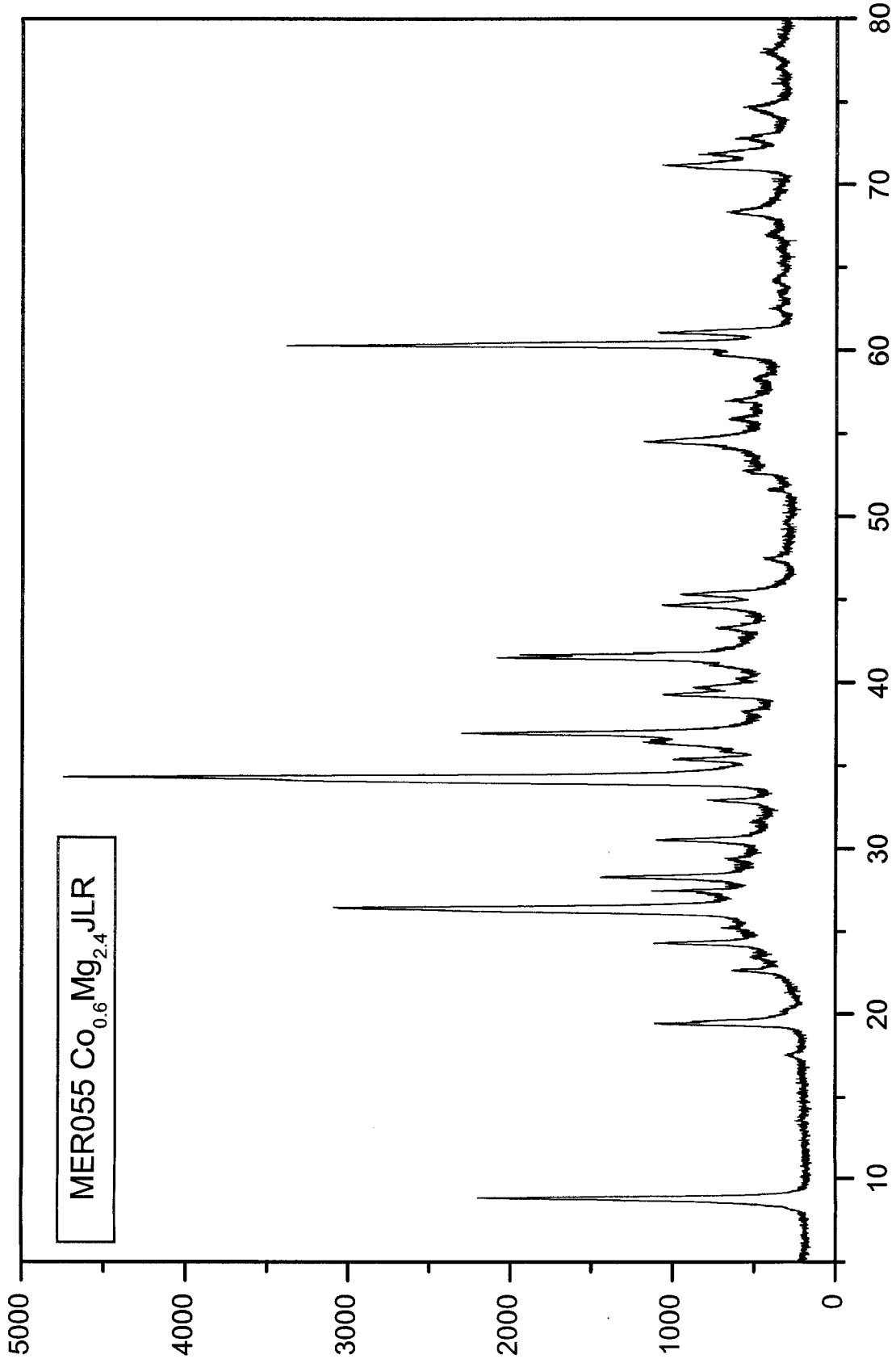
MER055 $Co_{0.6}Mg_{2.4}$JLR
5000
4000
3000
2000
1000
0
10
20
30
40
50
60
70
80

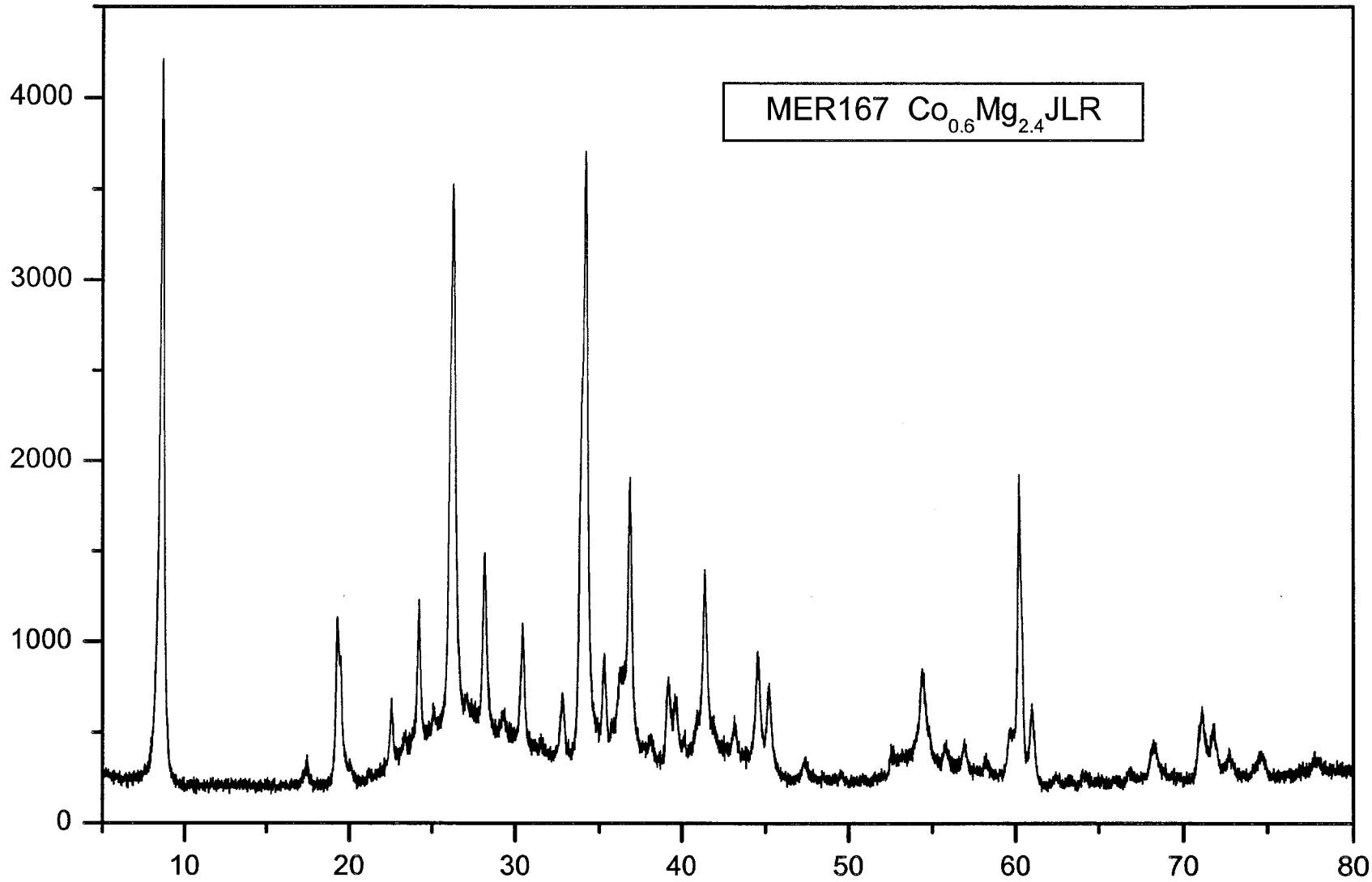
MER167 $Co_{0.6}Mg_{2.4}$JLR
4000
3000
2000
1000
0
10
20
30
40
50
60
70
80

A3

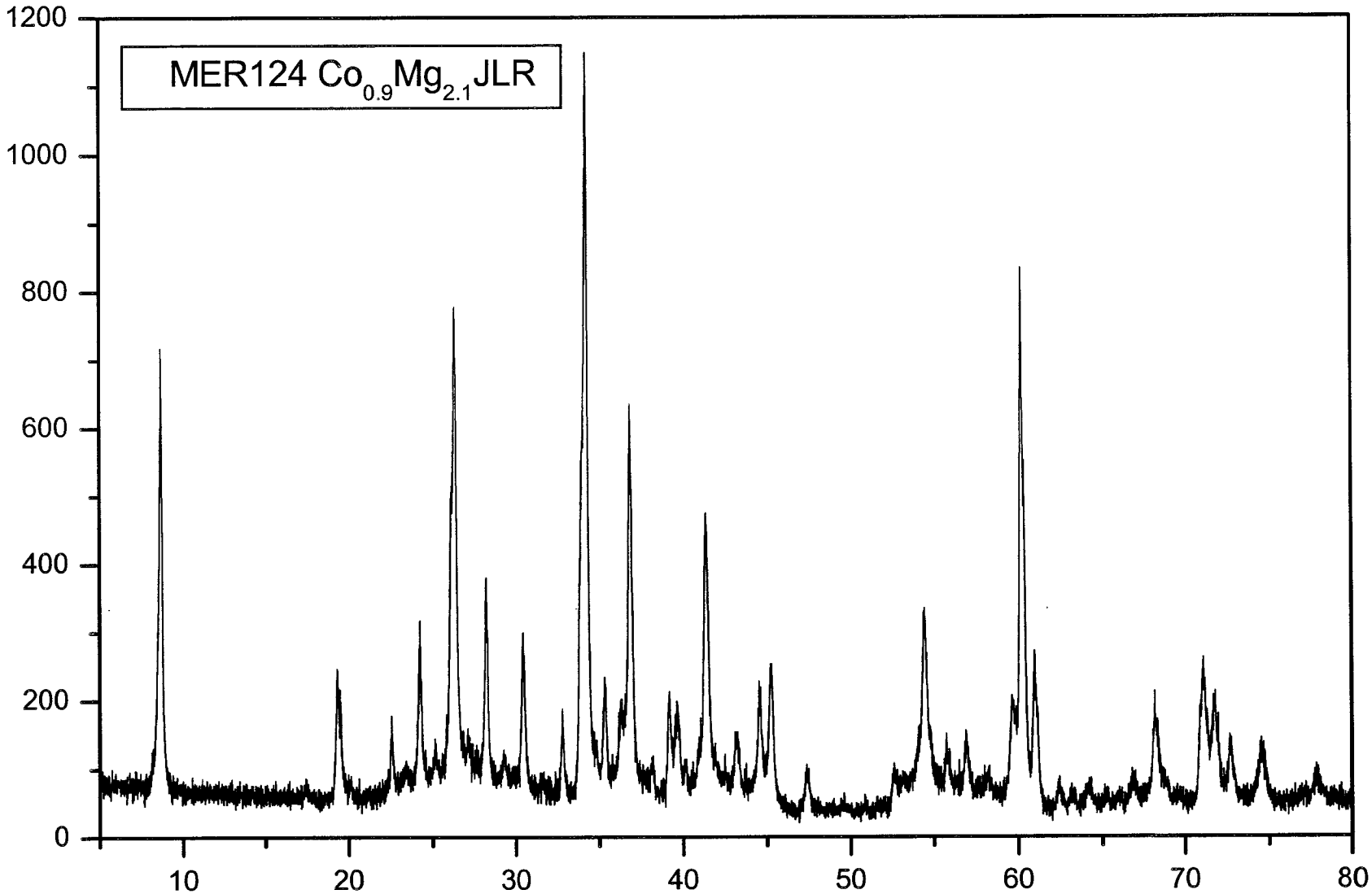
MER124 $Co_{0.9}Mg_{2.1}$JLR
1200
1000
800
600
400
200
0
10
20
30
40
50
60
70
80

A4

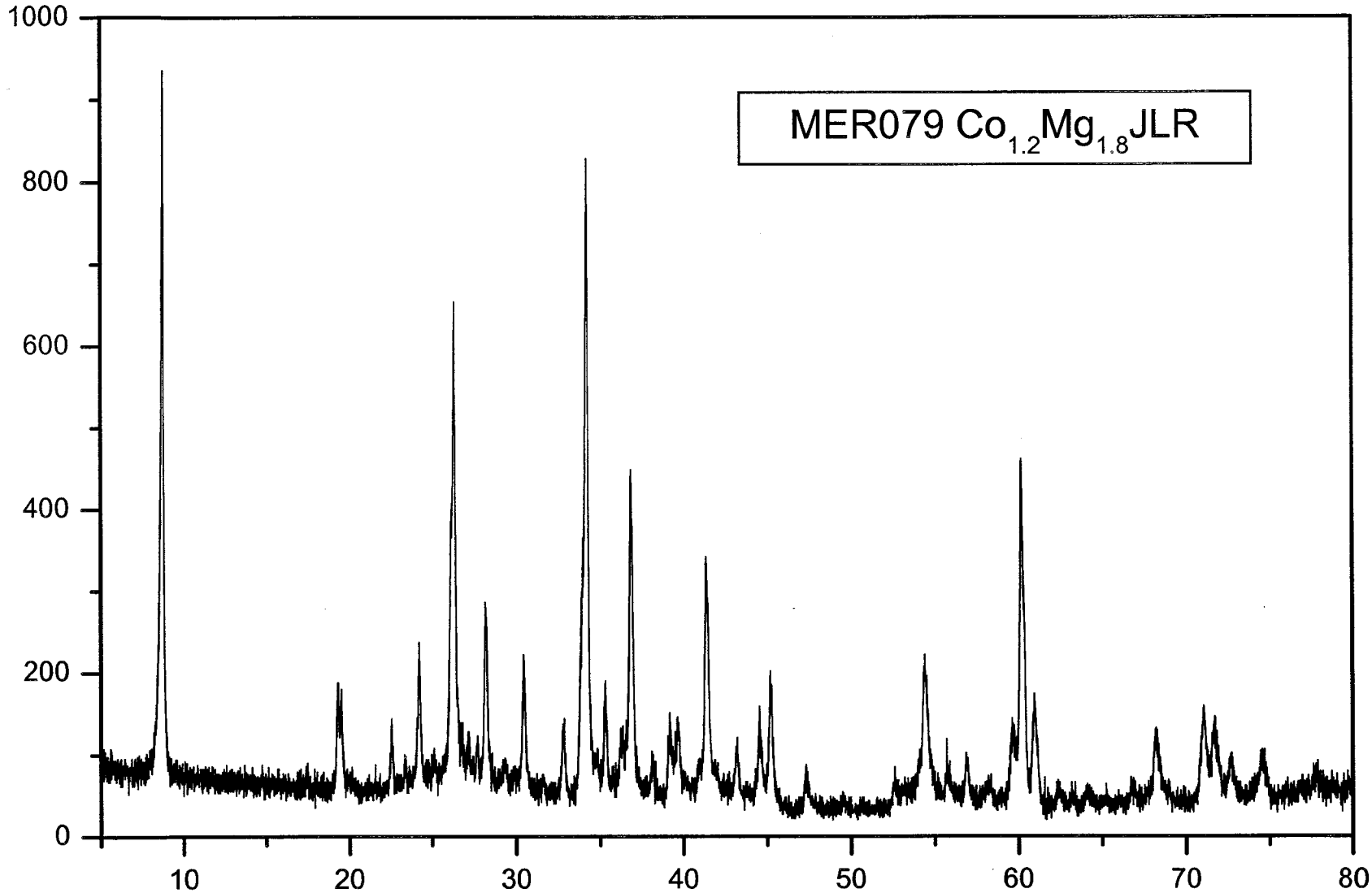
MER079 $Co_{1.2}Mg_{1.8}$JLR
1000
800
600
400
200
0
10
20
30
40
50
60
70
80

A5

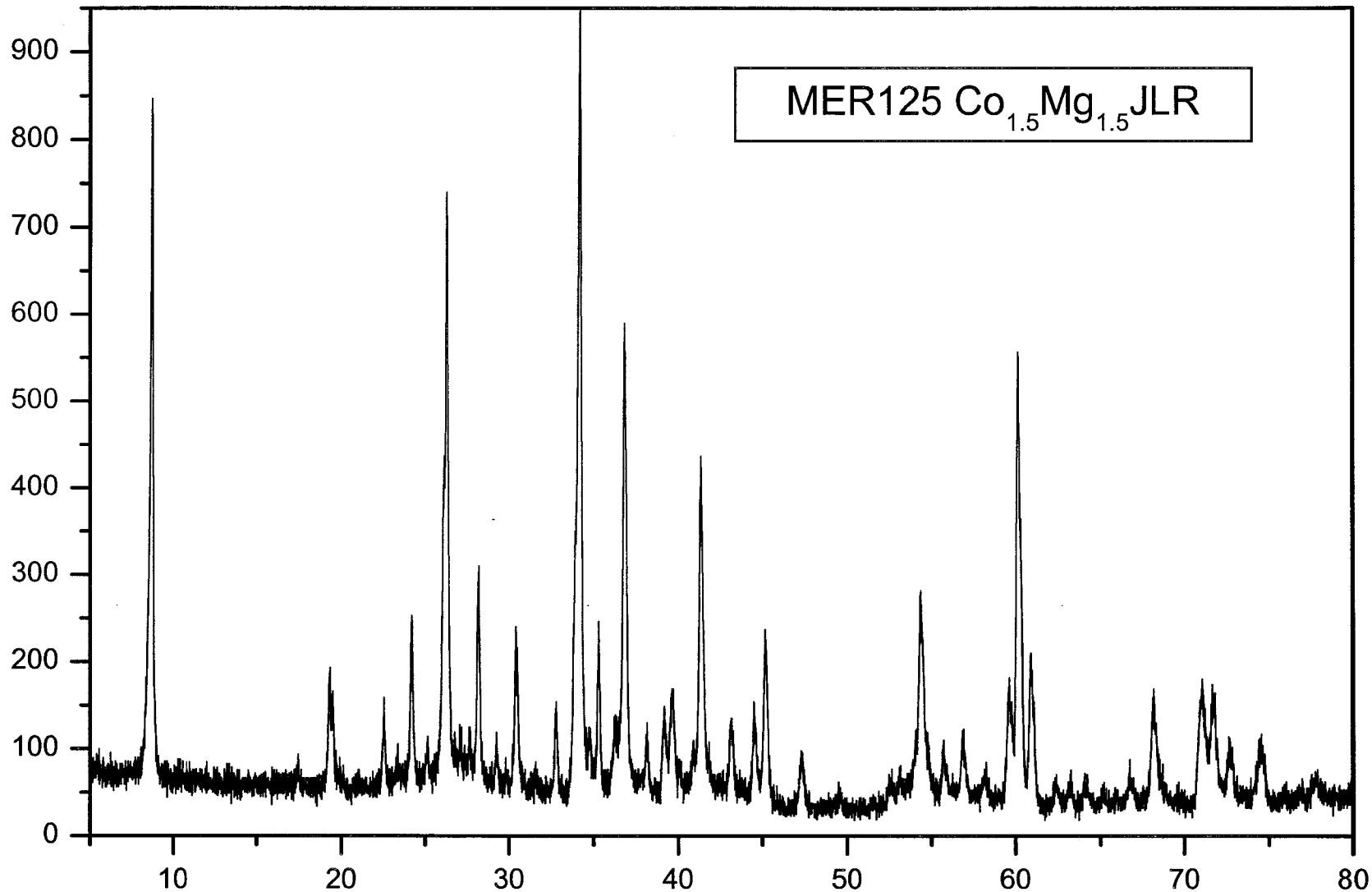
MER125 $Co_{1.5}Mg_{1.5}$JLR
900
800
700
600
500
400
300
200
100
0
10
20
30
40
50
60
70
80

A6

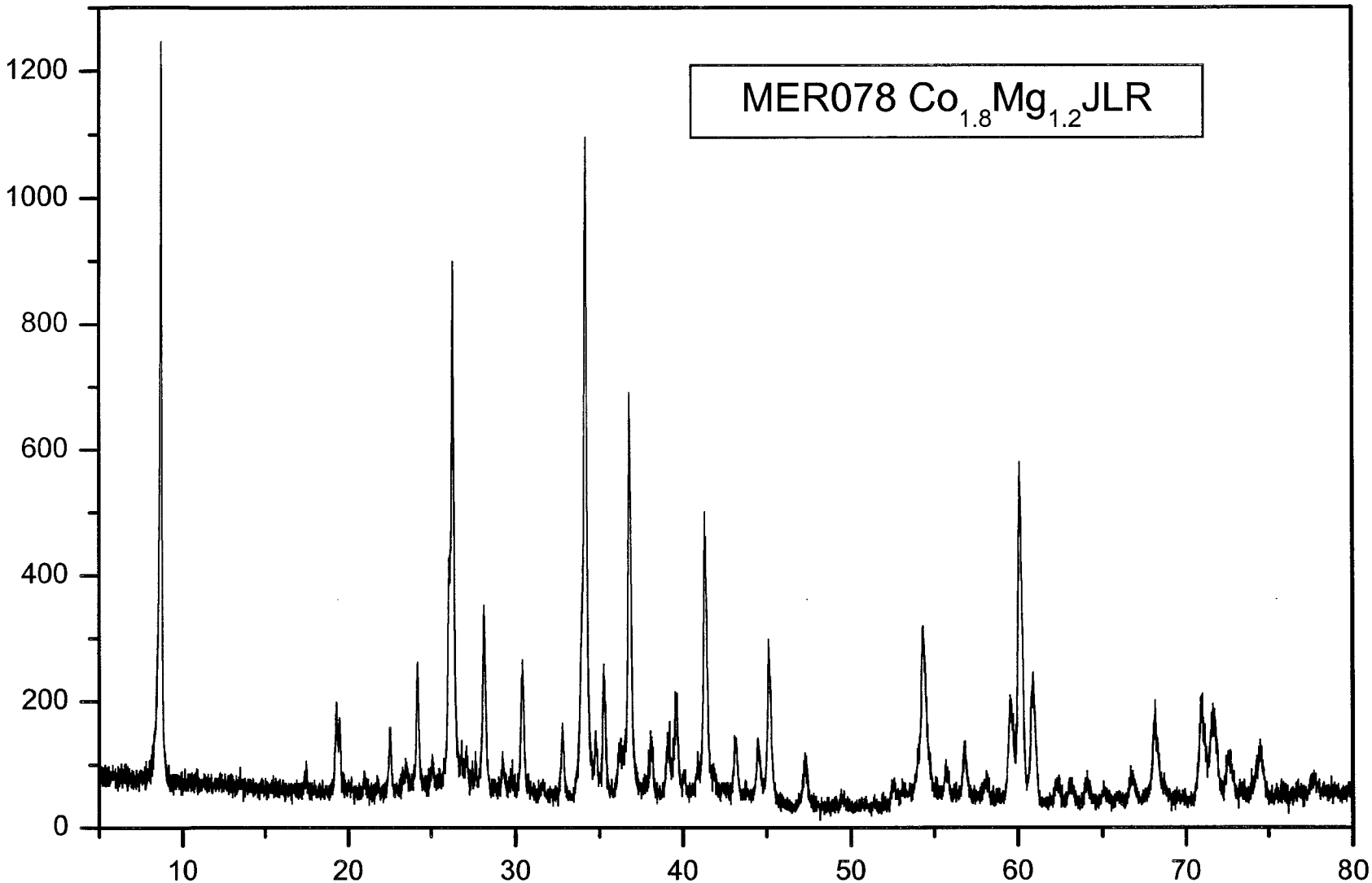
MER078 $Co_{1.8}Mg_{1.2}$JLR
1200
1000
800
600
400
200
0
10
20
30
40
50
60
70
80

A7

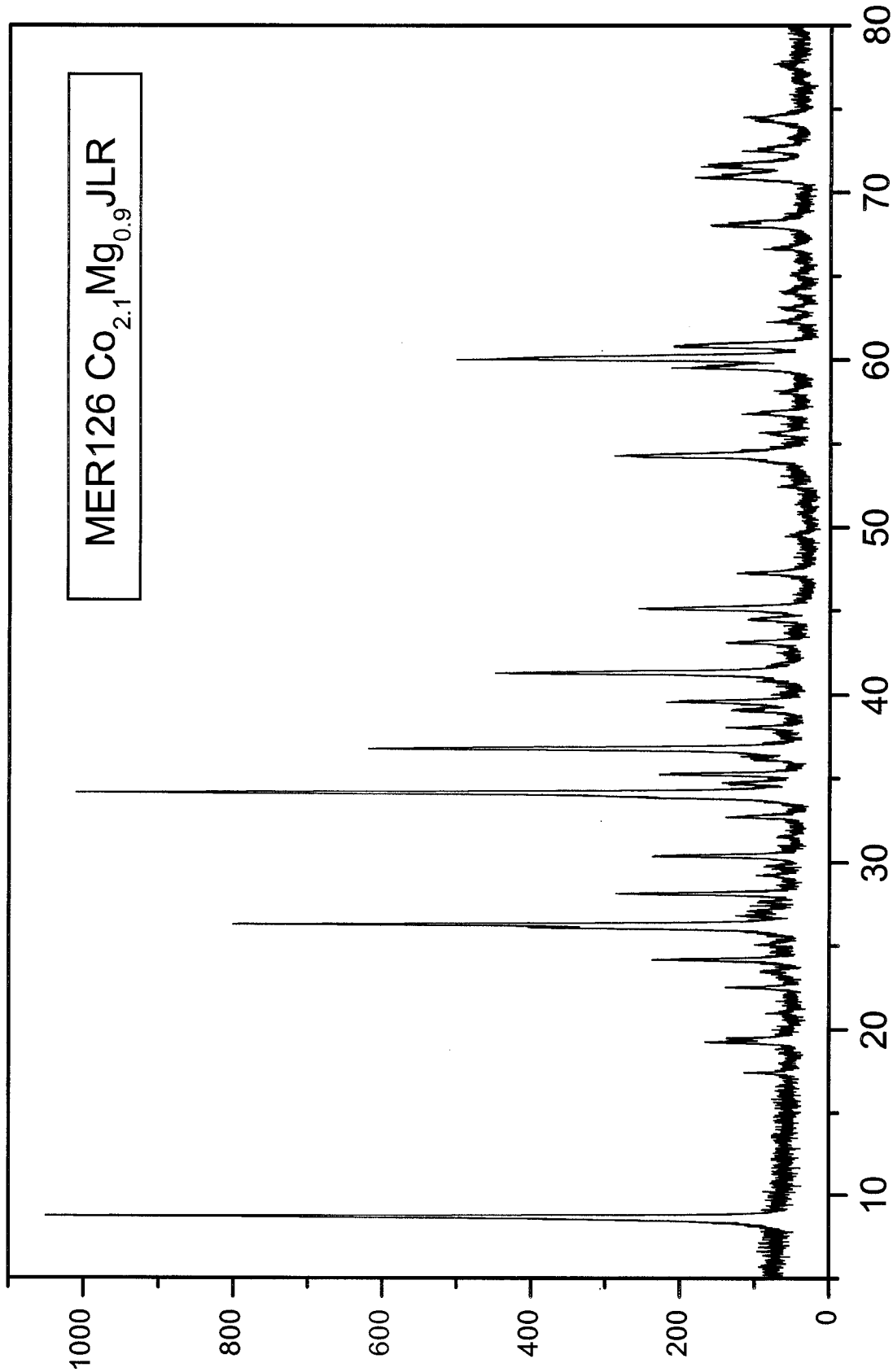
MER126 $Co_{2.1}Mg_{0.9}$JLR
0
200
400
600
800
1000
10
20
30
40
50
60
70
80

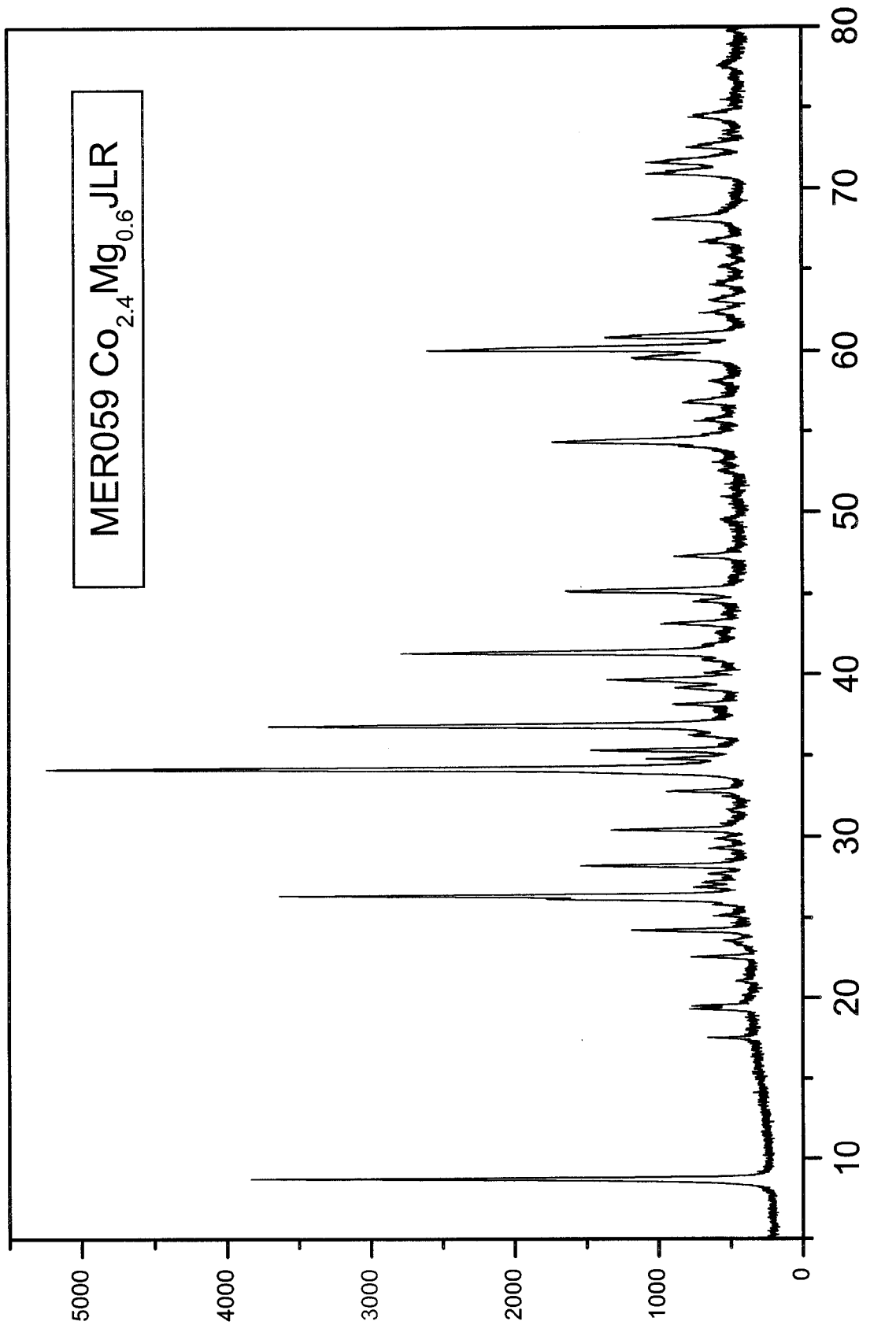
MER059 $Co_{2.4}Mg_{0.6}$JLR
0
1000
2000
3000
4000
5000
10
20
30
40
50
60
70
80

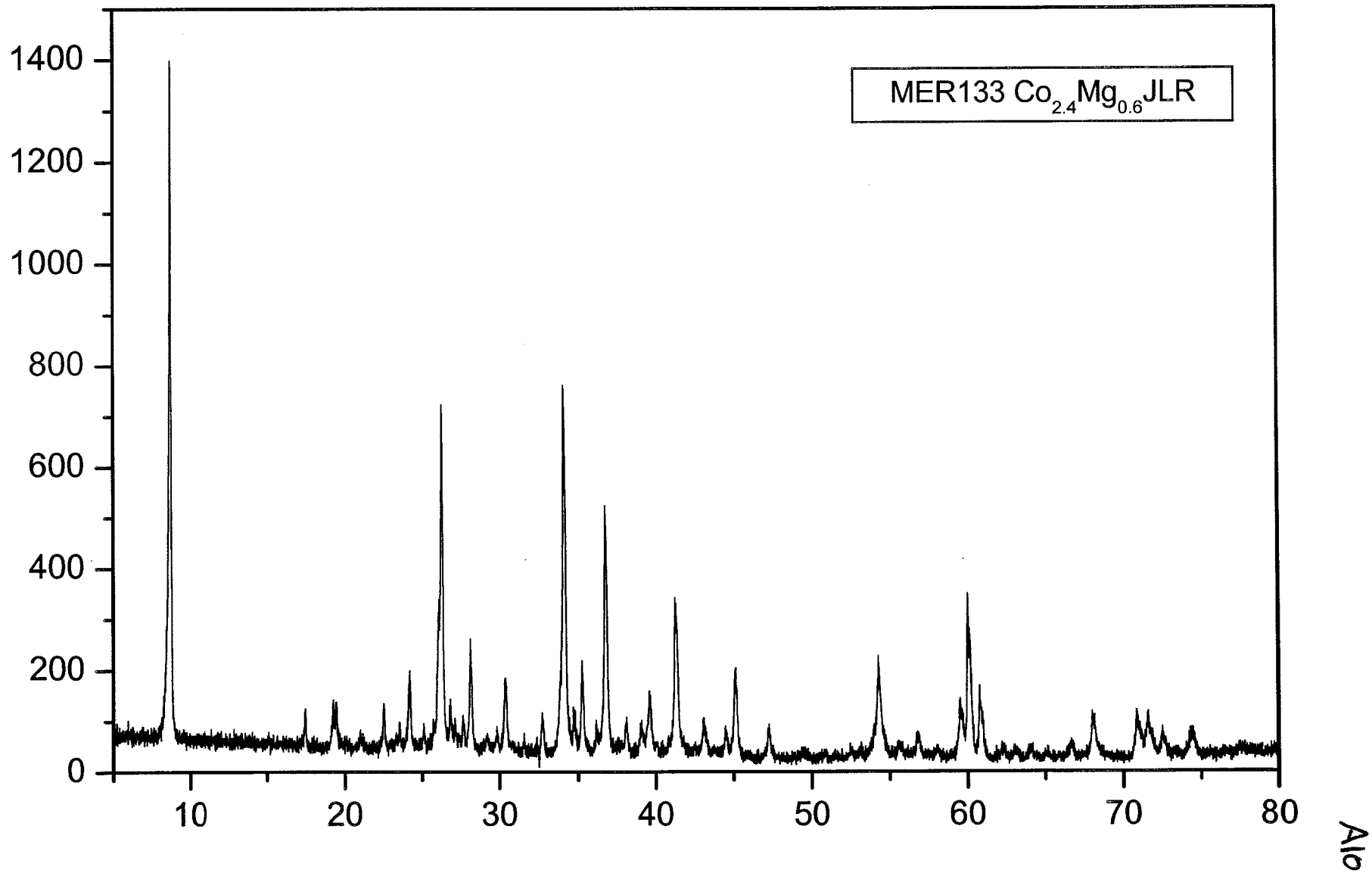
MER133 $Co_{2.4}Mg_{0.6}$JLR
1400
1200
1000
800
600
400
200
0
10
20
30
40
50
60
70
80
Alo

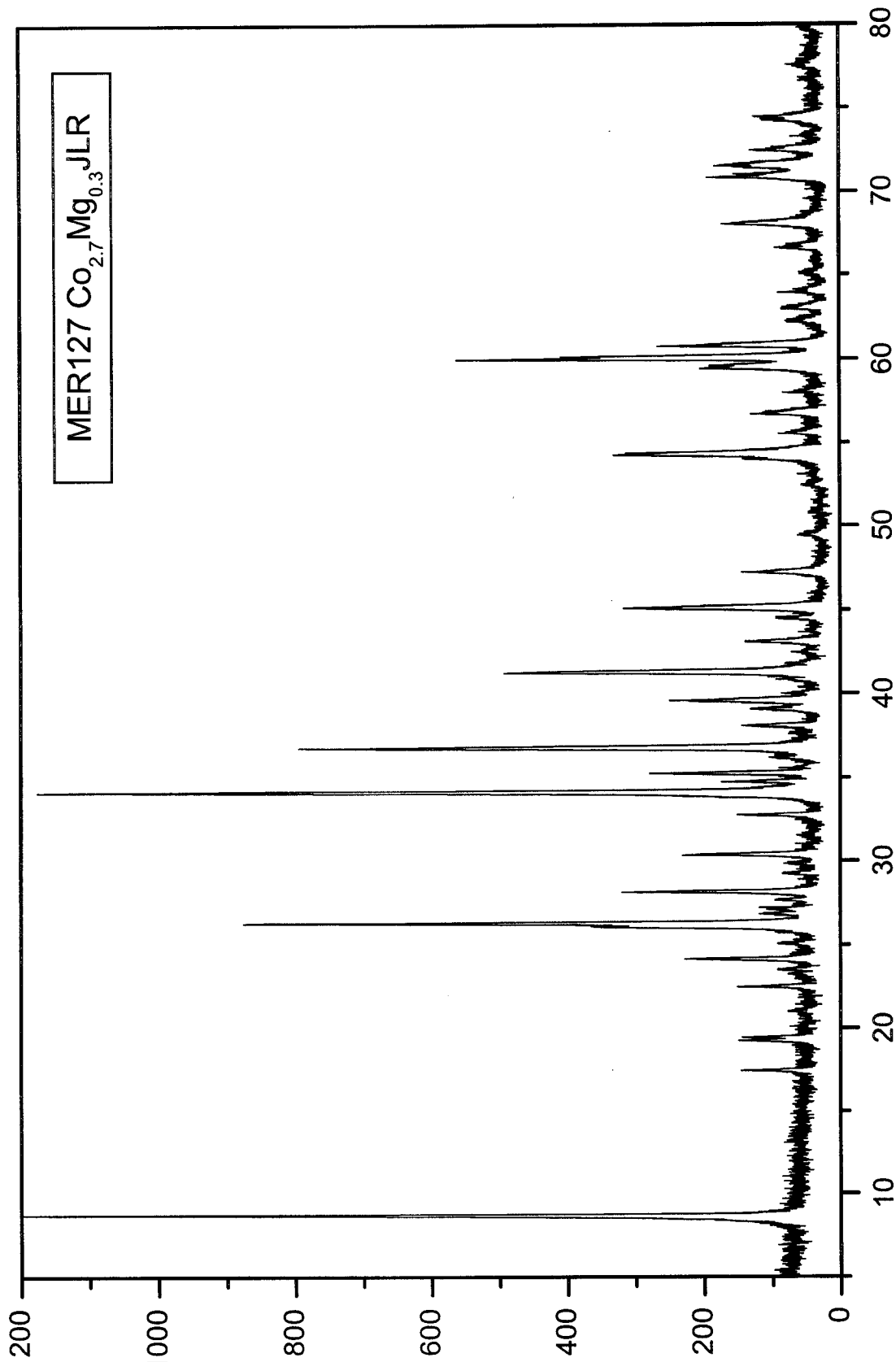
MER127 $Co_{2.7}Mg_{0.3}$JLR
0
200
400
600
800
1000
1200
10
20
30
40
50
60
70
80

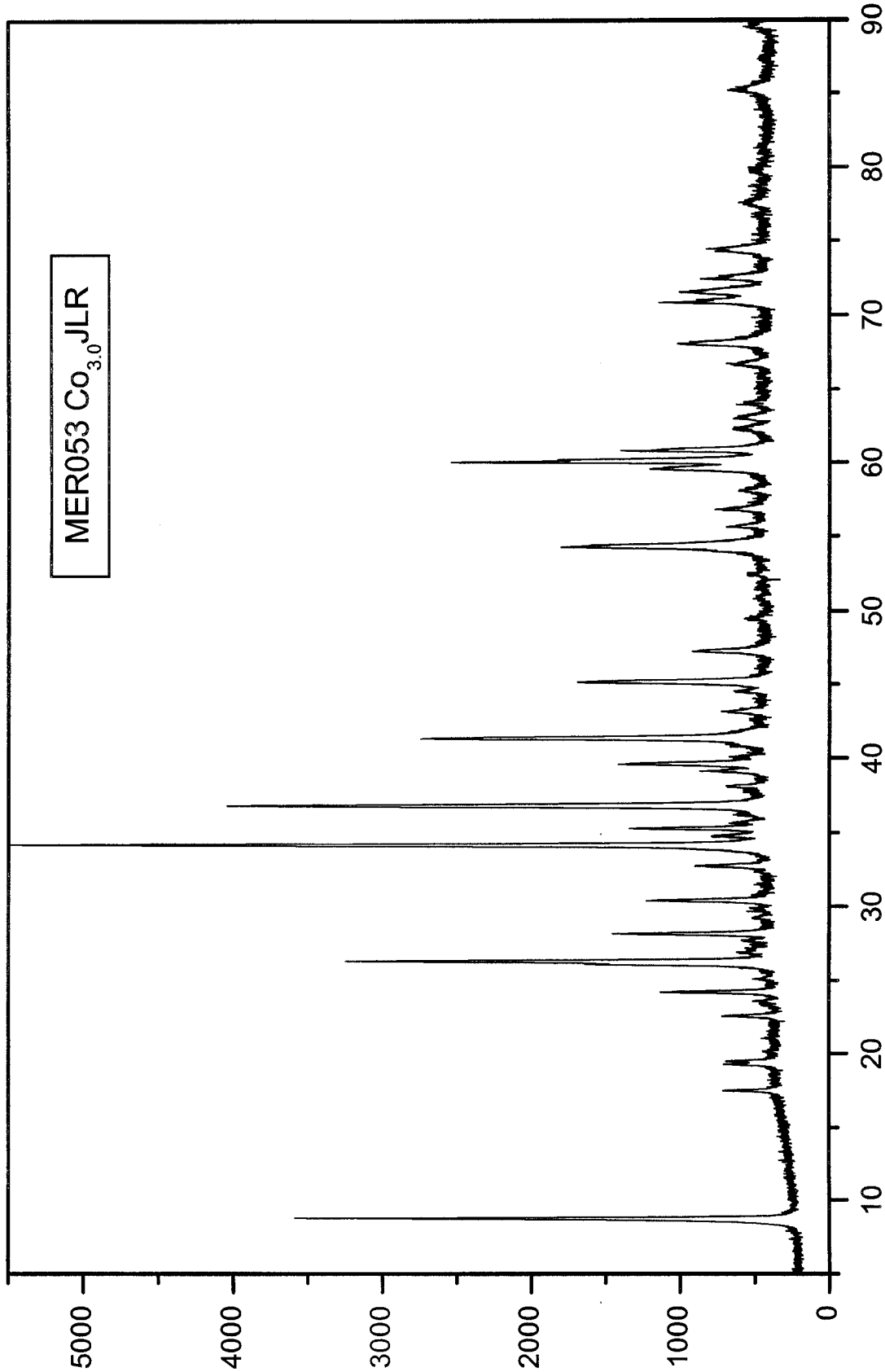
MER053 $Co_{3.0}$JLR
0
1000
2000
3000
4000
5000
10
20
30
40
50
60
70
80
90

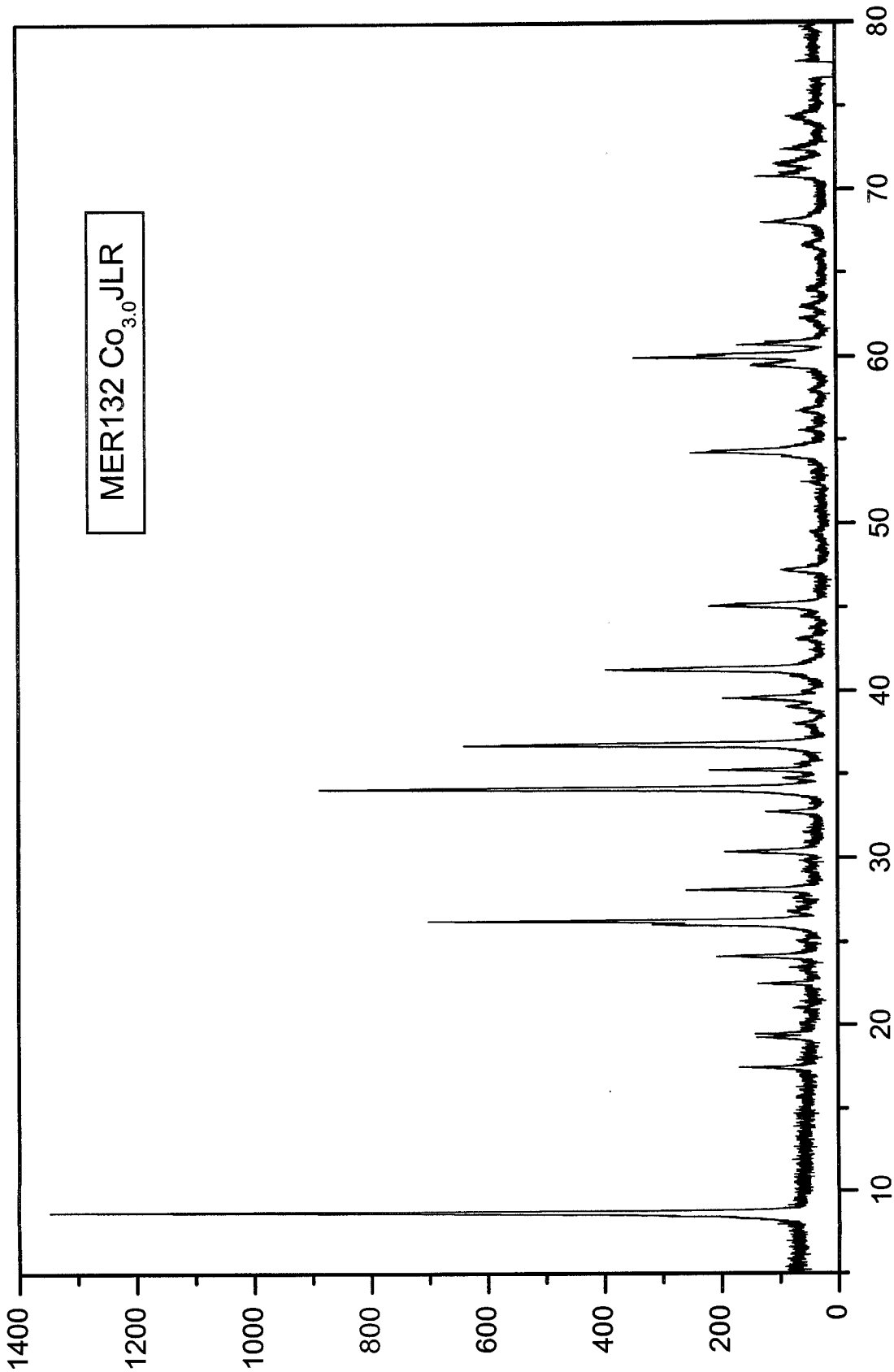
MER132 $Co_{3.0}$JLR
0
200
400
600
800
1000
1200
1400
10
20
30
40
50
60
70
80

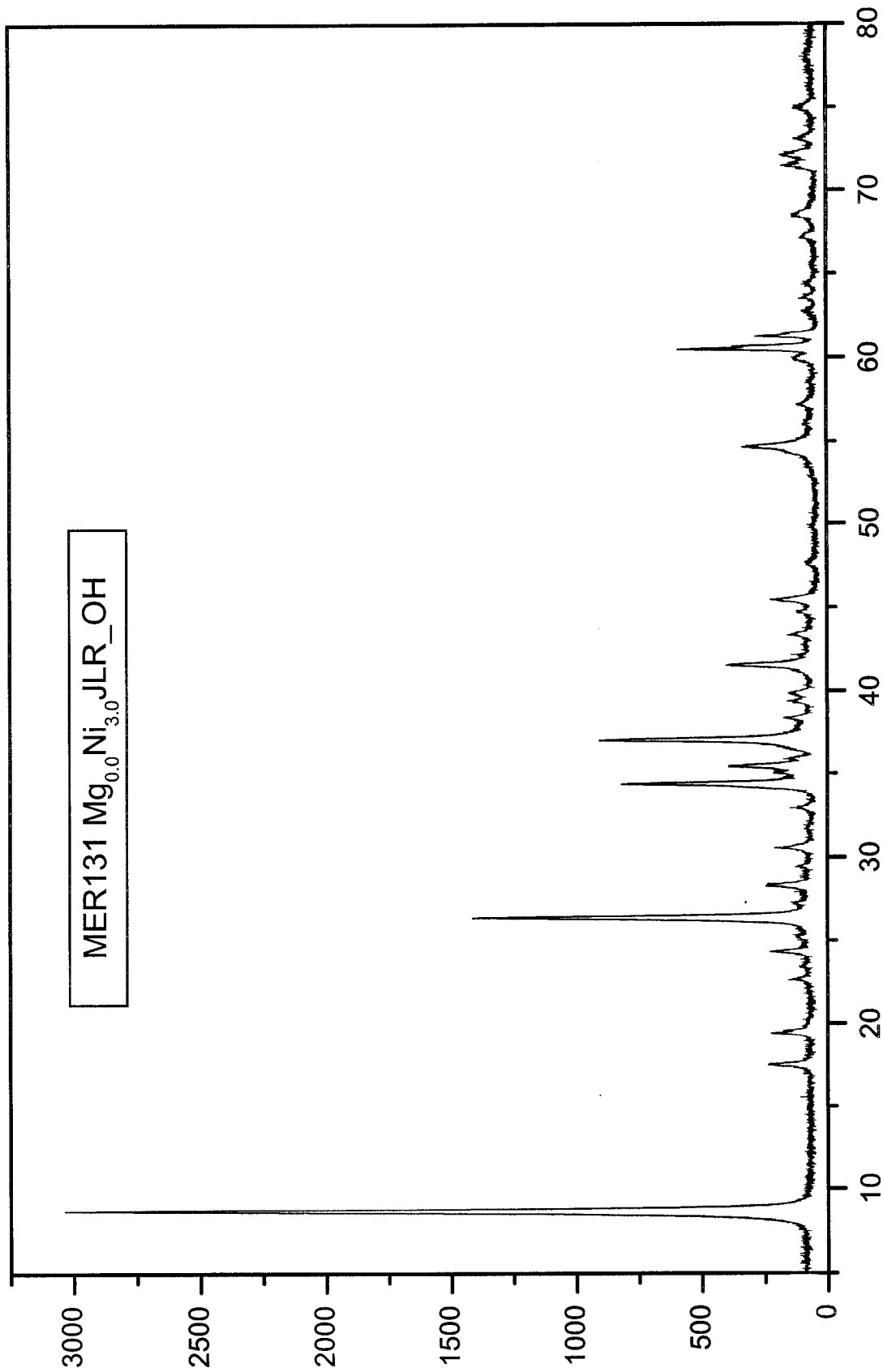
MER131 $Mg_{0.0}Ni_{3.0}$JLR_OH
0
500
1000
1500
2000
2500
3000
10
20
30
40
50
60
70
80

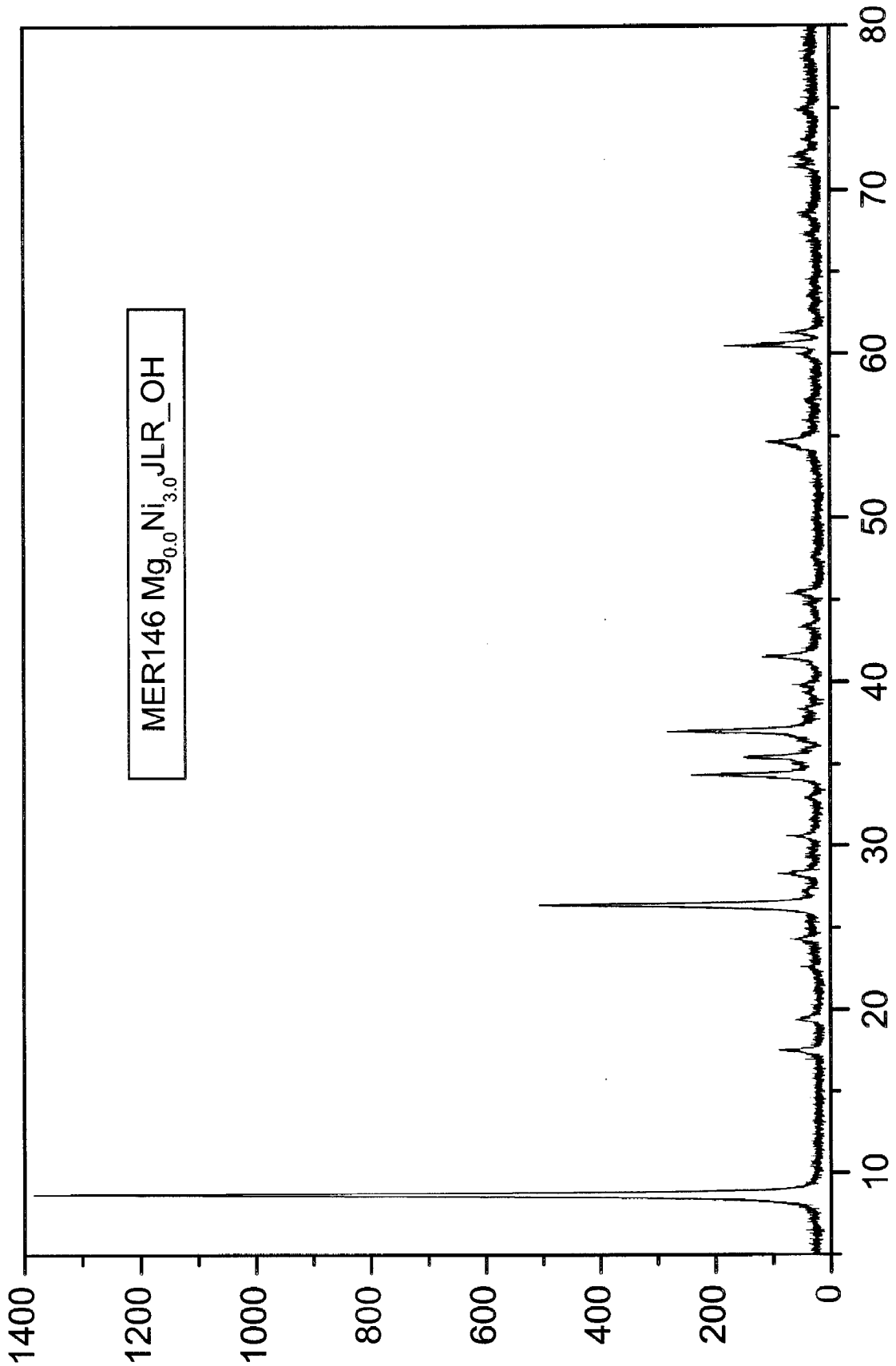
MER146 $Mg_{0.0}Ni_{3.0}$JLR_OH
0
200
400
600
800
1000
1200
1400
10
20
30
40
50
60
70
80

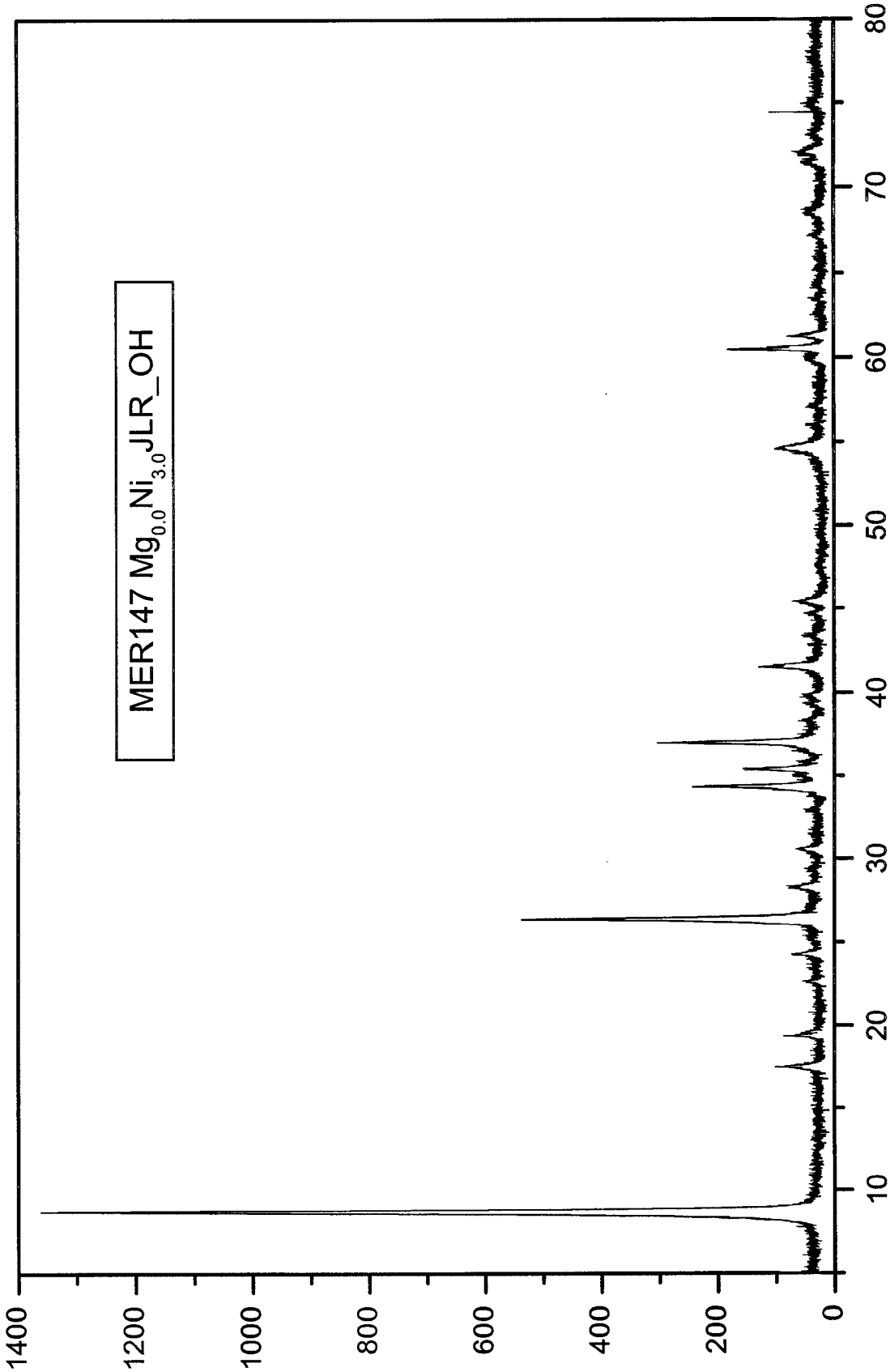
MER147 $Mg_{0.0}Ni_{3.0}$JLR_OH
0
200
400
600
800
1000
1200
1400
10
20
30
40
50
60
70
80

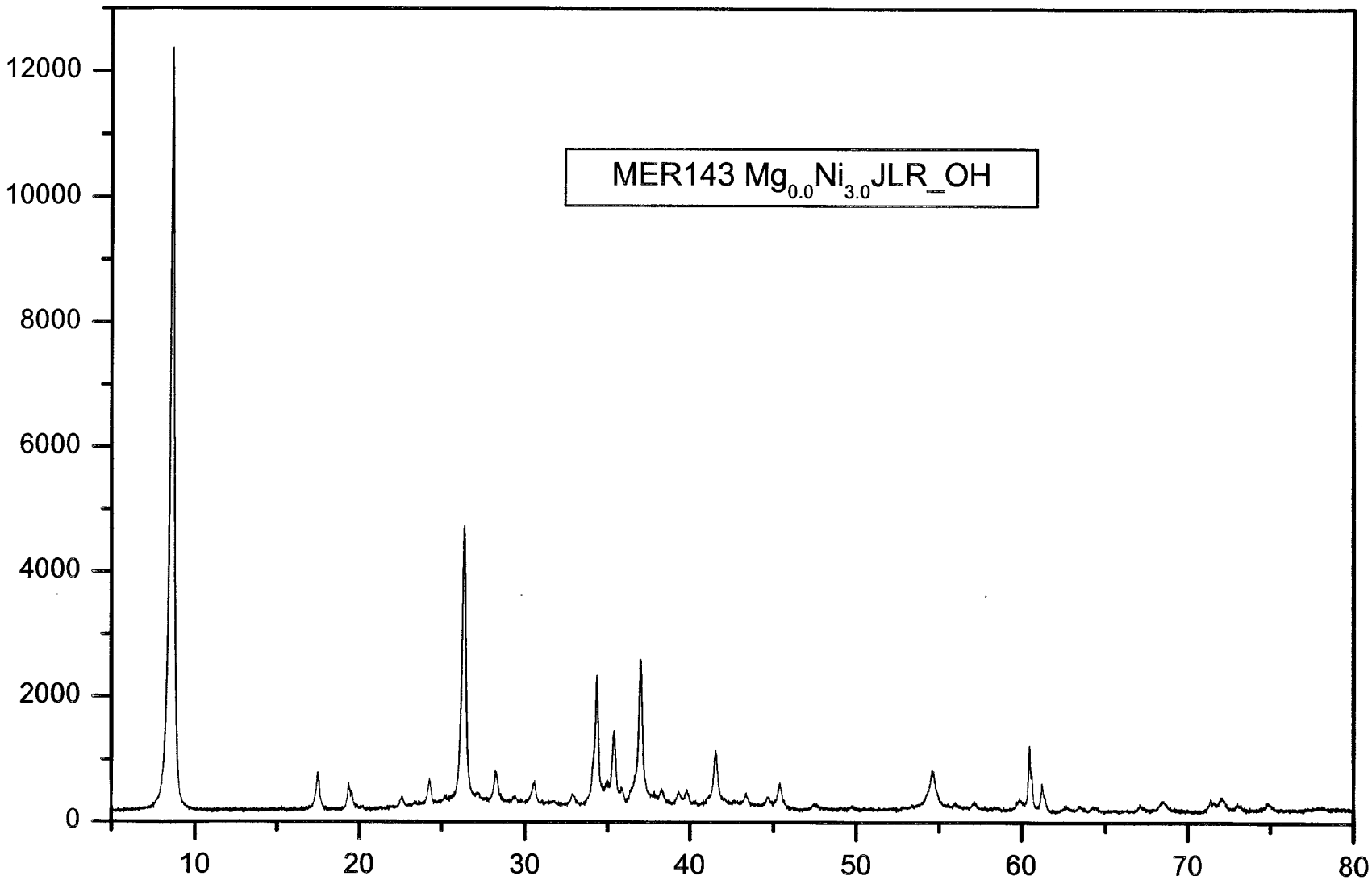
MER143 $Mg_{0.0}Ni_{3.0}$JLR_OH
12000
10000
8000
6000
4000
2000
0
10
20
30
40
50
60
70
80

A1-7

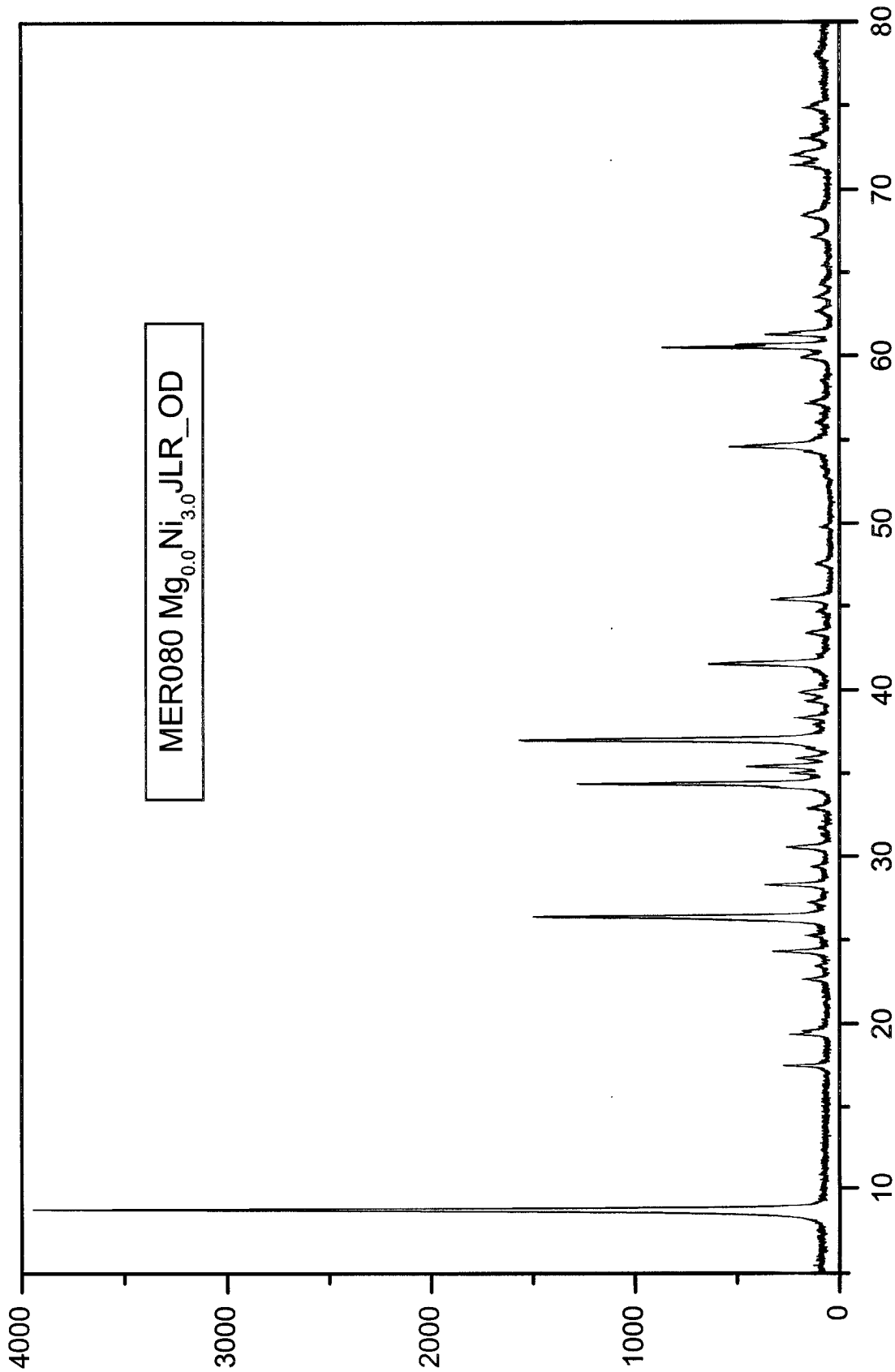
MER080 $Mg_{0.0}Ni_{3.0}$JLR_OD
0
1000
2000
3000
4000
10
20
30
40
50
60
70
80

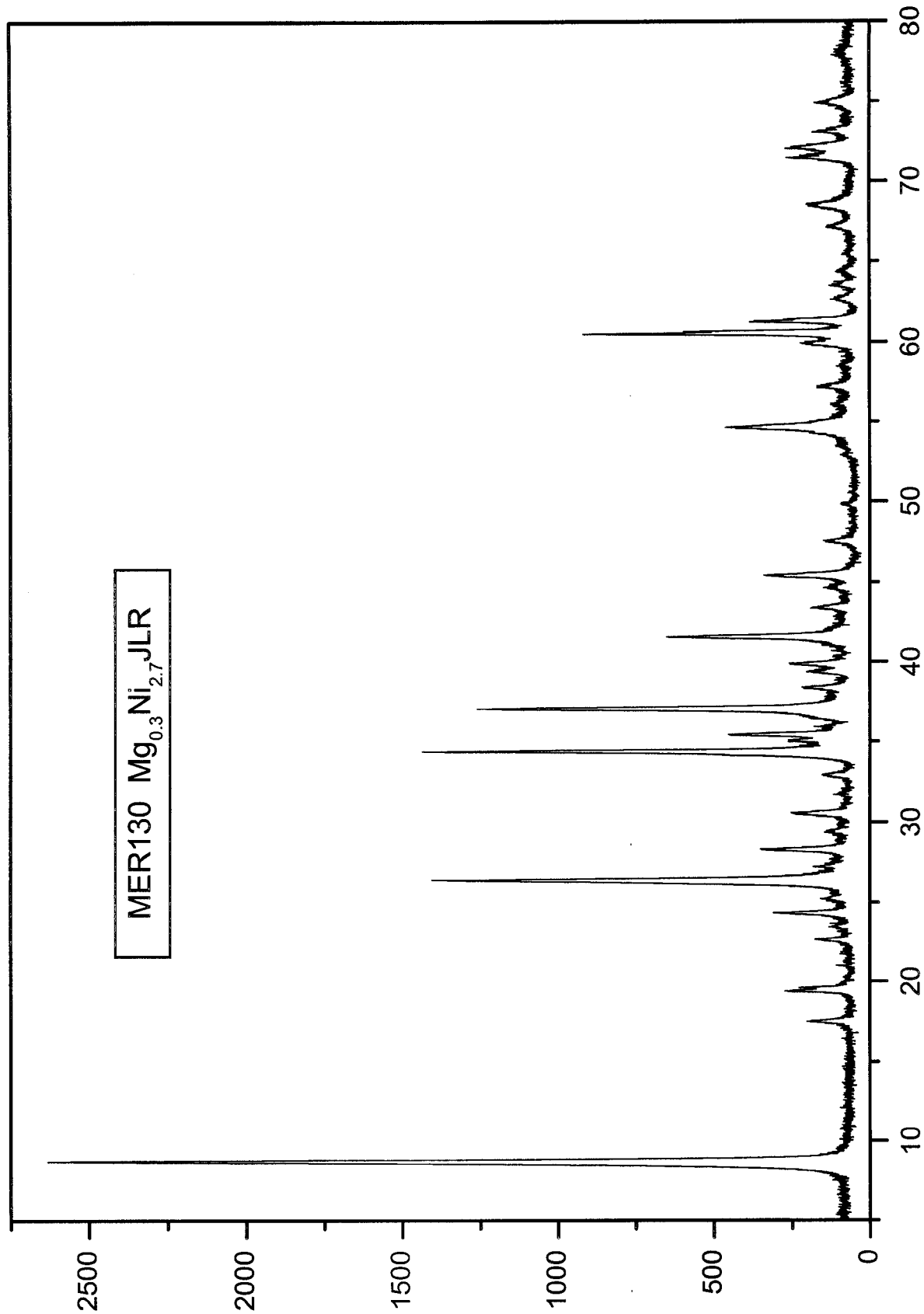
MER130 $Mg_{0.3}Ni_{2.7}$JLR
2500
2000
1500
1000
500
0
10
20
30
40
50
60
70
80

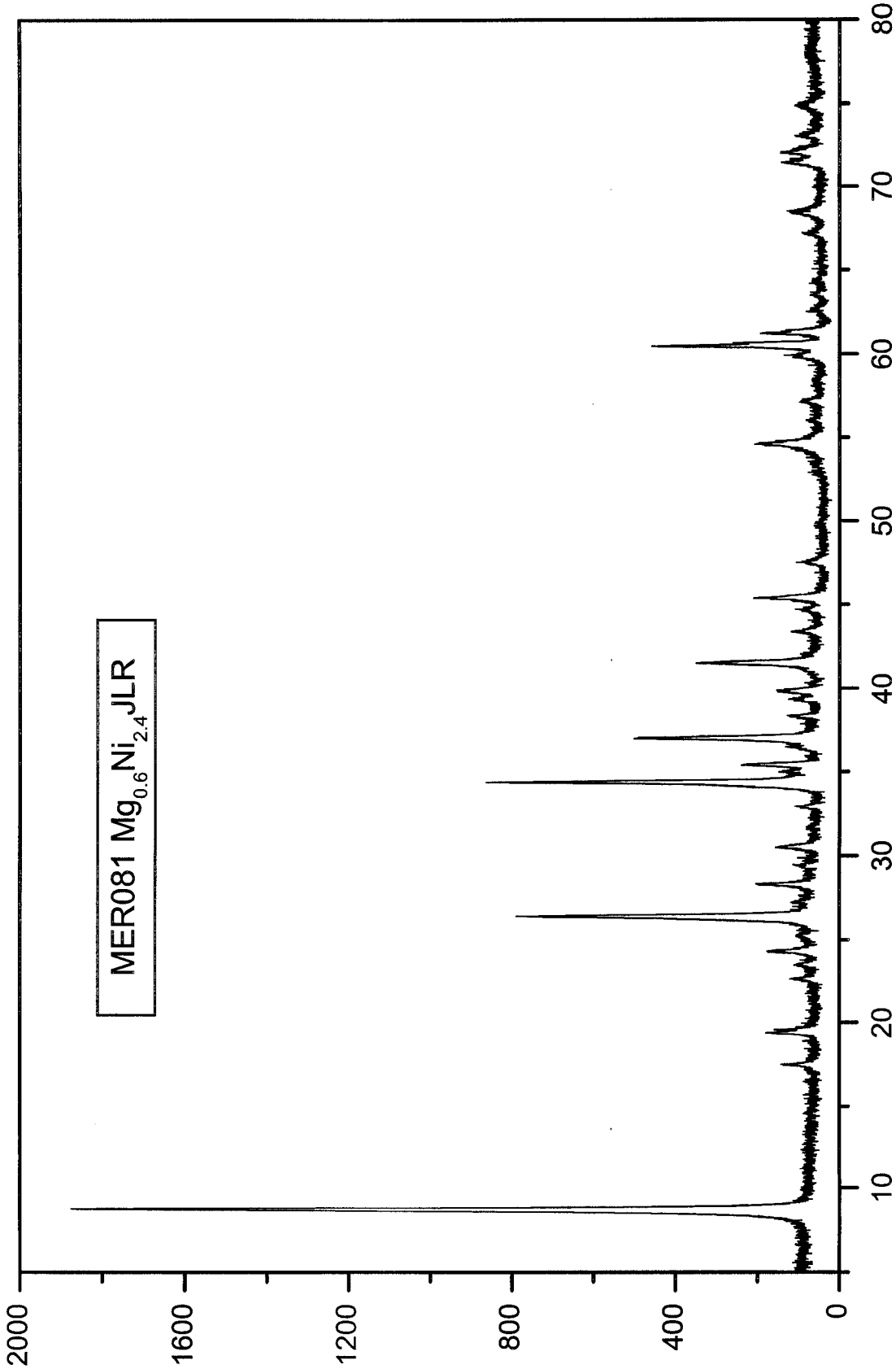
MER081 $Mg_{0.6}Ni_{2.4}$JLR
2000
1600
1200
800
400
0
10
20
30
40
50
60
70
80

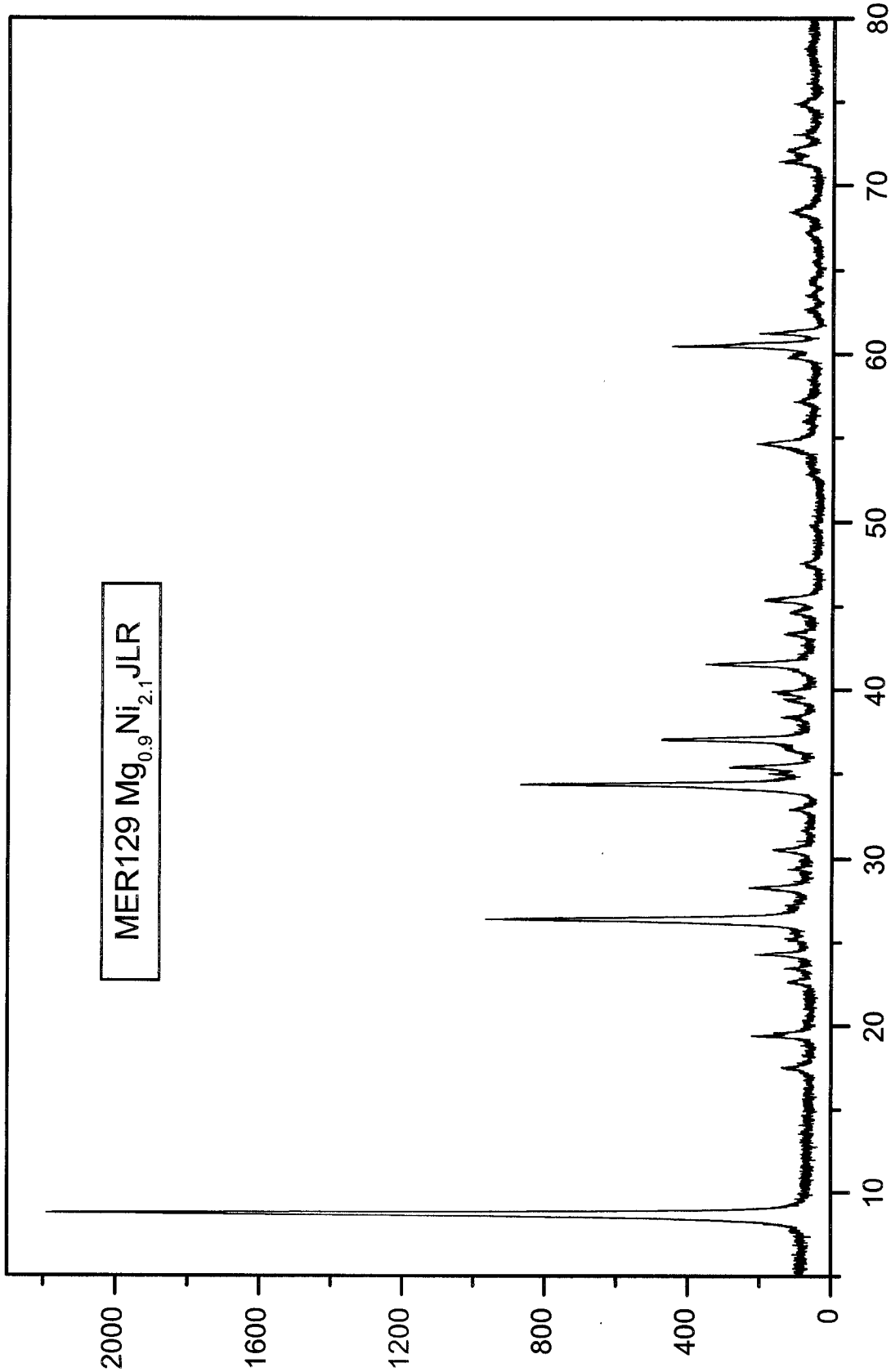
MER129 $Mg_{0.9}Ni_{2.1}$JLR
2000
1600
1200
800
400
0
10
20
30
40
50
60
70
80

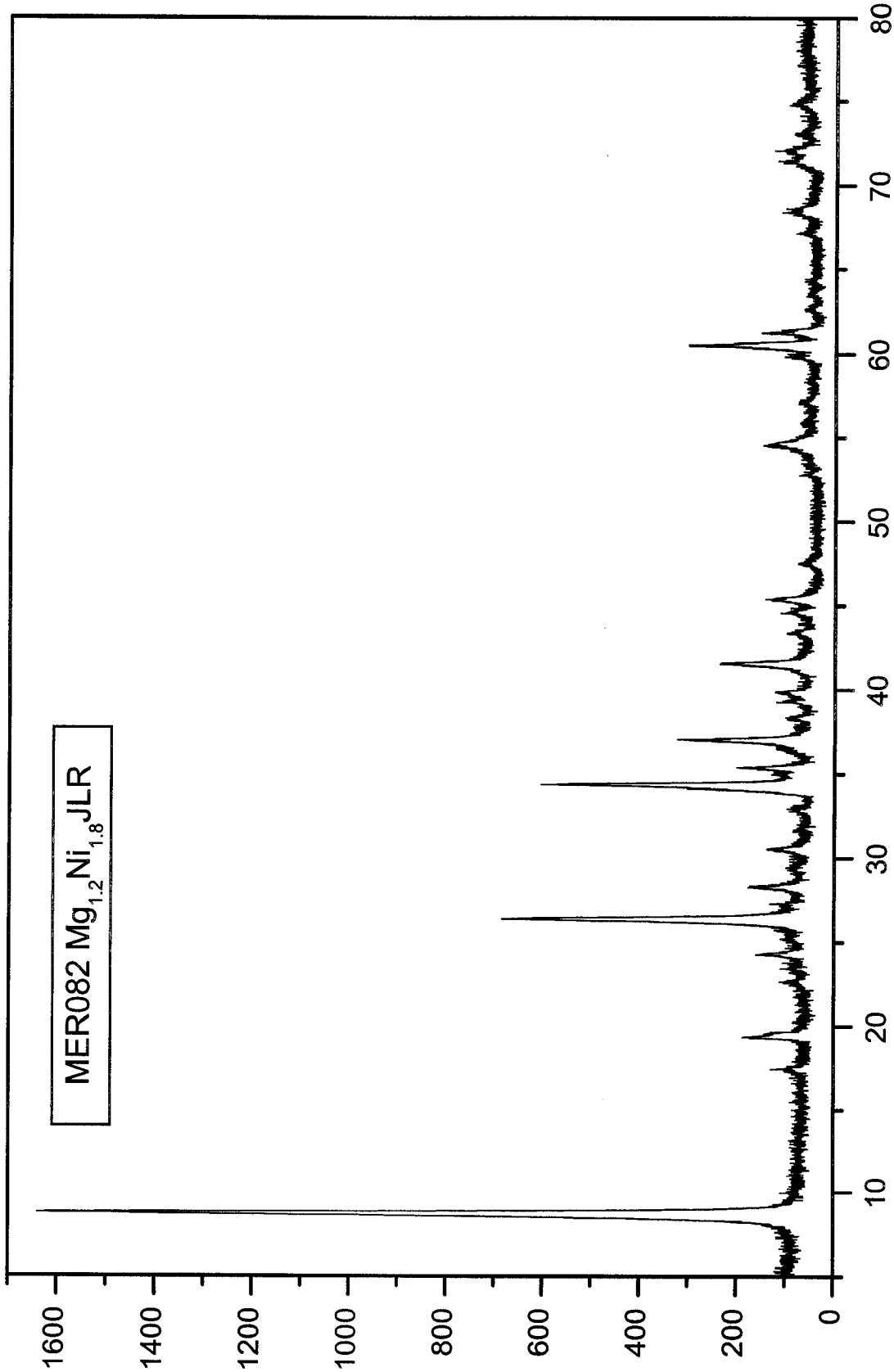
MER082 $Mg_{1.2}Ni_{1.8}$JLR
0
200
400
600
800
1000
1200
1400
1600
10
20
30
40
50
60
70
80

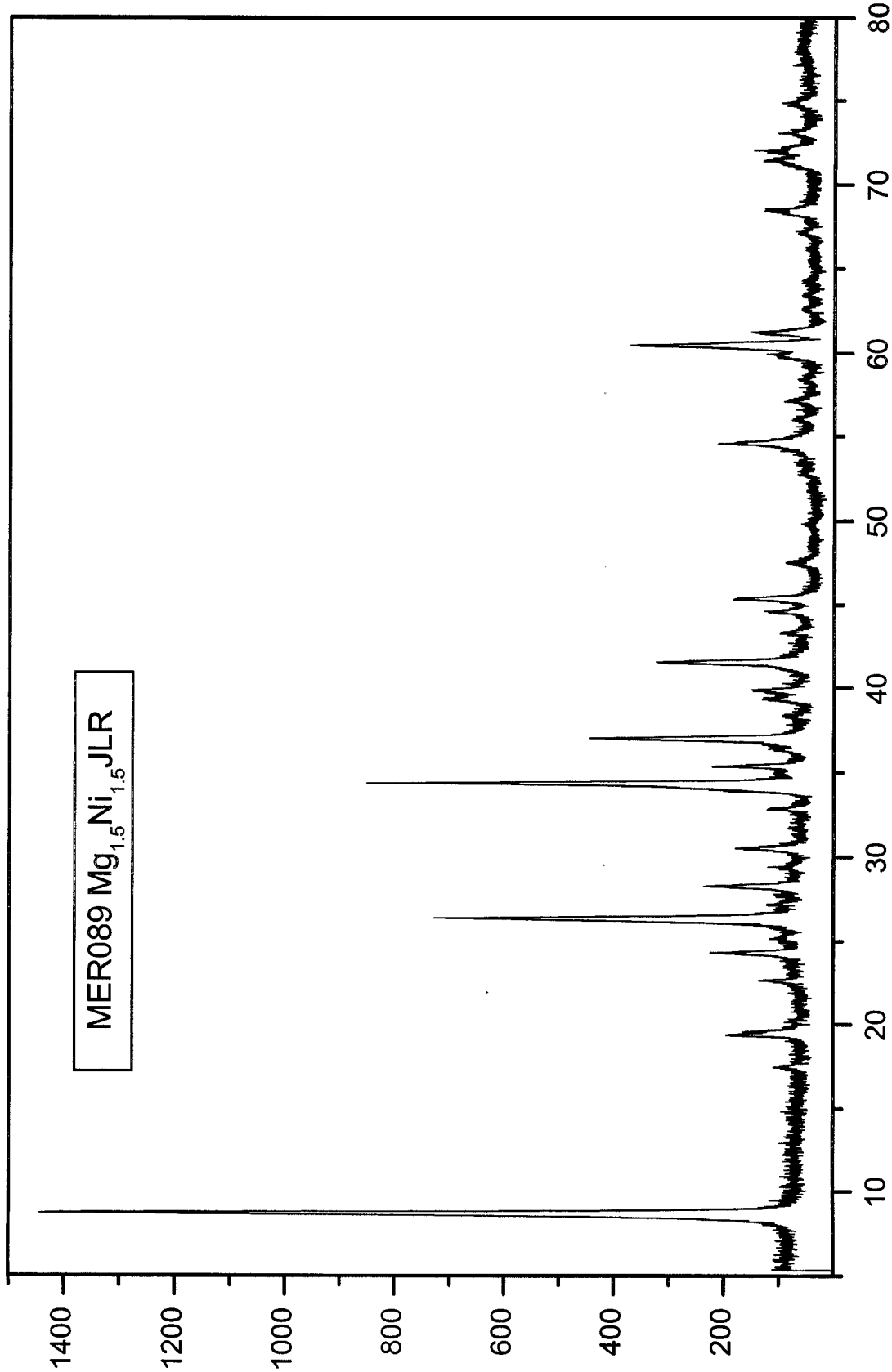
MER089 $Mg_{1.5}Ni_{1.5}$JLR
1400
1200
1000
800
600
400
200
10
20
30
40
50
60
70
80

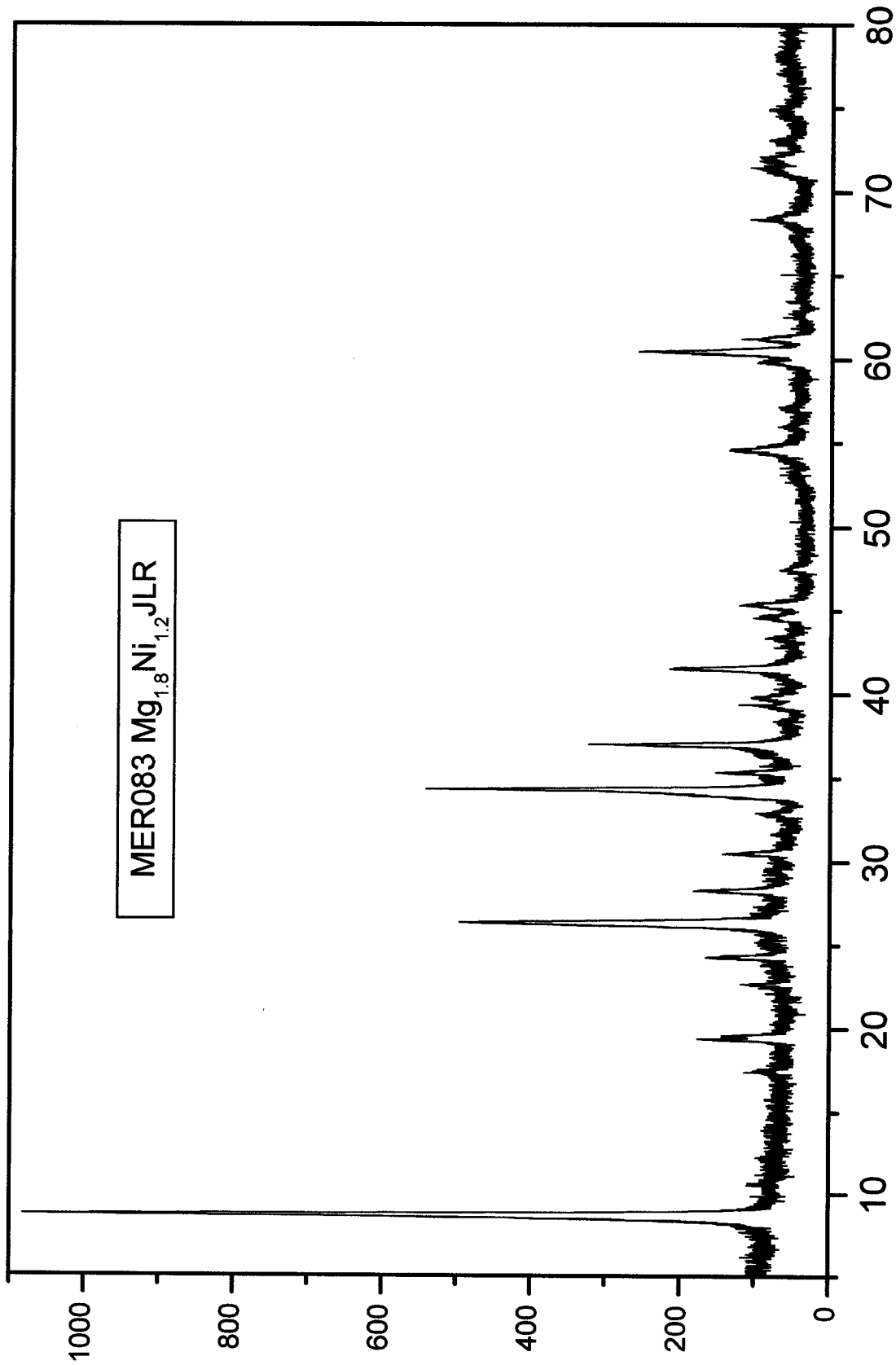
MER083 $Mg_{1.8}Ni_{1.2}$JLR
0
200
400
600
800
1000
10
20
30
40
50
60
70
80

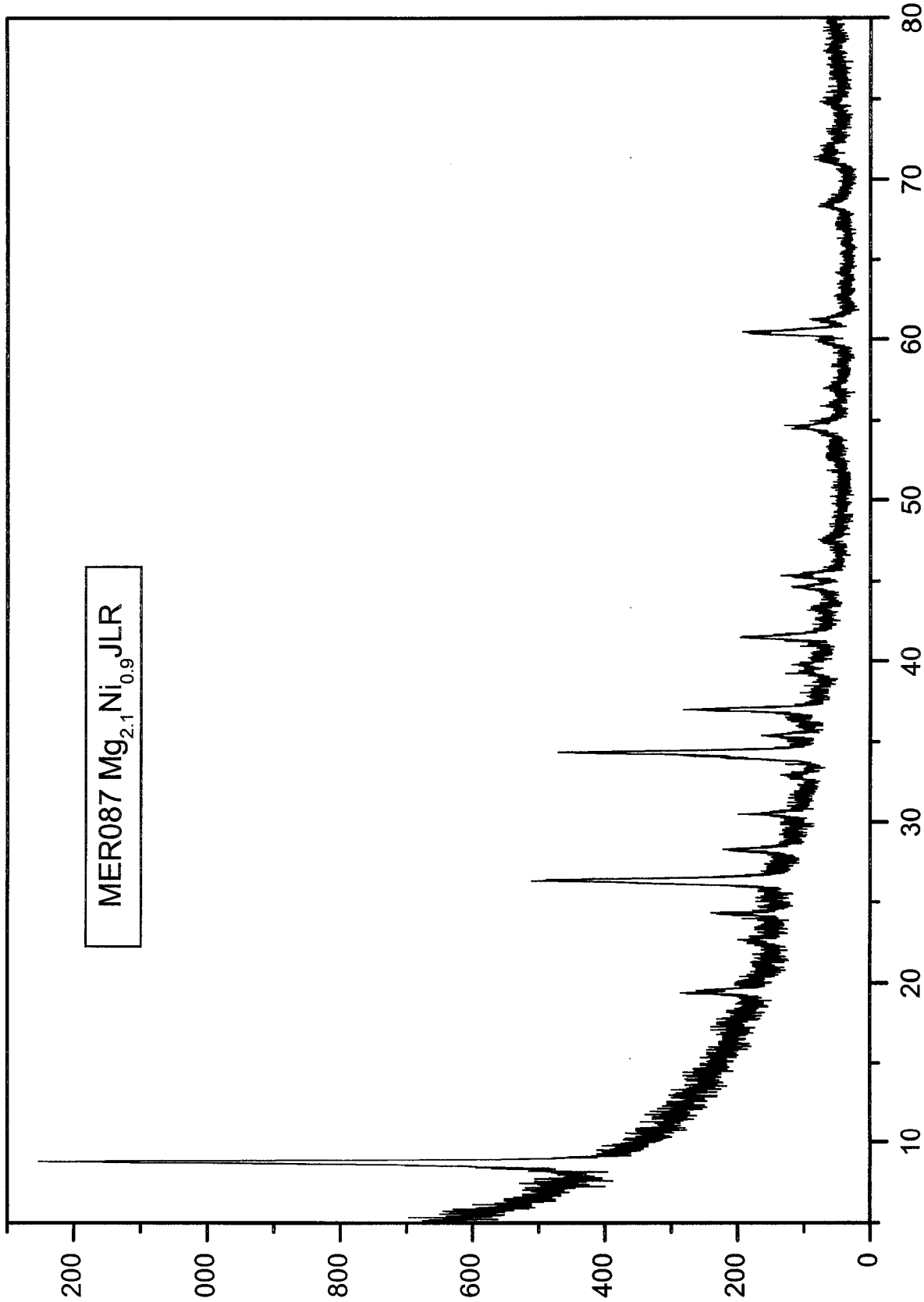
MER087 $Mg_{2.1}Ni_{0.9}$JLR
0
200
400
600
800
1000
1200
10
20
30
40
50
60
70
80

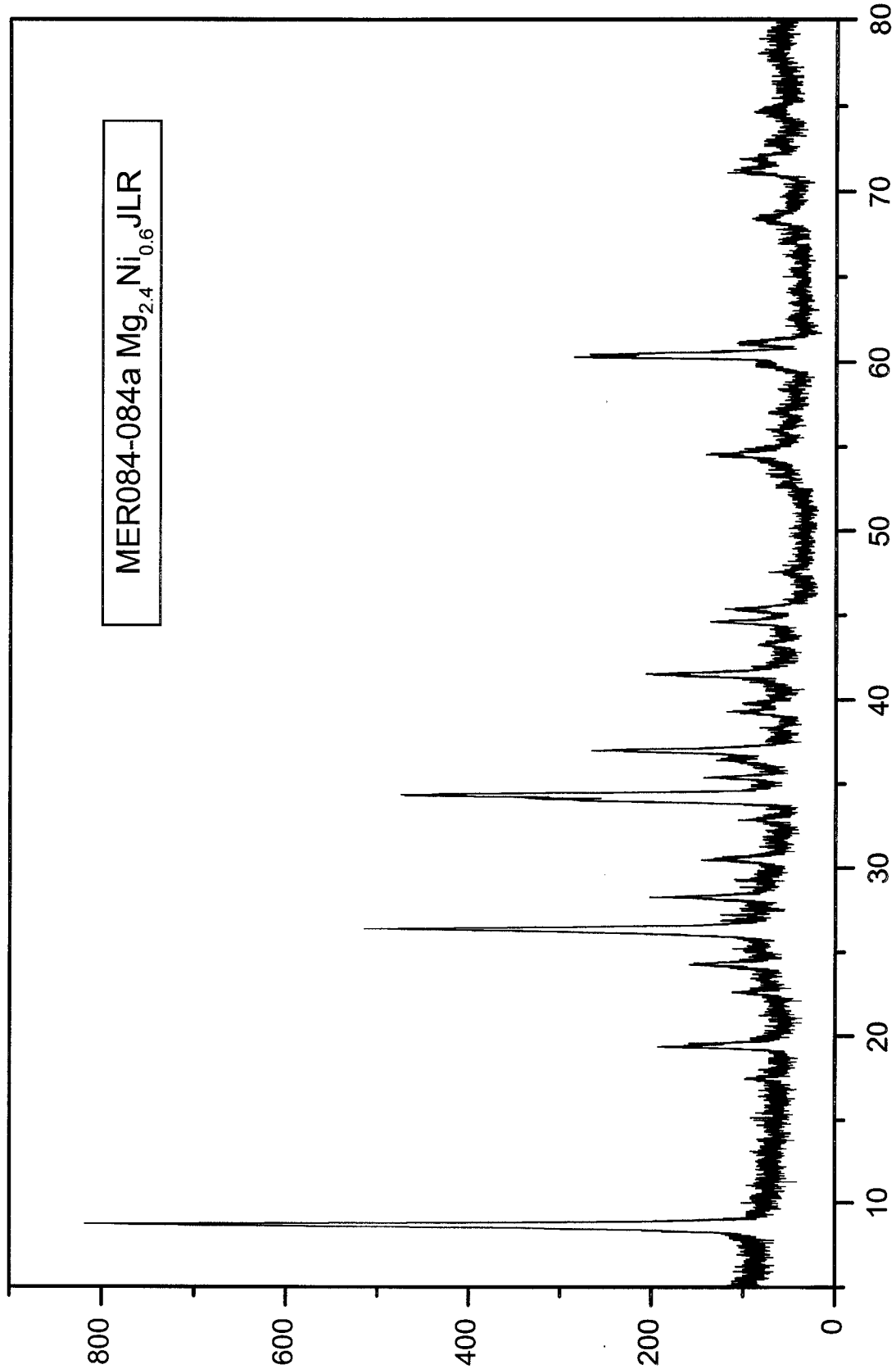
MER084-084a $Mg_{2.4}Ni_{0.6}$JLR
800
600
400
200
0
10
20
30
40
50
60
70
80

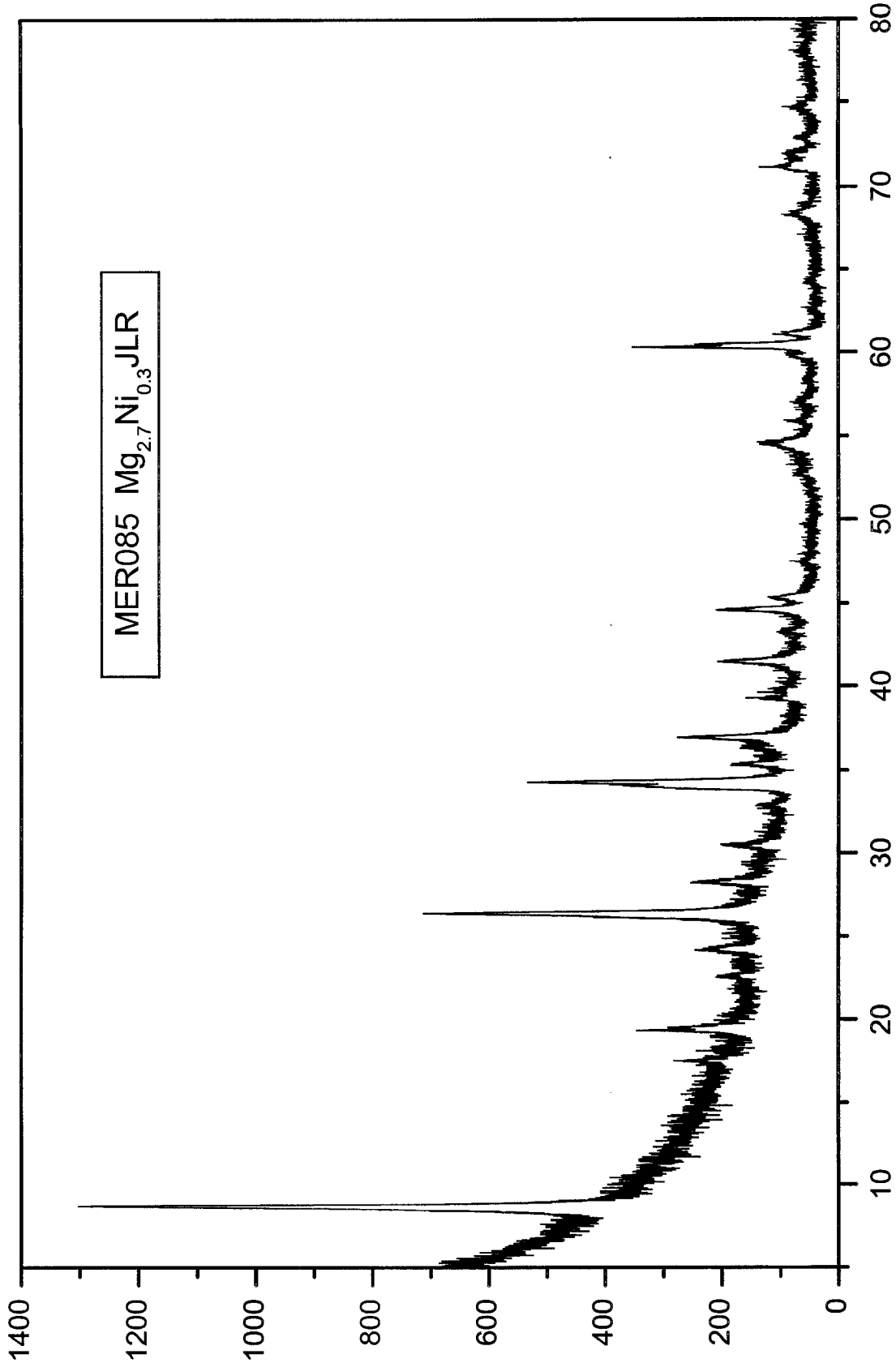
MER085 $Mg_{2.7}Ni_{0.3}$JLR
0
200
400
600
800
1000
1200
1400
10
20
30
40
50
60
70
80

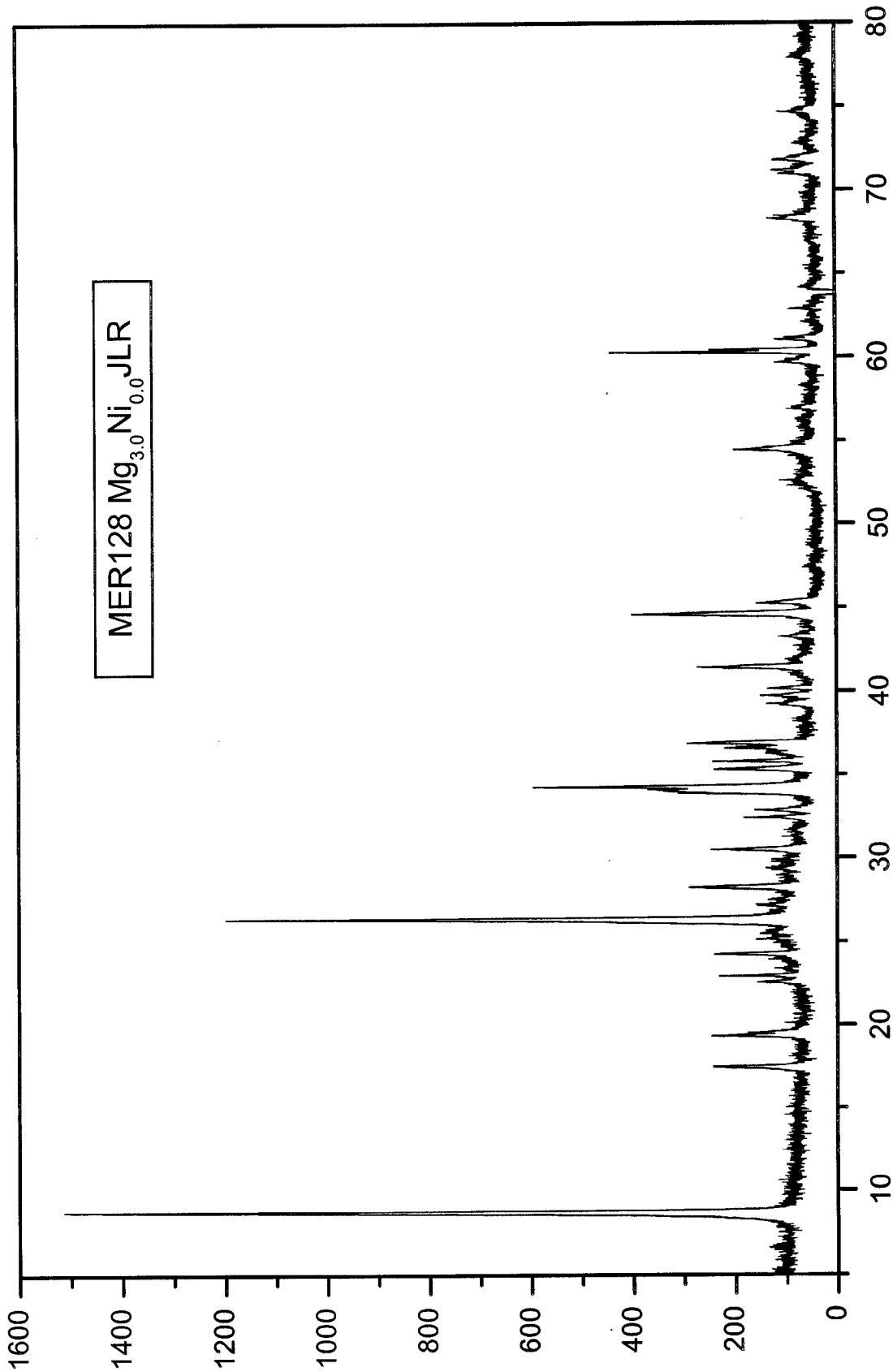
MER128 $Mg_{3.0}Ni_{0.0}$JLR
1600
1400
1200
1000
800
600
400
200
0
10
20
30
40
50
60
70
80

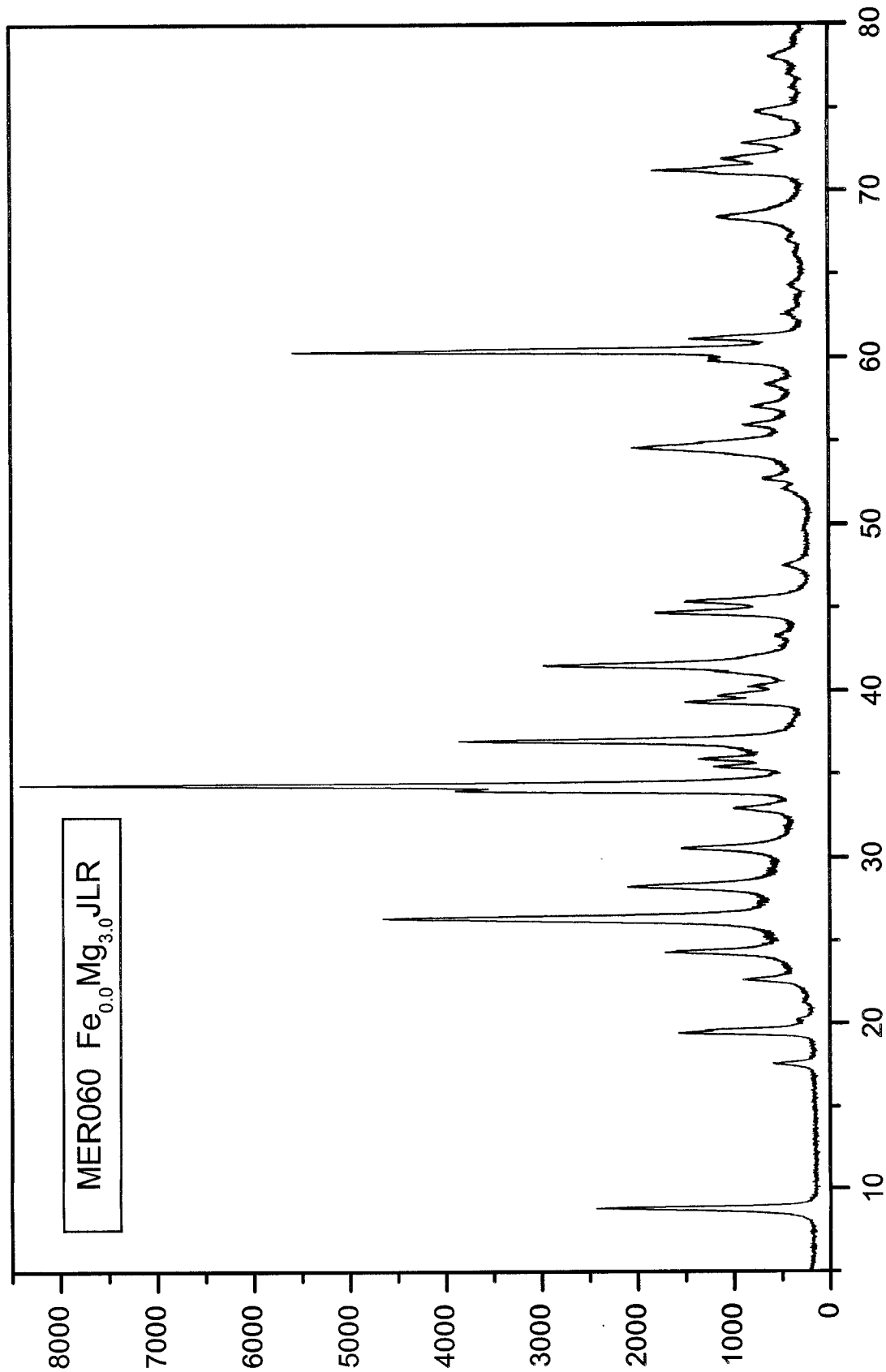
MER060 Fe0.0Mg3.0JLR
8000
7000
6000
5000
4000
3000
2000
1000
0
10
20
30
40
50
60
70
80

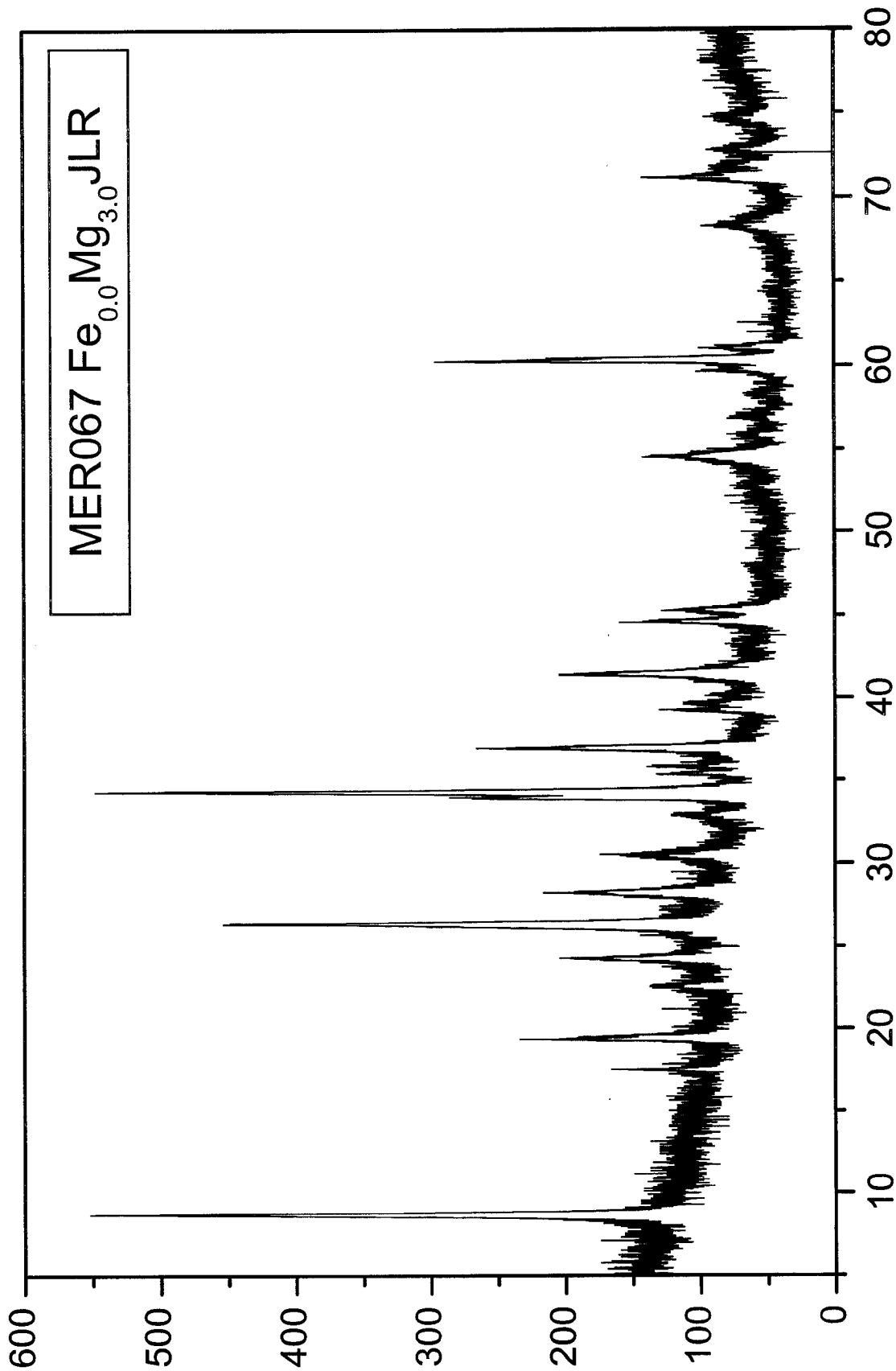
MER067 $Fe_{0.0}Mg_{3.0}$JLR
600
500
400
300
200
100
0
10
20
30
40
50
60
70
80

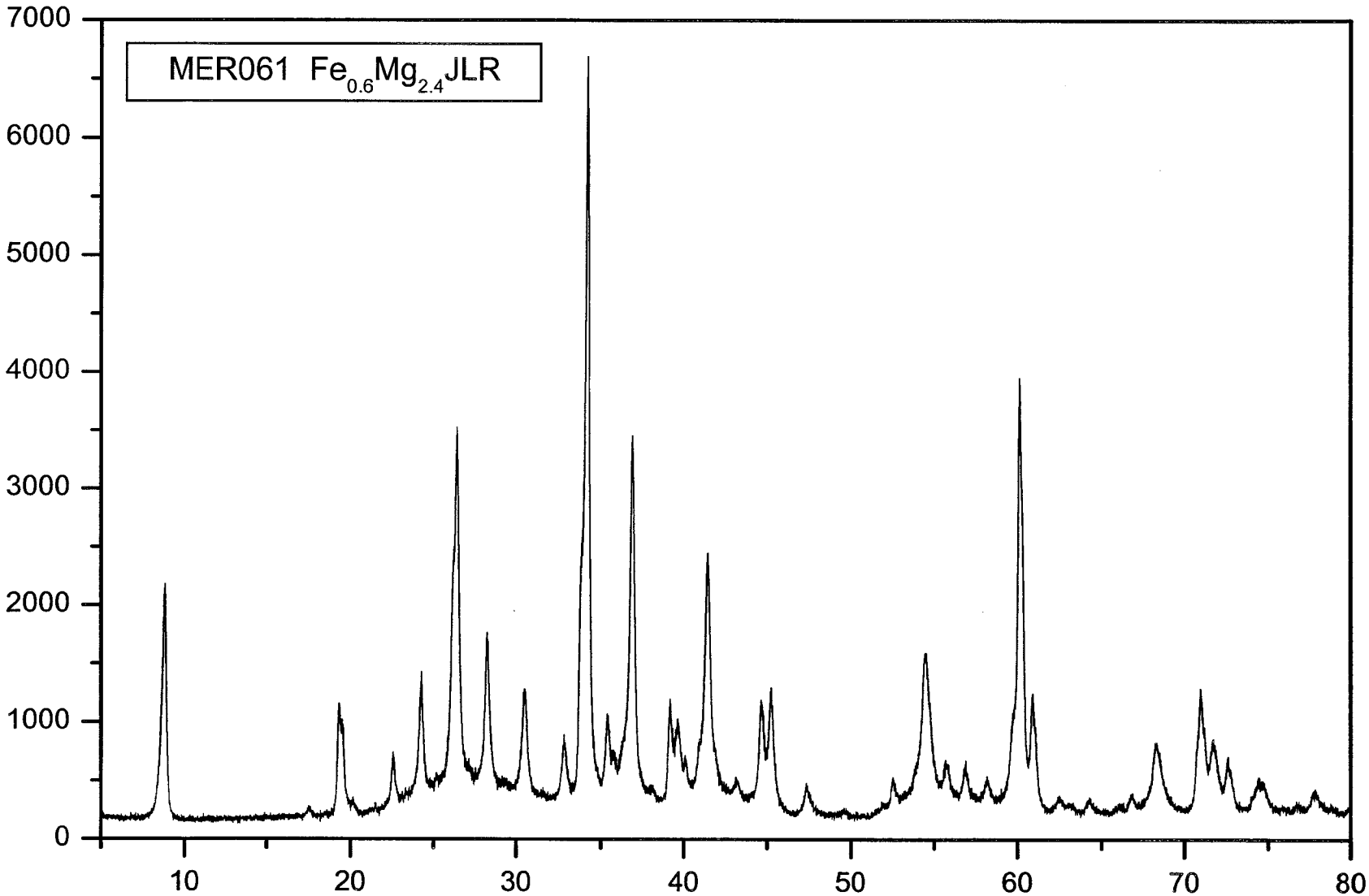
MER061 $Fe_{0.6}Mg_{2.4}$JLR
7000
6000
5000
4000
3000
2000
1000
0
10
20
30
40
50
60
70
80

A31

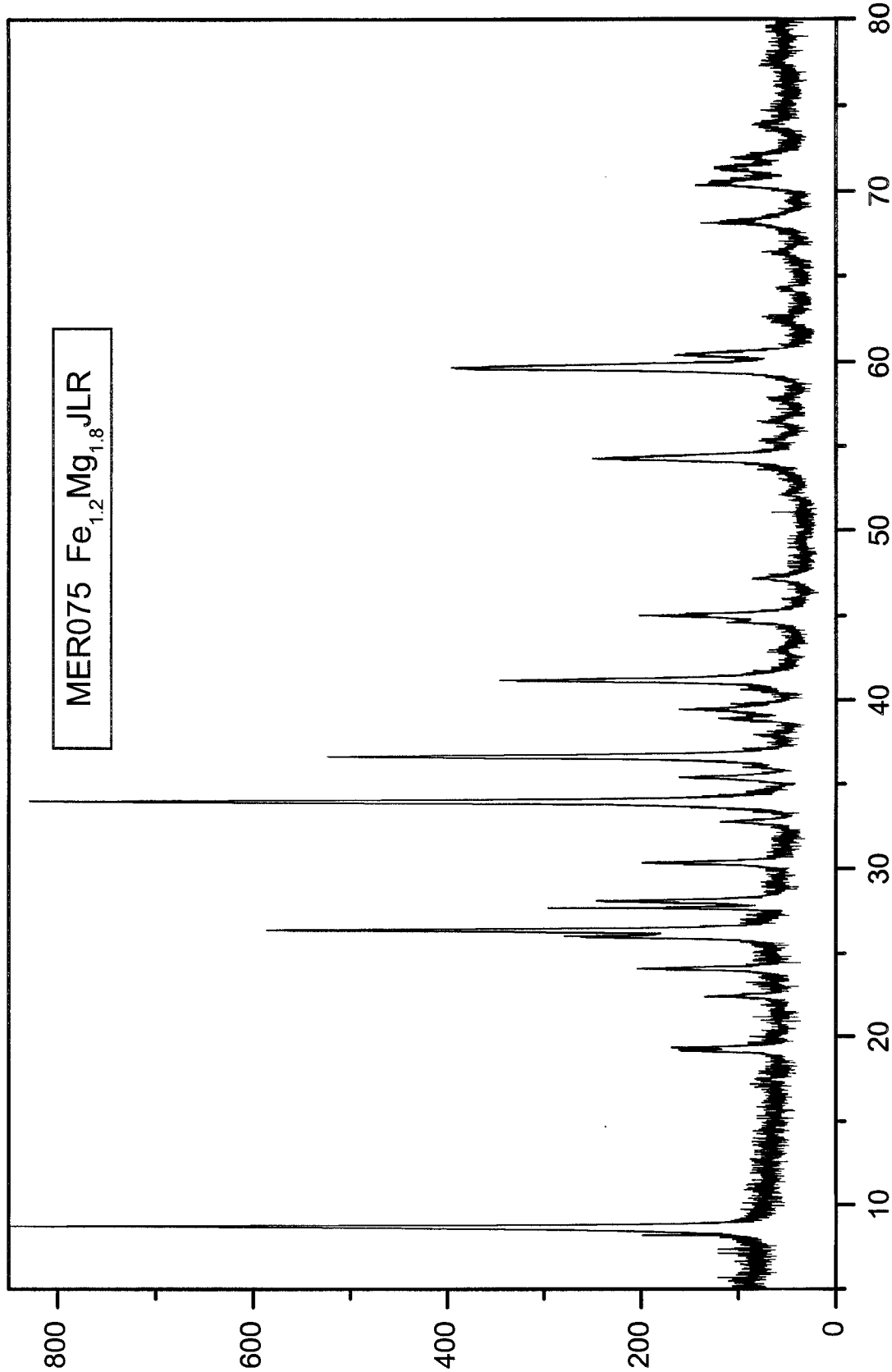
MER075 $Fe_{1.2}Mg_{1.8}$JLR
800
600
400
200
0
10
20
30
40
50
60
70
80

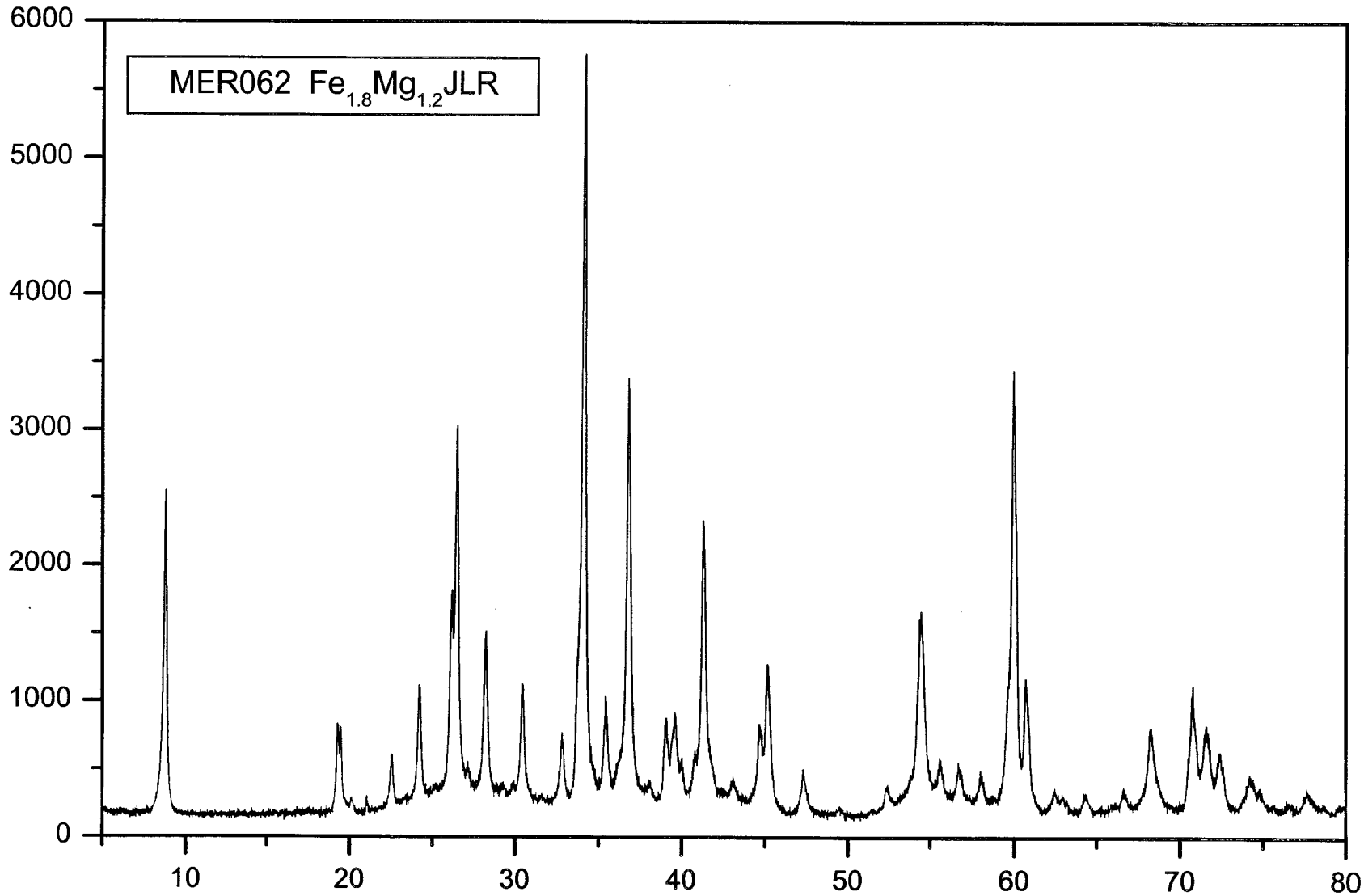
MER062 $Fe_{1.8}Mg_{1.2}$JLR
6000
5000
4000
3000
2000
1000
0
10
20
30
40
50
60
70
80

A33

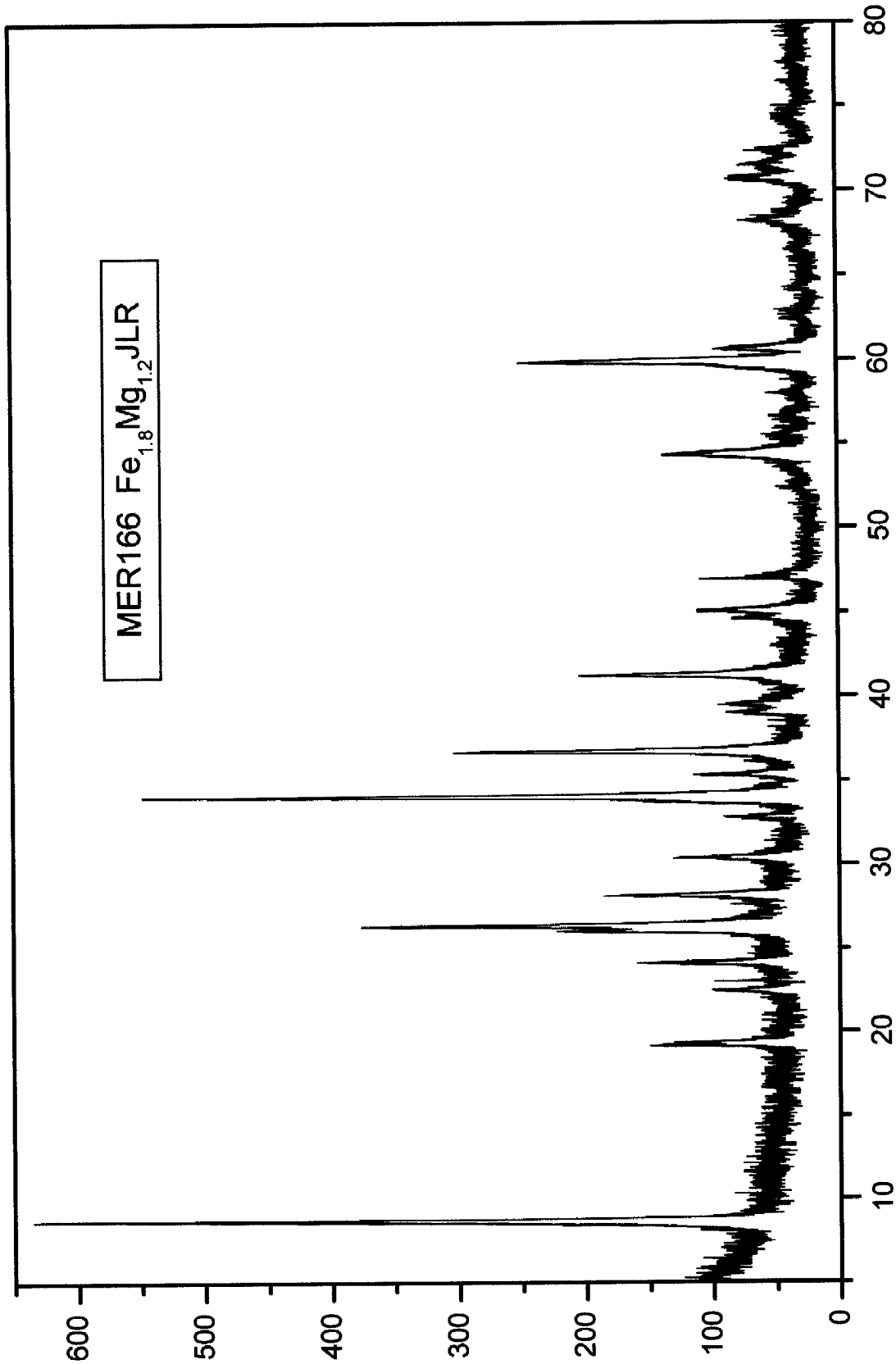
MER166 $Fe_{1.8}Mg_{1.2}$JLR
600
500
400
300
200
100
0
10
20
30
40
50
60
70
80

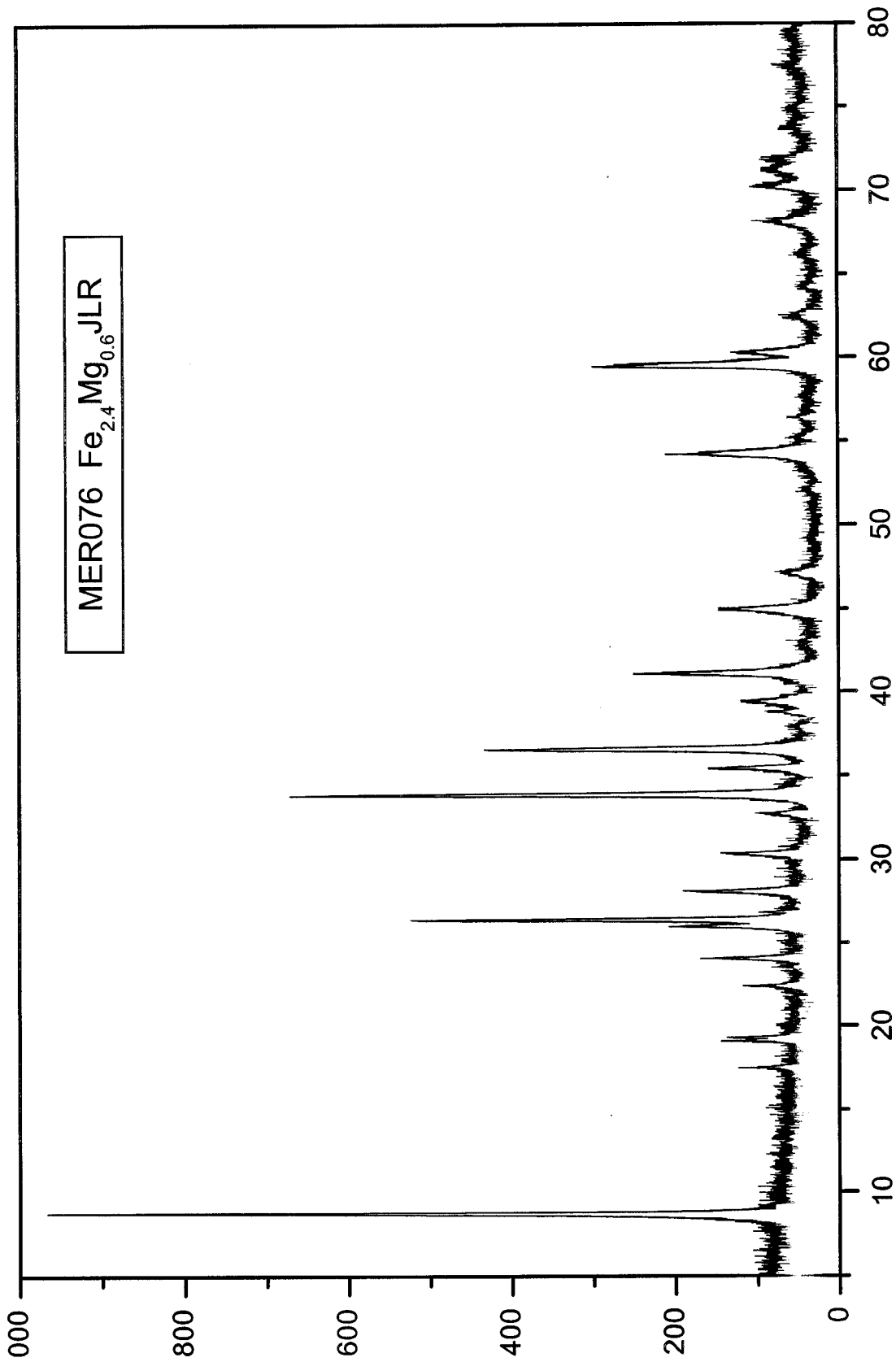
MER076 $Fe_{2.4}Mg_{0.6}$JLR
0
200
400
600
800
1000
10
20
30
40
50
60
70
80

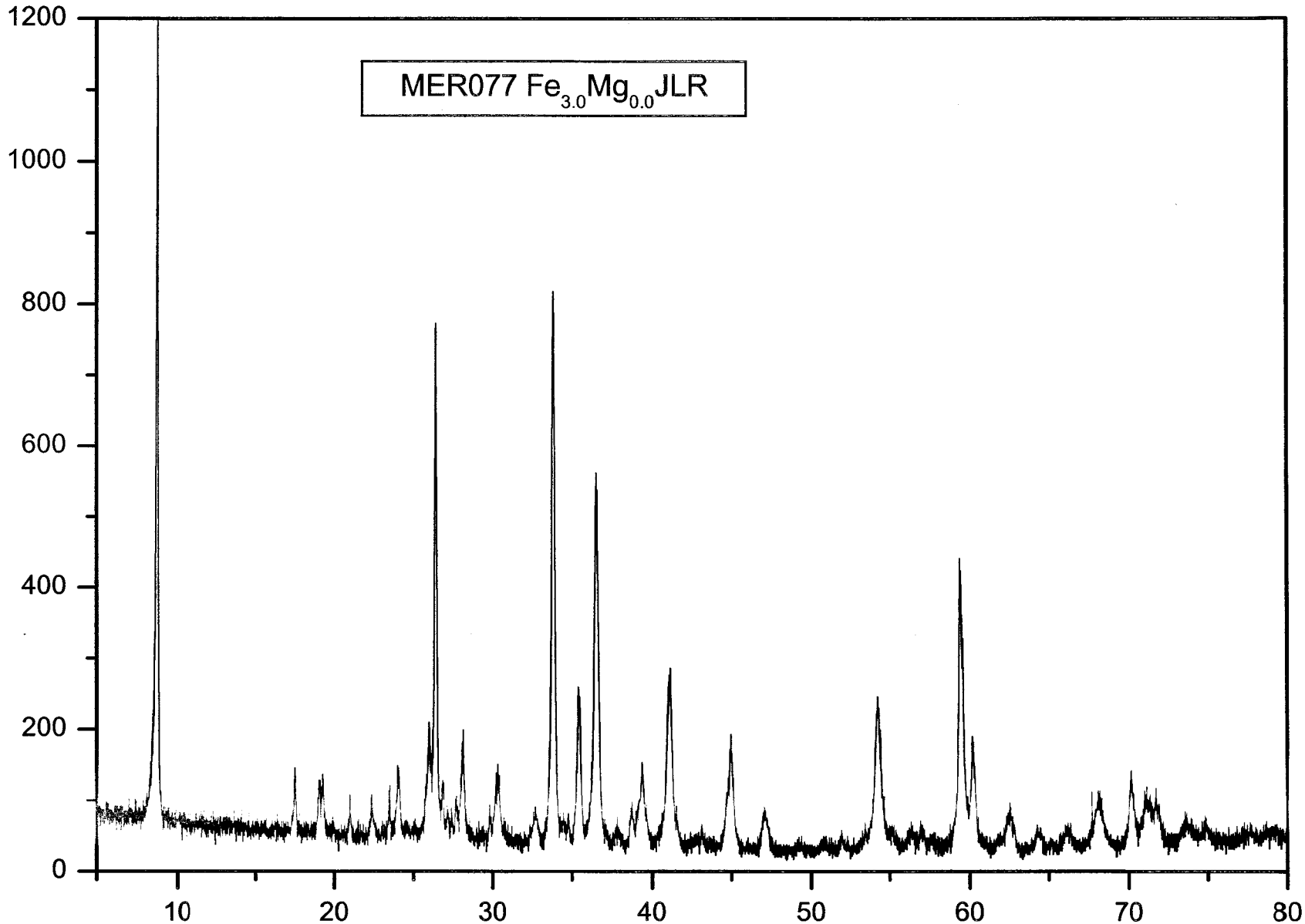
MER077 $Fe_{3.0}Mg_{0.0}$JLR
1200
1000
800
600
400
200
0
10
20
30
40
50
60
70
80

A36

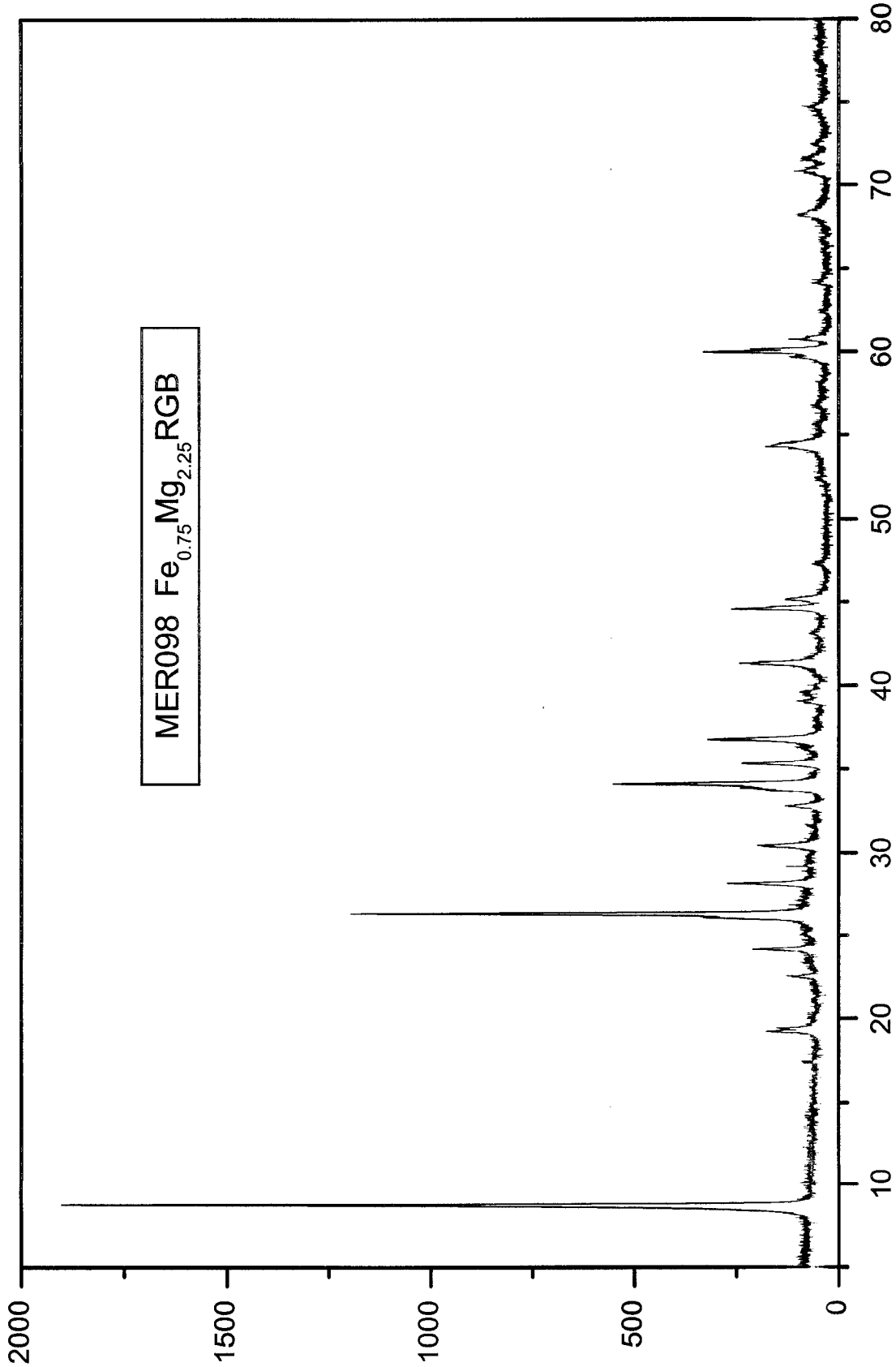
MER098 $Fe_{0.75}Mg_{2.25}RGB$
2000
1500
1000
500
0
10
20
30
40
50
60
70
80

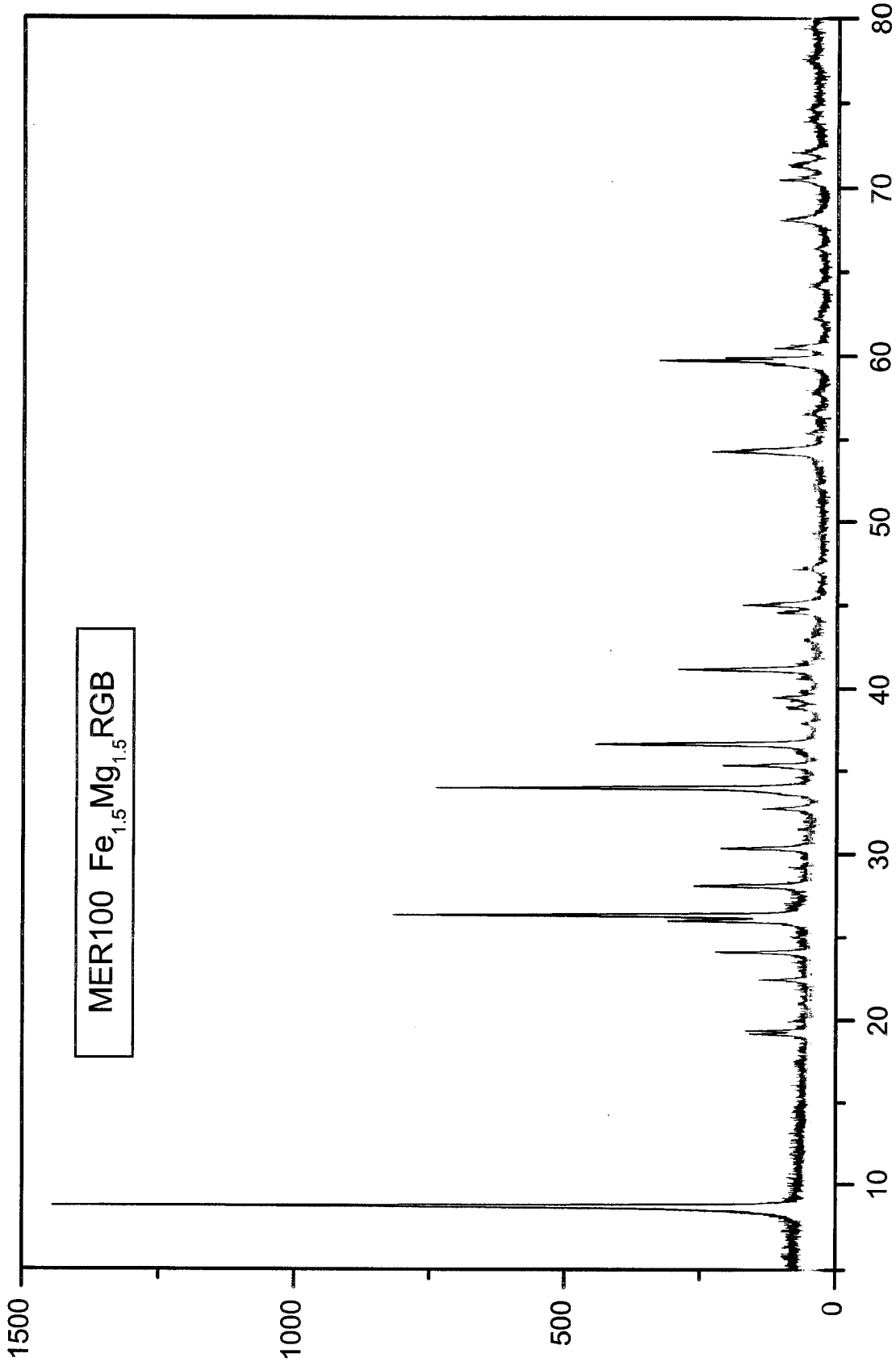
MER100 $Fe_{1.5}Mg_{1.5}$RGB
1500
1000
500
0
10
20
30
40
50
60
70
80

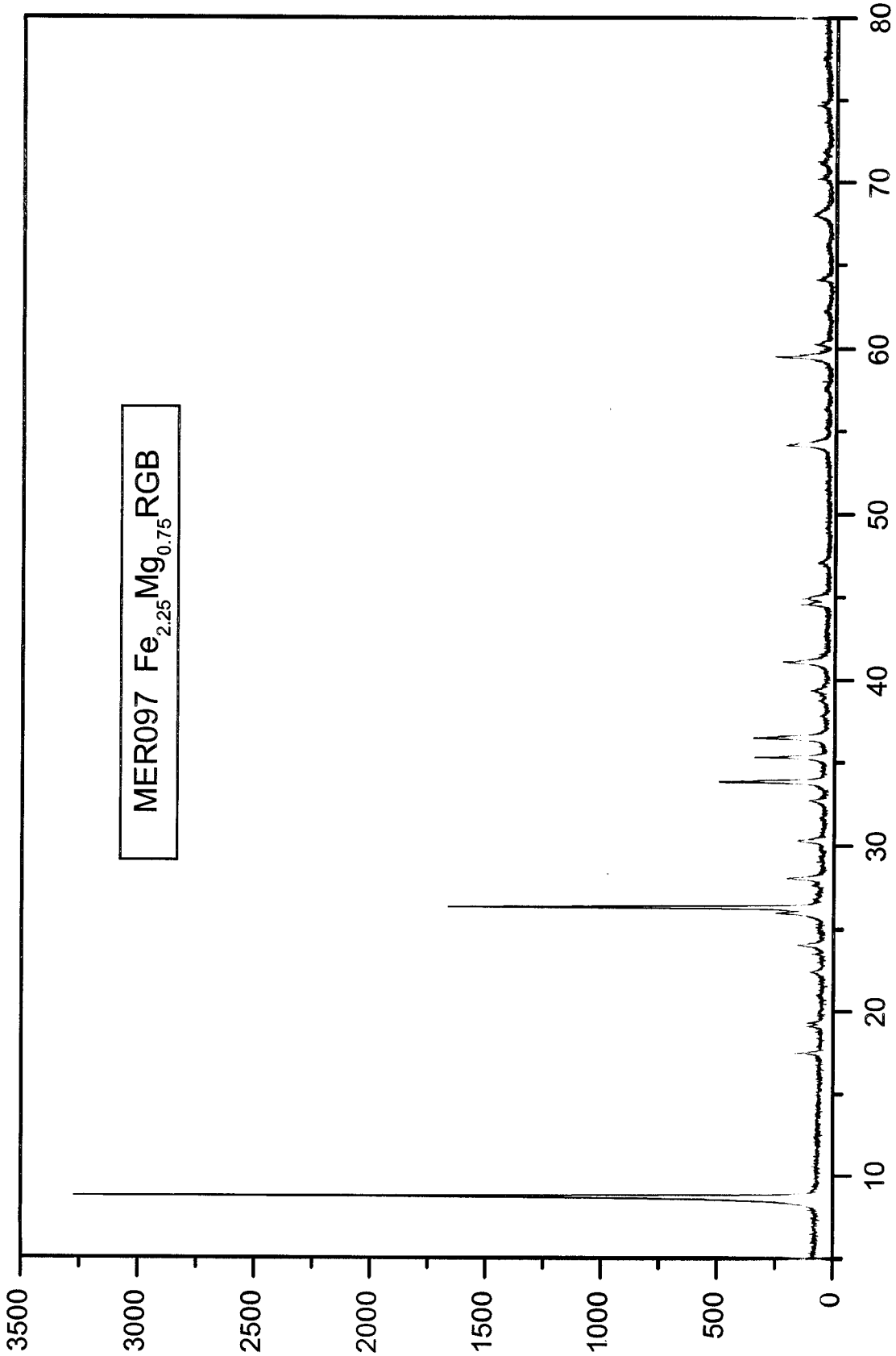
MER097 $Fe_{2.25}Mg_{0.75}RGB$
3500
3000
2500
2000
1500
1000
500
0
10
20
30
40
50
60
70
80

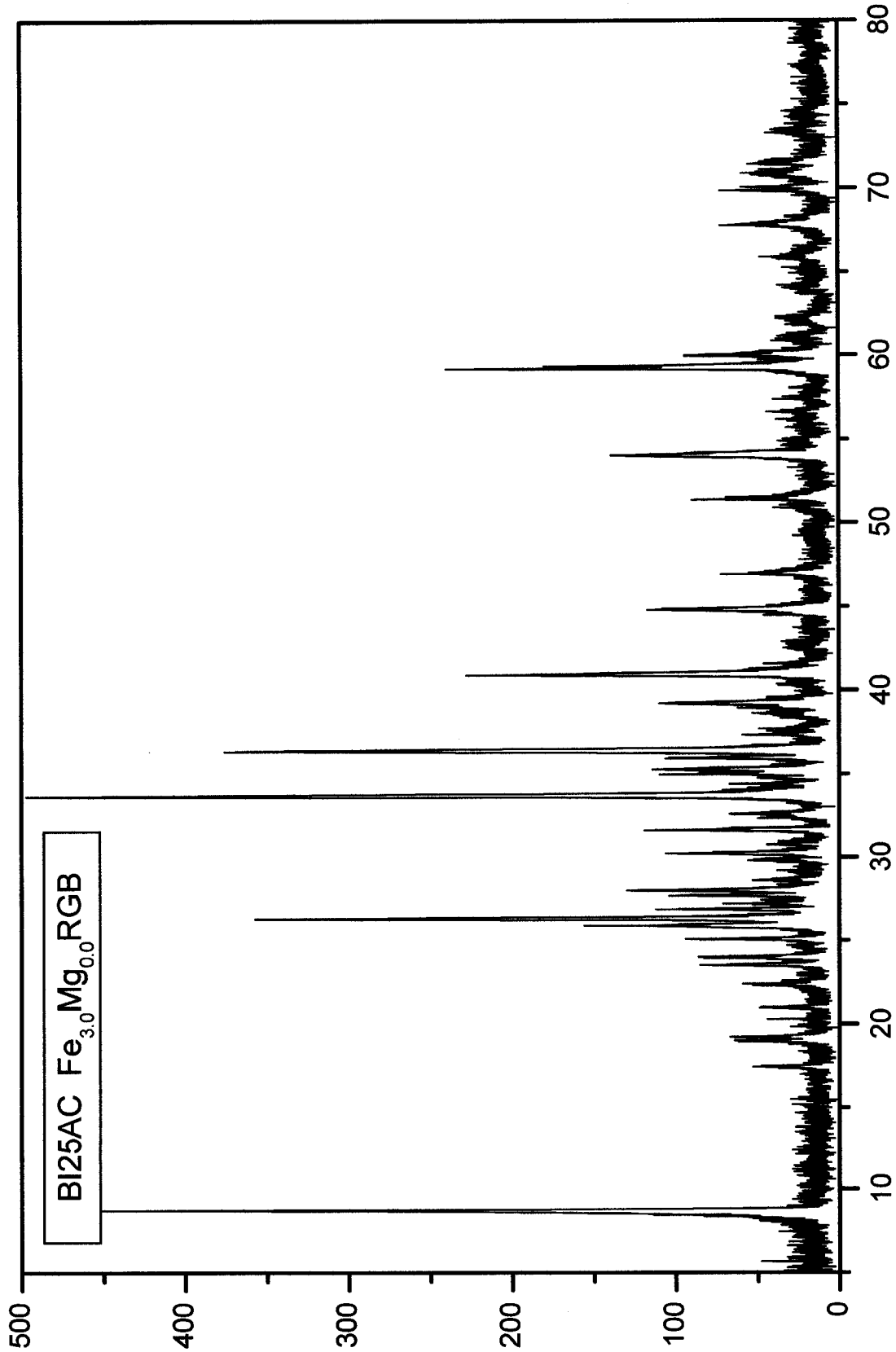
BI25AC Fe3.0Mg0.0RGB
500
400
300
200
100
0
10
20
30
40
50
60
70
80

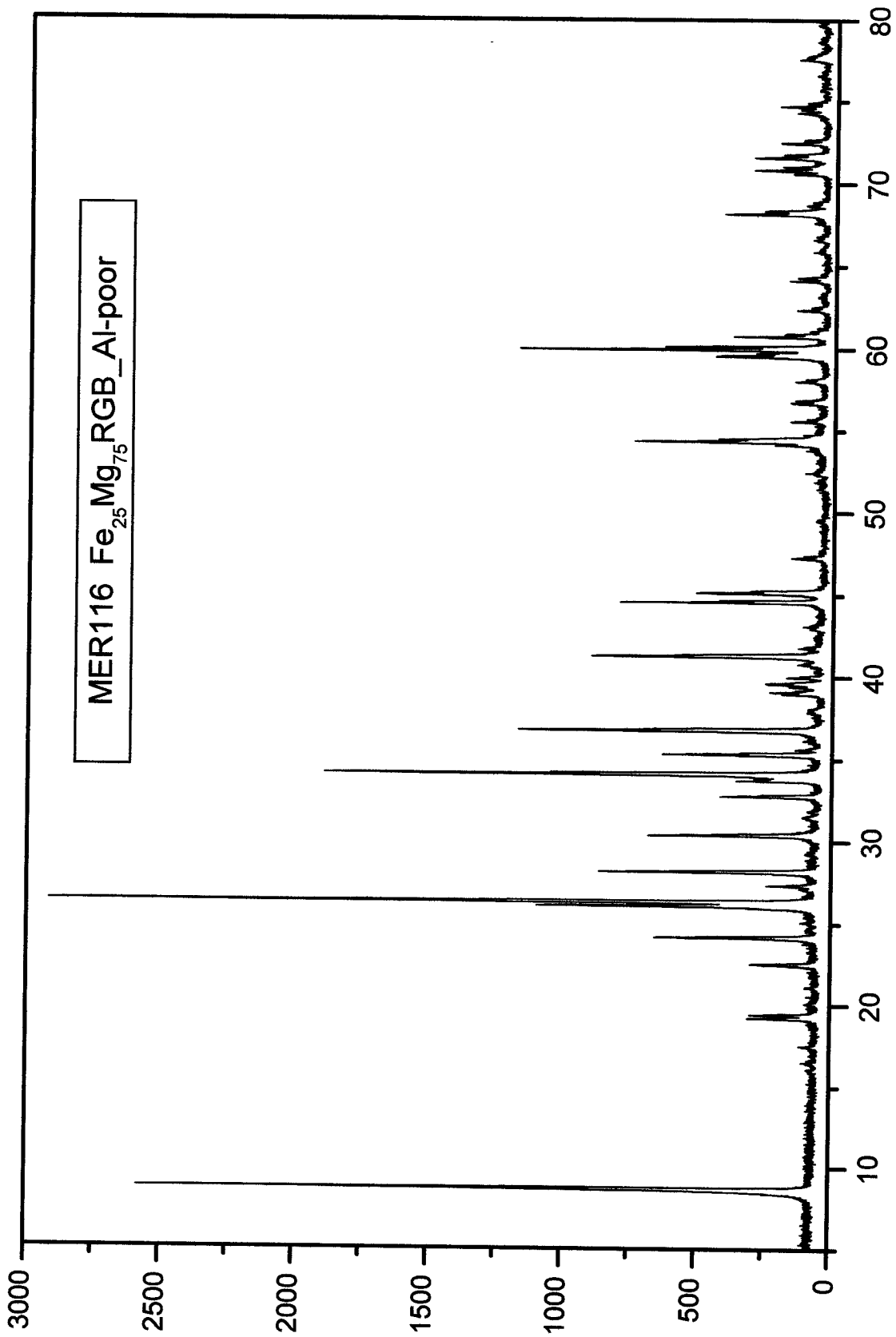
MER116 $Fe_{25}Mg_{75}$RGB_Al-poor
3000
2500
2000
1500
1000
500
0
10
20
30
40
50
60
70
80

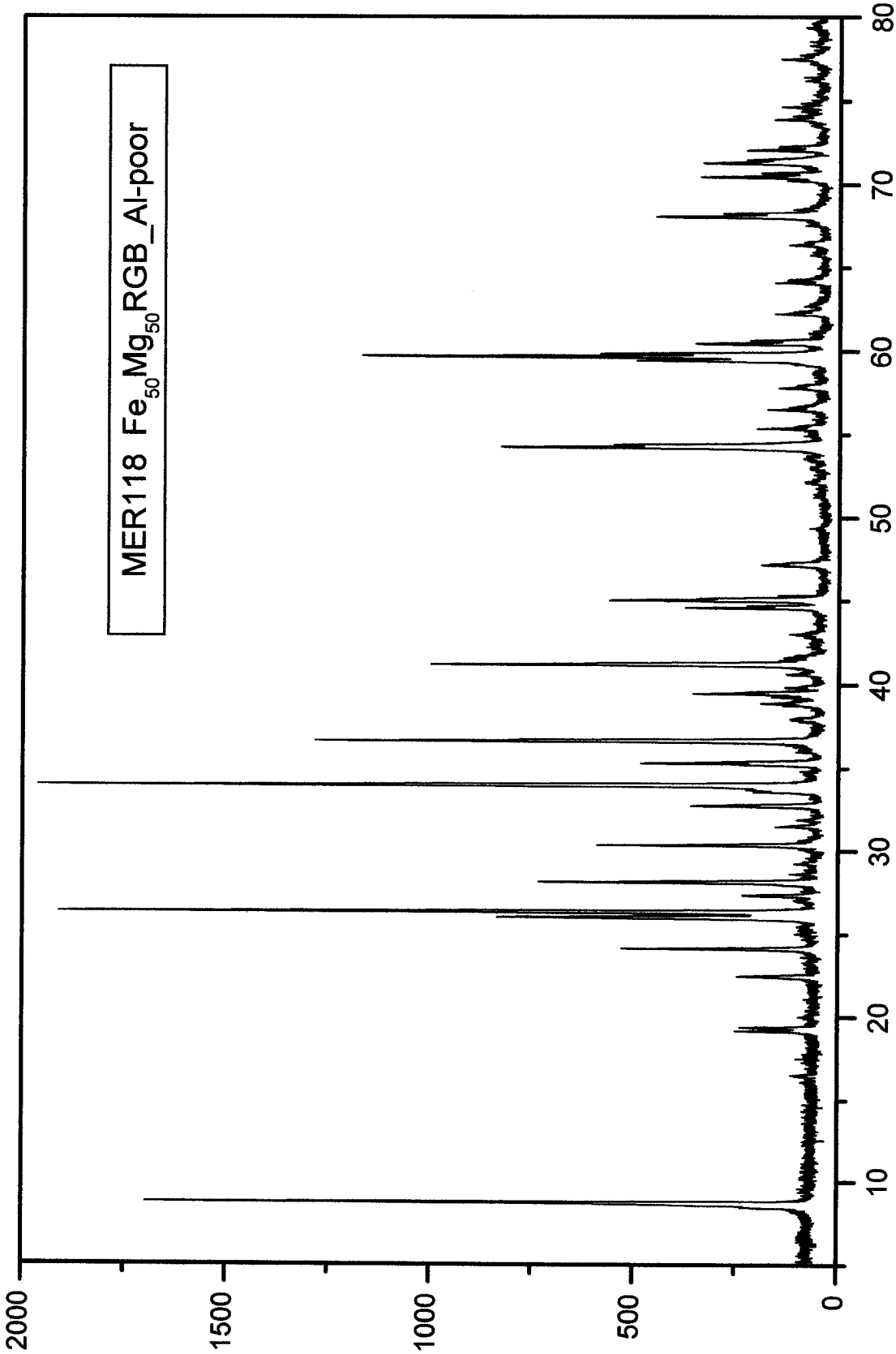
MER118 $Fe_{50}Mg_{50}$RGB_Al-poor
2000
1500
1000
500
0
10
20
30
40
50
60
70
80

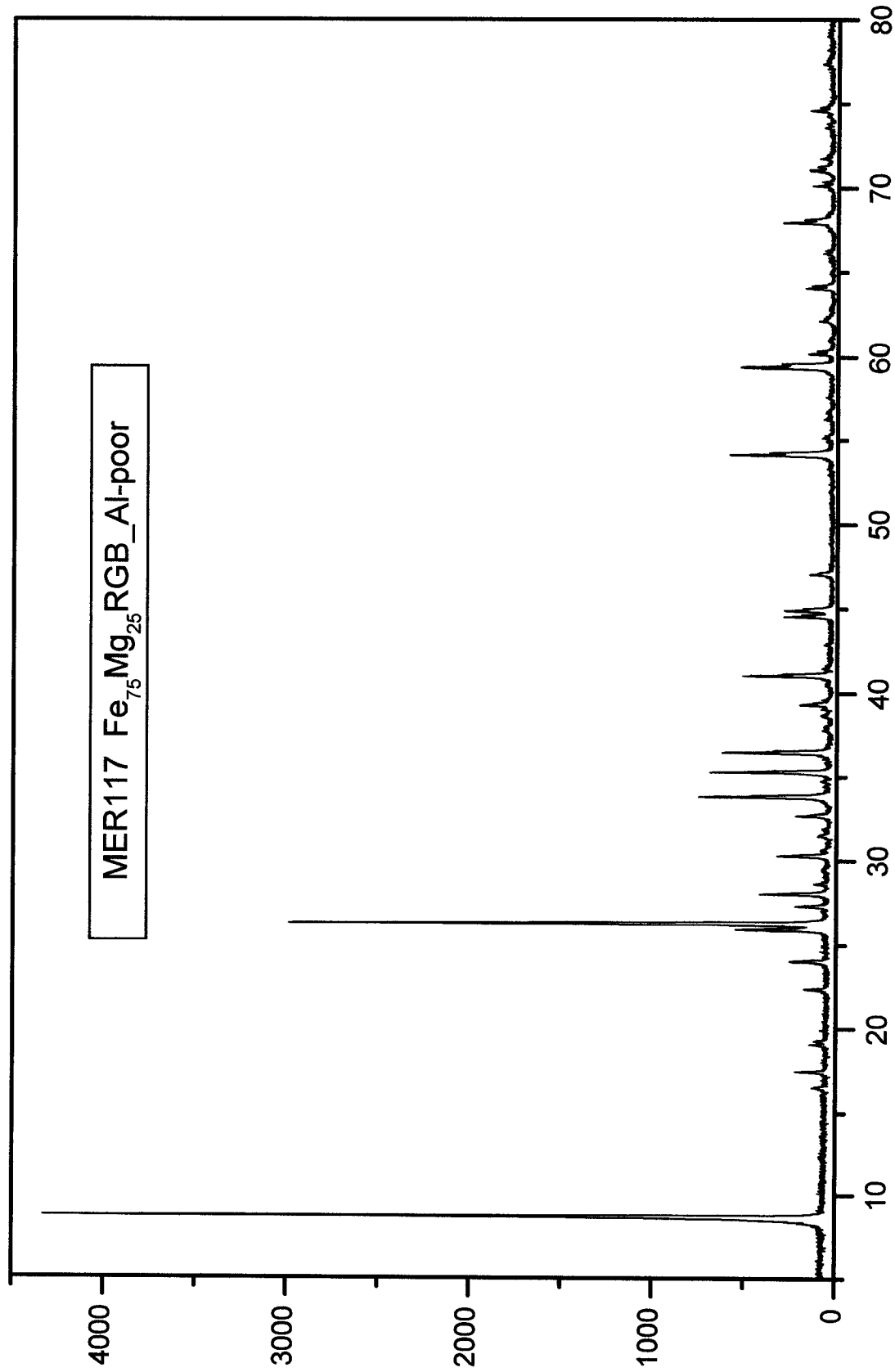
MER117 Fe75Mg25RGB_Al-poor
4000
3000
2000
1000
0
10
20
30
40
50
60
70
80

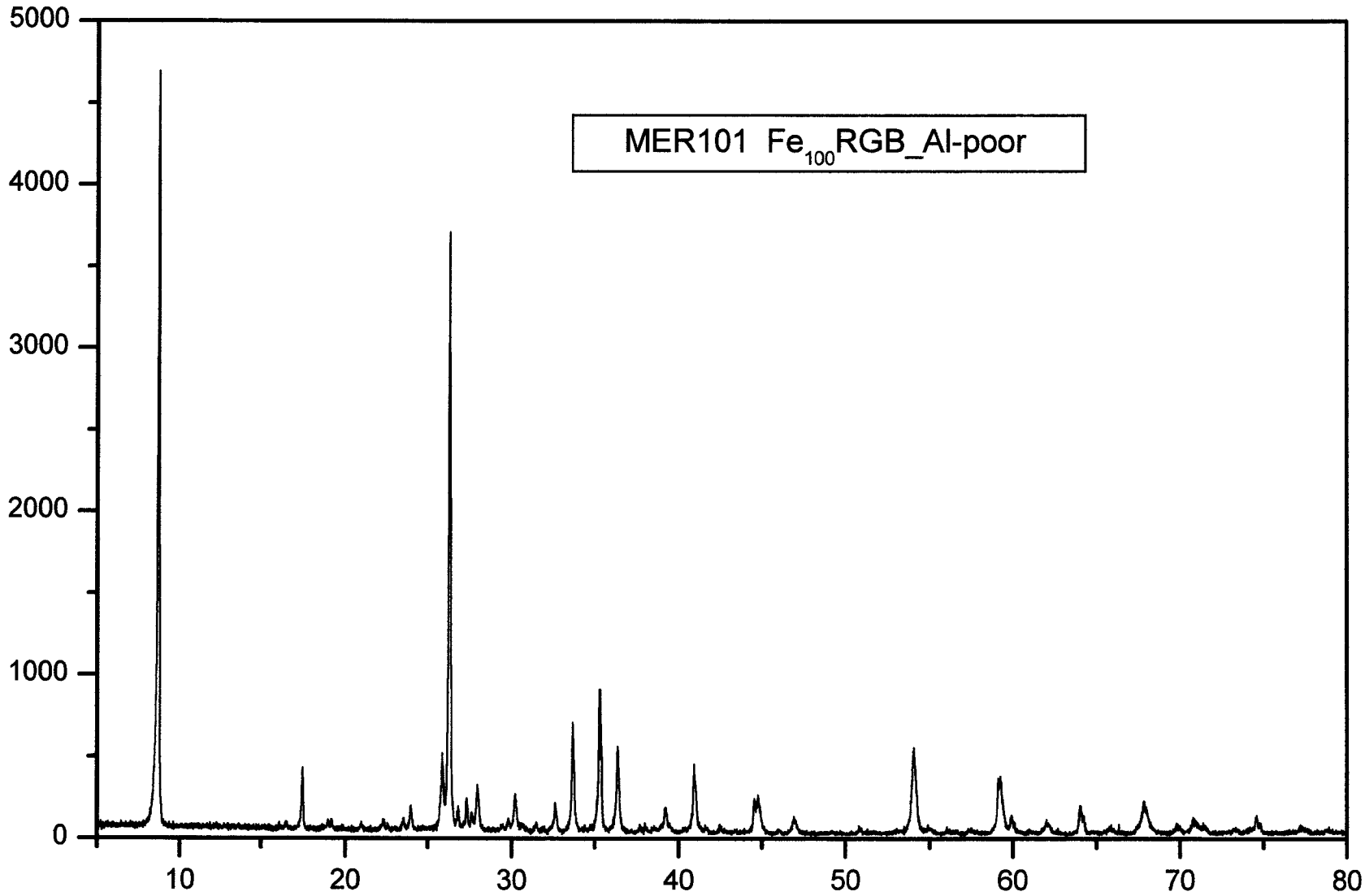
MER101 Fe100RGB_Al-poor
5000
4000
3000
2000
1000
0
10
20
30
40
50
60
70
80

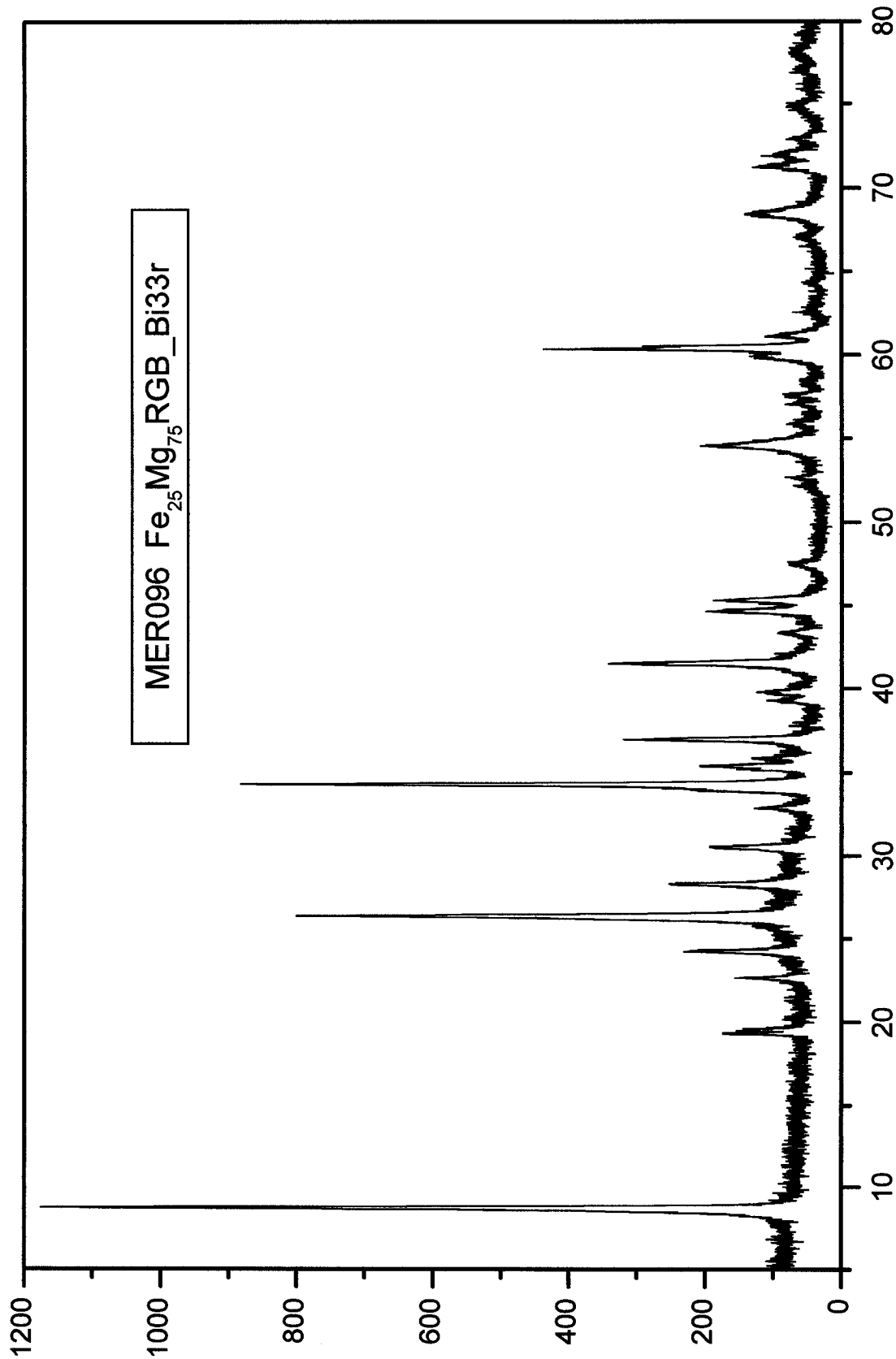
MER096 Fe25Mg75RGB_Bi33r
0
200
400
600
800
1000
1200
10
20
30
40
50
60
70
80

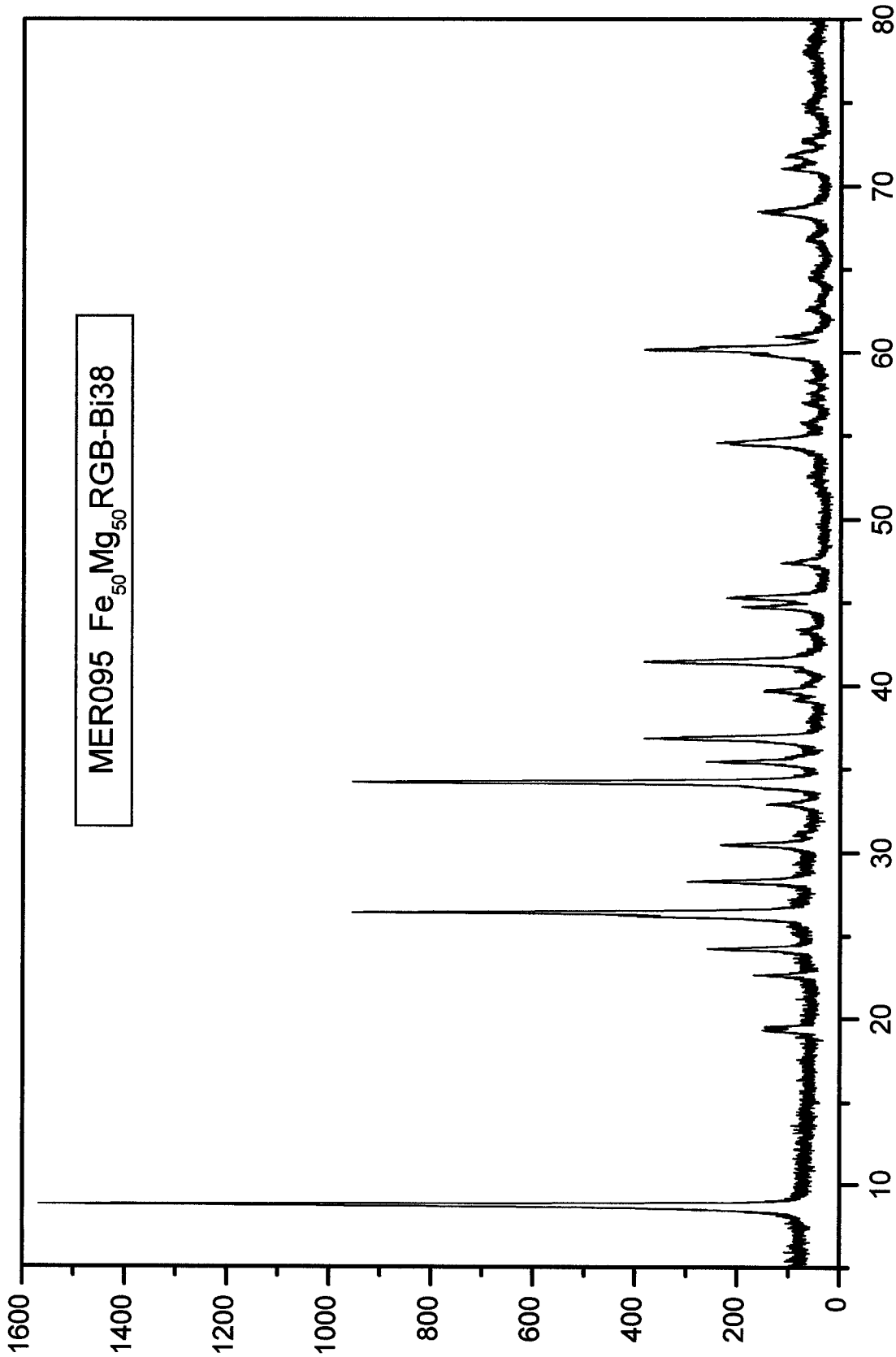
MER095 Fe50Mg50RGB-Bi38
1600
1400
1200
1000
800
600
400
200
0
10
20
30
40
50
60
70
80

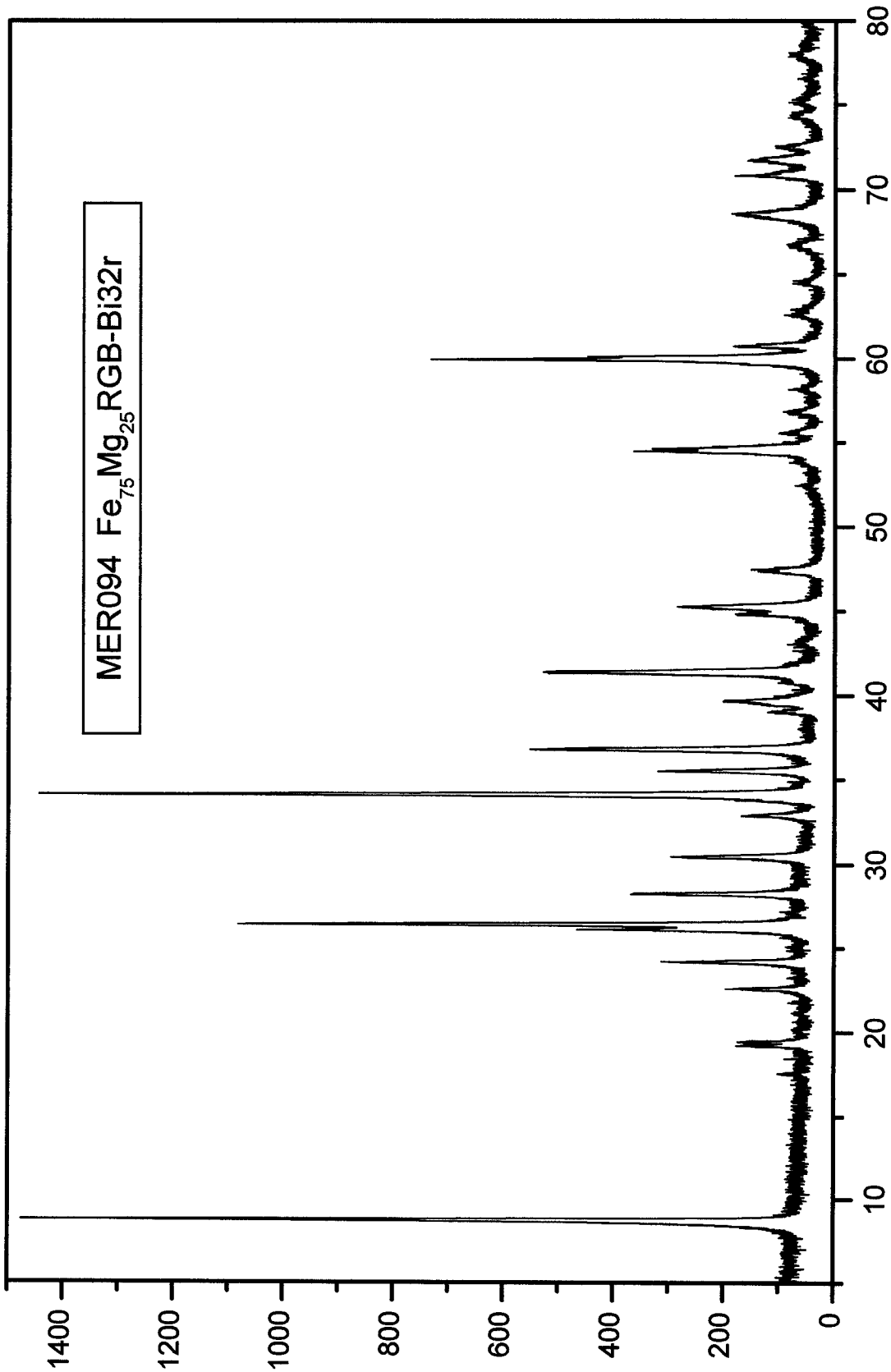
MER094 Fe75Mg25RGB-Bi32r
0
200
400
600
800
1000
1200
1400
10
20
30
40
50
60
70
80

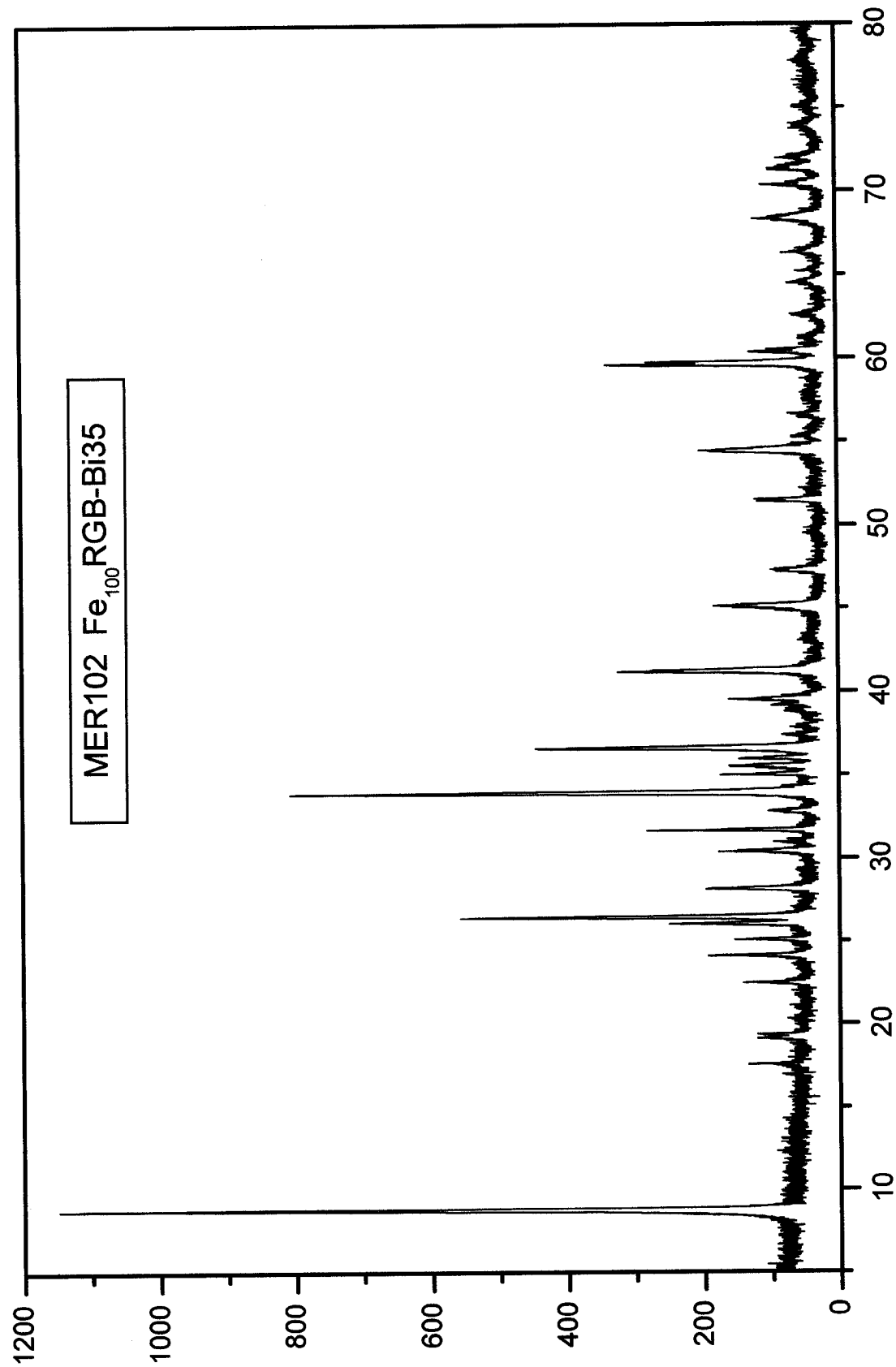
MER102 Fe100RGB-Bi35
1200
1000
800
600
400
200
0
10
20
30
40
50
60
70
80

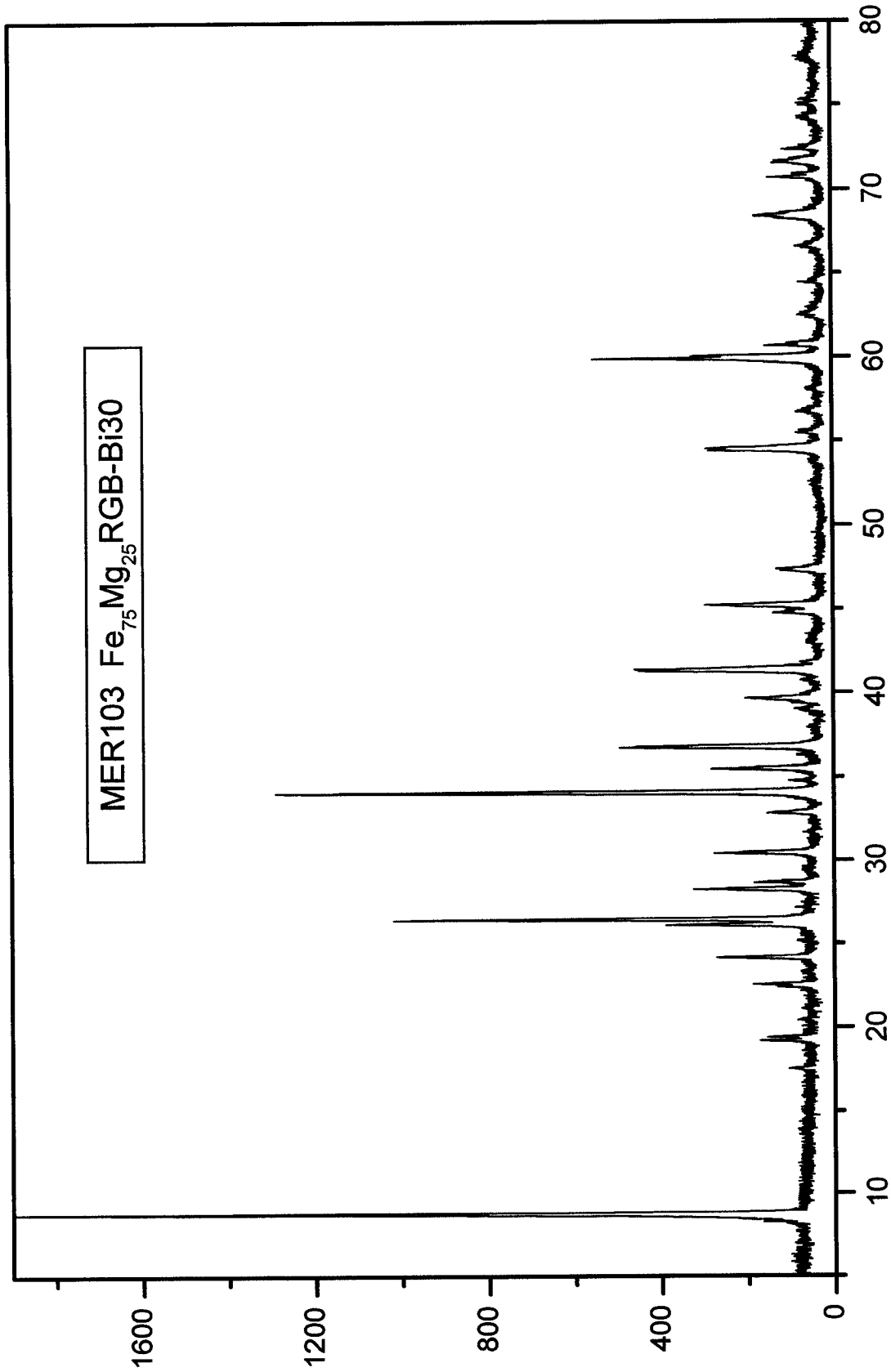
MER103 Fe75Mg25RGB-Bi30
0
400
800
1200
1600
10
20
30
40
50
60
70
80

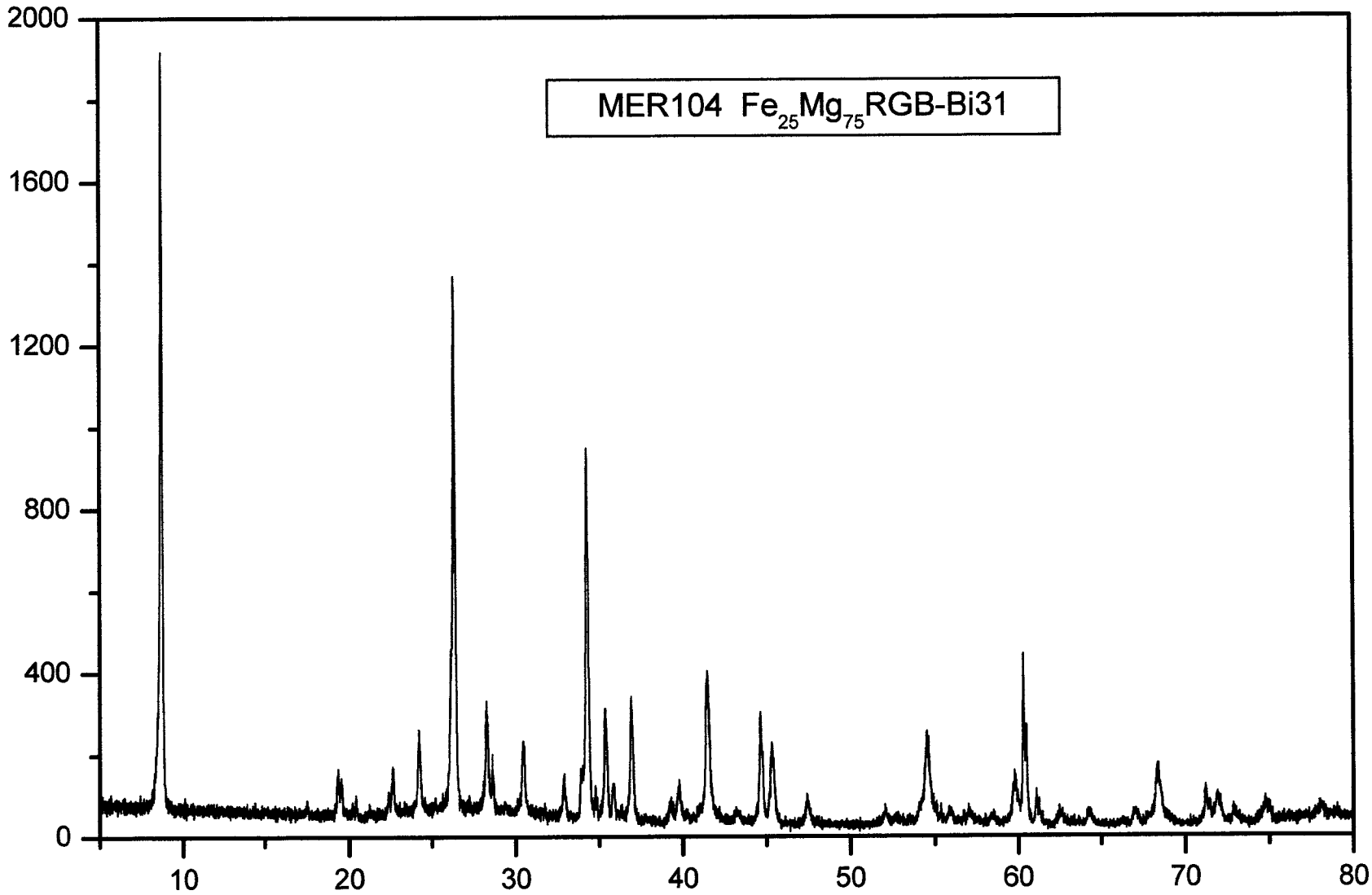
MER104 $Fe_{25}Mg_{75}$RGB-Bi31
2000
1600
1200
800
400
0
10
20
30
40
50
60
70
80

ASD

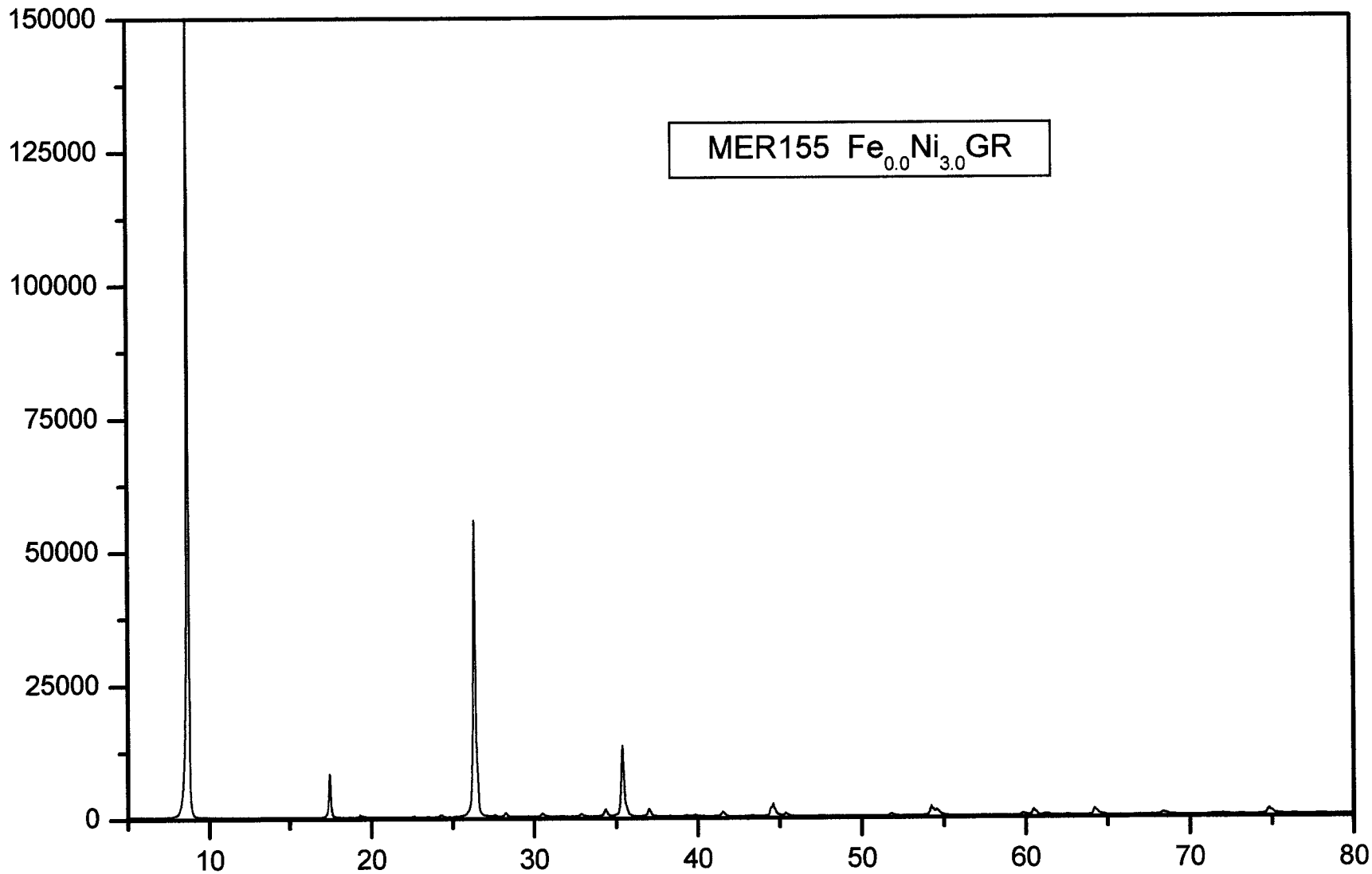
MER155 $Fe_{0.0}Ni_{3.0}GR$
150000
125000
100000
75000
50000
25000
0
10
20
30
40
50
60
70
80

A51

A51a

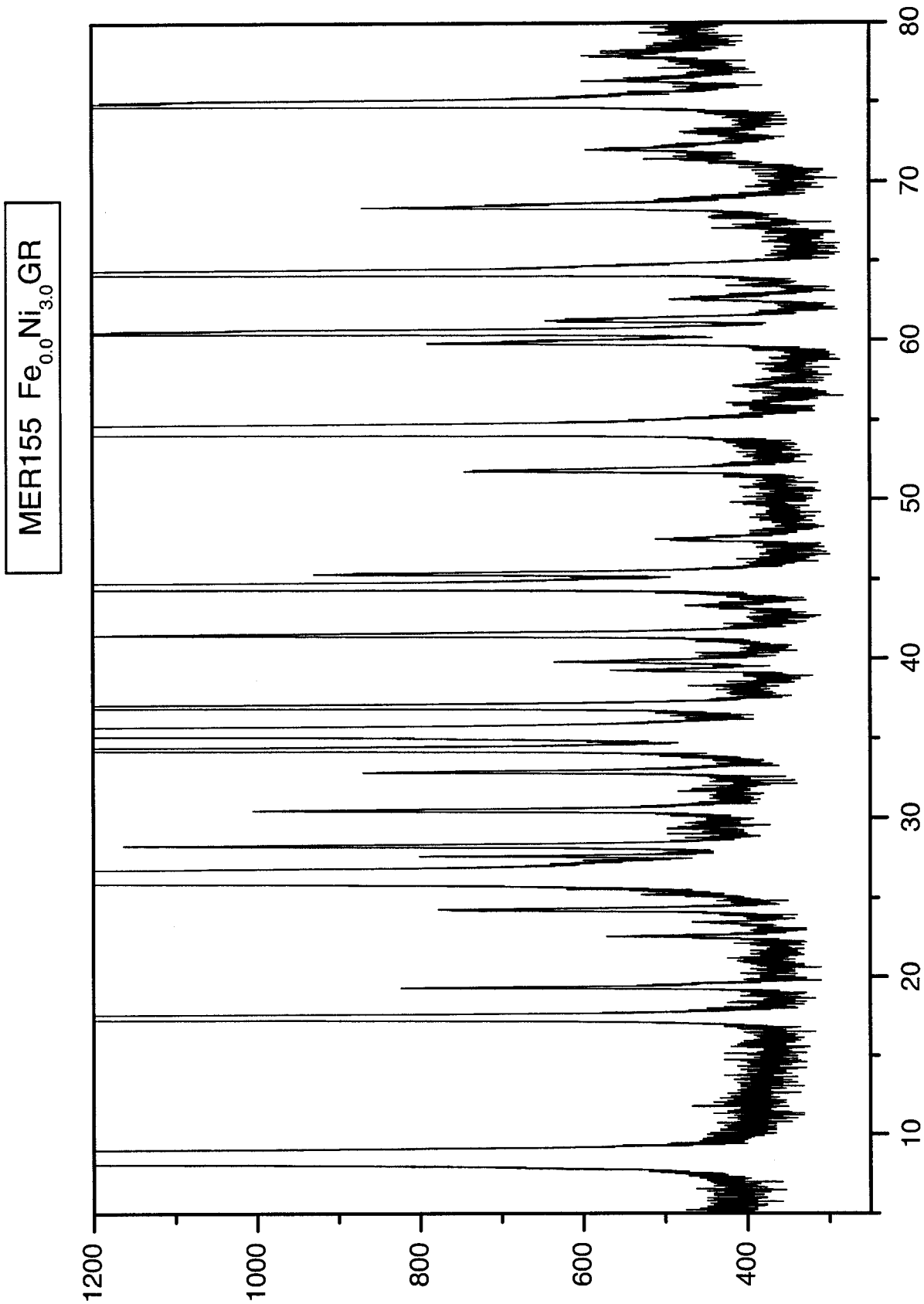

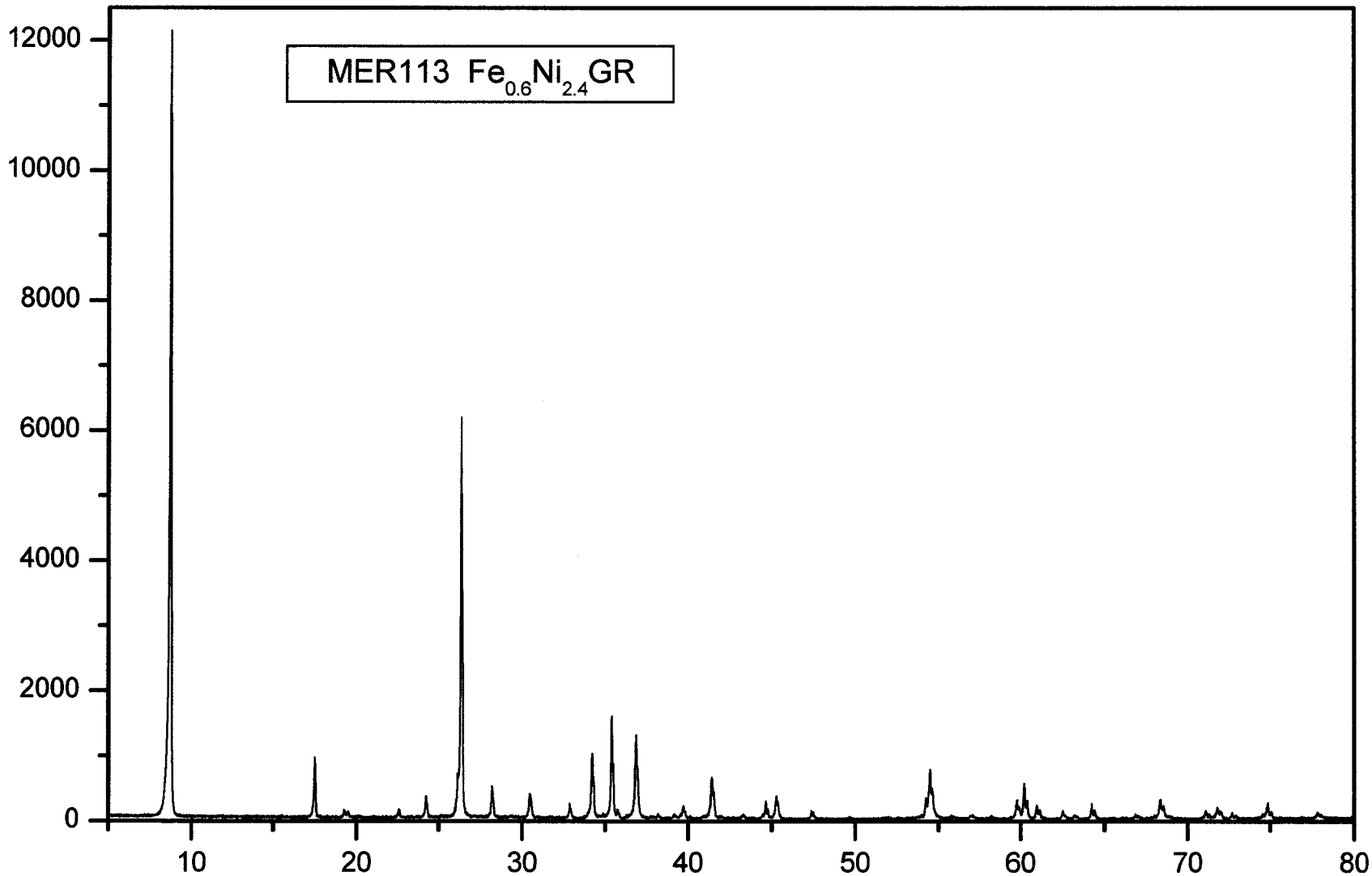
MER113 $Fe_{0.6}Ni_{2.4}GR$
12000
10000
8000
6000
4000
2000
0
10
20
30
40
50
60
70
80

AS2

A52a

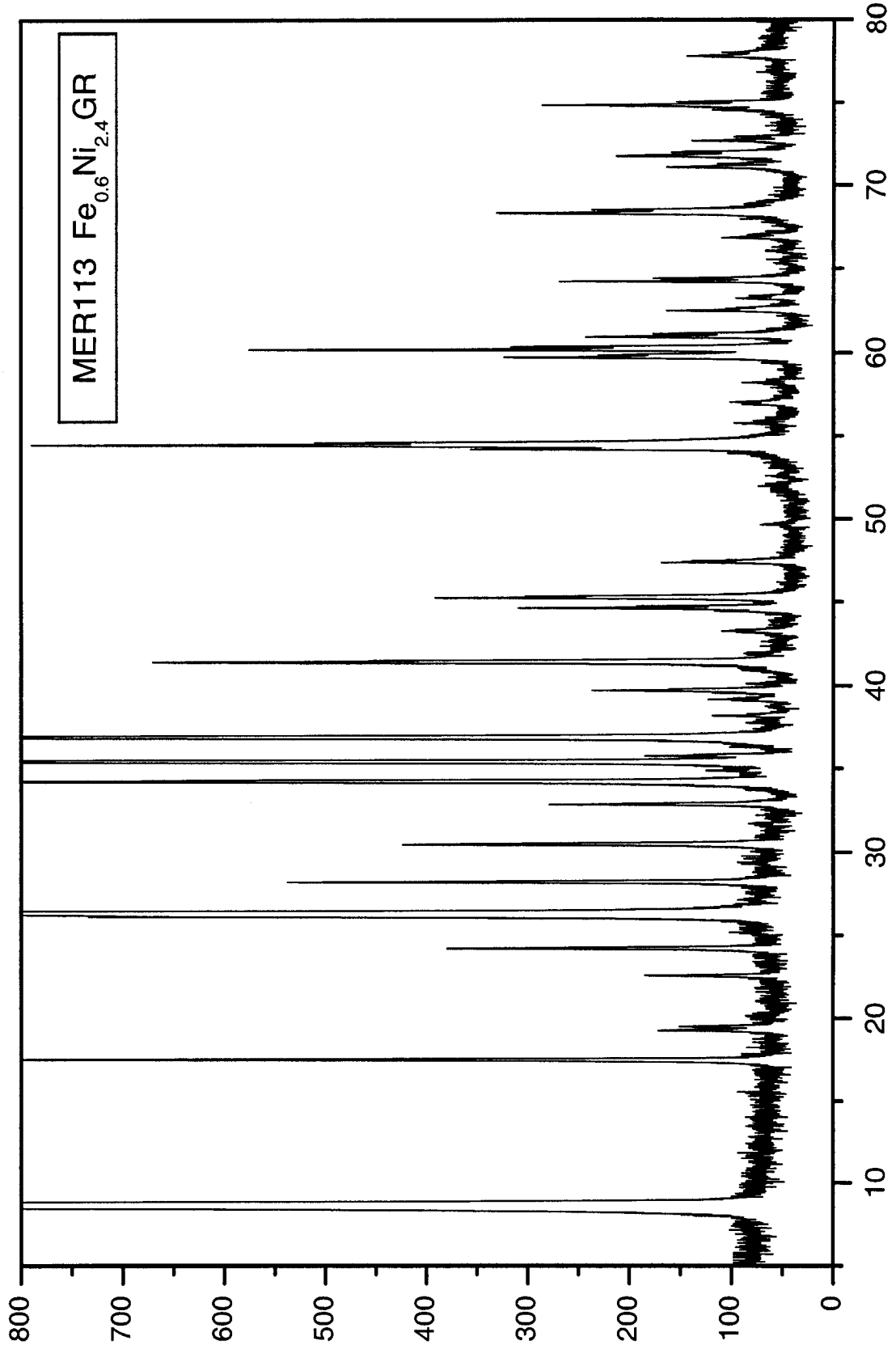
MER113 $Fe_{0.6}Ni_{2.4}GR$
800
700
600
500
400
300
200
100
0
10
20
30
40
50
60
70
80

A53

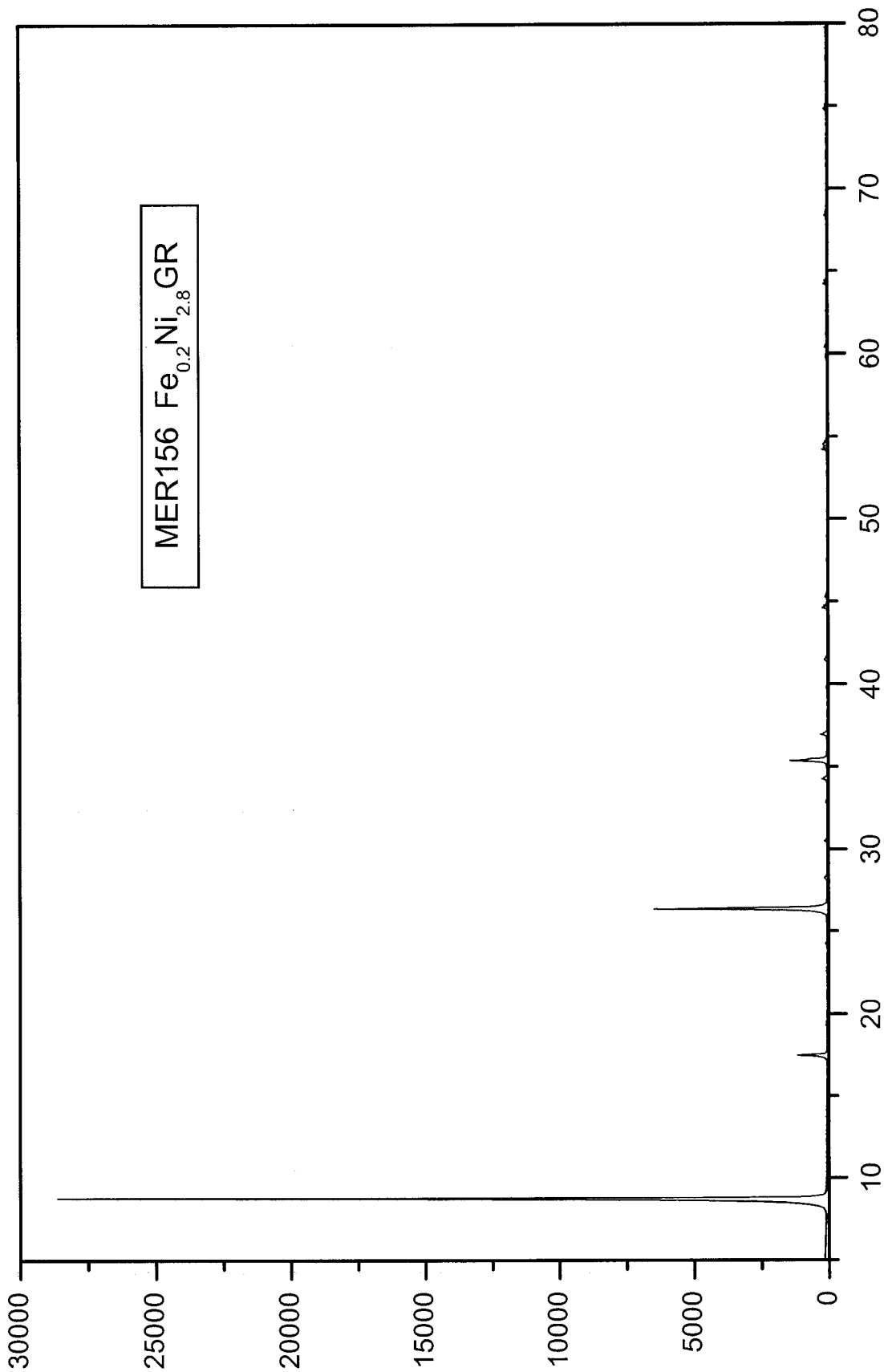
MER156 $Fe_{0.2}Ni_{2.8}GR$
30000
25000
20000
15000
10000
5000
0
10
20
30
40
50
60
70
80

A53a

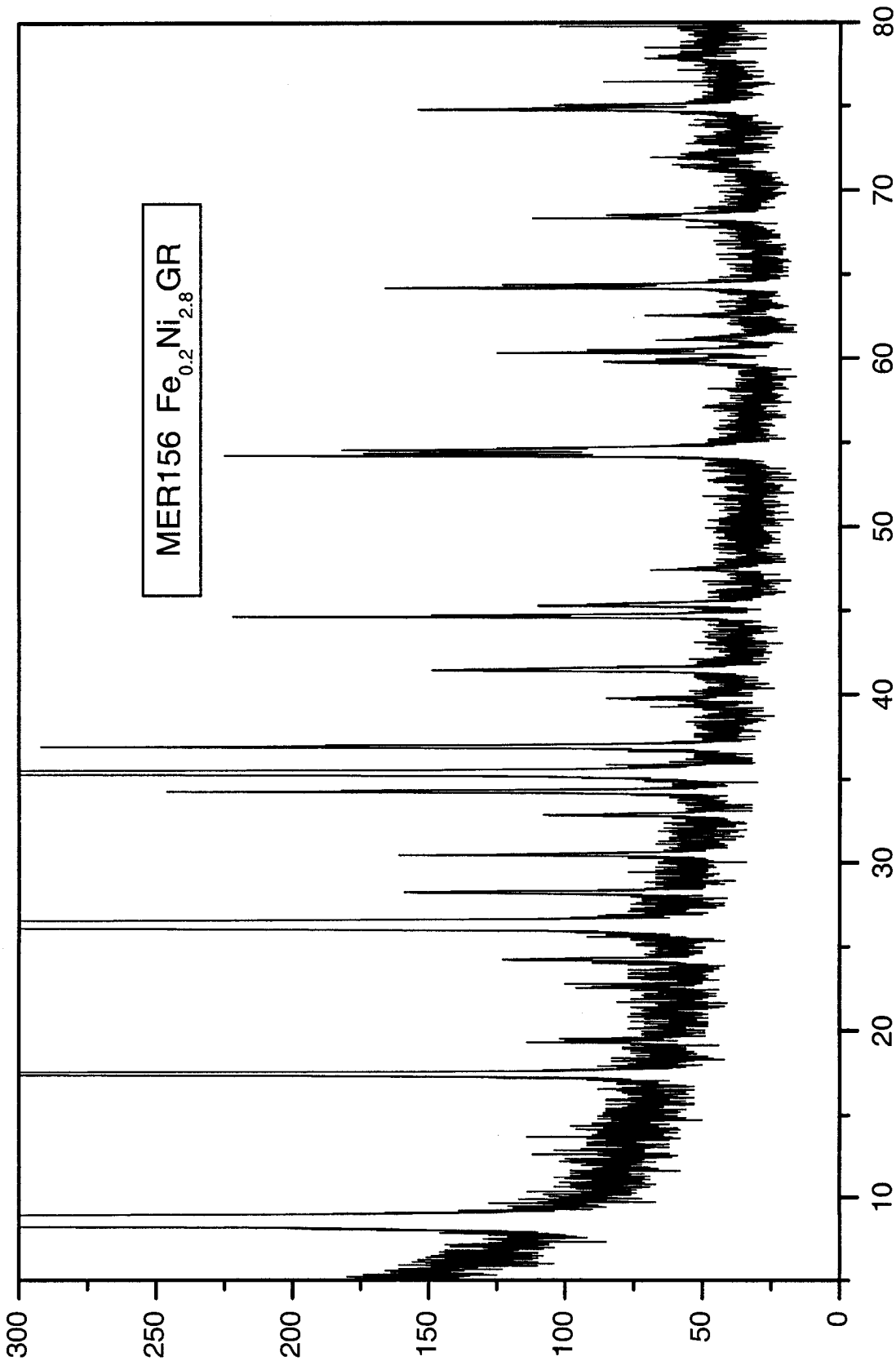
MER156 $Fe_{0.2}Ni_{2.8}GR$
300
250
200
150
100
50
0
10
20
30
40
50
60
70
80

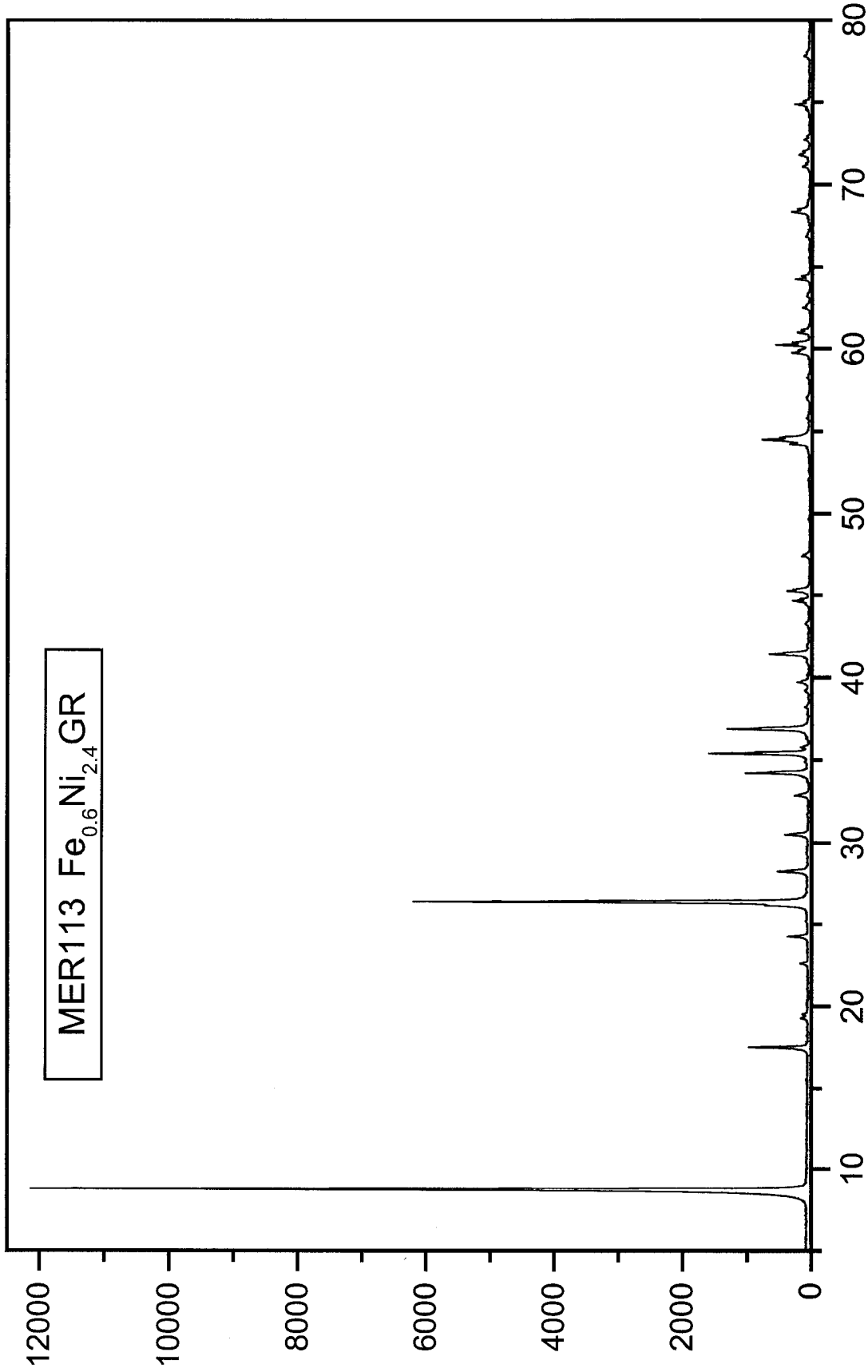
MER113 $Fe_{0.6}Ni_{2.4}GR$
12000
10000
8000
6000
4000
2000
0
10
20
30
40
50
60
70
80

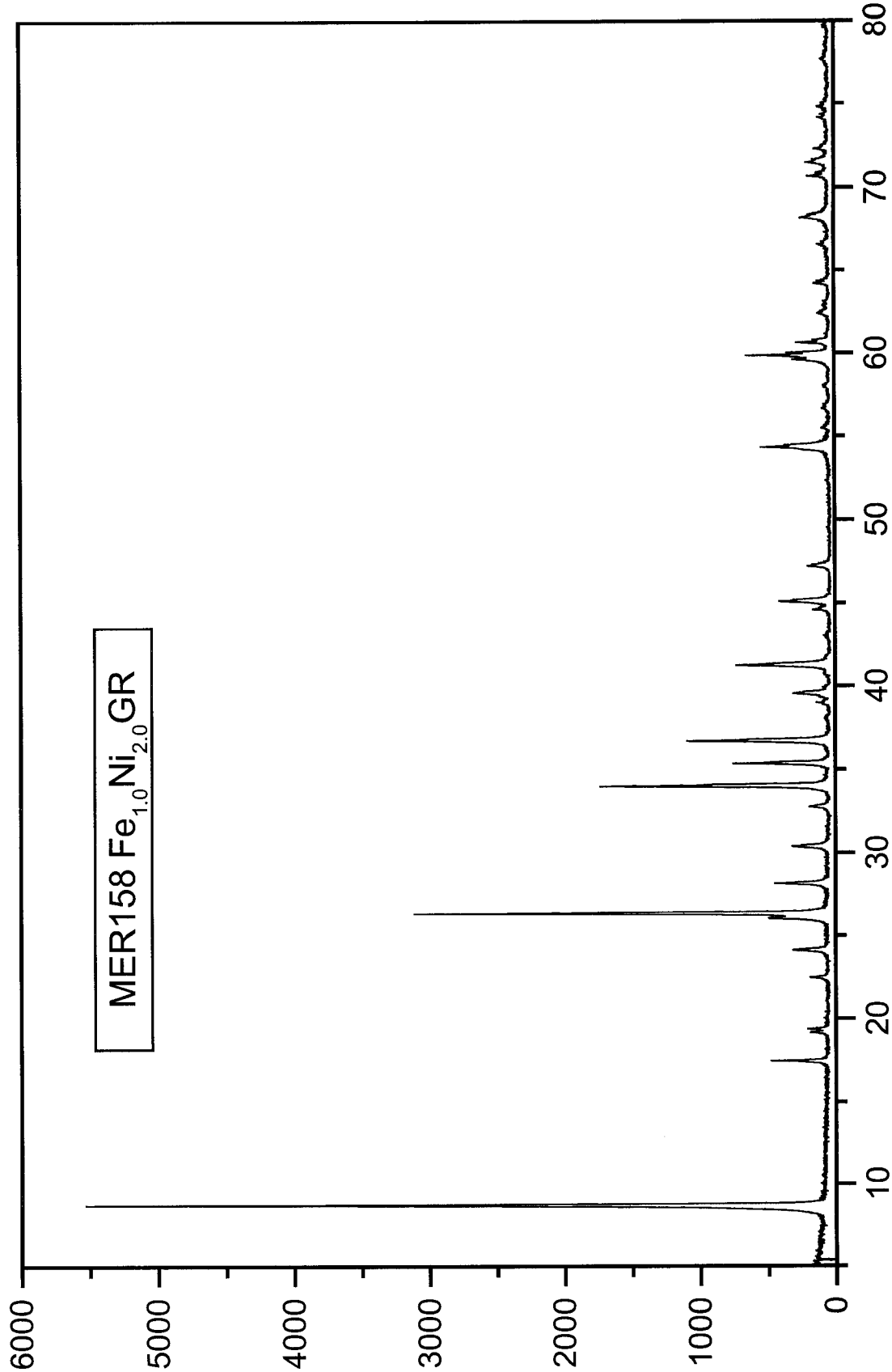
MER158 $Fe_{1.0}Ni_{2.0}$GR
6000
5000
4000
3000
2000
1000
0
10
20
30
40
50
60
70
80

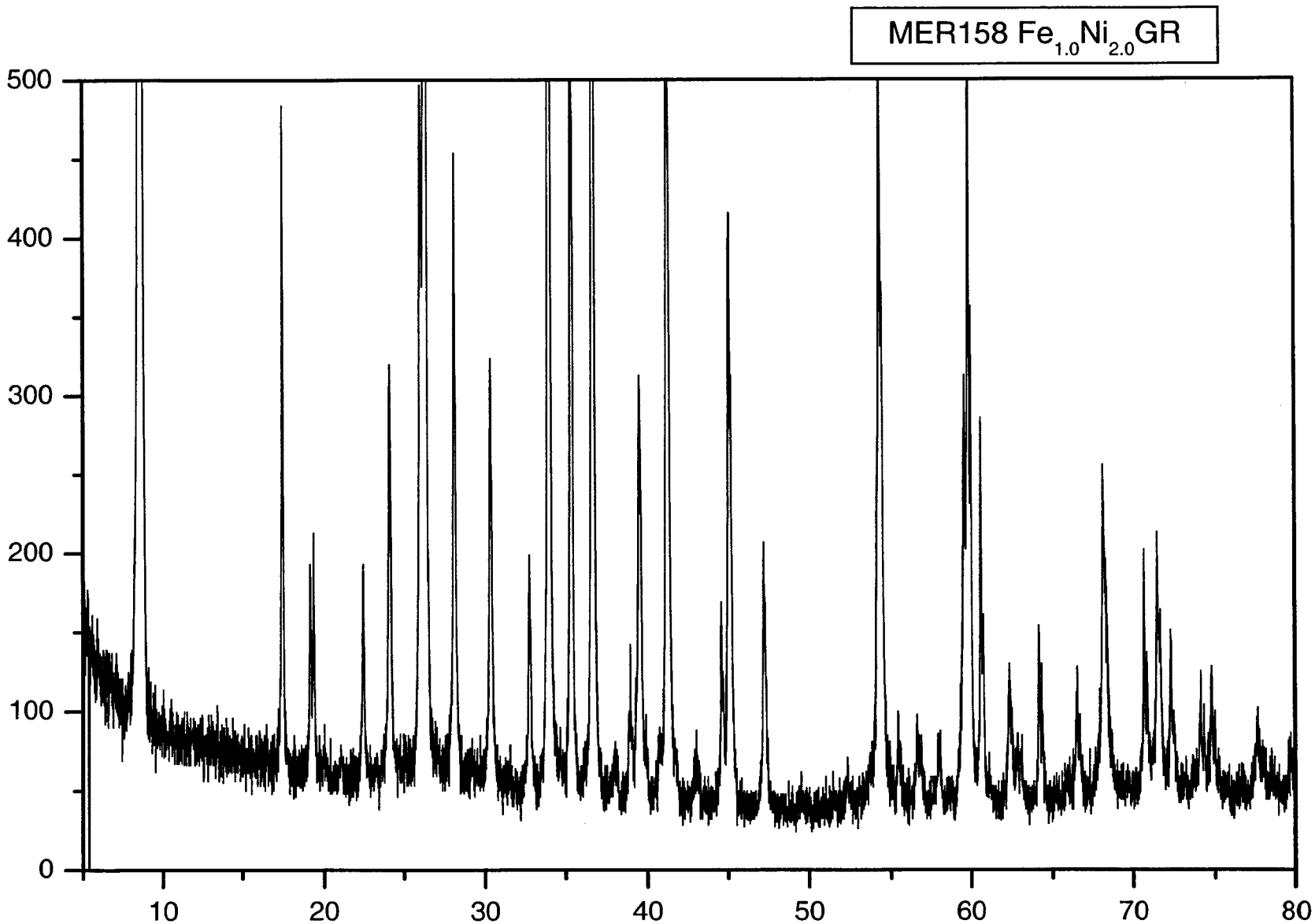

A55a

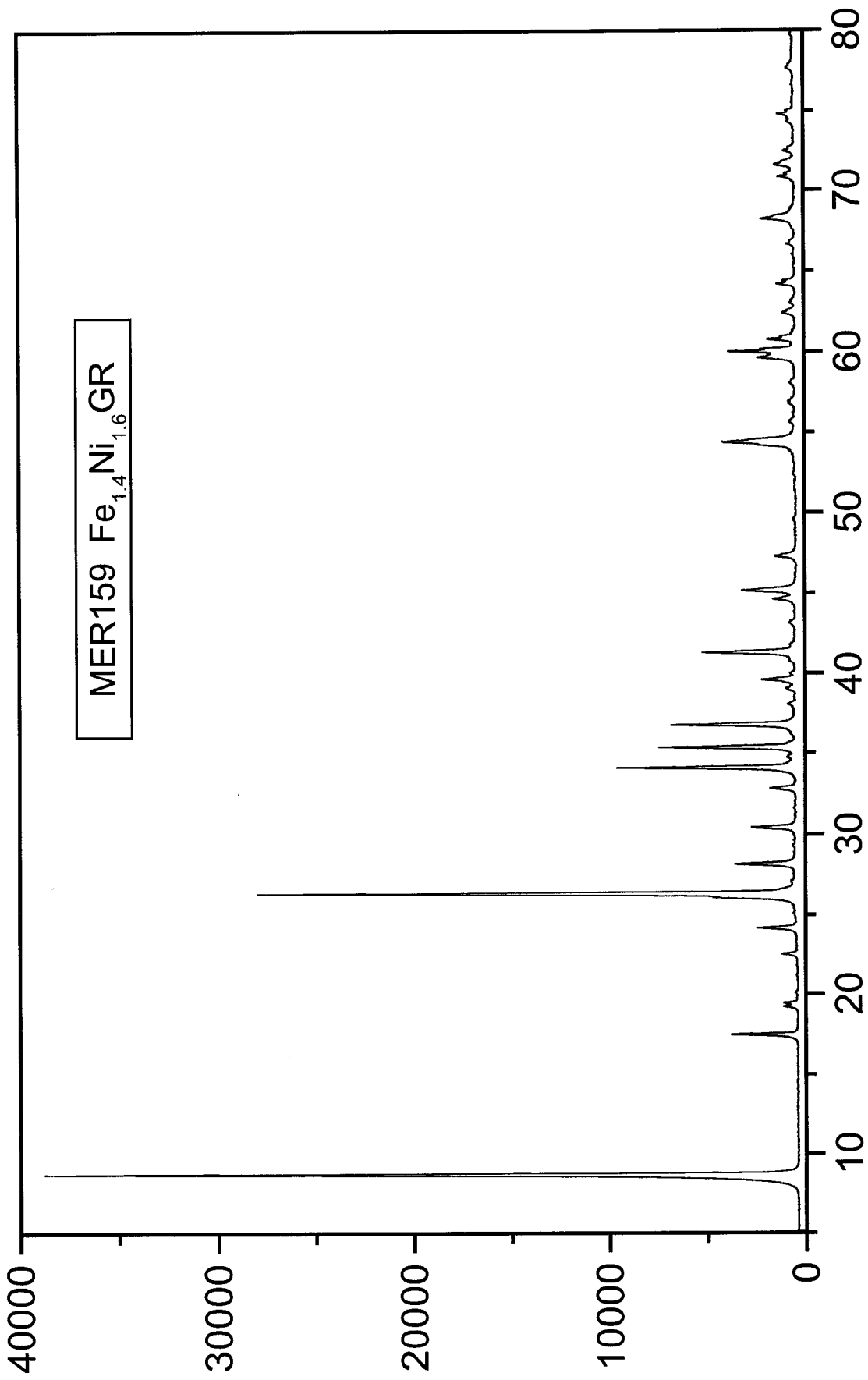
MER159 Fe1.4Ni1.6GR
40000
30000
20000
10000
0
10
20
30
40
50
60
70
80

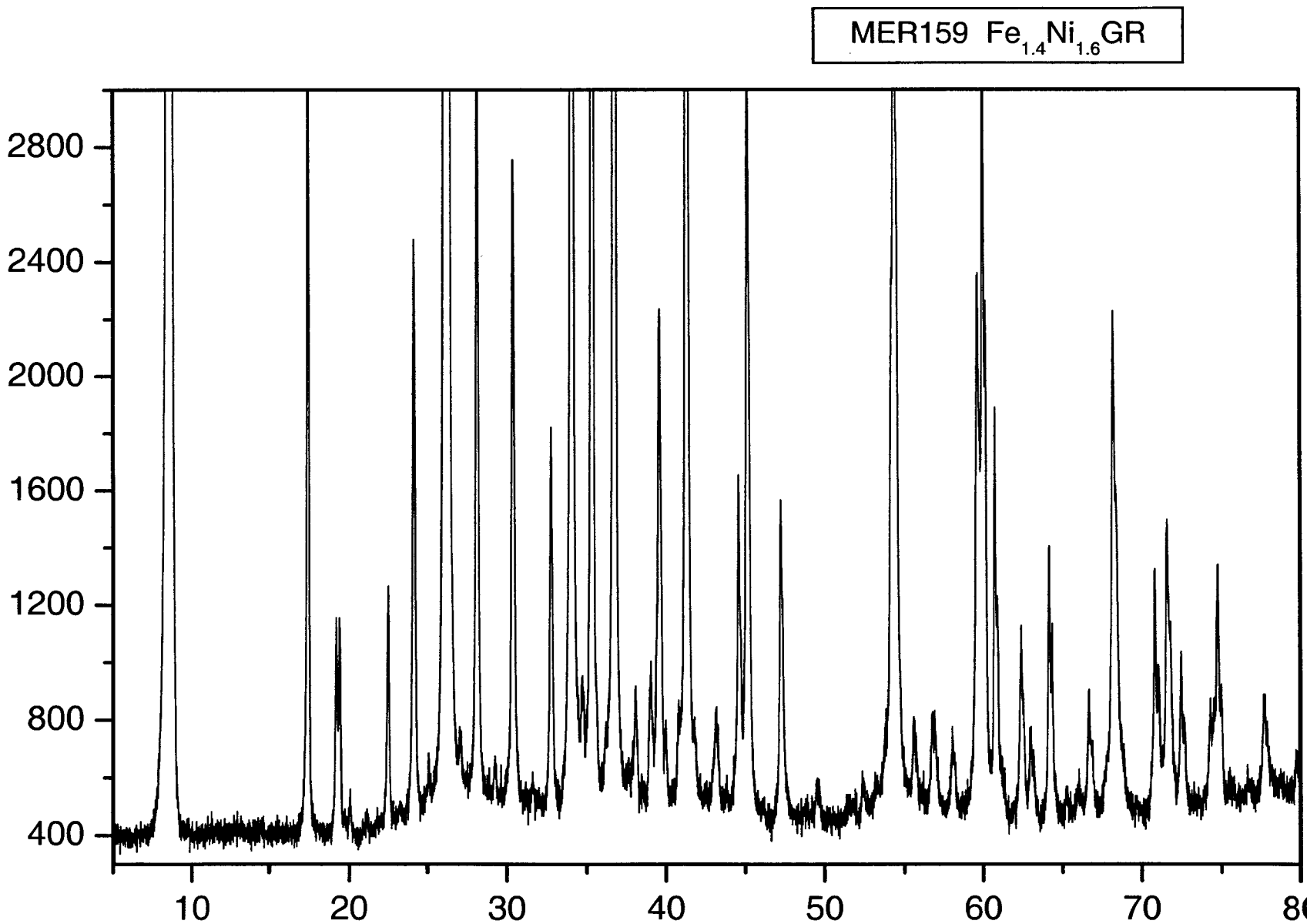
MER159 Fe1.4Ni1.6GR
2800
2400
2000
1600
1200
800
400
10
20
30
40
50
60
70
80

A56a

A57

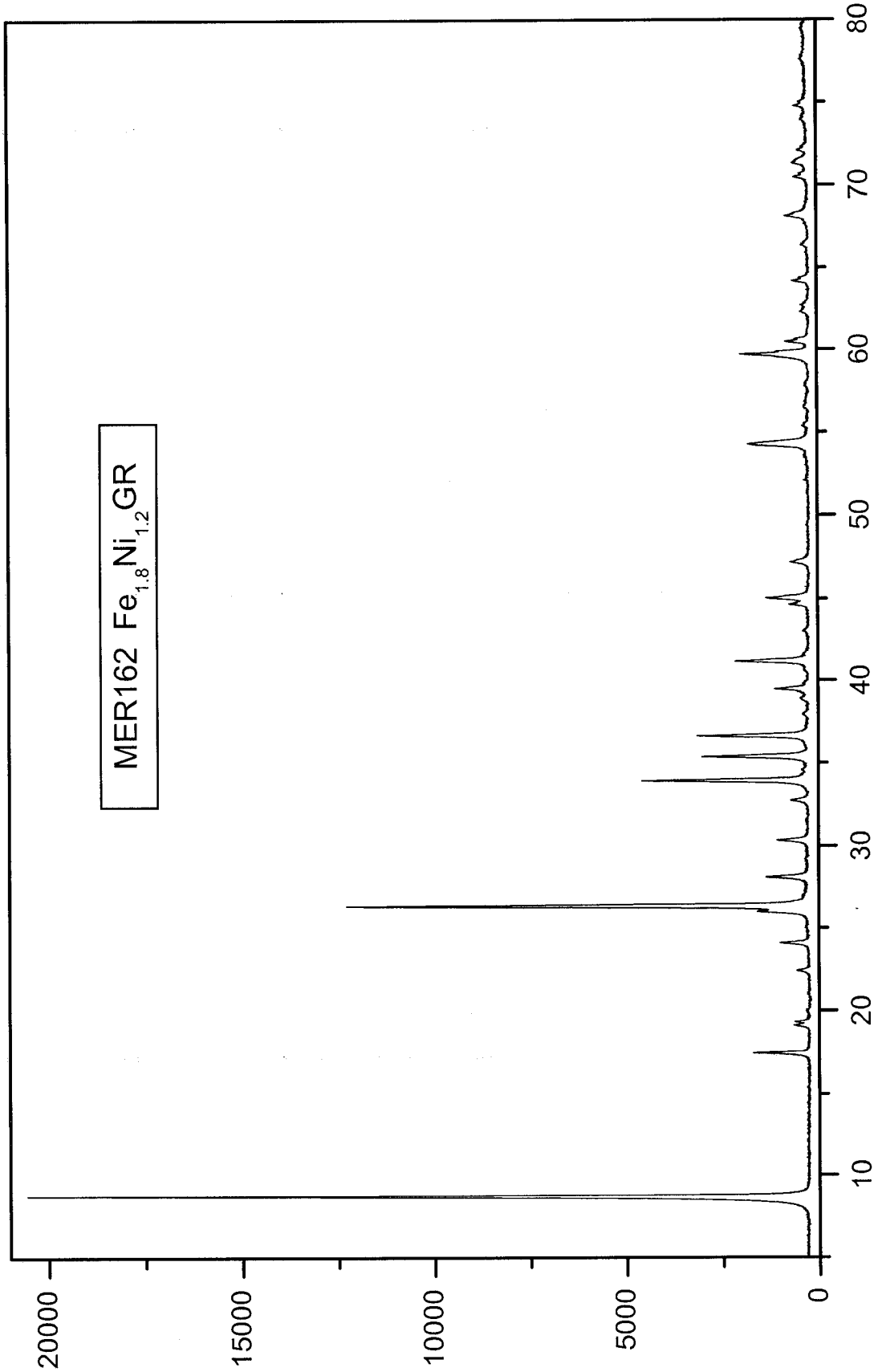
MER162 Fe1.8Ni1.2GR
20000
15000
10000
5000
0
10
20
30
40
50
60
70
80

A57a

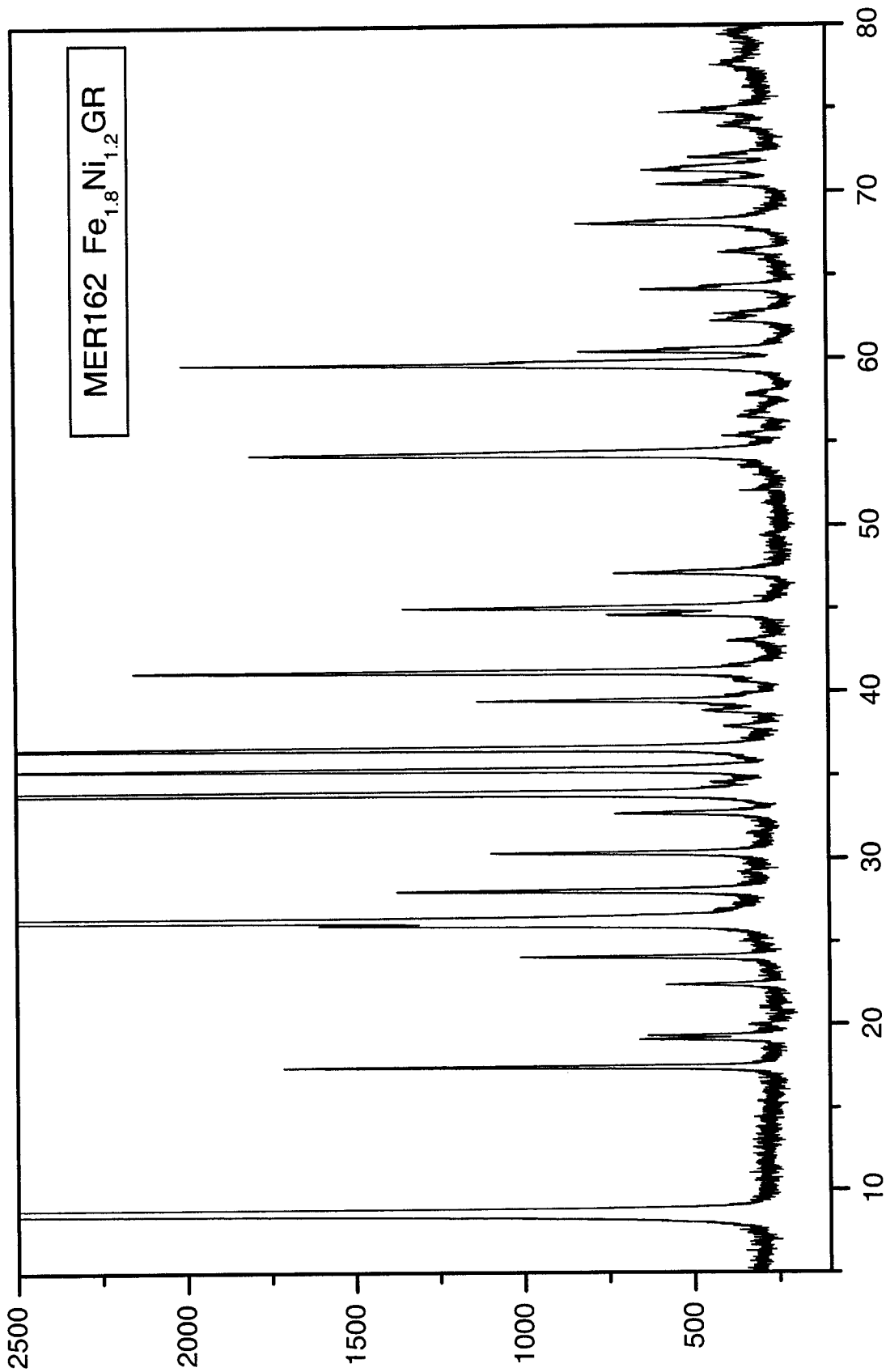
MER162 $Fe_{1.8}Ni_{1.2}GR$
2500
2000
1500
1000
500
10
20
30
40
50
60
70
80

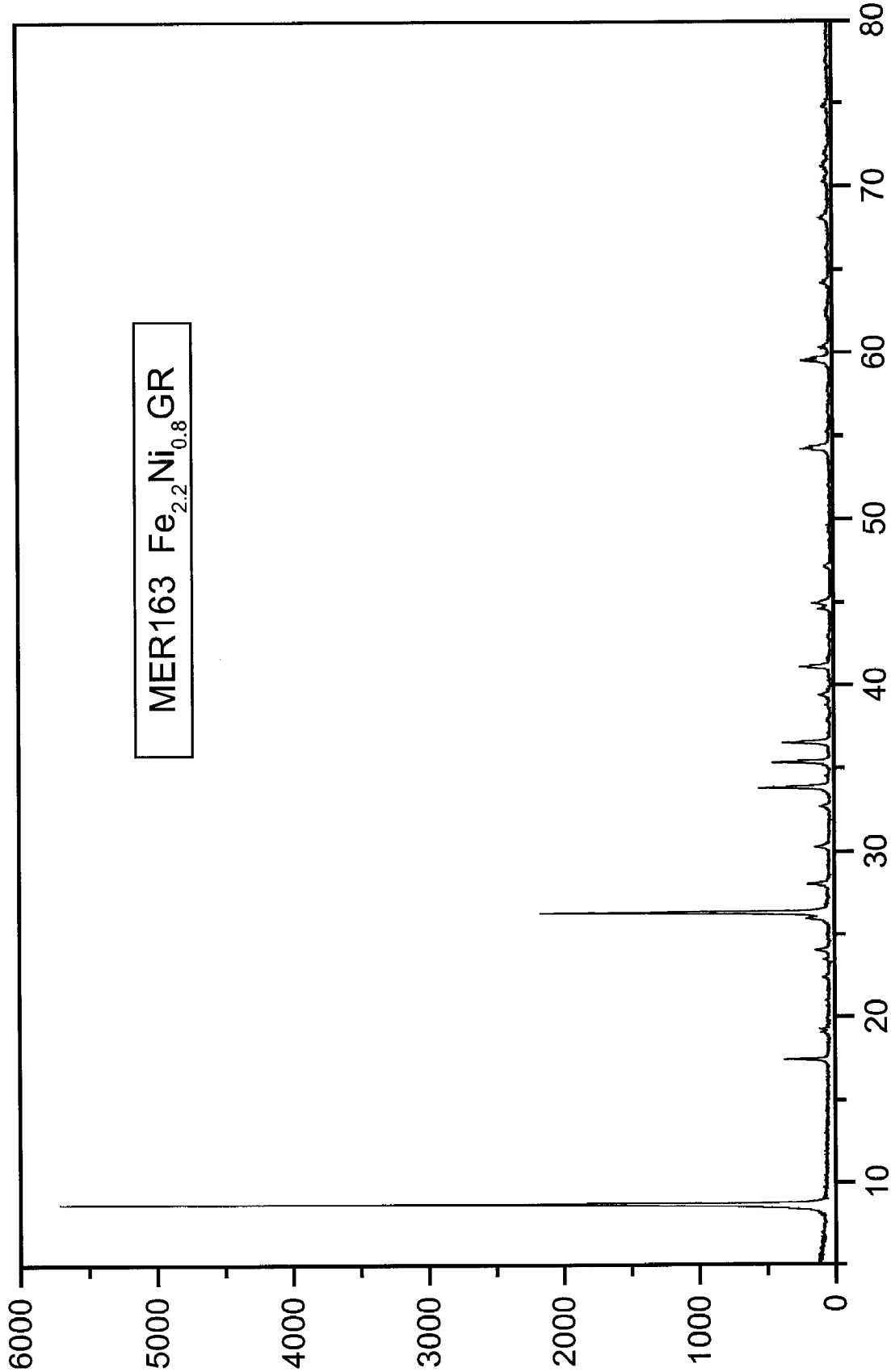
MER163 $Fe_{2.2}Ni_{0.8}GR$
6000
5000
4000
3000
2000
1000
0
10
20
30
40
50
60
70
80

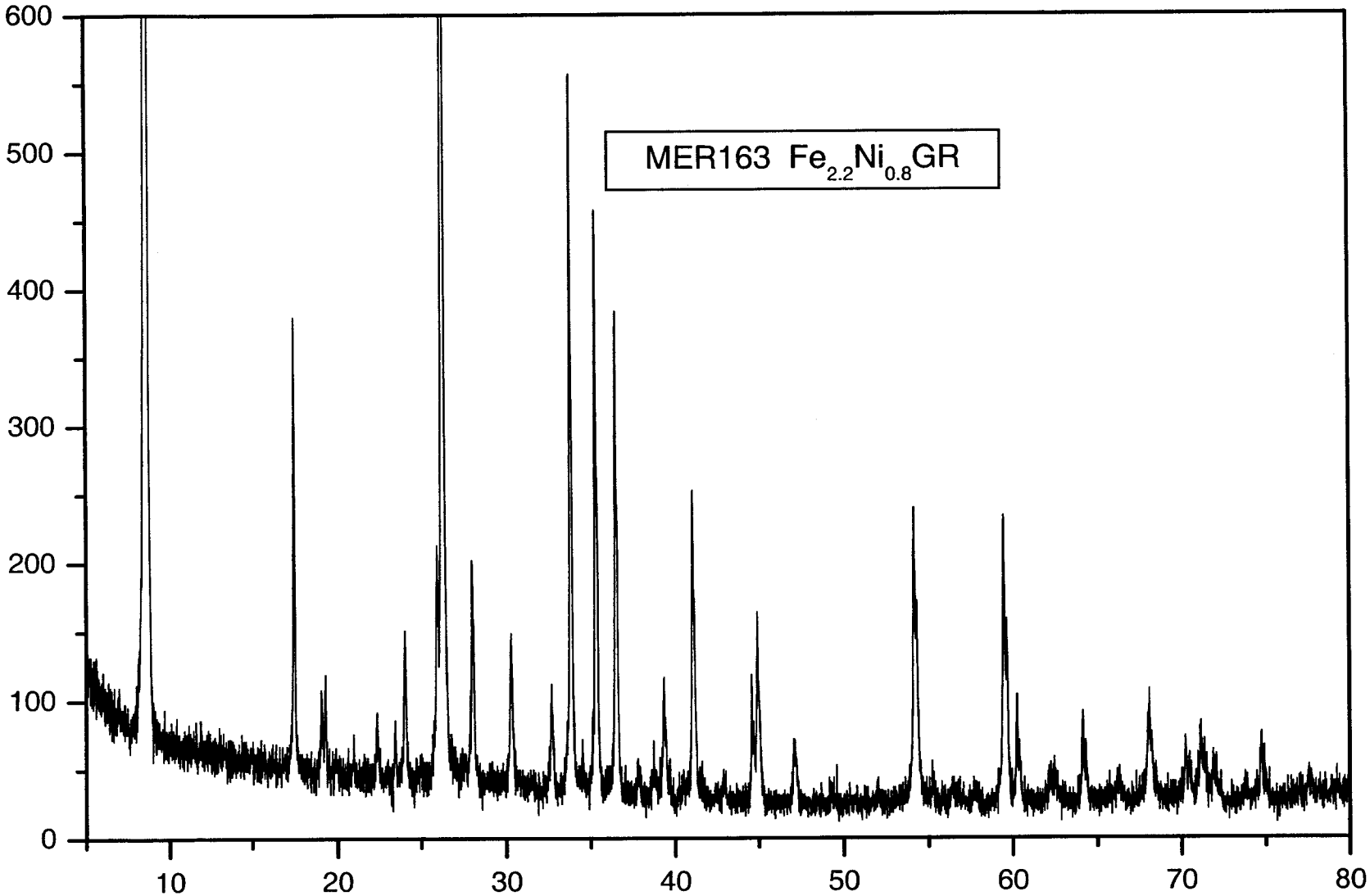
MER163 $Fe_{2.2}Ni_{0.8}GR$
600
500
400
300
200
100
0
10
20
30
40
50
60
70
80

A58a

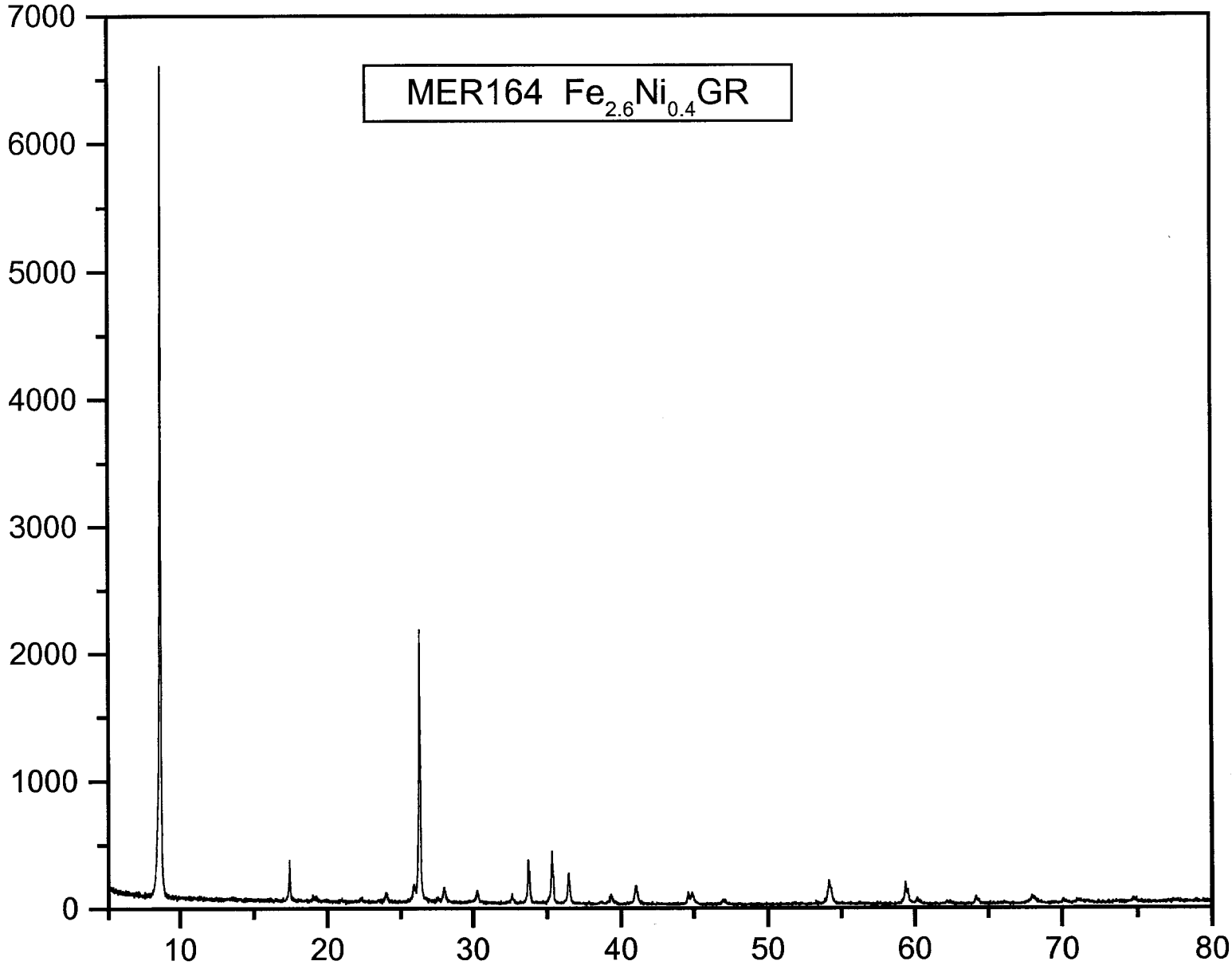
MER164 $Fe_{2.6}Ni_{0.4}GR$
7000
6000
5000
4000
3000
2000
1000
0
10
20
30
40
50
60
70
80

A59

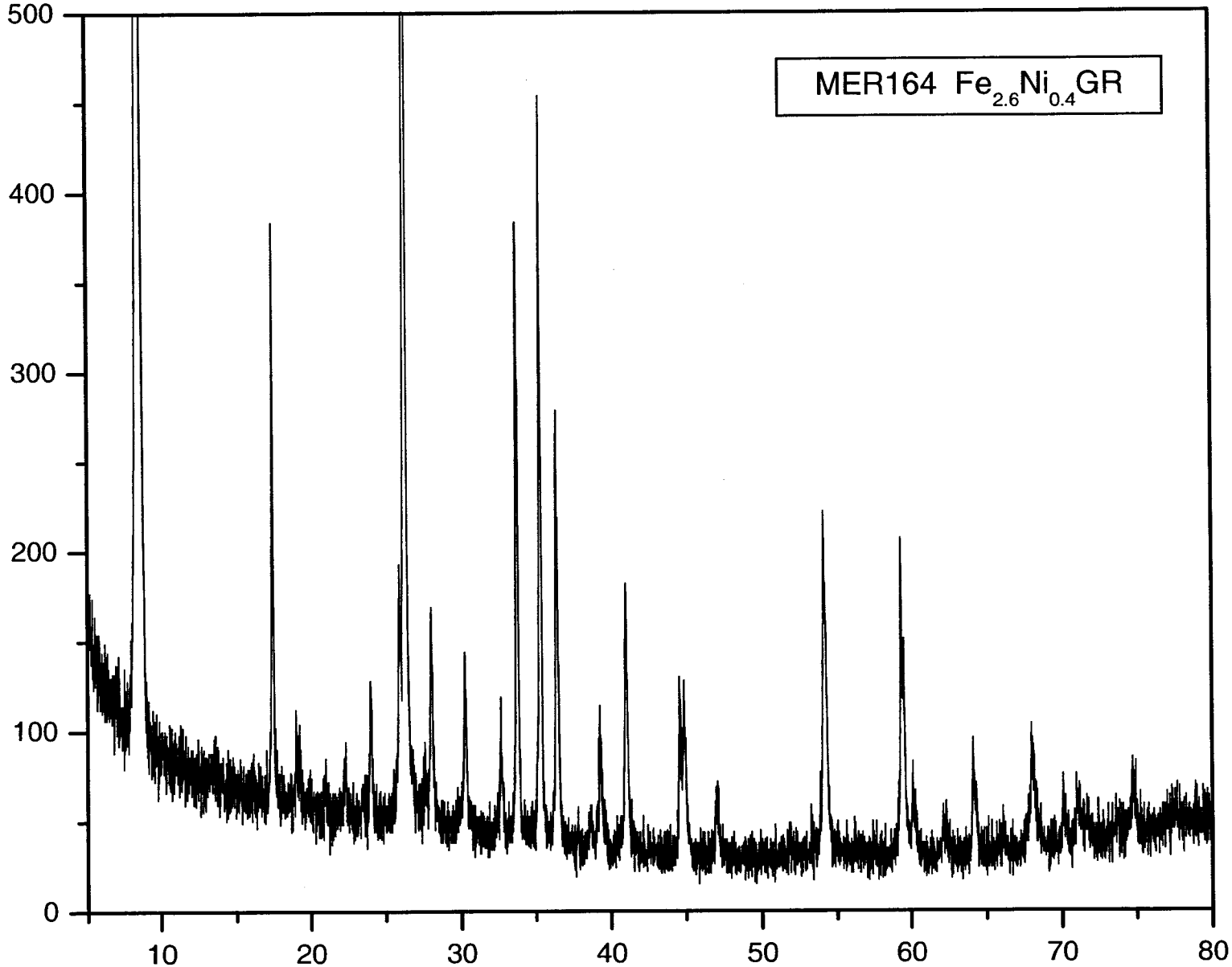

A59a

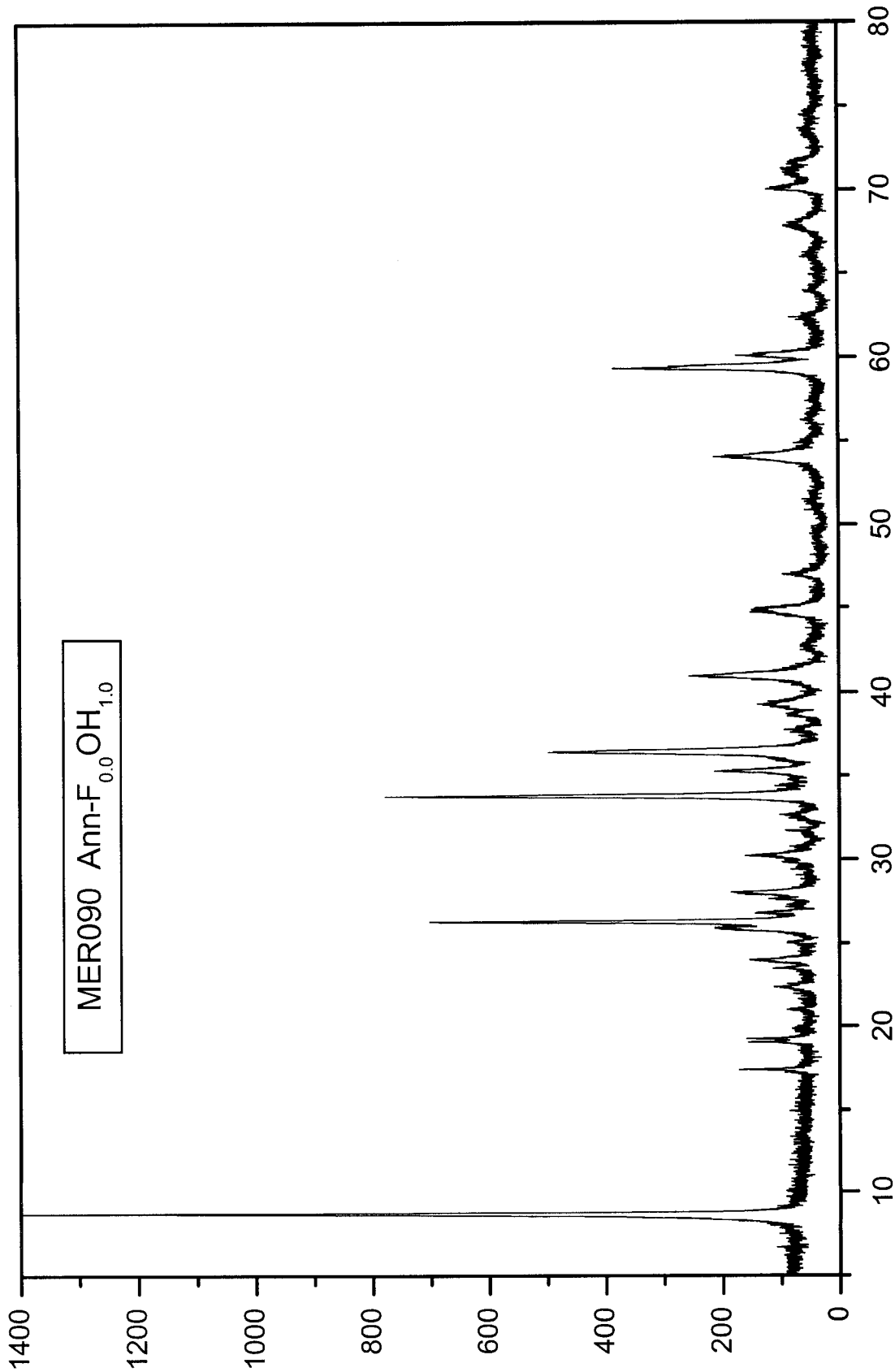
MER090 Ann-F0.0OH1.0
0
200
400
600
800
1000
1200
1400
10
20
30
40
50
60
70
80

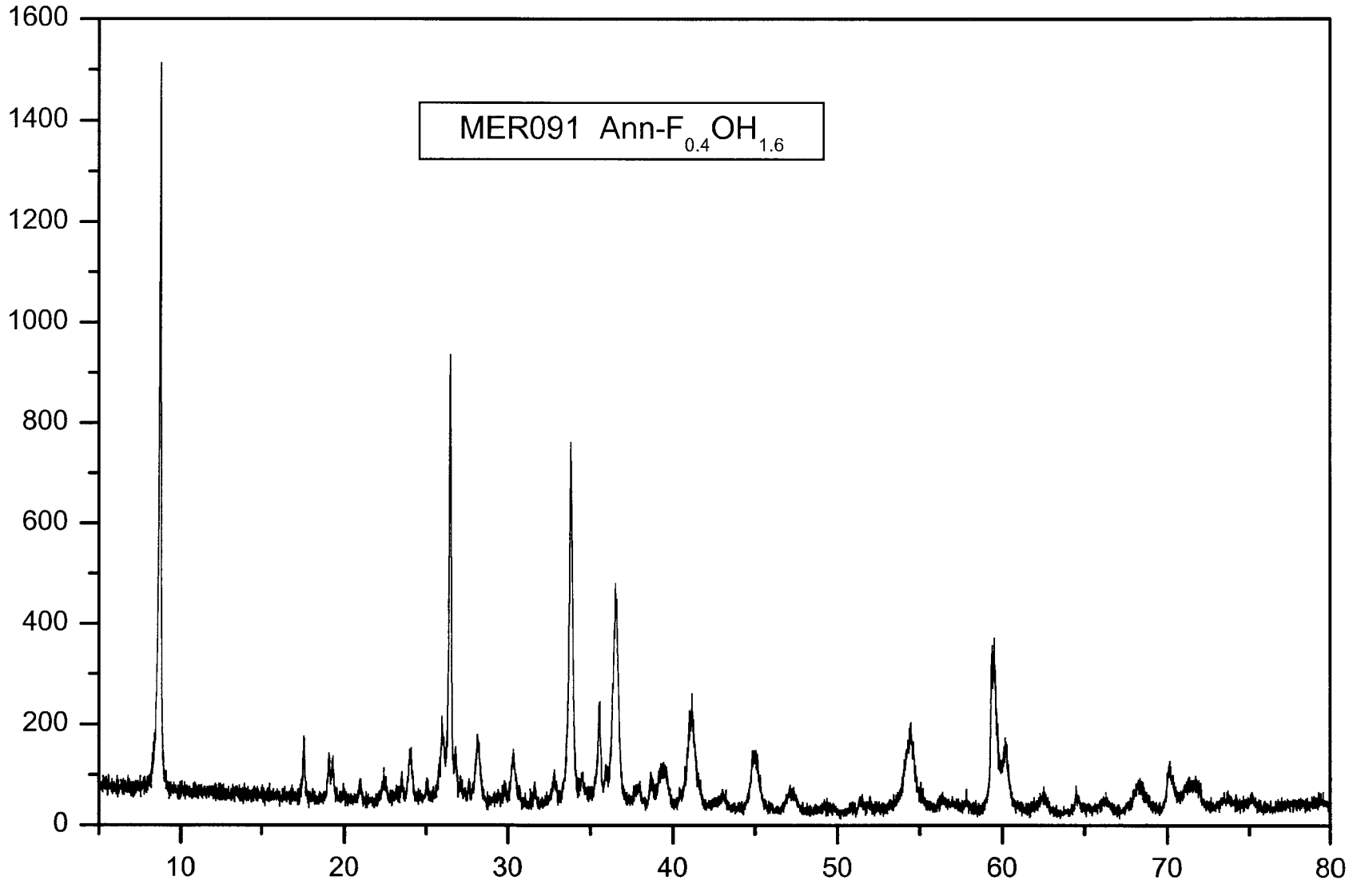
MER091 Ann-F0.4OH1.6
1600
1400
1200
1000
800
600
400
200
0
10
20
30
40
50
60
70
80

A61

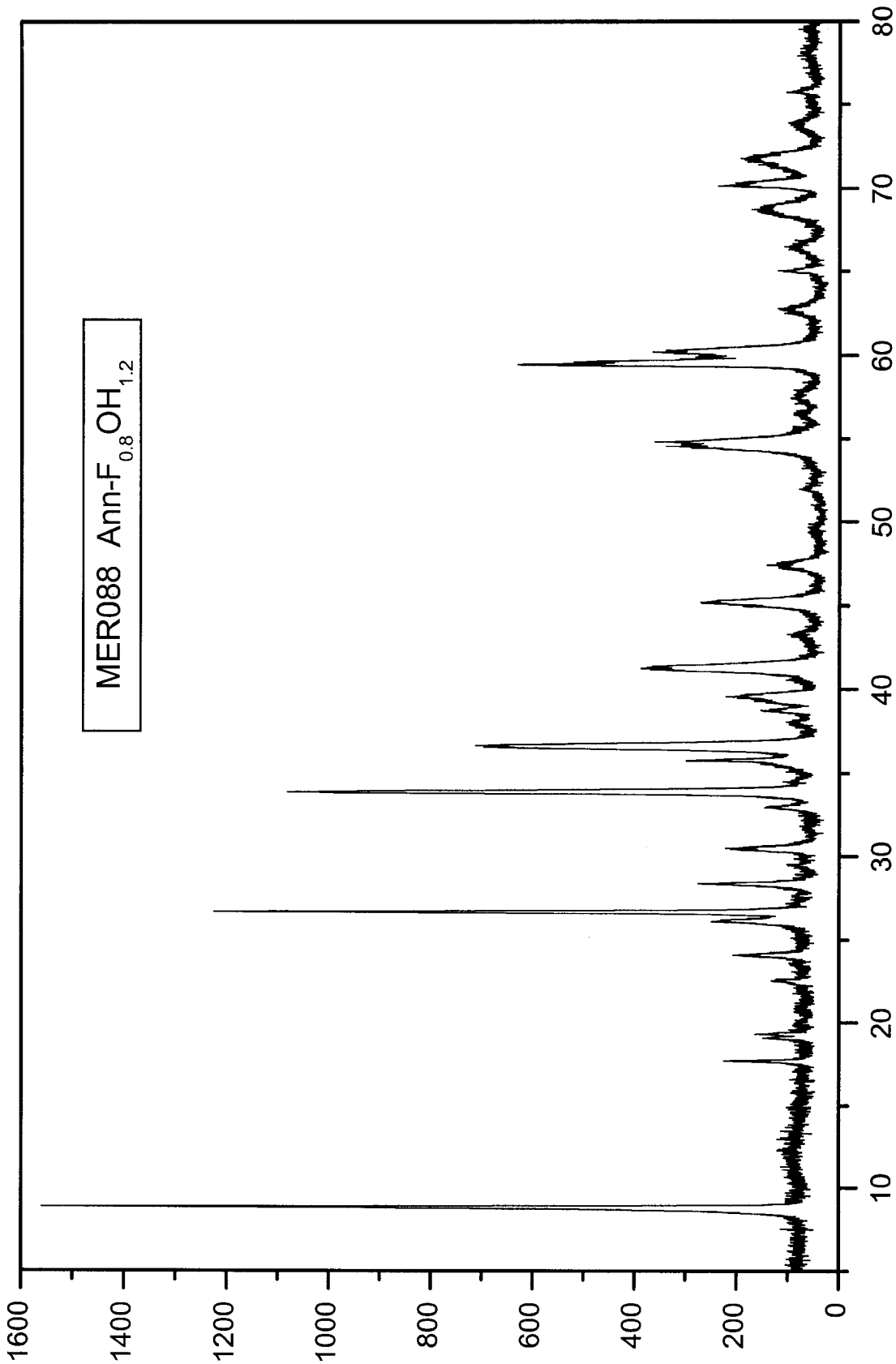
MER088 Ann-F0.8OH1.2
0
200
400
600
800
1000
1200
1400
1600
10
20
30
40
50
60
70
80

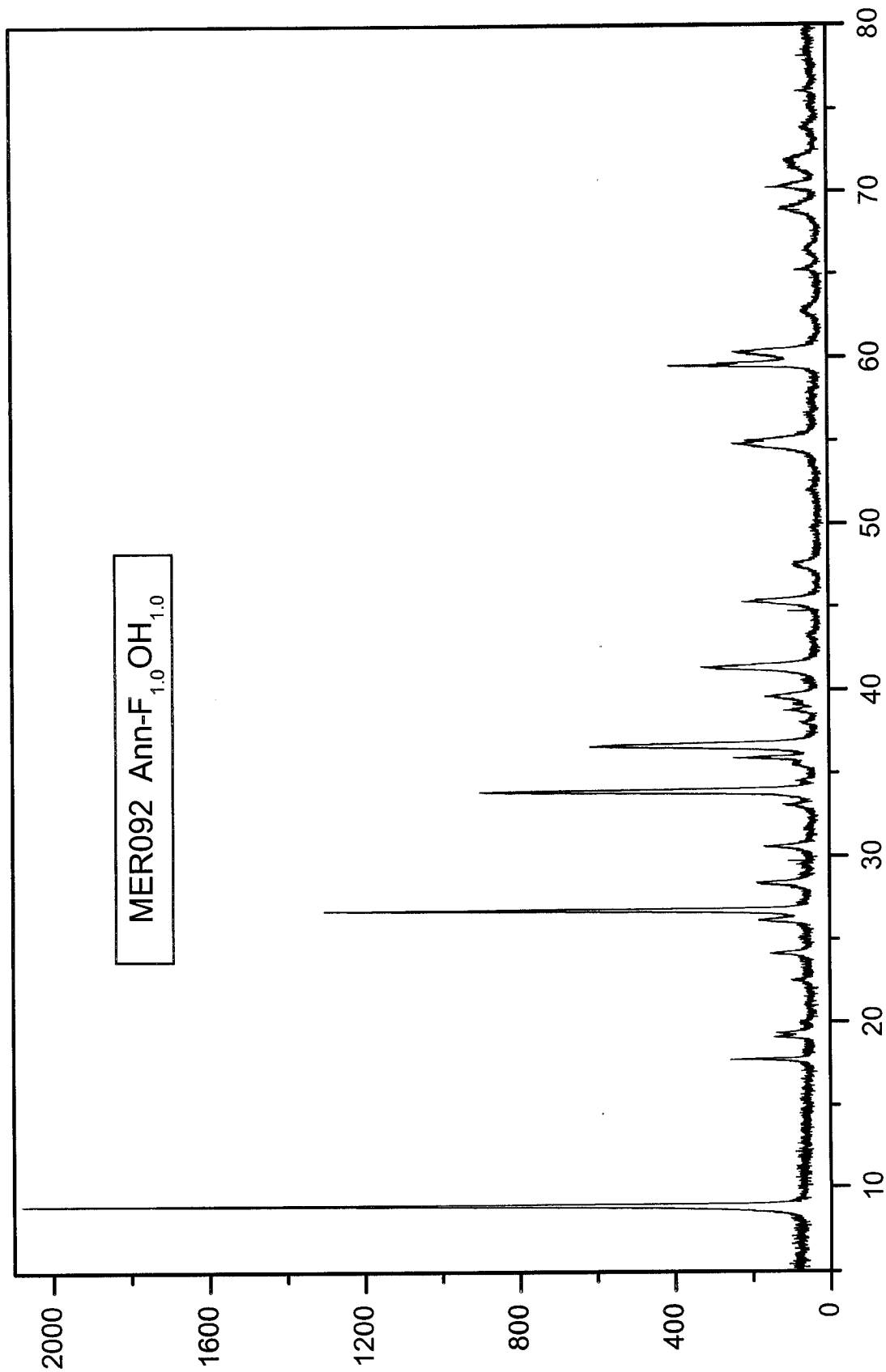
MER092 Ann-F1.0OH1.0
2000
1600
1200
800
400
0
10
20
30
40
50
60
70
80

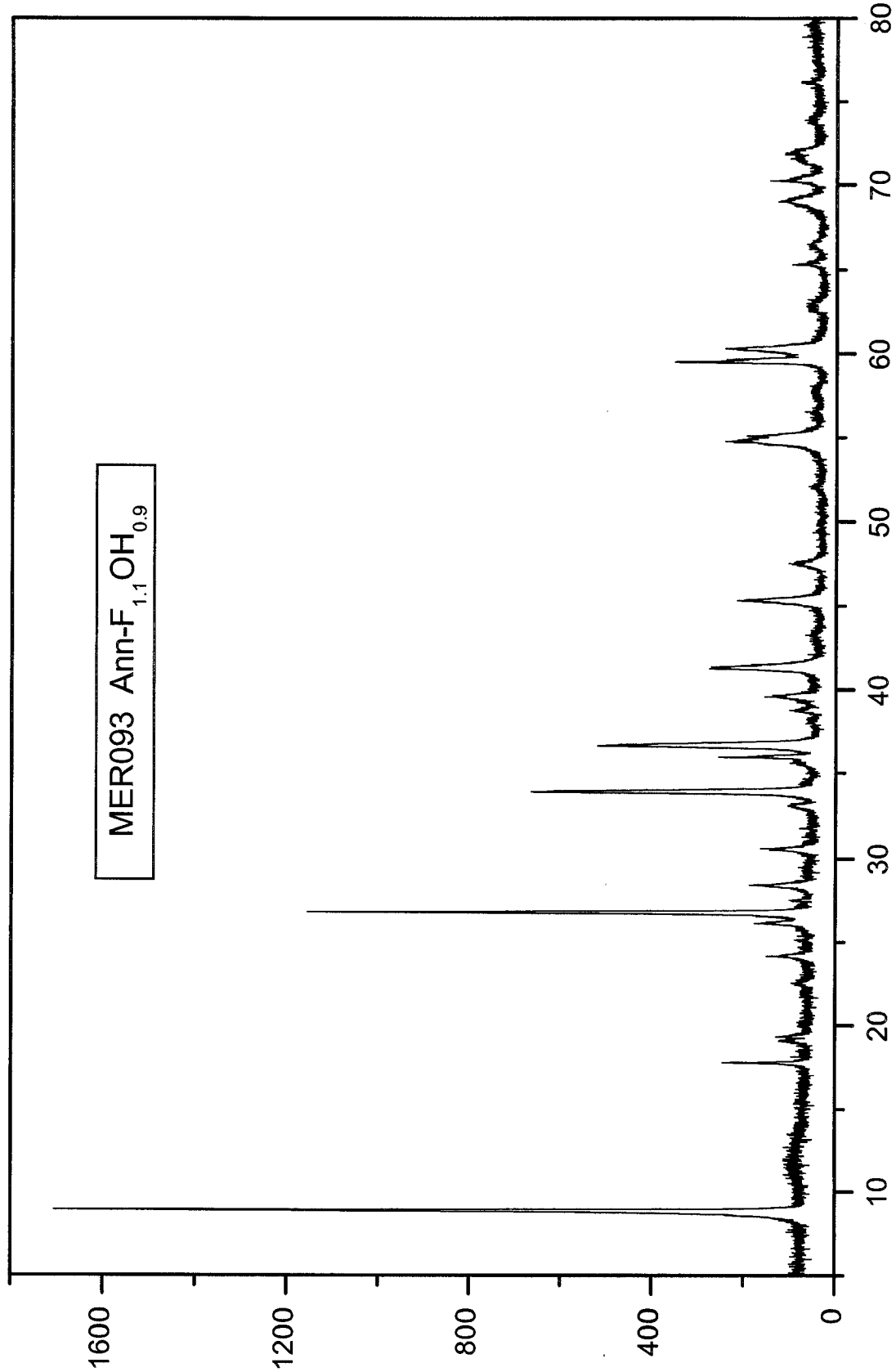
MER093 Ann-F1.1OH0.9
0
400
800
1200
1600
10
20
30
40
50
60
70
80

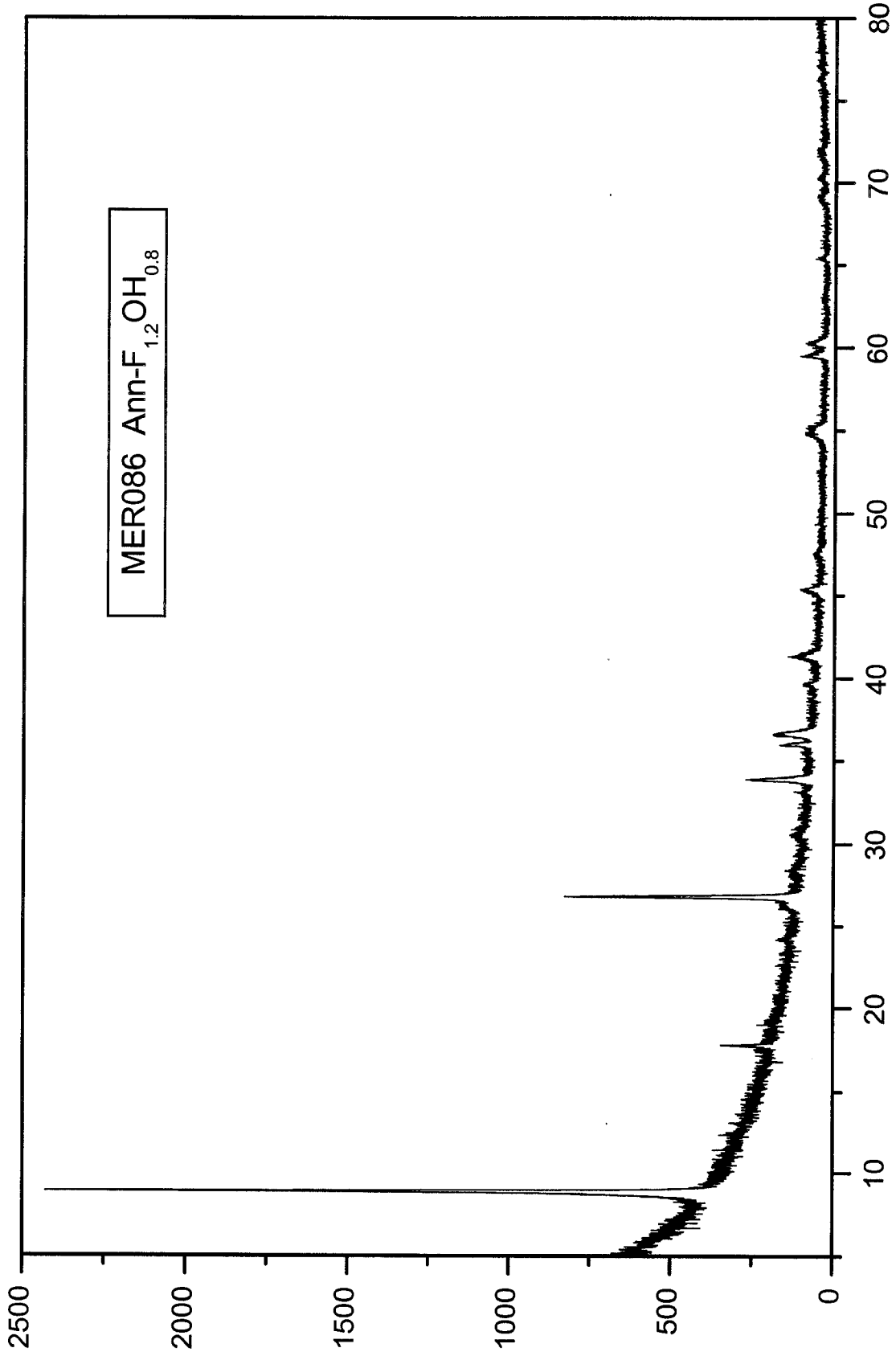
MER086 Ann-F1.2OH0.8
2500
2000
1500
1000
500
0
10
20
30
40
50
60
70
80

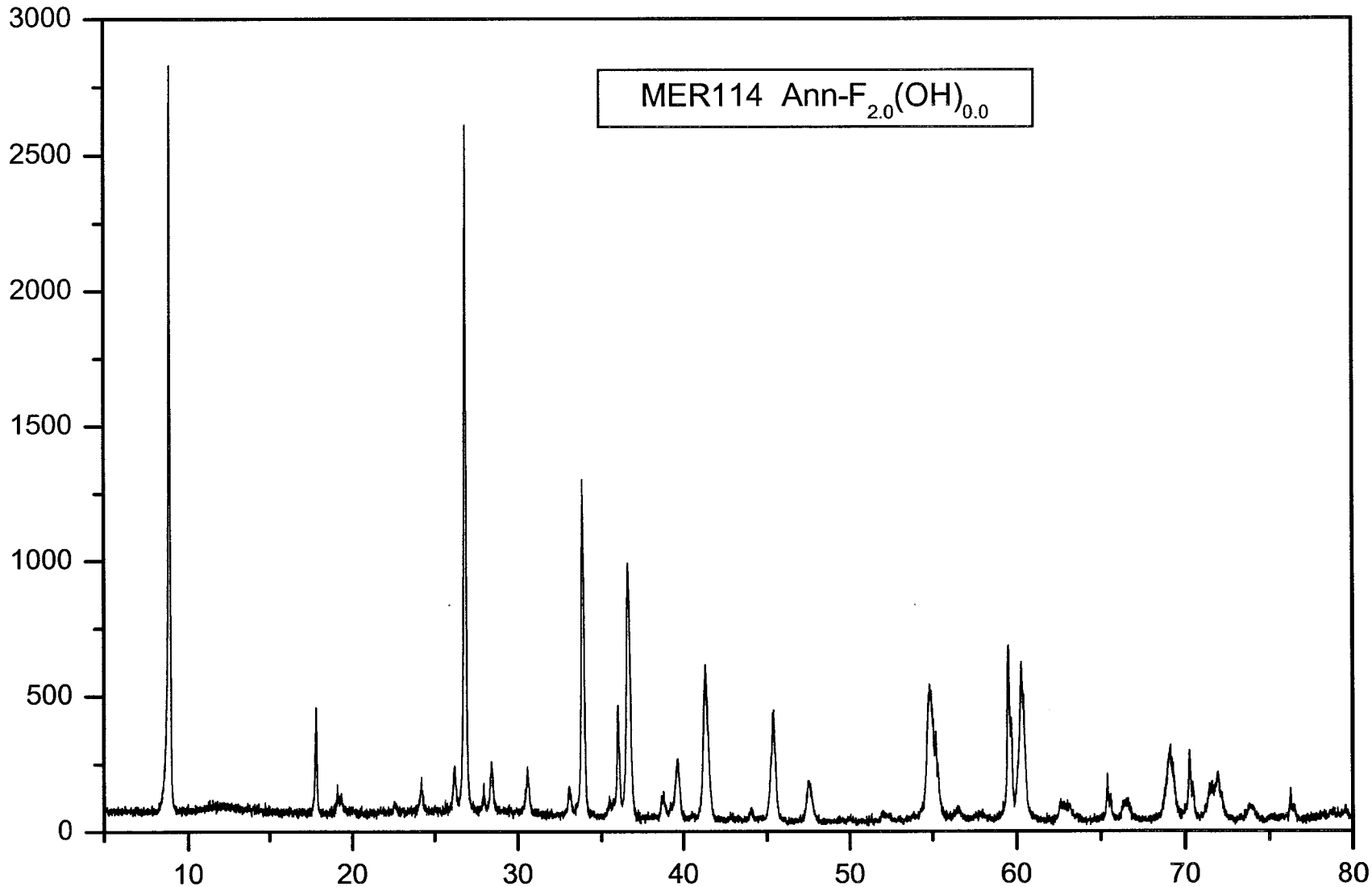
MER114 Ann-$F_{2.0}(OH)_{0.0}$
3000
2500
2000
1500
1000
500
0
10
20
30
40
50
60
70
80

A66

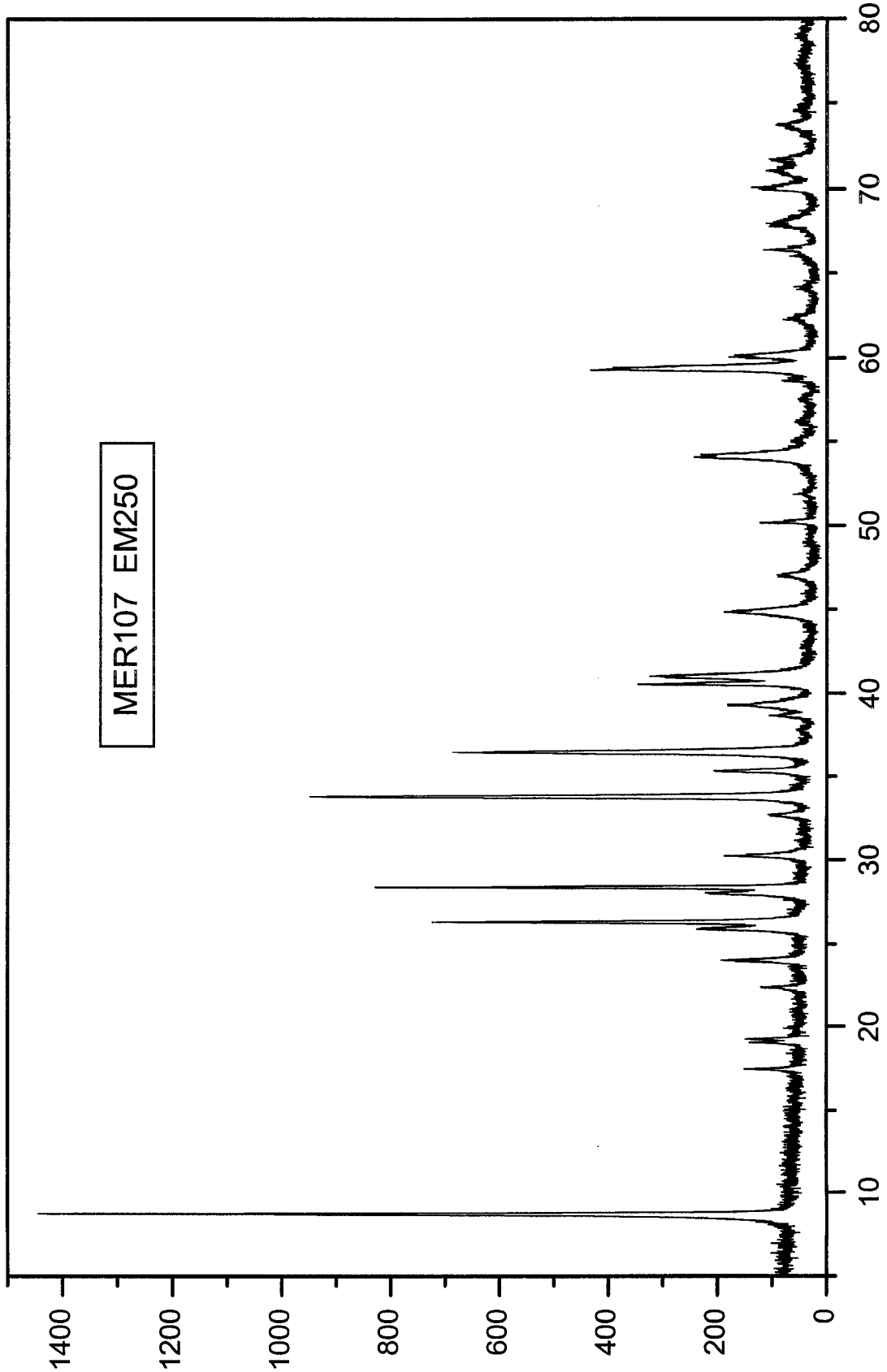
MER107 EM250
0
200
400
600
800
1000
1200
1400
10
20
30
40
50
60
70
80

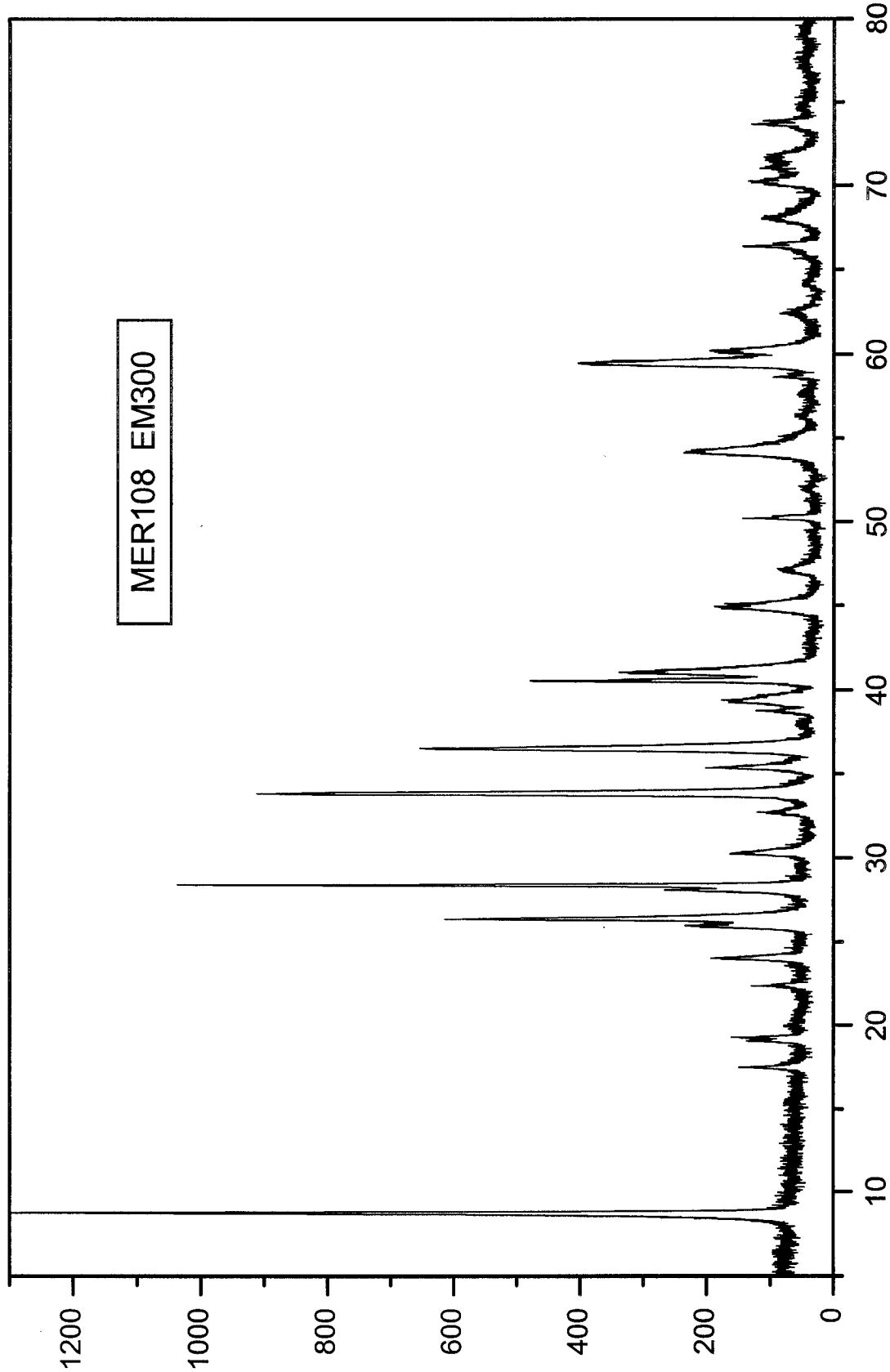
MER108 EM300
1200
1000
800
600
400
200
0
10
20
30
40
50
60
70
80

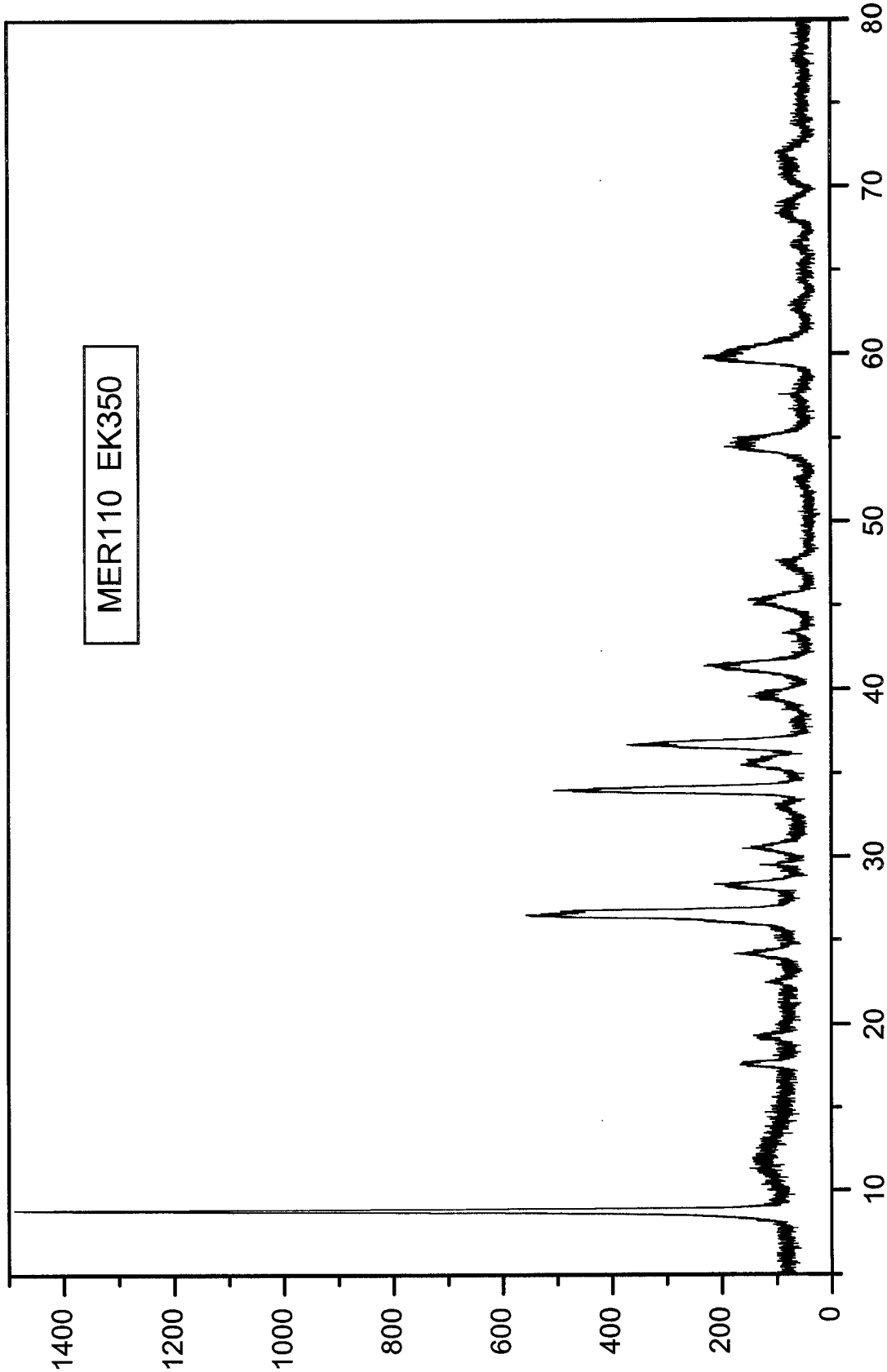
MER110 EK350
1400
1200
1000
800
600
400
200
0
10
20
30
40
50
60
70
80

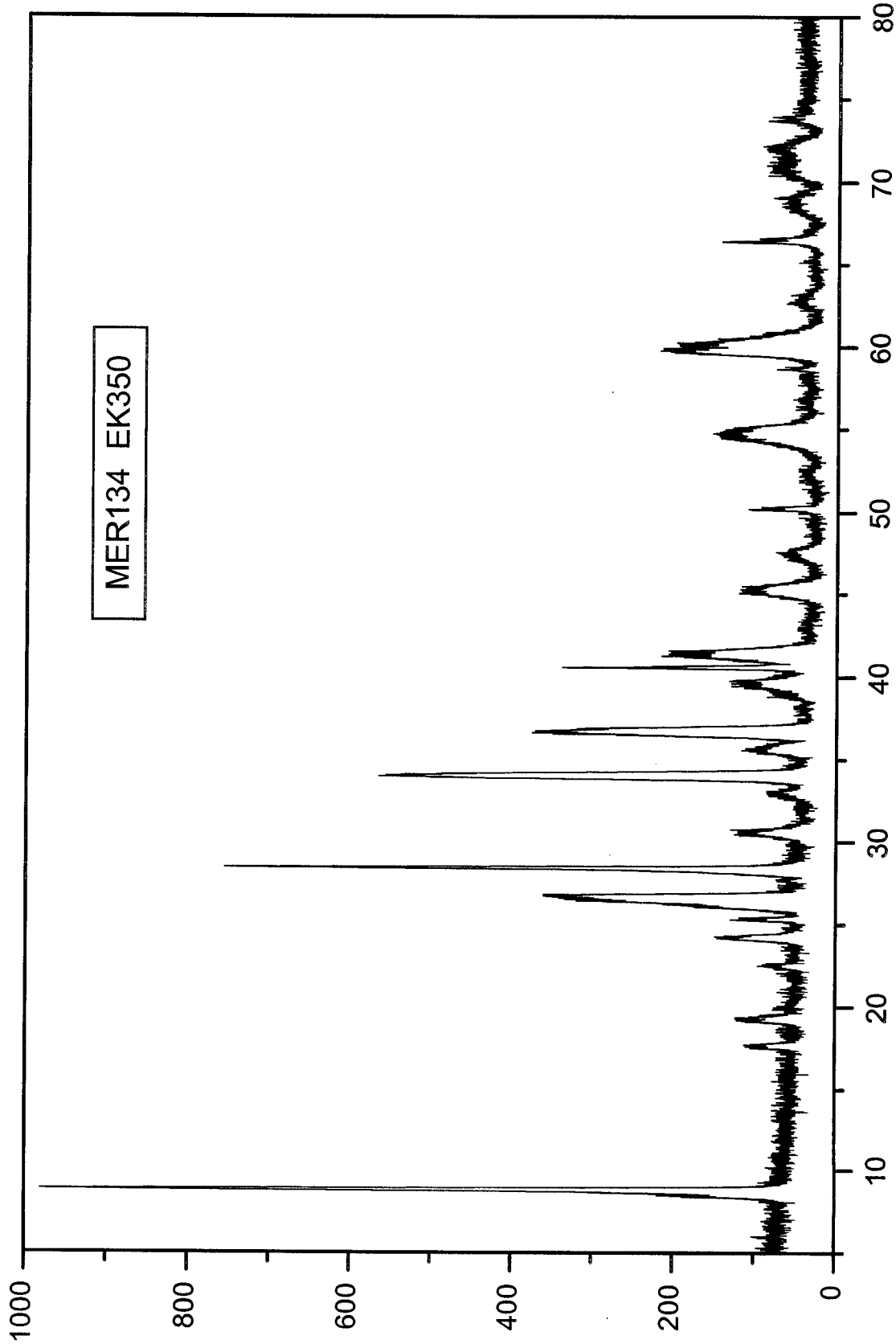
MER134 EK350
1000
800
600
400
200
0
10
20
30
40
50
60
70
80

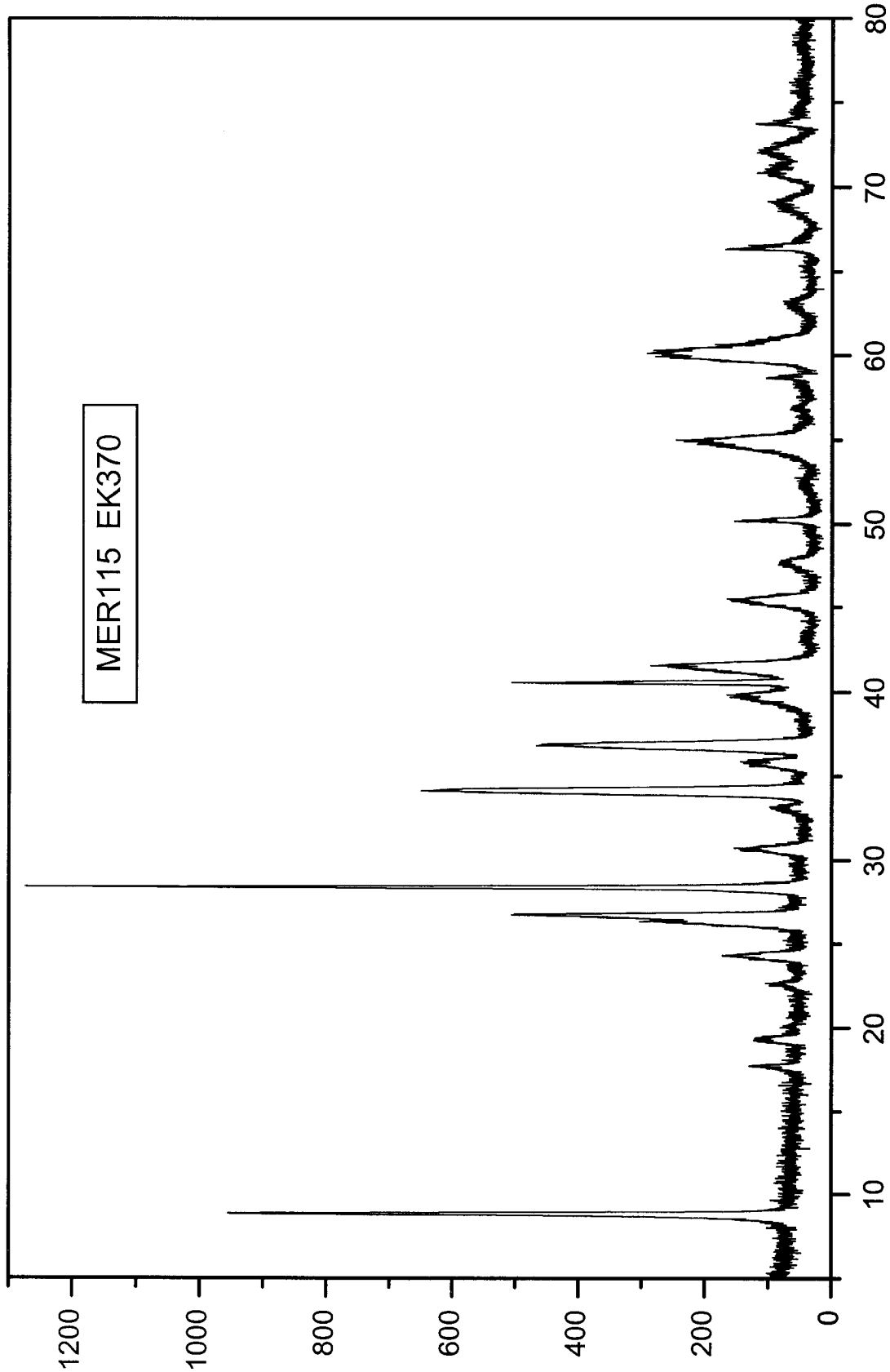
MER115 EK370
0
200
400
600
800
1000
1200
10
20
30
40
50
60
70
80

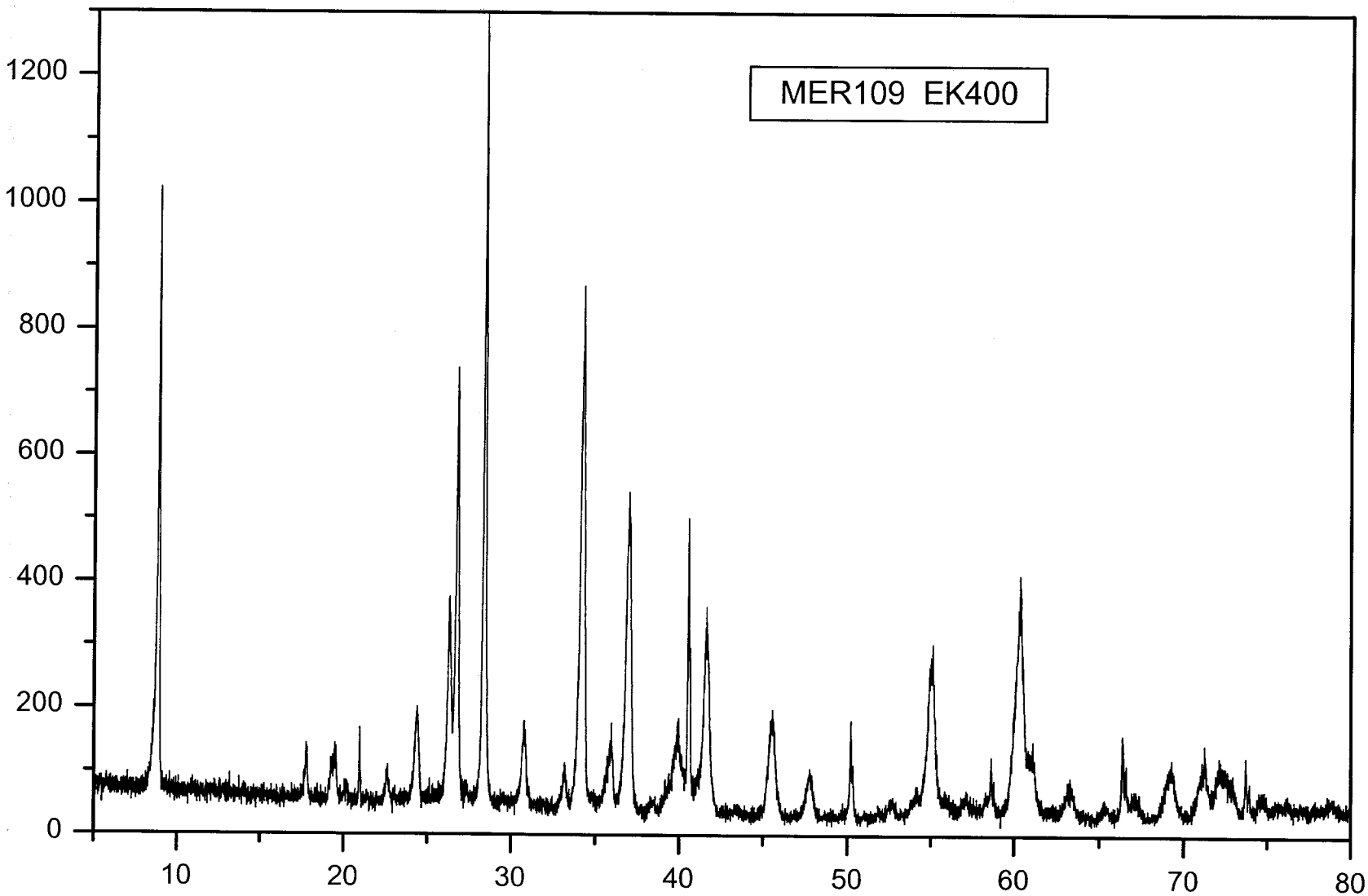

A42

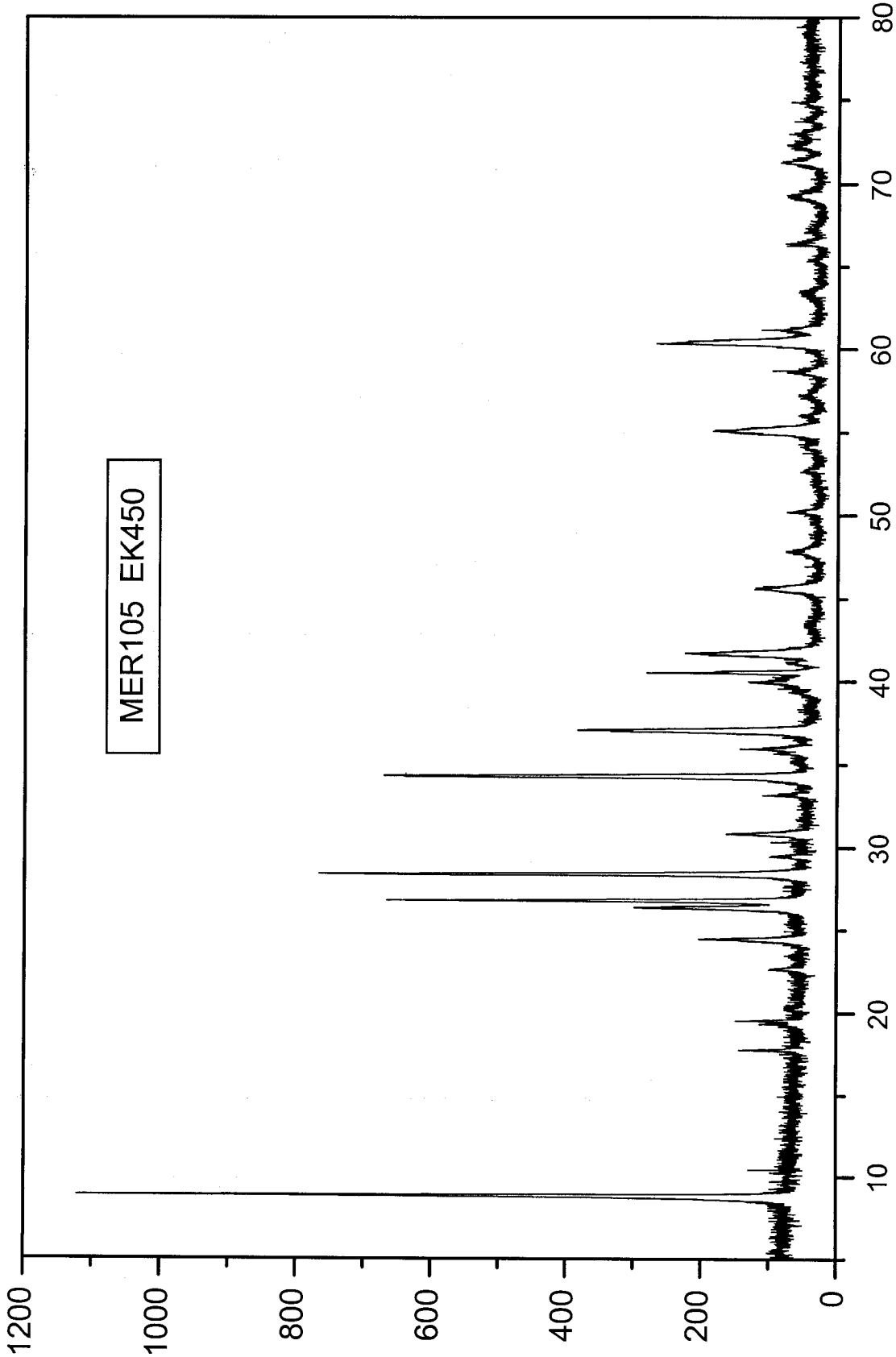
MER105 EK450
1200
1000
800
600
400
200
0
10
20
30
40
50
60
70
80

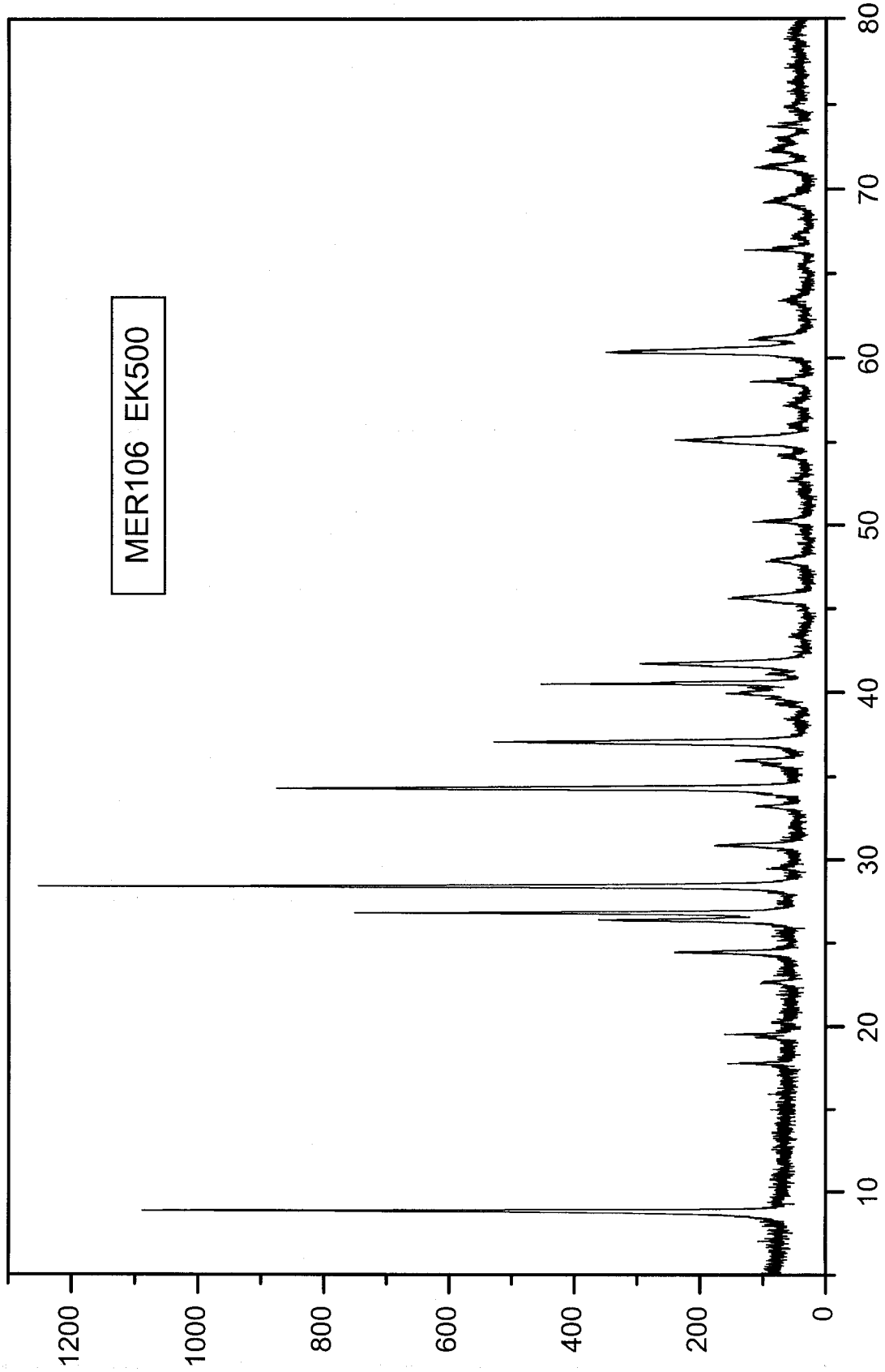
MER106 EK500
0
200
400
600
800
1000
1200
10
20
30
40
50
60
70
80

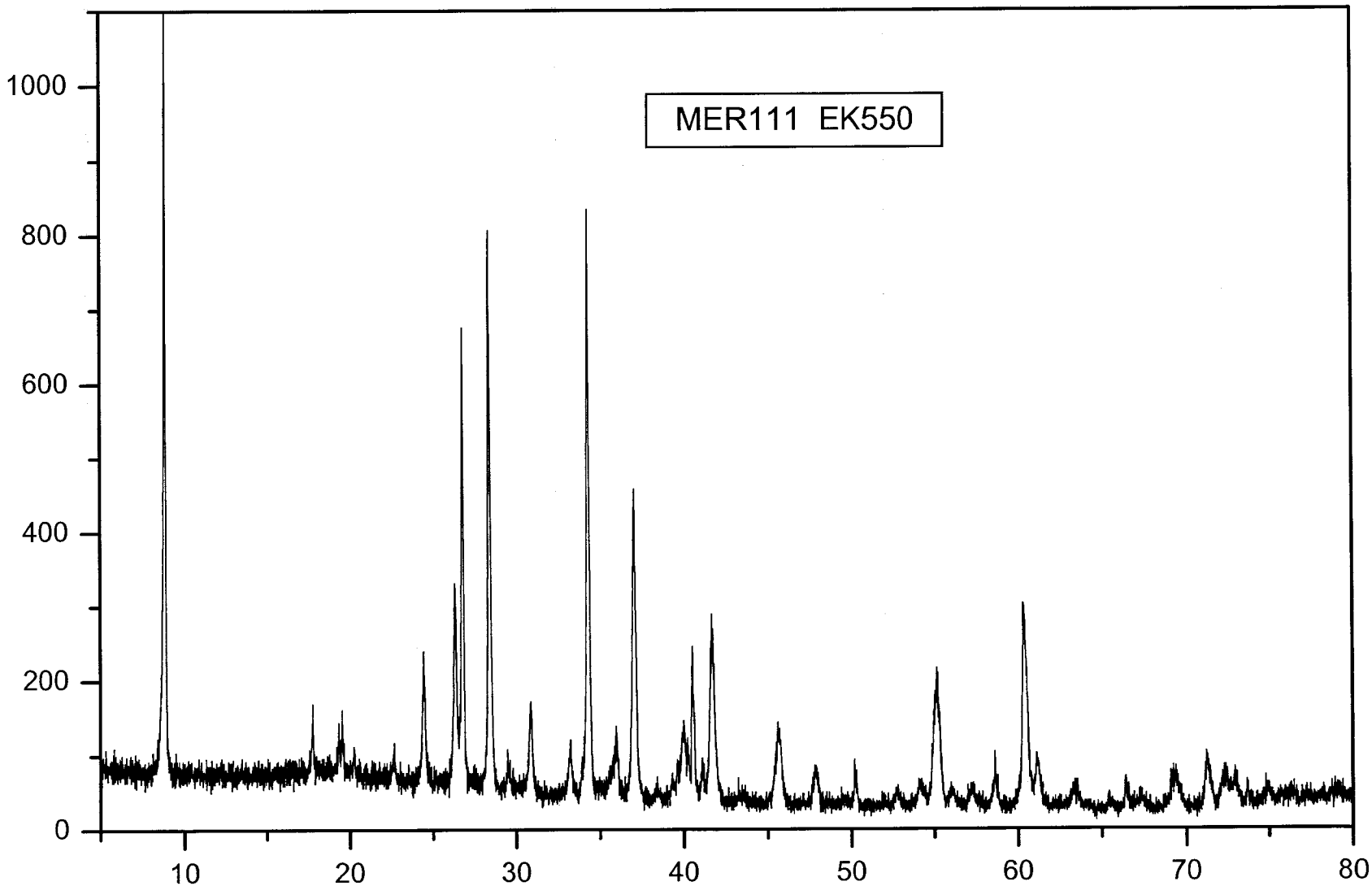

A45

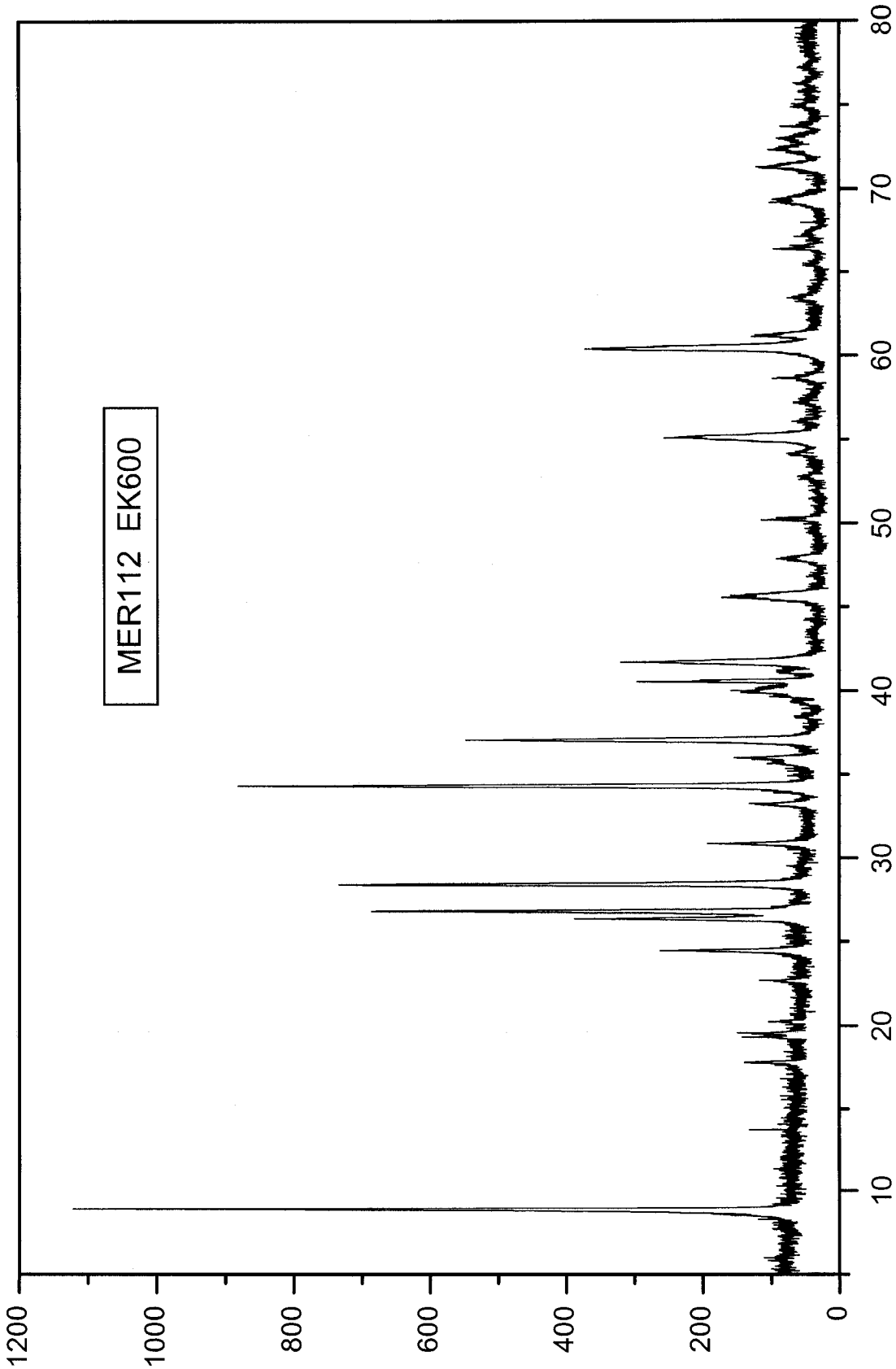
MER112 EK600
1200
1000
800
600
400
200
0
10
20
30
40
50
60
70
80

Appendix B. Mössbauer spectra

B1

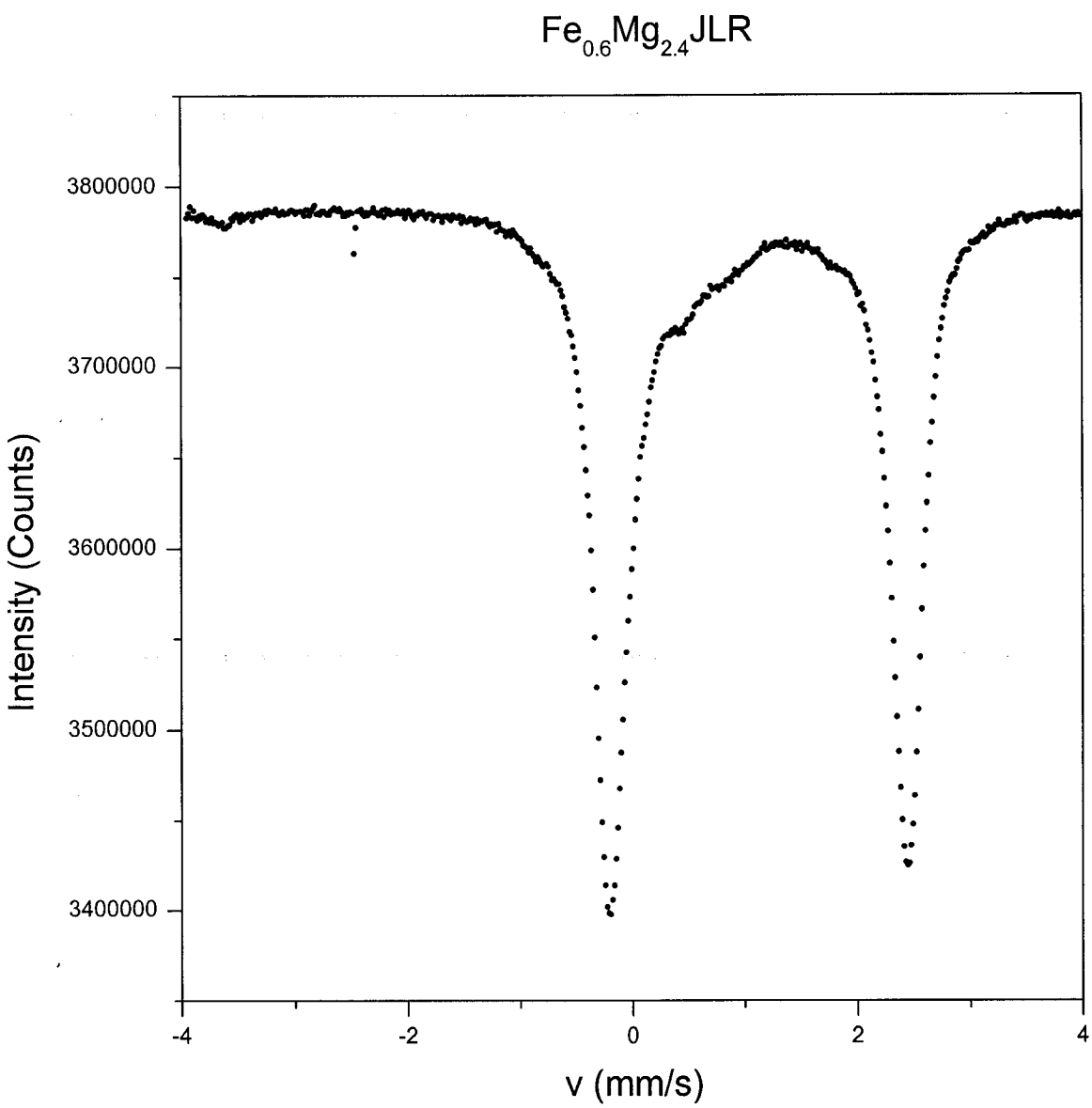
Fe0.6Mg2.4JLR
Intensity (Counts)
3800000
3700000
3600000
3500000
3400000
-4
-2
0
2
4
v (mm/s)

B2

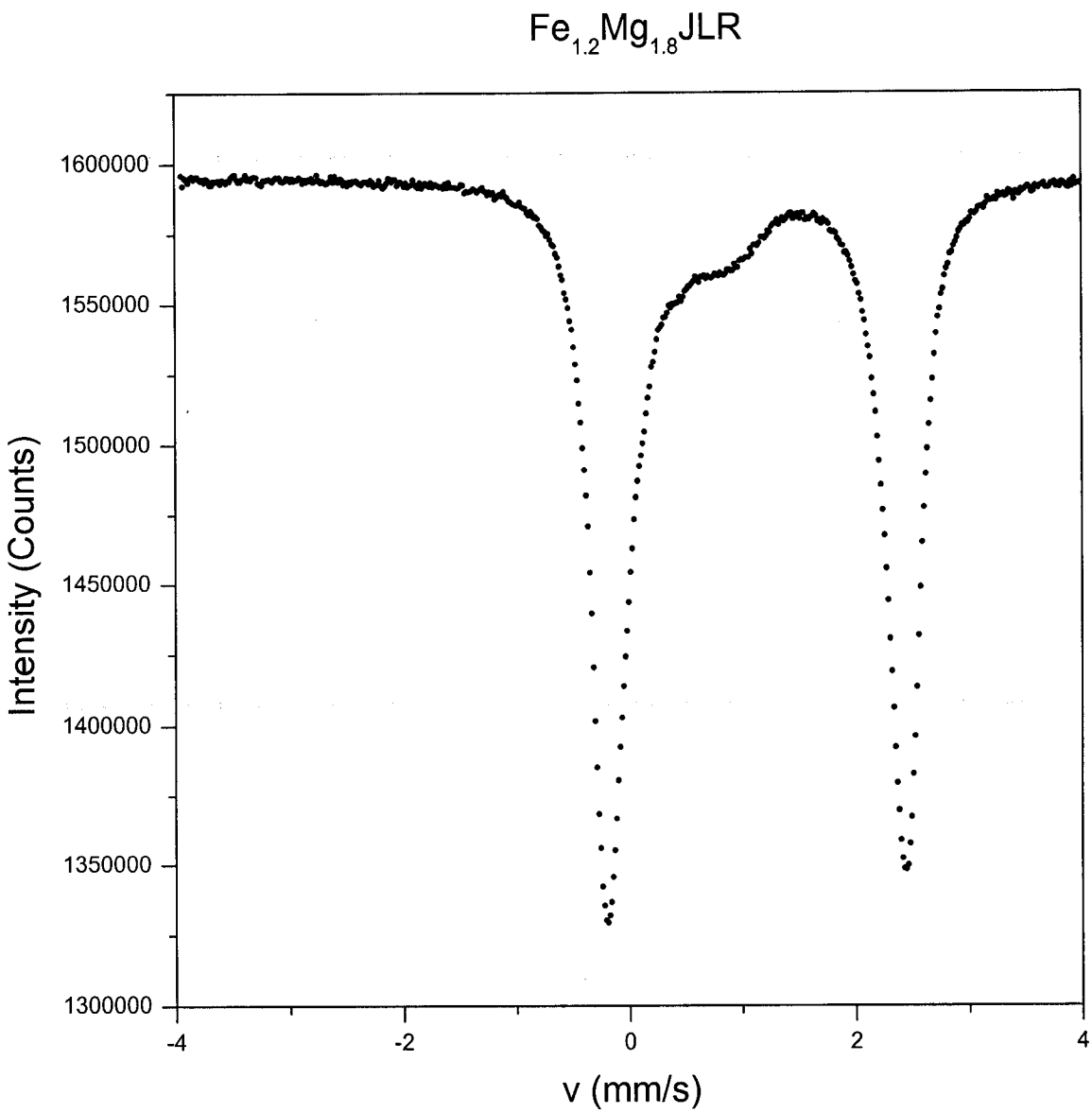
$Fe_{1.2}Mg_{1.8}JLR$
Intensity (Counts)
1600000
1550000
1500000
1450000
1400000
1350000
1300000
-4
-2
0
2
4
v (mm/s)

B3

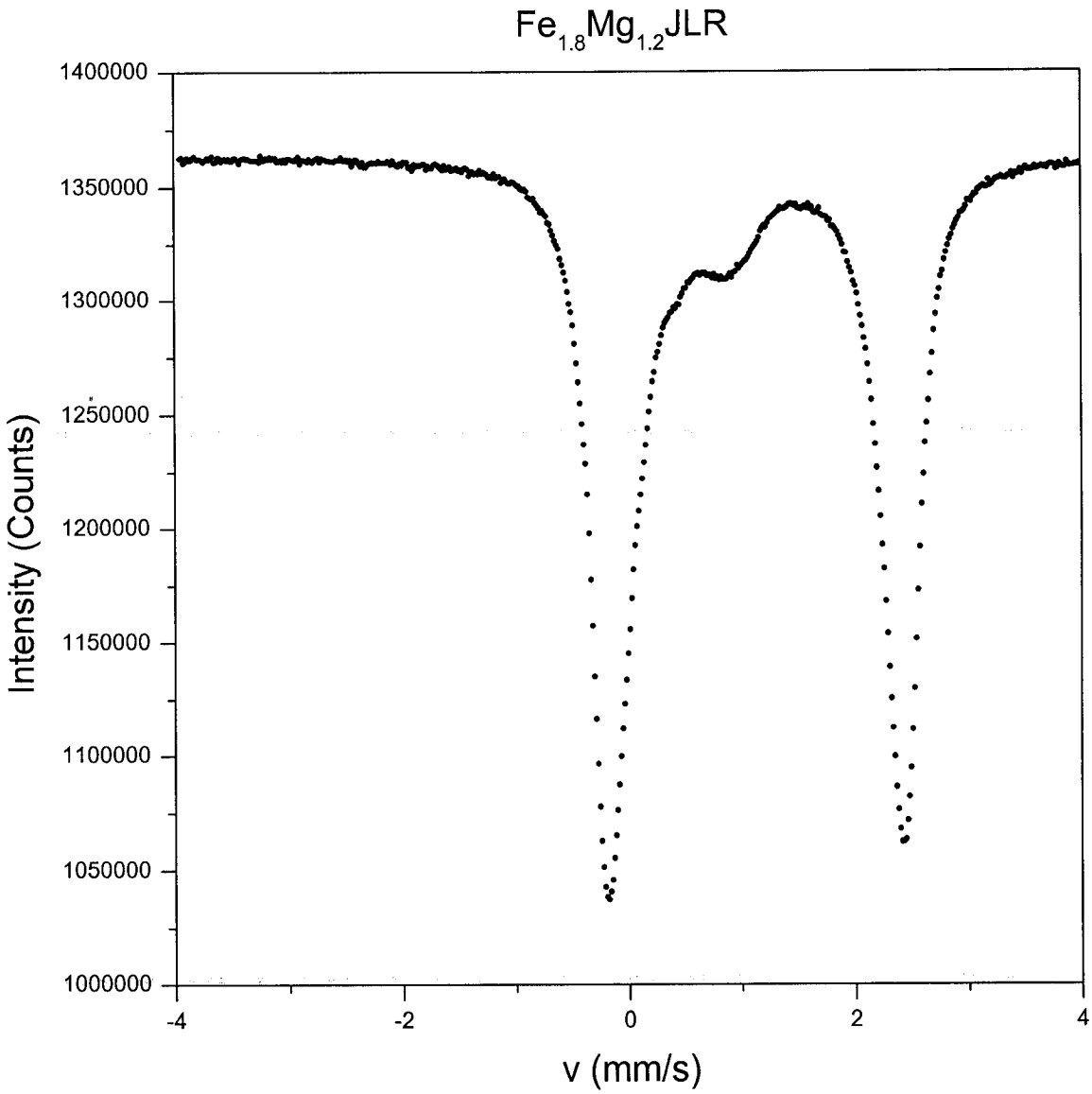
Fe1.8Mg1.2JLR
Intensity (Counts)
1400000
1350000
1300000
1250000
1200000
1150000
1100000
1050000
1000000
-4
-2
0
2
4
v (mm/s)

B4

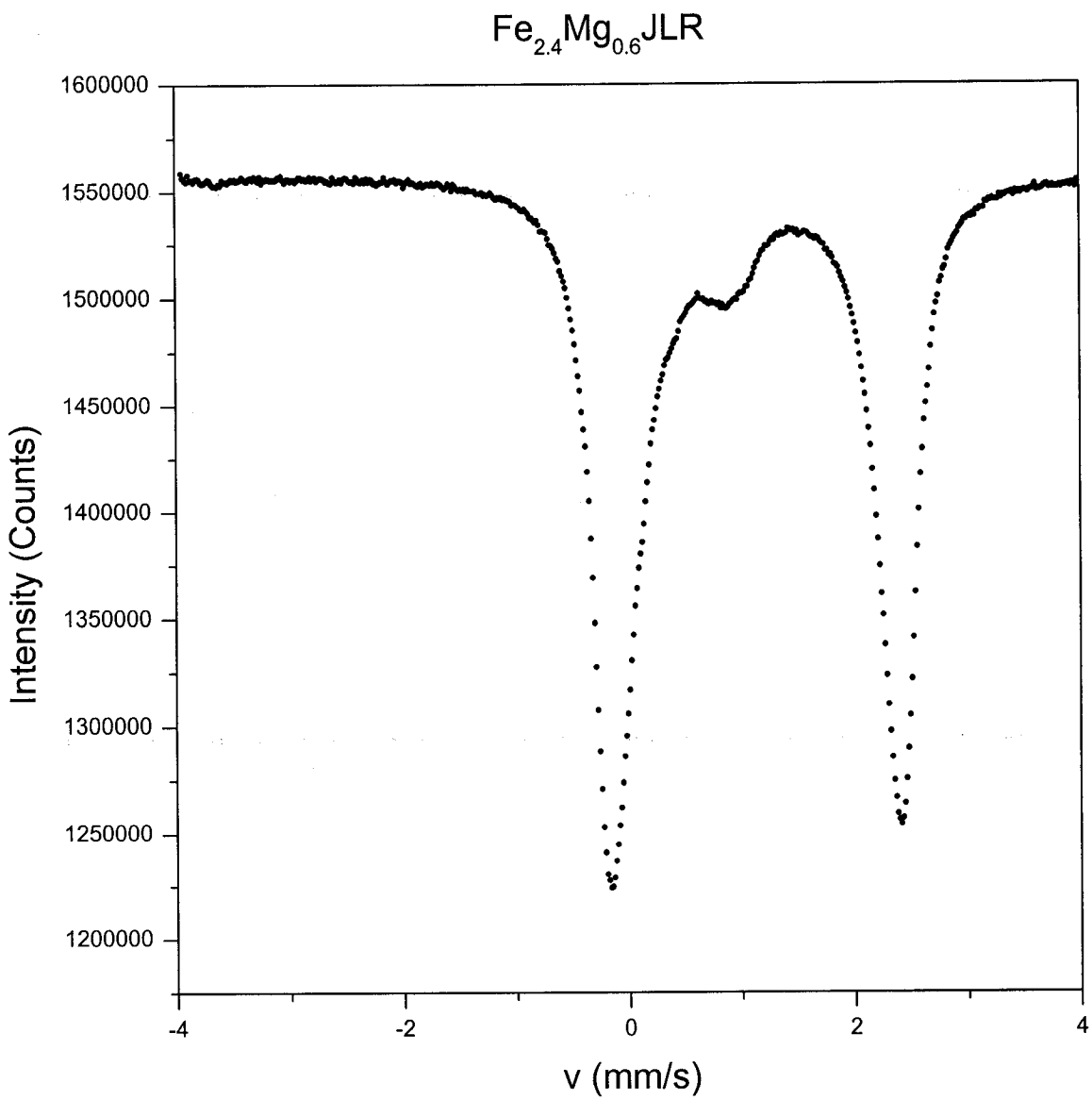
Fe2.4Mg0.6JLR
Intensity (Counts)
1600000
1550000
1500000
1450000
1400000
1350000
1300000
1250000
1200000
-4
-2
0
2
4
v (mm/s)

B5

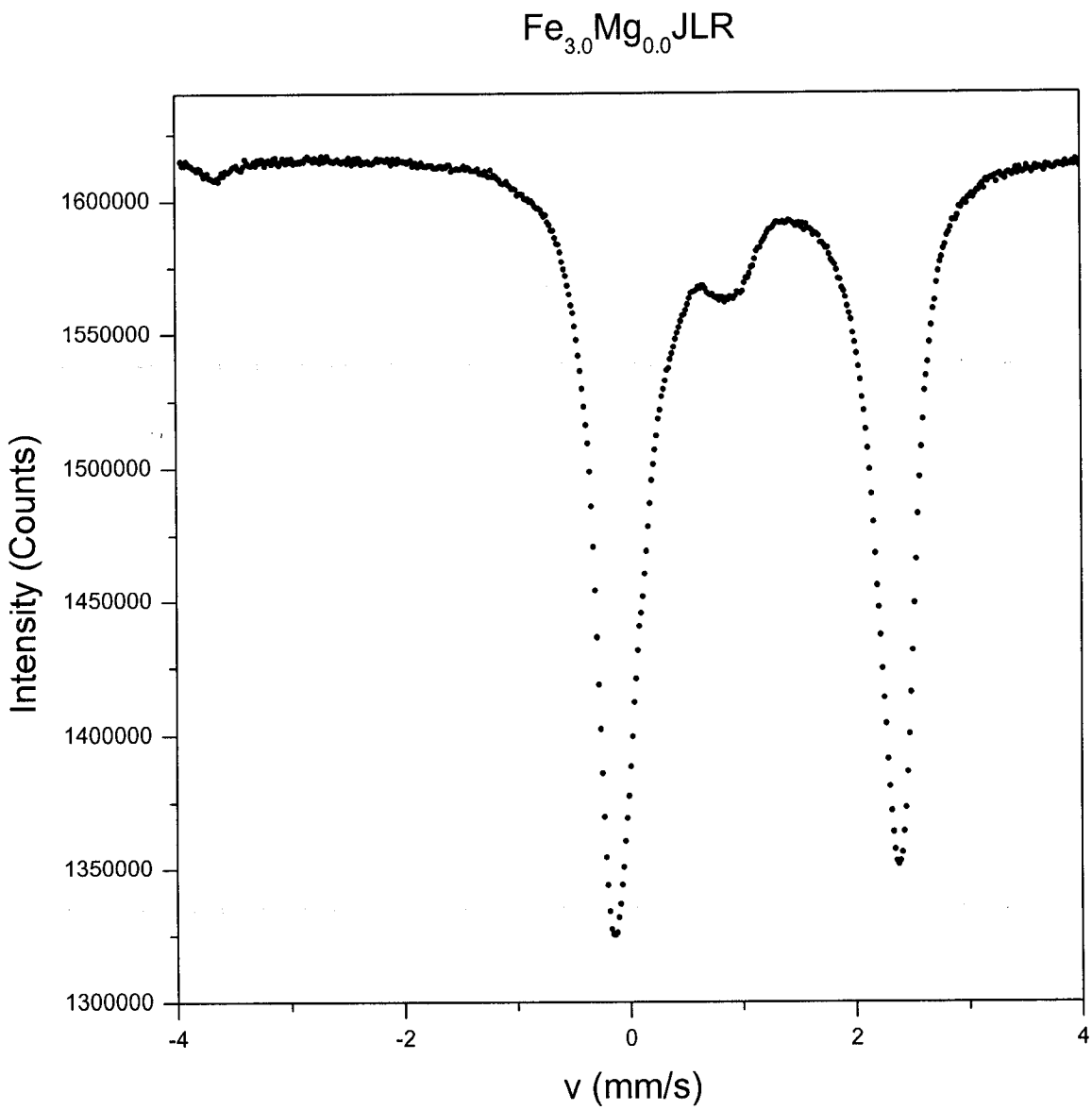
$Fe_{3.0}Mg_{0.0}JLR$
Intensity (Counts)
1600000
1550000
1500000
1450000
1400000
1350000
1300000
-4
-2
0
2
4
v (mm/s)

B6

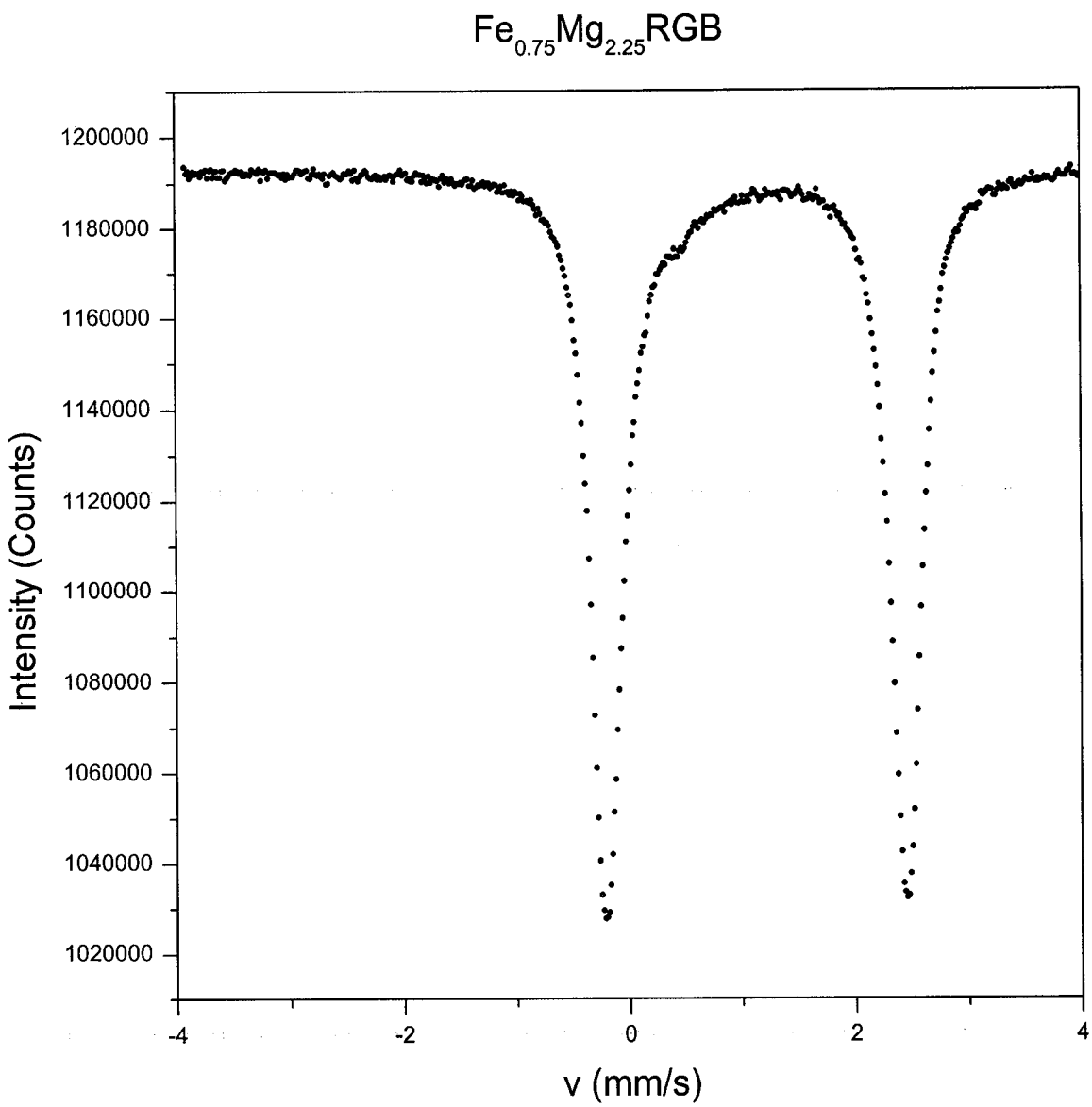
$Fe_{0.75}Mg_{2.25}RGB$
Intensity (Counts)
1200000
1180000
1160000
1140000
1120000
1100000
1080000
1060000
1040000
1020000
-4
-2
0
2
4
v (mm/s)

B7

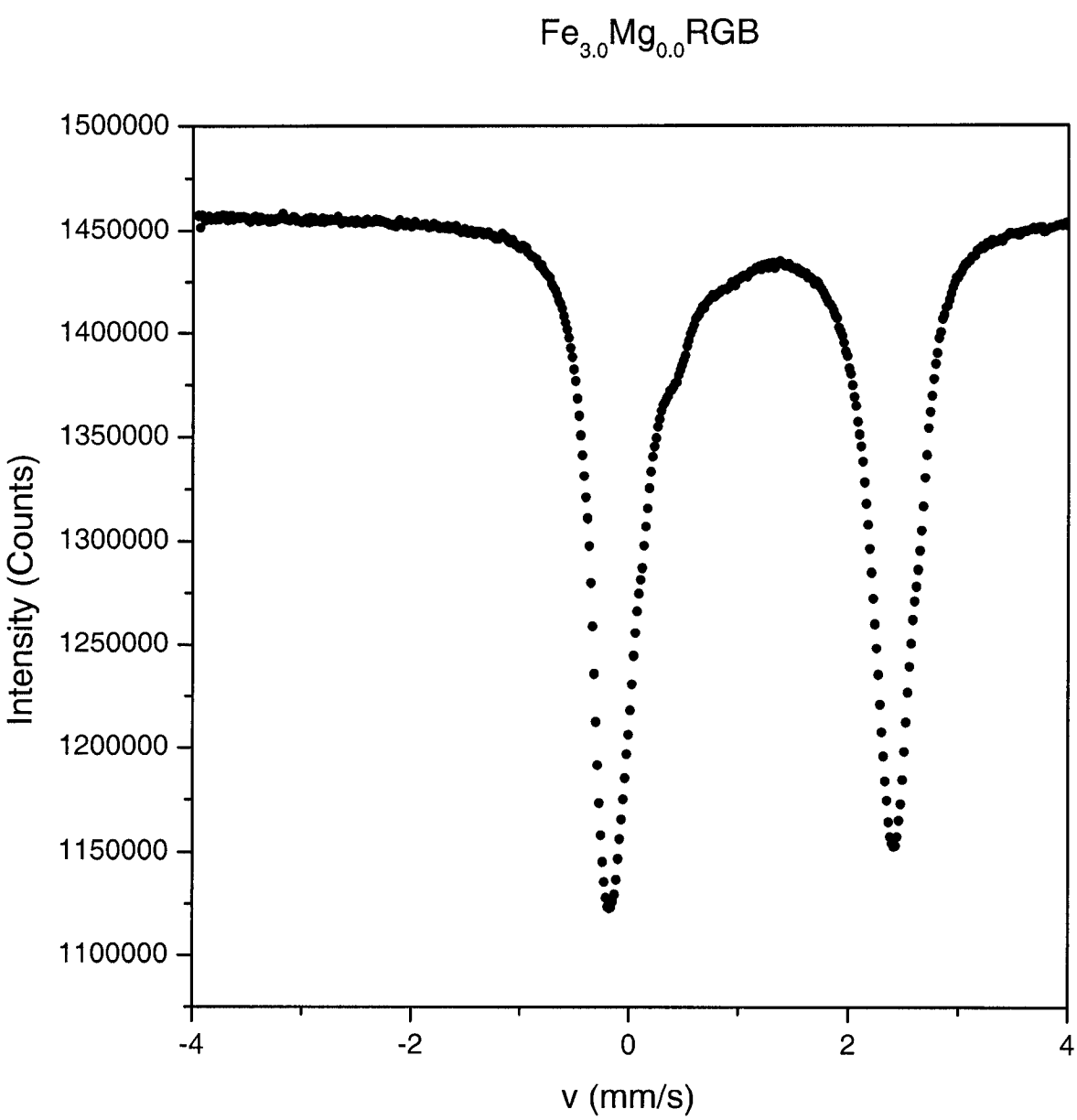
$Fe_{3.0}Mg_{0.0}RGB$
Intensity (Counts)
1500000
1450000
1400000
1350000
1300000
1250000
1200000
1150000
1100000
-4
-2
0
2
4
v (mm/s)

B8

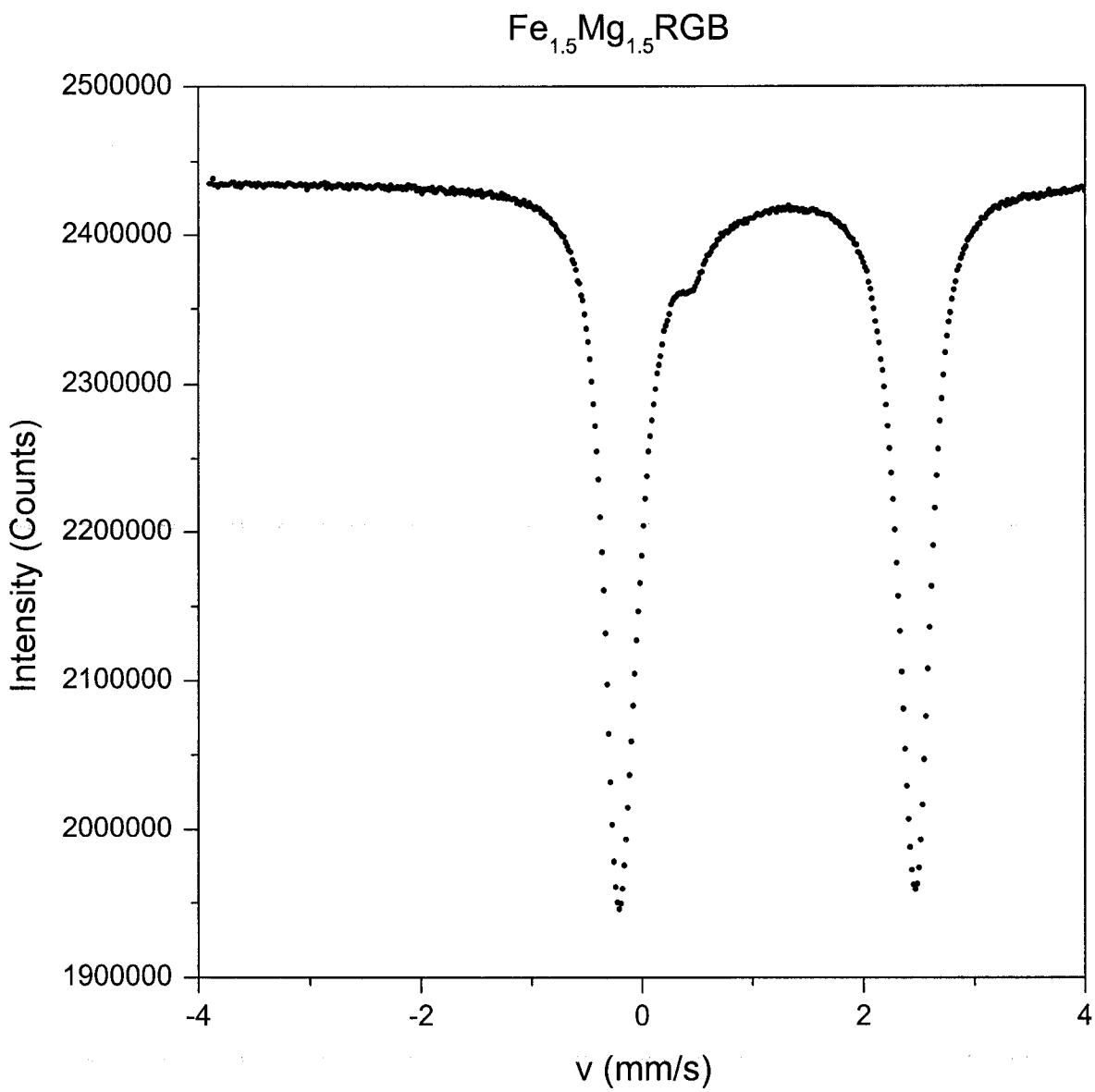
Fe1.5Mg1.5RGB
2500000
2400000
2300000
2200000
2100000
2000000
1900000
Intensity (Counts)
-4
-2
0
2
4
v (mm/s)

B9

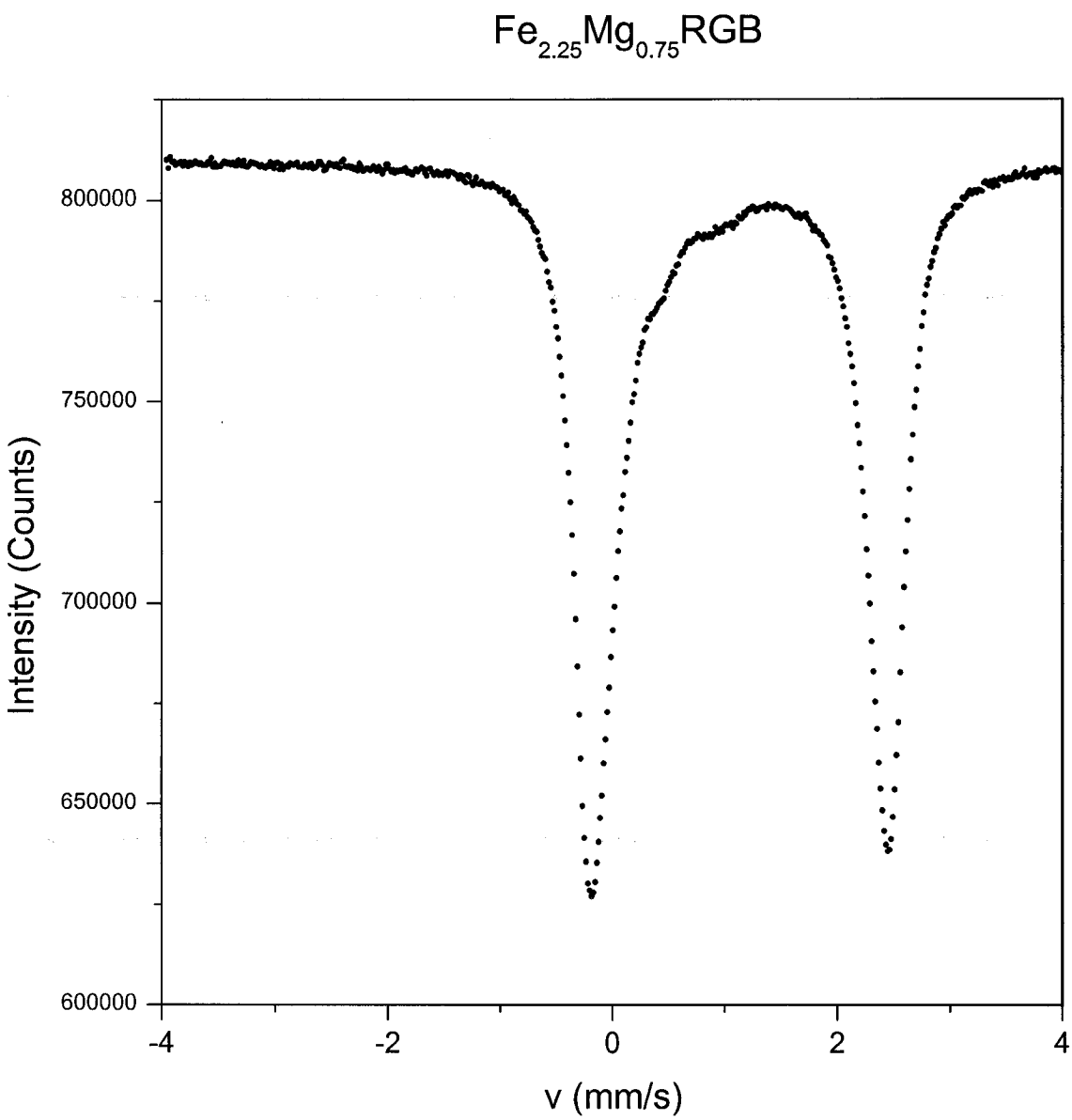
$Fe_{2.25}Mg_{0.75}RGB$
Intensity (Counts)
800000
750000
700000
650000
600000
-4
-2
0
2
4
v (mm/s)

B10

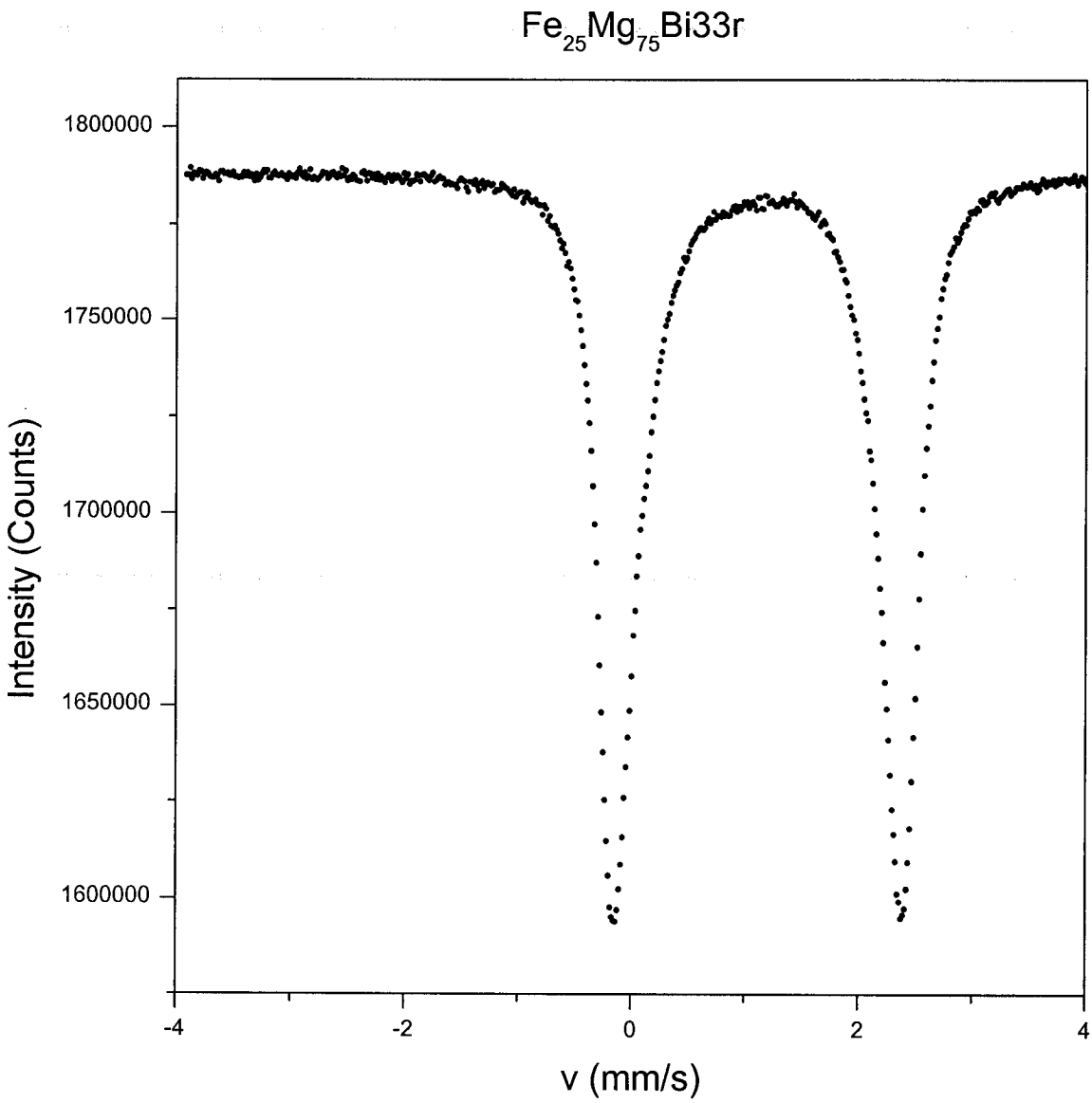
Fe25Mg75Bi33r
Intensity (Counts)
1800000
1750000
1700000
1650000
1600000
-4
-2
0
2
4
v (mm/s)

B11

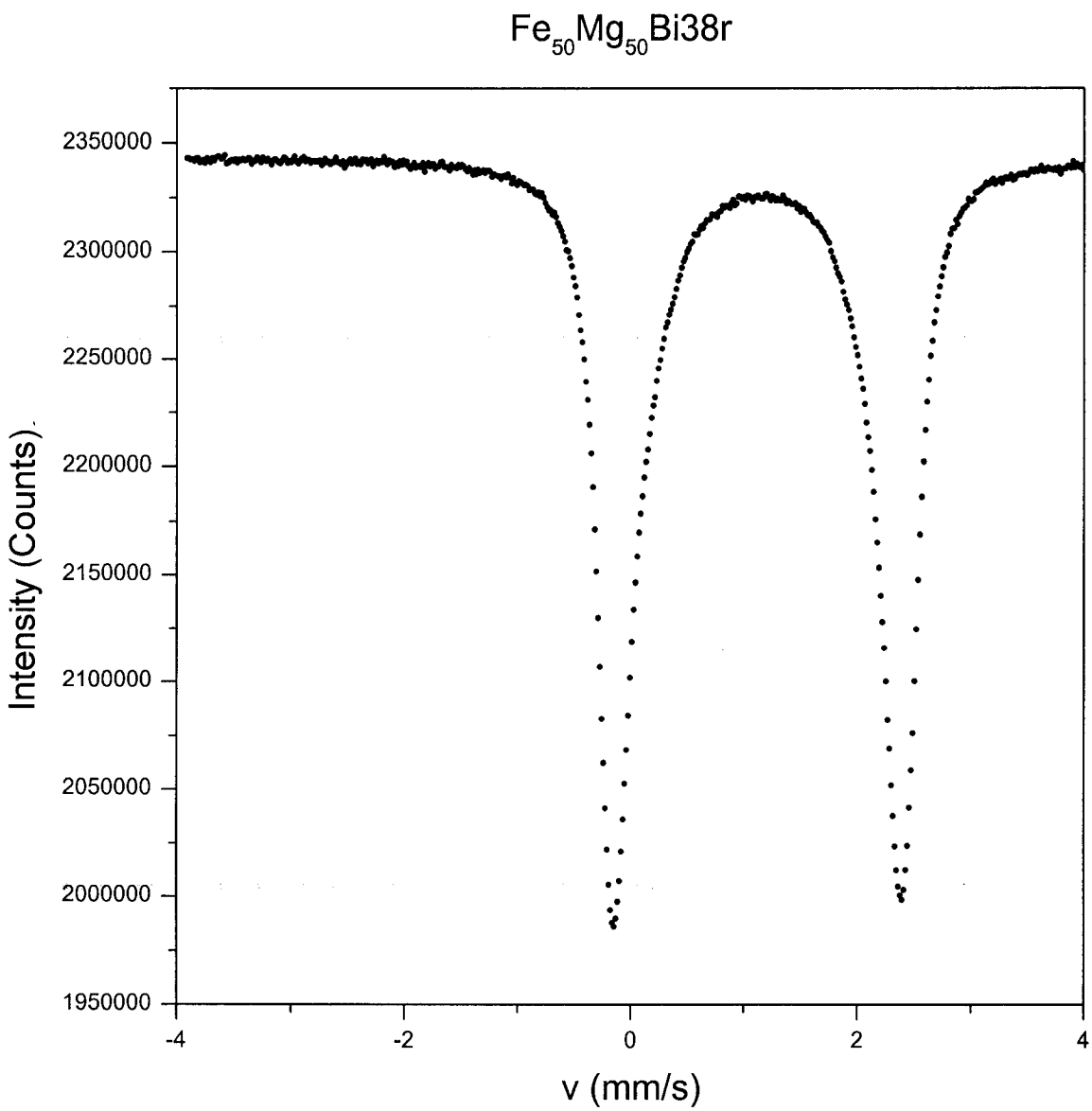
Fe50Mg50Bi38r
Intensity (Counts)
2350000
2300000
2250000
2200000
2150000
2100000
2050000
2000000
1950000
-4
-2
0
2
4
v (mm/s)

B12

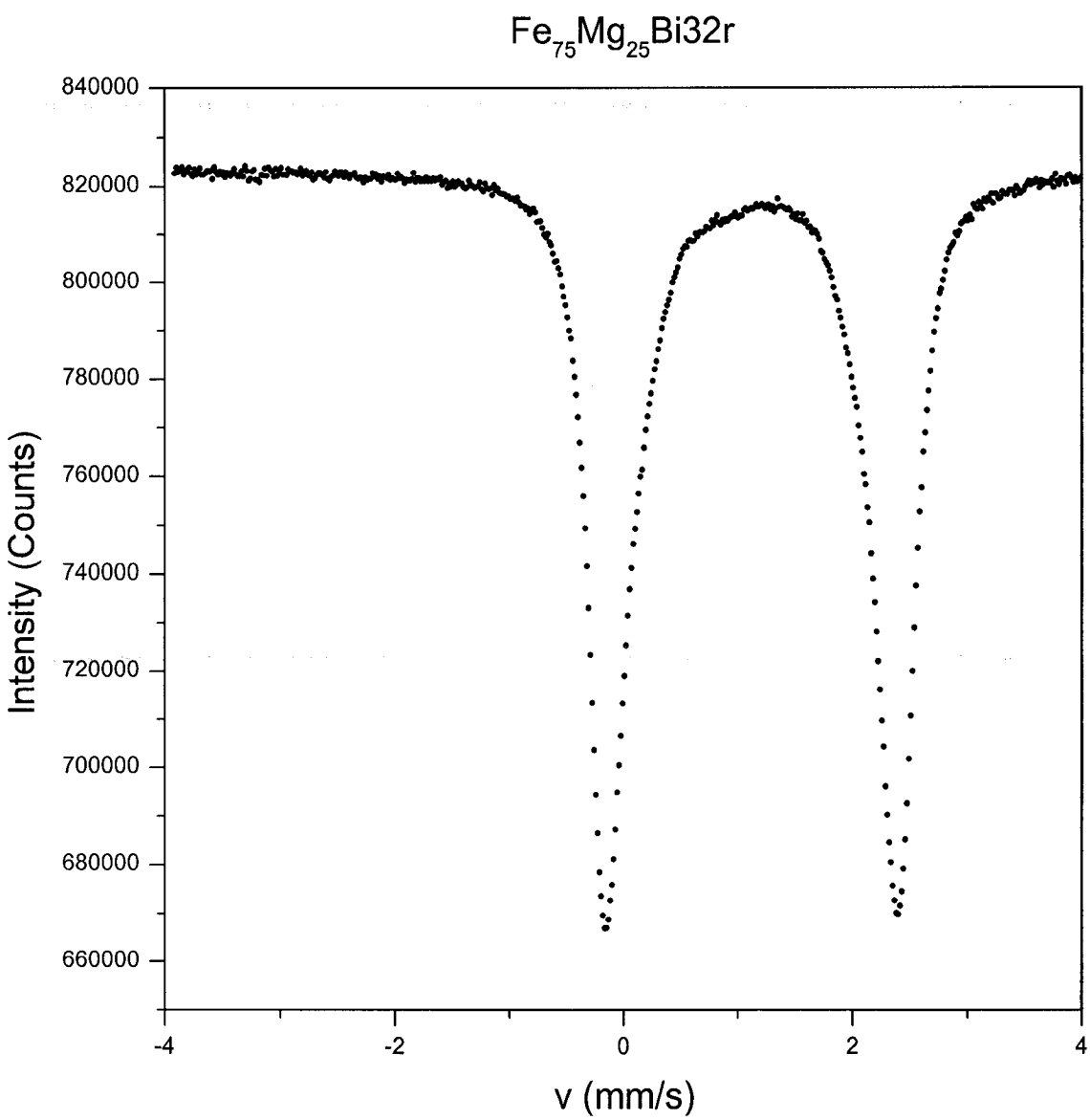
Fe75Mg25Bi32r
Intensity (Counts)
840000
820000
800000
780000
760000
740000
720000
700000
680000
660000
-4
-2
0
2
4
v (mm/s)

B13

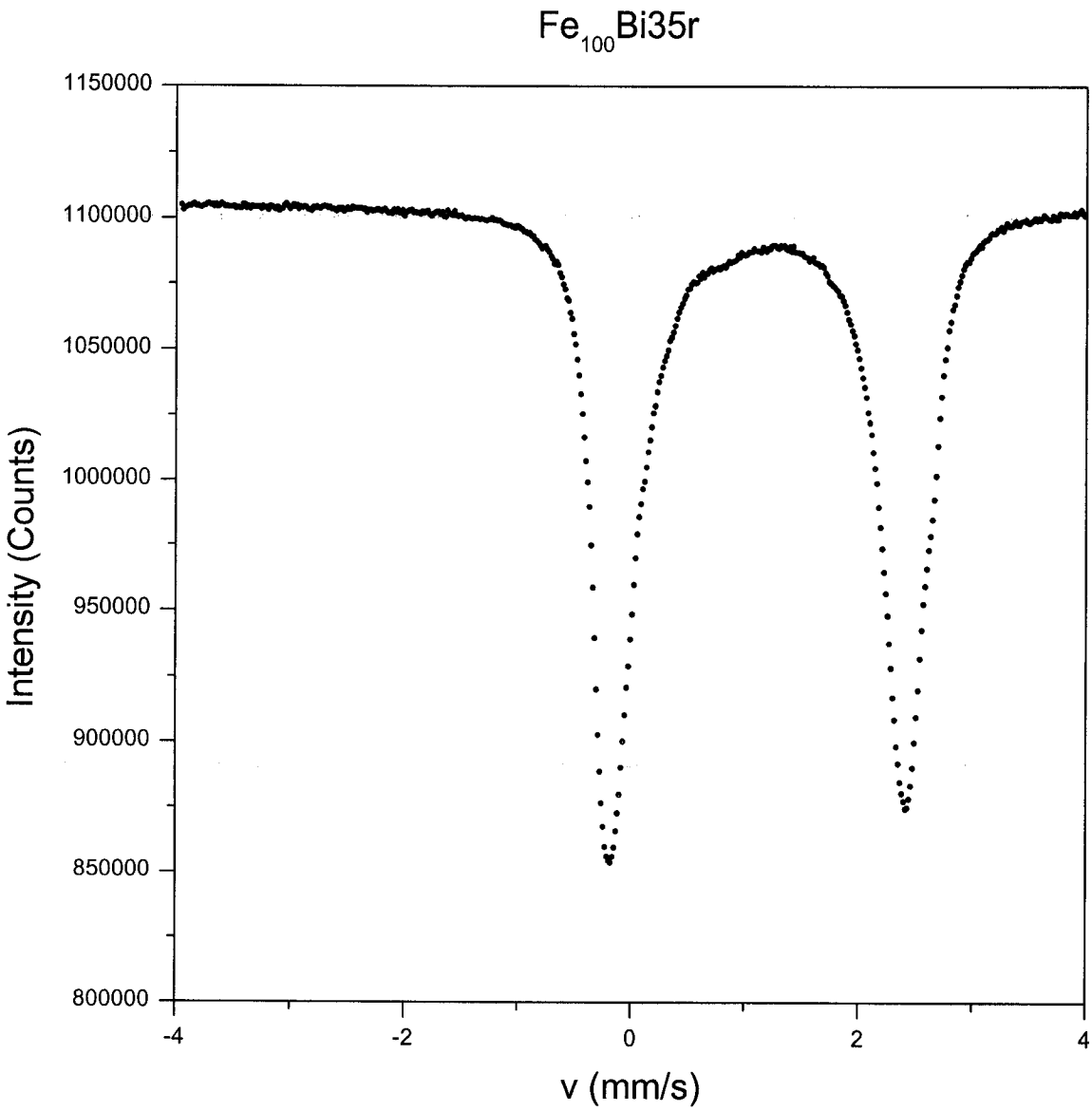
Fe100Bi35r
Intensity (Counts)
1150000
1100000
1050000
1000000
950000
900000
850000
800000
-4
-2
0
2
4
v (mm/s)

B14

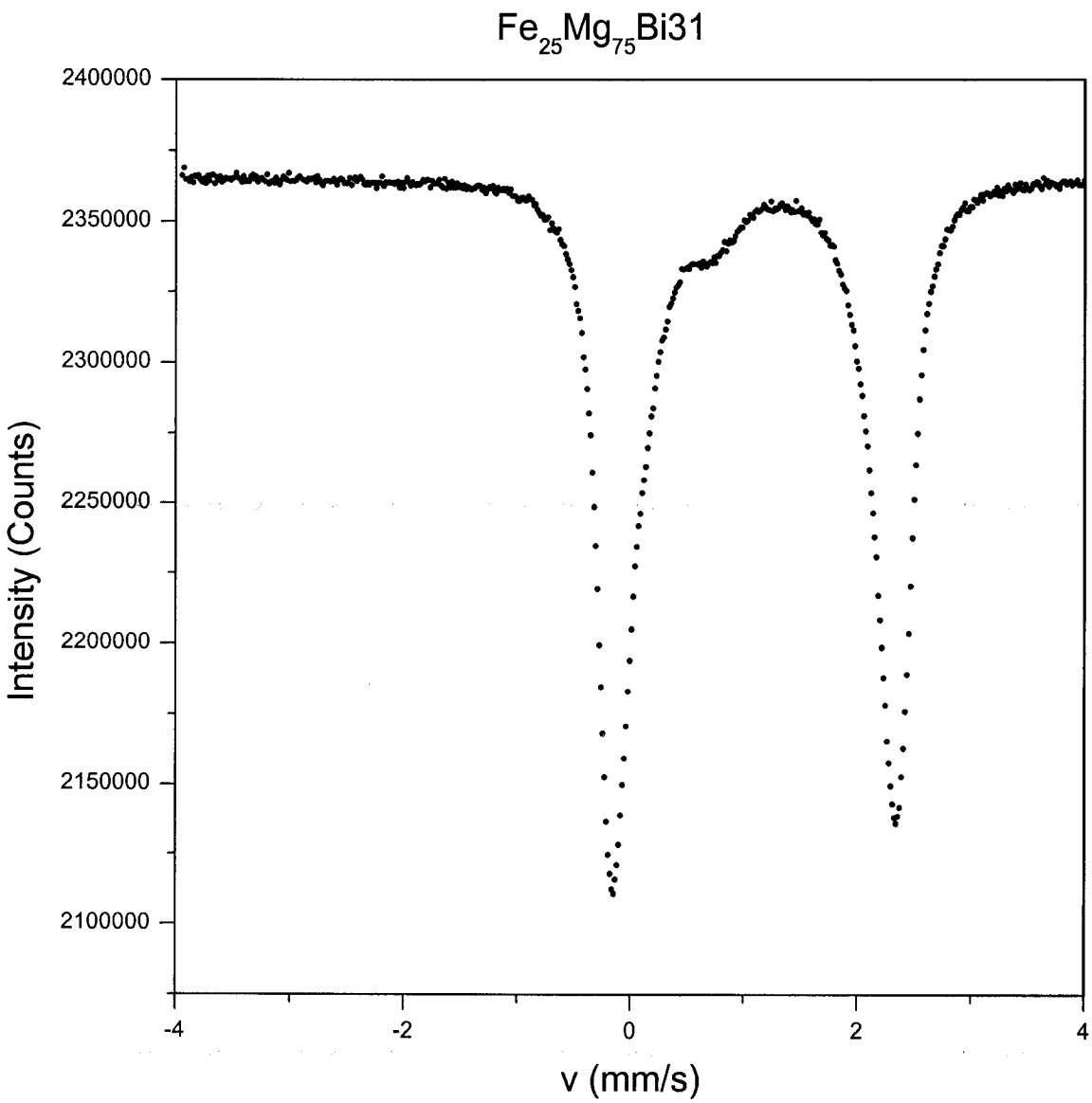
Fe25Mg75Bi31
Intensity (Counts)
2400000
2350000
2300000
2250000
2200000
2150000
2100000
-4
-2
0
2
4
v (mm/s)

B15

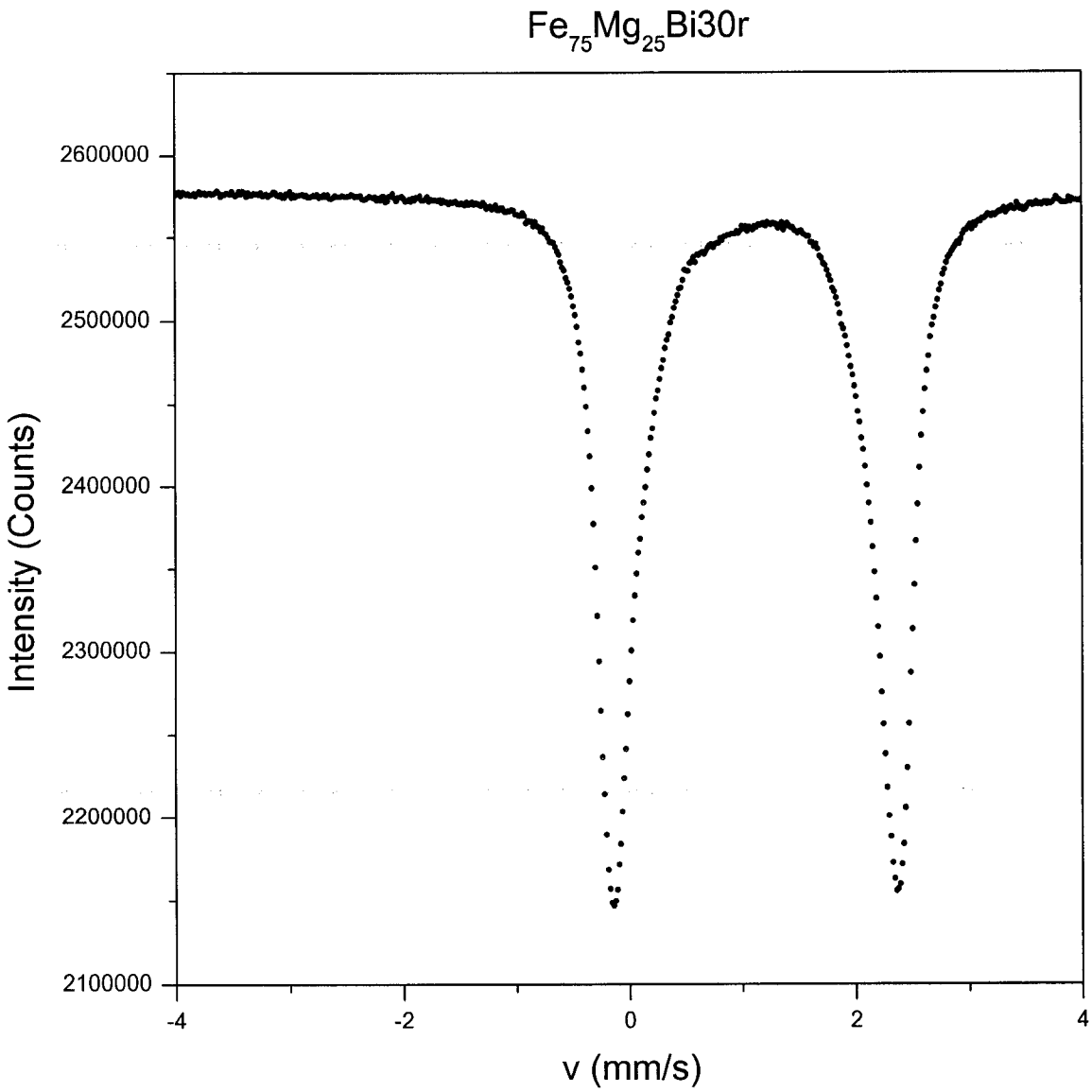
Fe75Mg25Bi30r
Intensity (Counts)
2600000
2500000
2400000
2300000
2200000
2100000
-4
-2
0
2
4
v (mm/s)

Appendix C. SEM micrographs and EDS X-ray microanalysis

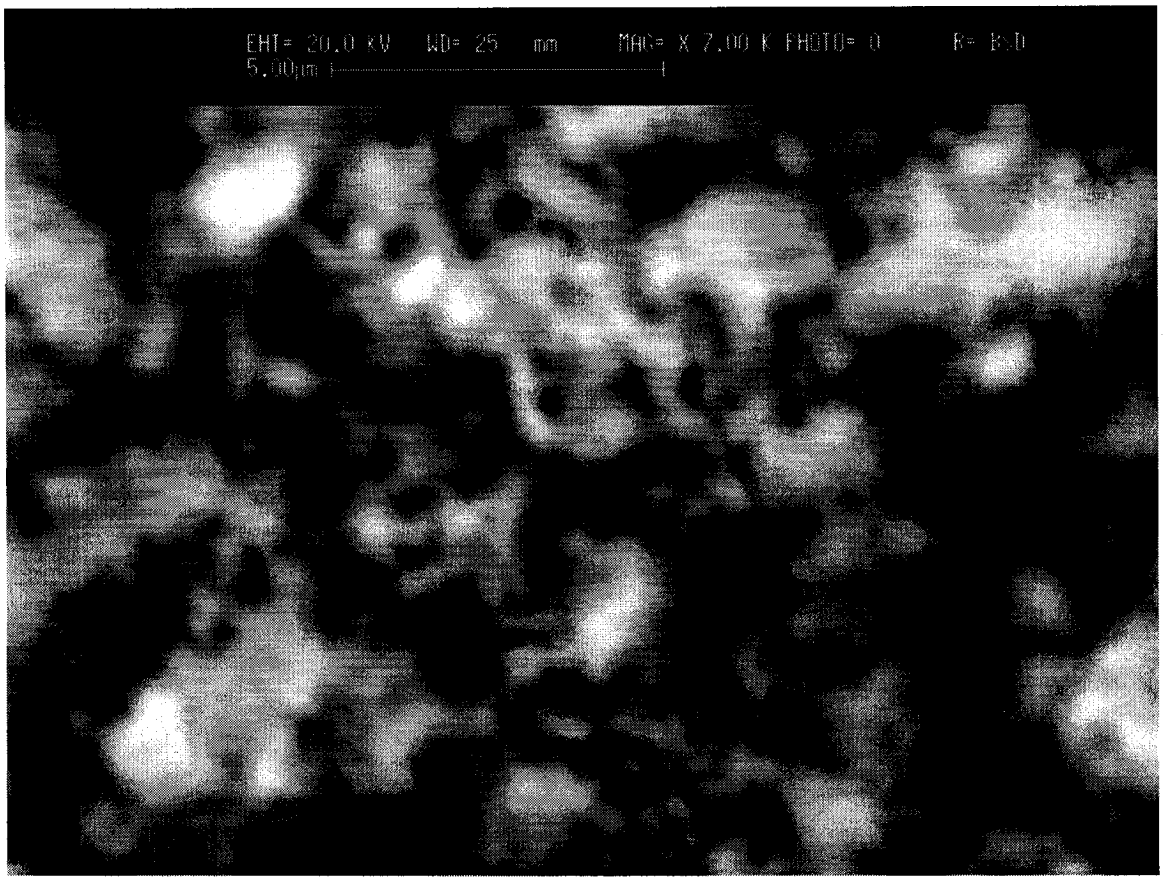

Micrograph CO07EDS1

$Co_{2.4}Mg_{0.6}$JLR

CO07EDS1

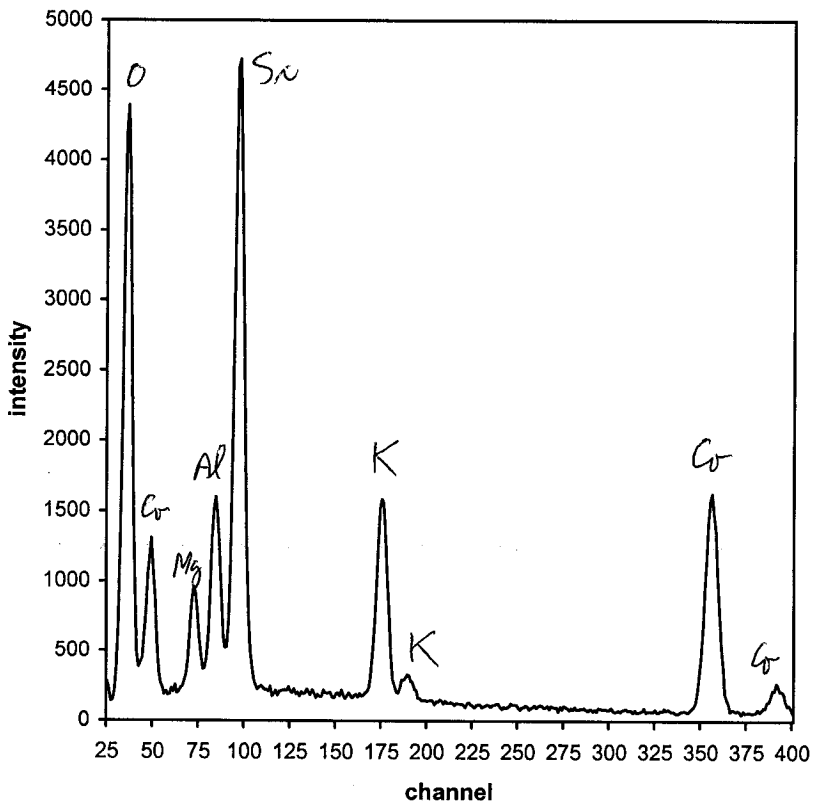
5000
4500
4000
3500
3000
2500
2000
1500
1000
500
0
intensity
O
Co
Mg
Al
Si
K
K
Co
Co
25 50 75 100 125 150 175 200 225 250 275 300 325 350 375 400
channel

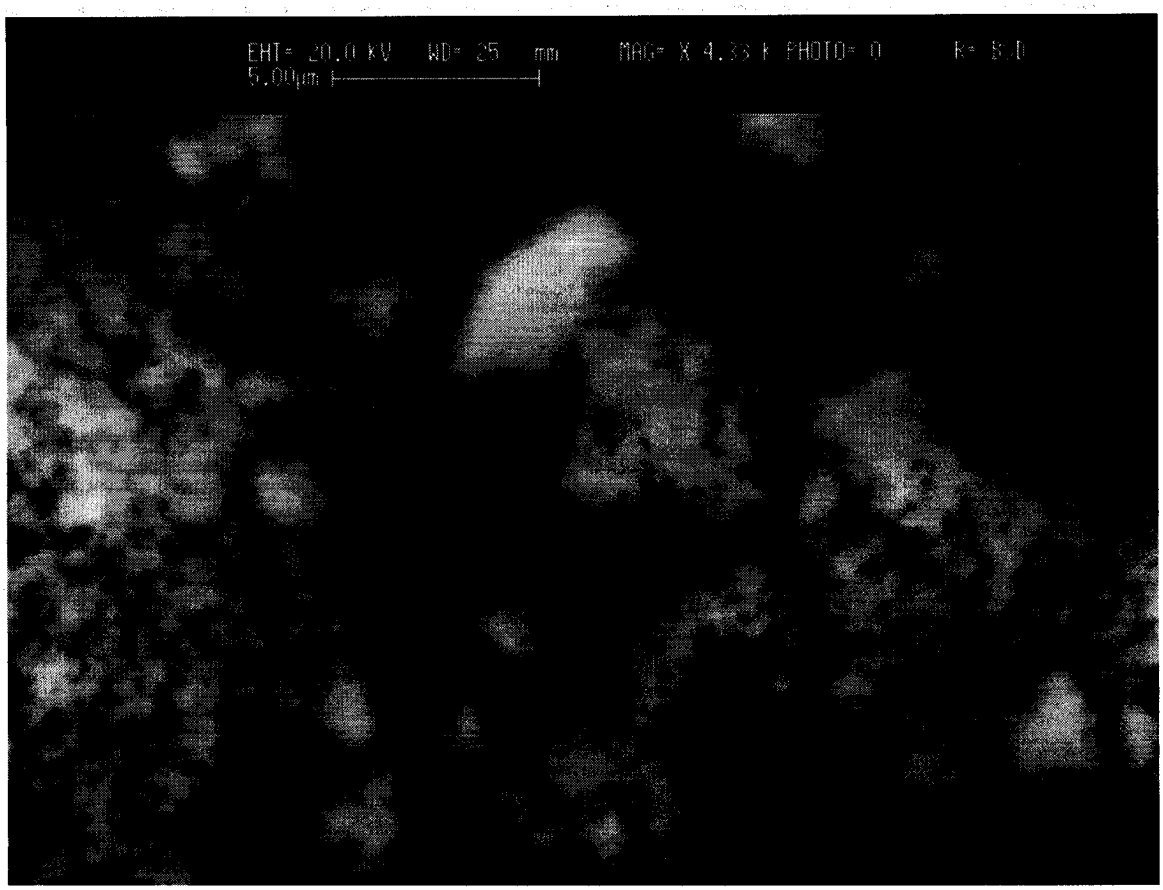

Micrograph CO07EDS2

$Co_{2.4}Mg_{0.6}$JLR

CO07EDS2

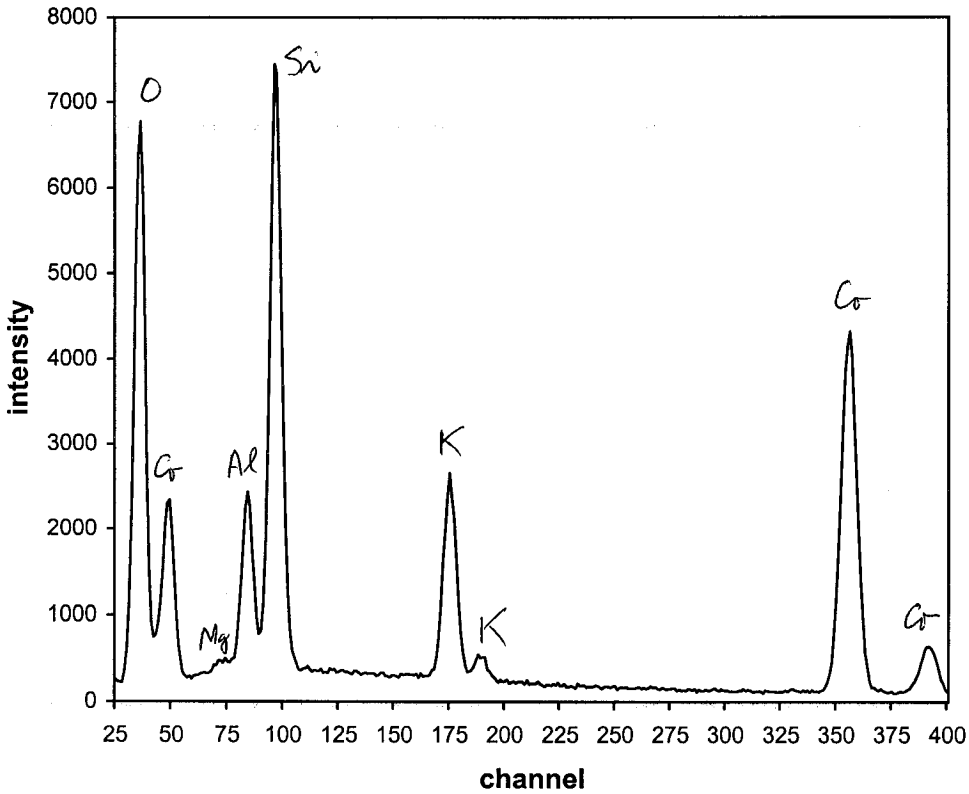
8000
7000
6000
5000
4000
3000
2000
1000
0
intensity
25 50 75 100 125 150 175 200 225 250 275 300 325 350 375 400
channel
O
Si
Au
Al
Mg
K
K
Au
Au

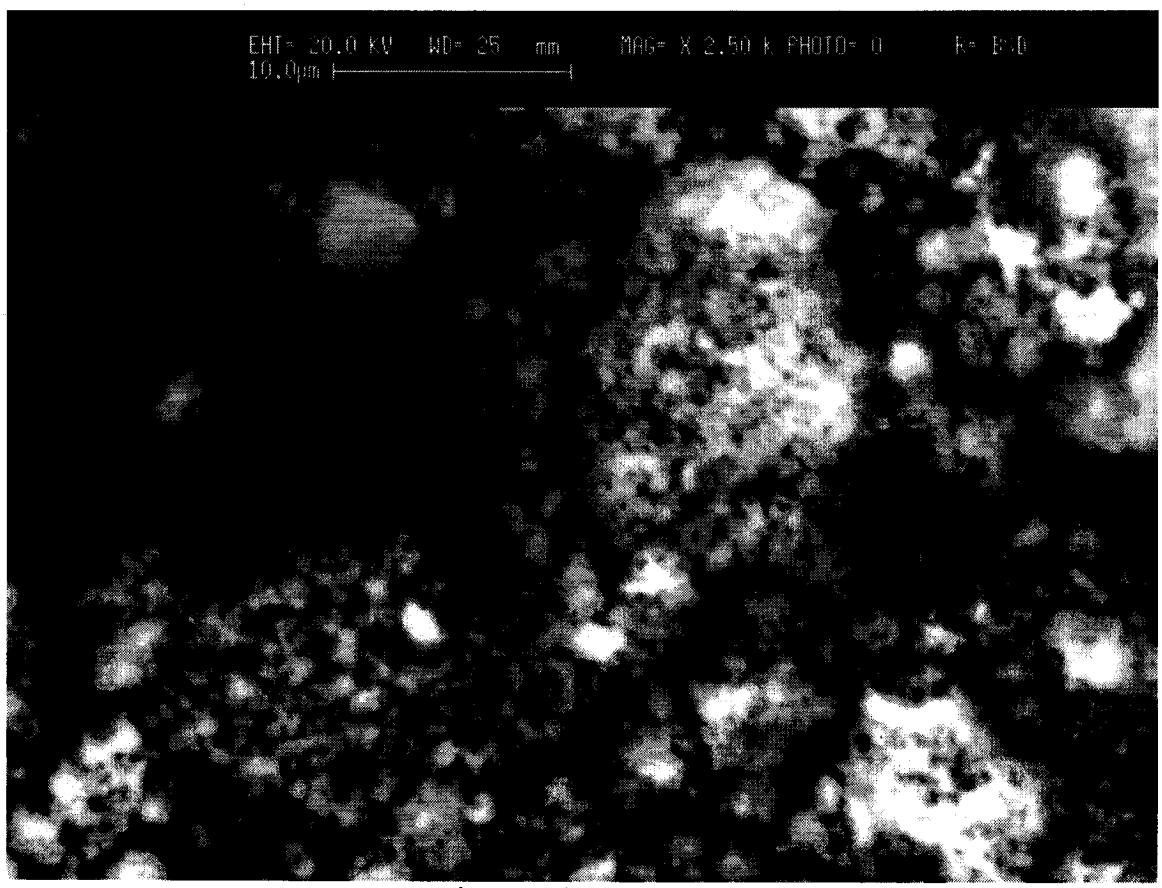

Micrograph CO07EDS3

$Co_{2.4}Mg_{0.6}$JLR

CO07EDS3

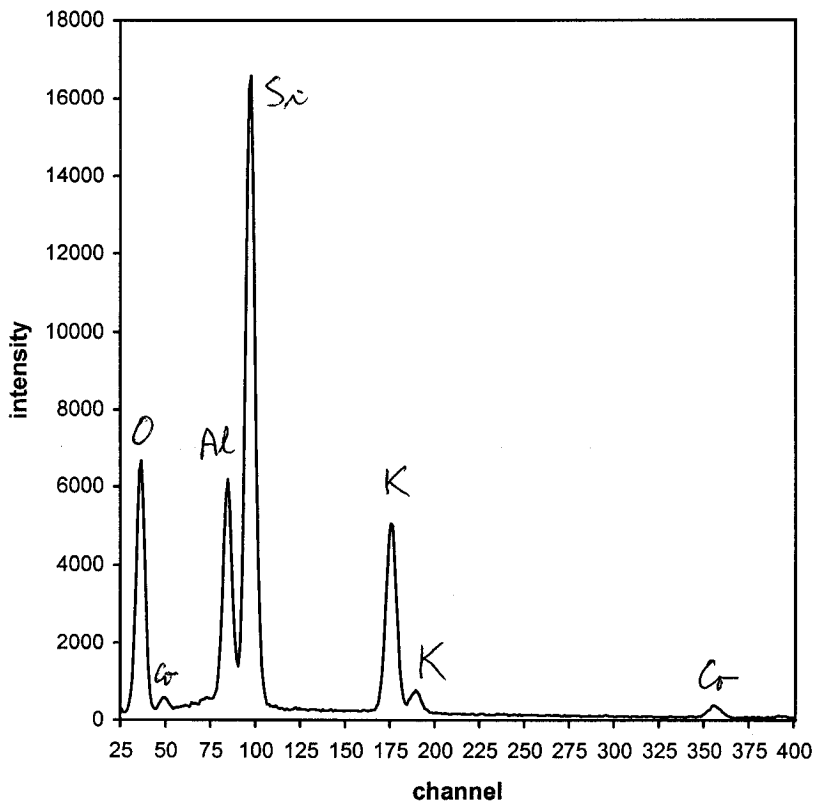
18000
16000
14000
12000
10000
8000
6000
4000
2000
0
intensity
O
Al
Si
K
K
Co
Co
25 50 75 100 125 150 175 200 225 250 275 300 325 350 375 400
channel

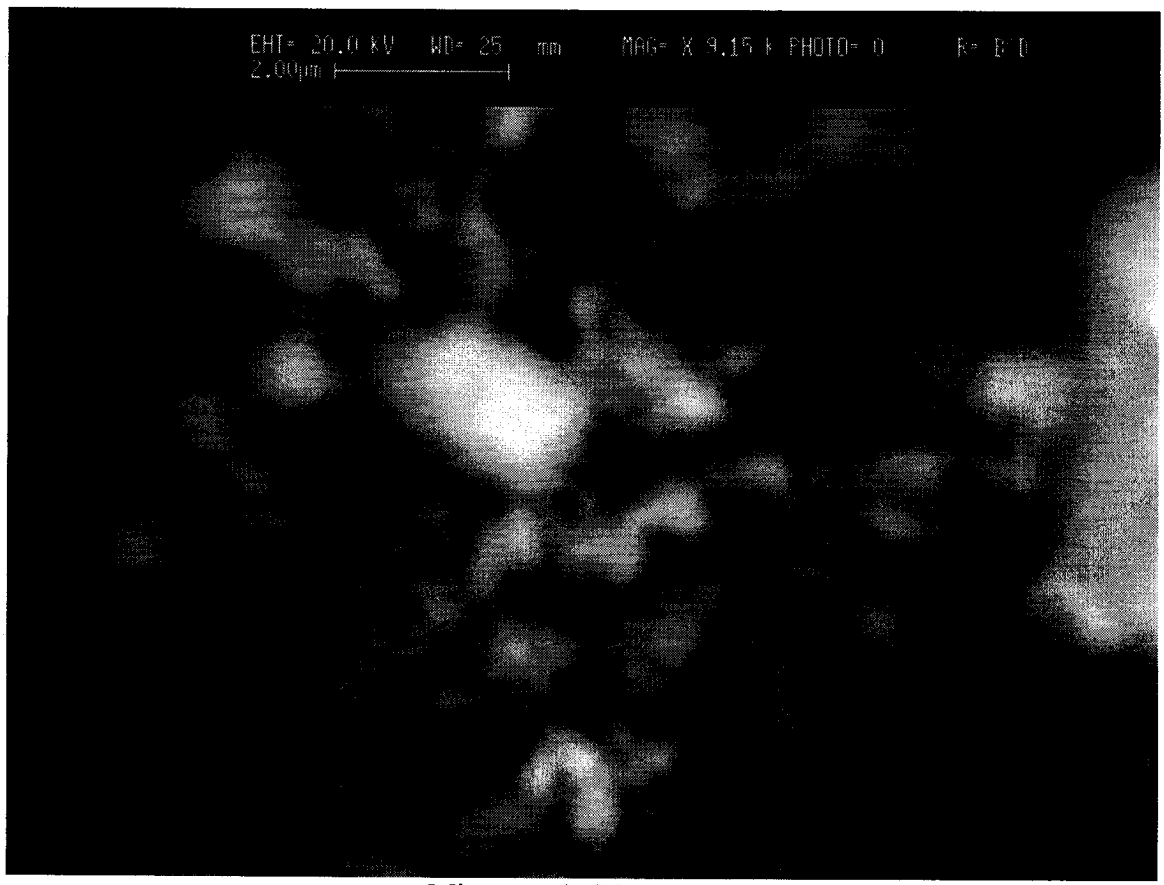

Micrograph CO07EDS4

$Co_{2.4}Mg_{0.6}JLR$

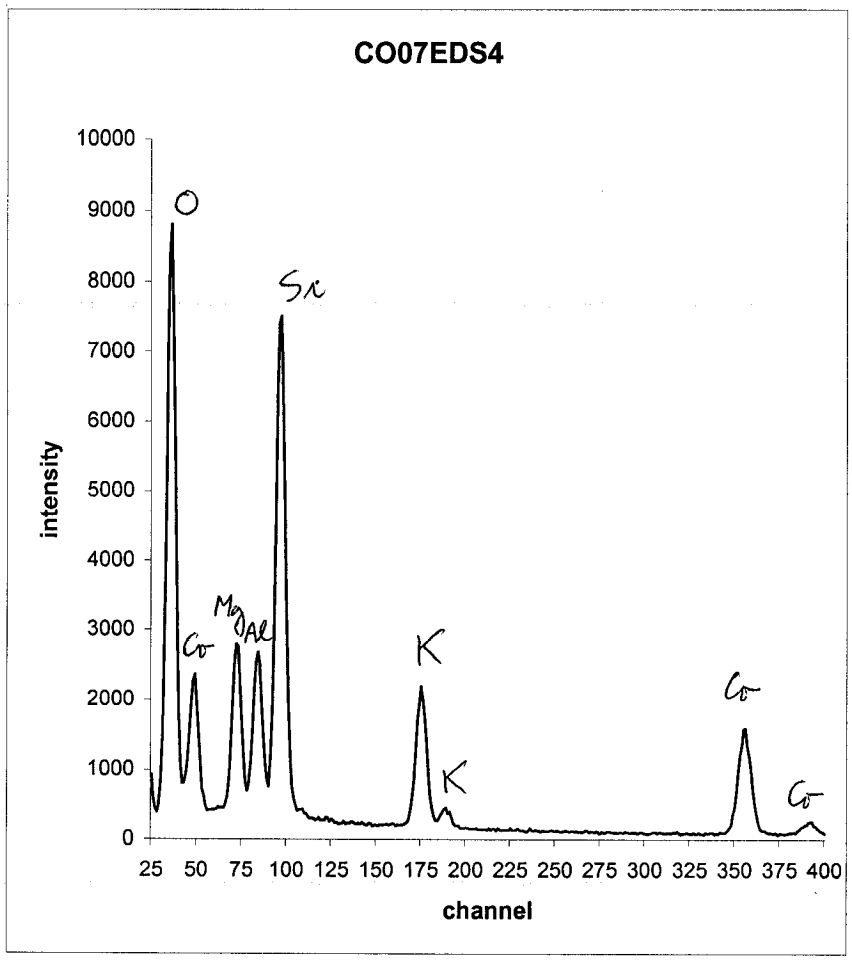
CO07EDS4
intensity
channel
10000
9000
8000
7000
6000
5000
4000
3000
2000
1000
0
25 50 75 100 125 150 175 200 225 250 275 300 325 350 375 400
O
Co
Mg
Al
Si
K
K
Co
Co

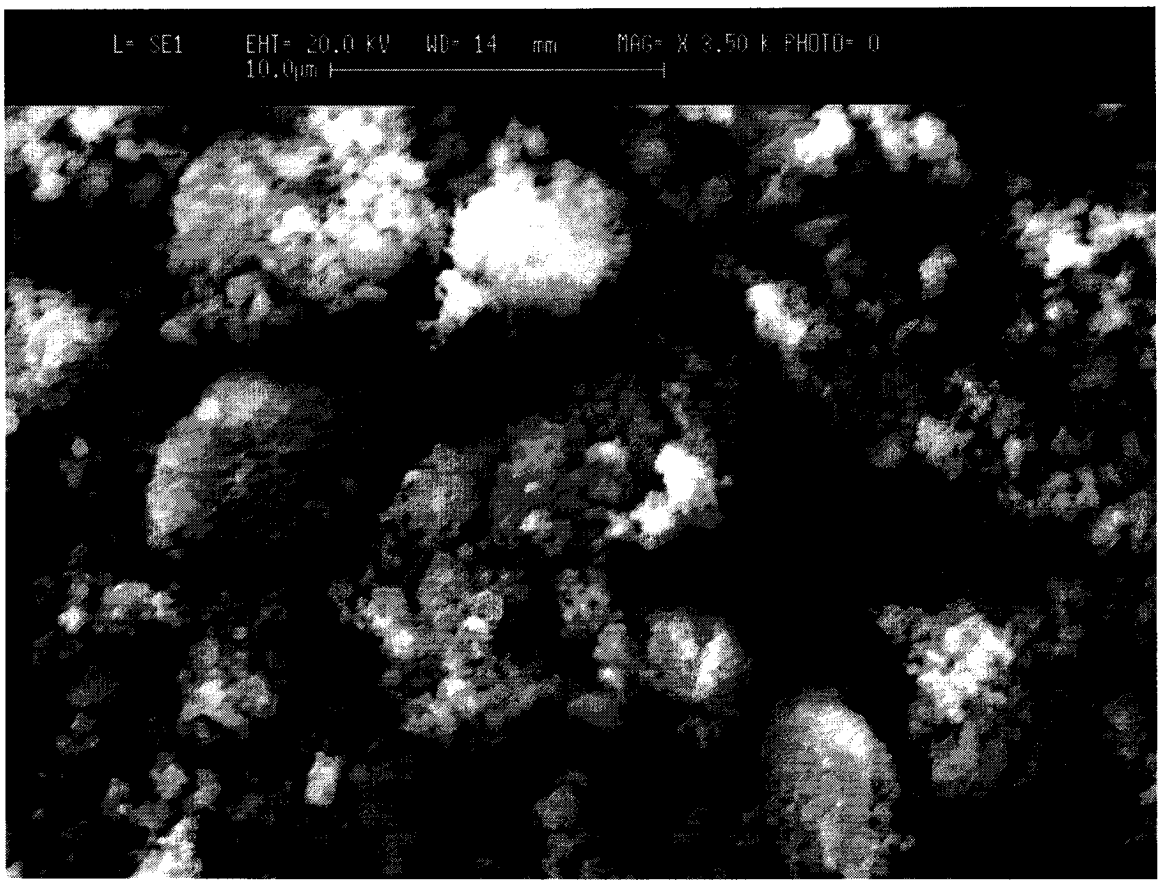

Micrograph CO07SE

$Co_{2.4}Mg_{0.6}$JLR

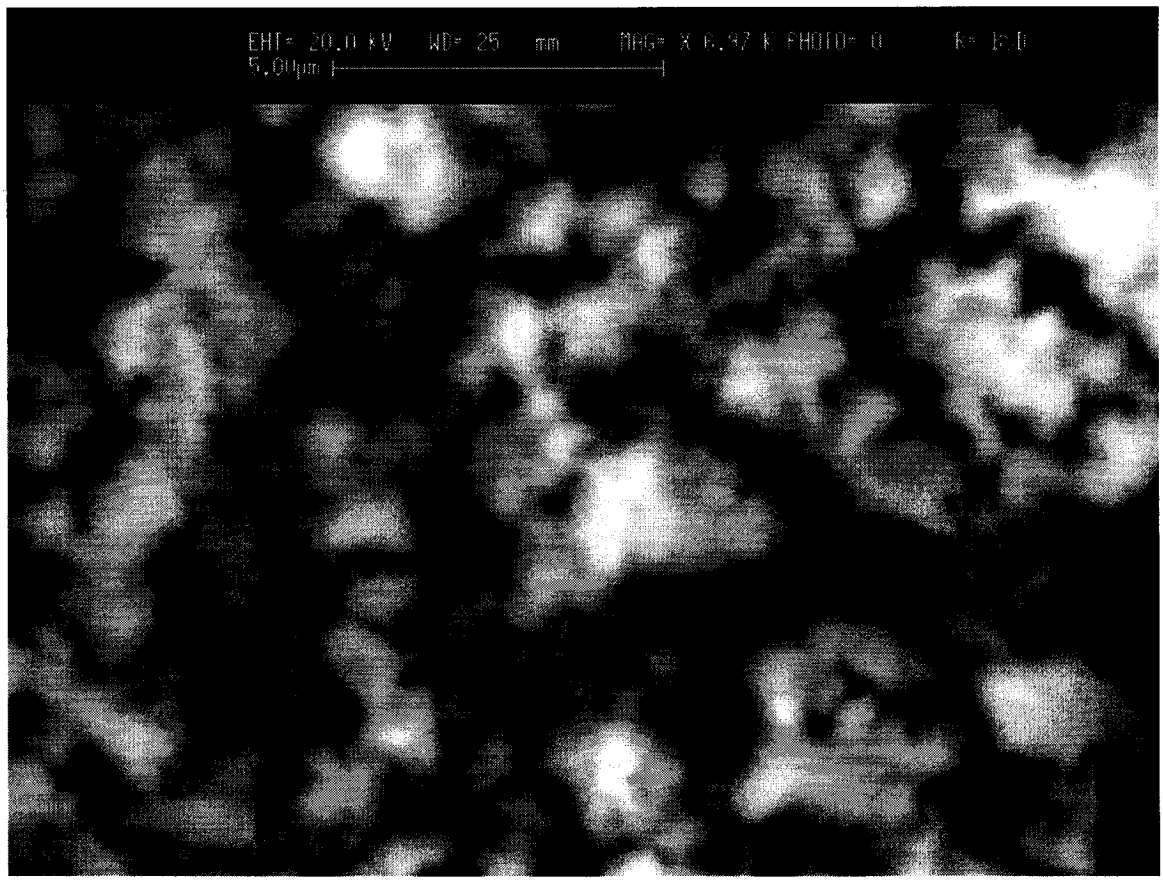

Micrograph IKO-BS1

IKO-Ann

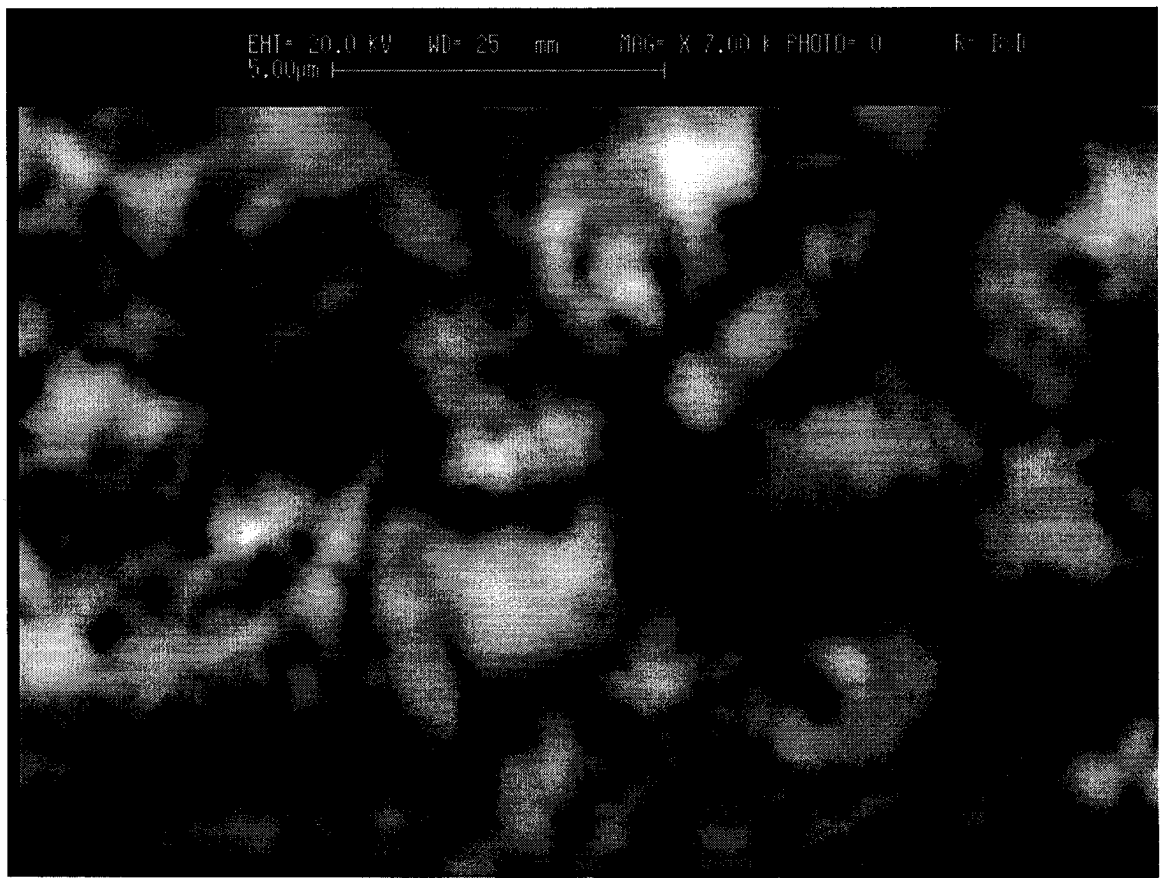

Micrograph IKO-BS2

IKO-Ann

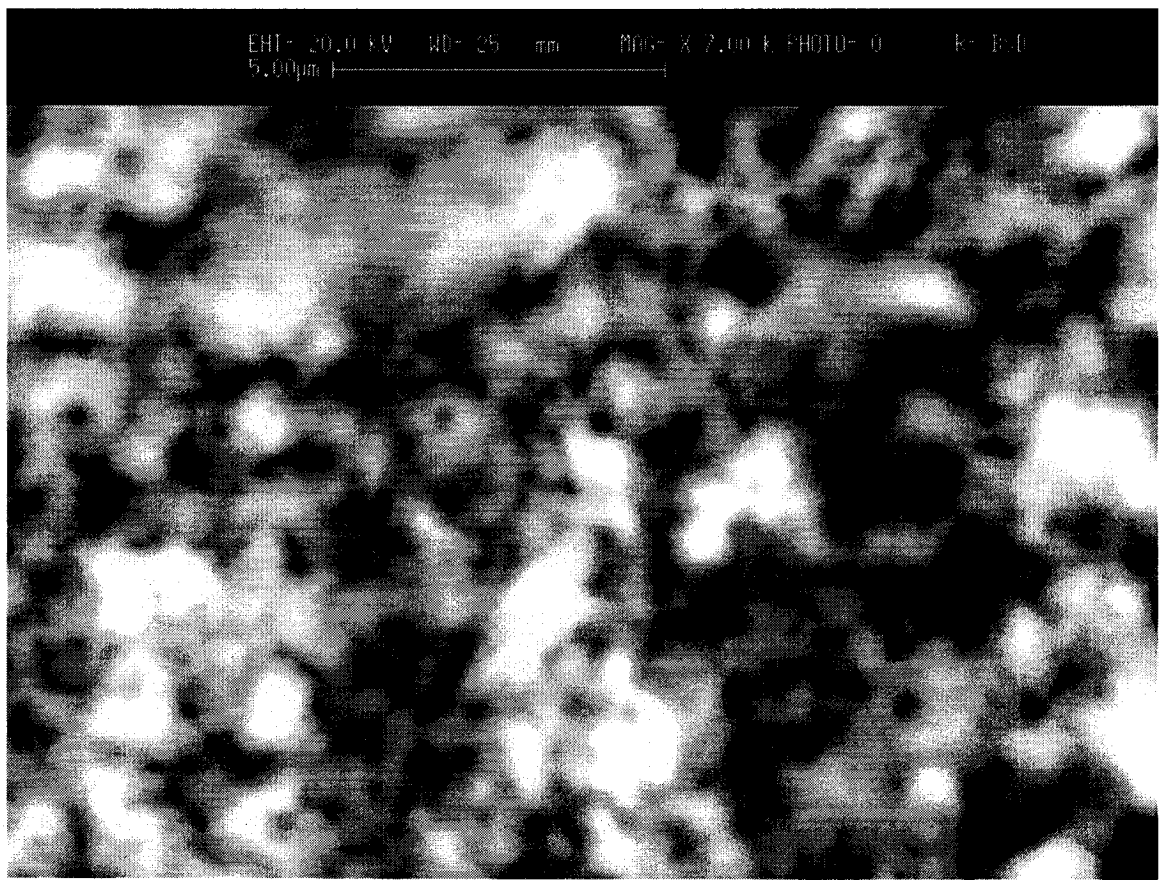

Micrograph IKO-BS3

IKO-Ann

IKOEDS1

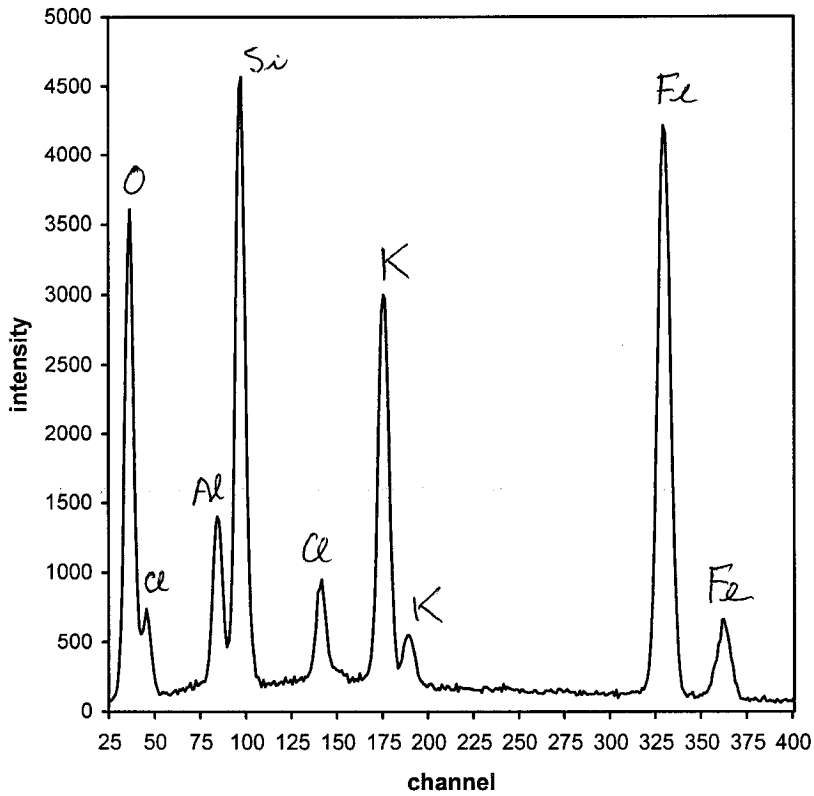
5000
4500
4000
3500
3000
2500
2000
1500
1000
500
0
intensity
O
Cl
Al
Si
Ca
K
K
Fe
Fe
25 50 75 100 125 150 175 200 225 250 275 300 325 350 375 400
channel

IKOEDS2

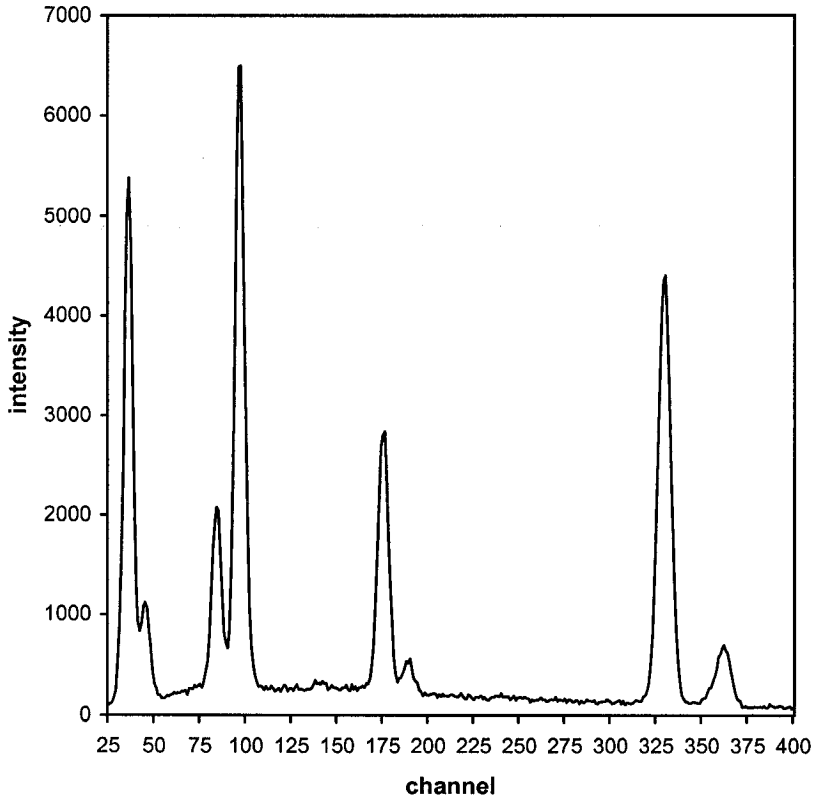
7000
6000
5000
4000
3000
2000
1000
0
intensity
25 50 75 100 125 150 175 200 225 250 275 300 325 350 375 400
channel

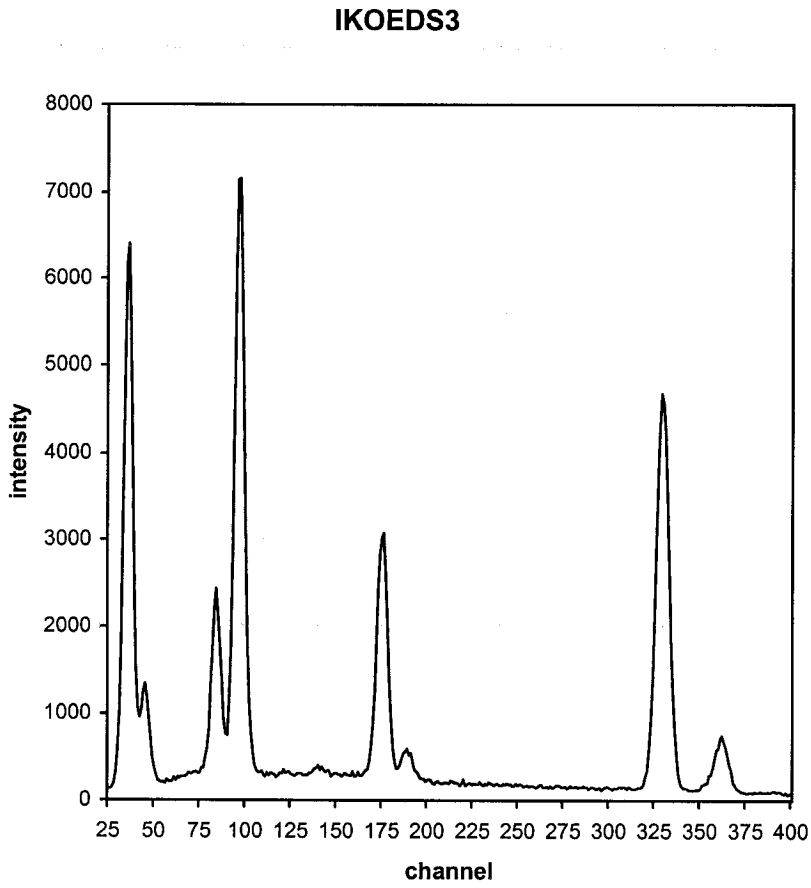
IKOEDS3
8000
7000
6000
5000
4000
3000
2000
1000
0
intensity
25 50 75 100 125 150 175 200 225 250 275 300 325 350 375 400
channel

Appendix D. Photomicrographs obtained by optical microscopy

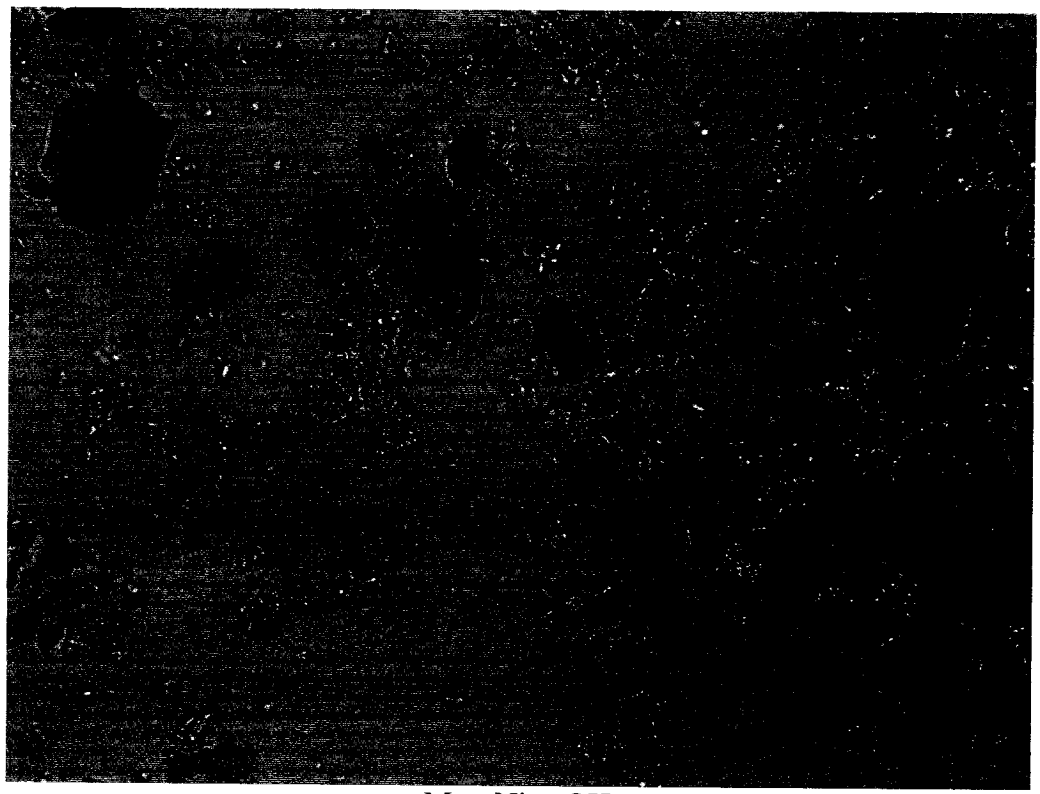

$Mg_{0.0}Ni_{3.0}$-OH

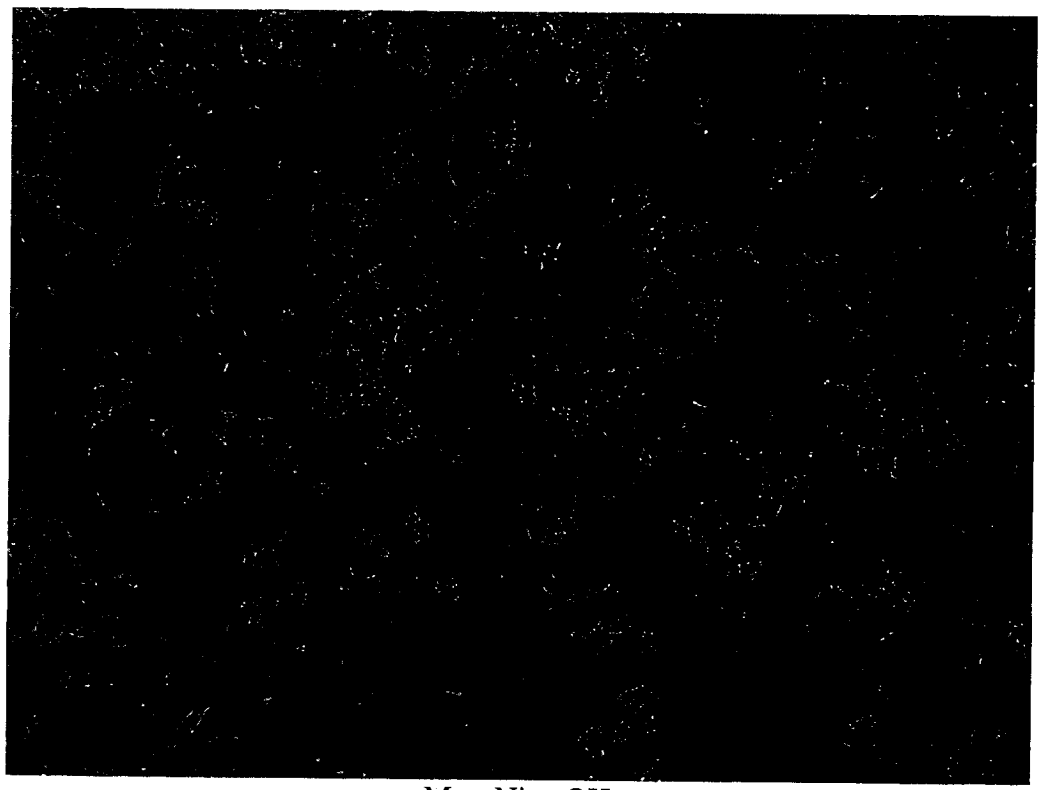

$Mg_{0.0}Ni_{3.0}$-OH

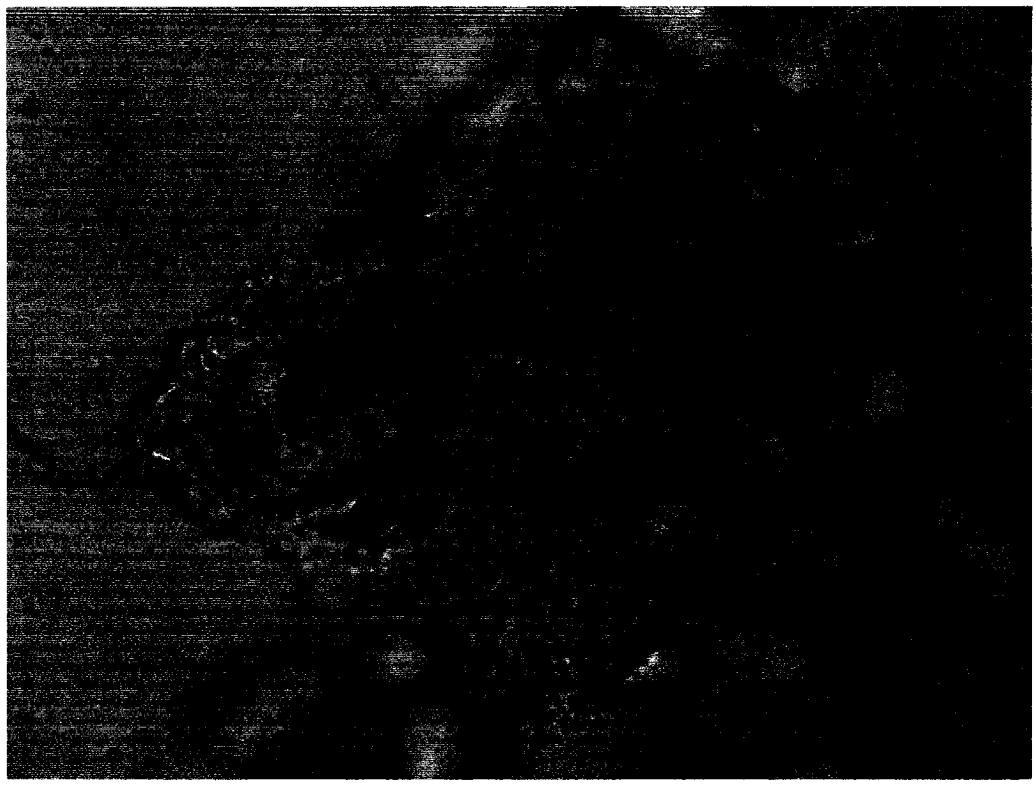

$Mg_{0.0}Ni_{3.0}$-OH

$Mg_{0.0}Ni_{3.0}$-OH

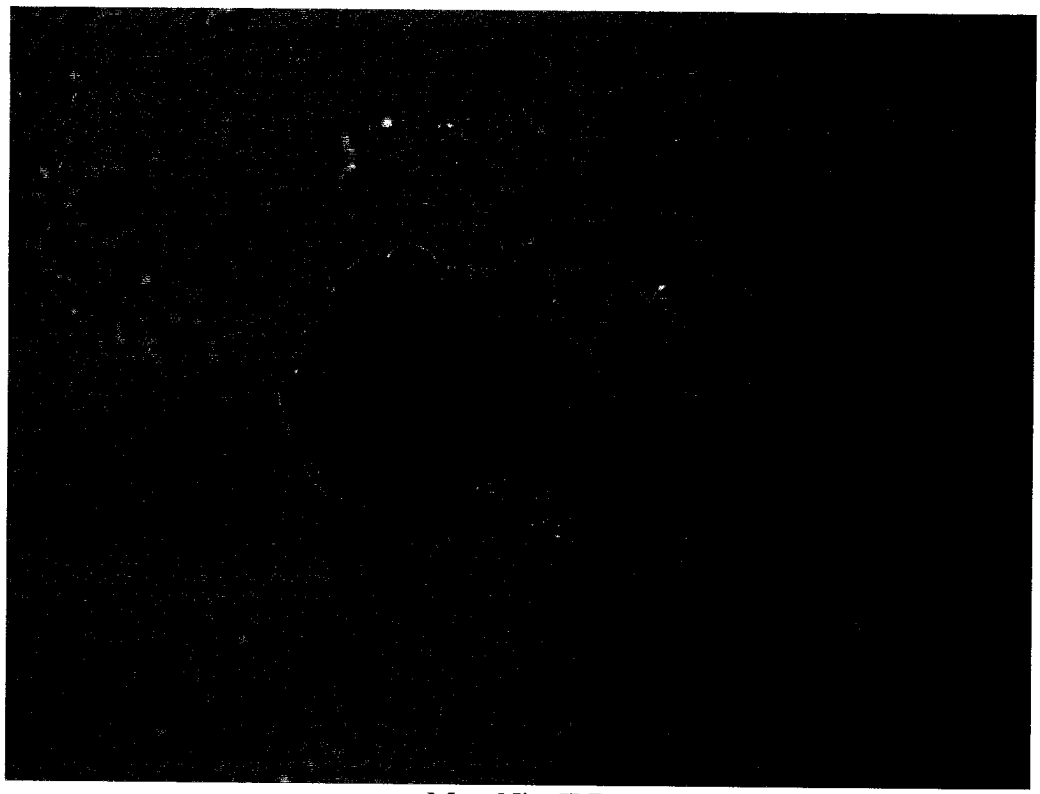

$Mg_{1.5}Ni_{1.5}JLR$

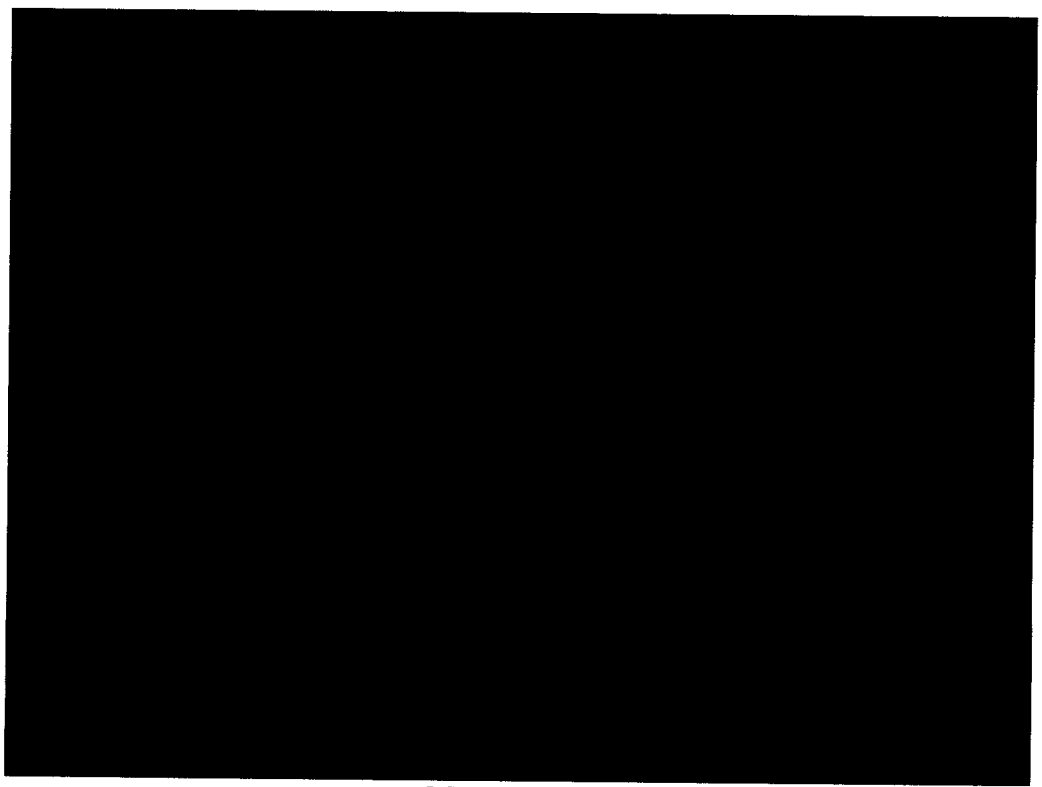

$Mg_{1.5}Ni_{1.5}JLR$

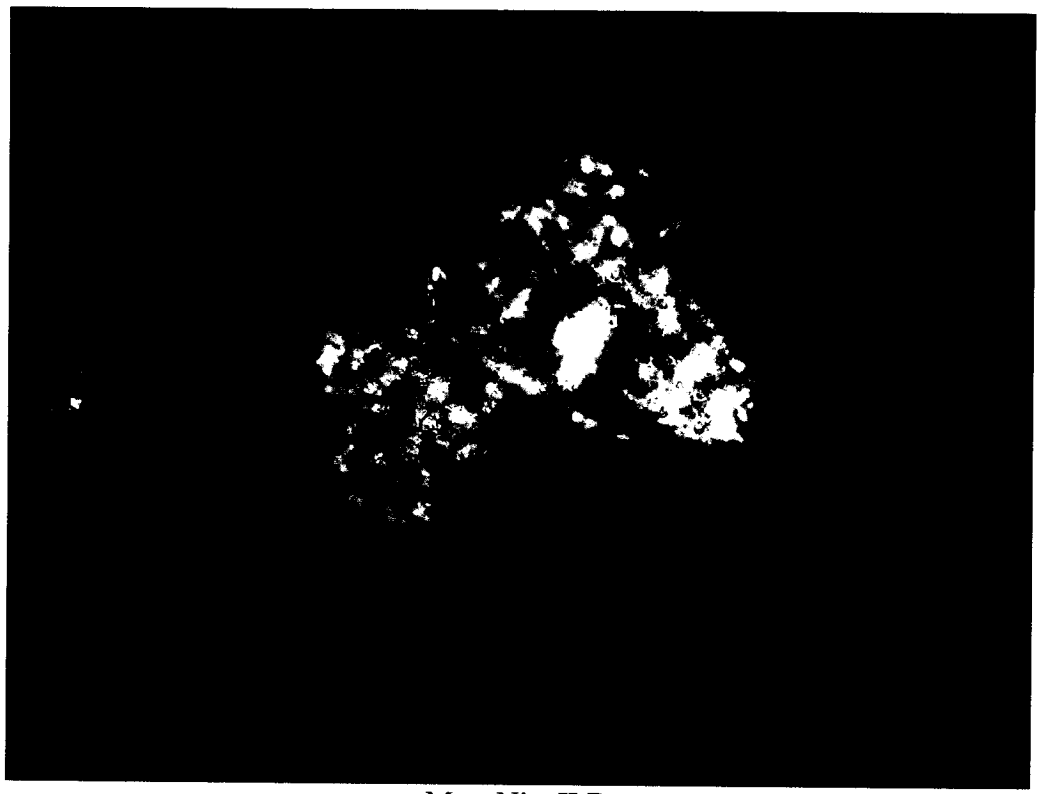

$Mg_{1.5}Ni_{1.5}JLR$

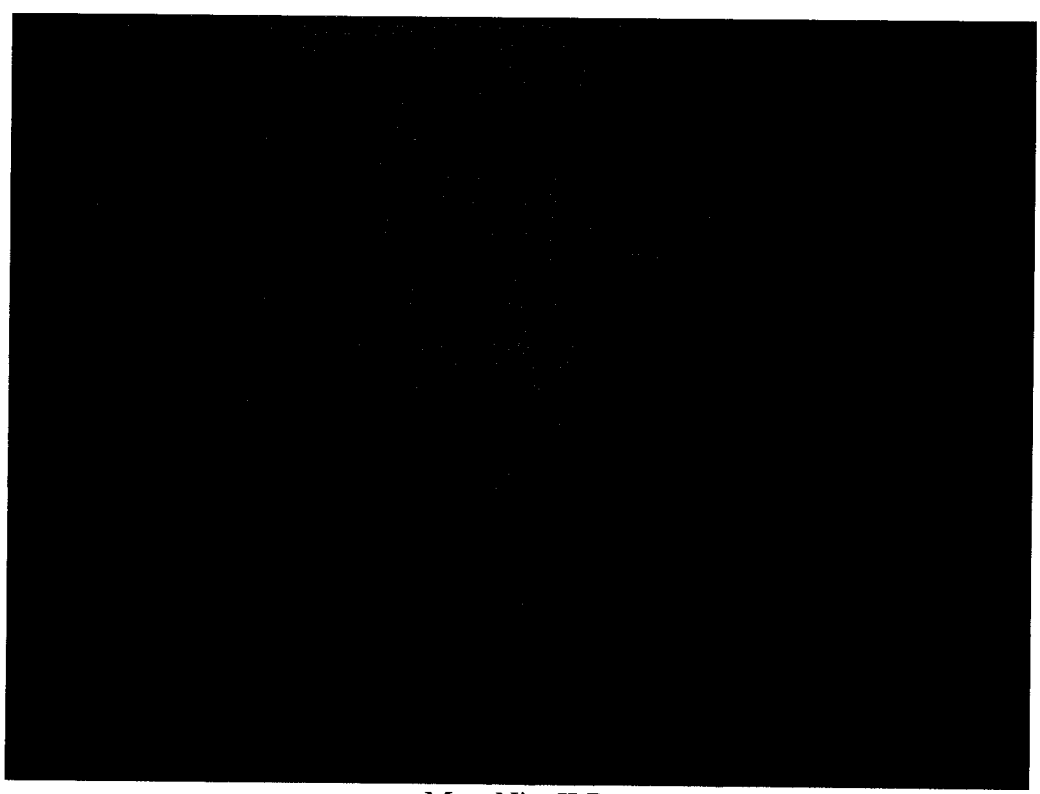

$Mg_{1.5}Ni_{1.5}JLR$

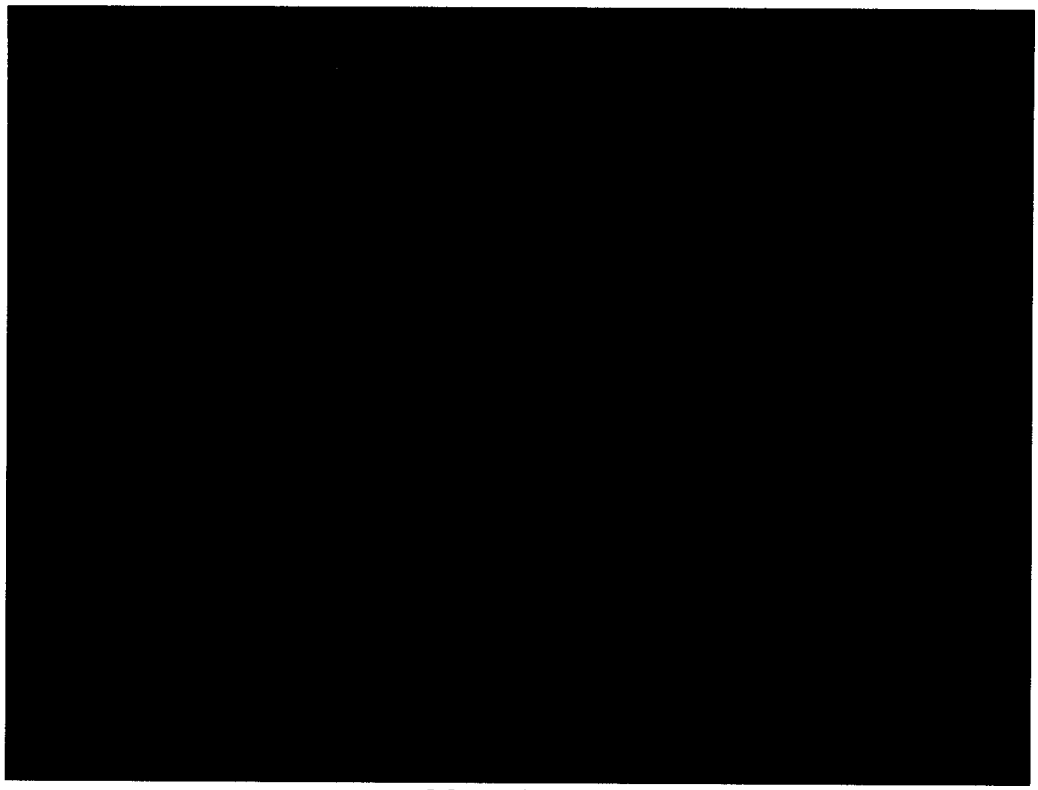

$Mg_{1.5}Ni_{1.5}JLR$

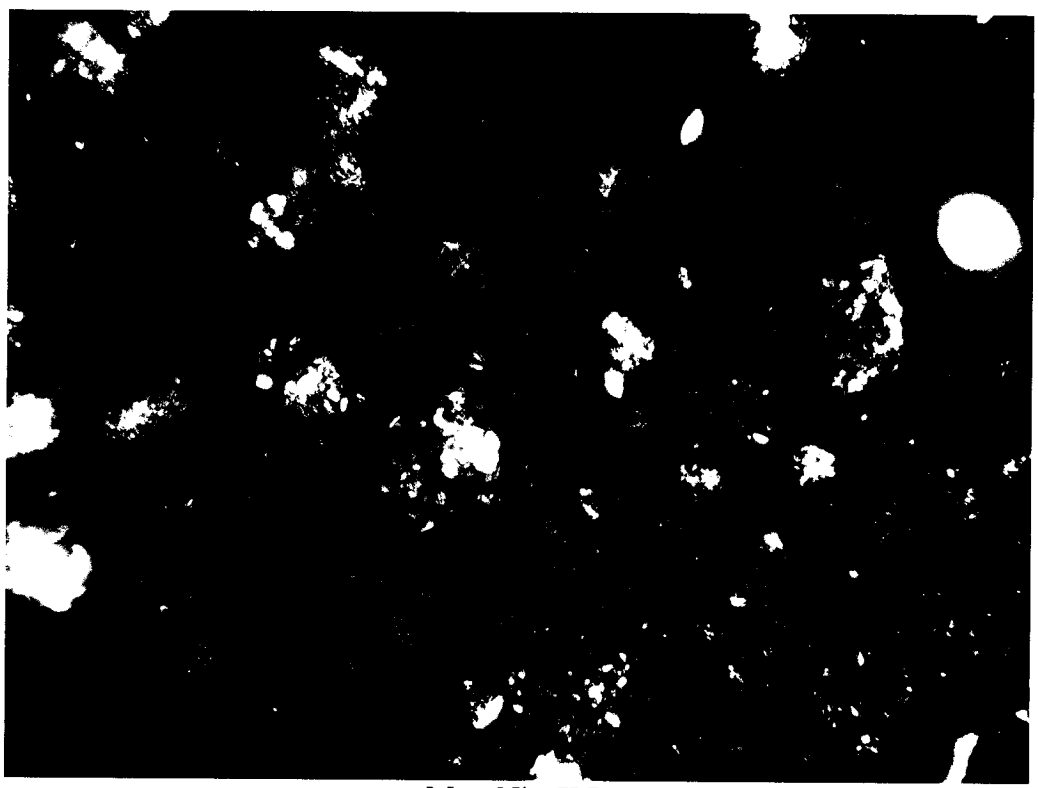

$Mg_{1.5}Ni_{1.5}JLR$

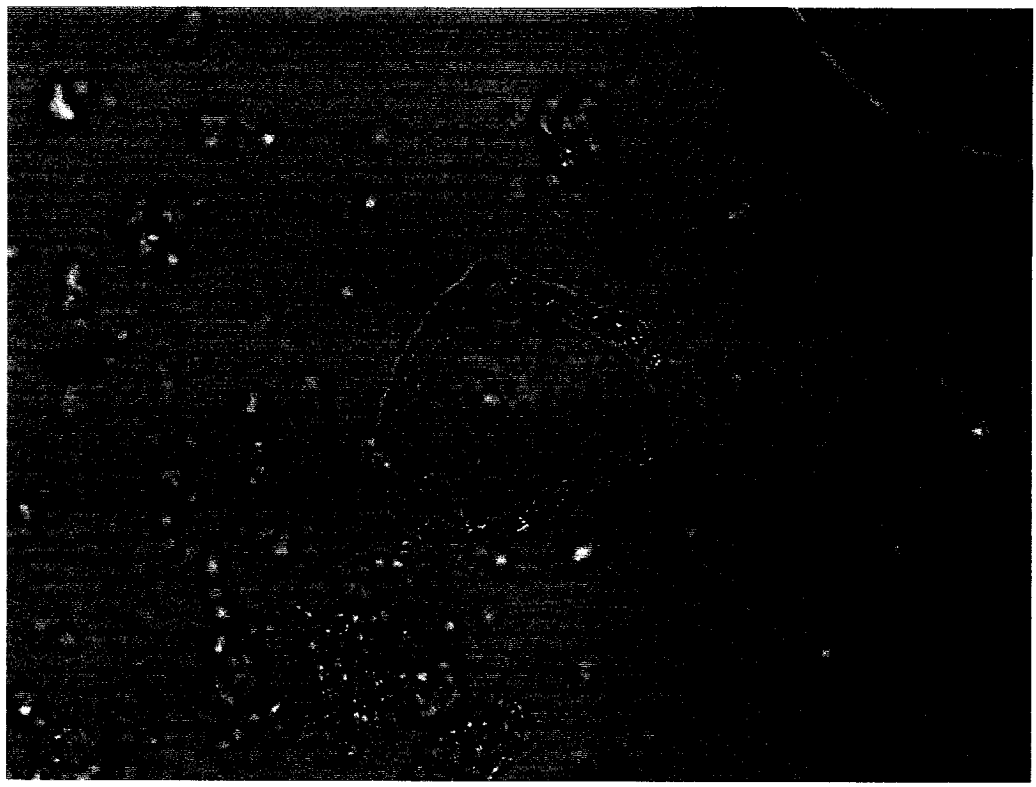

$Mg_{1.5}Ni_{1.5}JLR$

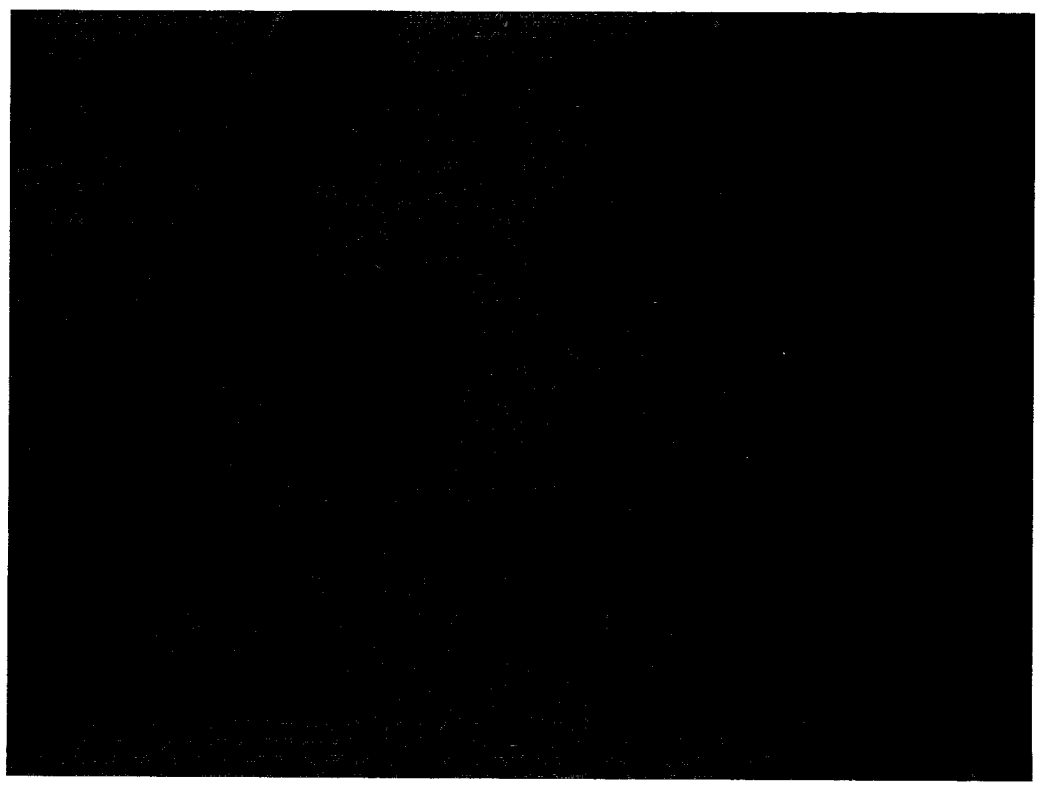

$Mg_{2.4}Ni_{0.6}JLR$

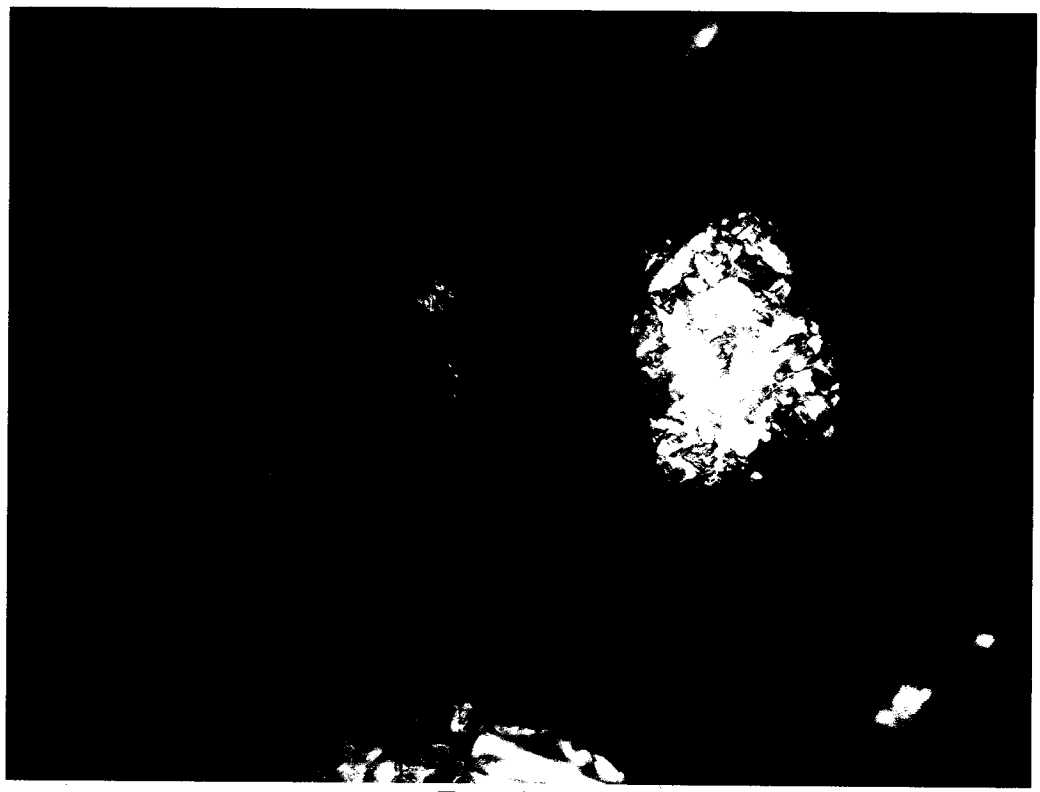

$Fe_{0.0}Ni_{3.0}GR$

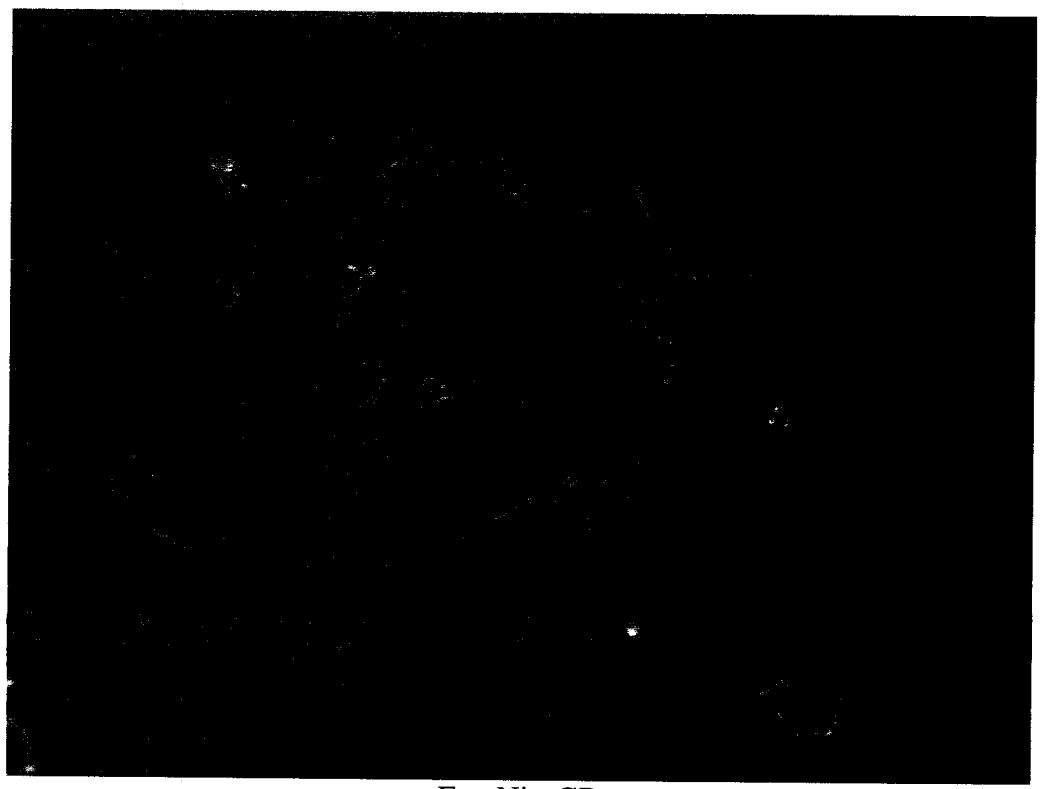

$Fe_{0.0}Ni_{3.0}GR$

$Fe_{0.0}Ni_{3.0}GR$

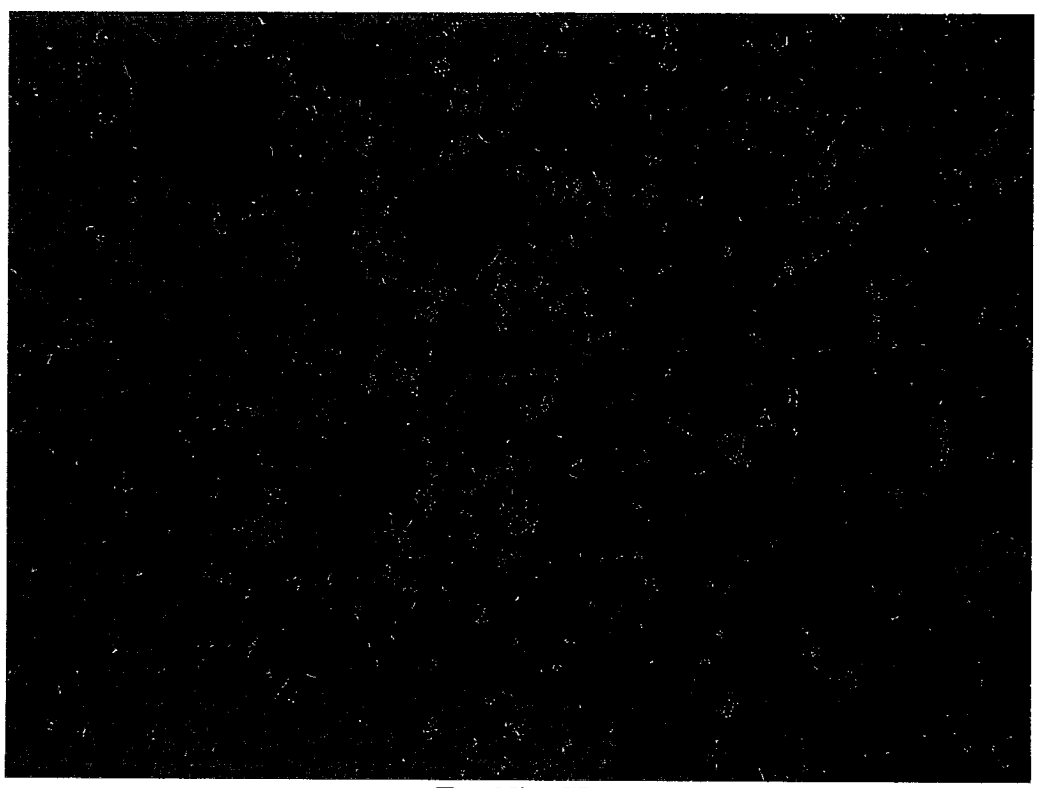

$Fe_{0.0}Ni_{3.0}GR$

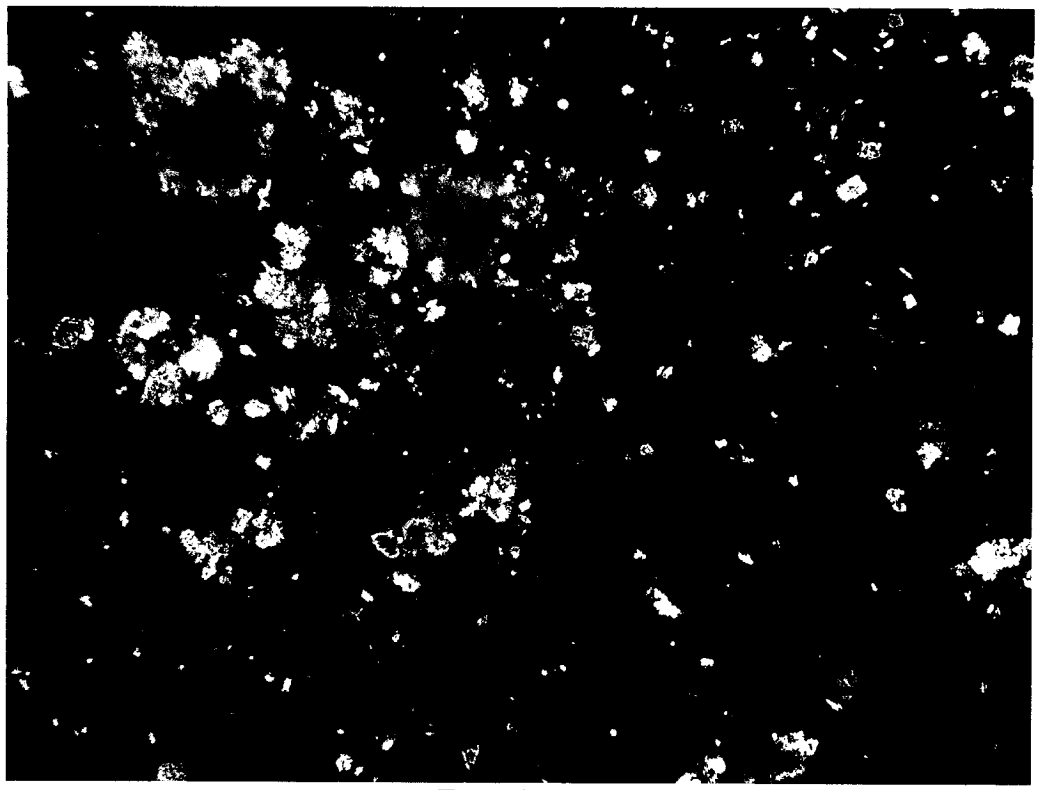

$Fe_{0.0}Ni_{3.0}GR$

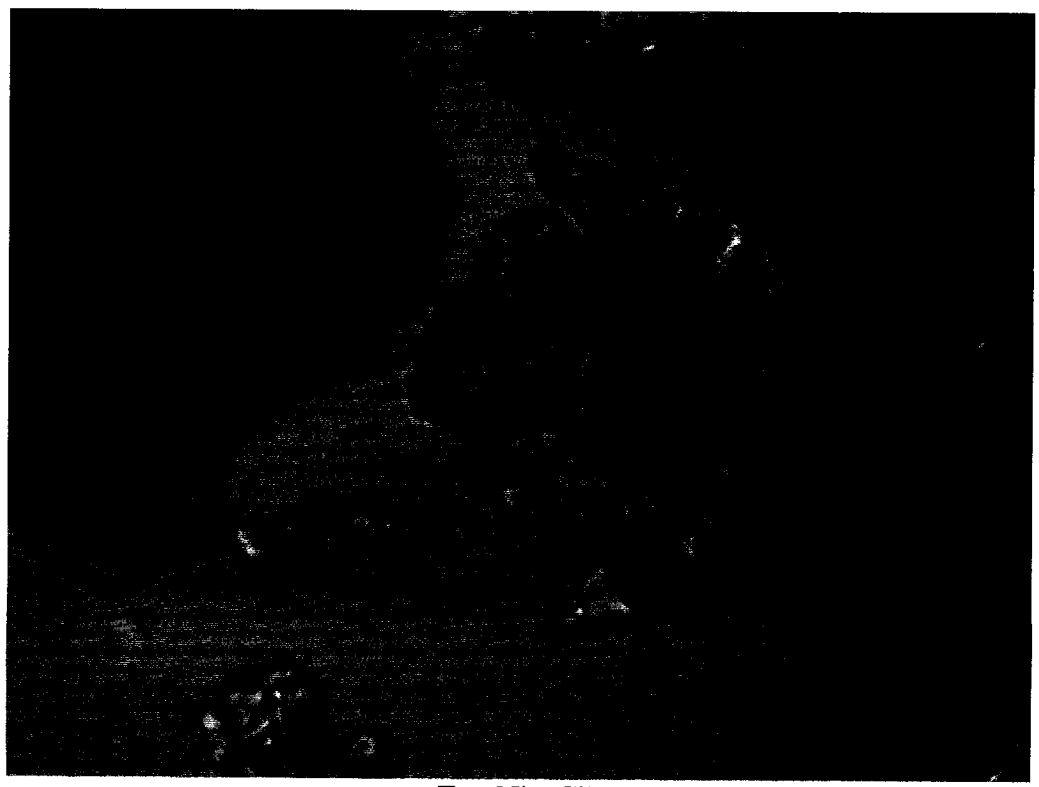

$Fe_{0.0}Ni_{3.0}GR$

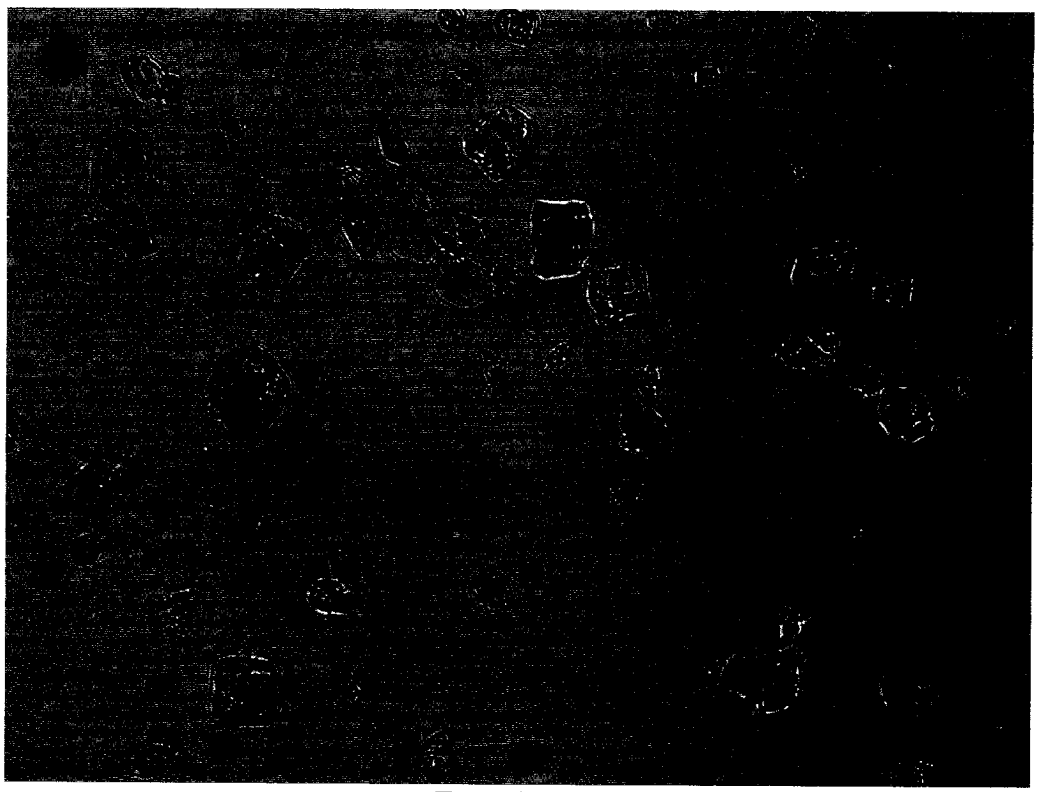

$Fe_{0.0}Ni_{3.0}GR$

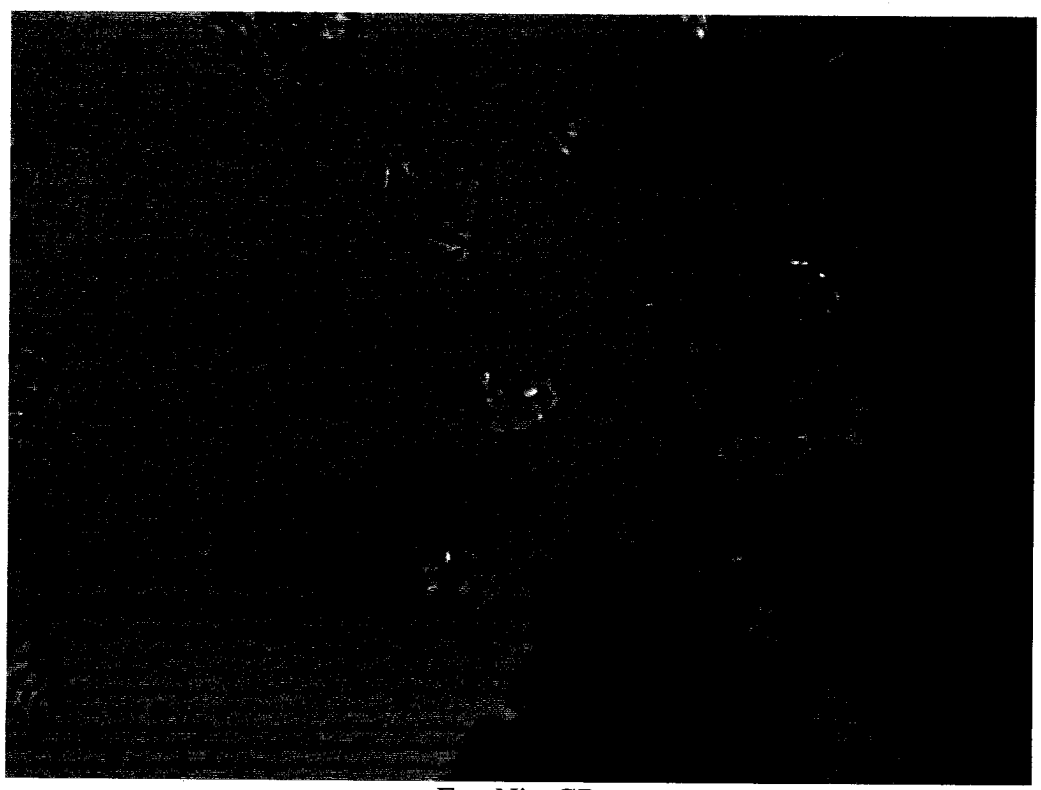

$Fe_{0.0}Ni_{3.0}GR$

Appendix E. Chromatograms collected by gas chromatography

IKO-Ann Run	Filename	Mass (mg)	N (%)	C (%)	H (%)	S (%)
	bbot042	0.303	6.51	72.53	6.09	7.44
	bbot043	0.516	6.51	72.53	6.09	7.44
	bbot044	0.208	6.51	72.53	6.09	7.44
	bbot045	0.854	6.51	72.53	6.09	7.44
	bbot046	0.925	6.51	72.53	6.09	7.44
	sul229	1.337	16.27	41.84	4.68	18.62
	sul230	0.638	16.27	41.84	4.68	18.62
	sul231	0.327	16.27	41.84	4.68	18.62
	sul232	0.569	16.27	41.84	4.68	18.62
	sul233	0.71	16.27	41.84	4.68	18.62
	iko01	4.947				
	iko02	5.164				
	iko03	0.195				
	iko04	0.260				
	iko05	0.813				
	iko06	0.964				
	iko07	0.268				
	iko08	0.237				
	iko09	1.321				
	iko10	0.527				
	blk098					
	blk099					
	blk100					
	blk101					
	blk102					
	blk103					
	blk104					
	vo001					
	vo002					
	vo003					
	vo004					

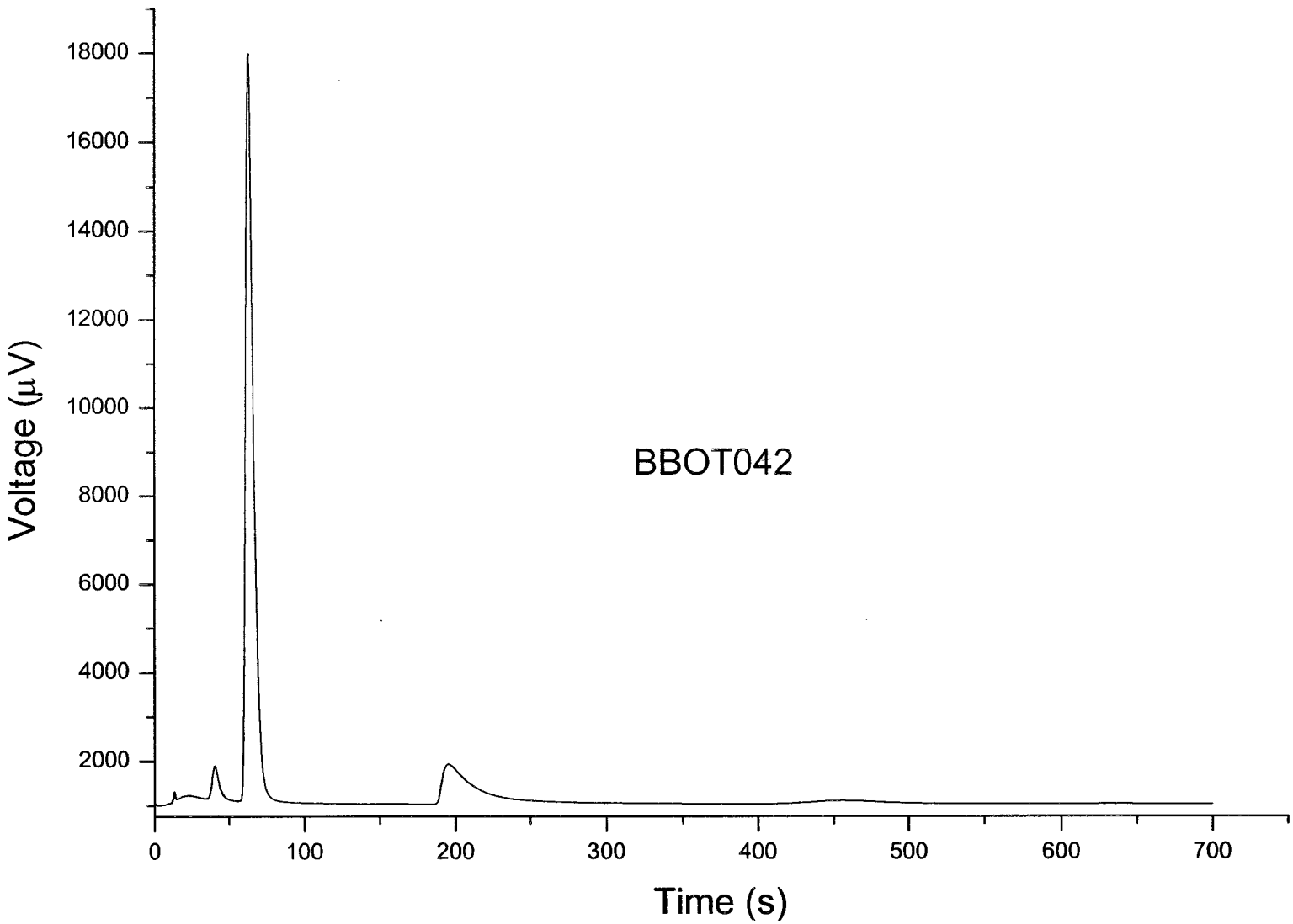
BBOT042
Voltage (μV)
18000
16000
14000
12000
10000
8000
6000
4000
2000
0
100
200
300
400
500
600
700
Time (s)

E2

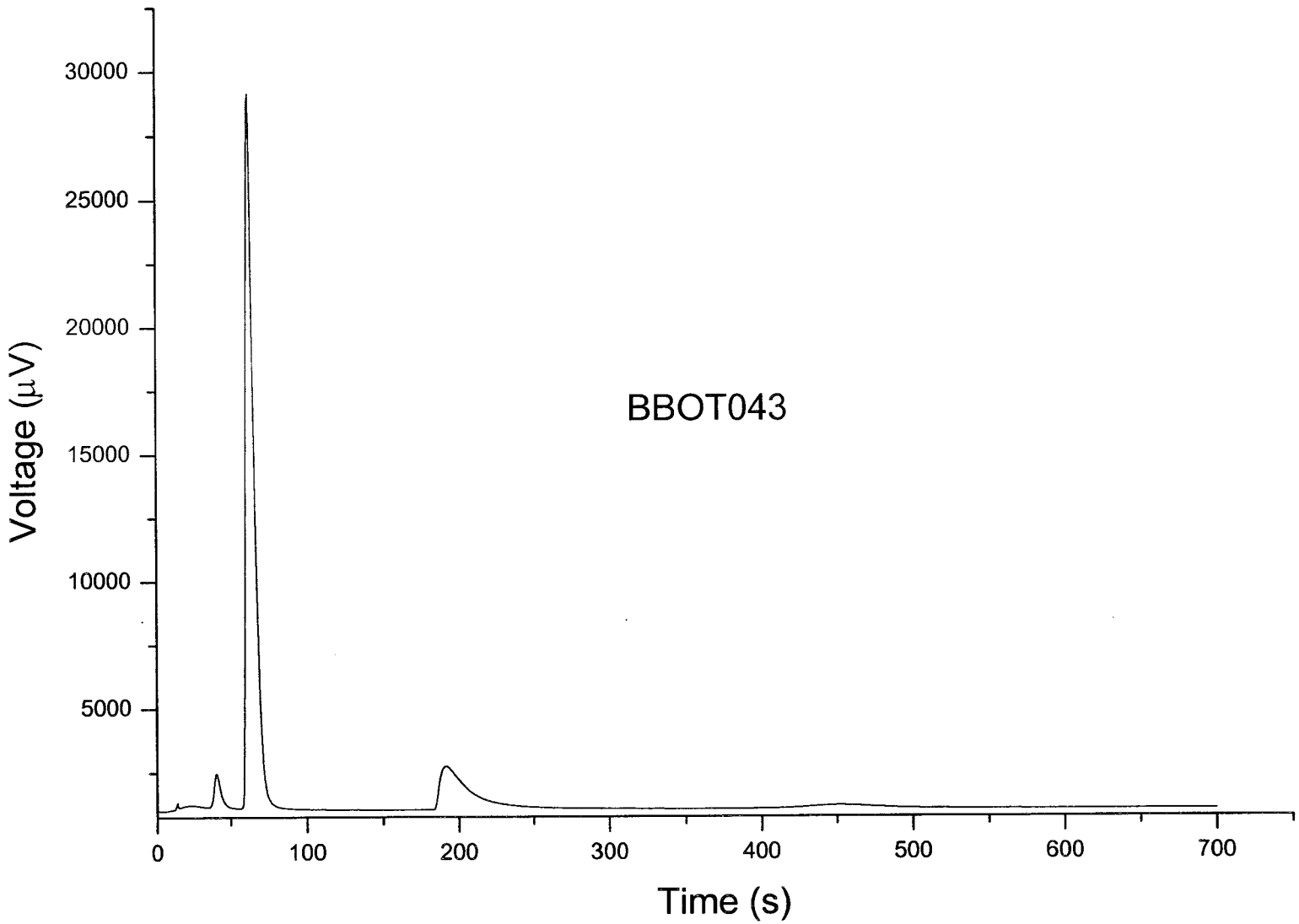
BBOT043
Voltage (μV)
30000
25000
20000
15000
10000
5000
0
100
200
300
400
500
600
700
Time (s)

E3

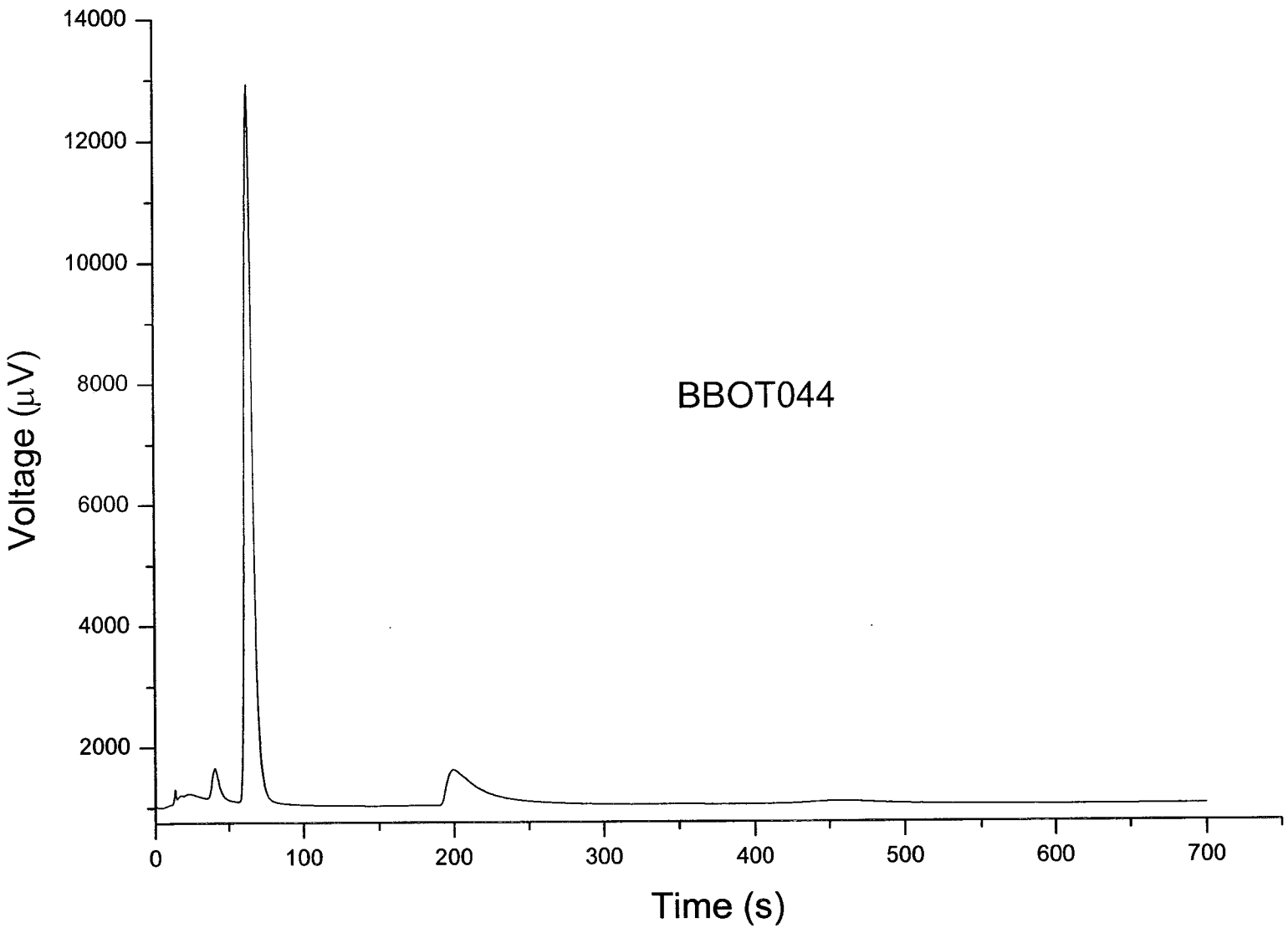
14000
12000
10000
8000
6000
4000
2000
Voltage (μV)
BBOT044
0
100
200
300
400
500
600
700
Time (s)

E4

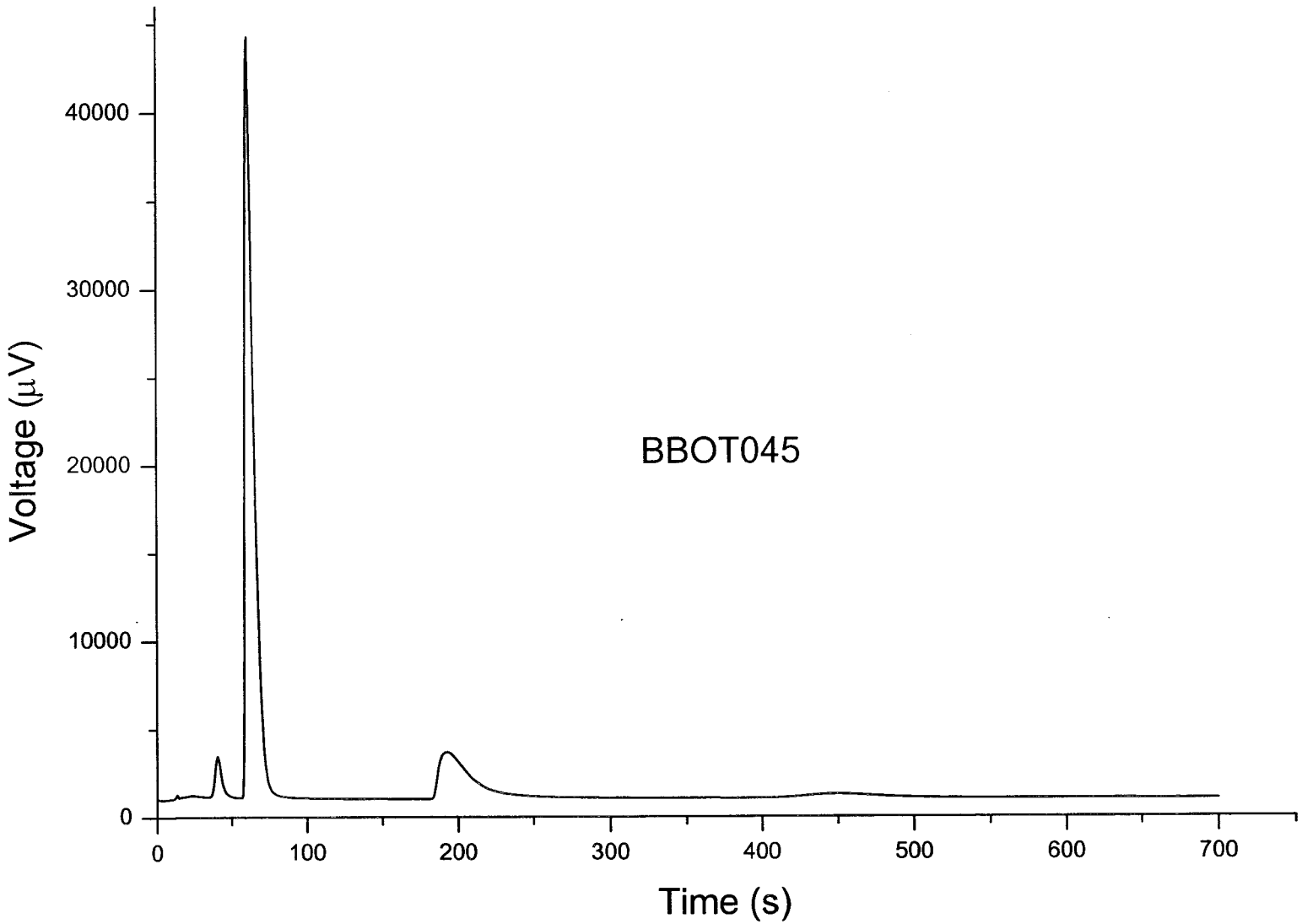
BBOT045
Voltage (μV)
40000
30000
20000
10000
0
0
100
200
300
400
500
600
700
Time (s)

E5

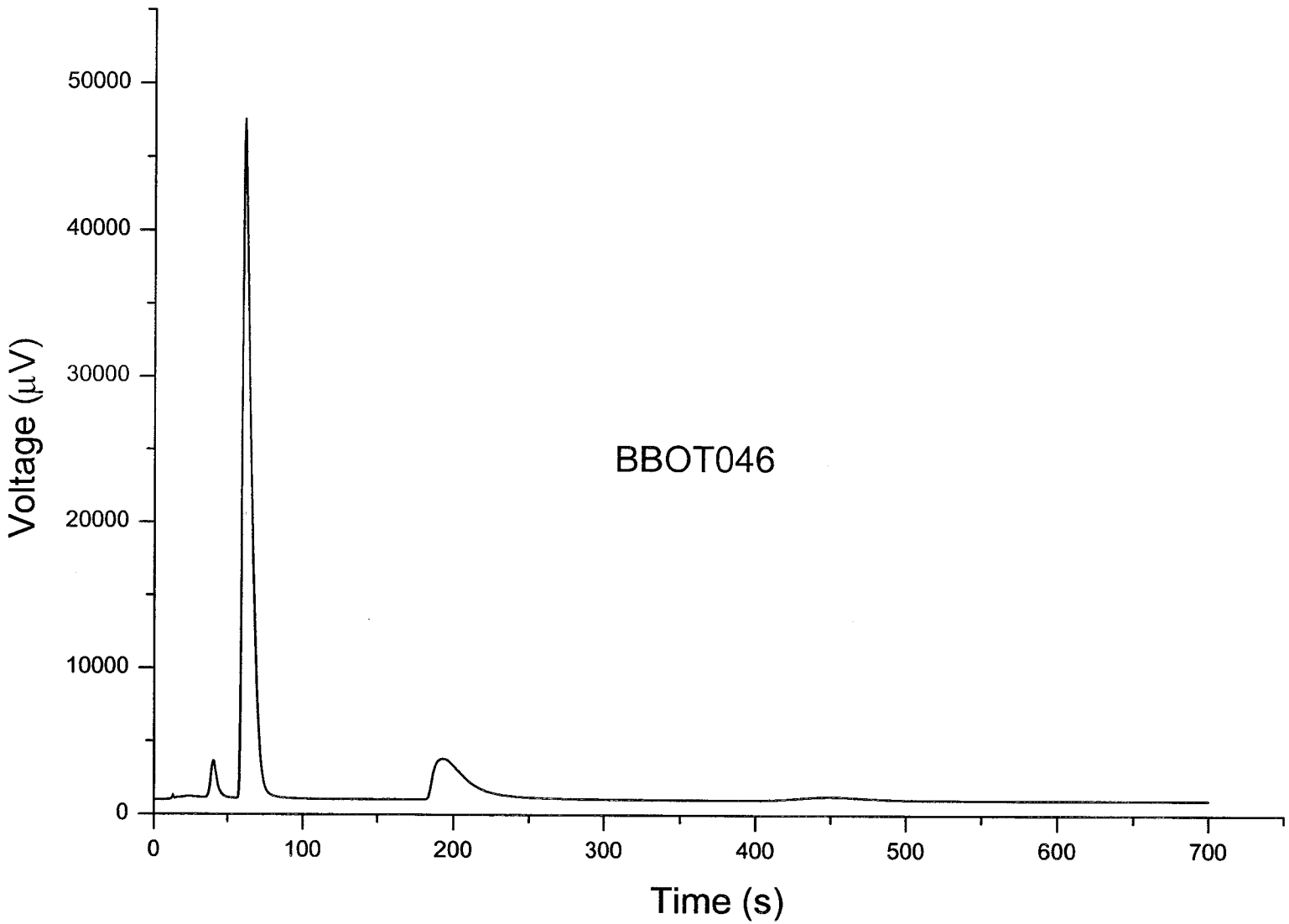
BBOT046
Voltage (μV)
50000
40000
30000
20000
10000
0
0
100
200
300
400
500
600
700
Time (s)

E7

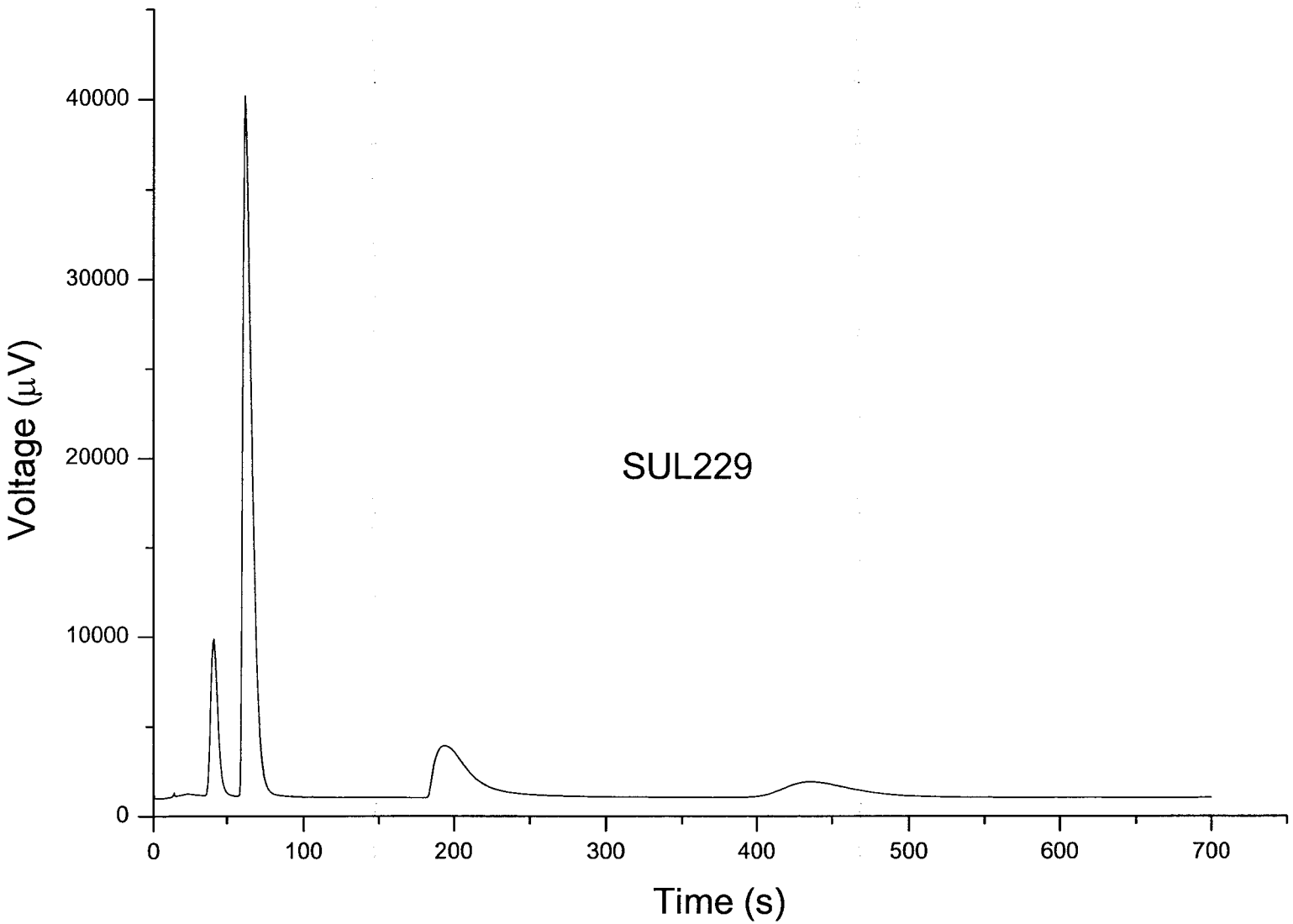
SUL229
Voltage (μV)
40000
30000
20000
10000
0
0
100
200
300
400
500
600
700
Time (s)

E8

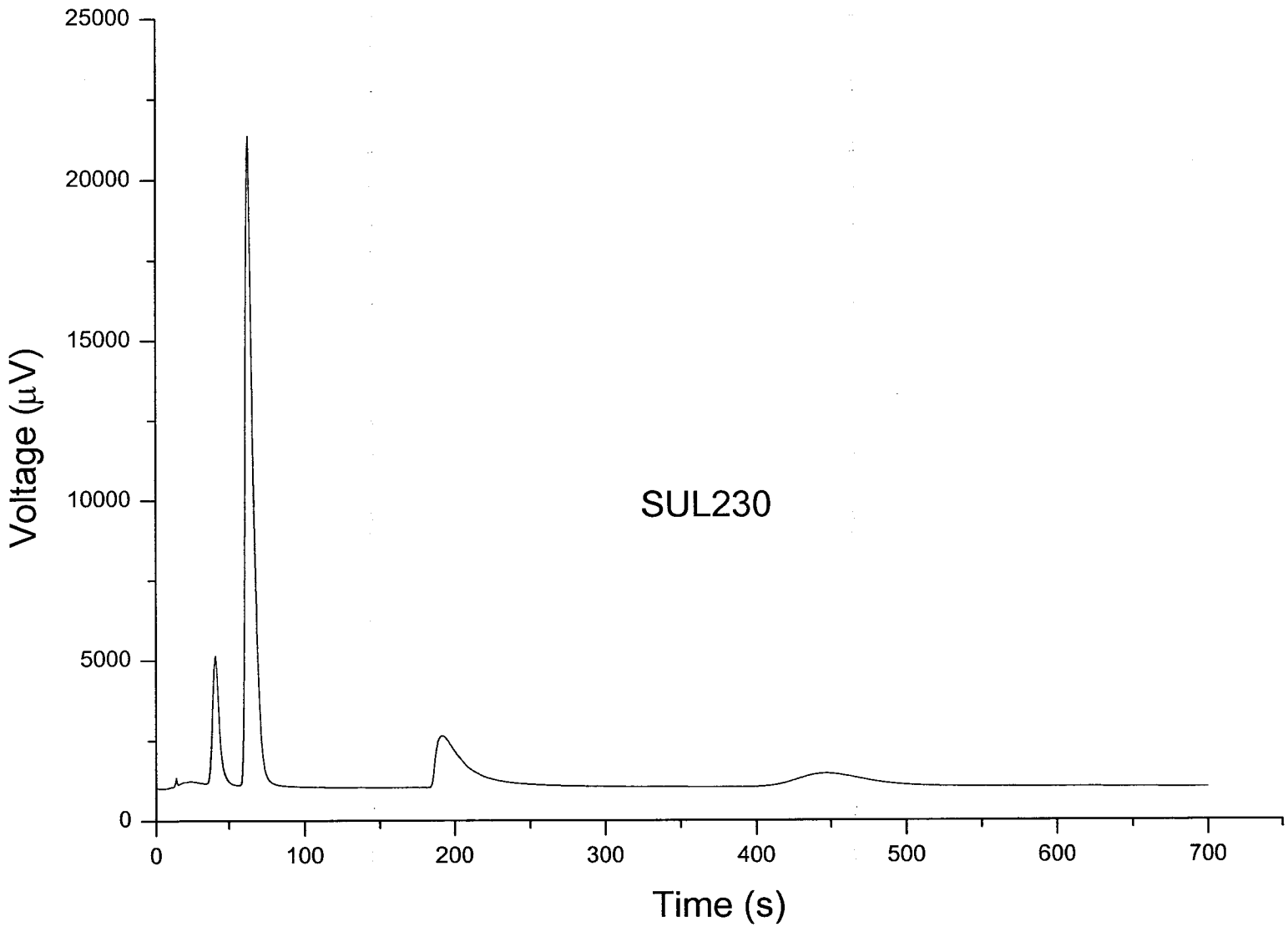
25000
20000
15000
10000
5000
0
Voltage (μV)
SUL230
0
100
200
300
400
500
600
700
Time (s)

E9

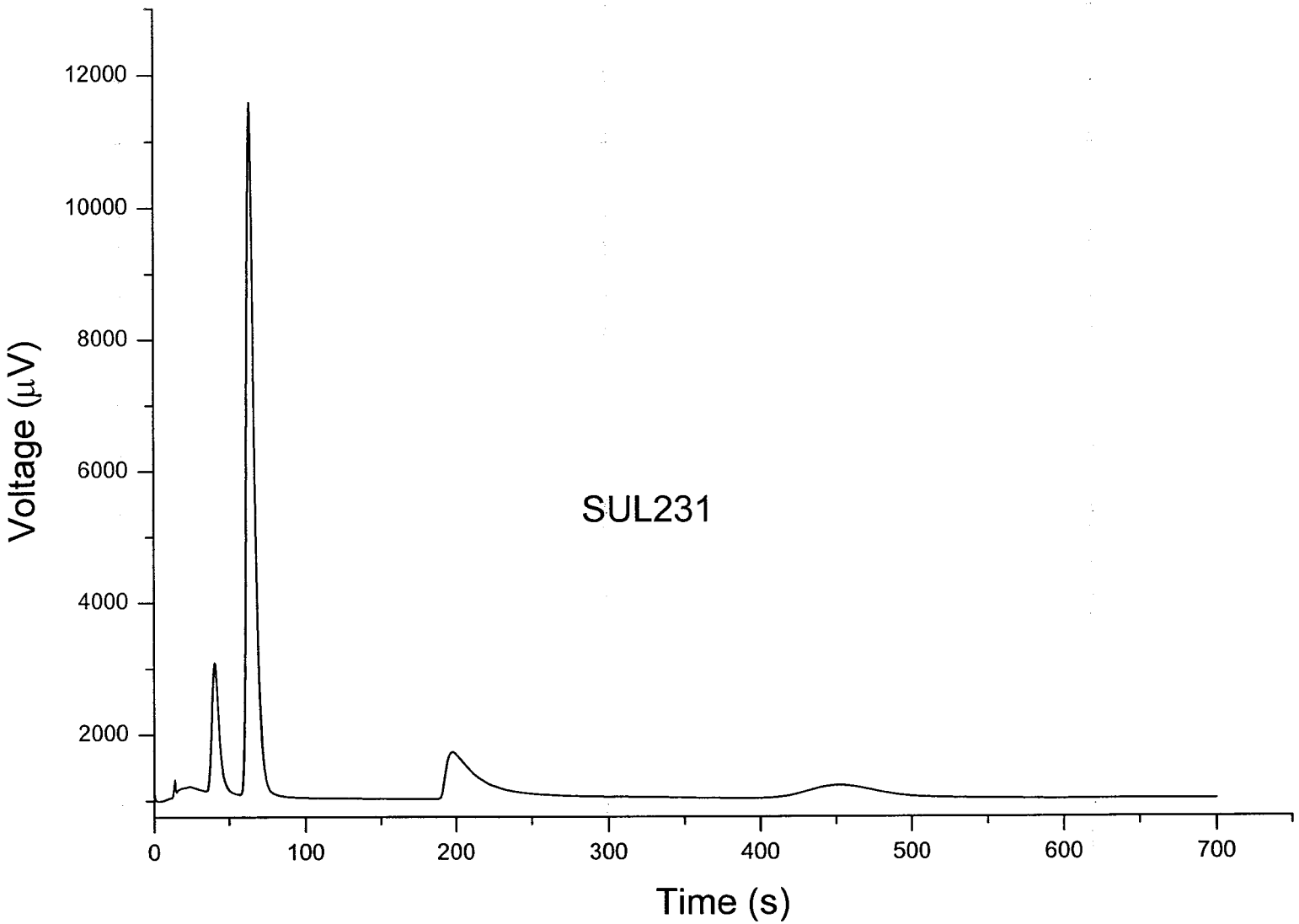
12000
10000
8000
6000
4000
2000
Voltage (μV)
SUL231
0
100
200
300
400
500
600
700
Time (s)

E10

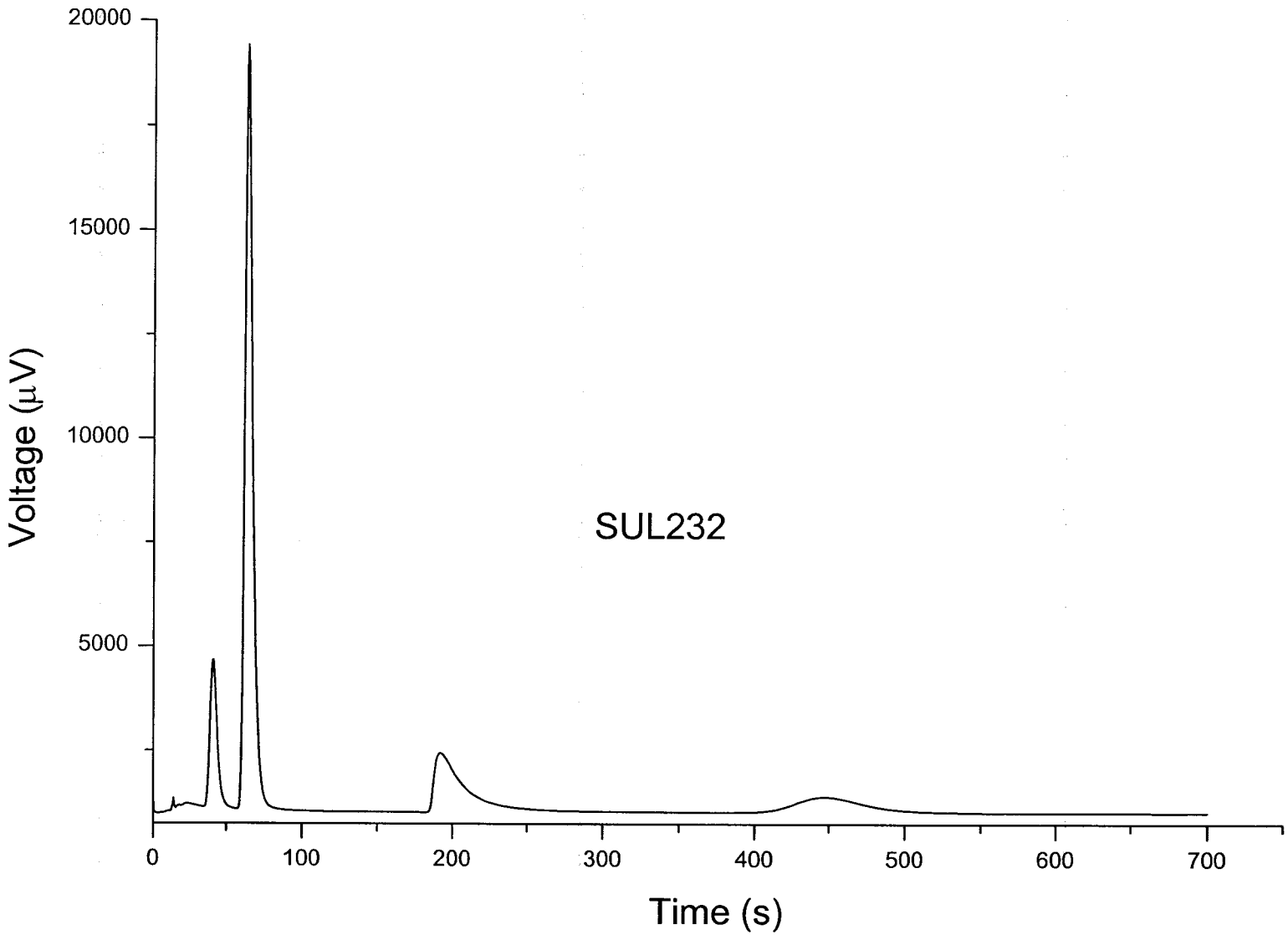
20000
15000
10000
5000
Voltage (μV)
SUL232
0
100
200
300
400
500
600
700
Time (s)

E11

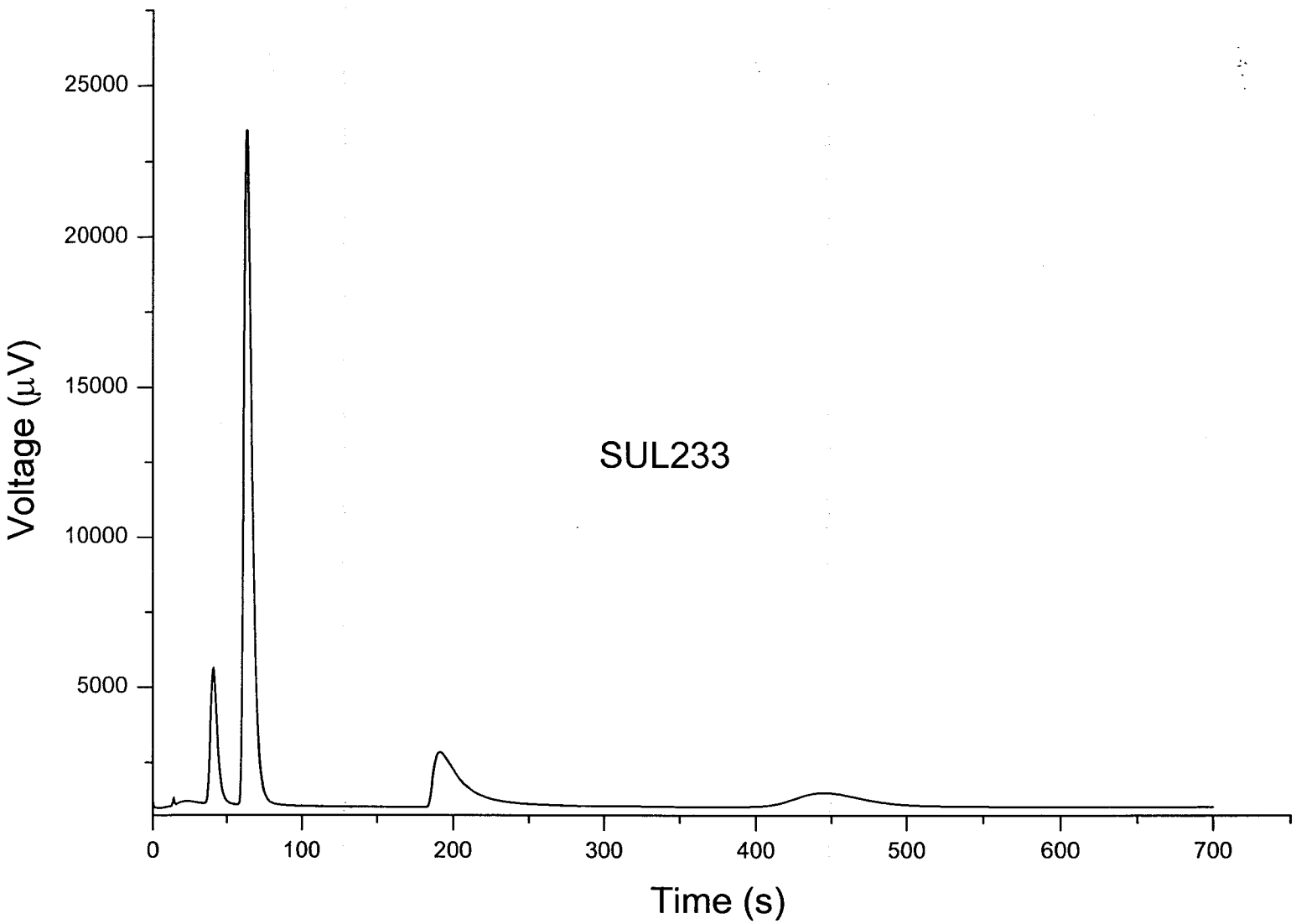
SUL233
Voltage (μV)
25000
20000
15000
10000
5000
0
100
200
300
400
500
600
700
Time (s)

E12

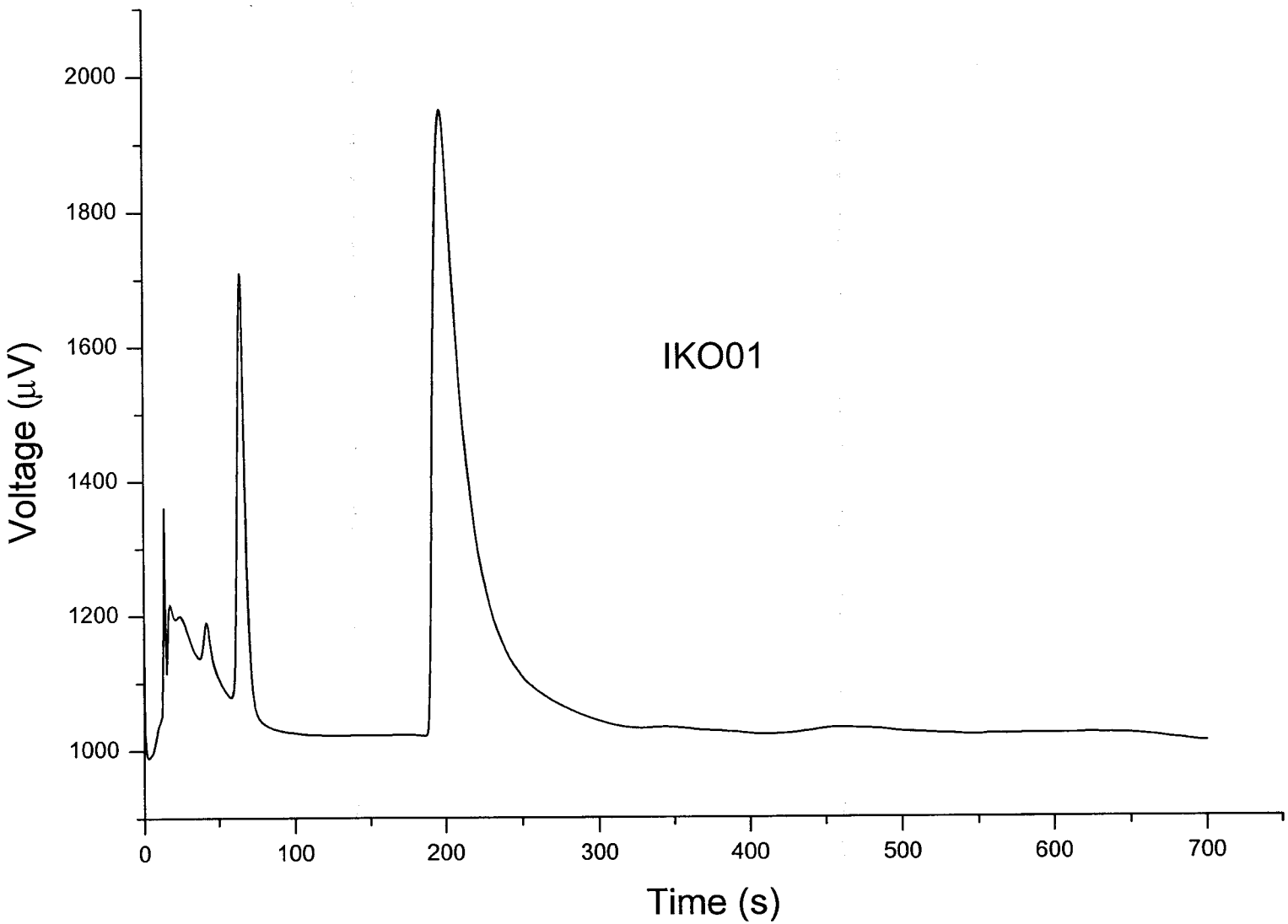
IKO01
Voltage (μV)
2000
1800
1600
1400
1200
1000
0
100
200
300
400
500
600
700
Time (s)

E13

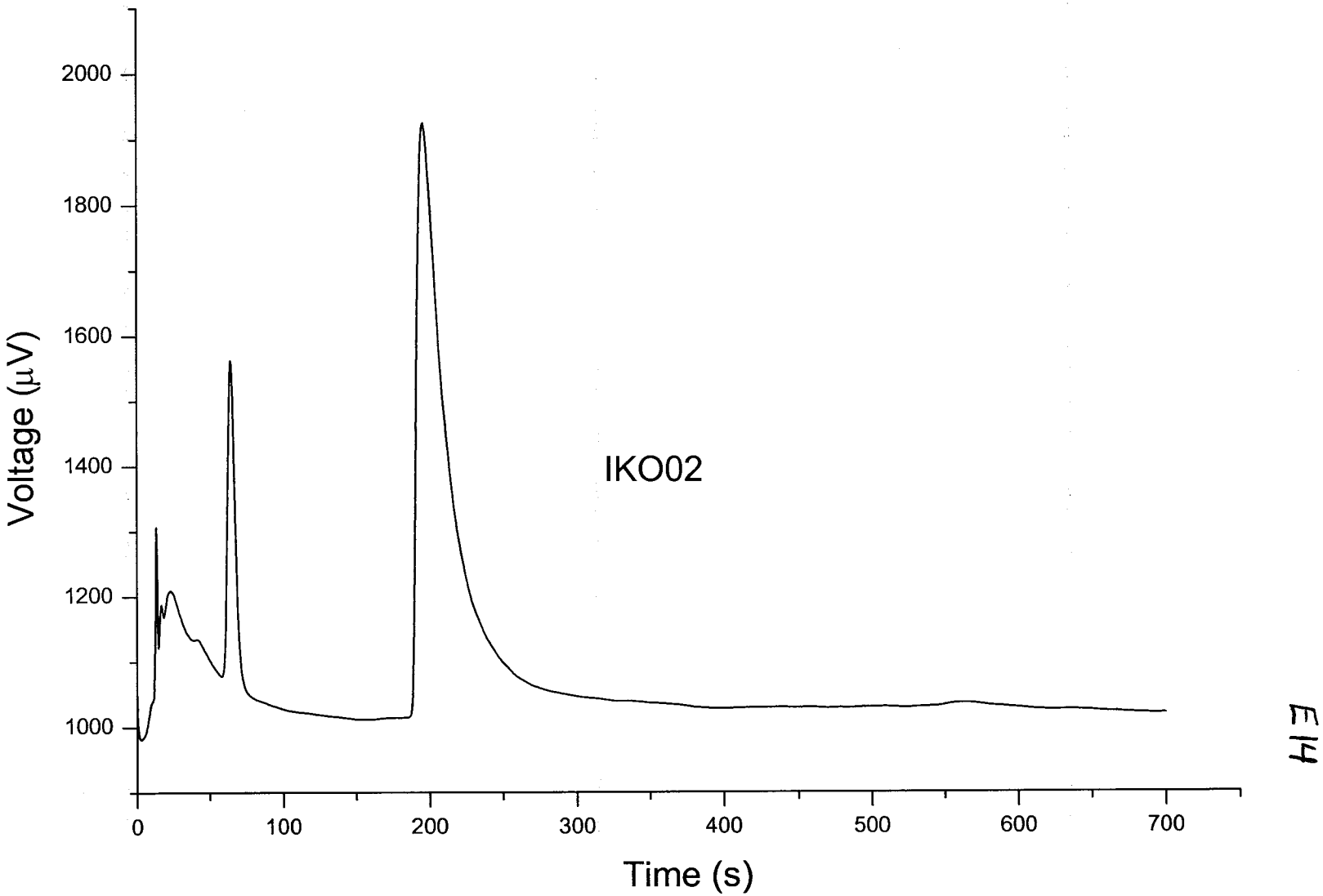
2000
1800
1600
1400
1200
1000
Voltage (μV)
IKO02
0
100
200
300
400
500
600
700
Time (s)

Fig 14

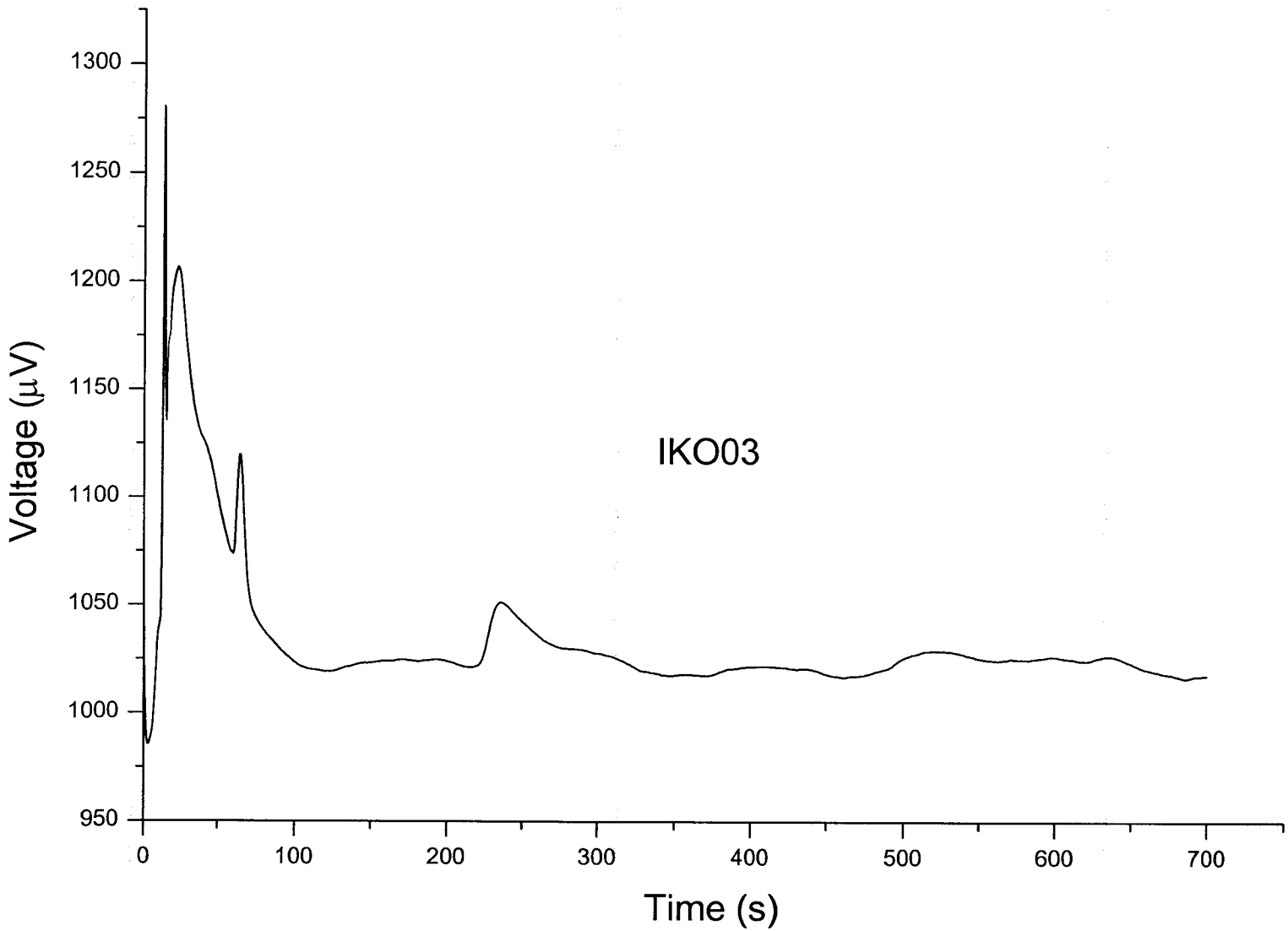
IKO03
Voltage (μV)
1300
1250
1200
1150
1100
1050
1000
950
0
100
200
300
400
500
600
700
Time (s)

E15

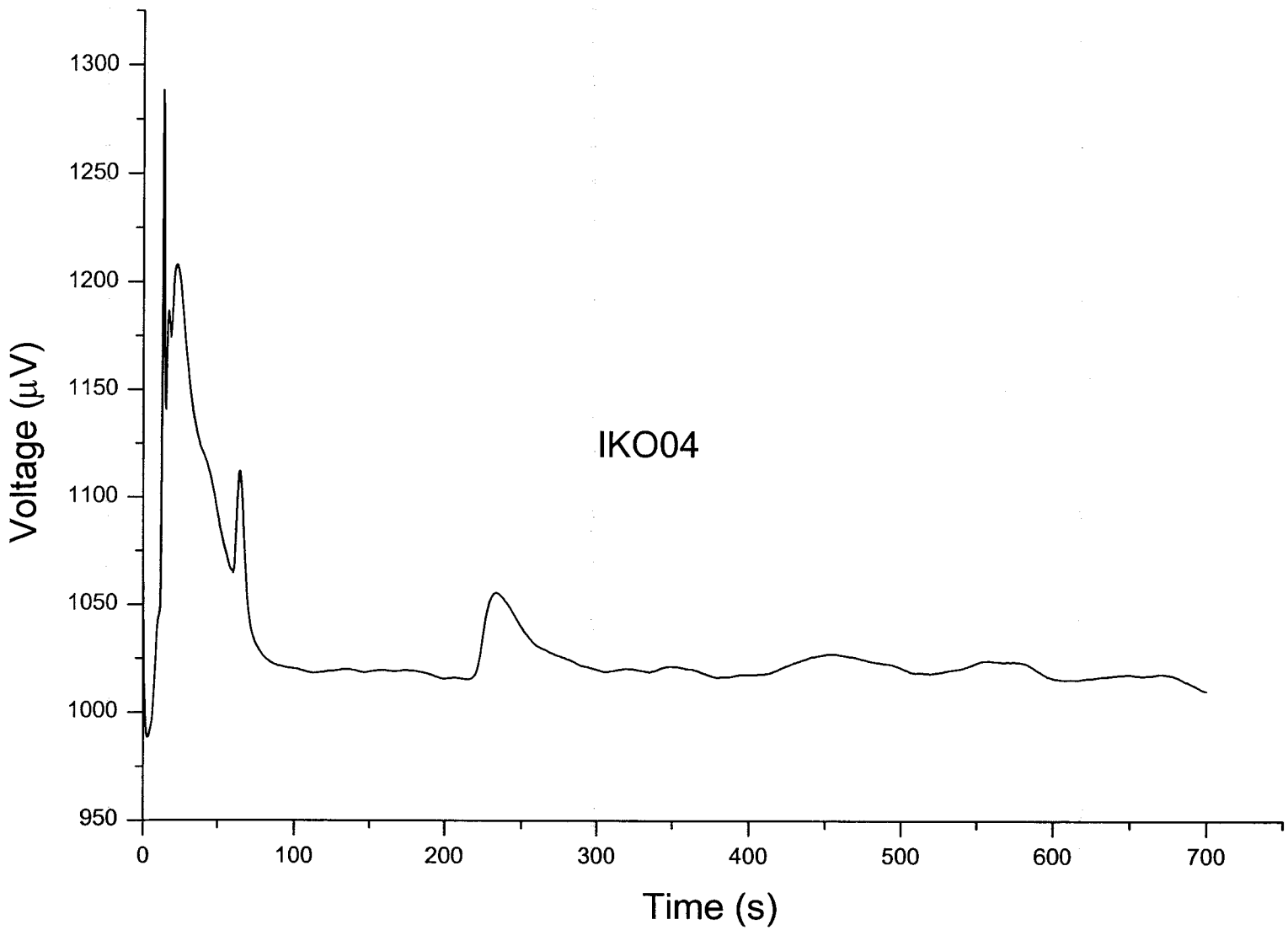
IKO04
Voltage (μV)
1300
1250
1200
1150
1100
1050
1000
950
0
100
200
300
400
500
600
700
Time (s)

E16

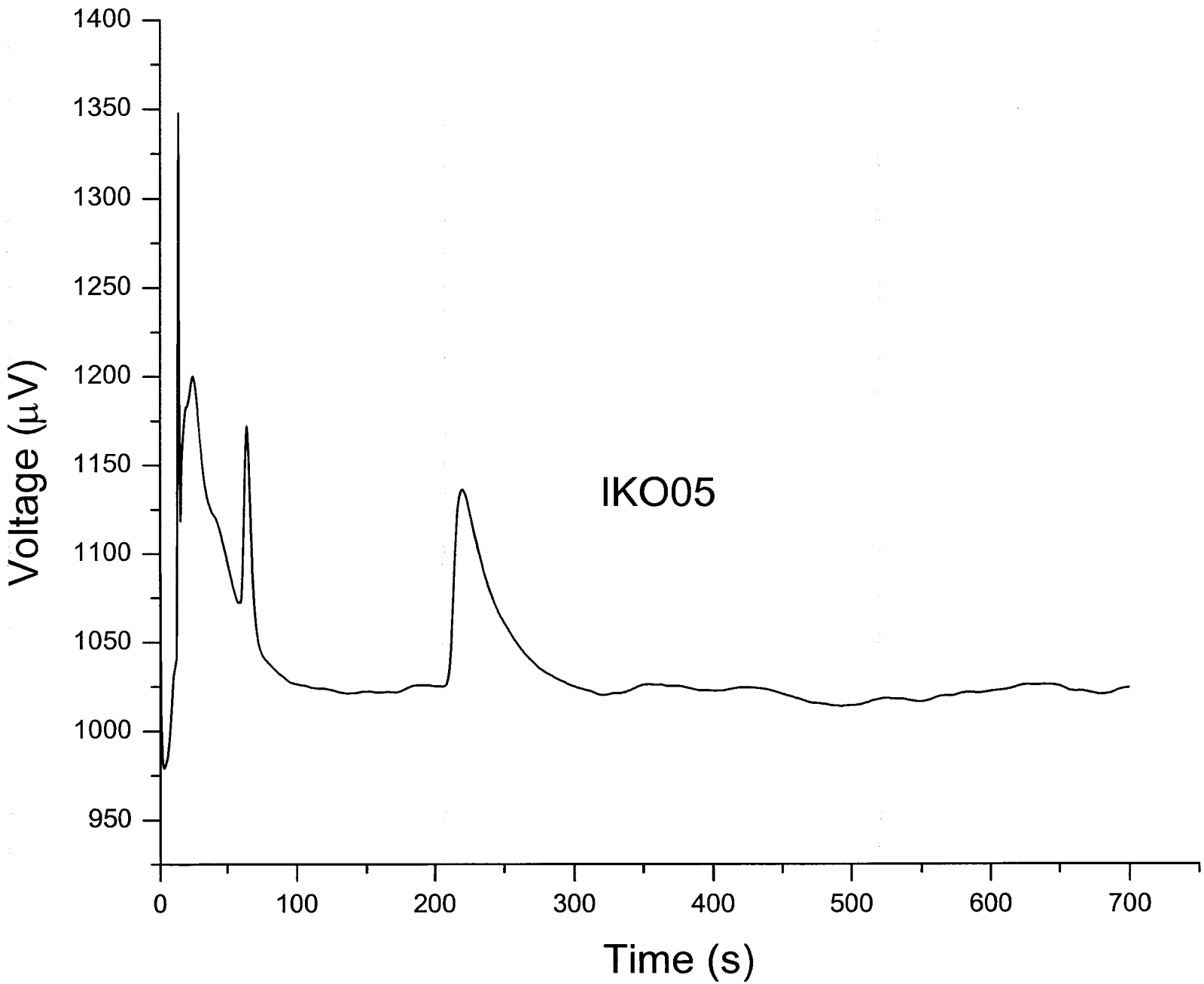
1400
1350
1300
1250
1200
1150
1100
1050
1000
950
Voltage (μV)
IKO05
0
100
200
300
400
500
600
700
Time (s)

E17

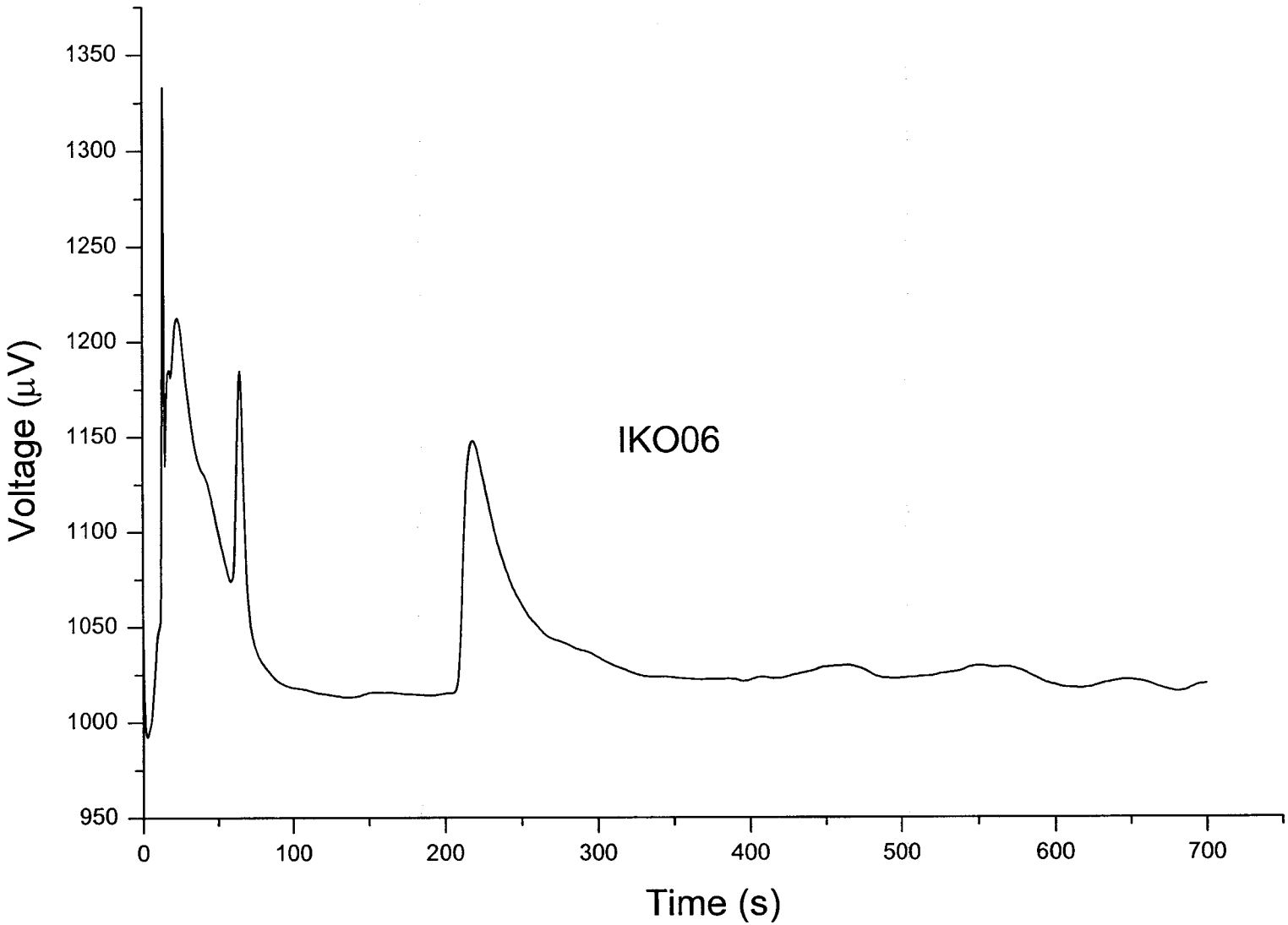
IKO06
Voltage (μV)
1350
1300
1250
1200
1150
1100
1050
1000
950
0
100
200
300
400
500
600
700
Time (s)

E18

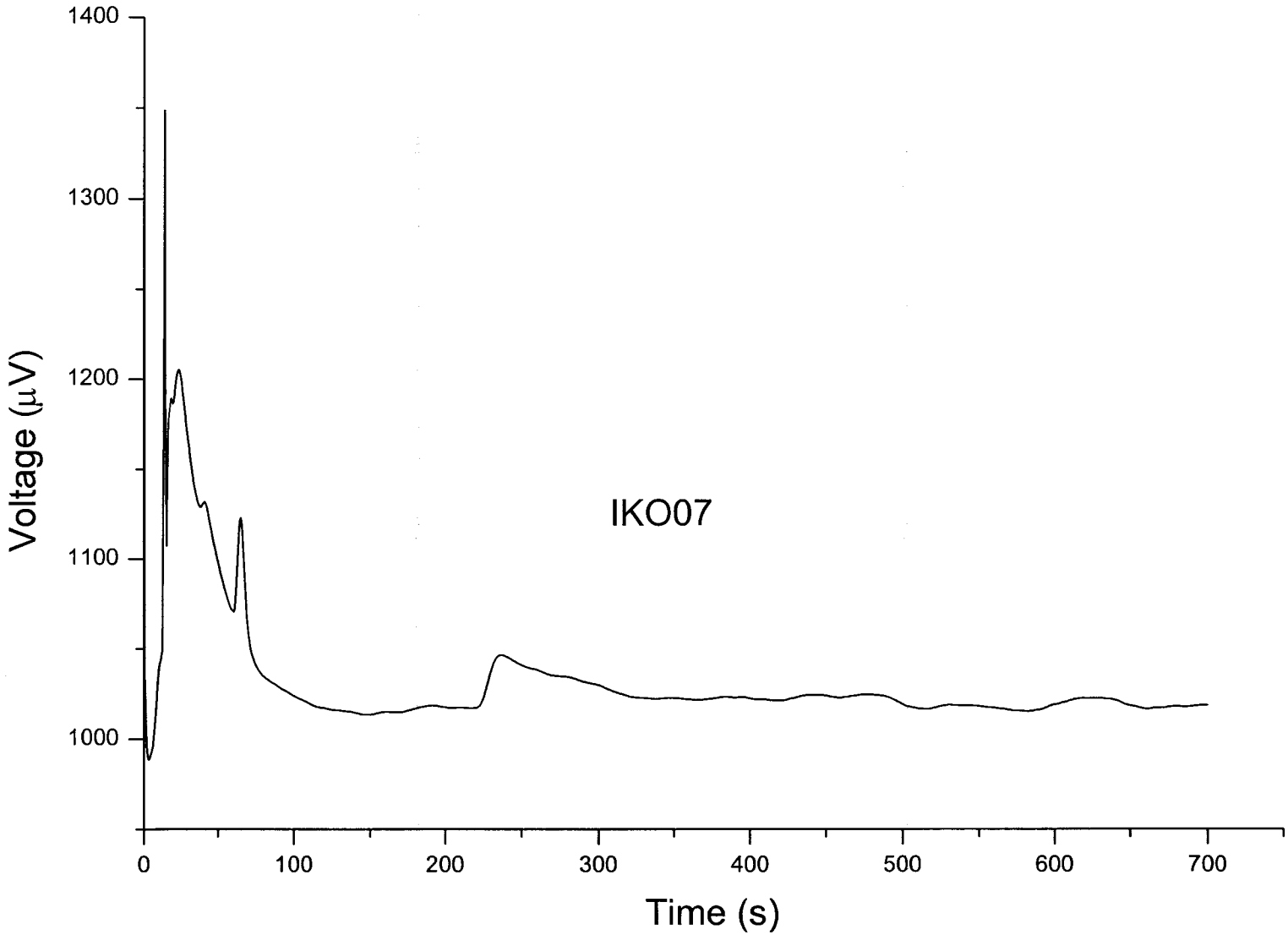
1400
1300
1200
1100
1000
Voltage (μV)
IKO07
0
100
200
300
400
500
600
700
Time (s)

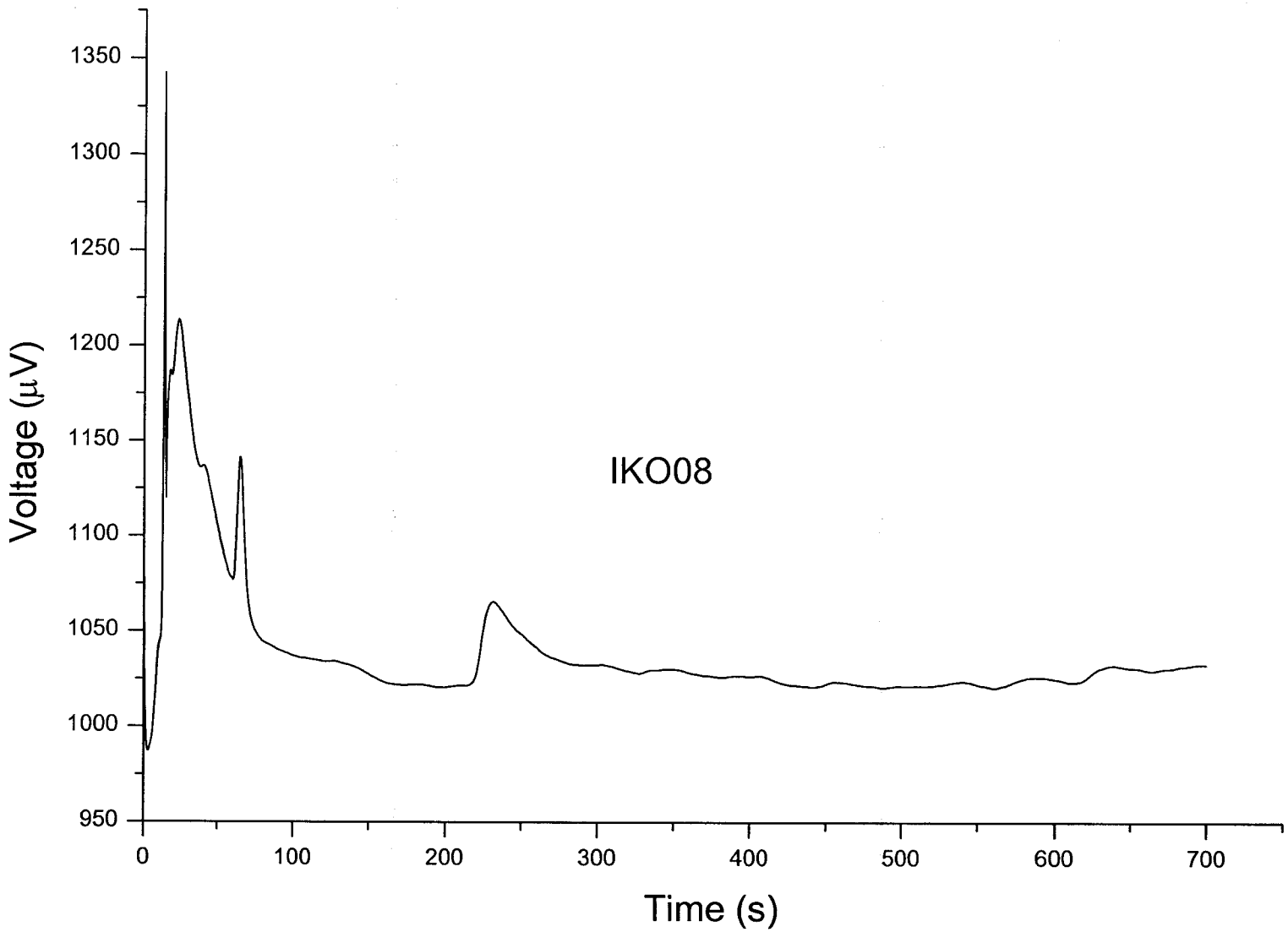
IKO08
Voltage (μV)
Time (s)
1350
1300
1250
1200
1150
1100
1050
1000
950
0
100
200
300
400
500
600
700

E20

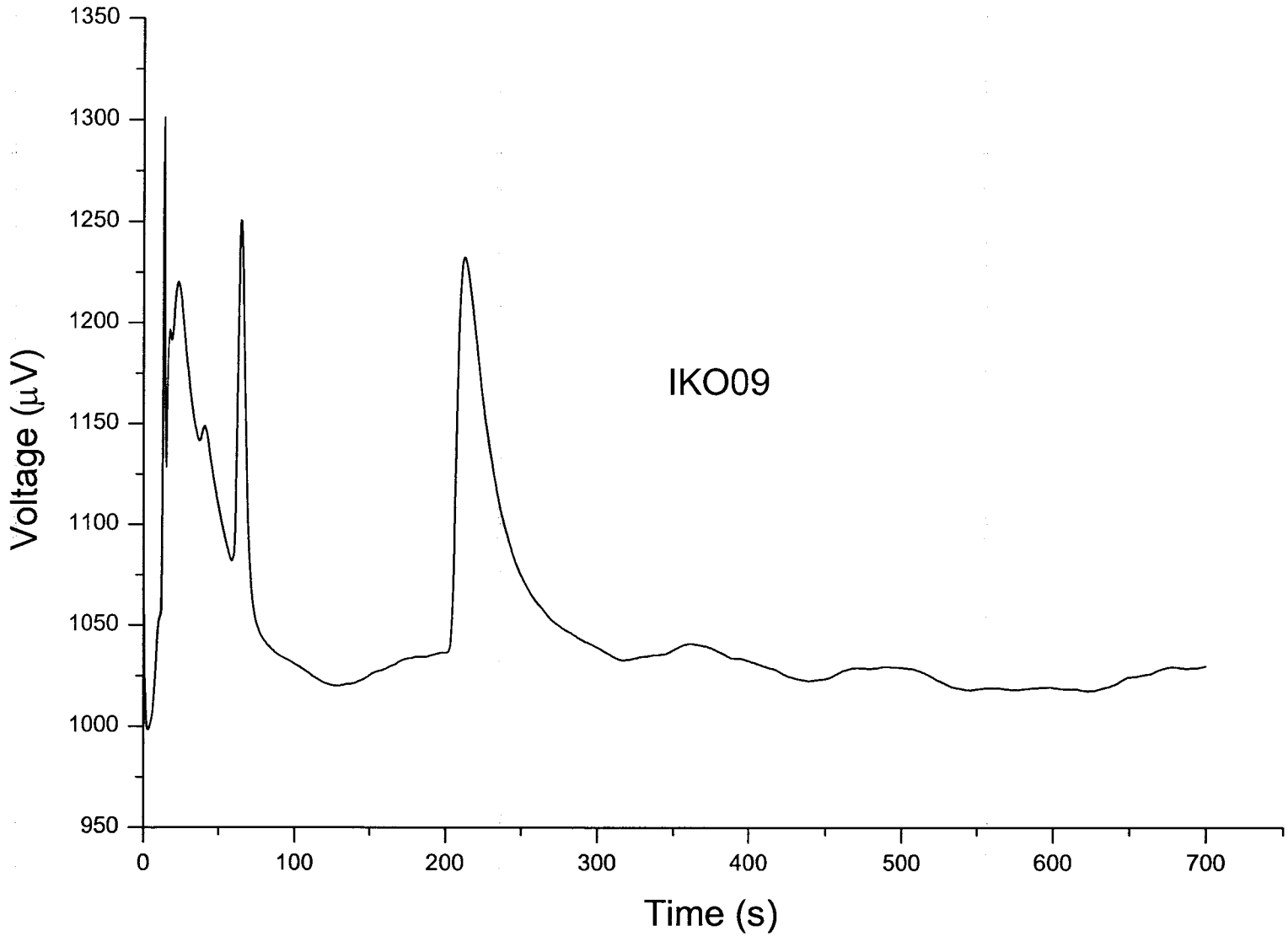
IKO09
Voltage (μV)
Time (s)
1350
1300
1250
1200
1150
1100
1050
1000
950
0
100
200
300
400
500
600
700

EZ1

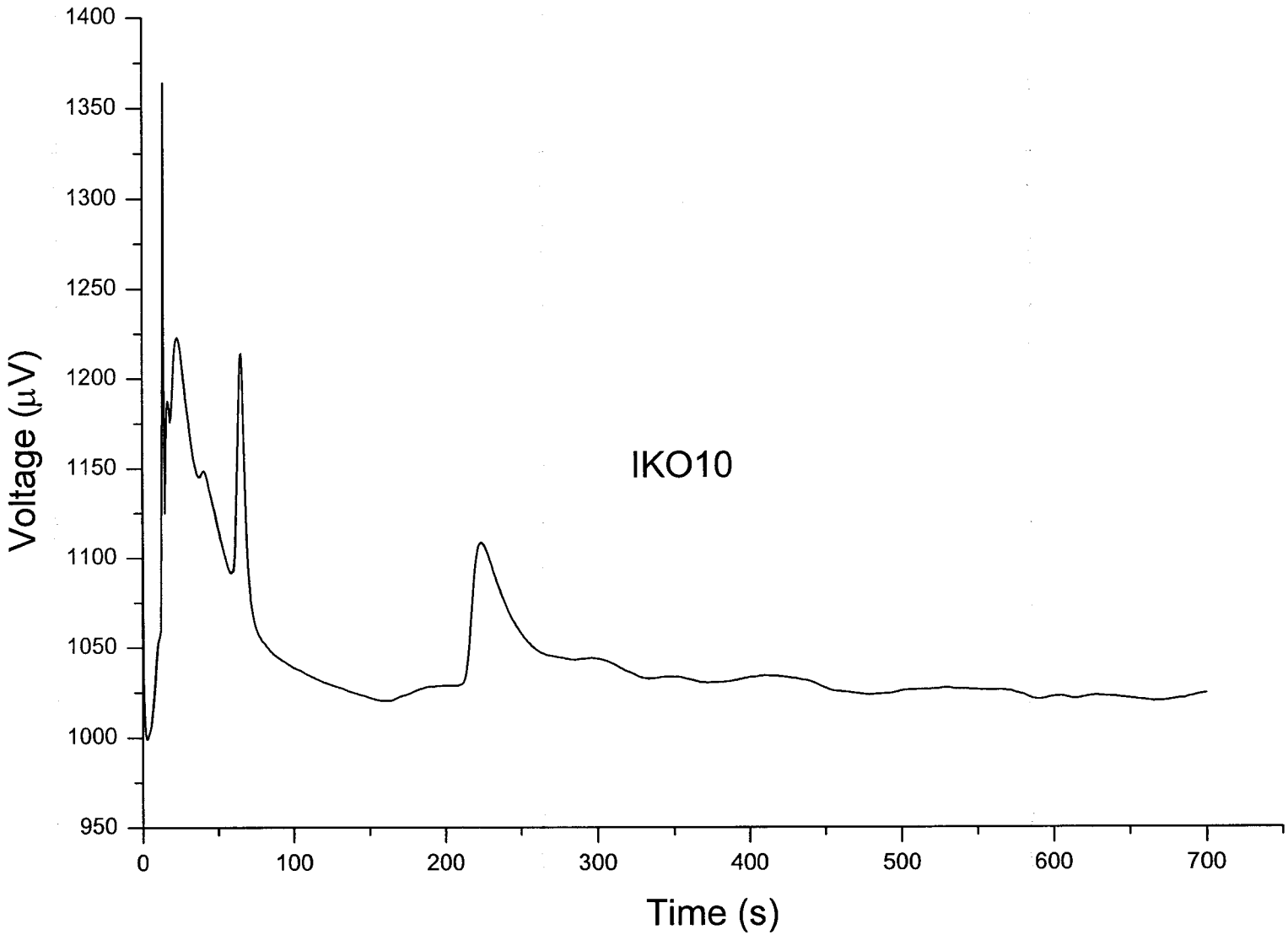
1400
1350
1300
1250
1200
1150
1100
1050
1000
950
Voltage (μV)
IKO10
0
100
200
300
400
500
600
700
Time (s)

E22

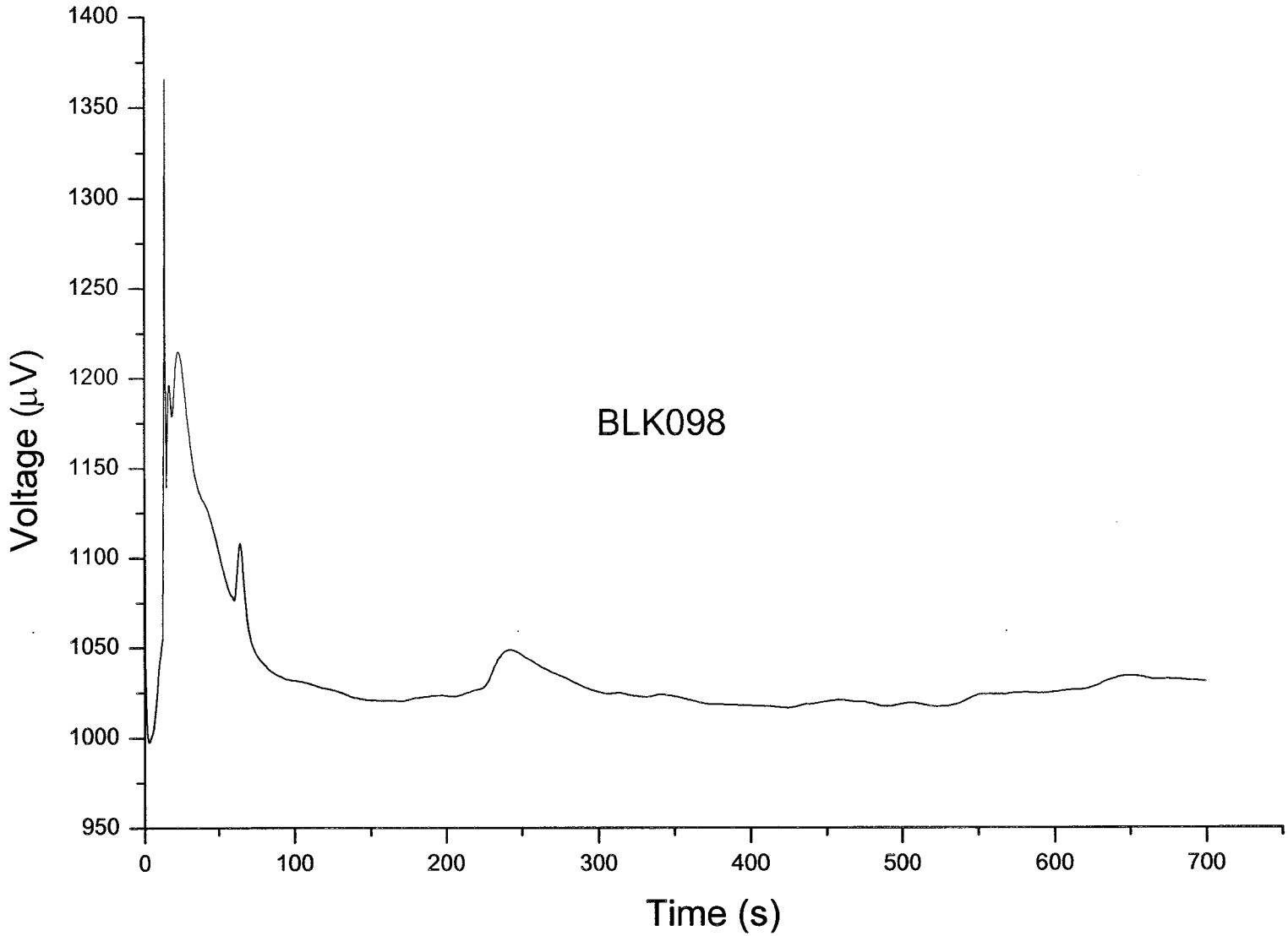
BLK098
Voltage (μV)
Time (s)
1400
1350
1300
1250
1200
1150
1100
1050
1000
950
0
100
200
300
400
500
600
700

E23

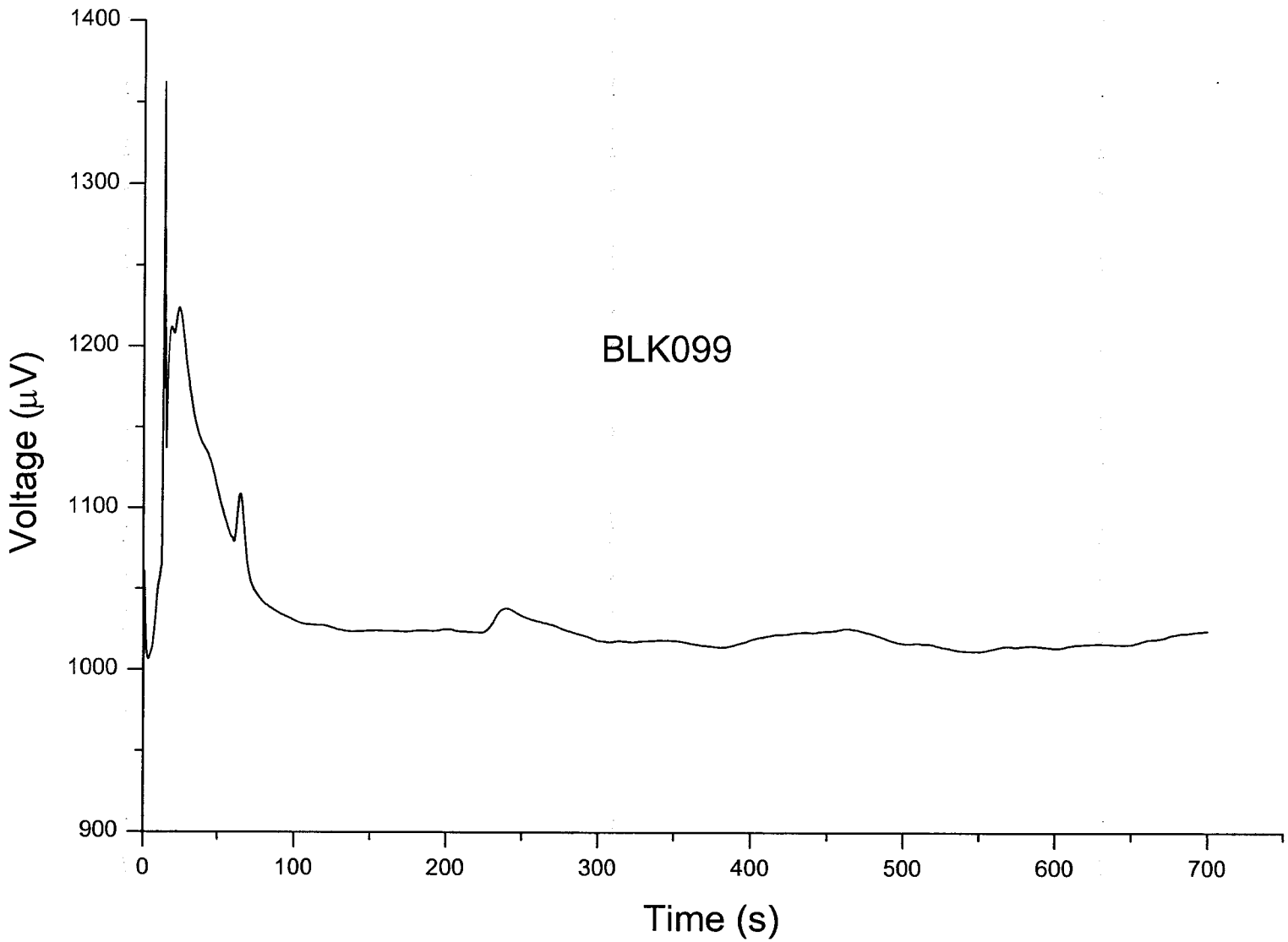
BLK099
Voltage (μV)
1400
1300
1200
1100
1000
900
0
100
200
300
400
500
600
700
Time (s)

E24

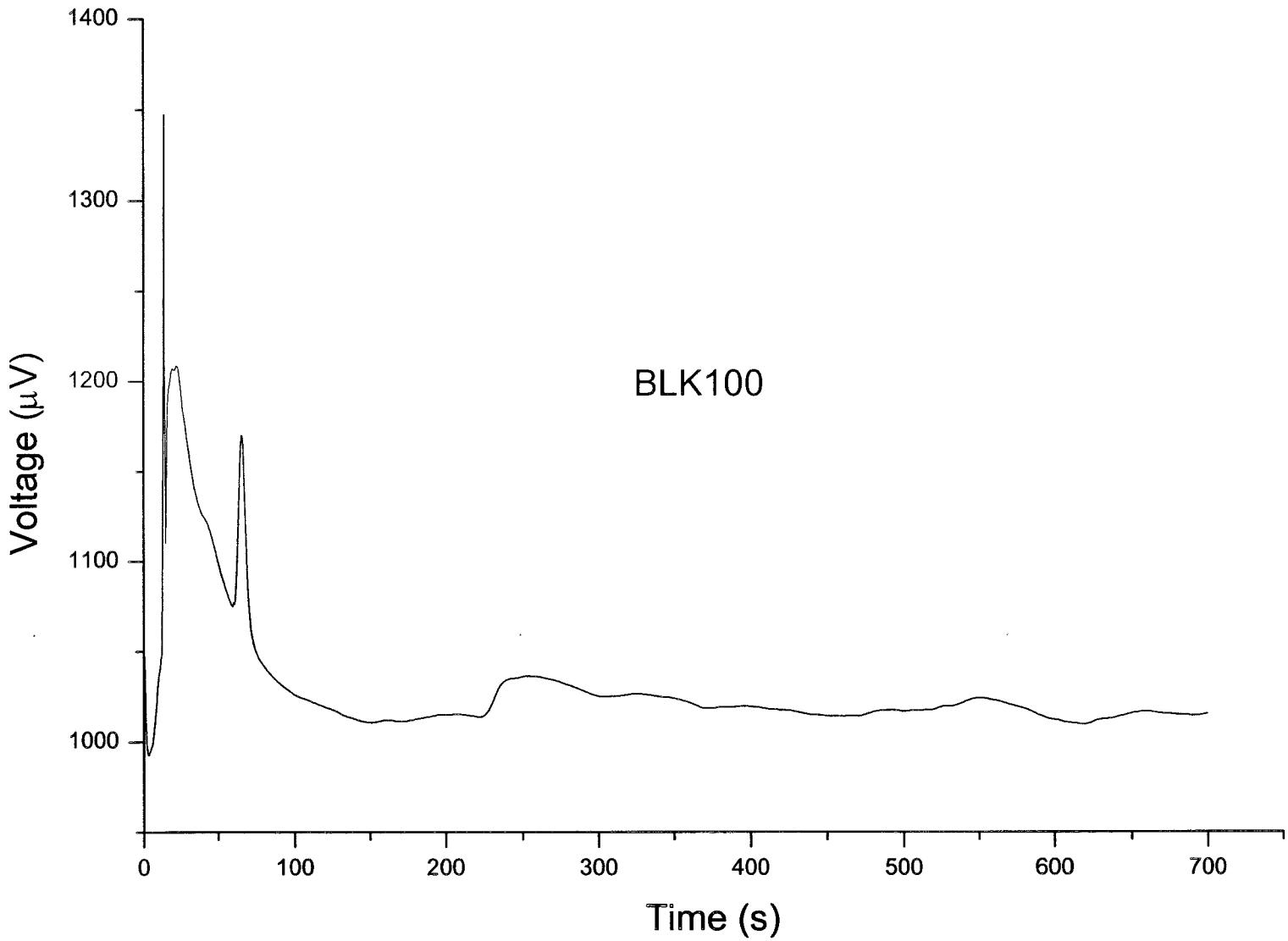
BLK100
Voltage (μV)
1400
1300
1200
1100
1000
0
100
200
300
400
500
600
700
Time (s)

E25

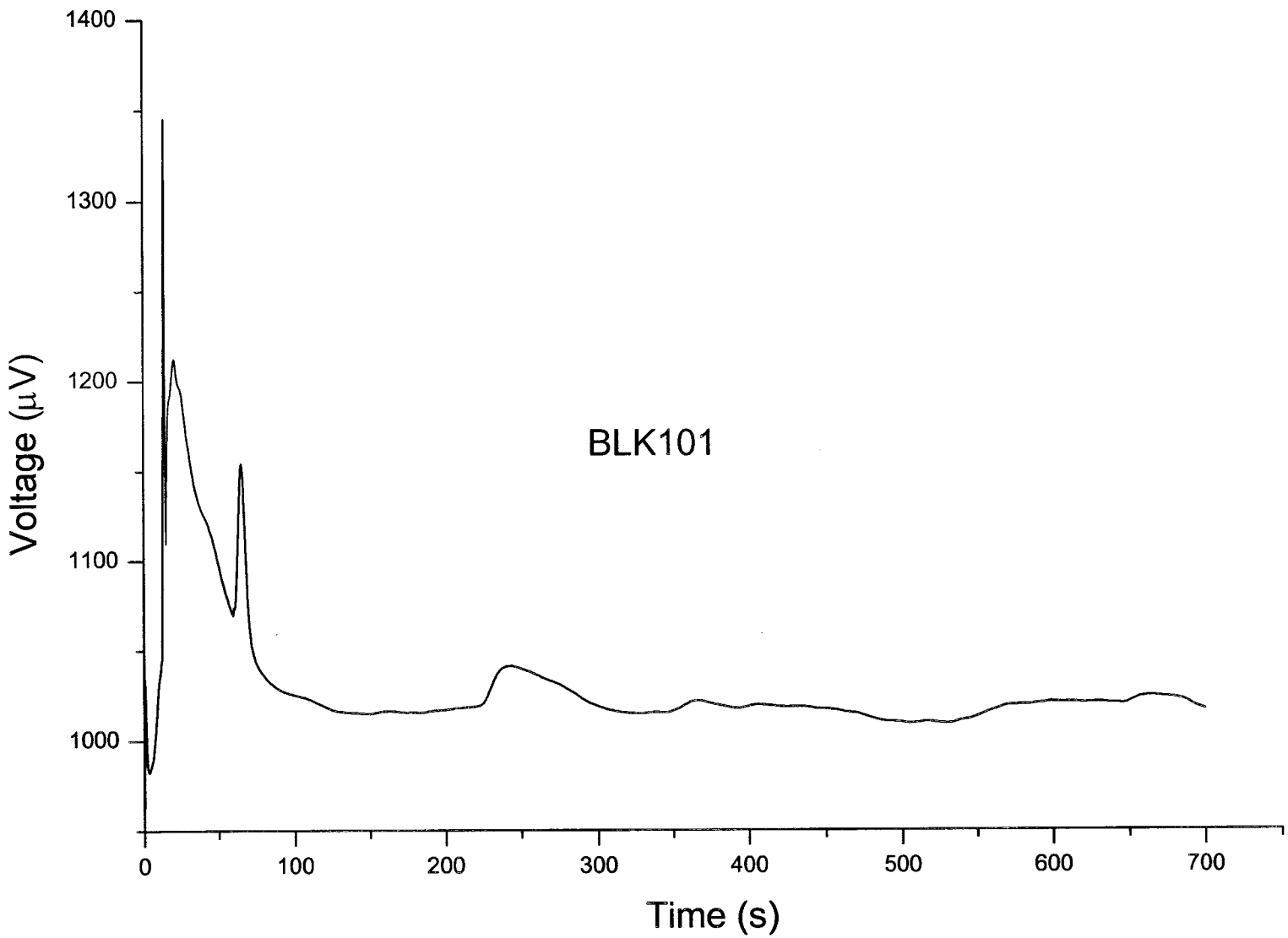
BLK101
Voltage (μV)
1400
1300
1200
1100
1000
0
100
200
300
400
500
600
700
Time (s)

E26

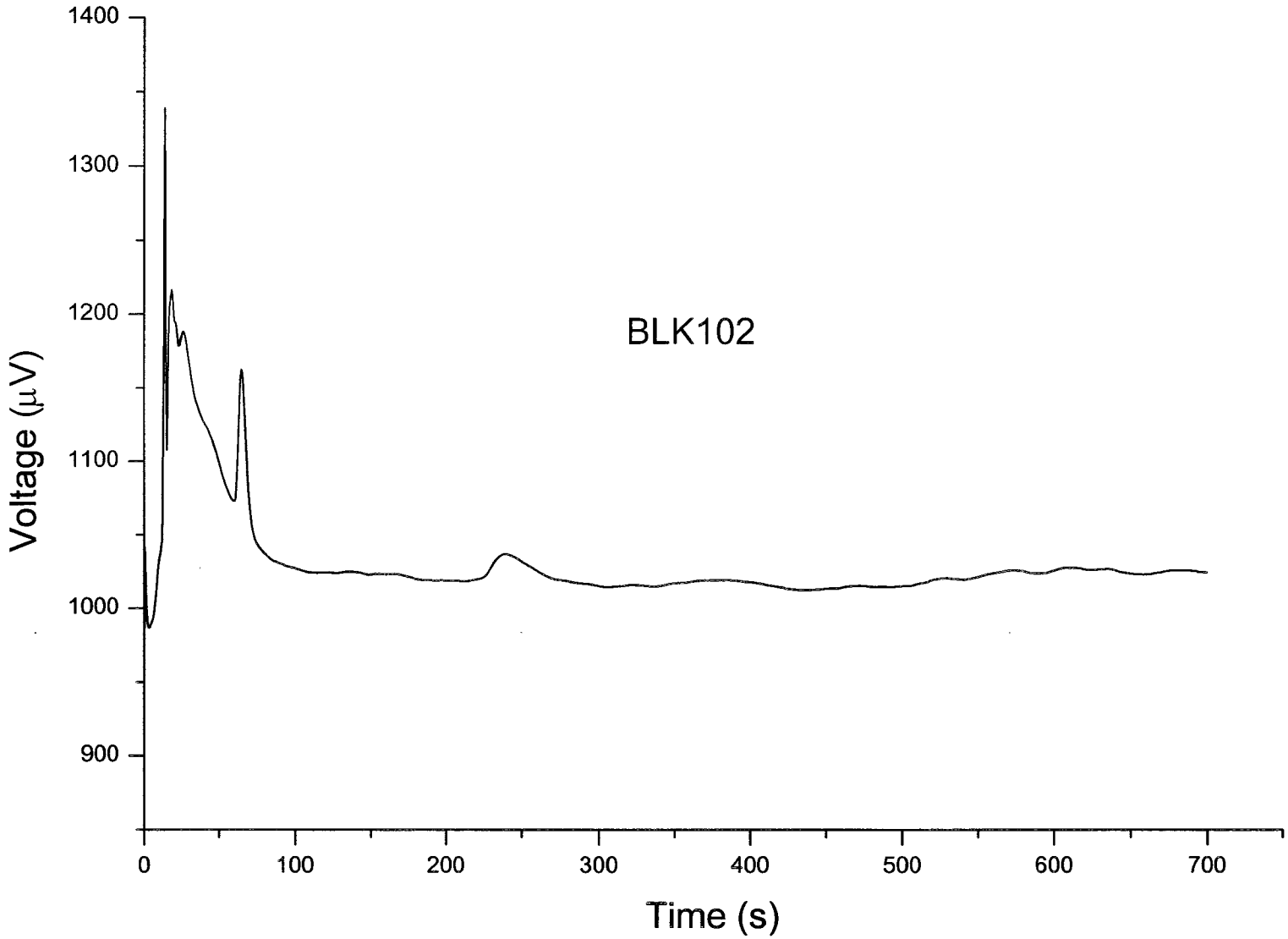
BLK102
Voltage (μV)
1400
1300
1200
1100
1000
900
0
100
200
300
400
500
600
700
Time (s)

E27

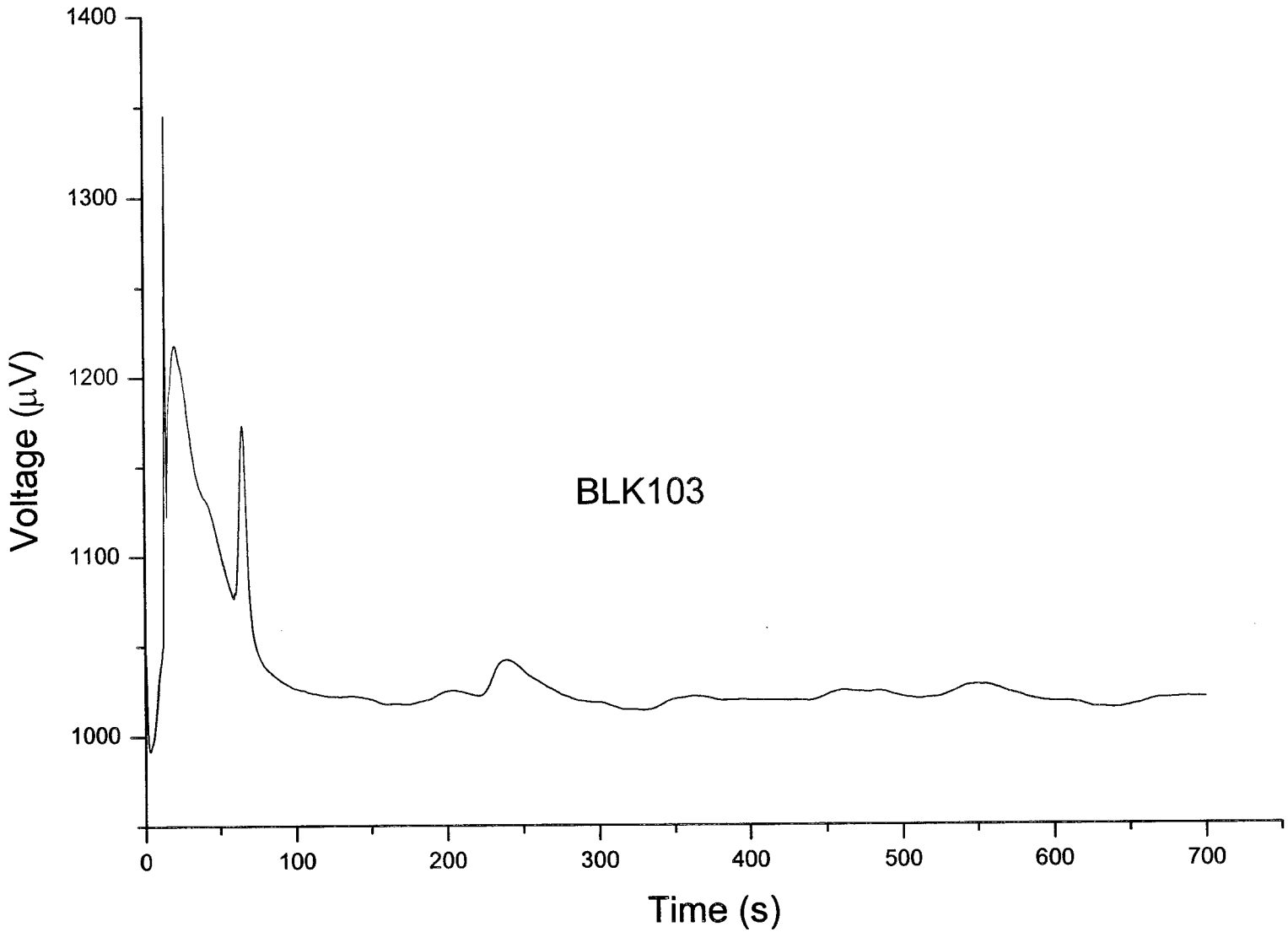
1400
1300
1200
1100
1000
Voltage (μV)
BLK103
0
100
200
300
400
500
600
700
Time (s)

E28

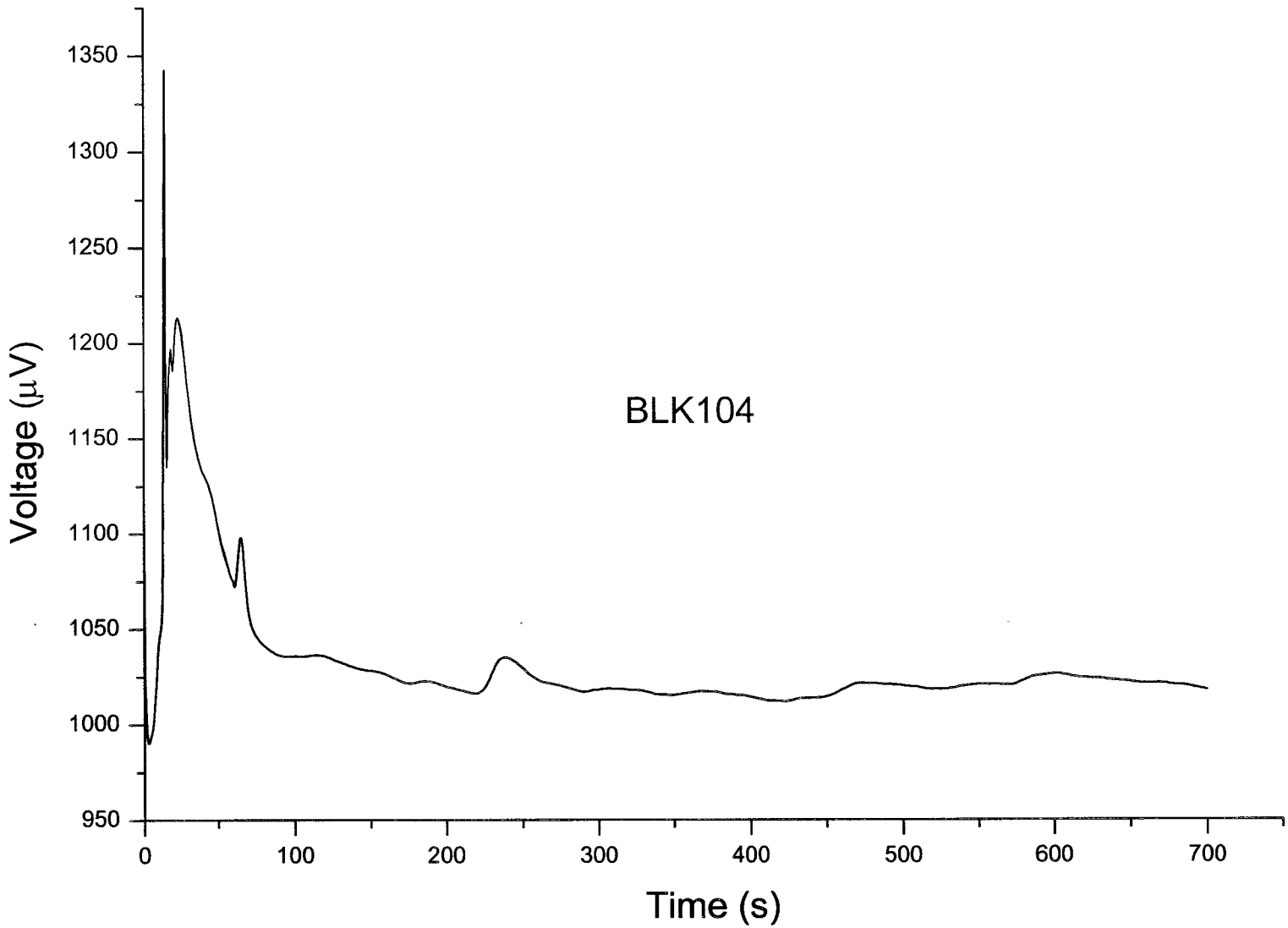
BLK104
Voltage (μV)
1350
1300
1250
1200
1150
1100
1050
1000
950
0
100
200
300
400
500
600
700
Time (s)

E29

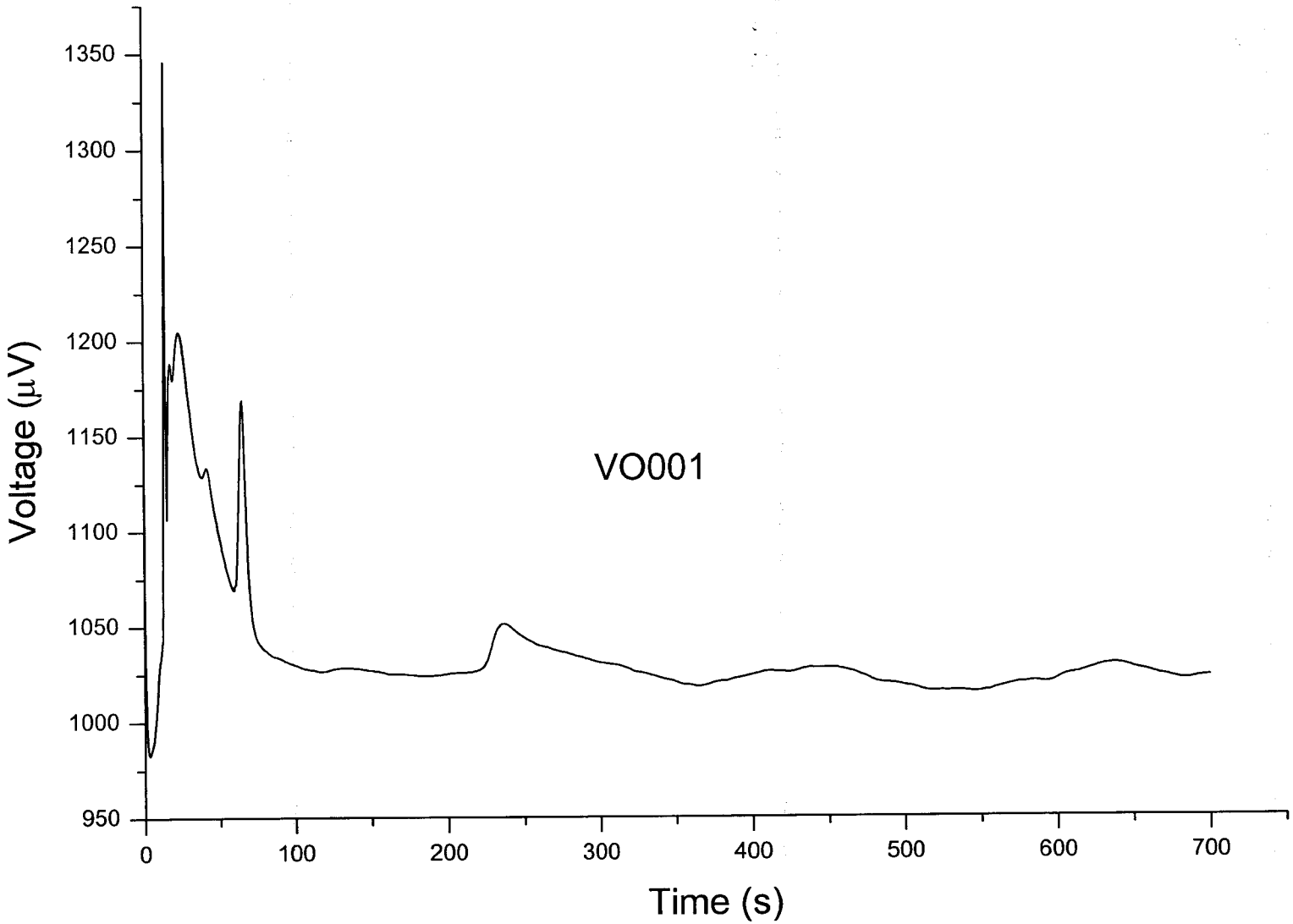
VO001
Voltage (μV)
Time (s)
1350
1300
1250
1200
1150
1100
1050
1000
950
0
100
200
300
400
500
600
700

E30

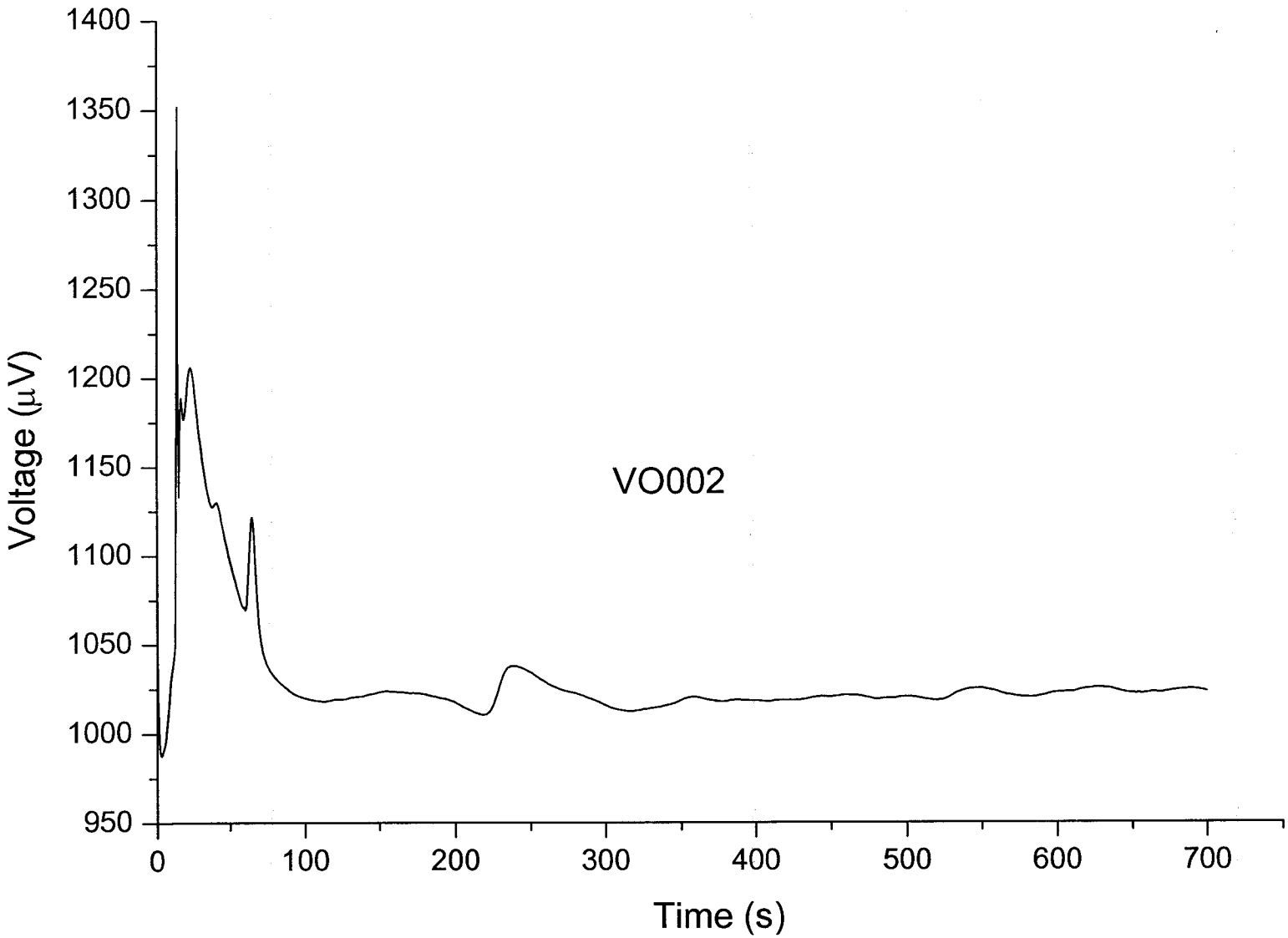
1400
1350
1300
1250
1200
1150
1100
1050
1000
950
Voltage (μV)
VO002
0
100
200
300
400
500
600
700
Time (s)

E31

E32

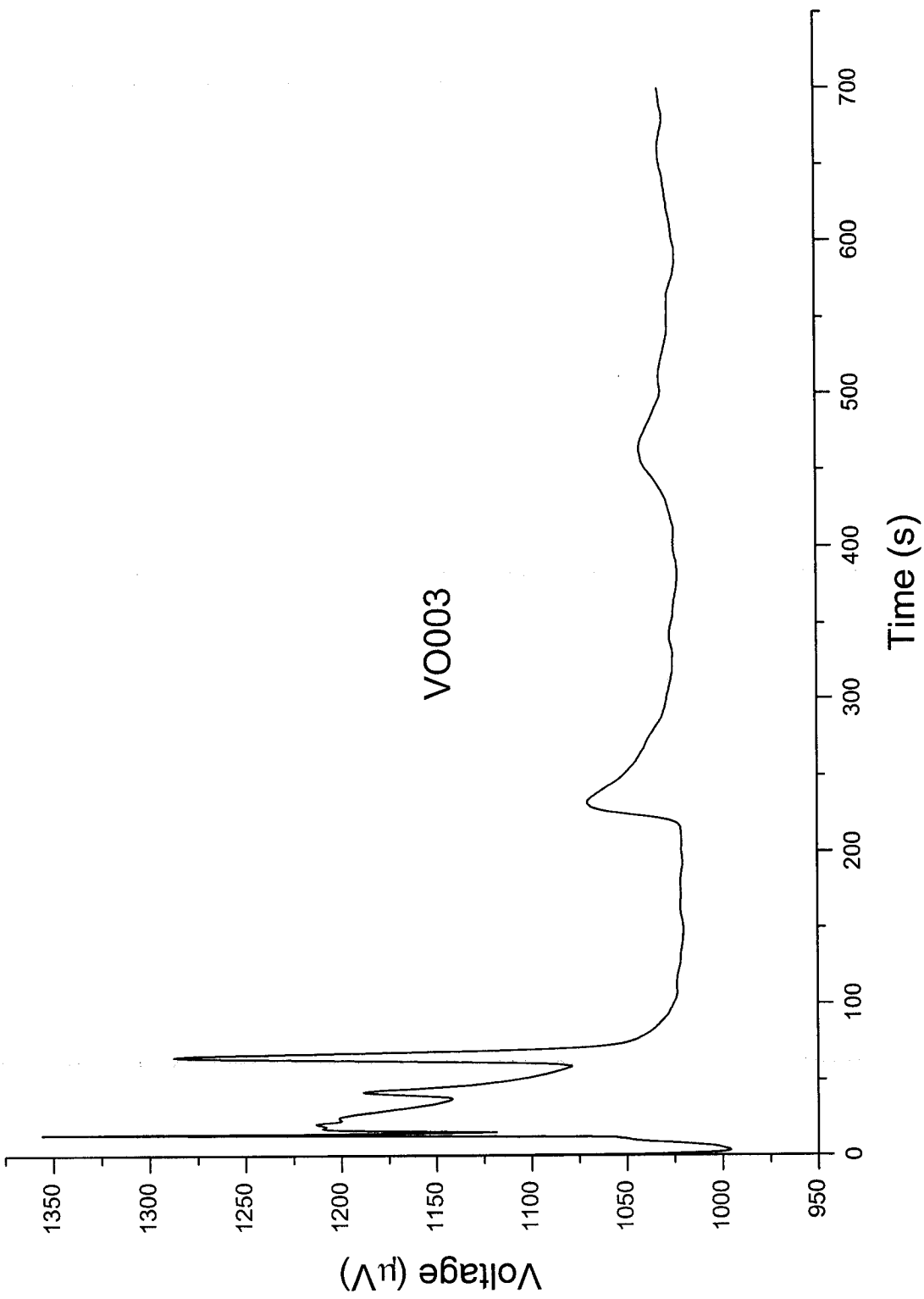
VO003
Voltage (μV)
Time (s)
1350
1300
1250
1200
1150
1100
1050
1000
950
0
100
200
300
400
500
600
700

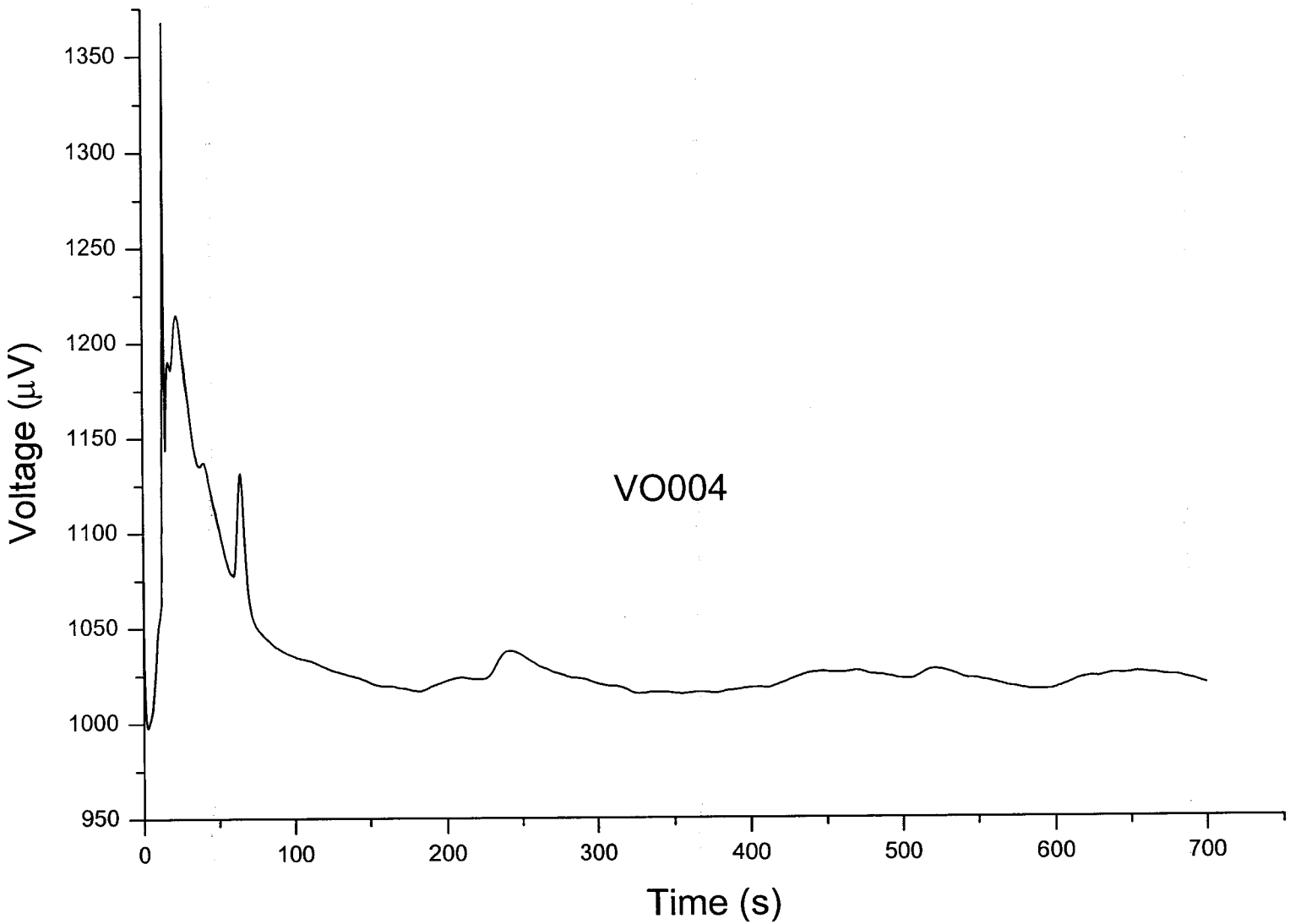
VO004
Voltage (μV)
1350
1300
1250
1200
1150
1100
1050
1000
950
0
100
200
300
400
500
600
700
Time (s)

E 33

Appendix F. Impurity reflections for the Co-Mg JLR series

Impurity or Low-Intensity Peak Identification / Designation	$Co_{0.3}Mg_{2.7}JLR$ MER123		$Co_{0.6}Mg_{2.4}JLR$ MER167		$Co_{0.9}Mg_{2.1}JLR$ MER124	
	$2\theta_{vis}$	d_{hkl}	$2\theta_{vis}$	d_{hkl}	$2\theta_{vis}$	d_{hkl}
1M 11-1; $2M_1$ 111					20.142	4.405
1M 02-1; $2M_1$ 02-2; Sa 20-1	21.266	4.175			21.179	4.192
$2M_1$ 112	21.861	4.062				
$2M_1$ 02-3; ?Sa130	23.275	3.819			23.396	3.799
Sa130						
2M1 11-4; Ol 111; Sa 22-1	25.147	3.538			25.127	3.541
Sa 11-2	25.525	3.487				
Sa 220						
$2M_1$ 114; Sa 00-2	27.188	3.277			27.138	3.283
Sa 040						
Sa 20-2						
$2M_1$ 02-5	29.346	3.041			29.286	3.047
Sa 131						
$2M_1$ 11-6; $2M_2$ 11-6; Ol 130	31.700	2.820			31.617	2.828
Sa 24-1; $2M_2$ 31-3,02-2,311						
1M 131,20-2; $2M_1$ 13-3,202; Ol 131	35.863	2.502				
$2M_2$ 31-4, 02-3, 312; Ol 112	36.355	2.469			36.299	2.473
$2M_2$ 31-5, 02-4, 313	38.200	2.354				
1M 22-1; $2M_1$ ...; $2M_2$ ...;	39.238	2.294				
1M 132,20-3; $2M_1$ ...; $2M_2$ ...	39.588	2.275				
1M 04-1; $2M_2$ ...; $2M_1$ ...	40.163	2.243				
$2M_2$ 31-7, 02-6; 1M 04-2; $2M_1$ 04-4	43.268	2.089			43.187	2.093
1M 005	44.572	2.031			44.548	2.032
1M 22-4; $2M_1$ 226; $2M_2$ 317,02-8,226;Ol 113; Sa 113					49.600	1.836
Sa 20-4,043					50.862	1.794
Sa 44-1; Ol 222,240						
1M 24-1,150; $2M_1$ 24-1; $2M_2$ 51-2	52.682	1.736			52.621	1.738
1M 31-2,...; $2M_1$ ...; $2M_2$ ...	53.279	1.718			53.238	1.719
1M 13-6,205; $2M_2$ ...; $2M_1$ ...	62.555	1.484			62.428	1.486
1M 062,331; $2M_1$ ...; $2M_2$ ...	63.369	1.467			63.257	1.469
1M 31-5, 313; $2M_1$ ...; $2M_2$ ...					65.299	1.428
1M 225; $2M_1$ ...; $2M_2$ ...	66.186	1.411			65.922	1.416
1M 063,332,33-4; $2M_1$ ...; $2M_2$ ...	66.863	1.398			66.856	1.398

Impurity or Low-Intensity Peak Identification / Designation	$Co_{1.2}Mg_{1.8}$JLR MER079		$Co_{1.5}Mg_{1.5}$JLR MER125		$Co_{1.8}Mg_{1.2}$JLR MER078	
	$2\theta_{vis}$	d_{hkl}	$2\theta_{vis}$	d_{hkl}	$2\theta_{vis}$	d_{hkl}
1M 11-1; $2M_1$ 11-1	20.015	4.433	20.123	4.409	20.103	4.413
1M 02-1; $2M_1$ 02-2; Sa 20-1			21.012	4.225	20.970	4.233
$2M_1$ 112					21.750	4.083
$2M_1$ 02-3; ?Sa130	23.375	3.803	23.370	3.803	23.292	3.816
Sa130					23.511	3.781
2M1 11-4; Ol 111; Sa 22-1	25.120	3.542	25.135	3.540	25.071	3.549
Sa 11-2						
Sa 220	26.755	3.329	26.783	3.326	26.812	3.322
$2M_1$ 114; Sa 20-2	27.163	3.280	27.132	3.284	27.114	3.286
Sa 040					27.448	3.247
Sa 20-2	27.677	3.221	27.659	3.223	27.660	3.222
$2M_1$ 02-5	29.319	3.044	29.259	3.050	29.249	3.051
Sa 131	29.889	2.987	29.824	2.993	29.782	2.997
$2M_1$ 11-6; $2M_2$ 11-6; Ol 130	31.569	2.832	31.570	2.832	31.600	2.829
Sa 24-1; $2M_2$ 31-3,02-2,311	34.827	2.574	34.789	2.577	34.755	2.579
1M 131,20-2; $2M_1$ 13-3,202; Ol 131	35.754	2.509	35.722	2.512		
$2M_2$ 31-4, 02-3, 312; Ol 112	36.299	2.473	36.287	2.474	36.206	2.479
$2M_2$ 31-5, 02-4, 313						
1M 22-1; $2M_1$ ...; $2M_2$ ...;						
1M 132,20-3; $2M_1$ ...; $2M_2$ ...						
1M 04-1; $2M_2$ ...; $2M_1$ ...						
$2M_2$ 31-7, 02-6; 1M 04-2; $2M_1$ 04-4	43.192	2.093	43.158	2.094	43.140	2.095
1M 005	44.500	2.034	44.529	2.033	44.495	2.035
1M 22-4; $2M_1$ 226; $2M_2$ 317,02-8,226;Ol 113; Sa 113	49.545	1.838	49.526	1.839	49.506	1.840
Sa 20-4,043						
Sa 44-1; Ol 222,240					51.429	1.775
1M 24-1,150; $2M_1$ 24-1; $2M_2$ 51-2	52.626	1.738	52.573	1.739	52.583	1.739
1M 31-2,...; $2M_1$ ...; $2M_2$ ...	53.171	1.721	53.119	1.723	53.232	1.719
1M 13-6,205; $2M_2$ ...; $2M_1$ ...	62.382	1.487	62.358	1.488	62.363	1.488
1M 062,331; $2M_1$ ...; $2M_2$ ...	63.207	1.470	63.170	1.471	63.082	1.473

Impurity or Low-Intensity Peak Identification / Designation	$Co_{2.1}Mg_{0.9}$JLR MER126		$Co_{2.4}Mg_{0.6}$JLR MER133		$Co_{2.7}Mg_{0.3}$JLR MER127		$Co_{3.0}Mg_{0.0}$JLR MER132	
	$2\theta_{vis}$	d_{hkl}	133b.prn	d_{hkl}	$2\theta_{vis}$	d_{hkl}	$2\theta_{vis}$	d_{hkl}
1M 11-1; $2M_1$ 11-1			20.095	4.415	20.096	4.415		
1M 02-1; $2M_1$ 02-2; Sa 20-1	20.97	4.233	21.007	4.226	21.000	4.227	21.016	4.224
$2M_1$ 112								
$2M_1$ 02-3; ?Sa130			23.297	3.815	23.295	3.815	23.267	3.820
Sa130	23.472	3.787	23.521	3.779	23.517	3.780	23.478	3.786
2M1 11-4; OI 111; Sa 22-1	25.044	3.553	25.098	3.545	25.074	3.549	25.041	3.553
Sa 11-2								
Sa 220	26.797	3.324	26.818	3.322	26.835	3.320	26.803	3.324
$2M_1$ 114; Sa 20-2	27.085	3.290	27.109	3.287	27.119	3.285	27.082	3.290
Sa 040	27.410	3.251	27.389	3.254	27.403	3.252	27.398	3.253
Sa 20-2	27.633	3.226	27.654	3.223	27.648	3.224	27.636	3.225
$2M_1$ 02-5	29.234	3.052	29.231	3.053	29.215	3.054	29.187	3.057
Sa 131	29.804	2.995	29.832	2.993	29.824	2.993	29.801	2.996
$2M_1$ 11-6; $2M_2$ 11-6; OI 130	31.537	2.835	31.569	2.832	31.517	2.836	31.519	2.836
Sa 24-1; $2M_2$ 31-3,02-2,311	34.74	2.580	34.742	2.580	34.744	2.580		
1M 131,20-2; $2M_1$ 13-3,202; OI 131								
$2M_2$ 31-4, 02-3, 312; OI 112	36.154	2.482	36.156	2.482	36.171	2.481		
$2M_2$ 31-5, 02-4, 313								
1M 22-1; $2M_1$ ...; $2M_2$ ...;								
1M 132,20-3; $2M_1$ ...; $2M_2$ ...								
1M 04-1; $2M_2$ ...; $2M_1$ ...								
$2M_2$ 31-7, 02-6; 1M 04-2; $2M_1$ 04-4	43.100	2.097	43.098	2.097	43.085	2.098	43.075	2.098
1M 005	44.487	2.035	44.508	2.034	44.522	2.033	44.443	2.037
1M 22-4; $2M_1$ 226; $2M_2$ 317,02-8,226;OI 113; Sa 113	49.483	1.841	49.494	1.840	49.437	1.842	49.455	1.841
Sa 20-4,043	50.825	1.795	50.808	1.796	50.840	1.795		
Sa 44-1; OI 222,240	51.414	1.776			51.431	1.775		
1M 24-1,150; $2M_1$ 24-1; $2M_2$ 51-2	52.500	1.742	52.498	1.742	52.449	1.743	52.405	1.745
1M 31-2,...; $2M_1$ ...; $2M_2$ ...	53.065	1.724	53.160	1.722	53.102	1.723	53.036	1.725
1M 13-6,205; $2M_2$ ...; $2M_1$ ...	62.288	1.489	62.245	1.490	62.250	1.490	62.254	1.490
1M 062,331; $2M_1$ ...; $2M_2$ ...	63.051	1.473	63.039	1.473	63.000	1.474	62.977	1.475

Appendix G. Impurity reflections for the Mg-Ni JLR series

Impurity or Low-Intensity Peak Identification / Designation	$Mg_{0.0}Ni_{3.0}$JLR_OH MER131 2θ	d_{hkl}	$Mg_{0.0}Ni_{3.0}$JLR_OD MER080 2θ	d_{hkl}	$Mg_{0.3}Ni_{2.7}$JLR MER130 2θ	d_{hkl}	$Mg_{0.6}Ni_{2.4}$JLR MER081 2θ	d_{hkl}
					19.871	4.464		
1M 11-1; $2M_1$ 11-1					20.242	4.383		
1M 02-1; $2M_1$ 02-2; Sa 20-1			21.265	4.175	21.006	4.226		
$2M_1$ 02-3; ?Sa130	23.426	3.794	23.434	3.793	23.452	3.790	23.483	3.785
Sa130								
2M1 11-4; Ol 111; Sa 22-1	25.206	3.530	25.246	3.525	25.211	3.530	25.240	3.526
Sa 11-2								
Sa 220								
$2M_1$ 114; Sa 20-2	27.236	3.272	27.233	3.272	27.222	3.273	27.215	3.274
Sa 040			27.674	3.221	27.676	3.221	27.616	3.227
$2M_1$ 02-5	29.418	3.034	29.388	3.037	29.388	3.037	29.443	3.031
Sa 131					29.847	2.991	29.872	2.989
$2M_1$ 11-6; $2M_2$ 11-6; Ol 130	31.672	2.823	31.713	2.819	31.718	2.819	31.681	2.822
Sa 24-1; $2M_2$ 31-3,02-2,311	35.025	2.560	35.006	2.561	35.037	2.559	34.982	2.563
1M 131,20-2; $2M_1$ 13-3,202; Ol 131	35.867	2.502	35.901	2.499	35.901	2.499		
$2M_2$ 31-4, 02-3, 312; Ol 112			36.473	2.461			36.478	2.461
			37.875	2.374				
$2M_2$ 31-5, 02-4, 313	38.338	2.346	38.338	2.346	38.347	2.345	38.345	2.346
1M 22-1; $2M_1$ ...; $2M_2$ ...;	39.325	2.289	39.335	2.289	39.380	2.286	39.350	2.288
1M 132,20-3; $2M_1$ ...; $2M_2$ ...	39.890	2.258	39.825	2.262	39.805	2.263	39.775	2.264
1M 04-1; $2M_2$ ...; $2M_1$ ...	40.311	2.236	40.297	2.236	40.305	2.236	40.309	2.236
$2M_2$ 31-7, 02-6; 1M 04-2; $2M_1$ 04-4	43.370	2.085	43.382	2.084	43.365	2.085	43.374	2.085
1M 22-4; $2M_1$ 226; $2M_2$ 317,02-8,226;Ol 113; Sa 113	49.828	1.829	49.752	1.831	49.807	1.829	49.894	1.826
	52.164	1.752	52.232	1.750				
1M 24-1,150; $2M_1$ 24-1; $2M_2$ 51-2	52.746	1.734	52.830	1.732	52.877	1.730	52.889	1.730
1M 31-2,...; $2M_1$ ...; $2M_2$ ...	53.450	1.713			53.458	1.713	53.482	1.712
1M 13-6,205; $2M_2$ ...; $2M_1$ ...	62.717	1.480	62.641	1.482	62.681	1.481	62.557	1.484
1M 062,331; $2M_1$ ...; $2M_2$ ...	63.470	1.464	63.499	1.464	63.505	1.464	63.482	1.464
1M 31-5, 313; $2M_1$ ...; $2M_2$ ...	65.467	1.425	65.440	1.425	65.445	1.425	65.414	1.426
1M 225; $2M_1$ ...; $2M_2$ ...			66.206	1.410	66.301	1.409	66.341	1.408

Impurity or Low-Intensity Peak Identification / Designation	$Mg_{0.9}Ni_{2.1}$JLR MER129		$Mg_{1.2}Ni_{1.8}$JLR MER082		$Mg_{1.5}Ni_{1.5}$JLR MER089		$Mg_{1.8}Ni_{1.2}$JLR MER083	
	2θ	d_{hkl}	2θ	d_{hkl}	2θ	d_{hkl}	2θ	d_{hkl}
					18.235	4.861		
					18.515	4.788		
					19.870	4.465		
1M 11-1; $2M_1$ 11-1	20.246	4.383			20.176	4.398	20.224	4.387
1M 02-1; $2M_1$ 02-2; Sa 20-1							21.332	4.162
$2M_1$ 02-3; ?Sa130	23.442	3.792	23.451	3.790			23.393	3.800
Sa130								
2M1 11-4; Ol 111; Sa 22-1	25.217	3.529	25.191	3.532	25.169	3.535	25.169	3.535
Sa 11-2								
Sa 220								
$2M_1$ 114; Sa 20-2	27.265	3.268	27.287	3.266	27.164	3.280	27.221	3.273
Sa 040								
							28.905	3.086
$2M_1$ 02-5	29.380	3.038	29.390	3.037	29.424	3.033	29.459	3.030
Sa 131								
$2M_1$ 11-6; $2M_2$ 11-6; Ol 130	31.690	2.821	31.763	2.815	31.719	2.819	31.715	2.819
					32.084	2.787		
Sa 24-1; $2M_2$ 31-3,02-2,311	34.991	2.562	34.978	2.563	34.965	2.564		
1M 131,20-2; $2M_1$ 13-3,202; Ol 131	35.889	2.500					35.803	2.506
$2M_2$ 31-4, 02-3, 312; Ol 112	36.485	2.461	36.504	2.459	36.417	2.465	36.384	2.467
	37.870	2.374						
$2M_2$ 31-5, 02-4, 313	38.330	2.346	38.339	2.346	38.322	2.347	38.331	2.346
1M 22-1; $2M_1$ ...; $2M_2$ ...;	39.355	2.288	39.315	2.290	39.350	2.288	39.335	2.289
1M 132,20-3; $2M_1$ ...; $2M_2$ ...	39.830	2.261	39.850	2.260	39.845	2.261	39.790	2.264
1M 04-1; $2M_2$ ...; $2M_1$ ...	40.303	2.236			40.266	2.238	40.314	2.235
$2M_2$ 31-7, 02-6; 1M 04-2; $2M_1$ 04-4	43.358	2.085	43.351	2.086	43.324	2.087	43.356	2.085
1M 22-4; $2M_1$ 226; $2M_2$ 317,02-8,226;Ol 113; Sa 113	49.747	1.831			49.806	1.829	49.768	1.831
1M 24-1,150; $2M_1$ 24-1; $2M_2$ 51-2	52.825	1.732	52.808	1.732	52.796	1.733	52.85	1.731
1M 31-2,...; $2M_1$ ...; $2M_2$ ...	53.352	1.716	53.323	1.717	53.347	1.716	53.295	1.718
1M 13-6,205; $2M_2$ ...; $2M_1$ ...	62.670	1.481	62.674	1.481	62.599	1.483	62.555	1.484
1M 062,331; $2M_1$ ...; $2M_2$ ...	63.493	1.464	63.484	1.464	63.448	1.465	63.500	1.464
1M 31-5, 313; $2M_1$ ...; $2M_2$ ...	65.434	1.425	65.326	1.427	65.497	1.424		
1M 225; $2M_1$ ...; $2M_2$ ...					66.167	1.411		

Impurity or Low-Intensity Peak Identification / Designation	$Mg_{2.1}Ni_{0.9}$JLR MER087		$Mg_{2.4}Ni_{0.6}$JLR MER084		$Mg_{2.7}Ni_{0.3}$JLR MER085		$Mg_{3.0}Ni_{0.0}$JLR MER128	
	2θ	d_{hkl}	2θ	d_{hkl}	2θ	d_{hkl}	2θ	d_{hkl}
							20.099	4.414
1M 11-1; $2M_1$ 11-1							20.650	4.298
1M 02-1; $2M_1$ 02-2; Sa 20-1							22.927	3.876
$2M_1$ 02-3; ?Sa130			23.374	3.803			23.385	3.801
Sa130							23.908	3.719
2M1 11-4; Ol 111; Sa 22-1	25.188	3.533	25.153	3.538			25.151	3.538
Sa 11-2							25.516	3.488
Sa 220							26.817	3.322
$2M_1$ 114; Sa 20-2			27.211	3.275			27.153	3.281
Sa 040							27.483	3.243
							28.975	3.079
$2M_1$ 02-5			29.295	3.046			29.318	3.044
Sa 131							29.877	2.988
							31.250	2.860
$2M_1$ 11-6; $2M_2$ 11-6; Ol 130			31.673	2.823			31.631	2.826
							32.380	2.763
Sa 24-1; $2M_2$ 31-3,02-2,311								
1M 131,20-2; $2M_1$ 13-3,202; Ol 131							35.757	2.509
$2M_2$ 31-4, 02-3, 312; Ol 112	36.447	2.463	36.400	2.466	36.342	2.470	36.301	2.473
							36.573	2.455
$2M_2$ 31-5, 02-4, 313			38.312	2.347			38.225	2.353
1M 22-1; $2M_1$ ...; $2M_2$ ...;	39.310	2.290	39.290	2.291	39.250	2.293	39.200	2.296
1M 132,20-3; $2M_1$ ...; $2M_2$ ...	39.840	2.261	39.770	2.265	39.725	2.267	39.730	2.267
1M 04-1; $2M_2$ ...; $2M_1$ ...	40.213	2.241	40.242	2.239			40.134	2.245
$2M_2$ 31-7, 02-6; 1M 04-2; $2M_1$ 04-4	43.305	2.088	43.263	2.090	43.254	2.090	43.237	2.091
							48.705	1.868
1M 22-4; $2M_1$ 226; $2M_2$ 317,02-8,226;Ol 113; Sa 113							49.631	1.835
1M 24-1,150; $2M_1$ 24-1; $2M_2$ 51-2	52.845	1.731	52.730	1.735	52.732	1.735	52.576	1.739
1M 31-2,...; $2M_1$ ...; $2M_2$ ...			53.321	1.717	53.307	1.717	53.211	1.720
							53.819	1.702
1M 13-6,205; $2M_2$ ...; $2M_1$ ...	62.685	1.481	62.607	1.483	62.520	1.484	62.089	1.494
1M 062,331; $2M_1$ ...; $2M_2$ ...	63.485	1.464	63.444	1.465	63.300	1.468	62.848	1.477
1M 31-5, 313; $2M_1$ ...; $2M_2$ ...			65.198	1.430			65.266	1.428
1M 225; $2M_1$ ...; $2M_2$ ...							66.085	1.413

Appendix H. Impurity reflections for the Fe-Mg JLR series

Impurity or Low-Intensity Peak Identification / Designation	$Fe_{0.0}Mg_{3.0}$JLR MER060		$Fe_{0.0}Mg_{3.0}$JLR MER067		$Fe_{0.6}Mg_{2.4}$JLR MER061		$Fe_{1.2}Mg_{1.8}$JLR MER166	
	2θ	d_{hkl}	2θ	d_{hkl}	2θ	d_{hkl}	2θ	d_{hkl}
1M 11-1; $2M_1$ 11-1; Ol 110	20.186	4.396			20.164	4.400	20.029	4.430
1M 02-1; $2M_1$ 02-2; Sa 20-1	21.223	4.183			21.513	4.127	21.072	4.213
$2M_1$ 02-3; ?Sa130					23.338	3.809	23.016	3.861
Sa130								
Sa13-1								
2M1 11-4; Ol 111; Sa 22-1								
Sa 11-2								
Sa 220							26.824	3.321
$2M_1$ 114; Sa 20-2					27.173	3.279	27.082	3.290
Sa 040								
Sa 00-2							27.587	3.231
$2M_1$ 02-5					29.338	3.042	29.338	3.042
Sa 131								
$2M_1$ 11-6; $2M_2$ 11-6; Ol 130					31.611	2.828		
$2M_2$ 31-4, 02-3, 312; Ol 112								
Sa 31-2								
Sa 24-1; $2M_2$ 31-3,02-2,311								
1M 131,20-2; $2M_1$ 13-3,202; Ol 131	35.858	2.502	35.800	2.506	35.784	2.507		
$2M_2$ 31-5, 02-4, 313					38.144	2.357	38.008	2.366
1M 22-1; $2M_1$ ...; $2M_2$ ...;	39.315	2.290	39.235	2.294	39.175	2.298	38.962	2.310
1M 132,20-3; $2M_1$ ...; $2M_2$ ...	39.700	2.269	39.652	2.271	39.615	2.273	39.466	2.281
1M 04-1; $2M_2$ ...; $2M_1$ ...	40.235	2.240	40.163	2.243	40.085	2.248		
$2M_2$ 31-7, 02-6; 1M 04-2; $2M_1$ 04-4; Mag 400	43.248	2.090	43.113	2.097	43.153	2.095	43.008	2.101
1M 22-4; $2M_1$ 226; $2M_2$ 317,02-8,226;Ol 113; Sa 113	49.796	1.830			49.610	1.836		
Sa 44-1								
Sa 20-4								
1M 24-1,150; $2M_1$ 24-1; $2M_2$ 51-2	52.124	1.753	52.052	1.756				
1M 31-2,...; $2M_1$ ...; $2M_2$ ...	52.706	1.735	52.74	1.734	52.542	1.740	52.319	1.747
Mag 511,333								
1M 13-6,205; $2M_2$ ...; $2M_1$ ...	62.620	1.482			62.415	1.487	62.403	1.487
1M 062,331; $2M_1$ ...; $2M_2$ ...; Mag 440	63.390	1.466			63.190	1.470	63.065	1.473
1M 31-5, 313; $2M_1$ ...; $2M_2$ ...								
1M 225; $2M_1$ ...; $2M_2$ ...	66.152	1.411			66.075	1.413		

Impurity or Low-Intensity Peak Identification / Designation	$Fe_{1.2}Mg_{1.8}$JLR MER062		$Fe_{1.8}Mg_{1.2}$JLR MER075		$Fe_{2.4}Mg_{0.6}$JLR MER076		$Fe_{3.0}Mg_{0.0}$JLR MER077	
	2θ	d_{hkl}	2θ	d_{hkl}	2θ	d_{hkl}	2θ	d_{hkl}
1M 11-1; $2M_1$ 11-1; Ol 110	20.100	4.414	19.981	4.440			19.931	4.451
1M 02-1; $2M_1$ 02-2; Sa 20-1	21.075	4.212					20.980	4.231
$2M_1$ 02-3; ?Sa130	23.288	3.817	23.215	3.828	23.517	3.780	23.498	3.783
Sa130								
Sa13-1							24.610	3.614
2M1 11-4; Ol 111; Sa 22-1			25.080	3.548	25.015	3.557	25.113	3.543
Sa 11-2								
Sa 220					26.822	3.321	26.815	3.322
$2M_1$ 114; Sa 20-2	27.163	3.280			27.042	3.295	27.136	3.283
Sa 040							27.382	3.255
Sa 00-2; ?Lct 400			**27.698**	**3.218**			27.682	3.220
$2M_1$ 02-5	29.288	3.047	29.093	3.067	29.463	3.029		
Sa 131	29.888	2.987					29.809	2.995
$2M_1$ 11-6; $2M_2$ 11-6; Ol 130	31.588	2.830						
$2M_2$ 31-4, 02-3, 312; Ol 112								
Sa 31-2							34.492	2.598
Sa 24-1; $2M_2$ 31-3,02-2,311							34.770	2.578
1M 131,20-2; $2M_1$ 13-3,202; Ol 131								
			35.99	2.493				
$2M_2$ 31-5, 02-4, 313	38.063	2.362	37.905	2.372	37.874	2.374	37.813	2.377
1M 22-1; $2M_1$ ...; $2M_2$ ...;	39.065	2.304	38.855	2.316	38.795	2.319	38.715	2.324
1M 132,20-3; $2M_1$ ...; $2M_2$ ...	39.600	2.274	39.445	2.283	39.365	2.287	39.365	2.287
1M 04-1; $2M_2$ ...; $2M_1$ ...	39.995	2.252	39.769	2.265				
$2M_2$ 31-7, 02-6; 1M 04-2; $2M_1$ 04-4; Mag 400	43.088	2.098	42.937	2.105	42.830	2.110	43.136	2.095
1M 22-4; $2M_1$ 226; $2M_2$ 317,02-8,226;Ol 113; Sa 113	49.538	1.839	49.287	1.847	49.179	1.851	49.278	1.848
Sa 20-4							50.851	1.794
1M 24-1,150; $2M_1$ 24-1; $2M_2$ 51-2			52.124	1.753	52.070	1.755	51.932	1.759
1M 31-2,...; $2M_1$ ...; $2M_2$ ...	52.400	1.745						
Mag 511,333							56.995	1.614
1M 13-6,205; $2M_2$ ...; $2M_1$ ...	62.370	1.488						
1M 062,331; $2M_1$ ...; $2M_2$ ...; Mag 440	62.940	1.476	62.700	1.481	62.555	1.484	62.509	1.485
1M 31-5, 313; $2M_1$ ...; $2M_2$ ...								
1M 225; $2M_1$ ...; $2M_2$ ...	65.963	1.415					65.140	1.431

Appendix I. Impurity reflections for the Fe-Mg RGB Al-normal series

Impurity or Low-Intensity Peak Identification / Designation	$Fe_{0.75}Mg_{2.25}RGB$ MER098		$Fe_{1.5}Mg_{1.5}RGB$ MER100		$Fe_{2.25}Mg_{0.75}RGB$ MER097		$Fe_{3.0}Mg_{0.0}RGB$ BI25AC	
	2θ	d_{hkl}	2θ	d_{hkl}	2θ	d_{hkl}	2θ	d_{hkl}
1M 11-1; $2M_1$ 11-1; Ol 110			20.003	4.435	19.943	4.449	19.862	4.466
1M 02-1; $2M_1$ 02-2; Sa 20-1	21.047	4.218	21.026	4.222	21.003	4.226	20.980	4.231
$2M_1$ 02-3; ?Sa130	23.348	3.807	23.485	3.785	23.046	3.856		
Sa130					23.543	3.776	23.509	3.781
2M1 11-4; Ol 111; Sa 22-1	25.094	3.546	25.012	3.557	25.103	3.545	25.065	3.550
Sa 11-2								
Sa 220	26.850	3.318			26.818	3.322	26.838	3.319
$2M_1$ 114; Sa 20-2	27.120	3.285	27.076	3.291	27.165	3.280	27.177	3.279
Sa 040	27.357	3.257	27.375	3.255	27.362	3.257	27.397	3.253
Sa 00-2	27.680	3.220	27.646	3.224	27.643	3.224	27.671	3.221
Kls 102							28.610	3.118
$2M_1$ 02-5; Ol 121,002	29.265	3.049	29.180	3.058			29.180	3.058
Sa 131							29.827	2.993
Sa 04-1,02-2							30.780	2.903
$2M_1$ 11-6; $2M_2$ 11-6; Ol 130	31.626	2.827	31.508	2.837	31.687	2.822	31.632	2.826
Sa 13-2							32.388	2.762
Sa 31-2							34.397	2.605
Kls 110; Sa 24-1; $2M_2$ 31-3,02-2,311	34.818	2.575	34.615	2.589			34.758	2.579
1M 131,20-2; $2M_1$ 13-3,202; Ol 131							34.999	2.562
$2M_2$ 31-4, 02-3, 312; Ol 112	36.327	2.471	36.171	2.481			35.931	2.497
							37.312	2.408
$2M_2$ 31-5, 02-4, 313	38.030	2.364	37.924	2.371	37.818	2.377	37.673	2.386
1M 22-1; $2M_1$ ...; $2M_2$ ...;	39.055	2.304	38.860	2.316	38.740	2.323	38.505	2.336
1M 132,20-3; $2M_1$ ...; $2M_2$ ...	39.615	2.273	39.455	2.282	39.375	2.287	39.235	2.294
1M 04-1; $2M_2$ ...; $2M_1$ ...	40.025	2.251	39.836	2.261	39.702	2.268	39.534	2.278
$2M_2$ 31-7, 02-6; 1M 04-2; $2M_1$ 04-4	43.097	2.097	43.018	2.101	42.937	2.105	42.775	2.112
1M 22-4; $2M_1$ 226; $2M_2$ 317,02-8,226;Ol 113; Sa 113			49.360	1.845	49.171	1.851	49.336	1.846
Sa 20-4					50.831	1.795	50.903	1.792
Sa 44-1; Ol 222,240					51.487	1.773	51.397	1.776
1M 24-1,150; $2M_1$ 24-1; $2M_2$ 51-2	52.467	1.743	52.217	1.750				
1M 31-2,...; $2M_1$ ...; $2M_2$ ...			53.486	1.712				
Sa 46-1; Ol 062							61.013	1.517
1M 13-6,205; $2M_2$ ...; $2M_1$ ...	62.425	1.486	62.228	1.491	62.296	1.489		
1M 062,331; $2M_1$ ...; $2M_2$ ...	63.187	1.470					62.144	1.492
1M 31-5, 313; $2M_1$ ...; $2M_2$ ...			65.111	1.431				
1M 225; $2M_1$ ...; $2M_2$ ...	66.057	1.413						

Appendix J. Impurity reflections for the Fe-Mg RGB Al-poor series

Impurity or Low-Intensity Peak Identification / Designation	$Fe_{25}Mg_{75}$RGB_poor MER116		$Fe_{50}Mg_{50}$RGB_Al-poor MER118		$Fe_{75}Mg_{25}$RGB_Al-poor MER117		Fe_{100}RGB_Al-poor MER101	
	2θ	d_{hkl}	2θ	d_{hkl}	2θ	d_{hkl}	2θ	d_{hkl}
Sa 222							46.004	1.971
$2M_2$ 31-9,317,02-8	49.505	1.840	49.370	1.844				
Sa 043,20-4							50.835	1.795
?1M 223	51.454	1.775	51.308	1.779				
?1M 134,20-5,115	51.863	1.762						
?1M 150,24-1	52.421	1.744	52.146	1.753	51.943	1.759		
?1M 310,31-2	53.110	1.723	52.971	1.727				
?1M 151,24-2			53.556	1.710	53.291	1.718	53.086	1.724
1M 006	54.136	1.693						
?$2M_2$ 31-11,319,02-10					56.678	1.623	56.567	1.626
1M 116	61.092	1.516	61.063	1.516	61.030	1.517	61.004	1.518
1M 06-2,331	63.162	1.471	62.708	1.480				
?$2M_2$ 31-13,31.11,02-12			65.100	1.432	64.949	1.435		
1M 225	65.874	1.417	65.773	1.419	65.623	1.422		
1M 02-7	67.634	1.384	67.571	1.385	67.467	1.387		
1M 04-6	68.653	1.366	68.521	1.368	68.381	1.371		
1M 40-1,26-1	70.590	1.333	70.255	1.339	69.912	1.344		
1M 170	73.884	1.282	73.535	1.287				
1M 226	74.507	1.273	74.389	1.274	74.278	1.276		

Appendix K. Impurity reflections for the Fe-Mg RGB Al-rich series

Impury or Low-intensity Peak Identification / Designation	$Fe_{25}Mg_{75}$RGB-Bi33r MER096		$Fe_{50}Mg_{50}$RGB-Bi38 MER095		$Fe_{75}Mg_{25}$RGB-Bi32r MER094	
	2θ	d_{hkl}	2θ	d_{hkl}	2θ	d_{hkl}
1M 11-1; $2M_1$ 111; $2M_2$ 20-2,111	20.186	4.396			20.128	4.408
1M 02-1; $2M_1$ 02-2	21.200	4.188	21.202	4.187	21.125	4.202
$2M_1$ 02-3					23.240	3.824
$2M_1$&$2M_2$ 11-4; Ol 111					25.084	3.547
Cor 012	25.630	3.473				
$2M_1$&$2M_2$ 114	27.272	3.267	27.208	3.275	27.220	3.274
$2M_1$ 02-5	29.448	3.031	29.398	3.036	29.347	3.041
Alm 400			31.094	2.874		
$2M_1$&$2M_2$ 11-6			31.625	2.827		
Cor 104	35.175	2.549				
Cor 110; 1M 20-2,131; $2M_1$ 13-3,202	35.813	2.505				
1M 11-4	37.813	2.377	37.844	2.375		
$2M_2$ 31-5,02-4,313			38.162			
1M 04-1			40.082	2.248	40.783	2.211
1M 04-2; $2M_1$ 04-4; $2M_2$ 315,31-7,02-6					43.073	2.098
Cor 113	43.353	2.085	43.347	2.086		
?1M 134,20-5	52.139	1.753	52.121	1.753		
?1M 150,24-1					52.438	1.744
Cor 024	52.666	1.737	52.614	1.738		
?1M 310,31-2					53.219	1.720
Cor 116	57.554	1.600	57.555	1.600		

Fe_{100}RGB-Bi35 MER102					
Identification	2θ	d_{hkl}	Identification	2θ	d_{hkl}
Fa 020	16.944	5.229	Fa 113,151	49.567	1.838
1M 11-1; $2M_1$ 111; $2M_2$ 20-2,111	20.279	4.376	Fa 222	51.382	1.777
1M 02-1; $2M_1$ 02-2	21.061	4.215	Fa 240	51.519	1.772
Fa 111	25.082	3.548	?1M 150,24-1	52.113	1.754
Fa 121,002	29.303	3.045	?1M 151,24-2	53.453	1.713
Alm 400	30.952	2.887	Fa 241	53.939	1.699
Fa 130	31.638	2.826	Fa 133	55.720	1.648
Fa 131; Alm 420	34.989	2.562	Fa 004	60.841	1.521
Fa 112	35.928	2.498	Fa 171	61.147	1.514
Fa 240,041	37.366	2.405	Fa 330	63.722	1.459
1M 11-4	37.936	2.370	Fa 170	65.232	1.429
Fa 210	38.337	2.346			
Fa 140	39.161	2.299			
1M 04-1	39.699	2.269			
1M 22-2	40.550	2.223			
1M 04-2; $2M_1$ 04-4; $2M_2$ 315,31-7,02-6	43.194	2.093			

K2

Impury or Low-intensity Peak Identification / Designation	$Fe_{25}Mg_{75}$RGB-Bi31 MER104		$Fe_{75}Mg_{25}$RGB-Bi30 MER103	
	2θ	d_{hkl}	2θ	d_{hkl}
1M 11-1; $2M_1$ 111; $2M_2$ 20-2,111	20.201	4.392	20.163	4.400
Ks 002	20.421	4.345	20.435	4.343
1M 02-1; $2M_1$ 02-2	21.217	4.184	21.106	4.206
Ks 101	22.368	3.971	22.398	3.966
$2M_1$ 02-3	23.263	3.821	23.323	3.811
$2M_1$&$2M_2$ 11-4; ?OI 111	25.150	3.538	25.188	3.533
$2M_1$&$2M_2$ 114	27.250	3.270	27.145	3.282
Ks 102	28.622	3.116	28.639	3.114
$2M_1$ 02-5	29.375	3.038	29.432	3.032
$2M_1$&$2M_2$ 11-6; OI 130			31.668	2.823
1M 130,20-1	33.961	2.638		
Ks 110	34.776	2.578	34.775	2.578
1M 20-2,131; $2M_1$ 13-3,202; ?OI 131	35.833	2.504		
$2M_2$ 312,02-3,31-4; ?OI 112			36.315	2.472
1M&$2M_1$ 11-4			37.973	2.368
1M 04-1	40.254	2.239		
1M 22-2			40.707	2.215
1M 221			41.780	2.160
1M 04-2; 2M1 04-4; 2M2 315,31-7,02-6	43.212	2.092	43.045	2.100
?1M 134,20-5	52.089	1.754		
?1M 150,24-1	52.775	1.733	52.389	1.745
?1M 310,31-2	53.531	1.710		
?1M 151,24-2			53.756	1.704
?1M 225	66.279	1.409	66.254	1.410

K3

Appendix L. Impurity reflections for the Fe-Ni GR series

Impurity or Low-Intensity Peak Identification / Designation	$Fe_{0.0}Ni_{3.0}GR$ MER155		$Fe_{0.2}Ni_{2.8}GR$ MER156		$Fe_{0.6}Ni_{2.4}GR$ MER113		$Fe_{1.0}Ni_{2.0}GR$ MER159	
	2θ	d_{hkl}	2θ	d_{hkl}	2θ	d_{hkl}	2θ	d_{hkl}
1M 11-1; $2M_1$ 111; $2M_2$ 20-2,111; Ol 110	20.179	4.397			20.099	4.414	20.095	4.415
1M 02-1; $2M_1$ 02-2; Sa 20-1	20.985	4.230	b.d.l.		21.184	4.191	21.125	4.202
							21.778	4.078
$2M_1$ 02-3; Sa130	23.479	3.786			23.347	3.807	23.263	3.821
$2M_1$&$2M_2$ 11-4; Ol 111; Sa 22-1	25.210	3.530			25.172	3.535	25.063	3.550
Sa 220								
$2M_1$&$2M_2$ 114; Sa 20-2					27.152	3.282	27.061	3.292
Sa 040								
Sa 00-2	27.628	3.226						
$2M_1$ 02-5; Ol 121,002	29.345	3.041			29.383	3.037	29.279	3.048
Sa 131	29.708	3.005						
$2M_1$&$2M_2$ 11-6; Ol 130	31.725	2.818			31.702	2.820	31.604	2.829
Sa 24-1; $2M_2$ 31-3,02-2,311							34.741	2.580
1M 131,20-2; $2M_1$ 13-3,202; Ol 131					35.773	2.508		
1M 11-4; $2M_1$ 117;$2M_2$ 31-5, 02-4, 313	38.280	2.349			38.207	2.354	38.095	2.360
1M 04-1	40.260	2.238			40.128	2.245	40.000	2.252
$2M_2$ 31-7, 02-6,315; 1M 04-2; $2M_1$ 04-4	43.359	2.085			43.284	2.089	43.170	2.094
$2M_2$ 31-9, 02-8, 317	49.808	1.829			49.656	1.835	49.571	1.837
?1M 223							51.570	1.771
?1M 20-5,134,115					51.992	1.757		
?1M 24-1,150					52.638	1.737	52.369	1.746
?1M 31-2,310					53.302	1.717		
1M 13-6,205; $2M_2$ ...; $2M_1$ ...	62.575	1.483			62.523	1.484	62.400	1.487
1M 062,331; $2M_1$ ...; $2M_2$ ...	63.429	1.465			63.235	1.469	63.017	1.474
$2M_2$ 31-13,31.11,02-12	65.596	1.422			65.418	1.425	65.260	1.429
1M 225; $2M_1$ ...; $2M_2$ ...	66.225	1.410			66.096	1.413	66.010	1.414

Impurity or Low-Intensity Peak	$Fe_{1.4}Ni_{1.6}GR$ MER158		$Fe_{1.8}Ni_{1.2}GR$ MER162		$Fe_{2.2}Ni_{0.8}GR$ MER163		$Fe_{2.6}Ni_{0.4}GR$ MER164	
	2θ	d_{hkl}	2θ	d_{hkl}	2θ	d_{hkl}	2θ	d_{hkl}
1M 11-1; $2M_1$ 11-1; OI 110	20.017	4.432	19.964	4.444	19.908	4.456	20.214	4.389
1M 02-1; $2M_1$ 02-2; Sa 20-1	21.067	4.214	21.010	4.225	20.954	4.236	20.923	4.242
$2M_1$ 02-3; Sa130	23.308	3.813	23.191	3.832	23.473	3.787	23.454	3.790
$2M_1$&$2M_2$ 11-4; OI 111; Sa 22-1			25.014	3.557	24.936	3.568	24.922	3.570
Sa 220					26.804	3.323	26.810	3.323
$2M_1$&$2M_2$ 114; Sa 20-2	27.106	3.287	26.987	3.301			26.974	3.303
Sa 040			27.261	3.269				
Sa 00-2					27.622	3.227	27.578	3.232
$2M_1$ 02-5; OI 121,002	29.253	3.050	29.222	3.054	29.162	3.060		
Sa 131							29.742	3.001
$2M_1$&$2M_2$ 11-6; OI 130	31.553	2.833	31.569	2.832	31.548	2.834		
Sa 24-1; $2M_2$ 31-3,02-2,311	34.643	2.587	34.592	2.591	34.516	2.596		
1M 131,20-2; $2M_1$ 13-3,202; OI 131								
1M 11-4; $2M_1$ 117;$2M_2$ 31-5, 02-4, 313	38.020	2.365	37.928	2.370	37.837	2.376	37.824	2.377
1M 04-1	39.902	2.258	39.797	2.263	39.720	2.267	39.638	2.272
$2M_2$ 31-7, 02-6,315; 1M 04-2; $2M_1$ 04-4	43.073	2.098	43.007	2.101	42.899	2.106		
$2M_2$ 31-9, 02-8, 317	49.523	1.839	49.393	1.844	49.318	1.846		
?1M 223	51.458	1.774						
?1M 20-5,134,115								
?1M 24-1,150	52.346	1.746	52.115	1.754	52.012	1.757		
?1M 31-2,310								
1M 13-6,205; $2M_2$ ...; $2M_1$ ...	62.371	1.488	62.274	1.490	62.222	1.491		
1M 062,331; $2M_1$ ...; $2M_2$ ...	62.929	1.476	62.694	1.481	62.563	1.484		
$2M_2$ 31-13,31.11,02-12			65.126	1.431				
1M 225; $2M_1$ ...; $2M_2$ ...	65.921	1.416	65.850	1.417				

Appendix M. Impurity reflections for the annite-fluoroannite series

Impurity or Low-Intensity Peak Identification / Designation	Ann-$F_{0.0}(OH)_{2.0}$ MER090		Ann-$F_{0.4}(OH)_{1.6}$ MER091		Ann-$F_{0.8}(OH)_{1.2}$ MER088		Ann-$F_{1.0}(OH)_{1.0}$ MER092	
1M 11-1; $2M_1$ 111; $2M_2$ 20-2,111	19.885	4.461	19.960	4.445	19.932	4.451	20.001	4.436
1M 02-1; $2M_1$ 02-2; Sa 20-1	20.982	4.231	20.970	4.233			21.109	4.205
Sa130	23.492	3.784	23.502	3.782				
Fa 111; Sa 22-1	25.029	3.555	25.030	3.555			25.064	3.550
Sa 220	26.817	3.322	26.814	3.322				
$2M_1$&$2M_2$ 114; Sa 20-2	27.173	3.279	27.118	3.286	27.163	3.280	27.215	3.274
Sa 040	27.398	3.253	27.382	3.255	27.386	3.254		
Sa 00-2	27.670	3.221	27.636	3.225	27.652	3.223		
$2M_1$ 02-5; OI 121,002	29.126	3.064			29.493	3.026	29.475	3.028
Sa 131	29.801	2.996	29.828	2.993	29.854	2.990		
Sa 04-1	30.754	2.905						
$2M_1$&$2M_2$ 11-6; Fa 130	31.654	2.824	31.629	2.827	31.674	2.823	31.653	2.824
Sa 13-2; $2M_2$ 31-3,02-2,311	34.420	2.603	34.505	2.597	34.516	2.596	34.538	2.595
Sa 24-1	34.738	2.580						
1M 131,20-2; $2M_1$ 13-3,202;							35.493	2.527
Fa 112; 2M2 31-4,312,02-3			35.950	2.496				
1M 11-4; $2M_1$ 117;$2M_2$ 31-5, 02-4, 313	37.735	2.382	37.938	2.370	37.996	2.366	38.020	2.365
1M 220							39.125	2.301
$2M_2$ 31-7, 02-6,315; 1M 04-2; $2M_1$ 04-4	42.750	2.113	43.028	2.100	43.283	2.089	43.179	2.093
$2M_2$ 31-9, 02-8, 317	49.226	1.850	49.373	1.844	49.517	1.839	49.733	1.832
Sa 043,20-4	50.885	1.793	50.896	1.793	50.867	1.794		
Sa 44-1	51.410	1.776	51.432	1.775				
?1M 24-1,150	51.870	1.761	51.976	1.758	51.952	1.759	52.028	1.756
?1M 24-2,151					53.450	1.713	53.591	1.709
1M 311,31-3	55.111							
1M 24-3,152	56.264		56.350	1.631	56.605	1.625	56.519	1.627
$2M_2$ 31-11,02-10,319			56.967	1.615	57.250	1.608	57.332	1.606
1M 15-3,242	57.492		57.836	1.593	57.900	1.591	57.940	1.590

M1

Impurity or Low-Intensity Peak Identification / Designation	Ann-$F_{1.1}(OH)_{0.9}$ MER093		Ann-$F_{1.2}(OH)_{0.8}$ MER086	Ann-$F_{1.6}(OH)_{0.4}$ MER114
1M 11-1; $2M_1$ 111; $2M_2$ 20-2,111	19.952	4.447		19.996
$2M_1$&$2M_2$ 11-4; Fa 111; Sa 22-1	25.134	3.540		25.034
$2M_1$&$2M_2$ 114; Sa 20-2	27.271	3.268		
Sa 040	27.507	3.240		
Tpz 120				27.928
$2M_1$ 02-5; Fa 121,002				29.461
Sa 131				29.922
$2M_1$&$2M_2$ 11-6; Fa 130	31.758	2.815		
1M 131,20-2; $2M_1$ 13-3,202;	35.481	2.528		35.494
1M 11-4; $2M_1$ 117;$2M_2$ 31-5, 02-4, 313	38.050	2.363		
1M 22-2				40.538
Tpz 123; 1M 04-2; $2M_1$ 04-4				42.908
$2M_2$ 31-7, 02-6,315; 1M 04-2; $2M_1$ 04-4	43.238	2.091		
?				44.0525
$2M_2$ 31-9, 02-8, 317	49.821	1.829		50.024
?1M 24-1,150	52.001	1.757		52.045
?1M 24-2,151				53.504
1M 006	55.101	1.665		55.189

M2

Appendix N. Impurity reflections for the annite-oxyannite-ferrioxyannite series

The impurity reflections observed in the diffractograms of these samples are reported in [Rancourt *et al.* 2001].

Appendix O. Mössbauer fitting parameters for RT thickness corrected spectra

Sample	A-/A+	BGD-fit counts	<Fe^{3+}>/Fe %	[Fe^{3+}]/Fe %	[Fe^{2+}]/Fe cnts * mm/s	$A_{<3+>}$	$A_{[3+]}$	$A_{[2+]}$	δ_0-[Fe2+] mm/s	δ_1-[Fe2+]	δ_0-[Fe3+] mm/s	δ_0-<Fe3+>
$Fe_{1.2}Mg_{1.8}$JLR	1	1362770	2.52	14.21	83.26	11100	62400	365600	1.1329	-0.0050	0.4180	0.2380
$Fe_{1.8}Mg_{1.2}$JLR	1	1594980	3.69	11.38	84.9	12700	39300	293000	1.1014	0.0071	0.3850	0.2460
$Fe_{2.4}Mg_{0.6}$JLR	1	1556450	4.4	13.11	82.49	21100	63000	396400	1.1266	-0.0026	0.4080	0.2130
$Fe_{0.75}Mg_{2.25}$RGB	1	1192480	3.2	3.5	93.3	5500	6000	159400	1.1077	0.0053	0.2900	0.2410
$Fe_{1.5}Mg_{1.5}$RGB	1	2434750	5.08	2.23	92.7	29200	12800	532700	1.1143	0.0051	0.4960	0.2240
$Fe_{2.25}Mg_{0.75}$RGB	1	809390	7.82	2.47	89.71	19620	6200	225000	1.0340	0.0097	0.4800	0.1700
$Fe_{3.0}Mg_{0.0}$RGB	1	1455820	6.57	3.08	90.35	32600	15300	449100	0.9786	0.0584	0.4810	0.2560
$Fe_{25}Mg_{75}$Bi33rRGB	1	1788010	-	2.42	97.58	-	5430	219400	1.1110	0.0022	0.5220	-
$Fe_{50}Mg_{50}$Bi38rRGB	1	2342770	-	4.85	95.15	-	20900	410200	1.0883	0.0124	0.5730	-
$Fe_{75}Mg_{25}$Bi32rRGB	1	822900	-	1.86	98.14	-	3830	202200	1.0916	0.0105	0.5670	-
Fe_{100}Bi35rRGB	1	1104250	-	5.26	94.74	-	18600	333900	0.9390	0.0688	0.5180	-
$Fe_{25}Mg_{75}$Bi31rRGB	1	2366490	-	10.88	89.12	-	30400	249500	1.0350	0.0228	0.3200	-
$Fe_{75}Mg_{25}$Bi30rRGB	1	2578100	-	3.51	96.49	-	18600	511500	1.1083	0.0012	0.4000	-

<Δ>-<Fe3+>	σ_Δ-<Fe3+>	<Δ>-[Fe3+]	σ_Δ-[Fe3+]	<Δ>-[Fe2+]-1	σ_Δ-[Fe2+]-1	p-1	<Δ>-[Fe2+]-2	σ_Δ-[Fe2+]-2	p-2	<Δ>-[Fe2+]-3	σ_Δ-[Fe2+]-3	p-3
mm/s	mm/s	mm/s	mm/s	mm/s	mm/s	%	mm/s	mm/s	%	mm/s	mm/s	%
0.332	0.163	0.929	0.472	2.6447	0.0942	38.1678	2.5045	0.2540	47.5	2.2120	0.3980	14.37
0.362	0.218	0.980	0.479	2.6519	0.0914	53.3151	2.5328	0.2603	39.7	2.1100	1.0600	6.98
0.298	0.214	0.975	0.413	2.6156	0.0978	37.0565	2.4440	0.2430	45.8	2.1070	0.9850	17.4
0.343	0.170	0.830	0.460	2.6712	0.1030	56.27	2.6090	0.2580	38.6	2.2600	1.3500	5.1
0.448	0.170	0.608	0.340	2.6867	0.1054	52.684	2.1300	1.2200	6.41	2.5975	0.2690	40.9
0.426	0.345	0.907	0.171	2.6718	0.0870	31.217	1.1960	1.3900	12.33	2.5657	0.2633	56.4
0.332	0.154	0.794	0.181	2.6050	0.1060	18.1134	2.0410	1.0750	15.96	2.5770	0.2810	65.9
-	-	0.560	0.290	2.5616	0.1262	50.0099	2.3470	0.3060	35	2.2600	0.6600	15
-	-	0.942	0.940	2.5626	0.1273	55.9431	2.3190	0.2430	17.3	2.1850	0.5610	26.7
-	-	0.586	0.242	2.5655	0.1316	50.7617	2.3340	0.3770	37.9	2.1130	0.9400	11.3
-	-	0.676	0.302	2.5950	0.2620	68.1267	1.9200	0.5960	15.4	2.6210	0.0890	16
-	-	0.689	0.481	2.1530	0.2760	27.1412	2.5000	0.7000	6.9	2.5142	0.1342	66
-	-	0.900	0.820	2.2020	0.2500	14.7818	2.1510	0.4920	22.6	2.5324	0.1358	62.6

Appendix P. Database of 1*M* crystal structure refinements

	Ref.		Samples	a	b	c	β
1	Brigatti & Davoli 1990	Bt	M14	5.343	9.258	10.227	100.26
2			M32	5.346	9.252	10.238	100.02
3			M13	5.355	9.251	10.246	100.15
4			M73	5.345	9.258	10.222	100.23
5			M62	5.337	9.242	10.211	100.15
6	Bigi & Brigatti 1994	Bt	M7	5.335	9.244	10.206	100.08
7	Brigatti *et al*. 1996a	ferri-Phl	S1	5.362	9.288	10.321	99.99
8			S2	5.3649	9.2924	10.3255	99.988
9	Brigatti *et al*. 1996b	Fe^{3+}-rich Phl	1	5.318	9.214	10.279	100.01
10			2	5.33	9.2346	10.301	99.92
11			3	5.333	9.238	10.267	99.96
12			4	5.329	9.228	10.258	100.03
13			5	5.3405	9.244	10.253	100.09
14			6	5.321	9.211	10.287	99.93
15			7	5.33	9.23	10.256	99.92
16			8	5.318	9.219	10.274	99.88
17			9	5.338	9.247	10.3	99.96
18			10	5.332	9.239	10.291	99.94
19			11	5.357	9.27	10.319	99.96
20			12	5.358	9.277	10.308	99.99
21			13	5.356	9.284	10.309	100.03
22	Donnay *et al*. 1964	syn	ferriannite	5.43	9.404	10.341	100.066
23	Hazen & Burnham 1973		Phl	5.3078	9.1901	10.1547	100.08
24			Ann	5.386	9.3241	10.2683	100.63
25	Russel & Guggenheim 1999		Phl	5.303	9.1805	10.2483	100.05
26			Bt-untreated	5.3346	9.2417	10.182	100.26
27			Bt-heat-treated	5.3099	9.185	10.093	100.07
28	Guggenheim 1981	Lepidolite	Radkovice	5.209	9.011	10.149	100.77
29	Hawthorne *et al*. 1999		Phl (Rb,Cs)	5.343	9.247	10.397	100.04
30	Hazen *et al*. 1981		trioc mica	5.329	9.23	10.2191	99.98
31	Joswig 1972		Phl	5.3141	9.2024	10.1645	100.05
32	Kato *et al*. 1979	Mn-Bt	No. 0	5.392	9.342	10.365	100.29
33		MnBaPhl	No. 1	5.380	9.295	10.318	99.96
34		MnBaPhl	No. 2	5.349	9.241	10.282	99.96
35		MnBaPhl	No. 5	5.330	9.245	10.24	99.92
36		kinoshitalite	No. 6	5.345	9.250	10.256	99.99
37	Brigatti *et al*. 2000a	Al-rich Bt	A4	5.352	9.268	10.255	100.27
38			GFS15a	5.339	9.232	10.208	100.3
39			H87	5.344	9.256	10.237	100.27
40			CC1	5.328	9.222	10.197	100.26
41			C3-31	5.347	9.257	10.211	100.27
42			B1	5.336	9.239	10.200	100.29
43	Knurr & Bailey 1986		Phl	5.316	9.221	10.282	99.90
44	Comodi *et al*. 1999	syn	No.1	5.486	9.506	10.818	99.67
45	Cs-ferriannite	"	No.2	5.480	9.498	10.820	99.76
46	MacKinney *et al*. 1988	clintonite	No.1	5.197	9.002	9.812	100.32
47			No.2	5.199	9.005	9.812	100.30
48			No.3	5.200	9.005	9.779	100.30
49	McCauley *et al*. 1973	syn	F-Phl	5.308	9.183	10.139	100.07

50	McCauley & Newham 1973	syn	BaLi-trioc	5.2858	9.1575	10.0375	100.124
51	Oberti *et al*. 1993	preiswerkite	KP9	5.225	9.050	9.791	100.27
52			KP17	5.228	9.049	9.819	100.4
53	Ohta *et al*. 1982		oxy-Bt	5.3204	9.210	10.104	100.102
54	Rayner 1974		Phl	5.322	9.206	10.24	100.03
55	Redhammer *et al*. 2000	syn, Rietveld	A44	5.3899	9.3367	10.3086	100.16
56	Ann-Syd	"	sd12no.12	5.3944	9.3454	10.3284	100.22
57		"	sd25no.10	5.3883	9.3365	10.3092	100.2
58		"	sd37no.10	5.3812	9.3234	10.2934	100.22
59		"	sd50no.10	5.3732	9.3097	10.2807	100.24
60		"	sd62no.10	5.3635	9.2929	10.2837	100.28
61		"	sd75no.10	5.3607	9.2874	10.2664	100.3
62		"	sd87no.10	5.3582	9.2819	10.2688	100.39
63		Syd	G-117	5.377	9.308	10.283	100.22
64	Robert & Gaspérin 1985	Zn-mica	hendricksite	5.340	9.254	10.235	100.07
65	Sartori 1976		Lepidolite	5.20	9.01	10.09	99.28
66	Takeda & Donnay 1966	syn	Li-F-mica	5.31	9.21	10.13	100.02
67	Takeda & Ross 1975		hy-Bt	5.331	9.231	10.173	100.16
68	Takéuchi 1965	syn	clintonite	5.194	9.003	9.802	100.1
69	Tateyama *et al*. 1974	syn	oct-vac	5.321	9.238	10.287	100.06
70	Toraya *et al*. 1977	syn	taeniolite	5.231	9.065	10.140	99.86
71	Toraya *et al*. 1978a	syn	Ge-mtm-like	5.421	9.353	10.533	100.14
72		"	Ge-taeniolite	5.395	9.341	10.547	99.87
73	Toraya *et al*. 1976	syn	mtm	5.253	9.086	10.159	99.89
74	Toraya *et al*. 1983	syn	Mn-F-Mg-mica	5.285	9.157	10.190	99.97
75	Toraya *et al*. 1978b	syn	Ge-Phl	5.417	9.345	10.468	100.03
76	Toraya & Marumo 1983	syn	Mg-Ge-F-mica	5.413	9.368	10.531	99.88
77	Toraya *et al*. 1978c	syn	F-Ph-like	5.292	9.164	10.143	100.07
78	Toraya & Marumo 1981	syn	x=.68	5.435	9.413	10.458	100.03
79	KMg[3-x]Mn[x]Ge3AlO10F2	"	x=1.96	5.489	9.509	10.462	100.12
80	Tyrna & Guggenheim 1991		norrishite	5.289	8.914	10.062	98.22
81	Guggenheim & Frimmel 1999		ferrokinoshitalite	5.389	9.337	10.054	100.53
82	Cruciani & Zanazzi 1994	Phl	1	5.325	9.236	10.242	100.12
83			2	5.313	9.210	10.286	99.91
84			3	5.321	9.219	10.124	100.15
85			4	5.327	9.228	10.217	100.05
86			5	5.324	9.217	10.230	100.04
87			6	5.316	9.202	10.212	100.12
88			7	5.310	9.200	10.277	99.92
89			8	5.315	9.200	10.193	100.01
90			9	5.317	9.211	10.228	100.01
91			10	5.319	9.217	10.208	100.03
92			11	5.319	9.212	10.251	100.04
93			12	5.330	9.229	10.196	100.06
94			14	5.320	9.218	10.217	100.11
95			15	5.335	9.242	10.202	100.05
96			16	5.322	9.223	10.190	100.02
97			17	5.334	9.240	10.225	100.06
98			18	5.314	9.204	10.182	100.03
99			19	5.338	9.244	10.259	100.12
100			21	5.336	9.244	10.089	100.29

101			22	5.336	9.245	10.079	100.30
102			23	5.337	9.249	10.096	100.31
103			24	5.339	9.251	10.298	99.86
104			25	5.337	9.243	10.298	99.92
105			26	5.331	9.228	10.240	100.02
106	Brigatti *et al*. 1991	Ti-Bt	8	5.317	9.207	10.232	99.98
107			9	5.306	9.190	10.163	100.11
108			10	5.322	9.228	10.102	100.25
109			11	5.315	9.204	10.168	100.13
110			12	5.314	9.190	10.160	100.18
111			15	5.329	9.235	10.190	100.20
112			16	5.333	9.256	10.186	100.17
113			17	5.323	9.215	10.210	100.14
114	Brigatti & Poppi 1993	Ba-rich trioc	18	5.320	9.207	10.100	100.24
115			19	5.331	9.230	10.160	100.19
116			20	5.323	9.219	10.219	100.03
117			21	5.326	9.222	10.223	100.04
118			22	5.330	9.245	10.192	100.35
119			23	5.328	9.219	10.233	99.88
120			24	5.328	9.224	10.247	100.01
121			25	5.333	9.241	10.180	100.10
122			26	5.322	9.209	10.163	100.17
123			27	5.318	9.214	10.164	100.11
124	Alietti *et al*. 1995	high-Al Phl	Phl1a	5.306	9.195	10.272	100.01
125			Phl1b	5.309	9.180	10.291	100.00
126			Phl2a	5.305	9.189	10.286	99.96
127			Phl3a	5.299	9.179	10.279	99.90
128			Phl4a	5.307	9.199	10.291	99.89
129	Alietti *et al*. 1997	clintonite	Cli5a	5.200	9.005	9.795	100.24
130			Cli7c	5.198	9.006	9.796	100.21
131			Cli8a	5.194	8.995	9.788	100.23
132			Cli8d	5.203	9.026	9.811	100.27
133			Cli9a	5.192	9.003	9.794	100.17
134			Cli9b	5.202	9.005	9.816	100.30
135	Brigatti *et al*. 2001	trioc	Tpp16-6a	5.330	9.239	10.305	99.89
136			Tax27-1	5.351	9.267	10.311	99.99
137			Taa11-1A	5.329	9.244	10.271	99.97
138			Tai17-1	5.3355	9.2457	10.294	99.94
139			Ta9	5.344	9.259	10.280	100.01
140			Li12a	5.331	9.227	10.275	99.96
141			Tpp16-6b	5.360	9.293	10.314	100.01
142			Tpp16-6c	5.3637	9.2908	10.321	99.995
143			Ma1	5.317	9.208	10.118	100.15
144	Takeda & Burnham 1969	syn	F-polylithionite	5.188	8.968	10.029	100.45
145	Tepikin *et al*. 1969		Bt	5.366	9.311	10.16	100.17
146	Semenova *et al*. 1977		tetraferri-Phl	5.358	9.297	10.318	100.02
147	Soboleva *et al*. 1977		paragonite	5.135	8.89	9.74	99.67
148	Semenova *et al*. 1983		tetraferri-Phl	5.341	9.259	10.297	99.95
149			tetraferri-Bt	5.373	9.311	10.306	100.1
150	Brigatti *et al*. 2000b	Fe-rich Phl	26	5.358	9.280	10.151	100.10
151			33	5.372	9.313	10.204	100.52
152			120	5.384	9.324	10.254	100.86

153	Redhammer & Roth 2002	syn	NiPhl#6	5.3023	9.1804	10.2911	99.921
154		"	Phl#2	5.3158	9.2036	10.31	99.891
155		"	CoAn#2	5.338	9.2465	10.341	99.977
156		"	Coni1.8#2	5.3225	9.2195	10.3125	99.949
157		"	A20#2	5.3257	9.2254	10.307	99.926
158		"	A20#4	5.3245	9.2245	10.305	99.927
159		"	A40#7	5.3295	9.2309	10.3074	99.944
160		"	A60#2	5.3384	9.2465	10.3061	99.951
161		"	Mgan1.2#1	5.3409	9.2536	10.3087	99.962
162		"	Mgan1.6#4	5.3257	9.2241	10.3056	99.932
163		"	Sd87#4	5.3649	9.2892	10.2698	100.242
164		"	GaPhl#1	5.3214	9.214	10.3896	99.717
165		Ann	Ann#1	5.4059	9.3639	10.3235	100.2
166		Syd	G-117	5.3741	9.3083	10.2829	100.22
167		Syd	Sdp#3	5.371	9.302	10.256	100.25
168	Redhammer pers. com.	syn	Nian#4	5.3023	9.1804	10.2911	99.921
169		"	Phl#1	5.3158	9.2036	10.3042	99.891
170		"	CoAn#1	5.338	9.2465	10.341	99.977

		T			M2	O1		
	c/a cosβ*	x/a	y/b	z/c = z'/c'	y/b	x/a	y/b	z/c = z'/c'
1	0.3409	0.0749	0.1668	0.2258	0.3454	0.0268	0	0.1690
2	0.3332	0.0752	0.1674	0.2262	0.3340	0.0236	0	0.1681
3	0.3372	0.0752	0.1666	0.2256	0.3342	0.0241	0	0.1694
4	0.3396	0.0748	0.1669	0.2257	0.3347	0.0267	0	0.1687
5	0.3372	0.0746	0.1666	0.2255	0.3350	0.0239	0	0.1698
6	0.3348	0.0752	0.1669	0.2258	0.3343	0.0247	0	0.1688
7	0.3339	0.0756	0.1667	0.2266	0.3328	-0.0024	0	0.1705
8	0.3338	0.0755	0.1666	0.2267	0.3328	-0.0020	0	0.1705
9	0.3360	0.0761	0.1666	0.2283	0.3323	0.0138	0	0.1703
10	0.3329	0.0761	0.1667	0.2283	0.3322	0.0134	0	0.1704
11	0.3330	0.0755	0.1666	0.2268	0.3340	0.0134	0	0.1705
12	0.3353	0.0760	0.1666	0.2271	0.3335	0.0150	0	0.1699
13	0.3363	0.0756	0.1667	0.2265	0.3335	0.016	0	0.1704
14	0.3334	0.0760	0.1668	0.2282	0.3320	0.0108	0	0.1704
15	0.3315	0.0759	0.1667	0.2278	0.3325	0.0112	0	0.1706
16	0.3315	0.0760	0.1665	0.2276	0.3320	0.0105	0	0.1714
17	0.3337	0.0758	0.1667	0.2275	0.3325	0.0106	0	0.1711
18	0.3332	0.0761	0.1667	0.2280	0.3326	0.0112	0	0.1701
19	0.3332	0.0759	0.1667	0.2268	0.3325	0.000	0	0.1717
20	0.3337	0.0755	0.1667	0.2267	0.3328	0.0012	0	0.1701
21	0.3352	0.0756	0.1667	0.2266	0.3329	0.0046	0	0.1695
22	0.3329	0.0750	0.1660	0.2240	0.3330	0.0150	0	0.1660
23	0.3348	0.0752	0.1668	0.2254	0.3315	0.0180	0	0.1675
24	0.3517	0.0703	0.1668	0.2246	0.3332	0.0427	0	0.1684
25	0.3372	0.0759	0.1668	0.2282	0.3318	-0.0001	0	0.1713
26	0.3400	0.0744	0.1666	0.2252	0.3333	0.0330	0	0.1668
27	0.3324	0.0734	0.1674	0.2232	0.3420	0.0310	0	0.1661
28	0.3641	0.0810	0.1686	0.2320	0.3289	0.0218	0	0.1750
29	0.3392	0.0785	0.1668	0.2328	0.3331	0.0419	0	0.1765
30	0.3323	0.0749	0.1667	0.2255	0.3337	0.0264	0	0.1669
31	0.3338	0.0755	0.1667	0.2257	0.3312	0.0171	0	0.1676
32	0.3434	0.0750	0.1670	0.2240	0.3320	0.015	0	0.165
33	0.3317	0.0746	0.1667	0.2258	0.3319	0.0229	0	0.1688
34	0.3325	0.0743	0.1672	0.2263	0.3332	0.0261	0	0.1688
35	0.3310	0.0755	0.1666	0.2260	0.3306	0.0027	0	0.1677
36	0.3329	0.0751	0.1667	0.2245	0.3306	-0.0070	0	0.1635
37	0.3416	0.0757	0.1671	0.2263	0.3332	0.0130	0	0.1704
38	0.3419	0.0758	0.1669	0.2264	0.3331	0.0162	0	0.1700
39	0.3415	0.0755	0.1671	0.2261	0.3331	0.0160	0	0.1705
40	0.3409	0.0757	0.1671	0.2265	0.3334	0.0156	0	0.1710
41	0.3405	0.0756	0.1671	0.2257	0.3333	0.0181	0	0.1700
42	0.3415	0.0756	0.1670	0.2258	0.3332	0.0169	0	0.1704
43	0.3325	0.0754	0.1668	0.2276	0.3320	0.0065	0	0.1709
44	0.3312	0.0797	0.1666	0.2384	0.3323	0.0588	0	0.1836
45	0.3347	0.0796	0.1666	0.2382	0.3319	0.0610	0	0.1838
46	0.3382	0.0705	0.1670	0.2101	0.3292	-0.0735	0	0.1523
47	0.3375	0.0703	0.1670	0.2100	0.3292	-0.0740	0	0.1528
48	0.3363	0.0703	0.1669	0.2096	0.3302	-0.0705	0	0.1508
49	0.3340	0.0751	0.1663	0.2245	0.3306	0.0274	0	0.1678

50	0.3338	0.0748	0.1670	0.2250	0.3335	0.0235	0	0.1598
51	0.3341	0.0709	0.1666	0.2126	0.3291	-0.0513	0	0.1598
52	0.3390	0.0740	0.1672	0.2139	0.3302	-0.0470	0	0.1651
53	0.3331	0.0730	0.1673	0.2228	0.3454	0.0177	0	0.1666
54	0.3351	0.0746	0.1664	0.2267	0.3319	0.0119	0	0.1698
55	0.3374	0.0746	0.1664	0.2254	0.3333	0.0457	0	0.1676
56	0.3397	0.0714	0.1668	0.2258	0.3333	0.0417	0	0.1722
57	0.3388	0.0729	0.1663	0.2263	0.3316	0.0342	0	0.1701
58	0.3394	0.0724	0.1667	0.2260	0.3323	0.0277	0	0.1700
59	0.3401	0.0720	0.1670	0.2261	0.3318	0.0216	0	0.1711
60	0.3422	0.0748	0.1674	0.2269	0.3327	0.0117	0	0.1734
61	0.3424	0.0740	0.1665	0.2266	0.3319	0.0069	0	0.1740
62	0.3456	0.0741	0.1673	0.2271	0.3327	0.0200	0	0.1748
63	0.3393	0.0754	0.1668	0.2258	0.3320	0.0158	0	0.1706
64	0.3351	0.0750	0.1668	0.2252	0.3317	0.0211	0	0.1671
65	0.3129	0.0810	0.1685	0.2320	0.3283	0.0214	0	0.1742
66	0.3319	0.0753	0.1665	0.2250	0.3308	0.0235	0	0.1664
67	0.3366	0.0745	0.1671	0.2242	0.3392	0.0165	0	0.1674
68	0.3309	0.0640	0.1680	0.208	0.330	-0.073	0	0.150
69	0.3377	0.0759	0.1665	0.2293	0.3325	0.0190	0	0.1686
70	0.3319	0.0757	0.1667	0.2283	0.3344	0.0494	0	0.1650
71	0.3421	0.0767	0.1678	0.2290	0.3362	-0.0140	0	0.1627
72	0.3351	0.0759	0.1669	0.2302	0.3363	-0.0158	0	0.1612
73	0.3322	0.0757	0.1667	0.2272	0.3336	0.0476	0	0.1669
74	0.3338	0.0756	0.1668	0.2271	0.3336	0.0470	0	0.1680
75	0.3366	0.0755	0.1668	0.2267	0.3317	-0.0269	0	0.1650
76	0.3338	0.0759	0.1669	0.2284	0.3340	-0.0180	0	0.1611
77	0.3351	0.0756	0.1665	0.2262	0.3321	0.0375	0	0.1669
78	0.3351	0.0752	0.1667	0.2249	0.3312	-0.0236	0	0.1626
79	0.3349	0.0744	0.1667	0.2224	0.3314	-0.0138	0	0.1608
80	0.2720	0.0629	0.1707	0.2270	0.3472	0.0450	0	0.1670
81	0.3409	0.0745	0.1664	0.2199	0.3331	0.0333	0	0.1578
82	0.3380	0.0758	0.1669	0.2273	0.3330	0.0120	0	0.1709
83	0.3332	0.0760	0.1668	0.2285	0.3323	0.0064	0	0.1709
84	0.3353	0.0749	0.1667	0.2244	0.3347	0.0256	0	0.1659
85	0.3347	0.0751	0.1668	0.2259	0.3356	0.0100	0	0.1695
86	0.3350	0.0754	0.1669	0.2265	0.3351	0.0095	0	0.1697
87	0.3375	0.0750	0.1668	0.2264	0.3354	0.0126	0	0.1677
88	0.3334	0.0761	0.1668	0.2279	0.3339	0.0145	0	0.1687
89	0.3333	0.0753	0.1668	0.2266	0.3367	0.0158	0	0.1701
90	0.3344	0.0754	0.1668	0.2268	0.3346	0.0081	0	0.1693
91	0.3342	0.0751	0.1669	0.2258	0.3358	0.0082	0	0.1693
92	0.3360	0.0756	0.1668	0.2271	0.3345	0.0069	0	0.1701
93	0.3342	0.0746	0.1670	0.2251	0.3373	0.0114	0	0.1684
94	0.3371	0.0750	0.1666	0.2263	0.3362	0.0194	0	0.1693
95	0.3337	0.0757	0.1673	0.2265	0.3351	0.0171	0	0.1701
96	0.3331	0.0748	0.1669	0.2257	0.3395	0.0061	0	0.1697
97	0.3349	0.0756	0.1669	0.2269	0.3349	0.0171	0	0.1692
98	0.3337	0.0754	0.1668	0.2264	0.3344	0.0113	0	0.1686
99	0.3377	0.0761	0.1666	0.2270	0.3345	0.0164	0	0.1687
100	0.3377	0.0738	0.1671	0.2222	0.3423	0.0255	0	0.1648

101	0.3377	0.0735	0.1669	0.2214	0.3427	0.0263	0	0.1646
102	0.3386	0.0738	0.1670	0.2222	0.3419	0.0272	0	0.1646
103	0.3303	0.0758	0.1666	0.2278	0.3323	0.0110	0	0.1701
104	0.3324	0.0758	0.1668	0.2279	0.3323	0.0112	0	0.1701
105	0.3342	0.0752	0.1669	0.2266	0.3369	0.0118	0	0.1699
106	0.3335	0.0756	0.1668	0.2269	0.3347	0.0171	0	0.1697
107	0.3362	0.0753	0.1668	0.2258	0.3353	0.0220	0	0.1682
108	0.3378	0.0743	0.167	0.2232	0.3353	0.0291	0	0.1673
109	0.3365	0.0749	0.1669	0.2255	0.3364	0.0212	0	0.1683
110	0.3379	0.075	0.1668	0.2258	0.3357	0.0214	0	0.1686
111	0.3386	0.0742	0.1671	0.225	0.3368	0.0174	0	0.1691
112	0.3372	0.0747	0.1669	0.2254	0.3353	0.0297	0	0.1678
113	0.3377	0.0759	0.1664	0.2268	0.3327	0.0145	0	0.1712
114	0.3375	0.0744	0.1671	0.2236	0.3415	0.0252	0	0.1665
115	0.3372	0.0744	0.1671	0.2241	0.3377	0.0165	0	0.1682
116	0.3344	0.0751	0.1668	0.2263	0.335	0.0107	0	0.1705
117	0.3346	0.0752	0.1668	0.2262	0.3354	0.009	0	0.1699
118	0.3435	0.0731	0.167	0.2231	0.3408	0.0357	0	0.1675
119	0.3295	0.0753	0.1667	0.2267	0.3338	0.0094	0	0.1706
120	0.3343	0.0755	0.1669	0.2262	0.3338	0.0092	0	0.1692
121	0.3348	0.0748	0.1669	0.2246	0.3356	0.0119	0	0.1673
122	0.3372	0.0755	0.1667	0.2246	0.3306	-0.0032	0	0.1641
123	0.3355	0.0753	0.1666	0.2244	0.3307	-0.0029	0	0.1641
124	0.3365	0.0767	0.1668	0.2284	0.3317	0.0049	0	0.1716
125	0.3366	0.0761	0.1667	0.2287	0.3316	0.0029	0	0.1721
126	0.3354	0.0766	0.1666	0.2284	0.3308	0.0013	0	0.1718
127	0.3335	0.0765	0.1667	0.2285	0.3309	-0.0064	0	0.1738
128	0.3331	0.0764	0.1667	0.2287	0.331	0.0031	0	0.1719
129	0.3349	0.0705	0.1667	0.21007	0.3299	-0.075	0	0.1511
130	0.3341	0.0703	0.1666	0.21015	0.3307	-0.0794	0	0.1504
131	0.3347	0.0702	0.1668	0.2101	0.3301	-0.0772	0	0.1514
132	0.3362	0.0703	0.1668	0.21011	0.3298	-0.0752	0	0.1513
133	0.3331	0.0703	0.1672	0.2102	0.3315	-0.0849	0	0.1533
134	0.3374	0.0707	0.167	0.2103	0.3296	-0.0715	0	0.1516
135	0.3321	0.076	0.16674	0.22814	0.3322	0.0143	0	0.1698
136	0.3343	0.0758	0.16669	0.22744	0.3331	0.0158	0	0.1703
137	0.3337	0.0757	0.16666	0.22758	0.3327	0.0134	0	0.1699
138	0.3330	0.07585	0.16666	0.22742	0.33252	0.0109	0	0.1695
139	0.3344	0.0758	0.16671	0.22728	0.3331	0.0219	0	0.169
140	0.3334	0.0758	0.16668	0.22792	0.3333	0.0226	0	0.1709
141	0.3345	0.0758	0.16661	0.22669	0.3327	0.003	0	0.1701
142	0.3340	0.07563	0.16664	0.22676	0.33267	0.0043	0	0.17
143	0.3353	0.07455	0.16694	0.22406	0.3396	0.0322	0	0.1661
144	0.3506	0.082	0.1686	0.2331	0.3286	0.0473	0	0.1684
145	0.3343	0.073	0.168	0.225	0.333	0.045	0	0.163
146	0.3351	0.07521	0.16668	0.22656	0.33269	-0.00155	0	0.17084
147	0.3186	0.08	0.17	0.22	0.322	-0.031	0	0.166
148	0.3331	0.07564	0.16676	0.22746	0.3323	0.00954	0	0.16975
149	0.3364	0.0761	0.1664	0.2264	0.3328	0.0117	0	0.1683
150	0.3322	0.0753	0.167	0.2254	0.3334	0.0305	0	0.1679
151	0.3468	0.0733	0.1664	0.2239	0.3308	0.0441	0	0.1668
152	0.3588	0.069	0.1668	0.2242	0.3338	0.041	0	0.1675

153	0.3344	0.07689	0.16663	0.23009	0.33198	0.00706	0	0.1733
154	0.3332	0.07651	0.16674	0.22952	0.33171	0.00995	0	0.17174
155	0.3356	0.0761	0.16668	0.22778	0.33147	0.01819	0	0.17061
156	0.3347	0.07637	0.16674	0.22848	0.3319	0.0141	0	0.1708
157	0.3336	0.07616	0.16672	0.22873	0.33241	0.00953	0	0.17173
158	0.3336	0.07621	0.1669	0.22879	0.33248	0.01106	0	0.17167
159	0.3340	0.07604	0.16684	0.22793	0.33302	0.01447	0	0.17135
160	0.3336	0.07557	0.16681	0.2275	0.33449	0.01183	0	0.17102
161	0.3339	0.07634	0.16674	0.22776	0.33387	0.01402	0	0.17123
162	0.3338	0.07576	0.16683	0.22793	0.33388	0.01118	0	0.17082
163	0.3404	0.07595	0.16683	0.22658	0.33139	-0.0004	0	0.17334
164	0.3295	0.07612	0.16673	0.22866	0.33269	0.00088	0	0.17107
165	0.3382	0.07218	0.1666	0.22473	0.33209	0.03927	0	0.16774
166	0.3395	0.0754	0.16681	0.22577	0.33199	0.01517	0	0.17068
167	0.3398	0.07587	0.16692	0.22617	0.33133	0.01258	0	0.17127
168	0.3344	0.0765	0.16676	0.22979	0.33207	0.0098	0	0.1731
169	0.3330	0.0762	0.1666	0.2296	0.3317	0.0113	0	0.1718
170	0.3356	0.076	0.16673	0.2277	0.3315	0.0183	0	0.17021

	O2			O3			O4		
	x/a	y/b	z/c = z'/c'	x/a	y/b	z/c = z'/c'	x/a	y/b	z/c = z'/c'
1	0.3192	0.2357	0.1682	0.1312	0.1678	0.3912	0.1286	0.5	0.3957
2	0.3221	0.2339	0.1695	0.1308	0.1673	0.3910	0.1293	0.5	0.3960
3	0.3203	0.2355	0.1668	0.1330	0.1676	0.3916	0.1304	0.5	0.3949
4	0.3195	0.2361	0.1681	0.1316	0.1677	0.3909	0.1291	0.5	0.3947
5	0.3207	0.2340	0.1681	0.1303	0.1676	0.3909	0.1305	0.5	0.3952
6	0.3219	0.2336	0.1683	0.1334	0.1675	0.3905	0.1301	0.5	0.3952
7	0.3360	0.2206	0.1704	0.1305	0.1669	0.3918	0.1335	0.5	0.3990
8	0.3357	0.2203	0.1706	0.1304	0.1671	0.3914	0.1331	0.5	0.3988
9	0.3285	0.2286	0.1703	0.1302	0.1668	0.3908	0.1322	0.5	0.3978
10	0.3281	0.2284	0.1703	0.1300	0.1667	0.3910	0.1326	0.5	0.3976
11	0.3285	0.2281	0.1700	0.1304	0.1670	0.3914	0.1314	0.5	0.3973
12	0.3283	0.2278	0.1698	0.1295	0.1674	0.3908	0.1308	0.5	0.3966
13	0.3271	0.2293	0.1695	0.1311	0.1671	0.3910	0.1309	0.5	0.3972
14	0.3296	0.2276	0.1704	0.1302	0.1666	0.3912	0.1320	0.5	0.3977
15	0.3296	0.2274	0.1707	0.1300	0.1668	0.3910	0.1323	0.5	0.3976
16	0.3286	0.2275	0.1708	0.1318	0.1670	0.3920	0.1329	0.5	0.3975
17	0.3301	0.2268	0.1708	0.1300	0.1670	0.3910	0.1327	0.5	0.3980
18	0.3291	0.2278	0.1700	0.1304	0.1668	0.3912	0.1324	0.5	0.3980
19	0.3317	0.2220	0.1715	0.1281	0.1677	0.3909	0.1338	0.5	0.3982
20	0.3342	0.2221	0.1700	0.1309	0.1670	0.3918	0.1330	0.5	0.3977
21	0.3320	0.2238	0.1699	0.1302	0.1671	0.3909	0.1327	0.5	0.3978
22	0.3200	0.2360	0.1670	0.1330	0.1660	0.3910	0.1340	0.5	0.4010
23	0.3248	0.2307	0.1677	0.1297	0.1664	0.3902	0.1330	0.5	0.4008
24	0.3031	0.2457	0.1670	0.1291	0.1674	0.3894	0.1239	0.5	0.3931
25	0.3364	0.2214	0.1714	0.1317	0.1677	0.3925	0.1309	0.5	0.3985
26	0.3154	0.2391	0.1670	0.1307	0.1668	0.3893	0.1299	0.5	0.3958
27	0.3155	0.2380	0.1645	0.1295	0.1694	0.3896	0.1359	0.5	0.4010
28	0.3252	0.2319	0.1680	0.1418	0.1768	0.3945	0.1076	0.5	0.4017
29	0.3171	0.2411	0.1748	0.1335	0.1684	0.3939	0.1288	0.5	0.4009
30	0.3198	0.2355	0.1672	0.1298	0.1670	0.3901	0.1336	0.5	0.3992
31	0.3255	0.2306	0.1680	0.1307	0.1666	0.3910	0.1323	0.5	0.4009
32	0.321	0.231	0.166	0.128	0.166	0.387	0.129	0.5	0.391
33	0.3224	0.2335	0.1674	0.1270	0.1678	0.3864	0.1290	0.5	0.3945
34	0.3187	0.2332	0.1670	0.1277	0.1681	0.3885	0.1304	0.5	0.3968
35	0.3336	0.2223	0.1677	0.1296	0.1671	0.3904	0.1299	0.5	0.3977
36	0.3364	0.2177	0.1654	0.1299	0.1674	0.3892	0.1308	0.5	0.3972
37	0.3272	0.2284	0.1692	0.1316	0.1690	0.3916	0.1280	0.5	0.3972
38	0.3264	0.2315	0.1692	0.1322	0.1685	0.3920	0.1285	0.5	0.3969
39	0.3270	0.2296	0.1690	0.1330	0.1690	0.3923	0.1263	0.5	0.3970
40	0.3271	0.2297	0.1689	0.1326	0.1693	0.3921	0.1269	0.5	0.3977
41	0.3252	0.2307	0.1681	0.1322	0.1686	0.3915	0.1280	0.5	0.3975
42	0.3256	0.2313	0.1685	0.1326	0.1687	0.3919	0.1268	0.5	0.3978
43	0.3321	0.2247	0.1703	0.1302	0.1669	0.3917	0.1392	0.5	0.3993
44	0.3117	0.2496	0.1824	0.1325	0.1664	0.3958	0.1322	0.5	0.4018
45	0.3119	0.2501	0.1844	0.1326	0.1662	0.3962	0.1325	0.5	0.4015
46	0.3627	0.1878	0.1512	0.1316	0.1689	0.3889	0.1277	0.5	0.3990
47	0.3631	0.1876	0.1513	0.1311	0.1685	0.3887	0.1281	0.5	0.3981
48	0.3609	0.1895	0.1500	0.1306	0.1681	0.3877	0.1291	0.5	0.3977
49	0.3208	0.2347	0.1682	0.1291	0.1661	0.3896	0.1327	0.5	0.4017

50	0.3139	0.2395	0.1609	0.1311	0.1671	0.3874	0.1309	0.5	0.3981
51	0.3546	0.1971	0.1593	0.1285	0.1685	0.3918	0.1335	0.5	0.3970
52	0.3559	0.1989	0.1584	0.1348	0.1703	0.3905	0.1252	0.5	0.3989
53	0.3217	0.2315	0.1645	0.1298	0.1697	0.3905	0.1335	0.5	0.4006
54	0.3279	0.2281	0.1693	0.1313	0.1674	0.3918	0.1309	0.5	0.4001
55	0.3138	0.2410	0.1777	0.1373	0.1675	0.3939	0.1367	0.5	0.3860
56	0.3085	0.2466	0.1744	0.1365	0.1665	0.3940	0.1323	0.5	0.3877
57	0.3158	0.2361	0.1752	0.1369	0.1670	0.3933	0.1309	0.5	0.3882
58	0.3201	0.2308	0.1758	0.1368	0.1678	0.3933	0.1329	0.5	0.3909
59	0.3251	0.2255	0.1759	0.1370	0.1690	0.3943	0.1332	0.5	0.3924
60	0.3290	0.2237	0.1770	0.1391	0.1689	0.3950	0.1310	0.5	0.3926
61	0.3333	0.2205	0.1768	0.1384	0.1697	0.3945	0.1309	0.5	0.3928
62	0.3343	0.2190	0.1766	0.1385	0.1700	0.3958	0.1289	0.5	0.3928
63	0.3260	0.2298	0.1695	0.1319	0.1679	0.3918	0.1271	0.5	0.3963
64	0.3242	0.2331	0.1674	0.1313	0.1663	0.3898	0.1297	0.5	0.3949
65	0.3251	0.2310	0.1680	0.1421	0.1768	0.3941	0.1107	0.5	0.4015
66	0.3218	0.2346	0.1670	0.1305	0.1665	0.3910	0.1329	0.5	0.4020
67	0.3240	0.2310	0.1660	0.1310	0.1684	0.3906	0.1312	0.5	0.3985
68	0.357	0.188	0.144	0.117	0.165	0.383	0.132	0.5	0.400
69	0.3294	0.2320	0.1720	0.1287	0.1668	0.3889	0.1360	0.5	0.3956
70	0.3075	0.2473	0.1650	0.1284	0.1668	0.3871	0.1333	0.5	0.3967
71	0.3345	0.2175	0.1578	0.1390	0.1729	0.3931	0.1130	0.5	0.3999
72	0.3376	0.2154	0.1603	0.1295	0.1676	0.3941	0.1350	0.5	0.4032
73	0.3088	0.2466	0.1666	0.1291	0.1667	0.3873	0.1333	0.5	0.3978
74	0.3104	0.2458	0.1680	0.1397	0.1668	0.3881	0.1335	0.5	0.3991
75	0.3464	0.2087	0.1645	0.1314	0.1668	0.3956	0.1371	0.5	0.4086
76	0.3392	0.2144	0.1606	0.1320	0.1678	0.3939	0.1338	0.5	0.4043
77	0.3150	0.2408	0.1669	0.1298	0.1665	0.3891	0.1336	0.5	0.4008
78	0.3428	0.2117	0.1630	0.1322	0.1665	0.3945	0.1355	0.5	0.4049
79	0.3371	0.2161	0.1602	0.1307	0.1670	0.3924	0.1324	0.5	0.4009
80	0.2970	0.2486	0.1615	0.1080	0.1787	0.3853	0.1090	0.5	0.3960
81	0.3134	0.2400	0.1586	0.1319	0.1659	0.3883	0.1229	0.5	0.3871
82	0.3290	0.2279	0.1703	0.1314	0.1675	0.3919	0.1304	0.5	0.3985
83	0.3316	0.2254	0.1712	0.1305	0.1670	0.3919	0.1329	0.5	0.3998
84	0.3199	0.2355	0.1658	0.1311	0.1672	0.3904	0.1312	0.5	0.4004
85	0.3286	0.2270	0.1685	0.1306	0.1677	0.3912	0.1318	0.5	0.3994
86	0.3291	0.2265	0.1693	0.1304	0.1675	0.3916	0.1323	0.5	0.3992
87	0.3254	0.2287	0.1684	0.1306	0.1676	0.3915	0.1348	0.5	0.4011
88	0.3257	0.2298	0.1694	0.1310	0.1676	0.3920	0.1313	0.5	0.3984
89	0.3258	0.2299	0.1685	0.1311	0.1678	0.3918	0.1303	0.5	0.4001
90	0.3299	0.2260	0.1690	0.1306	0.1675	0.3917	0.1321	0.5	0.3994
91	0.3305	0.2259	0.1687	0.1300	0.1679	0.3913	0.1331	0.5	0.3999
92	0.3307	0.2254	0.1698	0.1310	0.1676	0.3921	0.1318	0.5	0.3994
93	0.3275	0.2276	0.1677	0.1305	0.1680	0.3912	0.1321	0.5	0.3994
94	0.3234	0.2311	0.1687	0.1314	0.1679	0.3915	0.1302	0.5	0.4000
95	0.3254	0.2313	0.1701	0.1336	0.1682	0.3924	0.1301	0.5	0.3974
96	0.3304	0.2254	0.1688	0.1304	0.1685	0.3919	0.1343	0.5	0.4012
97	0.3260	0.2302	0.1687	0.1304	0.1673	0.3910	0.1313	0.5	0.3994
98	0.3273	0.2284	0.1683	0.1308	0.1671	0.3913	0.1318	0.5	0.3986
99	0.3267	0.2300	0.1688	0.1303	0.1662	0.3913	0.1328	0.5	0.3989
100	0.3179	0.2356	0.1628	0.1314	0.1699	0.3900	0.1288	0.5	0.3994

101	0.3185	0.2359	0.1620	0.1312	0.1697	0.3904	0.1311	0.5	0.3984
102	0.3169	0.2367	0.1628	0.1313	0.1697	0.3903	0.1278	0.5	0.3975
103	0.3295	0.2269	0.1699	0.1313	0.1669	0.3915	0.1313	0.5	0.3989
104	0.3295	0.2265	0.1701	0.1305	0.1668	0.3913	0.1331	0.5	0.3992
105	0.3276	0.2281	0.1692	0.1310	0.1677	0.3914	0.1314	0.5	0.3989
106	0.3256	0.2311	0.1692	0.1313	0.1673	0.3914	0.1311	0.5	0.3979
107	0.3222	0.2334	0.1672	0.1309	0.1672	0.3911	0.1317	0.5	0.4006
108	0.3187	0.2368	0.1663	0.1321	0.1687	0.3907	0.1308	0.5	0.4007
109	0.323	0.2327	0.1674	0.131	0.1676	0.3911	0.1312	0.5	0.3998
110	0.3225	0.233	0.1677	0.1307	0.1674	0.391	0.1311	0.5	0.3995
111	0.3243	0.2311	0.1678	0.1307	0.1683	0.391	0.1293	0.5	0.3964
112	0.3201	0.2368	0.1678	0.131	0.1679	0.3905	0.1291	0.5	0.3952
113	0.3249	0.2298	0.1697	0.1302	0.1671	0.3904	0.1293	0.5	0.3954
114	0.319	0.2352	0.1647	0.1316	0.1685	0.3906	0.1305	0.5	0.4013
115	0.3238	0.2305	0.1674	0.1316	0.1679	0.3912	0.1298	0.5	0.3988
116	0.3294	0.2267	0.169	0.1302	0.1675	0.3914	0.1312	0.5	0.3988
117	0.33	0.2264	0.1691	0.1304	0.1675	0.3913	0.1326	0.5	0.3992
118	0.3142	0.2376	0.1655	0.1339	0.1687	0.3905	0.1328	0.5	0.3968
119	0.3303	0.2265	0.1696	0.1295	0.1673	0.3911	0.1299	0.5	0.3973
120	0.3289	0.227	0.1691	0.1307	0.1676	0.3913	0.1306	0.5	0.3973
121	0.3272	0.2282	0.1666	0.1308	0.1675	0.391	0.1317	0.5	0.3984
122	0.3341	0.2206	0.1639	0.1307	0.1664	0.3911	0.1313	0.5	0.3985
123	0.3342	0.2211	0.1638	0.1311	0.1663	0.3909	0.131	0.5	0.3988
124	0.3333	0.224	0.1724	0.1308	0.167	0.3932	0.1328	0.5	0.3979
125	0.334	0.2228	0.1716	0.1305	0.1669	0.3928	0.1326	0.5	0.3985
126	0.3358	0.2214	0.1721	0.1313	0.1666	0.3927	0.1318	0.5	0.3993
127	0.3395	0.2182	0.1732	0.1322	0.1673	0.3937	0.1306	0.5	0.3997
128	0.334	0.2225	0.1717	0.1295	0.167	0.392	0.1319	0.5	0.3981
129	0.363	0.1876	0.1507	0.1308	0.1678	0.3892	0.13	0.5	0.396
130	0.3661	0.1845	0.1506	0.1296	0.167	0.3898	0.13	0.5	0.3928
131	0.364	0.1857	0.1507	0.1302	0.1678	0.3886	0.131	0.5	0.3948
132	0.3626	0.1879	0.1501	0.1309	0.1678	0.3896	0.1294	0.5	0.3954
133	0.3647	0.1829	0.1505	0.1319	0.1678	0.3918	0.1322	0.5	0.3893
134	0.3619	0.1882	0.151	0.1298	0.1686	0.3878	0.1293	0.5	0.3977
135	0.328	0.2277	0.1706	0.1299	0.1674	0.391	0.133	0.5	0.3976
136	0.3265	0.23	0.1697	0.1303	0.1669	0.3907	0.1324	0.5	0.3974
137	0.329	0.2284	0.1706	0.1302	0.1667	0.3904	0.1309	0.5	0.3962
138	0.329	0.2271	0.1697	0.1307	0.1669	0.3913	0.1322	0.5	0.3974
139	0.3232	0.233	0.1695	0.1306	0.1672	0.3905	0.1318	0.5	0.3963
140	0.3237	0.2331	0.1691	0.1295	0.167	0.3908	0.1323	0.5	0.3968
141	0.3336	0.2234	0.1702	0.1304	0.1668	0.3909	0.1327	0.5	0.3978
142	0.3334	0.2236	0.1703	0.13	0.1669	0.3911	0.1327	0.5	0.3983
143	0.3164	0.2389	0.165	0.1305	0.168	0.39	0.1308	0.5	0.4002
144	0.3126	0.2404	0.1648	0.1317	0.1779	0.3913	0.1107	0.5	0.3988
145	0.307	0.253	0.169	0.111	0.168	0.395	0.114	0.5	0.394
146	0.33582	0.22073	0.17003	0.13096	0.16695	0.3921	0.13395	0.5	0.39897
147	0.36	0.198	0.156	0.135	0.176	0.388	0.109	0.5	0.396
148	0.33024	0.22657	0.17035	0.12985	0.16688	0.3909	0.13287	0.5	0.39766
149	0.3291	0.2271	0.1666	0.1309	0.1679	0.3899	0.1306	0.5	0.3951
150	0.319	0.2376	0.1688	0.13	0.1636	0.3964	0.1299	0.5	0.3885
151	0.3101	0.2455	0.1670	0.1293	0.1659	0.3896	0.1235	0.5	0.3918
152	0.3026	0.2463	0.1675	0.128	0.1678	0.3894	0.1245	0.5	0.3941

153	0.33411	0.22589	0.17263	0.13163	0.16634	0.39342	0.13367	0.5	0.3994
154	0.33048	0.22662	0.17165	0.13068	0.16673	0.39172	0.13248	0.5	0.3988
155	0.32584	0.23063	0.1705	0.12987	0.16676	0.39048	0.13211	0.5	0.39758
156	0.32794	0.22891	0.17079	0.13136	0.16663	0.39129	0.13362	0.5	0.39809
157	0.33088	0.22634	0.17177	0.12998	0.16682	0.39159	0.13254	0.5	0.39761
158	0.32982	0.2271	0.17142	0.13084	0.16673	0.39157	0.13284	0.5	0.39918
159	0.32811	0.22858	0.17137	0.1303	0.16747	0.39006	0.1324	0.5	0.3963
160	0.32792	0.22795	0.17027	0.13012	0.16712	0.39127	0.133	0.5	0.39854
161	0.32827	0.22845	0.17024	0.13027	0.16727	0.38943	0.13309	0.5	0.39728
162	0.32878	0.22745	0.17055	0.13032	0.16706	0.3913	0.13321	0.5	0.3991
163	0.33672	0.2205	0.17265	0.13333	0.16776	0.39449	0.12691	0.5	0.39857
164	0.33456	0.22253	0.17097	0.13028	0.16729	0.39206	0.13357	0.5	0.39915
165	0.30853	0.24357	0.16801	0.12887	0.16638	0.38846	0.12753	0.5	0.39288
166	0.32658	0.22975	0.16961	0.13165	0.1679	0.39203	0.12709	0.5	0.39672
167	0.3285	0.22801	0.17015	0.13295	0.16808	0.39273	0.12562	0.5	0.39761
168	0.3313	0.2263	0.1731	0.1311	0.1665	0.3924	0.1324	0.5	0.3998
169	0.3296	0.2265	0.1722	0.1297	0.1667	0.3914	0.1317	0.5	0.3976
170	0.3257	0.2311	0.1698	0.1307	0.1667	0.3901	0.1324	0.5	0.3975

	M1-O3	M1-O4	<M1-O>	M2-O3	M2-O3'	M2-O4	<M2-O>	h_o
1	2.1025	2.0788	2.0946	2.1704	2.0868	1.9798	2.0790	2.1596
2	2.0980	2.0801	2.0920	2.0939	2.0916	2.0558	2.0804	2.1642
3	2.1032	2.0798	2.0954	2.0964	2.0801	2.0652	2.0806	2.1644
4	2.1042	2.0811	2.0965	2.0994	2.0836	2.0593	2.0808	2.1695
5	2.0969	2.0713	2.0884	2.0955	2.0881	2.0539	2.0791	2.1644
6	2.1051	2.0735	2.0946	2.1003	2.0759	2.0571	2.0778	2.1691
7	2.1002	2.0586	2.0863	2.0934	2.0988	2.0662	2.0861	2.1508
8	2.1048	2.0623	2.0906	2.0952	2.1019	2.0675	2.0882	2.1585
9	2.0908	2.0531	2.0782	2.0820	2.0881	2.0597	2.0766	2.1635
10	2.0925	2.0581	2.0810	2.0844	2.0945	2.0664	2.0818	2.1674
11	2.0917	2.0637	2.0824	2.0917	2.0900	2.0519	2.0779	2.1566
12	2.0944	2.0662	2.0850	2.0856	2.0935	2.0565	2.0785	2.1670
13	2.0975	2.0660	2.0870	2.0927	2.0878	2.0559	2.0788	2.1589
14	2.0868	2.0569	2.0769	2.0787	2.0893	2.0616	2.0765	2.1610
15	2.0897	2.0579	2.0791	2.0823	2.0927	2.0605	2.0785	2.1579
16	2.0880	2.0530	2.0763	2.0744	2.0784	2.0646	2.0725	2.1492
17	2.0967	2.0580	2.0838	2.0865	2.0963	2.0645	2.0824	2.1642
18	2.0930	2.0575	2.0812	2.0862	2.0918	2.0611	2.0797	2.1598
19	2.1029	2.0589	2.0882	2.0831	2.1120	2.0709	2.0887	2.1682
20	2.0994	2.0638	2.0875	2.0912	2.0952	2.0704	2.0856	2.1569
21	2.1050	2.0635	2.0912	2.0962	2.1005	2.0695	2.0887	2.1683
22	2.1245	2.0704	2.1065	2.1314	2.1111	2.0747	2.1057	2.1518
23	2.0795	2.0304	2.0631	2.0707	2.0832	2.0396	2.0645	2.1249
24	2.1215	2.1185	2.1205	2.1106	2.1080	2.0831	2.1005	2.2075
25	2.0833	2.0500	2.0722	2.0590	2.0682	2.0495	2.0589	2.1292
26	2.1007	2.0682	2.0898	2.0986	2.0882	2.0594	2.0821	2.1748
27	2.0984	2.0151	2.0706	2.1203	2.0872	1.9691	2.0589	2.1187
28	2.1274	2.1003	2.1183	1.9662	1.9708	1.9737	1.9702	2.0559
29	2.1035	2.0695	2.0922	2.0783	2.0733	2.0407	2.0641	2.1247
30	2.0940	2.0436	2.0772	2.0920	2.0941	2.0441	2.0767	2.1511
31	2.0806	2.0361	2.0658	2.0671	2.0786	2.0418	2.0625	2.1158
32	2.1312	2.1144	2.1256	2.1312	2.1345	2.1223	2.1293	2.2776
33	2.1332	2.1017	2.1227	2.1082	2.1418	2.0903	2.1134	2.2540
34	2.1130	2.0758	2.1006	2.0927	2.1191	2.0602	2.0907	2.2023
35	2.0953	2.0680	2.0862	2.0709	2.0962	2.0686	2.0786	2.1620
36	2.1083	2.0698	2.0954	2.0799	2.1036	2.0764	2.0866	2.1844
37	2.1129	2.0801	2.1020	2.0801	2.0838	2.0562	2.0734	2.1500
38	2.1004	2.0725	2.0911	2.0739	2.0730	2.0520	2.0663	2.1366
39	2.1088	2.0855	2.1010	2.0754	2.0716	2.0512	2.0661	2.1382
40	2.1034	2.0739	2.0936	2.0680	2.0678	2.0389	2.0582	2.1279
41	2.1077	2.0759	2.0971	2.0811	2.0781	2.0495	2.0696	2.1401
42	2.1034	2.0762	2.0944	2.0748	2.0705	2.0424	2.0626	2.1303
43	2.0863	2.0169	2.0632	2.0741	2.0861	2.0695	2.0766	2.1426
44	2.1393	2.1165	2.1317	2.1357	2.1382	2.1106	2.1282	2.1798
45	2.1349	2.1128	2.1276	2.1314	2.1328	2.1153	2.1265	2.1760
46	2.0579	2.0097	2.0418	2.0014	2.0264	2.0055	2.0111	2.0800
47	2.0557	2.0117	2.0410	2.0044	2.0304	2.0117	2.0155	2.0885
48	2.0556	2.0076	2.0396	2.0161	2.0351	2.0074	2.0195	2.0968
49	2.0778	2.0285	2.0614	2.0670	2.0879	2.0383	2.0644	2.1237
50	2.0915	2.0374	2.0735	2.0868	2.0748	2.0245	2.0620	2.1548
51	2.0377	1.9989	2.0247	1.9847	2.0390	2.0363	2.0200	2.0514

52	2.0739	2.0304	2.0594	2.0050	2.0150	2.0023	2.0074	2.0610
53	2.1004	2.0307	2.0772	2.1419	2.0877	1.9470	2.0588	2.1115
54	2.0882	2.0507	2.0757	2.0686	2.0786	2.0433	2.0635	2.1263
55	2.1155	2.0985	2.1098	2.1038	2.0649	2.1568	2.1085	2.2066
56	2.1090	2.1126	2.1102	2.1111	2.0693	2.1390	2.1065	2.1976
57	2.1149	2.1147	2.1148	2.0984	2.0678	2.1415	2.1025	2.1997
58	2.1172	2.0920	2.1088	2.0946	2.0650	2.1218	2.0938	2.1780
59	2.1172	2.0816	2.1053	2.0747	2.0571	2.1141	2.0820	2.1515
60	2.1151	2.0873	2.1058	2.0802	2.0413	2.0994	2.0736	2.1411
61	2.1201	2.0851	2.1084	2.0689	2.0445	2.1017	2.0717	2.1427
62	2.1147	2.0919	2.1071	2.0646	2.0371	2.0915	2.0644	2.1251
63	2.1127	2.0973	2.1075	2.0866	2.0914	2.0756	2.0845	2.1596
64	2.0997	2.0793	2.0929	2.0936	2.0910	2.0792	2.0879	2.1868
65	2.1166	2.1064	2.1132	1.9508	1.9915	1.9741	1.9721	2.0600
66	2.0778	2.0278	2.0611	2.0629	2.0774	2.0386	2.0596	2.1015
67	2.1017	2.0531	2.0855	2.1181	2.0835	2.0034	2.0683	2.1382
68	2.0336	1.9892	2.0188	2.0336	2.1153	2.0023	2.0504	2.1488
69	2.1031	2.0440	2.0834	2.0956	2.1026	2.0840	2.0941	2.2054
70	2.0764	2.0220	2.0583	2.0817	2.0802	2.0216	2.0612	2.1919
71	2.1793	2.1758	2.1782	2.1136	2.0806	2.0153	2.0698	2.1698
72	2.1105	2.0569	2.0926	2.1181	2.1163	2.0411	2.0918	2.1378
73	2.0812	2.0252	2.0626	2.0826	2.0834	2.0258	2.0639	2.1858
74	2.1142	2.0296	2.0860	2.1142	2.0431	2.0317	2.0630	2.1725
75	2.0980	2.0309	2.0757	2.0849	2.1027	2.0465	2.0780	2.0630
76	2.1223	2.0638	2.1028	2.1112	2.1102	2.0516	2.0910	2.1296
77	2.0822	2.0223	2.0622	2.0761	2.0816	2.0319	2.0632	2.1372
78	2.1133	2.0561	2.0942	2.1008	2.1084	2.0764	2.0952	2.1015
79	2.1418	2.1003	2.1280	2.1236	2.1388	2.1067	2.1230	2.1580
80	2.0938	2.1801	2.1226	2.0255	2.2360	1.8588	2.0401	2.2135
81	2.1113	2.1390	2.1205	2.1202	2.0933	2.1048	2.1061	2.2161
82	2.0931	2.0580	2.0814	2.0795	2.0772	2.0483	2.0683	2.1355
83	2.0852	2.0431	2.0712	2.0737	2.0830	2.0486	2.0684	2.1373
84	2.0896	2.0421	2.0738	2.0917	2.0777	2.0185	2.0626	2.1180
85	2.0939	2.0494	2.0791	2.0953	2.0846	2.0255	2.0685	2.1341
86	2.0889	2.0474	2.0751	2.0896	2.0836	2.0305	2.0679	2.1329
87	2.0877	2.0249	2.0668	2.0891	2.0785	2.0204	2.0627	2.1172
88	2.0879	2.0540	2.0766	2.0791	2.0789	2.0402	2.0661	2.1435
89	2.0862	2.0500	2.0741	2.0937	2.0762	2.0047	2.0582	2.1166
90	2.0873	2.0458	2.0735	2.0846	2.0806	2.0308	2.0653	2.1300
91	2.0908	2.0391	2.0736	2.0908	2.0844	2.0218	2.0657	2.1277
92	2.0884	2.0481	2.0750	2.0836	2.0782	2.0326	2.0648	2.1292
93	2.0947	2.0481	2.0792	2.1036	2.0853	2.0137	2.0675	2.1297
94	2.0940	2.0515	2.0799	2.0968	2.0766	2.0129	2.0621	2.1257
95	2.0982	2.0662	2.0875	2.0894	2.0683	2.0380	2.0652	2.1283
96	2.0919	2.0297	2.0712	2.1091	2.0818	1.9915	2.0608	2.1073
97	2.0944	2.0540	2.0809	2.0964	2.0884	2.0316	2.0722	2.1384
98	2.0836	2.0471	2.0714	2.0850	2.0780	2.0326	2.0652	2.1309
99	2.0881	2.0502	2.0755	2.1025	2.0892	2.0438	2.0785	2.1444
100	2.1137	2.0580	2.0951	2.1310	2.0816	1.9690	2.0605	2.1217
101	2.1091	2.0500	2.0894	2.1319	2.0806	1.9771	2.0632	2.1208
102	2.1116	2.0691	2.0974	2.1289	2.0809	1.9817	2.0638	2.1316
103	2.0957	2.0632	2.0849	2.0855	2.0905	2.0572	2.0777	2.1516

104	2.0937	2.0522	2.0799	2.0849	2.0932	2.0588	2.0790	2.1519
105	2.0951	2.0555	2.0819	2.1054	2.0849	2.0199	2.0701	2.1398
106	2.0889	2.0563	2.0781	2.0896	2.0792	2.0361	2.0683	2.1451
107	2.0828	2.0363	2.0673	2.0889	2.0736	2.0119	2.0582	2.1158
108	2.1008	2.0410	2.0808	2.0864	2.0700	2.0123	2.0562	2.1068
109	2.0885	2.0440	2.0736	2.0966	2.0761	2.0104	2.0610	2.1220
110	2.0850	2.0440	2.0714	2.0911	2.0761	2.0148	2.0607	2.1233
111	2.0996	2.0684	2.0892	2.1010	2.0820	2.0294	2.0708	2.1502
112	2.1030	2.0752	2.0937	2.0995	2.0838	2.0487	2.0774	2.1643
113	2.0920	2.0718	2.0853	2.0819	2.0860	2.0615	2.0765	2.1696
114	2.0959	2.0399	2.0772	2.1268	2.0738	1.9625	2.0543	2.1038
115	2.0953	2.0577	2.0827	2.1083	2.0769	2.0079	2.0644	2.1253
116	2.0891	2.0533	2.0772	2.0891	2.0847	2.0304	2.0681	2.1360
117	2.0910	2.0464	2.0761	2.0937	2.0851	2.0294	2.0694	2.1354
118	2.1151	2.0487	2.0929	2.1384	2.0684	2.0102	2.0723	2.1536
119	2.0882	2.0692	2.0819	2.0828	2.0938	2.0447	2.0737	2.1540
120	2.0941	2.0642	2.0841	2.0846	2.0858	2.0485	2.0730	2.1534
121	2.0941	2.0531	2.0804	2.0982	2.0839	2.0312	2.0711	2.1354
122	2.0806	2.0493	2.0701	2.0657	2.0785	2.0593	2.0678	2.1294
123	2.0821	2.0494	2.0712	2.0692	2.0773	2.0563	2.0676	2.1306
124	2.0755	2.0459	2.0657	2.0599	2.0722	2.0611	2.0644	2.1290
125	2.0760	2.0465	2.0662	2.0612	2.0770	2.0571	2.0651	2.1344
126	2.0767	2.0466	2.0667	2.0605	2.0731	2.0566	2.0634	2.1295
127	2.0751	2.0495	2.0666	2.0501	2.0641	2.0485	2.0542	2.1123
128	2.0809	2.0524	2.0714	2.0606	2.0859	2.0637	2.0700	2.1486
129	2.0460	2.0106	2.0342	2.0084	2.0306	2.0213	2.0201	2.0923
130	2.0345	2.0213	2.0301	2.0126	2.0337	2.0336	2.0266	2.1056
131	2.0461	2.0081	2.0334	2.0098	2.0334	2.0267	2.0233	2.1063
132	2.0479	2.0163	2.0374	2.0095	2.0298	2.0280	2.0224	2.0942
133	2.0324	2.0226	2.0291	2.0051	2.0150	2.0520	2.0240	2.1022
134	2.0591	2.0086	2.0423	2.0092	2.0404	2.0142	2.0213	2.1035
135	2.0977	2.0569	2.0841	2.0800	2.0957	2.0680	2.0812	2.1684
136	2.1026	2.0655	2.0903	2.0979	2.1000	2.0672	2.0884	2.1745
137	2.0961	2.0687	2.0870	2.0914	2.0935	2.0670	2.0839	2.1783
138	2.0950	2.0618	2.0839	2.0863	2.0913	2.0659	2.0811	2.1631
139	2.1033	2.0686	2.0917	2.0945	2.0956	2.0692	2.0864	2.1779
140	2.0923	2.0610	2.0819	2.0876	2.0961	2.0607	2.0814	2.1698
141	2.1050	2.0653	2.0918	2.0988	2.1014	2.0724	2.0909	2.1695
142	2.1038	2.0652	2.0909	2.0961	2.1042	2.0699	2.0901	2.1650
143	2.0941	2.0432	2.0771	2.1187	2.0815	1.9830	2.0611	2.1234
144	2.1144	2.0894	2.1061	1.9370	2.0217	1.9835	1.9807	2.0948
145	2.0406	2.1592	2.0802	2.0193	2.1700	2.0456	2.0783	2.1067
146	2.1007	2.0547	2.0853	2.0924	2.0936	2.0692	2.0851	2.1461
147	2.0911	2.0914	2.0912	1.8998	2.0041	2.0085	1.9708	2.0996
148	2.0976	2.0594	2.0848	2.0876	2.0983	2.0697	2.0852	2.1673
149	2.1227	2.0870	2.1108	2.1023	2.1051	2.0859	2.0977	2.1990
150	2.0379	2.1038	2.0599	2.0811	2.0750	2.1052	2.0871	2.1233
151	2.1034	2.1200	2.1089	2.0966	2.1015	2.0999	2.0993	2.2005
152	2.1221	2.1069	2.1171	2.1098	2.1076	2.0747	2.0973	2.1960
153	2.0702	2.0376	2.0594	2.0655	2.0688	2.0509	2.0618	2.1204
154	2.0857	2.0506	2.0740	2.0738	2.0851	2.0582	2.0724	2.1516
155	2.1007	2.0634	2.0883	2.0868	2.1003	2.0751	2.0874	2.1826

156	2.0920	2.0492	2.0777	2.0828	2.0849	2.0665	2.0781	2.1624
157	2.0887	2.0571	2.0782	2.0804	2.0911	2.0638	2.0784	2.1606
158	2.0899	2.0496	2.0765	2.0833	2.0868	2.0545	2.0749	2.1498
159	2.1043	2.0634	2.0906	2.0913	2.0965	2.0680	2.0853	2.1901
160	2.0965	2.0552	2.0827	2.0982	2.0953	2.0485	2.0806	2.1582
161	2.1103	2.0600	2.0935	2.1058	2.1024	2.0616	2.0899	2.1922
162	2.0927	2.0485	2.0780	2.0911	2.0905	2.0462	2.0759	2.1541
163	2.0952	2.0857	2.0920	2.0668	2.0702	2.0625	2.0665	2.1051
164	2.0921	2.0519	2.0787	2.0793	2.0937	2.0569	2.0766	2.1623
165	2.1266	2.1186	2.1240	2.1221	2.1291	2.1072	2.1195	2.2366
166	2.1106	2.0950	2.1054	2.0844	2.0908	2.0730	2.0828	2.1536
167	2.1082	2.0963	2.1042	2.0751	2.0797	2.0668	2.0738	2.1324
168	2.0763	2.0420	2.0649	2.0700	2.0751	2.0451	2.0634	2.1315
169	2.0848	2.0583	2.0760	2.0734	2.0906	2.0631	2.0757	2.1628
170	2.1045	2.0623	2.0905	2.0917	2.0980	2.0761	2.0886	2.1883

	psiM1	psiM2	delta	theta1	theta2	theta3	epsM1	<M-O>	<psi>
1	58.97	58.71	0.37	31.50	28.67	3.94	59.94	2.0842	58.796
2	58.85	58.66	0.25	29.71	30.08	0.39	60.01	2.0843	58.723
3	58.91	58.66	0.32	30.07	30.50	0.54	59.65	2.0855	58.741
4	58.84	58.58	0.34	29.93	30.24	0.72	59.86	2.0860	58.666
5	58.79	58.63	0.20	30.13	29.96	0.77	60.07	2.0822	58.686
6	58.82	58.53	0.37	29.91	30.47	0.54	59.63	2.0834	58.628
7	58.97	58.97	0.01	30.00	30.11	-0.09	60.04	2.0862	58.970
8	58.92	58.88	0.05	29.95	30.14	-0.03	60.07	2.0890	58.892
9	58.63	58.61	0.04	29.82	30.20	-0.27	59.99	2.0771	58.615
10	58.62	58.63	-0.01	29.83	30.11	-0.33	60.07	2.0815	58.626
11	58.81	58.74	0.10	29.94	29.93	0.30	60.07	2.0794	58.763
12	58.69	58.58	0.14	29.85	30.01	0.27	60.19	2.0807	58.617
13	58.85	58.72	0.18	29.86	30.22	0.18	59.89	2.0815	58.763
14	58.65	58.65	0.01	29.73	30.17	-0.42	60.00	2.0767	58.647
15	58.74	58.73	0.01	29.82	30.07	-0.21	60.09	2.0787	58.731
16	58.83	58.77	0.09	29.81	30.37	-0.30	59.93	2.0738	58.790
17	58.72	58.69	0.03	29.88	30.13	-0.15	60.10	2.0829	58.700
18	58.74	58.72	0.03	29.84	30.12	-0.18	60.03	2.0802	58.726
19	58.73	58.73	-0.01	30.06	29.97	0.06	60.46	2.0885	58.730
20	58.89	58.86	0.04	30.00	30.19	-0.06	59.99	2.0862	58.873
21	58.77	58.73	0.06	29.96	30.13	0.00	60.07	2.0895	58.744
22	59.29	59.27	0.01	30.00	30.34	-0.30	59.51	2.1060	59.278
23	59.00	59.03	-0.03	29.67	30.21	-0.62	59.98	2.0640	59.020
24	58.63	58.30	0.43	29.22	30.34	0.18	59.90	2.1072	58.412
25	59.09	58.86	0.29	29.56	30.59	-0.15	59.95	2.0633	58.938
26	58.65	58.52	0.17	29.79	30.27	0.03	59.78	2.0847	58.559
27	59.23	59.03	0.26	31.70	29.10	3.38	60.44	2.0628	59.099
28	60.97	58.55	3.44	25.85	34.41	1.77	59.49	2.0196	59.358
29	59.48	59.02	0.61	29.35	30.74	0.45	59.82	2.0735	59.178
30	58.82	58.81	0.01	30.12	29.94	0.21	60.10	2.0769	58.811
31	59.20	59.14	0.07	29.50	30.38	-0.66	59.92	2.0636	59.159
32	57.60	57.67	-0.08	29.76	30.11	-0.60	59.89	2.1281	57.647
33	57.93	57.77	0.20	29.45	30.15	-0.09	60.40	2.1165	57.826
34	58.39	58.22	0.22	29.75	30.01	0.38	60.43	2.0940	58.273
35	58.79	58.66	0.17	29.13	30.32	-0.68	60.22	2.0811	58.707
36	58.59	58.44	0.20	29.37	30.56	-0.60	60.07	2.0896	58.487
37	59.24	58.77	0.62	29.45	30.67	0.66	60.05	2.0829	58.927
38	59.28	58.87	0.54	29.57	30.72	0.48	59.87	2.0746	59.005
39	59.41	58.84	0.77	29.19	30.85	0.63	59.89	2.0777	59.030
40	59.46	58.87	0.78	29.29	30.81	0.81	59.97	2.0700	59.068
41	59.32	58.87	0.60	29.44	30.68	0.57	59.91	2.0787	59.017
42	59.43	58.91	0.70	29.24	30.76	0.57	59.87	2.0732	59.082
43	58.72	58.94	-0.28	30.65	30.13	-0.33	60.14	2.0721	58.868
44	59.25	59.19	0.07	29.55	30.16	-0.39	59.92	2.1294	59.213
45	59.24	59.23	0.02	29.59	30.23	-0.57	59.85	2.1269	59.232
46	59.38	58.86	0.70	28.68	31.35	-0.57	59.96	2.0214	59.034
47	59.23	58.79	0.58	28.78	31.21	-0.69	59.98	2.0240	58.939
48	59.07	58.73	0.46	29.08	30.95	-0.51	59.96	2.0262	58.839
49	59.00	59.05	-0.06	29.46	30.25	-0.98	59.99	2.0634	59.029
50	58.69	58.50	0.25	29.76	30.33	0.18	59.77	2.0659	58.566
51	59.56	59.48	0.12	29.56	30.62	-0.71	60.57	2.0216	59.510

52	59.98	59.11	1.17	28.49	31.85	0.15	59.75	2.0248	59.401
53	59.45	59.15	0.41	31.90	28.66	4.48	60.49	2.0650	59.251
54	59.19	58.99	0.27	29.48	30.49	-0.21	59.94	2.0675	59.055
55	58.47	58.45	0.03	31.24	31.08	0.24	59.18	2.1089	58.455
56	58.62	58.56	0.08	30.55	30.84	-0.06	59.12	2.1077	58.579
57	58.66	58.46	0.26	30.05	31.25	-0.43	59.12	2.1066	58.527
58	58.91	58.66	0.32	30.32	31.26	0.03	59.24	2.0988	58.744
59	59.27	58.89	0.51	30.23	31.51	0.24	59.43	2.0897	59.016
60	59.44	58.92	0.70	30.06	31.66	0.49	59.12	2.0844	59.093
61	59.46	58.86	0.80	29.92	31.84	0.49	59.31	2.0839	59.059
62	59.72	59.02	0.93	29.80	31.77	0.82	59.35	2.0786	59.254
63	59.18	58.80	0.50	29.16	30.69	-0.03	59.88	2.0922	58.928
64	58.50	58.42	0.11	29.49	30.41	-0.60	59.73	2.0896	58.449
65	60.83	58.52	3.28	25.44	33.73	1.56	60.23	2.0191	59.287
66	59.35	59.32	0.04	29.41	30.32	-0.80	60.01	2.0601	59.333
67	59.16	58.88	0.38	30.71	29.57	2.27	60.08	2.0740	58.970
68	57.85	58.40	-0.71	29.26	28.57	-1.44	61.43	2.0399	58.216
69	58.04	58.23	-0.23	30.49	30.02	-0.21	60.14	2.0905	58.165
70	57.83	57.88	-0.07	30.28	29.73	0.36	60.15	2.0602	57.862
71	60.13	58.39	2.39	27.52	31.93	2.77	59.52	2.1059	58.969
72	59.28	59.27	0.01	30.57	29.46	1.15	60.38	2.0921	59.275
73	58.00	58.03	-0.03	30.16	29.98	0.09	59.99	2.0635	58.020
74	58.62	58.23	0.50	30.11	31.49	0.12	58.51	2.0707	58.358
75	60.20	60.24	-0.04	30.03	30.35	-0.44	59.94	2.0772	60.227
76	59.58	59.39	0.25	29.98	30.20	0.54	60.04	2.0949	59.451
77	58.79	58.81	-0.02	29.85	30.21	-0.42	59.93	2.0629	58.801
78	59.88	59.90	-0.02	29.79	30.43	-0.69	59.84	2.0949	59.895
79	59.53	59.45	0.11	29.55	30.35	-0.48	60.04	2.1247	59.479
80	58.57	57.15	1.65	28.06	26.11	6.90	65.19	2.0676	57.622
81	58.50	58.26	0.31	29.17	30.40	-0.30	59.40	2.1109	58.337
82	59.14	58.92	0.29	29.62	30.33	0.15	59.97	2.0727	58.992
83	58.94	58.89	0.06	29.77	30.16	-0.21	60.09	2.0694	58.908
84	59.29	59.11	0.24	29.89	30.04	0.57	59.91	2.0664	59.169
85	59.12	58.94	0.23	30.16	29.87	0.98	60.11	2.0720	59.003
86	59.07	58.96	0.16	30.19	29.88	0.77	60.10	2.0703	58.995
87	59.19	59.12	0.09	30.55	29.93	0.89	60.04	2.0640	59.144
88	58.93	58.75	0.23	29.85	30.10	0.45	60.10	2.0696	58.812
89	59.32	59.06	0.35	30.06	29.76	1.34	60.08	2.0635	59.144
90	59.10	58.96	0.18	30.05	29.95	0.63	60.11	2.0681	59.005
91	59.13	59.00	0.17	30.34	29.76	1.10	60.24	2.0683	59.046
92	59.13	58.96	0.22	30.02	30.05	0.63	60.05	2.0682	59.020
93	59.19	59.00	0.25	30.47	29.65	1.58	60.16	2.0714	59.065
94	59.27	58.98	0.39	30.01	29.94	1.23	60.00	2.0680	59.073
95	59.35	58.98	0.49	29.91	30.38	0.99	59.81	2.0727	59.107
96	59.42	59.25	0.23	31.01	29.32	2.38	60.32	2.0643	59.308
97	59.08	58.94	0.19	29.98	29.89	0.66	60.06	2.0751	58.985
98	59.05	58.94	0.14	30.01	29.97	0.45	60.00	2.0673	58.976
99	58.89	58.94	-0.07	30.22	29.81	0.21	59.88	2.0775	58.928
100	59.58	59.01	0.77	30.79	29.44	3.65	60.20	2.0721	59.202
101	59.50	59.07	0.58	31.26	29.30	3.70	60.22	2.0719	59.215
102	59.46	58.91	0.75	30.67	29.44	3.47	60.20	2.0750	59.091
103	58.94	58.82	0.16	29.54	30.25	-0.24	59.97	2.0801	58.856

104	58.85	58.83	0.02	29.84	30.17	-0.27	60.02	2.0793	58.838
105	59.08	58.88	0.26	30.33	29.73	1.37	60.04	2.0740	58.945
106	58.93	58.76	0.21	29.98	30.02	0.60	59.96	2.0716	58.819
107	59.22	59.07	0.20	30.06	29.91	0.75	59.95	2.0612	59.120
108	59.59	59.18	0.54	29.92	30.33	1.20	59.98	2.0644	59.318
109	59.23	59.02	0.27	30.20	29.83	1.19	59.99	2.0652	59.086
110	59.17	58.99	0.23	30.15	29.92	0.92	59.94	2.0642	59.048
111	59.03	58.72	0.40	30.17	29.86	1.52	60.12	2.0769	58.825
112	58.88	58.61	0.36	29.91	30.03	0.96	60.05	2.0828	58.697
113	58.65	58.51	0.19	29.61	30.25	-0.06	59.97	2.0794	58.555
114	59.58	59.20	0.51	30.84	29.37	2.99	59.98	2.0620	59.326
115	59.32	59.02	0.40	30.26	29.79	1.67	59.93	2.0705	59.120
116	59.06	58.91	0.20	30.01	29.86	0.74	60.14	2.0711	58.958
117	59.05	58.94	0.15	30.27	29.84	0.86	60.10	2.0717	58.977
118	59.04	58.69	0.47	31.35	29.88	2.87	59.62	2.0792	58.808
119	58.85	58.71	0.18	29.66	29.86	0.33	60.26	2.0764	58.756
120	58.89	58.71	0.24	29.82	30.14	0.42	60.07	2.0767	58.770
121	59.12	58.97	0.20	30.19	29.87	0.92	60.04	2.0742	59.019
122	59.05	59.01	0.05	29.45	30.51	-0.89	59.82	2.0686	59.023
123	59.05	58.99	0.08	29.35	30.49	-0.90	59.80	2.0688	59.006
124	58.98	58.96	0.03	29.82	30.29	-0.39	60.05	2.0648	58.967
125	58.90	58.88	0.03	29.80	30.32	-0.45	60.01	2.0655	58.890
126	58.99	58.93	0.07	29.46	30.46	-0.78	59.90	2.0645	58.952
127	59.27	59.06	0.27	29.25	30.61	-0.54	59.95	2.0583	59.129
128	58.76	58.74	0.03	29.52	30.20	-0.59	60.25	2.0705	58.744
129	59.05	58.81	0.32	29.23	30.88	-0.69	59.98	2.0248	58.891
130	58.76	58.70	0.08	29.48	30.40	-0.68	60.10	2.0278	58.723
131	58.81	58.63	0.23	29.46	30.79	-0.63	60.04	2.0267	58.692
132	59.07	58.82	0.34	29.13	30.87	-0.72	60.01	2.0274	58.903
133	58.80	58.71	0.11	30.06	30.61	-0.21	60.01	2.0257	58.743
134	59.00	58.65	0.48	29.05	31.03	-0.54	60.13	2.0283	58.765
135	58.65	58.60	0.06	29.86	30.18	-0.12	60.21	2.0822	58.620
136	58.66	58.63	0.04	29.97	30.10	0.00	60.01	2.0890	58.637
137	58.54	58.49	0.07	29.70	30.08	-0.18	60.03	2.0849	58.508
138	58.74	58.69	0.06	29.82	30.18	-0.17	60.01	2.0821	58.704
139	58.63	58.54	0.12	29.93	30.19	0.09	60.01	2.0882	58.568
140	58.59	58.59	0.01	30.02	29.96	0.09	60.15	2.0816	58.589
141	58.76	58.75	0.02	29.91	30.12	-0.15	60.01	2.0912	58.752
142	58.82	58.81	0.02	29.90	30.09	-0.13	60.08	2.0904	58.811
143	59.26	58.99	0.35	30.60	29.39	2.27	60.09	2.0664	59.083
144	60.18	58.08	2.93	26.26	33.10	1.95	61.09	2.0225	58.776
145	59.58	59.55	0.01	27.28	27.04	0.28	63.38	2.0789	59.556
146	59.03	59.03	0.01	30.03	30.16	-0.11	60.02	2.0852	59.028
147	59.87	57.81	2.89	24.76	34.03	-0.60	60.74	2.0109	58.499
148	58.68	58.69	-0.01	29.87	30.09	-0.24	60.12	2.0851	58.687
149	58.61	58.39	0.29	29.79	30.44	0.21	60.01	2.1021	58.462
150	58.98	59.42	-0.58	30.05	29.21	-0.89	59.87	2.0780	59.275
151	58.55	58.39	0.21	28.76	30.38	-0.99	59.77	2.1025	58.447
152	58.76	58.43	0.43	29.45	30.26	0.48	60.01	2.1039	58.540
153	59.01	59.05	-0.05	29.90	30.25	-0.50	59.85	2.0610	59.041
154	58.75	58.73	0.04	29.70	30.28	-0.46	59.99	2.0729	58.736
155	58.49	58.48	0.02	29.70	30.29	-0.53	60.02	2.0877	58.484

156	58.64	58.65	0.00	29.94	30.37	-0.44	59.84	2.0780	58.647
157	58.68	58.68	0.00	29.87	30.08	-0.23	60.10	2.0783	58.683
158	58.83	58.80	0.04	29.84	30.18	-0.24	59.96	2.0754	58.807
159	58.41	58.32	0.12	30.01	30.22	0.15	60.07	2.0871	58.353
160	58.79	58.76	0.04	30.20	29.85	0.48	60.11	2.0813	58.770
161	58.43	58.37	0.08	30.18	30.08	0.34	60.02	2.0911	58.389
162	58.78	58.75	0.04	30.12	29.97	0.28	60.07	2.0766	58.758
163	59.79	59.38	0.55	28.94	30.85	-0.25	59.77	2.0750	59.518
164	58.66	58.63	0.05	29.93	30.08	-0.01	60.21	2.0773	58.637
165	58.23	58.15	0.10	29.38	30.13	-0.46	59.97	2.1210	58.179
166	59.24	58.87	0.49	29.13	30.63	-0.03	59.94	2.0903	58.992
167	59.56	59.06	0.66	28.77	30.93	-0.18	59.80	2.0840	59.227
168	58.93	58.90	0.03	29.71	30.24	-0.43	59.90	2.0639	58.910
169	58.61	58.60	0.01	29.64	30.14	-0.48	60.12	2.0758	58.603
170	58.44	58.41	0.04	29.75	30.42	-0.54	59.87	2.0892	58.418

		unshared edges M2			unshared edges M1		
	<e_u>M2	(O3-O3')	(O3-O4)	(O3'-O4)	(O3-O3)*2	(O3-O4)*4	<e_s>M1
1	3.0741	3.0746	3.0716	3.0759	3.1070	3.1098	3.1089
2	3.0777	3.0800	3.0746	3.0786	3.0957	3.1039	3.1012
3	3.0778	3.0811	3.0770	3.0753	3.1009	3.1114	3.1079
4	3.0756	3.0764	3.0735	3.0767	3.1051	3.1085	3.1074
5	3.0750	3.0726	3.0800	3.0724	3.0979	3.0915	3.0937
6	3.0697	3.0728	3.0622	3.0741	3.0967	3.1072	3.1037
7	3.0963	3.0936	3.1005	3.0947	3.1003	3.0950	3.0968
8	3.0964	3.0934	3.1014	3.0944	3.1055	3.0993	3.1014
9	3.0702	3.0694	3.0704	3.0709	3.0738	3.0736	3.0737
10	3.0787	3.0772	3.0802	3.0786	3.0788	3.0765	3.0773
11	3.0765	3.0760	3.0768	3.0768	3.0855	3.0857	3.0856
12	3.0724	3.0698	3.0775	3.0698	3.0895	3.0834	3.0855
13	3.0772	3.0788	3.0749	3.0780	3.0893	3.0960	3.0938
14	3.0714	3.0723	3.0704	3.0717	3.0691	3.0737	3.0722
15	3.0770	3.0759	3.0790	3.0762	3.0791	3.0779	3.0783
16	3.0694	3.0679	3.0697	3.0704	3.0791	3.0764	3.0773
17	3.0817	3.0789	3.0860	3.0801	3.0885	3.0827	3.0846
18	3.0785	3.0775	3.0789	3.0792	3.0821	3.0814	3.0816
19	3.0923	3.0826	3.1130	3.0814	3.1092	3.0827	3.0915
20	3.0919	3.0901	3.0959	3.0898	3.0985	3.0947	3.0960
21	3.0923	3.0889	3.0966	3.0914	3.1027	3.0948	3.0975
22	3.1354	3.1412	3.1225	3.1426	3.1221	3.1444	3.1370
23	3.0660	3.0666	3.0636	3.0676	3.0585	3.0659	3.0634
24	3.0955	3.1024	3.0826	3.1016	3.1217	3.1432	3.1360
25	3.0523	3.0519	3.0537	3.0513	3.0791	3.0796	3.0795
26	3.0755	3.0789	3.0675	3.0801	3.0830	3.0953	3.0912
27	3.0566	3.0399	3.0913	3.0387	3.1119	3.0674	3.0822
28	2.9104	2.9195	2.8921	2.9195	3.1863	3.2191	3.2082
29	3.0654	3.0683	3.0605	3.0674	3.1144	3.1257	3.1220
30	3.0772	3.0736	3.0832	3.0750	3.0828	3.0760	3.0783
31	3.0665	3.0686	3.0614	3.0697	3.0662	3.0771	3.0735
32	3.1163	3.1196	3.1087	3.1205	3.1015	3.1122	3.1087
33	3.0967	3.0937	3.1074	3.0889	3.1194	3.1137	3.1156
34	3.0784	3.0731	3.0938	3.0682	3.1068	3.0943	3.0985
35	3.0748	3.0744	3.0715	3.0786	3.0897	3.0910	3.0906
36	3.0792	3.0785	3.0816	3.0776	3.0969	3.0979	3.0976
37	3.0709	3.0684	3.0758	3.0684	3.1326	3.1267	3.1287
38	3.0636	3.0644	3.0653	3.0609	3.1112	3.1149	3.1137
39	3.0623	3.0640	3.0584	3.0644	3.1285	3.1349	3.1328
40	3.0518	3.0516	3.0534	3.0505	3.1226	3.1233	3.1231
41	3.0684	3.0690	3.0675	3.0685	3.1215	3.1252	3.1239
42	3.0594	3.0619	3.0545	3.0617	3.1172	3.1265	3.1234
43	3.0810	3.0682	3.1022	3.0727	3.0780	3.0426	3.0544
44	3.1661	3.1702	3.1562	3.1719	3.1636	3.1779	3.1732
45	3.1645	3.1689	3.1538	3.1710	3.1571	3.1716	3.1668
46	2.9808	2.9806	2.9795	2.9824	3.0409	3.0451	3.0437
47	2.9852	2.9853	2.9836	2.9867	3.0347	3.0390	3.0376
48	2.9893	2.9893	2.9883	2.9904	3.0275	3.0320	3.0305
49	3.0663	3.0689	3.0614	3.0686	3.0506	3.0655	3.0605
50	3.0456	3.0480	3.0385	3.0504	3.0604	3.0730	3.0688

51	3.0136	3.0002	3.0401	3.0005	3.0499	3.0107	3.0237
52	2.9835	2.9856	2.9797	2.9853	3.0821	3.0917	3.0885
53	3.0587	3.0438	3.0885	3.0437	3.1259	3.0855	3.0989
54	3.0632	3.0649	3.0615	3.0631	3.0822	3.0908	3.0879
55	3.1121	3.1042	3.1265	3.1055	3.1278	3.1073	3.1141
56	3.1128	3.1162	3.1049	3.1174	3.1120	3.1241	3.1201
57	3.1037	3.1081	3.0933	3.1096	3.1184	3.1332	3.1282
58	3.0974	3.0966	3.0981	3.0974	3.1289	3.1268	3.1275
59	3.0871	3.0810	3.0988	3.0816	3.1467	3.1281	3.1343
60	3.0758	3.0763	3.0738	3.0772	3.1391	3.1412	3.1405
61	3.0709	3.0674	3.0775	3.0679	3.1521	3.1415	3.1450
62	3.0656	3.0632	3.0699	3.0635	3.1558	3.1490	3.1513
63	3.0883	3.0926	3.0807	3.0917	3.1256	3.1395	3.1349
64	3.0808	3.0869	3.0669	3.0885	3.0779	3.0975	3.0910
65	2.9119	2.9155	2.9021	2.9182	3.1859	3.2008	3.1959
66	3.0680	3.0683	3.0622	3.0735	3.0669	3.0737	3.0715
67	3.0664	3.0618	3.0754	3.0620	3.1090	3.0980	3.1017
68	3.0246	3.0144	3.0386	3.0209	2.9710	2.9542	2.9598
69	3.0834	3.0727	3.0985	3.0790	3.0818	3.0521	3.0620
70	3.0239	3.0193	3.0304	3.0220	3.0241	3.0149	3.0179
71	3.0535	3.0703	3.0262	3.0640	3.2343	3.2898	3.2713
72	3.1147	3.1058	3.1318	3.1064	3.1311	3.1089	3.1163
73	3.0329	3.0315	3.0370	3.0302	3.0293	3.0305	3.0301
74	3.0377	3.0503	3.0091	3.0536	3.0548	3.0994	3.0845
75	3.1246	3.1231	3.1341	3.1166	3.1175	3.1217	3.1203
76	3.1173	3.1140	3.1239	3.1139	3.1439	3.1396	3.1410
77	3.0571	3.0567	3.0561	3.0584	3.0516	3.0572	3.0553
78	3.1395	3.1394	3.1380	3.1411	3.1345	3.1398	3.1380
79	3.1668	3.1661	3.1666	3.1677	3.1760	3.1775	3.1770
80	2.9602	2.9341	3.0804	2.8661	3.1859	3.0977	3.1271
81	3.1022	3.1188	3.0680	3.1199	3.0980	3.1483	3.1315
82	3.0682	3.0678	3.0652	3.0717	3.0941	3.0949	3.0946
83	3.0675	3.0650	3.0696	3.0680	3.0761	3.0717	3.0732
84	3.0662	3.0674	3.0614	3.0698	3.0828	3.0914	3.0885
85	3.0694	3.0662	3.0744	3.0676	3.0951	3.0887	3.0908
86	3.0689	3.0658	3.0753	3.0656	3.0877	3.0812	3.0834
87	3.0665	3.0602	3.0790	3.0603	3.0845	3.0701	3.0749
88	3.0596	3.0574	3.0625	3.0588	3.0838	3.0794	3.0809
89	3.0578	3.0578	3.0581	3.0574	3.0875	3.0909	3.0898
90	3.0652	3.0623	3.0698	3.0636	3.0857	3.0797	3.0817
91	3.0671	3.0600	3.0792	3.0622	3.0951	3.0772	3.0831
92	3.0646	3.0623	3.0685	3.0630	3.0879	3.0837	3.0851
93	3.0697	3.0648	3.0791	3.0651	3.1009	3.0896	3.0934
94	3.0610	3.0605	3.0600	3.0626	3.0954	3.0974	3.0967
95	3.0658	3.0662	3.0640	3.0670	3.1090	3.1117	3.1108
96	3.0673	3.0563	3.0867	3.0589	3.1082	3.0793	3.0889
97	3.0747	3.0739	3.0750	3.0753	3.0917	3.0926	3.0923
98	3.0644	3.0640	3.0643	3.0649	3.0760	3.0775	3.0770
99	3.0843	3.0861	3.0802	3.0866	3.0727	3.0809	3.0781
100	3.0584	3.0514	3.0708	3.0530	3.1411	3.1239	3.1297
101	3.0637	3.0533	3.0832	3.0547	3.1378	3.1090	3.1186
102	3.0598	3.0541	3.0694	3.0559	3.1391	3.1240	3.1291

103	3.0788	3.0806	3.0735	3.0825	3.0880	3.0961	3.0934
104	3.0812	3.0800	3.0828	3.0808	3.0835	3.0830	3.0832
105	3.0696	3.0679	3.0734	3.0674	3.0951	3.0928	3.0936
106	3.0633	3.0638	3.0623	3.0639	3.0807	3.0841	3.0829
107	3.0583	3.0585	3.0563	3.0599	3.0731	3.0783	3.0766
108	3.0590	3.0549	3.0631	3.0590	3.1135	3.1060	3.1085
109	3.0607	3.0599	3.0615	3.0607	3.0852	3.0865	3.0861
110	3.0593	3.0602	3.0601	3.0578	3.0768	3.0828	3.0808
111	3.0654	3.0621	3.0703	3.0638	3.1085	3.1000	3.1029
112	3.0714	3.0692	3.0706	3.0743	3.1082	3.1028	3.1046
113	3.0668	3.0689	3.0633	3.0681	3.0797	3.0872	3.0847
114	3.0559	3.0541	3.0596	3.0541	3.1028	3.1028	3.1028
115	3.0656	3.0662	3.0641	3.0663	3.0994	3.1043	3.1027
116	3.0676	3.0655	3.0711	3.0662	3.0884	3.0847	3.0859
117	3.0707	3.0671	3.0776	3.0673	3.0894	3.0816	3.0842
118	3.0656	3.0597	3.0735	3.0636	3.1193	3.1035	3.1088
119	3.0696	3.0695	3.0713	3.0678	3.0847	3.0865	3.0859
120	3.0683	3.0672	3.0710	3.0667	3.0919	3.0904	3.0909
121	3.0740	3.0717	3.0768	3.0735	3.0957	3.0914	3.0928
122	3.0701	3.0744	3.0628	3.0730	3.0648	3.0803	3.0751
123	3.0690	3.0740	3.0573	3.0758	3.0646	3.0826	3.0766
124	3.0636	3.0608	3.0676	3.0623	3.0711	3.0638	3.0662
125	3.0621	3.0617	3.0663	3.0584	3.0643	3.0646	3.0645
126	3.0611	3.0635	3.0554	3.0644	3.0618	3.0712	3.0680
127	3.0515	3.0537	3.0465	3.0545	3.0713	3.0795	3.0768
128	3.0646	3.0615	3.0684	3.0639	3.0725	3.0650	3.0675
129	2.9927	2.9919	2.9941	2.9922	3.0221	3.0218	3.0219
130	2.9992	2.9983	3.0002	2.9991	3.0080	3.0057	3.0064
131	2.9920	2.9885	2.9986	2.9887	3.0187	3.0101	3.0130
132	2.9964	2.9949	2.9953	2.9990	3.0291	3.0263	3.0272
133	2.9960	2.9883	3.0088	2.9909	3.0214	2.9986	3.0062
134	2.9892	2.9857	2.9960	2.9859	3.0365	3.0305	3.0325
135	3.0770	3.0711	3.0862	3.0736	3.0932	3.0778	3.0829
136	3.0884	3.0871	3.0905	3.0876	3.0933	3.0918	3.0923
137	3.0773	3.0776	3.0729	3.0816	3.0819	3.0843	3.0835
138	3.0797	3.0787	3.0801	3.0804	3.0862	3.0850	3.0854
139	3.0826	3.0807	3.0852	3.0820	3.0962	3.0921	3.0934
140	3.0769	3.0742	3.0831	3.0732	3.0818	3.0758	3.0778
141	3.0960	3.0941	3.0967	3.0972	3.1001	3.0968	3.0979
142	3.0968	3.0946	3.1001	3.0956	3.1013	3.0974	3.0987
143	3.0598	3.0575	3.0632	3.0588	3.0939	3.0918	3.0925
144	2.9111	2.8985	2.9426	2.8921	3.1908	3.1513	3.1645
145	3.0999	3.0871	3.1212	3.0913	3.1285	3.0903	3.1030
146	3.0965	3.0922	3.1001	3.0972	3.1043	3.0938	3.0973
147	2.8845	2.8850	2.8835	2.8851	3.1293	3.1337	3.1323
148	3.0857	3.0823	3.0896	3.0851	3.0903	3.0825	3.0851
149	3.0943	3.0911	3.0992	3.0927	3.1266	3.1182	3.1210
150	3.1124	3.1223	3.0921	3.1228	3.0364	3.0685	3.0578
151	3.0965	3.1094	3.0682	3.1118	3.0901	3.1293	3.1163
152	3.0952	3.0978	3.0899	3.0979	3.1291	3.1382	3.1352
153	3.0627	3.0640	3.0603	3.0637	3.0541	3.0599	3.0580
154	3.0679	3.0682	3.0673	3.0681	3.0690	3.0725	3.0713

155	3.0819	3.0811	3.0826	3.0822	3.0839	3.0839	3.0839
156	3.0737	3.0733	3.0735	3.0743	3.0725	3.0737	3.0733
157	3.0755	3.0735	3.0787	3.0743	3.0780	3.0737	3.0751
158	3.0740	3.0737	3.0731	3.0752	3.0760	3.0780	3.0774
159	3.0737	3.0696	3.0814	3.0702	3.0918	3.0813	3.0848
160	3.0813	3.0780	3.0872	3.0789	3.0906	3.0830	3.0855
161	3.0823	3.0782	3.0886	3.0800	3.0957	3.0867	3.0897
162	3.0741	3.0711	3.0789	3.0721	3.0820	3.0763	3.0782
163	3.0801	3.0871	3.0664	3.0868	3.1167	3.1388	3.1315
164	3.0710	3.0663	3.0802	3.0665	3.0828	3.0714	3.0752
165	3.1183	3.1238	3.1069	3.1243	3.1159	3.1334	3.1276
166	3.0878	3.0913	3.0803	3.0918	3.1257	3.1375	3.1336
167	3.0808	3.0878	3.0662	3.0883	3.1270	3.1497	3.1421
168	3.0603	3.0625	3.0558	3.0626	3.0571	3.0665	3.0634
169	3.0687	3.0685	3.0693	3.0682	3.0685	3.0699	3.0694
170	3.0813	3.0817	3.0794	3.0828	3.0828	3.0867	3.0854

	shared edges M1			shared edges M2				
	(O3-O3)*2	(O3-O4)*4	<e_s>M1	(O3-O3)*1	(O3-O4)*2	(O3-O3)*2	(O4-O4)*1	<e_s>M2
1	2.8336	2.7953	2.8081	2.8336	2.7953	2.8061	2.7357	2.7954
2	2.8325	2.7969	2.8088	2.8325	2.7969	2.8209	2.7332	2.8002
3	2.8423	2.7960	2.8114	2.8423	2.7960	2.8014	2.7657	2.8005
4	2.8405	2.8025	2.8152	2.8405	2.8025	2.8100	2.7558	2.8035
5	2.8268	2.7958	2.8062	2.8268	2.7958	2.8130	2.7517	2.7994
6	2.8523	2.7941	2.8135	2.8523	2.7941	2.8101	2.7464	2.8012
7	2.8340	2.7782	2.7968	2.8340	2.7782	2.8320	2.7261	2.7968
8	2.8418	2.7857	2.8044	2.8418	2.7857	2.8376	2.7281	2.8028
9	2.8352	2.7796	2.7981	2.8352	2.7796	2.8319	2.7237	2.7970
10	2.8347	2.7863	2.8024	2.8347	2.7863	2.8384	2.7342	2.8031
11	2.8249	2.7833	2.7972	2.8249	2.7833	2.8227	2.7265	2.7939
12	2.8286	2.7935	2.8052	2.8286	2.7935	2.8267	2.7338	2.8005
13	2.8378	2.7839	2.8019	2.8378	2.7839	2.8219	2.7260	2.7959
14	2.8285	2.7792	2.7956	2.8285	2.7792	2.8306	2.7245	2.7954
15	2.8261	2.7802	2.7955	2.8261	2.7802	2.8300	2.7242	2.7951
16	2.8209	2.7721	2.7884	2.8209	2.7721	2.8089	2.7305	2.7856
17	2.8366	2.7857	2.8027	2.8366	2.7857	2.8362	2.7298	2.8017
18	2.8325	2.7809	2.7981	2.8325	2.7809	2.8317	2.7247	2.7971
19	2.8324	2.7964	2.8084	2.8324	2.7964	2.8437	2.7406	2.8088
20	2.8336	2.7850	2.8012	2.8336	2.7850	2.8264	2.7426	2.7998
21	2.8457	2.7930	2.8106	2.8457	2.7930	2.8409	2.7394	2.8088
22	2.8821	2.7772	2.8122	2.8821	2.7772	2.8620	2.7114	2.8120
23	2.8184	2.7374	2.7644	2.8184	2.7374	2.8227	2.6548	2.7656
24	2.8737	2.8457	2.8550	2.8737	2.8457	2.8524	2.7716	2.8403
25	2.8072	2.7571	2.7738	2.8072	2.7571	2.7835	2.6951	2.7639
26	2.8542	2.7928	2.8132	2.8542	2.7928	2.8363	2.7333	2.8076
27	2.8159	2.7420	2.7667	2.8159	2.7420	2.7927	2.6618	2.7579
28	2.8196	2.7407	2.7670	2.8196	2.7407	2.5874	2.4645	2.6567
29	2.8284	2.7649	2.7861	2.8284	2.7649	2.7816	2.6701	2.7653
30	2.8348	2.7678	2.7901	2.8348	2.7678	2.8349	2.6997	2.7900
31	2.8132	2.7352	2.7612	2.8132	2.7352	2.8095	2.6504	2.7588
32	2.9237	2.8878	2.8997	2.9237	2.8878	2.9292	2.8573	2.9025
33	2.9105	2.8705	2.8839	2.9105	2.8705	2.9170	2.7770	2.8771
34	2.8648	2.8236	2.8373	2.8648	2.8236	2.8675	2.7339	2.8301
35	2.8311	2.7892	2.8032	2.8311	2.7892	2.8359	2.7031	2.7974
36	2.8616	2.8037	2.8230	2.8616	2.8037	2.8524	2.7248	2.8164
37	2.8362	2.7939	2.8080	2.8362	2.7939	2.7926	2.7116	2.7868
38	2.8227	2.7769	2.7922	2.8227	2.7769	2.7779	2.7104	2.7738
39	2.8285	2.7865	2.8005	2.8285	2.7865	2.7733	2.6990	2.7745
40	2.8189	2.7741	2.7890	2.8189	2.7741	2.7644	2.6807	2.7628
41	2.8329	2.7815	2.7986	2.8329	2.7815	2.7879	2.6976	2.7782
42	2.8250	2.7740	2.7910	2.8250	2.7740	2.7753	2.6806	2.7674
43	2.8171	2.7538	2.7749	2.8171	2.7538	2.8205	2.7445	2.7851
44	2.8805	2.8307	2.8473	2.8805	2.8307	2.8800	2.7665	2.8447
45	2.8748	2.8257	2.8421	2.8748	2.8257	2.8732	2.7752	2.8413
46	2.7736	2.6972	2.7227	2.7736	2.6972	2.7274	2.5754	2.6997
47	2.7737	2.7036	2.7269	2.7737	2.7036	2.7364	2.5933	2.7078
48	2.7813	2.7054	2.7307	2.7813	2.7054	2.7507	2.6012	2.7158
49	2.8219	2.7326	2.7624	2.8219	2.7326	2.8335	2.6344	2.7647
50	2.8516	2.7582	2.7893	2.8516	2.7582	2.8277	2.6636	2.7812

51	2.7031	2.6890	2.6937	2.7031	2.6890	2.7052	2.6491	2.6901
52	2.7758	2.6997	2.7251	2.7758	2.6997	2.6871	2.5679	2.6862
53	2.8064	2.7480	2.7675	2.8064	2.7480	2.7798	2.6559	2.7530
54	2.8182	2.7528	2.7746	2.8182	2.7528	2.8008	2.6684	2.7656
55	2.8492	2.8465	2.8474	2.8492	2.8465	2.7743	2.9862	2.8462
56	2.8474	2.8394	2.8421	2.8474	2.8394	2.7889	2.9315	2.8393
57	2.8576	2.8412	2.8467	2.8576	2.8412	2.7889	2.9078	2.8376
58	2.8531	2.8179	2.8297	2.8531	2.8179	2.7765	2.8689	2.8185
59	2.8335	2.8011	2.8119	2.8335	2.8011	2.7449	2.8407	2.7943
60	2.8355	2.7917	2.8063	2.8355	2.7917	2.7265	2.8217	2.7823
61	2.8361	2.7957	2.8092	2.8361	2.7957	2.7243	2.8141	2.7817
62	2.8157	2.7892	2.7981	2.8157	2.7892	2.7001	2.8022	2.7661
63	2.8432	2.8049	2.8177	2.8432	2.8049	2.8103	2.7297	2.8005
64	2.8568	2.8053	2.8224	2.8568	2.8053	2.8452	2.7549	2.8188
65	2.7874	2.7547	2.7656	2.7874	2.7547	2.6063	2.4525	2.6603
66	2.8040	2.7222	2.7495	2.8040	2.7222	2.8067	2.6286	2.7484
67	2.8288	2.7690	2.7889	2.8288	2.7690	2.7995	2.6908	2.7761
68	2.7777	2.7309	2.7465	2.7777	2.7309	2.8984	2.5819	2.7697
69	2.8626	2.8083	2.8264	2.8626	2.8083	2.8676	2.7918	2.8344
70	2.8461	2.7767	2.7999	2.8461	2.7767	2.8528	2.7082	2.8022
71	2.9219	2.8538	2.8765	2.9219	2.8538	2.7650	2.6186	2.7964
72	2.8307	2.7757	2.7940	2.8307	2.7757	2.8381	2.7039	2.7937
73	2.8548	2.7717	2.7994	2.8548	2.7717	2.8546	2.6967	2.8007
74	2.9236	2.7517	2.8090	2.9236	2.7517	2.8215	2.6878	2.7930
75	2.8085	2.7033	2.7384	2.8085	2.7033	2.8050	2.6188	2.7407
76	2.8516	2.7695	2.7968	2.8516	2.7695	2.8316	2.6764	2.7884
77	2.8336	2.7394	2.7708	2.8336	2.7394	2.8321	2.6541	2.7718
78	2.8353	2.7439	2.7743	2.8353	2.7439	2.8277	2.6733	2.7753
79	2.8745	2.8108	2.8321	2.8745	2.8108	2.8705	2.7334	2.8284
80	2.7179	2.9459	2.8699	2.7179	2.9459	2.8650	2.5298	2.8116
81	2.8693	2.8555	2.8601	2.8693	2.8555	2.8437	2.8298	2.8496
82	2.8197	2.7665	2.7842	2.8197	2.7665	2.7997	2.6956	2.7746
83	2.8160	2.7585	2.7777	2.8160	2.7585	2.8148	2.6917	2.7757
84	2.8218	2.7418	2.7684	2.8218	2.7418	2.8048	2.6474	2.7604
85	2.8211	2.7621	2.7817	2.8211	2.7621	2.8073	2.6842	2.7740
86	2.8144	2.7599	2.7780	2.8144	2.7599	2.8051	2.6927	2.7729
87	2.8143	2.7371	2.7628	2.8143	2.7371	2.7988	2.6742	2.7600
88	2.8155	2.7702	2.7853	2.8155	2.7702	2.8030	2.7034	2.7776
89	2.8064	2.7487	2.7680	2.8064	2.7487	2.7895	2.6546	2.7562
90	2.8118	2.7569	2.7752	2.8118	2.7569	2.8021	2.6857	2.7693
91	2.8118	2.7550	2.7740	2.8118	2.7550	2.8033	2.6813	2.7683
92	2.8126	2.7574	2.7758	2.8126	2.7574	2.7972	2.6885	2.7684
93	2.8171	2.7604	2.7793	2.8171	2.7604	2.8015	2.6834	2.7707
94	2.8211	2.7556	2.7774	2.8211	2.7556	2.7958	2.6624	2.7644
95	2.8186	2.7678	2.7848	2.8186	2.7678	2.7744	2.7063	2.7682
96	2.8007	2.7404	2.7605	2.8007	2.7404	2.7854	2.6645	2.7528
97	2.8262	2.7653	2.7856	2.8262	2.7653	2.8176	2.6835	2.7792
98	2.8114	2.7556	2.7742	2.8114	2.7556	2.8030	2.6895	2.7697
99	2.8284	2.7633	2.7850	2.8284	2.7633	2.8295	2.7105	2.7874
100	2.8293	2.7654	2.7867	2.8293	2.7654	2.7781	2.6470	2.7605
101	2.8192	2.7633	2.7819	2.8192	2.7633	2.7733	2.6789	2.7619
102	2.8252	2.7785	2.7941	2.8252	2.7785	2.7773	2.6749	2.7686

103	2.8342	2.7771	2.7961	2.8342	2.7771	2.8274	2.7021	2.7909
104	2.8332	2.7723	2.7926	2.8332	2.7723	2.8321	2.7101	2.7920
105	2.8246	2.7684	2.7871	2.8246	2.7684	2.8074	2.6943	2.7784
106	2.8221	2.7699	2.7873	2.8221	2.7699	2.8070	2.7053	2.7802
107	2.8122	2.7373	2.7623	2.8122	2.7373	2.7984	2.6508	2.7557
108	2.8211	2.7404	2.7673	2.8211	2.7404	2.7779	2.6377	2.7492
109	2.8157	2.7481	2.7707	2.8157	2.7481	2.7964	2.6640	2.7615
110	2.8147	2.7472	2.7697	2.8147	2.7472	2.7974	2.6679	2.7620
111	2.8233	2.7863	2.7986	2.8233	2.7863	2.7979	2.7180	2.7849
112	2.8336	2.7983	2.8101	2.8336	2.7983	2.8102	2.7372	2.7980
113	2.8324	2.7941	2.8069	2.8324	2.7941	2.8222	2.7372	2.8004
114	2.8186	2.7350	2.7629	2.8186	2.7350	2.7808	2.6244	2.7458
115	2.8203	2.7589	2.7794	2.8203	2.7589	2.7912	2.6741	2.7658
116	2.8141	2.7651	2.7814	2.8141	2.7651	2.8073	2.6898	2.7748
117	2.8187	2.7611	2.7803	2.8187	2.7611	2.8090	2.6940	2.7755
118	2.8573	2.7766	2.8035	2.8573	2.7766	2.7894	2.7385	2.7880
119	2.8155	2.7853	2.7954	2.8155	2.7853	2.8212	2.7078	2.7894
120	2.8251	2.7825	2.7967	2.8251	2.7825	2.8116	2.7175	2.7884
121	2.8209	2.7648	2.7835	2.8209	2.7648	2.8066	2.6965	2.7767
122	2.8147	2.7511	2.7723	2.8147	2.7511	2.8090	2.6884	2.7705
123	2.8193	2.7510	2.7738	2.8193	2.7510	2.8129	2.6795	2.7711
124	2.7928	2.7568	2.7688	2.7928	2.7568	2.7891	2.7227	2.7679
125	2.8018	2.7575	2.7723	2.8018	2.7575	2.7989	2.7144	2.7715
126	2.8066	2.7514	2.7698	2.8066	2.7514	2.8011	2.6924	2.7673
127	2.7913	2.7441	2.7598	2.7913	2.7441	2.7751	2.6737	2.7506
128	2.8071	2.7730	2.7844	2.8071	2.7730	2.8164	2.7143	2.7834
129	2.7589	2.7068	2.7242	2.7589	2.7068	2.7355	2.6378	2.7136
130	2.7401	2.7231	2.7288	2.7401	2.7231	2.7395	2.6914	2.7261
131	2.7627	2.7161	2.7317	2.7627	2.7161	2.7436	2.6624	2.7241
132	2.7569	2.7131	2.7277	2.7569	2.7131	2.7337	2.6479	2.7164
133	2.7190	2.7297	2.7262	2.7190	2.7297	2.6961	2.7636	2.7224
134	2.7820	2.7139	2.7366	2.7820	2.7139	2.7532	2.6095	2.7209
135	2.8342	2.7909	2.8053	2.8342	2.7909	2.8333	2.7372	2.8033
136	2.8488	2.7957	2.8134	2.8488	2.7957	2.8446	2.7431	2.8121
137	2.8419	2.7988	2.8132	2.8419	2.7988	2.8417	2.7428	2.8110
138	2.8339	2.7862	2.8021	2.8339	2.7862	2.8296	2.7351	2.8001
139	2.8477	2.8009	2.8165	2.8477	2.8009	2.8371	2.7521	2.8126
140	2.8309	2.7913	2.8045	2.8309	2.7913	2.8346	2.7427	2.8042
141	2.8483	2.7933	2.8116	2.8483	2.7933	2.8455	2.7406	2.8111
142	2.8436	2.7908	2.8084	2.8436	2.7908	2.8443	2.7333	2.8079
143	2.8230	2.7496	2.7741	2.8230	2.7496	2.8024	2.6464	2.7622
144	2.7752	2.7825	2.7801	2.7752	2.7825	2.6385	2.5071	2.6874
145	2.6209	2.8466	2.7713	2.6209	2.8466	2.8258	2.6583	2.7707
146	2.8310	2.7745	2.7934	2.8310	2.7745	2.8251	2.7292	2.7933
147	2.7746	2.7701	2.7716	2.7746	2.7701	2.6496	2.4737	2.6813
148	2.8371	2.7893	2.8052	2.8371	2.7893	2.8404	2.7368	2.8056
149	2.8720	2.8284	2.8429	2.8720	2.8284	2.8473	2.7765	2.8333
150	2.7189	2.7825	2.7613	2.7189	2.7825	2.7749	2.8578	2.7819
151	2.8546	2.8363	2.8424	2.8546	2.8363	2.8539	2.7760	2.8352
152	2.8675	2.8350	2.8458	2.8675	2.8350	2.8456	2.7588	2.8312
153	2.7957	2.7408	2.7591	2.7957	2.7408	2.7926	2.7033	2.7610
154	2.8251	2.7695	2.7880	2.8251	2.7695	2.8232	2.7107	2.7869

155	2.8533	2.7983	2.8166	2.8533	2.7983	2.8528	2.7407	2.8160
156	2.8401	2.7755	2.7970	2.8401	2.7755	2.8296	2.7339	2.7974
157	2.8245	2.7823	2.7964	2.8245	2.7823	2.8282	2.7341	2.7966
158	2.8300	2.7682	2.7888	2.8300	2.7682	2.8261	2.7078	2.7877
159	2.8553	2.8065	2.8228	2.8553	2.8065	2.8438	2.7575	2.8189
160	2.8335	2.7808	2.7984	2.8335	2.7808	2.8318	2.7233	2.7970
161	2.8689	2.8047	2.8261	2.8689	2.8047	2.8580	2.7473	2.8236
162	2.8318	2.7727	2.7924	2.8318	2.7727	2.8285	2.7122	2.7911
163	2.8010	2.7618	2.7749	2.8010	2.7618	2.7628	2.6839	2.7557
164	2.8289	2.7822	2.7978	2.8289	2.7822	2.8306	2.7236	2.7964
165	2.8951	2.8643	2.8746	2.8951	2.8643	2.8988	2.8059	2.8712
166	2.8369	2.8005	2.8126	2.8369	2.8005	2.8076	2.7216	2.7958
167	2.8283	2.7852	2.7996	2.8283	2.7852	2.7858	2.6908	2.7768
168	2.8104	2.7492	2.7696	2.8104	2.7492	2.8076	2.6874	2.7686
169	2.8232	2.7825	2.7961	2.8232	2.7825	2.8306	2.7256	2.7958
170	2.8657	2.7994	2.8215	2.8657	2.7994	2.8563	2.7441	2.8202

	Ref.		Samples	[Al3+]	[Ti4+]	[Fe3+]	[Fe2+]	[Mn2+]
1	Brigatti & Davoli 1990	Bt	M14	0	0.231	0.4465	0.786	0.0125
2			M32	0.0105	0.153	0.457	0.713	0.027
3			M13	0.052	0.23	0.338	0.907	0.033
4			M73	0.015	0.2505	0.357	0.8605	0.015
5			M62	0.052	0.196	0.394	0.9535	0.032
6	Bigi & Brigatti 1994	Bt	M7	0.045	0.2	0.5035	0.695	0.0215
7	Brigatti *et al*. 1996a	ferri-Phl	S1	0	0.01	0.08	0.17	0
8			S2	0	0	0.11	0.2	0.01
9	Brigatti *et al*. 1996b	Fe^{3+}-rich Phl	1	0	0.05	0.19	0.07	0
10			2	0	0.06	0.21	0.07	0.01
11			3	0	0.13	0.3	0.38	0.01
12			4	0	0.13	0.25	0.34	0.01
13			5	0	0.18	0.24	0.62	0.02
14			6	0	0.08	0.16	0.09	0
15			7	0	0.09	0.22	0.09	0
16			8	0	0.1	0.23	0.09	0
17			9	0	0.03	0.1	0.22	0.01
18			10	0	0.08	0.15	0.08	0.01
19			11	0	0.01	0.05	0.17	0
20			12	0	0.01	0.06	0.17	0.01
21			13	0	0.02	0.23	0.2	0
22	Donnay *et al*. 1964	syn	ferriannite				3	
23	Hazen & Burnham 1973		Phl					
24			Ann	0.09	0.22	0.19	2.22	0.05
25	Russel & Guggenheim 1999		Phl	0.495			0.12	
26			Bt-untreated		0.105	0.105	1.065	0.06
27			Bt-heat-treated		0.105	0.985	0.185	0.06
28	Guggenheim 1981	Lepidolite	Radkovice	1.3	0	0.008	0.002	0.03
29	Hawthorne *et al*. 1999		Phl (Rb,Cs)	0.38	0.04		1	0.04
30	Hazen *et al*. 1981		trioc mica	0	0.088		0.031	0.006
31	Joswig 1972		Phl	0.075	0.03		0.16	0
32	Kato *et al*. 1979	Mn-Bt	No. 0	0.22		0.33	0.02	1.36
33		MnBaPhl	No. 1	0		0.063	0.003	0.954
34		MnBaPhl	No. 2	0		0.026	0.485	0.485
35		MnBaPhl	No. 5	0.346		0.041	0.003	0.516
36		kinoshitalite	No. 6	0.223		0.045	0.003	0.522
37	Brigatti *et al*. 2000a	Al-rich Bt	A4	0.35	0.21	0.01	1.45	0.04
38			GFS15a	0.6	0.14		1.36	0.02
39			H87	0.5	0.16		1.46	0.03
40			CC1	0.64	0.17		1.33	0.04
41			C3-31	0.48	0.2		1.48	0.06
42			B1	0.54	0.17	0.01	1.41	0.03
43	Knurr & Bailey 1986		Phl	0.114	0.009	0.173	0	0.132
44	Comodi *et al*. 1999	syn	No.1			0.035	2.965	
45	Cs-ferriannite	"	No.2			0.035	2.965	
46	MacKinney *et al*. 1988	clintonite	No.1	0.82	0		0.07	
47			No.2	0.74	0		0.18	
48			No.3	0.7	0.01		0.11	
49	McCauley *et al*. 1973	syn	F-Phl					
50	McCauley & Newham 1973	syn	BaLi-trioc					
51	Oberti *et al*. 1993	preiswerkite	KP9	0.859	0.001		0.193	0.004

[Mg2+]	[Li1+]	[Ca2+]	[Na1+]	[Mn3+]	[Cr3+]	[Zn2+]	[Ni2+]	[Co2+]	Total	Vac	
1.4325	0.009								2.9175	0.0825	1
1.5025	0.012								2.875	0.125	2
1.3505	0.0155								2.926	0.074	3
1.3865	0.006								2.8905	0.1095	4
1.3535	0.0095								2.9905	0.0095	5
1.5355	0								3.0005	-0.0005	6
2.73	0								2.99	0.01	7
2.68	0								3	0	8
2.68									2.99	0.01	9
2.64									2.99	0.01	10
2.17									2.99	0.01	11
2.19									2.92	0.08	12
1.9									2.96	0.04	13
2.65									2.98	0.02	14
2.6									3	0	15
2.57									2.99	0.01	16
2.64									3	0	17
2.68									3	0	18
2.7									2.93	0.07	19
2.75									3	0	20
2.54									2.99	0.01	21
									3	0	22
3									3	0	23
0.12									2.89	0.11	24
2.28									2.895	0.105	25
1.57									2.905	0.095	26
1.57									2.905	0.095	27
0.05	1.48								2.87	0.13	28
1.2	0.34								3	0	29
2.457	0.225	0.005	0.11						2.922	0.078	30
2.705	0	0	0						2.97	0.03	31
1.2									3.13	-0.13	32
1.74				0.183					2.943	0.057	33
2.266				0.003					3.265	-0.265	34
2.098				0.217					3.221	-0.221	35
2.065				0.206					3.064	-0.064	36
0.77									2.83	0.17	37
0.73									2.85	0.15	38
0.7									2.85	0.15	39
0.73									2.91	0.09	40
0.7									2.92	0.08	41
0.83									2.99	0.01	42
2.506									2.934	0.066	43
									3	0	44
									3	0	45
2.11									3	0	46
2.08									3	0	47
2.18									3	0	48
2.97									2.97	0.03	49
2.23	0.77								3	0	50
1.927					0.01				2.994	0.006	51

52			KP17	0.934			0.174	0.003
53	Ohta *et al*. 1982		oxy-Bt	0.163	0.342	0.855	0.013	0.01
54	Rayner 1974		Phl		0.105		0.1	
55	Redhammer *et al*. 2000	syn, Rietveld	A44	0.096		0.312	2.592	
56	Ann-Syd	"	sd12no.12	0.11		0.08	2.8	
57		"	sd25no.10	0.26		0.08	2.62	
58		"	sd37no.10	0.33		0.04	2.62	
59		"	sd50no.10	0.51		0	2.43	
60		"	sd62no.10	0.6		0	2.37	
61		"	sd75no.10	0.75		0	2.18	
62		"	sd87no.10	0.78		0	2.17	
63		Syd	G-117	0.27	0.04	0.48	1.9	0.03
64	Robert & Gaspérin 1985	Zn-mica	hendricksite	0.07	0.07		0.25	0.4
65	Sartori 1976		Lepidolite	1.31				
66	Takeda & Donnay 1966	syn	Li-F-mica					
67	Takeda & Ross 1975		hy-Bt	0.163	0.342	0.855	0.013	0.01
68	Takéuchi 1965	syn	clintonite	0.72				
69	Tateyama *et al*. 1974	syn	oct-vac					
70	Toraya *et al*. 1977	syn	taeniolite					
71	Toraya *et al*. 1978a	syn	Ge-mtm-like					
72		"	Ge-taeniolite					
73	Toraya *et al*. 1976	syn	mtm					
74	Toraya *et al*. 1983	syn	Mn-F-Mg-mica					0.24
75	Toraya *et al*. 1978b	syn	Ge-Phl					
76	Toraya & Marumo 1983	syn	Mg-Ge-F-mica					
77	Toraya *et al*. 1978c	syn	F-Ph-like					
78	Toraya & Marumo 1981	syn	x=.68					0.68
79	KMg[3-x]Mn[x]Ge3AlO10F2	"	x=1.96					1.96
80	Tyrna & Guggenheim 1991		norrishite	0.005	0.01			
81	Guggenheim & Frimmel 1999		ferrokinoshitalite	0.01	0.17	0.15	1.72	0.08
82	Cruciani & Zanazzi 1994	Phl	1	0.352	0.122	0.04	0.759	0.006
83			2	0.107	0.065	0	0.191	0
84			3	0	0.234	0.1	0.308	0.01
85			4	0.123	0.149	0.163	0.651	0.009
86			5	0.096	0.143	0.117	0.464	0.006
87			6	0	0.142	0.014	0.145	0
88			7	0	0.089	0.059	0.105	0
89			8	0	0.19	0.008	0.203	0
90			9	0.08	0.134	0.021	0.389	0.003
91			10	0.08	0.15	0.035	0.657	0.007
92			11	0.186	0.118	0.05	0.445	0.004
93			12	0.054	0.239	0.223	0.517	0.006
94			14	0.039	0.205	0.03	0.269	0.002
95			15	0.138	0.211	0.162	0.645	0.004
96			16	0.168	0.248	0.044	0.391	0.004
97			17	0	0.172	0.002	0.237	0.005
98			18	0.07	0.09	0.079	0.184	0.002
99			19	0	0.161	0.021	0.24	0.005
100			21	0	0.607	0.216	0.536	0.005
101			22	0	0.65	0.207	0.514	0.006
102			23	0	0.592	0.196	0.55	0.003
103			24	0	0.017	0.05	0.107	0.004

1.908			0.01	3.029	-0.029	52
1.666				3.049	-0.049	53
2.765		0.03		3	0	54
				3	0	55
				2.99	0.01	56
				2.96	0.04	57
				2.99	0.01	58
				2.94	0.06	59
				2.97	0.03	60
				2.93	0.07	61
				2.95	0.05	62
0.11				2.83	0.17	63
1.57			0.54	2.9	0.1	64
	1.69			3	0	65
2.8	0.2			3	0	66
1.666				3.049	-0.049	67
2.18				2.9	0.1	68
2.84				2.84	0.16	69
2	1			3	0	70
2.5				2.5	0.5	71
2	1			3	0	72
2.5				2.5	0.5	73
2.44				2.68	0.32	74
3				3	0	75
2.64				2.64	0.36	76
2.75				2.75	0.25	77
2.32				3	0	78
1.04				3	0	79
0.025	1	1.96		3	0	80
0.74				2.87	0.13	81
1.651	0.004		0	2.934	0.066	82
2.546	0		0.072	2.981	0.019	83
2.1	0.005		0	2.757	0.243	84
1.81			0.003	2.908	0.092	85
2.12			0.012	2.958	0.042	86
2.499	0.001		0.079	2.88	0.12	87
2.648	0.002		0.019	2.922	0.078	88
2.509	0.001		0.07	2.981	0.019	89
2.36	0		0.013	3	0	90
2.067			0.001	2.997	0.003	91
2.175			0.005	2.983	0.017	92
1.863			0.001	2.903	0.097	93
2.316	0.001		0.053	2.915	0.085	94
1.695	0.005		0.016	2.876	0.124	95
2.13	0		0.007	2.992	0.008	96
2.537	0		0.005	2.958	0.042	97
2.52	0		0.018	2.963	0.037	98
2.566	0		0.002	2.995	0.005	99
1.49	0.005		0.001	2.86	0.14	100
1.527	0.006		0	2.91	0.09	101
1.556	0.006		0	2.903	0.097	102
2.82	0.001		0.001	3	0	103

104			25	0	0.023	0.072	0.043	0.005
105			26	0.049	0.273	0	0.509	0.003
106	Brigatti *et al*. 1991	Ti-Bt	8	0.2235	0.1445		0.3905	0.022
107			9	0.0015	0.1775		0.2805	0.0135
108			10	0.0915	0.523		0.5865	0.031
109			11	0.152	0.325		0.5045	0.0275
110			12	0.0385	0.268		0.4965	0.017
111			15	0.007	0.389		0.942	0.023
112			16	0.0795	0.231		1.24	0.023
113			17	0.1915	0.198		1.295	0.009
114	Brigatti & Poppi 1993	Ba-rich trioc	18	0.0085	0.4145	0.1825	0.0635	0.005
115			19	0.017	0.371	0.3925	0.5965	0.0095
116			20	0.932	0.138	0.412	0.389	0.026
117			21	0.1375	0.166	0.3835	0.312	0.0045
118			22	0.0005	0.4865	0	0.7445	0.0065
119			23	0.116	0.141	0.465	0.4175	0.009
120			24	0.128	0.1795	0.7175	0.2995	0.0095
121			25	0.2425	0.171	0.2345	0.7645	0.007
122			26	0.2015	0.0435	0	0.295	0.019
123			27	0.165	0.0255	0	0.272	0.004
124	Alietti *et al*. 1995	high-Al Phl	Phl1a	0.24	0.02	0.09	0.12	0.01
125			Phl1b	0.24	0.02	0.07	0.11	0.01
126			Phl2a	0.18	0.01	0.15	0.03	
127			Phl3a	0.47	0.01	0.15	0.07	0.04
128			Phl4a	0.2		0.11	0.04	0.01
129	Alietti *et al*. 1997	clintonite	Cli5a	0.68			0.11	
130			Cli7c	0.64			0.22	
131			Cli8a	0.76			0.15	
132			Cli8d	0.65			0.13	
133			Cli9a	0.67	0.01		0.16	
134			Cli9b	0.63	0.01		0.16	
135	Brigatti *et al*. 2001	trioc	Tpp16-6a		0.06	0.08	0.13	0
136			Tax27-1		0.08	0.04	0.43	0.01
137			Taa11-1A		0.1	0.06	0.6	0.01
138			Tai17-1		0.09	0.1	0.44	0.01
139			Ta9		0.09	0	1.14	0.04
140			Li12a		0.05	0	0.44	0
141			Tpp16-6b		0.01	0.01	0.6	0.01
142			Tpp16-6c		0.01	0	0.6	0.01
143			Ma1		0.33	0.03	0.35	0
144	Takeda & Burnham 1969	syn	F-polylithionite	1				
145	Tepikin *et al*. 1969		Bt	0.18	0.1	0.01	2.31	0.02
146	Semenova *et al*. 1977		tetraferri-Phl				0.16	0.01
147	Soboleva *et al*. 1977		paragonite	2				
148	Semenova *et al*. 1983		tetraferri-Phl				0.15	
149			tetraferri-Bt				1.37	0.01
150	Brigatti *et al*. 2000b	Fe-rich Phl	26	0.835	0.0235	0.242	1.627	0.0035
151			33	0.3485	0.108	0.159	2.2215	0.0785
152			120	0.1275	0.2475	0.214	2.288	0.01
153	Redhammer & Roth 2002	syn	NiPhl#6	0.04				
154		"	Phl#2	0.03				
155		"	CoAn#2	0.06				

2.853	0.001	0.003		3	0	104
2.066		0.017		2.917	0.083	105
2.1665		0.047		2.994	0.006	106
2.4245		0.025		2.9225	0.0775	107
1.603		0.0525		2.8875	0.1125	108
1.8995		0.0705		2.979	0.021	109
2.0875		0.0535		2.961	0.039	110
1.475		0.006		2.842	0.158	111
1.401		0.0055		2.98	0.02	112
1.244		0.0065		2.944	0.056	113
2.3265				3.0005	-0.0005	114
1.611				2.9975	0.0025	115
1.103				3	0	116
1.9965				3	0	117
1.7				2.938	0.062	118
1.8515				3	0	119
1.666				3	0	120
1.5805				3	0	121
2.441				3	0	122
2.5335				3	0	123
2.48				2.96	0.04	124
2.55				3	0	125
2.63				3	0	126
2.23				2.97	0.03	127
2.64				3	0	128
2.21				3	0	129
2.14				3	0	130
2.09				3	0	131
2.22				3	0	132
2.17				3.01	-0.01	133
2.2				3	0	134
2.73				3	0	135
2.39				2.95	0.05	136
2.23				3	0	137
2.36				3	0	138
1.73				3	0	139
2.51				3	0	140
2.36				2.99	0.01	141
2.38				3	0	142
2.07				2.78	0.22	143
	2			3	0	144
0.28	0.04			2.94	0.06	145
2.89				3.06	-0.06	146
				2	1	147
2.85				3	0	148
1.64				3.02	-0.02	149
0.0965	0.169	0.007		3.0035	-0.0035	150
0.0015	0.0815			2.9985	0.0015	151
0.104				2.991	0.009	152
			2.98	3.02	-0.02	153
2.98				3.01	-0.01	154
			2.94	3	0	155

156		"	Coni1.8#2	0.04				
157		"	A20#2	0.03			0.33	
158		"	A20#4	0.03			0.33	
159		"	A40#7	0.03			0.53	
160		"	A60#2	0.01			0.68	
161		"	Mgan1.2#1	0.01			0.82	
162		"	Mgan1.6#4	0.01			0.5	
163		"	Sd87#4	0.79			2.18	
164		"	GaPhl#1					
165		Ann	Ann#1	0.001	0.079	0.284	2.25	0.175
166		Syd	G-117	0.657	0.017	0.096	1.949	0.119
167		Syd	Sdp#3	0.272	0.036	0.476	1.903	0.035
168	Redhammer pers. com.	syn	Nian#4	0.04				
169		"	Phl#1	0.03				
170		"	CoAn#1	0.06				

			1.32	1.67	3.03	-0.03	156
2.68					3.04	-0.04	157
2.68					3.04	-0.04	158
2.45					3.01	-0.01	159
2.35					3.04	-0.04	160
2.19					3.02	-0.02	161
2.51					3.02	-0.02	162
					2.97	0.03	163
3					3	0	164
0.074					2.863	0.137	165
0.054		0.003			2.895	0.105	166
0.109					2.831	0.169	167
			2.98		3.02	-0.02	168
2.98					3.01	-0.01	169
				2.94	3	0	170

	O1-O2	O1-O2'	O2-O2'	<O-O>bas	O3-O1	O3-O2	O3-O2'	<O3-Obas>
1	2.6846	2.6860	2.6846	2.6851	2.7271	2.7242	2.7247	2.7253
2	2.6873	2.6883	2.6896	2.6884	2.7344	2.7157	2.7202	2.7234
3	2.6977	2.6775	2.6910	2.6887	2.7312	2.7423	2.7483	2.7406
4	2.6890	2.6820	2.6849	2.6853	2.7261	2.7219	2.7227	2.7236
5	2.6826	2.6858	2.6849	2.6844	2.7142	2.7202	2.7218	2.7187
6	2.6795	2.6894	2.6847	2.6845	2.7192	2.7066	2.7242	2.7167
7	2.7370	2.7359	2.7361	2.7363	2.7501	2.7492	2.7486	2.7493
8	2.7336	2.7411	2.7387	2.7378	2.7488	2.7434	2.7463	2.7462
9	2.6902	2.6878	2.6881	2.6887	2.7193	2.7211	2.7159	2.7188
10	2.6949	2.6955	2.6947	2.6950	2.7264	2.7267	2.7269	2.7267
11	2.6958	2.6981	2.6970	2.6970	2.7246	2.7263	2.7262	2.7257
12	2.6846	2.7017	2.6958	2.6940	2.7224	2.7219	2.7173	2.7205
13	2.6942	2.6975	2.6976	2.6964	2.7189	2.7234	2.7237	2.7220
14	2.6968	2.6880	2.6923	2.6923	2.7240	2.7261	2.7229	2.7243
15	2.6990	2.6959	2.6975	2.6975	2.7180	2.7162	2.7158	2.7167
16	2.6952	2.6916	2.6912	2.6927	2.7242	2.7180	2.7300	2.7241
17	2.7035	2.7036	2.7033	2.7035	2.7243	2.7256	2.7231	2.7243
18	2.7025	2.6957	2.6974	2.6985	2.7307	2.7303	2.7292	2.7301
19	2.7192	2.7301	2.7283	2.7259	2.7326	2.7245	2.7292	2.7288
20	2.7257	2.7289	2.7286	2.7277	2.7486	2.7457	2.7481	2.7475
21	2.7184	2.7260	2.7218	2.7221	2.7448	2.7375	2.7386	2.7403
22	2.7681	2.6998	2.7278	2.7319	2.7821	2.7663	2.7798	2.7761
23	2.6731	2.6791	2.6775	2.6766	2.7083	2.7103	2.7089	2.7092
24	2.6876	2.6983	2.6942	2.6934	2.7227	2.7232	2.7341	2.7267
25	2.7046	2.7007	2.7030	2.7028	2.7285	2.7229	2.7175	2.7230
26	2.6742	2.6762	2.6749	2.6751	2.7129	2.7083	2.7115	2.7109
27	2.6589	2.6635	2.6641	2.6622	2.7149	2.7053	2.7093	2.7098
28	2.6289	2.6197	2.6258	2.6248	2.7150	2.6952	2.6952	2.7018
29	2.6724	2.6771	2.6766	2.6754	2.7180	2.7171	2.7212	2.7188
30	2.6773	2.6783	2.6779	2.6778	2.7288	2.7227	2.7246	2.7253
31	2.6808	2.6803	2.6809	2.6807	2.7190	2.7157	2.7166	2.7171
32	2.7154	2.7227	2.7193	2.7191	2.7514	2.7478	2.7493	2.7495
33	2.7047	2.7008	2.7075	2.7043	2.7115	2.7214	2.7115	2.7148
34	2.6653	2.7023	2.6925	2.6867	2.7178	2.7198	2.7292	2.7223
35	2.7082	2.7209	2.7138	2.7143	2.7410	2.7382	2.7378	2.7390
36	2.7225	2.7432	2.7386	2.7348	2.7755	2.7536	2.7586	2.7626
37	2.7048	2.7057	2.7058	2.7055	2.7365	2.7298	2.7267	2.7310
38	2.7047	2.6774	2.6913	2.6911	2.7271	2.7257	2.7134	2.7221
39	2.6996	2.6980	2.6986	2.6987	2.7363	2.7313	2.7290	2.7322
40	2.6935	2.6861	2.6903	2.6899	2.7219	2.7211	2.7161	2.7197
41	2.6961	2.6966	2.6973	2.6967	2.7261	2.7273	2.7262	2.7265
42	2.7003	2.6829	2.6904	2.6912	2.7233	2.7250	2.7195	2.7226
43	2.7005	2.7022	2.6986	2.7004	2.7279	2.7310	2.7299	2.7296
44	2.7497	2.7382	2.7430	2.7436	2.7611	2.7720	2.7748	2.7693
45	2.7441	2.7386	2.7400	2.7409	2.7607	2.7596	2.7581	2.7595
46	2.8295	2.8297	2.8296	2.8296	2.8197	2.8133	2.8087	2.8139
47	2.8338	2.8318	2.8321	2.8326	2.8132	2.8134	2.8082	2.8116
48	2.8197	2.8185	2.8191	2.8191	2.8081	2.8053	2.8015	2.8050
49	2.6586	2.6720	2.6688	2.6665	2.6927	2.6963	2.6948	2.6946
50	2.6759	2.6311	2.6499	2.6523	2.7253	2.7045	2.7150	2.7149

51	2.7719	2.7848	2.7824	2.7797	2.7580	2.7575	2.7474	2.7543
52	2.7804	2.7701	2.7735	2.7747	2.7234	2.7474	2.7424	2.7377
53	2.6785	2.6824	2.6820	2.6810	2.7282	2.7200	2.7233	2.7238
54	2.6909	2.6875	2.6914	2.6899	2.7283	2.7255	2.7281	2.7273
55	2.6663	2.7325	2.7021	2.7003	2.7794	2.6629	2.7141	2.7188
56	2.7150	2.6835	2.6980	2.6989	2.7413	2.7041	2.7405	2.7287
57	2.6713	2.7350	2.7071	2.7045	2.7534	2.6774	2.7367	2.7225
58	2.6602	2.7522	2.7150	2.7091	2.7562	2.6672	2.7307	2.7180
59	2.6534	2.7688	2.7255	2.7159	2.7603	2.6733	2.7344	2.7227
60	2.6827	2.7509	2.7262	2.7199	2.7510	2.6716	2.7308	2.7178
61	2.6904	2.7595	2.7359	2.7286	2.7450	2.6729	2.7208	2.7129
62	2.6377	2.7928	2.7403	2.7236	2.7429	2.6881	2.7316	2.7209
63	2.7137	2.7135	2.7147	2.7139	2.7390	2.7374	2.7392	2.7385
64	2.6965	2.6846	2.6883	2.6898	2.7278	2.7285	2.7262	2.7275
65	2.6195	2.6267	2.6232	2.6231	2.7213	2.6549	2.7201	2.6988
66	2.6785	2.6691	2.6701	2.6726	2.7205	2.7159	2.7150	2.7171
67	2.6912	2.6859	2.6885	2.6886	2.7305	2.7281	2.7280	2.7289
68	2.8111	2.8317	2.8274	2.8234	2.7579	2.8477	2.8202	2.8086
69	2.7023	2.6760	2.6814	2.6866	2.7182	2.7045	2.6735	2.6987
70	2.6169	2.6170	2.6160	2.6166	2.6852	2.6842	2.6835	2.6843
71	2.7829	2.7647	2.7783	2.7753	2.9127	2.8922	2.9116	2.9055
72	2.7730	2.7732	2.7739	2.7734	2.9050	2.9137	2.9024	2.9070
73	2.6276	2.6217	2.6272	2.6255	2.6761	2.6781	2.6800	2.6781
74	2.6465	2.6423	2.6436	2.6441	2.6875	2.6586	2.7107	2.6856
75	2.8101	2.8072	2.8163	2.8112	2.8759	2.8885	2.8790	2.8811
76	2.7886	2.7847	2.7875	2.7869	2.9082	2.9035	2.9034	2.9050
77	2.6507	2.6511	2.6514	2.6511	2.6947	2.6974	2.6951	2.6957
78	2.8167	2.8094	2.8115	2.8125	2.8878	2.8841	2.8850	2.8856
79	2.8172	2.8206	2.8192	2.8190	2.8890	2.8931	2.8911	2.8911
80	2.5906	2.5932	2.6452	2.6097	2.6952	2.6650	2.6716	2.6772
81	2.7010	2.7021	2.7010	2.7014	2.7572	2.7558	2.7573	2.7568
82	2.6988	2.6950	2.6936	2.6958	2.7231	2.7219	2.7190	2.7213
83	2.7005	2.6944	2.6949	2.6966	2.7298	2.7238	2.7233	2.7257
84	2.6770	2.6727	2.6739	2.6745	2.7216	2.7168	2.7184	2.7190
85	2.6971	2.6976	2.6971	2.6973	2.7259	2.7252	2.7261	2.7257
86	2.6937	2.6974	2.6970	2.6960	2.7279	2.7249	2.7253	2.7261
87	2.6814	2.6880	2.6868	2.6854	2.7371	2.7218	2.7266	2.7285
88	2.6826	2.6809	2.6809	2.6814	2.7454	2.7285	2.7340	2.7360
89	2.6829	2.6813	2.6832	2.6824	2.7173	2.7197	2.7231	2.7201
90	2.6950	2.6956	2.6950	2.6952	2.7320	2.7278	2.7278	2.7292
91	2.6977	2.6970	2.6964	2.6970	2.7274	2.7259	2.7200	2.7244
92	2.6981	2.6975	2.6978	2.6978	2.7340	2.7292	2.7289	2.7307
93	2.6935	2.6979	2.6969	2.6961	2.7320	2.7265	2.7283	2.7289
94	2.6753	2.6887	2.6827	2.6822	2.7257	2.7168	2.7247	2.7224
95	2.6972	2.6857	2.6898	2.6909	2.7302	2.7093	2.7218	2.7205
96	2.7030	2.6992	2.6994	2.7005	2.7310	2.7237	2.7225	2.7257
97	2.6911	2.6930	2.6920	2.6920	2.7239	2.7242	2.7222	2.7234
98	2.6909	2.6840	2.6866	2.6872	2.7219	2.7185	2.7214	2.7206
99	2.6951	2.6935	2.6945	2.6944	2.7308	2.7383	2.7308	2.7333
100	2.6813	2.6820	2.6813	2.6815	2.7367	2.7255	2.7287	2.7303
101	2.6838	2.6798	2.6808	2.6815	2.7384	2.7378	2.7334	2.7365
102	2.6821	2.6802	2.6799	2.6807	2.7407	2.7304	2.7315	2.7342

103	2.7016	2.7058	2.7035	2.7036	2.7374	2.7318	2.7404	2.7365
104	2.6961	2.7076	2.7036	2.7024	2.7334	2.7304	2.7352	2.7330
105	2.6961	2.6940	2.6960	2.6954	2.7279	2.7232	2.7271	2.7261
106	2.6871	2.6766	2.6812	2.6817	2.7221	2.7195	2.7212	2.7209
107	2.6728	2.6689	2.6705	2.6707	2.7142	2.7183	2.7179	2.7168
108	2.6751	2.6738	2.6721	2.6737	2.7160	2.7058	2.7084	2.7101
109	2.6768	2.6757	2.6765	2.6763	2.7180	2.7186	2.7177	2.7181
110	2.6740	2.6711	2.6753	2.6735	2.7103	2.7142	2.7118	2.7121
111	2.6903	2.6872	2.6873	2.6882	2.7221	2.7212	2.7179	2.7204
112	2.6838	2.6804	2.6777	2.6806	2.7240	2.7161	2.7101	2.7167
113	2.6876	2.6857	2.6875	2.6869	2.6970	2.7033	2.7077	2.7027
114	2.6726	2.6722	2.6740	2.6729	2.7193	2.7176	2.7218	2.7196
115	2.6860	2.6907	2.6897	2.6888	2.7239	2.7163	2.7243	2.7215
116	2.6935	2.6971	2.6960	2.6956	2.7175	2.7252	2.7226	2.7218
117	2.6994	2.6968	2.6984	2.6982	2.7234	2.7253	2.7221	2.7236
118	2.6533	2.6964	2.6749	2.6749	2.7285	2.7166	2.7402	2.7284
119	2.6999	2.6953	2.6990	2.6981	2.7174	2.7225	2.7198	2.7199
120	2.6993	2.6951	2.6976	2.6973	2.7343	2.7268	2.7280	2.7297
121	2.6979	2.6975	2.6968	2.6974	2.7345	2.7330	2.7334	2.7336
122	2.7112	2.7147	2.7155	2.7138	2.7564	2.7632	2.7603	2.7600
123	2.7140	2.7117	2.7118	2.7125	2.7555	2.7613	2.7600	2.7590
124	2.6970	2.6967	2.6958	2.6965	2.7308	2.7240	2.7195	2.7248
125	2.6975	2.6978	2.7011	2.6988	2.7259	2.7325	2.7277	2.7287
126	2.6993	2.7066	2.7041	2.7033	2.7276	2.7260	2.7267	2.7268
127	2.7157	2.7122	2.7131	2.7136	2.7269	2.7236	2.7274	2.7260
128	2.6971	2.7058	2.7013	2.7014	2.7237	2.7246	2.7223	2.7235
129	2.8363	2.8315	2.8325	2.8334	2.8249	2.8196	2.8170	2.8205
130	2.8499	2.8555	2.8542	2.8532	2.8353	2.8369	2.8315	2.8346
131	2.8368	2.8435	2.8430	2.8411	2.8179	2.8155	2.8155	2.8163
132	2.8416	2.8353	2.8328	2.8366	2.8312	2.8315	2.8279	2.8302
133	2.8607	2.8665	2.8635	2.8636	2.8420	2.8414	2.8563	2.8466
134	2.8213	2.8289	2.8291	2.8265	2.8123	2.8099	2.8017	2.8080
135	2.6864	2.7052	2.6967	2.6961	2.7359	2.7217	2.7261	2.7279
136	2.7038	2.6990	2.7011	2.7013	2.7293	2.7325	2.7318	2.7312
137	2.6985	2.6966	2.6943	2.6965	2.7209	2.7152	2.7127	2.7162
138	2.6996	2.7035	2.7011	2.7014	2.7384	2.7324	2.7364	2.7357
139	2.6914	2.6909	2.6905	2.6909	2.7311	2.7212	2.7233	2.7252
140	2.6857	2.6801	2.6837	2.6832	2.7127	2.7292	2.7225	2.7215
141	2.7294	2.7262	2.7252	2.7269	2.7413	2.7398	2.7376	2.7396
142	2.7257	2.7269	2.7263	2.7263	2.7445	2.7430	2.7387	2.7421
143	2.6699	2.6632	2.6664	2.6665	2.7168	2.7164	2.7142	2.7158
144	2.5616	2.6245	2.6000	2.5953	2.7165	2.6699	2.6596	2.6820
145	2.7385	2.6365	2.6843	2.6864	2.7988	2.8032	2.6743	2.7588
146	2.7357	2.7382	2.7337	2.7359	2.7497	2.7532	2.7533	2.7521
147	2.6842	2.7409	2.7306	2.7185	2.6890	2.7123	2.6987	2.7000
148	2.7076	2.7071	2.7055	2.7068	2.7350	2.7292	2.7268	2.7303
149	2.7185	2.7228	2.7202	2.7205	2.7490	2.7556	2.7518	2.7522
150	2.6919	2.6865	2.6889	2.6891	2.7451	2.7668	2.7577	2.7565
151	2.6960	2.6831	2.6873	2.6888	2.7176	2.7309	2.7126	2.7204
152	2.6940	2.6913	2.6929	2.6927	2.7282	2.7208	2.7177	2.7222
153	2.7040	2.6779	2.6879	2.6899	2.7174	2.7304	2.7194	2.7224
154	2.6933	2.6908	2.6925	2.6922	2.7222	2.7217	2.7229	2.7223

155	2.6917	2.6940	2.6929	2.6929	2.7263	2.7281	2.7257	2.7267
156	2.6915	2.6885	2.6895	2.6899	2.7257	2.7235	2.7271	2.7254
157	2.6998	2.6980	2.6984	2.6987	2.7229	2.7231	2.7199	2.7220
158	2.6964	2.6958	2.6956	2.6959	2.7219	2.7218	2.7242	2.7226
159	2.6918	2.6951	2.6939	2.6936	2.7152	2.7077	2.7096	2.7108
160	2.7008	2.6998	2.7002	2.7003	2.7283	2.7295	2.7316	2.7298
161	2.7004	2.7009	2.7001	2.7005	2.7125	2.7150	2.7161	2.7145
162	2.6952	2.6950	2.6952	2.6951	2.7281	2.7262	2.7278	2.7274
163	2.7333	2.7390	2.7379	2.7368	2.7426	2.7395	2.7406	2.7409
164	2.7125	2.7054	2.7084	2.7088	2.7546	2.7496	2.7501	2.7514
165	2.7054	2.7061	2.7056	2.7057	2.7319	2.7254	2.7374	2.7316
166	2.7168	2.7114	2.7134	2.7138	2.7403	2.7404	2.7379	2.7395
167	2.7175	2.7157	2.7165	2.7165	2.7384	2.7346	2.7369	2.7366
168	2.6874	2.6850	2.6866	2.6863	2.7098	2.7105	2.7116	2.7106
169	2.6844	2.6964	2.6929	2.6912	2.7168	2.7126	2.7157	2.7150
170	2.6947	2.6903	2.6918	2.6922	2.7265	2.7294	2.7292	2.7283

	O1-O2	O1-O2'	O2-O2'	<O-O>bas	O3-O1	O3-O2	O3-O2'	<O3-Obas>
1	2.6846	2.6860	2.6846	2.6851	2.7271	2.7242	2.7247	2.7253
2	2.6873	2.6883	2.6896	2.6884	2.7344	2.7157	2.7202	2.7234
3	2.6977	2.6775	2.6910	2.6887	2.7312	2.7423	2.7483	2.7406
4	2.6890	2.6820	2.6849	2.6853	2.7261	2.7219	2.7227	2.7236
5	2.6826	2.6858	2.6849	2.6844	2.7142	2.7202	2.7218	2.7187
6	2.6795	2.6894	2.6847	2.6845	2.7192	2.7066	2.7242	2.7167
7	2.7370	2.7359	2.7361	2.7363	2.7501	2.7492	2.7486	2.7493
8	2.7336	2.7411	2.7387	2.7378	2.7488	2.7434	2.7463	2.7462
9	2.6902	2.6878	2.6881	2.6887	2.7193	2.7211	2.7159	2.7188
10	2.6949	2.6955	2.6947	2.6950	2.7264	2.7267	2.7269	2.7267
11	2.6958	2.6981	2.6970	2.6970	2.7246	2.7263	2.7262	2.7257
12	2.6846	2.7017	2.6958	2.6940	2.7224	2.7219	2.7173	2.7205
13	2.6942	2.6975	2.6976	2.6964	2.7189	2.7234	2.7237	2.7220
14	2.6968	2.6880	2.6923	2.6923	2.7240	2.7261	2.7229	2.7243
15	2.6990	2.6959	2.6975	2.6975	2.7180	2.7162	2.7158	2.7167
16	2.6952	2.6916	2.6912	2.6927	2.7242	2.7180	2.7300	2.7241
17	2.7035	2.7036	2.7033	2.7035	2.7243	2.7256	2.7231	2.7243
18	2.7025	2.6957	2.6974	2.6985	2.7307	2.7303	2.7292	2.7301
19	2.7192	2.7301	2.7283	2.7259	2.7326	2.7245	2.7292	2.7288
20	2.7257	2.7289	2.7286	2.7277	2.7486	2.7457	2.7481	2.7475
21	2.7184	2.7260	2.7218	2.7221	2.7448	2.7375	2.7386	2.7403
22	2.7681	2.6998	2.7278	2.7319	2.7821	2.7663	2.7798	2.7761
23	2.6731	2.6791	2.6775	2.6766	2.7083	2.7103	2.7089	2.7092
24	2.6876	2.6983	2.6942	2.6934	2.7227	2.7232	2.7341	2.7267
25	2.7046	2.7007	2.7030	2.7028	2.7285	2.7229	2.7175	2.7230
26	2.6742	2.6762	2.6749	2.6751	2.7129	2.7083	2.7115	2.7109
27	2.6589	2.6635	2.6641	2.6622	2.7149	2.7053	2.7093	2.7098
28	2.6289	2.6197	2.6258	2.6248	2.7150	2.6952	2.6952	2.7018
29	2.6724	2.6771	2.6766	2.6754	2.7180	2.7171	2.7212	2.7188
30	2.6773	2.6783	2.6779	2.6778	2.7288	2.7227	2.7246	2.7253
31	2.6808	2.6803	2.6809	2.6807	2.7190	2.7157	2.7166	2.7171
32	2.7154	2.7227	2.7193	2.7191	2.7514	2.7478	2.7493	2.7495
33	2.7047	2.7008	2.7075	2.7043	2.7115	2.7214	2.7115	2.7148
34	2.6653	2.7023	2.6925	2.6867	2.7178	2.7198	2.7292	2.7223
35	2.7082	2.7209	2.7138	2.7143	2.7410	2.7382	2.7378	2.7390
36	2.7225	2.7432	2.7386	2.7348	2.7755	2.7536	2.7586	2.7626
37	2.7048	2.7057	2.7058	2.7055	2.7365	2.7298	2.7267	2.7310
38	2.7047	2.6774	2.6913	2.6911	2.7271	2.7257	2.7134	2.7221
39	2.6996	2.6980	2.6986	2.6987	2.7363	2.7313	2.7290	2.7322
40	2.6935	2.6861	2.6903	2.6899	2.7219	2.7211	2.7161	2.7197
41	2.6961	2.6966	2.6973	2.6967	2.7261	2.7273	2.7262	2.7265
42	2.7003	2.6829	2.6904	2.6912	2.7233	2.7250	2.7195	2.7226
43	2.7005	2.7022	2.6986	2.7004	2.7279	2.7310	2.7299	2.7296
44	2.7497	2.7382	2.7430	2.7436	2.7611	2.7720	2.7748	2.7693
45	2.7441	2.7386	2.7400	2.7409	2.7607	2.7596	2.7581	2.7595
46	2.8295	2.8297	2.8296	2.8296	2.8197	2.8133	2.8087	2.8139
47	2.8338	2.8318	2.8321	2.8326	2.8132	2.8134	2.8082	2.8116
48	2.8197	2.8185	2.8191	2.8191	2.8081	2.8053	2.8015	2.8050
49	2.6586	2.6720	2.6688	2.6665	2.6927	2.6963	2.6948	2.6946
50	2.6759	2.6311	2.6499	2.6523	2.7253	2.7045	2.7150	2.7149

51	2.7719	2.7848	2.7824	2.7797	2.7580	2.7575	2.7474	2.7543
52	2.7804	2.7701	2.7735	2.7747	2.7234	2.7474	2.7424	2.7377
53	2.6785	2.6824	2.6820	2.6810	2.7282	2.7200	2.7233	2.7238
54	2.6909	2.6875	2.6914	2.6899	2.7283	2.7255	2.7281	2.7273
55	2.6663	2.7325	2.7021	2.7003	2.7794	2.6629	2.7141	2.7188
56	2.7150	2.6835	2.6980	2.6989	2.7413	2.7041	2.7405	2.7287
57	2.6713	2.7350	2.7071	2.7045	2.7534	2.6774	2.7367	2.7225
58	2.6602	2.7522	2.7150	2.7091	2.7562	2.6672	2.7307	2.7180
59	2.6534	2.7688	2.7255	2.7159	2.7603	2.6733	2.7344	2.7227
60	2.6827	2.7509	2.7262	2.7199	2.7510	2.6716	2.7308	2.7178
61	2.6904	2.7595	2.7359	2.7286	2.7450	2.6729	2.7208	2.7129
62	2.6377	2.7928	2.7403	2.7236	2.7429	2.6881	2.7316	2.7209
63	2.7137	2.7135	2.7147	2.7139	2.7390	2.7374	2.7392	2.7385
64	2.6965	2.6846	2.6883	2.6898	2.7278	2.7285	2.7262	2.7275
65	2.6195	2.6267	2.6232	2.6231	2.7213	2.6549	2.7201	2.6988
66	2.6785	2.6691	2.6701	2.6726	2.7205	2.7159	2.7150	2.7171
67	2.6912	2.6859	2.6885	2.6886	2.7305	2.7281	2.7280	2.7289
68	2.8111	2.8317	2.8274	2.8234	2.7579	2.8477	2.8202	2.8086
69	2.7023	2.6760	2.6814	2.6866	2.7182	2.7045	2.6735	2.6987
70	2.6169	2.6170	2.6160	2.6166	2.6852	2.6842	2.6835	2.6843
71	2.7829	2.7647	2.7783	2.7753	2.9127	2.8922	2.9116	2.9055
72	2.7730	2.7732	2.7739	2.7734	2.9050	2.9137	2.9024	2.9070
73	2.6276	2.6217	2.6272	2.6255	2.6761	2.6781	2.6800	2.6781
74	2.6465	2.6423	2.6436	2.6441	2.6875	2.6586	2.7107	2.6856
75	2.8101	2.8072	2.8163	2.8112	2.8759	2.8885	2.8790	2.8811
76	2.7886	2.7847	2.7875	2.7869	2.9082	2.9035	2.9034	2.9050
77	2.6507	2.6511	2.6514	2.6511	2.6947	2.6974	2.6951	2.6957
78	2.8167	2.8094	2.8115	2.8125	2.8878	2.8841	2.8850	2.8856
79	2.8172	2.8206	2.8192	2.8190	2.8890	2.8931	2.8911	2.8911
80	2.5906	2.5932	2.6452	2.6097	2.6952	2.6650	2.6716	2.6772
81	2.7010	2.7021	2.7010	2.7014	2.7572	2.7558	2.7573	2.7568
82	2.6988	2.6950	2.6936	2.6958	2.7231	2.7219	2.7190	2.7213
83	2.7005	2.6944	2.6949	2.6966	2.7298	2.7238	2.7233	2.7257
84	2.6770	2.6727	2.6739	2.6745	2.7216	2.7168	2.7184	2.7190
85	2.6971	2.6976	2.6971	2.6973	2.7259	2.7252	2.7261	2.7257
86	2.6937	2.6974	2.6970	2.6960	2.7279	2.7249	2.7253	2.7261
87	2.6814	2.6880	2.6868	2.6854	2.7371	2.7218	2.7266	2.7285
88	2.6826	2.6809	2.6809	2.6814	2.7454	2.7285	2.7340	2.7360
89	2.6829	2.6813	2.6832	2.6824	2.7173	2.7197	2.7231	2.7201
90	2.6950	2.6956	2.6950	2.6952	2.7320	2.7278	2.7278	2.7292
91	2.6977	2.6970	2.6964	2.6970	2.7274	2.7259	2.7200	2.7244
92	2.6981	2.6975	2.6978	2.6978	2.7340	2.7292	2.7289	2.7307
93	2.6935	2.6979	2.6969	2.6961	2.7320	2.7265	2.7283	2.7289
94	2.6753	2.6887	2.6827	2.6822	2.7257	2.7168	2.7247	2.7224
95	2.6972	2.6857	2.6898	2.6909	2.7302	2.7093	2.7218	2.7205
96	2.7030	2.6992	2.6994	2.7005	2.7310	2.7237	2.7225	2.7257
97	2.6911	2.6930	2.6920	2.6920	2.7239	2.7242	2.7222	2.7234
98	2.6909	2.6840	2.6866	2.6872	2.7219	2.7185	2.7214	2.7206
99	2.6951	2.6935	2.6945	2.6944	2.7308	2.7383	2.7308	2.7333
100	2.6813	2.6820	2.6813	2.6815	2.7367	2.7255	2.7287	2.7303
101	2.6838	2.6798	2.6808	2.6815	2.7384	2.7378	2.7334	2.7365
102	2.6821	2.6802	2.6799	2.6807	2.7407	2.7304	2.7315	2.7342

103	2.7016	2.7058	2.7035	2.7036	2.7374	2.7318	2.7404	2.7365
104	2.6961	2.7076	2.7036	2.7024	2.7334	2.7304	2.7352	2.7330
105	2.6961	2.6940	2.6960	2.6954	2.7279	2.7232	2.7271	2.7261
106	2.6871	2.6766	2.6812	2.6817	2.7221	2.7195	2.7212	2.7209
107	2.6728	2.6689	2.6705	2.6707	2.7142	2.7183	2.7179	2.7168
108	2.6751	2.6738	2.6721	2.6737	2.7160	2.7058	2.7084	2.7101
109	2.6768	2.6757	2.6765	2.6763	2.7180	2.7186	2.7177	2.7181
110	2.6740	2.6711	2.6753	2.6735	2.7103	2.7142	2.7118	2.7121
111	2.6903	2.6872	2.6873	2.6882	2.7221	2.7212	2.7179	2.7204
112	2.6838	2.6804	2.6777	2.6806	2.7240	2.7161	2.7101	2.7167
113	2.6876	2.6857	2.6875	2.6869	2.6970	2.7033	2.7077	2.7027
114	2.6726	2.6722	2.6740	2.6729	2.7193	2.7176	2.7218	2.7196
115	2.6860	2.6907	2.6897	2.6888	2.7239	2.7163	2.7243	2.7215
116	2.6935	2.6971	2.6960	2.6956	2.7175	2.7252	2.7226	2.7218
117	2.6994	2.6968	2.6984	2.6982	2.7234	2.7253	2.7221	2.7236
118	2.6533	2.6964	2.6749	2.6749	2.7285	2.7166	2.7402	2.7284
119	2.6999	2.6953	2.6990	2.6981	2.7174	2.7225	2.7198	2.7199
120	2.6993	2.6951	2.6976	2.6973	2.7343	2.7268	2.7280	2.7297
121	2.6979	2.6975	2.6968	2.6974	2.7345	2.7330	2.7334	2.7336
122	2.7112	2.7147	2.7155	2.7138	2.7564	2.7632	2.7603	2.7600
123	2.7140	2.7117	2.7118	2.7125	2.7555	2.7613	2.7600	2.7590
124	2.6970	2.6967	2.6958	2.6965	2.7308	2.7240	2.7195	2.7248
125	2.6975	2.6978	2.7011	2.6988	2.7259	2.7325	2.7277	2.7287
126	2.6993	2.7066	2.7041	2.7033	2.7276	2.7260	2.7267	2.7268
127	2.7157	2.7122	2.7131	2.7136	2.7269	2.7236	2.7274	2.7260
128	2.6971	2.7058	2.7013	2.7014	2.7237	2.7246	2.7223	2.7235
129	2.8363	2.8315	2.8325	2.8334	2.8249	2.8196	2.8170	2.8205
130	2.8499	2.8555	2.8542	2.8532	2.8353	2.8369	2.8315	2.8346
131	2.8368	2.8435	2.8430	2.8411	2.8179	2.8155	2.8155	2.8163
132	2.8416	2.8353	2.8328	2.8366	2.8312	2.8315	2.8279	2.8302
133	2.8607	2.8665	2.8635	2.8636	2.8420	2.8414	2.8563	2.8466
134	2.8213	2.8289	2.8291	2.8265	2.8123	2.8099	2.8017	2.8080
135	2.6864	2.7052	2.6967	2.6961	2.7359	2.7217	2.7261	2.7279
136	2.7038	2.6990	2.7011	2.7013	2.7293	2.7325	2.7318	2.7312
137	2.6985	2.6966	2.6943	2.6965	2.7209	2.7152	2.7127	2.7162
138	2.6996	2.7035	2.7011	2.7014	2.7384	2.7324	2.7364	2.7357
139	2.6914	2.6909	2.6905	2.6909	2.7311	2.7212	2.7233	2.7252
140	2.6857	2.6801	2.6837	2.6832	2.7127	2.7292	2.7225	2.7215
141	2.7294	2.7262	2.7252	2.7269	2.7413	2.7398	2.7376	2.7396
142	2.7257	2.7269	2.7263	2.7263	2.7445	2.7430	2.7387	2.7421
143	2.6699	2.6632	2.6664	2.6665	2.7168	2.7164	2.7142	2.7158
144	2.5616	2.6245	2.6000	2.5953	2.7165	2.6699	2.6596	2.6820
145	2.7385	2.6365	2.6843	2.6864	2.7988	2.8032	2.6743	2.7588
146	2.7357	2.7382	2.7337	2.7359	2.7497	2.7532	2.7533	2.7521
147	2.6842	2.7409	2.7306	2.7185	2.6890	2.7123	2.6987	2.7000
148	2.7076	2.7071	2.7055	2.7068	2.7350	2.7292	2.7268	2.7303
149	2.7185	2.7228	2.7202	2.7205	2.7490	2.7556	2.7518	2.7522
150	2.6919	2.6865	2.6889	2.6891	2.7451	2.7668	2.7577	2.7565
151	2.6960	2.6831	2.6873	2.6888	2.7176	2.7309	2.7126	2.7204
152	2.6940	2.6913	2.6929	2.6927	2.7282	2.7208	2.7177	2.7222
153	2.7040	2.6779	2.6879	2.6899	2.7174	2.7304	2.7194	2.7224
154	2.6933	2.6908	2.6925	2.6922	2.7222	2.7217	2.7229	2.7223

155	2.6917	2.6940	2.6929	2.6929	2.7263	2.7281	2.7257	2.7267
156	2.6915	2.6885	2.6895	2.6899	2.7257	2.7235	2.7271	2.7254
157	2.6998	2.6980	2.6984	2.6987	2.7229	2.7231	2.7199	2.7220
158	2.6964	2.6958	2.6956	2.6959	2.7219	2.7218	2.7242	2.7226
159	2.6918	2.6951	2.6939	2.6936	2.7152	2.7077	2.7096	2.7108
160	2.7008	2.6998	2.7002	2.7003	2.7283	2.7295	2.7316	2.7298
161	2.7004	2.7009	2.7001	2.7005	2.7125	2.7150	2.7161	2.7145
162	2.6952	2.6950	2.6952	2.6951	2.7281	2.7262	2.7278	2.7274
163	2.7333	2.7390	2.7379	2.7368	2.7426	2.7395	2.7406	2.7409
164	2.7125	2.7054	2.7084	2.7088	2.7546	2.7496	2.7501	2.7514
165	2.7054	2.7061	2.7056	2.7057	2.7319	2.7254	2.7374	2.7316
166	2.7168	2.7114	2.7134	2.7138	2.7403	2.7404	2.7379	2.7395
167	2.7175	2.7157	2.7165	2.7165	2.7384	2.7346	2.7369	2.7366
168	2.6874	2.6850	2.6866	2.6863	2.7098	2.7105	2.7116	2.7106
169	2.6844	2.6964	2.6929	2.6912	2.7168	2.7126	2.7157	2.7150
170	2.6947	2.6903	2.6918	2.6922	2.7265	2.7294	2.7292	2.7283

	T-O1	T-O2	T-O2'	<T-O>bas	T-O3	<T-O>
1	1.6538	1.6528	1.6558	1.6541	1.6645	1.6567
2	1.6648	1.6506	1.6518	1.6557	1.6615	1.6572
3	1.6511	1.6645	1.6603	1.6586	1.6743	1.6626
4	1.6553	1.6557	1.6522	1.6544	1.6618	1.6563
5	1.6472	1.6517	1.6564	1.6518	1.6625	1.6544
6	1.6542	1.6514	1.6550	1.6535	1.6551	1.6539
7	1.6801	1.6790	1.6806	1.6799	1.6789	1.6796
8	1.6803	1.6770	1.6840	1.6804	1.6752	1.6791
9	1.6592	1.6618	1.6579	1.6597	1.6449	1.6560
10	1.6639	1.6620	1.6645	1.6634	1.6509	1.6603
11	1.6572	1.6600	1.6601	1.6591	1.6645	1.6604
12	1.6574	1.6575	1.6635	1.6595	1.6536	1.6580
13	1.6561	1.6600	1.6599	1.6586	1.6605	1.6591
14	1.6623	1.6628	1.6582	1.6611	1.6517	1.6587
15	1.6616	1.6608	1.6604	1.6609	1.6488	1.6579
16	1.6558	1.6524	1.6622	1.6568	1.6640	1.6586
17	1.6628	1.6634	1.6632	1.6631	1.6587	1.6620
18	1.6660	1.6651	1.6642	1.6651	1.6543	1.6624
19	1.6723	1.6543	1.6862	1.6709	1.6679	1.6702
20	1.6763	1.6757	1.6779	1.6766	1.6761	1.6765
21	1.6758	1.6698	1.6768	1.6741	1.6679	1.6726
22	1.6836	1.6807	1.6819	1.6821	1.7004	1.6866
23	1.6508	1.6477	1.6506	1.6497	1.6477	1.6492
24	1.6560	1.6543	1.6651	1.6585	1.6632	1.6597
25	1.6629	1.6671	1.6575	1.6625	1.6580	1.6614
26	1.6511	1.6506	1.6517	1.6511	1.6442	1.6494
27	1.6436	1.6403	1.6424	1.6421	1.6537	1.6450
28	1.6344	1.6353	1.6364	1.6353	1.6219	1.6320
29	1.6492	1.6520	1.6571	1.6528	1.6494	1.6519
30	1.6550	1.6525	1.6544	1.6540	1.6566	1.6547
31	1.6536	1.6513	1.6523	1.6524	1.6544	1.6529
32	1.6858	1.6623	1.6885	1.6789	1.6624	1.6747
33	1.6636	1.6745	1.6679	1.6686	1.6321	1.6595
34	1.6585	1.6518	1.6733	1.6612	1.6426	1.6565
35	1.6731	1.6724	1.6759	1.6738	1.6583	1.6699
36	1.6930	1.6835	1.6942	1.6903	1.6636	1.6836
37	1.6646	1.6609	1.6649	1.6635	1.6681	1.6646
38	1.6557	1.6632	1.6479	1.6556	1.6633	1.6575
39	1.6591	1.6622	1.6561	1.6591	1.6742	1.6629
40	1.6532	1.6591	1.6517	1.6546	1.6617	1.6564
41	1.6578	1.6594	1.6592	1.6588	1.6659	1.6606
42	1.6537	1.6591	1.6509	1.6546	1.6670	1.6577
43	1.6632	1.6646	1.6610	1.6629	1.6622	1.6627
44	1.6882	1.6936	1.6923	1.6914	1.6786	1.6882
45	1.6853	1.6851	1.6815	1.6840	1.6848	1.6842
46	1.7291	1.7290	1.7278	1.7286	1.7261	1.7280
47	1.7288	1.7312	1.7276	1.7292	1.7252	1.7282
48	1.7248	1.7261	1.7235	1.7248	1.7136	1.7220
49	1.6358	1.6376	1.6447	1.6393	1.6482	1.6415
50	1.6668	1.6547	1.6544	1.6586	1.6047	1.6451

51	1.6824	1.6798	1.6914	1.6845	1.7266	1.6950
52	1.6762	1.6856	1.6855	1.6824	1.7058	1.6883
53	1.6506	1.6495	1.6514	1.6505	1.6683	1.6550
54	1.6522	1.6617	1.6564	1.6568	1.6648	1.6588
55	1.6614	1.6164	1.6497	1.6425	1.7101	1.6594
56	1.6524	1.6477	1.6373	1.6458	1.7102	1.6619
57	1.6574	1.6308	1.6639	1.6507	1.6949	1.6618
58	1.6603	1.6264	1.6657	1.6508	1.6953	1.6619
59	1.6601	1.6316	1.6687	1.6534	1.7023	1.6656
60	1.6646	1.6265	1.6685	1.6532	1.7014	1.6653
61	1.6561	1.6429	1.6709	1.6566	1.6966	1.6666
62	1.6516	1.6443	1.6713	1.6557	1.7044	1.6679
63	1.6646	1.6648	1.6686	1.6660	1.6799	1.6695
64	1.6611	1.6651	1.6506	1.6589	1.6587	1.6589
65	1.6379	1.6154	1.6524	1.6353	1.6168	1.6306
66	1.6501	1.6491	1.6467	1.6486	1.6559	1.6504
67	1.6570	1.6569	1.6552	1.6564	1.6663	1.6589
68	1.7249	1.7541	1.7302	1.7364	1.6892	1.7246
69	1.6677	1.6765	1.6361	1.6601	1.6166	1.6492
70	1.6384	1.6379	1.6370	1.6377	1.5864	1.6249
71	1.7526	1.7609	1.7580	1.7572	1.7025	1.7435
72	1.7554	1.7604	1.7550	1.7569	1.7031	1.7435
73	1.6310	1.6323	1.6336	1.6323	1.6023	1.6248
74	1.6392	1.6385	1.6357	1.6378	1.6167	1.6325
75	1.7406	1.7503	1.7425	1.7445	1.7410	1.7436
76	1.7555	1.7574	1.7533	1.7554	1.7171	1.7458
77	1.6395	1.6422	1.6417	1.6412	1.6268	1.6376
78	1.7473	1.7441	1.7435	1.7450	1.7466	1.7454
79	1.7472	1.7473	1.7505	1.7483	1.7509	1.7490
80	1.6348	1.6380	1.6324	1.6350	1.5781	1.6208
81	1.6740	1.6732	1.6753	1.6742	1.6646	1.6718
82	1.6602	1.6591	1.6560	1.6585	1.6596	1.6587
83	1.6650	1.6608	1.6601	1.6620	1.6557	1.6604
84	1.6512	1.6512	1.6499	1.6508	1.6543	1.6517
85	1.6589	1.6591	1.6613	1.6597	1.6630	1.6605
86	1.6601	1.6565	1.6612	1.6593	1.6631	1.6603
87	1.6599	1.6505	1.6613	1.6573	1.6598	1.6579
88	1.6624	1.6518	1.6610	1.6584	1.6613	1.6591
89	1.6502	1.6536	1.6551	1.6530	1.6583	1.6543
90	1.6617	1.6601	1.6614	1.6611	1.6609	1.6610
91	1.6596	1.6603	1.6567	1.6589	1.6636	1.6601
92	1.6618	1.6600	1.6617	1.6611	1.6655	1.6622
93	1.6598	1.6577	1.6595	1.6590	1.6675	1.6612
94	1.6506	1.6490	1.6585	1.6527	1.6617	1.6550
95	1.6603	1.6502	1.6505	1.6537	1.6666	1.6569
96	1.6602	1.6590	1.6590	1.6594	1.6678	1.6615
97	1.6611	1.6607	1.6595	1.6604	1.6521	1.6584
98	1.6582	1.6550	1.6574	1.6568	1.6534	1.6560
99	1.6625	1.6644	1.6623	1.6631	1.6593	1.6621
100	1.6536	1.6539	1.6554	1.6543	1.6659	1.6572
101	1.6494	1.6596	1.6511	1.6534	1.6761	1.6590
102	1.6535	1.6544	1.6548	1.6542	1.6699	1.6582

103	1.6666	1.6667	1.6694	1.6676	1.6609	1.6659
104	1.6672	1.6643	1.6689	1.6668	1.6575	1.6645
105	1.6599	1.6584	1.6603	1.6595	1.6618	1.6601
106	1.6537	1.6547	1.6514	1.6533	1.6577	1.6544
107	1.6475	1.6491	1.6488	1.6485	1.6539	1.6498
108	1.6442	1.6441	1.6403	1.6429	1.6652	1.6484
109	1.6496	1.6519	1.6484	1.6499	1.6576	1.6519
110	1.6462	1.6501	1.6483	1.6482	1.6520	1.6492
111	1.6542	1.6554	1.6499	1.6532	1.6648	1.6561
112	1.6549	1.6573	1.6435	1.6519	1.6553	1.6527
113	1.6477	1.6462	1.6630	1.6523	1.6443	1.6503
114	1.6475	1.6479	1.6498	1.6484	1.6599	1.6513
115	1.6537	1.6471	1.6546	1.6518	1.6710	1.6566
116	1.6550	1.6602	1.6585	1.6579	1.6614	1.6588
117	1.6586	1.6615	1.6585	1.6595	1.6620	1.6601
118	1.6444	1.6411	1.6540	1.6465	1.6785	1.6545
119	1.6569	1.6624	1.6592	1.6595	1.6574	1.6590
120	1.6626	1.6574	1.6611	1.6604	1.6660	1.6618
121	1.6622	1.6614	1.6609	1.6615	1.6677	1.6630
122	1.6790	1.6795	1.6818	1.6801	1.6656	1.6765
123	1.6779	1.6808	1.6783	1.6790	1.6660	1.6758
124	1.6615	1.6533	1.6579	1.6576	1.6671	1.6600
125	1.6594	1.6627	1.6625	1.6615	1.6631	1.6619
126	1.6618	1.6599	1.6645	1.6621	1.6645	1.6627
127	1.6630	1.6617	1.6646	1.6631	1.6728	1.6655
128	1.6633	1.6589	1.6669	1.6630	1.6556	1.6612
129	1.7332	1.7325	1.7323	1.7327	1.7267	1.7312
130	1.7429	1.7460	1.7452	1.7447	1.7320	1.7415
131	1.7353	1.7352	1.7390	1.7365	1.7194	1.7322
132	1.7369	1.7364	1.7342	1.7359	1.7328	1.7351
133	1.7513	1.7360	1.7556	1.7477	1.7507	1.7484
134	1.7287	1.7278	1.7300	1.7288	1.7143	1.7252
135	1.6658	1.6572	1.6676	1.6635	1.6533	1.6610
136	1.6645	1.6659	1.6658	1.6654	1.6579	1.6635
137	1.6633	1.6625	1.6569	1.6609	1.6471	1.6574
138	1.6669	1.6633	1.6680	1.6661	1.6617	1.6650
139	1.6627	1.6585	1.6609	1.6607	1.6524	1.6586
140	1.6527	1.6624	1.6570	1.6574	1.6484	1.6551
141	1.6766	1.6755	1.6753	1.6758	1.6679	1.6738
142	1.6759	1.6766	1.6747	1.6757	1.6704	1.6744
143	1.6465	1.6494	1.6443	1.6467	1.6527	1.6482
144	1.6423	1.6163	1.6557	1.6381	1.5628	1.6193
145	1.6831	1.6670	1.6172	1.6558	1.7031	1.6676
146	1.6789	1.6810	1.6795	1.6798	1.6820	1.6804
147	1.6688	1.6790	1.6749	1.6742	1.6140	1.6592
148	1.6701	1.6667	1.6652	1.6673	1.6576	1.6649
149	1.6751	1.6855	1.6845	1.6817	1.6590	1.6760
150	1.6586	1.6515	1.6501	1.6534	1.7093	1.6674
151	1.6529	1.6636	1.6461	1.6542	1.6624	1.6563
152	1.6573	1.6568	1.6545	1.6562	1.6636	1.6581
153	1.6566	1.6684	1.6487	1.6579	1.6557	1.6573
154	1.6621	1.6610	1.6618	1.6617	1.6474	1.6581

155	1.6604	1.6587	1.6622	1.6604	1.6570	1.6596
156	1.6609	1.6585	1.6601	1.6599	1.6537	1.6583
157	1.6628	1.6619	1.6613	1.6620	1.6535	1.6599
158	1.6633	1.6603	1.6611	1.6616	1.6523	1.6593
159	1.6594	1.6553	1.6588	1.6578	1.6460	1.6549
160	1.6629	1.6604	1.6653	1.6628	1.6624	1.6627
161	1.6625	1.6626	1.6661	1.6637	1.6415	1.6582
162	1.6622	1.6592	1.6621	1.6612	1.6584	1.6605
163	1.6699	1.6697	1.6723	1.6707	1.6969	1.6772
164	1.6726	1.6713	1.6711	1.6717	1.6733	1.6721
165	1.6657	1.6613	1.6692	1.6654	1.6636	1.6649
166	1.6648	1.6660	1.6657	1.6655	1.6825	1.6698
167	1.6659	1.6648	1.6670	1.6659	1.6810	1.6697
168	1.6547	1.6541	1.6532	1.6540	1.6484	1.6526
169	1.6596	1.6559	1.6643	1.6599	1.6424	1.6555
170	1.6618	1.6631	1.6610	1.6620	1.6540	1.6600

]	tauO1-T-O3	tauO2-T-O3	tauO2'-T-O3	<tau-api>	tauO1-T-O2	tauO1-T-O2'	tauO2'-T-O2	<tau-bas>
1	110.54	110.41	110.33	110.43	108.56	108.50	108.46	108.507
2	110.58	110.16	110.38	110.38	108.30	108.30	108.89	108.501
3	110.43	110.44	110.96	110.61	108.91	107.91	108.21	108.343
4	110.53	110.26	110.44	110.41	108.61	108.37	108.52	108.500
5	110.19	110.33	110.25	110.25	108.82	108.78	108.56	108.717
6	110.51	109.89	110.82	110.40	108.31	108.72	108.54	108.526
7	109.91	109.92	109.82	109.89	109.14	108.99	109.04	109.056
8	110.01	109.85	109.76	109.87	109.02	109.13	109.10	109.084
9	110.77	110.75	110.58	110.70	108.21	108.25	108.17	108.207
10	110.67	110.79	110.70	110.72	108.25	108.16	108.19	108.200
11	110.22	110.18	110.18	110.19	108.72	108.85	108.69	108.751
12	110.62	110.58	110.08	110.43	108.16	108.88	108.53	108.526
13	110.13	110.20	110.23	110.19	108.68	108.87	108.74	108.762
14	110.56	110.67	110.64	110.63	108.40	108.09	108.33	108.273
15	110.38	110.31	110.31	110.33	108.66	108.49	108.61	108.590
16	110.29	110.08	110.45	110.27	109.11	108.43	108.53	108.689
17	110.21	110.26	110.12	110.20	108.74	108.76	108.72	108.738
18	110.66	110.68	110.65	110.66	108.44	108.09	108.22	108.250
19	109.79	110.19	109.30	109.76	109.65	108.76	109.30	109.236
20	110.15	110.01	110.07	110.08	108.81	108.90	108.90	108.868
21	110.35	110.20	110.01	110.19	108.69	108.80	108.77	108.752
22	110.60	109.80	110.56	110.32	110.73	106.68	108.40	108.602
23	110.38	110.66	110.47	110.51	108.27	108.48	108.50	108.419
24	110.23	110.34	110.60	110.39	108.56	108.68	108.49	108.577
25	110.49	109.95	109.98	110.14	108.62	108.85	108.84	108.769
26	110.83	110.57	110.73	110.71	108.18	108.25	108.19	108.207
27	110.84	110.43	110.59	110.62	108.13	108.30	108.46	108.294
28	112.98	111.68	111.64	112.10	107.04	106.44	106.71	106.729
29	110.97	110.78	110.84	110.86	108.10	108.13	108.00	108.079
30	110.98	110.72	110.77	110.82	108.08	108.05	108.12	108.085
31	110.56	110.48	110.49	110.51	108.42	108.34	108.46	108.409
32	110.52	111.48	110.59	110.86	108.39	107.59	108.22	108.068
33	110.72	110.77	110.41	110.63	108.24	108.33	108.32	108.297
34	110.83	111.29	111.06	111.06	107.25	108.40	108.06	107.907
35	110.72	110.59	110.44	110.58	108.09	108.67	108.28	108.349
36	111.56	110.70	110.61	110.96	107.47	108.17	108.23	107.956
37	110.39	110.17	109.84	110.13	108.85	108.71	108.85	108.802
38	110.50	110.05	109.87	110.14	109.16	108.28	108.83	108.756
39	110.34	109.90	109.98	110.07	108.74	108.94	108.86	108.848
40	110.39	110.05	110.02	110.15	108.82	108.74	108.76	108.771
41	110.21	110.20	110.14	110.18	108.73	108.77	108.76	108.754
42	110.19	110.03	109.99	110.07	109.20	108.56	108.80	108.852
43	110.24	110.36	110.42	110.34	108.49	108.76	108.50	108.581
44	110.19	110.57	110.79	110.52	108.80	108.19	108.27	108.421
45	110.00	109.95	109.99	109.98	109.01	108.86	108.95	108.941
46	109.39	109.03	108.81	109.07	109.81	109.89	109.88	109.860
47	109.07	108.97	108.80	108.95	109.97	110.03	109.96	109.986
48	109.51	109.29	109.16	109.32	109.59	109.64	109.63	109.619
49	110.16	110.29	109.94	110.13	108.62	109.08	108.82	108.842
50	112.81	112.14	112.81	112.59	107.35	104.79	106.29	106.141

51	108.00	108.09	107.10	107.73	111.06	111.26	111.21	111.180
52	107.27	108.21	107.93	107.80	111.60	110.98	110.80	111.126
53	110.57	110.13	110.26	110.32	108.51	108.65	108.67	108.611
54	110.67	110.03	110.38	110.36	108.58	108.64	108.52	108.579
55	111.05	106.33	108.13	108.50	108.86	111.23	110.92	110.335
56	109.21	107.27	109.75	108.74	110.71	109.31	110.37	110.131
57	110.43	107.22	109.53	109.06	108.66	110.87	110.13	109.884
58	110.44	106.81	109.14	108.80	108.06	111.68	110.62	110.121
59	110.35	106.60	108.85	108.60	107.43	112.57	110.93	110.311
60	109.63	106.77	108.75	108.38	109.19	111.24	111.11	110.516
61	109.91	106.32	108.11	108.11	109.27	112.08	111.11	110.821
62	109.62	106.77	108.33	108.24	106.32	114.38	111.37	110.688
63	109.96	109.85	109.82	109.88	109.19	108.99	109.05	109.078
64	110.50	110.35	110.74	110.53	108.33	108.31	108.38	108.342
65	113.46	110.45	113.16	112.36	107.25	105.94	106.50	106.561
66	110.75	110.52	110.55	110.61	108.56	108.12	108.21	108.295
67	110.50	110.35	110.41	110.42	108.60	108.37	108.52	108.498
68	107.76	111.57	110.82	110.05	107.80	110.08	108.77	108.883
69	111.70	110.41	110.04	110.72	107.81	108.18	108.16	108.050
70	112.74	112.70	112.69	112.71	106.02	106.07	106.03	106.041
71	114.91	113.24	114.53	114.23	104.76	103.91	104.33	104.333
72	114.26	114.54	114.04	114.28	104.14	104.37	104.24	104.245
73	111.72	111.78	111.85	111.78	107.26	106.85	107.13	107.078
74	111.26	109.51	112.87	111.21	107.69	107.58	107.68	107.651
75	111.39	111.65	111.37	111.47	107.21	107.40	107.58	107.398
76	113.75	113.37	113.51	113.54	105.09	105.05	105.14	105.094
77	111.17	111.20	111.08	111.15	107.74	107.79	107.71	107.749
78	111.49	111.43	111.50	111.47	107.56	107.18	107.41	107.384
79	111.36	111.59	111.36	111.44	107.45	107.50	107.41	107.452
80	114.03	111.91	112.55	112.83	104.67	105.07	107.97	105.902
81	111.35	111.31	111.32	111.33	107.60	107.56	107.53	107.562
82	110.22	110.20	110.14	110.19	108.79	108.72	108.67	108.727
83	110.58	110.43	110.43	110.48	108.58	108.25	108.44	108.423
84	110.84	110.56	110.70	110.70	108.31	108.12	108.19	108.209
85	110.29	110.24	110.21	110.25	108.76	108.68	108.64	108.696
86	110.34	110.34	110.19	110.29	108.62	108.61	108.72	108.647
87	111.07	110.62	110.51	110.73	108.19	108.06	108.33	108.193
88	111.39	110.88	110.88	111.05	108.08	107.54	107.93	107.850
89	110.43	110.41	110.56	110.47	108.59	108.42	108.41	108.476
90	110.62	110.44	110.40	110.49	108.44	108.42	108.45	108.438
91	110.31	110.18	109.96	110.15	108.70	108.84	108.77	108.767
92	110.51	110.31	110.22	110.35	108.63	108.51	108.60	108.582
93	110.38	110.16	110.20	110.25	108.57	108.73	108.75	108.684
94	110.75	110.29	110.42	110.49	108.35	108.68	108.39	108.472
95	110.30	109.54	110.28	110.04	109.12	108.42	109.04	108.860
96	110.29	109.92	109.84	110.02	109.05	108.82	108.88	108.917
97	110.59	110.64	110.56	110.60	108.22	108.38	108.34	108.315
98	110.56	110.51	110.60	110.56	108.62	108.10	108.37	108.361
99	110.58	110.95	110.57	110.70	108.21	108.22	108.21	108.211
100	111.06	110.36	110.50	110.64	108.32	108.29	108.24	108.282
101	110.86	110.32	110.37	110.52	108.40	108.57	108.25	108.407
102	111.11	110.44	110.49	110.68	108.35	108.22	108.16	108.244

103	110.70	110.36	110.78	110.61	108.29	108.40	108.27	108.318
104	110.60	110.56	110.68	110.62	108.05	108.51	108.38	108.313
105	110.42	110.21	110.37	110.33	108.69	108.46	108.64	108.597
106	110.58	110.37	110.60	110.52	108.63	108.16	108.40	108.396
107	110.60	110.77	110.75	110.71	108.34	108.12	108.16	108.210
108	110.31	109.69	109.99	110.00	108.88	108.99	108.89	108.921
109	110.54	110.46	110.54	110.51	108.35	108.45	108.41	108.404
110	110.52	110.56	110.48	110.52	108.43	108.34	108.45	108.407
111	110.20	110.08	110.09	110.12	108.75	108.84	108.80	108.795
112	110.75	110.15	110.30	110.40	108.24	108.71	108.46	108.471
113	110.02	110.48	110.12	110.21	109.36	108.43	108.58	108.790
114	110.61	110.49	110.67	110.59	108.39	108.27	108.36	108.340
115	110.03	109.89	110.11	110.01	108.93	108.85	109.03	108.934
116	110.05	110.26	110.17	110.16	108.68	108.97	108.71	108.787
117	110.20	110.17	110.09	110.15	108.79	108.78	108.77	108.779
118	110.39	109.83	110.79	110.34	107.72	109.67	108.50	108.630
119	110.15	110.19	110.14	110.16	108.86	108.74	108.76	108.783
120	110.46	110.26	110.20	110.31	108.79	108.36	108.70	108.616
121	110.41	110.36	110.40	110.39	108.54	108.53	108.52	108.531
122	111.00	111.39	111.13	111.17	107.66	107.75	107.78	107.731
123	110.98	111.19	111.20	111.12	107.81	107.79	107.70	107.768
124	110.25	110.25	109.81	110.10	108.90	108.66	108.90	108.821
125	110.26	110.49	110.21	110.32	108.58	108.61	108.68	108.622
126	110.17	110.17	110.04	110.13	108.70	108.92	108.84	108.820
127	109.66	109.53	109.65	109.61	109.54	109.18	109.28	109.335
128	110.31	110.58	110.14	110.34	108.55	108.68	108.58	108.604
129	109.47	109.20	109.06	109.24	109.85	109.58	109.66	109.698
130	109.36	109.31	109.03	109.23	109.54	109.90	109.72	109.719
131	109.31	109.18	109.04	109.17	109.65	109.86	109.83	109.780
132	109.37	109.41	109.28	109.35	109.79	109.54	109.41	109.579
133	108.49	109.16	109.33	108.99	110.23	109.64	110.00	109.957
134	109.53	109.44	108.89	109.29	109.42	109.76	109.80	109.660
135	111.03	110.59	110.48	110.70	107.88	108.50	108.30	108.227
136	110.47	110.59	110.55	110.54	108.55	108.27	108.34	108.388
137	110.55	110.25	110.30	110.37	108.47	108.62	108.51	108.530
138	110.71	110.53	110.59	110.61	108.32	108.32	108.31	108.316
139	110.95	110.55	110.59	110.70	108.27	108.12	108.25	108.214
140	110.52	111.04	110.83	110.80	108.22	108.14	108.00	108.122
141	110.10	110.06	109.94	110.03	109.02	108.84	108.83	108.898
142	110.20	110.08	109.89	110.06	108.79	108.94	108.89	108.874
143	110.87	110.70	110.75	110.77	108.21	108.05	108.13	108.129
144	115.87	114.24	111.97	114.02	103.64	105.46	104.97	104.690
145	111.49	112.56	106.74	110.26	109.65	106.03	109.39	108.358
146	109.80	109.90	109.96	109.89	109.02	109.24	108.90	109.053
147	109.99	110.89	110.22	110.36	106.60	110.11	109.03	108.582
148	110.55	110.36	110.28	110.40	108.47	108.52	108.55	108.511
149	111.08	110.96	110.77	110.93	107.98	108.28	107.75	108.003
150	109.18	110.82	110.32	110.11	108.83	108.57	108.97	108.791
151	110.11	110.38	109.92	110.14	108.75	108.84	108.70	108.762
152	110.47	110.05	109.95	110.16	108.76	108.71	108.82	108.764
153	110.25	110.44	110.51	110.40	108.83	108.23	108.39	108.483
154	110.68	110.70	110.74	110.71	108.28	108.10	108.24	108.207

155	110.53	110.72	110.45	110.57	108.38	108.35	108.35	108.359
156	110.63	110.62	110.78	110.68	108.36	108.10	108.25	108.235
157	110.38	110.44	110.27	110.36	108.59	108.51	108.57	108.557
158	110.36	110.50	110.61	110.49	108.44	108.37	108.47	108.426
159	110.46	110.20	110.19	110.28	108.60	108.63	108.71	108.646
160	110.26	110.46	110.41	110.38	108.72	108.43	108.54	108.563
161	110.36	110.51	110.45	110.44	108.61	108.47	108.42	108.499
162	110.49	110.52	110.51	110.51	108.48	108.33	108.45	108.419
163	109.09	108.92	108.89	108.97	109.86	110.07	110.01	109.981
164	110.83	110.59	110.63	110.68	108.42	108.02	108.24	108.227
165	110.28	110.11	110.54	110.31	108.82	108.48	108.61	108.634
166	109.90	109.85	109.71	109.82	109.31	109.00	109.07	109.125
167	109.80	109.64	109.69	109.71	109.35	109.13	109.22	109.235
168	110.25	110.32	110.41	110.33	108.62	108.52	108.64	108.595
169	110.72	110.66	110.53	110.64	108.13	108.43	108.36	108.305
170	110.63	110.74	110.80	110.72	108.28	108.12	108.16	108.188

	alpha1	alpha2	alpha3	alpha4	alpha5	alpha6	alpha	alphaO2-O2'
1	108.747	131.285	131.285	108.706	108.696	131.259	5.64	5.66
2	107.273	132.636	132.718	107.325	107.319	132.699	6.34	6.36
3	107.718	132.096	131.847	108.075	108.216	132.237	6.01	5.74
4	108.757	131.273	131.121	108.812	108.862	131.251	5.60	5.50
5	107.449	132.506	132.593	107.439	107.417	132.529	6.28	6.33
6	107.392	132.598	132.788	107.281	107.216	132.593	6.34	6.48
7	96.939	143.079	143.044	96.944	96.947	143.076	11.53	11.51
8	96.987	142.950	143.134	96.917	96.898	142.924	11.52	11.63
9	103.062	136.985	136.905	103.060	103.071	136.960	8.47	8.43
10	103.006	137.020	137.010	102.979	102.976	136.998	8.51	8.51
11	102.827	137.167	137.214	102.799	102.787	137.160	8.59	8.63
12	103.079	136.791	137.202	102.946	102.863	136.813	8.49	8.74
13	103.765	136.149	136.272	103.785	103.768	136.199	8.11	8.16
14	102.043	137.959	137.795	102.163	102.204	138.002	8.95	8.82
15	102.091	137.910	137.852	102.133	102.148	137.925	8.94	8.90
16	102.187	137.922	137.773	102.154	102.171	137.857	8.92	8.86
17	101.745	138.268	138.260	101.734	101.733	138.257	9.13	9.13
18	102.299	137.785	137.598	102.329	102.360	137.755	8.85	8.74
19	98.371	141.449	141.783	98.340	98.307	141.492	10.81	10.98
20	98.213	141.726	141.830	98.210	98.201	141.745	10.89	10.94
21	99.697	140.321	140.447	99.570	99.543	140.253	10.18	10.29
22	106.596	133.731	132.239	107.145	107.593	133.571	6.52	5.54
23	104.958	134.973	135.134	104.934	104.900	135.007	7.53	7.62
24	116.951	122.981	123.226	116.916	116.800	123.077	1.55	1.71
25	97.444	142.540	142.481	97.517	97.528	142.589	11.26	11.21
26	111.443	128.571	128.598	111.412	111.395	128.563	4.29	4.32
27	110.604	129.243	129.439	110.665	110.627	129.357	4.68	4.75
28	105.285	134.493	134.374	105.457	105.513	134.571	7.27	7.15
29	113.074	126.827	126.982	113.098	113.055	126.906	3.46	3.53
30	108.563	131.431	131.455	108.555	108.548	131.435	5.72	5.74
31	104.666	135.316	135.320	104.686	104.688	135.330	7.66	7.66
32	105.260	134.727	134.869	105.175	105.133	134.715	7.40	7.50
33	106.732	133.031	133.135	106.951	106.975	133.210	6.56	6.52
34	107.905	131.666	132.662	107.790	107.538	131.943	6.09	6.64
35	98.729	141.311	141.514	98.506	98.466	141.178	10.69	10.86
36	95.405	144.311	144.891	95.273	95.233	144.279	12.30	12.61
37	102.998	136.971	137.007	103.006	103.002	136.987	8.50	8.51
38	104.405	135.587	135.088	104.759	104.914	135.677	7.69	7.30
39	103.852	136.150	136.113	103.867	103.876	136.149	8.07	8.04
40	103.711	136.252	136.134	103.826	103.865	136.298	8.11	8.01
41	104.766	135.174	135.221	104.796	104.793	135.209	7.60	7.62
42	104.629	135.426	135.056	104.802	104.900	135.430	7.63	7.38
43	100.215	139.916	139.848	100.092	100.085	139.805	9.93	9.94
44	119.286	120.754	120.512	119.326	119.461	120.654	0.32	0.16
45	119.914	120.152	120.002	119.897	119.963	120.069	0.04	-0.04
46	73.380	166.614	166.617	73.374	73.375	166.596	23.31	23.31
47	73.189	166.832	166.772	73.208	73.197	166.939	23.41	23.38
48	74.485	165.512	165.491	74.511	74.504	165.581	22.76	22.74
49	108.321	131.504	131.883	108.299	108.204	131.626	5.85	6.05
50	110.092	130.098	129.113	110.423	110.787	129.912	4.82	4.16

51	80.109	159.697	160.073	79.976	80.023	159.351	19.92	20.13
52	80.682	159.204	158.961	80.837	80.803	159.519	19.61	19.50
53	105.501	134.409	134.539	105.510	105.487	134.457	7.24	7.30
54	102.589	137.303	137.321	102.715	102.732	137.399	8.67	8.63
55	115.114	124.495	125.781	114.617	113.982	124.786	2.61	3.57
56	116.168	123.885	123.255	116.364	116.698	123.698	1.80	1.35
57	111.215	128.545	129.834	110.676	110.173	128.730	4.59	5.50
58	107.980	131.551	133.506	107.172	106.580	131.714	6.25	7.58
59	104.594	134.725	137.279	103.531	102.957	134.752	7.97	9.63
60	101.594	137.939	139.498	100.950	100.675	137.862	9.34	10.33
61	99.137	140.336	141.964	98.476	98.262	140.166	10.55	11.55
62	100.826	138.103	141.701	99.343	98.819	137.833	9.89	12.12
63	104.039	135.903	135.940	104.082	104.084	135.945	7.97	7.97
64	106.254	133.859	133.555	106.314	106.389	133.797	6.85	6.68
65	105.226	134.652	134.791	105.135	105.093	134.635	7.39	7.50
66	107.546	132.635	132.325	107.520	107.583	132.507	6.23	6.09
67	104.810	135.187	135.087	104.875	104.905	135.201	7.57	7.50
68	74.040	165.474	166.034	73.768	73.889	164.451	22.86	23.25
69	104.955	135.394	134.619	105.003	105.154	135.178	7.51	7.11
70	117.883	122.168	122.131	117.844	117.844	122.130	1.07	1.07
71	93.940	145.763	145.600	94.395	94.424	146.154	12.90	12.69
72	93.034	146.926	146.956	93.060	93.060	146.952	13.47	13.48
73	117.016	122.854	122.839	117.159	117.225	122.923	1.43	1.35
74	116.528	123.511	123.403	116.532	116.577	123.463	1.73	1.67
75	87.901	151.734	151.956	88.227	88.225	152.067	15.95	15.97
76	92.152	147.806	147.767	92.249	92.252	147.895	13.90	13.86
77	112.713	127.264	127.290	112.726	112.722	127.282	3.64	3.65
78	90.060	150.012	149.830	90.134	90.134	150.085	14.97	14.86
79	93.673	146.312	146.382	93.628	93.624	146.278	13.17	13.22
80	117.608	119.576	121.671	119.639	119.606	121.635	0.57	0.56
81	112.123	127.904	127.902	112.091	112.082	127.885	3.95	3.96
82	102.508	137.654	137.462	102.438	102.455	137.550	8.77	8.71
83	100.476	139.651	139.442	100.470	100.494	139.595	9.77	9.67
84	108.389	131.659	131.544	108.401	108.432	131.625	5.80	5.74
85	101.911	138.098	138.097	101.896	101.894	138.086	9.05	9.05
86	101.612	138.314	138.436	101.616	101.600	138.348	9.19	9.25
87	103.414	136.483	136.681	103.402	103.368	136.532	8.29	8.39
88	104.017	136.022	135.959	104.010	104.019	135.998	7.99	7.97
89	104.065	135.874	135.884	104.126	104.135	135.920	7.95	7.93
90	101.146	138.867	138.869	101.127	101.124	138.853	9.43	9.44
91	101.032	139.017	138.967	101.004	101.007	138.984	9.49	9.48
92	100.633	139.362	139.355	100.645	100.647	139.369	9.68	9.67
93	102.492	137.447	137.571	102.477	102.457	137.470	8.76	8.82
94	105.552	134.412	134.686	105.409	105.331	134.404	7.27	7.46
95	104.849	135.233	134.959	104.935	105.000	135.205	7.55	7.38
96	100.547	139.532	139.402	100.540	100.555	139.495	9.73	9.67
97	104.445	135.557	135.589	104.419	104.409	135.549	7.79	7.81
98	102.747	137.296	137.137	102.808	102.841	137.295	8.61	8.51
99	104.164	135.827	135.805	104.191	104.199	135.839	7.91	7.89
100	108.634	131.370	131.372	108.614	108.609	131.358	5.69	5.70
101	108.706	131.322	131.213	108.716	108.745	131.288	5.64	5.58
102	109.420	130.632	130.550	109.395	109.410	130.586	5.30	5.26

103	101.965	138.045	138.113	101.900	101.881	138.015	9.04	9.09
104	101.886	138.026	138.303	101.791	101.741	138.031	9.08	9.25
105	102.652	137.301	137.295	102.716	102.726	137.346	8.65	8.63
106	104.712	135.323	135.102	104.820	104.880	135.328	7.61	7.46
107	106.742	133.272	133.187	106.776	106.801	133.266	6.62	6.56
108	109.544	130.566	130.457	109.474	109.484	130.481	5.25	5.23
109	106.282	133.702	133.691	106.307	106.314	133.715	6.85	6.83
110	106.406	133.454	133.502	106.545	106.564	133.562	6.75	6.72
111	104.992	135.073	134.964	104.979	104.996	135.029	7.51	7.46
112	109.511	130.706	130.480	109.386	109.411	130.542	5.28	5.23
113	103.981	135.973	135.967	104.036	104.046	136.010	7.99	7.97
114	108.242	131.670	131.721	108.306	108.309	131.729	5.86	5.85
115	104.757	135.176	135.311	104.746	104.720	135.210	7.62	7.69
116	101.776	138.185	138.275	101.750	101.734	138.189	9.12	9.17
117	101.328	138.658	138.618	101.375	101.387	138.683	9.32	9.29
118	111.765	128.232	129.026	111.316	110.959	128.287	4.29	4.91
119	101.320	138.609	138.576	101.436	101.456	138.686	9.30	9.25
120	101.737	138.245	138.181	101.809	101.828	138.281	9.11	9.05
121	102.822	137.222	137.180	102.794	102.796	137.189	8.60	8.59
122	97.059	142.815	142.973	97.099	97.090	142.876	11.45	11.51
123	97.289	142.762	142.681	97.287	97.293	142.745	11.36	11.32
124	99.583	140.468	140.423	99.547	99.548	140.430	10.22	10.21
125	98.617	141.213	141.345	98.740	98.739	141.337	10.65	10.67
126	97.825	142.119	142.296	97.753	97.732	142.095	11.10	11.21
127	95.040	145.001	144.905	95.066	95.073	145.011	12.48	12.42
128	98.731	141.276	141.429	98.595	98.567	141.200	10.67	10.79
129	73.113	166.951	166.818	73.177	73.148	167.238	23.46	23.38
130	71.330	168.599	168.750	71.247	71.285	168.195	24.31	24.41
131	72.148	167.715	167.932	72.088	72.132	167.316	23.88	24.01
132	73.288	166.969	166.660	73.237	73.199	167.206	23.43	23.28
133	70.283	169.662	169.757	70.138	70.179	169.138	24.83	24.93
134	73.838	165.972	166.246	73.801	73.846	165.630	23.03	23.18
135	103.092	136.865	137.242	102.868	102.777	136.813	8.52	8.78
136	104.053	135.961	135.860	104.105	104.131	135.967	7.96	7.89
137	102.961	137.199	137.042	102.866	102.876	137.087	8.55	8.51
138	102.113	137.907	137.963	102.044	102.027	137.872	8.96	9.02
139	106.558	133.475	133.440	106.539	106.543	133.450	6.73	6.72
140	106.419	133.530	133.456	106.519	106.555	133.571	6.76	6.68
141	99.041	141.082	140.932	98.996	99.007	141.015	10.50	10.44
142	99.308	140.690	140.712	99.293	99.289	140.683	10.35	10.37
143	110.957	129.049	128.916	111.020	111.076	129.034	4.50	4.40
144	114.626	125.013	126.455	114.288	113.670	125.446	2.86	3.81
145	118.682	121.450	119.395	119.147	120.390	120.650	0.44	-1.19
146	97.203	142.952	142.880	97.046	97.039	142.810	11.45	11.46
147	81.957	156.773	158.412	81.397	81.576	155.589	18.82	19.81
148	101.572	138.518	138.442	101.510	101.512	138.452	9.23	9.22
149	102.123	137.890	137.951	102.049	102.030	137.852	8.96	9.02
150	109.990	130.025	129.913	110.034	110.076	130.009	4.99	4.91
151	116.003	124.106	123.786	116.025	116.160	123.970	1.97	1.79
152	116.958	123.031	122.989	116.987	117.017	123.027	1.51	1.47
153	100.155	140.002	139.401	100.416	100.519	140.057	9.86	9.48
154	101.502	138.476	138.446	101.554	101.565	138.506	9.23	9.20

155	104.794	135.201	135.247	104.768	104.755	135.198	7.61	7.64
156	103.276	136.750	136.676	103.297	103.312	136.743	8.36	8.31
157	101.325	138.698	138.648	101.333	101.341	138.691	9.34	9.31
158	101.958	138.070	138.038	101.945	101.948	138.052	9.03	9.02
159	103.229	136.750	136.827	103.200	103.184	136.752	8.39	8.44
160	102.595	137.411	137.387	102.603	102.608	137.410	8.70	8.69
161	103.045	136.979	136.969	103.017	103.014	136.956	8.49	8.49
162	102.232	137.766	137.763	102.236	102.237	137.769	8.88	8.88
163	97.071	142.846	143.011	97.043	97.029	142.852	11.46	11.55
164	98.209	141.817	141.668	98.297	98.319	141.858	10.88	10.78
165	114.925	125.080	125.088	114.916	114.909	125.078	2.54	2.55
166	103.844	136.186	136.061	103.890	103.918	136.181	8.06	7.99
167	102.610	137.389	137.353	102.633	102.641	137.395	8.69	8.66
168	101.260	138.720	138.691	101.309	101.319	138.749	9.36	9.32
169	101.893	137.986	138.297	101.816	101.763	138.012	9.07	9.25
170	104.934	135.099	134.993	104.964	104.989	135.087	7.52	7.46

	<Si4+>	<Al3+>	<Fe3+>	<Ge4+>	<Ti4+>	<Mg>	<Mn2+>	<Ga3+>
1	2.7805	1.185	0.0345					
2	2.7975	1.2025						
3	2.846	1.154						
4	2.742	1.258						
5	2.7905	1.2095						
6	2.8095	1.1905						
7	3.05		0.95					
8	3.05		0.95					
9	2.85	1.07	0.08					
10	2.85	1.1	0.05					
11	2.76	1.19	0.05					
12	2.74	1.15	0.11					
13	2.71	1.2	0.09					
14	2.84	1.04	0.12					
15	2.82	1.13	0.05					
16	2.81	1.14	0.05					
17	2.91	0.71	0.38					
18	2.82	1.11	0.07					
19	3.11	0	0.89					
20	3.07	0	0.93					
21	3.15	0.04	0.81					
22	3		1					
23	2.95	1.05						
24	2.81	1.19						
25	2.785	1.215						
26	2.97	1.005			0.025			
27	2.97	1.005			0.025			
28	3.49	0.51						
29	2.91	1.09						
30	3.312	0.042	0.646					
31	2.91	1.09						
32	2.69	1.29			0.02			
33	2.748	1.154	0.073		0.025			
34	2.857	1.073	0.05		0.02			
35	2.334	1.653			0.01			
36	2.052	1.938			0.01			
37	2.71	1.29						
38	2.69	1.31						
39	2.72	1.28						
40	2.68	1.32						
41	2.63	1.37						
42	2.62	1.38						
43	2.79	1.21						
44	3.075	0.025	0.9					
45	3.075	0.025	0.9					
46	1.08	2.92						
47	1.1	2.9						
48	1.32	2.68						
49	2.98	1.02						
50	2.84	1.16						
51	2.083	1.917						

52	2.123	1.877						
53	2.841	1.159						
54	2.88	1.12						
55	3	0.904	0.096					
56	2.85	1.15						
57	2.8	1.2						
58	2.66	1.34						
59	2.59	1.41						
60	2.43	1.57						
61	2.32	1.68						
62	2.28	1.72						
63	2.55	1.45						
64	2.92	1.08						
65	3.36	0.64						
66	3.25	0.75						
67	2.841	1.159						
68	1.05	2.95						
69	3.63	0.02	0.035			0.305		
70	4							
71				4				
72				4				
73	4							
74	3.82						0.18	
75		1		3				
76		0.28		3.72				
77	3.5	0.5						
78		1		3				
79		1		3				
80	3.94	0.06						
81	2.44	1.56						
82	2.826	1.174	0					
83	2.768	1.232	0					
84	2.926	0.967	0.107					
85	2.708	1.292	0					
86	2.735	1.265	0					
87	2.891	1.075	0.034					
88	2.922	1.067	0.011					
89	2.817	1.14	0.043					
90	2.707	1.293	0					
91	2.66	1.34	0					
92	2.729	1.271	0					
93	2.664	1.336	0					
94	2.88	1.12	0					
95	2.802	1.198	0					
96	2.717	1.283	0					
97	2.94	0.803	0.257					
98	2.864	1.136	0					
99	2.945	0.814	0.241					
100	2.73	1.255	0.015					
101	2.741	1.244	0.015					
102	2.736	1.223	0.041					
103	2.974	0.588	0.438					

104	2.93	0.675	0.395					
105	2.749	1.251	0					
106	2.8575	1.1425						
107	2.908	1.092						
108	2.9315	1.0685						
109	2.8675	1.1325						
110	2.9035	1.0965						
111	2.734	1.266						
112	2.808	1.192						
113	2.763	1.237						
114	2.939	1.061						
115	2.7485	1.2515						
116	2.679	1.321						
117	2.6805	1.3195						
118	3.2525	0.7475						
119	2.6525	1.3475						
120	2.6245	1.3755						
121	2.587	1.413						
122	2.199	1.801						
123	2.1685	1.8315						
124	2.74	1.26						
125	2.65	1.35						
126	2.60	1.40						
127	2.5	1.5						
128	2.6	1.4						
129	1.2	2.76	0.04					
130	1.19	2.79	0.02					
131	1.25	2.75						
132	1.24	2.76						
133	1.19	2.78	0.03					
134	1.28	2.7	0.02					
135	2.82	1.04	0.14					
136	2.94	0.78	0.28					
137	2.84	1.14	0.02					
138	2.82	1.1	0.08					
139	3	0.9	0.1					
140	3.01	0.92	0.07					
141	3.03	0.07	0.9					
142	3.02	0.06	0.92					
143	2.94	1.06	0					
144	4							
145	2.71	1.29						
146	2.98	0.08	0.85		0.03			
147	3.09	0.91						
148	2.98	0.55	0.45		0.02			
149	3.06	0.03	0.87					
150	2.9425	1.0575						
151	3.0935	0.9065						
152	3.1365	0.8635						
153	2.92	1.08						
154	2.92	1.08						
155	2.91	1.09						

156	2.91	1.09						
157	2.91	1.09						
158	2.91	1.09						
159	2.96	1.04						
160	2.91	1.09						
161	2.97	1.03						
162	2.94	1.06						
163	2.28	1.72						
164	3							1
165	2.826	0.98	0.194					
166	2.492	1.436	0.072					
167	2.55	1.45						
168	2.92	1.08						
169	2.92	1.08						
170	2.91	1.09						

	(A-O1)-in	(A-O2)in	<A-O>in	d-int	T-O-T thickness	K-O4
1	3.0293	3.0407	3.0369	3.3907	6.6727491	3.982256
2	3.0201	3.0287	3.0259	3.4083	6.6735063	3.992434
3	3.0286	3.0287	3.0286	3.3821	6.7035939	3.98285
4	3.0290	3.0414	3.0373	3.3860	6.6734712	3.970572
5	3.0192	3.0196	3.0194	3.3906	6.6605922	3.97226
6	3.0192	3.0145	3.0161	3.3857	6.6628013	3.971171
7	2.9303	2.9327	2.9319	3.4647	6.6997696	4.055641
8	2.9336	2.9342	2.9340	3.4690	6.7000202	4.0554
9	2.9778	2.9812	2.9801	3.4477	6.6747944	4.026749
10	2.9857	2.9865	2.9862	3.4567	6.6902503	4.034444
11	2.9838	2.9792	2.9807	3.4415	6.6707231	4.017605
12	2.9838	2.9741	2.9773	3.4310	6.6701748	4.006162
13	2.9932	2.9880	2.9897	3.4281	6.6663581	4.009531
14	2.9693	2.9729	2.9717	3.4533	6.6796025	4.029852
15	2.9737	2.9737	2.9737	3.4484	6.6542888	4.016821
16	2.9717	2.9762	2.9747	3.4616	6.660032	4.023352
17	2.9788	2.9779	2.9782	3.4675	6.677285	4.037617
18	2.9743	2.9784	2.9770	3.4471	6.689429	4.034336
19	2.9448	2.9550	2.9516	3.4874	6.676051	4.047102
20	2.9415	2.9403	2.9407	3.4523	6.6994522	4.037336
21	2.9517	2.9569	2.9552	3.4468	6.7046907	4.038246
22	3.0148	3.0746	3.0547	3.3939	6.7878811	4.082912
23	2.9691	2.9689	2.9689	3.3520	6.6459743	4.007186
24	3.1095	3.1598	3.1431	3.3802	6.7119091	3.967951
25	2.9129	2.9157	2.9148	3.4585	6.6325098	4.021325
26	3.0412	3.0562	3.0512	3.3451	6.6741138	3.965672
27	3.0178	3.0106	3.0130	3.2800	6.6574732	3.984968
28	2.9560	2.9467	2.9498	3.3965	6.5737035	4.010098
29	3.1461	3.1381	3.1408	3.5907	6.6470514	4.104508
30	3.0199	3.0224	3.0216	3.3635	6.7009226	4.017739
31	2.9697	2.9718	2.9711	3.3602	6.6483357	4.012429
32	2.9899	3.0236	3.0124	3.3790	6.8192577	3.987633
33	3.0418	3.0295	3.0336	3.4119	6.7506065	4.009117
34	3.0401	3.0181	3.0254	3.3946	6.7324544	4.018417
35	2.9228	2.9127	2.9161	3.3831	6.7037566	4.011572
36	2.8675	2.8657	2.8663	3.3285	6.7720479	4.011925
37	2.9801	2.9865	2.9844	3.4228	6.6679344	4.008237
38	2.9827	2.9971	2.9923	3.4041	6.6394221	3.986449
39	2.9890	2.9891	2.9890	3.4147	6.6582452	3.999284
40	2.9801	2.9778	2.9785	3.4035	6.6304316	3.990768
41	2.9955	2.9921	2.9932	3.3907	6.6567405	3.994036
42	2.9859	2.9930	2.9906	3.3948	6.6411197	3.99259
43	2.9514	2.9484	2.9494	3.4540	6.6749412	4.044611
44	3.3611	3.3578	3.3589	3.8989	6.7654275	4.284916
45	3.3665	3.3739	3.3715	3.9284	6.7350013	4.281366
46	2.4412	2.4387	2.4396	2.9262	6.72704	3.851838
47	2.4425	2.4377	2.4393	2.9309	6.722962	3.843347
48	2.4464	2.4426	2.4439	2.8916	6.7298568	3.826511
49	3.0109	3.0042	3.0065	3.3556	6.627253	4.010101
50	2.9444	2.9908	2.9753	3.1725	6.7086845	3.933725

51	2.5761	2.5718	2.5732	3.0726	6.5614873	3.824754
52	2.6174	2.5786	2.5915	3.1027	6.554995	3.85281
53	2.9654	2.9600	2.9618	3.2866	6.6607511	3.984912
54	2.9657	2.9677	2.9670	3.4176	6.6658651	4.034443
55	3.1374	3.1740	3.1618	3.5379	6.6090473	3.916878
56	3.1397	3.2067	3.1844	3.5305	6.6340479	3.940788
57	3.0940	3.1211	3.1121	3.5208	6.6255139	3.938783
58	3.0598	3.0763	3.0708	3.5226	6.6075149	3.959849
59	3.0325	3.0273	3.0291	3.5268	6.5901788	3.96989
60	2.9942	3.0119	3.0060	3.5577	6.5609131	3.97261
61	2.9731	2.9777	2.9762	3.5528	6.548114	3.967703
62	3.0301	2.9647	2.9865	3.5553	6.5450735	3.967616
63	3.0072	3.0112	3.0098	3.4380	6.6817978	4.010691
64	3.0007	3.0054	3.0038	3.3719	6.7054544	3.979562
65	2.9839	2.9206	2.9417	3.3870	6.5709145	3.998868
66	2.9897	2.9971	2.9946	3.3278	6.6476651	4.010147
67	2.9711	2.9729	2.9723	3.3338	6.6796568	3.990401
68	2.4366	2.4034	2.4145	2.8178	6.8322709	3.860041
69	2.9935	3.0181	3.0099	3.4614	6.6674785	4.00699
70	3.0679	3.0685	3.0683	3.2968	6.6934496	3.963131
71	2.8789	2.8689	2.8723	3.3062	7.0623173	4.148361
72	2.8621	2.8605	2.8610	3.3376	7.0533403	4.189609
73	3.0780	3.0786	3.0784	3.3367	6.671353	3.981199
74	3.0942	3.0975	3.0964	3.3721	6.6639811	4.005414
75	2.8301	2.8214	2.8243	3.3948	6.9132416	4.211855
76	2.8577	2.8561	2.8566	3.3358	7.038968	4.194544
77	3.0451	3.0452	3.0452	3.3336	6.65317	4.00269
78	2.8394	2.8485	2.8455	3.3545	6.9437109	4.169728
79	2.8939	2.8910	2.8920	3.3040	6.9952378	4.128974
80	3.1221	3.0337	3.0631	3.2532	6.7054754	3.943622
81	3.0183	3.0268	3.0240	3.1301	6.7545342	3.826674
82	2.9698	2.9766	2.9743	3.4382	6.644469	4.018002
83	2.9497	2.9586	2.9556	3.4674	6.6651754	4.050984
84	2.9978	3.0027	3.0011	3.3052	6.660314	3.990242
85	2.9560	2.9553	2.9556	3.3970	6.6632248	4.018068
86	2.9546	2.9555	2.9552	3.4135	6.6598213	4.021285
87	2.9527	2.9679	2.9629	3.3812	6.6719211	4.032308
88	2.9728	2.9853	2.9812	3.4251	6.698284	4.033151
89	2.9782	2.9721	2.9741	3.3935	6.6443785	4.016172
90	2.9446	2.9466	2.9460	3.4065	6.6658505	4.022885
91	2.9439	2.9418	2.9425	3.3956	6.6564265	4.019791
92	2.9446	2.9493	2.9478	3.4299	6.6640714	4.031571
93	2.9568	2.9547	2.9554	3.3718	6.6673941	4.009679
94	2.9915	2.9933	2.9927	3.3977	6.6606434	4.023418
95	2.9919	3.0022	2.9987	3.4175	6.6279938	3.992088
96	2.9367	2.9386	2.9380	3.3937	6.6408802	4.025872
97	2.9889	2.9867	2.9875	3.4002	6.6675646	4.021098
98	2.9504	2.9573	2.9550	3.3769	6.6494988	3.996522
99	2.9862	2.9896	2.9885	3.4089	6.6905089	4.028659
100	2.9936	2.9925	2.9929	3.2454	6.6813516	3.96487
101	2.9955	2.9876	2.9902	3.2302	6.6864175	3.950807
102	3.0008	3.0040	3.0029	3.2461	6.6868876	3.948529

103	2.9791	2.9734	2.9753	3.4489	6.6969634	4.047196
104	2.9775	2.9713	2.9733	3.4510	6.6930357	4.0495
105	2.9697	2.9718	2.9711	3.4171	6.666743	4.022445
106	2.9866	2.9901	2.9889	3.4135	6.6636983	4.009716
107	2.9885	2.9902	2.9896	3.3524	6.6527874	4.008112
108	3.0153	3.0175	3.0167	3.3129	6.6278488	3.983344
109	2.9891	2.9888	2.9889	3.3572	6.6523093	4.001834
110	2.9889	2.9910	2.9903	3.3600	6.6400364	3.995076
111	2.9814	2.9870	2.9851	3.3744	6.6545448	3.975564
112	3.0325	3.0373	3.0357	3.3647	6.6612475	3.962322
113	2.9783	2.9872	2.9843	3.4212	6.6293263	3.974041
114	2.9940	2.9922	2.9928	3.2859	6.65325	3.988657
115	2.9727	2.9777	2.9760	3.3532	6.6464947	3.987974
116	2.9624	2.9532	2.9563	3.4113	6.651524	4.013069
117	2.9537	2.9518	2.9524	3.4098	6.6566064	4.018529
118	3.0521	3.0416	3.0451	3.3320	6.6941343	3.978425
119	2.9644	2.9544	2.9577	3.4263	6.6549607	4.005279
120	2.9549	2.9609	2.9589	3.4135	6.6775606	4.009177
121	2.9534	2.9531	2.9532	3.3441	6.6781542	3.992871
122	2.8661	2.8637	2.8645	3.2804	6.7228985	3.986357
123	2.8675	2.8662	2.8666	3.2800	6.7261536	3.990492
124	2.9398	2.9505	2.9469	3.4825	6.6331582	4.025015
125	2.9365	2.9358	2.9360	3.4816	6.6530642	4.038669
126	2.9274	2.9266	2.9268	3.4851	6.6459209	4.045315
127	2.9028	2.9026	2.9026	3.5117	6.6142632	4.047363
128	2.9386	2.9364	2.9371	3.4828	6.6553042	4.035967
129	2.4314	2.4319	2.4317	2.9078	6.7312229	3.817061
130	2.4101	2.4054	2.4069	2.9025	6.7383305	3.786942
131	2.4213	2.4156	2.4175	2.9077	6.7246979	3.802875
132	2.4328	2.4355	2.4346	2.9058	6.7480155	3.817162
133	2.3993	2.3965	2.3974	2.9197	6.720448	3.752921
134	2.4489	2.4425	2.4446	2.9205	6.7372921	3.840997
135	2.9880	2.9850	2.9860	3.4584	6.6934601	4.036383
136	3.0033	3.0050	3.0044	3.4506	6.7041099	4.035465
137	2.9795	2.9852	2.9833	3.4468	6.669071	4.007923
138	2.9720	2.9737	2.9732	3.4400	6.6994907	4.029428
139	3.0187	3.0258	3.0234	3.4285	6.6950159	4.01195
140	3.0254	3.0155	3.0188	3.4348	6.6853664	4.015673
141	2.9500	2.9549	2.9533	3.4568	6.7002307	4.040453
142	2.9576	2.9578	2.9578	3.4599	6.70441	4.048464
143	3.0258	3.0255	3.0256	3.2940	6.6656624	3.985893
144	3.0290	2.9846	2.9994	3.2744	6.5882533	3.936129
145	3.0959	3.1934	3.1609	3.3401	6.6602451	3.941292
146	2.9329	2.9326	2.9327	3.4607	6.6999131	4.053783
147	2.6657	2.5082	2.5607	3.0597	6.5418968	3.803259
148	2.9695	2.9748	2.9730	3.4514	6.6907578	4.033117
149	2.9824	2.9691	2.9735	3.3922	6.7540469	4.008818
150	3.0471	3.0530	3.0511	3.3679	6.6258177	3.882552
151	3.1022	3.1316	3.1218	3.3495	6.6829716	3.931289
152	3.0901	3.1688	3.1426	3.3736	6.6967866	3.969772
153	2.9592	2.9612	2.9605	3.5045	6.6327085	4.048801
154	2.9723	2.9736	2.9731	3.4874	6.6693319	4.050515

155	3.0121	3.0147	3.0139	3.4737	6.7109157	4.049206
156	2.9874	2.9920	2.9905	3.4696	6.6877807	4.043568
157	2.9733	2.9758	2.9750	3.4876	6.6651231	4.036822
158	2.9790	2.9803	2.9798	3.4818	6.6689525	4.051963
159	2.9941	2.9950	2.9947	3.4796	6.6730017	4.023456
160	2.9846	2.9871	2.9863	3.4619	6.6891385	4.045601
161	2.9960	2.9911	2.9928	3.4637	6.6895852	4.033693
162	2.9761	2.9791	2.9781	3.4644	6.6867665	4.051325
163	2.9422	2.9426	2.9425	3.4943	6.6118516	4.028284
164	2.9435	2.9432	2.9433	3.5023	6.7382103	4.087528
165	3.1160	3.1492	3.1381	3.4122	6.7480936	3.9919
166	3.0035	3.0101	3.0079	3.4400	6.6797088	4.014914
167	2.9906	2.9940	2.9929	3.4420	6.6503688	4.013131
168	2.9700	2.9730	2.9720	3.5095	6.6277075	4.052862
169	2.9780	2.9777	2.9778	3.4933	6.6577299	4.036056
170	3.0109	3.0135	3.0126	3.4615	6.7231373	4.048389

	Groups	Al-apfu	<Fe3>	Shannon
1	[Ann-Phl]	1.185	0.0345	2.0864
2	[Ann-Phl]	1.213		2.0893
3	[Ann-Phl]	1.206		2.0888
4	[Ann-Phl]	1.273		2.0896
5	[Ann-Phl]	1.2615		2.0869
6	[Ann-Phl]	1.2355		2.0783
7	tetra-ferri-[Ann-Phl]	0	0.95	2.0881
8	tetra-ferri-[Ann-Phl]	0	0.95	2.0883
9	[Ann-Phl]	1.07	0.08	2.0818
10	[Ann-Phl]	1.1	0.05	2.0813
11	[Ann-Phl]	1.19	0.05	2.0826
12	[Ann-Phl]	1.15	0.11	2.0859
13	[Ann-Phl]	1.2	0.09	2.0886
14	[Ann-Phl]	1.04	0.12	2.0823
15	[Ann-Phl]	1.13	0.05	2.0796
16	[Ann-Phl]	1.14	0.05	2.0793
17	[Ann-Phl]	0.71	0.38	2.0878
18	[Ann-Phl]	1.11	0.07	2.0819
19	tetra-ferri-[Ann-Phl]	0	0.89	2.0913
20	tetra-ferri-[Ann-Phl]	0	0.93	2.0886
21	tetra-ferri-[Ann-Phl]	0.04	0.81	2.0846
22	tetra-ferri-[Ann-Phl]	0	1	2.1467
23	[Ann-Phl]	1.05		2.0867
24	[Ann-Phl]	1.28		2.1187
25	aluminous-[Ann-Phl]	1.71		2.0629
26	[Ann-Phl]	1.005		2.1075
27	oxy-Bt	1.005		2.0679
28	lepidolite	1.81		2.0325
29	{Rb,Cs}-Phl	1.47		2.0877
30	tetra-ferri-[Ann-Phl]	0.042	0.646	2.1018
31	[Ann-Phl]	1.165		2.0854
32	Mn-Bt	1.51		2.1098
33	Mn-Bt	1.154	0.073	2.1179
34	Mn-Bt	1.073	0.05	2.1026
35	Mn-Bt	1.999		2.0688
36	kinoshitalite	2.161		2.0832
37	aluminous-[Ann-Phl]	1.64		2.0943
38	aluminous-[Ann-Phl]	1.91		2.0784
39	aluminous-[Ann-Phl]	1.78		2.0862
40	aluminous-[Ann-Phl]	1.96		2.0725
41	aluminous-[Ann-Phl]	1.85		2.0845
42	aluminous-[Ann-Phl]	1.92		2.0763
43	aluminous-[Ann-Phl]	1.324		2.0826
44	Cs-tetra-ferri-Ann	0.025	0.9	2.1451
45	Cs-tetra-ferri-Ann	0.025	0.9	2.1451
46	clintonite	3.74		2.0375
47	clintonite	3.64		2.0447
48	clintonite	3.38		2.0454
49	F-Phl	1.02		2.0879
50	Ba-Li-trioc	1.16		2.097
51	preiswerkite	2.776		2.0376

52	preiswerkite	2.811		2.0312
53	oxy-Bt	1.322		2.0408
54	[Ann-Phl]	1.12		2.0875
55	Rietveld-[Ann-Syd]	1	0.096	2.1248
56	Rietveld-[Ann-Syd]	1.26		2.1343
57	Rietveld-[Ann-Syd]	1.46		2.1227
58	Rietveld-[Ann-Syd]	1.67		2.1182
59	Rietveld-[Ann-Syd]	1.92		2.1063
60	Rietveld-[Ann-Syd]	2.17		2.0983
61	Rietveld-[Ann-Syd]	2.43		2.0869
62	Rietveld-[Ann-Syd]	2.5		2.0841
63	aluminous-[Ann-Phl]	1.72		2.1026
64	Zn-Bt	1.15		2.1071
65	Lepidolite	1.95		2.0285
66	F-Li-Phl	0.75		2.0894
67	aluminous-[Ann-Phl]	1.322		2.0408
68	clintonite	3.67		2.0464
69	<Ti-rich>-Phl	0.02	0.035	2.0933
70	tainiolite	0		2.1
71	Ge-containing	0		2.1073
72	Ge-containing	0		2.1
73	tetrasilisic-Phl	0		2.1073
74	F-Mn-Mg-mica	0		2.1087
75	Ge-containing	1		2.0867
76	Ge-containing	0.28		2.1015
77	F-Phengite	0.5		2.097
78	Ge-containing	1		2.1116
79	Ge-containing	1		2.1586
80	norrishite	0.065		2.0503
81	ferro-kinoshitalite	1.57		2.1185
82	aluminous-[Ann-Phl]	1.526	0	2.0775
83	aluminous-[Ann-Phl]	1.339	0	2.0797
84	[Ann-Phl]	0.967	0.107	2.0918
85	aluminous-[Ann-Phl]	1.415	0	2.0864
86	aluminous-[Ann-Phl]	1.361	0	2.0832
87	[Ann-Phl]	1.075	0.034	2.086
88	[Ann-Phl]	1.067	0.011	2.0865
89	[Ann-Phl]	1.14	0.043	2.0816
90	aluminous-[Ann-Phl]	1.373	0	2.0835
91	aluminous-[Ann-Phl]	1.42	0	2.0886
92	aluminous-[Ann-Phl]	1.457	0	2.079
93	aluminous-[Ann-Phl]	1.39	0	2.0831
94	[Ann-Phl]	1.159	0	2.0828
95	aluminous-[Ann-Phl]	1.336	0	2.0837
96	aluminous-[Ann-Phl]	1.451	0	2.0738
97	[Ann-Phl]	0.803	0.257	2.0865
98	[Ann-Phl]	1.206	0	2.0816
99	[Ann-Phl]	0.814	0.241	2.0851
100	[Ann-Phl]	1.255	0.015	2.0747
101	[Ann-Phl]	1.244	0.015	2.0709
102	[Ann-Phl]	1.223	0.041	2.0743
103	[Ann-Phl]	0.588	0.438	2.0871

104	[Ann-Phl]	0.675	0.395	2.085
105	[Ann-Phl]	1.3	0	2.0863
106	aluminous-[Ann-Phl]	1.366		2.0746
107	[Ann-Phl]	1.0935		2.0882
108	[Ann-Phl]	1.16		2.0767
109	[Ann-Phl]	1.2845		2.0744
110	[Ann-Phl]	1.135		2.0843
111	[Ann-Phl]	1.273		2.0973
112	[Ann-Phl]	1.2715		2.0992
113	aluminous-[Ann-Phl]	1.4285		2.0956
114	[Ann-Phl]	1.0695		2.0672
115	[Ann-Phl]	1.2685		2.074
116	aluminous-[Ann-Phl]	2.253		2.0224
117	aluminous-[Ann-Phl]	1.457		2.0687
118	[Ann-Phl]	0.748		2.0857
119	aluminous-[Ann-Phl]	1.4635		2.0712
120	aluminous-[Ann-Phl]	1.5035		2.0603
121	aluminous-[Ann-Phl]	1.6555		2.0749
122	aluminous-[Ann-Phl]	2.0025		2.0792
123	aluminous-[Ann-Phl]	1.9965		2.0811
124	aluminous-[Ann-Phl]	1.5		2.0733
125	aluminous-[Ann-Phl]	1.59		2.072
126	aluminous-[Ann-Phl]	1.58		2.0721
127	aluminous-[Ann-Phl]	1.97		2.0577
128	aluminous-[Ann-Phl]	1.6		2.0728
129	clintonite	3.44	0.04	2.047
130	clintonite	3.43	0.02	2.0516
131	clintonite	3.51		2.0428
132	clintonite	3.41		2.0492
133	clintonite	3.45	0.03	2.0478
134	clintonite	3.33	0.02	2.0507
135	[Ann-Phl]	1.04	0.14	2.085
136	[Ann-Phl]	0.78	0.28	2.0937
137	[Ann-Phl]	1.14	0.02	2.0937
138	[Ann-Phl]	1.1	0.08	2.0899
139	[Ann-Phl]	0.9	0.1	2.1075
140	[Ann-Phl]	0.92	0.07	2.0936
141	tetra-ferri-[Ann-Phl]	0.07	0.9	2.0988
142	tetra-ferri-[Ann-Phl]	0.06	0.92	2.0987
143	[Ann-Phl]	1.06	0	2.0893
144	lepidolite	1		2.0517
145	aluminous-[Ann-Phl]	1.47		2.1214
146	tetra-ferri-[Ann-Phl]	0.08	0.85	2.0878
147	paragonite	2.91		2.0045
148	tetra-ferri-[Ann-Phl]	0.55	0.45	2.0897
149	tetra-ferri-[Ann-Phl]	0.03	0.87	2.1136
150	aluminous-[Ann-Phl]	1.8925		2.0631
151	[Ann-Phl]	1.255		2.1056
152	[Ann-Phl]	0.991		2.1105
153	[Ann-Phl]			2.0536
154	[Ann-Phl]	1.11		2.0844
155	[Ann-Phl]	1.15		2.1075

156	[Ann-Phl]	1.13		2.0837
157	[Ann-Phl]	1.12		2.0898
158	[Ann-Phl]	1.12		2.0898
159	[Ann-Phl]	1.07		2.095
160	[Ann-Phl]	1.1		2.098
161	[Ann-Phl]	1.04		2.1017
162	[Ann-Phl]	1.07		2.0953
163	aluminous-[Ann-Phl]	2.51		2.0828
164	Ga-Phl	0		2.0867
165	[Ann-Phl]	0.981	0.194	2.1336
166	aluminous-[Ann-Phl]	2.093	0.072	2.0907
167	aluminous-[Ann-Phl]	1.722		2.1029
168	[Ann-Phl]	1.12		2.0536
169	[Ann-Phl]	1.11		2.0844
170	[Ann-Phl]	1.15		2.1075

Appendix Q. Database of $2M_1$ crystal structure refinements

Q1

No.	Reference	Sample	a	b	c	β	UC Vol.
1	[Rule & Bailey 1985]	Ph	5.2153	9.043	19.974	95.789	937.2
2	[Lin & Guggenheim 1983]	Li-Ca-Be-micas	5.058	8.763	19.111	95.39	843.3
3	[Lin & Bailey 1984]	Paragonite	5.128	8.898	19.287	94.35	877.5
4	[Radoslovich 1960]	Mu	5.189	8.995	20.097	95.18	934.2
5	[Sartori 1976]	Lepidolite	5.209	9.053	20.185	99.125	939.8
6	[Bigi & Brigatti 1994]	Bt	5.339	9.249	20.196	95.06	993.4
7	[Birle & Tettenhorst 1968]	Mu	5.19384	8.996	20.096	95.18	935.1
8	[Brigatti *et al*. 1998]	GA1	5.226	9.074	20.039	95.74	945.5
9	Mu	RA1	5.182	8.982	20.002	95.72	926.4
10		A4b	5.186	8.991	20.029	95.77	929.2
11		GFS13Ab	5.192	9.013	20.056	95.83	933.7
12		H87b	5.209	9.035	20.066	95.68	939.7
13		CC1b	5.186	9.005	20.031	95.78	930.7
14		C3-29b	5.188	8.996	20.082	95.78	932.5
15		B1b	5.187	9.004	20.036	95.73	931.1
16		C6Cb	5.186	9.003	20.030	95.84	930.3
17		C6Bb	5.196	8.997	20.034	95.80	931.8
18		C3-31b	5.197	9.022	20.176	95.79	941.2
19	[Brigatti *et al*. 2000]	Bt	5.335	9.242	20.181	95.20	991.0
20	[Brigatti *et al*. 2001]	Westland	5.192	9.011	20.028	95.74	932.3
21	Cr-Mu	Campbell	5.175	8.979	19.915	95.66	920.9
22		Anatoki	5.206	9.040	20.058	95.79	939.2
23	[Bohlen *et al*. 1980]	Bt - Au Sable	5.357	9.245	20.234	94.978	998.3
24	[Takeda & Ross 1975]	Bt - Ruiz Peak	5.329	9.234	20.098	95.09	985.1
25	[Comodi & Zanazzi 2000]	As-is	5.140	8.911	19.380	94.62	884.8
26	***Paragonite***	***dehydroxylated***	5.182	9.117	19.550	92.70	922.6
27	[Guggenheim *et al*. 1987]	Panasqueira	5.1579	8.9505	20.071	95.75	921.9
28	Mu	Keystone	5.200	9.021	20.07	95.71	936.8
29	[Guven 1971]	Ph	5.2112	9.0383	19.9473	95.769	934.8
30		Mu	5.1906	9.0080	20.0470	95.757	932.6
31	[Knurr & Bailey 1986]	Mn-Mu	5.2044	9.018	20.073	95.82	937.2
32	[Richardson & Richardson 1982]	Mu	5.1988	9.0266	20.1058	95.782	938.7
33	[Swanson & Bailey 1981]	Lepidolite	5.199	9.206	19.969	95.41	951.5
34	[Takéuchi 1965]	Margarite	5.11	8.87	19.18	95.43	865.4
35	[Ohta *et al*. (1982)]	Bt	5.3175	9.212	19.976	95.09	974.7
36	[Catti et al. 1989]	Mu-RT	5.191	9.006	20.068	95.77	933.4
37	[Pavase *et al*. 1999]	before heating	5.21397	9.0521	19.9968	95.736	939.1
38	Ph	after heating	5.21482	9.0621	20.0042	95.740	940.6
39	[Catti *et al*. 1994]	Mu	5.2108	9.0399	20.021	95.76	938.3
40	[Sidorenko *et al*. 1977]	Paragonite	5.135	8.894	19.36	94.17	881.8
41	[Novak *et al*. 1999]	polylithionite (R14)	5.187	8.979	19.881	95.11	922.3
42		boro-Mu (R15)	5.090	8.822	19.819	95.62	885.7
43		boro-Mu (LTM)	5.075	8.794	19.815	95.59	880.1
44	[Ivaldi *et al*. 2001]	yellowish	5.2132	9.051	19.937	95.76	936.0
45	Ph	greenish	5.225	9.057	19.956	95.73	939.7
46	[Smyth *et al*. 2000]	synthetic Ph	5.2046	9.0368	19.886	95.615	930.8

Appendix R. Database of $2M_2$ crystal structure refinements

No.	Reference	Sample	a	b	c	β	UC Vol.
1	[Guggenheim 1981]	Lepidolite	9.023	5.197	20.171	99.48	932.95
2	[Sartori *et al*. 1973]	Lepidolite	9.040	5.220	20.210	99.58	940.39
3	[Takeda *et al*. 1971]	Mu	9.032	5.200	20.15	99.77	932.65
4	[Zhoukhlistov *et al*. 1973]	dioc-Mica	8.965	5.175	20.31	100.67	925.97

Appendix S. Database of 2*O* crystal structure refinements

No.	Reference	Space group	Sample	a	b	c	UC Vol.
1	[Giuseppetti & Tadini 1972]	*Pnmn*	Anandite	5.468	9.489	19.963	1035.80
2	[Filut *et al*. 1985]	*Pnmn*	Anandite	5.439	9.509	19.878	1028.08
3	[Ferraris *et al*. 2001]	*Ccmm*	Phl	5.2781	9.141	20.124	970.92

Appendix T. Database of 3*T* crystal structure refinements

No.	Reference	Sample	a	c
1	[Brown 1978]	Lepidolite	5.200	29.76
2	[Guven & Burnham 1967]	Mu	5.1963	29.9705
3	[Pavlishin *et al*. 1981]	Protolithionite	5.307	29.754
4	[Sidorenko *et al*. 1977]	Paragonite	5.132	28.72
5	[Ivaldi *et al*. 2001]	yellowish (3TY)	5.220	29.762
6	Ph	greenish (3TG)	5.228	29.73
7	[Weiss *et al*. 1993]	Protolithionite	5.309	29.818
8	[Amisano-Canesi *et al*. 1994]	KZ	5.212	29.804
9	phengitic Mu	DM	5.215	29.755
10	[Pavase *et al*. 1997]	before heating	5.21379	29.7382
11	Ph	after heating	5.2137	29.7366
12	[Smyth *et al*. 2000]	synthetic Ph	5.2110	29.689

Appendix U. Maple worksheets used for stacking polytype derivation

Stacking polytype 2*M*1 derivation

Let us first write the fractional atomic coordinates in the *Standard C2/m* 1-layer unit-cell.

The interlayer cations (K) are at the following positions within the C 1 2/*m* 1 space group (sg No. 12):

Multplicity, Wyckoff letter, Site symmetry (1/2,1/2,0)+

2 *b* 2/*m* (0,1/2,0)

```
> with(linalg): K[1] := [0,1/2,1]; K[2]:= [1/2,0,1];K[3]:= [1/2,0,0];K[4]:= [0,1/2,0];
Warning, new definition for norm
Warning, new definition for trace
```

$$K_1 := \left[0, \frac{1}{2}, 1\right]$$

$$K_2 := \left[\frac{1}{2}, 0, 1\right]$$

$$K_3 := \left[\frac{1}{2}, 0, 0\right]$$

$$K_4 := \left[0, \frac{1}{2}, 0\right]$$

The M1 cations are at the following positions within the *C* 1 2/*m* 1 space group (sg No. 12):

Multplicity, Wyckoff letter, Site symmetry, Coordinates (1/2,1/2,0)+

2 *c* 2/*m* (0,0,1/2)

```
> M1[1] := [0,0,1/2]; M1[2]:= evalm(M1[1]+[1/2,1/2,0]);M1[3] := [3/2,1/2,1/2];
```

$$M1_1 := \left[0, 0, \frac{1}{2}\right]$$

$$M1_2 := \left[\frac{1}{2}, \frac{1}{2}, \frac{1}{2}\right]$$

$$M1_3 := \left[\frac{3}{2}, \frac{1}{2}, \frac{1}{2}\right]$$

The M2 cations are at the following positions within the C 1 2/*m* 1 space group (s.g. No. 12):

Multplicity, Wyckoff letter, Site symmetry, Coordinates (1/2,1/2,0)+

4 *h* 2 (1) 0 , y ,1/2 (2) 0, -y , 1/2

```
> M2[1] := [0,M2y,1/2]; M2[2]:= [M2[1][1],-M2[1][2]+1,M2[1][3]];
  M2[3]:=evalm(M2[1]+[1/2,1/2,0]);M2[4]:=evalm(M2[2]+[1/2,-1/2,0]);
  M2[5]:=[1,M2[1][2],1/2];M2[6]:=[M2[1][1]+1,-M2[1][2],1/2];
```

$$M2_1 := \left[0, M2y, \frac{1}{2}\right]$$

$$M2_2 := \left[0, -M2y + 1, \frac{1}{2}\right]$$

$$M2_3 := \left[\frac{1}{2}, \frac{1}{2} + M2y, \frac{1}{2}\right]$$

$$M2_4 := \left[\frac{1}{2}, \frac{1}{2} - M2y, \frac{1}{2}\right]$$

$$M2_5 := \left[1,\ M2y,\ \frac{1}{2}\right]$$

$$M2_6 := \left[1,\ -M2y,\ \frac{1}{2}\right]$$

The O4 oxygen atoms are at the following positions within the C 1 2/*m* 1 space group (s.g. No. 12; unique axis *b*):

Multplicity, Wyckoff letter, Site symmetry, Coordinates (1/2,1/2,0)+

4 *i* *m* (1) x , 0 , z
(2) -x , 0 , -z
(3) 1/2 + x , 1/2 , z
(4) 1/2 - x , 1/2 , -z

```
> O4[1]:=[O4x,1/2,O4z];  O4[2]:= [-O4[1][1]+1,O4[1][2],-O4[1][3]+1];
  O4[3]:=[O4[1][1]+1/2,O4[1][2]-1/2,O4[1][3]];
  O4[4]:=[-O4[1][1]+1/2,O4[1][2]-1/2,-O4[1][3]+1];
```

$$O4_1 := \left[O4x,\ \frac{1}{2},\ O4z\right]$$

$$O4_2 := \left[-O4x + 1,\ \frac{1}{2},\ -O4z + 1\right]$$

$$O4_3 := \left[O4x + \frac{1}{2},\ 0,\ O4z\right]$$

$$O4_4 := \left[-O4x + \frac{1}{2},\ 0,\ -O4z + 1\right]$$

The O3 oxygen atoms are at the following positions within the C 1 2/*m* 1 space group (s.g. No. 12; unique axis *b*):

Multplicity, Wyckoff letter, Site symmetry, Coordinates (1/2,1/2,0)+

8 *j* 1 (1) x , y , z
(2) -x , y , -z
(3) -x , - y , - z
(4) x , -y , z
(5) 1/2 + x , 1/2 + y , z
(6) 1/2 - x , 1/2 + y , -z
(7) 1/2 - x , 1/2 - y , -z
(8) 1/2 + x , 1/2 - y , z

```
> O3[1]:=[O3x,O3y,O3z];  O3[2]:= [-O3[1][1]+1,O3[1][2],-O3[1][3]+1];
  O3[3]:=[-O3[1][1]+1,-O3[1][2]+1,-O3[1][3]+1];
  O3[4]:=[O3[1][1],-O3[1][2]+1,O3[1][3]];
  O3[5]:=[O3[1][1]+1/2,O3[1][2]+1/2,O3[1][3]];
  O3[6]:=[1/2-O3[1][1],1/2+O3[1][2],-O3[1][3]+1];
  O3[7]:=[1/2-O3[1][1],1/2-O3[1][2],-O3[1][3]+1];
  O3[8]:=[1/2+O3[1][1],1/2-O3[1][2],O3[1][3]];
```

$$O3_1 := [O3x,\ O3y,\ O3z]$$

$$O3_2 := [-O3x + 1,\ O3y,\ -O3z + 1]$$

$$O3_3 := [-O3x + 1,\ -O3y + 1,\ -O3z + 1]$$

$$O3_4 := [O3x,\ -O3y + 1,\ O3z]$$

$$O3_5 := \left[O3x + \frac{1}{2},\ O3y + \frac{1}{2},\ O3z\right]$$

$$O3_6 := \left[\frac{1}{2} - O3x,\ O3y + \frac{1}{2},\ -O3z + 1\right]$$

$$O3_7 := \left[\frac{1}{2} - O3x, \frac{1}{2} - O3y, -O3z + 1\right]$$

$$O3_8 := \left[O3x + \frac{1}{2}, \frac{1}{2} - O3y, O3z\right]$$

The T cations are at the following positions within the C 1 2/*m* 1 space group (s.g. No. 12; unique axis *b*):

Multplicity, Wyckoff letter, Site symmetry, Coordinates (1/2,1/2,0)+

8 *j* 1 (1) x , y , z
(2) -x , y , -z
(3) -x , - y , - z
(4) x , -y , z
(5) 1/2 + x , 1/2 + y , z
(6) 1/2 - x , 1/2 + y , -z
(7) 1/2 - x , 1/2 - y , -z
(8) 1/2 + x , 1/2 - y , z

```
> T[1]:=[Tx,Ty,Tz];  T[2]:= [-T[1][1]+1,T[1][2],-T[1][3]+1];
  T[3]:=[-T[1][1]+1,-T[1][2]+1,-T[1][3]+1];
  T[4]:=[T[1][1],-T[1][2]+1,T[1][3]];
  T[5]:=[T[1][1]+1/2,T[1][2]+1/2,T[1][3]];
  T[6]:=[1/2-T[1][1],1/2+T[1][2],-T[1][3]+1];
  T[7]:=[1/2-T[1][1],1/2-T[1][2],-T[1][3]+1];
  T[8]:=[1/2+T[1][1],1/2-T[1][2],T[1][3]];
```

$$T_1 := [Tx, Ty, Tz]$$

$$T_2 := [-Tx + 1, Ty, -Tz + 1]$$

$$T_3 := [-Tx + 1, -Ty + 1, -Tz + 1]$$

$$T_4 := [Tx, -Ty + 1, Tz]$$

$$T_5 := \left[Tx + \frac{1}{2}, Ty + \frac{1}{2}, Tz\right]$$

$$T_6 := \left[\frac{1}{2} - Tx, Ty + \frac{1}{2}, -Tz + 1\right]$$

$$T_7 := \left[\frac{1}{2} - Tx, \frac{1}{2} - Ty, -Tz + 1\right]$$

$$T_8 := \left[Tx + \frac{1}{2}, \frac{1}{2} - Ty, Tz\right]$$

The O1 oxygen atoms are at the following positions within the C 1 2/*m* 1 space group (s.g. No. 12; unique axis *b*):

Multplicity, Wyckoff letter, Site symmetry, Coordinates (1/2,1/2,0)+

4 *i* *m* (1) x , 0 , z
(2) -x , 0 , -z
(3) 1/2 + x , 1/2 , z
(4) 1/2 - x , 1/2 , -z

```
> O1[1]:=[O1x,0,O1z];  O1[2]:= [-O1[1][1]+1,O1[1][2],-O1[1][3]+1];
  O1[3]:=[1/2+O1[1][1],1/2,O1[1][3]];
  O1[4]:=[1/2-O1[1][1],1/2,-O1[1][3]+1];
```

$$O1_1 := [O1x, 0, O1z]$$

$$O1_2 := [-O1x + 1, 0, -O1z + 1]$$

$$O1_3 := \left[\frac{1}{2} + O1x, \frac{1}{2}, O1z\right]$$

$$O1_4 := \left[\frac{1}{2} - O1x, \frac{1}{2}, -O1z + 1\right]$$

The O2 oxygen atoms are at the following positions within the C 1 2/*m* 1 space group (s.g. No. 12; unique axis *b*):

Multplicity, Wyckoff letter, Site symmetry, Coordinates (1/2,1/2,0)+

8	*j*	1	(1)	x	y	z
			(2)	-x	y	-z
			(3)	-x	- y	- z
			(4)	x	-y	z
			(5)	1/2 + x	1/2 + y	z
			(6)	1/2 - x	1/2 + y	-z
			(7)	1/2 - x	1/2 - y	-z
			(8)	1/2 + x	1/2 - y	z

```
> O2[1]:=[O2x,O2y,O2z]; O2[2]:= [-O2[1][1]+1,O2[1][2],-O2[1][3]+1];
  O2[3]:=[-O2[1][1]+1,-O2[1][2]+1,-O2[1][3]+1];
  O2[4]:=[O2[1][1],-O2[1][2]+1,O2[1][3]]; O2[5]:=[O2[1][1]+1/2,O2[1][2]+1/2,O2[1][3]];
  O2[6]:=[1/2-O2[1][1],1/2+O2[1][2],-O2[1][3]+1];
  O2[7]:=[1/2-O2[1][1],1/2-O2[1][2],-O2[1][3]+1];
  O2[8]:=[1/2+O2[1][1],1/2-O2[1][2],O2[1][3]];
```

$$O2_1 := [O2x, O2y, O2z]$$

$$O2_2 := [-O2x + 1, O2y, -O2z + 1]$$

$$O2_3 := [-O2x + 1, -O2y + 1, -O2z + 1]$$

$$O2_4 := [O2x, -O2y + 1, O2z]$$

$$O2_5 := \left[O2x + \frac{1}{2}, O2y + \frac{1}{2}, O2z\right]$$

$$O2_6 := \left[\frac{1}{2} - O2x, O2y + \frac{1}{2}, -O2z + 1\right]$$

$$O2_7 := \left[\frac{1}{2} - O2x, \frac{1}{2} - O2y, -O2z + 1\right]$$

$$O2_8 := \left[O2x + \frac{1}{2}, \frac{1}{2} - O2y, O2z\right]$$

```
> R[60] := [[1/2,-3/2,0],[1/2,1/2,0],[0,0,1]];
```

$$R_{60} := \left[\left[\frac{1}{2}, \frac{-3}{2}, 0\right], \left[\frac{1}{2}, \frac{1}{2}, 0\right], [0, 0, 1]\right]$$

```
> R[-60] := inverse(R[60]);
```

$$R_{-60} := \begin{bmatrix} \frac{1}{2} & \frac{3}{2} & 0 \\ \frac{-1}{2} & \frac{1}{2} & 0 \\ 0 & 0 & 1 \end{bmatrix}$$

Transformation to a metric orthogonal **abc** coordinate system with cation M1 at (0,0,0):

```
> Tometric := [[1,0,-c1M/a1M*cos(pi-beta1M)],[0,1,0],[0,0,1]];
```

$$Tometric := \left[\left[1, 0, -\frac{c1M\cos(-\pi + beta1M)}{a1M}\right], [0, 1, 0], [0, 0, 1]\right]$$

```
> metricTo1M := inverse(Tometric);
```

$$metricTo1M := \begin{bmatrix} 1 & 0 & \frac{c1M\cos(-\pi + beta1M)}{a1M} \\ 0 & 1 & 0 \\ 0 & 0 & 1 \end{bmatrix}$$

```
> for i from 1  to 8 do  O2metric[i]:= evalm(Tometric&*O2[i]
  +[1/2*c1M/a1M*cos(pi-beta1M),0,-1/2]) od;
```

$$O2metric_1 := \left[O2x - \frac{c1M\cos(-\pi + beta1M)\,O2z}{a1M} + \frac{1}{2}\frac{c1M\cos(-\pi + beta1M)}{a1M},\ O2y,\ O2z - \frac{1}{2} \right]$$

$$O2metric_2 := \left[-O2x + 1 - \frac{c1M\cos(-\pi + beta1M)\,(-O2z + 1)}{a1M} + \frac{1}{2}\frac{c1M\cos(-\pi + beta1M)}{a1M},\ O2y,\ -O2z + \frac{1}{2} \right]$$

$$O2metric_3 := \left[-O2x + 1 - \frac{c1M\cos(-\pi + beta1M)\,(-O2z + 1)}{a1M} + \frac{1}{2}\frac{c1M\cos(-\pi + beta1M)}{a1M},\ -O2y + 1,\ -O2z + \frac{1}{2} \right]$$

$$O2metric_4 := \left[O2x - \frac{c1M\cos(-\pi + beta1M)\,O2z}{a1M} + \frac{1}{2}\frac{c1M\cos(-\pi + beta1M)}{a1M},\ -O2y + 1,\ O2z - \frac{1}{2} \right]$$

$$O2metric_5 := \left[O2x + \frac{1}{2} - \frac{c1M\cos(-\pi + beta1M)\,O2z}{a1M} + \frac{1}{2}\frac{c1M\cos(-\pi + beta1M)}{a1M},\ O2y + \frac{1}{2},\ O2z - \frac{1}{2} \right]$$

$$O2metric_6 := \left[\frac{1}{2} - O2x - \frac{c1M\cos(-\pi + beta1M)\,(-O2z + 1)}{a1M} + \frac{1}{2}\frac{c1M\cos(-\pi + beta1M)}{a1M},\ O2y + \frac{1}{2},\ -O2z + \frac{1}{2} \right]$$

$$O2metric_7 := \left[\frac{1}{2} - O2x - \frac{c1M\cos(-\pi + beta1M)\,(-O2z + 1)}{a1M} + \frac{1}{2}\frac{c1M\cos(-\pi + beta1M)}{a1M},\ \frac{1}{2} - O2y,\ -O2z + \frac{1}{2} \right]$$

$$O2metric_8 := \left[O2x + \frac{1}{2} - \frac{c1M\cos(-\pi + beta1M)\,O2z}{a1M} + \frac{1}{2}\frac{c1M\cos(-\pi + beta1M)}{a1M},\ \frac{1}{2} - O2y,\ O2z - \frac{1}{2} \right]$$

```
> for i from 1  to 8 do  Tmetric[i]:= evalm(Tometric&*T[i]
  +[1/2*c1M/a1M*cos(pi-beta1M),0,-1/2]) od;
```

$$Tmetric_1 := \left[Tx - \frac{c1M\cos(-\pi + beta1M)\,Tz}{a1M} + \frac{1}{2}\frac{c1M\cos(-\pi + beta1M)}{a1M},\ Ty,\ Tz - \frac{1}{2} \right]$$

$$Tmetric_2 := \left[-Tx + 1 - \frac{c1M\cos(-\pi + beta1M)\,(-Tz + 1)}{a1M} + \frac{1}{2}\frac{c1M\cos(-\pi + beta1M)}{a1M},\ Ty,\ -Tz + \frac{1}{2} \right]$$

$$Tmetric_3 := \left[-Tx + 1 - \frac{c1M\cos(-\pi + beta1M)\,(-Tz + 1)}{a1M} + \frac{1}{2}\frac{c1M\cos(-\pi + beta1M)}{a1M},\ -Ty + 1,\ -Tz + \frac{1}{2} \right]$$

$$Tmetric_4 := \left[Tx - \frac{c1M\cos(-\pi + beta1M)\,Tz}{a1M} + \frac{1}{2}\frac{c1M\cos(-\pi + beta1M)}{a1M},\ -Ty + 1,\ Tz - \frac{1}{2} \right]$$

$$Tmetric_5 := \left[Tx + \frac{1}{2} - \frac{c1M\cos(-\pi + beta1M)\,Tz}{a1M} + \frac{1}{2}\frac{c1M\cos(-\pi + beta1M)}{a1M},\ Ty + \frac{1}{2},\ Tz - \frac{1}{2} \right]$$

$$Tmetric_6 := \left[\frac{1}{2} - Tx - \frac{c1M\cos(-\pi + beta1M)\,(-Tz + 1)}{a1M} + \frac{1}{2}\frac{c1M\cos(-\pi + beta1M)}{a1M},\ Ty + \frac{1}{2},\ -Tz + \frac{1}{2} \right]$$

$$Tmetric_7 := \left[\frac{1}{2} - Tx - \frac{c1M\cos(-\pi + beta1M)\,(-Tz + 1)}{a1M} + \frac{1}{2}\frac{c1M\cos(-\pi + beta1M)}{a1M},\ \frac{1}{2} - Ty,\ -Tz + \frac{1}{2} \right]$$

$$Tmetric_8 := \left[Tx + \frac{1}{2} - \frac{c1M\cos(-\pi + beta1M)\,Tz}{a1M} + \frac{1}{2}\frac{c1M\cos(-\pi + beta1M)}{a1M},\ \frac{1}{2} - Ty,\ Tz - \frac{1}{2} \right]$$

```
> for i from 1  to 4 do  O1metric[i]:= evalm(Tometric&*O1[i]
  +[1/2*c1M/a1M*cos(pi-beta1M),0,-1/2]) od;
```

$$O1metric_1 := \left[O1x - \frac{c1M\cos(-\pi + beta1M)\,O1z}{a1M} + \frac{1}{2}\frac{c1M\cos(-\pi + beta1M)}{a1M},\ 0,\ O1z - \frac{1}{2} \right]$$

$$O1metric_2 := \left[-O1x + 1 - \frac{c1M\cos(-\pi + beta1M)\,(-O1z + 1)}{a1M} + \frac{1}{2}\frac{c1M\cos(-\pi + beta1M)}{a1M},\ 0,\ -O1z + \frac{1}{2} \right]$$

$$O1metric_3 := \left[\frac{1}{2} + O1x - \frac{c1M\cos(-\pi + beta1M)\,O1z}{a1M} + \frac{1}{2}\frac{c1M\cos(-\pi + beta1M)}{a1M},\ \frac{1}{2},\ O1z - \frac{1}{2} \right]$$

$$O1metric_4 := \left[\frac{1}{2} - O1x - \frac{c1M\cos(-\pi + beta1M)\,(-O1z + 1)}{a1M} + \frac{1}{2}\frac{c1M\cos(-\pi + beta1M)}{a1M},\ \frac{1}{2},\ -O1z + \frac{1}{2} \right]$$

```
> for i from 1  to 4 do  O4metric[i]:= evalm(Tometric&*O4[i]
  +[1/2*c1M/a1M*cos(pi-beta1M),0,-1/2])  od;
```

$$O4metric_1 := \left[O4x - \frac{c1M\cos(-\pi + beta1M)\,O4z}{a1M} + \frac{1}{2}\frac{c1M\cos(-\pi + beta1M)}{a1M},\ \frac{1}{2},\ O4z - \frac{1}{2} \right]$$

$$O4metric_2 := \left[-O4x + 1 - \frac{c1M\cos(-\pi + beta1M)\,(-O4z+1)}{a1M} + \frac{1}{2}\frac{c1M\cos(-\pi+beta1M)}{a1M}, \frac{1}{2}, -O4z + \frac{1}{2} \right]$$

$$O4metric_3 := \left[O4x + \frac{1}{2} - \frac{c1M\cos(-\pi + beta1M)\,O4z}{a1M} + \frac{1}{2}\frac{c1M\cos(-\pi+beta1M)}{a1M}, 0, O4z - \frac{1}{2} \right]$$

$$O4metric_4 := \left[-O4x + \frac{1}{2} - \frac{c1M\cos(-\pi + beta1M)\,(-O4z+1)}{a1M} + \frac{1}{2}\frac{c1M\cos(-\pi+beta1M)}{a1M}, 0, -O4z + \frac{1}{2} \right]$$

```
> for i from 1  to 8 do  O3metric[i]:= evalm(Tometric&*O3[i]
  +[1/2*c1M/a1M*cos(pi-beta1M),0,-1/2]) od;
```

$$O3metric_1 := \left[O3x - \frac{c1M\cos(-\pi + beta1M)\,O3z}{a1M} + \frac{1}{2}\frac{c1M\cos(-\pi+beta1M)}{a1M}, O3y, O3z - \frac{1}{2} \right]$$

$$O3metric_2 := \left[-O3x + 1 - \frac{c1M\cos(-\pi + beta1M)\,(-O3z+1)}{a1M} + \frac{1}{2}\frac{c1M\cos(-\pi+beta1M)}{a1M}, O3y, -O3z + \frac{1}{2} \right]$$

$$O3metric_3 := \left[-O3x + 1 - \frac{c1M\cos(-\pi + beta1M)\,(-O3z+1)}{a1M} + \frac{1}{2}\frac{c1M\cos(-\pi+beta1M)}{a1M}, -O3y + 1, -O3z + \frac{1}{2} \right]$$

$$O3metric_4 := \left[O3x - \frac{c1M\cos(-\pi + beta1M)\,O3z}{a1M} + \frac{1}{2}\frac{c1M\cos(-\pi+beta1M)}{a1M}, -O3y + 1, O3z - \frac{1}{2} \right]$$

$$O3metric_5 := \left[O3x + \frac{1}{2} - \frac{c1M\cos(-\pi + beta1M)\,O3z}{a1M} + \frac{1}{2}\frac{c1M\cos(-\pi+beta1M)}{a1M}, O3y + \frac{1}{2}, O3z - \frac{1}{2} \right]$$

$$O3metric_6 := \left[\frac{1}{2} - O3x - \frac{c1M\cos(-\pi + beta1M)\,(-O3z+1)}{a1M} + \frac{1}{2}\frac{c1M\cos(-\pi+beta1M)}{a1M}, O3y + \frac{1}{2}, -O3z + \frac{1}{2} \right]$$

$$O3metric_7 := \left[\frac{1}{2} - O3x - \frac{c1M\cos(-\pi + beta1M)\,(-O3z+1)}{a1M} + \frac{1}{2}\frac{c1M\cos(-\pi+beta1M)}{a1M}, \frac{1}{2} - O3y, -O3z + \frac{1}{2} \right]$$

$$O3metric_8 := \left[O3x + \frac{1}{2} - \frac{c1M\cos(-\pi + beta1M)\,O3z}{a1M} + \frac{1}{2}\frac{c1M\cos(-\pi+beta1M)}{a1M}, \frac{1}{2} - O3y, O3z - \frac{1}{2} \right]$$

```
> for i from 1  to 6 do  M2metric[i]:= evalm(Tometric&*M2[i]
  +[1/2*c1M/a1M*cos(pi-beta1M),0,-1/2]) od:
> for i from 1  to 4 do  Kmetric[i]:= evalm(Tometric&*K[i]
  +[1/2*c1M/a1M*cos(pi-beta1M),0,-1/2]) od:
> for i from 1  to 3 do  M1metric[i]:= evalm(Tometric&*M1[i]
  +[1/2*c1M/a1M*cos(pi-beta1M),0,-1/2]) od:
> layer[1] :=
  [Kmetric[1],Kmetric[2],Kmetric[3],Kmetric[4],M1metric[1],M1metric[2],M1metric[3],M2metric
  [1],M2metric[2],M2metric[3],M2metric[4],M2metric[5],M2metric[6],O4metric[1],O4metric[2],O
  4metric[3],O4metric[4],O3metric[1],O3metric[2],O3metric[3],O3metric[4],O3metric[5],O3metr
  ic[6],O3metric[7],O3metric[8],Tmetric[1],Tmetric[2],Tmetric[3],Tmetric[4],Tmetric[5],Tmet
  ric[6],Tmetric[7],Tmetric[8],O1metric[1],O1metric[2],O1metric[3],O1metric[4],O2metric[1],
  O2metric[2],O2metric[3],O2metric[4],O2metric[5],O2metric[6],O2metric[7],O2metric[8]];
```

$layer_1 := [Kmetric_1, Kmetric_2, Kmetric_3, Kmetric_4, M1metric_1, M1metric_2, M1metric_3, M2metric_1, M2metric_2, M2metric_3, M2metric_4, M2metric_5, M2metric_6, O4metric_1, O4metric_2, O4metric_3, O4metric_4, O3metric_1, O3metric_2, O3metric_3, O3metric_4, O3metric_5, O3metric_6, O3metric_7, O3metric_8, Tmetric_1, Tmetric_2, Tmetric_3, Tmetric_4, Tmetric_5, Tmetric_6, Tmetric_7, Tmetric_8, O1metric_1, O1metric_2, O1metric_3, O1metric_4, O2metric_1, O2metric_2, O2metric_3, O2metric_4, O2metric_5, O2metric_6, O2metric_7, O2metric_8]$

```
> Zadjust := [[1,0,0],[0,1,0],[0,0,1/2]];
```

$$Zadjust := \left[[1, 0, 0], [0, 1, 0], \left[0, 0, \frac{1}{2} \right] \right]$$

```
> print(M1metric[1]);print(M1metric[2]);print(M1metric[3]);
```

$$[0, 0, 0]$$

$$\left[\frac{1}{2}, \frac{1}{2}, 0 \right]$$

$$\left[\frac{3}{2}, \frac{1}{2}, 0\right]$$

```
> print(M2metric[1]);print(M2metric[2]);print(M2metric[5]);print(M2metric[6]);
```

$$[0, M2y, 0]$$
$$[0, -M2y + 1, 0]$$
$$[1, M2y, 0]$$
$$[1, -M2y, 0]$$

```
>
>
>
> for i from 1 to 45 do layer_1_coordinates[i] :=
  evalm(Zadjust&*R[-60]&*layer[1][i]+[3/4,1/4,0]) od:
> Tocprime := [[1,0,-c1M/a1M*cos(pi-beta1M)],[0,1,0],[0,0,1]];
```

$$Tocprime := \left[\left[1, 0, -\frac{c1M\cos(-\pi + beta1M)}{a1M}\right], [0, 1, 0], [0, 0, 1]\right]$$

```
> cprimeTo2M1 := inverse(Tocprime);
```

$$cprimeTo2M1 := \begin{bmatrix} 1 & 0 & \frac{c1M\cos(-\pi + beta1M)}{a1M} \\ 0 & 1 & 0 \\ 0 & 0 & 1 \end{bmatrix}$$

```
> evalm(Tocprime&*cprimeTo2M1);
```

$$\begin{bmatrix} 1 & 0 & 0 \\ 0 & 1 & 0 \\ 0 & 0 & 1 \end{bmatrix}$$

```
> for i from 1 to 45 do layer_1_coordinates2M1[i] :=evalm(
  cprimeTo2M1&*layer_1_coordinates[i])  od;
```

$$layer\_1\_coordinates2M1_1 := \left[\frac{3}{2}, \frac{1}{4}\frac{c1M\cos(-\pi + beta1M)}{a1M} + \frac{1}{2}, \frac{1}{4}\right]$$

$$layer\_1\_coordinates2M1_2 := \left[1, \frac{1}{4}\frac{c1M\cos(-\pi + beta1M)}{a1M}, \frac{1}{4}\right]$$

$$layer\_1\_coordinates2M1_3 := \left[1, -\frac{1}{4}\frac{c1M\cos(-\pi + beta1M)}{a1M}, \frac{-1}{4}\right]$$

$$layer\_1\_coordinates2M1_4 := \left[\frac{3}{2}, \frac{1}{2} - \frac{1}{4}\frac{c1M\cos(-\pi + beta1M)}{a1M}, \frac{-1}{4}\right]$$

$$layer\_1\_coordinates2M1_5 := \left[\frac{3}{4}, \frac{1}{4}, 0\right]$$

$$layer\_1\_coordinates2M1_6 := \left[\frac{7}{4}, \frac{1}{4}, 0\right]$$

$$layer\_1\_coordinates2M1_7 := \left[\frac{9}{4}, \frac{-1}{4}, 0\right]$$

$$layer\_1\_coordinates2M1_8 := \left[\frac{3}{2}M2y + \frac{3}{4}, \frac{1}{2}M2y + \frac{1}{4}, 0\right]$$

$$layer\_1\_coordinates2M1_9 := \left[-\frac{3}{2}M2y + \frac{9}{4}, -\frac{1}{2}M2y + \frac{3}{4}, 0\right]$$

$$layer\_1\_coordinates2M1_{10} := \left[\frac{7}{4} + \frac{3}{2}M2y, \frac{1}{2}M2y + \frac{1}{4}, 0\right]$$

$$layer\_1\_coordinates2M1_{11} := \left[\frac{7}{4} - \frac{3}{2}M2y, \frac{1}{4} - \frac{1}{2}M2y, 0\right]$$

$$layer\_1\_coordinates2M1_{12} := \left[\frac{5}{4} + \frac{3}{2}M2y, -\frac{1}{4} + \frac{1}{2}M2y, 0\right]$$

$$layer\_1\_coordinates2M1_{13} := \left[\frac{5}{4} - \frac{3}{2}\,M2y,\ -\frac{1}{4} - \frac{1}{2}\,M2y,\ 0\right]$$

$$layer\_1\_coordinates2M1_{14} := \left[\begin{array}{l}\frac{1}{2}\,O4x - \frac{1}{2}\,\frac{c1M\cos(-\pi + beta1M)\,O4z}{a1M} + \frac{1}{4}\,\frac{c1M\cos(-\pi + beta1M)}{a1M} + \frac{3}{2} + \frac{c1M\cos(-\pi + beta1M)\left(\frac{1}{2}\,O4z - \frac{1}{4}\right)}{a1M}, \\ -\frac{1}{2}\,O4x + \frac{1}{2}\,\frac{c1M\cos(-\pi + beta1M)\,O4z}{a1M} - \frac{1}{4}\,\frac{c1M\cos(-\pi + beta1M)}{a1M} + \frac{1}{2}, \frac{1}{2}\,O4z - \frac{1}{4}\end{array}\right]$$

$$layer\_1\_coordinates2M1_{15} := \left[\begin{array}{l}-\frac{1}{2}\,O4x + 2 - \frac{1}{2}\,\frac{c1M\cos(-\pi + beta1M)\,(-O4z + 1)}{a1M} + \frac{1}{4}\,\frac{c1M\cos(-\pi + beta1M)}{a1M} + \frac{c1M\cos(-\pi + beta1M)\left(-\frac{1}{2}\,O4z + \frac{1}{4}\right)}{a1M}, \\ \frac{1}{2}\,O4x + \frac{1}{2}\,\frac{c1M\cos(-\pi + beta1M)\,(-O4z + 1)}{a1M} - \frac{1}{4}\,\frac{c1M\cos(-\pi + beta1M)}{a1M}, -\frac{1}{2}\,O4z + \frac{1}{4}\end{array}\right]$$

$$layer\_1\_coordinates2M1_{16} := \left[\begin{array}{l}\frac{1}{2}\,O4x + 1 - \frac{1}{2}\,\frac{c1M\cos(-\pi + beta1M)\,O4z}{a1M} + \frac{1}{4}\,\frac{c1M\cos(-\pi + beta1M)}{a1M} + \frac{c1M\cos(-\pi + beta1M)\left(\frac{1}{2}\,O4z - \frac{1}{4}\right)}{a1M}, \\ -\frac{1}{2}\,O4x + \frac{1}{2}\,\frac{c1M\cos(-\pi + beta1M)\,O4z}{a1M} - \frac{1}{4}\,\frac{c1M\cos(-\pi + beta1M)}{a1M}, \frac{1}{2}\,O4z - \frac{1}{4}\end{array}\right]$$

$$layer\_1\_coordinates2M1_{17} := \left[\begin{array}{l}-\frac{1}{2}\,O4x + 1 - \frac{1}{2}\,\frac{c1M\cos(-\pi + beta1M)\,(-O4z + 1)}{a1M} + \frac{1}{4}\,\frac{c1M\cos(-\pi + beta1M)}{a1M} + \frac{c1M\cos(-\pi + beta1M)\left(-\frac{1}{2}\,O4z + \frac{1}{4}\right)}{a1M}, \\ \frac{1}{2}\,O4x + \frac{1}{2}\,\frac{c1M\cos(-\pi + beta1M)\,(-O4z + 1)}{a1M} - \frac{1}{4}\,\frac{c1M\cos(-\pi + beta1M)}{a1M}, -\frac{1}{2}\,O4z + \frac{1}{4}\end{array}\right]$$

$$layer\_1\_coordinates2M1_{18} := \left[\begin{array}{l}\frac{1}{2}\,O3x - \frac{1}{2}\,\frac{c1M\cos(-\pi + beta1M)\,O3z}{a1M} + \frac{1}{4}\,\frac{c1M\cos(-\pi + beta1M)}{a1M} + \frac{3}{2}\,O3y + \frac{3}{4} + \frac{c1M\cos(-\pi + beta1M)\left(\frac{1}{2}\,O3z - \frac{1}{4}\right)}{a1M}, \\ -\frac{1}{2}\,O3x + \frac{1}{2}\,\frac{c1M\cos(-\pi + beta1M)\,O3z}{a1M} - \frac{1}{4}\,\frac{c1M\cos(-\pi + beta1M)}{a1M} + \frac{1}{2}\,O3y + \frac{1}{4}, \frac{1}{2}\,O3z - \frac{1}{4}\end{array}\right]$$

$$layer\_1\_coordinates2M1_{19} := \left[-\frac{1}{2} O3x + \frac{5}{4} - \frac{1}{2} \frac{c1M \cos(-\pi + beta1M)\,(-O3z + 1)}{a1M} + \frac{1}{4} \frac{c1M \cos(-\pi + beta1M)}{a1M} + \frac{3}{2} O3y + \frac{c1M \cos(-\pi + beta1M) \left(-\frac{1}{2} O3z + \frac{1}{4} \right)}{a1M}, \right.$$

$$\left. \frac{1}{2} O3x - \frac{1}{4} + \frac{1}{2} \frac{c1M \cos(-\pi + beta1M)\,(-O3z + 1)}{a1M} - \frac{1}{4} \frac{c1M \cos(-\pi + beta1M)}{a1M} + \frac{1}{2} O3y, -\frac{1}{2} O3z + \frac{1}{4} \right]$$

$$layer\_1\_coordinates2M1_{20} := \left[-\frac{1}{2} O3x + \frac{11}{4} - \frac{1}{2} \frac{c1M \cos(-\pi + beta1M)\,(-O3z + 1)}{a1M} + \frac{1}{4} \frac{c1M \cos(-\pi + beta1M)}{a1M} - \frac{3}{2} O3y + \frac{c1M \cos(-\pi + beta1M) \left(-\frac{1}{2} O3z + \frac{1}{4} \right)}{a1M}, \right.$$

$$\left. \frac{1}{2} O3x + \frac{1}{2} \frac{c1M \cos(-\pi + beta1M)\,(-O3z + 1)}{a1M} - \frac{1}{4} \frac{c1M \cos(-\pi + beta1M)}{a1M} - \frac{1}{2} O3y + \frac{1}{4}, -\frac{1}{2} O3z + \frac{1}{4} \right]$$

$$layer\_1\_coordinates2M1_{21} := \left[\right.$$

$$\frac{1}{2} O3x - \frac{1}{2} \frac{c1M \cos(-\pi + beta1M)\,O3z}{a1M} + \frac{1}{4} \frac{c1M \cos(-\pi + beta1M)}{a1M} - \frac{3}{2} O3y + \frac{9}{4} + \frac{c1M \cos(-\pi + beta1M) \left(\frac{1}{2} O3z - \frac{1}{4} \right)}{a1M},$$

$$\left. -\frac{1}{2} O3x + \frac{1}{2} \frac{c1M \cos(-\pi + beta1M)\,O3z}{a1M} - \frac{1}{4} \frac{c1M \cos(-\pi + beta1M)}{a1M} - \frac{1}{2} O3y + \frac{3}{4}, \frac{1}{2} O3z - \frac{1}{4} \right]$$

$$layer\_1\_coordinates2M1_{22} := \left[\right.$$

$$\frac{1}{2} O3x + \frac{7}{4} - \frac{1}{2} \frac{c1M \cos(-\pi + beta1M)\,O3z}{a1M} + \frac{1}{4} \frac{c1M \cos(-\pi + beta1M)}{a1M} + \frac{3}{2} O3y + \frac{c1M \cos(-\pi + beta1M) \left(\frac{1}{2} O3z - \frac{1}{4} \right)}{a1M},$$

$$\left. -\frac{1}{2} O3x + \frac{1}{2} \frac{c1M \cos(-\pi + beta1M)\,O3z}{a1M} - \frac{1}{4} \frac{c1M \cos(-\pi + beta1M)}{a1M} + \frac{1}{2} O3y + \frac{1}{4}, \frac{1}{2} O3z - \frac{1}{4} \right]$$

$$layer\_1\_coordinates2M1_{23} := \left[\right.$$

$$\frac{7}{4} - \frac{1}{2} O3x - \frac{1}{2} \frac{c1M \cos(-\pi + beta1M)\,(-O3z + 1)}{a1M} + \frac{1}{4} \frac{c1M \cos(-\pi + beta1M)}{a1M} + \frac{3}{2} O3y + \frac{c1M \cos(-\pi + beta1M) \left(-\frac{1}{2} O3z + \frac{1}{4} \right)}{a1M},$$

$$\left. \frac{1}{2} O3x + \frac{1}{2} \frac{c1M \cos(-\pi + beta1M)\,(-O3z + 1)}{a1M} - \frac{1}{4} \frac{c1M \cos(-\pi + beta1M)}{a1M} + \frac{1}{2} O3y + \frac{1}{4}, -\frac{1}{2} O3z + \frac{1}{4} \right]$$

$$layer\_1\_coordinates2M1_{24} := \left[\right.$$

$$\frac{7}{4}-\frac{1}{2}O3x-\frac{1}{2}\frac{c1M\cos(-\pi+beta1M)\,(-O3z+1)}{a1M}+\frac{1}{4}\frac{c1M\cos(-\pi+beta1M)}{a1M}-\frac{3}{2}O3y+\frac{c1M\cos(-\pi+beta1M)\left(-\frac{1}{2}O3z+\frac{1}{4}\right)}{a1M},$$

$$\frac{1}{2}O3x+\frac{1}{2}\frac{c1M\cos(-\pi+beta1M)\,(-O3z+1)}{a1M}-\frac{1}{4}\frac{c1M\cos(-\pi+beta1M)}{a1M}-\frac{1}{2}O3y+\frac{1}{4},-\frac{1}{2}O3z+\frac{1}{4}\Bigg]$$

$$layer\_1\_coordinates2M1_{25}:=\Bigg[$$

$$\frac{1}{2}O3x+\frac{7}{4}-\frac{1}{2}\frac{c1M\cos(-\pi+beta1M)\,O3z}{a1M}+\frac{1}{4}\frac{c1M\cos(-\pi+beta1M)}{a1M}-\frac{3}{2}O3y+\frac{c1M\cos(-\pi+beta1M)\left(\frac{1}{2}O3z-\frac{1}{4}\right)}{a1M},$$

$$-\frac{1}{2}O3x+\frac{1}{2}\frac{c1M\cos(-\pi+beta1M)\,O3z}{a1M}-\frac{1}{4}\frac{c1M\cos(-\pi+beta1M)}{a1M}-\frac{1}{2}O3y+\frac{1}{4},\frac{1}{2}O3z-\frac{1}{4}\Bigg]$$

$$layer\_1\_coordinates2M1_{26}:=\Bigg[$$

$$\frac{1}{2}Tx-\frac{1}{2}\frac{c1M\cos(-\pi+beta1M)\,Tz}{a1M}+\frac{1}{4}\frac{c1M\cos(-\pi+beta1M)}{a1M}+\frac{3}{2}Ty+\frac{3}{4}+\frac{c1M\cos(-\pi+beta1M)\left(\frac{1}{2}Tz-\frac{1}{4}\right)}{a1M},$$

$$-\frac{1}{2}Tx+\frac{1}{2}\frac{c1M\cos(-\pi+beta1M)\,Tz}{a1M}-\frac{1}{4}\frac{c1M\cos(-\pi+beta1M)}{a1M}+\frac{1}{2}Ty+\frac{1}{4},\frac{1}{2}Tz-\frac{1}{4}\Bigg]$$

$$layer\_1\_coordinates2M1_{27}:=\Bigg[$$

$$-\frac{1}{2}Tx+\frac{5}{4}-\frac{1}{2}\frac{c1M\cos(-\pi+beta1M)\,(-Tz+1)}{a1M}+\frac{1}{4}\frac{c1M\cos(-\pi+beta1M)}{a1M}+\frac{3}{2}Ty+\frac{c1M\cos(-\pi+beta1M)\left(-\frac{1}{2}Tz+\frac{1}{4}\right)}{a1M},$$

$$\frac{1}{2}Tx-\frac{1}{4}+\frac{1}{2}\frac{c1M\cos(-\pi+beta1M)\,(-Tz+1)}{a1M}-\frac{1}{4}\frac{c1M\cos(-\pi+beta1M)}{a1M}+\frac{1}{2}Ty,-\frac{1}{2}Tz+\frac{1}{4}\Bigg]$$

$$layer\_1\_coordinates2M1_{28}:=\Bigg[$$

$$-\frac{1}{2}Tx+\frac{11}{4}-\frac{1}{2}\frac{c1M\cos(-\pi+beta1M)\,(-Tz+1)}{a1M}+\frac{1}{4}\frac{c1M\cos(-\pi+beta1M)}{a1M}-\frac{3}{2}Ty+\frac{c1M\cos(-\pi+beta1M)\left(-\frac{1}{2}Tz+\frac{1}{4}\right)}{a1M},$$

$$\frac{1}{2}Tx+\frac{1}{2}\frac{c1M\cos(-\pi+beta1M)\,(-Tz+1)}{a1M}-\frac{1}{4}\frac{c1M\cos(-\pi+beta1M)}{a1M}-\frac{1}{2}Ty+\frac{1}{4},-\frac{1}{2}Tz+\frac{1}{4}\Bigg]$$

$$layer\_1\_coordinates2M1_{29}:=\Bigg[$$

$$\frac{1}{2}Tx-\frac{1}{2}\frac{c1M\cos(-\pi+beta1M)\,Tz}{a1M}+\frac{1}{4}\frac{c1M\cos(-\pi+beta1M)}{a1M}-\frac{3}{2}Ty+\frac{9}{4}+\frac{c1M\cos(-\pi+beta1M)\left(\frac{1}{2}Tz-\frac{1}{4}\right)}{a1M},$$

$$-\frac{1}{2}Tx+\frac{1}{2}\frac{c1M\cos(-\pi+beta1M)\,Tz}{a1M}-\frac{1}{4}\frac{c1M\cos(-\pi+beta1M)}{a1M}-\frac{1}{2}Ty+\frac{3}{4},\frac{1}{2}Tz-\frac{1}{4}\Bigg]$$

$$layer\_1\_coordinates2M1_{30}:=\Bigg[$$

$$\frac{1}{2}Tx+\frac{7}{4}-\frac{1}{2}\frac{c1M\cos(-\pi+beta1M)\,Tz}{a1M}+\frac{1}{4}\frac{c1M\cos(-\pi+beta1M)}{a1M}+\frac{3}{2}Ty+\frac{c1M\cos(-\pi+beta1M)\left(\frac{1}{2}Tz-\frac{1}{4}\right)}{a1M},$$

$$-\frac{1}{2}Tx+\frac{1}{2}\frac{c1M\cos(-\pi+beta1M)\,Tz}{a1M}-\frac{1}{4}\frac{c1M\cos(-\pi+beta1M)}{a1M}+\frac{1}{2}Ty+\frac{1}{4},\frac{1}{2}Tz-\frac{1}{4}\Bigg]$$

$$layer\_1\_coordinates2M1_{31}:=\Bigg[$$

$$\frac{7}{4}-\frac{1}{2}Tx-\frac{1}{2}\frac{c1M\cos(-\pi+beta1M)\,(-Tz+1)}{a1M}+\frac{1}{4}\frac{c1M\cos(-\pi+beta1M)}{a1M}+\frac{3}{2}Ty+\frac{c1M\cos(-\pi+beta1M)\left(-\frac{1}{2}Tz+\frac{1}{4}\right)}{a1M},$$

$$\frac{1}{2}Tx+\frac{1}{2}\frac{c1M\cos(-\pi+beta1M)\,(-Tz+1)}{a1M}-\frac{1}{4}\frac{c1M\cos(-\pi+beta1M)}{a1M}+\frac{1}{2}Ty+\frac{1}{4},-\frac{1}{2}Tz+\frac{1}{4}\Bigg]$$

$$layer\_1\_coordinates2M1_{32}:=\Bigg[$$

$$\frac{7}{4}-\frac{1}{2}Tx-\frac{1}{2}\frac{c1M\cos(-\pi+beta1M)\,(-Tz+1)}{a1M}+\frac{1}{4}\frac{c1M\cos(-\pi+beta1M)}{a1M}-\frac{3}{2}Ty+\frac{c1M\cos(-\pi+beta1M)\left(-\frac{1}{2}Tz+\frac{1}{4}\right)}{a1M},$$

$$\frac{1}{2}Tx+\frac{1}{2}\frac{c1M\cos(-\pi+beta1M)\,(-Tz+1)}{a1M}-\frac{1}{4}\frac{c1M\cos(-\pi+beta1M)}{a1M}-\frac{1}{2}Ty+\frac{1}{4},-\frac{1}{2}Tz+\frac{1}{4}\Bigg]$$

$$layer\_1\_coordinates2M1_{33}:=\Bigg[$$

$$\frac{1}{2}Tx+\frac{7}{4}-\frac{1}{2}\frac{c1M\cos(-\pi+beta1M)\,Tz}{a1M}+\frac{1}{4}\frac{c1M\cos(-\pi+beta1M)}{a1M}-\frac{3}{2}Ty+\frac{c1M\cos(-\pi+beta1M)\left(\frac{1}{2}Tz-\frac{1}{4}\right)}{a1M},$$

$$-\frac{1}{2}Tx+\frac{1}{2}\frac{c1M\cos(-\pi+beta1M)\,Tz}{a1M}-\frac{1}{4}\frac{c1M\cos(-\pi+beta1M)}{a1M}-\frac{1}{2}Ty+\frac{1}{4},\frac{1}{2}Tz-\frac{1}{4}\Bigg]$$

$$layer\_1\_coordinates2M1_{34}:=\Bigg[$$

$$\frac{1}{2}O1x-\frac{1}{2}\frac{c1M\cos(-\pi+beta1M)\,O1z}{a1M}+\frac{1}{4}\frac{c1M\cos(-\pi+beta1M)}{a1M}+\frac{3}{4}+\frac{c1M\cos(-\pi+beta1M)\left(\frac{1}{2}O1z-\frac{1}{4}\right)}{a1M},$$

$$-\frac{1}{2}O1x+\frac{1}{2}\frac{c1M\cos(-\pi+beta1M)\,O1z}{a1M}-\frac{1}{4}\frac{c1M\cos(-\pi+beta1M)}{a1M}+\frac{1}{4},\frac{1}{2}O1z-\frac{1}{4}\Bigg]$$

$$layer\_1\_coordinates2M1_{35} := \left[-\frac{1}{2} O1x + \frac{5}{4} - \frac{1}{2}\frac{c1M\cos(-\pi + beta1M)\,(-O1z+1)}{a1M} + \frac{1}{4}\frac{c1M\cos(-\pi + beta1M)}{a1M} + \frac{c1M\cos(-\pi + beta1M)\left(-\frac{1}{2}O1z + \frac{1}{4}\right)}{a1M}, \right.$$

$$\left. \frac{1}{2} O1x - \frac{1}{4} + \frac{1}{2}\frac{c1M\cos(-\pi + beta1M)\,(-O1z+1)}{a1M} - \frac{1}{4}\frac{c1M\cos(-\pi + beta1M)}{a1M}, -\frac{1}{2}O1z + \frac{1}{4} \right]$$

$$layer\_1\_coordinates2M1_{36} := \left[\frac{7}{4} + \frac{1}{2} O1x - \frac{1}{2}\frac{c1M\cos(-\pi + beta1M)\,O1z}{a1M} + \frac{1}{4}\frac{c1M\cos(-\pi + beta1M)}{a1M} + \frac{c1M\cos(-\pi + beta1M)\left(\frac{1}{2}O1z - \frac{1}{4}\right)}{a1M}, \right.$$

$$\left. -\frac{1}{2} O1x + \frac{1}{2}\frac{c1M\cos(-\pi + beta1M)\,O1z}{a1M} - \frac{1}{4}\frac{c1M\cos(-\pi + beta1M)}{a1M} + \frac{1}{4}, \frac{1}{2}O1z - \frac{1}{4} \right]$$

$$layer\_1\_coordinates2M1_{37} := \left[\frac{7}{4} - \frac{1}{2} O1x - \frac{1}{2}\frac{c1M\cos(-\pi + beta1M)\,(-O1z+1)}{a1M} + \frac{1}{4}\frac{c1M\cos(-\pi + beta1M)}{a1M} + \frac{c1M\cos(-\pi + beta1M)\left(-\frac{1}{2}O1z + \frac{1}{4}\right)}{a1M}, \right.$$

$$\left. \frac{1}{2} O1x + \frac{1}{2}\frac{c1M\cos(-\pi + beta1M)\,(-O1z+1)}{a1M} - \frac{1}{4}\frac{c1M\cos(-\pi + beta1M)}{a1M} + \frac{1}{4}, -\frac{1}{2}O1z + \frac{1}{4} \right]$$

$$layer\_1\_coordinates2M1_{38} := \left[\frac{1}{2} O2x - \frac{1}{2}\frac{c1M\cos(-\pi + beta1M)\,O2z}{a1M} + \frac{1}{4}\frac{c1M\cos(-\pi + beta1M)}{a1M} + \frac{3}{2}O2y + \frac{3}{4} + \frac{c1M\cos(-\pi + beta1M)\left(\frac{1}{2}O2z - \frac{1}{4}\right)}{a1M}, \right.$$

$$\left. -\frac{1}{2} O2x + \frac{1}{2}\frac{c1M\cos(-\pi + beta1M)\,O2z}{a1M} - \frac{1}{4}\frac{c1M\cos(-\pi + beta1M)}{a1M} + \frac{1}{2}O2y + \frac{1}{4}, \frac{1}{2}O2z - \frac{1}{4} \right]$$

$$layer\_1\_coordinates2M1_{39} := \left[-\frac{1}{2} O2x + \frac{5}{4} - \frac{1}{2}\frac{c1M\cos(-\pi + beta1M)\,(-O2z+1)}{a1M} + \frac{1}{4}\frac{c1M\cos(-\pi + beta1M)}{a1M} + \frac{3}{2}O2y \right.$$

$$\left. + \frac{c1M\cos(-\pi + beta1M)\left(-\frac{1}{2}O2z + \frac{1}{4}\right)}{a1M}, \right.$$

$$\left. \frac{1}{2} O2x - \frac{1}{4} + \frac{1}{2}\frac{c1M\cos(-\pi + beta1M)\,(-O2z+1)}{a1M} - \frac{1}{4}\frac{c1M\cos(-\pi + beta1M)}{a1M} + \frac{1}{2}O2y, -\frac{1}{2}O2z + \frac{1}{4} \right]$$

$$layer\_1\_coordinates2M1_{40} := \left[-\frac{1}{2} O2x + \frac{11}{4} - \frac{1}{2}\frac{c1M\cos(-\pi + beta1M)\,(-O2z+1)}{a1M} + \frac{1}{4}\frac{c1M\cos(-\pi + beta1M)}{a1M} - \frac{3}{2}O2y \right.$$

$$+\frac{c1M\cos(-\pi+beta1M)\left(-\frac{1}{2}O2z+\frac{1}{4}\right)}{a1M},$$

$$\frac{1}{2}O2x+\frac{1}{2}\frac{c1M\cos(-\pi+beta1M)(-O2z+1)}{a1M}-\frac{1}{4}\frac{c1M\cos(-\pi+beta1M)}{a1M}-\frac{1}{2}O2y+\frac{1}{4},-\frac{1}{2}O2z+\frac{1}{4}\Bigg]$$

$$layer\_1\_coordinates2M1_{41}:=\Bigg[$$

$$\frac{1}{2}O2x-\frac{1}{2}\frac{c1M\cos(-\pi+beta1M)\,O2z}{a1M}+\frac{1}{4}\frac{c1M\cos(-\pi+beta1M)}{a1M}-\frac{3}{2}O2y+\frac{9}{4}+\frac{c1M\cos(-\pi+beta1M)\left(\frac{1}{2}O2z-\frac{1}{4}\right)}{a1M},$$

$$-\frac{1}{2}O2x+\frac{1}{2}\frac{c1M\cos(-\pi+beta1M)\,O2z}{a1M}-\frac{1}{4}\frac{c1M\cos(-\pi+beta1M)}{a1M}-\frac{1}{2}O2y+\frac{3}{4},\frac{1}{2}O2z-\frac{1}{4}\Bigg]$$

$$layer\_1\_coordinates2M1_{42}:=\Bigg[$$

$$\frac{1}{2}O2x+\frac{7}{4}-\frac{1}{2}\frac{c1M\cos(-\pi+beta1M)\,O2z}{a1M}+\frac{1}{4}\frac{c1M\cos(-\pi+beta1M)}{a1M}+\frac{3}{2}O2y+\frac{c1M\cos(-\pi+beta1M)\left(\frac{1}{2}O2z-\frac{1}{4}\right)}{a1M},$$

$$-\frac{1}{2}O2x+\frac{1}{2}\frac{c1M\cos(-\pi+beta1M)\,O2z}{a1M}-\frac{1}{4}\frac{c1M\cos(-\pi+beta1M)}{a1M}+\frac{1}{2}O2y+\frac{1}{4},\frac{1}{2}O2z-\frac{1}{4}\Bigg]$$

$$layer\_1\_coordinates2M1_{43}:=\Bigg[$$

$$\frac{7}{4}-\frac{1}{2}O2x-\frac{1}{2}\frac{c1M\cos(-\pi+beta1M)(-O2z+1)}{a1M}+\frac{1}{4}\frac{c1M\cos(-\pi+beta1M)}{a1M}+\frac{3}{2}O2y+\frac{c1M\cos(-\pi+beta1M)\left(-\frac{1}{2}O2z+\frac{1}{4}\right)}{a1M},$$

$$\frac{1}{2}O2x+\frac{1}{2}\frac{c1M\cos(-\pi+beta1M)(-O2z+1)}{a1M}-\frac{1}{4}\frac{c1M\cos(-\pi+beta1M)}{a1M}+\frac{1}{2}O2y+\frac{1}{4},-\frac{1}{2}O2z+\frac{1}{4}\Bigg]$$

$$layer\_1\_coordinates2M1_{44}:=\Bigg[$$

$$\frac{7}{4}-\frac{1}{2}O2x-\frac{1}{2}\frac{c1M\cos(-\pi+beta1M)(-O2z+1)}{a1M}+\frac{1}{4}\frac{c1M\cos(-\pi+beta1M)}{a1M}-\frac{3}{2}O2y+\frac{c1M\cos(-\pi+beta1M)\left(-\frac{1}{2}O2z+\frac{1}{4}\right)}{a1M},$$

$$\frac{1}{2}O2x+\frac{1}{2}\frac{c1M\cos(-\pi+beta1M)(-O2z+1)}{a1M}-\frac{1}{4}\frac{c1M\cos(-\pi+beta1M)}{a1M}-\frac{1}{2}O2y+\frac{1}{4},-\frac{1}{2}O2z+\frac{1}{4}\Bigg]$$

$$layer\_1\_coordinates2M1_{45}:=\Bigg[$$

$$\frac{1}{2}O2x+\frac{7}{4}-\frac{1}{2}\frac{c1M\cos(-\pi+beta1M)\,O2z}{a1M}+\frac{1}{4}\frac{c1M\cos(-\pi+beta1M)}{a1M}-\frac{3}{2}O2y+\frac{c1M\cos(-\pi+beta1M)\left(\frac{1}{2}O2z-\frac{1}{4}\right)}{a1M},$$

$$-\frac{1}{2}O2x+\frac{1}{2}\frac{c1M\cos(-\pi+beta1M)\,O2z}{a1M}-\frac{1}{4}\frac{c1M\cos(-\pi+beta1M)}{a1M}-\frac{1}{2}O2y+\frac{1}{4},\frac{1}{2}O2z-\frac{1}{4}\Bigg]$$

```
> for i from 1 to 45 do layer_2_coordinates[i]
  :=evalm(R[60]&*Zadjust&*layer[1][i]+[1/2-1/2*c1M/a1M*cos(pi-beta1M),0,1/2]+[3/4,1/4,0])
  od:
> for i from 1 to 45 do layer_2_coordinates2M1[i] :=evalm(
  cprimeTo2M1&*layer_2_coordinates[i]) od;
```

$$layer\_2\_coordinates2M1_1:=\left[\frac{1}{2},\frac{1}{2}-\frac{1}{4}\frac{c1M\cos(-\pi+beta1M)}{a1M},\frac{3}{4}\right]$$

$$layer\_2\_coordinates2M1_2:=\left[\frac{3}{2},\frac{1}{2}-\frac{1}{4}\frac{c1M\cos(-\pi+beta1M)}{a1M},\frac{3}{4}\right]$$

$$layer\_2\_coordinates2M1_3:=\left[\frac{3}{2},\frac{1}{4}\frac{c1M\cos(-\pi+beta1M)}{a1M}+\frac{1}{2},\frac{1}{4}\right]$$

$$layer\_2\_coordinates2M1_4:=\left[\frac{1}{2},\frac{1}{4}\frac{c1M\cos(-\pi+beta1M)}{a1M}+\frac{1}{2},\frac{1}{4}\right]$$

$$layer\_2\_coordinates2M1_5:=\left[\frac{5}{4},\frac{1}{4},\frac{1}{2}\right]$$

$$layer\_2\_coordinates2M1_6:=\left[\frac{3}{4},\frac{3}{4},\frac{1}{2}\right]$$

$$layer\_2\_coordinates2M1_7:=\left[\frac{5}{4},\frac{5}{4},\frac{1}{2}\right]$$

$$layer\_2\_coordinates2M1_8:=\left[\frac{5}{4}-\frac{3}{2}M2y,\frac{1}{2}M2y+\frac{1}{4},\frac{1}{2}\right]$$

$$layer\_2\_coordinates2M1_9:=\left[\frac{3}{2}M2y-\frac{1}{4},-\frac{1}{2}M2y+\frac{3}{4},\frac{1}{2}\right]$$

$$layer\_2\_coordinates2M1_{10}:=\left[\frac{3}{4}-\frac{3}{2}M2y,\frac{3}{4}+\frac{1}{2}M2y,\frac{1}{2}\right]$$

$$layer\_2\_coordinates2M1_{11}:=\left[\frac{3}{2}M2y+\frac{3}{4},-\frac{1}{2}M2y+\frac{3}{4},\frac{1}{2}\right]$$

$$layer\_2\_coordinates2M1_{12}:=\left[\frac{7}{4}-\frac{3}{2}M2y,\frac{3}{4}+\frac{1}{2}M2y,\frac{1}{2}\right]$$

$$layer\_2\_coordinates2M1_{13}:=\left[\frac{7}{4}+\frac{3}{2}M2y,-\frac{1}{2}M2y+\frac{3}{4},\frac{1}{2}\right]$$

$$layer\_2\_coordinates2M1_{14}:=\Bigg[$$

$$\frac{1}{2}O4x-\frac{1}{2}\frac{c1M\cos(-\pi+beta1M)\,O4z}{a1M}-\frac{1}{4}\frac{c1M\cos(-\pi+beta1M)}{a1M}+\frac{1}{2}+\frac{c1M\cos(-\pi+beta1M)\left(\frac{1}{2}O4z+\frac{1}{4}\right)}{a1M},$$

$$\frac{1}{2}O4x-\frac{1}{2}\frac{c1M\cos(-\pi+beta1M)\,O4z}{a1M}+\frac{1}{4}\frac{c1M\cos(-\pi+beta1M)}{a1M}+\frac{1}{2},\frac{1}{2}O4z+\frac{1}{4}\Bigg]$$

$$layer\_2\_coordinates2M1_{15}:=\Bigg[$$

$$-\frac{1}{2}O4x+1-\frac{1}{2}\frac{c1M\cos(-\pi+beta1M)\,(-O4z+1)}{a1M}-\frac{1}{4}\frac{c1M\cos(-\pi+beta1M)}{a1M}+\frac{c1M\cos(-\pi+beta1M)\left(-\frac{1}{2}O4z+\frac{3}{4}\right)}{a1M},$$

$$-\frac{1}{2}O4x+1-\frac{1}{2}\frac{c1M\cos(-\pi+beta1M)\,(-O4z+1)}{a1M}+\frac{1}{4}\frac{c1M\cos(-\pi+beta1M)}{a1M},-\frac{1}{2}O4z+\frac{3}{4}\Bigg]$$

$$layer\_2\_coordinates2M1_{16}:=\Bigg[$$

$$\frac{1}{2}O4x-\frac{1}{2}\frac{c1M\cos(-\pi+beta1M)\,O4z}{a1M}-\frac{1}{4}\frac{c1M\cos(-\pi+beta1M)}{a1M}+\frac{3}{2}+\frac{c1M\cos(-\pi+beta1M)\left(\frac{1}{2}O4z+\frac{1}{4}\right)}{a1M},$$

$$\frac{1}{2}O4x-\frac{1}{2}\frac{c1M\cos(-\pi+beta1M)\,O4z}{a1M}+\frac{1}{4}\frac{c1M\cos(-\pi+beta1M)}{a1M}+\frac{1}{2},\frac{1}{2}O4z+\frac{1}{4}\Bigg]$$

$$layer\_2\_coordinates2M1_{17}:=\Bigg[$$

$$-\frac{1}{2}O4x+\frac{3}{2}-\frac{1}{2}\frac{c1M\cos(-\pi+beta1M)\,(-O4z+1)}{a1M}-\frac{1}{4}\frac{c1M\cos(-\pi+beta1M)}{a1M}+\frac{c1M\cos(-\pi+beta1M)\left(-\frac{1}{2}O4z+\frac{3}{4}\right)}{a1M},$$

$$-\frac{1}{2}O4x+\frac{1}{2}-\frac{1}{2}\frac{c1M\cos(-\pi+beta1M)\,(-O4z+1)}{a1M}+\frac{1}{4}\frac{c1M\cos(-\pi+beta1M)}{a1M},-\frac{1}{2}O4z+\frac{3}{4}\Bigg]$$

$$layer\_2\_coordinates2M1_{18}:=\Bigg[$$

$$\frac{1}{2}O3x-\frac{1}{2}\frac{c1M\cos(-\pi+beta1M)\,O3z}{a1M}-\frac{1}{4}\frac{c1M\cos(-\pi+beta1M)}{a1M}-\frac{3}{2}O3y+\frac{5}{4}+\frac{c1M\cos(-\pi+beta1M)\left(\frac{1}{2}O3z+\frac{1}{4}\right)}{a1M},$$

$$\frac{1}{2}O3x-\frac{1}{2}\frac{c1M\cos(-\pi+beta1M)\,O3z}{a1M}+\frac{1}{4}\frac{c1M\cos(-\pi+beta1M)}{a1M}+\frac{1}{2}O3y+\frac{1}{4},\frac{1}{2}O3z+\frac{1}{4}\Bigg]$$

$$layer\_2\_coordinates2M1_{19}:=\Bigg[-\frac{1}{2}O3x+\frac{7}{4}-\frac{1}{2}\frac{c1M\cos(-\pi+beta1M)\,(-O3z+1)}{a1M}-\frac{1}{4}\frac{c1M\cos(-\pi+beta1M)}{a1M}-\frac{3}{2}O3y$$
$$+\frac{c1M\cos(-\pi+beta1M)\left(-\frac{1}{2}O3z+\frac{3}{4}\right)}{a1M},$$

$$-\frac{1}{2}O3x+\frac{3}{4}-\frac{1}{2}\frac{c1M\cos(-\pi+beta1M)\,(-O3z+1)}{a1M}+\frac{1}{4}\frac{c1M\cos(-\pi+beta1M)}{a1M}+\frac{1}{2}O3y,-\frac{1}{2}O3z+\frac{3}{4}\Bigg]$$

$$layer\_2\_coordinates2M1_{20}:=\Bigg[-\frac{1}{2}O3x+\frac{1}{4}-\frac{1}{2}\frac{c1M\cos(-\pi+beta1M)\,(-O3z+1)}{a1M}-\frac{1}{4}\frac{c1M\cos(-\pi+beta1M)}{a1M}+\frac{3}{2}O3y$$
$$+\frac{c1M\cos(-\pi+beta1M)\left(-\frac{1}{2}O3z+\frac{3}{4}\right)}{a1M},$$

$$-\frac{1}{2}O3x+\frac{5}{4}-\frac{1}{2}\frac{c1M\cos(-\pi+beta1M)\,(-O3z+1)}{a1M}+\frac{1}{4}\frac{c1M\cos(-\pi+beta1M)}{a1M}-\frac{1}{2}O3y,-\frac{1}{2}O3z+\frac{3}{4}\Bigg]$$

$$layer\_2\_coordinates2M1_{21} := \left[\frac{1}{2} O3x - \frac{1}{2} \frac{c1M \cos(-\pi + beta1M)\, O3z}{a1M} - \frac{1}{4} \frac{c1M \cos(-\pi + beta1M)}{a1M} + \frac{3}{2} O3y - \frac{1}{4} + \frac{c1M \cos(-\pi + beta1M) \left(\frac{1}{2} O3z + \frac{1}{4} \right)}{a1M}, \right.$$

$$\left. \frac{1}{2} O3x - \frac{1}{2} \frac{c1M \cos(-\pi + beta1M)\, O3z}{a1M} + \frac{1}{4} \frac{c1M \cos(-\pi + beta1M)}{a1M} - \frac{1}{2} O3y + \frac{3}{4}, \frac{1}{2} O3z + \frac{1}{4} \right]$$

$$layer\_2\_coordinates2M1_{22} := \left[\frac{1}{2} O3x + \frac{3}{4} - \frac{1}{2} \frac{c1M \cos(-\pi + beta1M)\, O3z}{a1M} - \frac{1}{4} \frac{c1M \cos(-\pi + beta1M)}{a1M} - \frac{3}{2} O3y + \frac{c1M \cos(-\pi + beta1M) \left(\frac{1}{2} O3z + \frac{1}{4} \right)}{a1M}, \right.$$

$$\left. \frac{1}{2} O3x + \frac{3}{4} - \frac{1}{2} \frac{c1M \cos(-\pi + beta1M)\, O3z}{a1M} + \frac{1}{4} \frac{c1M \cos(-\pi + beta1M)}{a1M} + \frac{1}{2} O3y, \frac{1}{2} O3z + \frac{1}{4} \right]$$

$$layer\_2\_coordinates2M1_{23} := \left[\frac{3}{4} - \frac{1}{2} O3x - \frac{1}{2} \frac{c1M \cos(-\pi + beta1M)\, (-O3z + 1)}{a1M} - \frac{1}{4} \frac{c1M \cos(-\pi + beta1M)}{a1M} - \frac{3}{2} O3y + \frac{c1M \cos(-\pi + beta1M) \left(-\frac{1}{2} O3z + \frac{3}{4} \right)}{a1M}, \right.$$

$$\left. -\frac{1}{2} O3x + \frac{3}{4} - \frac{1}{2} \frac{c1M \cos(-\pi + beta1M)\, (-O3z + 1)}{a1M} + \frac{1}{4} \frac{c1M \cos(-\pi + beta1M)}{a1M} + \frac{1}{2} O3y, -\frac{1}{2} O3z + \frac{3}{4} \right]$$

$$layer\_2\_coordinates2M1_{24} := \left[\frac{3}{4} - \frac{1}{2} O3x - \frac{1}{2} \frac{c1M \cos(-\pi + beta1M)\, (-O3z + 1)}{a1M} - \frac{1}{4} \frac{c1M \cos(-\pi + beta1M)}{a1M} + \frac{3}{2} O3y + \frac{c1M \cos(-\pi + beta1M) \left(-\frac{1}{2} O3z + \frac{3}{4} \right)}{a1M}, \right.$$

$$\left. \frac{3}{4} - \frac{1}{2} O3x - \frac{1}{2} \frac{c1M \cos(-\pi + beta1M)\, (-O3z + 1)}{a1M} + \frac{1}{4} \frac{c1M \cos(-\pi + beta1M)}{a1M} - \frac{1}{2} O3y, -\frac{1}{2} O3z + \frac{3}{4} \right]$$

$$layer\_2\_coordinates2M1_{25} := \left[\frac{1}{2} O3x + \frac{3}{4} - \frac{1}{2} \frac{c1M \cos(-\pi + beta1M)\, O3z}{a1M} - \frac{1}{4} \frac{c1M \cos(-\pi + beta1M)}{a1M} + \frac{3}{2} O3y + \frac{c1M \cos(-\pi + beta1M) \left(\frac{1}{2} O3z + \frac{1}{4} \right)}{a1M}, \right.$$

$$\left. \frac{1}{2} O3x - \frac{1}{2} \frac{c1M \cos(-\pi + beta1M)\, O3z}{a1M} + \frac{1}{4} \frac{c1M \cos(-\pi + beta1M)}{a1M} - \frac{1}{2} O3y + \frac{3}{4}, \frac{1}{2} O3z + \frac{1}{4} \right]$$

$$layer\_2\_coordinates2M1_{26} := \left[\right.$$

$$\frac{1}{2}Tx-\frac{1}{2}\frac{c1M\cos(-\pi+beta1M)\,Tz}{a1M}-\frac{1}{4}\frac{c1M\cos(-\pi+beta1M)}{a1M}-\frac{3}{2}Ty+\frac{5}{4}+\frac{c1M\cos(-\pi+beta1M)\left(\frac{1}{2}Tz+\frac{1}{4}\right)}{a1M},$$

$$\frac{1}{2}Tx-\frac{1}{2}\frac{c1M\cos(-\pi+beta1M)\,Tz}{a1M}+\frac{1}{4}\frac{c1M\cos(-\pi+beta1M)}{a1M}+\frac{1}{2}Ty+\frac{1}{4},\frac{1}{2}Tz+\frac{1}{4}\Bigg]$$

$$layer\_2\_coordinates2M1_{27}:=\Bigg[$$

$$-\frac{1}{2}Tx+\frac{7}{4}-\frac{1}{2}\frac{c1M\cos(-\pi+beta1M)\,(-Tz+1)}{a1M}-\frac{1}{4}\frac{c1M\cos(-\pi+beta1M)}{a1M}-\frac{3}{2}Ty+\frac{c1M\cos(-\pi+beta1M)\left(-\frac{1}{2}Tz+\frac{3}{4}\right)}{a1M},$$

$$-\frac{1}{2}Tx+\frac{3}{4}-\frac{1}{2}\frac{c1M\cos(-\pi+beta1M)\,(-Tz+1)}{a1M}+\frac{1}{4}\frac{c1M\cos(-\pi+beta1M)}{a1M}+\frac{1}{2}Ty,-\frac{1}{2}Tz+\frac{3}{4}\Bigg]$$

$$layer\_2\_coordinates2M1_{28}:=\Bigg[$$

$$-\frac{1}{2}Tx+\frac{1}{4}-\frac{1}{2}\frac{c1M\cos(-\pi+beta1M)\,(-Tz+1)}{a1M}-\frac{1}{4}\frac{c1M\cos(-\pi+beta1M)}{a1M}+\frac{3}{2}Ty+\frac{c1M\cos(-\pi+beta1M)\left(-\frac{1}{2}Tz+\frac{3}{4}\right)}{a1M},$$

$$-\frac{1}{2}Tx+\frac{5}{4}-\frac{1}{2}\frac{c1M\cos(-\pi+beta1M)\,(-Tz+1)}{a1M}+\frac{1}{4}\frac{c1M\cos(-\pi+beta1M)}{a1M}-\frac{1}{2}Ty,-\frac{1}{2}Tz+\frac{3}{4}\Bigg]$$

$$layer\_2\_coordinates2M1_{29}:=\Bigg[$$

$$\frac{1}{2}Tx-\frac{1}{2}\frac{c1M\cos(-\pi+beta1M)\,Tz}{a1M}-\frac{1}{4}\frac{c1M\cos(-\pi+beta1M)}{a1M}+\frac{3}{2}Ty-\frac{1}{4}+\frac{c1M\cos(-\pi+beta1M)\left(\frac{1}{2}Tz+\frac{1}{4}\right)}{a1M},$$

$$\frac{1}{2}Tx-\frac{1}{2}\frac{c1M\cos(-\pi+beta1M)\,Tz}{a1M}+\frac{1}{4}\frac{c1M\cos(-\pi+beta1M)}{a1M}-\frac{1}{2}Ty+\frac{3}{4},\frac{1}{2}Tz+\frac{1}{4}\Bigg]$$

$$layer\_2\_coordinates2M1_{30}:=\Bigg[$$

$$\frac{1}{2}Tx+\frac{3}{4}-\frac{1}{2}\frac{c1M\cos(-\pi+beta1M)\,Tz}{a1M}-\frac{1}{4}\frac{c1M\cos(-\pi+beta1M)}{a1M}-\frac{3}{2}Ty+\frac{c1M\cos(-\pi+beta1M)\left(\frac{1}{2}Tz+\frac{1}{4}\right)}{a1M},$$

$$\frac{1}{2}Tx+\frac{3}{4}-\frac{1}{2}\frac{c1M\cos(-\pi+beta1M)\,Tz}{a1M}+\frac{1}{4}\frac{c1M\cos(-\pi+beta1M)}{a1M}+\frac{1}{2}Ty,\frac{1}{2}Tz+\frac{1}{4}\Bigg]$$

$$layer\_2\_coordinates2M1_{31}:=\Bigg[$$

$$\frac{3}{4}-\frac{1}{2}Tx-\frac{1}{2}\frac{c1M\cos(-\pi+beta1M)\,(-Tz+1)}{a1M}-\frac{1}{4}\frac{c1M\cos(-\pi+beta1M)}{a1M}-\frac{3}{2}Ty+\frac{c1M\cos(-\pi+beta1M)\left(-\frac{1}{2}Tz+\frac{3}{4}\right)}{a1M}.$$

$$-\frac{1}{2}Tx+\frac{3}{4}-\frac{1}{2}\frac{c1M\cos(-\pi+beta1M)\,(-Tz+1)}{a1M}+\frac{1}{4}\frac{c1M\cos(-\pi+beta1M)}{a1M}+\frac{1}{2}Ty,-\frac{1}{2}Tz+\frac{3}{4}\Bigg]$$

$$layer\_2\_coordinates2M1_{32}:=\Bigg[$$

$$\frac{3}{4}-\frac{1}{2}Tx-\frac{1}{2}\frac{c1M\cos(-\pi+beta1M)\,(-Tz+1)}{a1M}-\frac{1}{4}\frac{c1M\cos(-\pi+beta1M)}{a1M}+\frac{3}{2}Ty+\frac{c1M\cos(-\pi+beta1M)\left(-\frac{1}{2}Tz+\frac{3}{4}\right)}{a1M},$$

$$\frac{3}{4}-\frac{1}{2}Tx-\frac{1}{2}\frac{c1M\cos(-\pi+beta1M)\,(-Tz+1)}{a1M}+\frac{1}{4}\frac{c1M\cos(-\pi+beta1M)}{a1M}-\frac{1}{2}Ty,-\frac{1}{2}Tz+\frac{3}{4}\Bigg]$$

$$layer\_2\_coordinates2M1_{33}:=\Bigg[$$

$$\frac{1}{2}Tx+\frac{3}{4}-\frac{1}{2}\frac{c1M\cos(-\pi+beta1M)\,Tz}{a1M}-\frac{1}{4}\frac{c1M\cos(-\pi+beta1M)}{a1M}+\frac{3}{2}Ty+\frac{c1M\cos(-\pi+beta1M)\left(\frac{1}{2}Tz+\frac{1}{4}\right)}{a1M},$$

$$\frac{1}{2}Tx-\frac{1}{2}\frac{c1M\cos(-\pi+beta1M)\,Tz}{a1M}+\frac{1}{4}\frac{c1M\cos(-\pi+beta1M)}{a1M}-\frac{1}{2}Ty+\frac{3}{4},\frac{1}{2}Tz+\frac{1}{4}\Bigg]$$

$$layer\_2\_coordinates2M1_{34}:=\Bigg[$$

$$\frac{1}{2}O1x-\frac{1}{2}\frac{c1M\cos(-\pi+beta1M)\,O1z}{a1M}-\frac{1}{4}\frac{c1M\cos(-\pi+beta1M)}{a1M}+\frac{5}{4}+\frac{c1M\cos(-\pi+beta1M)\left(\frac{1}{2}O1z+\frac{1}{4}\right)}{a1M},$$

$$\frac{1}{2}O1x-\frac{1}{2}\frac{c1M\cos(-\pi+beta1M)\,O1z}{a1M}+\frac{1}{4}\frac{c1M\cos(-\pi+beta1M)}{a1M}+\frac{1}{4},\frac{1}{2}O1z+\frac{1}{4}\Bigg]$$

$$layer\_2\_coordinates2M1_{35}:=\Bigg[$$

$$-\frac{1}{2}O1x+\frac{7}{4}-\frac{1}{2}\frac{c1M\cos(-\pi+beta1M)\,(-O1z+1)}{a1M}-\frac{1}{4}\frac{c1M\cos(-\pi+beta1M)}{a1M}+\frac{c1M\cos(-\pi+beta1M)\left(-\frac{1}{2}O1z+\frac{3}{4}\right)}{a1M},$$

$$-\frac{1}{2}O1x+\frac{3}{4}-\frac{1}{2}\frac{c1M\cos(-\pi+beta1M)\,(-O1z+1)}{a1M}+\frac{1}{4}\frac{c1M\cos(-\pi+beta1M)}{a1M},-\frac{1}{2}O1z+\frac{3}{4}\Bigg]$$

$$layer\_2\_coordinates2M1_{36}:=\Bigg[$$

$$\frac{1}{2}O1x-\frac{1}{2}\frac{c1M\cos(-\pi+beta1M)\,O1z}{a1M}-\frac{1}{4}\frac{c1M\cos(-\pi+beta1M)}{a1M}+\frac{3}{4}+\frac{c1M\cos(-\pi+beta1M)\left(\frac{1}{2}O1z+\frac{1}{4}\right)}{a1M},$$

$$\frac{1}{2}O1x-\frac{1}{2}\frac{c1M\cos(-\pi+beta1M)\,O1z}{a1M}+\frac{1}{4}\frac{c1M\cos(-\pi+beta1M)}{a1M}+\frac{3}{4},\frac{1}{2}O1z+\frac{1}{4}\Bigg]$$

$$layer\_2\_coordinates2M1_{37} := \left[\right.$$

$$\frac{3}{4} - \frac{1}{2} O1x - \frac{1}{2} \frac{c1M \cos(-\pi + beta1M)\,(-O1z + 1)}{a1M} - \frac{1}{4} \frac{c1M \cos(-\pi + beta1M)}{a1M} + \frac{c1M \cos(-\pi + beta1M)\left(-\frac{1}{2} O1z + \frac{3}{4}\right)}{a1M},$$

$$-\frac{1}{2} O1x + \frac{3}{4} - \frac{1}{2} \frac{c1M \cos(-\pi + beta1M)\,(-O1z + 1)}{a1M} + \frac{1}{4} \frac{c1M \cos(-\pi + beta1M)}{a1M}, -\frac{1}{2} O1z + \frac{3}{4} \left.\right]$$

$$layer\_2\_coordinates2M1_{38} := \left[\right.$$

$$\frac{1}{2} O2x - \frac{1}{2} \frac{c1M \cos(-\pi + beta1M)\,O2z}{a1M} - \frac{1}{4} \frac{c1M \cos(-\pi + beta1M)}{a1M} - \frac{3}{2} O2y + \frac{5}{4} + \frac{c1M \cos(-\pi + beta1M)\left(\frac{1}{2} O2z + \frac{1}{4}\right)}{a1M},$$

$$\frac{1}{2} O2x - \frac{1}{2} \frac{c1M \cos(-\pi + beta1M)\,O2z}{a1M} + \frac{1}{4} \frac{c1M \cos(-\pi + beta1M)}{a1M} + \frac{1}{2} O2y + \frac{1}{4}, \frac{1}{2} O2z + \frac{1}{4} \left.\right]$$

$$layer\_2\_coordinates2M1_{39} := \left[-\frac{1}{2} O2x + \frac{7}{4} - \frac{1}{2} \frac{c1M \cos(-\pi + beta1M)\,(-O2z + 1)}{a1M} - \frac{1}{4} \frac{c1M \cos(-\pi + beta1M)}{a1M} - \frac{3}{2} O2y \right.$$

$$+ \frac{c1M \cos(-\pi + beta1M)\left(-\frac{1}{2} O2z + \frac{3}{4}\right)}{a1M},$$

$$-\frac{1}{2} O2x + \frac{3}{4} - \frac{1}{2} \frac{c1M \cos(-\pi + beta1M)\,(-O2z + 1)}{a1M} + \frac{1}{4} \frac{c1M \cos(-\pi + beta1M)}{a1M} + \frac{1}{2} O2y, -\frac{1}{2} O2z + \frac{3}{4} \left.\right]$$

$$layer\_2\_coordinates2M1_{40} := \left[-\frac{1}{2} O2x + \frac{1}{4} - \frac{1}{2} \frac{c1M \cos(-\pi + beta1M)\,(-O2z + 1)}{a1M} - \frac{1}{4} \frac{c1M \cos(-\pi + beta1M)}{a1M} + \frac{3}{2} O2y \right.$$

$$+ \frac{c1M \cos(-\pi + beta1M)\left(-\frac{1}{2} O2z + \frac{3}{4}\right)}{a1M},$$

$$-\frac{1}{2} O2x + \frac{5}{4} - \frac{1}{2} \frac{c1M \cos(-\pi + beta1M)\,(-O2z + 1)}{a1M} + \frac{1}{4} \frac{c1M \cos(-\pi + beta1M)}{a1M} - \frac{1}{2} O2y, -\frac{1}{2} O2z + \frac{3}{4} \left.\right]$$

$$layer\_2\_coordinates2M1_{41} := \left[\right.$$

$$\frac{1}{2} O2x - \frac{1}{2} \frac{c1M \cos(-\pi + beta1M)\,O2z}{a1M} - \frac{1}{4} \frac{c1M \cos(-\pi + beta1M)}{a1M} + \frac{3}{2} O2y - \frac{1}{4} + \frac{c1M \cos(-\pi + beta1M)\left(\frac{1}{2} O2z + \frac{1}{4}\right)}{a1M},$$

$$\frac{1}{2} O2x - \frac{1}{2} \frac{c1M \cos(-\pi + beta1M)\,O2z}{a1M} + \frac{1}{4} \frac{c1M \cos(-\pi + beta1M)}{a1M} - \frac{1}{2} O2y + \frac{3}{4}, \frac{1}{2} O2z + \frac{1}{4} \left.\right]$$

$$layer\_2\_coordinates2M1_{42} := \left[\right.$$

$$\frac{1}{2}O2x+\frac{3}{4}-\frac{1}{2}\frac{c1M\cos(-\pi+beta1M)\,O2z}{a1M}-\frac{1}{4}\frac{c1M\cos(-\pi+beta1M)}{a1M}-\frac{3}{2}O2y+\frac{c1M\cos(-\pi+beta1M)\left(\frac{1}{2}O2z+\frac{1}{4}\right)}{a1M},$$

$$\frac{1}{2}O2x+\frac{3}{4}-\frac{1}{2}\frac{c1M\cos(-\pi+beta1M)\,O2z}{a1M}+\frac{1}{4}\frac{c1M\cos(-\pi+beta1M)}{a1M}+\frac{1}{2}O2y,\frac{1}{2}O2z+\frac{1}{4}\Bigg]$$

$$layer\_2\_coordinates2M1_{43}:=\Bigg[$$

$$\frac{3}{4}-\frac{1}{2}O2x-\frac{1}{2}\frac{c1M\cos(-\pi+beta1M)\,(-O2z+1)}{a1M}-\frac{1}{4}\frac{c1M\cos(-\pi+beta1M)}{a1M}-\frac{3}{2}O2y+\frac{c1M\cos(-\pi+beta1M)\left(-\frac{1}{2}O2z+\frac{3}{4}\right)}{a1M},$$

$$-\frac{1}{2}O2x+\frac{3}{4}-\frac{1}{2}\frac{c1M\cos(-\pi+beta1M)\,(-O2z+1)}{a1M}+\frac{1}{4}\frac{c1M\cos(-\pi+beta1M)}{a1M}+\frac{1}{2}O2y,-\frac{1}{2}O2z+\frac{3}{4}\Bigg]$$

$$layer\_2\_coordinates2M1_{44}:=\Bigg[$$

$$\frac{3}{4}-\frac{1}{2}O2x-\frac{1}{2}\frac{c1M\cos(-\pi+beta1M)\,(-O2z+1)}{a1M}-\frac{1}{4}\frac{c1M\cos(-\pi+beta1M)}{a1M}+\frac{3}{2}O2y+\frac{c1M\cos(-\pi+beta1M)\left(-\frac{1}{2}O2z+\frac{3}{4}\right)}{a1M},$$

$$\frac{3}{4}-\frac{1}{2}O2x-\frac{1}{2}\frac{c1M\cos(-\pi+beta1M)\,(-O2z+1)}{a1M}+\frac{1}{4}\frac{c1M\cos(-\pi+beta1M)}{a1M}-\frac{1}{2}O2y,-\frac{1}{2}O2z+\frac{3}{4}\Bigg]$$

$$layer\_2\_coordinates2M1_{45}:=\Bigg[$$

$$\frac{1}{2}O2x+\frac{3}{4}-\frac{1}{2}\frac{c1M\cos(-\pi+beta1M)\,O2z}{a1M}-\frac{1}{4}\frac{c1M\cos(-\pi+beta1M)}{a1M}+\frac{3}{2}O2y+\frac{c1M\cos(-\pi+beta1M)\left(\frac{1}{2}O2z+\frac{1}{4}\right)}{a1M},$$

$$\frac{1}{2}O2x-\frac{1}{2}\frac{c1M\cos(-\pi+beta1M)\,O2z}{a1M}+\frac{1}{4}\frac{c1M\cos(-\pi+beta1M)}{a1M}-\frac{1}{2}O2y+\frac{3}{4},\frac{1}{2}O2z+\frac{1}{4}\Bigg]$$

>

Stacking polytype 2*M*2 derivation

Let us first write the fractional atomic coordinates in the *Standard C2/m* 1-layer unit-cell.

The interlayer cations (K) are at the following positions within the *C* 1 2/*m* 1 space group (sg No. 12):

Multplicity, Wyckoff letter, Site symmetry (1/2,1/2,0)+

2 *b* 2/*m* (0,1/2,0)

```
> with(linalg): K[1] := [0,1/2,0]; K[2]:= [-1/2,0,0]; K[3]:= [1/2,0,1]; K[4]:= [1/2,0,0];
Warning, new definition for norm
Warning, new definition for trace
```

$$K_1 := \left[0, \frac{1}{2}, 0\right]$$

$$K_2 := \left[\frac{-1}{2}, 0, 0\right]$$

$$K_3 := \left[\frac{1}{2}, 0, 1\right]$$

$$K_4 := \left[\frac{1}{2}, 0, 0\right]$$

The M1 cations are at the following positions within the *C* 1 2/*m* 1 space group (sg No. 12):

Multplicity, Wyckoff letter, Site symmetry, Coordinates (1/2,1/2,0)+

2 *c* 2/*m* (0,0,1/2)

```
> M1[1] := [0,0,1/2]; M1[2]:= evalm(M1[1]+[1/2,1/2,0]);M1[3] := [3/2,1/2,1/2];
```

$$M1_1 := \left[0, 0, \frac{1}{2}\right]$$

$$M1_2 := \left[\frac{1}{2}, \frac{1}{2}, \frac{1}{2}\right]$$

$$M1_3 := \left[\frac{3}{2}, \frac{1}{2}, \frac{1}{2}\right]$$

The M2 cations are at the following positions within the C 1 2/*m* 1 space group (s.g. No. 12):

Multplicity, Wyckoff letter, Site symmetry, Coordinates (1/2,1/2,0)+

4 *h* 2 (1) 0 , y ,1/2 (2) 0, -y , 1/2

```
> M2[1] := [0,M2y,1/2]; M2[2]:= [M2[1][1],-M2[1][2],M2[1][3]];
  M2[3]:=evalm(M2[1]+[1/2,1/2,0]);M2[4]:=evalm(M2[2]+[1/2,1/2,0]);
  M2[5]:=[0,M2[1][2],1/2];M2[6]:=[M2[1][1],-M2[1][2]+1,1/2];
```

$$M2_1 := \left[0, M2y, \frac{1}{2}\right]$$

$$M2_2 := \left[0, -M2y, \frac{1}{2}\right]$$

$$M2_3 := \left[\frac{1}{2}, \frac{1}{2} + M2y, \frac{1}{2}\right]$$

$$M2_4 := \left[\frac{1}{2}, \frac{1}{2} - M2y, \frac{1}{2}\right]$$

$$M2_5 := \left[0,\ M2y,\ \frac{1}{2}\right]$$

$$M2_6 := \left[0,\ -M2y + 1,\ \frac{1}{2}\right]$$

The O4 oxygen atoms are at the following positions within the $C\ 1\ 2/m\ 1$ space group (s.g. No. 12; unique axis b):

Multplicity, Wyckoff letter, Site symmetry, Coordinates (1/2,1/2,0)+

4 *i* *m* (1) x , 0 , z
(2) -x , 0 , -z
(3) 1/2 + x , 1/2 , z
(4) 1/2 - x , 1/2 , -z

```
> O4[1]:=[O4x,1/2,O4z];  O4[2]:= [-O4[1][1]+1,O4[1][2],-O4[1][3]+1];
  O4[3]:=[O4[1][1]+1/2,O4[1][2]+1/2-1,O4[1][3]];
  O4[4]:=[-O4[1][1]+1/2,O4[1][2]+1/2-1,-O4[1][3]+1];
```

$$O4_1 := \left[O4x,\ \frac{1}{2},\ O4z\right]$$

$$O4_2 := \left[-O4x + 1,\ \frac{1}{2},\ -O4z + 1\right]$$

$$O4_3 := \left[O4x + \frac{1}{2},\ 0,\ O4z\right]$$

$$O4_4 := \left[-O4x + \frac{1}{2},\ 0,\ -O4z + 1\right]$$

The O3 oxygen atoms are at the following positions within the C 1 $2/m$ 1 space group (s.g. No. 12; unique axis b):

Multplicity, Wyckoff letter, Site symmetry, Coordinates (1/2,1/2,0)+

8 *j* 1 (1) x , y , z
(2) -x , y , -z
(3) -x , - y , - z
(4) x , -y , z
(5) 1/2 + x , 1/2 + y , z
(6) 1/2 - x , 1/2 + y , -z
(7) 1/2 - x , 1/2 - y , -z
(8) 1/2 + x , 1/2 - y , z

```
> O3[1]:=[O3x,O3y,O3z];  O3[2]:= [-O3[1][1]+1,O3[1][2],-O3[1][3]+1];
  O3[3]:=[-O3[1][1]+1,-O3[1][2]+1,-O3[1][3]+1];
  O3[4]:=[O3[1][1],-O3[1][2]+1,O3[1][3]];
  O3[5]:=[O3[1][1]+1/2,O3[1][2]+1/2,O3[1][3]];
  O3[6]:=[1/2-O3[1][1],1/2+O3[1][2],-O3[1][3]+1];
  O3[7]:=[1/2-O3[1][1],1/2-O3[1][2],-O3[1][3]+1];
  O3[8]:=[1/2+O3[1][1],1/2-O3[1][2],O3[1][3]];
```

$$O3_1 := [O3x,\ O3y,\ O3z]$$

$$O3_2 := [-O3x + 1,\ O3y,\ -O3z + 1]$$

$$O3_3 := [-O3x + 1,\ -O3y + 1,\ -O3z + 1]$$

$$O3_4 := [O3x,\ -O3y + 1,\ O3z]$$

$$O3_5 := \left[O3x + \frac{1}{2},\ O3y + \frac{1}{2},\ O3z\right]$$

$$O3_6 := \left[\frac{1}{2} - O3x,\ O3y + \frac{1}{2},\ -O3z + 1\right]$$

$$O3_7 := \left[\frac{1}{2} - O3x, \frac{1}{2} - O3y, -O3z + 1\right]$$

$$O3_8 := \left[O3x + \frac{1}{2}, \frac{1}{2} - O3y, O3z\right]$$

The T cations are at the following positions within the C 1 2/*m* 1 space group (s.g. No. 12; unique axis *b*):

Multplicity, Wyckoff letter, Site symmetry, Coordinates (1/2,1/2,0)+

8 *j* 1 (1) x , y , z
(2) -x , y , -z
(3) -x , - y , - z
(4) x , -y , z
(5) 1/2 + x , 1/2 + y , z
(6) 1/2 - x , 1/2 + y , -z
(7) 1/2 - x , 1/2 - y , -z
(8) 1/2 + x , 1/2 - y , z

```
> T[1]:=[Tx,Ty,Tz];
  T[2]:= [-T[1][1]+1,T[1][2],-T[1][3]+1];
  T[3]:=[-T[1][1]+1,-T[1][2]+1,-T[1][3]+1];
  T[4]:=[T[1][1],-T[1][2]+1,T[1][3]];
  T[5]:=[T[1][1]+1/2,T[1][2]+1/2,T[1][3]];
  T[6]:=[1/2-T[1][1],1/2+T[1][2],-T[1][3]+1];
  T[7]:=[1/2-T[1][1],1/2-T[1][2],-T[1][3]+1];
  T[8]:=[1/2+T[1][1],1/2-T[1][2],T[1][3]];
```

$$T_1 := [Tx, Ty, Tz]$$

$$T_2 := [-Tx + 1, Ty, -Tz + 1]$$

$$T_3 := [-Tx + 1, -Ty + 1, -Tz + 1]$$

$$T_4 := [Tx, -Ty + 1, Tz]$$

$$T_5 := \left[Tx + \frac{1}{2}, Ty + \frac{1}{2}, Tz\right]$$

$$T_6 := \left[\frac{1}{2} - Tx, Ty + \frac{1}{2}, -Tz + 1\right]$$

$$T_7 := \left[\frac{1}{2} - Tx, \frac{1}{2} - Ty, -Tz + 1\right]$$

$$T_8 := \left[Tx + \frac{1}{2}, \frac{1}{2} - Ty, Tz\right]$$

The O1 oxygen atoms are at the following positions within the C 1 2/*m* 1 space group (s.g. No. 12; unique axis *b*):

Multplicity, Wyckoff letter, Site symmetry, Coordinates (1/2,1/2,0)+

4 *i* *m* (1) x , 0 , z
(2) -x , 0 , -z
(3) 1/2 + x , 1/2 , z
(4) 1/2 - x , 1/2 , -z

```
> O1[1]:=[O1x,0,O1z];  O1[2]:= [-O1[1][1]+1,O1[1][2],-O1[1][3]+1];
  O1[3]:=[1/2+O1[1][1],1/2,O1[1][3]];
  O1[4]:=[1/2-O1[1][1],1/2,-O1[1][3]+1];
```

$$O1_1 := [O1x, 0, O1z]$$

$$O1_2 := [-O1x + 1, 0, -O1z + 1]$$

$$O1_3 := \left[\frac{1}{2} + O1x, \frac{1}{2}, O1z\right]$$

$$O1_4 := \left[\frac{1}{2} - O1x, \frac{1}{2}, -O1z + 1\right]$$

The O2 oxygen atoms are at the following positions within the C 1 2/*m* 1 space group (s.g. No. 12; unique axis *b*):

Multplicity, Wyckoff letter, Site symmetry, Coordinates (1/2,1/2,0)+

8 *j* 1 (1) x , y , z
(2) -x , y , -z
(3) -x , -y , -z
(4) x , -y , z
(5) 1/2 + x , 1/2 + y , z
(6) 1/2 - x , 1/2 + y , -z
(7) 1/2 - x , 1/2 - y , -z
(8) 1/2 + x , 1/2 - y , z

```
> O2[1]:=[O2x,O2y,O2z];
  O2[2]:= [-O2[1][1]+1,O2[1][2],-O2[1][3]+1];
  O2[3]:=[-O2[1][1]+1,-O2[1][2]+1,-O2[1][3]+1];
  O2[4]:=[O2[1][1],-O2[1][2]+1,O2[1][3]];
  O2[5]:=[O2[1][1]+1/2,O2[1][2]+1/2,O2[1][3]];
  O2[6]:=[1/2-O2[1][1],1/2+O2[1][2],-O2[1][3]+1];
  O2[7]:=[1/2-O2[1][1],1/2-O2[1][2],-O2[1][3]+1];
  O2[8]:=[1/2+O2[1][1],1/2-O2[1][2],O2[1][3]];
```

$$O2_1 := [O2x, O2y, O2z]$$

$$O2_2 := [-O2x + 1, O2y, -O2z + 1]$$

$$O2_3 := [-O2x + 1, -O2y + 1, -O2z + 1]$$

$$O2_4 := [O2x, -O2y + 1, O2z]$$

$$O2_5 := \left[O2x + \frac{1}{2}, O2y + \frac{1}{2}, O2z\right]$$

$$O2_6 := \left[\frac{1}{2} - O2x, O2y + \frac{1}{2}, -O2z + 1\right]$$

$$O2_7 := \left[\frac{1}{2} - O2x, \frac{1}{2} - O2y, -O2z + 1\right]$$

$$O2_8 := \left[O2x + \frac{1}{2}, \frac{1}{2} - O2y, O2z\right]$$

```
> R[60] := [[1/2,-3/2,0],[1/2,1/2,0],[0,0,1]];
```

$$R_{60} := \left[\left[\frac{1}{2}, \frac{-3}{2}, 0\right], \left[\frac{1}{2}, \frac{1}{2}, 0\right], [0, 0, 1]\right]$$

```
> R[120] := [[-1/2,-3/2,0],[1/2,-1/2,0],[0,0,1]];
```

$$R_{120} := \left[\left[\frac{-1}{2}, \frac{-3}{2}, 0\right], \left[\frac{1}{2}, \frac{-1}{2}, 0\right], [0, 0, 1]\right]$$

Transformation to a metric orthogonal **abc** coordinate system with cation M1 at (0,0,0):

```
> Tometric := [[1,0,-c1M/a1M*cos(pi-beta1M)],[0,1,0],[0,0,1]];
```

$$Tometric := \left[\left[1, 0, -\frac{c1M\cos(-\pi + beta1M)}{a1M}\right], [0, 1, 0], [0, 0, 1]\right]$$

```
> metricTo1M := inverse(Tometric);
```

$$metricTo1M := \begin{bmatrix} 1 & 0 & \frac{c1M\cos(-\pi + beta1M)}{a1M} \\ 0 & 1 & 0 \\ 0 & 0 & 1 \end{bmatrix}$$

```
> for i from 1  to 8 do  O2metric[i]:= evalm(Tometric&*O2[i]
```

```
+[1/2*c1M/a1M*cos(pi-beta1M),0,-1/2]) od;
```

$$O2metric_1 := \left[O2x - \frac{c1M\cos(-\pi + beta1M)\,O2z}{a1M} + \frac{1}{2}\frac{c1M\cos(-\pi + beta1M)}{a1M},\ O2y,\ O2z - \frac{1}{2} \right]$$

$$O2metric_2 := \left[-O2x + 1 - \frac{c1M\cos(-\pi + beta1M)\,(-O2z + 1)}{a1M} + \frac{1}{2}\frac{c1M\cos(-\pi + beta1M)}{a1M},\ O2y,\ -O2z + \frac{1}{2} \right]$$

$$O2metric_3 := \left[-O2x + 1 - \frac{c1M\cos(-\pi + beta1M)\,(-O2z + 1)}{a1M} + \frac{1}{2}\frac{c1M\cos(-\pi + beta1M)}{a1M},\ -O2y + 1,\ -O2z + \frac{1}{2} \right]$$

$$O2metric_4 := \left[O2x - \frac{c1M\cos(-\pi + beta1M)\,O2z}{a1M} + \frac{1}{2}\frac{c1M\cos(-\pi + beta1M)}{a1M},\ -O2y + 1,\ O2z - \frac{1}{2} \right]$$

$$O2metric_5 := \left[O2x + \frac{1}{2} - \frac{c1M\cos(-\pi + beta1M)\,O2z}{a1M} + \frac{1}{2}\frac{c1M\cos(-\pi + beta1M)}{a1M},\ O2y + \frac{1}{2},\ O2z - \frac{1}{2} \right]$$

$$O2metric_6 := \left[\frac{1}{2} - O2x - \frac{c1M\cos(-\pi + beta1M)\,(-O2z + 1)}{a1M} + \frac{1}{2}\frac{c1M\cos(-\pi + beta1M)}{a1M},\ O2y + \frac{1}{2},\ -O2z + \frac{1}{2} \right]$$

$$O2metric_7 := \left[\frac{1}{2} - O2x - \frac{c1M\cos(-\pi + beta1M)\,(-O2z + 1)}{a1M} + \frac{1}{2}\frac{c1M\cos(-\pi + beta1M)}{a1M},\ \frac{1}{2} - O2y,\ -O2z + \frac{1}{2} \right]$$

$$O2metric_8 := \left[O2x + \frac{1}{2} - \frac{c1M\cos(-\pi + beta1M)\,O2z}{a1M} + \frac{1}{2}\frac{c1M\cos(-\pi + beta1M)}{a1M},\ \frac{1}{2} - O2y,\ O2z - \frac{1}{2} \right]$$

```
> for i from 1  to 8 do  Tmetric[i]:= evalm(Tometric&*T[i]
+[1/2*c1M/a1M*cos(pi-beta1M),0,-1/2]) od;
```

$$Tmetric_1 := \left[Tx - \frac{c1M\cos(-\pi + beta1M)\,Tz}{a1M} + \frac{1}{2}\frac{c1M\cos(-\pi + beta1M)}{a1M},\ Ty,\ Tz - \frac{1}{2} \right]$$

$$Tmetric_2 := \left[-Tx + 1 - \frac{c1M\cos(-\pi + beta1M)\,(-Tz + 1)}{a1M} + \frac{1}{2}\frac{c1M\cos(-\pi + beta1M)}{a1M},\ Ty,\ -Tz + \frac{1}{2} \right]$$

$$Tmetric_3 := \left[-Tx + 1 - \frac{c1M\cos(-\pi + beta1M)\,(-Tz + 1)}{a1M} + \frac{1}{2}\frac{c1M\cos(-\pi + beta1M)}{a1M},\ -Ty + 1,\ -Tz + \frac{1}{2} \right]$$

$$Tmetric_4 := \left[Tx - \frac{c1M\cos(-\pi + beta1M)\,Tz}{a1M} + \frac{1}{2}\frac{c1M\cos(-\pi + beta1M)}{a1M},\ -Ty + 1,\ Tz - \frac{1}{2} \right]$$

$$Tmetric_5 := \left[Tx + \frac{1}{2} - \frac{c1M\cos(-\pi + beta1M)\,Tz}{a1M} + \frac{1}{2}\frac{c1M\cos(-\pi + beta1M)}{a1M},\ Ty + \frac{1}{2},\ Tz - \frac{1}{2} \right]$$

$$Tmetric_6 := \left[\frac{1}{2} - Tx - \frac{c1M\cos(-\pi + beta1M)\,(-Tz + 1)}{a1M} + \frac{1}{2}\frac{c1M\cos(-\pi + beta1M)}{a1M},\ Ty + \frac{1}{2},\ -Tz + \frac{1}{2} \right]$$

$$Tmetric_7 := \left[\frac{1}{2} - Tx - \frac{c1M\cos(-\pi + beta1M)\,(-Tz + 1)}{a1M} + \frac{1}{2}\frac{c1M\cos(-\pi + beta1M)}{a1M},\ \frac{1}{2} - Ty,\ -Tz + \frac{1}{2} \right]$$

$$Tmetric_8 := \left[Tx + \frac{1}{2} - \frac{c1M\cos(-\pi + beta1M)\,Tz}{a1M} + \frac{1}{2}\frac{c1M\cos(-\pi + beta1M)}{a1M},\ \frac{1}{2} - Ty,\ Tz - \frac{1}{2} \right]$$

```
> for i from 1  to 4 do  O1metric[i]:= evalm(Tometric&*O1[i]
+[1/2*c1M/a1M*cos(pi-beta1M),0,-1/2]) od;
```

$$O1metric_1 := \left[O1x - \frac{c1M\cos(-\pi + beta1M)\,O1z}{a1M} + \frac{1}{2}\frac{c1M\cos(-\pi + beta1M)}{a1M},\ 0,\ O1z - \frac{1}{2} \right]$$

$$O1metric_2 := \left[-O1x + 1 - \frac{c1M\cos(-\pi + beta1M)\,(-O1z + 1)}{a1M} + \frac{1}{2}\frac{c1M\cos(-\pi + beta1M)}{a1M},\ 0,\ -O1z + \frac{1}{2} \right]$$

$$O1metric_3 := \left[\frac{1}{2} + O1x - \frac{c1M\cos(-\pi + beta1M)\,O1z}{a1M} + \frac{1}{2}\frac{c1M\cos(-\pi + beta1M)}{a1M},\ \frac{1}{2},\ O1z - \frac{1}{2} \right]$$

$$O1metric_4 := \left[\frac{1}{2} - O1x - \frac{c1M\cos(-\pi + beta1M)\,(-O1z + 1)}{a1M} + \frac{1}{2}\frac{c1M\cos(-\pi + beta1M)}{a1M},\ \frac{1}{2},\ -O1z + \frac{1}{2} \right]$$

```
> for i from 1  to 4 do  O4metric[i]:= evalm(Tometric&*O4[i]
+[1/2*c1M/a1M*cos(pi-beta1M),0,-1/2])  od;
```

$$O4metric_1 := \left[O4x - \frac{c1M\cos(-\pi + beta1M)\,O4z}{a1M} + \frac{1}{2}\frac{c1M\cos(-\pi + beta1M)}{a1M},\ \frac{1}{2},\ O4z - \frac{1}{2} \right]$$

$$O4metric_2 := \left[-O4x + 1 - \frac{c1M\cos(-\pi + beta1M)\,(-O4z+1)}{a1M} + \frac{1}{2}\frac{c1M\cos(-\pi + beta1M)}{a1M}, \frac{1}{2}, -O4z + \frac{1}{2} \right]$$

$$O4metric_3 := \left[O4x + \frac{1}{2} - \frac{c1M\cos(-\pi + beta1M)\,O4z}{a1M} + \frac{1}{2}\frac{c1M\cos(-\pi + beta1M)}{a1M}, 0, O4z - \frac{1}{2} \right]$$

$$O4metric_4 := \left[-O4x + \frac{1}{2} - \frac{c1M\cos(-\pi + beta1M)\,(-O4z+1)}{a1M} + \frac{1}{2}\frac{c1M\cos(-\pi + beta1M)}{a1M}, 0, -O4z + \frac{1}{2} \right]$$

```
> for i from 1  to 8 do  O3metric[i]:= evalm(Tometric&*O3[i]
  +[1/2*c1M/a1M*cos(pi-beta1M),0,-1/2]) od;
```

$$O3metric_1 := \left[O3x - \frac{c1M\cos(-\pi + beta1M)\,O3z}{a1M} + \frac{1}{2}\frac{c1M\cos(-\pi + beta1M)}{a1M}, O3y, O3z - \frac{1}{2} \right]$$

$$O3metric_2 := \left[-O3x + 1 - \frac{c1M\cos(-\pi + beta1M)\,(-O3z+1)}{a1M} + \frac{1}{2}\frac{c1M\cos(-\pi + beta1M)}{a1M}, O3y, -O3z + \frac{1}{2} \right]$$

$$O3metric_3 := \left[-O3x + 1 - \frac{c1M\cos(-\pi + beta1M)\,(-O3z+1)}{a1M} + \frac{1}{2}\frac{c1M\cos(-\pi + beta1M)}{a1M}, -O3y + 1, -O3z + \frac{1}{2} \right]$$

$$O3metric_4 := \left[O3x - \frac{c1M\cos(-\pi + beta1M)\,O3z}{a1M} + \frac{1}{2}\frac{c1M\cos(-\pi + beta1M)}{a1M}, -O3y + 1, O3z - \frac{1}{2} \right]$$

$$O3metric_5 := \left[O3x + \frac{1}{2} - \frac{c1M\cos(-\pi + beta1M)\,O3z}{a1M} + \frac{1}{2}\frac{c1M\cos(-\pi + beta1M)}{a1M}, O3y + \frac{1}{2}, O3z - \frac{1}{2} \right]$$

$$O3metric_6 := \left[\frac{1}{2} - O3x - \frac{c1M\cos(-\pi + beta1M)\,(-O3z+1)}{a1M} + \frac{1}{2}\frac{c1M\cos(-\pi + beta1M)}{a1M}, O3y + \frac{1}{2}, -O3z + \frac{1}{2} \right]$$

$$O3metric_7 := \left[\frac{1}{2} - O3x - \frac{c1M\cos(-\pi + beta1M)\,(-O3z+1)}{a1M} + \frac{1}{2}\frac{c1M\cos(-\pi + beta1M)}{a1M}, \frac{1}{2} - O3y, -O3z + \frac{1}{2} \right]$$

$$O3metric_8 := \left[O3x + \frac{1}{2} - \frac{c1M\cos(-\pi + beta1M)\,O3z}{a1M} + \frac{1}{2}\frac{c1M\cos(-\pi + beta1M)}{a1M}, \frac{1}{2} - O3y, O3z - \frac{1}{2} \right]$$

```
> for i from 1  to 6 do  M2metric[i]:= evalm(Tometric&*M2[i]
  +[1/2*c1M/a1M*cos(pi-beta1M),0,-1/2]) od:
> for i from 1  to 4 do  Kmetric[i]:= evalm(Tometric&*K[i]
  +[1/2*c1M/a1M*cos(pi-beta1M),0,-1/2]) od:
> for i from 1  to 3 do  M1metric[i]:= evalm(Tometric&*M1[i]
  +[1/2*c1M/a1M*cos(pi-beta1M),0,-1/2]) od:
> layer[1] :=
  [Kmetric[1],Kmetric[2],Kmetric[3],Kmetric[4],M1metric[1],M1metric[2],M1metric[3],M2metric
  [1],M2metric[2],M2metric[3],M2metric[4],M2metric[5],M2metric[6],O4metric[1],O4metric[2],O
  4metric[3],O4metric[4],O3metric[1],O3metric[2],O3metric[3],O3metric[4],O3metric[5],O3metr
  ic[6],O3metric[7],O3metric[8],Tmetric[1],Tmetric[2],Tmetric[3],Tmetric[4],Tmetric[5],Tmet
  ric[6],Tmetric[7],Tmetric[8],O1metric[1],O1metric[2],O1metric[3],O1metric[4],O2metric[1],
  O2metric[2],O2metric[3],O2metric[4],O2metric[5],O2metric[6],O2metric[7],O2metric[8]];
```

$layer_1 := [Kmetric_1, Kmetric_2, Kmetric_3, Kmetric_4, M1metric_1, M1metric_2, M1metric_3, M2metric_1, M2metric_2, M2metric_3, M2metric_4, M2metric_5, M2metric_6, O4metric_1, O4metric_2, O4metric_3, O4metric_4, O3metric_1, O3metric_2, O3metric_3, O3metric_4, O3metric_5, O3metric_6, O3metric_7, O3metric_8, Tmetric_1, Tmetric_2, Tmetric_3, Tmetric_4, Tmetric_5, Tmetric_6, Tmetric_7, Tmetric_8, O1metric_1, O1metric_2, O1metric_3, O1metric_4, O2metric_1, O2metric_2, O2metric_3, O2metric_4, O2metric_5, O2metric_6, O2metric_7, O2metric_8]$

```
> Zadjust := [[1,0,0],[0,1,0],[0,0,1/2]];
```

$$Zadjust := \left[[1, 0, 0], [0, 1, 0], \left[0, 0, \frac{1}{2} \right] \right]$$

```
> print(M1metric[1]);print(M1metric[2]);print(M1metric[3]);
```

$$[0, 0, 0]$$

$$\left[\frac{1}{2}, \frac{1}{2}, 0 \right]$$

$$\left[\frac{3}{2}, \frac{1}{2}, 0\right]$$

```
> print(M2metric[1]);print(M2metric[2]);print(M2metric[5]);print(M2metric[6]);
```

$$[0, M2y, 0]$$

$$[0, -M2y, 0]$$

$$[0, M2y, 0]$$

$$[0, -M2y + 1, 0]$$

```
> for i from 1 to 45 do layer_1_coordinates[i] :=
  evalm(Zadjust&*R[120]&*layer[1][i]+[1/4,-1/4,0]) od:
> Tocprime := [[1,0,0],[0,1,-c1M/a1M*cos(pi-beta1M)],[0,0,1]];
```

$$Tocprime := \left[[1, 0, 0], \left[0, 1, -\frac{c1M\cos(-\pi + beta1M)}{a1M}\right], [0, 0, 1]\right]$$

```
> cprimeTo2M2a_unique := inverse(Tocprime);
```

$$cprimeTo2M2a\_unique := \begin{bmatrix} 1 & 0 & 0 \\ 0 & 1 & \frac{c1M\cos(-\pi + beta1M)}{a1M} \\ 0 & 0 & 1 \end{bmatrix}$$

```
> abc2M2a_unique_TO_b_unique := [[0,1,0],[-1,0,0],[0,0,1]];
```

$$abc2M2a\_unique\_TO\_b\_unique := [[0, 1, 0], [-1, 0, 0], [0, 0, 1]]$$

```
> for i from 1 to 45 do layer_1_coordinates2M2[i] :=evalm(
  a_unique_TO_b_unique&*cprimeTo2M2a_unique&*layer_1_coordinates[i])  od;
```

$$layer\_1\_coordinates2M2_1 := a\_unique\_TO\_b\_unique\ \&* \left[-\frac{1}{4}\frac{c1M\cos(-\pi + beta1M)}{a1M} - \frac{1}{2}, \frac{-1}{2}, \frac{-1}{4}\right]$$

$$layer\_1\_coordinates2M2_2 := a\_unique\_TO\_b\_unique\ \&* \left[\frac{1}{2} - \frac{1}{4}\frac{c1M\cos(-\pi + beta1M)}{a1M}, \frac{-1}{2}, \frac{-1}{4}\right]$$

$$layer\_1\_coordinates2M2_3 := a\_unique\_TO\_b\_unique\ \&* \left[\frac{1}{4}\frac{c1M\cos(-\pi + beta1M)}{a1M}, 0, \frac{1}{4}\right]$$

$$layer\_1\_coordinates2M2_4 := a\_unique\_TO\_b\_unique\ \&* \left[-\frac{1}{4}\frac{c1M\cos(-\pi + beta1M)}{a1M}, 0, \frac{-1}{4}\right]$$

$$layer\_1\_coordinates2M2_5 := a\_unique\_TO\_b\_unique\ \&* \left[\frac{1}{4}, \frac{-1}{4}, 0\right]$$

$$layer\_1\_coordinates2M2_6 := a\_unique\_TO\_b\_unique\ \&* \left[\frac{-3}{4}, \frac{-1}{4}, 0\right]$$

$$layer\_1\_coordinates2M2_7 := a\_unique\_TO\_b\_unique\ \&* \left[\frac{-5}{4}, \frac{1}{4}, 0\right]$$

$$layer\_1\_coordinates2M2_8 := a\_unique\_TO\_b\_unique\ \&* \left[-\frac{3}{2}M2y + \frac{1}{4}, -\frac{1}{2}M2y - \frac{1}{4}, 0\right]$$

$$layer\_1\_coordinates2M2_9 := a\_unique\_TO\_b\_unique\ \&* \left[\frac{3}{2}M2y + \frac{1}{4}, \frac{1}{2}M2y - \frac{1}{4}, 0\right]$$

$$layer\_1\_coordinates2M2_{10} := a\_unique\_TO\_b\_unique\ \&* \left[-\frac{3}{4} - \frac{3}{2}M2y, -\frac{1}{2}M2y - \frac{1}{4}, 0\right]$$

$$layer\_1\_coordinates2M2_{11} := a\_unique\_TO\_b\_unique\ \&* \left[-\frac{3}{4} + \frac{3}{2}M2y, \frac{1}{2}M2y - \frac{1}{4}, 0\right]$$

$$layer\_1\_coordinates2M2_{12} := a\_unique\_TO\_b\_unique\ \&* \left[-\frac{3}{2}M2y + \frac{1}{4}, -\frac{1}{2}M2y - \frac{1}{4}, 0\right]$$

$$layer\_1\_coordinates2M2_{13} := a\_unique\_TO\_b\_unique\ \&* \left[\frac{3}{2}M2y - \frac{5}{4}, \frac{1}{2}M2y - \frac{3}{4}, 0\right]$$

$$layer\_1\_coordinates2M2_{14} := a\_unique\_TO\_b\_unique\ \&* \left[\right.$$

$$-\frac{1}{2}\,O4x+\frac{1}{2}\,\frac{c1M\cos(-\pi+beta1M)\,O4z}{a1M}-\frac{1}{4}\,\frac{c1M\cos(-\pi+beta1M)}{a1M}-\frac{1}{2},$$

$$-\frac{1}{2}+\frac{1}{2}\,O4x-\frac{1}{2}\,\frac{c1M\cos(-\pi+beta1M)\,O4z}{a1M}+\frac{1}{4}\,\frac{c1M\cos(-\pi+beta1M)}{a1M}+\frac{c1M\cos(-\pi+beta1M)\left(\frac{1}{2}\,O4z-\frac{1}{4}\right)}{a1M},\frac{1}{2}\,O4z-\frac{1}{4}\Bigg]$$

$$layer\_1\_coordinates2M2_{15}:=a\_unique\_TO\_b\_unique\ \&*\Bigg[$$

$$\frac{1}{2}\,O4x-1+\frac{1}{2}\,\frac{c1M\cos(-\pi+beta1M)\,(-O4z+1)}{a1M}-\frac{1}{4}\,\frac{c1M\cos(-\pi+beta1M)}{a1M},$$

$$-\frac{1}{2}\,O4x-\frac{1}{2}\,\frac{c1M\cos(-\pi+beta1M)\,(-O4z+1)}{a1M}+\frac{1}{4}\,\frac{c1M\cos(-\pi+beta1M)}{a1M}+\frac{c1M\cos(-\pi+beta1M)\left(-\frac{1}{2}\,O4z+\frac{1}{4}\right)}{a1M},$$

$$-\frac{1}{2}\,O4z+\frac{1}{4}\Bigg]$$

$$layer\_1\_coordinates2M2_{16}:=a\_unique\_TO\_b\_unique\ \&*\Bigg[-\frac{1}{2}\,O4x+\frac{1}{2}\,\frac{c1M\cos(-\pi+beta1M)\,O4z}{a1M}-\frac{1}{4}\,\frac{c1M\cos(-\pi+beta1M)}{a1M},$$

$$\frac{1}{2}\,O4x-\frac{1}{2}\,\frac{c1M\cos(-\pi+beta1M)\,O4z}{a1M}+\frac{1}{4}\,\frac{c1M\cos(-\pi+beta1M)}{a1M}+\frac{c1M\cos(-\pi+beta1M)\left(\frac{1}{2}\,O4z-\frac{1}{4}\right)}{a1M},\frac{1}{2}\,O4z-\frac{1}{4}\Bigg]$$

$$layer\_1\_coordinates2M2_{17}:=a\_unique\_TO\_b\_unique\ \&*\Bigg[$$

$$\frac{1}{2}\,O4x+\frac{1}{2}\,\frac{c1M\cos(-\pi+beta1M)\,(-O4z+1)}{a1M}-\frac{1}{4}\,\frac{c1M\cos(-\pi+beta1M)}{a1M},$$

$$-\frac{1}{2}\,O4x-\frac{1}{2}\,\frac{c1M\cos(-\pi+beta1M)\,(-O4z+1)}{a1M}+\frac{1}{4}\,\frac{c1M\cos(-\pi+beta1M)}{a1M}+\frac{c1M\cos(-\pi+beta1M)\left(-\frac{1}{2}\,O4z+\frac{1}{4}\right)}{a1M},$$

$$-\frac{1}{2}\,O4z+\frac{1}{4}\Bigg]$$

$$layer\_1\_coordinates2M2_{18}:=a\_unique\_TO\_b\_unique\ \&*\Bigg[$$

$$-\frac{1}{2}\,O3x+\frac{1}{2}\,\frac{c1M\cos(-\pi+beta1M)\,O3z}{a1M}-\frac{1}{4}\,\frac{c1M\cos(-\pi+beta1M)}{a1M}-\frac{3}{2}\,O3y+\frac{1}{4},$$

$$-\frac{1}{4}+\frac{1}{2}\,O3x-\frac{1}{2}\,\frac{c1M\cos(-\pi+beta1M)\,O3z}{a1M}+\frac{1}{4}\,\frac{c1M\cos(-\pi+beta1M)}{a1M}-\frac{1}{2}\,O3y+\frac{c1M\cos(-\pi+beta1M)\left(\frac{1}{2}\,O3z-\frac{1}{4}\right)}{a1M},$$

$$\frac{1}{2}\,O3z-\frac{1}{4}\Bigg]$$

$$layer\_1\_coordinates2M2_{19}:=a\_unique\_TO\_b\_unique\ \&*\Bigg[$$

$$\frac{1}{2}O3x-\frac{1}{4}+\frac{1}{2}\frac{c1M\cos(-\pi+beta1M)\,(-O3z+1)}{a1M}-\frac{1}{4}\frac{c1M\cos(-\pi+beta1M)}{a1M}-\frac{3}{2}O3y,$$

$$\frac{1}{4}-\frac{1}{2}O3x-\frac{1}{2}\frac{c1M\cos(-\pi+beta1M)\,(-O3z+1)}{a1M}+\frac{1}{4}\frac{c1M\cos(-\pi+beta1M)}{a1M}-\frac{1}{2}O3y+\frac{c1M\cos(-\pi+beta1M)\left(-\frac{1}{2}O3z+\frac{1}{4}\right)}{a1M},$$

$$-\frac{1}{2}O3z+\frac{1}{4}\Bigg]$$

$$layer\_1\_coordinates2M2_{20} := a\_unique\_TO\_b\_unique\ \&*\Bigg[$$

$$\frac{1}{2}O3x-\frac{7}{4}+\frac{1}{2}\frac{c1M\cos(-\pi+beta1M)\,(-O3z+1)}{a1M}-\frac{1}{4}\frac{c1M\cos(-\pi+beta1M)}{a1M}+\frac{3}{2}O3y,-\frac{1}{4}-\frac{1}{2}O3x$$

$$-\frac{1}{2}\frac{c1M\cos(-\pi+beta1M)\,(-O3z+1)}{a1M}+\frac{1}{4}\frac{c1M\cos(-\pi+beta1M)}{a1M}+\frac{1}{2}O3y+\frac{c1M\cos(-\pi+beta1M)\left(-\frac{1}{2}O3z+\frac{1}{4}\right)}{a1M},$$

$$-\frac{1}{2}O3z+\frac{1}{4}\Bigg]$$

$$layer\_1\_coordinates2M2_{21} := a\_unique\_TO\_b\_unique\ \&*\Bigg[$$

$$-\frac{1}{2}O3x+\frac{1}{2}\frac{c1M\cos(-\pi+beta1M)\,O3z}{a1M}-\frac{1}{4}\frac{c1M\cos(-\pi+beta1M)}{a1M}+\frac{3}{2}O3y-\frac{5}{4},$$

$$-\frac{3}{4}+\frac{1}{2}O3x-\frac{1}{2}\frac{c1M\cos(-\pi+beta1M)\,O3z}{a1M}+\frac{1}{4}\frac{c1M\cos(-\pi+beta1M)}{a1M}+\frac{1}{2}O3y+\frac{c1M\cos(-\pi+beta1M)\left(\frac{1}{2}O3z-\frac{1}{4}\right)}{a1M},$$

$$\frac{1}{2}O3z-\frac{1}{4}\Bigg]$$

$$layer\_1\_coordinates2M2_{22} := a\_unique\_TO\_b\_unique\ \&*\Bigg[$$

$$-\frac{1}{2}O3x-\frac{3}{4}+\frac{1}{2}\frac{c1M\cos(-\pi+beta1M)\,O3z}{a1M}-\frac{1}{4}\frac{c1M\cos(-\pi+beta1M)}{a1M}-\frac{3}{2}O3y,$$

$$-\frac{1}{4}+\frac{1}{2}O3x-\frac{1}{2}\frac{c1M\cos(-\pi+beta1M)\,O3z}{a1M}+\frac{1}{4}\frac{c1M\cos(-\pi+beta1M)}{a1M}-\frac{1}{2}O3y+\frac{c1M\cos(-\pi+beta1M)\left(\frac{1}{2}O3z-\frac{1}{4}\right)}{a1M},$$

$$\frac{1}{2}O3z-\frac{1}{4}\Bigg]$$

$$layer\_1\_coordinates2M2_{23} := a\_unique\_TO\_b\_unique\ \&*\Bigg[$$

$$-\frac{3}{4}+\frac{1}{2}O3x+\frac{1}{2}\frac{c1M\cos(-\pi+beta1M)\,(-O3z+1)}{a1M}-\frac{1}{4}\frac{c1M\cos(-\pi+beta1M)}{a1M}-\frac{3}{2}O3y,-\frac{1}{4}-\frac{1}{2}O3x$$

$$-\frac{1}{2}\frac{c1M\cos(-\pi+beta1M)\,(-O3z+1)}{a1M}+\frac{1}{4}\frac{c1M\cos(-\pi+beta1M)}{a1M}-\frac{1}{2}O3y+\frac{c1M\cos(-\pi+beta1M)\left(-\frac{1}{2}O3z+\frac{1}{4}\right)}{a1M},$$

$$-\frac{1}{2}O3z+\frac{1}{4}\Bigg]$$

$$layer\_1\_coordinates2M2_{24} := a\_unique\_TO\_b\_unique\ \&*\Bigg[$$

$$-\frac{3}{4}+\frac{1}{2}O3x+\frac{1}{2}\frac{c1M\cos(-\pi+beta1M)\,(-O3z+1)}{a1M}-\frac{1}{4}\frac{c1M\cos(-\pi+beta1M)}{a1M}+\frac{3}{2}O3y,-\frac{1}{4}-\frac{1}{2}O3x$$

$$-\frac{1}{2}\frac{c1M\cos(-\pi+beta1M)\,(-O3z+1)}{a1M}+\frac{1}{4}\frac{c1M\cos(-\pi+beta1M)}{a1M}+\frac{1}{2}O3y+\frac{c1M\cos(-\pi+beta1M)\left(-\frac{1}{2}O3z+\frac{1}{4}\right)}{a1M},$$

$$-\frac{1}{2}O3z+\frac{1}{4}\Bigg]$$

$$layer\_1\_coordinates2M2_{25} := a\_unique\_TO\_b\_unique\ \&*\Bigg[$$

$$-\frac{1}{2}O3x-\frac{3}{4}+\frac{1}{2}\frac{c1M\cos(-\pi+beta1M)\,O3z}{a1M}-\frac{1}{4}\frac{c1M\cos(-\pi+beta1M)}{a1M}+\frac{3}{2}O3y,$$

$$-\frac{1}{4}+\frac{1}{2}O3x-\frac{1}{2}\frac{c1M\cos(-\pi+beta1M)\,O3z}{a1M}+\frac{1}{4}\frac{c1M\cos(-\pi+beta1M)}{a1M}+\frac{1}{2}O3y+\frac{c1M\cos(-\pi+beta1M)\left(\frac{1}{2}O3z-\frac{1}{4}\right)}{a1M},$$

$$\frac{1}{2}O3z-\frac{1}{4}\Bigg]$$

$$layer\_1\_coordinates2M2_{26} := a\_unique\_TO\_b\_unique\ \&*\Bigg[$$

$$-\frac{1}{2}Tx+\frac{1}{2}\frac{c1M\cos(-\pi+beta1M)\,Tz}{a1M}-\frac{1}{4}\frac{c1M\cos(-\pi+beta1M)}{a1M}-\frac{3}{2}Ty+\frac{1}{4},$$

$$-\frac{1}{4}+\frac{1}{2}Tx-\frac{1}{2}\frac{c1M\cos(-\pi+beta1M)\,Tz}{a1M}+\frac{1}{4}\frac{c1M\cos(-\pi+beta1M)}{a1M}-\frac{1}{2}Ty+\frac{c1M\cos(-\pi+beta1M)\left(\frac{1}{2}Tz-\frac{1}{4}\right)}{a1M},\frac{1}{2}Tz-\frac{1}{4}\Bigg]$$

$$layer\_1\_coordinates2M2_{27} := a\_unique\_TO\_b\_unique\ \&*\Bigg[$$

$$\frac{1}{2}Tx-\frac{1}{4}+\frac{1}{2}\frac{c1M\cos(-\pi+beta1M)\,(-Tz+1)}{a1M}-\frac{1}{4}\frac{c1M\cos(-\pi+beta1M)}{a1M}-\frac{3}{2}Ty,$$

$$\frac{1}{4}-\frac{1}{2}Tx-\frac{1}{2}\frac{c1M\cos(-\pi+beta1M)\,(-Tz+1)}{a1M}+\frac{1}{4}\frac{c1M\cos(-\pi+beta1M)}{a1M}-\frac{1}{2}Ty+\frac{c1M\cos(-\pi+beta1M)\left(-\frac{1}{2}Tz+\frac{1}{4}\right)}{a1M},$$

$$-\frac{1}{2}Tz+\frac{1}{4}\Bigg]$$

$$layer\_1\_coordinates2M2_{28} := a\_unique\_TO\_b\_unique \;\&^{*}\left[\begin{array}{l} \frac{1}{2}Tx - \frac{7}{4} + \frac{1}{2}\frac{c1M\cos(-\pi + beta1M)\,(-Tz+1)}{a1M} - \frac{1}{4}\frac{c1M\cos(-\pi + beta1M)}{a1M} + \frac{3}{2}Ty, \\ -\frac{1}{4} - \frac{1}{2}Tx - \frac{1}{2}\frac{c1M\cos(-\pi + beta1M)\,(-Tz+1)}{a1M} + \frac{1}{4}\frac{c1M\cos(-\pi + beta1M)}{a1M} + \frac{1}{2}Ty + \frac{c1M\cos(-\pi + beta1M)\left(-\frac{1}{2}Tz + \frac{1}{4}\right)}{a1M}, \\ -\frac{1}{2}Tz + \frac{1}{4} \end{array}\right]$$

$$layer\_1\_coordinates2M2_{29} := a\_unique\_TO\_b\_unique \;\&^{*}\left[\begin{array}{l} -\frac{1}{2}Tx + \frac{1}{2}\frac{c1M\cos(-\pi + beta1M)\,Tz}{a1M} - \frac{1}{4}\frac{c1M\cos(-\pi + beta1M)}{a1M} + \frac{3}{2}Ty - \frac{5}{4}, \\ -\frac{3}{4} + \frac{1}{2}Tx - \frac{1}{2}\frac{c1M\cos(-\pi + beta1M)\,Tz}{a1M} + \frac{1}{4}\frac{c1M\cos(-\pi + beta1M)}{a1M} + \frac{1}{2}Ty + \frac{c1M\cos(-\pi + beta1M)\left(\frac{1}{2}Tz - \frac{1}{4}\right)}{a1M}, \frac{1}{2}Tz - \frac{1}{4} \end{array}\right]$$

$$layer\_1\_coordinates2M2_{30} := a\_unique\_TO\_b\_unique \;\&^{*}\left[\begin{array}{l} -\frac{1}{2}Tx - \frac{3}{4} + \frac{1}{2}\frac{c1M\cos(-\pi + beta1M)\,Tz}{a1M} - \frac{1}{4}\frac{c1M\cos(-\pi + beta1M)}{a1M} - \frac{3}{2}Ty, \\ -\frac{1}{4} + \frac{1}{2}Tx - \frac{1}{2}\frac{c1M\cos(-\pi + beta1M)\,Tz}{a1M} + \frac{1}{4}\frac{c1M\cos(-\pi + beta1M)}{a1M} - \frac{1}{2}Ty + \frac{c1M\cos(-\pi + beta1M)\left(\frac{1}{2}Tz - \frac{1}{4}\right)}{a1M}, \frac{1}{2}Tz - \frac{1}{4} \end{array}\right]$$

$$layer\_1\_coordinates2M2_{31} := a\_unique\_TO\_b\_unique \;\&^{*}\left[\begin{array}{l} -\frac{3}{4} + \frac{1}{2}Tx + \frac{1}{2}\frac{c1M\cos(-\pi + beta1M)\,(-Tz+1)}{a1M} - \frac{1}{4}\frac{c1M\cos(-\pi + beta1M)}{a1M} - \frac{3}{2}Ty, \\ -\frac{1}{4} - \frac{1}{2}Tx - \frac{1}{2}\frac{c1M\cos(-\pi + beta1M)\,(-Tz+1)}{a1M} + \frac{1}{4}\frac{c1M\cos(-\pi + beta1M)}{a1M} - \frac{1}{2}Ty + \frac{c1M\cos(-\pi + beta1M)\left(-\frac{1}{2}Tz + \frac{1}{4}\right)}{a1M}, \\ -\frac{1}{2}Tz + \frac{1}{4} \end{array}\right]$$

$$layer\_1\_coordinates2M2_{32} := a\_unique\_TO\_b\_unique \;\&^{*}\left[\begin{array}{l} -\frac{3}{4} + \frac{1}{2}Tx + \frac{1}{2}\frac{c1M\cos(-\pi + beta1M)\,(-Tz+1)}{a1M} - \frac{1}{4}\frac{c1M\cos(-\pi + beta1M)}{a1M} + \frac{3}{2}Ty, \\ -\frac{1}{4} - \frac{1}{2}Tx - \frac{1}{2}\frac{c1M\cos(-\pi + beta1M)\,(-Tz+1)}{a1M} + \frac{1}{4}\frac{c1M\cos(-\pi + beta1M)}{a1M} + \frac{1}{2}Ty + \frac{c1M\cos(-\pi + beta1M)\left(-\frac{1}{2}Tz + \frac{1}{4}\right)}{a1M}, \end{array}\right]$$

$$-\frac{1}{2}Tz+\frac{1}{4}\Bigg]$$

$$layer\_1\_coordinates2M2_{33} := a\_unique\_TO\_b\_unique\ \&*\Bigg[$$

$$-\frac{1}{2}Tx-\frac{3}{4}+\frac{1}{2}\frac{c1M\cos(-\pi+beta1M)\,Tz}{a1M}-\frac{1}{4}\frac{c1M\cos(-\pi+beta1M)}{a1M}+\frac{3}{2}Ty,$$

$$-\frac{1}{4}+\frac{1}{2}Tx-\frac{1}{2}\frac{c1M\cos(-\pi+beta1M)\,Tz}{a1M}+\frac{1}{4}\frac{c1M\cos(-\pi+beta1M)}{a1M}+\frac{1}{2}Ty+\frac{c1M\cos(-\pi+beta1M)\left(\frac{1}{2}Tz-\frac{1}{4}\right)}{a1M},\frac{1}{2}Tz-\frac{1}{4}\Bigg]$$

$$layer\_1\_coordinates2M2_{34} := a\_unique\_TO\_b\_unique\ \&*\Bigg[$$

$$-\frac{1}{2}O1x+\frac{1}{2}\frac{c1M\cos(-\pi+beta1M)\,O1z}{a1M}-\frac{1}{4}\frac{c1M\cos(-\pi+beta1M)}{a1M}+\frac{1}{4},$$

$$-\frac{1}{4}+\frac{1}{2}O1x-\frac{1}{2}\frac{c1M\cos(-\pi+beta1M)\,O1z}{a1M}+\frac{1}{4}\frac{c1M\cos(-\pi+beta1M)}{a1M}+\frac{c1M\cos(-\pi+beta1M)\left(\frac{1}{2}O1z-\frac{1}{4}\right)}{a1M},\frac{1}{2}O1z-\frac{1}{4}\Bigg]$$

$$layer\_1\_coordinates2M2_{35} := a\_unique\_TO\_b\_unique\ \&*\Bigg[$$

$$\frac{1}{2}O1x-\frac{1}{4}+\frac{1}{2}\frac{c1M\cos(-\pi+beta1M)\,(-O1z+1)}{a1M}-\frac{1}{4}\frac{c1M\cos(-\pi+beta1M)}{a1M},$$

$$\frac{1}{4}-\frac{1}{2}O1x-\frac{1}{2}\frac{c1M\cos(-\pi+beta1M)\,(-O1z+1)}{a1M}+\frac{1}{4}\frac{c1M\cos(-\pi+beta1M)}{a1M}+\frac{c1M\cos(-\pi+beta1M)\left(-\frac{1}{2}O1z+\frac{1}{4}\right)}{a1M},$$

$$-\frac{1}{2}O1z+\frac{1}{4}\Bigg]$$

$$layer\_1\_coordinates2M2_{36} := a\_unique\_TO\_b\_unique\ \&*\Bigg[$$

$$-\frac{3}{4}-\frac{1}{2}O1x+\frac{1}{2}\frac{c1M\cos(-\pi+beta1M)\,O1z}{a1M}-\frac{1}{4}\frac{c1M\cos(-\pi+beta1M)}{a1M},$$

$$-\frac{1}{4}+\frac{1}{2}O1x-\frac{1}{2}\frac{c1M\cos(-\pi+beta1M)\,O1z}{a1M}+\frac{1}{4}\frac{c1M\cos(-\pi+beta1M)}{a1M}+\frac{c1M\cos(-\pi+beta1M)\left(\frac{1}{2}O1z-\frac{1}{4}\right)}{a1M},\frac{1}{2}O1z-\frac{1}{4}\Bigg]$$

$$layer\_1\_coordinates2M2_{37} := a\_unique\_TO\_b\_unique\ \&*\Bigg[$$

$$\frac{1}{2}O1x-\frac{3}{4}+\frac{1}{2}\frac{c1M\cos(-\pi+beta1M)\,(-O1z+1)}{a1M}-\frac{1}{4}\frac{c1M\cos(-\pi+beta1M)}{a1M},$$

$$-\frac{1}{4}-\frac{1}{2}O1x-\frac{1}{2}\frac{c1M\cos(-\pi+beta1M)\,(-O1z+1)}{a1M}+\frac{1}{4}\frac{c1M\cos(-\pi+beta1M)}{a1M}+\frac{c1M\cos(-\pi+beta1M)\left(-\frac{1}{2}O1z+\frac{1}{4}\right)}{a1M},$$

$$-\frac{1}{2}\,O1z+\frac{1}{4}\Bigg]$$

$$layer\_1\_coordinates2M2_{38} := a\_unique\_TO\_b\_unique\ \&*\Bigg[$$

$$-\frac{1}{2}\,O2x+\frac{1}{2}\,\frac{c1M\cos(-\pi+beta1M)\,O2z}{a1M}-\frac{1}{4}\,\frac{c1M\cos(-\pi+beta1M)}{a1M}-\frac{3}{2}\,O2y+\frac{1}{4},$$

$$-\frac{1}{4}+\frac{1}{2}\,O2x-\frac{1}{2}\,\frac{c1M\cos(-\pi+beta1M)\,O2z}{a1M}+\frac{1}{4}\,\frac{c1M\cos(-\pi+beta1M)}{a1M}-\frac{1}{2}\,O2y+\frac{c1M\cos(-\pi+beta1M)\left(\frac{1}{2}\,O2z-\frac{1}{4}\right)}{a1M},$$

$$\frac{1}{2}\,O2z-\frac{1}{4}\Bigg]$$

$$layer\_1\_coordinates2M2_{39} := a\_unique\_TO\_b\_unique\ \&*\Bigg[$$

$$\frac{1}{2}\,O2x-\frac{1}{4}+\frac{1}{2}\,\frac{c1M\cos(-\pi+beta1M)\,(-O2z+1)}{a1M}-\frac{1}{4}\,\frac{c1M\cos(-\pi+beta1M)}{a1M}-\frac{3}{2}\,O2y,$$

$$\frac{1}{4}-\frac{1}{2}\,O2x-\frac{1}{2}\,\frac{c1M\cos(-\pi+beta1M)\,(-O2z+1)}{a1M}+\frac{1}{4}\,\frac{c1M\cos(-\pi+beta1M)}{a1M}-\frac{1}{2}\,O2y+\frac{c1M\cos(-\pi+beta1M)\left(-\frac{1}{2}\,O2z+\frac{1}{4}\right)}{a1M},$$

$$-\frac{1}{2}\,O2z+\frac{1}{4}\Bigg]$$

$$layer\_1\_coordinates2M2_{40} := a\_unique\_TO\_b\_unique\ \&*\Bigg[$$

$$\frac{1}{2}\,O2x-\frac{7}{4}+\frac{1}{2}\,\frac{c1M\cos(-\pi+beta1M)\,(-O2z+1)}{a1M}-\frac{1}{4}\,\frac{c1M\cos(-\pi+beta1M)}{a1M}+\frac{3}{2}\,O2y,-\frac{1}{4}-\frac{1}{2}\,O2x$$

$$-\frac{1}{2}\,\frac{c1M\cos(-\pi+beta1M)\,(-O2z+1)}{a1M}+\frac{1}{4}\,\frac{c1M\cos(-\pi+beta1M)}{a1M}+\frac{1}{2}\,O2y+\frac{c1M\cos(-\pi+beta1M)\left(-\frac{1}{2}\,O2z+\frac{1}{4}\right)}{a1M},$$

$$-\frac{1}{2}\,O2z+\frac{1}{4}\Bigg]$$

$$layer\_1\_coordinates2M2_{41} := a\_unique\_TO\_b\_unique\ \&*\Bigg[$$

$$-\frac{1}{2}\,O2x+\frac{1}{2}\,\frac{c1M\cos(-\pi+beta1M)\,O2z}{a1M}-\frac{1}{4}\,\frac{c1M\cos(-\pi+beta1M)}{a1M}+\frac{3}{2}\,O2y-\frac{5}{4},$$

$$-\frac{3}{4}+\frac{1}{2}\,O2x-\frac{1}{2}\,\frac{c1M\cos(-\pi+beta1M)\,O2z}{a1M}+\frac{1}{4}\,\frac{c1M\cos(-\pi+beta1M)}{a1M}+\frac{1}{2}\,O2y+\frac{c1M\cos(-\pi+beta1M)\left(\frac{1}{2}\,O2z-\frac{1}{4}\right)}{a1M},$$

$$\frac{1}{2}\,O2z-\frac{1}{4}\Bigg]$$

$$layer\_1\_coordinates2M2_{42} := a\_unique\_TO\_b\_unique \&* \left[-\frac{1}{2} O2x - \frac{3}{4} + \frac{1}{2}\frac{c1M\cos(-\pi + beta1M)\, O2z}{a1M} - \frac{1}{4}\frac{c1M\cos(-\pi + beta1M)}{a1M} - \frac{3}{2} O2y, -\frac{1}{4} + \frac{1}{2} O2x - \frac{1}{2}\frac{c1M\cos(-\pi + beta1M)\, O2z}{a1M} + \frac{1}{4}\frac{c1M\cos(-\pi + beta1M)}{a1M} - \frac{1}{2} O2y + \frac{c1M\cos(-\pi + beta1M)\left(\frac{1}{2} O2z - \frac{1}{4}\right)}{a1M}, \frac{1}{2} O2z - \frac{1}{4} \right]$$

$$layer\_1\_coordinates2M2_{43} := a\_unique\_TO\_b\_unique \&* \left[-\frac{3}{4} + \frac{1}{2} O2x + \frac{1}{2}\frac{c1M\cos(-\pi + beta1M)\,(-O2z + 1)}{a1M} - \frac{1}{4}\frac{c1M\cos(-\pi + beta1M)}{a1M} - \frac{3}{2} O2y, -\frac{1}{4} - \frac{1}{2} O2x - \frac{1}{2}\frac{c1M\cos(-\pi + beta1M)\,(-O2z + 1)}{a1M} + \frac{1}{4}\frac{c1M\cos(-\pi + beta1M)}{a1M} - \frac{1}{2} O2y + \frac{c1M\cos(-\pi + beta1M)\left(-\frac{1}{2} O2z + \frac{1}{4}\right)}{a1M}, -\frac{1}{2} O2z + \frac{1}{4} \right]$$

$$layer\_1\_coordinates2M2_{44} := a\_unique\_TO\_b\_unique \&* \left[-\frac{3}{4} + \frac{1}{2} O2x + \frac{1}{2}\frac{c1M\cos(-\pi + beta1M)\,(-O2z + 1)}{a1M} - \frac{1}{4}\frac{c1M\cos(-\pi + beta1M)}{a1M} + \frac{3}{2} O2y, -\frac{1}{4} - \frac{1}{2} O2x - \frac{1}{2}\frac{c1M\cos(-\pi + beta1M)\,(-O2z + 1)}{a1M} + \frac{1}{4}\frac{c1M\cos(-\pi + beta1M)}{a1M} + \frac{1}{2} O2y + \frac{c1M\cos(-\pi + beta1M)\left(-\frac{1}{2} O2z + \frac{1}{4}\right)}{a1M}, -\frac{1}{2} O2z + \frac{1}{4} \right]$$

$$layer\_1\_coordinates2M2_{45} := a\_unique\_TO\_b\_unique \&* \left[-\frac{1}{2} O2x - \frac{3}{4} + \frac{1}{2}\frac{c1M\cos(-\pi + beta1M)\, O2z}{a1M} - \frac{1}{4}\frac{c1M\cos(-\pi + beta1M)}{a1M} + \frac{3}{2} O2y, -\frac{1}{4} + \frac{1}{2} O2x - \frac{1}{2}\frac{c1M\cos(-\pi + beta1M)\, O2z}{a1M} + \frac{1}{4}\frac{c1M\cos(-\pi + beta1M)}{a1M} + \frac{1}{2} O2y + \frac{c1M\cos(-\pi + beta1M)\left(\frac{1}{2} O2z - \frac{1}{4}\right)}{a1M}, \frac{1}{2} O2z - \frac{1}{4} \right]$$

```
> for i from 1 to 45 do layer_2_coordinates[i]
  :=evalm(R[60]&*Zadjust&*layer[1][i]+[0,1/2-1/2*c1M/a1M*cos(pi-beta1M),1/2]+[1/4,-1/4,0])
  od:
> for i from 1 to 45 do layer_2_coordinates2M2[i] :=evalm(
  a_unique_TO_b_unique&*cprimeTo2M2a_unique&*layer_2_coordinates[i]) od;
```

$$layer\_2\_coordinates2M2_1 := a\_unique\_TO\_b\_unique \&* \left[\frac{1}{4}\frac{c1M\cos(-\pi + beta1M)}{a1M} - \frac{1}{2}, \frac{1}{2}, \frac{1}{4}\right]$$

$$layer\_2\_coordinates2M2_2 := a\_unique\_TO\_b\_unique \&* \left[\frac{1}{4}\frac{c1M\cos(-\pi + beta1M)}{a1M}, 0, \frac{1}{4}\right]$$

$$layer\_2\_coordinates2M2_3 := a\_unique\_TO\_b\_unique \&* \left[\frac{1}{2} - \frac{1}{4}\frac{c1M\cos(-\pi + beta1M)}{a1M}, \frac{1}{2}, \frac{3}{4}\right]$$

$$layer\_2\_coordinates2M2_4 := a\_unique\_TO\_b\_unique \&* \left[\frac{1}{4}\frac{c1M\cos(-\pi + beta1M)}{a1M} + \frac{1}{2}, \frac{1}{2}, \frac{1}{4}\right]$$

$$layer\_2\_coordinates2M2_5 := a\_unique\_TO\_b\_unique \&* \left[\frac{1}{4}, \frac{1}{4}, \frac{1}{2}\right]$$

$$layer\_2\_coordinates2M2_6 := a\_unique\_TO\_b\_unique \&* \left[\frac{-1}{4}, \frac{3}{4}, \frac{1}{2}\right]$$

$$layer\_2\_coordinates2M2_7 := a\_unique\_TO\_b\_unique \&* \left[\frac{1}{4}, \frac{5}{4}, \frac{1}{2}\right]$$

$$layer\_2\_coordinates2M2_8 := a\_unique\_TO\_b\_unique \&* \left[-\frac{3}{2}M2y + \frac{1}{4}, \frac{1}{4} + \frac{1}{2}M2y, \frac{1}{2}\right]$$

$$layer\_2\_coordinates2M2_9 := a\_unique\_TO\_b\_unique \&* \left[\frac{3}{2}M2y + \frac{1}{4}, \frac{1}{4} - \frac{1}{2}M2y, \frac{1}{2}\right]$$

$$layer\_2\_coordinates2M2_{10} := a\_unique\_TO\_b\_unique \&* \left[-\frac{1}{4} - \frac{3}{2}M2y, \frac{3}{4} + \frac{1}{2}M2y, \frac{1}{2}\right]$$

$$layer\_2\_coordinates2M2_{11} := a\_unique\_TO\_b\_unique \&* \left[-\frac{1}{4} + \frac{3}{2}M2y, \frac{3}{4} - \frac{1}{2}M2y, \frac{1}{2}\right]$$

$$layer\_2\_coordinates2M2_{12} := a\_unique\_TO\_b\_unique \&* \left[-\frac{3}{2}M2y + \frac{1}{4}, \frac{1}{4} + \frac{1}{2}M2y, \frac{1}{2}\right]$$

$$layer\_2\_coordinates2M2_{13} := a\_unique\_TO\_b\_unique \&* \left[\frac{3}{2}M2y - \frac{5}{4}, \frac{3}{4} - \frac{1}{2}M2y, \frac{1}{2}\right]$$

$$layer\_2\_coordinates2M2_{14} := a\_unique\_TO\_b\_unique \&* \left[\begin{array}{l} \frac{1}{2}O4x - \frac{1}{2}\frac{c1M\cos(-\pi + beta1M)\,O4z}{a1M} + \frac{1}{4}\frac{c1M\cos(-\pi + beta1M)}{a1M} - \frac{1}{2}, \\ \frac{1}{2} + \frac{1}{2}O4x - \frac{1}{2}\frac{c1M\cos(-\pi + beta1M)\,O4z}{a1M} - \frac{1}{4}\frac{c1M\cos(-\pi + beta1M)}{a1M} + \frac{c1M\cos(-\pi + beta1M)\left(\frac{1}{2}O4z + \frac{1}{4}\right)}{a1M}, \frac{1}{2}O4z + \frac{1}{4} \end{array}\right]$$

$$layer\_2\_coordinates2M2_{15} := a\_unique\_TO\_b\_unique \&* \left[\begin{array}{l} -\frac{1}{2}O4x - \frac{1}{2}\frac{c1M\cos(-\pi + beta1M)\,(-O4z + 1)}{a1M} + \frac{1}{4}\frac{c1M\cos(-\pi + beta1M)}{a1M}, \\ 1 - \frac{1}{2}O4x - \frac{1}{2}\frac{c1M\cos(-\pi + beta1M)\,(-O4z + 1)}{a1M} - \frac{1}{4}\frac{c1M\cos(-\pi + beta1M)}{a1M} + \frac{c1M\cos(-\pi + beta1M)\left(-\frac{1}{2}O4z + \frac{3}{4}\right)}{a1M}, \\ -\frac{1}{2}O4z + \frac{3}{4} \end{array}\right]$$

$$layer\_2\_coordinates2M2_{16} := a\_unique\_TO\_b\_unique \&* \left[\right.$$

$$\frac{1}{2}\,O4x-\frac{1}{2}\,\frac{c1M\cos(-\pi+beta1M)\,O4z}{a1M}+\frac{1}{4}\,\frac{c1M\cos(-\pi+beta1M)}{a1M}+\frac{1}{2},$$

$$\frac{1}{2}+\frac{1}{2}\,O4x-\frac{1}{2}\,\frac{c1M\cos(-\pi+beta1M)\,O4z}{a1M}-\frac{1}{4}\,\frac{c1M\cos(-\pi+beta1M)}{a1M}+\frac{c1M\cos(-\pi+beta1M)\left(\frac{1}{2}\,O4z+\frac{1}{4}\right)}{a1M},\frac{1}{2}\,O4z+\frac{1}{4}\Bigg]$$

$$layer\_2\_coordinates2M2_{17}:=a\_unique\_TO\_b\_unique\ \&*\Bigg[$$

$$-\frac{1}{2}\,O4x+\frac{1}{2}-\frac{1}{2}\,\frac{c1M\cos(-\pi+beta1M)\,(-O4z+1)}{a1M}+\frac{1}{4}\,\frac{c1M\cos(-\pi+beta1M)}{a1M},$$

$$\frac{1}{2}-\frac{1}{2}\,O4x-\frac{1}{2}\,\frac{c1M\cos(-\pi+beta1M)\,(-O4z+1)}{a1M}-\frac{1}{4}\,\frac{c1M\cos(-\pi+beta1M)}{a1M}+\frac{c1M\cos(-\pi+beta1M)\left(-\frac{1}{2}\,O4z+\frac{3}{4}\right)}{a1M},$$

$$-\frac{1}{2}\,O4z+\frac{3}{4}\Bigg]$$

$$layer\_2\_coordinates2M2_{18}:=a\_unique\_TO\_b\_unique\ \&*\Bigg[$$

$$\frac{1}{2}\,O3x-\frac{1}{2}\,\frac{c1M\cos(-\pi+beta1M)\,O3z}{a1M}+\frac{1}{4}\,\frac{c1M\cos(-\pi+beta1M)}{a1M}-\frac{3}{2}\,O3y+\frac{1}{4},$$

$$\frac{1}{4}+\frac{1}{2}\,O3x-\frac{1}{2}\,\frac{c1M\cos(-\pi+beta1M)\,O3z}{a1M}-\frac{1}{4}\,\frac{c1M\cos(-\pi+beta1M)}{a1M}+\frac{1}{2}\,O3y+\frac{c1M\cos(-\pi+beta1M)\left(\frac{1}{2}\,O3z+\frac{1}{4}\right)}{a1M},$$

$$\frac{1}{2}\,O3z+\frac{1}{4}\Bigg]$$

$$layer\_2\_coordinates2M2_{19}:=a\_unique\_TO\_b\_unique\ \&*\Bigg[$$

$$-\frac{1}{2}\,O3x+\frac{3}{4}-\frac{1}{2}\,\frac{c1M\cos(-\pi+beta1M)\,(-O3z+1)}{a1M}+\frac{1}{4}\,\frac{c1M\cos(-\pi+beta1M)}{a1M}-\frac{3}{2}\,O3y,$$

$$\frac{3}{4}-\frac{1}{2}\,O3x-\frac{1}{2}\,\frac{c1M\cos(-\pi+beta1M)\,(-O3z+1)}{a1M}-\frac{1}{4}\,\frac{c1M\cos(-\pi+beta1M)}{a1M}+\frac{1}{2}\,O3y+\frac{c1M\cos(-\pi+beta1M)\left(-\frac{1}{2}\,O3z+\frac{3}{4}\right)}{a1M},$$

$$-\frac{1}{2}\,O3z+\frac{3}{4}\Bigg]$$

$$layer\_2\_coordinates2M2_{20}:=a\_unique\_TO\_b\_unique\ \&*\Bigg[$$

$$-\frac{1}{2}\,O3x-\frac{3}{4}-\frac{1}{2}\,\frac{c1M\cos(-\pi+beta1M)\,(-O3z+1)}{a1M}+\frac{1}{4}\,\frac{c1M\cos(-\pi+beta1M)}{a1M}+\frac{3}{2}\,O3y,$$

$$\frac{5}{4}-\frac{1}{2}\,O3x-\frac{1}{2}\,\frac{c1M\cos(-\pi+beta1M)\,(-O3z+1)}{a1M}-\frac{1}{4}\,\frac{c1M\cos(-\pi+beta1M)}{a1M}-\frac{1}{2}\,O3y+\frac{c1M\cos(-\pi+beta1M)\left(-\frac{1}{2}\,O3z+\frac{3}{4}\right)}{a1M},$$

$$-\frac{1}{2}O3z+\frac{3}{4}\Bigg]$$

$$layer\_2\_coordinates2M2_{21} := a\_unique\_TO\_b\_unique \&* \Bigg[$$

$$\frac{1}{2}O3x-\frac{1}{2}\frac{c1M\cos(-\pi+beta1M)\,O3z}{a1M}+\frac{1}{4}\frac{c1M\cos(-\pi+beta1M)}{a1M}+\frac{3}{2}O3y-\frac{5}{4},$$

$$\frac{3}{4}+\frac{1}{2}O3x-\frac{1}{2}\frac{c1M\cos(-\pi+beta1M)\,O3z}{a1M}-\frac{1}{4}\frac{c1M\cos(-\pi+beta1M)}{a1M}-\frac{1}{2}O3y+\frac{c1M\cos(-\pi+beta1M)\left(\frac{1}{2}O3z+\frac{1}{4}\right)}{a1M},$$

$$\frac{1}{2}O3z+\frac{1}{4}\Bigg]$$

$$layer\_2\_coordinates2M2_{22} := a\_unique\_TO\_b\_unique \&* \Bigg[$$

$$\frac{1}{2}O3x-\frac{1}{4}-\frac{1}{2}\frac{c1M\cos(-\pi+beta1M)\,O3z}{a1M}+\frac{1}{4}\frac{c1M\cos(-\pi+beta1M)}{a1M}-\frac{3}{2}O3y,$$

$$\frac{3}{4}+\frac{1}{2}O3x-\frac{1}{2}\frac{c1M\cos(-\pi+beta1M)\,O3z}{a1M}-\frac{1}{4}\frac{c1M\cos(-\pi+beta1M)}{a1M}+\frac{1}{2}O3y+\frac{c1M\cos(-\pi+beta1M)\left(\frac{1}{2}O3z+\frac{1}{4}\right)}{a1M},$$

$$\frac{1}{2}O3z+\frac{1}{4}\Bigg]$$

$$layer\_2\_coordinates2M2_{23} := a\_unique\_TO\_b\_unique \&* \Bigg[$$

$$-\frac{1}{4}-\frac{1}{2}O3x-\frac{1}{2}\frac{c1M\cos(-\pi+beta1M)\,(-O3z+1)}{a1M}+\frac{1}{4}\frac{c1M\cos(-\pi+beta1M)}{a1M}-\frac{3}{2}O3y,$$

$$\frac{3}{4}-\frac{1}{2}O3x-\frac{1}{2}\frac{c1M\cos(-\pi+beta1M)\,(-O3z+1)}{a1M}-\frac{1}{4}\frac{c1M\cos(-\pi+beta1M)}{a1M}+\frac{1}{2}O3y+\frac{c1M\cos(-\pi+beta1M)\left(-\frac{1}{2}O3z+\frac{3}{4}\right)}{a1M},$$

$$-\frac{1}{2}O3z+\frac{3}{4}\Bigg]$$

$$layer\_2\_coordinates2M2_{24} := a\_unique\_TO\_b\_unique \&* \Bigg[$$

$$-\frac{1}{4}-\frac{1}{2}O3x-\frac{1}{2}\frac{c1M\cos(-\pi+beta1M)\,(-O3z+1)}{a1M}+\frac{1}{4}\frac{c1M\cos(-\pi+beta1M)}{a1M}+\frac{3}{2}O3y,$$

$$\frac{3}{4}-\frac{1}{2}O3x-\frac{1}{2}\frac{c1M\cos(-\pi+beta1M)\,(-O3z+1)}{a1M}-\frac{1}{4}\frac{c1M\cos(-\pi+beta1M)}{a1M}-\frac{1}{2}O3y+\frac{c1M\cos(-\pi+beta1M)\left(-\frac{1}{2}O3z+\frac{3}{4}\right)}{a1M},$$

$$-\frac{1}{2}O3z+\frac{3}{4}\Bigg]$$

$$layer\_2\_coordinates2M2_{25} := a\_unique\_TO\_b\_unique \&* \left[\begin{array}{l} \frac{1}{2} O3x - \frac{1}{4} - \frac{1}{2} \frac{c1M \cos(-\pi + beta1M)\, O3z}{a1M} + \frac{1}{4} \frac{c1M \cos(-\pi + beta1M)}{a1M} + \frac{3}{2} O3y, \\ \frac{3}{4} + \frac{1}{2} O3x - \frac{1}{2} \frac{c1M \cos(-\pi + beta1M)\, O3z}{a1M} - \frac{1}{4} \frac{c1M \cos(-\pi + beta1M)}{a1M} - \frac{1}{2} O3y + \frac{c1M \cos(-\pi + beta1M) \left(\frac{1}{2} O3z + \frac{1}{4} \right)}{a1M}, \\ \frac{1}{2} O3z + \frac{1}{4} \end{array} \right]$$

$$layer\_2\_coordinates2M2_{26} := a\_unique\_TO\_b\_unique \&* \left[\begin{array}{l} \frac{1}{2} Tx - \frac{1}{2} \frac{c1M \cos(-\pi + beta1M)\, Tz}{a1M} + \frac{1}{4} \frac{c1M \cos(-\pi + beta1M)}{a1M} - \frac{3}{2} Ty + \frac{1}{4}, \\ \frac{1}{4} + \frac{1}{2} Tx - \frac{1}{2} \frac{c1M \cos(-\pi + beta1M)\, Tz}{a1M} - \frac{1}{4} \frac{c1M \cos(-\pi + beta1M)}{a1M} + \frac{1}{2} Ty + \frac{c1M \cos(-\pi + beta1M) \left(\frac{1}{2} Tz + \frac{1}{4} \right)}{a1M}, \frac{1}{2} Tz + \frac{1}{4} \end{array} \right]$$

$$layer\_2\_coordinates2M2_{27} := a\_unique\_TO\_b\_unique \&* \left[\begin{array}{l} -\frac{1}{2} Tx + \frac{3}{4} - \frac{1}{2} \frac{c1M \cos(-\pi + beta1M)\, (-Tz + 1)}{a1M} + \frac{1}{4} \frac{c1M \cos(-\pi + beta1M)}{a1M} - \frac{3}{2} Ty, \\ \frac{3}{4} - \frac{1}{2} Tx - \frac{1}{2} \frac{c1M \cos(-\pi + beta1M)\, (-Tz + 1)}{a1M} - \frac{1}{4} \frac{c1M \cos(-\pi + beta1M)}{a1M} + \frac{1}{2} Ty + \frac{c1M \cos(-\pi + beta1M) \left(-\frac{1}{2} Tz + \frac{3}{4} \right)}{a1M}, \\ -\frac{1}{2} Tz + \frac{3}{4} \end{array} \right]$$

$$layer\_2\_coordinates2M2_{28} := a\_unique\_TO\_b\_unique \&* \left[\begin{array}{l} -\frac{1}{2} Tx - \frac{3}{4} - \frac{1}{2} \frac{c1M \cos(-\pi + beta1M)\, (-Tz + 1)}{a1M} + \frac{1}{4} \frac{c1M \cos(-\pi + beta1M)}{a1M} + \frac{3}{2} Ty, \\ \frac{5}{4} - \frac{1}{2} Tx - \frac{1}{2} \frac{c1M \cos(-\pi + beta1M)\, (-Tz + 1)}{a1M} - \frac{1}{4} \frac{c1M \cos(-\pi + beta1M)}{a1M} - \frac{1}{2} Ty + \frac{c1M \cos(-\pi + beta1M) \left(-\frac{1}{2} Tz + \frac{3}{4} \right)}{a1M}, \\ -\frac{1}{2} Tz + \frac{3}{4} \end{array} \right]$$

$$layer\_2\_coordinates2M2_{29} := a\_unique\_TO\_b\_unique \&* \left[\begin{array}{l} \frac{1}{2} Tx - \frac{1}{2} \frac{c1M \cos(-\pi + beta1M)\, Tz}{a1M} + \frac{1}{4} \frac{c1M \cos(-\pi + beta1M)}{a1M} + \frac{3}{2} Ty - \frac{5}{4}, \end{array} \right.$$

$$\frac{3}{4}+\frac{1}{2}Tx-\frac{1}{2}\frac{c1M\cos(-\pi+beta1M)\,Tz}{a1M}-\frac{1}{4}\frac{c1M\cos(-\pi+beta1M)}{a1M}-\frac{1}{2}Ty+\frac{c1M\cos(-\pi+beta1M)\left(\frac{1}{2}Tz+\frac{1}{4}\right)}{a1M},\frac{1}{2}Tz+\frac{1}{4}\Bigg]$$

$$layer\_2\_coordinates2M2_{30} := a\_unique\_TO\_b\_unique\ \&*\Bigg[$$

$$\frac{1}{2}Tx-\frac{1}{4}-\frac{1}{2}\frac{c1M\cos(-\pi+beta1M)\,Tz}{a1M}+\frac{1}{4}\frac{c1M\cos(-\pi+beta1M)}{a1M}-\frac{3}{2}Ty,$$

$$\frac{3}{4}+\frac{1}{2}Tx-\frac{1}{2}\frac{c1M\cos(-\pi+beta1M)\,Tz}{a1M}-\frac{1}{4}\frac{c1M\cos(-\pi+beta1M)}{a1M}+\frac{1}{2}Ty+\frac{c1M\cos(-\pi+beta1M)\left(\frac{1}{2}Tz+\frac{1}{4}\right)}{a1M},\frac{1}{2}Tz+\frac{1}{4}\Bigg]$$

$$layer\_2\_coordinates2M2_{31} := a\_unique\_TO\_b\_unique\ \&*\Bigg[$$

$$-\frac{1}{4}-\frac{1}{2}Tx-\frac{1}{2}\frac{c1M\cos(-\pi+beta1M)\,(-Tz+1)}{a1M}+\frac{1}{4}\frac{c1M\cos(-\pi+beta1M)}{a1M}-\frac{3}{2}Ty,$$

$$\frac{3}{4}-\frac{1}{2}Tx-\frac{1}{2}\frac{c1M\cos(-\pi+beta1M)\,(-Tz+1)}{a1M}-\frac{1}{4}\frac{c1M\cos(-\pi+beta1M)}{a1M}+\frac{1}{2}Ty+\frac{c1M\cos(-\pi+beta1M)\left(-\frac{1}{2}Tz+\frac{3}{4}\right)}{a1M},$$

$$-\frac{1}{2}Tz+\frac{3}{4}\Bigg]$$

$$layer\_2\_coordinates2M2_{32} := a\_unique\_TO\_b\_unique\ \&*\Bigg[$$

$$-\frac{1}{4}-\frac{1}{2}Tx-\frac{1}{2}\frac{c1M\cos(-\pi+beta1M)\,(-Tz+1)}{a1M}+\frac{1}{4}\frac{c1M\cos(-\pi+beta1M)}{a1M}+\frac{3}{2}Ty,$$

$$\frac{3}{4}-\frac{1}{2}Tx-\frac{1}{2}\frac{c1M\cos(-\pi+beta1M)\,(-Tz+1)}{a1M}-\frac{1}{4}\frac{c1M\cos(-\pi+beta1M)}{a1M}-\frac{1}{2}Ty+\frac{c1M\cos(-\pi+beta1M)\left(-\frac{1}{2}Tz+\frac{3}{4}\right)}{a1M},$$

$$-\frac{1}{2}Tz+\frac{3}{4}\Bigg]$$

$$layer\_2\_coordinates2M2_{33} := a\_unique\_TO\_b\_unique\ \&*\Bigg[$$

$$\frac{1}{2}Tx-\frac{1}{4}-\frac{1}{2}\frac{c1M\cos(-\pi+beta1M)\,Tz}{a1M}+\frac{1}{4}\frac{c1M\cos(-\pi+beta1M)}{a1M}+\frac{3}{2}Ty,$$

$$\frac{3}{4}+\frac{1}{2}Tx-\frac{1}{2}\frac{c1M\cos(-\pi+beta1M)\,Tz}{a1M}-\frac{1}{4}\frac{c1M\cos(-\pi+beta1M)}{a1M}-\frac{1}{2}Ty+\frac{c1M\cos(-\pi+beta1M)\left(\frac{1}{2}Tz+\frac{1}{4}\right)}{a1M},\frac{1}{2}Tz+\frac{1}{4}\Bigg]$$

$$layer\_2\_coordinates2M2_{34} := a\_unique\_TO\_b\_unique\ \&*\Bigg[$$

$$\frac{1}{2}O1x-\frac{1}{2}\frac{c1M\cos(-\pi+beta1M)\,O1z}{a1M}+\frac{1}{4}\frac{c1M\cos(-\pi+beta1M)}{a1M}+\frac{1}{4},$$

$$\frac{1}{4}+\frac{1}{2}\,O1x-\frac{1}{2}\,\frac{c1M\cos(-\pi+beta1M)\,O1z}{a1M}-\frac{1}{4}\,\frac{c1M\cos(-\pi+beta1M)}{a1M}+\frac{c1M\cos(-\pi+beta1M)\left(\frac{1}{2}\,O1z+\frac{1}{4}\right)}{a1M},\ \frac{1}{2}\,O1z+\frac{1}{4}\Bigg]$$

$$layer\_2\_coordinates2M2_{35} := a\_unique\_TO\_b\_unique\ \&*\Bigg[$$

$$-\frac{1}{2}\,O1x+\frac{3}{4}-\frac{1}{2}\,\frac{c1M\cos(-\pi+beta1M)\,(-O1z+1)}{a1M}+\frac{1}{4}\,\frac{c1M\cos(-\pi+beta1M)}{a1M},$$

$$\frac{3}{4}-\frac{1}{2}\,O1x-\frac{1}{2}\,\frac{c1M\cos(-\pi+beta1M)\,(-O1z+1)}{a1M}-\frac{1}{4}\,\frac{c1M\cos(-\pi+beta1M)}{a1M}+\frac{c1M\cos(-\pi+beta1M)\left(-\frac{1}{2}\,O1z+\frac{3}{4}\right)}{a1M},$$

$$-\frac{1}{2}\,O1z+\frac{3}{4}\Bigg]$$

$$layer\_2\_coordinates2M2_{36} := a\_unique\_TO\_b\_unique\ \&*\Bigg[$$

$$\frac{1}{2}\,O1x-\frac{1}{2}\,\frac{c1M\cos(-\pi+beta1M)\,O1z}{a1M}+\frac{1}{4}\,\frac{c1M\cos(-\pi+beta1M)}{a1M}-\frac{1}{4},$$

$$\frac{3}{4}+\frac{1}{2}\,O1x-\frac{1}{2}\,\frac{c1M\cos(-\pi+beta1M)\,O1z}{a1M}-\frac{1}{4}\,\frac{c1M\cos(-\pi+beta1M)}{a1M}+\frac{c1M\cos(-\pi+beta1M)\left(\frac{1}{2}\,O1z+\frac{1}{4}\right)}{a1M},\ \frac{1}{2}\,O1z+\frac{1}{4}\Bigg]$$

$$layer\_2\_coordinates2M2_{37} := a\_unique\_TO\_b\_unique\ \&*\Bigg[$$

$$-\frac{1}{2}\,O1x-\frac{1}{2}\,\frac{c1M\cos(-\pi+beta1M)\,(-O1z+1)}{a1M}+\frac{1}{4}\,\frac{c1M\cos(-\pi+beta1M)}{a1M}-\frac{1}{4},$$

$$\frac{3}{4}-\frac{1}{2}\,O1x-\frac{1}{2}\,\frac{c1M\cos(-\pi+beta1M)\,(-O1z+1)}{a1M}-\frac{1}{4}\,\frac{c1M\cos(-\pi+beta1M)}{a1M}+\frac{c1M\cos(-\pi+beta1M)\left(-\frac{1}{2}\,O1z+\frac{3}{4}\right)}{a1M},$$

$$-\frac{1}{2}\,O1z+\frac{3}{4}\Bigg]$$

$$layer\_2\_coordinates2M2_{38} := a\_unique\_TO\_b\_unique\ \&*\Bigg[$$

$$\frac{1}{2}\,O2x-\frac{1}{2}\,\frac{c1M\cos(-\pi+beta1M)\,O2z}{a1M}+\frac{1}{4}\,\frac{c1M\cos(-\pi+beta1M)}{a1M}-\frac{3}{2}\,O2y+\frac{1}{4},$$

$$\frac{1}{4}+\frac{1}{2}\,O2x-\frac{1}{2}\,\frac{c1M\cos(-\pi+beta1M)\,O2z}{a1M}-\frac{1}{4}\,\frac{c1M\cos(-\pi+beta1M)}{a1M}+\frac{1}{2}\,O2y+\frac{c1M\cos(-\pi+beta1M)\left(\frac{1}{2}\,O2z+\frac{1}{4}\right)}{a1M},$$

$$\frac{1}{2}\,O2z+\frac{1}{4}\Bigg]$$

$$layer\_2\_coordinates2M2_{39} := a\_unique\_TO\_b\_unique\ \&*\Bigg[$$

$$-\frac{1}{2}O2x+\frac{3}{4}-\frac{1}{2}\frac{c1M\cos(-\pi+beta1M)\,(-O2z+1)}{a1M}+\frac{1}{4}\frac{c1M\cos(-\pi+beta1M)}{a1M}-\frac{3}{2}O2y,$$

$$\frac{3}{4}-\frac{1}{2}O2x-\frac{1}{2}\frac{c1M\cos(-\pi+beta1M)\,(-O2z+1)}{a1M}-\frac{1}{4}\frac{c1M\cos(-\pi+beta1M)}{a1M}+\frac{1}{2}O2y+\frac{c1M\cos(-\pi+beta1M)\left(-\frac{1}{2}O2z+\frac{3}{4}\right)}{a1M},$$

$$-\frac{1}{2}O2z+\frac{3}{4}\Bigg]$$

$$layer\_2\_coordinates2M2_{40} := a\_unique\_TO\_b\_unique\ \&*\Bigg[$$

$$-\frac{1}{2}O2x-\frac{3}{4}-\frac{1}{2}\frac{c1M\cos(-\pi+beta1M)\,(-O2z+1)}{a1M}+\frac{1}{4}\frac{c1M\cos(-\pi+beta1M)}{a1M}+\frac{3}{2}O2y,$$

$$\frac{5}{4}-\frac{1}{2}O2x-\frac{1}{2}\frac{c1M\cos(-\pi+beta1M)\,(-O2z+1)}{a1M}-\frac{1}{4}\frac{c1M\cos(-\pi+beta1M)}{a1M}-\frac{1}{2}O2y+\frac{c1M\cos(-\pi+beta1M)\left(-\frac{1}{2}O2z+\frac{3}{4}\right)}{a1M},$$

$$-\frac{1}{2}O2z+\frac{3}{4}\Bigg]$$

$$layer\_2\_coordinates2M2_{41} := a\_unique\_TO\_b\_unique\ \&*\Bigg[$$

$$\frac{1}{2}O2x-\frac{1}{2}\frac{c1M\cos(-\pi+beta1M)\,O2z}{a1M}+\frac{1}{4}\frac{c1M\cos(-\pi+beta1M)}{a1M}+\frac{3}{2}O2y-\frac{5}{4},$$

$$\frac{3}{4}+\frac{1}{2}O2x-\frac{1}{2}\frac{c1M\cos(-\pi+beta1M)\,O2z}{a1M}-\frac{1}{4}\frac{c1M\cos(-\pi+beta1M)}{a1M}-\frac{1}{2}O2y+\frac{c1M\cos(-\pi+beta1M)\left(\frac{1}{2}O2z+\frac{1}{4}\right)}{a1M},$$

$$\frac{1}{2}O2z+\frac{1}{4}\Bigg]$$

$$layer\_2\_coordinates2M2_{42} := a\_unique\_TO\_b\_unique\ \&*\Bigg[$$

$$\frac{1}{2}O2x-\frac{1}{4}-\frac{1}{2}\frac{c1M\cos(-\pi+beta1M)\,O2z}{a1M}+\frac{1}{4}\frac{c1M\cos(-\pi+beta1M)}{a1M}-\frac{3}{2}O2y,$$

$$\frac{3}{4}+\frac{1}{2}O2x-\frac{1}{2}\frac{c1M\cos(-\pi+beta1M)\,O2z}{a1M}-\frac{1}{4}\frac{c1M\cos(-\pi+beta1M)}{a1M}+\frac{1}{2}O2y+\frac{c1M\cos(-\pi+beta1M)\left(\frac{1}{2}O2z+\frac{1}{4}\right)}{a1M},$$

$$\frac{1}{2}O2z+\frac{1}{4}\Bigg]$$

$$layer\_2\_coordinates2M2_{43} := a\_unique\_TO\_b\_unique\ \&*\Bigg[$$

$$-\frac{1}{4}-\frac{1}{2}O2x-\frac{1}{2}\frac{c1M\cos(-\pi+beta1M)\,(-O2z+1)}{a1M}+\frac{1}{4}\frac{c1M\cos(-\pi+beta1M)}{a1M}-\frac{3}{2}O2y,$$

$$\frac{3}{4}-\frac{1}{2}\,O2x-\frac{1}{2}\,\frac{c1M\cos(-\pi+beta1M)\,(-O2z+1)}{a1M}-\frac{1}{4}\,\frac{c1M\cos(-\pi+beta1M)}{a1M}+\frac{1}{2}\,O2y+\frac{c1M\cos(-\pi+beta1M)\left(-\frac{1}{2}\,O2z+\frac{3}{4}\right)}{a1M},$$

$$-\frac{1}{2}\,O2z+\frac{3}{4}\Bigg]$$

$$layer\_2\_coordinates2M2_{44} := a\_unique\_TO\_b\_unique\ \&*\Bigg[$$

$$-\frac{1}{4}-\frac{1}{2}\,O2x-\frac{1}{2}\,\frac{c1M\cos(-\pi+beta1M)\,(-O2z+1)}{a1M}+\frac{1}{4}\,\frac{c1M\cos(-\pi+beta1M)}{a1M}+\frac{3}{2}\,O2y,$$

$$\frac{3}{4}-\frac{1}{2}\,O2x-\frac{1}{2}\,\frac{c1M\cos(-\pi+beta1M)\,(-O2z+1)}{a1M}-\frac{1}{4}\,\frac{c1M\cos(-\pi+beta1M)}{a1M}-\frac{1}{2}\,O2y+\frac{c1M\cos(-\pi+beta1M)\left(-\frac{1}{2}\,O2z+\frac{3}{4}\right)}{a1M},$$

$$-\frac{1}{2}\,O2z+\frac{3}{4}\Bigg]$$

$$layer\_2\_coordinates2M2_{45} := a\_unique\_TO\_b\_unique\ \&*\Bigg[$$

$$\frac{1}{2}\,O2x-\frac{1}{4}-\frac{1}{2}\,\frac{c1M\cos(-\pi+beta1M)\,O2z}{a1M}+\frac{1}{4}\,\frac{c1M\cos(-\pi+beta1M)}{a1M}+\frac{3}{2}\,O2y,$$

$$\frac{3}{4}+\frac{1}{2}\,O2x-\frac{1}{2}\,\frac{c1M\cos(-\pi+beta1M)\,O2z}{a1M}-\frac{1}{4}\,\frac{c1M\cos(-\pi+beta1M)}{a1M}-\frac{1}{2}\,O2y+\frac{c1M\cos(-\pi+beta1M)\left(\frac{1}{2}\,O2z+\frac{1}{4}\right)}{a1M},$$

$$\frac{1}{2}\,O2z+\frac{1}{4}\Bigg]$$

>

Stacking polytype 2O derivation

Let us first write the fractional atomic coordinates in the *Standard C2/m* 1-layer unit-cell.

The interlayer cations (K) are at the following positions within the C 1 2/*m* 1 space group (sg No. 12):

Multplicity, Wyckoff letter, Site symmetry (1/2,1/2,0)+

2 *b* 2/*m* (0,1/2,0)

```
> with(linalg): K[1] := [0,1/2,0]; K[2]:= [1/2,0,0];
Warning, new definition for norm
Warning, new definition for trace
```

$$K_1 := \left[0, \frac{1}{2}, 0\right]$$

$$K_2 := \left[\frac{1}{2}, 0, 0\right]$$

The M1 cations are at the following positions within the *C* 1 2/*m* 1 space group (sg No. 12):

Multplicity, Wyckoff letter, Site symmetry, Coordinates (1/2,1/2,0)+

2 *c* 2/*m* (0,0,1/2)

```
> M1[1] := [0,0,1/2]; M1[2]:= evalm(M1[1]+[1/2,1/2,0]);
```

$$M1_1 := \left[0, 0, \frac{1}{2}\right]$$

$$M1_2 := \left[\frac{1}{2}, \frac{1}{2}, \frac{1}{2}\right]$$

The M2 cations are at the following positions within the C 1 2/*m* 1 space group (s.g. No. 12):

Multplicity, Wyckoff letter, Site symmetry, Coordinates (1/2,1/2,0)+

4 *h* 2 (1) 0 , y ,1/2 (2) 0, -y , 1/2

```
> M2[1] := [0,M2y,1/2]; M2[2]:= [M2[1][1],-M2[1][2]+1,M2[1][3]];
  M2[3]:=evalm(M2[1]+[1/2,1/2,0]); M2[4]:=evalm(M2[2]+[1/2,-1/2,0]);
```

$$M2_1 := \left[0, M2y, \frac{1}{2}\right]$$

$$M2_2 := \left[0, -M2y + 1, \frac{1}{2}\right]$$

$$M2_3 := \left[\frac{1}{2}, \frac{1}{2} + M2y, \frac{1}{2}\right]$$

$$M2_4 := \left[\frac{1}{2}, \frac{1}{2} - M2y, \frac{1}{2}\right]$$

The O4 oxygen atoms are at the following positions within the C 1 2/*m* 1 space group (s.g. No. 12; unique axis *b*):

Multplicity, Wyckoff letter, Site symmetry, Coordinates (1/2,1/2,0)+

4 *i* *m* (1) x , 0 , z
(2) -x , 0 , -z
(3) 1/2 + x , 1/2 , z

(4) 1/2 - x , 1/2 , -z

```
> O4[1]:=[O4x,1/2,O4z];  O4[2]:= [-O4[1][1]+1,O4[1][2],-O4[1][3]+1];
  O4[3]:=[O4[1][1]+1/2,O4[1][2]-1/2,O4[1][3]];
  O4[4]:=[-O4[1][1]+1/2,O4[1][2]-1/2,-O4[1][3]+1];
```

$$O4_1 := \left[O4x, \frac{1}{2}, O4z \right]$$

$$O4_2 := \left[-O4x + 1, \frac{1}{2}, -O4z + 1 \right]$$

$$O4_3 := \left[O4x + \frac{1}{2}, 0, O4z \right]$$

$$O4_4 := \left[-O4x + \frac{1}{2}, 0, -O4z + 1 \right]$$

The O3 oxygen atoms are at the following positions within the C 1 2/*m* 1 space group (s.g. No. 12; unique axis *b*):

Multplicity, Wyckoff letter, Site symmetry, Coordinates (1/2,1/2,0)+

8 *j* 1 (1) x , y , z
(2) -x , y , -z
(3) -x , - y , - z
(4) x , -y , z
(5) 1/2 + x , 1/2 + y , z
(6) 1/2 - x , 1/2 + y , -z
(7) 1/2 - x , 1/2 - y , -z
(8) 1/2 + x , 1/2 - y , z

```
> O3[1]:=[O3x,O3y,O3z];  O3[2]:= [-O3[1][1]+1,O3[1][2],-O3[1][3]+1];
  O3[3]:=[-O3[1][1]+1,-O3[1][2]+1,-O3[1][3]+1];
  O3[4]:=[O3[1][1],-O3[1][2]+1,O3[1][3]];
  O3[5]:=[O3[1][1]+1/2,O3[1][2]+1/2,O3[1][3]];
  O3[6]:=[1/2-O3[1][1],1/2+O3[1][2],-O3[1][3]+1];
  O3[7]:=[1/2-O3[1][1],1/2-O3[1][2],-O3[1][3]+1];
  O3[8]:=[1/2+O3[1][1],1/2-O3[1][2],O3[1][3]];
```

$$O3_1 := [O3x, O3y, O3z]$$

$$O3_2 := [-O3x + 1, O3y, -O3z + 1]$$

$$O3_3 := [-O3x + 1, -O3y + 1, -O3z + 1]$$

$$O3_4 := [O3x, -O3y + 1, O3z]$$

$$O3_5 := \left[O3x + \frac{1}{2}, O3y + \frac{1}{2}, O3z \right]$$

$$O3_6 := \left[\frac{1}{2} - O3x, O3y + \frac{1}{2}, -O3z + 1 \right]$$

$$O3_7 := \left[\frac{1}{2} - O3x, \frac{1}{2} - O3y, -O3z + 1 \right]$$

$$O3_8 := \left[O3x + \frac{1}{2}, \frac{1}{2} - O3y, O3z \right]$$

The T cations are at the following positions within the C 1 2/*m* 1 space group (s.g. No. 12; unique axis *b*):

Multplicity, Wyckoff letter, Site symmetry, Coordinates (1/2,1/2,0)+

8 *j* 1 (1) x , y , z
(2) -x , y , -z
(3) -x , - y , - z

(4) x , -y , z
(5) 1/2 + x , 1/2 + y , z
(6) 1/2 - x , 1/2 + y , -z
(7) 1/2 - x , 1/2 - y , -z
(8) 1/2 + x , 1/2 - y , z

```
> T[1]:=[Tx,Ty,Tz]; T[2]:= [-T[1][1]+1,T[1][2],-T[1][3]+1];
  T[3]:=[-T[1][1]+1,-T[1][2]+1,-T[1][3]+1];
  T[4]:=[T[1][1],-T[1][2]+1,T[1][3]];
  T[5]:=[T[1][1]+1/2,T[1][2]+1/2,T[1][3]];
  T[6]:=[1/2-T[1][1],1/2+T[1][2],-T[1][3]+1];
  T[7]:=[1/2-T[1][1],1/2-T[1][2],-T[1][3]+1];
  T[8]:=[1/2+T[1][1],1/2-T[1][2],T[1][3]];
```

$$T_1 := [Tx, Ty, Tz]$$

$$T_2 := [-Tx + 1, Ty, -Tz + 1]$$

$$T_3 := [-Tx + 1, -Ty + 1, -Tz + 1]$$

$$T_4 := [Tx, -Ty + 1, Tz]$$

$$T_5 := \left[Tx + \frac{1}{2}, Ty + \frac{1}{2}, Tz\right]$$

$$T_6 := \left[\frac{1}{2} - Tx, Ty + \frac{1}{2}, -Tz + 1\right]$$

$$T_7 := \left[\frac{1}{2} - Tx, \frac{1}{2} - Ty, -Tz + 1\right]$$

$$T_8 := \left[Tx + \frac{1}{2}, \frac{1}{2} - Ty, Tz\right]$$

The O1 oxygen atoms are at the following positions within the C 1 2/*m* 1 space group (s.g. No. 12; unique axis *b*):

Multplicity, Wyckoff letter, Site symmetry, Coordinates (1/2,1/2,0)+

4 *i* *m* (1) x , 0 , z
(2) -x , 0 , -z
(3) 1/2 + x , 1/2 , z
(4) 1/2 - x , 1/2 , -z

```
> O1[1]:=[O1x,0,O1z];  O1[2]:= [-O1[1][1]+1,O1[1][2],-O1[1][3]+1];
  O1[3]:=[1/2+O1[1][1],1/2,O1[1][3]]; O1[4]:=[1/2-O1[1][1],1/2,-O1[1][3]+1];
```

$$O1_1 := [O1x, 0, O1z]$$

$$O1_2 := [-O1x + 1, 0, -O1z + 1]$$

$$O1_3 := \left[\frac{1}{2} + O1x, \frac{1}{2}, O1z\right]$$

$$O1_4 := \left[\frac{1}{2} - O1x, \frac{1}{2}, -O1z + 1\right]$$

The O2 oxygen atoms are at the following positions within the C 1 2/*m* 1 space group (s.g. No. 12; unique axis *b*):

Multplicity, Wyckoff letter, Site symmetry, Coordinates (1/2,1/2,0)+

8 *j* 1 (1) x , y , z
(2) -x , y , -z
(3) -x , - y , - z
(4) x , -y , z
(5) 1/2 + x , 1/2 + y , z
(6) 1/2 - x , 1/2 + y , -z
(7) 1/2 - x , 1/2 - y , -z

(8) 1/2 + x , 1/2 - y , z

```
> O2[1]:=[O2x,O2y,O2z];
  O2[2]:= [-O2[1][1]+1,O2[1][2],-O2[1][3]+1];
  O2[3]:=[-O2[1][1]+1,-O2[1][2]+1,-O2[1][3]+1];
  O2[4]:=[O2[1][1],-O2[1][2]+1,O2[1][3]];
  O2[5]:=[O2[1][1]+1/2,O2[1][2]+1/2,O2[1][3]];
  O2[6]:=[1/2-O2[1][1],1/2+O2[1][2],-O2[1][3]+1];
  O2[7]:=[1/2-O2[1][1],1/2-O2[1][2],-O2[1][3]+1];
  O2[8]:=[1/2+O2[1][1],1/2-O2[1][2],O2[1][3]];
```

$$O2_1 := [O2x, O2y, O2z]$$

$$O2_2 := [-O2x + 1, O2y, -O2z + 1]$$

$$O2_3 := [-O2x + 1, -O2y + 1, -O2z + 1]$$

$$O2_4 := [O2x, -O2y + 1, O2z]$$

$$O2_5 := \left[O2x + \frac{1}{2}, O2y + \frac{1}{2}, O2z\right]$$

$$O2_6 := \left[\frac{1}{2} - O2x, O2y + \frac{1}{2}, -O2z + 1\right]$$

$$O2_7 := \left[\frac{1}{2} - O2x, \frac{1}{2} - O2y, -O2z + 1\right]$$

$$O2_8 := \left[O2x + \frac{1}{2}, \frac{1}{2} - O2y, O2z\right]$$

```
> R[180] := [[-1,0,0],[0,-1,0],[0,0,1]];
```

$$R_{180} := [[-1, 0, 0], [0, -1, 0], [0, 0, 1]]$$

Transformation to a metric orthogonal **abc** coordinate system with cation M1 at (0,0,0):

```
> for i from 1  to 8 do  O2metric[i]:=
  evalm([O2[i][1]-c1M/a1M*cos(pi-beta1M)*O2[i][3]+1/2*c1M/a1M*cos(pi-beta1M),O2[i][2],O2[i]
  [3]-1/2]) od:
> for i from 1  to 8 do  Tmetric[i]:=
  evalm([T[i][1]-c1M/a1M*cos(pi-beta1M)*T[i][3]+1/2*c1M/a1M*cos(pi-beta1M),T[i][2],T[i][3]-
  1/2]) od;
```

$$Tmetric_1 := \left[Tx - \frac{c1M\cos(\pi - beta1M)\,Tz}{a1M} + \frac{1}{2}\frac{c1M\cos(\pi - beta1M)}{a1M}, Ty, Tz - \frac{1}{2}\right]$$

$$Tmetric_2 := \left[-Tx + 1 - \frac{c1M\cos(\pi - beta1M)\,(-Tz + 1)}{a1M} + \frac{1}{2}\frac{c1M\cos(\pi - beta1M)}{a1M}, Ty, -Tz + \frac{1}{2}\right]$$

$$Tmetric_3 := \left[-Tx + 1 - \frac{c1M\cos(\pi - beta1M)\,(-Tz + 1)}{a1M} + \frac{1}{2}\frac{c1M\cos(\pi - beta1M)}{a1M}, -Ty + 1, -Tz + \frac{1}{2}\right]$$

$$Tmetric_4 := \left[Tx - \frac{c1M\cos(\pi - beta1M)\,Tz}{a1M} + \frac{1}{2}\frac{c1M\cos(\pi - beta1M)}{a1M}, -Ty + 1, Tz - \frac{1}{2}\right]$$

$$Tmetric_5 := \left[Tx + \frac{1}{2} - \frac{c1M\cos(\pi - beta1M)\,Tz}{a1M} + \frac{1}{2}\frac{c1M\cos(\pi - beta1M)}{a1M}, Ty + \frac{1}{2}, Tz - \frac{1}{2}\right]$$

$$Tmetric_6 := \left[\frac{1}{2} - Tx - \frac{c1M\cos(\pi - beta1M)\,(-Tz + 1)}{a1M} + \frac{1}{2}\frac{c1M\cos(\pi - beta1M)}{a1M}, Ty + \frac{1}{2}, -Tz + \frac{1}{2}\right]$$

$$Tmetric_7 := \left[\frac{1}{2} - Tx - \frac{c1M\cos(\pi - beta1M)\,(-Tz + 1)}{a1M} + \frac{1}{2}\frac{c1M\cos(\pi - beta1M)}{a1M}, \frac{1}{2} - Ty, -Tz + \frac{1}{2}\right]$$

$$Tmetric_8 := \left[Tx + \frac{1}{2} - \frac{c1M\cos(\pi - beta1M)\,Tz}{a1M} + \frac{1}{2}\frac{c1M\cos(\pi - beta1M)}{a1M}, \frac{1}{2} - Ty, Tz - \frac{1}{2}\right]$$

```
> for i from 1  to 4 do  O1metric[i]:=
  evalm([O1[i][1]-c1M/a1M*cos(pi-beta1M)*O1[i][3]+1/2*c1M/a1M*cos(pi-beta1M),O1[i][2],O1[i]
  [3]-1/2]) od;
```

$$O1metric_1 := \left[O1x - \frac{c1M\cos(\pi - beta1M)\,O1z}{a1M} + \frac{1}{2}\frac{c1M\cos(\pi - beta1M)}{a1M},\ 0,\ O1z - \frac{1}{2} \right]$$

$$O1metric_2 := \left[-O1x + 1 - \frac{c1M\cos(\pi - beta1M)\,(-O1z + 1)}{a1M} + \frac{1}{2}\frac{c1M\cos(\pi - beta1M)}{a1M},\ 0,\ -O1z + \frac{1}{2} \right]$$

$$O1metric_3 := \left[\frac{1}{2} + O1x - \frac{c1M\cos(\pi - beta1M)\,O1z}{a1M} + \frac{1}{2}\frac{c1M\cos(\pi - beta1M)}{a1M},\ \frac{1}{2},\ O1z - \frac{1}{2} \right]$$

$$O1metric_4 := \left[\frac{1}{2} - O1x - \frac{c1M\cos(\pi - beta1M)\,(-O1z + 1)}{a1M} + \frac{1}{2}\frac{c1M\cos(\pi - beta1M)}{a1M},\ \frac{1}{2},\ -O1z + \frac{1}{2} \right]$$

```
> for i from 1  to 4 do  O4metric[i]:=
evalm([O4[i][1]-c1M/a1M*cos(pi-beta1M)*O4[i][3]+1/2*c1M/a1M*cos(pi-beta1M),O4[i][2],O4[i]
[3]-1/2]) od;
```

$$O4metric_1 := \left[O4x - \frac{c1M\cos(\pi - beta1M)\,O4z}{a1M} + \frac{1}{2}\frac{c1M\cos(\pi - beta1M)}{a1M},\ \frac{1}{2},\ O4z - \frac{1}{2} \right]$$

$$O4metric_2 := \left[-O4x + 1 - \frac{c1M\cos(\pi - beta1M)\,(-O4z + 1)}{a1M} + \frac{1}{2}\frac{c1M\cos(\pi - beta1M)}{a1M},\ \frac{1}{2},\ -O4z + \frac{1}{2} \right]$$

$$O4metric_3 := \left[O4x + \frac{1}{2} - \frac{c1M\cos(\pi - beta1M)\,O4z}{a1M} + \frac{1}{2}\frac{c1M\cos(\pi - beta1M)}{a1M},\ 0,\ O4z - \frac{1}{2} \right]$$

$$O4metric_4 := \left[-O4x + \frac{1}{2} - \frac{c1M\cos(\pi - beta1M)\,(-O4z + 1)}{a1M} + \frac{1}{2}\frac{c1M\cos(\pi - beta1M)}{a1M},\ 0,\ -O4z + \frac{1}{2} \right]$$

```
> for i from 1  to 8 do  O3metric[i]:=
evalm([O3[i][1]-c1M/a1M*cos(pi-beta1M)*O3[i][3]+1/2*c1M/a1M*cos(pi-beta1M),O3[i][2],O3[i]
[3]-1/2]) od;
```

$$O3metric_1 := \left[O3x - \frac{c1M\cos(\pi - beta1M)\,O3z}{a1M} + \frac{1}{2}\frac{c1M\cos(\pi - beta1M)}{a1M},\ O3y,\ O3z - \frac{1}{2} \right]$$

$$O3metric_2 := \left[-O3x + 1 - \frac{c1M\cos(\pi - beta1M)\,(-O3z + 1)}{a1M} + \frac{1}{2}\frac{c1M\cos(\pi - beta1M)}{a1M},\ O3y,\ -O3z + \frac{1}{2} \right]$$

$$O3metric_3 := \left[-O3x + 1 - \frac{c1M\cos(\pi - beta1M)\,(-O3z + 1)}{a1M} + \frac{1}{2}\frac{c1M\cos(\pi - beta1M)}{a1M},\ -O3y + 1,\ -O3z + \frac{1}{2} \right]$$

$$O3metric_4 := \left[O3x - \frac{c1M\cos(\pi - beta1M)\,O3z}{a1M} + \frac{1}{2}\frac{c1M\cos(\pi - beta1M)}{a1M},\ -O3y + 1,\ O3z - \frac{1}{2} \right]$$

$$O3metric_5 := \left[O3x + \frac{1}{2} - \frac{c1M\cos(\pi - beta1M)\,O3z}{a1M} + \frac{1}{2}\frac{c1M\cos(\pi - beta1M)}{a1M},\ O3y + \frac{1}{2},\ O3z - \frac{1}{2} \right]$$

$$O3metric_6 := \left[\frac{1}{2} - O3x - \frac{c1M\cos(\pi - beta1M)\,(-O3z + 1)}{a1M} + \frac{1}{2}\frac{c1M\cos(\pi - beta1M)}{a1M},\ O3y + \frac{1}{2},\ -O3z + \frac{1}{2} \right]$$

$$O3metric_7 := \left[\frac{1}{2} - O3x - \frac{c1M\cos(\pi - beta1M)\,(-O3z + 1)}{a1M} + \frac{1}{2}\frac{c1M\cos(\pi - beta1M)}{a1M},\ \frac{1}{2} - O3y,\ -O3z + \frac{1}{2} \right]$$

$$O3metric_8 := \left[O3x + \frac{1}{2} - \frac{c1M\cos(\pi - beta1M)\,O3z}{a1M} + \frac{1}{2}\frac{c1M\cos(\pi - beta1M)}{a1M},\ \frac{1}{2} - O3y,\ O3z - \frac{1}{2} \right]$$

```
> for i from 1  to 4 do  M2metric[i]:=
evalm([M2[i][1]-c1M/a1M*cos(pi-beta1M)*M2[i][3]+1/2*c1M/a1M*cos(pi-beta1M),M2[i][2],M2[i]
[3]-1/2]) od;
```

$$M2metric_1 := [0,\ M2y,\ 0]$$

$$M2metric_2 := [0,\ -M2y + 1,\ 0]$$

$$M2metric_3 := \left[\frac{1}{2},\ \frac{1}{2} + M2y,\ 0 \right]$$

$$M2metric_4 := \left[\frac{1}{2},\ \frac{1}{2} - M2y,\ 0 \right]$$

```
> for i from 1  to 2 do  Kmetric[i]:=
evalm([K[i][1]-c1M/a1M*cos(pi-beta1M)*K[i][3]+1/2*c1M/a1M*cos(pi-beta1M),K[i][2],K[i][3]-
1/2]) od;
```

$$Kmetric_1 := \left[\frac{1}{2}\frac{c1M\cos(\pi - beta1M)}{a1M}, \frac{1}{2}, \frac{-1}{2}\right]$$

$$Kmetric_2 := \left[\frac{1}{2}+\frac{1}{2}\frac{c1M\cos(\pi - beta1M)}{a1M}, 0, \frac{-1}{2}\right]$$

```
> for i from 1  to 2 do  M1metric[i]:=
evalm([M1[i][1]-c1M/a1M*cos(pi-beta1M)*M1[i][3]+1/2*c1M/a1M*cos(pi-beta1M),M1[i][2],M1[i]
[3]-1/2]) od;
```

$$M1metric_1 := [0, 0, 0]$$

$$M1metric_2 := \left[\frac{1}{2}, \frac{1}{2}, 0\right]$$

```
> layer[1] :=
[Kmetric[1],Kmetric[2],M1metric[1],M1metric[2],M2metric[1],M2metric[2],M2metric[3],M2metr
ic[4],O4metric[1],O4metric[2],O4metric[3],O4metric[4],O3metric[1],O3metric[2],O3metric[3]
,O3metric[4],O3metric[5],O3metric[6],O3metric[7],O3metric[8],Tmetric[1],Tmetric[2],Tmetri
c[3],Tmetric[4],Tmetric[5],Tmetric[6],Tmetric[7],Tmetric[8],O1metric[1],O1metric[2],O1met
ric[3],O1metric[4],O2metric[1],O2metric[2],O2metric[3],O2metric[4],O2metric[5],O2metric[6
],O2metric[7],O2metric[8]];
```

$layer_1 := [Kmetric_1, Kmetric_2, M1metric_1, M1metric_2, M2metric_1, M2metric_2, M2metric_3, M2metric_4, O4metric_1, O4metric_2,$
$O4metric_3, O4metric_4, O3metric_1, O3metric_2, O3metric_3, O3metric_4, O3metric_5, O3metric_6, O3metric_7, O3metric_8, Tmetric_1,$
$Tmetric_2, Tmetric_3, Tmetric_4, Tmetric_5, Tmetric_6, Tmetric_7, Tmetric_8, O1metric_1, O1metric_2, O1metric_3, O1metric_4, O2metric_1,$
$O2metric_2, O2metric_3, O2metric_4, O2metric_5, O2metric_6, O2metric_7, O2metric_8]$

```
> Zadjust := [[1,0,0],[0,1,0],[0,0,1/2]];
```

$$Zadjust := \left[[1, 0, 0], [0, 1, 0], \left[0, 0, \frac{1}{2}\right]\right]$$

```
> for i from 1 to 40 do layer_1_coordinates[i] :=evalm(R[180]&*Zadjust&*layer[1][i]) od;
```

$$layer\_1\_coordinates_1 := \left[-\frac{1}{2}\frac{c1M\cos(\pi - beta1M)}{a1M}, \frac{-1}{2}, \frac{-1}{4}\right]$$

$$layer\_1\_coordinates_2 := \left[-\frac{1}{2}-\frac{1}{2}\frac{c1M\cos(\pi - beta1M)}{a1M}, 0, \frac{-1}{4}\right]$$

$$layer\_1\_coordinates_3 := [0, 0, 0]$$

$$layer\_1\_coordinates_4 := \left[\frac{-1}{2}, \frac{-1}{2}, 0\right]$$

$$layer\_1\_coordinates_5 := [0, -M2y, 0]$$

$$layer\_1\_coordinates_6 := [0, M2y - 1, 0]$$

$$layer\_1\_coordinates_7 := \left[\frac{-1}{2}, -\frac{1}{2} - M2y, 0\right]$$

$$layer\_1\_coordinates_8 := \left[\frac{-1}{2}, -\frac{1}{2} + M2y, 0\right]$$

$$layer\_1\_coordinates_9 := \left[-O4x + \frac{c1M\cos(\pi - beta1M)\,O4z}{a1M} - \frac{1}{2}\frac{c1M\cos(\pi - beta1M)}{a1M}, \frac{-1}{2}, \frac{1}{2}O4z - \frac{1}{4}\right]$$

$$layer\_1\_coordinates_{10} := \left[O4x - 1 + \frac{c1M\cos(\pi - beta1M)\,(-O4z+1)}{a1M} - \frac{1}{2}\frac{c1M\cos(\pi - beta1M)}{a1M}, \frac{-1}{2}, -\frac{1}{2}O4z + \frac{1}{4}\right]$$

$$layer\_1\_coordinates_{11} := \left[-O4x - \frac{1}{2} + \frac{c1M\cos(\pi - beta1M)\,O4z}{a1M} - \frac{1}{2}\frac{c1M\cos(\pi - beta1M)}{a1M}, 0, \frac{1}{2}O4z - \frac{1}{4}\right]$$

$$layer\_1\_coordinates_{12} := \left[O4x - \frac{1}{2} + \frac{c1M\cos(\pi - beta1M)\,(-O4z+1)}{a1M} - \frac{1}{2}\frac{c1M\cos(\pi - beta1M)}{a1M}, 0, -\frac{1}{2}O4z + \frac{1}{4}\right]$$

$$layer\_1\_coordinates_{13} := \left[-O3x + \frac{c1M\cos(\pi - beta1M)\,O3z}{a1M} - \frac{1}{2}\frac{c1M\cos(\pi - beta1M)}{a1M}, -O3y, \frac{1}{2}O3z - \frac{1}{4}\right]$$

$$layer\_1\_coordinates_{14} := \left[O3x - 1 + \frac{c1M\cos(\pi - beta1M)\,(-O3z+1)}{a1M} - \frac{1}{2}\frac{c1M\cos(\pi - beta1M)}{a1M},\ -O3y,\ -\frac{1}{2}O3z + \frac{1}{4} \right]$$

$$layer\_1\_coordinates_{15} := \left[O3x - 1 + \frac{c1M\cos(\pi - beta1M)\,(-O3z+1)}{a1M} - \frac{1}{2}\frac{c1M\cos(\pi - beta1M)}{a1M},\ O3y - 1,\ -\frac{1}{2}O3z + \frac{1}{4} \right]$$

$$layer\_1\_coordinates_{16} := \left[-O3x + \frac{c1M\cos(\pi - beta1M)\,O3z}{a1M} - \frac{1}{2}\frac{c1M\cos(\pi - beta1M)}{a1M},\ O3y - 1,\ \frac{1}{2}O3z - \frac{1}{4} \right]$$

$$layer\_1\_coordinates_{17} := \left[-O3x - \frac{1}{2} + \frac{c1M\cos(\pi - beta1M)\,O3z}{a1M} - \frac{1}{2}\frac{c1M\cos(\pi - beta1M)}{a1M},\ -O3y - \frac{1}{2},\ \frac{1}{2}O3z - \frac{1}{4} \right]$$

$$layer\_1\_coordinates_{18} := \left[-\frac{1}{2} + O3x + \frac{c1M\cos(\pi - beta1M)\,(-O3z+1)}{a1M} - \frac{1}{2}\frac{c1M\cos(\pi - beta1M)}{a1M},\ -O3y - \frac{1}{2},\ -\frac{1}{2}O3z + \frac{1}{4} \right]$$

$$layer\_1\_coordinates_{19} := \left[-\frac{1}{2} + O3x + \frac{c1M\cos(\pi - beta1M)\,(-O3z+1)}{a1M} - \frac{1}{2}\frac{c1M\cos(\pi - beta1M)}{a1M},\ -\frac{1}{2} + O3y,\ -\frac{1}{2}O3z + \frac{1}{4} \right]$$

$$layer\_1\_coordinates_{20} := \left[-O3x - \frac{1}{2} + \frac{c1M\cos(\pi - beta1M)\,O3z}{a1M} - \frac{1}{2}\frac{c1M\cos(\pi - beta1M)}{a1M},\ -\frac{1}{2} + O3y,\ \frac{1}{2}O3z - \frac{1}{4} \right]$$

$$layer\_1\_coordinates_{21} := \left[-Tx + \frac{c1M\cos(\pi - beta1M)\,Tz}{a1M} - \frac{1}{2}\frac{c1M\cos(\pi - beta1M)}{a1M},\ -Ty,\ \frac{1}{2}Tz - \frac{1}{4} \right]$$

$$layer\_1\_coordinates_{22} := \left[Tx - 1 + \frac{c1M\cos(\pi - beta1M)\,(-Tz+1)}{a1M} - \frac{1}{2}\frac{c1M\cos(\pi - beta1M)}{a1M},\ -Ty,\ -\frac{1}{2}Tz + \frac{1}{4} \right]$$

$$layer\_1\_coordinates_{23} := \left[Tx - 1 + \frac{c1M\cos(\pi - beta1M)\,(-Tz+1)}{a1M} - \frac{1}{2}\frac{c1M\cos(\pi - beta1M)}{a1M},\ Ty - 1,\ -\frac{1}{2}Tz + \frac{1}{4} \right]$$

$$layer\_1\_coordinates_{24} := \left[-Tx + \frac{c1M\cos(\pi - beta1M)\,Tz}{a1M} - \frac{1}{2}\frac{c1M\cos(\pi - beta1M)}{a1M},\ Ty - 1,\ \frac{1}{2}Tz - \frac{1}{4} \right]$$

$$layer\_1\_coordinates_{25} := \left[-Tx - \frac{1}{2} + \frac{c1M\cos(\pi - beta1M)\,Tz}{a1M} - \frac{1}{2}\frac{c1M\cos(\pi - beta1M)}{a1M},\ -Ty - \frac{1}{2},\ \frac{1}{2}Tz - \frac{1}{4} \right]$$

$$layer\_1\_coordinates_{26} := \left[-\frac{1}{2} + Tx + \frac{c1M\cos(\pi - beta1M)\,(-Tz+1)}{a1M} - \frac{1}{2}\frac{c1M\cos(\pi - beta1M)}{a1M},\ -Ty - \frac{1}{2},\ -\frac{1}{2}Tz + \frac{1}{4} \right]$$

$$layer\_1\_coordinates_{27} := \left[-\frac{1}{2} + Tx + \frac{c1M\cos(\pi - beta1M)\,(-Tz+1)}{a1M} - \frac{1}{2}\frac{c1M\cos(\pi - beta1M)}{a1M},\ -\frac{1}{2} + Ty,\ -\frac{1}{2}Tz + \frac{1}{4} \right]$$

$$layer\_1\_coordinates_{28} := \left[-Tx - \frac{1}{2} + \frac{c1M\cos(\pi - beta1M)\,Tz}{a1M} - \frac{1}{2}\frac{c1M\cos(\pi - beta1M)}{a1M},\ -\frac{1}{2} + Ty,\ \frac{1}{2}Tz - \frac{1}{4} \right]$$

$$layer\_1\_coordinates_{29} := \left[-O1x + \frac{c1M\cos(\pi - beta1M)\,O1z}{a1M} - \frac{1}{2}\frac{c1M\cos(\pi - beta1M)}{a1M},\ 0,\ \frac{1}{2}O1z - \frac{1}{4} \right]$$

$$layer\_1\_coordinates_{30} := \left[O1x - 1 + \frac{c1M\cos(\pi - beta1M)\,(-O1z+1)}{a1M} - \frac{1}{2}\frac{c1M\cos(\pi - beta1M)}{a1M},\ 0,\ -\frac{1}{2}O1z + \frac{1}{4} \right]$$

$$layer\_1\_coordinates_{31} := \left[-\frac{1}{2} - O1x + \frac{c1M\cos(\pi - beta1M)\,O1z}{a1M} - \frac{1}{2}\frac{c1M\cos(\pi - beta1M)}{a1M},\ \frac{-1}{2},\ \frac{1}{2}O1z - \frac{1}{4} \right]$$

$$layer\_1\_coordinates_{32} := \left[-\frac{1}{2} + O1x + \frac{c1M\cos(\pi - beta1M)\,(-O1z+1)}{a1M} - \frac{1}{2}\frac{c1M\cos(\pi - beta1M)}{a1M},\ \frac{-1}{2},\ -\frac{1}{2}O1z + \frac{1}{4} \right]$$

$$layer\_1\_coordinates_{33} := \left[-O2x + \frac{c1M\cos(\pi - beta1M)\,O2z}{a1M} - \frac{1}{2}\frac{c1M\cos(\pi - beta1M)}{a1M},\ -O2y,\ \frac{1}{2}O2z - \frac{1}{4} \right]$$

$$layer\_1\_coordinates_{34} := \left[O2x - 1 + \frac{c1M\cos(\pi - beta1M)\,(-O2z+1)}{a1M} - \frac{1}{2}\frac{c1M\cos(\pi - beta1M)}{a1M},\ -O2y,\ -\frac{1}{2}O2z + \frac{1}{4} \right]$$

$$layer\_1\_coordinates_{35} := \left[O2x - 1 + \frac{c1M\cos(\pi - beta1M)\,(-O2z+1)}{a1M} - \frac{1}{2}\frac{c1M\cos(\pi - beta1M)}{a1M},\ O2y - 1,\ -\frac{1}{2}O2z + \frac{1}{4} \right]$$

$$layer\_1\_coordinates_{36} := \left[-O2x + \frac{c1M\cos(\pi - beta1M)\,O2z}{a1M} - \frac{1}{2}\frac{c1M\cos(\pi - beta1M)}{a1M},\ O2y - 1,\ \frac{1}{2}O2z - \frac{1}{4} \right]$$

$$layer\_1\_coordinates_{37} := \left[-O2x - \frac{1}{2} + \frac{c1M\cos(\pi - beta1M)\,O2z}{a1M} - \frac{1}{2}\frac{c1M\cos(\pi - beta1M)}{a1M},\ -O2y - \frac{1}{2},\ \frac{1}{2}O2z - \frac{1}{4} \right]$$

$$layer\_1\_coordinates_{38} := \left[-\frac{1}{2} + O2x + \frac{c1M\cos(\pi - beta1M)\,(-O2z+1)}{a1M} - \frac{1}{2}\frac{c1M\cos(\pi - beta1M)}{a1M}, -O2y - \frac{1}{2}, -\frac{1}{2}O2z + \frac{1}{4} \right]$$

$$layer\_1\_coordinates_{39} := \left[-\frac{1}{2} + O2x + \frac{c1M\cos(\pi - beta1M)\,(-O2z+1)}{a1M} - \frac{1}{2}\frac{c1M\cos(\pi - beta1M)}{a1M}, -\frac{1}{2} + O2y, -\frac{1}{2}O2z + \frac{1}{4} \right]$$

$$layer\_1\_coordinates_{40} := \left[-O2x - \frac{1}{2} + \frac{c1M\cos(\pi - beta1M)\,O2z}{a1M} - \frac{1}{2}\frac{c1M\cos(\pi - beta1M)}{a1M}, -\frac{1}{2} + O2y, \frac{1}{2}O2z - \frac{1}{4} \right]$$

```
> for i from 1 to 40 do layer_2_coordinates[i] :=evalm( Zadjust&*layer[1][i]+[0,0,1/2]) od;
```

$$layer\_2\_coordinates_{1} := \left[\frac{1}{2}\frac{c1M\cos(\pi - beta1M)}{a1M}, \frac{1}{2}, \frac{1}{4} \right]$$

$$layer\_2\_coordinates_{2} := \left[\frac{1}{2} + \frac{1}{2}\frac{c1M\cos(\pi - beta1M)}{a1M}, 0, \frac{1}{4} \right]$$

$$layer\_2\_coordinates_{3} := \left[0, 0, \frac{1}{2} \right]$$

$$layer\_2\_coordinates_{4} := \left[\frac{1}{2}, \frac{1}{2}, \frac{1}{2} \right]$$

$$layer\_2\_coordinates_{5} := \left[0, M2y, \frac{1}{2} \right]$$

$$layer\_2\_coordinates_{6} := \left[0, -M2y + 1, \frac{1}{2} \right]$$

$$layer\_2\_coordinates_{7} := \left[\frac{1}{2}, \frac{1}{2} + M2y, \frac{1}{2} \right]$$

$$layer\_2\_coordinates_{8} := \left[\frac{1}{2}, \frac{1}{2} - M2y, \frac{1}{2} \right]$$

$$layer\_2\_coordinates_{9} := \left[O4x - \frac{c1M\cos(\pi - beta1M)\,O4z}{a1M} + \frac{1}{2}\frac{c1M\cos(\pi - beta1M)}{a1M}, \frac{1}{2}, \frac{1}{2}O4z + \frac{1}{4} \right]$$

$$layer\_2\_coordinates_{10} := \left[-O4x + 1 - \frac{c1M\cos(\pi - beta1M)\,(-O4z+1)}{a1M} + \frac{1}{2}\frac{c1M\cos(\pi - beta1M)}{a1M}, \frac{1}{2}, -\frac{1}{2}O4z + \frac{3}{4} \right]$$

$$layer\_2\_coordinates_{11} := \left[O4x + \frac{1}{2} - \frac{c1M\cos(\pi - beta1M)\,O4z}{a1M} + \frac{1}{2}\frac{c1M\cos(\pi - beta1M)}{a1M}, 0, \frac{1}{2}O4z + \frac{1}{4} \right]$$

$$layer\_2\_coordinates_{12} := \left[-O4x + \frac{1}{2} - \frac{c1M\cos(\pi - beta1M)\,(-O4z+1)}{a1M} + \frac{1}{2}\frac{c1M\cos(\pi - beta1M)}{a1M}, 0, -\frac{1}{2}O4z + \frac{3}{4} \right]$$

$$layer\_2\_coordinates_{13} := \left[O3x - \frac{c1M\cos(\pi - beta1M)\,O3z}{a1M} + \frac{1}{2}\frac{c1M\cos(\pi - beta1M)}{a1M}, O3y, \frac{1}{2}O3z + \frac{1}{4} \right]$$

$$layer\_2\_coordinates_{14} := \left[-O3x + 1 - \frac{c1M\cos(\pi - beta1M)\,(-O3z+1)}{a1M} + \frac{1}{2}\frac{c1M\cos(\pi - beta1M)}{a1M}, O3y, -\frac{1}{2}O3z + \frac{3}{4} \right]$$

$$layer\_2\_coordinates_{15} := \left[-O3x + 1 - \frac{c1M\cos(\pi - beta1M)\,(-O3z+1)}{a1M} + \frac{1}{2}\frac{c1M\cos(\pi - beta1M)}{a1M}, -O3y + 1, -\frac{1}{2}O3z + \frac{3}{4} \right]$$

$$layer\_2\_coordinates_{16} := \left[O3x - \frac{c1M\cos(\pi - beta1M)\,O3z}{a1M} + \frac{1}{2}\frac{c1M\cos(\pi - beta1M)}{a1M}, -O3y + 1, \frac{1}{2}O3z + \frac{1}{4} \right]$$

$$layer\_2\_coordinates_{17} := \left[O3x + \frac{1}{2} - \frac{c1M\cos(\pi - beta1M)\,O3z}{a1M} + \frac{1}{2}\frac{c1M\cos(\pi - beta1M)}{a1M}, O3y + \frac{1}{2}, \frac{1}{2}O3z + \frac{1}{4} \right]$$

$$layer\_2\_coordinates_{18} := \left[\frac{1}{2} - O3x - \frac{c1M\cos(\pi - beta1M)\,(-O3z+1)}{a1M} + \frac{1}{2}\frac{c1M\cos(\pi - beta1M)}{a1M}, O3y + \frac{1}{2}, -\frac{1}{2}O3z + \frac{3}{4} \right]$$

$$layer\_2\_coordinates_{19} := \left[\frac{1}{2} - O3x - \frac{c1M\cos(\pi - beta1M)\,(-O3z+1)}{a1M} + \frac{1}{2}\frac{c1M\cos(\pi - beta1M)}{a1M}, \frac{1}{2} - O3y, -\frac{1}{2}O3z + \frac{3}{4} \right]$$

$$layer\_2\_coordinates_{20} := \left[O3x + \frac{1}{2} - \frac{c1M\cos(\pi - beta1M)\,O3z}{a1M} + \frac{1}{2}\frac{c1M\cos(\pi - beta1M)}{a1M}, \frac{1}{2} - O3y, \frac{1}{2}O3z + \frac{1}{4} \right]$$

$$layer\_2\_coordinates_{21} := \left[Tx - \frac{c1M\cos(\pi - beta1M)\,Tz}{a1M} + \frac{1}{2}\frac{c1M\cos(\pi - beta1M)}{a1M},\ Ty,\ \frac{1}{2}Tz + \frac{1}{4} \right]$$

$$layer\_2\_coordinates_{22} := \left[-Tx + 1 - \frac{c1M\cos(\pi - beta1M)\,(-Tz + 1)}{a1M} + \frac{1}{2}\frac{c1M\cos(\pi - beta1M)}{a1M},\ Ty,\ -\frac{1}{2}Tz + \frac{3}{4} \right]$$

$$layer\_2\_coordinates_{23} := \left[-Tx + 1 - \frac{c1M\cos(\pi - beta1M)\,(-Tz + 1)}{a1M} + \frac{1}{2}\frac{c1M\cos(\pi - beta1M)}{a1M},\ -Ty + 1,\ -\frac{1}{2}Tz + \frac{3}{4} \right]$$

$$layer\_2\_coordinates_{24} := \left[Tx - \frac{c1M\cos(\pi - beta1M)\,Tz}{a1M} + \frac{1}{2}\frac{c1M\cos(\pi - beta1M)}{a1M},\ -Ty + 1,\ \frac{1}{2}Tz + \frac{1}{4} \right]$$

$$layer\_2\_coordinates_{25} := \left[Tx + \frac{1}{2} - \frac{c1M\cos(\pi - beta1M)\,Tz}{a1M} + \frac{1}{2}\frac{c1M\cos(\pi - beta1M)}{a1M},\ Ty + \frac{1}{2},\ \frac{1}{2}Tz + \frac{1}{4} \right]$$

$$layer\_2\_coordinates_{26} := \left[\frac{1}{2} - Tx - \frac{c1M\cos(\pi - beta1M)\,(-Tz + 1)}{a1M} + \frac{1}{2}\frac{c1M\cos(\pi - beta1M)}{a1M},\ Ty + \frac{1}{2},\ -\frac{1}{2}Tz + \frac{3}{4} \right]$$

$$layer\_2\_coordinates_{27} := \left[\frac{1}{2} - Tx - \frac{c1M\cos(\pi - beta1M)\,(-Tz + 1)}{a1M} + \frac{1}{2}\frac{c1M\cos(\pi - beta1M)}{a1M},\ \frac{1}{2} - Ty,\ -\frac{1}{2}Tz + \frac{3}{4} \right]$$

$$layer\_2\_coordinates_{28} := \left[Tx + \frac{1}{2} - \frac{c1M\cos(\pi - beta1M)\,Tz}{a1M} + \frac{1}{2}\frac{c1M\cos(\pi - beta1M)}{a1M},\ \frac{1}{2} - Ty,\ \frac{1}{2}Tz + \frac{1}{4} \right]$$

$$layer\_2\_coordinates_{29} := \left[O1x - \frac{c1M\cos(\pi - beta1M)\,O1z}{a1M} + \frac{1}{2}\frac{c1M\cos(\pi - beta1M)}{a1M},\ 0,\ \frac{1}{2}O1z + \frac{1}{4} \right]$$

$$layer\_2\_coordinates_{30} := \left[-O1x + 1 - \frac{c1M\cos(\pi - beta1M)\,(-O1z + 1)}{a1M} + \frac{1}{2}\frac{c1M\cos(\pi - beta1M)}{a1M},\ 0,\ -\frac{1}{2}O1z + \frac{3}{4} \right]$$

$$layer\_2\_coordinates_{31} := \left[\frac{1}{2} + O1x - \frac{c1M\cos(\pi - beta1M)\,O1z}{a1M} + \frac{1}{2}\frac{c1M\cos(\pi - beta1M)}{a1M},\ \frac{1}{2},\ \frac{1}{2}O1z + \frac{1}{4} \right]$$

$$layer\_2\_coordinates_{32} := \left[\frac{1}{2} - O1x - \frac{c1M\cos(\pi - beta1M)\,(-O1z + 1)}{a1M} + \frac{1}{2}\frac{c1M\cos(\pi - beta1M)}{a1M},\ \frac{1}{2},\ -\frac{1}{2}O1z + \frac{3}{4} \right]$$

$$layer\_2\_coordinates_{33} := \left[O2x - \frac{c1M\cos(\pi - beta1M)\,O2z}{a1M} + \frac{1}{2}\frac{c1M\cos(\pi - beta1M)}{a1M},\ O2y,\ \frac{1}{2}O2z + \frac{1}{4} \right]$$

$$layer\_2\_coordinates_{34} := \left[-O2x + 1 - \frac{c1M\cos(\pi - beta1M)\,(-O2z + 1)}{a1M} + \frac{1}{2}\frac{c1M\cos(\pi - beta1M)}{a1M},\ O2y,\ -\frac{1}{2}O2z + \frac{3}{4} \right]$$

$$layer\_2\_coordinates_{35} := \left[-O2x + 1 - \frac{c1M\cos(\pi - beta1M)\,(-O2z + 1)}{a1M} + \frac{1}{2}\frac{c1M\cos(\pi - beta1M)}{a1M},\ -O2y + 1,\ -\frac{1}{2}O2z + \frac{3}{4} \right]$$

$$layer\_2\_coordinates_{36} := \left[O2x - \frac{c1M\cos(\pi - beta1M)\,O2z}{a1M} + \frac{1}{2}\frac{c1M\cos(\pi - beta1M)}{a1M},\ -O2y + 1,\ \frac{1}{2}O2z + \frac{1}{4} \right]$$

$$layer\_2\_coordinates_{37} := \left[O2x + \frac{1}{2} - \frac{c1M\cos(\pi - beta1M)\,O2z}{a1M} + \frac{1}{2}\frac{c1M\cos(\pi - beta1M)}{a1M},\ O2y + \frac{1}{2},\ \frac{1}{2}O2z + \frac{1}{4} \right]$$

$$layer\_2\_coordinates_{38} := \left[\frac{1}{2} - O2x - \frac{c1M\cos(\pi - beta1M)\,(-O2z + 1)}{a1M} + \frac{1}{2}\frac{c1M\cos(\pi - beta1M)}{a1M},\ O2y + \frac{1}{2},\ -\frac{1}{2}O2z + \frac{3}{4} \right]$$

$$layer\_2\_coordinates_{39} := \left[\frac{1}{2} - O2x - \frac{c1M\cos(\pi - beta1M)\,(-O2z + 1)}{a1M} + \frac{1}{2}\frac{c1M\cos(\pi - beta1M)}{a1M},\ \frac{1}{2} - O2y,\ -\frac{1}{2}O2z + \frac{3}{4} \right]$$

$$layer\_2\_coordinates_{40} := \left[O2x + \frac{1}{2} - \frac{c1M\cos(\pi - beta1M)\,O2z}{a1M} + \frac{1}{2}\frac{c1M\cos(\pi - beta1M)}{a1M},\ \frac{1}{2} - O2y,\ \frac{1}{2}O2z + \frac{1}{4} \right]$$

Stacking polytype 3*T* derivation

Let us first write the fractional atomic coordinates in the *Standard C2/m* 1-layer unit-cell.

The interlayer cations (K) are at the following positions within the C 1 2/*m* 1 space group (sg No. 12):

Multplicity, Wyckoff letter, Site symmetry (1/2,1/2,0)+

2 *b* 2/*m* (0,1/2,0)

```
> with(linalg): K[1] := [0,1/2,1]; K[2]:= [-1/2,0,1];K[3]:= [1/2,0,1];K[4]:= [1/2,0,0];
Warning, new definition for norm
Warning, new definition for trace
```

$$K_1 := \left[0, \frac{1}{2}, 1\right]$$

$$K_2 := \left[\frac{-1}{2}, 0, 1\right]$$

$$K_3 := \left[\frac{1}{2}, 0, 1\right]$$

$$K_4 := \left[\frac{1}{2}, 0, 0\right]$$

The M1 cations are at the following positions within the *C* 1 2/*m* 1 space group (sg No. 12):

Multplicity, Wyckoff letter, Site symmetry, Coordinates (1/2,1/2,0)+

2 *c* 2/*m* (0,0,1/2)

```
> M1[1] := [0,0,1/2]; M1[2]:= evalm(M1[1]+[1/2,1/2,0]);M1[3] := [3/2,1/2,1/2];
```

$$Ml_1 := \left[0, 0, \frac{1}{2}\right]$$

$$Ml_2 := \left[\frac{1}{2}, \frac{1}{2}, \frac{1}{2}\right]$$

$$Ml_3 := \left[\frac{3}{2}, \frac{1}{2}, \frac{1}{2}\right]$$

The M2 cations are at the following positions within the C 1 2/*m* 1 space group (s.g. No. 12):

Multplicity, Wyckoff letter, Site symmetry, Coordinates (1/2,1/2,0)+

4 *h* 2 (1) 0 , y ,1/2 (2) 0, -y , 1/2

```
> M2[1] := [0,yM2,1/2]; M2[2]:= [M2[1][1],-M2[1][2]+1,M2[1][3]];
  M2[3]:=evalm(M2[1]+[1/2,1/2,0]);M2[4]:=evalm(M2[2]+[1/2,-1/2,0]);M2[5]:=[0,0,0]:M2[6]:=[0
  ,0,0]:
```

$$M2_1 := \left[0, yM2, \frac{1}{2}\right]$$

$$M2_2 := \left[0, -yM2 + 1, \frac{1}{2}\right]$$

$$M2_3 := \left[\frac{1}{2}, \frac{1}{2} + yM2, \frac{1}{2}\right]$$

$$M2_4 := \left[\frac{1}{2}, \frac{1}{2} - yM2, \frac{1}{2}\right]$$

The O4 oxygen atoms are at the following positions within the C 1 2/*m* 1 space group (s.g. No. 12; unique axis *b*):

Multplicity, Wyckoff letter, Site symmetry, Coordinates (1/2,1/2,0)+

4 *i* *m* (1) x , 0 , z
(2) -x , 0 , -z
(3) 1/2 + x , 1/2 , z
(4) 1/2 - x , 1/2 , -z

```
> O4[1]:=[O4x,1/2,O4z];  O4[2]:= [1-O4[1][1],O4[1][2],-O4[1][3]+1];
  O4[3]:=[O4[1][1]+1/2,O4[1][2]-1/2,O4[1][3]];
  O4[4]:=[-O4[1][1]+1/2,O4[1][2]-1/2,-O4[1][3]+1];
```

$$O4_1 := \left[O4x, \frac{1}{2}, O4z \right]$$

$$O4_2 := \left[1 - O4x, \frac{1}{2}, -O4z + 1 \right]$$

$$O4_3 := \left[O4x + \frac{1}{2}, 0, O4z \right]$$

$$O4_4 := \left[-O4x + \frac{1}{2}, 0, -O4z + 1 \right]$$

The O3 oxygen atoms are at the following positions within the C 1 2/*m* 1 space group (s.g. No. 12; unique axis *b*):

Multplicity, Wyckoff letter, Site symmetry, Coordinates (1/2,1/2,0)+

8 *j* 1 (1) x , y , z
(2) -x , y , -z
(3) -x , - y , - z
(4) x , -y , z
(5) 1/2 + x , 1/2 + y , z
(6) 1/2 - x , 1/2 + y , -z
(7) 1/2 - x , 1/2 - y , -z
(8) 1/2 + x , 1/2 - y , z

```
> O3[1]:=[O3x,O3y,O3z];  O3[2]:= [-O3[1][1]+1,O3[1][2],-O3[1][3]+1];
  O3[3]:=[-O3[1][1]+1,-O3[1][2]+1,-O3[1][3]+1];
  O3[4]:=[O3[1][1],-O3[1][2]+1,O3[1][3]];
  O3[5]:=[O3[1][1]+1/2,O3[1][2]+1/2,O3[1][3]];
  O3[6]:=[1/2-O3[1][1],1/2+O3[1][2],-O3[1][3]+1];
  O3[7]:=[1/2-O3[1][1],1/2-O3[1][2],-O3[1][3]+1];
  O3[8]:=[1/2+O3[1][1],1/2-O3[1][2],O3[1][3]];
```

$$O3_1 := [O3x, O3y, O3z]$$

$$O3_2 := [-O3x + 1, O3y, -O3z + 1]$$

$$O3_3 := [-O3x + 1, -O3y + 1, -O3z + 1]$$

$$O3_4 := [O3x, -O3y + 1, O3z]$$

$$O3_5 := \left[O3x + \frac{1}{2}, O3y + \frac{1}{2}, O3z \right]$$

$$O3_6 := \left[\frac{1}{2} - O3x, O3y + \frac{1}{2}, -O3z + 1 \right]$$

$$O3_7 := \left[\frac{1}{2} - O3x, \frac{1}{2} - O3y, -O3z + 1 \right]$$

$$O3_8 := \left[O3x + \frac{1}{2}, \frac{1}{2} - O3y, O3z \right]$$

The T cations are at the following positions within the C 1 2/*m* 1 space group (s.g. No. 12; unique axis *b*):

Multplicity, Wyckoff letter, Site symmetry, Coordinates (1/2,1/2,0)+

8 *j* 1 (1) x , y , z
(2) -x , y , -z
(3) -x , - y , - z
(4) x , -y , z
(5) 1/2 + x , 1/2 + y , z
(6) 1/2 - x , 1/2 + y , -z
(7) 1/2 - x , 1/2 - y , -z
(8) 1/2 + x , 1/2 - y , z

```
> T[1]:=[Tx,Ty,Tz];
  T[2]:= [-T[1][1]+1,T[1][2],-T[1][3]+1];
  T[3]:=[-T[1][1]+1,-T[1][2]+1,-T[1][3]+1];
  T[4]:=[T[1][1],-T[1][2]+1,T[1][3]];
  T[5]:=[T[1][1]+1/2,T[1][2]+1/2,T[1][3]];
  T[6]:=[1/2-T[1][1],1/2+T[1][2],-T[1][3]+1];
  T[7]:=[1/2-T[1][1],1/2-T[1][2],-T[1][3]+1];
  T[8]:=[1/2+T[1][1],1/2-T[1][2],T[1][3]];
```

$$T_1 := [Tx, Ty, Tz]$$

$$T_2 := [-Tx + 1, Ty, -Tz + 1]$$

$$T_3 := [-Tx + 1, -Ty + 1, -Tz + 1]$$

$$T_4 := [Tx, -Ty + 1, Tz]$$

$$T_5 := \left[Tx + \frac{1}{2}, Ty + \frac{1}{2}, Tz\right]$$

$$T_6 := \left[\frac{1}{2} - Tx, Ty + \frac{1}{2}, -Tz + 1\right]$$

$$T_7 := \left[\frac{1}{2} - Tx, \frac{1}{2} - Ty, -Tz + 1\right]$$

$$T_8 := \left[Tx + \frac{1}{2}, \frac{1}{2} - Ty, Tz\right]$$

The O1 oxygen atoms are at the following positions within the C 1 2/*m* 1 space group (s.g. No. 12; unique axis *b*):

Multplicity, Wyckoff letter, Site symmetry, Coordinates (1/2,1/2,0)+

4 *i* *m* (1) x , 0 , z
(2) -x , 0 , -z
(3) 1/2 + x , 1/2 , z
(4) 1/2 - x , 1/2 , -z

```
> O1[1]:=[O1x,0,O1z];  O1[2]:= [-O1[1][1]+1,O1[1][2],-O1[1][3]+1];
  O1[3]:=[1/2+O1[1][1],1/2,O1[1][3]];
  O1[4]:=[1/2-O1[1][1],1/2,-O1[1][3]+1];
```

$$O1_1 := [O1x, 0, O1z]$$

$$O1_2 := [-O1x + 1, 0, -O1z + 1]$$

$$O1_3 := \left[\frac{1}{2} + O1x, \frac{1}{2}, O1z\right]$$

$$O1_4 := \left[\frac{1}{2} - O1x, \frac{1}{2}, -O1z + 1\right]$$

The O2 oxygen atoms are at the following positions within the C 1 2/*m* 1 space group (s.g. No. 12; unique axis *b*):

Multplicity, Wyckoff letter, Site symmetry, Coordinates (1/2,1/2,0)+

8	*j*	1	(1)	x	y	z
			(2)	-x	y	-z
			(3)	-x	-y	-z
			(4)	x	-y	z
			(5)	1/2 + x	1/2 + y	z
			(6)	1/2 - x	1/2 + y	-z
			(7)	1/2 - x	1/2 - y	-z
			(8)	1/2 + x	1/2 - y	z

```
> O2[1]:=[O2x,O2y,O2z];        O2[2]:= [-O2[1][1]+1,O2[1][2],-O2[1][3]+1];
  O2[3]:=[-O2[1][1]+1,-O2[1][2]+1,-O2[1][3]+1];
  O2[4]:=[O2[1][1],-O2[1][2]+1,O2[1][3]];
  O2[5]:=[O2[1][1]+1/2,O2[1][2]+1/2,O2[1][3]];
  O2[6]:=[1/2-O2[1][1],1/2+O2[1][2],-O2[1][3]+1];
  O2[7]:=[1/2-O2[1][1],1/2-O2[1][2],-O2[1][3]+1];
  O2[8]:=[1/2+O2[1][1],1/2-O2[1][2],O2[1][3]];
```

$$O2_1 := [O2x, O2y, O2z]$$

$$O2_2 := [-O2x + 1, O2y, -O2z + 1]$$

$$O2_3 := [-O2x + 1, -O2y + 1, -O2z + 1]$$

$$O2_4 := [O2x, -O2y + 1, O2z]$$

$$O2_5 := \left[O2x + \frac{1}{2}, O2y + \frac{1}{2}, O2z\right]$$

$$O2_6 := \left[\frac{1}{2} - O2x, O2y + \frac{1}{2}, -O2z + 1\right]$$

$$O2_7 := \left[\frac{1}{2} - O2x, \frac{1}{2} - O2y, -O2z + 1\right]$$

$$O2_8 := \left[O2x + \frac{1}{2}, \frac{1}{2} - O2y, O2z\right]$$

```
> R[120] := [[-1/2,-3/2,0],[1/2,-1/2,0],[0,0,1]];
```

$$R_{120} := \left[\left[\frac{-1}{2}, \frac{-3}{2}, 0\right], \left[\frac{1}{2}, \frac{-1}{2}, 0\right], [0, 0, 1]\right]$$

```
> R[-120] := inverse(R[120]);
```

$$R_{-120} := \begin{bmatrix} \frac{-1}{2} & \frac{3}{2} & 0 \\ \frac{-1}{2} & \frac{-1}{2} & 0 \\ 0 & 0 & 1 \end{bmatrix}$$

Transformation to a metric orthogonal **abc** coordinate system with cation M1 at (0,0,0):

```
> Tometric := [[1,0,-c1M/a1M*cos(pi-beta1M)],[0,1,0],[0,0,1]];
```

$$Tometric := \left[\left[1, 0, -\frac{c1M \cos(\pi - beta1M)}{a1M}\right], [0, 1, 0], [0, 0, 1]\right]$$

```
> metricTo1M := inverse(Tometric);
```

$$metricTo1M := \begin{bmatrix} 1 & 0 & \frac{c1M \cos(\pi - beta1M)}{a1M} \\ 0 & 1 & 0 \\ 0 & 0 & 1 \end{bmatrix}$$

```
> for i from 1  to 8 do  O2metric[i]:= evalm(Tometric&*O2[i]
  +[1/2*c1M/a1M*cos(pi-beta1M),0,-1/2]) od:
> for i from 1  to 8 do  Tmetric[i]:= evalm(Tometric&*T[i]
```

```
  +[1/2*c1M/a1M*cos(pi-beta1M),0,-1/2]) od:
> for i from 1  to 4 do  O1metric[i]:= evalm(Tometric&*O1[i]
  +[1/2*c1M/a1M*cos(pi-beta1M),0,-1/2]) od;
```

$$O1metric_1 := \left[O1x - \frac{c1M\cos(\pi - beta1M)\,O1z}{a1M} + \frac{1}{2}\frac{c1M\cos(\pi - beta1M)}{a1M},\ 0,\ O1z - \frac{1}{2} \right]$$

$$O1metric_2 := \left[-O1x + 1 - \frac{c1M\cos(\pi - beta1M)\,(-O1z + 1)}{a1M} + \frac{1}{2}\frac{c1M\cos(\pi - beta1M)}{a1M},\ 0,\ -O1z + \frac{1}{2} \right]$$

$$O1metric_3 := \left[\frac{1}{2} + O1x - \frac{c1M\cos(\pi - beta1M)\,O1z}{a1M} + \frac{1}{2}\frac{c1M\cos(\pi - beta1M)}{a1M},\ \frac{1}{2},\ O1z - \frac{1}{2} \right]$$

$$O1metric_4 := \left[\frac{1}{2} - O1x - \frac{c1M\cos(\pi - beta1M)\,(-O1z + 1)}{a1M} + \frac{1}{2}\frac{c1M\cos(\pi - beta1M)}{a1M},\ \frac{1}{2},\ -O1z + \frac{1}{2} \right]$$

```
> for i from 1  to 4 do  O4metric[i]:= evalm(Tometric&*O4[i]
  +[1/2*c1M/a1M*cos(pi-beta1M),0,-1/2])  od;
```

$$O4metric_1 := \left[O4x - \frac{c1M\cos(\pi - beta1M)\,O4z}{a1M} + \frac{1}{2}\frac{c1M\cos(\pi - beta1M)}{a1M},\ \frac{1}{2},\ O4z - \frac{1}{2} \right]$$

$$O4metric_2 := \left[1 - O4x - \frac{c1M\cos(\pi - beta1M)\,(-O4z + 1)}{a1M} + \frac{1}{2}\frac{c1M\cos(\pi - beta1M)}{a1M},\ \frac{1}{2},\ -O4z + \frac{1}{2} \right]$$

$$O4metric_3 := \left[O4x + \frac{1}{2} - \frac{c1M\cos(\pi - beta1M)\,O4z}{a1M} + \frac{1}{2}\frac{c1M\cos(\pi - beta1M)}{a1M},\ 0,\ O4z - \frac{1}{2} \right]$$

$$O4metric_4 := \left[-O4x + \frac{1}{2} - \frac{c1M\cos(\pi - beta1M)\,(-O4z + 1)}{a1M} + \frac{1}{2}\frac{c1M\cos(\pi - beta1M)}{a1M},\ 0,\ -O4z + \frac{1}{2} \right]$$

```
> for i from 1  to 8 do  O3metric[i]:= evalm(Tometric&*O3[i]
  +[1/2*c1M/a1M*cos(pi-beta1M),0,-1/2]) od;
```

$$O3metric_1 := \left[O3x - \frac{c1M\cos(\pi - beta1M)\,O3z}{a1M} + \frac{1}{2}\frac{c1M\cos(\pi - beta1M)}{a1M},\ O3y,\ O3z - \frac{1}{2} \right]$$

$$O3metric_2 := \left[-O3x + 1 - \frac{c1M\cos(\pi - beta1M)\,(-O3z + 1)}{a1M} + \frac{1}{2}\frac{c1M\cos(\pi - beta1M)}{a1M},\ O3y,\ -O3z + \frac{1}{2} \right]$$

$$O3metric_3 := \left[-O3x + 1 - \frac{c1M\cos(\pi - beta1M)\,(-O3z + 1)}{a1M} + \frac{1}{2}\frac{c1M\cos(\pi - beta1M)}{a1M},\ -O3y + 1,\ -O3z + \frac{1}{2} \right]$$

$$O3metric_4 := \left[O3x - \frac{c1M\cos(\pi - beta1M)\,O3z}{a1M} + \frac{1}{2}\frac{c1M\cos(\pi - beta1M)}{a1M},\ -O3y + 1,\ O3z - \frac{1}{2} \right]$$

$$O3metric_5 := \left[O3x + \frac{1}{2} - \frac{c1M\cos(\pi - beta1M)\,O3z}{a1M} + \frac{1}{2}\frac{c1M\cos(\pi - beta1M)}{a1M},\ O3y + \frac{1}{2},\ O3z - \frac{1}{2} \right]$$

$$O3metric_6 := \left[\frac{1}{2} - O3x - \frac{c1M\cos(\pi - beta1M)\,(-O3z + 1)}{a1M} + \frac{1}{2}\frac{c1M\cos(\pi - beta1M)}{a1M},\ O3y + \frac{1}{2},\ -O3z + \frac{1}{2} \right]$$

$$O3metric_7 := \left[\frac{1}{2} - O3x - \frac{c1M\cos(\pi - beta1M)\,(-O3z + 1)}{a1M} + \frac{1}{2}\frac{c1M\cos(\pi - beta1M)}{a1M},\ \frac{1}{2} - O3y,\ -O3z + \frac{1}{2} \right]$$

$$O3metric_8 := \left[O3x + \frac{1}{2} - \frac{c1M\cos(\pi - beta1M)\,O3z}{a1M} + \frac{1}{2}\frac{c1M\cos(\pi - beta1M)}{a1M},\ \frac{1}{2} - O3y,\ O3z - \frac{1}{2} \right]$$

```
> for i from 1  to 6 do  M2metric[i]:= evalm(Tometric&*M2[i]
  +[1/2*c1M/a1M*cos(pi-beta1M),0,-1/2]) od:
> for i from 1  to 4 do  Kmetric[i]:= evalm(Tometric&*K[i]
  +[1/2*c1M/a1M*cos(pi-beta1M),0,-1/2]) od:
> for i from 1  to 3 do  M1metric[i]:= evalm(Tometric&*M1[i]
  +[1/2*c1M/a1M*cos(pi-beta1M),0,-1/2]) od;
```

$$M1metric_1 := [0, 0, 0]$$

$$M1metric_2 := \left[\frac{1}{2}, \frac{1}{2}, 0 \right]$$

$$M1metric_3 := \left[\frac{3}{2}, \frac{1}{2}, 0 \right]$$

```
> layer[1] :=
  [Kmetric[1],Kmetric[2],Kmetric[3],Kmetric[4],M1metric[1],M1metric[2],M1metric[3],M2metric
  [1],M2metric[2],M2metric[3],M2metric[4],M2metric[5],M2metric[6],O4metric[1],O4metric[2],O
  4metric[3],O4metric[4],O3metric[1],O3metric[2],O3metric[3],O3metric[4],O3metric[5],O3metr
  ic[6],O3metric[7],O3metric[8],Tmetric[1],Tmetric[2],Tmetric[3],Tmetric[4],Tmetric[5],Tmet
  ric[6],Tmetric[7],Tmetric[8],O1metric[1],O1metric[2],O1metric[3],O1metric[4],O2metric[1],
  O2metric[2],O2metric[3],O2metric[4],O2metric[5],O2metric[6],O2metric[7],O2metric[8]];
```

$$layer_1 := [Kmetric_1, Kmetric_2, Kmetric_3, Kmetric_4, M1metric_1, M1metric_2, M1metric_3, M2metric_1, M2metric_2, M2metric_3, M2metric_4, M2metric_5, M2metric_6, O4metric_1, O4metric_2, O4metric_3, O4metric_4, O3metric_1, O3metric_2, O3metric_3, O3metric_4, O3metric_5, O3metric_6, O3metric_7, O3metric_8, Tmetric_1, Tmetric_2, Tmetric_3, Tmetric_4, Tmetric_5, Tmetric_6, Tmetric_7, Tmetric_8, O1metric_1, O1metric_2, O1metric_3, O1metric_4, O2metric_1, O2metric_2, O2metric_3, O2metric_4, O2metric_5, O2metric_6, O2metric_7, O2metric_8]$$

```
> Zadjust := [[1,0,0],[0,1,0],[0,0,1/3]];
```

$$Zadjust := \left[[1, 0, 0], [0, 1, 0], \left[0, 0, \frac{1}{3}\right]\right]$$

```
> print(M1metric[1]);print(M1metric[2]);print(M1metric[3]);
```

$$[0, 0, 0]$$

$$\left[\frac{1}{2}, \frac{1}{2}, 0\right]$$

$$\left[\frac{3}{2}, \frac{1}{2}, 0\right]$$

```
> print(M2metric[1]);print(M2metric[2]);print(M2metric[5]);print(M2metric[6]);
```

$$[0, yM2, 0]$$

$$[0, -yM2 + 1, 0]$$

$$\left[\frac{1}{2}\frac{c1M\cos(\pi - beta1M)}{a1M}, 0, \frac{-1}{2}\right]$$

$$\left[\frac{1}{2}\frac{c1M\cos(\pi - beta1M)}{a1M}, 0, \frac{-1}{2}\right]$$

```
>
>
>
> for i from 1 to 45 do layer_1_coordinates[i] :=
  evalm(Zadjust&*layer[1][i]+[0,-1/3*(1/2-1/2*c1M/a1M*cos(pi-beta1M)),0]) od:
> aNbNcN_To_Hexagonal := [[0,2,0],[-1,1,0],[0,0,1]];
```

$$aNbNcN\_To\_Hexagonal := [[0, 2, 0], [-1, 1, 0], [0, 0, 1]]$$

```
> Hexagonal_To_aNbNcN := inverse(aNbNcN_To_Hexagonal);
```

$$Hexagonal\_To\_aNbNcN := \begin{bmatrix} \frac{1}{2} & -1 & 0 \\ \frac{1}{2} & 0 & 0 \\ 0 & 0 & 1 \end{bmatrix}$$

```
> for i from 1 to 45 do layer_1_coordinates3Tsg151[i] :=evalm(
  aNbNcN_To_Hexagonal&*layer_1_coordinates[i]) od;
```

$$layer\_1\_coordinates3Tsg151_1 := \left[\frac{2}{3} + \frac{1}{3}\frac{c1M\cos(\pi - beta1M)}{a1M}, \frac{2}{3}\frac{c1M\cos(\pi - beta1M)}{a1M} + \frac{1}{3}, \frac{1}{6}\right]$$

$$layer\_1\_coordinates3Tsg151_2 := \left[-\frac{1}{3} + \frac{1}{3}\frac{c1M\cos(\pi - beta1M)}{a1M}, \frac{2}{3}\frac{c1M\cos(\pi - beta1M)}{a1M} + \frac{1}{3}, \frac{1}{6}\right]$$

$$layer\_1\_coordinates3Tsg151_3 := \left[-\frac{1}{3} + \frac{1}{3}\frac{c1M\cos(\pi - beta1M)}{a1M}, -\frac{2}{3} + \frac{2}{3}\frac{c1M\cos(\pi - beta1M)}{a1M}, \frac{1}{6}\right]$$

$$layer\_1\_coordinates3Tsg151_4 := \left[-\frac{1}{3} + \frac{1}{3}\frac{c1M\cos(\pi - beta1M)}{a1M}, -\frac{2}{3} - \frac{1}{3}\frac{c1M\cos(\pi - beta1M)}{a1M}, \frac{-1}{6}\right]$$

$$layer\_1\_coordinates3Tsg151_5 := \left[-\frac{1}{3}+\frac{1}{3}\frac{c1M\cos(\pi-beta1M)}{a1M}, -\frac{1}{6}+\frac{1}{6}\frac{c1M\cos(\pi-beta1M)}{a1M}, 0\right]$$

$$layer\_1\_coordinates3Tsg151_6 := \left[\frac{2}{3}+\frac{1}{3}\frac{c1M\cos(\pi-beta1M)}{a1M}, -\frac{1}{6}+\frac{1}{6}\frac{c1M\cos(\pi-beta1M)}{a1M}, 0\right]$$

$$layer\_1\_coordinates3Tsg151_7 := \left[\frac{2}{3}+\frac{1}{3}\frac{c1M\cos(\pi-beta1M)}{a1M}, -\frac{7}{6}+\frac{1}{6}\frac{c1M\cos(\pi-beta1M)}{a1M}, 0\right]$$

$$layer\_1\_coordinates3Tsg151_8 := \left[2\,yM2-\frac{1}{3}+\frac{1}{3}\frac{c1M\cos(\pi-beta1M)}{a1M}, yM2-\frac{1}{6}+\frac{1}{6}\frac{c1M\cos(\pi-beta1M)}{a1M}, 0\right]$$

$$layer\_1\_coordinates3Tsg151_9 := \left[-2\,yM2+\frac{5}{3}+\frac{1}{3}\frac{c1M\cos(\pi-beta1M)}{a1M}, -yM2+\frac{5}{6}+\frac{1}{6}\frac{c1M\cos(\pi-beta1M)}{a1M}, 0\right]$$

$$layer\_1\_coordinates3Tsg151_{10} := \left[\frac{2}{3}+2\,yM2+\frac{1}{3}\frac{c1M\cos(\pi-beta1M)}{a1M}, yM2-\frac{1}{6}+\frac{1}{6}\frac{c1M\cos(\pi-beta1M)}{a1M}, 0\right]$$

$$layer\_1\_coordinates3Tsg151_{11} := \left[\frac{2}{3}-2\,yM2+\frac{1}{3}\frac{c1M\cos(\pi-beta1M)}{a1M}, -\frac{1}{6}-yM2+\frac{1}{6}\frac{c1M\cos(\pi-beta1M)}{a1M}, 0\right]$$

$$layer\_1\_coordinates3Tsg151_{12} := \left[-\frac{1}{3}+\frac{1}{3}\frac{c1M\cos(\pi-beta1M)}{a1M}, -\frac{1}{3}\frac{c1M\cos(\pi-beta1M)}{a1M}-\frac{1}{6}, \frac{-1}{6}\right]$$

$$layer\_1\_coordinates3Tsg151_{13} := \left[-\frac{1}{3}+\frac{1}{3}\frac{c1M\cos(\pi-beta1M)}{a1M}, -\frac{1}{3}\frac{c1M\cos(\pi-beta1M)}{a1M}-\frac{1}{6}, \frac{-1}{6}\right]$$

$$layer\_1\_coordinates3Tsg151_{14} := \left[\frac{2}{3}+\frac{1}{3}\frac{c1M\cos(\pi-beta1M)}{a1M}, -O4x+\frac{c1M\cos(\pi-beta1M)\,O4z}{a1M}-\frac{1}{3}\frac{c1M\cos(\pi-beta1M)}{a1M}+\frac{1}{3}, \frac{1}{3}\,O4z-\frac{1}{6}\right]$$

$$layer\_1\_coordinates3Tsg151_{15} := \left[\frac{2}{3}+\frac{1}{3}\frac{c1M\cos(\pi-beta1M)}{a1M}, -\frac{2}{3}+O4x+\frac{c1M\cos(\pi-beta1M)\,(-O4z+1)}{a1M}-\frac{1}{3}\frac{c1M\cos(\pi-beta1M)}{a1M}, -\frac{1}{3}\,O4z+\frac{1}{6}\right]$$

$$layer\_1\_coordinates3Tsg151_{16} := \left[-\frac{1}{3}+\frac{1}{3}\frac{c1M\cos(\pi-beta1M)}{a1M}, -O4x-\frac{2}{3}+\frac{c1M\cos(\pi-beta1M)\,O4z}{a1M}-\frac{1}{3}\frac{c1M\cos(\pi-beta1M)}{a1M}, \frac{1}{3}\,O4z-\frac{1}{6}\right]$$

$$layer\_1\_coordinates3Tsg151_{17} := \left[-\frac{1}{3}+\frac{1}{3}\frac{c1M\cos(\pi-beta1M)}{a1M}, -\frac{2}{3}+O4x+\frac{c1M\cos(\pi-beta1M)\,(-O4z+1)}{a1M}-\frac{1}{3}\frac{c1M\cos(\pi-beta1M)}{a1M}, -\frac{1}{3}\,O4z+\frac{1}{6}\right]$$

$$layer\_1\_coordinates3Tsg151_{18} := \left[2\,O3y-\frac{1}{3}+\frac{1}{3}\frac{c1M\cos(\pi-beta1M)}{a1M}, -O3x+\frac{c1M\cos(\pi-beta1M)\,O3z}{a1M}-\frac{1}{3}\frac{c1M\cos(\pi-beta1M)}{a1M}+O3y-\frac{1}{6}, \frac{1}{3}\,O3z-\frac{1}{6}\right]$$

$$layer\_1\_coordinates3Tsg151_{19} := \left[2\,O3y-\frac{1}{3}+\frac{1}{3}\frac{c1M\cos(\pi-beta1M)}{a1M}, O3x-\frac{7}{6}+\frac{c1M\cos(\pi-beta1M)\,(-O3z+1)}{a1M}-\frac{1}{3}\frac{c1M\cos(\pi-beta1M)}{a1M}+O3y, -\frac{1}{3}\,O3z+\frac{1}{6}\right]$$

$$layer\_1\_coordinates3Tsg151_{20} := \left[-2\,O3y+\frac{5}{3}+\frac{1}{3}\frac{c1M\cos(\pi-beta1M)}{a1M}, O3x-\frac{1}{6}+\frac{c1M\cos(\pi-beta1M)\,(-O3z+1)}{a1M}-\frac{1}{3}\frac{c1M\cos(\pi-beta1M)}{a1M}-O3y, -\frac{1}{3}\,O3z+\frac{1}{6}\right]$$

$$layer\_1\_coordinates3Tsg151_{21} := \left[-2\,O3y+\frac{5}{3}+\frac{1}{3}\frac{c1M\cos(\pi-beta1M)}{a1M}, -O3x+\frac{c1M\cos(\pi-beta1M)\,O3z}{a1M}-\frac{1}{3}\frac{c1M\cos(\pi-beta1M)}{a1M}-O3y+\frac{5}{6}, \frac{1}{3}\,O3z-\frac{1}{6}\right]$$

$$layer\_1\_coordinates3Tsg151_{22} := \left[2\,O3y+\frac{2}{3}+\frac{1}{3}\frac{c1M\cos(\pi-beta1M)}{a1M}, -O3x+\frac{c1M\cos(\pi-beta1M)\,O3z}{a1M}-\frac{1}{3}\frac{c1M\cos(\pi-beta1M)}{a1M}+O3y-\frac{1}{6}, \frac{1}{3}\,O3z-\frac{1}{6}\right]$$

$$layer\_1\_coordinates3Tsg151_{23} := \left[2\,O3y + \frac{2}{3} + \frac{1}{3}\frac{c1M\cos(\pi - beta1M)}{a1M},\ -\frac{1}{6} + O3x + \frac{c1M\cos(\pi - beta1M)\,(-O3z+1)}{a1M} - \frac{1}{3}\frac{c1M\cos(\pi - beta1M)}{a1M} + O3y,\ -\frac{1}{3}O3z + \frac{1}{6}\right]$$

$$layer\_1\_coordinates3Tsg151_{24} := \left[\frac{2}{3} - 2\,O3y + \frac{1}{3}\frac{c1M\cos(\pi - beta1M)}{a1M},\ O3x - \frac{1}{6} + \frac{c1M\cos(\pi - beta1M)\,(-O3z+1)}{a1M} - \frac{1}{3}\frac{c1M\cos(\pi - beta1M)}{a1M} - O3y,\ -\frac{1}{3}O3z + \frac{1}{6}\right]$$

$$layer\_1\_coordinates3Tsg151_{25} := \left[\frac{2}{3} - 2\,O3y + \frac{1}{3}\frac{c1M\cos(\pi - beta1M)}{a1M},\ -O3x - \frac{1}{6} + \frac{c1M\cos(\pi - beta1M)\,O3z}{a1M} - \frac{1}{3}\frac{c1M\cos(\pi - beta1M)}{a1M} - O3y,\ \frac{1}{3}O3z - \frac{1}{6}\right]$$

$$layer\_1\_coordinates3Tsg151_{26} := \left[2\,Ty - \frac{1}{3} + \frac{1}{3}\frac{c1M\cos(\pi - beta1M)}{a1M},\ -Tx + \frac{c1M\cos(\pi - beta1M)\,Tz}{a1M} - \frac{1}{3}\frac{c1M\cos(\pi - beta1M)}{a1M} + Ty - \frac{1}{6},\ \frac{1}{3}Tz - \frac{1}{6}\right]$$

$$layer\_1\_coordinates3Tsg151_{27} := \left[2\,Ty - \frac{1}{3} + \frac{1}{3}\frac{c1M\cos(\pi - beta1M)}{a1M},\ Tx - \frac{7}{6} + \frac{c1M\cos(\pi - beta1M)\,(-Tz+1)}{a1M} - \frac{1}{3}\frac{c1M\cos(\pi - beta1M)}{a1M} + Ty,\ -\frac{1}{3}Tz + \frac{1}{6}\right]$$

$$layer\_1\_coordinates3Tsg151_{28} := \left[-2\,Ty + \frac{5}{3} + \frac{1}{3}\frac{c1M\cos(\pi - beta1M)}{a1M},\ Tx - \frac{1}{6} + \frac{c1M\cos(\pi - beta1M)\,(-Tz+1)}{a1M} - \frac{1}{3}\frac{c1M\cos(\pi - beta1M)}{a1M} - Ty,\ -\frac{1}{3}Tz + \frac{1}{6}\right]$$

$$layer\_1\_coordinates3Tsg151_{29} := \left[-2\,Ty + \frac{5}{3} + \frac{1}{3}\frac{c1M\cos(\pi - beta1M)}{a1M},\ -Tx + \frac{c1M\cos(\pi - beta1M)\,Tz}{a1M} - \frac{1}{3}\frac{c1M\cos(\pi - beta1M)}{a1M} - Ty + \frac{5}{6},\ \frac{1}{3}Tz - \frac{1}{6}\right]$$

$$layer\_1\_coordinates3Tsg151_{30} := \left[2\,Ty + \frac{2}{3} + \frac{1}{3}\frac{c1M\cos(\pi - beta1M)}{a1M},\ -Tx + \frac{c1M\cos(\pi - beta1M)\,Tz}{a1M} - \frac{1}{3}\frac{c1M\cos(\pi - beta1M)}{a1M} + Ty - \frac{1}{6},\ \frac{1}{3}Tz - \frac{1}{6}\right]$$

$$layer\_1\_coordinates3Tsg151_{31} := \left[2\,Ty + \frac{2}{3} + \frac{1}{3}\frac{c1M\cos(\pi - beta1M)}{a1M},\ -\frac{1}{6} + Tx + \frac{c1M\cos(\pi - beta1M)\,(-Tz+1)}{a1M} - \frac{1}{3}\frac{c1M\cos(\pi - beta1M)}{a1M} + Ty,\ -\frac{1}{3}Tz + \frac{1}{6}\right]$$

$$layer\_1\_coordinates3Tsg151_{32} := \left[\frac{2}{3} - 2\,Ty + \frac{1}{3}\frac{c1M\cos(\pi - beta1M)}{a1M},\ Tx - \frac{1}{6} + \frac{c1M\cos(\pi - beta1M)\,(-Tz+1)}{a1M} - \frac{1}{3}\frac{c1M\cos(\pi - beta1M)}{a1M} - Ty,\ -\frac{1}{3}Tz + \frac{1}{6}\right]$$

$$layer\_1\_coordinates3Tsg151_{33} := \left[\frac{2}{3} - 2\,Ty + \frac{1}{3}\frac{c1M\cos(\pi - beta1M)}{a1M},\ -Tx - \frac{1}{6} + \frac{c1M\cos(\pi - beta1M)\,Tz}{a1M} - \frac{1}{3}\frac{c1M\cos(\pi - beta1M)}{a1M} - Ty,\ \frac{1}{3}Tz - \frac{1}{6}\right]$$

$$layer\_1\_coordinates3Tsg151_{34} := \left[-\frac{1}{3} + \frac{1}{3}\frac{c1M\cos(\pi - beta1M)}{a1M},\ -O1x + \frac{c1M\cos(\pi - beta1M)\,O1z}{a1M} - \frac{1}{3}\frac{c1M\cos(\pi - beta1M)}{a1M} - \frac{1}{6},\ \frac{1}{3}O1z - \frac{1}{6}\right]$$

$$layer\_1\_coordinates3Tsg151_{35} := \left[-\frac{1}{3} + \frac{1}{3}\frac{c1M\cos(\pi - beta1M)}{a1M},\ O1x - \frac{7}{6} + \frac{c1M\cos(\pi - beta1M)\,(-O1z+1)}{a1M} - \frac{1}{3}\frac{c1M\cos(\pi - beta1M)}{a1M},\ -\frac{1}{3}O1z + \frac{1}{6}\right]$$

$$layer\_1\_coordinates3Tsg151_{36} := \left[\frac{2}{3} + \frac{1}{3}\frac{c1M\cos(\pi - beta1M)}{a1M},\ -O1x + \frac{c1M\cos(\pi - beta1M)\,O1z}{a1M} - \frac{1}{3}\frac{c1M\cos(\pi - beta1M)}{a1M} - \frac{1}{6},\ \frac{1}{3}O1z - \frac{1}{6}\right]$$

$$layer\_1\_coordinates3Tsg151_{37} :=$$

$$\left[\frac{2}{3}+\frac{1}{3}\frac{c1M\cos(\pi-beta1M)}{a1M},-\frac{1}{6}+O1x+\frac{c1M\cos(\pi-beta1M)\,(-O1z+1)}{a1M}-\frac{1}{3}\frac{c1M\cos(\pi-beta1M)}{a1M},-\frac{1}{3}O1z+\frac{1}{6}\right]$$

$layer\_1\_coordinates3Tsg151_{38} :=$

$$\left[2\,O2y-\frac{1}{3}+\frac{1}{3}\frac{c1M\cos(\pi-beta1M)}{a1M},-O2x+\frac{c1M\cos(\pi-beta1M)\,O2z}{a1M}-\frac{1}{3}\frac{c1M\cos(\pi-beta1M)}{a1M}+O2y-\frac{1}{6},\frac{1}{3}O2z-\frac{1}{6}\right]$$

$layer\_1\_coordinates3Tsg151_{39} :=\left[2\,O2y-\frac{1}{3}+\frac{1}{3}\frac{c1M\cos(\pi-beta1M)}{a1M},\right.$

$$\left.O2x-\frac{7}{6}+\frac{c1M\cos(\pi-beta1M)\,(-O2z+1)}{a1M}-\frac{1}{3}\frac{c1M\cos(\pi-beta1M)}{a1M}+O2y,-\frac{1}{3}O2z+\frac{1}{6}\right]$$

$layer\_1\_coordinates3Tsg151_{40} :=\left[-2\,O2y+\frac{5}{3}+\frac{1}{3}\frac{c1M\cos(\pi-beta1M)}{a1M},\right.$

$$\left.O2x-\frac{1}{6}+\frac{c1M\cos(\pi-beta1M)\,(-O2z+1)}{a1M}-\frac{1}{3}\frac{c1M\cos(\pi-beta1M)}{a1M}-O2y,-\frac{1}{3}O2z+\frac{1}{6}\right]$$

$layer\_1\_coordinates3Tsg151_{41} :=$

$$\left[-2\,O2y+\frac{5}{3}+\frac{1}{3}\frac{c1M\cos(\pi-beta1M)}{a1M},-O2x+\frac{c1M\cos(\pi-beta1M)\,O2z}{a1M}-\frac{1}{3}\frac{c1M\cos(\pi-beta1M)}{a1M}-O2y+\frac{5}{6},\frac{1}{3}O2z-\frac{1}{6}\right]$$

$layer\_1\_coordinates3Tsg151_{42} :=$

$$\left[2\,O2y+\frac{2}{3}+\frac{1}{3}\frac{c1M\cos(\pi-beta1M)}{a1M},-O2x+\frac{c1M\cos(\pi-beta1M)\,O2z}{a1M}-\frac{1}{3}\frac{c1M\cos(\pi-beta1M)}{a1M}+O2y-\frac{1}{6},\frac{1}{3}O2z-\frac{1}{6}\right]$$

$layer\_1\_coordinates3Tsg151_{43} :=\left[2\,O2y+\frac{2}{3}+\frac{1}{3}\frac{c1M\cos(\pi-beta1M)}{a1M},\right.$

$$\left.-\frac{1}{6}+O2x+\frac{c1M\cos(\pi-beta1M)\,(-O2z+1)}{a1M}-\frac{1}{3}\frac{c1M\cos(\pi-beta1M)}{a1M}+O2y,-\frac{1}{3}O2z+\frac{1}{6}\right]$$

$layer\_1\_coordinates3Tsg151_{44} :=\left[\frac{2}{3}-2\,O2y+\frac{1}{3}\frac{c1M\cos(\pi-beta1M)}{a1M},\right.$

$$\left.O2x-\frac{1}{6}+\frac{c1M\cos(\pi-beta1M)\,(-O2z+1)}{a1M}-\frac{1}{3}\frac{c1M\cos(\pi-beta1M)}{a1M}-O2y,-\frac{1}{3}O2z+\frac{1}{6}\right]$$

$layer\_1\_coordinates3Tsg151_{45} :=$

$$\left[\frac{2}{3}-2\,O2y+\frac{1}{3}\frac{c1M\cos(\pi-beta1M)}{a1M},-O2x-\frac{1}{6}+\frac{c1M\cos(\pi-beta1M)\,O2z}{a1M}-\frac{1}{3}\frac{c1M\cos(\pi-beta1M)}{a1M}-O2y,\frac{1}{3}O2z-\frac{1}{6}\right]$$

```
> for i from 1 to 45 do layer_2_coordinates[i]
  :=evalm(R[120]&*Zadjust&*layer[1][i]+[1/2*(1/2-1/2*c1M/a1M*cos(pi-beta1M)),1/6*(1/2-1/2*c
  1M/a1M*cos(pi-beta1M)),1/3]) od:
> for i from 1 to 45 do layer_2_coordinates3Tsg151[i] :=evalm(
  aNbNcN_To_Hexagonal&*layer_2_coordinates[i]) od;
```

$$layer\_2\_coordinates3Tsg151_1 :=\left[-\frac{2}{3}\frac{c1M\cos(\pi-beta1M)}{a1M}-\frac{1}{3},\frac{1}{3}-\frac{1}{3}\frac{c1M\cos(\pi-beta1M)}{a1M},\frac{1}{2}\right]$$

$$layer\_2\_coordinates3Tsg151_2 :=\left[-\frac{2}{3}\frac{c1M\cos(\pi-beta1M)}{a1M}-\frac{1}{3},-\frac{2}{3}-\frac{1}{3}\frac{c1M\cos(\pi-beta1M)}{a1M},\frac{1}{2}\right]$$

$$layer\_2\_coordinates3Tsg151_3 :=\left[\frac{2}{3}-\frac{2}{3}\frac{c1M\cos(\pi-beta1M)}{a1M},\frac{1}{3}-\frac{1}{3}\frac{c1M\cos(\pi-beta1M)}{a1M},\frac{1}{2}\right]$$

$$layer\_2\_coordinates3Tsg151_4 :=\left[\frac{2}{3}+\frac{1}{3}\frac{c1M\cos(\pi-beta1M)}{a1M},\frac{2}{3}\frac{c1M\cos(\pi-beta1M)}{a1M}+\frac{1}{3},\frac{1}{6}\right]$$

$$layer\_2\_coordinates3Tsg151_5 :=\left[\frac{1}{6}-\frac{1}{6}\frac{c1M\cos(\pi-beta1M)}{a1M},-\frac{1}{6}+\frac{1}{6}\frac{c1M\cos(\pi-beta1M)}{a1M},\frac{1}{3}\right]$$

$$layer\_2\_coordinates3Tsg151_6 :=\left[\frac{1}{6}-\frac{1}{6}\frac{c1M\cos(\pi-beta1M)}{a1M},\frac{5}{6}+\frac{1}{6}\frac{c1M\cos(\pi-beta1M)}{a1M},\frac{1}{3}\right]$$

$$layer\_2\_coordinates3Tsg151_7 :=\left[\frac{7}{6}-\frac{1}{6}\frac{c1M\cos(\pi-beta1M)}{a1M},\frac{11}{6}+\frac{1}{6}\frac{c1M\cos(\pi-beta1M)}{a1M},\frac{1}{3}\right]$$

$$layer\_2\_coordinates3Tsg151_{8} := \left[-yM2 + \frac{1}{6} - \frac{1}{6}\frac{c1M\cos(\pi - beta1M)}{a1M},\ yM2 - \frac{1}{6} + \frac{1}{6}\frac{c1M\cos(\pi - beta1M)}{a1M},\ \frac{1}{3} \right]$$

$$layer\_2\_coordinates3Tsg151_{9} := \left[yM2 - \frac{5}{6} - \frac{1}{6}\frac{c1M\cos(\pi - beta1M)}{a1M},\ -yM2 + \frac{5}{6} + \frac{1}{6}\frac{c1M\cos(\pi - beta1M)}{a1M},\ \frac{1}{3} \right]$$

$$layer\_2\_coordinates3Tsg151_{10} := \left[-yM2 + \frac{1}{6} - \frac{1}{6}\frac{c1M\cos(\pi - beta1M)}{a1M},\ \frac{5}{6} + yM2 + \frac{1}{6}\frac{c1M\cos(\pi - beta1M)}{a1M},\ \frac{1}{3} \right]$$

$$layer\_2\_coordinates3Tsg151_{11} := \left[yM2 + \frac{1}{6} - \frac{1}{6}\frac{c1M\cos(\pi - beta1M)}{a1M},\ -yM2 + \frac{5}{6} + \frac{1}{6}\frac{c1M\cos(\pi - beta1M)}{a1M},\ \frac{1}{3} \right]$$

$$layer\_2\_coordinates3Tsg151_{12} := \left[\frac{1}{3}\frac{c1M\cos(\pi - beta1M)}{a1M} + \frac{1}{6},\ \frac{2}{3}\frac{c1M\cos(\pi - beta1M)}{a1M} - \frac{1}{6},\ \frac{1}{6} \right]$$

$$layer\_2\_coordinates3Tsg151_{13} := \left[\frac{1}{3}\frac{c1M\cos(\pi - beta1M)}{a1M} + \frac{1}{6},\ \frac{2}{3}\frac{c1M\cos(\pi - beta1M)}{a1M} - \frac{1}{6},\ \frac{1}{6} \right]$$

$$layer\_2\_coordinates3Tsg151_{14} := \left[O4x - \frac{c1M\cos(\pi - beta1M)\,O4z}{a1M} + \frac{1}{3}\frac{c1M\cos(\pi - beta1M)}{a1M} - \frac{1}{3},\right.$$
$$\left. O4x - \frac{c1M\cos(\pi - beta1M)\,O4z}{a1M} + \frac{2}{3}\frac{c1M\cos(\pi - beta1M)}{a1M} + \frac{1}{3},\ \frac{1}{3}O4z + \frac{1}{6} \right]$$

$$layer\_2\_coordinates3Tsg151_{15} := \left[\frac{2}{3} - O4x - \frac{c1M\cos(\pi - beta1M)\,(-O4z + 1)}{a1M} + \frac{1}{3}\frac{c1M\cos(\pi - beta1M)}{a1M},\right.$$
$$\left. \frac{4}{3} - O4x - \frac{c1M\cos(\pi - beta1M)\,(-O4z + 1)}{a1M} + \frac{2}{3}\frac{c1M\cos(\pi - beta1M)}{a1M},\ -\frac{1}{3}O4z + \frac{1}{2} \right]$$

$$layer\_2\_coordinates3Tsg151_{16} := \left[O4x + \frac{2}{3} - \frac{c1M\cos(\pi - beta1M)\,O4z}{a1M} + \frac{1}{3}\frac{c1M\cos(\pi - beta1M)}{a1M},\right.$$
$$\left. O4x - \frac{c1M\cos(\pi - beta1M)\,O4z}{a1M} + \frac{2}{3}\frac{c1M\cos(\pi - beta1M)}{a1M} + \frac{1}{3},\ \frac{1}{3}O4z + \frac{1}{6} \right]$$

$$layer\_2\_coordinates3Tsg151_{17} := \left[\frac{2}{3} - O4x - \frac{c1M\cos(\pi - beta1M)\,(-O4z + 1)}{a1M} + \frac{1}{3}\frac{c1M\cos(\pi - beta1M)}{a1M},\right.$$
$$\left. -O4x - \frac{c1M\cos(\pi - beta1M)\,(-O4z + 1)}{a1M} + \frac{2}{3}\frac{c1M\cos(\pi - beta1M)}{a1M} + \frac{1}{3},\ -\frac{1}{3}O4z + \frac{1}{2} \right]$$

$$layer\_2\_coordinates3Tsg151_{18} := \left[O3x - \frac{c1M\cos(\pi - beta1M)\,O3z}{a1M} + \frac{1}{3}\frac{c1M\cos(\pi - beta1M)}{a1M} - O3y + \frac{1}{6},\right.$$
$$\left. O3x - \frac{c1M\cos(\pi - beta1M)\,O3z}{a1M} + \frac{2}{3}\frac{c1M\cos(\pi - beta1M)}{a1M} + O3y - \frac{1}{6},\ \frac{1}{3}O3z + \frac{1}{6} \right]$$

$$layer\_2\_coordinates3Tsg151_{19} := \left[-O3x + \frac{7}{6} - \frac{c1M\cos(\pi - beta1M)\,(-O3z + 1)}{a1M} + \frac{1}{3}\frac{c1M\cos(\pi - beta1M)}{a1M} - O3y,\right.$$
$$\left. -O3x + \frac{5}{6} - \frac{c1M\cos(\pi - beta1M)\,(-O3z + 1)}{a1M} + \frac{2}{3}\frac{c1M\cos(\pi - beta1M)}{a1M} + O3y,\ -\frac{1}{3}O3z + \frac{1}{2} \right]$$

$$layer\_2\_coordinates3Tsg151_{20} := \left[-O3x - \frac{c1M\cos(\pi - beta1M)\,(-O3z + 1)}{a1M} + \frac{1}{3}\frac{c1M\cos(\pi - beta1M)}{a1M} + O3y + \frac{1}{6},\right.$$
$$\left. -O3x + \frac{11}{6} - \frac{c1M\cos(\pi - beta1M)\,(-O3z + 1)}{a1M} + \frac{2}{3}\frac{c1M\cos(\pi - beta1M)}{a1M} - O3y,\ -\frac{1}{3}O3z + \frac{1}{2} \right]$$

$$layer\_2\_coordinates3Tsg151_{21} := \left[O3x - \frac{c1M\cos(\pi - beta1M)\,O3z}{a1M} + \frac{1}{3}\frac{c1M\cos(\pi - beta1M)}{a1M} + O3y - \frac{5}{6},\right.$$
$$\left. O3x - \frac{c1M\cos(\pi - beta1M)\,O3z}{a1M} + \frac{2}{3}\frac{c1M\cos(\pi - beta1M)}{a1M} - O3y + \frac{5}{6},\ \frac{1}{3}O3z + \frac{1}{6} \right]$$

$$layer\_2\_coordinates3Tsg151_{22} := \left[O3x - \frac{c1M\cos(\pi - beta1M)\,O3z}{a1M} + \frac{1}{3}\frac{c1M\cos(\pi - beta1M)}{a1M} - O3y + \frac{1}{6},\right.$$
$$\left. O3x + \frac{5}{6} - \frac{c1M\cos(\pi - beta1M)\,O3z}{a1M} + \frac{2}{3}\frac{c1M\cos(\pi - beta1M)}{a1M} + O3y,\ \frac{1}{3}O3z + \frac{1}{6} \right]$$

$$layer\_2\_coordinates3Tsg151_{23} := \left[-O3x - \frac{c1M\cos(\pi - beta1M)\,(-O3z+1)}{a1M} + \frac{1}{3}\frac{c1M\cos(\pi - beta1M)}{a1M} - O3y + \frac{1}{6}, \right.$$
$$\left. -O3x + \frac{5}{6} - \frac{c1M\cos(\pi - beta1M)\,(-O3z+1)}{a1M} + \frac{2}{3}\frac{c1M\cos(\pi - beta1M)}{a1M} + O3y, -\frac{1}{3}O3z + \frac{1}{2} \right]$$

$$layer\_2\_coordinates3Tsg151_{24} := \left[-O3x - \frac{c1M\cos(\pi - beta1M)\,(-O3z+1)}{a1M} + \frac{1}{3}\frac{c1M\cos(\pi - beta1M)}{a1M} + O3y + \frac{1}{6}, \right.$$
$$\left. \frac{5}{6} - O3x - \frac{c1M\cos(\pi - beta1M)\,(-O3z+1)}{a1M} + \frac{2}{3}\frac{c1M\cos(\pi - beta1M)}{a1M} - O3y, -\frac{1}{3}O3z + \frac{1}{2} \right]$$

$$layer\_2\_coordinates3Tsg151_{25} := \left[O3x - \frac{c1M\cos(\pi - beta1M)\,O3z}{a1M} + \frac{1}{3}\frac{c1M\cos(\pi - beta1M)}{a1M} + O3y + \frac{1}{6}, \right.$$
$$\left. O3x - \frac{c1M\cos(\pi - beta1M)\,O3z}{a1M} + \frac{2}{3}\frac{c1M\cos(\pi - beta1M)}{a1M} - O3y + \frac{5}{6}, \frac{1}{3}O3z + \frac{1}{6} \right]$$

$$layer\_2\_coordinates3Tsg151_{26} := \left[Tx - \frac{c1M\cos(\pi - beta1M)\,Tz}{a1M} + \frac{1}{3}\frac{c1M\cos(\pi - beta1M)}{a1M} - Ty + \frac{1}{6}, \right.$$
$$\left. Tx - \frac{c1M\cos(\pi - beta1M)\,Tz}{a1M} + \frac{2}{3}\frac{c1M\cos(\pi - beta1M)}{a1M} + Ty - \frac{1}{6}, \frac{1}{3}Tz + \frac{1}{6} \right]$$

$$layer\_2\_coordinates3Tsg151_{27} := \left[-Tx + \frac{7}{6} - \frac{c1M\cos(\pi - beta1M)\,(-Tz+1)}{a1M} + \frac{1}{3}\frac{c1M\cos(\pi - beta1M)}{a1M} - Ty, \right.$$
$$\left. -Tx + \frac{5}{6} - \frac{c1M\cos(\pi - beta1M)\,(-Tz+1)}{a1M} + \frac{2}{3}\frac{c1M\cos(\pi - beta1M)}{a1M} + Ty, -\frac{1}{3}Tz + \frac{1}{2} \right]$$

$$layer\_2\_coordinates3Tsg151_{28} := \left[-Tx - \frac{c1M\cos(\pi - beta1M)\,(-Tz+1)}{a1M} + \frac{1}{3}\frac{c1M\cos(\pi - beta1M)}{a1M} + Ty + \frac{1}{6}, \right.$$
$$\left. -Tx + \frac{11}{6} - \frac{c1M\cos(\pi - beta1M)\,(-Tz+1)}{a1M} + \frac{2}{3}\frac{c1M\cos(\pi - beta1M)}{a1M} - Ty, -\frac{1}{3}Tz + \frac{1}{2} \right]$$

$$layer\_2\_coordinates3Tsg151_{29} := \left[Tx - \frac{c1M\cos(\pi - beta1M)\,Tz}{a1M} + \frac{1}{3}\frac{c1M\cos(\pi - beta1M)}{a1M} + Ty - \frac{5}{6}, \right.$$
$$\left. Tx - \frac{c1M\cos(\pi - beta1M)\,Tz}{a1M} + \frac{2}{3}\frac{c1M\cos(\pi - beta1M)}{a1M} - Ty + \frac{5}{6}, \frac{1}{3}Tz + \frac{1}{6} \right]$$

$$layer\_2\_coordinates3Tsg151_{30} := \left[Tx - \frac{c1M\cos(\pi - beta1M)\,Tz}{a1M} + \frac{1}{3}\frac{c1M\cos(\pi - beta1M)}{a1M} - Ty + \frac{1}{6}, \right.$$
$$\left. Tx + \frac{5}{6} - \frac{c1M\cos(\pi - beta1M)\,Tz}{a1M} + \frac{2}{3}\frac{c1M\cos(\pi - beta1M)}{a1M} + Ty, \frac{1}{3}Tz + \frac{1}{6} \right]$$

$$layer\_2\_coordinates3Tsg151_{31} := \left[-Tx - \frac{c1M\cos(\pi - beta1M)\,(-Tz+1)}{a1M} + \frac{1}{3}\frac{c1M\cos(\pi - beta1M)}{a1M} - Ty + \frac{1}{6}, \right.$$
$$\left. -Tx + \frac{5}{6} - \frac{c1M\cos(\pi - beta1M)\,(-Tz+1)}{a1M} + \frac{2}{3}\frac{c1M\cos(\pi - beta1M)}{a1M} + Ty, -\frac{1}{3}Tz + \frac{1}{2} \right]$$

$$layer\_2\_coordinates3Tsg151_{32} := \left[-Tx - \frac{c1M\cos(\pi - beta1M)\,(-Tz+1)}{a1M} + \frac{1}{3}\frac{c1M\cos(\pi - beta1M)}{a1M} + Ty + \frac{1}{6}, \right.$$
$$\left. \frac{5}{6} - Tx - \frac{c1M\cos(\pi - beta1M)\,(-Tz+1)}{a1M} + \frac{2}{3}\frac{c1M\cos(\pi - beta1M)}{a1M} - Ty, -\frac{1}{3}Tz + \frac{1}{2} \right]$$

$$layer\_2\_coordinates3Tsg151_{33} := \left[Tx - \frac{c1M\cos(\pi - beta1M)\,Tz}{a1M} + \frac{1}{3}\frac{c1M\cos(\pi - beta1M)}{a1M} + Ty + \frac{1}{6}, \right.$$
$$\left. Tx - \frac{c1M\cos(\pi - beta1M)\,Tz}{a1M} + \frac{2}{3}\frac{c1M\cos(\pi - beta1M)}{a1M} - Ty + \frac{5}{6}, \frac{1}{3}Tz + \frac{1}{6} \right]$$

$$layer\_2\_coordinates3Tsg151_{34} := \left[O1x - \frac{c1M\cos(\pi - beta1M)\,O1z}{a1M} + \frac{1}{3}\frac{c1M\cos(\pi - beta1M)}{a1M} + \frac{1}{6}, \right.$$
$$\left. O1x - \frac{c1M\cos(\pi - beta1M)\,O1z}{a1M} + \frac{2}{3}\frac{c1M\cos(\pi - beta1M)}{a1M} - \frac{1}{6}, \frac{1}{3}O1z + \frac{1}{6} \right]$$

$$layer\_2\_coordinates3Tsg151_{35} := \left[-O1x + \frac{7}{6} - \frac{c1M\cos(\pi - beta1M)\,(-O1z+1)}{a1M} + \frac{1}{3}\frac{c1M\cos(\pi - beta1M)}{a1M}, \right.$$
$$\left. -O1x + \frac{5}{6} - \frac{c1M\cos(\pi - beta1M)\,(-O1z+1)}{a1M} + \frac{2}{3}\frac{c1M\cos(\pi - beta1M)}{a1M}, -\frac{1}{3}O1z + \frac{1}{2} \right]$$

$$layer\_2\_coordinates3Tsg151_{36} := \left[O1x - \frac{c1M\cos(\pi - beta1M)\,O1z}{a1M} + \frac{1}{3}\frac{c1M\cos(\pi - beta1M)}{a1M} + \frac{1}{6}, \right.$$
$$\left. \frac{5}{6} + O1x - \frac{c1M\cos(\pi - beta1M)\,O1z}{a1M} + \frac{2}{3}\frac{c1M\cos(\pi - beta1M)}{a1M}, \frac{1}{3}O1z + \frac{1}{6} \right]$$

$$layer\_2\_coordinates3Tsg151_{37} := \left[-O1x - \frac{c1M\cos(\pi - beta1M)\,(-O1z+1)}{a1M} + \frac{1}{3}\frac{c1M\cos(\pi - beta1M)}{a1M} + \frac{1}{6}, \right.$$
$$\left. -O1x + \frac{5}{6} - \frac{c1M\cos(\pi - beta1M)\,(-O1z+1)}{a1M} + \frac{2}{3}\frac{c1M\cos(\pi - beta1M)}{a1M}, -\frac{1}{3}O1z + \frac{1}{2} \right]$$

$$layer\_2\_coordinates3Tsg151_{38} := \left[O2x - \frac{c1M\cos(\pi - beta1M)\,O2z}{a1M} + \frac{1}{3}\frac{c1M\cos(\pi - beta1M)}{a1M} - O2y + \frac{1}{6}, \right.$$
$$\left. O2x - \frac{c1M\cos(\pi - beta1M)\,O2z}{a1M} + \frac{2}{3}\frac{c1M\cos(\pi - beta1M)}{a1M} + O2y - \frac{1}{6}, \frac{1}{3}O2z + \frac{1}{6} \right]$$

$$layer\_2\_coordinates3Tsg151_{39} := \left[-O2x + \frac{7}{6} - \frac{c1M\cos(\pi - beta1M)\,(-O2z+1)}{a1M} + \frac{1}{3}\frac{c1M\cos(\pi - beta1M)}{a1M} - O2y, \right.$$
$$\left. -O2x + \frac{5}{6} - \frac{c1M\cos(\pi - beta1M)\,(-O2z+1)}{a1M} + \frac{2}{3}\frac{c1M\cos(\pi - beta1M)}{a1M} + O2y, -\frac{1}{3}O2z + \frac{1}{2} \right]$$

$$layer\_2\_coordinates3Tsg151_{40} := \left[-O2x - \frac{c1M\cos(\pi - beta1M)\,(-O2z+1)}{a1M} + \frac{1}{3}\frac{c1M\cos(\pi - beta1M)}{a1M} + O2y + \frac{1}{6}, \right.$$
$$\left. -O2x + \frac{11}{6} - \frac{c1M\cos(\pi - beta1M)\,(-O2z+1)}{a1M} + \frac{2}{3}\frac{c1M\cos(\pi - beta1M)}{a1M} - O2y, -\frac{1}{3}O2z + \frac{1}{2} \right]$$

$$layer\_2\_coordinates3Tsg151_{41} := \left[O2x - \frac{c1M\cos(\pi - beta1M)\,O2z}{a1M} + \frac{1}{3}\frac{c1M\cos(\pi - beta1M)}{a1M} + O2y - \frac{5}{6}, \right.$$
$$\left. O2x - \frac{c1M\cos(\pi - beta1M)\,O2z}{a1M} + \frac{2}{3}\frac{c1M\cos(\pi - beta1M)}{a1M} - O2y + \frac{5}{6}, \frac{1}{3}O2z + \frac{1}{6} \right]$$

$$layer\_2\_coordinates3Tsg151_{42} := \left[O2x - \frac{c1M\cos(\pi - beta1M)\,O2z}{a1M} + \frac{1}{3}\frac{c1M\cos(\pi - beta1M)}{a1M} - O2y + \frac{1}{6}, \right.$$
$$\left. O2x + \frac{5}{6} - \frac{c1M\cos(\pi - beta1M)\,O2z}{a1M} + \frac{2}{3}\frac{c1M\cos(\pi - beta1M)}{a1M} + O2y, \frac{1}{3}O2z + \frac{1}{6} \right]$$

$$layer\_2\_coordinates3Tsg151_{43} := \left[-O2x - \frac{c1M\cos(\pi - beta1M)\,(-O2z+1)}{a1M} + \frac{1}{3}\frac{c1M\cos(\pi - beta1M)}{a1M} - O2y + \frac{1}{6}, \right.$$
$$\left. -O2x + \frac{5}{6} - \frac{c1M\cos(\pi - beta1M)\,(-O2z+1)}{a1M} + \frac{2}{3}\frac{c1M\cos(\pi - beta1M)}{a1M} + O2y, -\frac{1}{3}O2z + \frac{1}{2} \right]$$

$$layer\_2\_coordinates3Tsg151_{44} := \left[-O2x - \frac{c1M\cos(\pi - beta1M)\,(-O2z+1)}{a1M} + \frac{1}{3}\frac{c1M\cos(\pi - beta1M)}{a1M} + O2y + \frac{1}{6}, \right.$$
$$\left. \frac{5}{6} - O2x - \frac{c1M\cos(\pi - beta1M)\,(-O2z+1)}{a1M} + \frac{2}{3}\frac{c1M\cos(\pi - beta1M)}{a1M} - O2y, -\frac{1}{3}O2z + \frac{1}{2} \right]$$

$$layer\_2\_coordinates3Tsg151_{45} := \left[O2x - \frac{c1M\cos(\pi - beta1M)\,O2z}{a1M} + \frac{1}{3}\frac{c1M\cos(\pi - beta1M)}{a1M} + O2y + \frac{1}{6}, \right.$$
$$\left. O2x - \frac{c1M\cos(\pi - beta1M)\,O2z}{a1M} + \frac{2}{3}\frac{c1M\cos(\pi - beta1M)}{a1M} - O2y + \frac{5}{6}, \frac{1}{3}O2z + \frac{1}{6} \right]$$

```
> for i from 1 to 45 do layer_3_coordinates[i]
  :=evalm(R[-120]&*Zadjust&*layer[1][i]+[-(1/2*(1/2-1/2*c1M/a1M*cos(pi-beta1M))),1/6*(1/2-1
  /2*c1M/a1M*cos(pi-beta1M)),2/3]) od:
> for i from 1 to 45 do layer_3_coordinates3Tsg151[i] :=evalm(
  aNbNcN_To_Hexagonal&*layer_3_coordinates[i]) od;
```

$$layer\_3\_coordinates3Tsg151_1 := \left[-\frac{1}{3}+\frac{1}{3}\frac{c1M\cos(\pi-beta1M)}{a1M}, -\frac{2}{3}-\frac{1}{3}\frac{c1M\cos(\pi-beta1M)}{a1M}, \frac{5}{6}\right]$$

$$layer\_3\_coordinates3Tsg151_2 := \left[\frac{2}{3}+\frac{1}{3}\frac{c1M\cos(\pi-beta1M)}{a1M}, \frac{1}{3}-\frac{1}{3}\frac{c1M\cos(\pi-beta1M)}{a1M}, \frac{5}{6}\right]$$

$$layer\_3\_coordinates3Tsg151_3 := \left[-\frac{1}{3}+\frac{1}{3}\frac{c1M\cos(\pi-beta1M)}{a1M}, \frac{1}{3}-\frac{1}{3}\frac{c1M\cos(\pi-beta1M)}{a1M}, \frac{5}{6}\right]$$

$$layer\_3\_coordinates3Tsg151_4 := \left[-\frac{2}{3}\frac{c1M\cos(\pi-beta1M)}{a1M}-\frac{1}{3}, \frac{1}{3}-\frac{1}{3}\frac{c1M\cos(\pi-beta1M)}{a1M}, \frac{1}{2}\right]$$

$$layer\_3\_coordinates3Tsg151_5 := \left[\frac{1}{6}-\frac{1}{6}\frac{c1M\cos(\pi-beta1M)}{a1M}, \frac{1}{3}-\frac{1}{3}\frac{c1M\cos(\pi-beta1M)}{a1M}, \frac{2}{3}\right]$$

$$layer\_3\_coordinates3Tsg151_6 := \left[-\frac{5}{6}-\frac{1}{6}\frac{c1M\cos(\pi-beta1M)}{a1M}, -\frac{2}{3}-\frac{1}{3}\frac{c1M\cos(\pi-beta1M)}{a1M}, \frac{2}{3}\right]$$

$$layer\_3\_coordinates3Tsg151_7 := \left[-\frac{11}{6}-\frac{1}{6}\frac{c1M\cos(\pi-beta1M)}{a1M}, -\frac{2}{3}-\frac{1}{3}\frac{c1M\cos(\pi-beta1M)}{a1M}, \frac{2}{3}\right]$$

$$layer\_3\_coordinates3Tsg151_8 := \left[-yM2+\frac{1}{6}-\frac{1}{6}\frac{c1M\cos(\pi-beta1M)}{a1M}, -2\,yM2+\frac{1}{3}-\frac{1}{3}\frac{c1M\cos(\pi-beta1M)}{a1M}, \frac{2}{3}\right]$$

$$layer\_3\_coordinates3Tsg151_9 := \left[yM2-\frac{5}{6}-\frac{1}{6}\frac{c1M\cos(\pi-beta1M)}{a1M}, 2\,yM2-\frac{5}{3}-\frac{1}{3}\frac{c1M\cos(\pi-beta1M)}{a1M}, \frac{2}{3}\right]$$

$$layer\_3\_coordinates3Tsg151_{10} := \left[-\frac{5}{6}-yM2-\frac{1}{6}\frac{c1M\cos(\pi-beta1M)}{a1M}, -\frac{2}{3}-2\,yM2-\frac{1}{3}\frac{c1M\cos(\pi-beta1M)}{a1M}, \frac{2}{3}\right]$$

$$layer\_3\_coordinates3Tsg151_{11} := \left[yM2-\frac{5}{6}-\frac{1}{6}\frac{c1M\cos(\pi-beta1M)}{a1M}, -\frac{2}{3}+2\,yM2-\frac{1}{3}\frac{c1M\cos(\pi-beta1M)}{a1M}, \frac{2}{3}\right]$$

$$layer\_3\_coordinates3Tsg151_{12} := \left[-\frac{2}{3}\frac{c1M\cos(\pi-beta1M)}{a1M}+\frac{1}{6}, \frac{1}{3}-\frac{1}{3}\frac{c1M\cos(\pi-beta1M)}{a1M}, \frac{1}{2}\right]$$

$$layer\_3\_coordinates3Tsg151_{13} := \left[-\frac{2}{3}\frac{c1M\cos(\pi-beta1M)}{a1M}+\frac{1}{6}, \frac{1}{3}-\frac{1}{3}\frac{c1M\cos(\pi-beta1M)}{a1M}, \frac{1}{2}\right]$$

$$layer\_3\_coordinates3Tsg151_{14} :=$$

$$\left[-O4x+\frac{c1M\cos(\pi-beta1M)\,O4z}{a1M}-\frac{2}{3}\frac{c1M\cos(\pi-beta1M)}{a1M}-\frac{1}{3}, -\frac{2}{3}-\frac{1}{3}\frac{c1M\cos(\pi-beta1M)}{a1M}, \frac{1}{3}O4z+\frac{1}{2}\right]$$

$$layer\_3\_coordinates3Tsg151_{15} :=$$

$$\left[-\frac{4}{3}+O4x+\frac{c1M\cos(\pi-beta1M)\,(-O4z+1)}{a1M}-\frac{2}{3}\frac{c1M\cos(\pi-beta1M)}{a1M}, -\frac{2}{3}-\frac{1}{3}\frac{c1M\cos(\pi-beta1M)}{a1M}, -\frac{1}{3}O4z+\frac{5}{6}\right]$$

$$layer\_3\_coordinates3Tsg151_{16} :=$$

$$\left[-O4x+\frac{c1M\cos(\pi-beta1M)\,O4z}{a1M}-\frac{2}{3}\frac{c1M\cos(\pi-beta1M)}{a1M}-\frac{1}{3}, \frac{1}{3}-\frac{1}{3}\frac{c1M\cos(\pi-beta1M)}{a1M}, \frac{1}{3}O4z+\frac{1}{2}\right]$$

$$layer\_3\_coordinates3Tsg151_{17} :=$$

$$\left[O4x-\frac{1}{3}+\frac{c1M\cos(\pi-beta1M)\,(-O4z+1)}{a1M}-\frac{2}{3}\frac{c1M\cos(\pi-beta1M)}{a1M}, \frac{1}{3}-\frac{1}{3}\frac{c1M\cos(\pi-beta1M)}{a1M}, -\frac{1}{3}O4z+\frac{5}{6}\right]$$

$$layer\_3\_coordinates3Tsg151_{18} :=$$

$$\left[-O3x+\frac{c1M\cos(\pi-beta1M)\,O3z}{a1M}-\frac{2}{3}\frac{c1M\cos(\pi-beta1M)}{a1M}-O3y+\frac{1}{6}, -2\,O3y+\frac{1}{3}-\frac{1}{3}\frac{c1M\cos(\pi-beta1M)}{a1M}, \frac{1}{3}O3z+\frac{1}{2}\right]$$

$$layer\_3\_coordinates3Tsg151_{19} := \left[O3x-\frac{5}{6}+\frac{c1M\cos(\pi-beta1M)\,(-O3z+1)}{a1M}-\frac{2}{3}\frac{c1M\cos(\pi-beta1M)}{a1M}-O3y,\right.$$

$$\left.-2\,O3y+\frac{1}{3}-\frac{1}{3}\frac{c1M\cos(\pi-beta1M)}{a1M}, -\frac{1}{3}O3z+\frac{5}{6}\right]$$

$$layer\_3\_coordinates3Tsg151_{20} := \left[O3x-\frac{11}{6}+\frac{c1M\cos(\pi-beta1M)\,(-O3z+1)}{a1M}-\frac{2}{3}\frac{c1M\cos(\pi-beta1M)}{a1M}+O3y,\right.$$

$$-\frac{5}{3}+2\,O3y-\frac{1}{3}\frac{c1M\cos(\pi-beta1M)}{a1M},-\frac{1}{3}O3z+\frac{5}{6}\Bigg]$$

$$layer\_3\_coordinates3Tsg151_{21}:=$$

$$\left[-O3x+\frac{c1M\cos(\pi-beta1M)\,O3z}{a1M}-\frac{2}{3}\frac{c1M\cos(\pi-beta1M)}{a1M}+O3y-\frac{5}{6},-\frac{5}{3}+2\,O3y-\frac{1}{3}\frac{c1M\cos(\pi-beta1M)}{a1M},\frac{1}{3}O3z+\frac{1}{2}\right]$$

$$layer\_3\_coordinates3Tsg151_{22}:=$$

$$\left[-O3x-\frac{5}{6}+\frac{c1M\cos(\pi-beta1M)\,O3z}{a1M}-\frac{2}{3}\frac{c1M\cos(\pi-beta1M)}{a1M}-O3y,-\frac{2}{3}-2\,O3y-\frac{1}{3}\frac{c1M\cos(\pi-beta1M)}{a1M},\frac{1}{3}O3z+\frac{1}{2}\right]$$

$$layer\_3\_coordinates3Tsg151_{23}:=\left[O3x-\frac{5}{6}+\frac{c1M\cos(\pi-beta1M)\,(-O3z+1)}{a1M}-\frac{2}{3}\frac{c1M\cos(\pi-beta1M)}{a1M}-O3y,\right.$$

$$\left.-\frac{2}{3}-2\,O3y-\frac{1}{3}\frac{c1M\cos(\pi-beta1M)}{a1M},-\frac{1}{3}O3z+\frac{5}{6}\right]$$

$$layer\_3\_coordinates3Tsg151_{24}:=\left[-\frac{5}{6}+O3x+\frac{c1M\cos(\pi-beta1M)\,(-O3z+1)}{a1M}-\frac{2}{3}\frac{c1M\cos(\pi-beta1M)}{a1M}+O3y,\right.$$

$$\left.-\frac{2}{3}+2\,O3y-\frac{1}{3}\frac{c1M\cos(\pi-beta1M)}{a1M},-\frac{1}{3}O3z+\frac{5}{6}\right]$$

$$layer\_3\_coordinates3Tsg151_{25}:=$$

$$\left[-O3x+\frac{c1M\cos(\pi-beta1M)\,O3z}{a1M}-\frac{2}{3}\frac{c1M\cos(\pi-beta1M)}{a1M}+O3y-\frac{5}{6},-\frac{2}{3}+2\,O3y-\frac{1}{3}\frac{c1M\cos(\pi-beta1M)}{a1M},\frac{1}{3}O3z+\frac{1}{2}\right]$$

$$layer\_3\_coordinates3Tsg151_{26}:=$$

$$\left[-Tx+\frac{c1M\cos(\pi-beta1M)\,Tz}{a1M}-\frac{2}{3}\frac{c1M\cos(\pi-beta1M)}{a1M}-Ty+\frac{1}{6},-2\,Ty+\frac{1}{3}-\frac{1}{3}\frac{c1M\cos(\pi-beta1M)}{a1M},\frac{1}{3}Tz+\frac{1}{2}\right]$$

$$layer\_3\_coordinates3Tsg151_{27}:=$$

$$\left[Tx-\frac{5}{6}+\frac{c1M\cos(\pi-beta1M)\,(-Tz+1)}{a1M}-\frac{2}{3}\frac{c1M\cos(\pi-beta1M)}{a1M}-Ty,-2\,Ty+\frac{1}{3}-\frac{1}{3}\frac{c1M\cos(\pi-beta1M)}{a1M},-\frac{1}{3}Tz+\frac{5}{6}\right]$$

$$layer\_3\_coordinates3Tsg151_{28}:=$$

$$\left[Tx-\frac{11}{6}+\frac{c1M\cos(\pi-beta1M)\,(-Tz+1)}{a1M}-\frac{2}{3}\frac{c1M\cos(\pi-beta1M)}{a1M}+Ty,-\frac{5}{3}+2\,Ty-\frac{1}{3}\frac{c1M\cos(\pi-beta1M)}{a1M},-\frac{1}{3}Tz+\frac{5}{6}\right]$$

$$layer\_3\_coordinates3Tsg151_{29}:=$$

$$\left[-Tx+\frac{c1M\cos(\pi-beta1M)\,Tz}{a1M}-\frac{2}{3}\frac{c1M\cos(\pi-beta1M)}{a1M}+Ty-\frac{5}{6},-\frac{5}{3}+2\,Ty-\frac{1}{3}\frac{c1M\cos(\pi-beta1M)}{a1M},\frac{1}{3}Tz+\frac{1}{2}\right]$$

$$layer\_3\_coordinates3Tsg151_{30}:=$$

$$\left[-Tx-\frac{5}{6}+\frac{c1M\cos(\pi-beta1M)\,Tz}{a1M}-\frac{2}{3}\frac{c1M\cos(\pi-beta1M)}{a1M}-Ty,-\frac{2}{3}-2\,Ty-\frac{1}{3}\frac{c1M\cos(\pi-beta1M)}{a1M},\frac{1}{3}Tz+\frac{1}{2}\right]$$

$$layer\_3\_coordinates3Tsg151_{31}:=$$

$$\left[Tx-\frac{5}{6}+\frac{c1M\cos(\pi-beta1M)\,(-Tz+1)}{a1M}-\frac{2}{3}\frac{c1M\cos(\pi-beta1M)}{a1M}-Ty,-\frac{2}{3}-2\,Ty-\frac{1}{3}\frac{c1M\cos(\pi-beta1M)}{a1M},-\frac{1}{3}Tz+\frac{5}{6}\right]$$

$$layer\_3\_coordinates3Tsg151_{32}:=$$

$$\left[-\frac{5}{6}+Tx+\frac{c1M\cos(\pi-beta1M)\,(-Tz+1)}{a1M}-\frac{2}{3}\frac{c1M\cos(\pi-beta1M)}{a1M}+Ty,-\frac{2}{3}+2\,Ty-\frac{1}{3}\frac{c1M\cos(\pi-beta1M)}{a1M},-\frac{1}{3}Tz+\frac{5}{6}\right]$$

$$layer\_3\_coordinates3Tsg151_{33}:=$$

$$\left[-Tx+\frac{c1M\cos(\pi-beta1M)\,Tz}{a1M}-\frac{2}{3}\frac{c1M\cos(\pi-beta1M)}{a1M}+Ty-\frac{5}{6},-\frac{2}{3}+2\,Ty-\frac{1}{3}\frac{c1M\cos(\pi-beta1M)}{a1M},\frac{1}{3}Tz+\frac{1}{2}\right]$$

$$layer\_3\_coordinates3Tsg151_{34}:=$$

$$\left[-O1x+\frac{c1M\cos(\pi-beta1M)\,O1z}{a1M}-\frac{2}{3}\frac{c1M\cos(\pi-beta1M)}{a1M}+\frac{1}{6},\frac{1}{3}-\frac{1}{3}\frac{c1M\cos(\pi-beta1M)}{a1M},\frac{1}{3}O1z+\frac{1}{2}\right]$$

$$layer\_3\_coordinates3Tsg151_{35} := \left[O1x - \frac{5}{6} + \frac{c1M\cos(\pi - beta1M)\,(-O1z+1)}{a1M} - \frac{2}{3}\frac{c1M\cos(\pi - beta1M)}{a1M}, \frac{1}{3} - \frac{1}{3}\frac{c1M\cos(\pi - beta1M)}{a1M}, -\frac{1}{3}O1z + \frac{5}{6} \right]$$

$$layer\_3\_coordinates3Tsg151_{36} := \left[-\frac{5}{6} - O1x + \frac{c1M\cos(\pi - beta1M)\,O1z}{a1M} - \frac{2}{3}\frac{c1M\cos(\pi - beta1M)}{a1M}, -\frac{2}{3} - \frac{1}{3}\frac{c1M\cos(\pi - beta1M)}{a1M}, \frac{1}{3}O1z + \frac{1}{2} \right]$$

$$layer\_3\_coordinates3Tsg151_{37} := \left[O1x - \frac{5}{6} + \frac{c1M\cos(\pi - beta1M)\,(-O1z+1)}{a1M} - \frac{2}{3}\frac{c1M\cos(\pi - beta1M)}{a1M}, -\frac{2}{3} - \frac{1}{3}\frac{c1M\cos(\pi - beta1M)}{a1M}, -\frac{1}{3}O1z + \frac{5}{6} \right]$$

$$layer\_3\_coordinates3Tsg151_{38} := \left[-O2x + \frac{c1M\cos(\pi - beta1M)\,O2z}{a1M} - \frac{2}{3}\frac{c1M\cos(\pi - beta1M)}{a1M} - O2y + \frac{1}{6}, -2\,O2y + \frac{1}{3} - \frac{1}{3}\frac{c1M\cos(\pi - beta1M)}{a1M}, \frac{1}{3}O2z + \frac{1}{2} \right]$$

$$layer\_3\_coordinates3Tsg151_{39} := \left[O2x - \frac{5}{6} + \frac{c1M\cos(\pi - beta1M)\,(-O2z+1)}{a1M} - \frac{2}{3}\frac{c1M\cos(\pi - beta1M)}{a1M} - O2y, \right.$$
$$\left. -2\,O2y + \frac{1}{3} - \frac{1}{3}\frac{c1M\cos(\pi - beta1M)}{a1M}, -\frac{1}{3}O2z + \frac{5}{6} \right]$$

$$layer\_3\_coordinates3Tsg151_{40} := \left[O2x - \frac{11}{6} + \frac{c1M\cos(\pi - beta1M)\,(-O2z+1)}{a1M} - \frac{2}{3}\frac{c1M\cos(\pi - beta1M)}{a1M} + O2y, \right.$$
$$\left. -\frac{5}{3} + 2\,O2y - \frac{1}{3}\frac{c1M\cos(\pi - beta1M)}{a1M}, -\frac{1}{3}O2z + \frac{5}{6} \right]$$

$$layer\_3\_coordinates3Tsg151_{41} := \left[-O2x + \frac{c1M\cos(\pi - beta1M)\,O2z}{a1M} - \frac{2}{3}\frac{c1M\cos(\pi - beta1M)}{a1M} + O2y - \frac{5}{6}, -\frac{5}{3} + 2\,O2y - \frac{1}{3}\frac{c1M\cos(\pi - beta1M)}{a1M}, \frac{1}{3}O2z + \frac{1}{2} \right]$$

$$layer\_3\_coordinates3Tsg151_{42} := \left[-O2x - \frac{5}{6} + \frac{c1M\cos(\pi - beta1M)\,O2z}{a1M} - \frac{2}{3}\frac{c1M\cos(\pi - beta1M)}{a1M} - O2y, -\frac{2}{3} - 2\,O2y - \frac{1}{3}\frac{c1M\cos(\pi - beta1M)}{a1M}, \frac{1}{3}O2z + \frac{1}{2} \right]$$

$$layer\_3\_coordinates3Tsg151_{43} := \left[O2x - \frac{5}{6} + \frac{c1M\cos(\pi - beta1M)\,(-O2z+1)}{a1M} - \frac{2}{3}\frac{c1M\cos(\pi - beta1M)}{a1M} - O2y, \right.$$
$$\left. -\frac{2}{3} - 2\,O2y - \frac{1}{3}\frac{c1M\cos(\pi - beta1M)}{a1M}, -\frac{1}{3}O2z + \frac{5}{6} \right]$$

$$layer\_3\_coordinates3Tsg151_{44} := \left[-\frac{5}{6} + O2x + \frac{c1M\cos(\pi - beta1M)\,(-O2z+1)}{a1M} - \frac{2}{3}\frac{c1M\cos(\pi - beta1M)}{a1M} + O2y, \right.$$
$$\left. -\frac{2}{3} + 2\,O2y - \frac{1}{3}\frac{c1M\cos(\pi - beta1M)}{a1M}, -\frac{1}{3}O2z + \frac{5}{6} \right]$$

$$layer\_3\_coordinates3Tsg151_{45} := \left[-O2x + \frac{c1M\cos(\pi - beta1M)\,O2z}{a1M} - \frac{2}{3}\frac{c1M\cos(\pi - beta1M)}{a1M} + O2y - \frac{5}{6}, -\frac{2}{3} + 2\,O2y - \frac{1}{3}\frac{c1M\cos(\pi - beta1M)}{a1M}, \frac{1}{3}O2z + \frac{1}{2} \right]$$

>

Appendix V. Results pertaining to Section 5.1

MER135			MER136			MER137		
2θvis	2θprf	Diff.	$2\theta_{vis}$	$2\theta_{prf}$	Diff.	$2\theta_{vis}$	$2\theta_{prf}$	Diff.
8.735	8.7097	0.0253	8.710	8.6966	0.0134	8.735	8.7126	0.0224
17.460	17.4572	0.0028	17.445	17.4358	0.0092	17.465	17.4535	0.0115
19.030	19.0264	0.0036	19.020	18.9992	0.0208	19.020	19.0236	-0.0036
19.245	19.2449	0.0001	19.240	19.2243	0.0157	19.250	19.2426	0.0074
22.345	22.3334	0.0116	22.340	22.3017	0.0383	22.340	22.3284	0.0116
23.990	23.9788	0.0112	23.990	23.9607	0.0293	24.010	23.9777	0.0323
25.920	25.8993	0.0207	25.905	25.8803	0.0247	25.890	25.8952	-0.0052
26.310	26.2939	0.0161	26.290	26.2716	0.0184	26.290	26.2875	0.0025
28.015	28.0166	-0.0016	28.005	28.0057	-0.0007	28.005	28.0168	-0.0118
30.235	30.2340	0.0010	30.220	30.2125	0.0075	30.260	30.2312	0.0288
32.640	32.6362	0.0038	32.645	32.6092	0.0358	32.650	32.6276	0.0224
33.735	33.7454	-0.0104	33.700	33.7281	-0.0281	33.740	33.7454	-0.0054
35.275	35.2779	-0.0029	35.280	35.2611	0.0189	35.280	35.2771	0.0029
36.440	36.4132	0.0268	36.440	36.3969	0.0431	36.420	36.4148	0.0052
38.675	38.6142	0.0608 *	38.615	38.5955	0.0195	38.655	38.6190	0.0360
39.260	39.2702	-0.0102	39.260	39.2494	0.0106	39.295	39.2628	0.0322
40.970	40.9740	-0.0040	40.980	40.9553	0.0247	40.980	40.9686	0.0114
44.855	44.8319	0.0231	44.840	44.7900	0.0500	44.835	44.8085	0.0265
47.000	46.9805	0.0195	46.980	46.9677	0.0123	46.980	46.9743	0.0057
54.080	54.0713	0.0087	54.100	54.0452	0.0548	54.100	54.0663	0.0337
55.050	55.0299	0.0201	55.030	55.0220	0.0080	55.080	55.0420	0.0380
56.150	56.2319	-0.0819 *	56.165	56.1975	-0.0325	56.195	56.1883	0.0067
57.480	57.5104	-0.0304	57.525	57.4797	0.0453	57.500	57.4973	0.0027
59.300	59.3191	-0.0191	59.290	59.2927	-0.0027	59.320	59.3132	0.0068
60.060	60.0720	-0.0120	60.040	60.0493	-0.0093	60.070	60.0712	-0.0012
62.300	62.1947	0.1053 *	60.055	60.0493	0.0057	62.280	62.1961	0.0839 *
64.060	64.0548	0.0052	62.330	62.1934	0.1366 *	64.100	64.0648	0.0352
65.975	65.9374	0.0376	64.100	64.0394	0.0606	65.935	65.9576	-0.0226
67.885	67.8920	-0.0070	66.000	65.9295	0.0705	67.930	67.8793	0.0507
69.965	69.9900	-0.0250	67.945	67.8622	0.0828	69.955	69.9808	-0.0258
70.950	70.9307	0.0193	69.980	69.9621	0.0179	70.980	70.9296	0.0504
71.605	71.5960	0.0090	70.950	70.9184	0.0316	71.565	71.5913	-0.0263
			71.570	71.5845	-0.0145			
	Av. Diff. =	0.0049		Av. Diff. =	0.0213		Av. Diff. =	0.0123
	$\sigma_{Diff.}$ =	0.0161		$\sigma_{Diff.}$ =	0.0261		$\sigma_{Diff.}$ =	0.0207

*Outliar

Table V.1. Comparison of line positions evaluated by visual estimation, $2\theta_{vis}$,and FP line-profile fitting, $2\theta_{prf}$, for various diffractograms

MER138			MER139			MER149		
$2\theta_{vis}$	$2\theta_{prf}$	Diff.	$2\theta_{vis}$	$2\theta_{prf}$	Diff.	$2\theta_{vis}$	$2\theta_{prf}$	Diff.
8.730	8.7126	0.0174	8.74	8.7149	0.0251	8.698	8.6798	0.0182
17.465	17.4539	0.0111	17.47	17.4553	0.0147	17.432	17.4231	0.0089
19.020	19.0192	0.0008	19.02	19.0267	-0.0067	18.982	18.9833	-0.0013
19.250	19.2465	0.0035	19.245	19.2483	-0.0033	19.219	19.2122	0.0068
22.330	22.3311	-0.0011	22.31	22.3290	-0.0190	22.323	22.2903	0.0327
23.970	23.9829	-0.0129	23.98	23.9805	-0.0005	23.966	23.9500	0.0160
25.895	25.9013	-0.0063	25.875	25.8996	-0.0246	25.854	25.8690	-0.0150
26.285	26.2970	-0.0120	26.29	26.2906	-0.0006	26.258	26.2589	-0.0009
28.000	28.0230	-0.0230	28.025	28.0255	-0.0005	28.004	27.9870	0.0170
30.230	30.2300	0.0000	30.24	30.2344	0.0056	30.206	30.2043	0.0017
32.630	32.6313	-0.0013	32.625	32.6294	-0.0044	32.623	32.6052	0.0178
33.740	33.7463	-0.0063	33.755	33.7454	0.0096	33.721	33.7126	0.0084
35.260	35.2775	-0.0175	35.28	35.2771	0.0029	35.253	35.2472	0.0058
36.410	36.4129	-0.0029	36.45	36.4124	0.0376	36.4	36.3824	0.0176
38.630	38.6147	0.0153	38.66	38.6135	0.0465	38.617	38.5797	0.0373
39.290	39.2607	0.0293	39.255	39.2579	-0.0029	39.253	39.2306	0.0224
40.975	40.9749	0.0001	40.995	40.9748	0.0202	40.956	40.9449	0.0111
44.800	44.8126	-0.0126	44.85	44.8080	0.0420	44.808	44.7791	0.0289
47.005	46.9795	0.0255	46.985	46.9788	0.0062	46.972	46.9409	0.0311
54.045	54.0639	-0.0189	54.1	54.0662	0.0338	54.069	54.0462	0.0228
55.020	55.0125	0.0075	55.04	55.0359	0.0041	54.985	55.0120	-0.0270
56.160	56.1658	-0.0058	56.14	56.1816	-0.0416	56.163	56.1603	0.0027
57.500	57.5031	-0.0031	57.5	57.5034	-0.0034	57.459	57.4264	0.0326
59.260	59.3089	-0.0489 *	59.305	59.3155	-0.0105	59.282	59.2870	-0.0050
60.085	60.0695	0.0155	60.04	60.0749	-0.0349	60.04	60.0403	-0.0003
62.290	62.2156	0.0744 *	62.28	62.1956	0.0844 *	62.227	62.1772	0.0498
64.050	64.0346	0.0154	64.1	64.0419	0.0581	64.034	64.0524	-0.0184
65.950	65.9527	-0.0027	66.025	65.9799	0.0451	66.04	65.9463	0.0937 *
67.890	67.8836	0.0064	67.915	67.8777	0.0373	67.882	67.8628	0.0192
69.960	69.9831	-0.0231	69.985	69.9849	0.0001	69.955	69.9614	-0.0064
70.900	70.9204	-0.0204	70.985	70.9281	0.0569	70.895	70.9060	-0.0110
71.575	71.5890	-0.0140	71.6	71.5914	0.0086	71.59	71.5691	0.0209
	Av. Diff. =	-0.0012		Av. Diff. =	0.0097		Av. Diff. =	0.0111
	$\sigma_{Diff.}$ =	0.0140		$\sigma_{Diff.}$ =	0.0253		$\sigma_{Diff.}$ =	0.0175

*Outliar

Table V.1. Continued.

MER150			MER151			MER152		
$2\theta_{vis}$	$2\theta_{prf}$	Diff.	$2\theta_{vis}$	$2\theta_{prf}$	Diff.	$2\theta_{vis}$	$2\theta_{prf}$	Diff.
8.685	8.6709	0.0141	8.684	8.6729	0.0111	8.682	8.6732	0.0088
17.432	17.4182	0.0138	17.432	17.4104	0.0216	17.417	17.4156	0.0014
18.997	18.9890	0.0080	18.980	18.9843	-0.0043	18.977	18.9783	-0.0013
19.211	19.2112	-0.0002	19.196	19.2071	-0.0111	19.204	19.2062	-0.0022
22.309	22.2937	0.0153	22.324	22.3029	0.0211	22.295	22.2901	0.0049
23.958	23.9438	0.0142	23.962	23.9394	0.0226	23.954	23.9386	0.0154
25.861	25.8586	0.0024	25.866	25.8612	0.0048	25.863	25.8522	0.0108
26.263	26.2544	0.0086	26.262	26.2515	0.0105	26.259	26.2549	0.0041
27.991	27.9802	0.0108	28.010	27.9727	0.0373	27.993	27.9848	0.0082
30.205	30.1923	0.0127	30.208	30.1967	0.0113	30.204	30.1886	0.0154
32.594	32.5856	0.0084	32.610	32.5917	0.0183	32.625	32.5943	0.0307
33.705	33.7004	0.0046	33.718	33.7050	0.0130	33.721	33.7033	0.0177
35.257	35.2300	0.0270	35.262	35.2390	0.0230	35.242	35.2352	0.0068
36.393	36.3670	0.0260	36.358	36.3701	-0.0121	36.392	36.3716	0.0204
38.595	38.5697	0.0253	38.584	38.5682	0.0158	38.603	38.5660	0.0370
39.257	39.2162	0.0408	39.226	39.2203	0.0057	39.229	39.2271	0.0019
40.946	40.9262	0.0198	40.976	40.9295	0.0465	40.948	40.9353	0.0127
44.79	44.7616	0.0284	44.810	44.7702	0.0398	44.813	44.7546	0.0584
46.951	46.9347	0.0163	46.962	46.9471	0.0149	46.968	46.9340	0.0340
54.056	54.0246	0.0314	54.052	54.0278	0.0242	54.095	54.0345	0.0605
54.99	54.9843	0.0057	54.950	54.9594	-0.0094	55.065	55.0316	0.0334
56.16	56.1553	0.0047	56.166	56.2157	-0.0497	56.126	56.1787	-0.0527
57.478	57.4673	0.0107	57.524	57.4771	0.0469	57.511	57.4301	0.0809
59.296	59.2711	0.0249	59.304	59.2777	0.0263	59.276	59.2761	-0.0001
60.023	60.0286	-0.0056	60.008	60.0303	-0.0223	60.057	60.0331	0.0239
62.211	62.1570	0.0540	62.218	62.1538	0.0642	62.243	62.1742	0.0688
64.049	64.0213	0.0277	64.058	64.0165	0.0415	63.993	64.0135	-0.0205
66.036	65.9254	0.1106 *	66.058	65.9404	0.1176 *	66.095	65.8798	0.2152 *
67.88	67.8376	0.0424	67.890	67.8585	0.0315	67.923	67.8576	0.0654
69.951	69.9423	0.0087	69.968	69.9405	0.0275	69.970	69.9572	0.0128
70.958	70.8988	0.0592	70.926	70.9044	0.0216	70.940	70.9070	0.0330
71.536	71.5504	-0.0144	71.562	71.5666	-0.0046	71.574	71.5816	-0.0076
	Av. Diff. =	0.0176		Av. Diff. =	0.0157		Av. Diff. =	0.0188
	$\sigma_{Diff.}$ =	0.0163		$\sigma_{Diff.}$ =	0.0229		$\sigma_{Diff.}$ =	0.0277

*Outliar

Table V.1. Continued.

MER153			MER145			MER148		
$2\theta_{vis}$	$2\theta_{prf}$	Diff.	$2\theta_{vis}$	$2\theta_{prf}$	Diff.	$2\theta_{vis}$	$2\theta_{prf}$	Diff.
8.680	8.6734	0.0066	21.360	21.3558	0.0042	21.374	21.3629	0.0111
17.429	17.4173	0.0117	28.440	28.4415	-0.0015	28.450	28.4503	-0.0003
18.974	18.9762	-0.0022	30.390	30.3877	0.0023	30.386	30.3870	-0.0010
19.214	19.1945	0.0195	37.450	37.4488	0.0012	37.451	37.4506	0.0004
22.308	22.2906	0.0174	43.510	43.5102	-0.0002	43.510	43.5125	-0.0025
23.949	23.9427	0.0063	47.300	47.3014	-0.0014	47.309	47.3064	0.0026
25.868	25.8574	0.0106	48.965	48.9611	0.0039	48.958	48.9638	-0.0058
26.258	26.2539	0.0041	53.990	53.9896	0.0004	53.991	53.9929	-0.0019
27.976	27.9798	-0.0038	56.120	56.1153	0.0047	56.118	56.1230	-0.0050
30.196	30.1796	0.0164	63.220	63.2158	0.0042	63.212	63.2224	-0.0104
32.613	32.5857	0.0273	67.540	67.5404	-0.0004	67.550	67.5525	-0.0025
33.699	33.7054	-0.0064	69.135	69.1309	0.0041	69.121	69.1328	-0.0118
35.256	35.2376	0.0184	71.740	71.7429	-0.0029	71.733	71.7400	-0.0070
36.412	36.3723	0.0397	75.835	75.8335	0.0015	75.845	75.8503	-0.0053
	38.5645		76.375	76.3700	0.0050	76.359	76.3734	-0.0144
39.256	39.2276	0.0284	83.850	83.8445	0.0055	83.836	83.8505	-0.0145
40.954	40.9377	0.0163	87.775	87.7772	-0.0022	87.783	87.7935	-0.0105
44.786	44.7725	0.0135	88.025	88.0202	0.0048	88.030	88.0334	-0.0034
46.993	46.9438	0.0492	94.940	94.9241	0.0159	94.946	94.9554	-0.0094
54.057	54.0272	0.0298	99.640	99.6419	-0.0019	99.638	99.6554	-0.0174
55.011	54.9715	0.0395						
56.143	56.1552	-0.0122						
57.573	57.5574	0.0156		Av. Diff. =	0.0024		Av. Diff. =	-0.0054
59.273	59.2777	-0.0047		$\sigma_{Diff.}$ =	0.0042		$\sigma_{Diff.}$ =	0.0068
60.041	60.0293	0.0117	SRM640c_6NOV2001			MER064		
62.237	62.0570	0.1800 *	$2\theta_{vis}$	$2\theta_{prf}$	Diff.	$2\theta_{vis}$	$2\theta_{prf}$	Diff.
64.016	64.0040	0.0120	28.445	28.4443	0.0007	28.470	28.4628	0.0072
65.987	65.9194	0.0676	47.305	47.3036	0.0014	47.320	47.3177	0.0023
67.911	67.8662	0.0448	56.115	56.1151	-0.0001	56.140	56.1338	0.0062
69.951	69.9468	0.0042	69.125	69.1227	0.0023	69.145	69.1381	0.0069
70.939	70.8902	0.0488	76.370	76.3686	0.0014	76.380	76.3841	-0.0041
71.573	71.5403	0.0327	88.020	88.0185	0.0015			
			94.945	94.9423	0.0027			
	Av. Diff. =	0.0188		Av. Diff. =	0.0014		Av. Diff. =	0.0037
	$\sigma_{Diff.}$ =	0.0189		$\sigma_{Diff.}$ =	0.0009		$\sigma_{Diff.}$ =	0.0048

*Outliar

Table V.1. Continued.

MER154			MER140			MER165		
$2\theta_{vis}$	$2\theta_{prf}$	Diff.	$2\theta_{vis}$	$2\theta_{prf}$	Diff.	$2\theta_{vis}$	$2\theta_{prf}$	Diff.
21.363	21.3562	0.0068	21.365	21.3418	0.0232	21.364	21.3481	0.0159
28.443	28.4374	0.0056	28.451	28.4256	0.0254	28.444	28.4249	0.0191
30.384	30.3841	-0.0001	30.396	30.3692	0.0268	30.390	30.3747	0.0153
37.445	37.4419	0.0031	37.451	37.4297	0.0213	37.444	37.4337	0.0103
43.504	43.5056	-0.0016	43.512	43.4965	0.0155	43.509	43.5012	0.0078
47.297	47.2997	-0.0027	47.300	47.2889	0.0111	47.296	47.2889	0.0071
48.960	48.9557	0.0043	48.956	48.9456	0.0104	48.959	48.9507	0.0083
53.983	53.9848	-0.0018	53.982	53.9756	0.0064	53.982	53.9809	0.0011
56.119	56.1182	0.0008	56.113	56.1041	0.0089	56.109	56.1067	0.0023
63.212	63.2203	-0.0083	63.209	63.2023	0.0067	63.203	63.2054	-0.0024
67.545	67.5488	-0.0038	67.537	67.5291	0.0079	67.531	67.5319	-0.0009
71.736	71.7408	-0.0048	69.113	69.1059	0.0071	69.100	69.1061	-0.0061
75.841	75.8477	-0.0067	71.734	71.7240	0.0100	71.730	71.7276	0.0024
76.356	76.3684	-0.0124	75.820	75.8208	-0.0008	75.823	75.8249	-0.0019
83.841	83.8463	-0.0053	76.360	76.3514	0.0086	76.354	76.3494	0.0046
87.784	87.7900	-0.0060	79.850	79.8507	-0.0007	79.850	79.8467	0.0033
88.015	88.0197	-0.0047	83.825	83.8210	0.0040	83.828	83.8230	0.0050
94.935	94.9443	-0.0093	87.769	87.7683	0.0007	87.765	87.7675	-0.0025
			88.012	88.0024	0.0096	88.008	88.0006	0.0074
			94.926	94.9244	0.0016	94.921	94.9205	0.0005
	Av. Diff. =	-0.0026	95.643	95.6453	-0.0023	95.649	95.6481	0.0009
	$\sigma_{Diff.}$ =	0.00529	99.603	99.6110	-0.0080	99.609	99.6124	-0.0034
s002_hkl								
$2\theta_{vis}$	$2\theta_{prf}$	Diff.						
28.465	28.4589	0.0061		Av. Diff. =	0.0088		Av. Diff. =	0.0043
47.320	47.3126	0.0074		$\sigma_{Diff.}$ =	0.00916		$\sigma_{Diff.}$ =	0.00664
56.135	56.1288	0.0062						
69.130	69.1330	-0.0030						
76.380	76.3759	0.0041						
88.030	88.0288	0.0012						
94.950	94.9512	-0.0012						
106.705	106.7079	-0.0029						
114.090	114.0912	-0.0012						
127.545	127.5420	0.0030						
	Av. Diff. =	0.0020						
	$\sigma_{Diff.}$ =	0.00393						

Table V.1. Continued.

Diffractograms considered	Specimen Characteristics	Visual		FP fitting	
		$(\sigma_j)_{av}$ [a]	$(\sigma_j)_{sd}$ [a]	$(\sigma_j)_{av}$ [a]	$(\sigma_j)_{sd}$ [a]
149-150-151-152-153	same IKO-Ann smear, left goniometer, repeated measurements under various experimental configurations	0.0128	0.0058	0.0078	0.0049
135-137-139	smears of different size-fractions of IKO-Ann, right goniometer, same experimental configuration	0.0138	0.0066	0.0050	0.0060
136-138	smears of different size-fractions of IKO-Ann, left goniometer, same experimental configuration	0.0130	0.0084	0.0129	0.0047
145-148-154-6NOV[b]	various smears of SRMs, left goniometer, various experimental configurations	0.0048	0.0019	0.0052	0.0030
140-165	right goniometer, different smears of SRMs, different experimental configurations	0.0033	0.0020	0.0021	0.0013

[a] These values are expressed in °2θ and are computed excluding individual σ_j values greater than 0.03 °2θ.

[b] 6NOV refers to the series of diffractograms SRM640c_6NOV2001.

Table V.2. Comparison of $(\sigma_j)_{av}$ and $(\sigma_j)_{sd}$ values computed using individual $K\alpha_1$ line positions evaluated by the visual estimation and the FP line-profile fitting methods (Table V.1) for various sets of diffractograms of a given sample.

Appendix W. Summary of lattice parameter results

Sample	Diffractogram	*a* (Å)	*b* (Å)	*c* (Å)	β (°)	UC Vol.[1] (Å^3)	$N_{refl.}$[2]	N_{hkl}[3]
Co-Mg JLR								
$Co_{0.3}Mg_{2.7}$JLR	MER123	5.3163	9.2064	10.3019	99.926	496.67	33	55
$Co_{0.6}Mg_{2.4}$JLR	MER055	5.3146	9.2053	10.2994	99.921	496.34	36	60
"	MER167	5.3182	9.2106	10.3128	99.899	497.64	36	60
$Co_{0.9}Mg_{2.1}$JLR	MER124	5.3191	9.2115	10.3160	99.905	497.92	36	60
$Co_{1.2}Mg_{1.8}$JLR	MER079	5.3222	9.2160	10.3172	99.900	498.52	36	60
$Co_{1.5}Mg_{1.5}$JLR	MER125	5.3232	9.2177	10.3177	99.909	498.71	36	60
$Co_{1.8}Mg_{1.2}$JLR	MER078	5.3285	9.2271	10.3247	99.920	500.04	36	60
$Co_{2.1}Mg_{0.9}$JLR	MER126	5.3334	9.2373	10.3360	99.905	501.63	37	61
$Co_{2.4}Mg_{0.6}$JLR	MER059	5.3309	9.2341	10.3232	99.914	500.58	34	57
"	MER133	5.3333	9.2379	10.3250	99.911	501.11	34	55
$Co_{2.7}Mg_{0.3}$JLR	MER127	5.3370	9.2438	10.3392	99.907	502.47	36	60
$Co_{3.0}Mg_{0.0}$JLR	MER053	5.3358	9.2420	10.3288	99.913	501.74	36	60
"	MER132	5.3389	9.2469	10.3379	99.915	502.74	36	60
Mg-Ni JLR								
$Mg_{0.0}Ni_{3.0}$JLR-OH	MER131	5.2962	9.1741	10.2775	99.895	491.93	35	59
"	MER146	5.2976	9.1751	10.2721	99.899	491.85	28	44
"	MER147	5.2974	9.1761	10.2846	99.879	492.52	27	43
"	MER143	5.2989	9.1789	10.2829	99.885	492.72	33	55
$Mg_{0.0}Ni_{3.0}$JLR-OD	MER080	5.2977	9.1744	10.2876	99.887	492.58	35	59
$Mg_{0.3}Ni_{2.7}$JLR	MER130	5.2977	9.1769	10.2802	99.892	492.36	35	59
$Mg_{0.6}Ni_{2.4}$JLR	MER081	5.2987	9.1773	10.2913	99.891	493.00	35	59
$Mg_{0.9}Ni_{2.1}$JLR	MER129	5.2978	9.1764	10.2871	99.895	492.67	35	59
$Mg_{1.2}Ni_{1.8}$JLR	MER082	5.2994	9.1793	10.2911	99.881	493.18	35	59
$Mg_{1.5}Ni_{1.5}$JLR	MER089	5.2969	9.1765	10.2949	99.876	492.99	35	59
$Mg_{1.8}Ni_{1.2}$JLR	MER083	5.2991	9.1779	10.3002	99.885	493.51	35	59
$Mg_{2.1}Ni_{0.9}$JLR	MER087	5.2985	9.1756	10.2972	99.890	493.18	35	59
$Mg_{2.4}Ni_{0.6}$JLR	MER084-84a	5.3056	9.1908	10.2920	99.906	494.38	33	56
$Mg_{2.7}Ni_{0.3}$JLR	MER085	5.3108	9.1995	10.3006	99.901	495.76	33	54
$Mg_{3.0}Ni_{0.0}$JLR	MER128-1	5.3149	9.2052	10.3080	99.906	496.80	33	54
Fe-Mg JLR								
$Fe_{0.0}Mg_{3.0}$JLR	MER060	5.3091	9.1947	10.2902	99.919	494.81	42	70
"	MER067	5.3142	9.2047	10.2935	99.909	496.00	28	46
"	MER066	5.3130	9.2037	10.2938	99.910	495.85	32	53
$Fe_{0.6}Mg_{2.4}$JLR	MER061	5.3260	9.2231	10.2983	99.937	498.29	42	68
$Fe_{1.2}Mg_{1.8}$JLR	MER062	5.3432	9.2538	10.2939	99.974	501.29	39	65
"	MER166	5.3472	9.2615	10.3008	99.967	502.43	35	59
$Fe_{1.8}Mg_{1.2}$JLR	MER075	5.3672	9.2953	10.3064	99.991	506.39	36	59
$Fe_{2.4}Mg_{0.6}$JLR	MER076	5.3753	9.3101	10.2978	100.023	507.48	36	61
$Fe_{3.0}Mg_{0.0}$JLR	MER077	5.3993	9.3500	10.3248	100.049	513.24	35	59

[1] UC Vol.: unit cell volume.

[2] $N_{refl.}$: number of reflections used in the refinement.

[3] N_{hkl}: number of *hkl* values successfully assigned in the refinement.

Sample	Diffractogram	*a* (Å)	*b* (Å)	*c* (Å)	β (°)	UC Vol.[1] ($Å^3$)	$N_{refl.}$[2]	N_{hkl}[3]
Fe-Mg RGBn								
$Fe_{0.75}Mg_{2.25}RGB$	MER098	5.3360	9.2427	10.3021	99.944	500.46	36	59
$Fe_{1.5}Mg_{1.5}RGB$	MER100	5.3595	9.2831	10.3167	99.977	505.52	35	58
$Fe_{0.75}Mg_{2.25}RGB$	MER097	5.3737	9.3076	10.3138	100.005	508.01	36	59
$Fe_{3.0}Mg_{0.0}RGB$	BI25AC	5.4045	9.3594	10.3272	100.051	514.36	33	54
Fe-Mg RGBp								
$Fe_{25}Mg_{75}RGBp$	MER116	5.3379	9.2453	10.3127	99.939	501.30	36	59
$Fe_{50}Mg_{50}RGBp$	MER118	5.3604	9.2845	10.3161	99.976	505.66	35	58
$Fe_{75}Mg_{25}RGBp$	MER117	5.3834	9.3244	10.3220	100.010	510.25	36	59
$Fe_{100}RGBp$	MER101	5.4059	9.3630	10.3265	100.049	514.66	36	59
Fe-Mg RGBr								
$Fe_{25}Mg_{75}Bi33r$	MER096	5.3094	9.1967	10.2882	99.905	494.87	33	56
$Fe_{25}Mg_{75}Bi38r$	MER095	5.3223	9.2165	10.2746	99.943	496.43	34	57
$Fe_{75}Mg_{25}Bi32r$	MER094	5.3392	9.2465	10.2533	100.006	498.49	35	56
$Fe_{100}Bi35r$	MER102	5.3724	9.3069	10.2642	100.049	505.34	35	57
$Fe_{25}Mg_{75}Bi31r$	MER104	5.3095	9.1958	10.3003	99.897	495.43	36	59
$Fe_{75}Mg_{25}Bi30r$	MER103	5.3471	9.2580	10.2722	99.986	500.81	35	57
Fe-Ni GR								
$Fe_{0.0}Ni_{3.0}GR$	MER155	5.2968	9.1774	10.2957	99.871	493.07	34	54
"	NIAN30GR	5.2958	9.1716	10.2919	99.872	492.49	35	59
$Fe_{0.2}Ni_{2.8}GR$	MER156	5.3063	9.1912	10.2966	99.897	494.70	31	48
"	NIAN28GR	5.3036	9.1862	10.2916	99.890	493.95	35	59
$Fe_{0.6}Ni_{2.4}GR$	MER113	5.3197	9.2133	10.2911	99.927	496.84	38	62
"	NIAN24GR	5.3238	9.2198	10.3001	99.922	498.01	37	61
$Fe_{1.0}Ni_{2.0}GR$	MER159	5.3359	9.2419	10.3029	99.943	500.44	38	62
"	NIAN20GR	5.3327	9.2370	10.2937	99.949	499.42	37	61
$Fe_{1.4}Ni_{1.6}GR$	MER158	5.3471	9.2614	10.3021	99.966	502.48	36	59
"	NIAN16GR	5.3466	9.2606	10.3015	99.964	502.36	37	61
$Fe_{1.8}Ni_{1.2}GR$	MER162	5.3612	9.2850	10.3045	99.984	505.18	36	59
"	NIAN12GR	5.3577	9.2804	10.3010	99.981	504.43	36	59
$Fe_{2.2}Ni_{0.8}GR$	MER163	5.3745	9.3077	10.3065	100.011	507.72	36	59
"	NIAN08GR	5.3713	9.3026	10.2976	100.018	506.70	36	59
$Fe_{2.6}Ni_{0.4}GR$	MER164	5.3862	9.3291	10.3097	100.031	510.13	32	51
"	NIAN04GR	5.3825	9.3208	10.3007	100.033	508.875	36	59

[1] UC Vol.: unit cell volume.

[2] $N_{refl.}$: number of reflections used in the refinement.

[3] N_{hkl}: number of *hkl* values successfully assigned in the refinement.

Sample	Diffractogram	*a* (Å)	*b* (Å)	*c* (Å)	β (°)	UC Vol.[1] (Å^3)	$N_{refl.}$[2]	N_{hkl}[3]
Ann-F(OH)								
Ann-$F_{0.0}(OH)_{2.0}$	MER090	5.3869	9.3294	10.3418	99.992	511.86	32	53
Ann-$F_{0.4}(OH)_{1.6}$	MER091	5.3812	9.3197	10.2604	100.095	506.60	32	52
Ann-$F_{0.8}(OH)_{1.2}$	MER088	5.3660	9.2914	10.1989	100.133	500.56	31	48
Ann-$F_{1.0}(OH)_{1.0}$	MER092	5.3779	9.3142	10.1499	100.187	500.40	31	50
Ann-$F_{1.1}(OH)_{0.9}$	MER093	5.3775	9.3141	10.1495	100.174	500.36	33	54
Ann-$F_{1.2}(OH)_{0.8}$	MER086	5.3762	9.3097	10.1357	100.182	499.31	24	37
Ann-$F_{1.6}(OH)_{0.4}$	MER114	5.3765	9.3098	10.1303	100.192	499.06	34	56
Ann-oxy-ferrioxy								
EM250	MER107	5.3878	9.3327	10.3135	100.037	510.65	31	52
EM300	MER108	5.3797	9.3200	10.2973	100.040	508.39	30	50
EK350	MER110	5.3580	9.2788	10.2562	100.016	502.12	24	39
EM350	MER134	5.3612	9.2865	10.2634	100.048	503.14	23	35
EK370	MER115	5.3338	9.2411	10.1346	100.103	491.79	26	43
EM400	MER109	5.3125	9.1982	10.1396	100.042	487.89	29	49
EM450	MER105	5.3080	9.1963	10.1394	100.037	487.37	30	51
EM500	MER106	5.3076	9.1938	10.1298	100.062	486.70	31	52
EM550	MER111	5.3068	9.1909	10.1312	100.052	486.56	31	52
EM600	MER112	5.3065	9.1916	10.1237	100.059	486.20	31	52
IKO-Ann[4]	Left Gonio.							
L	MER136	5.3941	9.3419	10.3165	100.049	511.88	32	53
W	MER138	5.3944	9.3438	10.3244	100.038	512.43	32	53
W	MER149	5.3964	9.3453	10.3285	100.014	512.94	30	48
W	MER150	5.3964	9.3433	10.3269	100.056	512.69	30	46
W	MER151	5.3968	9.3450	10.3251	100.043	512.75	29	46
W	MER152	5.3953	9.3445	10.3203	100.048	512.33	27	44
W	MER153	5.3951	9.3448	10.3230	100.041	512.47	29	48
	Right Gonio.							
S	MER135	5.3930	9.3426	10.3215	100.039	512.08	32	53
W	MER137	5.3935	9.3428	10.3165	100.037	511.90	32	53
L	MER139	5.3927	9.3421	10.3174	100.042	511.82	32	53
Ann M.Sc.								
HK-550	[Mercier 1996]	5.3997	9.3538	10.3167	100.051	513.08	30	50
HK-596	"	5.3919	9.3411	10.2896	100.059	510.28	33	55
HK-650	"	5.3940	9.3428	10.3105	100.043	511.64	31	52
HK-700	"	5.3994	9.3547	10.3200	100.051	513.26	30	50
HK-750	"	5.3990	9.3537	10.3122	100.062	512.76	26	40
RB-7	"	5.4062	9.3626	10.3289	100.051	514.78	30	48
RB-22[5]	"	5.4054	9.3603	10.3442	100.060	515.33	30	52

[1] UC Vol.: unit cell volume.

[2] $N_{refl.}$: number of reflections used in the refinement.

[3] N_{hkl}: number of *hkl* values successfully assigned in the refinement.

[4] W = all size fractions; S = small size fraction, d < 1 μm; L = large size fraction, d > 1 μm (see [Rancourt *et al*. 2001]).

[5] Powder pattern meaured using a Gandolfi camera that used CoKα radiation (λ = 1.7902 Å assumed in the refinement).

Appendix X. C++ program used for synthetic error evaluation of lattice parameters

```
/* Program SyntheticErrorEvaluation.cpp */
#include <stdio.h>
#include <stdlib.h>
#include <io.h>
#include <math.h>
#include <iostream.h>
#include <dir.h>
#include <fstream.h>
#include <cstring.h>
#include <process.h>
#include <conio.h>


/* ran1 subroutine of Numerical Recipes */

#define IA 16807
#define IM 2147483647
#define AM (1.0/IM)
#define IQ 127773
#define IR 2836
#define NTAB 32
#define NDIV (1+(IM-1)/NTAB)
#define EPS 1.2e-7
#define RNMX (1.0-EPS)

float ran1(long *idum)
{
        int j;
 long k;
 static long iy=0;
 static long iv[NTAB];
 float temp;

 if (*idum <= 0 || !iy) {
        if (-(*idum) < 1) *idum=1;
  else *idum = -(*idum);
  for (j=NTAB+7;j>=0;j--) {
        k=(*idum)/IQ;
   *idum=IA*(*idum-k*IQ)-IR*k;
   if (*idum < 0) *idum += IM;
   if (j < NTAB) iv[j] = *idum;
  }
  iy=iv[0];
 }
 k=(*idum)/IQ;
 *idum=IA*(*idum-k*IQ)-IR*k;
 if (*idum < 0) *idum += IM;
 j=iy/NDIV;
 iy=iv[j];
 iv[j] = *idum;
 if ((temp=AM*iy) > RNMX) return RNMX;
 else return temp;
}

/* gasdev(long *idum) function of Numerical Recipes */
```

```
/* Returns a normally distributed deviate with zero mean and unit variance,
using ran1(idum) as the source of uniform deviates */

float gasdev(long *idum)

{
//          float ran1(long *idum);
 static int iset=0;
 static float gset;
 float fac,rsq,v1,v2;

 if (iset == 0) {
          do {
                    v1=2.0*ran1(idum)-1.0;
     v2=2.0*ran1(idum)-1.0;
     rsq=v1*v1+v2*v2;
   } while (rsq >= 1.0 || rsq == 0.0);
   fac=sqrt(-2.0*log(rsq)/rsq);
   gset=v1*fac;
   iset=1;
   return v2*fac;
 } else {
                    iset = 0;
    return gset;
 }
}
void spawnl_example(void)
{
  int result;

//  result = spawnl(P_WAIT, "c:\\users\\patrick\\programCPP\\celref.bat", NULL);
  result = spawnl(P_WAIT, "celref.bat", "celref.bat", NULL);
  if (result == -1)
  {
    perror("Error from spawnl");
    exit(1);
  }
}



main() {

          const int MAX = 100;
  char buf[100], buf2[100];

  const float uncertainty = .02;

  FILE* DataStats =fopen("datastats.fil", "w");
  FILE* OrgFileIn = fopen("ikoann.dat", "r");
  FILE* RunFileIn;// = fopen("runfile.dat", "w");
  FILE* RunFileOut;// = fopen("runfile.out", "r");

  int i;
  long idum;
  float angle;
```

```
idum = -1;
ran1(&idum);



for(i=1; i<1000;i++)
   ran1(&idum);

i=0;
while (i < MAX) {
 RunFileIn = fopen("runfile.dat", "w");
 fseek(OrgFileIn, 0, SEEK_SET);
 fgets(buf, sizeof(buf), OrgFileIn);
 fprintf(RunFileIn, "%s", buf);
 fgets(buf, sizeof(buf), OrgFileIn);
 fprintf(RunFileIn, "%s", buf);
 fgets(buf, sizeof(buf), OrgFileIn);
 fprintf(RunFileIn, "%s", buf);
 while (!feof(OrgFileIn)) {
        fgets(buf, 39, OrgFileIn);
  fprintf(RunFileIn, "%s", buf);
  if (strncmp(buf, "      ", 6) == 0) {
   fgets(buf, sizeof(buf), OrgFileIn);
   sscanf(buf, "%f", &angle);
   fprintf(RunFileIn, "%9.5f  1.00000\n", angle + gasdev(&idum)*uncertainty);
  }
 }
 fclose(RunFileIn);

 spawnl_example();

 RunFileOut = fopen("runfile.out", "r");
 while (!feof(RunFileOut)) {
        fgets(buf, sizeof(buf), RunFileOut);
  if(strncmp(buf, "    DIRECT CELL", 15)== 0)
        strcpy(buf2,buf);
 }
 fclose(RunFileOut);
 fprintf(DataStats, "%s\n", buf2);

        i += 1;
        }

fclose(DataStats);
fclose(OrgFileIn);

return 0;
}
```